CERN-Proceedings-2012-002

Proceedings
of the

13th INTERNATIONAL CONFERENCE ON NUCLEAR REACTION MECHANISMS

Varenna (Italy), Villa Monastero, 11-15 June 2012

Edited by Francesco Cerutti, Mark Chadwick,
Alfredo Ferrari, and Toshihiko Kawano,
with Simone Bottoni and Luna Pellegri

CERN
GENEVA
2012

CERN-Proceedings-2012-002
available at http://cdsweb.cern.ch/record/1495183
ISSN 2078-8835
ISBN 978-92-9083-382-6

IL NUCLEARE

3

La Fisica Nucleare ha portato a scoperte fondamentali ed è tuttora un campo di indagine alle frontiere della ricerca che permette in modo peculiare ed esclusivo lo studio della materia elementare in condizioni estreme.

Non meno importante è il suo utilizzo in ricerche e applicazioni tecnologiche di immediato interesse per la Società, tra cui oggi sono di particolare importanza la produzione controllata e sicura di energia e le applicazioni mediche per la diagnosi e la terapia di tumori.

Conclusioni analoghe si raggiungono se si considerano le ricerche sulla radioattività: accanto a studi di carattere fondamentale, le applicazioni di tipo medico ed industriale, per il controllo ambientale, la sicurezza, la datazione di reperti sono innumerevoli.

Questa collana si propone la pubblicazione di testi volti a descrivere questa variegata moltitudine di argomenti e a rappresentare una fonte di informazioni obiettive e documentate.

Proceedings of the 13th International Conference on Nuclear Reaction Mechanisms

Varenna (Italy), Villa Monastero,
11–15 June 2012

a cura di

Francesco Cerutti, Mark Chadwick,
Alfredo Ferrari, and Toshihiko Kawano,
with Simone Bottoni and Luna Pellegri

CERN–Proceedings–2012–002.

www.aracneeditrice.it
info@aracneeditrice.it

via Raffaele Garofalo, 133/A–B
00173 Roma
(06) 93781065

ISBN 978-88-548-5882-4

I edizione: marzo 2013

FOREWORD

The 13th edition of the Varenna Conference on Nuclear Reaction Mechanisms (NRM) is dedicated both to Professors Mitsuji Kawai and Arthur Kerman, whose lasting and major contributions to nuclear physics are briefly recalled in the following pages. It was an honor and a great pleasure to listen to their talks in the traditional Wednesday evening special session, as well as to benefit from their assiduous participation during the Conference week.

This featured, as is usual, 18 regular sessions, embracing the scope – well-established and coherently evolving – of the Varenna NRM meetings, which includes nuclear structure and reaction modelling, fission, nuclear data compilation and interpretation, detector performances, facilities programs, and applications such as nuclear astrophysics, hadrontherapy, and nuclear energy. The discussion of the various topics has been substantiated by more than 90 oral presentations, documented in the rich collection of papers this book comprises (and in the videos available on the Conference website), and animated by the stimulating interaction of young scientists and renowned experts, both long standing and recent members of the Varenna "family", according to the well-chosen expression by Ettore Gadioli, the father of this Conference series.

Encouraged by the broad and lively participation last June, with an attendance level that challenged the Villa Monastero's capacity, and by the valuable support of many colleagues and different institutions, we look forward with enthusiasm to future editions. See you in 2015!

Francesco Cerutti *Mark Chadwick* *Alfredo Ferrari* *Toshihiko Kawano*

DEDICATION

MITSUJI KAWAI graduated from University of Tokyo in 1953. He became a professor of Kyushu University in 1976, and had led the theoretical nuclear physics laboratory since then. Currently he is a professor emeritus at Kyushu University, and is still very active in the theoretical nuclear physics field on both research and education.

Prof. Kawai's first paper appeared in 1954, concerning *High energy nucleon scattering by nuclei*. Since then he has published several hundred papers and co-authored several text books including the famous *Nuclear Matter and Nuclear Reaction* (North-Holland, 1968), often referred to as the Kikuchi-Kawai book. His book *Nuclear Reaction Theory* (Asakura Shoten, in Japanese), co-authored with Prof. Yoshida of Tohoku University, is one of the most comprehensive textbooks on the nuclear reaction theories in the world nowadays. He also has served on important committees including Science Council of Japan, Center for Nuclear Study (University of Tokyo), Yukawa Institute for Theoretical Physics (Kyoto University), Research Center for Nuclear Physics (Osaka University), and so forth.

His involvement is extended over a wide range of nuclear reaction theories. For example, he first wrote the scattering matrix as a sum of the direct reaction and the compound reaction parts, which became a standard formula of the statistical nuclear reaction theory. This formula has a very important feature, because the second term (the fluctuation part) disappears by energy-average. His very famous paper Kawai-Kerman-McVoy, often called KKM, *Modification of Hauser-Feshbach calculations by direct-reaction channel coupling* published in 1973, has been cited more than 100 times and has provided an important basis for theories on statistical compound nuclear reactions.

In 1980 Feshbach-Kerman-Koonin (FKK) first published a paper on the statistical multistep compound (MSC) and direct (MSD) reaction theories to deal with the preequilibrium process in the quantum mechanical framework. Despite many publications of FKK calculations since 1980, Prof. Kawai first pointed out a problem in the approximation made by FKK in the MSD theory. This gave rise to a lot of discussions on the validity of the FKK theory, and finally it was concluded in 1998 that the approximation cannot be justified. A paper on the Semi-Classical Distorted Wave model (SCDW) published in 1990 by Luo and Kawai is one of the MSD theories, which calculates the nucleon inelastic scattering process that leaves the residual nucleus in its continuum state. The model was extended to the two-step reaction in 1992, and it has been successfully applied to the pre-equilibrium process as an adjustable-parameter-free MSD theory.

Prof. Kawai made significant contributions to the direct nuclear reaction theories. In 1965, his computer code DWBA2 that calculates the reaction process based on the distorted wave Born approximation (DWBA) was made available to many experimentalists to analyze their experimental data. His contributions also include the second-order DWBA calculations, Coupled (Reaction) Rearrangement Channels (CRC) and Continuum Discretized Coupled Channels (CDCC) methods. Although the stripping and pick up reactions, in which rearrangement is involved, are often analyzed by a perturbation theory based on a simple DWBA, he developed the CRC method to solve these reaction processes rigorously, and proposed a method to calculate microscopically the form-factor for one-nucleon transfer. In addition, the theory was further extended to include a two-step process where the rearrangement is involved. His research includes not only derivation of the fundamental equations but also development of numerical methods to solve the coupled equations.

The CDCC method allowed to calculate complicated direct reaction mechanisms, e.g. the projectile break-up in deuteron induced reactions. Since 1986, when a series of papers on CDCC were published, CDCC has become very popular because of the increasing interest in the reactions where loosely bound nuclei are involved, such as halo nuclei or rare isotopes. Even for

nucleon or heavy-ion induced reactions on a light element, CDCC can be applied as long as the reaction system can be reduced to a three-body problem. The paper entitled *Continuum-Discretized Coupled-Channels calculations for 3-Body models of deuteron-nucleus reactions* published in 1987 has been cited more than 200 times. Nowadays CDCC is one of the most powerful tools to understand nuclei off-stability, related to key issues in nuclear astrophysics.

Professor MITSUJI KAWAI

Professor **ARTHUR KERMAN** is one of the most renowned scientists in nuclear physics, with seminal contributions in numerous areas, and with long connections to the Varenna conference research focus areas. His impact includes basic science advances; nuclear science impacting applications; teaching; and advisory roles for the US government.

Arthur is a native of Montreal, and moved to the US as a professor at MIT. He was Director of the Center for Theoretical Physics from 1976-1983 and of the Laboratory for Nuclear Science from 1983-1992. He has longstanding advisory roles at the US National Laboratories, especially Los Alamos, Livermore, and Oak Ridge, and at the Department of Energy. In these positions he has been a tireless advocate for experimental and theoretical nuclear physics, for high-performance computing, and for the importance of bringing high-quality science to bear on problems of national importance.

Arthur's work in multistep reaction physics, beginning with a quantum formulation of the importance of doorway states and intermediate structure, culminated in his FKK theory with Feshbach and Koonin. Since its publication, this theory has transformed the preequilibrium reaction community's efforts. His other research advances are too numerous to list in full, but include Feshbach resonances and Bose-Einstein condensates, quark physics, Hartree-Fock methods in fission, time-dependent variational principle methods, and so on. He is a Fellow of the APS, the American Academy of Arts and Sciences, and the New York Academy of Sciences.

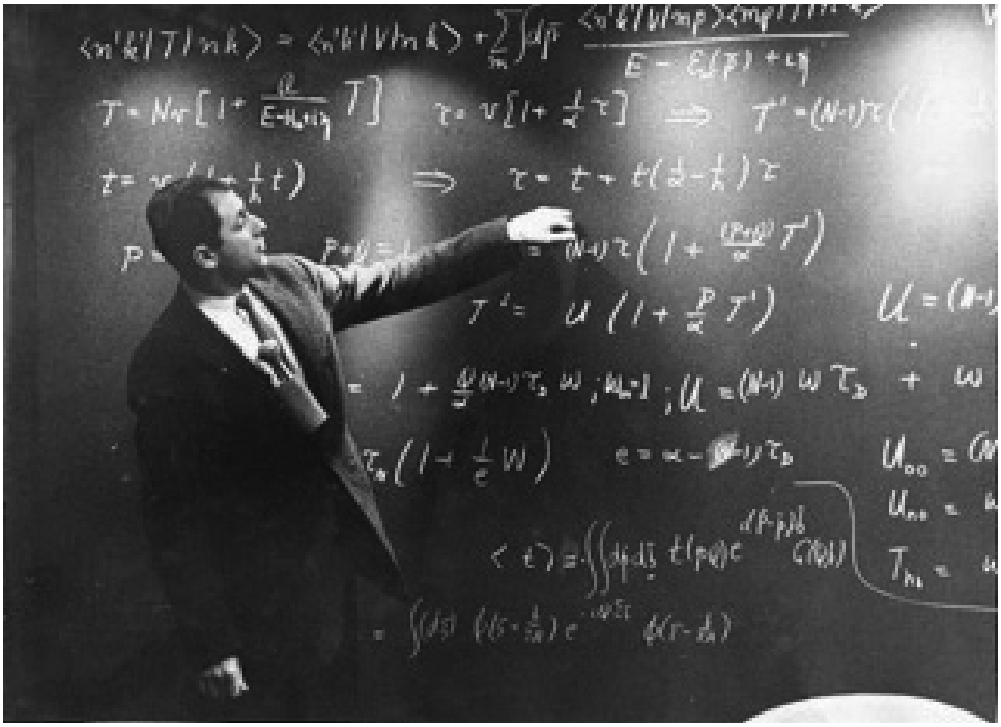

Professor ARTHUR KERMAN

CHAIRMEN OF THE CONFERENCE

M.B. Chadwick	Los Alamos	**A. Ferrari**	CERN

SCIENTIFIC SECRETARIES

F. Cerutti	CERN	**T. Kawano**	Los Alamos

ORGANIZING COMMITTEE

G. Battistoni	Milano	**F. Camera**	Milano
F. Cerutti	CERN	**M.B. Chadwick**	Los Alamos
A. Ferrari	CERN	**A. Guglielmetti**	Milano
T. Kawano	Los Alamos	**A. Mairani**	Pavia
P. Sala	Milano	**E. Tomasi Gustafson**	Saclay

INTERNATIONAL ADVISORY COMMITTEE

K. Amos	Melbourne	**F. Ballarini**	Pavia
E. Bauge	Bruyères-le-Châtel	**A. Bonaccorso**	Pisa
T. Borello Lewin	São Paulo	**B.A. Brown**	MSU East Lansing
R. Capote	IAEA	**S.H. Connell**	Johannesburg
L. Corradi	Legnaro	**A.A. Cowley**	iThemba LABS
V. Demetriou	Demokritos	**F.S. Dietrich**	Livermore
J. Escher	Livermore	**E. Gadioli**	Milano
S. Goriely	Bruxelles	**M. Herman**	BNL
H. Horiuchi	Osaka	**A. Kerman**	MIT
A. Koning	Petten	**A. Kreiner**	Buenos Aires
S. Leray	Saclay	**A. Mengoni**	Tokyo
T. Motobayashi	RIKEN	**K. Parodi**	Heidelberg
R.J. Peterson	Boulder	**L. Pinsky**	Houston
A. Plompen	Geel	**L. Sajo Bohus**	Caracas
L. Sihver	Göteborg	**K. Tanaka**	KEK
H. Toki	Osaka		

SECRETARY'S OFFICE

T. T. Böhlen	CERN	**S. Bottoni**	Milano
A. Mairani	Pavia	**L. Pellegri**	Milano
D. Pifferetti	Milano	**I. Rinaldi**	Heidelberg

ACKNOWLEDGMENTS

The Conference was supported by

- Los Alamos National Laboratory, USA
- CERN, European Organization for Nuclear Research, Switzerland
- DSM, IRFU, CEA, Saclay, France
- Department of Physics, University of Milano, Italy
- National Institute of Nuclear Physics (INFN), Italy
- "Piero Caldirola" International Centre for the Promotion of Science, Italy

The chairmen and the members of the Organizing Committee of the Conference wish to express their deepest appreciation and thanks to all these Institutions.

CONFERENCE PROGRAM

Monday, June 11

9:00 – 11:00 Chairman: ***M.B. Chadwick***

H.A. Weidenmuller	Some open problems in the statistical theory of nuclear reactions (30')
M. Herman	Nuclear reaction modeling in nuclear data evaluation (30')
M. Yahiro	Microscopic approach to the scattering of unstable nuclei at intermediate incident energies (30')
M. Jandel	Nuclear data for neutron induced reactions on U-235 measured at DANCE (30')

11:30 – 13:00 Chairman: ***T. Kawano***

H. Horiuchi	Cluster gas states in light nuclei (30')
P. Navratil	Ab initio calculations of light ion reactions (20')
K. Minomo	Eikonal reaction theory for neutron removal reactions (20')
L.W. Townsend	Derivation of eikonal corrections to the phase shift operator in the analytical abrasion ablation model (20')

15:00 – 17:10 Chairman: ***L. Canton***

F.S. Dietrich	Importance of final state fluctuations in radiative capture reactions and applications to surrogate reaction measurements (30')
A. Palffy	Level density for large number of particle hole states (20')
T. Furumoto	What is imaginary part of coupling potential in coupled channel calculation? (20')
N. Pietralla	Emerging simplicity: Evidence for the formation of collectivity from hadronic and EM probes (20')
G. Royer	Rotating quasi molecular states in light nuclear systems (20')
P. Fraser	Investigation of nuclei far from stability by the use of mirror systems (20')

17:35 – 19:15 Chairman: ***N. Pietralla***

K. Ogata	Breakup of ^{22}C studied by CDCC with Cluster Orbital Shell Model wave functions (20')
T. Matsumoto	CDCC analysis for breakup of three body projectiles (20')
S. Watanabe	Comparison of breakup processes of ^{6}He and ^{6}Li with four body CDCC (20')
T. Borello Lewin	Resonances near the 4α threshold through the ^{12}C(^{6}Li,d) reaction (20')
K.C.C. Pires	Study of the ^{6}He,^{7}Be+^{9}Be reactions at low energy (20')

Tuesday, June 12

9:00 – 11:00 Chairman: ***L. Pinsky***

A. Mairani	FLUKA Monte Carlo calculations for hadrontherapy application (20')
I. Rinaldi	Imaging techniques in ion beam therapy: status and perspective (20')
R. Peloso	Application of the HICAM camera for imaging of prompt gamma rays in measurements of proton beam range (20')
M. Bruzzi	A monolithic silicon detector for pre treatments verification in intensity modulated radiotherapy (20')
L. Sajo Bohus	An alternative source for Venezuelan nuclear energy production: The Thorium Molten Salt Reactor (20')
Anna Ferrari	Neutronics analysis around the spallation target for the MYRRHA ADS design (20')

11:30 – 13:00 Chairman: ***B.A. Brown***

F.M. Nunes	Status of reaction theory for (d,p) reactions and exotic nuclei (30')
A.N. Antonov	Analysis of elastic scattering of ^{6,8}He and ^{11}Li on protons and ^{6}He on ^{12}C using microscopic optical potential (20')
P. Danielewicz	Symmetry energy from isobaric analog states (20')
J.A. Tostevin	Probes of nucleon single particle configurations and correlations (20')

15:00 – 16:40 Chairman: ***M. Herman***

A. Bacquias	Study of (n,xnγ) reactions on ^{235,238}U (20')
J. Duan	Further analysis about predicted levels of ^{9}Be based on the neutron double differential cross sections at E_p=18 MeV (20')
A. Blanc	Neutron inelastic scattering cross section measurements on ^{175}Lu (20')
S.P. Simakov	48Ti(n,n'γ)γ production reaction as a candidate for a reference cross section (20')
T. Marchi	^{8}B production measurement at LNL (20')

17:15 – 18:35 Chairman: ***G. Casini***

E. Rapisarda	The observation of a strong E0 component in the 2+2 - 2+1 transition in ^{184}Hg from the β decay of laser ionized thallium isotopes: a strong signature for shape coexistence (20')
J.J. van Zyl	Angular distributions of the analysing power in the excitation of low lying states of ^{56}Co (20')
G. Baiocco	Towards a reconstruction of thermal properties of light nuclei from fusion evaporation reactions (20')
B. Carlson	The compound nucleus: sequential evaporation vs. statistical multifragmentation (20')

WINE PARTY

from 20:15 at Villa Cipressi Chairman: ***W.A. Richter***

Wednesday, June 13

9:00 – 11:10 Chairman: ***F.M. Nunes***

E. Fioretto	Recent results with the magnetic spectrometer PRISMA (30')
T.T. Böhlen	Fragmentation measurement of 400MeV/u ^{12}C ions on C and Au targets with the FIRST experiment (20')
J. Dudouet	95MeV/u ^{12}C nuclear fragmentation measurements on thin targets for hadrontherapy (20')
E. De Lucia	Measurement of charged and neutral particles production from an 80 MeV/A hadron therapy carbon beam fragmentation (20')
R.J. Peterson	Scaling of hadronic continuum spectra from carbon (20')
K. Tanaka	J-PARC status after the earthquake on 2011 March 11 (20')

*11:35 – 13:05 Chairman: A****lfredo Ferrari***

A. Plompen	Neutron inelastic scattering, recent experiments and their interpretation (30')
E. Chiaveri	Outlook and perspective for the n_TOF Experiment at CERN (30')
G. Casini	The Fazia initiative: more powerful detectors for a more detailed investigation on the origin and the decay of charged fragments (30')

EVENING SESSION

in honor of Profs. KERMAN and KAWAI

21:00 – 23:00 Chairman: ***E. Gadioli***

K. Schoenberg	LANSCE present and future: A tribute to the contributions of Arthur Kerman (15')
M.N. Kreisler	Three decades of interacting with Arthur Kerman (15')
A. Kerman	(30')
T. Kawano	Scary equations (30')
M. Kawai	(30')

Thursday, June 14

9:00 – 11:00 Chairman: ***E. Chiaveri***

P. Sala	FLUKA: Recent developments (20')
A. Boudard	Extension of the Liege intra nuclear cascade model to light ion induced collisions for medical and space applications (20')
L. Sihver	PHITS - Applications to radiation biology and radiotherapy (20')
A.M. Adamczyk	Electromagnetic dissociation cross sections for double nucleon removal using Weisskopf Ewing theory (20')
L. Heilbronn	Modeling accelerator based secondary neutron production measurements (20')
Z. Basrak	Scaling of energy deposit in central heavy ion reactions at intermediate energies (20')

11:30 – 13:00 Chairman: ***R.J. Peterson***

B.A. Brown	Structure aspects of direct and sequential two nucleon transfer reactions (30')
G. Potel	Study of pairing correlations in nuclei with two nucleon transfer reactions (20')
A. Volya	Pairing forces in nuclei (20')
M. Bondì	Selectivity of the two neutron transfer reaction (^{18}O,^{16}O) (20')

15:00 – 17:00 Chairman: ***F. Camera***

E. Farnea	Recent results using the AGATA Demonstrator at LNL (20')
T. Kröll	Spectroscopy of neutron rich nuclei at REX ISOLDE with MINIBALL (20')
L. Pellegri	Measurement of high energy gamma rays with large volume $LaBr_3$(Ce) scintillators (20')
F. Quarati	Scintillators with high energy resolution and low intrinsic activity (20')
S. Bottoni	Reaction dynamics and gamma spectroscopy of Ne isotopes by the heavy ion reaction ^{22}Ne + ^{208}Pb (20')
S. Barlini	Effects of energetic heavy ion irradiation on digital PSA performed with silicon detectors (20')

17:30 – 19:20 Chairman: ***H. Horiuchi***

H. Lenske	Strangeness production on nuclei (30')
B. Ramstein	One and two pion production in pp and np reactions with HADES (20')
G. Boca	The PANDA experiment (20')
A. Sanchez Lorente	Production of double lambda hypernuclei at the PANDA experiment (20')
D. Watts	Meson photoproduction from the nucleon at CLAS (20')

Friday, June 15

9:00 – 11:00 Chairman: H. Lenske

M.B. Chadwick	Overview of fission research for precise criticality modelling (20')
D. Tarrio	Measurement of the fission fragment angular distribution for Th-232(n,f) at the CERN n_TOF facility (20')
P. Talou	Monte Carlo Hauser Feshbach calculations of prompt fission neutrons and gamma rays (20')
A. Al Adili	Angular dependent TKE and mass distributions in ^{234}U(n,f) (20')
Y. Ayyad	Transient effects in proton induced fission of ^{208}Pb (20')
O. Delaune	Evolution of fission fragment isotopic yields with excitation energy (20')

11:30 – 13:00 Chairman: ***P.M. Milazzo***

D.P. McNabb	Plasma Nuclear Science (30')
E. Betak	Construction of deformed neutron stars steming from DBHF (20')
Y. Iwata	The synthesis of neutron rich heavy elements due to quasi fission events (20')
W.A. Richter	Review of nuclear structure calculations in the sd shell for the rp process (20')

15:00 – 17:00 Chairman: ***D.P. McNabb***

P.M. Milazzo	Nuclear astrophysics at n_TOF, CERN (20')
S.M. Grimes	Hauser Feshbach Calculations for Deformed Nuclei (20')
M. Dupuis	Microscopic models for direct inelastic scattering and pre equilibrium emission: spherical and axially deformed targets (20')
G. Blanchon	Nucleon elastic scattering off doubly closed shell nuclei within HF+RPA with Gogny force (20')
M.P.W. Chin	Processing of incident neutron sub library from ENDF/B VII.1, JENDL 4.0 and JEFF 3.1.1 (20')
A. Hurst	Improved capture gamma ray libraries for nuclear applications (20')

17.30 – 18.30 Chairman: ***P. Sala***

T. Fukui	Determination of ^{8}B(p,γ)^{9}C reaction rate from ^{9}C breakup (20')
M. Avrigeanu	Consistent analysis of all inclusive deuteron induced reactions at low energies (20')
M.V. Garzelli	Micro black hole formation and evaporation in ultra high energy cosmic ray interactions with the Earth's atmosphere (20')

TABLE OF CONTENTS

LIST OF PARTICIPANTS

Anne Marie Adamczyk	University of Tennessee, Knoxville, TN, USA
Ali Al-Adili	Uppsala University, Uppsala, Sweden
Anton N. Antonov	Bulgarian Academy of Sciences, Sofia, Bulgaria
Marilena Avrigeanu	Horia Hulubei National Institute for Physics and Nuclear Engineering, Bucharest-Magurele, Romania
Yassid Ayyad	University of Santiago de Compostela, Spain
Antoine Bacquias	Université de Strasbourg, Strasbourg, France
Giorgio Baiocco	University and INFN of Bologna, Italy and CNRS, ENSICAEN, Caen , France
Sandro Barlini	University and INFN of Firenze, Italy
Zoran Basrak	Ruđer Bošković Institute, Zagreb, Croatia
Eric Bauge	CEA, DAM, DIF Arpajon, France
Emil Betak	Institute of Physics, Bratislava, Slovakia
Aurélien Blanc	CEA, DAM, DIF Arpajon, France
Guillaume Blanchon	CEA, DAM, DIF Arpajon, France
Gianluigi Boca	GSI, Darmstadt, Germany
Karoly Bodor	Hungarian Academy of Sciences KFKI Atomic Energy Research Institute, Budapest, Hungary
Till T. Böhlen	CERN, Geneva, Switzerland
Mariangela Bondì	University of Catania, Italy
Thereza Borello Lewin	Universidade de São Paulo, São Paulo, Brazil
Simone Bottoni	University and INFN of Milano, Italy
Alain Boudard	CEA Saclay, FRANCE
B. Alex Brown	Michigan State University, Michigan, USA
Mara Bruzzi	University and INFN of Firenze, Italy
Franco Camera	University and INFN of Milano, Italy
Luciano Canton	INFN of Padova, Italy
Francesco Cappuzzello	University of Catania e INFN-Laboratori Nazionali del Sud, Italy
Stefano Carboni	University and INFN of Firenze, Italy
Brett V. Carlson	Instituto Tecnológico de Aeronáutica, São José dos Campos, Brazil
Giovanni Casini	University and INFN of Firenze, Italy
Francesco Cerutti	CERN, Geneva, Switzerland
Mark B. Chadwick	Los Alamos National Laboratory, Los Alamos,USA
Enrico Chiaveri	CEA Saclay, FRANCE and CERN, Geneva, Switzerland
Mary P.W. Chin	CERN, Geneva, Switzerland
Jean Colin	LPC Caen, France
Pawel Danielewicz	Michigan State University, Michigan, USA
Erika De Lucia	University anf INFN of Roma, Italy

Olivier Delaune	GANIL, CEA/DSM-CNRS/IN2P3,Caen, France
Frank S. Dietrich	Lawrence Livermore National Laboratory, Livermore, USA
Junfeng Duan	Uppsala University, Uppsala, Sweden
Jérémie Dudouet	LPC Caen, France
Marc Dupuis	CEA, DAM, DIF Arpajon, France
Enrico Farnea	INFN of Padova, Italy
Alfredo Ferrari	CERN, Geneva, Switzerland
Enrico Fioretto	INFN and LNL, Legnaro (PD), Italy
Paul R. Fraser	INFN of Padova, Italy
Tokuro Fukui	Osaka University, Japan
Takenori Furumoto	RIKEN Nishina Center, Japan
Maria Vittoria Garzelli	University of Nova Gorica, Slovenia
Steve M. Grimes	Ohio University, USA
Lawrence Heilbronn	University of Tennessee, USA
Michal W. Herman	Brookhaven National Laboratory, NY, USA
Hisashi Horiuchi	Osaka University, Japan
Aaron Hurst	Lawrence Berkeley National Laboratory, CA,USA
Yoritaka Iwata	GSI, Darmstadt, Germany
Marian Jandel	Los Alamos National Laboratory, Los Alamos,USA
Mitsuji Kawai	Kyushu University, Fukuoka, Japan
Toshihiko Kawano	Los Alamos National Laboratory, Los Alamos,USA
Arthur Kerman	Michigan State University, Michigan, USA
Michael N. Kreisler	Department of Energy, Washington, DC, USA
Thorsten Kröll	Institut für Kernphysik, Darmstadt, Germany
Horst Lenske	Institut für Theoretische Physik, Giessen, Germany
Andrea Mairani	CNAO, Pavia, Italy
Yury Malyshkin	Goethe-Universität Frankfurt, Germany
Tommaso Marchi	University of Padova and LNL, Padova, Italy
Takuma Matsumoto	Kyushu University, Fukuoka, Japan
Dennis P. McNabb	Lawrence Livermore National Laboratory, Livermore, USA
Paolo Milazzo	INFN of Trieste, Italy
Kosho Minomo	Kyushu University, Fukuoka, Japan
Petr Navratil	TRIUMF, Vancouver, Canada
Filomena M. Nunes	Michigan State University, Michigan, USA
Kazuyuki Ogata	Osaka University, Japan
Adriana Palffy	Max-Planck-Institut für Kernphysik, Heidelberg, Germany
Luna Pellegri	University and INFN of Milano, Italy
Roberta Peloso	Politecnico and INFN of Milano, Italy
R. Jerry Peterson	University of Colorado,USA
Norbert Pietralla	Institut für Kernphysik, Darmstadt, Germany
Kelly C.C. Pires	Universidade de São Paulo, São Paulo, Brazil
Arjan Plompen	EC-JRC-IRMM, Geel, Belgium
Grégory Potel	Universidad de Sevilla, Spain
Francesco Quarati	Delft University of Technology, The Netherlands

Beatrice Ramstein	Institut de Physique Nucléaire, CNRS/IN2P3, Orsay, France
Elisa Rapisarda	University of Leauven, Belgium
Werner A. Richter	iThemba Labs, Somerset West, South Africa
Ilaria Rinaldi	Heidelberg Ion Beam Theraphy Center, Germany
Guy Royer	Laboratoire Subatech, Nantes, France
Laszlo Sajo Bohus	Universidad Simón Bolívar, Caracas, Venezuela
Paola Sala	INFN of Milano, Italy
Alicia Sanchez Lorente	Helmholtz Institut Mainz, Germany
Lembit Sihver	Chalmers University of Technology, Sweden
Stanislav P. Simakov	IAEA, Vienna, Austria
Patrick Talou	Los Alamos National Laboratory, Los Alamos,USA
Kazuhiro Tanaka	KEK, Japan
Diego Tarrío	University of Santiago de Compostela, Spain
Jeffrey A. Tostevin	Michigan State University, Michigan, USA
Lawrence W. Townsend	University of Tennessee, USA
J.J. van Zyl	Stellenbosch University, Matieland, South Africa
Alexander Volya	Florida State University, Tallahassee, FL, USA
Shin Watanabe	Kyushu University, Fukuoka, Japan
Dan Watts	SUPA, University of Edinburgh, UK
Hans A. Weidenmuller	Max-Planck-Institut für Kernphysik, Heidelberg, Germany
Masanobu Yahiro	Kyushu University, Fukuoka, Japan

Three Decades of Interacting with Arthur Kerman

Michael N. Kreisler
SAIC Contractor to the National Nuclear Security Administration U.S. Department of Energy
Washington, DC

Professor Emeritus
Department of Physics
University of Massachusetts Amherst
Amherst, MA

Abstract

For many years, Arthur Kerman has been a leading force in pushing for new initiatives in science. In this paper, we present a short review of our mutual interactions on many of these efforts.

1 Introduction

Let me begin by introducing myself. For those of you who do not know me, I have spent the past 40 years holding various positions, including being a Professor in the Department of Physics at the University of Massachusetts Amherst, a consultant at both Lawrence Livermore National Laboratory and Los Alamos National Laboratory, the Division Leader at Livermore for Nuclear Physics, Elementary Particle Physics and Accelerator Physics, a Science Advisor to the National Nuclear Security Administration in Washington, DC and a consulting employee of SAIC while continuing to serve as an Advisor to the NNSA. In all of these roles, I have been lucky enough to interact often with Professor Arthur Kerman, one of our guests of honor at this conference. In the short time available, I'd like to reminisce a bit on some of those interactions. For those of you who would like a short story even shorter, it might suffice to say that whenever you work on an exciting new science project, Arthur is sure to tell you that he was involved in the very early stages of that project. While it sometimes seems impossible for him to have actually done as much as he says, I know from experience that it really is true. So let's begin.

The hero of our story can be seen in Figure 1, a picture that was used with a short biography at the start of one of the many advisory committees on which Arthur has sat. To give you a flavor of the breadth of his activities in the advisory capacity, I list a few of the committees in Figure 2. As you can see, in addition to his responsibilities at M.I.T., Arthur has served on the National Academy of Sciences Committee on Inertial Confinement Fusion, on the NIF Programs Review Committee at Livermore, on the Directorate and Division Review Committees at Livermore; the RHIC Policy Committee at Brookhaven, the SLAC Scientific Policy Committee; the Secretary of Energy Fusion Policy Advisory Committee; the White House Science Council Panel on Science and Technology in the Government and many, many other important and influential bodies. Clearly the scientific community and those in positions of setting policy relevant to science highly value Arthur's contributions. There is the opinion in some circles that if you want to find Arthur, just set up an important advisory committee and he will be there at the first meeting.

2 Directorate Review Committee

My first memory of interacting with Arthur concerns one of those advisory committees: Specifically, I was asked to serve on the Director's Review Committee (DRC) for the Physics Directorate at Lawrence Livermore National Laboratory. At the time, these committees were relatively new (Arthur had strongly advocated for their formation) and were asked for their advice not only on the work that was on-going but also for their suggestions on future directions. As such they often wielded a lot of power. The meeting of the DRC was a three-day affair covering the many science areas of the Directorate. As the "new boy" on the Committee, I took careful notes on both the presentations and the lively discussions that followed each talk. I was quite impressed not only with the breadth of the science being presented -- nuclear physics, atomic physics and materials science – to name just a few – but also with the active questioning across such a wide array of topics from my colleagues on the Committee—from Arthur in particular. Arthur had a question or two for most speakers. I noticed that he never seemed to take notes even though the DRC had to produce a written summary of their observations and findings to present to the Director and the Associate Director sometime after the meeting.

After the meeting, Arthur, the chair of the DRC, asked me to write up my notes in the form of a report. I felt honored to be asked to do so and worked for quite some time to prepare my input to the report for him. Once my report was done, it is my understanding that Arthur labeled that write-up as the DRC report and went alone to see both of the senior LLNL administrators to report personally on the recommendations of the DRC. I learned an important lesson from that experience – The important aspects of a review are not what is written –rather senior administrators are much more likely to pay attention to a one-on-one report and critique of their programs. The written report becomes archival quickly while the oral comments often lead to change when change is needed.

3 The Superconducting Super Collider (SSC)

Many years ago, when the U.S, was beginning to formulate plans to build the next generation of high energy particle accelerators, there was a call for proposals for the site of this major scientific prize. To many of us in academia, Massachusetts seemed to be the perfect place to house the SSC: (1) Massachusetts is home to a very large number of Universities active in High Energy Physics – with many of the scientific leaders of the field resident there. (2) A large military base was being decommissioned providing more than ample space for the accelerator complex. Such a space avoided any complications regarding ownership of the land and interactions with home- or business-owners. And (3) the governor of a neighboring state suggested using a newly constructed nuclear power plant in his state as a source of electrical power for the SSC.

All of the stars seemed to be aligned. Arthur took the lead role in gathering together leaders in HEP from the Massachusetts academic community. There were about 7 private universities (including Harvard, MIT, Boston College, Boston University, Brandeis, Tufts, etc.) and one public University (University of Massachusetts Amherst). We met many times at MIT to plan our proposal – our group included Roy Schwitters of Harvard who eventually became the Director of the ill-fated SSC project. During a few hectic months, we became experts in geology - was the land suitable for tunneling - and a variety of other engineering aspects. We submitted a beautiful proposal that would have won—in my opinion—except for one minor problem. A project of this size – several billion US dollars – had to have the support of the Governor of the home state. Unfortunately, Governor Mike Dukakis decided this project wasn't high on his list of priorities and chose not to support it. (For those of you who remember, Dukakis was not known for his political acumen as evidenced by his overwhelming loss in presidential politics.)

4 The French Program

At the NNSA, I manage an international agreement between the CEA/DAM in France and the NNSA/DP in the United States entitled " Cooperation in Fundamental Science Supporting Stockpile Stewardship". Under this agreement, scientists at Livermore, Los Alamos and Sandia National Laboratories in the US are encouraged to collaborate with their counterparts at CEA (Bruyeres-le-Chatel) on unclassified basic science projects, leading to publications in the open literature. This effort began in 1998 when Daniel Gogny was assigned to spend time at Livermore investigating possible collaborations. Various meetings then occurred between scientific leaders of both sides over the next few years, with a formal agreement document signed in 2002.

Arthur was present at all of the formative meetings, strongly urging that the agreement go forward. To be sure, there was always a very strong nuclear physics component in the interactions between the two countries – collaborations that preceded the international agreement. Under the agreement, there continue to be fruitful collaborations in nuclear physics.

In addition to his pushing for this agreement, Arthur has always attended the General Meetings at which each of the active projects reports on the progress of their collaborative research. Held every two years, these meetings alternate to sites in the two countries. In Figure 3, we have a picture that was taken at the official banquet held at the Chateau D'Artigny near Tours in France. Obviously it was a great scientific meeting and the banquet was extremely well received. See Figure 4 for another picture from that affair.

5 N Division Advisory Committee

I served as the leader of the Livermore division that was concerned with Nuclear Physics, Elementary Particle Physics and Accelerator Physics. Some of the major projects during the time I was leader included: Building the SLAC-LBNL-LLNL B Factory; Accelerator Production of Tritium; Accelerator Transmutation of Waste; PEREGRINE – a program to improve the treatment of cancer; the Rare Isotope Accelerator; proton radiography; improved nuclear data; measurements of important nuclear cross sections such as Pu(n,2n); and a host of other efforts.

During the 8 or 9 years that I served as leader, Arthur was always there to provide advice. For example, he was a charter member of the N Division Advisory Committee that met annually to review all our programs. A picture from one of those meetings is shown in Figure 5. (Arthur was never shy about offering his advice and served on every committee that met during my tenure there.)

6 "Arthur-isms"

Having had the pleasure of working with him for many years, I have also had the chance to observe him up close and personal. You might find some of these observations interesting.

1. Despite the ubiquity of laptops, IPAD's and Smart Phones, Arthur does not use the computer. He gets emails but only when he has someone print the message for him. Perhaps not being tied to the Internet allows him to get so much done.

2. He seems semi-indestructible. He and I took an overnight "red-eye" flight from California to Boston for an all-day presentation to the MIT Nuclear Engineering Department regarding either the Accelerator Production of Tritium or Accelerator Transmutation of Waste Project. We both had heavy loads consisting of briefcases and suitcases. We arrived at location of the briefing early in the morning. I struggled up the two flights of stairs hoping that some young graduate student would take pity on me and help (to no avail). When I reached the landing, I turned around and to my surprise, I saw Arthur trotting up the same set of stairs with his luggage as though he were completely fresh and ten years younger than me.

3. That is not to say he hasn't been ill. A few years ago, Arthur was hospitalized and for that reason was forced to cancel some of his schedule. In particular, he had been planning on joining the group that was going to France for a meeting regarding the International Agreement on Fundamental Science that was mentioned earlier. That episode was quite serious – not for the medical reasons about which I am not expert—but for another factor that many thought was life threatening. Arthur was hospitalized just a few weeks before the French meeting. We assumed that he had bought an inexpensive non-refundable airline ticket. We were sure that if he had to cancel his trip and as a result LOST the money on the ticket, that fact would kill him! As it turns out, Arthur had been smart – as usual – and had not bought such a ticket and all ended well.

4. As a long-time consultant to Livermore, Arthur has – as you might expect—become an expert on how to enjoy his time in the Livermore valley. On one of his visits, I offered to drive him from the lab to his residence near the lab. I remind you that the laboratory treats its consultants very well – providing more than adequate per diem allowances so that one can stay in any of the many hotels within a 20-mile radius of the lab. Eager to see what arrangements a senior consultant had made, I was unprepared to see that Arthur lived in a trailer park in a fairly old Airstream trailer (Figure 6). Somehow, it did not fit with my preconceptions.

As it turns out, this trailer had some history and involved a battle between Arthur and the lab. I believe Arthur wanted to park the trailer at the lab when he wasn't visiting- moving it during those periods when it was occupied. The lab management (the budget folks) did not want that to happen. You'll have to ask Arthur for all the details.

5. When I retired from Livermore and when I went to Washington on assignment, I often was given a two-person office to use. Almost invariably, my office partner turned out to be Arthur. Since we each tend to have busy schedules, this never posed a problem – in fact I admit to enjoying the many discussions such close proximity encourages.

6. I was fortunate enough to attend Arthur's 80th birthday celebration at MIT, along with many of the country's luminaries in science who took time to attend. It was an impressive gathering.

7. Arthur either knows everyone of importance or had them as students. I continue to be amazed at his ability to get appointments with everyone in DOE or at the laboratories – Steve Chu, Steve Koonin as well as the laboratory directors. If you want something done, convince Arthur and he'll be an influential advocate.

8. Finally, I leave you with one of Arthur's many wise observations that I treasure. We have often argued about which of the many scientific facility investments should be made by the U.S. government – through either the Department of Energy or the National Science Foundation. In this era of tight budgets, one spends a great deal of effort making choices that are extremely difficult. Arthur's constant argument – with which I completely agree – is that the United States now spends a smaller percentage of the Gross National Product on science than it did years ago. If we want a robust economy in the future led by inventive bright young scientific minds, we should not be choosing which scientific endeavor to pursue from a menu – WE SHOULD BE DOING THEM ALL!!

So, thank you Arthur and I look forward to many more years of interacting with you.

Arthur Kerman

Fig.1: Arthur Kerman

- National Academy of Sciences –Committee on Inertial Confinement Fusion
- NIF Program Review Committee
- Livermore Directorate Review Committee
- Livermore/Los Alamos Division(s) Review Committee(s)
- RHIC Policy Committee- Brookhaven
- SLAC Scientific Policy Committee
- Secretary of Energy Fusion Policy Advisory Committee
- White House Science council Panel on Science and Technology in the Government
- LANSCE Advisory Board

Fig. 2: A few of the Advisory Committees on which he has served (away from MIT)

Fig.3: General Meeting under the DOE/NNSA CEA/DAM Agreement Held in France.

Fig. 4: Dinner at one of the General Meetings

Fig. 5: Arthur (see arrow) served on every advisory panel for the LLNL Division on Nuclear Physics, Elementary Particle Physics and Accelerator Physics.

Fig.6: Arthur's Luxury Hotel near Livermore

Some Open Problems in the Statistical Theory of Nuclear Reactions

Hans A. Weidenmüller
Max-Planck-Institut für Kernphysik, Saupfercheckweg 1, D-69117 Heidelberg, Germany

Abstract
I address three important problems in the statistical theory of nuclear reactions and in two cases sketch the solutions.

1 Introduction

The Varenna meeting honoured M. Kawai and A. Kerman for their contributions to the theory of nuclear reactions. Much of the work of these authors relates to statistical properties of the scattering matrix. For that reason, I chose to speak about three open problems in the statistical theory. For each of these problems, a paper presenting a partial or complete solution has recently become available in the arXiv, or will become available shortly. This is why I keep this summary very short. In the first two cases I include a description of the solution found.

2 Distribution of Neutron Widths and Random–Matrix Theory

Random–Matrix theory (RMT) predicts that the reduced s–wave neutron widths Γ_n^0 follow the Porter–Thomas distribution (PTD)

$$P(y) = \frac{\exp\{-y/2\}}{(2\pi y)^{1/2}} \, . \tag{1}$$

Here y is the ratio $\Gamma_n^0/\langle\Gamma_n^0\rangle$ where brackets denote the average value. Early analyses using the Nuclear Data Ensemble (NDE) supported that prediction [1]. A recent test in the Pt isotopes (about 450 resonances) rejected the PTD with 99.997 per cent significance [2]. A recent re–analysis of the NDE (1245 widths) rejects the PTD with 98.17 per cent significance [3]. These results are at variance with other work: The analysis of amplitude and width correlations for 1117 amplitudes from inelastic proton scattering at TUNL supports RMT [4]. So do large–scale shell model calculations in the $1p$ shell [5]. Still, the results of Refs. [2,3] question the validity of RMT in nuclei.

The method of analysis used in Refs. [2,3] uses an energy–dependent cutoff on the magnitude of the reduced neutron widths. That cutoff effectively removes p–wave reduced widths with their characteristic linear dependence on resonance energy. Recent simulations [6] have shown that that method introduces a heavy bias. For the NDE the bias is so strong that the conclusions of Ref. [2] cannot be upheld. Consistency of the NDE with RMT is likely, in contrast to the claims in Ref. [2]. The case of the Pt isotopes is special: Close to the mass numbers of these nuclei the s–wave neutron strength function has a maximum. That maximum is caused by a single–particle threshold state (the $4s$–state of the shell model). Such a state modifies the energy dependence of s–wave neutron widths. That modification is the likely cause of the disagreement with the PTD in these isotopes [6]. In summary, the distribution of neutron widths does not refute RMT.

3 Fluctuations of the Scattering Matrix and Quantum Chaos

In the RMT approach to the statistical theory of nuclear reactions [7], the statistical scattering matrix is written as

$$S_{ab}(E) = \delta_{ab} - 2i\pi \sum_{\mu\nu} W_{a\mu} D^{-1}_{\mu\nu} W_{\nu b} \tag{2}$$

where

$$D_{\mu\nu} = E\delta_{\mu\nu} - H_{\mu\nu} + i\pi \sum_c W_{\mu c} W_{c\nu} \, . \tag{3}$$

Here $a, b, c, \ldots$ denote the channels, $\mu, \nu, \ldots$ denote vectors in the Hilbert space $\mathcal{H}$ of quasibound states, $W_{a\mu}$ are real energy–independent coupling amplitudes, and H is the projection of the Hamiltonian onto $\mathcal{H}$. The matrix S is endowed with statistical properties by assuming that H is a member of the GOE, the random–matrix ensemble of real symmetric matrices. Why is that assumption justified? There are two arguments. (i) Spectral fluctuations in nuclei agree with predictions of RMT. That was discussed in Section 2. (ii) Nuclei are chaotic quantum systems. That takes a little more explanation.

The spectral fluctuation properties of time–reversal invariant and rotationally symmetric bound quantum systems that are fully chaotic in the classical limit, agree with those of the GOE. That fact, conjectured in Ref. [8], was recently demonstrated for generic chaotic quantum systems [9] and proved for the case of chaotic graphs [10]. In both cases, given the eigenvalues E_μ of the system, one considers the level density $\rho(E) = \sum_\mu \delta(E - E_\mu)$ as a function of energy E and calculates the level correlation function $\langle \rho(E+\varepsilon)\rho(E-\varepsilon)\rangle$ as a function of ε. The brackets denote the energy average. The calculation involves the semiclassical approximation and shows that both level correlation functions agree with the GOE expression. Although the demonstration is confined to the level–level correlator, it is reasonable to assume that equality holds also for all higher level correlation functions, and that chaotic quantum systems generically have the same spectral fluctuation properties as predicted by RMT. By implication chaotic nuclear dynamics would then cause RMT spectral fluctuations.

Scattering happens on open quantum systems and is characterized by the scattering matrix. In full analogy to the case of bound chaotic quantum systems, we ask whether the S–matrix correlation function

$$\langle S_{ab}(E+\varepsilon) S^*_{cd}(E-\varepsilon)\rangle - \langle S_{ab}\rangle \langle S^*_{cd}\rangle \tag{4}$$

for scattering on chaotic quantum systems is the same as predicted in the framework of Eqs. (3, 4) with H replaced by the GOE. The latter is known in the form of a triple integral [7]. That is an important question: An affirmative answer would show that the RMT description of the scattering matrix in Eqs. (3, 4) and the results derived from it apply universally to chaotic quantum systems.

Little is known analytically about the S–matrix for quantum chaotic scattering in general, but progress was made recently for chaotic scattering on quantum graphs [11]. The problem was extensively studied in Refs. [12,13] where a formal expression for the S–matrix was derived and used for extensive numerical simulations. Using that expression and the supersymmetry approach of Ref. [10], the authors of Ref. [11] showed that the S–matrix correlation function for chaotic scattering on graphs is identical to the GOE expression of Ref. [7]. The authors also derived analytical expressions for all S–matrix correlation functions in the Ericson regime and, thus, the complete distribution of the S–matrix in that regime. Their result shows that the distribution of S–matrix elements is Gaussian only for strong absorption in all channels ($\langle S_{ab}\rangle = 0$ for all a, b).

4 Nuclear Excitation by Lasers

Efforts are under way to generate a multi–MeV zeptosecond pulsed laser beam by coherent Compton backscattering of laser light on a "sheet" of relativistic electrons [14]. That sheet is produced when the pulse of a primary laser beam of very high intensity passes through a sufficiently thin target foil. The device is presently under construction at the Nuclear Physics Pillar of the Extreme Light Infrastructure (ELI) in Romania [15]. These facts call for a theoretical exploration of the expected nuclear excitation processes.

The characteristic energy scales are: Photon energy $E_L \approx$ several MeV, number of photons per laser pulse $N \approx 10^2 - 10^4$, pulse width ≈ 50 keV, effective width for dipole photon absorption $N\Gamma_{\rm dip}$ with $\Gamma_{\rm dip} \approx$ several keV, spreading width for any simple nuclear mode of excitation $\Gamma \approx$ several MeV.

These figures suggest the following three regimes for the nuclear excitation process. (i) In the perturbative regime (basically defined by $N\Gamma_{\rm dip} << \Gamma$, the nuclear giant dipole mode is excited once or twice [16]. Coherent excitation of many close–lying states with spin/parity 1^- carries a unique experimental signal [17]. (ii) In the quasi–adiabatic regime where $N\Gamma_{\rm dip} \approx \Gamma$ the compound nucleus equilibrates about as fast as it gets excited by photon absorption. Excitation to several 100 MeV is possible, accompanied by neutron emission with subsequent excitation of the daughter nuclei by further dipole absorption. (iii) In the strongly non–adiabatic regime ($N\Gamma_{\rm dip} >> \Gamma$) the nucleus evaporates by multiple nucleon emission.

For the quasiadiabatic regime the theoretical approach developed for pre–equilibrium reactions seems adequate. A set of coupled time–dependent master equations would describe photon absorption, induced photon emission, internal nuclear equlibration, and neutron decay processes for a chain of nuclei. To that end the densities of particle–hole states at high excitation energies (several 100 MeV) and large particle-hole numbers are needed. In Ref. [18] we have developed an approach to calculate such densities. That is described in the contribution by A. Palffy to this Conference.

In summary, laser–induced nuclear reactions promise to yield novel nuclear–physics information. In the quasi–adiabatic regime, the population of compound–nucleus states far above the Yrast line will make level densities at high excitation energies accessible for the first time. Multiple neutron evaporation may lead to proton–rich nuclei far from the valley of stability.

References

[1] O. Bohigas, R. U. Haq, A. Pandey, in "Nuclear Data for Science and Technology", K. H. Böckhoff, editor, D. Reidel, Dordrecht, 1983, p. 809.

[2] P. E. Koehler et al., Phys. Rev. Lett. **105** (2010) 072502.

[3] P. E. Koehler, Phys. Rev. C **84** (2011) 034312.

[4] H. L. Harney, Phys. Rev. Lett. **53** (1984) 537; J. F. Shriner Jr., G. E. Mitchell, and E. G. Bilpuch, Phys. Rev. Lett. **59** (1987) 435.

[5] V. B. Zelevinsky et al., Phys. Rep. **276** (1996) 85.

[6] J. F. Shriner, Jr., H. A. Weidenmüller, and G. E. Mitchell, arXiv 1209.2439.

[7] J. J. M. Verbaarschot, H. A. Weidenmüller, and M. R. Zirnbauer, Phys. Rep. **129** (1985) 367.

[8] O. Bohigas, M.-J. Giannoni, and C. Schmit, Phys. Rev. Lett. **52** (1984) 1.

[9] S. Heusler at al., Phys. Rev. Lett. **98** (2007) 044103.

[10] S. Gnutzmann and A. Altland, Phys. Rev. Lett. **93** (2004) 194101.

[11] Z. Pluhar and H. A. Weidenmüller, to be submitted.

[12] T. Kottos and U. Smilansky, Phys. Rev. Lett. **85** (2000) 968.

[13] T. Kottos and U. Smilansky, J. Phys. A: Math. Gen. **36** (2003) 3501.

[14] G. Mourou and T. Tajima, Science **331** (20100) 41.

[15] ELI URL: extreme-light-infrastructure.eu 2012.

[16] H. A. Weidenmüller, Phys. Rev. Lett. **106** (2011) 122502.

[17] B. Dietz and H. A. Weidenmüller, Phys. Lett. B **693** (2010) 316.

[18] A. Palffy and H. A. Weidenmüller, arXiv 1206.1542.

Microscopic approach to the scattering of unstable nuclei at intermediate incident energies

M. Yahiro[1]*, K. Ogata*[2]*, T. Matsumoto*[1] *and K. Minomo*[1]
[1]Department of Physics, Kyushu University, Fukuoka 812-8581, Japan
[2]Research Center for Nuclear Physics (RCNP), Osaka University, Osaka 567-0047, Japan

Abstract
This article presents the theoretical foundation of the continuum discretized coupled-channels method (CDCC). The validity of the Glauber model is also shown by extending the multiple scattering theory for nucleon-nucleus scattering to nucleus-nucleus scattering. The multiple scattering theory is applied to the scattering of unstable nuclei. This presentation is based on the recent review article on CDCC (arXiv:1203.5392[nucl-th]).

1 Introduction

Nuclear reaction is one of fundamental reactions in Nature and a good tool of understanding nucleon-nucleon (NN), nucleon-nucleus (NA) and nucleus-nucleus (AA) interactions and eventually structures of nuclei. One of the most important current subjects in nuclear physics is understanding of unstable nuclei. Unstable nuclei have exotic properties such as the halo structure [1–3] and the loss of magicity in the "island of inversion" [4–9]. The term "island of inversion" was introduced by Warburton [4] to the region of unstable nuclei from ^{30}Ne to ^{34}Mg. In the island of inversion, the first-excited states have low excitation energies and large $B(E2)$ values [5–9]. This indicates that the $N = 20$ magic number is not valid. anymore. These novel quantum properties have inspired a lot of works.

Important experimental tools of analyzing properties of unstable nuclei are the reaction cross section $\sigma_{\rm R}$ or the interaction cross section $\sigma_{\rm I}$ and the nucleon-removal cross section σ_{-n} [1–3, 10]. The experimental exploration of halo nuclei is moving from lighter nuclei such as He and C isotopes to relatively heavier nuclei such as Ne isotopes. Very lately $\sigma_{\rm I}$ was measured by Takechi *et al*. [11] for $^{28-32}$Ne located near or in the island of inversion. Furthermore, a halo structure of ^{31}Ne was reported by Nakamura *et al*. [12] with the experiment on σ_{-n}.

Understanding of unstable nuclei can be made by high-accuracy measurements and accurate theoretical analyses. The scattering of unstable nuclei have two features. The projectile is fragile and hence the projectile breakup is important. Measurements of the elastic scattering are not easy because of weak intensity of the secondary beam, and consequently, there is no reliable phenomenological optical potential. Therefore it is important to construct the microscopic reaction theory. This is a goal of the nuclear reaction theory.

A pioneering work on the microscopic description of NA scattering was done by Watson [13]. Kerman, McManus and Thaler (KMT) reformulated the multiple scattering theory as a series expansion in terms of an underlying NN t matrix [14]. The KMT theory was extended to AA scattering [15]. Another important microscopic model is the Glauber model [16]. This model is useful particularly for inclusive reactions. The theoretical foundation of the model can be obtained by the theory of Ref. 15. We show the details in Sec. 3.1. The Glauber model is based on the eikonal and the adiabatic approximation. The adiabatic approximation makes the breakup cross section diverge when the Coulomb interaction is included. Hence the Glauber model was mainly applied to lighter targets in which the Coulomb interaction is negligible. A way of making Coulomb corrections to the model has been proposed [17,18].

The continuum discretized coupled-channels method (CDCC) [19–21] is a fully quantum-mechanical method of treating the projectile breakup process in exclusive reactions such as elastic and inelastic scattering, elastic-breakup reactions and transferred reactions. The theoretical foundation of CDCC is shown

by clarifying the relation between the Faddeev method and CDCC [22–24]. We will show the detail in Sec. 2. Recent development and applications of CDCC are shown in Ref. [21].

The microscopic optical potential can be constructed by the g-matrix folding model [25–33]. For NA scattering, the folding model has succeeded in describing the elastic scattering systematically [32]. In general, the microscopic optical potential constructed is non-local, but it can be localized with the Brieva-Rook method [27]. The validity of this localization is shown in Ref. 34. For AA scattering at intermediate and high incident energies, the folding model is also successful in describing the scattering, since the projectile breakup is weak. This is discussed in Sec. 3. One can use the microscopic optical potential as an input of CDCC calculations.

2 Theoretical foundation

Following Refs. 22–24, We consider the projectile (P) that is composed of two particles b and c. In this case, the scattering of P on a target (A) can be described by the A+b+c three-body system. The three-body scattering is governed by the three-body Schrödinger equation

$$[H - E]\Psi = 0 \tag{1}$$

with the Hamiltonian

$$H = K_r + K_R + v(\mathbf{r}) + U_b(\mathbf{r}_b) + U_c(\mathbf{r}_c), \tag{2}$$

where K_r and K_R are the kinetic energy operators associated with the relative coordinate $\mathbf{r}$ between b and c and the relative coordinate $\mathbf{R}$ between P and A, respectively, and $v(\mathbf{r})$ is the interaction between b and c, while U_b (U_c) is an optical potential between b (c) on A.

In CDCC, the total wave function Ψ is expanded in terms of the complete set of eigenfunctions of Hamiltonian $h = K_r + v(\mathbf{r})$ [19,20]. The eigenfunctions consist of bound and continuum states. The continuum states are characterized by orbital angular momentum ℓ and linear momentum k of the b+c subsystem. They are truncated as

$$k \le k_{\max}, \quad \ell \le \ell_{\max}. \tag{3}$$

After making the truncations, we further discretize the k contiuum. Hence the modelspace $\mathcal{P}'$ is described as

$$\mathcal{P}' = \sum_{i=0}^{N} |\phi_i\rangle\langle\phi_i|, \tag{4}$$

where the ϕ_i represent the bound and discretized-continuum states of h and N is the number of the ϕ_i. The total wave function Ψ is hence approximated into

$$\Psi \approx \Psi_{\rm CDCC} \equiv \mathcal{P}'\Psi = \sum_{i=0}^{N} \phi_i(\boldsymbol{r})\chi_i(\boldsymbol{R}), \tag{5}$$

where the coefficient $\chi_i(\boldsymbol{R})$ describes a motion of P in its state ϕ_i. The approximate total wave function $\Psi_{\rm CDCC}$ is obtained by solving the three-body Schrödinger equation (1) in the modelspace $\mathcal{P}'$:

$$\mathcal{P}'[H - E]\mathcal{P}'\Psi_{\rm CDCC} = 0. \tag{6}$$

The S-matrix elements calculated with CDCC depend on the size of the modelspace P'. This artifact should be removed by confirming that the calculated S-matrix elements converge as the modelspace is enlarged. Actually the convergence was first shown in Refs. 19,20,35. The next question to be addressed is whether the converged S-matrix elements are exact.

CDCC is based on three approximations, the ℓ-truncation, the k-truncation and the discretization of k-continuum. The ℓ-truncation is most essential among these approximations, as shown below. Now we introduce the projection operator $\mathcal{P}$ that only selects ℓ up to $\ell_{\max}$. Obviously, $\mathcal{P}'$ tends to $\mathcal{P}$ in the limit of large $k_{\max}$ and small width of momentum bin. The component $\mathcal{P}\Psi$ has no asymptotic amplitudes in the rearrangement channels. For example, let us consider a simple case of $\ell_{\max} = 0$. In this case, $\mathcal{PUP}$ is the average of $U = U_b + U_c$ over the angle of vector $\mathbf{r}$. Hence the potential $\mathcal{PUP}$ becomes a function of r and R. Thus $\mathcal{PUP}$ is a three-body potential that vanishes at large R and/or large r, so that it does not generate any rearrangement channel.

The insertion of three-body distorting potentials does not change the mathematical properties of the Faddeev equations [36]. Now we consider $\mathcal{PUP}$ as such a distorting potential in order to obtain the distorted Faddeev equations,

$$(E - K_r - K_R - v - \mathcal{PUP})\psi_A = v(\psi_b + \psi_c), \tag{7}$$

$$(E - K_r - K_R - U_b)\psi_b = (U_b - \mathcal{P}U_b\mathcal{P})\psi_A + U_b\psi_c, \tag{8}$$

$$(E - K_r - K_R - U_c)\psi_c = (U_c - \mathcal{P}U_c\mathcal{P})\psi_A + U_c\psi_b, \tag{9}$$

where ψ_A, ψ_b and ψ_c satisfy the relation $\Psi = \psi_A + \psi_b + \psi_c$. If Eqs. (7)-(9) are added, the original three-body Schrödinger equqtion (1) is recovered. In an iterative approach to Eqs. (7)-(9), the zeroth order solution for ψ_A is obtained by setting the right-hand side of (7) to zero. The zeroth order solution is nothing but $\Psi_{\rm CDCC}$. When $\Psi_{\rm CDCC}$ is inserted in Eqs. (8)-(9), the equations do not generate any disconnected diagram, since $\Psi_{\rm CDCC}$ has no rearrangement channel in the asymptotic region. Furthermore, the subtractions, $U_b - \mathcal{P}U_b\mathcal{P}$ and $U_c - \mathcal{P}U_c\mathcal{P}$, sizably weaken couplings of $\Psi_{\rm CDCC}$ with ψ_b and ψ_c. Thus $\Psi_{\rm CDCC}$ is a good solution to the three-body Schrödinger equation (1), when $\ell_{\max}$ is large enough. Very lately, the CDCC solution was compared with the Faddeev solution through numerical calculations. The two solutions agree with each other [24].

3 Microscopic reaction theory for AA scattering

The most fundamental equation to describe AA scattering is the many-body Schrödinger equation with the realistic NN interaction v_{ij}:

$$(K + h_{\rm P} + h_{\rm T} + \sum_{i\in{\rm P}, j\in{\rm T}} v_{ij} - E)\hat{\Psi}^{(+)} = 0\,, \tag{10}$$

where K is the kinetic-energy operator for the relative motion between P and T and $h_{\rm P}$ ($h_{\rm A}$) is the internal Hamiltonian of P (T). The scattering of P from T can be described with a series of multiple scattering in terms of v_{ij}. In the series, one can first take a summation of ladder diagrams between the same NN pair. The summation can be described by an effective NN interaction τ_{ij} in nuclear medium. Taking a resummation of the series in terms of τ_{ij}, one can get the many-body Schrödinger equation with τ_{ij} [15]:

$$(K + h_{\rm P} + h_{\rm T} + \sum_{i\in{\rm P}, j\in{\rm T}} \tau_{ij} - E)\hat{\Psi}^{(+)} = 0\,. \tag{11}$$

Here the number of v_{ij} between P and T is assumed to be much larger than 1 and the antisymmetrization between incident nucleons in P and target nucleons in T can be approximated by using τ_{ij} that is properly symmetrical with respect to the exchange of the colliding nucleons. The first assumption is good for AA scattering, and the second one is known to be accurate at intermediate and high incident energies [37,38]. This theory of Ref. 15 is an extension of the KMT theory [14] for NA scattering to AA scattering.

Since τ_{ij} describes NN scattering in nuclear medium, the Brueckner g-matrix is commonly used as τ_{ij} in many applications; see for example Refs. 25–33. The g-matrix interaction does not include any effect induced by finite nucleus, e.g. effects of target collective excitations, because the interaction is evaluated in infinite nuclear matter.

3.1 Validity of the Glauber model

We show the validity of the Glauber model by using the many-body Schrödinger equation (11) with the effective NN interaction, following Ref. 15. The Glauber model is based on the eikonal approximation for NN scattering and the eikonal and adiabatic approximations for AA scattering. The condition for the eikonal approximation to be good for NN collision in both free space and AA scattering is that

$$|v(\boldsymbol{r})/e| \ll 1, \quad ka \gg 1 \,, \tag{12}$$

where e (k) is a kinetic energy (wave number) of NN collision, $\boldsymbol{r}$ is the relative coordinate between two nucleons and a is a range of the realistic NN interaction v. This condition is not well satisfied for the realistic NN potential that has a strong short-ranged repulsive core; for example, $v \sim 2000$ MeV at $r = 0$ for AV18 [39]. In fact, the eikonal approximation is not good for NN scattering at intermediate energies, as shown in the left panel of Fig. 1. To avoid this problem, a slowly-varying function such as the Gaussian form has been used as a profile function in the Glauber model [40].

The usage of slowly-varying profile function and hence of slowing-varying NN interaction can be justified by using the many-body Schrödinger equation (11). Applying the adiabtic and eikonal approximations to Eq. (11), one can obtain the S-matrix of AA scattering as

$$S = \exp\Big[-\frac{i}{\hbar v_{\rm rel}} \sum_{ij} \int_{-\infty}^{\infty} dz_{ij} \tau_{ij} \Big], \tag{13}$$

where $v_{\rm rel}$ stands for a velocity of P relative to A and z_{ij} is the z-component of the relative coordinate $\boldsymbol{r}_{ij}$ between two nucleons. In general, τ_{ij} has much milder r dependence than the bare NN potential v_{ij} [15]. In the case of large incident energies, for instance, τ_{ij} is reduced to the t-matrix of NN scattering that is a product of v_{ij} and the wave operator of NN scattering. When v_{ij} has a strong repulsive core at small r, the wave operator is largely suppressed there. This leads to the fact that the t matrix is a slowly-varying function of r [15]. The g matrix [26] proposed by Jeukenne, Lejeune and Mahaux (JLM) keeps this property. The g matrix is thus more suitable than v_{ij} as an input of the Glauber model. In fact, as shown in the right panel of Fig. 1, the eikonal approximation is quite good for NN scattering at intermediate energies, say 150 MeV, when the JLM g matrix is used. The usage of the g-matrix interaction has another merit in the sense that the effective interaction includes nuclear medium effects.

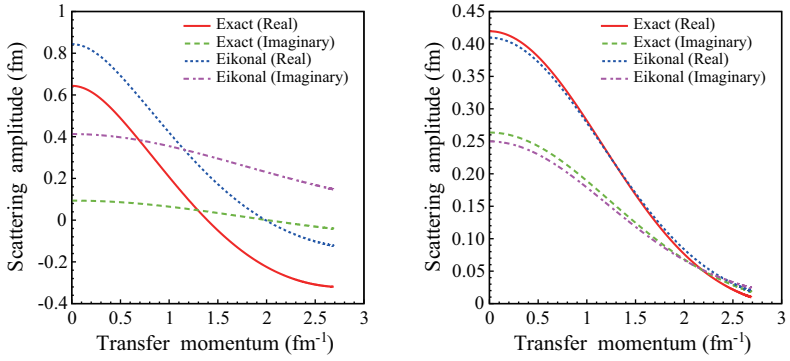

Fig. 1: (Color online) The on-shell NN scattering amplitude $f_{\rm NN}(\boldsymbol{q})$ at the laboratory energy $E_{\rm NN} = 150$ MeV calculated with the bare NN potential AV18 in the left panel and with the JLM g matrix [26] in the right panel. The solid (dashed) and dotted (dash-dotted) lines show, respectively, the real and imaginary parts of $f_{\rm NN}(\boldsymbol{q})$ of the exact (eikonal) calculation.

3.2 Application of the g-matrix folding model to AA scattering

Following Refs. 41–43, we consider two types of effective NN interactions in the folding model: the Love-Franey t-matrix interaction ($t_{\rm LF}$) [44], and the Melbourne interaction ($g_{\rm MB}$) [32] constructed from the Bonn-B realistic NN interaction [45]. For stable nuclei, we take the phenomenological proton-density [46] deduced from the electron scattering by unfolding the finite-size effect of the proton charge. The neutron density is assumed to have the same geometry as the corresponding proton one, since in the present case the proton RMS radius deviates from the neutron one only by less than 1% in the Hartree-Fock (HF) calculation. For Ne isotopes, the densities are constructed by antisymmetrized molecular dynamics (AMD) [47] with the Gogny D1S interaction [48,49]

Figure 2 shows the results of the g- and t-matrix folding models for the angular distribution of ^{12}C+^{12}C elastic scattering at 135 MeV/nucleon in the left panel and 74.25 MeV in the right panel. In the left panel, the g-matrix folding model (solid line) well reproduces the data [50] with no free parameter, whereas the t-matrix folding model (dashed line) does not. Also for the low incident energy in the right panel, the g-matrix folding model (solid line) yields better agreement with the data [51] than the t-matrix folding model (dashed line). For scattering angles larger than 50 degree, the solid line does not reproduce the data perfectly. The deviation may come from effects of collective projectile and target excitations that are not included in the g-matrix. The g-matrix folding model is thus quite reliable particularly for intermediate incident energies.

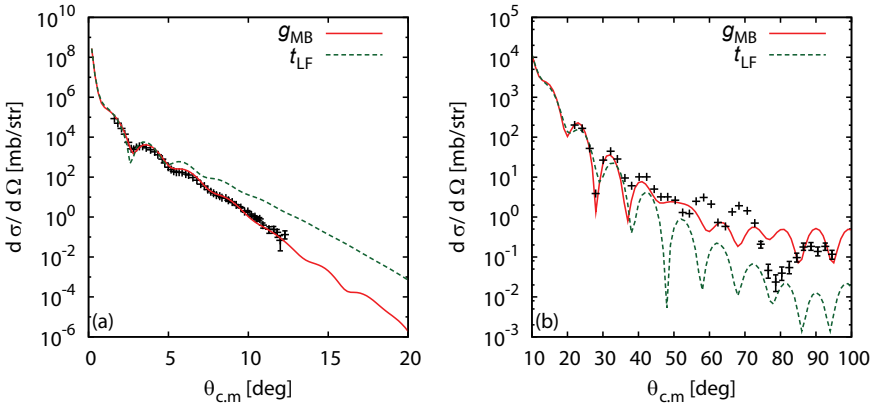

Fig. 2: (Color online) Angular distributions of ^{12}C+^{12}C elastic cross sections at 135 MeV/nucleon in the left panel and 74.25 MeV in the right panel. The solid (dashed) line stands for the results of DFM calculations with $g_{\rm MB}$ ($t_{\rm LF}$). The data is taken from Ref. [50] in the left panel and from Ref. [51] in the right panel.

The left panel of Fig. 3 shows the reaction cross sections for the scattering of ^{12}C from ^{12}C, ^{20}Ne, ^{23}Na, and ^{27}Al targets. The dotted and solid lines represent results of the g-folding calculations before and after the normalization with $F = 0.978$, respectively. Before the normalization procedure, the dotted line slightly overestimates the mean values of data for $A = 20$–27. After the normalization procedure, the solid line agrees with the mean values of data for all the targets. The normalization procedure is thus reliable. The dashed line corresponds to the results of the t-folding calculations with no normalization. The medium effect reduces the theoretical reaction cross sections by about 15% for all the targets.

The right panel of Fig. 3 represents $\sigma_{\rm R}$ for $^{20-32}$Ne + ^{12}C systems at 240 MeV/nucleon. The g-matrix folding model with the AMD density (solid line) reproduces the data [11], whereas the spherical Hatree-Fock (HF) calculation with the Gogny D1S interaction (dotted line) underestimates the data. It

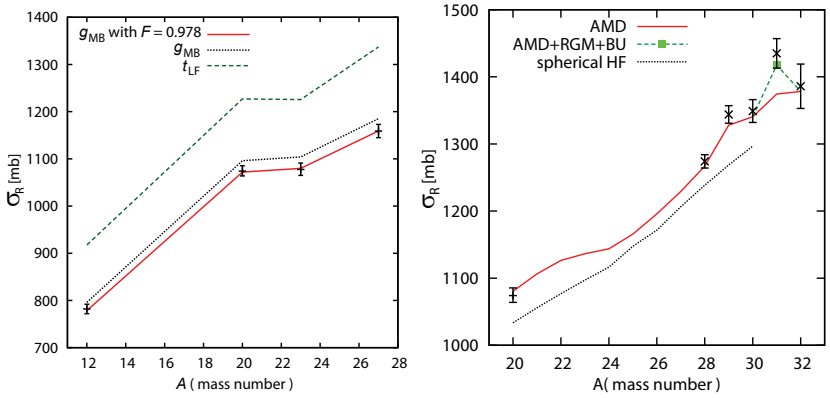

Fig. 3: (Color online) Reaction cross sections for the scattering of ^{12}C on stable nuclei from $A = 12$ to 27 in the left panel and for the scattering of Ne isotopes from a ^{12}C target at 240 MeV/nucleon in the right panel. In the left panel, the data at 250.8 MeV/nucleon for ^{12}C and ^{27}Al are taken from Ref. [52]. The data at 240 MeV/nucleon for ^{20}Ne and ^{23}Na are deduced from measured σ_I at around 1 GeV/nucleon [53,54] with the Glauber model [11]. The solid (dotted) line stands for the results of the g-matrix folding model after (before) the normalization with $F = 0.978$, whereas the dashed line corresponds to results of the t-matrix folding model. In the right panel, the solid (dotted) line represents the results of AMD (spherical HF) calculations. The dashed line with a closed square is the result of the AMD calculation with the tail and breakup corrections. The closed square represents the result of the AMD+RGM calculation with breakup correction. The experimental data for $A = 28 - 32$ are taken from Ref. 11.

should be noted that the nuclei with $A > 30$ are unbound in the spherical calculations, where A is the mass number of P. The enhancement from the dotted line to the solid line stems from the deformation of P. The g-matrix folding model with the AMD density thus yields results consistent with the data except ^{31}Ne. The underestimation of this model for ^{31}Ne comes from the inaccuracy of the AMD density in its tail region.

The tail correction to the AMD density can be made as below. The ground state of ^{31}Ne is described by the ^{30}Ne+n cluster model with excitations of ^{30}Ne. The cluster-model calculation can be done with the resonating group method (RGM) in which the ground and excited states of ^{30}Ne are constructed with AMD. This AMD+RGM calculation is quite time consuming, but it is done for ^{31}Ne. The tail correction to σ_R is 35 mb. The reaction cross section with the tail correction (a square symbol) well reproduces the experimental data [11] with no adjustable parameter. Consequently, ^{31}Ne is a halo nucleus with large deformation.

4 Summary

We have shown recent developments of CDCC and the microscopic reaction theory as an underlying theory of CDCC. This talk is based on the recent review article of Ref. 21.

First we have shown the theoretical foundation of CDCC by comparing the Faddeev method and CDCC. The primary approximation in CDCC is the ℓ-truncation P. The ℓ-truncation changes the two-body potentials, U_b and U_c, to three-body ones. The theoretical foundation of the ℓ-truncation is investigated with the distorted Faddeev equations where the three-body potentials $\mathcal{P}U_b\mathcal{P}$ and $\mathcal{P}U_c\mathcal{P}$ are inserted. The CDCC solution is the zeroth-order solution to the distorted Faddeev equations. The first-order solution is strongly weakened by the suppression of coupling potentials, $U_b - \mathcal{P}U_b\mathcal{P}$ and $U_c - \mathcal{P}U_c\mathcal{P}$.

The CDCC solution is thus a good solution to the three-body Schrödinger equation, when $\ell_{\max}$ is large enough. The theoretical statement based on the distorted Faddeev equations is numerically confirmed to be true by a direct comparison between the CDCC and Faddeev solutions [24].

As an underlying theory of CDCC, we have constructed a microscopic reaction theory for AA scattering, using the multiple scattering theory. This is an extension of the KMT theory for nucleon-nucleus scattering to nucleus-nucleus scattering. The input of the theory is the g-matrix NN interaction instead of the realistic one. The g-matrix has much milder r-dependence, so that the Glauber model becomes reliable when the model starts from the microscopic reaction theory of Ref. 15. The Glauber model is applicable for the scattering of lighter projectiles from lighter targets at intermediate and high incident energies, since Coulomb breakup is weak there.

Using the g-matrix folding model, one can construct the microscopic optical potential with projectile and target densities calculated by fully microscopic structure theories such as AMD and HF. This fully microscopic framework has been applied to the scattering of stable nuclei and unstable neutron-rich Ne-isotopes at intermediate incident energies with success of reproducing the data. In "the Island of inversion" region, the nuclei are strongly deformed, and ^{31}Ne is a halo nucleus with strong deformation. The reliable microscopic optical potential can be used as an input of CDCC calculations. This microscopic version of CDCC is quite useful to analyze the scattering of unstable nuclei.

References

[1] I. Tanihata, *et al*., Phys. Lett. B **289**, 261 (1992).
I. Tanihata, J. Phys. G **22**, 157 (1996).

[2] A. S. Jensen, *et al*., Rev. Mod. Phys. **76**, 215 (2004).

[3] B. Jonson, Phys. Rep. **389**, 1 (2004).

[4] E. K. Warburton, J. A. Becker, and B. A. Brown, Phys. Rev. C **41**, 1147 (1990).

[5] T. Motobayashi *et al*., Phys. Lett. B **346**, 9 (1995).

[6] E. Caurier, F. Nowacki, A. Poves, J. Retamosa, Phys. Rev. C **58**, 2033 (1998).

[7] Y. Utsuno, T. Otsuka, T. Mizusaki, M. Honma, Phys. Rev. C **60**, 054315 (1999).

[8] H. Iwasaki *et al*., Phys. Lett. B **522**, 227 (2001).

[9] Y. Yanagisawa *et al*., Phys. Lett. B **566**, 84 (2003).

[10] A. Gade, *et al*., Phys. Rev. C **77**, 044306 (2008).

[11] M. Takechi *et al*., Nucl. Phys. **A834**, 412c (2010).

[12] T. Nakamura, *et al*., Phys. Rev. Lett. **103**, 262501 (2009).

[13] K. M. Watson, Phys. Rev. **89**, 575 (1953).

[14] A. K. Kerman, H. McManus, and A. M. Thaler, Ann. Phys.(N.Y.) 8, **51** (1959).

[15] M. Yahiro, K. Minomo, K. Ogata, and M. Kawai, Prog. Theor. Phys. **120**, 767 (2008).

[16] R.J. Glauber, *in Lectures in Theoretical Physics* (Interscience, New York, 1959), Vol. 1, p.315.

[17] B. Abu-Ibrahim and Y. Suzuki, Prog. Theor. Phys. **112** (2004), 1013; B. Abu-Ibrahim and Y. Suzuki, Prog. Theor. Phys. **114** (2005), 901.

[18] P. Capel, D. Baye, and Y. Suzuki, Phys. Rev. C **78** (2008), 054602.

[19] M. Kamimura, M. Yahiro, Y. Iseri, Y. Sakuragi, H. Kameyama and M. Kawai, Prog. Theor. Phys. Suppl. **89** (1986), 1.

[20] N. Austern, Y. Iseri, M. Kamimura, M. Kawai, G. Rawitscher and M. Yahiro, Phys. Rep. **154** (1987), 125.

[21] M. Yahiro, K. Ogata, T. Matsumoto and K. Minomo, Prog. Theory. Exp. Phys. **1** (2012), 01A209 [arXiv:1203.5392 [nucl-th]].

[22] N. Austern, M. Yahiro, and M. Kawai, Phys. Rev. Lett. **63** (1989), 2649.

[23] N. Austern, M. Kawai, and M. Yahiro, Phys. Rev. C **53** (1996), 314.
[24] A. Deltuva, A.M. Moro, E. Cravo, F.M. Nunes, and A.C. Fonseca, Phys. Rev. C **76** (2007), 064602.
[25] G. Bertsch, J. Borysowicz, M. McManus, and W.G. Love, Nucl. Phys. A**284**, 399(1977).
[26] J.-P. Jeukenne, A. Lejeune and C. Mahaux, Phys. Rev. C**16**, 80 (1977); ibid. Phys. Rep. **25**, 83 (1976).
[27] F.A. Brieva and J.R. Rook, Nucl. Phys. A**291**, 299 (1977); ibid. 291, 317 (1977); ibid. 297, 206 (1978).
[28] G. R. Satchler, Phys. Rep. **55**, 183-254 (1979).
[29] G. R. Satchler, "Direct Nuclear Reactions", Oxfrod University Press, (1983).
[30] N. Yamaguchi, S. Nagata and T. Matsuda, Prog. Theor. Phys. **70**, 459 (1983); N. Yamaguchi, S. Nagata and J. Michiyama, Prog. Theor. Phys. **76**, 1289 (1986).
[31] L. Rikus, K. Nakano and H. V. von Geramb, Nucl. Phys. A**414**, 413 (1984); L. Rikus and H.V. von Geramb, Nucl. Phys. A**426**, 496 (1984).
[32] K. Amos, P. J. Dortmans, H. V. von Geramb, S. Karataglidis, and J. Raynal, in *Advances in Nuclear Physics*, edited by J. W. Negele and E. Vogt(Plenum, New York, 2000) Vol. 25, p. 275.
[33] T. Furumoto, Y. Sakuragi, and Y. Yamamoto, Phys. Rev. C**78**, 044610 (2008); *ibid*., C**79**, 011601(R) (2009); *ibid*., C**80**, 044614 (2009).
[34] K. Minomo, K. Ogata, M. Kohno, Y. R. Shimizu and M. Yahiro, J. Phys. G **37**, 085011 (2010) [arXiv:0911.1184 [nucl-th]].
[35] R. A. D. Piyadasa, M. Kawai, M. Kamimura and M. Yahiro, Phys. Rev. C **60**, 044611(1999); R. A.D. Piyadasa, M. Yahiro, M. Kamimura and M. Kawai, Prog. Theor. Phys. **81**, 910 (1989).
[36] M.C. Birse and E. F. Redish, Nucl. Phys. A**406**, 149.
[37] G. Takeda and K. M. Watson, Phys. Rev. **97**, 1336(1955).
[38] A. Picklesimer and R. M. Thaler, Phys. Rev. C**23**, 42(1981).
[39] R. B. Wiringa, V. G. J. Stoks and R. Schiavilla, Phys. Rev. C**51**, 38 (1995).
[40] R.J. Glauber and G. Matthiae, Nucl. Phys. B**21**, 135 (1970).
[41] K. Minomo, T. Sumi, M. Kimura, K. Ogata, Y. R. Shimizu, and M. Yahiro, Phys. Rev. C **84**, 034602 (2011).
[42] K. Minomo, T. Sumi, M. Kimura, K. Ogata, Y. R. Shimizu and M. Yahiro, Phys. Rev. Lett. **108** (2012), 052503.
[43] T. Sumi *et al*., Phys. Rev. C **85** (2012), 064613.
[44] W. G. Love and M. A. Franey, Phys. Rev. C**24**, 1073 (1981); M. A. Franey and W. G. Love, Phys. Rev. C**31**, 488 (1985).
[45] R. Machleidt, K. Holinde, and Ch. Elster, Phys. Rep. **149**, 1(1987).
[46] H. de Vries, C. W. de Jager, and C. de Vries, At. Data Nucl. Data Tables **36**, 495 (1987).
[47] M. Kimura and H. Horiuchi, Prog. Theor. Phys. 111, 841 (2004); M. Kimura, Phys. Rev. C 75, 041302 (2007). M. Kimura, arXiv:1105.3281 (2011) [nucl-th].
[48] J. Decharge and D. Gogny, Phys. Rev. C **21** (1980), 1568.
[49] J. F. Berger, M. Girod, and D. Gogny, Comp. Phys. Comm. **63** (1991), 1365.
[50] T. Ichihara *et al*., Nucl. Phys. A**569** 287c-296c(1994).
[51] R. G. Stokstad, *et al*., Phys. Rev. C **20**, 655 (1979).
[52] M. Takechi, *et al*., Phys. Rev. C **79**, 061601(R) (2009).
[53] T. Suzuki *et al*., Phys. Rev. Lett. **75**, 3241 (1995).
[54] L. Chulkov *et al*., Nucl. Phys. **A603** 219, (1996).

Derivation of Eikonal Corrections to the Phase Shift Operators in the Analytical Abrasion-Ablation Model

Santosh Bhatt, Lawrence W. Townsend
The University of Tennessee, Knoxville, TN-37996-2300, USA

Abstract
The analytical abrasion-ablation model has been used for quantitative predictions of the neutron and light ion spectra from nucleus-nucleus and nucleon-nucleus collisions. The abrasion stage of the present model utilizes Glauber's multiple scattering theory and applies a small angle approximation. However the validity of the small angle approximation for the current model is unclear for systems with three or more particles in the final state as well as for light ions and nucleons. In this work, we have re-derived the phase shift operator, χ, for the calculation of nuclear cross-sections in of the abrasion-ablation model using an approximation developed by Wallace based on converting the partial wave series to a Fourier Bessel expansion, using Legendre functions and thereby eliminating the small angle approximation. We have computed differential cross-sections for various projectile-target data sets at different energies and scattering angles, and compare our model results to results from the previous model and published experimental data.

1 Introduction

The ionizing space radiation environment is a major concern in planning for deep space, long duration exploratory missions. The space ionizing radiation environment is very complex in nature and consists of wide varieties of particles over a large energy range. Analytical models for quantitative prediction of neutrons and light ions spectra from high and intermediate energy interactions provide a basis for modelling of production and transport of ion fragments produced during such interactions, while also providing important insight in the assessment of radiation damage during long duration deep space missions [1],[2]. The analytical abrasion-ablation model, based on Eikonal approximations as derived in the Glauber multiple scattering theory, has been widely used to describe the physics of secondary particle production and transport during high energy nucleus-nucleus and nucleon-nucleus collisions[3],[4].

The abrasion-ablation model is based on a fragmentation theory that describes the secondary particle production from high energy interactions as a two step process[4], [5]. In the first step, the abrasion or knockout process, an incoming projectile, P, moving with some initial velocity (momentum) collides with a relatively stationary target T. During collision their overlapping volumes get sheared off and produce light ion and nucleon clusters. After the collision the remaining parts of the projectile and target nuclei continue in their original trajectory with near pre-collision velocities. However, the projectile pre-fragment is now in excited state and emits nucleons, light ion clusters and gamma rays to decay to ground state. This second step is known as the ablation process. The abrasion-ablation model usually takes into account only projectile fragmentation. Target fragmentation is generally accounted for by swapping the projectile and target in the model with appropriate frame transformations. Theoretical formulations of the abrasion process are often based on Glauber multiple scattering theory and apply the optical limit potential approximation to the nucleus-nucleus multiple scattering series expansion in terms of an Eikonal approximation [4],[6], while the ablation part of the

model is based on the classical evaporation model of Weiskopf and Ewing, which treats the particle emission as a statistical process [5],[7].

The motivation behind this work is the inherent small angle approximation used in Eikonal expansions in the Glauber multiple scattering series, which serve as the foundation in the formulation of the abrasion model. The Eikonal expansions in the Glauber model are treated in terms of a high energy, small angle approximation, which assumes that the total Eikonal phase for the scattering is equal to the sum of individual phases for the scattering of the projectile by the target and also confines the scattering to the plane of the incident momentum [3], [4]. While the Glauber model has been successfully used in many applications, the validity of the model for three or more particles in the final state is unclear and, since light ion transport ($Z \leq 2$) is basically a three dimensional problem, it cannot be properly described by the Glauber model, which is limited to the plane of incident momentum [3],[8]. In this work, we have used the higher order correction terms to the phase shift operator in the calculation of the scattering amplitude in the Glauber model, as developed by Wallace who converted the partial wave series into a Fourier-Bessel expansion, based on expansion of the Legendre polynomials [9],[10], [11]. This creates an infinite series for the phase shift operator, where the leading term is same as the Glauber model and higher order terms are corrections to the phase shift operator. The expansion is exact in the sense that no small angle approximation is made. Based on Wallace's approach, we have developed four higher order correction terms to the phase shift operator for use in the development of the abrasion model. We have also used Gaussian approximations for the nuclear densities for the purpose of computational simplicity. A comparison of predictions incorporating two and four higher order terms to the phase shift with predictions from the previous model and experimental data [12] for various heavy ion data sets is presented.

2 Abrasion-Ablation Formulation

2.1 Abrasion Formalism

During a nuclear interaction, the cross section for abrading '*n*' projectile nucleons can be given as [13]:

$$\sigma_n = \binom{A_P}{n} 2\pi \int \left[1 - P\left(\vec{b}\right)\right]^n P\left(\vec{b}\right)^{A_F} b\,db \tag{1}$$

Where the binomial coefficient $\binom{A_P}{n}$ describes the number of possible combinations of nucleons that can be emitted from an ensemble of A_P identical nucleons with $A_F = A_P - n$.

In the above Eq.(1), $P(\vec{b})$ is the nucleon non-removal probability expressed as a function of impact parameter *'b'* and can be expressed as:

$$P\left(\vec{b}\right) = \exp\left[\frac{-2\,\mathrm{Im}\,\chi\left(\vec{b}\right)}{A_P}\right] \tag{2}$$

with the Eikonal phase function $\chi\left(\vec{b}\right)$ given in terms of Glauber model by Eq.(3):

$$\chi\left(\vec{b}\right) = -\frac{1}{\hbar v}\int_{-\infty}^{\infty} V\left(\vec{r}\right) dz \tag{3}$$

In the above Eq.(3), $V\left(\vec{r}\right)$ is the optical potential and 'v' is the relative velocity of the incoming particle in the incident momentum plane 'z'.

Eq.(1) treats all nucleons as identical objects. To differentiate between protons and neutrons in the projectile nucleus, a simple approach of substituting the binomial in Eq.(1) for all nucleons with binomials for protons and neutrons can be used [14]. Thus substituting Eq.(2) into Eq.(1) and separating the binomials to account for nucleon species, we can rewrite Eq.(1) as

$$\sigma_{nz} = \binom{N_P}{n}\binom{Z_P}{z} 2\pi\int\left[1-\exp\left[\frac{-2\,\mathrm{Im}\,\chi\left(\vec{b}\right)}{A_P}\right]\right]^{n+z}\left(\exp\left[\frac{-2\,\mathrm{Im}\,\chi\left(\vec{b}\right)}{A_P}\right]\right)^{A_P-n-z} bdb \tag{4}$$

where σ_{nz} is the cross section for abrading n out of N_P neutrons and z out of Z_P protons. It is implicitly assumed in the above expression, for simplicity, that the neutron and proton distributions in the projectile are completely uncorrelated.

The total absorption cross section be expressed in terms of abrasion cross section as a summation over all projectile nucleons as

$$\sigma_{abs} = \sum_{n=1}^{A_P}\sigma_n \tag{5}$$

which is

$$\sigma_{abs} = 2\pi\int\left[1-P\left(\vec{b}\right)^{A_P}\right] bdb \tag{6}$$

The momentum distributions of the projectile fragments are derived using the work by Haneishi and Fujita [15] for the derivation of nucleon momentum distributions in the rest frame of the projectile and can be expressed as

$$n(\boldsymbol{p}) = n_0\sum_{i=1}^{3} C_i \exp\left(\frac{-p_n^2}{2{p_i}^2}\right) \tag{7}$$

where p_n is the momentum of the nucleon in the projectile rest frame, p_i is the momentum width parameter given in terms of the Fermi momentum k_F and n_0 is the normalization constant. . The values for C_i and p_i are taken from Cucinotta et al. [3].

For the abrasion process, the nucleon momentum distribution can now be given as

$$\left(\frac{d^3\sigma}{d{p_n}^3}\right)_{abr} = \left(\sum_{1}^{n}\sigma_n\right)\left(n_0\sum_{i=1}^{3} C_i \exp\left(\frac{-p_n^2}{2{p_i}^2}\right)\right) \tag{8}$$

2.2 Ablation Formalism

In the ablation process, the excited prefragment nuclei from the abrasion process give up their excess energy and decay to their ground states by evaporating nucleons, light ion clusters and gamma rays. The nucleon emission spectra from the ablation process are described by using the Weisskopf-Ewing statistical decay model, which describes the probability of emission as a competing process [14], [7]. The probability function for the emission of particles used herein is from the works by Cucinotta et al. [3] and Kikuchi and Kawai [16], and is given as

$$P_i(j,E_i)=\frac{2\mu_i g_i E_i \sigma_{CN} w_0(E_j^*-E_i)}{\int_0^{(E_l^*-S_j)} P_l(j,E)dE} \tag{9}$$

The neutron momentum distribution for the ablation process can be described in terms of this probability function as

$$\left(\frac{d^3\sigma}{dp^3}\right)_{abl}=\sum_j \sigma_{abr}\left(A_j,Z_j,E_j^*\right)P_i\left(j,\boldsymbol{k}\right) \tag{10}$$

where the total momentum distribution from both abrasion and ablation processes is

$$\left(\frac{d^3\sigma}{dp^3}\right)_{total}=\left(\frac{d^3\sigma}{dp^3}\right)_{abr}+\left(\frac{d^3\sigma}{dp^3}\right)_{abl} \tag{11}$$

3 Derivation of the Phase Function Correction Terms

Wallace obtains the higher order correction terms to the phase shift operator in the Glauber model by deriving a relationship between partial wave representation and impact parameter representation of the scattering amplitude using an expansion of Legendre polynomials in terms of zero order Bessel functions [9],[17]. In his work, Wallace formulates a relationship between the Eikonal phase factor and the phase shift, thus creating an infinite series, where the first term is same as the Glauber model and higher order terms are correction terms. The total Eikonal phase is the sum of the zero order term and higher order correction terms in Wallace's model. Each term can be expressed as [11], [18]

$$\chi_n(b)=-\frac{(\mu)^{n+1}}{k(n+1)!}\left[\left(\frac{b}{k}\frac{\partial}{\partial b}-\frac{\partial}{\partial k}\right)\frac{1}{k}\right]^n\int_{-\infty}^{\infty}V^{n+1}\left((b^2+z^2)^{1/2}\right)dz \tag{12}$$

with $r=(b^2+z^2)^{1/2}$.

Calculation of the phase function requires knowledge of the optical potential. For purposes of this work, we use the optical potential term as given in [2] for the nucleus-nucleus scattering and its further approximation in the context of high energy scattering, using a one body Schrodinger equation, as

$$V(\vec{r})=\frac{2mA_P{}^2A_T{}^2}{N}\int d^3z\ \rho_T\left(\vec{z}\right)\int d^3y\rho_P\left(\vec{x}+\vec{y}+\vec{z}\right)\tilde{t}\left(e,\vec{y}\right) \tag{13}$$

with $\rho_T(\vec{z})$ and $\rho_P(\vec{x}+\vec{y}+\vec{z})$ being the target and projectile single particle nuclear densities respectively and $\tilde{t}(e,\vec{y})$ being the two particle transition amplitude. The single particle densities, calculated from their experimentally determined charge distributions, were assumed in previous work [19], to have Harmonic Well (HW) distributions for lighter nuclei (A≤ 20) and Wood-Saxon distribution for the heavier nuclei (A > 20). For the purpose of simplicity, in this work the densities have been assumed to have simple Gaussian distributionsl, given as

$$\rho_A(\vec{r}) = C_i \exp(-D_i r^2) \tag{14}$$

with $i = P,T$ representing the projectile and target constituents respectively. A justification of this simplification is presented in more detail in [1].

Using the single particle densities from Eq. (14) and applying them to calculate the optical potential, we can now write the zero order phase function term and the four higher order correction terms as

$$\chi_0(b) = \frac{1}{2}\sqrt{\frac{\pi}{N}} M \exp\left(-Nb^2\right) \tag{15}$$

$$\chi_1(b) = \frac{1}{4k}\sqrt{\frac{\pi}{2N}} M^2 \left(4Nb^2+1\right)\exp(-2Nb^2) \tag{16}$$

$$\chi_2 = -\frac{1}{12k^2}\sqrt{\frac{\pi}{3N}} M^3 \left(-36\, b^4 N^2\right)\exp\left(-3Nb^2\right) \tag{17}$$

$$\chi_3 = \frac{1}{48k^3}\sqrt{\frac{\pi}{4N}} M^4 \left(-24b^2N - 192b^4N^2 + 512b^6N^3 - 3\right)\exp(-4Nb^2) \tag{18}$$

$$\chi_4 = -\frac{1}{240k^4}\sqrt{\frac{\pi}{5N}} M^5 \left(8000b^6N^3 - 10000b^8N^4\right)\exp(-5Nb^2) \tag{19}$$

with $\chi(b) = \chi_0(b) + \chi_1(b) + \chi_2(b) + \chi_3(b) + \chi_4(b) + \ldots\ldots$

$$M = \pi^3 A_P A_T C_T C_P \sigma(e)\left[\alpha(e)+i\right](2\pi B(e))^{-\frac{3}{2}}\left(\left(D_P + \frac{1}{2B(e)}\right)\right)^{-\frac{3}{2}}\left\{D_T + D_P - \frac{D_P^2}{\left(D_P + \frac{1}{2B(e)}\right)}\right\}^{-\frac{3}{2}} \tag{20}$$

$$N = \left(\left\{D_P - \frac{D_P^2}{\left(D_P + \frac{1}{2B(e)}\right)}\right\} - \frac{\left\{D_P - \frac{D_P^2}{\left(D_P + \frac{1}{2B(e)}\right)}\right\}^2}{\left\{D_T + D_P - \frac{D_P^2}{\left(D_P + \frac{1}{2B(e)}\right)}\right\}}\right) \tag{21}$$

In the above equations, it can be clearly seen that the zero order term is exactly the same as the Glauber model and the higher order terms are correction terms.

4 Results and Conclusion

The study showed that the contributions of the higher order terms in the calculation of total and abrasion cross sections were only significant for the first two correction terms, especially at the lower energy regions. The contributions of the correction terms became smaller with increasing energy and were not significant enough for the third and fourth order correction terms. Comparison to the experimental data [12] show that the neutron double differential cross section predictions improved with the addition of two higher order correction terms. At angles larger than 30 degrees, the current work under predicts the cross section, which is due to the lack of isobar formation and decay channel in the current model. Overall there was a significant improvement in cross section prediction with addition of two correction terms, while third and fourth order term contributions were not significant.

The comparisons for two and four correction terms and the comparison to the experimental data are shown below:

Energy (**MeV/N**)	$\sigma_{\sum_{i=1}\chi_i}$ (mb)	$\sigma_{\sum_{i=0}^{1}\chi_i}$ (mb)	$\sigma_{\sum_{i=0}^{2}\chi_i}$ (mb)	$\sigma_{\sum_{i=0}^{3}\chi_i}$ (mb)	$\sigma_{\sum_{i=0}^{4}\chi_i}$ (mb)
100	784.32	1368.40	1640.73	1690.05	1688.81
200	774.21	1074.81	1119.02	1122.45	1122.45
300	773.91	1022.38	1050.22	1051.92	1051.92
500	780.40	1035.56	1060.73	1062.08	1062.82
1000	783.19	1004.09	1019.68	1020.28	1020.28
3000	781.38	864.69	866.73	866.76	866.76
5000	781.60	833.82	834.58	834.59	834.59
10000	781.97	805.01	805.15	805.15	805.15

Table 1: Total Abrasion Cross Section with Correction Terms for ^{12}C on ^{27}Al at 10 Degrees

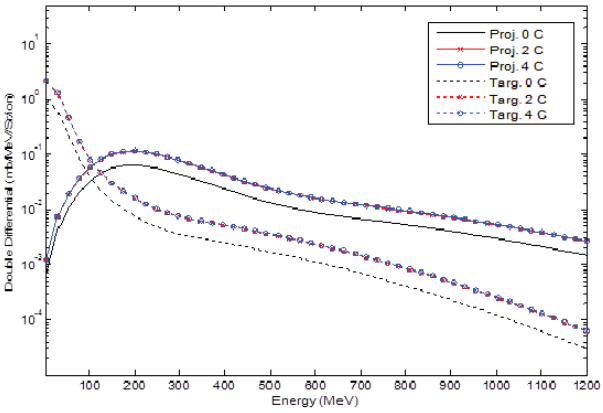

Fig.1: Comparison of neutron differential cross section from abrasion process for 400 MeV/nucleon ^{14}N on ^{12}C at 40^0 scattering angle for 0, 2 and 4 correction terms.

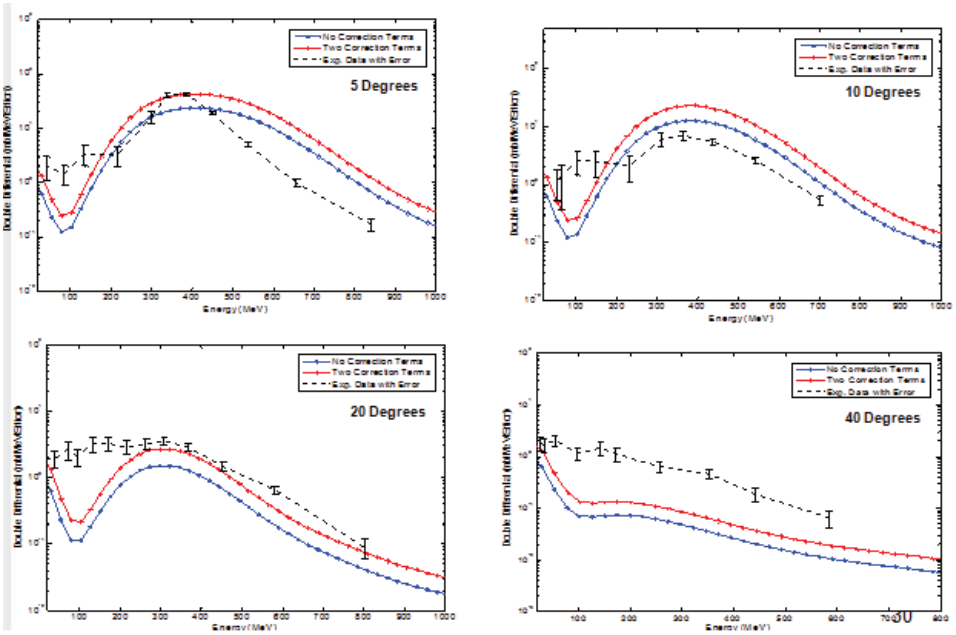

Fig. 2: Comparison to the experimental data for 400 MeV/nucleon ^{14}N beam colliding on ^{12}C Target

References

[1] S. Bhatt, "Derivation of Correction Terms to the Eikonal Approximations in the Formulation of Analytical Abrasion-Ablation Model," PhD Nuclear Engineering, Department of Nuclear Engineering, University of Tennessee, 2012.

[2] J. W. Wilson, W. Schimmerling, L. Townsend, G. S. Khandelwal, F. Khan, J. E. Nearly, F. A. Cucinotta, and J. Norbury, "Transport methods and interactions for space radiation," *National Technical Information Service*, NASA RP-1257, 1991.

[3] F. A. Cucinotta, J. W. Wilson, and L. W. Townsend, "Abrasion-ablation model for neutron production in heavy ion collisions," *Nuclear physics. A*, vol. 619, pp. 202-12, 1997.

[4] J. Bowman, W. Swiatecki, and C. Tsang, "Abrasion and ablation of heavy ions," *LBL-2908, University of California*, pp. 391-394, 1973.

[5] J. Hufner, K. Schafer, and B. Schurmann, "Abalation abrasion in reactions between relativistic heavy ions," *Physical Review A*, vol. 12, pp. 1888-1897, 1975.

[6] J. W. Wilson, "Multiple scattering of heavy ions, Glauber theory, and optical model," *Physics Letters B*, vol. 52, pp. 149-152, 1974B.

[7] V. F. Weisskopf and D. H. Ewing, "On the yield of nuclear reactions with heavy elements," *Physical Review*, vol. 57, pp. 472-485, 1940.

[8] F. A. Cucinotta, "Theory of alpha-nucleus collisions at high energies," Ph.D Dissertation, Physics Department, Old Dominion University, 1988.

[9] S. Wallace, "High energy expansion of scattering amplitudes," *Physical Review D,* vol. 8, 1973.

[10] S. J. Wallace, "Multiple-scattering eikonal expansion: systematic corrections to the Glauver theory," *Physcial Review C,* vol. 8, pp. 2043-2055, 1971.

[11] D. Waxman, C. Wilkin, J. F. Germond, and R. J. Lombard, "Eikonal corrections for spin-orbit potentials," *Physical Review C,* vol. 24, pp. 578-582, 1981.

[12] T. Nakamura and L. Heilbronn, "Handbook on Secondary Particle Production and Transport by High-Energy Heavy Ions,". CD ROM, New Jersery (NJ): World Scientific, 2006.

[13] M. Bleszynski and C. Sander, "Geometrical Aspects of high energy peripheral scattering," *Nuclear Physics A* vol. 326, pp. 525-535, 1979.

[14] J. Hufner, "Heavy fragments produced in proton-nucleus and nucleus-nucleus collisions at relativistic energies," *Physics Reports,* vol. 125, pp. 129-185, 1985.

[15] Y. Haneishi and T. Fujita, "Problem of backward proton production.," *Physical Review C,* vol. 33, pp. 260-274, 1986.

[16] K. Kikuchi and M. Kawai, "Nuclear matter and nuclear reactions," pp. 260-268, 1968.

[17] S. J. Wallace, "Eikonal Expansion * +," *Physics Review Letters,* vol. 27, 1971.

[18] F. Carstoiu and R. J. Lombard, "Eikonal expansions for total cross sections of heavy ions," *Physical Review C,* vol. 48, 1993.

[19] L.W. Townsend, "Abrasion cross sections for ^{20}Ne projectiles at 2.1 GeV/nucleon," *Canadian Journal of Physics*, vol. 61, pp. 93-98, 1983.

Eikonal reaction theory for neutron removal reactions

Kosho Minomo, Takuma Matsumoto, Kazuyuki Ogata, and Masanobu Yahiro
Department of Physics, Kyushu University, Fukuoka 812-8581, Japan
Research Center for Nuclear Physics (RCNP), Osaka University, Ibaraki 567-0047, Japan

Abstract
We present an accurate method of treating neutron removal reactions and it's applications. According to the method, the nuclear and Coulomb breakup processes are consistently treated by the method of the continuum discretized coupled channels. This method is referred to as the eikonal reaction theory (ERT). We analyze the two types of removal reactions of ^{31}Ne and ^{6}He with ERT.

1 Introduction

Unstable nuclei have exotic properties such as the halo structure [1–3] and the change of magicity for nuclei in the region called "island of inversion" [4]. One of the important experimental tools for exploring such exotic properties is the nucleon removal reaction; see for example Ref. [5]. Very recently, a halo structure of ^{31}Ne has been reported following the experiment on the one-neutron removal reaction σ_{-n} at 230 MeV/nucleon not only for a ^{12}C target but also for a ^{208}Pb target [6]. This is the heaviest halo nucleus at the present stage confirmed experimentally, which also resides within the region of "island of inversion".

The nucleon removal reaction is composed of the exclusive elastic breakup component and the inclusive nucleon-stripping component. For analyses of such exclusive and inclusive reactions, Glauber model [7] is often used. This model, however, becomes breakdown for Coulomb breakup reactions because of the adiabatic approximation. Meanwhile, the method of continuum discretized coupled channels (CDCC) [8, 9] is highly reliable for describing exclusive reactions but not applicable to inclusive reactions. Both method have different demerits.

In this paper, we introduce an accurate method of treating the one-neutron removal reaction at intermediate incident energies induced by both nuclear and Coulomb interactions. In the method, the nuclear and Coulomb breakup processes are accurately treated using CDCC without making the adiabatic approximation to the latter, so that the calculated cross section is reliable even in the presence of the Coulomb interaction. Thus, this method called the eikonal reaction theory (ERT) [10] is an essential extension of the Glauber model and CDCC. ERT is applied to the one-neutron removal from ^{31}Ne and the two-neutron removal from ^{6}He for both light (^{12}C) and heavy (^{208}Pb) targets and we show that ERT is useful for describing neutron removal reactions.

2 Eikonal reaction theory (ERT)

We consider as the scattering of a two-body projectile (P) composed of a core nucleus (c) and a valence neutron (n). Including a target (A), we take the three-body (c+n+A) system shown as Fig. 1

The starting point is the three-body Schrödinger equation,

$$\left[-\frac{\hbar^2}{2\mu}\nabla^2_{\boldsymbol{R}} + h_{\rm P} + U_{\rm c}^{(\rm Nucl)}(r_{\rm c}) + U_{\rm c}^{(\rm Coul)}(r_{\rm c}) + U_n^{(\rm Nucl)}(r_n) - E\right]\Psi(\boldsymbol{R},\boldsymbol{r}) = 0\,, \tag{1}$$

where μ is the reduced mass between P and A. The three-dimensional vector $\boldsymbol{R} = (\boldsymbol{b}, Z)$ stands for the coordinate between P and A, whereas $\boldsymbol{r}_x$ ($x = n$ or c) is the coordinate between x and A and $\boldsymbol{r}$ means the coordinate between c and n. The operator $h_{\rm P}$ is the internal Hamiltonian of the projectile. $U_n^{(\rm Nucl)}$ is the nuclear part of the optical potential between n and A, and $U_{\rm c}^{(\rm Nucl)}$ and $U_{\rm c}^{(\rm Coul)}$ are, respectively, the nuclear and Coulomb parts of the optical potential between c and A.

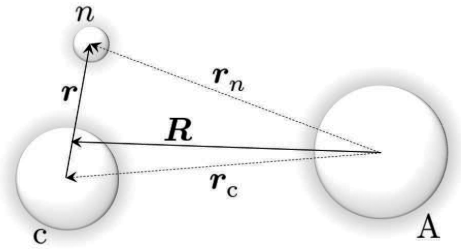

Fig. 1: The three-body model for a two-body projectile

First we make a product assumption for the total wave function so that it is devided into the plane wave part $\hat{O}$ and the remainder ψ,

$$\Psi = \hat{O}\psi(\boldsymbol{R}, \boldsymbol{r}) \,, \tag{2}$$

$$\hat{O} \equiv \frac{1}{\sqrt{\hbar\hat{v}}} e^{i\hat{K}\cdot Z} \,, \quad \hat{K} \equiv \frac{\sqrt{2\mu(E - h_{\rm P})}}{\hbar} \,, \quad \hat{v} \equiv \frac{\hbar\hat{K}}{\mu} \,. \tag{3}$$

we apply the eikonal approximation to the product form (2), namely, $\nabla^2_{\boldsymbol{R}}\psi$ is neglected in the kinetic energy term. It leads to the following equation,

$$i\frac{d\psi}{dZ} = \hat{O}^\dagger U \hat{O}\psi. \tag{4}$$

The scattering matrix as a formal solution to Eq.(4) is

$$S = \exp\Big[-i\mathcal{P}\int_{-\infty}^{\infty} dZ \hat{O}^\dagger \Big(U_c^{(\rm Nucl)} + U_c^{(\rm Coul)} + U_n^{(\rm Nucl)} \Big) \hat{O} \Big]. \tag{5}$$

Here, $\mathcal{P}$ is the "time" ordering (Z ordering) operator which describes the multistep scattering processes accurately.

In the Glauber model, the adiabatic approximation is made, in which $h_{\rm P}$ is replaced with the ground-state energy of the projectile, and hence $\hat{O}^\dagger U \hat{O}$ and $\mathcal{P}$ in Eq. 5 are reduced to $U/(\hbar v_0)$ and 1, respectively, where v_0 is the velocity of P in the ground state relative to A. At intermediate energies, this treatment is known to be valid for short-range nuclear interactions, but not for the long-range Coulomb interactions. Therefore, we make the adiabatic approximation in the evaluation of only $\hat{O}^\dagger U_n^{(\rm Nucl)} \hat{O}$, i.e., we use

$$\hat{O}^\dagger U_n^{(\rm Nucl)} \hat{O} \to U_n^{(\rm Nucl)}/(\hbar v_0) \,. \tag{6}$$

$U_n^{(\rm Nucl)}/(\hbar v_0)$ is just a number so that this term is commutable with the operators $\hat{O}$ and $\mathcal{P}$. As a result, S can be separated into the core part $S_{\rm c}$ and the neutron part S_n,

$$S \approx S_{\rm c} S_n \tag{7}$$

with

$$S_{\rm c} \equiv \exp\left[-i\mathcal{P}\int_{-\infty}^{\infty} dZ \hat{O}^\dagger \Big(U_{\rm c}^{(\rm Nucl)} + U_{\rm c}^{(\rm Coul)} \Big) \hat{O} \right] , \tag{8}$$

$$S_n \equiv \exp\left[-\frac{i}{\hbar v_0}\int_{-\infty}^{\infty} dZ \, U_n^{(\rm Nucl)} \right] . \tag{9}$$

This separation of S is the essence of ERT. It should be noted that one cannot evaluate $S_{\rm c}$ directly with Eq. (8), since it includes the operators $\hat{O}$ and $\mathcal{P}$.

The one-neutron removal cross section is composed of stripping ($\sigma_{n:\rm str}$) and elastic breakup ($\sigma_{\rm bu}$) cross sections.

$$\sigma_{-n} = \sigma_{n:\rm str} + \sigma_{\rm bu} \tag{10}$$

$\sigma_{n:\rm str}$ and are written by $S_{\rm c}, S_n$ and the projectile ground-state wave function φ_0,

$$\begin{aligned} \sigma_{n:\rm str} &= \int d^2\boldsymbol{b}\langle\varphi_0||S_{\rm c}|^2(1-|S_n|^2)|\varphi_0\rangle \\ &= [\sigma_{\rm R} - \sigma_{\rm bu}] - [\sigma_{\rm R}(-n) - \sigma_{\rm bu}(-n)], \end{aligned} \tag{11}$$

where $\sigma_{\rm R}, \sigma_{\rm bu}$ are the total reaction and elastic breakup cross sections, respectively,

$$\sigma_{\rm R} = \int d^2\boldsymbol{b}\left[1 - \left|\langle\varphi_0|S_cS_n|\varphi_0\rangle\right|^2\right], \tag{12}$$

$$\sigma_{\rm bu} = \int d^2\boldsymbol{b}\left[\langle\varphi_0||S_cS_n|^2|\varphi_0\rangle - \left|\langle\varphi_0|S_cS_n|\varphi_0\rangle\right|^2\right], \tag{13}$$

and $\sigma_{\rm R}(-n), \sigma_{\rm bu}(-n)$ correspond to the total reaction and elastic breakup, respectively, in which $S_{\rm c}S_n$ is replaced with $S_{\rm c}$. They are solution to the following equation,

$$\left[-\frac{\hbar^2}{2\mu}\nabla^2_{\boldsymbol{R}} + h_{\rm P} + U_{\rm c}^{(\rm Nucl)}(r_{\rm c}) + U_{\rm c}^{(\rm Coul)}(r_{\rm c}) - E\right]\Psi(\boldsymbol{R},\boldsymbol{r}) = 0\,. \tag{14}$$

Eqs.(1) and (14) can be solved with CDCC. This means that ERT makes CDCC applicable to inclusive reactions.

3 One-neutron removal from ^{31}Ne

We apply ERT to the one-neutron removal reactions for the ^{31}Ne+^{12}C scattering at 230 MeV/nucleon and the ^{31}Ne+^{208}Pb scattering at 234 MeV/nucleon with a three-body (^{30}Ne+n+A) model. The optical potentials for the n-target and ^{30}Ne-target subsystems are obtained by folding the effective nucleon-nucleon interaction [11] with one-body nuclear densities. The densities of P and A are constructed by the same method as in Ref. [12]. We assume the ground state of ^{31}Ne to be either the $^{30}{\rm Ne}(0^+)\otimes 1{\rm p}3/2$ or the $^{30}{\rm Ne}(0^+)\otimes 0{\rm f}7/2$, with the one-neutron separation energy $S_n = 0.33$ MeV [13]. As for the breakup states, we include s-, p-, d-, f-, and g-waves up to the relative momentum between ^{30}Ne and n of 0.8 fm^{-1}. For more detailed numerical inputs, see Ref. [10].

Table 1 shows the elastic-breakup cross section $\sigma_{\rm bu}$, the one-neutron stripping cross section $\sigma_{n:\rm str}$, the one-neutron removal cross section σ_{-n}, and the spectroscopic factor $\mathcal{S} = \sigma_{-n}^{\rm exp}/\sigma_{-n}^{\rm th}$ for ^{12}C and ^{208}Pb targets. $\mathcal{S}$ calculated with the 1p3/2 ground-state neutron configuration little depends on the target and less than unity, but that with the 0f7/2 configuration does not satisfy these conditions. Therefore, we can infer that the major component of the ground state of ^{31}Ne is $^{30}{\rm Ne}(0^+)\otimes 1{\rm p}3/2$ with $\mathcal{S}\sim 0.69$. We adopt this configuration in the following.

Since the potential between ^{30}Ne and n is not well known, we change each of the potential parameters by 30% and see how this ambiguity of the potential affects the resulting value of $\mathcal{S}$. We obtain $\mathcal{S} = 0.693 \pm 0.133 \pm 0.061$ for a ^{12}C target and $\mathcal{S} = 0.682 \pm 0.133 \pm 0.062$ for a ^{208}Pb target; the second and third numbers following the mean value stand for the theoretical and experimental uncertainties, respectively. Thus, $\mathcal{S}$ includes a sizable theoretical uncertainty. This situation completely changes if we look at the asymptotic normalization coefficient $C_{\rm ANC}$, i.e., $C_{\rm ANC} = 0.320 \pm 0.010 \pm 0.028$ fm$^{-1/2}$ for a ^{12}C target and $C_{\rm ANC} = 0.318 \pm 0.008 \pm 0.029$ fm$^{-1/2}$ for a ^{208}Pb target. Thus, $C_{\rm ANC}$ has a

Table 1: Integrated cross sections and the spectroscopic factor for the ^{31}Ne-^{12}C scattering at 230 MeV/nucleon and the ^{31}Ne-^{208}Pb scattering at 234 MeV/nucleon. The cross sections are presented in unit of mb and the data are taken from Ref. 6.

	^{12}C target			^{208}Pb target		
	$p_{3/2}$	$f_{7/2}$	Exp.	$p_{3/2}$	$f_{7/2}$	Exp.
$\sigma_{\rm EB}$	23.3	3.3		799.5	73.0	(540)
$\sigma_{n:\rm str}$	90	29		244	53	
σ_{-n}	114	32	79	1044	126	712
$\mathcal{S}$	0.693	2.47		0.682	5.65	

much smaller theoretical uncertainty than $\mathcal{S}$. This means that the one-nucleon removal reaction is quite peripheral.

The experimental value of S_n has a large error, $S_n = 0.29 \pm 1.64$ MeV [13], so we also see the S_n dependence of $C_{\rm ANC}$ and $\mathcal{S}$ When $S_n = 0.1$ MeV, $C_{\rm ANC} = 0.128 \pm 0.003 \pm 0.011$ fm$^{-1/2}$ and $\mathcal{S} = 0.530 \pm 0.084 \pm 0.047$ for a ^{12}C target, and $C_{\rm ANC} = 0.105 \pm 0.004 \pm 0.010$ fm$^{-1/2}$ and $\mathcal{S} = 0.358 \pm 0.057 \pm 0.033$ for a ^{208}Pb target. These values are plotted in Fig. 2. $C_{\rm ANC}$ and $\mathcal{S}$ are sensitive to the value of S_n. We can see from the S_n dependence of $\mathcal{S}$ for a ^{208}Pb target that $\mathcal{S} < 1$ when $S_n < 0.6$ MeV. It is thus necessary to determine S_n experimentally in the future to evaluate $C_{\rm ANC}$ and $\mathcal{S}$ properly. However, we can say at least that $C_{\rm ANC}$ has a smaller theoretical error and weaker target dependence than $\mathcal{S}$ for any value of S_n.

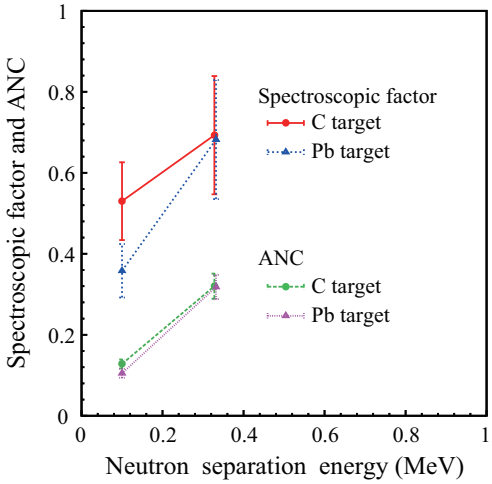

Fig. 2:

4 Two-neutron removal from ^{6}He

ERT could be easily extended to three-body projectile. Combining this four-body ERT with four-body CDCC [14, 15], we can calculate two-neutron removal cross sections. ERT is applied to two-neutron removal reactions of ^{6}He on ^{12}C and ^{208}Pb targets at 240 MeV/nucleon. In this case, the projectile is treated as a three-body ($\alpha + n + n$) system and hence four-body CDCC is used.

We use the microscopic folding potentials obtained by folding the Melbourne nucleon-nucleon

g-matrix interaction [16] with the densities obtained by the spherical Hartree-Fock calculation with the Gogny D1S interaction. [17, 18] The present framework has no adjustable parameters. the three-body calculation of ^{6}He and the model space of the reaction calculation is the same as in Ref. [15], with which good convergence is achieved.

Table 2: Integrated cross sections for two-neutron removal reaction of ^{6}He on ^{12}C and ^{208}Pb targets at 240 MeV/nucleon. The cross sections are presented in unit of mb and the experimental data are taken from Ref. [19].

	^{12}C target		^{208}Pb target	
	Calc.	Exp.	Calc.	Exp.
$\sigma_{n:\mathrm{str}}$	153.4	127 ± 14	353.6	320 ± 90
$\sigma_{2n:\mathrm{str}}$	29.0	33 ± 23	148.9	180 ± 100
σ_{-2n}	198.5	190 ± 18	1016.6	1150 ± 90

Table 2 shows the one- and two-neutron stripping cross sections, $\sigma_{n:\mathrm{str}}$ and $\sigma_{2n:\mathrm{str}}$, respectively, and the two-neutron removal cross section σ_{-2n}. The present framework well reproduces the experimental data [19] with no adjustable parameters. Thus, we can clearly see the reliability of ERT for two-neutron removal reactions on both light and heavy targets.

5 Summary

We have presented an accurate method, which called the eikonal reaction theory (ERT), of treating the neutron removal reaction at intermediate energies. According to the method, the nuclear and Coulomb breakup processes are accurately and consistently treated by the framework of CDCC. ERT is an extention of the Glauber model and CDCC.

C_{ANC} and $\mathcal{S}$ of the last neutron in ^{31}Ne are evaluated from the measured one-neutron removal reaction. For the $1p3/2$ orbit, $\mathcal{S}$ and C_{ANC} have weak target dependence and $\mathcal{S} < 1$. On the other hand, for the $1f7/2$ orbit, $\mathcal{S}$ and C_{ANC} have strong target dependence and $\mathcal{S} > 1$. These results indicate that the last neutron mainly occupy the $1p3/2$ orbit. C_{ANC} has a smaller theoretical error and weaker target-dependence than $\mathcal{S}$. Thus, C_{ANC} is determined more accurately than $\mathcal{S}$. This means that the one-neutron removal reaction is quite peripheral. We could understand the one-neutron removal from ^{31}Ne within the naive shell model.

The application of ERT to two-neutron removal reactions of ^{6}He is also shown. The present framework well reproduces the experimental data with no adjustable parameters. It was clearly shown that ERT is useful for describing neutron-removal reactions.

acknowledgements

The computation was carried out using the computer facilities at the Research Institute for Information Technology, Kyushu University. This research was supported in part by Grant-in-Aid of the Japan Society for the Promotion of Science (JSPS).

References

[1] I. Tanihata *et al.*, Phys. Lett. B **289** (1992), 261.
I. Tanihata, J. of Phys. G **22** (1996), 157.

[2] A. S. Jensen *et al.*, Rev. Mod. Phys. **76** (2004), 215.

[3] B. Jonson, Phys. Rep. **389** (2004), 1.

[4] E. K. Warburton, J. A. Becker, and B. A. Brown, Phys. Rev. C **41** (1990), 1147.

[5] A. Gade *et al*., Phys. Rev. C **77** (2008), 044306.
[6] T. Nakamura *et al*., Phys. Rev. Lett. **103** (2009), 262501.
[7] R. J. Glauber, in *L*ectures in Theoretical Physics Vol. 1 (Interscience, New York, 1959), p. 315.
[8] M. Kamimura, M. Yahiro, Y. Iseri, Y. Sakuragi, H. Kameyama, and M. Kawai, Prog. Theor. Phys. Suppl. Vol. 89 (1986), 1.
[9] N. Austern, Y. Iseri, M. Kamimura, M. Kawai, G. Rawitscher, and M. Yahiro, Phys. Rep. **154** (1987), 125.
[10] Yahiro, M., Ogata, K., Minomo, K.: Eikonal Reaction Theory for Neutron Removal Reaction. Prog. Theo. Phys. **126**, 167 (2011).
[11] B. Abu-Ibrahim, W. Horiuchi, A. Kohama, and Y. Suzuki, Phys. Rev. C **77** (2008), 034607.
[12] W. Horiuchi, Y. Suzuki, P. Capel, and D. Baye, Phys. Rev. C **81** (2010), 024606.
[13] B. Jurado et al., Phys. Lett. B **649** (2007), 43.
[14] M. Rodríguez-Gallardo, J. M. Arias, J. Gómez-Camacho, A. M. Moro, I. J. Thompson and J. A. Tostevin, Phys. Rev. C **80** (2009), 051601(R).
[15] T. Matsumoto, K. Katō, and M. Yahiro, Phys. Rev. C **82** (2010), 051602, arXiv:1006.0668.
[16] K. Amos, P. J. Dortmans, H. V. von Geramb, S. Karataglidis, and J. Raynal, in *Advances in Nuclear Physics*, edited by J. W. Negele and E. Vogt(Plenum, New York, 2000) Vol. 25, p. 275.
[17] J. Decharge and D. Gogny, Phys. Rev. C **21** (1980), 1568.
[18] J. F. Berger, M. Girod, and D. Gogny, Comp. Phys. Comm. **63** (1991), 365.
[19] T. Aumann *et al*., Phys. Rev. C **59**, 1252 (1999).

Ab initio calculations of light-ion reactions

Petr Navrátil[1,2]*, Sofia Quaglioni*[2]*, Simone Baroni*[3]*, and Robert Roth*[4]
[1]TRIUMF, 4004 Wesbrook Mall, Vancouver, BC V6T 2A3, Canada
[2]Lawrence Livermore National Laboratory, P.O. Box 808, L-414, Livermore, CA 94551, USA
[3]Physique Nucléaire Théorique, Université Libre de Bruxelles, C.P. 229, B-1050 Bruxelles, Belgium
[4]Institut für Kernphysik, Technische Universität Darmstadt, 64289 Darmstadt, Germany

Abstract
In recent years, significant progress has been made in *ab initio* nuclear structure and reaction calculations based on input from QCD employing Hamiltonians constructed within chiral effective field theory. In this contribution, we present one of such promising techniques capable of describing simultaneously both bound and scattering states in light nuclei. By combining the resonating-group method (RGM) with the *ab initio* no-core shell model (NCSM), we complement a microscopic cluster approach with the use of realistic interactions and a microscopic and consistent description of the clusters. We discuss applications to light nuclei scattering, radiative capture and fusion reactions.

1 Introduction

Nuclei are quantum many-body systems with both bound and unbound states. One of the major challenges for theoretical nuclear physics is to provide a unified description of structural and reaction properties of nuclei that is based on the fundamental underlying physics: the constituent nucleons and the QCD-based realistic interactions among them. A predictive theory of reactions of light nuclei is needed for many reasons.

First, it would greatly help our understanding of nuclear reactions important for astrophysics. Some of the outstanding light-nucleus uncertainty sources in astrophysics applications include: reactions leading to the nucleosynthesis of ^{8}B (and the production of the solar neutrinos measured in terrestrial experiments) such as the ^{7}Be$(p,\gamma)^8$B and ^{3}He$(\alpha,\gamma)^7$Be radiative capture rates; the thermonuclear reaction rates of α capture on ^{8}Be and ^{12}C nuclei during the stellar helium burning.

Furthermore, nuclear reactions are one of the best tools for studying exotic nuclei, which have become the focus of the next generation experiments with rare-isotope beams. These are nuclei for which most low-lying states are unbound, so that a rigorous analysis requires scattering boundary conditions. In addition, much of the information we have on the structure of these short-lived systems is inferred from reactions with other nuclei.

Finally, low-energy fusion reactions represent the primary energy-generation mechanism in stars, and could potentially be used for future energy generation on earth. Examples of these latter reactions include the d+^{3}H$\rightarrow$ n+^{4}He fusion used at ITER and at the National Ignition Facility (NIF). Even though there have been many experimental investigations of the cross sections of this reaction, there are still open issues. A first-principles theory based on accurate two-nucleon (NN) and three-nucleon (NNN) forces will provide the predictive power to reduce the uncertainty in the reaction rate at very low temperatures; provide an understanding of the reaction rate dependence on the polarization induced by the strong magnetic fields (characteristic of both inertial and magnetic confinement); and clarify the influence of non-local thermal equilibrium in plasma environments.

In this contribution, we describe the recently introduced *ab initio* many-body approach to reactions on light nuclei [1] that combines the resonating-group method (RGM) [2] with the *ab initio* no-core shell model (NCSM) [3]. We discuss examples of calculations relevant for nuclear astrophysics, ^{7}Be$(p,\gamma)^8$B radiative capture, calculations of the d-^{3}He and d-^{3}H fusion reactions, and investigations of the ground-state (g.s.) resonance of the exotic nucleus ^{7}He.

2 *Ab initio* NCSM/RGM

The *ab initio* nuclear reaction approach that we are developing is an extension of the *ab initio* no-core shell model (NCSM) [3]. The innovation which allows us to go beyond bound states and treat reactions is the use of cluster basis states in the spirit of the resonating-group method,

$$|\Phi^{J^\pi T}_{\nu r}\rangle = \Big[\big(\,|A{-}a\,\alpha_1 I_1^{\pi_1} T_1\rangle\,|a\,\alpha_2 I_2^{\pi_2} T_2\rangle\,\big)^{(sT)}\,Y_\ell\,(\hat{r}_{A-a,a})\Big]^{(J^\pi T)}\,\frac{\delta(r-r_{A-a,a})}{r r_{A-a,a}}\,, \tag{1}$$

in which each nucleon cluster is described within the NCSM. The above translational invariant cluster basis states describe two nuclei (a target and a projectile composed of $A{-}a$ and a nucleons, respectively) whose centers of mass are separated by the relative coordinate $\vec{r}_{A-a,a}$ and that are traveling in a $^{2s}\ell_J$ wave or relative motion (with s the channel spin, ℓ the relative momentum, and J the total angular momentum of the system). Additional quantum numbers characterizing the basis states are parity $\pi = \pi_1\pi_2(-1)^\ell$ and total isospin T. For the intrinsic (antisymmetric) wave functions of the two nuclei we employ the eigenstates $|A{-}a\,\alpha_1 I_1^{\pi_1} T_1\rangle$ and $|a\,\alpha_2 I_2^{\pi_2} T_2\rangle$ of the $(A-a)$- and a-nucleon intrinsic Hamiltonians, respectively, as obtained within the NCSM approach. These are characterized by the spin-parity, isospin and energy labels $I_i^{\pi_i}, T_i$, and α_i, respectively, where $i = 1, 2$. In our notation, all these quantum numbers are grouped into a cumulative index $\nu = \{A{-}a\,\alpha_1 I_1^{\pi_1} T_1;\, a\,\alpha_2 I_2^{\pi_2} T_2;\, s\ell\}$. Finally, we note that the channel states (1) are not antisymmetric with respect to exchanges of nucleons pertaining to different clusters. Therefore, to preserve the Pauli principle one has to introduce the appropriate inter-cluster antisymmetrizer, schematically $\hat{\mathcal{A}}_\nu = \sqrt{\frac{(A-a)!a!}{A!}}\left(1 + \sum_{P\neq id}(-)^p P\right)$, where the sum runs over all possible permutations of nucleons P different from the identical one that can be carried out between two different clusters and p is the number of interchanges characterizing them.

The channel states (1), fully antisimmetrized by the action of the antisymmetrization operator $\hat{A}_\nu$, are used as a continuous basis set to expand the many-body wave function,

$$|\Psi^{J^\pi T}\rangle \;=\; \sum_\nu \int dr r^2\,\hat{\mathcal{A}}_\nu |\Phi^{J^\pi T}_{\nu r}\rangle \frac{[\mathcal{N}^{-1/2}\chi]^{J^\pi T}_\nu(r)}{r}\,, \tag{2}$$

where $\chi^{J^\pi T}_\nu(r)$ represent continuous amplitudes determined by solving the orthogonalized RGM equations:

$$\sum_{\nu'} \int dr' r'^2 [\mathcal{N}^{-\frac{1}{2}}\mathcal{H}\,\mathcal{N}^{-\frac{1}{2}}]^{J^\pi T}_{\nu\nu'}(r,r')\frac{\chi^{J^\pi T}_{\nu'}(r')}{r'} = E\,\frac{\chi^{J^\pi T}_\nu(r)}{r}. \tag{3}$$

Here $\mathcal{N}^{J^\pi T}_{\nu\nu'}(r,r')$ and $\mathcal{H}^{J^\pi T}_{\nu\nu'}(r,r')$, commonly referred to as integration kernels, are respectively the overlap (or norm) and Hamiltonian matrix elements over the antisymmetrized basis (1), *i.e.*:

$$\mathcal{N}^{J^\pi T}_{\nu'\nu}(r',r) = \left\langle \Phi^{J^\pi T}_{\nu' r'}\right|\hat{\mathcal{A}}_{\nu'}\hat{\mathcal{A}}_\nu\left|\Phi^{J^\pi T}_{\nu r}\right\rangle\,,\; \mathcal{H}^{J^\pi T}_{\nu'\nu}(r',r) = \left\langle \Phi^{J^\pi T}_{\nu' r'}\right|\hat{\mathcal{A}}_{\nu'} H \hat{\mathcal{A}}_\nu\left|\Phi^{J^\pi T}_{\nu r}\right\rangle \tag{4}$$

where H is the microscopic $A-$nucleon Hamiltonian and E is the total energy in the center of mass (c.m.) frame. The calculation of the above many-body matrix elements, which contain all the nuclear structure and antisymmetrization properties of the system under consideration, represents the main task in performing RGM calculations. Further details are given in Refs. [4,5]. In the applications presented in Sec. 3 and 4 we employ SRG-evolved [6,7] chiral N^{3}LO [8] NN potentials (SRG-N^{3}LO).

3 Applications

3.1 The ^{7}Be(p,γ)^{8}B radiative capture

The ^{7}Be$(p,\gamma)^8$B radiative capture is the final step in the nucleosynthetic chain leading to ^{8}B and one of the main inputs of the standard model of solar neutrinos. Recently, we have performed the first *ab initio* many-body calculation [9], of this reaction starting from the SRG-N^{3}LO NN interaction with $\Lambda = 1.86$

fm^{-1}. Using p-^{7}Be channel states including the five lowest $N_{\max} = 10$ eigenstates of ^{7}Be (the $\frac{3}{2}^-$ ground and the $\frac{1}{2}^-$,$\frac{7}{2}^-$, and first and second $\frac{5}{2}^-$ excited states), we solved Eq. (3) first with bound-state boundary conditions to find the bound state of ^{8}B, and then with scattering boundary conditions to find the p-^{7}Be scattering wave functions. Former and latter wave functions were later used to calculate the capture cross section, which, at solar energies, is dominated by non-resonant $E1$ transitions from p-^{7}Be S- and D-waves into the weakly-bound ground state of ^{8}B. All stages of the calculation were based on the same harmonic oscillator (HO) frequency of $\hbar\Omega = 18$ MeV, which minimizes the g.s. energy of ^{7}Be. The largest model space achievable for the present calculation within the full NCSM basis is $N_{\max} = 10$. At this basis size, the ^{7}Be g.s. energy is very close to convergence as indicated by a fairly flat frequency dependence in the range $16 \leq \hbar\Omega \leq 20$ MeV, and the vicinity to the $N_{\max} = 12$ result obtained within the importance-truncated NCSM [10, 11]. The choice of $\Lambda = 1.86$ fm^{-1} in the SRG evolution of the N^{3}LO NN interaction leads to a single 2^+ bound state for ^{8}B with a separation energy of 136 keV quite close to the observed one (137 keV). This is very important for the description of the low-energy behavior of the ^{7}Be$(p,\gamma)^8$B astrophysical S-factor, known as S_{17}. We note that the NNN interaction induced by the SRG evolution of the NN potential is repulsive in the Λ-range $\sim$ 1.8-2.1 fm^{-1}, and, in very light nuclei, its contributions are canceled to a good extent by those of the initial attractive chiral NNN force (which is also SRG evolved) [12, 13].

The resulting S_{17} astrophysical factor is compared to several experimental data sets in Figure 1. Energy dependence and absolute magnitude follow closely the trend of the indirect Coulomb breakup measurements of Shümann et al. [14, 15], while somewhat underestimating the direct data of Junghans *et al*. [16]. The resonance, particularly evident in these and Filippone's data, is due to the $M1$ capture, which does not contribute to a theoretical calculation outside of the narrow ^{8}B 1^+ resonance and is negligible at astrophysical energies [17, 18]. The $M1$ operator, for which any dependence upon two-body currents needs to be included explicitly, poses more uncertainties than the Siegert's $E1$ operator. We plan to calculate its contribution in the future. The shape is also quite similar to that obtained within the microscopic three-cluster model [19] (see the dashed line in Fig. 1 (a)) used, after scaling to the data, in the most recent S_{17} evaluation [18]. The contributions from the initial 1^-, 2^- and 3^- partial waves are shown in panel (b) of Fig. 1.

The convergence of our results with respect to the size of the HO model space was assessed by means of calculations up to $N_{\max} = 12$ within the importance-truncation NCSM scheme [10, 11] with (due to computational limitations) only the first three eigenstates of ^{7}Be. The $N_{\max} = 10$ and 12 S-factors are very close. As for the convergence in the number of ^{7}Be states, we explored it by means of calculations including up to 8 ^{7}Be eigenstates in a $N_{\max} = 8$ basis (larger $N_{\max}$ values are currently out of reach with more then five ^{7}Be states). Based on this analysis, we conclude that the use of an

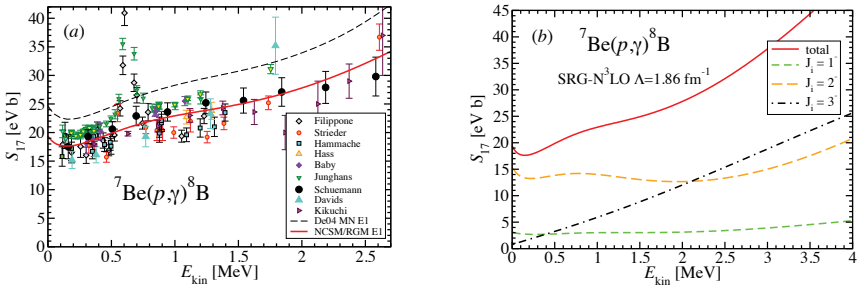

Fig. 1: Calculated ^{7}Be$(p,\gamma)^8$B S-factor as function of the energy in the c.m. compared to data and the microscopic cluster-model calculations of Ref. [19] with the Minnesota (MN) interaction (a). Only $E1$ transitions were considered. Initial-state partial wave contributions are shown in panel (b). Calculation as described in the text.

$N_{\max} = 10$ HO model space is justified and the limitation to five ^{7}Be eigenstates is quite reasonable. Finally, our calculated $S_{17}(0) = 19.4(7)$ MeV b is on the lower side, but consistent with the latest evaluation 20.8 ± 0.7(expt)± 1.4(theory) [18].

3.2 The ^{3}H$(d,n)^4$He and ^{3}He$(d,p)^4$He fusion reactions

The ^{3}H$(d,n)^4$He and ^{3}He$(d,p)^4$He fusion reactions have important implications first and foremost for fusion energy generation, but also for nuclear astrophysics, and atomic physics. Indeed, the deuterium-tritium fusion is the easiest reaction to achieve on earth and is pursued by research facilities directed at reaching fusion power by either inertial (*e.g.*, NIF) or magnetic (*e.g.*, ITER) confinement. Both ^{3}H$(d,n)^4$He and ^{3}He$(d,p)^4$He affect the predictions of Big Bang nucleosynthesis for light-nucleus abundances. In addition, the deuterium-^{3}He fusion is also an object of interest for atomic physics, due to the substantial electron-screening effects presented by this reaction.

In the following we present the first *ab initio* many-body calculations [20] of these reactions starting from the SRG-N^{3}LO NN interaction with $\Lambda = 1.5$ fm^{-1}, for which we reproduce the experimental Q-value of both reactions within 1%. We adopted HO model spaces up to $N_{\max} = 13$ with a frequency of $\hbar\Omega = 14$ MeV. The channel basis includes n-^{4}He (p-^{4}He), d-^{3}H (d-^{3}He), d^*-^{3}H (d^*-^{3}He) and d'^*-^{3}H (d'^*-^{3}He) binary cluster states, where d^* and d'^* denote $^3S_1$-$^3D_1$ and $^3D_2$ deuterium excited pseudostates, respectively, and the ^{3}H (^{3}He) and ^{4}He nuclei are in their ground state.

Figure 2 (left) presents the results obtained for the ^{3}He$(d,p)^4$He S-factor. The deuteron deformation and its virtual breakup, approximated by means of d pseudostates, play a crucial role. The S-factor increases dramatically with the number of pseudostates until convergence is reached for $9d^* + 5d'^*$. The dependence upon the HO basis size is illustrated by the ^{3}H$(d,n)^4$He results of Fig. 2 (right). The convergence is satisfactory and we expect that an $N_{\max}$=15 calculation, which is currently out of reach, would not yield significantly different results. The experimental position of the ^{3}He$(d,p)^4$He S-factor is reproduced within few tens of keV. Correspondingly, we find an overall fair agreement with experiment for this reaction, if we exclude the region at very low energy, where the accelerator data are enhanced by laboratory electron screening. The ^{3}H$(d,n)^4$He S-factor is not described as well with Λ=1.5 fm^{-1}. Due to the very low activation energy of this reaction, the S-factor (particularly peak position and height) is extremely sensitive to higher-order effects in the nuclear interaction, such as three-nucleon force (not yet included in the calculation) and missing isospin-breaking effects in the integration kernels (which are obtained in the isospin formalism). To compensate for these missing higher-order effects in the interaction and reproduce the position of the ^{3}H$(d,n)^4$He S-factor, we performed additional calculations using lower Λ values. This led to the theoretical S-factor of Fig. 2 (right) (obtained for Λ=1.45 fm^{-1}), that is in overall better agreement with data, although it presents a slightly narrower and somewhat overestimated

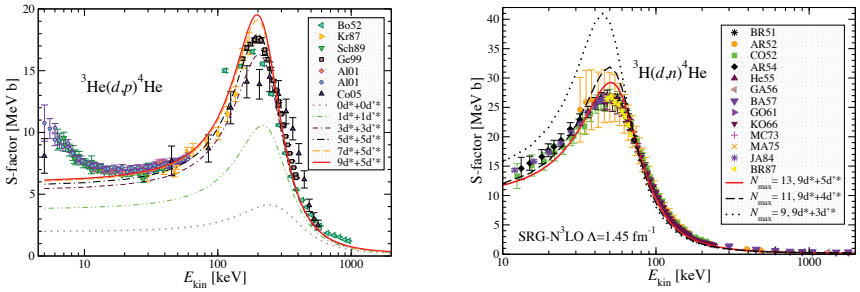

Fig. 2: Calculated S-factor of the ^{3}He$(d,p)^4$He (left) and ^{3}H$(d,n)^4$He (right) reaction compared to experimental data. Left: Convergence with the number of deuterium pseudostates in the $^3S_1$-$^3D_1$ (d^*) and $^3D_2$ (d'^*) channels. Right: Convergence with the size of the basis $N_{\max}$.

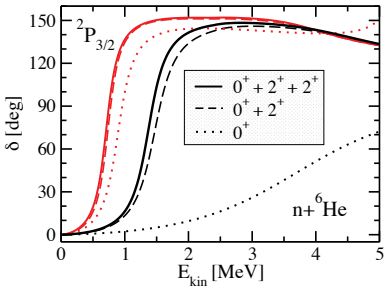

Fig. 3: Dependence of the NCSM/RGM (blue lines) and NCSMC (red lines) ^{6}He + n diagonal phase shifts of the ^{7}He $3/2^-$ g.s. on the number of ^{6}He states included in the binary-cluster basis. The short-dashed, dashed, and solid curves correspond to calculations with the ^{6}He 0^+ g.s. only, $0^+, 2^+$ states, and $0^+, 2^+, 2^+$ states, respectively.

peak. This calculation would suggest that some electron-screening enhancement could also be present in the ^{3}H$(d,n)^4$He measured S factor below 10 keV c.m. energy. However, these results cannot be considered conclusive until more accurate calculations using a complete nuclear interaction (that includes the three-nucleon force) are performed. Work in this direction is under way.

4 No-core shell model with continuum: Application to unbound ^{7}He

We can improve on the NCSM/RGM formalism with a more general unified approach, the no-core shell model with continuum (NCSMC), based on the coupling of the A-nucleon NCSM eigenstates with the NCSM/RGM binary-cluster states. We augment the NCSM/RGM ansatz for the A-body wave function by means of an expansion over A-body NCSM eigenstates $|A\lambda J^\pi T\rangle$ according to:

$$|\Psi_A^{J^\pi T}\rangle = \sum_\lambda c_\lambda |A\lambda J^\pi T\rangle + \sum_\nu \int dr\, r^2 \frac{[\mathcal{N}^{-1/2}\chi]_\nu(r)}{r} \hat{\mathcal{A}}_\nu |\Phi_{\nu r}^{J^\pi T}\rangle, \tag{5}$$

The NCSM sector of the basis provides an effective description of the short- to medium-range A-body structure, while the NCSM/RGM cluster states make the theory able to handle the scattering physics of the system. The discrete, c_λ, and the continuous, $\chi_\nu(r)$ (see Eq. 2) unknowns of the NCSMC wave functions are obtained as solutions of coupled equations that generalize Eq. 3.

This formalism can be applied successfully even to exotic unbound systems like ^{7}He. The ground state of this nucleus is a $3/2^-$ resonance at 0.43 MeV above the neutron and ^{6}He threshold. In Fig. 3, we present the dependence of the $3/2^-$ g.s. phase shifts on the number of ^{6}He eigenstates included in the NCSM/RGM (blue lines) and NCSMC (red lines) calculations. The NCSM/RGM calculation with the ^{6}He target restricted to its g.s. does not produce a ^{7}He $3/2^-$ resonance (the phase shift does not reach 90 degrees). A $^2P_{3/2}$ resonance does appear once the 2_1^+ state of ^{6}He is coupled, and the resonance position further moves to lower energy with the inclusion of the second 2^+ state of ^{6}He. On the contrary, the $^2P_{3/2}$ resonance is already present in the NCSMC calculation that includes four $3/2^-$ NCSM ^{7}He eignestates with only the g.s. of ^{6}He. Adding the 2_1^+ state of ^{6}He generates a modest shift of the resonance to a still lower energy while the second 2^+ state of ^{6}He has no significant influence. We further observe that the resonance position in the NCSMC calculation is lower than the NCSM/RGM one by about 0.7 MeV. This difference is due to the additional correlations brought by the ^{7}He eigenstates that are coupled to the n+^{6}He binary-cluster states in the NCSMC and that compensate for higher excited states of the ^{6}He target omitted in the NCSM/RGM sector of the basis. While NCSM/RGM calculations with a large number of cluster excited states can become prohibitively expensive, the coupling of a few NCSM eigenstates of the composite system is straightforward. More details can be found in Ref. [21].

5 Conclusions and Outlook

We gave an overview of the NCSM/RGM, an *ab initio* many-body approach capable of providing a unified description of structural and reaction properties of light nuclei, by combining the RGM with the use of realistic interactions, and a microscopic and consistent description of the nucleon clusters, achieved via the *ab initio* NCSM. Since the publication of the first results [1,4,22], obtained for nucleon-nucleus collisions, the NSCM/RGM has grown into a powerful approach for the description of light-ion fusion reactions. The formalism has been extended to include two-nucleon (deuteron) projectiles [5], as well as complex reactions with both nucleon-nucleus and deuteron-nucleus channels [20], based on realistic NN interactions. Further extensions of the approach to include the three-nucleon components of the nuclear interaction and three-cluster channel states are under way.

Acknowledgements

Computing support for this work came from the LLNL institutional Computing Grand Challenge program, the Jülich supercomputer Centre and Oak Ridge Leadership Computing Facility at ORNL. Prepared in part by LLNL under Contract DE-AC52-07NA27344. Support from the U. S. DOE/SC/NP (Work Proposal No. SCW1158) and the Natural Sciences and Engineering Research Council of Canada (NSERC) Grant No. 401945-2011 is acknowledged. TRIUMF receives funding via a contribution through the National Research Council Canada. This work is supported in part by the Deutsche Forschungsgemeinschaft through contract SFB 634 and by the Helmholtz International Center for FAIR within the framework of the LOEWE program launched by the State of Hesse.

References

[1] S. Quaglioni and P. Navrátil, *Phys. Rev. Lett.* **101** (2008), 092501
[2] K. Wildermuth and Y. C. Tang, *A unified theory of the nucleus* (Vieweg, Braunschweig) (1977)
[3] P. Navrátil, J. P. Vary, and B. R. Barrett, *Phys. Rev. Lett.* **84** (2000), 5728
[4] S. Quaglioni and P. Navrátil, *Phys. Rev. C* **79** (2009), 044606
[5] P. Navrátil and S. Quaglioni, *Phys. Rev. C* **83** (2011), 044609
[6] S. K. Bogner, R. J. Furnstahl, and R. J. Perry, *Phys. Rev. C* **75** (2007), 061001
[7] R. Roth, S. Reinhardt and H. Hergert, *Phys. Rev. C* **77** (2008), 064003
[8] D. R. Entem and R. Machleidt, *Phys. Rev. C* **68** (2003), 041001
[9] P. Navrátil, R. Roth, and S. Quaglioni, *Physics Letters B* **704** (2011), 379 – 383
[10] R. Roth and P. Navrátil, *Phys. Rev. Lett.* **99** (2007), 092501
[11] R. Roth, *Phys. Rev. C* **79**, (2009) 064324
[12] E. D. Jurgenson, P. Navrátil, and R. J. Furnstahl, *Phys. Rev. Lett.* **103** (2009), 082501
[13] E. D. Jurgenson, P. Navrátil, and R. J. Furnstahl, *Phys. Rev. C* **83** (2011), 034301
[14] F. Schümann *et al.*, *Phys. Rev. Lett.* **73** (2003), 232501
[15] F. Schümann *et al.*, *Phys. Rev. C* **73** (2006), 015806
[16] A. R. Junghans *et al.*, *Phys. Rev. C* **68** (2003), 065803
[17] E. Adelberger E *et al.*, *Rev. Mod. Phys.* **83** (2011), 195
[18] E. Adelberger *et al.*, *Rev. Mod. Phys.* **70** (1998), 1265
[19] P. Descouvemont, Phys. Rev. C **70** (2004), 065802
[20] P. Navrátil and S. Quaglioni, *Phys. Rev. Lett.* **108** (2012), 042503
[21] S. Baroni, P. Navrátil, and S. Quaglioni, arXiv:1210:1897 [nucl-th]
[22] P. Navrátil, R. Roth and S. Quaglioni, *Phys. Rev. C* **82** (2010), 034609

Importance of final-state fluctuations in radiative capture reactions and applications to surrogate reaction measurements

F. S. Dietrich
Lawrence Livermore National Laboratory, Livermore, CA 94551, USA

Abstract
Fluctuation effects in the final state of a direct reaction leading to unbound states were studied by Kerman and McVoy (KM). A simplified form of the KM theory has provided the key to the interpretation of a $^{89}\mathrm{Y}(\vec{p},\gamma)^{90}\mathrm{Zr}^*$ measurement in which the residual $^{90}\mathrm{Zr}^*$ nucleus was formed at excitation energies up to ≈28 MeV, well above the proton separation energy in $^{90}\mathrm{Zr}$. The same modified KM theory can be applied to other processes, such as the use of the (d,p) reaction to insert a neutron into a target to form a compound nucleus, as an alternative to direct formation by neutron bombardment. This is an example of the surrogate reaction mechanism, currently being developed for the indirect measurement of reactions on unstable targets. Leakage of the final-state neutron into the continuum invalidates the mechanism and thus its magnitude must be estimated. We use the modified KM theory to estimate this effect.

1 Introduction

A treatment of fluctuation effects in the final state of a direct reaction leading to highly-excited states in the residual nucleus was given by Kerman and McVoy (KM) [1], using an extension of the reaction framework developed by Kawai, Kerman and McVoy (KKM) [2]. The KM theory provides a basis for understanding the formation and subsequent decay of a compound nucleus B^* resulting from direct reactions such as $\mathrm{A}(d,p)\mathrm{B}^*$.

We will show how a simplified form of the KM theory provided the key to the interpretation of the $^{89}\mathrm{Y}(\vec{p},\gamma)^{90}\mathrm{Zr}^*$ reaction measurement [3] with 19.6-MeV polarized protons, in which the residual $^{90}\mathrm{Zr}^*$ nucleus was formed at excitation energies up to ≈28 MeV, well above the proton separation energy in $^{90}\mathrm{Zr}$. A straightforward extension of the direct-semidirect capture theory to unbound final states completely failed to explain the observed gamma spectra and angular distributions, but the addition of an absorptive term for the final-state proton obtained from the modified KM theory solved the problem and yielded an excellent reproduction of the observed gamma spectra, angular distributions, and analyzing powers [3].

The same modified KM theory can be applied to other direct reactions forming an unstable final state. A case of contemporary interest is the use of the (d,p) reaction to insert a neutron into a target to form an unstable compound nucleus, as an alternative to direct formation of the compound system by neutron bombardment. This is an example of the surrogate reaction mechanism, which is being developed for the indirect measurement of statistical reactions on rare or unstable targets. This topic has been covered in a recent review article [4]. Since it is assumed in applications of the surrogate reaction technique that the final-state neutron damps into a compound nucleus, leakage of the captured neutron into the continuum invalidates the surrogate mechanism, and thus its magnitude must be estimated. The modified KM theory (as well as closely related approaches [5,6]) can estimate the leakage fraction, and preliminary estimates have been made [4]. Since the direct-semidirect (n,γ) radiative-capture reaction deposits a neutron into a nucleus in a manner similar to the (d,p) stripping reaction, we can use the capture reaction to get an estimate of the leakage. We show estimates of the leakage probability as a function of the orbital angular momentum of the deposited neutron, and conclude that it is significant (of the order of 50% for low angular momenta).

It has so far been assumed that the surrogate compound nucleus decays according to simple Hauser-Feshbach branching ratios, but this ignores possible correlations between the decay channels and the direct-reaction formation process. This part of the problem will require application of the full KM theory.

We now show a few of the key results from the KKM, KM, and direct-semidirect capture theories that will be relevant to the following discussion.

In KKM [2], the S matrix element connecting entrance channel c and exit channel c' is written as an optical-potential background term plus a sum over resonances identified by q,

$$S_{cc'}(E) = \overline{S}_{cc'}(E) - i\sum_q \frac{g_{qc}g_{qc'}}{E-\mathscr{E}_q}, \tag{1}$$

where g_{qc} is an amplitude for decay from the state q into the channel c, and $\mathscr{E}_q$ is the (complex) energy of q. By construction, the energy average over an interval containing many states q is zero. The fluctuation (compound) cross section in the large width-to-spacing limit, $\Gamma/D \gg 1$, is defined in terms of certain averages over the resonance parameters,

$$X_{cc'} = \left(\frac{2\pi}{D\Gamma}\right)^{1/2} \langle g_{qc}g^*_{qc'}\rangle_q. \tag{2}$$

In KM [1], it was recognized that population of resonances q in a 2-body entrance channel c could be accomplished via a direct transfer reaction as well. An example would be the replacement of the absorption reaction $n + \mathrm{A} \rightarrow \mathrm{B}^*$ by the stripping reaction $\mathrm{A}(d,p)\mathrm{B}^*$. The expression in KM analogous to Eq. 1 is for the T matrix,

$$T_{Rc} = \overline{T}_{Rc} + \sum_q \frac{M_{Rq}g_{qc}}{E-\mathscr{E}_q}, \tag{3}$$

where $\overline{T}_{Rc}$ is the usual direct amplitude (calculated, e.g., in DWBA) and M_{Rq} is the replacement for the KKM amplitude g_{qc}. The factor M_{Rq} is defined in terms of an amplitude $m_{Rc_1}(r)$ for finding the deposited particle at position r in channel c_1,

$$m_{Rc_1}(r) = \frac{1}{2\pi}\sum_{c_0}\int dr' M^R_{c_0}(r')\mathscr{G}^{(+)}_{c_0c_1}(r',r), \tag{4}$$

where $M^R_{c_0}(r')$ is the direct-reaction amplitude for depositing the particle at spatial position r' in channel c_0, which is then propagated to position r in channel c_1 by the Green's function $\mathscr{G}^{(+)}$. Then M_{Rq} is

$$M_{Rq} = \sum_{c_1}\int dr V_{qc_1}(r) m_{Rc_1}(r), \tag{5}$$

where $V_{qc_1}(r)$ is the interaction that captures the particle at r in channel c_1 into the resonant state q. The main result from KM that is relevant to the present work was obtained by calculating the inclusive cross section, i.e., the sum over all final channels c. After several approximations, KM found the expression

$$\sum_c \langle\sigma^{fl}_{Rc}\rangle \approx -4\pi\sum_{c_1}\int dr\,|m_{Rc_1}(r)|^2\,W_{c_1}(r), \tag{6}$$

where $W_{c_1}(r)$ is the imaginary part of the optical potential acting on the captured particle after the transfer reaction.

Direct-semidirect capture (DSD) is a well-known process that may be regarded as the DWBA theory for radiative capture, mainly useful for nucleons. One calculates matrix elements of an effective radial operator, which for electric radiation of multipolarity L is

$$Q_L = q_L r^L + \left(\frac{1}{E_\gamma - E_{res} + i\Gamma/2} - \frac{1}{E_\gamma + E_{res}}\right) h'_L(r), \tag{7}$$

where the first term represents direct capture and q_L is a kinematic effective charge. The second (semidirect) term describes capture through excitation and subsequent gamma emission of a giant resonance at excitation energy E_{res} with width Γ; $h'_L(r)$ is a radial form factor describing the excitation. The second part of the semidirect term represents excitation by the particle in the final state (core polarization). Nearly all calculations preceding the work described here [3], such as that described in Ref. [7], were for capture of a continuum nucleon into a bound final state.

2 Radiative capture to unbound states

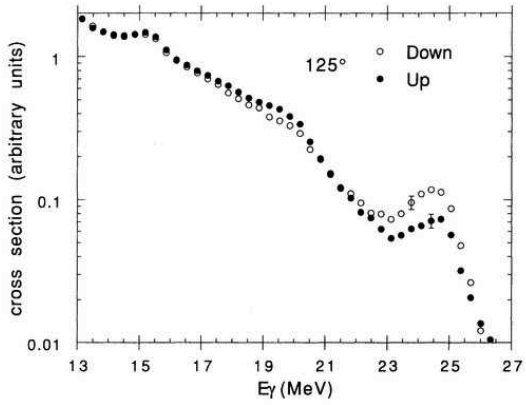

Fig. 1: Gamma spectra at 125^o from the ^{89}Y($\vec{p}$,$\vec{\gamma}$) reaction with protons protons polarized up and down along an axis perpendicular to the reaction plane.

We describe the work on radiative capture in chronological order to emphasize the important contributions of Prof. Arthur Kerman to this project. Before this work, several candidate mechanisms were proposed to explain the spectra of nucleon-induced gamma spectra populating both bound and unbound final states. These included equilibrium statistical emission, preequilibrium or multistep reactions (e.g., intermediate nucleon emission preceding the gamma), and DSD (although this had been implemented only for direct capture in light nuclei [8]).

To clarify this problem, we carried out measurements of the angular distributions and analyzing power of gammas emitted in the ^{89}Y($\vec{p}$,$\vec{\gamma}$) reaction with 19.6 MeV polarized protons [3]. Spectra were measured at 5 angles between 30^o and 150^o with both signs of the proton polarization along an axis perpendicular to the reaction plane. The spectra at 125^o, shown in Fig. 1, exhibit significant polarization effects above ≈17 MeV. Gammas above 19.6 MeV correspond to bound final states in the residual ^{90}Zr; those below, to states in which the captured proton is unbound and may be emitted into the continuum.

To explain the results, we first implemented a straightforward DSD capture calculation with a continuum (optical-model) final state wave function, similar to what was done in Ref. [8]. This calculation underestimated the magnitude of the cross section by 7 orders of magnitude. We soon realized that this discrepancy was due to the fact that the emission of the captured proton was suppressed by the Coulomb barrier, and that instead the proton was absorbed.

At this point Prof. Kerman pointed out that the KM paper could be applied to this problem. We implemented Eqs. 4 and 6 shown above, using an on-shell approximation for the Green's function in Eq. 4, and found that the discrepancy in the magnitude was reduced to a mere 2 orders of magnitude! We then calculated the full Green's function and obtained an excellent reproduction of the angular distributions

and analyzing powers as well as the spectral shapes. During this last stage we re-examined the theory and found that the inclusive cross section, which is all that is needed for the present case, can be derived more easily by applying closure to the final states, without requiring the approximations used to get the KM expression of Eq. 6. The resultant expressions are given in Ref. [3], in which the double-differential cross section for the full extended DSD theory can be expressed as a sum of two components,

$$\frac{d\sigma}{dE_\gamma d\Omega_\gamma} = \sigma_1 + \sigma_2, \tag{8}$$

where σ_1 is identical to the KM expression of Eq. 6 (in a slightly different notation) and represents compound-nucleus absorption in the final state. σ_2 is the direct escape contribution, which is the straightforward extension of DSD using a continuum final state wave function. This term is negligible in the present case as noted above, but, as will be seen below, it is significant for neutron capture since there is no Coulomb barrier.

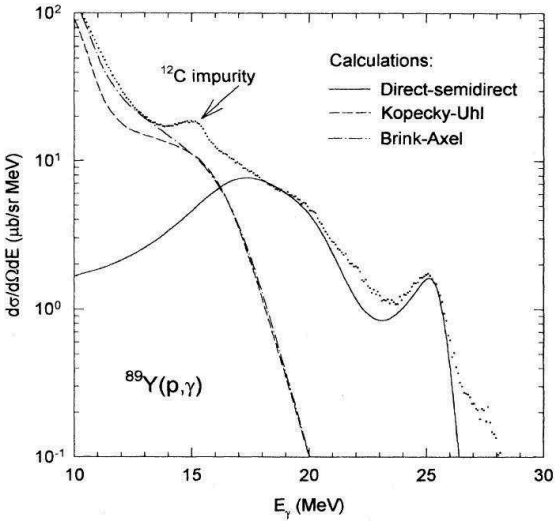

Fig. 2: 90^o spectrum of the gammas from the $^{89}\mathrm{Y}(p,\gamma)$ reaction, together with the full DSD and Hauser-Feshbach calculations.

Figure 2 shows the gamma spectrum at 90^o, together with the extended DSD calculations and equilibrium statistical (Hauser-Feshbach) calculations of the spectra using two commonly used models for the gamma strength function. We see that there is no apparent need for reaction mechanisms other than those shown in the figure, at least up to ≈20 MeV incident energy. In carrying out this calculation, we have included direct E1, E2, and E3 radiation as well as semidirect E1.

3 Application to surrogate reactions

The compound nuclear reaction, illustrated in the top portion of Fig. 3, may be difficult or impossible to measure if the target A is rare or unstable. An alternative approach, the surrogate reaction technique [4], involves forming the *same* compound nucleus in a direct reaction on a different target, as shown in the bottom portion of the figure. Corrections using nuclear reaction theory are required, since the spin-parity distribution of the compound system is different in the two cases, and the final state of the direct reaction may emit particles before an equilibrium compound nucleus is formed (i.e., incomplete or partial

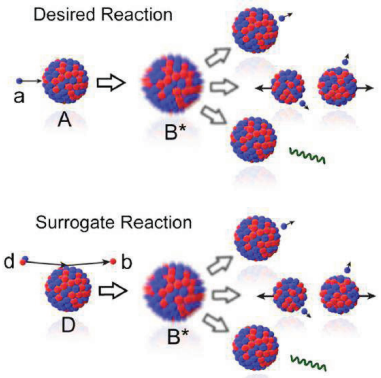

Fig. 3: Schematic picture of the formation of a compound nucleus B^* via either an absorption reaction $a + A \rightarrow B^*$, or a direct interaction $D(d,b)B^*$. In both cases, the compound nucleus subsequently decays into the various open channels.

fusion). Note that the relation between the desired and surrogate reactions is exactly the same as between the KKM and KM theories.

A particularly interesting case is the use of a (d,p) reaction as a surrogate for neutron absorption on an unstable target, since it may be useful for the determination of astrophysical neutron capture reactions. Since the (n,γ) process described by the extended DSD theory and the (d,p) reaction deposit a neutron onto a target in a similar manner, we can use a DSD calculation to give relevant estimates of both the spin distributions and the compound formation probability. The compound formation probability is easily obtainable since the calculation separately identifies the compound formation and the neutron escape (σ_1 and σ_2, respectively, in Eq. 8).

In Fig. 4 we show calculations of the cross sections and compound formation probabilities for the $^{89}\mathrm{Y}(n,\gamma)$ reaction at 19.6 MeV incident energy. These quantities are shown as a function of the orbital angular momentum L of the captured neutron, for three values of the energy available for neutron escape, 1, 5, and 11 MeV.

The upper panels of the graph show a striking odd-even effect in the dependence of the cross section on L. This is a consequence of the single-particle spectroscopy of the captured neutron in the potential well of the ^{89}Y target, and can be associated with the alternation of even and odd parities in the major shells in a harmonic oscillator potential. The lower panels show that for low L and low escape energies the compound formation probability is rather low, of the order of 0.5. For increasing L, the angular momentum barrier increases and eventually becomes large enough to inhibit escape, so that the formation probability approaches unity. Both of these effects are large enough that they will need to be carefully taken into account in the analysis of (d,p) surrogate reactions. Some preliminary escape calculations for (d,p) surrogate reactions using a similar reaction theory [5,6] have been reported in Ref. [4].

4 Conclusions

The extended DSD theory, supplemented by Hauser-Feshbach, describes capture to both bound and unbound regions. Together with further work not shown here, there is no evident need for multistep contributions up to approximately 33 MeV. The theoretical result for inclusive reactions agrees with the expression in KM, but obtaining it does not require detailed treatment of resonance structure as in KM.

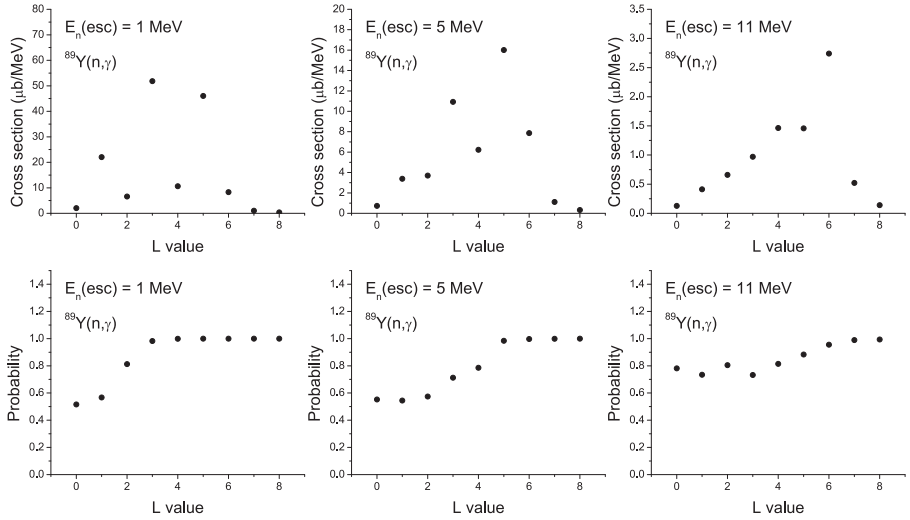

Fig. 4: Cross section and compound-nucleus formation probability for radiative capture to unbound final states in the $^{89}\mathrm{Y}(n,\gamma)$ reaction at 19.6 MeV incident energy, as a function of the orbital angular momentum of the neutron following capture. Results are shown for final-state neutron escape energies of 1, 5, and 11 MeV. The upper graphs show the cross sections, which are the angle-integrated values calculated from the extended DSD theory. The lower graphs show the probability that a compound nucleus is formed.

The theory predicts the ratio of compound formation to direct escape of the particle after capture. In comparing $^{89}\mathrm{Y}(p,\gamma)$ and $^{89}\mathrm{Y}(n,\gamma)$, we find that for protons the compound formation dominates hugely because of the Coulomb barrier. However, for neutrons, the neutron escapes a significant fraction of the time.

The calculation of escape vs. compound formation for neutron capture has been useful in understanding and quantifying the challenges in using (d,p) as a surrogate reaction to form the same compound nucleus as in neutron absorption.

It is important to realize that the treatment of inclusive reactions discussed here is not sufficient to understand possible correlations between compound decay channels and the formation of the compound nucleus by a direct reaction. If these are important, the statistical properties of the full KM theory will be required. As a pertinent example, the cross sections for formation of the compound resonances in the (d,p) reaction may very well be correlated with the neutron decay widths of these resonances.

Acknowledgements

The author is grateful for the opportunities he has had over several decades for discussions and collaborations with Arthur Kerman on many projects, including the ones described here. This work was performed under the auspices of the U.S. Department of Energy by Lawrence Livermore National Laboratory under Contract DE-AC52-07NA27344.

References

[1] A. K. Kerman and K. W. McVoy, Ann. Phys. (N.Y.) **122**, 197 (1979).
[2] M. Kawai, A. K. Kerman, and K. W. McVoy, Ann. Phys. (N.Y.) **75**, 156 (1973).
[3] W. E. Parker *et al*., Phys. Rev. C **52**, 252 (1995).
[4] J. E. Escher *et al*., Rev. Mod. Phys. **84**, 353 (2012).
[5] T. Udagawa and T. Tamura, Phys. Rev. Lett. **45**, 1311 (1980).
[6] T. Udagawa and T. Tamura, Phys. Rev. C **24**, 1348 (1981).
[7] F. S. Dietrich, D. W. Heikkinen, K. A. Snover, and K. Ebisawa, Phys. Rev. Lett. **38**, 156 (1977).
[8] H. R. Weller *et al*., Phys. Rev. C **25**, 2921 (1982).

Further analysis about predicted levels of ^{9}Be based on neutron double differential cross sections at E_p=18 MeV

Junfeng Duan[1], Jingshang Zhang[2]

[1]Division of applied nuclear physics, Department of physics and astronomy, Uppsala University, Box 516, 751 20, Uppsala, Sweden

[2]China Institute of Atomic Energy, PO Box 275(41), Beijing 102413, People's Republic of China

Abstract

The calculation of the neutron double differential cross sections for p+^{9}Be reaction is performed. The secondary outgoing neutrons only coming from the (n,np2α) reaction channel through four different emission processes, are illustrated in detail. Since two predicted levels of ^{9}Be, i.e., E(Jπ)Γ=9(5/2^{+})1000 and 10(5/2^{+})1000 have been proposed in 2009, in this work those two predicted levels are analyzed further based on the neutron double differential cross sections at E_p=18 MeV. The calculated results indicate that the fittings would be improved obviously while the predicted levels have been employed.

1 Introduction

^{9}Be has been selected as the material for controlled thermonuclear reactors for a long time. For improving neutron economy in thermal and fast-fission reactors and in the design of accelerator-driven spallation neutron sources, ^{9}Be is still a very useful material[1], because of the relatively large (n,2n) cross section, low mass and low neutron-capture cross section.

A model for description of light particles induced light nucleus reaction was proposed in 1999[2] and improved in 2009 by Jingshang Zhang[3]. The key point of this model is that the angular momentum and parity conservation is taken into account properly in the emission process from a compound nucleus to the discrete levels of the residual nuclei with pre-equilibrium mechanism. The double-differential cross sections of total outgoing neutrons for a series of light nucleus reactions, such as ^{6,7}Li[4,5], ^{10,11}B[6,7], ^{12}C[2], ^{14}N[8], ^{16}O[9] and ^{19}F[10], have been analyzed successfully by using this model. Furthermore, in 2009[11], the calculation and analysis of the double-differential cross sections from neutron induced ^{9}Be reactions had been performed based on the updated level schemes[12]. The model calculations are very sensitive to the level schemes, because all of the residual states are discrete levels in light nucleus reactions. Although the updated level scheme of ^{9}Be had been employed in the calculation, there were still some deficiencies between contributions from the 9th and 10th levels. In view of the much higher energy interval, we predicted that there were two new levels between the 9th level 7.94(5/2^{-}) and the 10th level 11.238(7/2^{+}). The calculated results indicted the fittings would be improved obviously, while the predicted levels 9.0(5/2^{+}) and 10.0(5/2^{+}) had been employed in the calculation[11]. Now, in this work, the calculation and analysis of the double-differential cross sections from p+^{9}Be reactions are performed to verify the validity of those two predicted levels. The level scheme of ^{9}Be employed in this calculation has been listed in Table I including those two predicted levels.

Energy(MeV)	Spin and parity	Energy width (keV)
g.s.	$3/2^-$	stable
1.684	$1/2^+$	217
2.4294	$5/2^-$	0.78
2.78	$1/2^-$	1080
3.049	$5/2^+$	282
4.704	$3/2^+$	743
5.59	$3/2^-$	1330
6.38	$7/2^-$	1210
6.76	$9/2^+$	1330
7.94	$5/2^-$	1000
*9.0	$5/2^+$	1000
*10.0	$5/2^+$	1000
11.283	$7/2^-$	575
11.81	$5/2^-$	400
13.79	$?^-$	590
14.3922	$3/2^-$	0.381
14.48	$5/2^-$	800
15.10	?	350
15.97	?	300
16.671	$5/2^-$	41
16.9752	$1/2^-$	0.389
17.298	$5/2^-$	200
17.493	$7/2^+$	47

Table 1. The level scheme of ^{9}Be taken from Ref[12]

*Labels the predicted levels; g.s. =ground state; ? indictes the abcent data

The emitted neutron of p+^{9}Be reactions only come from the (p,np2α) channel with four different reaction approaches. On the basis of the statistical theory[3], we calculate the total outgoing neutron double differential cross sections at 18 MeV incident proton energies using updated levels, while two predicted levels are (or not) employed. The results show that two predicted levels, i.e., E(Jπ)Γ=9.0(5/2$^+$)1000 and 10.0(5/2$^+$)1000, as labeled asterisk in Table I, obviously improve the agreement with the experimental data[13].

This article proceeds as follow. In Sec.II, the opened channels of p+^{9}Be reaction are analyzed in detail. The comparisons are performed between the model calculation and the experimental data in next section, while the two predicted levels are (or not) employed. In the last section a brief summary is given.

2 Reaction channels

In view of p+^{9}Be reactions with incident proton energy $E_p \leq 20$MeV, the opened reaction channels, the corresponding reaction Q-values and the threshold energy E_{th} in unit of MeV are listed as follows

(1)

$$p+{}^9Be \rightarrow {}^{10}B \rightarrow \begin{cases} \gamma+{}^{10}B & Q=6.586 & E_{th}=0.0000 \\ n+{}^9B & Q=-1.85 & E_{th}=2.0571 \\ p+{}^9Be & Q=0.00 & E_{th}=0.0000 \\ \alpha+{}^6Li & Q=2.127 & E_{th}=0.0000 \\ {}^3He+{}^7Li & Q=-11.202 & E_{th}=12.4558 \\ d+{}^8Be & Q=0.559 & E_{th}=0.0000 \\ t+{}^7Be & Q=-12.082 & E_{th}=13.4342 \\ {}^5He+{}^5Li & Q=-4.434 & E_{th}=4.9303 \end{cases}$$

After the neutron is emitted from the compound nucleus ^{10}B, the residual nucleus is ^{9}B which could emit the proton continuously with the residual nucleus ^{8}Be. ^{8}Be is unstable and can be separated into two alpha particles. Thus, this reaction is one of decay modes to the (p, np2α) reaction channel. The residual nucleus ^{9}Be* is yielded through proton emission. Of course the proton emission leaving ^{9}Be in the ground belongs to (n, p) channel. In fact, neutron can be emitted from ^{9}Be* in first three levels with unstable residual nucleus ^{8}Be, which belongs to (n, pn2α) channel. Furthermore, the alpha particles emission will appear above the fourth level of ^{9}Be with unstable residual nucleus ^{5}He which can be separated into neutron and alpha spontaneously, therefore this decay mode also belongs to (n, pn2α) channel. In this calculation ^{5}He emission is taken into account with unstable residual nucleus ^{5}Li, as well known, which can be separated into proton and alpha particle. Hence, this reaction also is one of decay modes to the (p, np2α) reaction channel. The reaction mechanisms to ^{9}Be(p,np2α) channel involved in the model calculation are shown as follows

$$p+{}^{9}Be \rightarrow {}^{10}B \rightarrow \left\{ \begin{array}{l} n+{}^{9}B \rightarrow p+{}^{8}Be \rightarrow 2\alpha \\ p+{}^{9}Be \rightarrow \left\{ \begin{array}{ll} k \le 3 & n+{}^{8}Be \rightarrow 2\alpha \\ k \ge 4 & \alpha+{}^{5}He \rightarrow n+\alpha \end{array} \right. \\ {}^{5}He+{}^{5}Li \rightarrow n+\alpha+{}^{5}Li \rightarrow p+\alpha \end{array} \right\} \rightarrow (p,np2\alpha) \tag{2}$$

The symbol k refers to the order number of the excited level of the ^{9}Be.

3 Calculated results and analysis

The LUNF code[8] based on the light nucleus reaction model for p+^{9}Be reactions has been developed and used for calculating all kinds of the reaction cross sections, the angular distributions and the double-differential cross sections of all kinds of outgoing particles from each partial reaction channel.

The calculation of the double-differential cross sections of total outgoing neutron from each reaction channels has been performed. The comparisons of the calculated results, which the predicted levels have been employed (red solid line) or not been employed (black dash line), with the experimental data measured by V.V. Verbinski[13] in 1969 are shown in Fig.1 and Fig.2 at E_p=18 MeV for outgoing angles of 0^0, 20^0, 40^0, 60^0, 80^0, 100^0, 120^0, 145^0 and 170^0, respectively. As shown in the two figures, all of the fittings agree very well with the measurements after the predicted levels 9.0(5/2$^+$)1000 and 10.0(5/2$^+$)1000 have been added to the level scheme of ^{9}Be, otherwise the calculated results would deviate obviously from the experimental measurements.

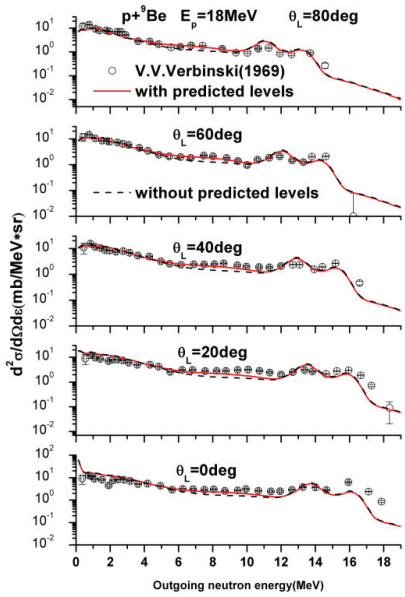

Fig.1: The energy-angular spectra of 0^0, 20^0, 40^0,60^0 and 80^0 at E_p=18MeV. The red solid lines and the black dash lines correspond to the results that the predicted levels have or not been added, respectively. The experimental data are taken from Ref[13].

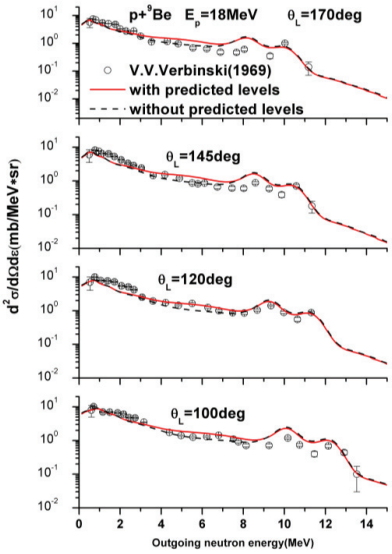

Fig.2: The same as FIG.1 but for outgoing angles of 100^0, 120^0, 145^0 and 170^0.

In p+^{9}Be reaction, the total outgoing neutron energy angular spectrum mainly comes from the contribution of the (p, np2α) reaction, as given by Eq.(2), which include four reaction mechanisms. Actually, the mechanisms related to the predicted levels are (p, pn)^{8}Be* and (p, pα)^{5}He* reaction modes. As an example, for $\Theta_L=60^0$ at E_p=18 MeV, the partial spectra of the emitted neutron from (p, pn)^{8}Be* and (p, pα)^{5}He* are shown in Fig.3 and Fig.4. Obviously, the predicted levels 9.0($5/2^+$) and 10.0($5/2^+$) can emit the secondary neutron and α particle from (p,pn)^{8}Be* and (p, pα)^{5}He*, respectively, so each level could give two neutron spectra. Therefore, four new outgoing neutron partial spectra are added. From Fig.3 and Fig.4, one can see that there are obvious contributions coming from the predicted levels to the total spectrum. And if they were absent in the model calculation, the results of total double-differential cross sections would deviate obviously from the experimental measurements in the outgoing neutron region 5 – 10 MeV.

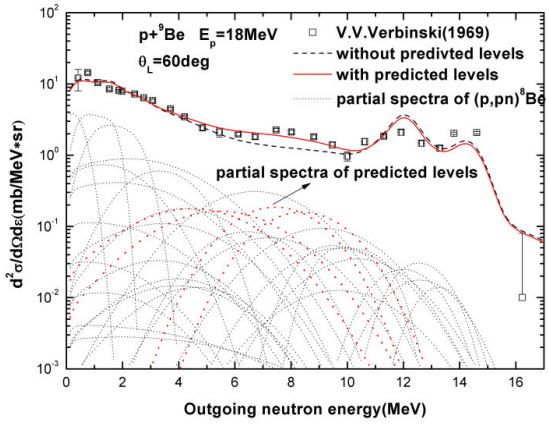

Fig.3: The comparison between the calculated results, which the predicted levels have been employed(red solid line) or not been employed (black dash line), and experimental data with Outgoing angle of 60^0 at E_p=18 MeV. The red dot lines correspond to the partial spectra of predicted levels through $(p,pn)^8Be^*$ reaction.

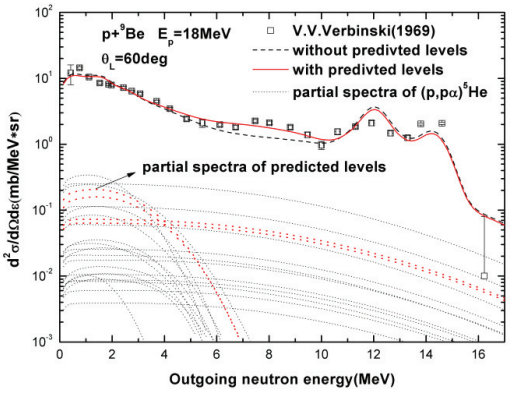

Fig.4: The same as FIG.3 but for $(p,p\alpha)^5He^*$ reaction.

4 Summary

The total outgoing neutron energy-angular spectra for p+^{9}Be reactions have been calculated and analyzed by the statistical theory for light nucleus reactions. In p+^{9}Be reactions, the total outgoing neutron energy-angular spectra mainly come from (p,pn2α) reaction channel with four different reaction processes.

The calculated results indicate the fittings would be improved obviously, while the predicted levels 9.0($5/2^{+}$) and 10.0($5/2^{+}$) have been employed both for the situation of neutron or proton inducing. In this calculation we further verified the validity of the predicted levels. Although the same spins, parities and energy width with the situation of neutron inducing have been adopted in this calculation, they are not precise enough. At last, we hope the two predicted levels could be validated by experiment.

References

[1] Schulke A. W., Jr Proc. 8_{th} Mtg Int. Collaboration Advanced Neutron Sources (ICANS-VIII). Rutherford-Appleton Laboratory, Report No. RAL-85-110(1985).

[2] J.S.Zhang, Y.L.Han and L.G.Cao, Nucl.Sci.Eng. 133(1999)218.

[3] J.S.Zhang, *Statistical Theory for Neutron Induced Light Nucleus Reaction* (Science Press, Beijing, 2009).

[4] Zhang Jing-Shang and Han Yin-Lu, Commum.Theor.Phys. (Beijing,China) 36(2001)437.

[5] Zhang Jing-Shang and Han Yin-Lu, Commum.Theor.Phys. (Beijing,China) 37(2002)465.

[6] Zhang Jing-Shang, Commum.Theor.Phys. (Beijing,China) 39(2003)433.

[7] Zhang Jing-Shang, Commum.Theor.Phys. (Beijing,China) 39(2003)83.

[8] Yan Yu-Liang et al., Commum.Theor.Phys. (Beijing,China) 44(2005)128.

[9] Duan Jun-Feng et al., Commum.Theor.Phys. (Beijing,China) 44(2005)701.

[10] Duan Jun-Feng et al., Commum.Theor.Phys. (Beijing,China) 47(2007)102.

[11] J.F.Duan et al. Phys.Rev.C 80, 064612(2009).

[12] D.R.Tilley et al., Nucl.Phys. A745,155(2004).

[13] V.V.Verbinski et al. Phys.Rev 177, 1671(1969).

Nucleon elastic scattering off doubly closed-shell nuclei within HF+RPA with Gogny force

G. Blanchon, M. Dupuis, H. Arellano and N. Vinh Mau.
CEA, DAM, DIF F-91297 Arpajon, France

Abstract
The nucleon-nucleus optical potential is determined within the Hartree-Fock (HF) approximation and the Random Phase Approximation (RPA) using the Gogny D1S force consistently. The scattering problem is solved for the calculated non-local potential without any localization procedure. An application is presented for proton scattering off ^{40}Ca and ^{208}Pb.

1 Introduction

Nucleon elastic scattering has been studied with several microscopic approaches, among them we can cite the nuclear structure method: HF+RPA [1,2], the nuclear matter method [3], the Faddeev RPA [4], the coupled channels method [5] and the coupled-cluster theory [6]. The nuclear matter method provides a satisfactory description of nucleon elastic scattering at incident energies above approximately 50 MeV, but an accurate description at lower energy has not yet been completed. In this work, we use the nuclear structure method without some of the approximations used in a previous work [2] and with a better description of the target spectroscopic information. We couple the elastic channel to all the excitations in the target predicted by the RPA method [7]. We use the Gogny D1S force [8] consistently to generate both the HF and the RPA contributions to the optical potential. In particular we do not approximate the intermediate propagator by a Coulomb wave and we generate the HF propagator in the continuum (including resonances). We show the effect of a RPA treatment of the target's excitations compared to a particle-hole treatment on the reaction cross section. We also study the impact of the correct treatment of the intermediate propagator on the reaction cross section.

2 Formalism

The nuclear structure approach is exposed in Ref. [1]. At the HF+RPA approximation, the optical potential reads,

$$V = V_{HF} + V_{RPA} - V_{ph}. \tag{1}$$

The HF contribution is

$$V_{HF}(\mathbf{r},\mathbf{r'}) = \int d\mathbf{r}_1 v(\mathbf{r},\mathbf{r}_1)\rho(\mathbf{r}_1)\delta(\mathbf{r}-\mathbf{r'}) - v(\mathbf{r},\mathbf{r'})\rho(\mathbf{r},\mathbf{r'}), \tag{2}$$

where $\rho(\mathbf{r})$ and $\rho(\mathbf{r},\mathbf{r}')$ are respectively the local and non-local matter densities of the target's ground state. V_{HF} is obtained in coordinate space [9] in order to get the correct asymptotic behavior of the wave functions. The first term in the right hand of Eq. 2 is the direct term which is local. The second term, the exchange term, is non-local because of the finite range of the Gogny interaction v. The Gogny interaction is real, so is V_{HF}.
The RPA contribution is

$$\begin{aligned} V_{RPA}(\mathbf{r},\mathbf{r}',E) &= \lim_{\eta\to 0^+} \sum_{N\neq 0,ijkl} \sum\!\!\!\!\!\!\int_{\lambda} \chi_{ij}^{(N)}\chi_{kl}^{(N)} \left(\frac{n_\lambda}{E-\epsilon_\lambda+E_N-i\eta} + \frac{1-n_\lambda}{E-\epsilon_\lambda-E_N+i\eta} \right) \\ &\times F_{ij\lambda}(\mathbf{r})F^*_{kl\lambda}(\mathbf{r}'), \end{aligned} \tag{3}$$

where there is a summation over discrete λ states and an integration over continuum λ states. n_λ is the occupation number of λ state. We couple the elastic channel to all the excitations in the target predicted by the RPA/D1S method [7]. We consider excitations with total angular momentum J from 0 to 14 for all parities. $\chi_{ij}^{(N)}$ and E_N are respectively the RPA amplitudes and the energy of the N^{th} excited state. In Eqs. 3 and 5,

$$F_{ij\lambda}(\mathbf{r}) = \int d^3\mathbf{r}_1 \phi_i^*(\mathbf{r}_1) v(\mathbf{r},\mathbf{r}_1)[1-P]\phi_\lambda(\mathbf{r})\phi_j(\mathbf{r}_1), \tag{4}$$

where P is an operator exchanging two particles. The ϕ's are solutions of $(T+V_{HF})\phi = \epsilon\phi$. Spin of the particles is taken into account but not explicitly written in the present equations for simplicity.
The particle-hole potential V_{ph} accounting for double counting in V_{RPA} in Eq. 1 reads,

$$\begin{aligned} V_{ph}(\mathbf{r},\mathbf{r}',E) &= \lim_{\eta\to 0^+} \sum_{N\neq 0,ijkl} \sum\!\!\!\!\!\!\int_\lambda n_j(1-n_i)\delta_{ik}\delta_{jl}\left(\frac{n_\lambda}{E-\epsilon_\lambda+\epsilon_i-\epsilon_j-i\eta}+\frac{1-n_\lambda}{E-\epsilon_\lambda-\epsilon_i+\epsilon_j+i\eta}\right) \\ &\times \quad F_{ij\lambda}(\mathbf{r})F^*_{kl\lambda}(\mathbf{r}'). \end{aligned} \tag{5}$$

The potential V in Eq. 1 is non-local, complex and energy dependent. In configuration space, it reads

$$\langle \mathbf{r}|V|\mathbf{r'}\rangle = V(\mathbf{r},\mathbf{r'}) = V(r,r',\cos(\mathbf{r},\mathbf{r'})). \tag{6}$$

The partial wave expansion of the potential is

$$V(\mathbf{r},\mathbf{r'}) = \sum_{jlm} \mathcal{Y}^m_{jl1/2}(\hat{\mathbf{r}})\nu_{jl}(r,r')\mathcal{Y}^{m\dagger}_{jl1/2}(\hat{\mathbf{r}}'). \tag{7}$$

The integro-differential Schrödinger equation,

$$-\frac{\hbar^2}{2\mu}\left[f''_{jl}(r) - \frac{l(l+1)}{r^2}f_{jl}(r)\right] + r\int \nu_{jl}(r,r')f_{jl}(r')r'dr' = Ef_{jl}(r), \tag{8}$$

is solved for each partial wave (j,l), where $f_{jl}(r) = r\phi_{jl}(r)$ and E is the incident beam energy. Solutions of these equations are obtained following R. H. Hooverman's method for discrete states [10] and J. Raynal's method for continuum states [11].

3 Results

The phase-shifts for a proton scattered off ^{40}Ca in HF approximation are shown in Fig. 1. We observe several resonances for different partial waves when the phase-shift δ increases rapidly through an odd multiple of $\pi/2$. The Levinson theorem, that relates the value of the phase-shift at zero energy to the number, N_{jl}, of bound states for a given (j,l) is verified thus $\delta_{jl}(0)(rad/\pi) = N_{jl}$. The ϕ_λ's are then used to determine V_{RPA} and V_{ph}, Eqs. 3 and 5.

In Figs. 2 and 3, we look at the contribution of the imaginary part of the RPA potential summed over all partial waves that reads,

$$W(R,s) = \sum_{lj} \frac{2j+1}{4\pi}\mathcal{I}m(\nu^{lj}_{RPA}(r,r')) \tag{9}$$

with $R = \frac{1}{2}(r+r')$ and $s = r-r'$. In particular we consider the diagonal contribution, $W(R,0)$ for protons scattered off ^{208}Pb at several incident energies. By convention, the imaginary part of the RPA potential is positive for an absorptive potential. We only consider the coupling to the first 3^- excitation at 3.4 MeV in ^{208}Pb. $W(R,0)$ is picked at the surface of the nucleus due to collectivity of the first 3^- excitation. Indeed the potential qualitatively behaves as the square of the radial transition density

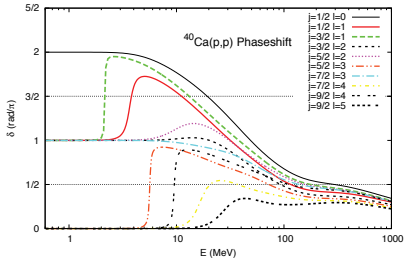

Fig. 1: p + ^{40}Ca HF phase-shift for different partial waves (j, l) *vs.* incident energy.

for a given RPA excited state. The radial transition density is well known to be surface-peaked in the case of a vibrational collective state such as the first 3^- excitation in ^{208}Pb. In Fig. 3, we see that the contribution to the potential increases from zero incident energy to about 30 MeV then decreases as the incident energy increases. This behavior is dictated by two factors. *(i)* For E < 3.4 MeV the channel is not open so $\mathcal{I}mV_{RPA} = 0$. At E = 3.4 MeV and above the channel is open and give a contribution to $\mathcal{I}mV_{RPA}$. *(ii)* The intermediate wave ϕ_λ oscillates more and more as E increases, since the intermediate wave energy, that is $\epsilon_\lambda = E - E_{RPA}$, increases as well. Slow as well as rapid oscillations kill $\mathcal{I}mV_{RPA}$. Consequently, $W(R, 0)$ increases between E = 3.4 MeV and 30 MeV and then decreases for higher incident energies.

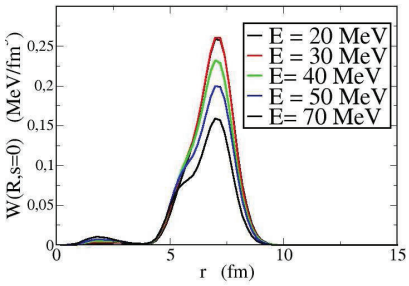

Fig. 2: $W(R, 0)$, Eq. 9, for p+^{208}Pb scattering for several incident energies. Coupling to the first 3^- excited state at E_{exc} =3.4 MeV.

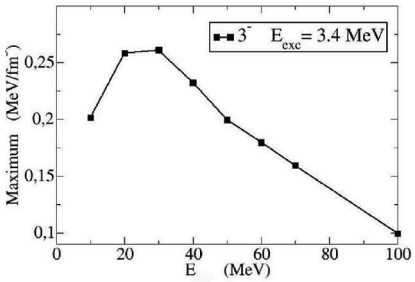

Fig. 3: Same as Fig. 2 but with the maximum value of W(R,0) *vs.* proton incident energy, E.

In Figs. 4 and 5, we display the imaginary part of the RPA potential for p + ^{208}Pb at E = 3.5 MeV. We consider the first partial wave $j = 1/2$ and $l = 0$ and couple to the first 3^- state. The two lines in red and blue in Fig. 4 indicate the two R values for which we show the non-locality in Fig. 5. The potential non-locality is almost Gaussian, but with a small emissive part (negative potential) at $s \approx 1.5$ fm. Our results confirm that the choice of a Gaussian non-locality by Perey and Buck for their phenomenological non-local optical potential [12] is a good approximation.

In Figs. 6 and 7, we present some reaction cross section calculations, σ_R, for p+^{40}Ca and for several incident energies. We see that the contribution of the RPA potential to the absorption is null for small incident energies as no inelastic channel is open. The contribution increases as inelastic channels open. In Fig. 6, we compare the reaction cross section obtained from $V_{HF} + \mathcal{I}mV_{RPA}$ (rpa) without removing the

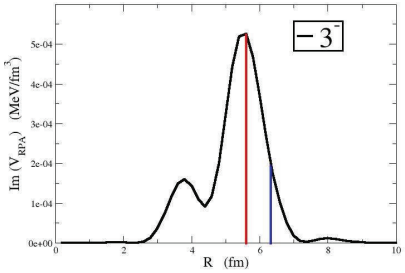

Fig. 4: Im$\nu_{RPA}(r,r)$ for p+^{208}Pb scattering for $j = 1/2$ and $l = 0$. Coupling to the first 3^- excited state E$_{exc}$ =3.4 MeV.

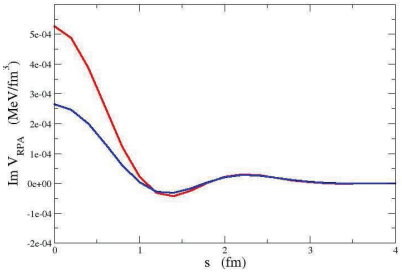

Fig. 5: Non-locality for the two values of R defined in Fig. 4 in red ($R \approx 5.5$ fm) and in blue ($R \approx 6.2$ fm).

double counting term V_{ph} and the one from $V_{HF} + 2\mathcal{I}mV_{ph}$ (2ph). In both cases we use distorted waves in the HF field (DW) to estimate ϕ_λ. Below 40 MeV incident energy, $V_{HF} + \mathcal{I}mV_{RPA}$ provides more absorption than $V_{HF} + 2\mathcal{I}mV_{ph}$ due to collectivity. Above 40 MeV, both cross sections are equivalent because in the RPA description of the target high energy excited states are near from being pure ph excitations and the ph contribution is double counted in RPA.

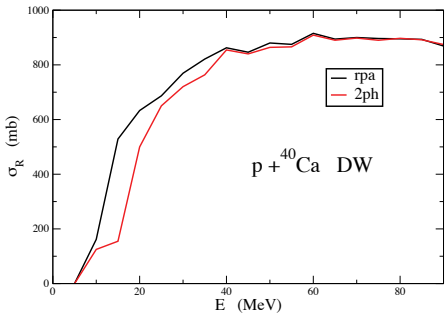

Fig. 6: Reaction cross sections for p+^{40}Ca for $V_{HF} + \mathcal{I}mV_{RPA}$ and $V_{HF} + 2\mathcal{I}mV_{ph}$ with ϕ_λ a distorted wave.

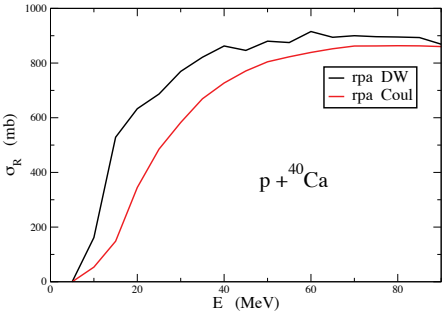

Fig. 7: Reaction cross sections for p+^{40}Ca for $V_{HF} + \mathcal{I}mV_{RPA}$ with ϕ_λ a distorted wave (DW) and a Coulomb wave (Coul).

In Fig. 7, we compare the reaction cross sections for $V_{HF} + \mathcal{I}mV_{RPA}$ calculated with ϕ_λ treated as a Coulomb wave (Coul) or as a distorted wave (DW). The DW treatment of the intermediate wave increases the absorption. It is explained by the action of the HF field that concentrates the ϕ_λ wave function at small radii and by the inclusion of resonances as depicted in Fig. 1. To illustrate this last feature, we show on Fig. 8 the effect of resonances on the reaction cross section σ_R calculated considering only the coupling to the first 1^- state in ^{40}Ca. We compare σ_R obtained with a distorted wave (DW) or a Coulomb wave (Coul) for ϕ_λ. The effect of resonances is important and considerably increases the absorption. We indicate to which resonance each of the bumps corresponds.

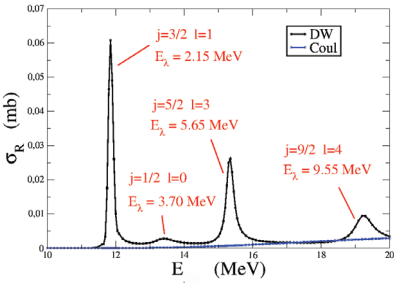

Fig. 8: Reaction cross section *vs.* incident proton energy with $V = V_{HF} + \mathcal{I}mV_{RPA}$. Coupling to the first 1^- in ^{40}Ca (E$_{exc}$=9.7 MeV). Comparison between ϕ_λ treated as a Coulomb wave (Coul) or a wave distorted by the HF potential (DW).

4 Conclusion

We have presented a calculation of nucleon-nucleus scattering within the nuclear structure approach. The optical potential is determined within the HF+RPA approximation. The Gogny D1S force is used consistently to generate the HF and the RPA contributions to the optical potential. As expected, we find that the RPA treatment increases the absorption compared to a particle-hole treatment of the target's excitations. Moreover, calculations performed with correct DW intermediate waves increases the absorption compared to the one obtained with Coulomb functions. Calculations taking into account the real part of V_{RPA} and damping widths in the intermediate propagator, are under progress. Preliminary results already show the importance of the real part of V_{RPA} in the determination of reaction cross section. In further calculations, we plan to take into account phenomena such as the coupling to excited states not described by RPA, the formation of an intermediate deuteron and the double charge exchange process.

Acknowledgements

We wish to thank P. Chau and G. Gosselin for their help in parallel computation.

References

[1] N. Vinh Mau, Theory of nuclear structure (IAEA, Vienna, 1970) p. 931.
[2] N. Vinh Mau and A. Bouyssy, Nucl. Phys. **A257**, 189 (1976).
[3] J. Hüfner and C. Mahaux, Ann. Phys. **73**, 525 (1972).
[4] S. J. Waldecker, C. Barbieri, and W. H. Dickhoff, Phys. Rev C **84**, 034616 (2011).
[5] G. P. A. Nobre et al., Phys. Rev. C **84**, 064609 (2011).
[6] G. Hagen and N. Michel, Phys. Rev. C **86**, 021602(R) (2012).
[7] J. Dechargé, D. Gogny, Phys. Rev. C **21**, 1568 (1980).
[8] J.-F. Berger, M. Girod, and D. Gogny, Comput. Phys. Commun. **63**, 365 (1991).
[9] K. T. R. Davies, S. J. Krieger, and M. Baranger, Nucl. Phys. **84** 545 (1966).
[10] R. H. Hooverman, Nucl. Phys. **A189**, 155 (1972).
[11] J. Raynal, computer code DWBA98, 1998, (NEA 1209/05).
[12] F. Perey and B. Buck, Nucl. Phys. **32** 353 (1962).

Impact of collective excitations on direct pre-equilibrium emission: axially-symmetric-deformed nuclei

*M. Dupuis, S.Péru, E. Bauge and T. Kawano**
CEA, DAM, DIF

Abstract
A microscopic calculation of the first order of direct pre-equilibrium neutron emission for 10-20 MeV neutron scattering off ^{238}U is presented. Cross sections are obtained solving coupled channel equations. The JLM folding model is used to calculate the relevant coupling potentials. Spectroscopic information are calculated from the QRPA model with the Gogny D1S interaction. No arbitrary renormalization process enters our analyzes. Predictions are in good agreement with the data at high emission energy and illustrate the importance of the collective excitations in the modeling of the pre-equilibrium reaction mechanism for a deformed target.

1 Introduction

Pre-equilibrium models usually use adjustable parameters, so predictions cannot be easily extrapolated to domains where data are missing. Furthermore, some measurements have not yet been well explained: the high energy part of the neutron emission spectrum for neutron scattering on ^{238}U was only understood using a very empirical approach [1,2], that consists in adding fictitious collective levels in the low energy spectrum to describe the measured cross section. To improve the modeling of direct pre-equilibrium emission, we developed reaction models that only rely on a microscopic description of the target states, and that use realistic two-body interactions between the projectile and the target nucleons. In [3], a microscopic calculation of the direct pre-equilibrium neutron emission at first order was performed for neutron scattering off ^{90}Zr and ^{208}Pb. In this previous work, target excited states were described as one phonon excitations of the correlated Ground State (GS) predicted by the Random Phase Approximation (RPA) model. This approach, that describes on an equal footing direct inelastic scattering and direct pre-equilibrium emission (first step), provided an accurate description of the high energy neutron emission without any arbitrary normalization. It also demonstrated the importance of collective excitations for this reaction mechanism. In this work, we extend this approach to treat the case of axially deformed targets. Inelastic scattering cross sections are obtained solving coupled channel (CC) equations. The JLM convolution model [4] is used to calculate the diagonal potentials and the transition potentials corresponding to one phonon excitations. A Quasi-particle RPA (QRPA) calculation [5, 6] with the Gogny D1S interaction [7] has been performed to obtain the relevant spectroscopic information.

The theoretical description of direct pre-equilibrium emission is explained in Sec.2. In Sec. 3 we present the QRPA description of the target excitations. In Sec. 4, we explain the coupling scheme adopted in CC calculations and how coupling potentials are calculated, then we present and discuss the results obtained for ^{238}U. We give the conclusions and perspectives of this work in Sec.5.

2 Reaction theory

In the case of inelastic nucleon scattering, the double differential cross section for direct pre-equilibrium emission of a nucleon at the outgoing energy E_f in the range $[E_\mathrm{f}, E_\mathrm{f} + \Delta E]$ reads

$$\frac{d^2\sigma(\mathbf{k}_i, \mathbf{k}_f)}{d\Omega_\mathrm{f} dE_\mathrm{f}} = \frac{1}{\Delta E} \int_{E_f}^{E_\mathrm{f}+\Delta E} dE \sum_n f_n(E_\mathrm{i} - E - E_n) \frac{d\sigma_n(\mathbf{k}_i, \mathbf{k})}{d\Omega_\mathrm{f}} \,, \tag{1}$$

*Los Alamos National Laboratory

where $E_{\rm i} = \frac{k_i^2}{2\mu}$ is the nucleon incident energy, and $E = \frac{k^2}{2\mu}$. The differential cross section $\frac{d\sigma_n}{d\Omega}$ corresponds to the inelastic scattering to a discrete state of excitation energy E_n in the target nucleus. The distribution $f_n(E)$ accounts for the finite width (damping and escape) of this excitation. In [3], these individual cross sections were calculated within the DWBA approximation. For strongly deformed nuclei, it becomes necessary to use a coupled channel approach as very collective states lie at low energy.

To obtain the coupled channels equations for direct inelastic scattering to discrete states, one starts from the Schrödinger equation

$$(H-E)|\Psi\rangle = 0 \ , \ \ H = H_A + T + V \ , \tag{2}$$

where V is a two-body interaction acting between the projectile and the target nucleons, H_A the target Hamiltonian, and T the kinetic energy operator. We develop $|\Psi\rangle$ on the solutions $|n\rangle$ of H_A, namely $|\Psi\rangle = \sum_{n=0}^{\infty} u_n|n\rangle$, where u_n include the relative movement of the projectile and the target, and the spin+isospin wave functions of the projectile nucleon. We introduce the Feshbach projection operators

$$P = |0\rangle\langle 0| + \sum_{n=1}^{k} |n\rangle\langle n| \ , \ \ Q = \hat{1} - P = \sum_{m>k} |m\rangle\langle m| \ , \tag{3}$$

where the sum over n represents a finite set of target excited states, and $|0\rangle$ is the target GS. The definition of this set will be discussed later on. Applying these projection operators on (2), one gets the equation for $P|\Psi\rangle$:

$$(T + V_{\rm eff})\, P|\Psi\rangle = EP|\Psi\rangle \ , \ V_{\rm eff} = P\left(V + VQ\frac{1}{E - QHQ + i\eta}QV\right)P \ . \tag{4}$$

Projecting Eq.(4) on the GS $|0\rangle$ and the excited states $\{|n\rangle\}$ for $n \leq k$, one gets the set of coupled equations

$$(E_i - T_0 - U_{00})\,|u_0\rangle = \sum_{i=1}^{k} U_{0n}|u_n\rangle \ \text{ and } \ (E_f - T_0 - U_{nn})\,|u_n\rangle = \sum_{n'\neq n}^{k} U_{nn'}|u_{n'}\rangle \ \ \forall n \leq 4 \ , \tag{5}$$

where $E_{\rm f} = E_{\rm i} - E_n$. The coupling potentials $U_{nn'}$ are the matrix elements of the effective interaction between the target states, namely $U_{nn'} = (n|V_{\rm eff}|n')$. The parentheses mean integration over all the coordinates of the target nucleons. Individual cross sections for each inelastic channel are calculated from the solutions $|u_n\rangle$ of these equations.

3 QRPA description of the target excitations

A detailed presentation of the QRPA method and its implementation with the Gogny force is provided in [5]. We just remind here that axially-symmetric-deformed Hartree-Fock-Bogoliubov (HFB) calculations are performed imposing T, TP2, axial and left-right symmetry. Then the projection K of the angular momentum J on the symmetry axis and the parity π are good quantum numbers. In the QRPA formalism, the intrinsic excitations of the target are described as one phonon excitation of the correlated ground state $|0_I\rangle$, namely

$$|\alpha K^\pi\rangle = \Theta^+_{\alpha K^\pi}|0_I\rangle = \frac{1}{2}\sum_{ij\in(K^\pi)}\left(X_{ij}^{\alpha K^\pi}\eta^+_{ip_i\Omega_i}\eta^+_{jp_j\Omega_j} - (-)^K Y_{ij}^{\alpha K^\pi}\eta_{ip_i-\Omega_i}\eta_{jp_j-\Omega_j}\right)|0_I\rangle \ , \tag{6}$$

with $\Theta_{\alpha K^\pi}|0_I\rangle = 0$. For an even-even nucleus, the GS is such as $K^\pi = 0^+$. Two-quasiparticles (2-qp) unperturbed excitations of the uncorrelated HFB mean field $|HFB\rangle$ are defined as $|\beta K^\pi\rangle = \eta^+_{ip_i\Omega_i}\eta^+_{jp_h\Omega_j}|HFB\rangle$, where the projections Ω and the parities π of the quasi-particle creation operators

η^+ are such as $\Omega_i + \Omega_j = K$ and $p_i p_j = \pi$. Target states in the laboratory frame are obtained after projection over the total angular momentum

$$|\alpha J M K^\pi\rangle = \mathcal{N} \int d\Omega {\mathcal{D}^J_{MK}}^*(\Omega) R(\Omega) |\alpha K^\pi\rangle + (-)^{J+K} {\mathcal{D}^J_{M-K}}^*(\Omega) R(\Omega) |\alpha \bar{K}^\pi\rangle \ , \tag{7}$$

where $\mathcal{N}$ is a normalization factor, the $\mathcal{D}^J_{MK}$'s are rotation matrix elements, and $R(\Omega)$ is the rotation operator. For the GS and each excitation (6), we obtain a rotational band in the laboratory frame with total angular momenta and parities $J^\pi \geq K^\pi$ if $K > 0$, $J^\pi = 0^+,\ 2^+,\ 4^+$ ... if $K^\pi = 0^+$, and $J^\pi = 1^-,\ 3^-,\ 5^-$ ... if $K^\pi = 0^-$. Excitation energies of the states $|\alpha J M K^\pi\rangle$ are given by the approximation $E_{\alpha K J \pi} = E_{\alpha K^\pi} + \frac{J(J+1)-K^2}{2\mathcal{I}}$, where the energies $E_{\alpha K^\pi}$ are the QRPA equations solutions, and $\mathcal{I}$ is the moment of inertia of the target in its GS.

We introduce the deformed radial GS density $\rho^{0_I,\alpha K^\pi}(\mathbf{r})$ and transition densities $\rho^{0_I,\alpha K^\pi}(\mathbf{r})$

$$\rho^{0_I}(\mathbf{r}) = \langle 0_I | \sum_{i=1}^{A} \delta(\mathbf{r} - \mathbf{r}_i) | 0_I \rangle \ \ , \ \ \rho^{0_I,\alpha K^\pi}(\mathbf{r}) = \langle \alpha K^\pi | \sum_{i=1}^{A} \delta(\mathbf{r} - \mathbf{r}_i) | 0_I \rangle \ . \tag{8}$$

where $\mathbf{r}_i$ is the coordinate of one of the target nucleons. The reduced transition probability of multipolarity $L \geq K$, associated to a transition between a state belonging to the GS band and a state belonging to a rotational band built on an intrinsic excitation of projection K and parity π, reads

$$B(E_L) \sim \int \rho^{0_I,\alpha K^\pi}_L(r) r^{L+2} dr \ \text{ for } \ L > 2 \ , \ \text{ with } \ \rho^{0_I,\alpha K^\pi}_L(r) = \int d\Omega \rho^{0_I,\alpha K^\pi}(\mathbf{r}) Y^L_K(\Omega) \ . \tag{9}$$

This relation holds in the case of a well deformed target for which the rotational approximation, defined as $\int d\Omega d\Omega' \equiv \int d\Omega \delta(\Omega - \Omega')$, applies.

QRPA calculations with the D1S interaction were performed for ^{238}U in a 13 harmonic oscillator major shells basis (see details in [6]). To characterize the collective content of the target spectrum predicted by the QRPA model, we compare the response functions (9) calculated with unperturbed 2-qp excitations, Fig. 1-(a), to those obtained with QRPA excitations, Fig. 1(b). The displayed $L = 3$ response functions correspond to all intrinsic excitations with total angular momentum projections $K \leq 3$. The QRPA response is considerably stronger than the unperturbed one for $E_n < 7$ MeV. It includes very collective transitions below 3 MeV, and two large peaks at 4.5 and 6.5 MeV that forms the Low Energy Octupole Resonance. Those differences between collective and unperturbed responses are also observed for the other angular momentum transfers up to L=8. As we will see, these collective excitations will strongly impact on the inelastic scattering predictions.

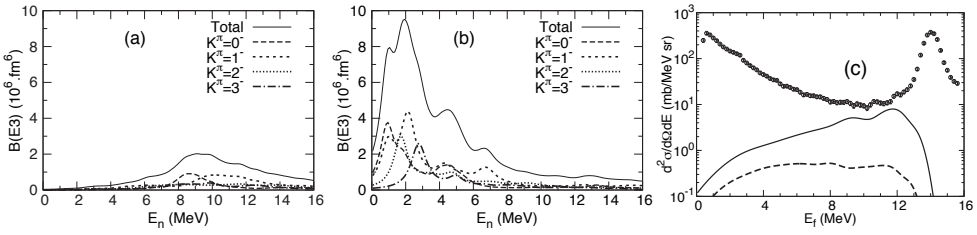

Fig. 1: (a) 2-qp and (b) QRPA $L = 3$ reduced transition probabilities in ^{238}U. Response functions have been folded with a 2 MeV-width Lorentz distribution. The different K components are labeled on the plots. Full black curves correspond to the sum over the K components. (c) Direct pre-equilibrium contribution to the (n,n') double differential cross-section at the outgoing angle $\theta_{c.m.} = 30°$, calculated with QRPA excitations (full curve) or 2-qp excitations (dashed curve), for 14.1 MeV neutron scattering on ^{238}U. The (n,xn) data are from [11].

4 Direct pre-equilibrium emission model for an axially-symmetric deformed target

4.1 Transition potentials and coupling scheme

In our approach, we represent the target spectrum with all the rotational bands built on each intrinsic excitation predicted by the QRPA model. All discrete inelastic scattering cross sections in (1) that correspond to the excitation of each of these states need to be calculated. Coupled channels calculations are performed coupling the rotational band built on the GS (GS band) to the rotational band built on a single intrinsic excitation (excited band). This calculation is repeated for each intrinsic excitation. The coupling potentials $U_{nn'}$ in Eq. (5) are calculated folding the QRPA radial densities (8) with a two-body effective interaction (4). In our applications, we use the folding method described in [4]. The JLM interaction as defined in [8] as been selected to represent the effective interaction. We precise that only direct potentials are used. As the JLM interaction was adjusted without considering knock-out exchange, its energy dependence is expected to approximately account for exchange effects.

The JLM interaction accounts for couplings to all non-elastic channels. Consequently, care should be taken when performing CC calculation. First, the imaginary part of the JLM interaction is reduced, as explained in [4], in order to compensate for the flux lost by the elastic channel when it is coupled to the inelastic channels of the GS band. Moreover, as this effective interaction is now adjusted to fit elastic and inelastic scattering to the GS band, it already includes, in principle, the couplings to all channels outside the GS band. Consequently, the couplings between excited bands are not included in our calculations. We remark that when we couple the GS band to one excited band, the effective interaction should also be renormalized to compensate for the additional absorption. However, as the flux in a single excited band remains small compared to the one in the GS band, we did not apply any additional renormalization.

The approximation of the present model, that limits the coupling to a single excited band, may be discussed as opening the couplings to more excitations may perturb the angular distributions calculated for the different inelastic channels. Note that if such a calculation was performed, the effective interaction should be renormalized each time the coupling scheme is extended. However, as we are interested in the direct pre-equilibrium emission cross-section that corresponds to a sum of many contributions, results should not be too sensitive to the details of individual inelastic channels.

4.2 Results for ^{238}U

We present the direct pre-equilibrium cross-sections (1) calculated with the model described in the previous section. All the intrinsic excitations with $K^{\pm} = 0^{\pm}$ to $8^{\pm}$ predicted by the QRPA model are included in the calculations. The coupled equations (5) are solved with the the code ECIS [9]. Rotational band states (7) are considered up to a total angular momentum $J = 8$, and the coupling potentials in Eq. (5) up to an orbital angular momentum transfer $L = 8$. These truncations ensure a good convergence of the calculations. The spreading functions $f_n(E)$ in Eq. (1) are obtained with the method used in Ref. [3].

Figure 1(c) displays the neutron spectrum for 14.1 MeV neutron scattering off ^{238}U at the emission angle $\theta_{c.m.} = 30°$. On this plot, the direct pre-equilibrium (n,n') cross-sections calculated with QRPA excitations and 2-qp excitations are compared. The cross-section obtained with QRPA excitations is considerably larger, following the behavior of response functions discussed in Sec.3. This illustrates the impact of collective transitions that are not described with 2-qp excitations.

We display on Fig. 2 the QRPA pre-equilibrium emission along with contributions to the (n,xn) cross sections arising from other reaction mechanisms, namely elastic scattering and inelastic scattering to the GS band states, evaporation from the Compound Nucleus (CN) and from the fission fragments. These other contributions are calculated following the method described in [10]. Predictions are compared to (n,xn) experimental data for the three incident energies 11.8 MeV, 14.1 MeV and 18 MeV, and the three outgoing angles $\theta_{c.m.} = 30°$, $90°$ and $120°$. We discuss the displayed spectra in term of excitation energies, namely $E^* = E_{\rm i} - E_{\rm f}$. We first focus on the high energy part of the spectra that corresponds to $E^* < 4$ MeV. At the three displayed incident energies, the predicted cross sections are

almost always in good agreement with the data. In previous analyzes [1, 2], the high energy emission was always underestimated by the pre-equilibrium calculations, and empirical collective states were introduced to obtain a good fit of the experimental cross sections. The present result proves what was postulated in these empirical analyzes: collective transitions, which are now predicted from a well established nuclear structure model, have to be included to describe correctly the direct neutron emission. Exceptions to this good agreement are observed at $E_{\rm i} = 11.8$ and 14.1 MeV for $\theta_{c.m.} = 30^{\circ}$. In the first case, data are largely underestimated only for $E^* = 1 - 2$ MeV. The shape of the experimental elastic peak suggests that a distribution broader than the Gaussian shape assumed in the present calculation should be used. This may improve agreement with the data at high emission energy. In the second case, predictions lie 20% below the data for $E^* = 1 - 4$ MeV This discrepancy is hard to interpret. Studies with other targets at the same incident energy should be perform to test if the same discrepancy remains. At energies E^* =4-9 MeV for $E_{\rm i} = 14.1$, and E^* =4-12 MeV for $E_{\rm i} = 18$ MeV, our predictions clearly underestimate the data. This is discussed in the next section.

4.3 Discussion

In neutron induced reactions, the high energy neutron emission is known to come from a direct inelastic scattering process that excites discrete states in the target. Moreover, the most part of this contribution comes from vibrational collective states which are well described with one phonon excitations predicted by the (Q)RPA model. The good agreement with the data at high emission energy confirms that the excitation of one phonon states, limited to natural parity transitions, is correctly described in the present approach. Thus, as our model does not involve any arbitrary renormalization process, we can state that the discrepancy between our calculations and the data observed a lower emission energy comes from other important reaction mechanisms that are either missing in the present analysis or not well described. First, non-natural parity excitations, that produce up to 20% of the direct pre-equilibrium cross-section for neutron scattering on ^{208}Pb (see [3]), are not yet included. The excitation of two-phonons states via a one or a two-steps process could also provide a non negligible contribution. A good treatment of these two mechanisms could reduced the discrepancy with the data. As seen on Fig.2, evaporation from fission fragments provides non-negligible neutron emission cross sections in the same energy range than the direct pre-equilibrium emission. As this contribution is calculated from a phenomenological model, different parameters set and/or approximations could eventually improve the agreement with the data. In our analysis, we have neglected the Multi-Step Compound (MSC) pre-equilibrium emission mechanism. However, the magnitude of the calculated cross-section varies greatly between different MSC model implementations. A careful study of this process, based on microscopic ingredients, should be performed to measure its actual contribution to the neutron emission.

5 Conclusions

We have presented a microscopic calculation of direct pre-equilibrium emission for 10-20 MeV neutron scattering off the axially deformed nucleus ^{238}U. Our model is based on a microscopic description of the target states, limited to one phonon excitations, provided by the QRPA model implemented with the Gogny D1S interaction. We demonstrate that the large collective content of the target spectrum predicted by the QRPA model allows us to explain the direct neutron emission observed a high energy. Our model does not include any arbitrary renormalization process. However, discrepancies between the predicted cross sections and data appear at lower emission energy and need to be understood. First, the present study is being extended to other targets to provide a better overview of the present model qualities. Non-natural-parity transitions will soon be included in the calculation and effect of two-phonons transitions on the direct pre-equilibrium cross section will also be studied. The description of other reaction mechanisms, such as MSC and evaporation from fission fragments, should also be improved.

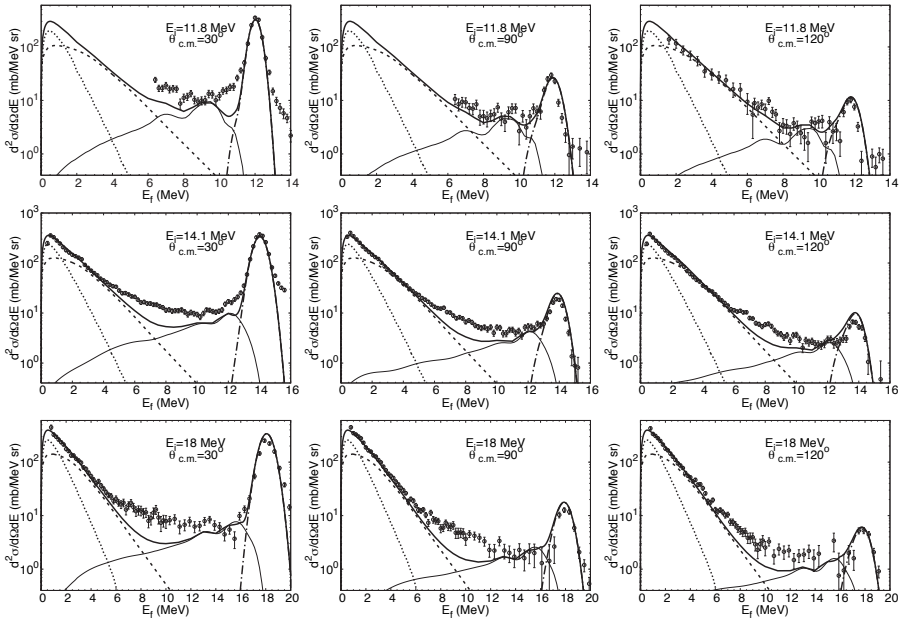

Fig. 2: Double differential (n,xn) cross sections for a ^{238}U target. Incident energies $E_{\rm i}$ and outgoing angles $\theta_{c.m.}$ are given on each plot. Thin full curves correspond to the direct pre-equilibrium emission calculated with QRPA excitations, dashed curves to the evaporation from fission fragments, dotted curves to the evaporation from the CN, dashed-dotted curves to the elastic scattering and inelastic scattering to the GS band states, and thick full curves to the sum of these contributions. Open circles represent data from [11–13].

Acknowledgments

We wish to thank J.-P. Delaroche for enlightening discussions and J. Raynal for his constant support with the code ECIS.

References

[1] T. Miura, M. Baba M. Ibaraki et al, Annals of Nuclear Energy **28**, 937 (2000).

[2] M. Chadwick et al, Nuclear Data Sheets **107**, 2931 (2006).

[3] M. Dupuis, T. Kawano, J.-P. Delaroche and E. Bauge, Phys.Rev.C **83**, 014602 (2011).

[4] E. Bauge et $al.$, Phys.Rev.C **61**, 034306 (2000).

[5] S. Péru and H. Goutte, Phys. Rev. C **78**, 024305 (2008).

[6] S. Peru et $al.$, Phys.Rev.C **83**, 014314 (2011).

[7] J.F. Berger, M. Girod and D. Gogny Comp.Phys.Comm. **63**, 365 (1991).

[8] E. Bauge, J.-P. Delarcoche and M. Giraud, Phys.Rev.C **63**, 024607 (2001).

[9] J.Raynal, CEA report No.CEA-N-2772, 1994.

[10] T. Kawano, T. Ohsawa, M. Baba and T. Nakagawa, Phys. Rev. C, **63**, 034601 (2001)

[11] M. Baba, H. Wakabayashi, N. Ito, K. Maeda and N. Irakawa, J. Nucl. Sci. Technol. **27**, 601 (1990).

[12] M. Baba et $al.$, in *proc. of Int. Conf. on Nuclear Data for Science and Technology*, Jülich, Germany, 1991, edited by S. M. Qaim (Springer-Verlag, Berlin/Heidelberg, 1992), p.349.

[13] Shen Guanren et al,Chinese Physics **8**, 1000 (1988).

What is imaginary part of coupling potential in coupled channel calculation?

T. Furumoto[1] *and Y. Sakuragi*[2,1]
[1] RIKEN Nishina Center, Wako, Saitama 351-0198, Japan
[2] Department of Physics, Osaka City University, Osaka 558-8585, Japan

Abstract
We have analyzed the energy dependence of the coupling effect in the microscopic coupled channel (MCC) method and its relation to the elastic and inelastic-scattering angular distributions in detail in the case of the ^{12}C + ^{12}C system in the energy range of $E = 100$ – 400 MeV/u. The large channel coupling effect is clearly seen in the elastic cross section although the incident energies are high enough. The dynamical polarization potential is derived to investigate the channel coupling effect. We also analyze the role of the imaginary part of the coupling potential on the elastic and inelastic cross sections.

1 Introduction

The collective excitation of nuclei is known to play an important role in heavy-ion (HI) reactions. The strong coupling among the ground and low-lying collective states of colliding nuclei requires a non-perturbative treatment to properly account for the coupling effects on the elastic and inelastic scatterings. The coupled-channel (CC) method is one of the most reliable and established reaction theory to study the role of nuclear excitations in HI reactions and to extract nuclear-structure information through the CC analyses of the experimental data [1]. For the last several decades, the CC calculation technique has been developed from the microscopic view point. That is so-called as microscopic coupled-channels (MCC) method, which have been proposed on the basis of microscopic optical potential models [2]. In the MCC method, the diagonal and coupling potentials used in the CC calculations are constructed by the double-folding model (DFM) with the use of an effective nucleon-nucleon (NN) interaction.

On the early stage of the MCC studies of HI reactions, the effective NN interactions called the M3Y interaction or its density-dependent version called DDM3Y (including its modified versions) have been used in constructing the diagonal and coupling potentials [2,3]. These interactions, especially the density-dependent versions, have been prove to give a good account of the strength and shape of the internuclear potentials. However, all these effective NN interactions have real part only and, therefore, one has to add an phenomenological imaginary part by hand to the diagonal and coupling potentials obtained by the DFM calculations with the real NN interactions, which makes the results of CC calculations still ambiguous. It is of particular importance to note that the channel-coupling effects largely depend on the real to imaginary ratio of the coupling potentials [4,5].

Recently, a microscopic interaction model that predicts complex optical potentials for HI systems has been proposed and successfully applied to HI elastic scattering over the wide range of incident energies [6–8]. In this model, a new type of complex effective NN interaction called CEG07 was constructed on the basis of the Breuckner G-matrix theory and the CEG07 interaction is doubly folded with the nucleon density distributions of the colliding nuclei giving a complex optical potential for the HI system. It is rather straightforward to generalize the successful microscopic theory for complex HI optical potential to the study of inelastic scattering of HI system that excites low-lying collective excited states. Namely, it is just to replace the real effective NN interaction (such as the DDM3Y one) by the complex one (CEG07) in the DFM calculation of the diagonal and coupling potentials within the MCC framework. This kind of MCC method based on the complex NN interaction was first applied to the elastic and inelastic scattering of ^{16}O + ^{16}O system at medium energies [9].

Here, it should be noted that the microscopic HI optical potentials predicted by the DFM with CEG07 shows a characteristic energy dependence. The real part of the HI optical potential becomes shallower as the increase of the incident energy and changes its sign from negative (attractive) to positive (repulsive) at the incident energy per nucleon around 300 MeV/u region, whereas the imaginary part of the optical potential gradually increase with the increase of the incident energy [8]. Although the precise energy region where the attractive to repulsive transition occurs is still to be examined through experimental confirmation [10], there is no doubt that the real to imaginary ratio of the optical potentials must drastically change in such medium to high energy region.

This kind of characteristic behavior of the microscopic optical potential will manifest itself also in the complex coupling potentials calculated with the CEG07 interaction within the MCC framework. In the present paper, we study the energy dependence of the real and imaginary part of the coupling potentials derived from the CEG07 interaction and investigate its relation to the channel-coupling effects on the elastic and inelastic scattering of the ^{12}C + ^{12}C system in the MCC framework. Particular attention will be paid to the characteristic energy dependence of the so-called dynamical polarization potential (DPP) and its relation to the energy dependence of the real to imaginary ratio of the coupling potential predicted by the microscopic interaction model with the CEG07 interaction.

2 Formalism

We apply the complex G-matrix interaction CEG07 to analyze the channel-coupling effect on elastic cross section and the energy dependence of the inelastic cross section through the MCC calculation based on the double-folding model. The detail of the MCC calculation for the heavy-ion system is presented in Refs. [3,11,12]. The effective NN interaction used in the present MCC calculation is the CEG07b interactions [6,13]. The CEG07b includes the three-body force (TBF) effect that is found to be essentially important to predict proper shape and strength of the nucleus-nucleus interaction consistent with the observed elastic scattering data [6–8].

The imaginary part of the calculated potential in the MCC method is multiplied by a renormalization factor N_W, the value of which is the only free parameter in the CEG07 folding model. In the previous analyses [6,7,9], its values were determined so as to reproduce the experimental data on the elastic and inelastic-scattering cross sections to be compared with the calculated ones. However, there exist no experimental data to be compared with the calculations in the high energy region $E = 100 - 400$ MeV/u and we fix the N_W value to unity unless otherwise mentioned as in Ref. [8].

We discuss the channel-coupling effect not only in the calculated cross sections but also in terms of the wavefunction-equivalent dynamical polarization potential (DPP), $U^{(J)}_{\rm DPP}$, that is J-dependent and defined in Ref. [11] in the framework of the coupled-channel method.

3 Results

We apply the MCC with the CEG07 G-matrix interaction to the ^{12}C + ^{12}C elastic and inelastic scattering at four incident energies, E = 100, 200, 300, and 400 MeV/u and first analyze the energy dependence of the channel coupling effect in the elastic cross sections. In the present MCC calculation, the single and mutual excitations to the 2^+_1 (4.44 MeV), 0^+_2 (7.65 MeV), 3^-_1 (9.64 MeV), and 2^+_2 (10.3 MeV) excited states of ^{12}C are taken into account. The diagonal and transition densities among the ground state and those excited states are taken from Ref. [14] obtained by the 3α-RGM calculation. In this paper, we call the CC calculation that takes account of the full combination of excited states of the projectile and target nuclei as the full-CC calculation. However, the single and mutual excitations to the 2^+_1 state are found to play a dominant role in the elastic and inelastic scattering discussed here.

First, we plot the energy dependence of the real and imaginary part of the coupling potential between the elastic channel and the 2^+_1 single-excitation channel (Fig. 1). Here, the real and imaginary parts of the coupling potential have similar strength at $E = 100$ MeV/u. In the energy evolution, the

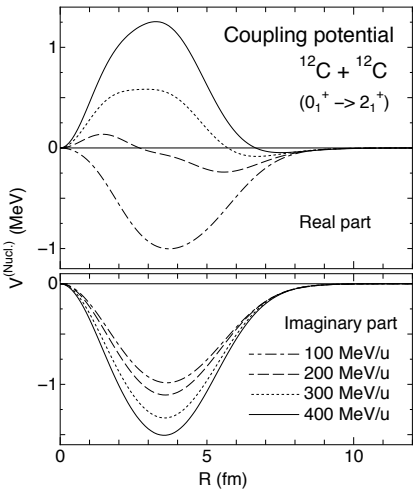

Fig. 1: The real and imaginary parts of the coupling potential between the elastic channel and the single-excitation channel to the 2_1^+ state at $E = 100$, 200, 300, and 400 MeV/u.

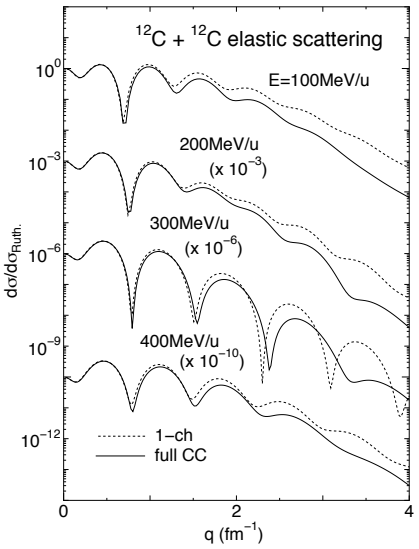

Fig. 2: Rutherford ratio of the elastic-scattering cross sections, displayed as the functions of the momentum transfer q. The dotted and solid curves are the results of single-channel and full-CC calculations, respectively.

real part of the coupling potential changes its sign between 200 and 300 MeV/u in the same manner as in the case of the diagonal potential [8], while the strength of the imaginary part gradually increases monotonically.

Figure 2 shows the angular distributions of the ^{12}C + ^{12}C elastic-scattering cross sections calculated at the four incident energies. The relativistic-kinematics correction has been made in all the CC calculations presented in this paper. The dotted and solid curves are the results of the single-channel and full-CC calculations, respectively. The sizable channel coupling effect is clearly seen in the elastic cross sections at all incident energies including the highest one. It is found that the dominant contribution to the channel-coupling effects on the elastic scattering comes from the 2_1^+ single-excitation channel. In the comparison of the single channel calculation with the full-CC one, it is seen that the diffraction pattern of the cross sections slightly shifts backward and the cross sections decreases at large angles by the channel-coupling effect. Although the effect on the cross sections looks similar to all the incident energies, the contents of the effect are very different as shown below in terms of the DPP.

Figures 3 to 6 show the complex DPP for $J = 20$, 40, 60 and 80 at all incident energies. The oscillation of the DPP is mainly due to the oscillation of the elastic-channel wave function that appears in the denominator in the definition of the DPP [5]. The oscillation, however, does not lead to any anomaly in the calculated cross sections because the DPP multiplied by the elastic-channel wave function in the CC equations is a smooth function of the radial valiable R. It should be noted that the DPP at short distances less than about 3 fm plays little role in the scattering because of the strong absorption in this region [8] and we here discuss the DPP outside the strong absorption region ($R \geq 3$ fm). In this region, the J dependence of DPP is rather small at all energies. The real part of the DPP shows the transition from positive (repulsive) to negative (attractive) around 200 MeV/u, whereas the imaginary part changes its sign from negative to positive at the surface region.

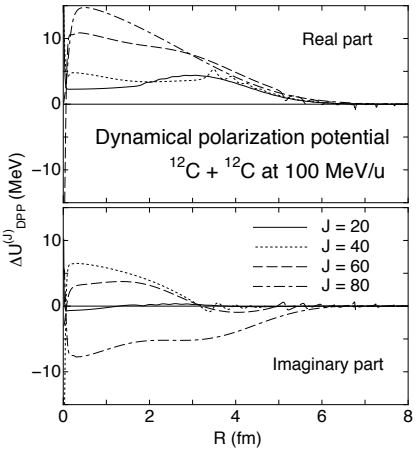

Fig. 3: Real (upper) and imaginary (lower) parts of the dynamical polarization potentials at $E = 100$ MeV/u. The solid, dotted, dashed, and dot-dashed curves are the results for $J = 20, 40, 60$, and 80, respectively.

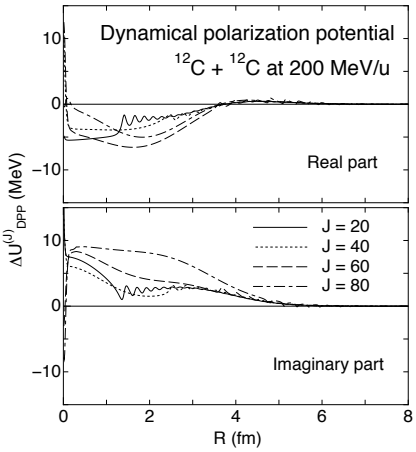

Fig. 4: The same as Fig. 3 but at $E = 200$ MeV/u.

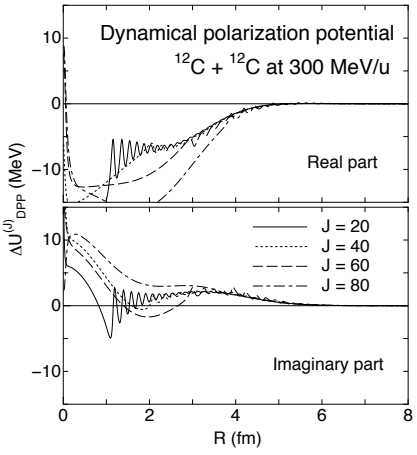

Fig. 5: The same as Fig. 3 but at $E = 300$ MeV/u.

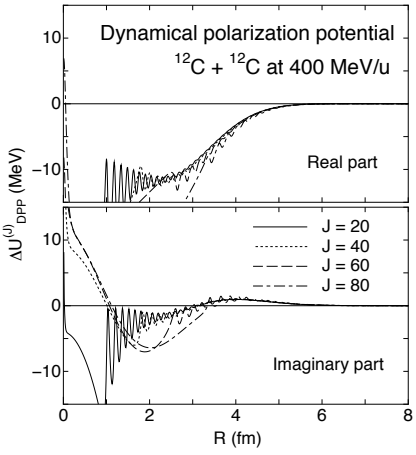

Fig. 6: The same as Fig. 3 but at $E = 400$ MeV/u.

The sign and the strength of the DPP have a close relation to the relative sign and the strength of the real and imaginary parts of the coupling potential [5]. Therefore, the characteristic energy evolution of the DPP can be easily understood through the energy dependence of the complex coupling potential shown in Fig, 1. For example, the negative (attractive) sign of the real part of DPP at 300 and 400 MeV/u is the result of the different sign of the real and imaginary parts of the coupling potential at those energies, whereas the positive sign of the imaginary part of DPP at 200 and 300 MeV/u can be understood by the dominance of the imaginary coupling at the sensitive region ($R \geq 3$ fm) at these energies [5].

Next, we discuss the role of the real and imaginary parts of the complex coupling potentials on the elastic and inelastic cross sections. As we have shown in Fig, 1, the real part of the coupling potentials drastically changes with energy and so does the real to imaginary ratio of the coupling potentials. There-

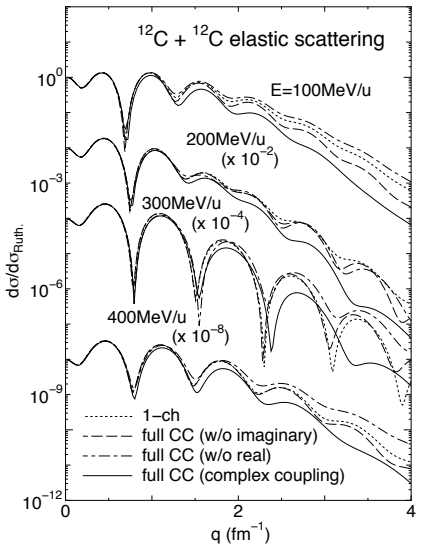

Fig. 7: The effect of the real and imaginary coupling on the elastic cross sections. The solid, dotted, dashed, and dot-dashed curves are the results of the full-CC, single-channel, full-CC without imaginary coupling, and full-CC without real coupling calculations, respectively.

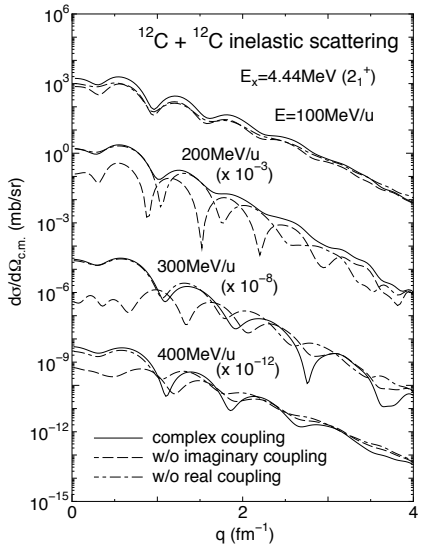

Fig. 8: The effect of the real and imaginary coupling on the inelastic cross sections. The solid, dashed, dot-dashed curves are the results of the full-CC, full-CC without imaginary coupling, and full-CC without real coupling calculations, respectively.

fore, both the real and imaginary parts of the coupling potentials play an important role in the elastic scattering and the complex coupling gives rise to the large channel-coupling effects. In fact, if we switch off either the real part or the imaginary part from the coupling potentials, the channel coupling effect becomes small and very different from that with the complex coupling as shown in Figure 7.

The complexness of the coupling potentials has more essential importance in the inelastic scattering. Figure 8 compares the inelastic-scattering cross sections for the single excitation to the 2_1^+ state. The solid curves are the full-CC calculation with the complex coupling (solid) which are compared with the CC calculations without the imaginary coupling (dashed curves) and those without the real coupling (dot-dashed curves). At 100 MeV/u, both the real and imaginary coupling play comparable roles in the inelastic cross section. In the cases of 200–400 MeV/u, the drastic difference between the solid and the dashed curves indicates the decisive role of the imaginary coupling that dominate the whole strength of the inelastic cross sections, especially at forward angles .

These can be understood with the relative strength of the real and imaginary part of the coupling potential around the nuclear surface region shown in Fig. 1, namely by notifying the similar strength of the real and imaginary parts at 100 MeV/u and the large strength of the imaginary part relative to the real one around the nuclear surface region at 200–400 MeV/u. For the highest energy, 400 MeV, the strength of the real part grows up again and its effect is visible in the cross section although the imaginary part still has a dominant role at this energy.

These results suggest that the measurement of the strength of inelastic cross sections at forward angles would provide a crucial test of the validity of the present microscopic interaction model to be used for generating the complex coupling potentials for inelastic excitations of colliding nuclei [15]. Such an experimental test will add another evidence of the validity of the present DFM based on the complex

G-matrix interaction CEG07, which has already been established in the construction of the microscopic optical potentials for heavy ions [6–8]. In addition, the observation of the inelastic cross section at those high energies will be a start to answer for the question "What is imaginary part of coupling potential in coupled channel calculation?", which is the tile of this paper.

4 Summary

The channel coupling effect on the elastic cross section is investigated with the microscopic coupled channel (MCC) method using the complex G-matrix interaction CEG07 for the ^{12}C + ^{12}C system at $E =$ 100, 200, 300, and 400 MeV/u. The channel coupling effect is clearly seen at all the incident energies. The dynamical polarization potential (DPP) has been derived to investigate the channel coupling effect in detail. The real part of the DPP shows the transition from repulsion to attraction as the increase of the incident energy, whereas the imaginary part of the DPP changes its sign from negative to positive. These characteristic energy dependence of the DPP can be understand by the drastic energy dependence of the real and imaginary parts of the coupling potential predicted by the DFM with the CEG07 G-matrix interaction that is successful in the analyses of elastic scattering of heavy ions [6–8].

We also investigate the effect of the real and imaginary coupling potentials on the elastic and inelastic cross sections. Both the real and imaginary parts of the complex coupling potential have large channel coupling effects on elastic scattering. The imaginary part of the coupling potential dominate the whole strength of the inelastic cross sections at forward angles at higher energies, 200–400 MeV/u, which is also understood from the energy evolution of the real and imaginary parts of the coupling potential predicted by the DFM. Since the magnitude of the inelastic cross section at forward angle at these energies are very sensitive to the strength of the imaginary part of the coupling potential, the experimental measurement of the forward-angle cross sections will remove the ambiguity of the imaginary-coupling strength in the theoretical models.

Acknowledgments

One of authors (T.F.) is supported by the Special Postdoctoral Researcher Program of RIKEN.

References

[1] G. R. Satchler, *Direct Nuclear Reactions* (Oxford University, Oxford, 1983)
[2] G. R. Satchler and W. G. Love, Phys. Rep. 55, 183 (1979)
[3] D. T. Khoa and G. R. Satchler, Nucl. Phys. A668, 3 (2000)
[4] Y. Sakuragi, M. Yahiro and M. Kamimura, Prog. Theor. Phys. Suppl. 89, 136 (1986)
[5] Y. Sakuragi, Phys. Rev. C 35, 2161 (1987)
[6] T. Furumoto, Y. Sakuragi and Y. Yamamoto, Phys. Rev. C 80, 044614 (2009)
[7] T. Furumoto, Y. Sakuragi and Y. Yamamoto, Phys. Rev. C 79, 011601(R) (2009)
[8] T. Furumoto, Y. Sakuragi and Y. Yamamoto, Phys. Rev. C 82, 044612 (2010)
[9] M. Takashina, T. Furumoto and Y. Sakuragi, Phys. Rev. C 81, 047605 (2010)
[10] C. L. Guo, G. L. Zhang, I. Tanihata and X. Y. Le, Chin. Phys. C 36, 047605 (2012)
[11] Y. Sakuragi, M. Yahiro and M. Kamimura, Prog. Theor. Phys. 70, 1047 (1983)
[12] M. Katsuma, Y. Sakuragi, S. Okabe and Y. Kondo, Prog. Theor. Phys. 107, 377 (2002)
[13] T. Furumoto, Y. Sakuragi and Y. Yamamoto, Phys. Rev. C 78, 044610 (2008)
[14] M. Kamimura, Nucl. Phys. A351, 456 (1981)
[15] T. Furumoto and Y. Sakuragi, in preparation.

Reaction theory for studying rare isotopes

F.M. Nunes, J. Liu, N.B. Nguyen, L. Titus and N.J. Upadhyay
National Superconducting Cyclotron Laboratory and Department of Physics and Astronomy, Michigan State University, East Lansing, MI 48824, USA

Abstract
Rare isotopes are often studied through nuclear reactions. Reliable reaction theory is needed to be able to extract the desired information from data. In these proceedings we briefly summarize some of the advances in reactions theory, including tests on exisiting models to better understand their range of validity and accuracy. We focus on deuteron induced reactions for which a number of important benchmarks have been recently performed.

1 Motivation

Low energy nuclear physics has seen for the last couple of decades important investments toward more powerful accelerators. Laboratories such as RIKEN (Japan), GSI (Germany) and NSCL/FRIB (USA) have either completed or are in the process of building new facilities with increased capabilities. This means that one can explore new isotopes, but also it represents increased particle production rates which then allows for more detailed reaction studies.

Nuclear reactions are the most diverse tool for studying the properties of nuclei. Through the wide range of kinematic choices, one can probe the surface, the asymptotic behavior, excitations, deformations, etc, etc. It is thus of paramount importance for the low energy programs to have reliable reaction theory that enables a meaningful analysis of the data.

The study of reactions with rare isotopes can provide critical information for structure many-body theories, which in turn will test assumptions made on the effective nucleon-nucleon interaction. This is ultimately the big goal of our field, to understand the force that binds nucleons together to make the matter that surrounds us. Studying rare isotopes provides a level of sensitivity to parts of the nuclear force which is otherwise hidden, for example the isospin dependence, the density dependence and role of many-body forces. To have a many-body structure theory with predictable power, one needs to include reactions with rare isotopes in the study.

One of the most important physics questions in our time, is to know how and where the heavy elements were formed. Although we do not fully have an answer to this question, we certainly know that part of the elements were formed in hot explosive environments and involved neutron rich isotopes, many nucleons away from stability (the so-called r-process). Neutron capture reactions relevant for the r-process may never be measured in the laboratory because they involve species that decay quickly, but there are indirect methods involving nuclear reactions from which one can extract the information of astrophysical interest [1]. Here again, reactions with rare isotopes play an important role.

With reactions playing such an important role, both for understanding the nuclear force, and the origin of the elements, it is critical to have reliable reaction theory. Here we briefly summarize some advances made in benchmarking existing theories, and present some ongoing efforts to advance the methods used today. We focus on deuteron induced reactions, and mostly on one nucleon transfer A(d,p)B. For closed shell targets, this problem can be addressed within a three-body model $n + p + A$ and the ingredients of the theory are effective interactions which can be constrained by elastic scattering thus reducing ambiguities. In Section II we discuss some of the existing theories and the underlying assumptions, in Section III we summarize some of the results obtained in the comparisons, and in Section IV an overview of current and future work is presented.

2 General aspects of theories for A(d,p)B reactions

Most of us learned about the distorted wave Born approximation (DWBA) in our graduate studies [1]. This method, in its common implementation, assumes the transfer proceeds through a single step, and takes an effective d-A interaction to represent the incoming wave and a p-B interaction for the outgoing wave. DWBA continues to be the most popular method to analyse (d,p) transfer angular distributions [2]. DWBA neglects deuteron breakup, beyond what might be included in the d-A potential, an assumption that has been long questioned given the loosely bound nature of the deuteron (2.2 MeV).

Specifically to address this drawback of DWBA, the adiabatic wave method (ADWA) was developed. In this method the deuteron continuum is explicitly included, although in a simplified form [3–5]. The approximations in ADWA work best if np are close together and thus should be adequate to compute transfer cross sections in post-form.

To include deuteron breakup in a more detailed manner, the continuum discretized coupled channel (CDCC) method [6, 7] was constructed. In CDCC, the three-body wavefunction is expanded in the full set of eigenstates of the $n - p$ subsystem. Given the necessary truncations of the basis, this method is not exact, particularly when rearrangment channels are involved.

In order to solve the three-body problem $n + p + A$ exactly, it is best to include explicitly in the basis the rearrangement channels. The Faddeev method [8] starts then from this overcomplete basis, includes all Jacobi components providing additional flexibility to describe what happens not only when the neutron and proton are close and correlated, but also when the $n - p$ subsystem has absorbed a large part of the energy of the system and are no longer spatially correlated. The Faddeev-AGS method [9, 10] transcribes the problem into a T-matrix integral equation in momentum space and together with techniques specifically developed to handle Coulomb, can provide exact solutions to $d + A \rightarrow d + A$, $d + A \rightarrow p + B$, $d + A \rightarrow n + B'$ and $d + A \rightarrow n + p + A$.

3 Comparing methods for A(d,p)B reactions

3.1 DWBA versus ADWA

Recent work [11] analysed angular distributions resulting from the reaction ^{10}Be(d,p)^{11}Be for a wide range of energies. Spectroscopic factors for the ground state and the first excited state of ^{11}Be were extracted using DWBA and subsequently finite range ADWA. Three important conclusions can be drawn from the study: i) the spectroscopic factors extracted show a large dependence on beam energy for DWBA while virtually no dependence is observed for ADWA, ii) the spectrosopic factors depend strongly on the choice of the optical potentials in DWBA but a much weaker dependence is found in ADWA and iii) the overall magnitude of the spectroscopic factors obtained with ADWA is systematically smaller than with DWBA.

The first point can be understood based on the fact that DWBA leaves out important physics in the dynamics, namely deuteron breakup. By including it, ADWA is able to capture the dependence on beam energy reliably. The second point is related to this fact that ADWA is constructed solely on nucleon-optical potentials which are better understood. We will come back to the dependence on optical potentials in 4.1. Finally, the last aspect is criticial for the interpretation of the results obtained through (d,p) experiments. When reduction factors are discussed (e.g. [12]) and interpreted as missing correlations in the many-body structure theory, one needs to consider deuteron breakup in the analysis.

In Fig.1 we compare DWBA and ADWA for another reaction of interest ^{132}Sn(d,p)^{133}Sn(g.s.) at $E_{\rm d}$ = 9.5 MeV [13]. This reaction was recently measured and offers an excellent example of the sort of reactions one needs to describe. Shown are the angular distribution as a function of the center of mass angle and the interactions included in the DWBA and ADWA calculations are the same as those in [13]. ADWA predicts a cross section around 20% larger than DWBA and consequently the extracted spectroscopic factor is 20% smaller.

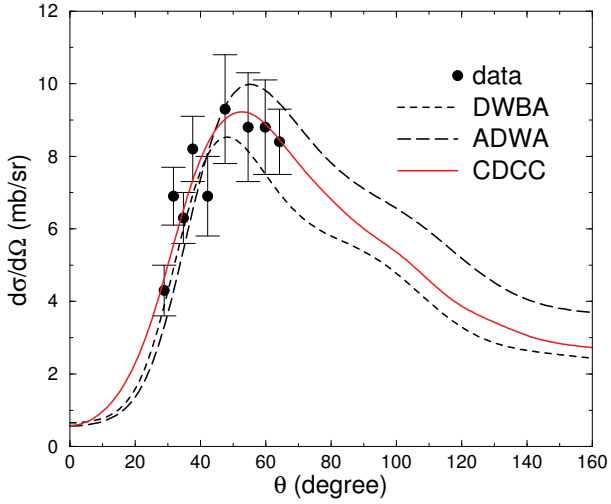

Fig. 1: Comparing methods for ^{132}Sn(d,p)^{133}Sn(g.s.) at $E_{\rm d}$ = 9.5 MeV. Angular distributions as a function of the center of mass angle for DWBA (black dashed), ADWA (blue long-dashed), CDCC (red solid) and experiment (black circles) [13].

3.2 Zero range versus finite range ADWA

The study of Nguyen et al. [14] compares, in a systematic manner, the zero-range ADWA [3] and the finite-range ADWA [4]. A large number of cases were chosen with the condition that data exist and ADWA provides a good description of the angular distribution. Results show that the zero-range approximation introduces an error of the order of 10% for low energy (d,p), and this value increases to 50% or more for higher energies. Although the work in [14] concentrates on the ground state, recent work developed by Liu *et al.* for (d,p) reactions populating excited states [15] show similar trends. In [15] a comparison with DWBA was also made but for many cases the standard optical potential parameterizations did not provide an adequate description of the angular distribution, confirming the strong sensitivity to the details of the optical potential found in [11]. Since it is not computationally demanding, results in [14, 15] provide a clear preference for the use of the finite-range ADWA in the analysis of (d,p), over its zero-range counterpart or the traditional DWBA. From now on we will use ADWA to refer to the finite-range version only.

3.3 ADWA versus Faddeev

Since ADWA provides a practical way in which to analyse (d,p) data, if one is to replace DWBA by ADWA as the working tool for experimentalists, it is necessary to better understand the validity of the approximations and the type of precision obtained in ADWA. After all, it does assume a Sturmian expansion truncated to one term [4]. From its formalism one expects ADWA to do better for low energy, but it was unclear at what beam energy would it breakup down.[1] With this motivation in mind, a comparison of ADWA with Faddeev was performed in [16]. Results for a number of reactions, at a wide range of energies, demonstrate that ADWA compares very well with the exact Faddeev-AGS transfer cross sections for reactions at around 10 MeV/u. Indeed for s-wave final states the agreement was close

[1] Unfortunately the name ADWA is misleading because adiabatic usually refers to a high energy approximation. This is not the case for the method introduced in [4].

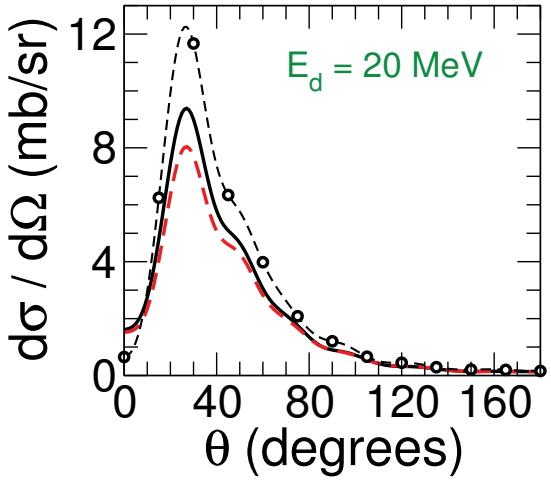

Fig. 2: Optical potential dependence of the angular distribution of ^{208}Pb(d,p)^{209}Pb at $E_{\rm d}$ = 20 MeV. We compare CH89 [18] with KD [19] and BG [20]. All calculations performed within CDCC.

to perfect. However the agreement deteriorates with beam energy and with increasing angular momentum transfer. Both these points can be well understood given that in ADWA one assumes that the full three-body deuteron wave has the same radial behaviour as the first term of the Sturmian expansion and that would naturally apply to low energy and zero angular momentum. We also found in [16] a larger sensitivity to the energy at which the optical potential parameters were obtained for reactions at higher beam energies. Note that global parameterizations of optical potentials are always energy dependent and the Faddeev-AGS formulation in [16] uses a fixed energy independent Hamiltonian.

3.4 CDCC versus Faddeev and ADWA

Most recently, a detailed comparison between CDCC and Faddeev has been completed [17]. In this work, all relevant channels (elastic, breakup and transfer) are studied. Given the difficulties in obtaining convergence for breakup channels, the comparison was performed neglecting the spin of the nucleons. Here we focus on the results for transfer. As for ADWA, very good agreement is found for reactions around 10 MeV/u, where most experiments in ISOL facilties take place. However that agreement is somewhat lost at the higher energies, where a larger dependence on the interactions is present. One can therefore unambiguously validate CDCC and ADWA against the exact calculations only for the lower energies.

ADWA can be thought of as a simplified CDCC calculation. One would then expect that CDCC remains valid in regions where ADWA is not. Particularly, since CDCC takes the expansion in $n-p$ partial waves explicitly up to convergence, we expected it would do much better than ADWA in cases where the angular momentum transfer is not zero. Results for (d,p) reactions on ^{12}C or ^{48}Ca do not show this trend. The examples studied in [17] suggest a similar level of agreement of ADWA and CDCC with the exact Faddeev calculations.

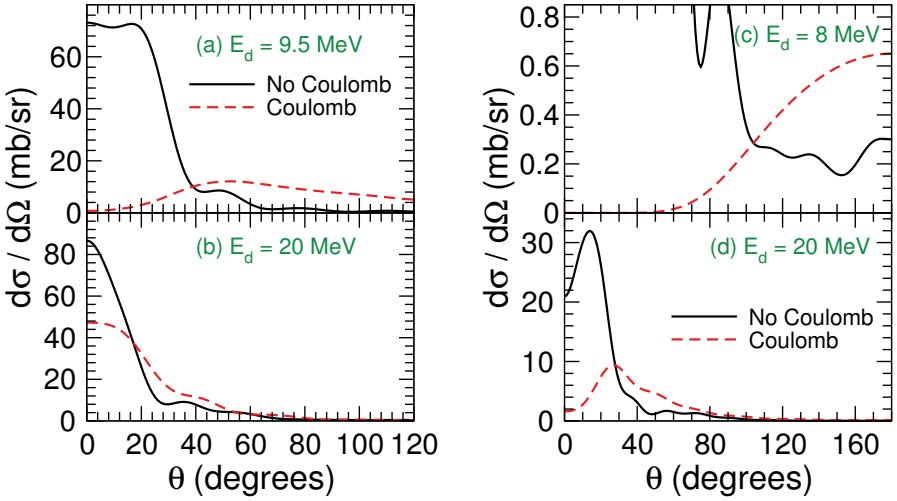

Fig. 3: Coulomb effects on the breakup cross sections for ^{132}Sn(d,p)^{133}Sn(g.s.) at (a) $E_{\rm d}$ = 9.5 MeV and (b) $E_{\rm d}$ = 50 MeV and for ^{208}Pb(d,p)^{209}Pb(g.s.) at (c) $E_{\rm d}$ = 8 MeV and (d) $E_{\rm d}$ = 20 MeV.

4 Outlook

4.1 Better constraints on the optical potential

Given the interest in neutron-rich heavy isotopes in connection to the r-process, it is important to understand the dependence on the nucleon optical potential. We performed CDCC calculations for a number of cases, exploring different nucleon-nucleus parameterizations [18–20]. In Fig.2 we present results for the angular distributions following ^{208}Pb(d,p)^{209}Pb at $E_{\rm d}$ = 20 MeV. While all these potentials provide identical $p - Pb$ elastic angular distributions at 10 MeV, the corresponding (d,p) transfer distributions differ considerably. Even constraining the optical potential with elastic is not sufficient to obtain the desired accuracy. This result suggests that one does need to combine data with microscopic theory to reduce the ambiguities in the optical potential.

One aspect of the optical potentials that arises naturally from microscopic theories and is most often neglected in reaction calculations is non-locality. The connection of the optical potentials with many-body structure models, including non-locality, requires additional efforts in the future.

4.2 The Coulomb problem

One interesting outcomes from these comparative studies [16, 17] was a better understanding of the limitations of the present implementation of Faddeev-AGS [10]. Of particular relevance is the Coulomb force which is well known to create problems in three-body reactions models. The development of Coulomb screening and renormalization techniques were essential to enable the application of the method to nuclear reactions [10]. However only light to medium nuclei can be tackled, while much of the interest in the future lies in nuclei with $Z > 20$. ^{132}Sn is a cornerstone example since it is one of the only bound doubly magic nuclei, far from stability, and accessible to experimental studies. In Fig.1 we show the angular distribution for the transfer ^{132}Sn(d,p)^{133}Sn(g.s.) at $E_{\rm d}$ = 9.5 MeV computed in DWBA, ADWA and CDCC (multiplied by the appropriate statistical factor to correct for neglecting spin). No Faddeev solution could be obtained for this case.

Since Coulomb represents large technical difficulties, it is fair to ask to what extent is it important

in transfer reactions, and in the analysis of (d,p) angular distributions. We performed CDCC calculations in the energy range where it was demonstrated to be valid, for a number of cases, to explore this aspect. For light systems $A \approx 12$ Coulomb has a small effect in the transfer cross section and could be safely neglected or approximated. Fig.3 shows the effect on heavy systems. At sub-Coulomb energies, the reaction dynamics is dictated by the Coulomb force and therefore one cannot expect any sensible answer when ignoring the Coulomb interactions (Fig3(c)). The other panels in Fig. 3 show clearly that the Coulomb effect in (d,p) reactions above the Coulomb barrier is still very important for these heavier systems. Thus, it is critical to treat the Coulomb force in the three-body problem accurately.

This problem is being addressed by the TORUS collaboration [21]. A new method that does not rely on Coulomb screening, has recently been suggested to enable the treatment of Coulomb for any case [22]. Work along these lines is in progress.

References

[1] Ian Thompson and Filomena Nunes, Nuclear Reactions for Astrophysics, Cambridge University Press, Cambridge 2009.

[2] M.B. Tsang *et al.*, Phys. Rev. Lett. 95, 222501 (2005); Phys. Rev. Lett. 102, 062501 (2009).

[3] R.C. Johnson and P.J.R. Soper, Phys. Rev. C 1, 976 (1970).

[4] R.C. Johnson and P.C. Tandy, Nucl. Phys. A235, 56 (1974).

[5] R.C. Johnson, in "Reaction Mechanisms for Rare Isotope Beams", 2nd Argonne/MSU/JINA/INT RIA workshop. MSU, East Lansing, 9-12 March, 2005, (ed. by B.A. Brown) AIP Conf. Conf. Procs. 79, 128 (2005).

[6] N. Austern, Y. Iseri, M. Kamimura, M. Kawai, G. Rawitsher, and M. Yahiro, Phys. Rep. **154**, 125 (1987).

[7] F.M. Nunes, Scholarpedia, 6(9):10497 (2011).

[8] L. D. Faddeev, Zh. Eksp. Theor. Fiz. 39, 1459 (1960); [Sov. Phys. JETP **12**, 1014 (1961)].

[9] E. O. Alt, P. Grassberger, and W. Sandhas, Nucl. Phys. **B2**, 167 (1967).

[10] A. Deltuva, Phys. Rev. C 79, 021602(R) (2009); Phys. Rev. C 79, 054603 (2009).

[11] K.T. Schmitt *et al.*, Phys. Rev. Lett. 108, 192701 (2012).

[12] Jenny Lee *et al.*, Phys. Rev. Lett. 104, 112701 (2010).

[13] Kate Jones *et al.*, Phys. Rev. C 84, 034601 (2011).

[14] N.B. Nguyen, F.M. Nunes and R.C. Johnson, Phys. Rev. C 82, 014611 (2010).

[15] Jiawen Liu, final report for the REU program, Department of Physics, Michigan State University, August 2012.

[16] F. M. Nunes and A. Deltuva, Phys. Rev. C 84, 034607 (2011).

[17] N.J. Upadhyay, A. Deltuva and F.M. Nunes, Phys. Rev. C 85, 054621 (2012).

[18] R. L. Varner *et al.*, Phys. Rep. **201**, 57 (1991).

[19] A.J. Koning and J.P. Delaroche, Nucl. Phys. A 713, 231 (2003).

[20] F. D. Becchetti, Jr. and G. W. Greenlees, Phys. Rev. 182, 1190 (1969).

[21] DOE Topical Collaborations in nuclear theory, Theory Of Reactions of Unstable iSotopes (www.reactiontheory.org).

[22] A.M. Mukhamedzhanov, V. Eremenko and A. Sattarov, Phys. Rev. C 86, 034001 (2012).

Coherence and the Successive Contribution in Two–Neutron Transfer reactions

G. Potel[1]*, A. Idini*[2,3]*, F. Barranco*[4]*, E. Vigezzi*[3] *and R.A. Broglia*[2,3,5]
[1]CEA, Centre de Saclay, IRFU, Service de Physique Nucléaire, F-91191 Gif-sur-Yvette, France.
[2]Dipartimento di Fisica, Università di Milano, Via Celoria 16, 20133 Milano, Italy.
[3] INFN, Sezione di Milano Via Celoria 16, 20133 Milano, Italy.
[4] Departamento de Fisica Aplicada III, Universidad de Sevilla, Escuela Superior de Ingenieros, Sevilla, 41092 Camino de los Descubrimientos s/n, Spain.
[5] The Niels Bohr Institute, University of Copenhagen, Blegdamsvej 17, 2100 Copenhagen Ø, Denmark.

Abstract
In this short letter we briefly address two important points of two–neutron transfer reactions, namely the successive nature of the process and the role of pairing correlations during this sequential transfer. The discussion is made within the 2–step DWBA formalism. The calculations were carried out making use of software specifically developed for this purpose, which includes successive, simultaneous and non–orthogonality contributions to the process. Microscopic form factors are used which take into account the relevant structure aspects of the process, such as the nature of the single–particle wavefunctions, the spectroscopic factors, and the interaction potential responsible for the transfer.

1 Introduction

The specific probe to study the superconducting state is Cooper pair tunneling. Therefore, important progress in the understanding of pairing in atomic nuclei may arise from the systematic study of two–particle transfer reactions. Although this subject of research started about the time of the BCS papers, the quantitative calculation of absolute cross sections taking properly into account the full non–locality of the Cooper pairs (correlation length much larger than nuclear dimensions) is still an open question, which we address here within the 2–step DWBA reaction mechanism (see, for example, [1,5,7,10]). This method have been successfully applied to obtain absolute values of the two–neutron transfer differential cross sections without free parameters [1, 7–9].

In the two following sections we will stress the sequential nature of two–neutron transfer processes, and how the pairing correlations are kept during the whole process despite the separation of the two neutrons forming the correlated Cooper pair. We will do so in the context of the study of the reaction $A + a(= b + 2) \rightarrow B(= A + 2) + b$, which will virtually populate several states of the intermediate nuclei $f(= b + 1)$ and $F(= A + 1)$.

2 Successive process

Let us consider the exact eigenfunction $\left|\Psi^{(+)}(\xi_b, \xi_A, \mathbf{r}_{b1}, \mathbf{r}_{b2}, \mathbf{R})\right\rangle$, with energy E, of the Hamiltonian

$$H = H_a(\xi_b, \mathbf{r}_{b1}, \mathbf{r}_{b2}) + H_A(\xi_A) + T_{aA}(R) + V(\xi_b, \xi_A, \mathbf{r}_{b1}, \mathbf{r}_{b2}, \mathbf{R}), \tag{1}$$

written in the *prior* representation. In the above expression, ξ_b, ξ_A stand for the spatial coordinates of the nucleons in the cores b, A, while $\mathbf{r}_{b1}, \mathbf{r}_{b2}$ are the coordinates of neutrons $1, 2$ with respect to core b and $\mathbf{R}$ is the relative coordinate between the cores. Spin degrees of freedom are not explicitly taken into account for the sake of simplicity. Since we are interested in the two–neutron transfer process from core

b (i.e., nucleus a) to core A (nucleus B), we need to evaluate the transition amplitude

$$T_{2NT} = \left\langle \chi_\beta(\mathbf{R})\phi_b(\xi_b)\psi_B(\xi_A,\mathbf{r}_{A1},\mathbf{r}_{A2}) \right| \left[V(\xi_b,\xi_A,\mathbf{r}_{b1},\mathbf{r}_{b2},\mathbf{R}) - U(\mathbf{R})\right] \left|\Psi^{(+)}(\xi_b,\xi_A,\mathbf{r}_{b1},\mathbf{r}_{b2},\mathbf{R})\right\rangle, \tag{2}$$

where the wavefunction $|\chi_\beta(\mathbf{R})\phi_b(\xi_b)\psi_B(\xi_A,\mathbf{r}_{A1},\mathbf{r}_{A2})\rangle$ corresponds to the final channel, in the sense that, when $\mathbf{R}\to\infty$ so that the residual nucleus can be collected in the detector, it describes a state in which the two transferred neutrons are bounded to the core A to form the nucleus B. The distorted wave $|\chi_\beta(\mathbf{R})\rangle$ is the solution of the Scrhödinger equation with the optical potential $U(\mathbf{R})$, and we schematically write the structure part as

$$|\psi_B(\xi_A,\mathbf{r}_{A1},\mathbf{r}_{A2}))\rangle = |\phi_A(\xi_A)\rangle \sum_n S_n(B)|\varphi_n^A(\mathbf{r}_{A1})\varphi_n^A(\mathbf{r}_{A2})\rangle. \tag{3}$$

Similarly, the asymptotic form of the wavefunction of the entrance channel is $|\chi_\alpha(\mathbf{R})\psi_a(\xi_b,\mathbf{r}_{b1},\mathbf{r}_{b2})\phi_A(\xi_A)\rangle$, with

$$|\psi_a(\xi_b,\mathbf{r}_{b1},\mathbf{r}_{b2}))\rangle = |\phi_b(\xi_b)\rangle \sum_m S_m(a)|\varphi_m^b(\mathbf{r}_{b1})\varphi_m^b(\mathbf{r}_{b2})\rangle. \tag{4}$$

We could of course be more general in our description by coupling the two–neutron states to different configurations of the cores b and A, but this would not change the conclusions of the present letter and we can safely avoid the extra complication.

The 2–step DWBA consists in approximating $\left|\Psi^{(+)}(\xi_b,\xi_A,\mathbf{r}_{b1},\mathbf{r}_{b2},\mathbf{R})\right\rangle$ by a state containing the entrance channel and the one–neutron transfer channels,

$$\begin{aligned}\left|\Psi^{(+)}\right\rangle \approx{}& |\chi_\alpha(\mathbf{R})\psi_a(\xi_b,\mathbf{r}_{b1},\mathbf{r}_{b2})\psi_A(\xi_A)\rangle \\ &+ \sum_n |\chi_n(\mathbf{R})\psi_{fn}(\xi_b,\mathbf{r}_{b1})\psi_{Fn}(\xi_A,\mathbf{r}_{A2})\rangle,\end{aligned} \tag{5}$$

with

$$\begin{aligned}|\psi_{fn}(\xi_b,\mathbf{r}_{b1})\rangle &= |\phi_b(\xi_b))\rangle|\varphi_n^b(\mathbf{r}_{b1})\rangle, \\ |\psi_{Fn}(\xi_A,\mathbf{r}_{A2})\rangle &= |\phi_A(\xi_A)\rangle|\varphi_n^A(\mathbf{r}_{A2})\rangle.\end{aligned} \tag{6}$$

We can split in four terms the interaction V defined in (1) and write it as

$$V = V_{bA}(\xi_b,\xi_A,\mathbf{R}) + V_1(\mathbf{r}_{A1}) + V_2(\mathbf{r}_{A2}) + V_{res}(\xi_b,\xi_A,\mathbf{r}_{b1},\mathbf{r}_{b2},\mathbf{R}), \tag{7}$$

where we expect the residual term $V_{res}(\xi_b,\xi_A,\mathbf{r}_{b1},\mathbf{r}_{b2},\mathbf{R})$ to be small. If, in addition, we define the optical potential such as

$$U(\mathbf{R}) = \langle\phi_b(\xi_b)\phi_A(\xi_A)|V_{bA}(\xi_b,\xi_A,\mathbf{R})|\phi_b(\xi_b)\phi_A(\xi_A)\rangle, \tag{8}$$

we are left with just the single–particle term $V_1(\mathbf{r}_{A1}) + V_2(\mathbf{r}_{A2})$ as the interaction potential responsible for the transfer. The substitution of (5) in (2) gives rise to three terms, corresponding to the simultaneous, non–orthogonality and successive contributions [5, 10]. The simultaneous and non–orthogonality terms arise because of the finite overlap between the wavefunctions $\varphi^b(\mathbf{r})$ and $\varphi^A(\mathbf{r})$. In fact, as a two–particle transfer reaction is a process in which two nucleon change state, it is of (at least) second order in the single–particle interaction potential $V_1(\mathbf{r}_{A1}) + V_2(\mathbf{r}_{A2})$. It is then not surprising that the non–orthogonal amplitude tend to cancel the simultaneous transfer contribution, which is only a spurious consequence of the fact that the initial and final states are described with non–orthogonal wavefunctions. This cancellation is exact if the number of intermediate states form a complete basis of the two–particle Hilbert space, and the two–neutron transfer reaction is a pure successive, two–step process. In Fig. 1 we

show an actual numerical realization of this cancellation. To further emphasize this important point, let us consider the following complete set of orthogonal wavefunctions:

$$
\begin{aligned}
&|\widetilde{\varphi}_0^b(\mathbf{r}_b)\rangle = |\varphi_0^b(\mathbf{r}_b)\rangle,\\
&|\widetilde{\varphi}_0^A(\mathbf{r}_A)\rangle = |\varphi_0^A(\mathbf{r}_A)\rangle - \langle\widetilde{\varphi}_0^b(\mathbf{r}_b)|\varphi_0^A(\mathbf{r}_A)\rangle\ |\widetilde{\varphi}_0^b(\mathbf{r}_b)\rangle,\\
&|\widetilde{\varphi}_1^b(\mathbf{r}_b)\rangle = |\varphi_1^b(\mathbf{r}_b)\rangle - \langle\widetilde{\varphi}_0^b(\mathbf{r}_b)|\varphi_1^b(\mathbf{r}_b)\rangle\ |\widetilde{\varphi}_0^b(\mathbf{r}_b)\rangle - \langle\widetilde{\varphi}_0^A(\mathbf{r}_A)|\varphi_1^b(\mathbf{r}_b)\rangle\ |\widetilde{\varphi}_0^A(\mathbf{r}_A)\rangle,\\
&|\widetilde{\varphi}_1^A(\mathbf{r}_A)\rangle = |\varphi_1^A(\mathbf{r}_A)\rangle - \langle\widetilde{\varphi}_0^b(\mathbf{r}_b)|\varphi_1^A(\mathbf{r}_A)\rangle\ |\widetilde{\varphi}_0^b(\mathbf{r}_b)\rangle\\
&\qquad - \langle\widetilde{\varphi}_0^A(\mathbf{r}_A)|\varphi_1^A(\mathbf{r}_A)\rangle\ |\widetilde{\varphi}_0^A(\mathbf{r}_A)\rangle - \langle\widetilde{\varphi}_1^b(\mathbf{r}_b)|\varphi_1^A(\mathbf{r}_A)\rangle\ |\widetilde{\varphi}_1^b(\mathbf{r}_b)\rangle,\\
&\vdots\\
&|\widetilde{\varphi}_k^b(\mathbf{r}_b)\rangle = |\varphi_k^b(\mathbf{r}_b)\rangle - \sum_{n=0}^{k-1}\langle\widetilde{\varphi}_n^b(\mathbf{r}_b)|\varphi_k^b(\mathbf{r}_b)\rangle\ |\widetilde{\varphi}_n^b(\mathbf{r}_b)\rangle\\
&\qquad - \sum_{m=0}^{k-1}\langle\widetilde{\varphi}_m^A(\mathbf{r}_A)|\varphi_k^b(\mathbf{r}_b)\rangle\ |\widetilde{\varphi}_m^A(\mathbf{r}_A)\rangle,\\
&|\widetilde{\varphi}_k^A(\mathbf{r}_A)\rangle = |\varphi_k^A(\mathbf{r}_A)\rangle - \sum_{n=0}^{k}\langle\widetilde{\varphi}_n^b(\mathbf{r}_b)|\varphi_k^A(\mathbf{r}_A)\rangle\ |\widetilde{\varphi}_n^b(\mathbf{r}_b)\rangle\\
&\qquad - \sum_{m=0}^{k-1}\langle\widetilde{\varphi}_m^A(\mathbf{r}_A)|\varphi_k^A(\mathbf{r}_A)\rangle\ |\widetilde{\varphi}_m^A(\mathbf{r}_A)\rangle.
\end{aligned}
\tag{9}
$$

Noting that all the overlaps in the above expressions tend to zero as $\mathbf{R}\to\infty$, it is clear that $|\widetilde{\varphi}_n(\mathbf{r})\rangle \to |\varphi_n(\mathbf{r})\rangle$ when $\mathbf{R}\to\infty$, and we can use the channel states

$$|\psi_a(\xi_b,\mathbf{r}_{b1},\mathbf{r}_{b2}))\rangle = |\phi_b(\xi_b)\rangle\sum_m S_m(a)|\widetilde{\varphi}_m^b(\mathbf{r}_{b1})\widetilde{\varphi}_m^b(\mathbf{r}_{b2})\rangle, \tag{10}$$

$$|\psi_B(\xi_A,\mathbf{r}_{A1},\mathbf{r}_{A2}))\rangle = |\phi_A(\xi_A)\rangle\sum_n S_n(B)|\widetilde{\varphi}_n^A(\mathbf{r}_{A1})\widetilde{\varphi}_n^A(\mathbf{r}_{A2})\rangle \tag{11}$$

instead of (3) and (4), as they are asymptotically identical. When we express the transition amplitude in terms of the new set, the first term of (5) gives no contribution. We turn our attention to the contribution to the transition amplitude (2) of the second term, for which we need the distorted waves in the intermediate channels $\chi_n(\mathbf{R})$, that is

$$\chi_n(\mathbf{R}) = -\frac{2\mu}{\hbar^2}\int d\mathbf{R}' G_n(\mathbf{R},\mathbf{R}')\langle\widetilde{\varphi}_n^A(\mathbf{r}_{A2})|V_2(\mathbf{r}_{A2})|\widetilde{\varphi}_n^b(\mathbf{r}_{b2})\rangle, \tag{12}$$

where the Green function $G_n(\mathbf{R},\mathbf{R}')$ is the solution of

$$\left(-\nabla_{\mathbf{R}}^2 - k_n^2 + \frac{2\mu}{\hbar^2}U(\mathbf{R})\right)G_n(\mathbf{R},\mathbf{R}') = \delta(\mathbf{R}-\mathbf{R}'). \tag{13}$$

The Green function $G_n(\mathbf{R},\mathbf{R}')$ propagates each virtual intermediate state with a kinetic energy

$$\frac{\hbar^2 k_n^2}{2\mu} = E - \varepsilon_{fn} - \varepsilon_{Fn}, \tag{14}$$

where $\varepsilon_{fn},\varepsilon_{Fn}$ are the internal energies of nuclei f,F in the intermediate channel n. We thus obtain an expression for the transition amplitude

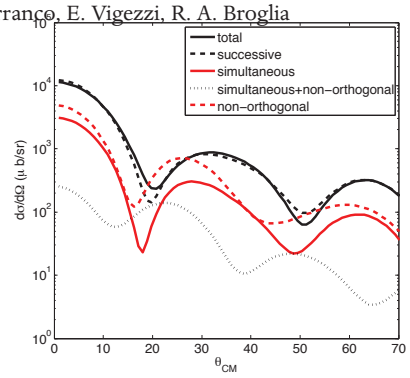

Fig. 1: Contributions to the total two–neutron transfer cross section of the different amplitudes (simultaneous, successive and non–orthogonal), for the ^{112}Sn(p,t)^{110}Sn reaction at a laboratory energy of 26 MeV. Note that the simultaneous and non–orthogonal contributions are in anti–phase, so that the contribution corresponding to the coherent superposition of these two amplitudes tend to cancel. The calculated total cross section thus essentially coincides with the successive contribution.

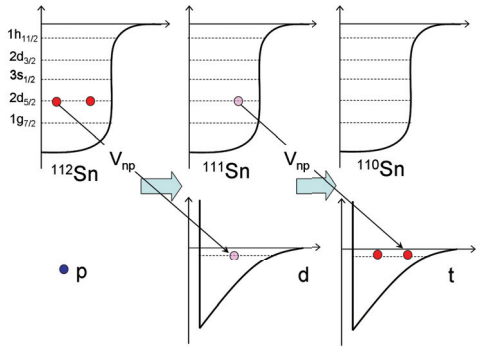

Fig. 2: Depiction of one of the successive single–particle orbital transfer processes contributing to the total successive amplitude in the ^{112}Sn(p,t)^{110}Sn reaction. All five contributions (arising from the $(1g_{7/2})^2, (2d_{5/2})^2, (3s_{1/2})^2, (2d_{3/2})^2, (1h_{11/2})^2$ configurations) contribute coherently to the total cross section.

$$T_{2NT} = T_{succ} = -\frac{4\mu}{\hbar^2}\sum_n \langle \widetilde{\varphi}_n^A(\mathbf{r}_{A1})|V_1(\mathbf{r}_{A1})|\widetilde{\varphi}_n^b(\mathbf{r}_{b1})\rangle \times \int d\mathbf{R}' G_n(\mathbf{R},\mathbf{R}')\langle \widetilde{\varphi}_n^A(\mathbf{r}_{A2})|V_2(\mathbf{r}_{A2})|\widetilde{\varphi}_n^b(\mathbf{r}_{b2})\rangle \quad (15)$$

which only contains a successive, two–step term. This is clearly a direct consequence of neglecting the residual interaction V_{res} in (7), which should be much smaller than the mean field single particle potential $V_1(\mathbf{r}), V_2(\mathbf{r})$. This is in general the case, but the validity of this approximation can break down in particular cases. For example, if some relevant intermediate states are strongly off shell (i.e. the kinetic energy (14) becomes negative), their contribution is significantly quenched. An interesting case can arise when this situation becomes operative for all possible intermediate states, in which case they can only be virtually populated, thus emphasizing the role of simultaneous transfer through the residual interaction V_{res}.

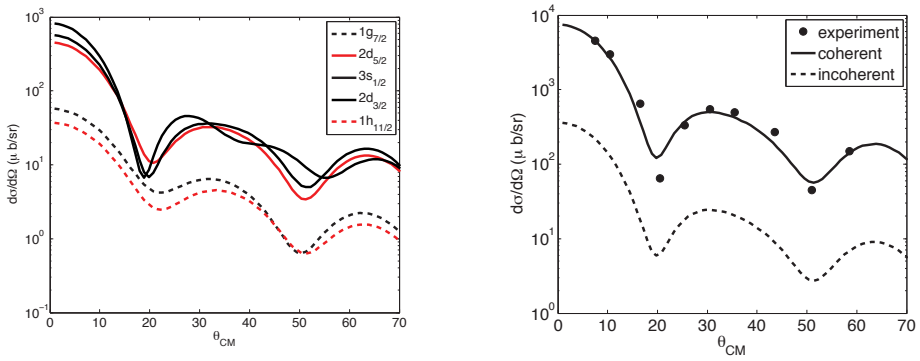

Fig. 3: In the left figure we show the contributions to the total ^{112}Sn(p,t)^{110}Sn cross section of each $(nl_j)^2$ configuration. The figure in the right–hand side compares the coherent (σ) with the incoherent (σ_{inc}, see text) cross sections for the same reaction, together with the experimental data [6].

3 Coherence of the successive transfer

We wish to emphasize that the fact that the transfer process arises through the successive migration of the neutrons from one core to the other by no means imply any correlation loss. The two nucleons are correlated over a distance $\xi = \hbar v_F/E_{corr}$, where v_F is the Fermi velocity and E_{corr} plays the role of the pairing gap for open shell, super- fluid, nuclei. In the case of, e.g., ^{210}Pb, $E_{corr} \approx 1.2$ MeV. Thus $\xi = 25$ fm. Of course, if the two nucleons are subject to an external field (the central potential generated by, e.g., the ^{208}Pb core), they cannot move away from each other more than 14 fm, in keeping with the fact that the radius of ^{208}Pb is ≈ 7 fm. On the other hand, in a heavy ion reaction with e.g. impact parameter 17 fm, the central single–particle potential acting on one of the two nucleons to be transferred is much stronger than typical values of the pairing field V_{res}. It will thus be this potential responsible for the transfer of one partner of the Cooper pair, and this two–step process will take place without loose of (pairing) correlation between the two nucleons, because the Cooper pair is equally well formed in the intermediate states, where the relative distance between the two neutrons is always less than 15 fm.

To illustrate this point, we present the results of the 2–step DWBA formalism applied to the ^{212}Sn$(p,t)^{210}$Sn reaction with a proton beam of energy $E_p = 26$ MeV. The ^{212}Sn is a superfluid nucleus, and in its ground state the valence neutrons form a Cooper pair condensate. This state of correlated pairs of neutrons can be described by mixing single-particle configurations corresponding to the outer shell, namely the $1g_{7/2}, 2d_{5/2}, 3s_{1/2}, 2d_{3/2}, 1h_{11/2}$ orbitals. Being a collective mode, this state is characterized by an enhanced absolute value of the two-nucleon differential cross section, measured in terms of the average pure two-particle units [2–4]. As we have exemplified in Fig.1, each single–particle orbital contribution $T(nl_j)$ to the total transition amplitude (see Fig. 2) arise essentially from a successive process. Despite that, they all contribute coherently to the total cross section σ, so

$$\sigma \sim |T(1g_{7/2}) + T(2d_{5/2}) + T(3s_{1/2}) + T(2d_{3/2}) + T(1h_{11/2})|^2. \tag{16}$$

In Fig.3 we compare this two–neutron transfer cross section, together with the experimental points, with the uncorrelated result σ_{unc} obtained by combining incoherently the transition amplitudes, schematically

$$\sigma_{inc} \sim |T(1g_{7/2})|^2 + |T(2d_{5/2})|^2 + |T(3s_{1/2})|^2 + |T(2d_{3/2})|^2 + |T(1h_{11/2})|^2. \tag{17}$$

That the uncorrelated cross section fall well below the data while the correlated cross section reproduce the experimental findings testifies to the fact that the pairing correlations among the two transferred neutrons is not lost during the two–step process.

4 Conclusions

It is well established that single Cooper pair transfer is the specific tool to probe pairing correlations in nuclei. The reaction formalism of 2–step DWBA have proved to be successful in predicting the absolute values of the differential transfer cross sections in a number of scenarios [1, 7–9], thus allowing to quantitatively assess the nature of such correlations through two–neutron transfer reaction experiments. In this paper we emphasize that, under most circumstances, these reactions consist in the successive transfer of the pair of nucleons. This is a consequence of neglecting the residual interaction V_{res} which, as a rule, is considerably smaller than the mean field potential. However, we also point out that, due to Q–value effects, the intermediate channels could be closed in some cases, a situation in which the successive transfer would be significantly quenched. Financial support from the Ministry of Science and Innovation of Spain grants FPA2009–07653 and ACI2009–1056 are acknowledged by FB and GP and by FB respectively.

References

[1] B. F. Bayman and J. Chen, *One-step and two-step contributions to two-nucleon transfer reactions*, Phys. Rev. C **26** (1982), 1509.

[2] R. A. Broglia, C. Riedel, and T. Udagawa, *Coherence properties of two-neutron transfer reactions and their relation to inelastic scattering*, Nuclear Physics A **169** (1971), 225.

[3] R. A. Broglia, C. Riedel, and T. Udagawa, *Sum rules and two-particle units in the analysis of two-neutron transfer reactions*, Nuclear Physics A **184** (1972), 23.

[4] R.A. Broglia, O. Hansen, and C. Riedel, *Two–neutron transfer reactions and the pairing model*, Advances in Nuclear Physics **6** (1973), 287.

[5] R.A. Broglia and A. Winther, *Heavy ion reactions, 2nd ed.*, Westview Press, Perseus Books, Boulder, 2005.

[6] P. Guazzoni, L. Zetta, A. Covello, A. Gargano, B. F. Bayman, G. Graw, R. Hertenberger, H.-F. Wirth, and M. Jaskola, *Spectroscopy of* ^{110}*Sn via the high-resolution* $^{112}Sn(p,t)$ ^{110}*Sn reaction*, Phys. Rev. C **74** (2006), 054605.

[7] M. Igarashi, K. Kubo, and K. Yagi, *Two–nucleon transfer mechanisms*, Phys. Rep. **199** (1991), 1.

[8] G. Potel, F. Barranco, F. Marini, A. Idini, E. Vigezzi, and R. A. Broglia, *Calculation of the Transition from Pairing Vibrational to Pairing Rotational Regimes between Magic Nuclei* ^{100}*Sn and* ^{132}*Sn via Two-Nucleon Transfer Reactions*, Physical Review Letters **107** (2011), 092501.

[9] G. Potel, F. Barranco, E. Vigezzi, and R. A. Broglia, *Evidence for phonon mediated pairing interaction in the halo of the nucleus* ^{11}*Li*, Phys. Rev. Lett. **105** (2010), 172502.

[10] G. Potel, A. Idini, F. Barranco, E. Vigezzi, and R. A. Broglia, *Single Cooper pair transfer in stable and in exotic nuclei*, arXiv:0906.4298v3 [nucl-th] (2009).

Scaling of energy deposition in central heavy-ion reactions at intermediate energies

Z. Basrak[1]*, *Ph. Eudes*[2], *M. Zorić*[1] *and F. Sébille*[2]
[1] Ruđer Bošković Institute, P.O.Box 180, HR-10 002 Zagreb, Croatia
[2] SUBATECH, EMN-IN2P3/CNRS-Université de Nantes, P.O.Box 20722, F-44 307 Nantes, France

Abstract
Semiclassical transport simulation of heavy-ion reactions (HIR) between about the Fermi energy and 100A MeV reveals a perfect linear correlation between the maximal excitation energy put into a nuclear system and the incident energy. This scaling feature becomes a universal property of HIR independent of reaction entrance channel parameters (system size, asymmetry and energy) when these excitation maxima are expressed in units of the system available energy. The constancy of the excitation energy fraction in the system available energy is on the best corroborate by those analysis of experimental data which do not presume a reaction mechanism dominating the collision process.

1 Introduction

For central HIR at low energies system undergoes fusion and fusion-like slow, essentially mean-field–transformation processes. With increasing incident energy $E_{\rm in}$ a much faster and considerably more violent reaction mechanism sets in and reaction becomes dominated by elementary nucleon-nucleon (NN) collisions. In fusion the entire available energy of the reaction is deposited via thermal excitation, whereas at higher energy a considerable fraction of the available energy is deposited into system via compression. By increasing $E_{\rm in}$ one expects that only a fraction of the available energy is effectively deposited into the reaction system and becomes dissipated during the reaction course. It is commonly admitted that this fraction should monotonically decrease with the increase of $E_{\rm in}$.

For $E_{\rm in}$ from about the Fermi energy $E_{\rm F}$ to several 100A MeV, the energy transformation is determined by those processes which govern heating and compression of a reacting system. The time scales involved are of the order of time which reaction partners need to bypass each other [1,2]. Projectile energy per nucleon $E_{\rm in}$ and reaction geometry (impact parameter and system mass asymmetry) determine the dominant reaction mechanism. Consequently, the course of a HIR is "decided" in the very first instances of a collision [3,4]. In central, the most violent collisions the largest fraction of the entrance channel energy is converted into internal degrees of freedom. Thus, the central collisions are of our greatest interest.

Table 1: Systems and energies studied for central collisions.

System	Incident energy (A MeV)
^{40}Ar+^{27}Al	25, 41, 53, 65, 77, 99
^{36}Ar+^{58}Ni	52, 74, 95
^{40}Ar+^{107}Ag	20, 30, 40, 45, 50, 75, 100
^{40}Ar+^{197}Au	50, 75, 100
^{36}Ar+^{36}Ar	32, 40, 52, 74
^{58}Ni+^{58}Ni	52, 74, 90
^{129}Xe+^{120}Sn	25, 32, 39, 45, 50, 75, 100
^{197}Au+^{197}Au	20, 30, 40, 60, 80, 100

We have shown theoretically that an intermediate energy HIR follows a two-stage scenario, a prompt first compact-stage and a second after-breakup one [4]. The emission pattern of central collisions is characterized by a copious and prompt dynamical emission occurring during the compact and prior-to-scission reaction phase [4–6]. This is the main system-cooling component and the amount of deposited energy into the compact system linearly increases with the projectile energy [7]. These results witness the above conclusion that global characteristics of HIR exit channel are determined in the first prompt reaction stage underlying the interest in studying the first instances of nuclear collisions.

*basrak@irb.hr

In this work we theoretically examine how much of the system energy may be temporarily stocked into the reaction system in the form of excitation energy as a function of $E_{\rm in}$, system size $A_{\rm sys}$ and system mass asymmetry. Four mass symmetric and four mass asymmetric central reactions were studied at several energies (see Tab. 1 for a review). Comparison with the pertinent results deduced from HIR experiments is presented too.

2 Transport model

Simulation was carried out within a semiclassical microscopic transport approach of Boltzmann's type using the Landau-Vlasov (LV) model [8]. The highly nonlinear LV equation $\frac{\partial f}{\partial t} + \{f, H\} = I_{\rm coll}(f)$ is solved by the test-particle method. $f(\mathbf{r}, \mathbf{p}; t)$ is the one-body density distribution function describing the spatio-temporal evolution of the system governed by the effective Hamiltonian H consisting of the self-consistent nuclear and Coulomb fields. The D1-G1 momentum-dependent interaction due to Gogny (the incompressibility module K_∞=228 MeV and the effective mass m^*/m=0.67) [9] was used to describe the nuclear mean-field potential. $\{\ ,\ \}$ stands for the Poisson brackets and $I_{\rm coll}$ is the collision integral. The effects of the Pauli-suppressed two-body residual NN collisions are treated on average in the Uehling-Uhlenbeck approximation taking the isospin- and energy-dependent free-scattering value for the NN cross section. Such an approach is very successful in reproducing a variety of global experimental dynamical observables because they are adequately described by the time evolution of the one-body density. Thus, the LV model is especially appropriate for describing the early stages of HIR, when the system is hot and compressed.

The observable studied is the thermal component (heat), i.e. one of the two main intrinsic-energy deposition components of the early-reaction-stage energy transformation. Heat is stocked into the compact system predominantly by NN collisions which occurs in the overlap zone. In the most of cases under study the time is too short for the full relaxation of the pressure tensor and establishment of a global equilibrium in momentum space. Therefore, it is more correct to name this component the excitation energy $E_{\rm x}$. Detailed definition of the transformation of the (system) available energy $E^{\rm c.m.}_{\rm avail}$ into intrinsic and collective degrees of freedom may be found elsewhere [7,10,11]. $E^{\rm c.m.}_{\rm avail}$ is defined as the center-of-mass system energy per nucleon $E^{\rm c.m.}_{\rm avail} = \frac{E_{\rm P}}{A_{\rm P}} \frac{A_{\rm P} A_{\rm T}}{(A_{\rm P}+A_{\rm T})^2}$, where $E_{\rm P}/A_{\rm P} = E_{\rm in}$ and $A_{\rm P}(A_{\rm T})$ is the projectile (target) number of nucleons.

3 Excitation energy versus incident energy

As an example of the time evolution of excitation energy per nucleon the inset of Fig. 1 shows $E_{\rm x}/A$ for the Au+Au reaction at six energies studied. Within a laps of time of merely 40–75 fm/c after the contact of colliding nuclei occurring at 0 fm/c the excitation energy per nucleon $E_{\rm x}/A$ reaches a maximum and then its value decreases almost as rapidly as it increased. The maxima are reached earlier and their height increases and width decreases with increasing $E_{\rm in}$. The regular and nearly symmetric rise and decrease of $E_{\rm x}/A$ with the reaction time is a common behavior for all reactions studied. The observed regularity suggests that maxima of $E_{\rm x}/A$ are proportional to the total energy deposited during HIR.

We are examining the maximal energy that may be dissipated in HIR. Thus, we take the maxima of $E_{\rm x}/A$ which we denote by $(E_{\rm x}/A)_{\rm max}$. The value of $(E_{\rm x}/A)_{\rm max}$ can readily and accurately be extracted from the simulation results. Figure 1 depicts how these maxima depends on $E^{\rm c.m.}_{\rm avail}$ for all studied HIR. Abscissa value is shifted for the threshold, the Coulomb barrier energy. With this correction the linear fit over all data points crosses abscissa axis closer to the origin of the graph. All data points lie very close to the fit line. One is facing a peculiar universal linear rise which is independent of $A_{\rm sys}$ and mass asymmetry in the full and a rather large span of $E_{\rm in}$ covered in this study.

An important question is whether the existing central HIR experimental data support our simulation results and in particular whether $E_{\rm x}$ linearly depends on $E_{\rm in}$. Most of the energy put into the system during the early reaction phase is released by the emission of particles and light and interme-

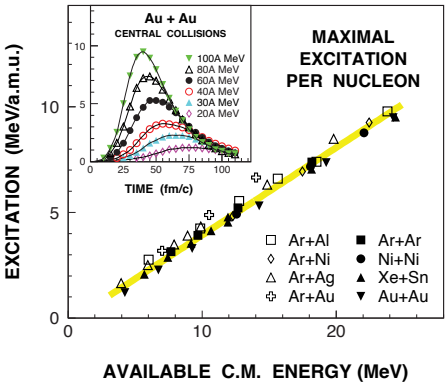

Fig. 1: (Color online.) Simulation results of the thermal excitation energy per nucleon $E_{\rm x}/A$ for central collisions. *Inset*: Time evolution of $E_{\rm x}/A$ for the Au+Au reaction at the indicated energies. At each time step considered are particles that are bound in large fragments, in fact the early compact system.
Main figure: Excitation maxima $(E_{\rm x}/A)_{\rm max}$ as a function of the system available energy $E^{\rm c.m.}_{\rm avail}$ for the mass asymmetric (open symbols) and the mass symmetric (filled symbols) systems studied. The thick grey line is due to the best linear fit to all data points.

diate mass fragments owing to the thermal excitation component $E_{\rm x}$. At energies below $100A$ MeV the compression-decompression process contributes a little in the total (kinetic) energy dissipation in HIR [12]. At the instant at which the maximum $(E_{\rm x}/A)_{\rm max}$ is reached a negligible emission occurs and at energies of our interest it amounts at most 3–5 % of the total system mass [7]. Thus, conjunction of the $(E_{\rm x}/A)_{\rm max}$ with the total (kinetic) energy released in HIR seems to be a natural assumption. One must keep in mind, however, that a simulation maximum is reached prior to although very close (of the order of ∼5–10 fm/c) to the time at which the total momentum distribution becomes locally spherical, i.e., the instant at which the local equilibrium has been reached in each part of the compact subsystem of bound particles [10]. Nevertheless, the system is far from a global equilibrium [7] and comparison with experimental $E_{\rm x}/A$ is not straightforward. Consequently, one must bear in mind that one should limit the comparison to general trend of experimental data, i.e. to the degree of linearity of $(E_{\rm x}/A)$ as a function of $E^{\rm c.m.}_{\rm avail}$ without seeking to reproduce the simulation absolute value. $(E_{\rm x}/A)_{\rm max}$ is reached during the very first reaction phase and if experimental data would display the same slope that could not but be a fortuitous result. Indeed, experimental data is registered at an infinite time. Hence, it reflects an integral of the full reaction history. Anyway, the simulation maxima $(E_{\rm x}/A)_{\rm max}$ should be compared with either the maximal value of $E_{\rm x}/A$ obtained in an experiment or with the most probable value of $E_{\rm x}/A$ depending on the nature of the distribution.

Figure 2 displays a collection of experimental data on $E_{\rm x}/A$ and total energy dissipated in central HIR published in periodics during the last two decades [13–26]. Because energy dependence is crucial for our comparison from the figure are dropped all single-energy results. Each reaction system is depicted by its symbol while the different measurements of the same system are distinguished by color (on line). To avoid of entirely spoiling the figure the error bars, typically of 5–15 %, are not displayed. To guide the eye, points belonging to the same system and the same analysis are connected and they mostly display close-to-linear dependence on $E^{\rm c.m.}_{\rm avail}$. Unlike the simulation result on $(E_{\rm x}/A)_{\rm max}$ (cf. the thick grey line in Fig. 2) the experimental data points span a large domain of the $E_{\rm x}/A$ vs. $E^{\rm c.m.}_{\rm avail}$ plane: The extracted excitations per nucleon lie between one third and almost the full accessible system energy $E^{\rm c.m.}_{\rm avail}$. One may speculate that the different approaches used in extracting from experiments the pertinent information on the global energy deposition in HIR might be at the origin of these much more scattered results. Indeed, in a HIR experiment one does not have a direct access to the excitation energies involved. To obtain $E_{\rm x}/A$ one needs to reconstruct from detected reaction products the total excitation $E_{\rm x}$ of an assumed primary emission source but also the source mass A. There is an evident difficulty to restore the break-up stage using exclusively asymptotic experimental information which is further obscured by an important role played by primary fragments internal excitation causing the in-flight emission. To overcome these uncontrolled issues one has to resort to certain more or less justified physical assumptions or/and to use theoretical predictions as a guide for data analysis. Anyhow, data analyzed on a same

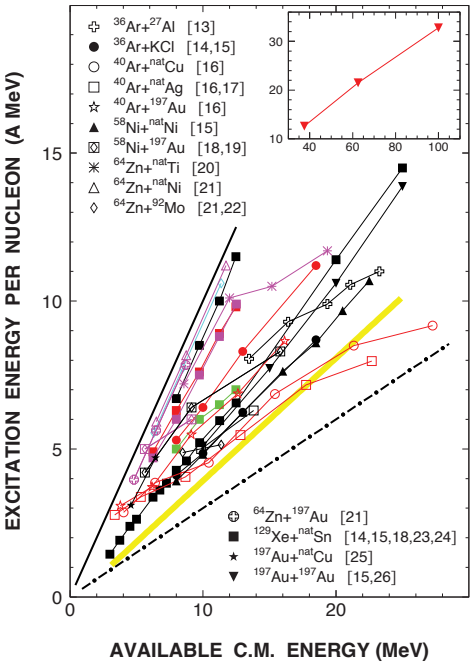

Fig. 2: (Color online.) Experimentally evaluated total excitation energy per nucleon or total dissipated energy per nucleon as a function of system available energy. Each reaction is represented by its own symbol and by color are distinguished different analyses of the same reaction. The thick full line corresponds to the $E_{\rm avail}^{\rm c.m.}$ and displays the upper energy limit which may be reached in HIR while the thick dash-dotted line depicts 30 % of this limit. The only data on the total $E_{\rm x}/A$ above 100A MeV are for the Au+Au reaction at $E_{\rm in}$=150A, 250A and 400A MeV [26]. They are shown in the inset. The axes aspect ratio of both the inset and the main diagram is the same so that the slope in both is the same. The very thick grey line is due to the best linear fit to the simulation results of Fig. 1.

footing seems to fall into much narrower zones of the $E_{\rm avail}^{\rm c.m.}$ vs. $E_{\rm x}/A$ plane.

4 Excitation share in the system available energy

A universal linear dependence of $(E_{\rm x}/A)_{\rm max}$ on $E_{\rm avail}^{\rm c.m.}$ as well as its nearly exact crossing of the origin in Fig. 1 has an important and remarkable consequence: Expressing the value of maximal excitation in percentage of the system available energy one obtains that the relative fraction of $(E_{\rm x}/A)_{\rm max}$ in $E_{\rm avail}^{\rm c.m.}$ has an almost constant value as can be seen in Fig. 3a). The exception to this constancy is for symmetric systems at $E_{\rm in} < E_{\rm F}$ which occurs because when $E_{\rm in}$ decreases below $E_{\rm F}$[1] the value of the maximum $(E_{\rm x}/A)_{\rm max}$ decreases faster than $E_{\rm avail}^{\rm c.m.}$ itself is decreasing. This is a consequence of an ever slower and slower the early compact system energy transformation as $E_{\rm in}$ decreases with an ever more broadened maximum (cf. inset in Fig. 1). Therefore, at these lower $E_{\rm in}$ the maximum $(E_{\rm x}/A)_{\rm max}$ is no more proportional on the same manner to the total energy deposited in HIR as for $E_{\rm in} \gtrsim E_{\rm F}$: These simulation $(E_{\rm x}/A)_{\rm max}$ cannot be compared with an experimental $E_{\rm x}/A$ of fusion reaction, i.e. of adiabatic-like processes. With this restriction in mind, from Fig. 3a) one infers that share of $E_{\rm x}/A$ in $E_{\rm avail}^{\rm c.m.}$ weekly depends on either reaction system or incident energy $E_{\rm in}$ and amounts 0.39±0.03 of $E_{\rm avail}^{\rm c.m.}$. In other words, during the early energy transformation in HIR the maximal excitation energy that may be deposited in the system is a constant which amounts about 40 % of the system available energy. Let us underline that this constancy of the maximum-of-excitation-energy share in available energy is evidenced in the fairly broad range of $E_{\rm in}$ (quotient of the highest and the lowest $E_{\rm avail}^{\rm c.m.}$ covered in the simulation is $\sim$9) and it is nearly independent of system size (studied is the range of $60 \lesssim A_{\rm sys} \lesssim 400$ nucleons) and mass asymmetry ($A_{\rm P} : A_{\rm T}$ is varied between 1:1 and 1:5).

Linear dependence of $E_{\rm x}/A$ on $E_{\rm avail}^{\rm c.m.}$ is not sufficient to obtain a constancy of its fraction in available energy: The line passing through data points should also pass close to the origin of the $E_{\rm avail}^{\rm c.m.}$ vs. $E_{\rm x}/A$ plane. As an example in Fig. 3b) are shown results for the Xe+Sn system which have been

[1] For mass symmetric systems $E_{\rm F}$ corresponds to $E_{\rm avail}^{\rm c.m.} \approx 8A$ MeV.

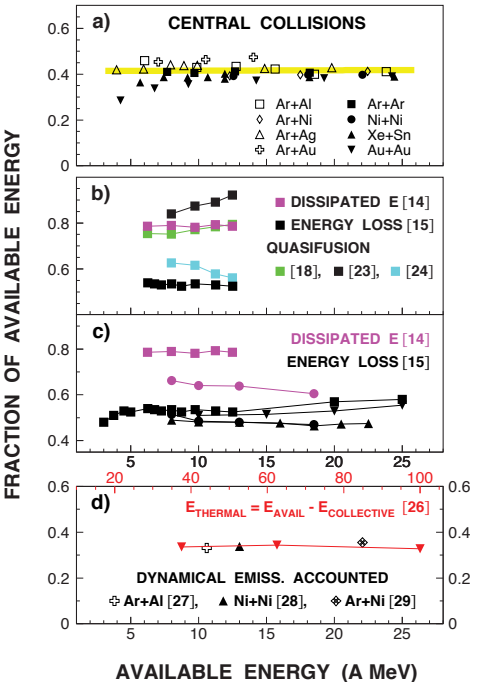

Fig. 3: (Color online.) Ratio of the excitation energy per nucleon and the corresponding $E^{\rm c.m.}_{\rm avail}$ as a function of this same available energy $E^{\rm c.m.}_{\rm avail}$. Symbols used to distinguish different systems are the same as in Fig. 2.
Panel a): Simulation results of Fig. 1.
Panel b): Five different analysis of the Xe+Sn reaction for $25A \leq E_{\rm in} \leq 50A$ MeV.
Panel c): Ratio values reported in the analyses based on the pure kinematical considerations.
Panel d): Ratio values reported in analyses which thoroughly accounted for the pre-equilibrium emission component as well as the results on the total thermal energy reported above $100A$ MeV and for which the abscissae labels above the panel frame are relative to.

extensively studied by the INDRA collaboration. Displayed are five analyses of apparently the same data set for $25A \leq E_{\rm in} \leq 50A$ MeV [14,15,18,23,24]. Each analysis has used its own approach in selecting data by centrality and its own philosophy in extracting the total excitation $E_{\rm x}$ and the primary source mass A. Reported $E_{\rm x}/A$ differ substantially among them: The absolute value at the same $E_{\rm in}$ differs up to 80 %. Moreover, some of presumed single-source (quasifusion) analyses display a rising fraction of $E_{\rm x}/A$ in $E^{\rm c.m.}_{\rm avail}$ as $E_{\rm in}$ increases [18,23], other falling fraction as $E_{\rm in}$ increases [24], whereas the most probable dissipated energy [14] and the total energy loss [15] displays a weak if any dependence on $E_{\rm in}$.

Dissipated energy and total energy loss are the analyses inspired by the kinematical arguments and do not require presumption on the dominant reaction mechanism. Their drawback is in their applicability to the mass-symmetric systems only. Figure 3c) displays results for all systems studied by these two approaches in a fairly broad range of $E_{\rm in}$. The total energy loss within the error bars gives the same constant value for all four systems studied. The results of Figure 3c) are rather weekly depending on $E_{\rm in}$ and may be considered constant. Another example of cases with the constant fraction of $E_{\rm x}/A$ in $E^{\rm c.m.}_{\rm avail}$ is shown in Fig. 3d). Displayed are three single-energy studies that carefully accounted for the copious midrapidity emission [27–29] which occurs during the compact and prior-to-scission reaction phase discussed in Sect. 1 as well as the only $E_{\rm x}/A$ result reported so far above $100A$ MeV. Within blast model extracted is the total thermal energy for the Au+Au reaction from $150A$ to $400A$ MeV [26]. These Au+Au data have recently been revised [30] but a strict linearity of the studied ratio as a function of $E_{\rm in}$ did not change so that the value of our fraction should merely be slightly increased.

5 Conclusions

In conclusion, a semiclassical transport model study of the early reaction phase of central heavy-ion collisions at intermediate energies has been carried out for a variety of system masses, mass asymmetries, and energies below $100A$ MeV. It has been found that the maxima of the excitation energy $E_{\rm x}$ deposited

at this early reaction stage into the reaction system represents a constant fraction of about 40 % of the total center-of-mass available energy of the system $E_{\mathrm{avail}}^{\mathrm{c.m.}}$. In heavy-ion experiments extracted total dissipated energy per nucleon and total energy loss deduced on kinematical arguments display a similar constancy of their share in the system available energy. A similar result may be found in total excitation energy extracted from experimental observations under condition that the pre-equilibrium emission is properly accounted for. This indicates that the stopping power of nuclear matter is significant even below the threshold of nucleon excitation and that it does not change appreciably over a wide range of incident energies, a result corroborated experimentally [31].

References

[1] D. Durand, E. Suraud and B. Tamain, Nuclear Dynamics in the Nucleonic Regime, (Institute of Physics Publishing, Bristol and Philadelphia, 2001).

[2] R. Bass, Nuclear Reactions with Heavy Ions, (Springer, Berlin, 1980).

[3] A. Bonasera, R. Coniglione and P. Sapienza, *Eur. Phys. J.* A **30** (2006) 47.

[4] Ph. Eudes, Z. Basrak and F. Sébille, *Phys. Rev.* C **56** (1997) 2003.

[5] F. Haddad, Ph. Eudes, Z. Basrak and F. Sébille, *Phys. Rev.* C **60** (1999) 031603.

[6] Z. Basrak and Ph. Eudes, *Eur. Phys. J.* A **9** (2000) 207; Ph. Eudes, Z. Basrak and F. Sébille, *Proc. 36th Int. Winter Meeting on Nucl. Phys. (Bormio)* ed. Iori I (University of Milan Press, Milan, 1998), p. 277.

[7] I. Novosel, Z. Basrak, Ph. Eudes, F. Haddad and F. Sébille, *Phys. Lett.* B **625** (2005) 26.

[8] B. Remaud, F. Sébille, C. Grégoire, L. Vinet and Y. Raffray, *Nucl. Phys.* A **447** (1985) 555c; F. Sébille, G. Royer, C. Grégoire, B. Remaud and P. Schuck, *Nucl. Phys.* A **501** (1989) 137.

[9] J. Dechargé and D. Gogny, *Phys. Rev.* C **21** (1980) 1568.

[10] P. Abgrall, F. Haddad, V. de la Mota and F. Sébille, *Phys. Rev.* C **49** (1994) 1040.

[11] V. de la Mota, F. Sébille, M. Farine, B. Remaud and P. Schuck, *Phys. Rev.* C **46** (1992) 677.

[12] J. Pochodzalla, *Prog. Part. Nucl. Phys.* **39** (1997) 443.

[13] J. Péter, *et al. Nucl. Phys.* A **593** (1995) 95.

[14] V. Métivier, *et al.* (INDRA Collaboration), *Nucl. Phys.* A **672** (2000) 357.

[15] G. Lehaut, *Ph.D. Thesis* (Université de Caen, Caen, France, 2009).

[16] Sun Rulin, *et al. Phys. Rev. Lett.* **84** (2000) 43.

[17] E. Vient, *et al. Nucl. Phys.* A **571** (1994) 588.

[18] B. Borderie, *et al.* (INDRA Collaboration), *Nucl. Phys.* A **734** (2004) 495.

[19] N. Bellaize, *et al.* (INDRA Collaboration), *Nucl. Phys.* A **709** (2002) 367.

[20] J.C. Steckmeyer, *et al. Phys. Rev. Lett.* **76** (1996) 4895.

[21] J. Wang, *et al.* (NIMROD Collaboration), *Phys. Rev.* C **72** (2005) 024603.

[22] J. Wang, *et al.* (NIMROD Collaboration), *Phys. Rev.* C **71** (2005) 054608.

[23] N. Le Neindre, *et al.* (INDRA and ALADIN Collaborations), *Nucl. Phys.* A **795** (2007) 47.

[24] E. Bonnet, *et al.* (INDRA and ALADIN Collaborations), *Phys. Rev. Lett.* **105** (2010) 142701.

[25] M. D'Agostino, *et al.* (MULTICS-MINIBALL Collaborations), *Nucl. Phys.* A **724** (2003) 455.

[26] W. Reisdorf, *et al.* (FOPI Collaboration), *Nucl. Phys.* A *612* (1997) 493.

[27] G. Lanzanò, *et al.* (ARGOS Collaboration), *Nucl. Phys.* A *683* (2001) 566.

[28] D. Thériault, *et al.* (INDRA Collaboration), *Phys. Rev.* C *71* (2005) 014610.

[29] D. Doré, *et al.* (INDRA Collaboration), *Phys. Lett.* B *491* (2000) 15.

[30] W. Reisdorf, *et al.* (FOPI Collaboration), *Nucl. Phys.* A *848* (2010) 366.

[31] G. Lehaut, *et al.* (INDRA and ALADIN Collaborations), *Phys. Rev. Lett.* **104** (2010) 232701.

Scaling of hadronic continuum spectra from carbon

R. J. (Jerry) Peterson
Department of Physics, University of Colorado

Scaling in nuclear reaction studies is found when two or more experimental observables can be combined into a single variable that permits comparison of a range of data. The most familiar example combines inclusive scattering doubly differential cross section data points with three-momentum transfer q and energy transfer ω to a single nucleon within a complex nuclear target to form the scaling variable[1]

$$y = \sqrt{(\omega(\omega + 2m))} - q,$$

with M the struck nucleon mass. This variable is the least internal nucleon momentum that can scatter a beam particle with q and ω. Nuclear responses measured by scattering experiments that measure doubly differential cross sections to the continuum are presented in this variable as

$$F(y) = d^2\sigma / d\Omega d\omega * q / (d\sigma / d\Omega * A_{eff} * \sqrt{((M^2 + (q + y))^2)}).$$

These responses yield patterns for electron scattering [1] which do not vary with q or ω, or with beam energy and scattering angle. An industry now uses these responses to understand the dynamics of nucleons within nuclei.

Can the same procedure yield scaling for continuum spectra measured with hadron beams, both scattering and charge exchange? The answer is not obvious, since one of the conditions for scaling to apply is that the beam interacts with each bound nucleon once and only once, incoherently and following the impulse approximation. The large cross sections with hadrons make multiple collisions common, violating the impulse approximation, and experimental conditions may not be consistent with the quasifree condition. If scaling is found with hadrons, there can be new opportunities to understand nucleon dynamics, since hadron beams offer access to all six spin/isospin single nucleon responses of nuclei. Moreover, the measured responses are not just of the bound nucleons, but measures of their interactions with another hadron within the nuclear medium.

The richest array of hadron continuum data at intermediate energies is found for a carbon sample. There are scaling systems other than the y-scaling used here, but several of these scale as well as y-scaling. See Ref. 2 for a recent comparison of carbon data in several scaling formats.

Care is needed with the parameters entering F(y). The singly-differential cross sections for the hadron striking a nucleon off the mass shell are taken in the optimum frame method.[3] The number of nucleons struck one and only once (A_{eff}) is calculated in a Glauber expression[4], using in-medium hadron-nucleon total cross sections at 70% of their free space values. The energy transfer ω to the one struck nucleon is taken from the beam energy loss, a binding energy of 20 MeV for carbon, a Coulomb energy for charge changing reactions, and the recoil of the A=11 system. Details are found in Ref. 2.

'Scaling of the first kind' is defined as invariance of the responses for a given beam and target as the scattering angle is changed. Figure 1 shows data for 795 MeV (p,px)[5] and 950 MeV/c (π^-,π^-x)[6]. The line at y=0 denotes free scattering, with negative y for lower energy losses ω. For both reactions the responses rise with larger scattering angle, more so with protons, but the responses at very negative y agree. The curve represents the expectation of a non relativisitic Fermi gas (NRFG) with k_F=228 MeV/c. Responses at negative y exceed this curve, since they arise from interactions or correlations among the bound nucleons. This is the region where responses are of greatest interest.

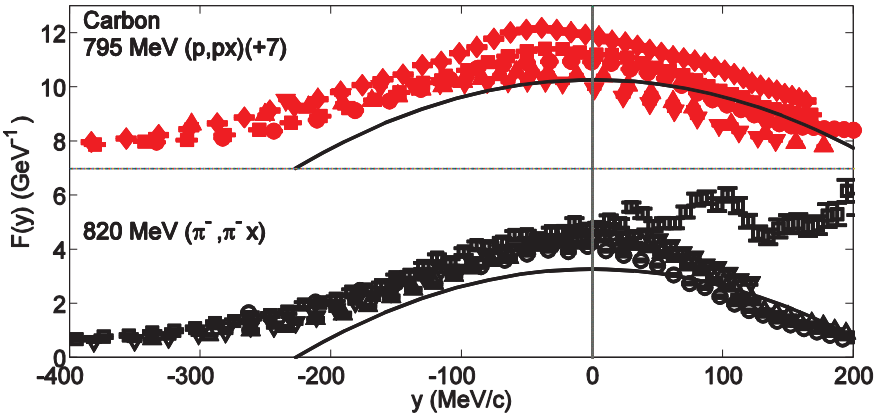

Fig.1: Proton and pion continuum spectra are displayed in the y-scaling format at proton angles of 13, 15, 20, 25, 30 deg[5] and pion q=350, 450, 550, 650 MeV/c.[6] Responses all rise with q, but agree closely for y<0. The curves show the expectations for a NRFG.

Data for scattering without charge exchange (NCX) with three hadron beams are shown in Fig. 2, all with q near 500 MeV/c. This q is consistent with the quasifree conditions. The agreement among the data from three beams and several beam energies demonstrates a new 'scaling of the third kind' with invariance among hadron species. The role of correlations at negative y is found to agree for all, above the NRFG curve and the dashed curve that represents a 'universal' fit to electron scattering responses.[7]

Charge exchange (SCX) data from (p,nx)[8] and (π^-,π^0x)[9] reactions with q near 500 MeV/c are shown in Fig. 3. Less agreement among the results is noted, with these SCX responses showing a stronger rise at positive y than was noted for NCX. This rise is due to isovector pion production, and NCX reactions have much less coupling to isovector responses. Again, the responses for SCX are stronger at negative y than would be expected for the simple NRFG.

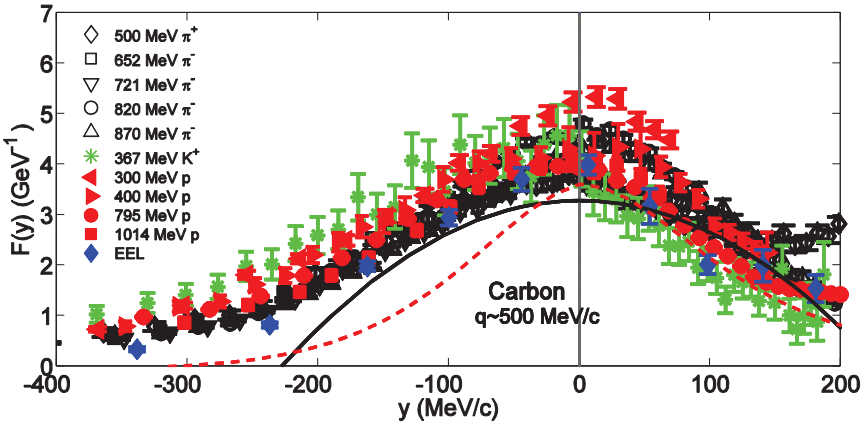

Fig.2: A collection of hadron y-scaling responses with q near 500 MeV/c is compared with the NRFG expectation and a curve from high energy electron scattering.[7] Longitudinal electron responses are also shown at q=550 MeV/c.[10]

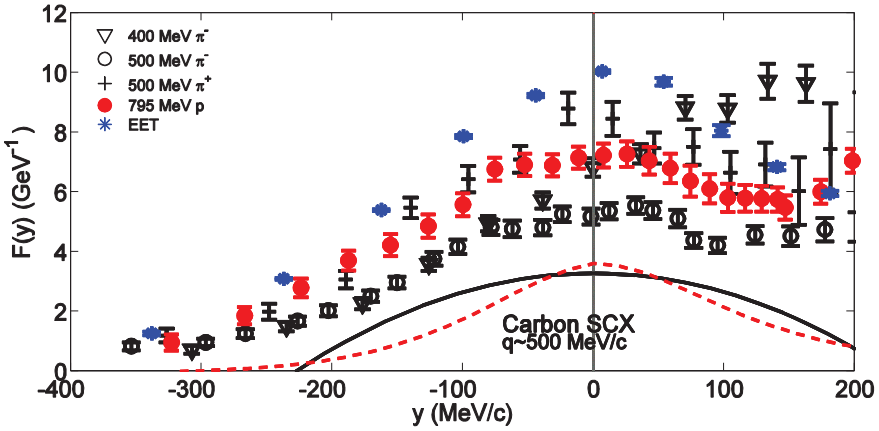

Fig.3: As Fig.2, but for hadronic charge exchange data. Transverse electron responses are also shown.[10]

Scaling of the first kind, independent of q, is found for all hadron NCX reactions over a useful range of momentum transfers, as shown in Fig. 4. Values of the responses were interpolated to be shown at fixed values of y=-170 and -300 MeV/c. Over a range of q from 400 to 600 MeV/c the responses are constant to within 2.7% (4.1%) at y=-170(-300) MeV/c. The 30 data points in this range at y=-170 MeV/c come from eight experiments, each with a systematic uncertainty near 10 %, implying a scatter of 3.9% in their average. The data agree with one another within the expected accuracy, for scaling of the first kind. Electron scattering from proton charge in carbon[10]

('longitudinal') at y=-170 (-300) MeV/c and q=550 MeV/c gives a response of 2.37 (0.69) GeV^{-1}, compared with 2.76 (1.25)GeV^{-1} for hadrons with q from 400 to 600 MeV/c. The hadronic responses are stronger because NCX scattering is more strongly isoscalar than is electron scattering, gaining more from nuclear collectivity.

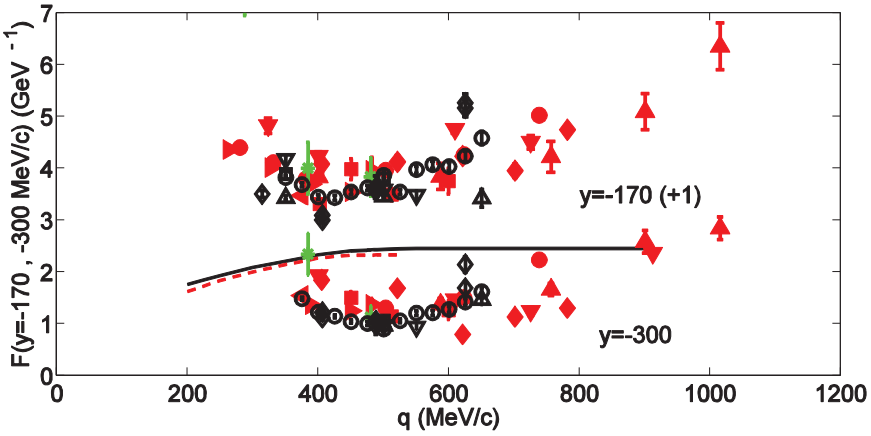

Fig.4: Hadronic y-scaling responses interpolated for fixed values of y are shown. The solid curve is the expectation of a Pauli-blocked NRFG, and the dashed curve arises from a slab model. The text demonstrates that 'scaling of the first kind' is found for q= 400-600 MeV/c.

The similar average of SCX responses of carbon for q=400 to 600 MeV/c and y=-170 (-300) MeV/c is 3.17 (1.26) GeV^{-1}, with a scatter of 5.6(10)% from 18(16) data points from five experiments. Scaling is not followed as well for isovector charge exchange as it is for NCX. The isovector ('transverse') electron scattering[10] response at q=550 MeV/c for y=-170(-300) MeV/c is 5.13(1.83) GeV^{-1}. Hadronic responses are weaker than those for electrons in the isovector channel.

The quasifree condition requires that incident and exiting nucleon kinetic energies be much larger than internal nucleon energies. Figure 5 shows interpolated NCX responses at y=-170 and -300 MeV/c for three hadron beams over a range of incident kinetic energies. The results change only slowly with higher beam energies, demonstrating that the quasifree condition is met surprisingly well.

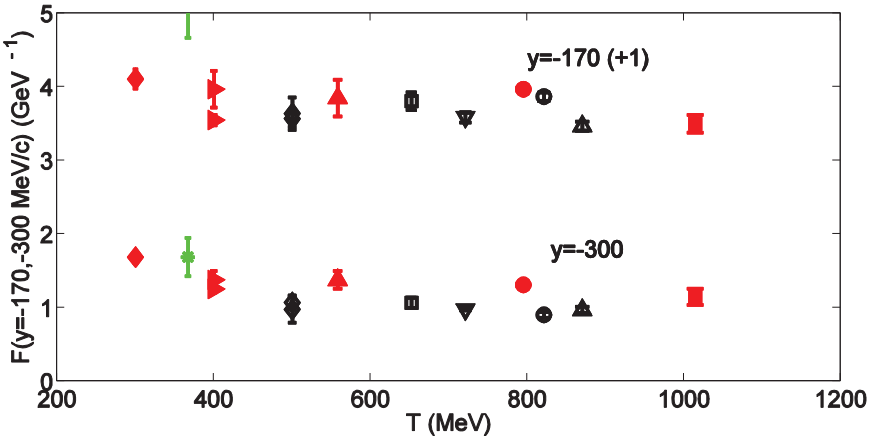

Fig.5: Hadronic NCX responses at fixed y are shown for a range of beam energies, demonstrating that the quasifree condition is met for these data.

These results are encouraging, indicating that the wealth of possible experiments with hadron beams can be used to infer universal nuclear responses for at least one nucleus. With the opportunities for spin transfer studies, hadron experiments can be expected to yield new insights into the spin and isospin single nucleon responses of nuclei, giving new insights into the dynamics of nucleons within nuclei.

This work was supported in part by the USDOE and the Chancellor of the University of Colorado at Boulder.

References

[1] D. B. Day et al., Ann. Rev. Nucl. Part. Sci. 40, 357 (1990).
[2] R. J.Peterson, Phys. Rev. C 85, 064616 (2012).
[3] S. A. Gurvitz, Phys. Rev. C 33,422 (1986).
[4] J. Ouyang et al., Phys. Rev. C47, 2809 (1993).
[5] R. E. Chrien et al., Phys. Rev. C 21, 1014 (1980).
[6] Y. Fujii et al., Phys. Rev. C 64, 034608 (2001).
[7] N. Antonov et al., Phys. Rev. C 71, 014317 (2005).
[8] D. L. Prout et al., Phys. Rev. C 52, 228 (1995).
[9] R.J. Peterson et al., Phys. Lett. B 238 (1992).
[10] J. M.Finn et al. , Phys. Rev. C 29, 2230 (1984).

Probes of nucleon single-particle configurations and correlations

J.A. Tostevin
NSCL, Michigan State University, East Lansing, Michigan 48824-1321, USA and Department of Physics, Faculty of Engineering and Physical Sciences, University of Surrey, Guildford, Surrey GU2 7XH, UK

Our theoretical understanding of the behaviour of nucleon single-particle states in the most highly-asymmetric nuclei has prospered from quantitative information derived from direct knockout (nucleon removal) and transfer reactions. Recent reaction studies propose both more quantitative assessments and links to microscopic structure models, e.g. [1], and probes of developments in shell-model effective interactions. Of particular value at intermediate energies have been the fast one- and two-nucleon removal mechanisms and transfer reactions. In particular, studies of well-bound and loosely-bound nucleon removal and the fast two-nucleon removal mechanism are now available, e.g. [2], providing quantitative predictions and experimental tests for both ab initio and truncated-basis structure models and of their inclusion of two-nucleon correlation effects [3,4]. Fast nucleon pickup reactions have also recently been suggested [5] as a probe for the migration/fragmentation of high-L intruder states, e.g. near traditional closed shells. This talk will review recent analyses and future possibilities for both spectroscopy and as probes of wave functions calculated with modern many-body methods.

References

[1] G.F. Grinyer et al., Phys. Rev. Lett. 106, 162502 (2011); Ø. Jensen, G. Hagen, M. Hjorth-Jensen, B. Alex Brown, and A. Gade, Phys. Rev. Lett. 107, 032501 (2011)

[2] D. Santiago- Gonzalez et al., Phys. Rev. C 83 061305 (2011); N. Kobayashi, T. Nakamura, J.A. Tostevin et al., submitted (2012)

[3] E.C. Simpson and J.A. Tostevin, Phys. Rev. C 82, 044616 (2010)

[4] E.C. Simpson, J.A. Tostevin, Phys. Rev. C 83, 014605 (2011)

[5] A. Gade, J.A. Tostevin et al., Phys. Rev. C 83, 054324 (2011); S. McDaniel, A. Gade, J. A. Tostevin et al., Phys. Rev. C 85, 014610 (2012)

^{175}Lu(n,n'γ) gamma-ray production cross section measurements

A. Blanc[1*], *G. Boutoux*[2], *A. Ebran*[1], *B. Jurado*[2], *V. Méot*[1], *O. Roig*[1], *C. Theroine*[1]
[1]CEA DAM DIF, F-91297 Arpajon, FRANCE
[2]Centre d'Etudes Nucléaires de Bordeaux Gradignan (CENBG), Institut National de Physique Nucléaire et de Physique des Particules, (IN2P3), BP 120, Le Haut Vigneau, F-33175 Gradignan, FRANCE

Abstract
Neutron inelastic scattering cross section on Lutetium 175 have recently been measured at various energies between 0.4 and 1.7 MeV using the 4 MV accelerator at CEA DAM-DIF. A High Purity Germanium detector has been used in order to measure the gamma-rays following the (n,n') reaction and thus extract the gamma-rays production cross-sections for low-lying levels transitions. These results have been compared to a TALYS calculation and are generally in good agreement. Results and calculations will be fully discussed for one of the gamma-ray transition at 396.3 keV.

1 Introduction

Fundamental nuclear physics and applications in reactor physics and astrophysics require accurate neutron-induced radiative capture cross section data. CEA DAM-DIF has started in 2007 a program aiming at measuring neutron-induced cross-sections for many Lu isotopes [1]. Because of target radioactivity, direct measurements for short-lived nuclei, such as the ^{173}Lu nucleus, are very challenging and does not allow to extract cross sections above a few hundred of keV. Therefore, complementary measurements, using indirect way of determining information for cross sections, are needed.

In the $70's$, Britt and Cramer proposed the surrogate method [3] for the indirect measurement of actinide's fission cross section. In this method, the cross section is determined using an alternate reaction (or surrogate reaction) which proceed through the same compound nucleus as the direct reaction. In 2010, fission cross sections of $^{242,243}Cm$ and ^{241}Am have been measured by Kessedjian et al. [4] using the surrogate method. From 1 to 6 MeV, the results are consistent with the neutron induced fission cross section measurements, but these results are still discussed [2].

The validity of the surrogate method when applied to the neutron-induced radiative capture has not been demonstrated yet. In this context, the $^{174}Yb(^3He,p)$ reaction has been studied in 2010 at Orsay [5]. This reaction is the surrogate of the well know $^{175}Lu(n,\gamma)$ reaction. The surrogate data present large discrepancies with respect to the neutron-induced data. Indeed, the average spins obtained for the surrogate reaction is 3 to 4 $\hbar$ higher than in the neutron-induced reaction [5]. In order to confirm these results we performed a new experiment in April 2012 using the K150 cyclotron at Texas A&M University which aims to study the $^{174}Yb(p,d)$ reaction as a surrogate of the $^{172}Yb(n,\gamma)$.

The Orsay experiment results have been interpreted using optical model calculations. These calculations have been performed at CEA DAM-DIF using the TALYS code [6]. TALYS is a computer code developed by NRG-Petten and CEA DAM-DIF for analysis and evaluation of nuclear reactions which uses a parameter library including ENSDF data [7]. It is built on various models such as pre-equilibrium, direct, fission models and optical model for which potential for neutrons can be read as external input. Recently, Garret et al. [8] used the $^{175}Lu(n,n'\gamma)$ reaction in order to accurately measure rotational bands and isomeric states in ^{175}Lu. Below 800 keV, most of ^{175}Lu low-lying levels are very well know. Therefore, for the calculations, all these levels have been included as discrete levels and a continuum was used above 800 keV. The optical model potential used for neutrons was evaluated on $n+^{181}Ta$ data [9] and was adjusted to reproduce the ^{175}Lu total cross section [10].

*Corresponding author, currently at Institut Laue-Langevin, email: blanc@ill.fr.

In the present work we measured the angle integrated gamma-rays production cross sections from the $^{175}Lu(n,n'\gamma)$ using a High Purity Germanium detector (HPGe). Results and TALYS calculation have been compared in the 0.4 to 1.7 MeV incident neutron energy range. The Sec. 2 and 3 respectively detail the experimental setup and the data analysis. Results and discussions are presented in detail in Sec. 4 for the gamma-ray transition at 396.3 keV.

2 Experimental setup

The $^{175}Lu(n,n'\gamma)$ measurement has been performed at the 4 MV accelerator at CEA DAM-DIF. The 4 MV accelerator produces a pulsed proton beam with a 400 ns period which impinges a titanium-tritium target (945 $\mu g/m^2$). The neutrons are produced by the $T(p,n)^3He$ reaction which emits nearly mono-energetic neutrons for which the energy directly depends on the θ_{neut} angle between the proton beam axis and the direction of the neutron emission [11]. Actually, at a fixed θ_{neut} angle the neutron energy distribution is driven by the protons energy loss inside the titanium-tritium target. This energy distribution can be calculated from the proton energy loss per length unit in Titanium provided by SRIM [12]. For instance, at zero degree, a proton beam of $E_p = 2500$ keV produces neutrons in the 1640 to 1720 keV range with a 1673 keV mean energy. This energy distribution is narrow enough that the neutron are considered nearly mono-energetic.

Since the ^{175}Lu is the most abundant isotope (97.41%), $\sim 30g$ of a Lutetium oxide powder was compressed inside polyethylene cylinder (3 cm in diameter and length) and used as a ^{175}Lu target. Its mass and volume were accurately measured and it contained 9.663×10^{22} ^{175}Lu nuclei, the uncertainty being negligible. The sample was placed, at zero degree, ~ 10 cm from the neutron production target. The gamma-ray production cross-sections were thus measured at six neutron mean energies: 458, 594, 682, 789, 1155 and 1673 keV.

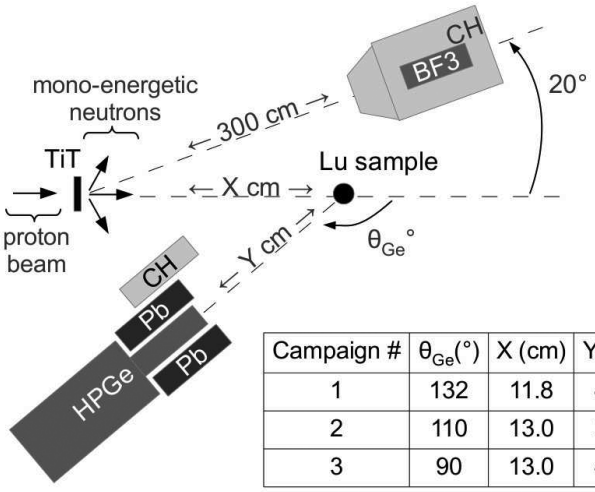

Campaign #	θ_{Ge}(°)	X (cm)	Y (cm)
1	132	11.8	40.2
2	110	13.0	39.8
3	90	13.0	45.0

Fig. 1: Schematic view of the experimental setup (not to scale).

The experimental setup consists of a 40% HPGe detector and a BF3 proportional counter for neutron fluence calculation (see Fig. 1). The Germanium detector was placed at a θ_{Ge} angle with respect to the proton beam axis. Three measurement campaigns, at three θ_{Ge} angle ($90°$, $110°$ and $132°$) were performed in order to extract gamma-rays angular distribution. The θ_{Ge} angle uncertainty was estimated to be $\pm 1.5°$. The exact positions of the Lu sample with respect to titanium-tritium target as well as the

position of the HPGe detector with respect to the sample depends on the measurement campaign and are reported Fig. 1. Note that, in order to reduce gamma-ray background, the Germanium detector was shielded with $\sim$ 10 cm of lead. A set of polyethylene was added in order to prevent damage on the Germanium Crystal due to fast neutrons coming from the neutron production target. An accurately calibrated BF3 counter, placed at 3 meters from the neutron production target, at 20 degrees with respect to the proton beam axis allows precise measurement of the neutron fluence in the sample.

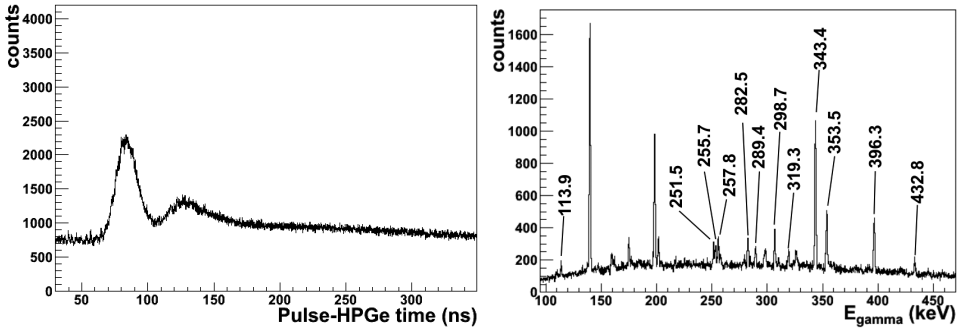

Fig. 2: (left) TAC spectrum for $E_n = 1155\ keV$ and $\theta = 110°$. (right) Energy spectrum for $E_n = 1155\ keV$ and $\theta = 110°$ gated on gamma-rays peak (see text for more details). All observed gamma-rays from $^{175}Lu(n,n'\gamma)$ have been labelled.

Events which are not in time with gamma-rays from the $^{175}Lu(n,n'\gamma)$ reaction are considered to be uncorrelated background. They mainly come from radioactive elements or thermal neutron capture and their effect can be significantly reduced using the time of flight (TOF) technique. As mentioned above, the proton beam is pulsed and can be used as a START for a time measurement. We thus used a Time Amplitude Converter (TAC) electronic module in order to measure the time between a pulse and a Germanium signal. The Fig. 2 (left) shows a typical TAC spectrum. The first peak at $\sim$ 85 ns is populated by gamma-rays which first hit the Germanium detector. The second peak at $\sim$ 130 ns with a long tail is due to the neutrons. The flat background is due to uncorrelated events. The Germanium detector time resolution was measured and found to be $\sim$ 10 ns. This value is too low to distinguish the prompt gamma-rays (from the neutron production target) from the signal coming from the $^{175}Lu(n,n'\gamma)$ reaction. The width of the gate used to select the signal has been determined using the delayed ^{175}Lu transition at 396.3 keV and was estimated to be 10 half time, i.e. 32.8 ns. Fig. 2 (right) shows a typical energy spectrum gated on signal. 12 gamma-rays from neutron inelastic scattering on ^{175}Lu have been identified: 113.9, 251.5, 255.7, 257.8, 282.5, 289.4, 298.7, 319.3, 343.4, 353.5, 396.3 and 432.8.0 keV. The other gamma-rays observed on Fig. 2 (right) mostly come from neutron capture on the Germanium detector.

Experimental setup performances have been measured using calibrated ^{241}Am, ^{133}Ba and ^{152}Eu gamma-ray sources. The energy resolution of the Germanium detector was found close to 2 keV at 1.4 MeV. The setup efficiency at the full energy peak was measured at various gamma-ray energies. Measurements have been compared with a simulation performed using the GEANT4 software [13]. They are in very good agreement above 250 keV [14].

3 Data analysis

TALYS provides angle integrated gamma-rays production cross section for all gamma-rays transitions from discrete levels. In order to compare calculations with measurements, we need to calculate the angle

integrated cross section from the measured gamma-ray yields. To do so we first need to extract from the data the differential production cross section at a θ_{Ge} angle. It was calculated from the following expression:

$$\frac{d\sigma}{d\Omega}(\theta_{Ge}) = \frac{N_\gamma(\theta_{Ge})}{\epsilon \cdot N_{nucl} \cdot \Phi_{neut}} \tag{1}$$

where

$\epsilon =$ correction factor including solid angle subtended by the detector (in sr unit),
$N_\gamma(\theta_{Ge}) =$ gamma-ray yield corrected for the dead time of the acquisition. The dead time correction depends on the trigger rate and range from 0.78 to 0.97,
$\Phi_{neut} =$ neutron fluence in the Lu sample,
$N_{nucl} =$ number of ^{175}Lu nuclei in the Lu sample,

The correction factor ϵ was determined using GEANT4 simulations which include the setup efficiency (see Sec. 2) and the gamma-ray attenuation in the Lu sample. It ranges from 3.23×10^{-4} to 4.92×10^{-4} sr according to the setup and the gamma-ray energy. Its relative uncertainty has been estimated to 5%. As described in Sec. 2, the neutron fluence in the sample Φ_{neut} was calculated from the measurement of the BF3 detector with an uncertainty better than 5%. Note that the energy and fluence variations of the incident neutrons over the sample due to the $T(p,n)^3He$ reaction have been neglected [11]. The neutron attenuation in the sample has also been neglected because of the very low density of the Lu sample (below $1.9\ g \cdot cm^{-3}$).

The angle-integrated gamma-ray production cross section as well as the angular distribution were then obtained for each transition. The gamma-ray angular distribution is symmetric about $90°$ and can be expressed as a series of even order Legendre polynomials [15,16]:

$$\frac{d\sigma}{d\Omega}(\theta_{Ge}) = \frac{\sigma}{4\pi} \sum_\nu c_\nu P_\nu cos(\theta_{Ge}) \tag{2}$$

where

$\nu = 0, 2, 4, ...,$
$\sigma =$ angle integrated cross section,
$c_\nu =$ coefficient of the angular distribution with $c_0 = 1$,
$P_\nu = \nu^{\text{th}}$ order Legendre polynomial.

The range of the ν index is determined by vector momentum coupling conditions, in particular, $\nu < 2 \cdot l_n$, where l_n is the angular momentum transferred by the incident neutron [15]. A calculation performed using the TALYS code shows that in the 0.2 to 1.7 MeV range, the neutron transmission coefficient for $l_n = 3$ is negligible with respect to $l_n = [0, 1, 2]$ [14]. Therefore, ν vary in the range $[0, 4]$ and the angular distribution can be well described with up to 4^{th} order Legendre polynomial [**?**,14]. The differential cross section has been measured at three different θ_{Ge} angle. It results in a system of three equations 2 with three parameters which can be analytically calculated: σ (the angle integrated cross section) and, c_2 and c_4 (the coefficients of the angular distribution).

Note that the effect of the neutron energy distribution in the Lu sample cannot be neglected. It has been included in the analysis by convolving the expected neutron energy distribution in the Lu sample to the TALYS calculation. This energy distribution is mainly due to:

– the proton energy loss in neutron production target (see Sec. 2) which has be calculated using

SRIM [12],

– the multiple scattering in the Lu sample which has been calculated using MCNP [18].

As a result, the calculated cross section decrease from less than 0.01% to 3.56%, depending on the transition and the neutron energy.

4 Results for the gamma-ray at 396.3 keV

The gamma-rays production cross section were obtained for eight transitions: $251.5, 257.9, 282.5, 298.7, 319.3, 343.4, 396.3$ and $432.7\ keV$. They are all above $250\ keV$ where the setup efficiency is well-reproduced by the GEANT4 simulation (see Sec. 2). All of them have been studied in detail in [14]. For the sake of clarity, only one will be discussed in the present proceeding. Since it has been used to determine the width of the gate used to select signal events (see Sec. 2), the delayed transition at $396.3\ keV$ has been chosen.

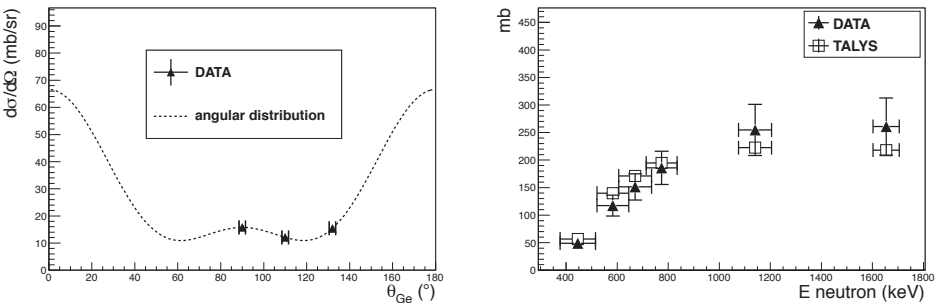

Fig. 3: Results for the gamma-ray at $396.3\ keV$. (left) Measured differential cross section as a function of θ_{Ge} (full triangles) for $E_n = 1155keV$. The analytically calculated angular distribution is also plotted (dashed line). (right) Gamma-ray production cross section as a function of the incident neutron energy (full triangles). The TALYS calculation is also plotted (open squares).

The Fig. 3 (left) displays the three measured differential cross sections at three different θ_{Ge} angle for the gamma-ray at $396.3\ keV$ and a $1155\ keV$ mean incident neutron energy. As described in Sec. 3, the angular distribution was analytically calculated from these measurements and the result is also plotted Fig. 3 (left, dashed line). The two "wells" at $\sim 60°$ and $\sim 120°$ illustrates that the effect of the fourth order Legendre polynomial in equation 2 is not negligible. The angle integrated production cross section is then extracted from the angular distribution. The angle integrated cross section as a function of the incident neutron mean energy is plotted Fig. 3 (right, full triangles). As expected the cross section increases with neutron energy increasing and reach a plateau from where the gamma-ray production is mainly driven by the feeding of the corresponding low-lying level. The TALYS calculation convolved with the neutron energy distribution (see Sec. 3) is also plotted Fig. 3 (right, open squares). Results and calculation are in good agreement over the whole neutron energy range studied in the present work.

5 Conclusion

In the present work, gamma-rays production cross section for the $^{175}Lu(n, n'\gamma)$ reaction have been measured using a 40% HPGe detector. The experiment has been performed at the CEA DAM-DIF 4 MV

accelerator using a nearly mono-energetic incident neutron beam ranging from 0.4 to 1.7 MeV. Differential cross sections have been measured at three HPGe angles with respect to the beam axis. Angular distribution and angle integrated cross sections were then extracted analytically for eight gamma-ray transitions. Optical model calculations has been performed using the TALYS code with a phenomenological potential used during the analysis of the Orsay surrogate experiment [5]. Measurements and calculations are generally in good agreement. These results validate the optical model calculations used for the Orsay experiment. It also validate calculations which, in the same way, will be performed for further experiment aiming at testing the validity of the surrogate method for neutron induced capture cross section measurements in the ^{175}Lu region.

Acknowledgements

The authors thank P. Romain for performing the TALYS calculations and the 4 MV accelerator operations staff for accelerator maintenance and operation.

References

[1] E. Bauge et al., Eur. Phys. J. A (2012) 48: 113

[2] P. Romain, B. Morillon, and H. Duarte, Phys. Rev. C 85, 044603 (2012)

[3] J.D. Cramer & H.C. Britt. Nucl. Sci. Eng. 41, no. 177 (1970)

[4] G. Kessedjian, B. Jurado, M. Aiche & G. Barreau et al., *Neutron-induced fission cross sections of short-lived actinides with the surrogate reaction method* Physics Letters B, vol. 692, pages 297-301 (2010)

[5] G. Boutoux et al., *Study of the surrogate-reaction method applied to neutron-induced capture cross sections* Physics Letters B, vol. 712, 319-325 (2012)

[6] A.J. Koning, S. Hilaire, M.C. Duijvestijn, TALYS: Comprehensive nuclear reaction modeling, in: Proceedings of the International Conference on Nuclear Data for Science and Technology - ND2004, 26 September-1 October 2004, Santa Fe, AIP Conf. Proc. 769 (2005) 1154-1159.

[7] NNDC On-Line Data Service from the ENSDF database, file revised as of 2011. M. R. Bhat, Evaluated Nuclear Structure Data File (ENSDF), Nuclear Data for Science and Technology, page 817, edited by S. M. Qaim (Springer-Verlag, Berlin, Germany, 1992).

[8] P.E. Garrett et al., *Rotational bands and isomeric states in* ^{175}Lu, Phys.Rev C 69, 017302 (2004)

[9] P. Romain and J.P. Delaroche, Proceedings of the Specialist' Meeting on the Nucleon Nucleus Optical Model up to 200 MeV, Bruyères-le-Châtel (1996)

[10] K.Wisshak, F.Voss, F.Kappeler & L.Kazakov, *Stellar neutron capture cross sections of the Lu isotopes*, Phys.Rev. C 73, 015807 (2006)

[11] H. Liskien and A. Paulsen, Atomic Data and Nuclear Data Tables 11, 569 (1973).

[12] http://www.srim.org/

[13] http://geant4.cern.ch/

[14] A. Blanc et al., to be published

[15] E. Sheldon & D.K. Van Patter, Compound Inelastic Nucleon and Gamma-Ray Angular Distributions for Even- and Odd-Mass Nuclei Review of Modern Physics, vol. 38, no. 1, 143 (1966)

[16] M.K. Banerjee & C.A. Levinson, Direct interaction theory of inelastic scattering Part I Annals of Physics:2, 471-498 (1957)

[17] Y.J. Ko et al., Thulium-169 neutrons inelastic scattering cross section measurements via the $^{169}Tm(n, n'\gamma)$ reaction, Nuclear Physics A, 679, 147-162 (2000)

[18] http://mcnpx.lanl.gov/

Selectivity of the (^{18}O,^{16}O) two-neutron transfer reaction

M.Bondì[1,2],C. Agodi[2], F.Cappuzzello[1,2], D.Carbone[1,2], M.Cavallaro[1,2], A.Cunsolo[1,2], M.De Napoli[3], A.Foti[1,3], D.Nicolosi[1,2], S.Tropea[1,2].

1. Dipartimento di Fisica e Astronomia, Università degli Studi di Catania, Catania, Italy
2. Istituto Nazionale di Fisica Nucleare – Laboratori Nazionali del Sud, Catania, Italy
3. Istituto Nazionale di Fisica Nucleare – Sezione Catania, Catania, Italy

Abstract

A study about the selectivity of the ^{12}C(^{18}O,^{16}O)^{14}C two-neutron transfer reaction was done at the Catania INFN-LNS laboratory at 84 MeV incident energy, that corresponds to about three times the Coulomb barrier. The ejectiles produced in the reactions were momentum analyzed and identified by the MAGNEX spectrometer. The achieved mass resolution in the particle identification (about 1/160) has allowed to identify the different reaction products (mainly isotopes of C, N, O, F, Ne). The integrated cross sections show an enhanced yield for the two-neutron transfer compared to the one-neutron transfer.

The *Q*-value spectrum was extracted and several known bound and resonant states were identified. In particular states with 2p-4h configuration respect to the ^{16}O core are mainly populated by the (^{18}O,^{16}O). This result is a first evidence that the (^{18}O,^{16}O) reaction proceeds mainly by the direct transfer of the neutron pair, instead of a second order process.

1 Introduction

Two-neutron transfer reactions are useful probes to study details of the neutron-neutron correlations beyond the nuclear mean field, in particular they play an important role to test the pairing interaction between the nucleons. The concept of pairing force was introduced in the thirties to explain the major stability of even-even nuclei respect odd systems [1]. In the two-neutron transfer reactions this force favors the direct transfer of a pair coupled to $L = 0$ angular momentum, in addition to the standard uncorrelated sequential transfer of two single nucleons [2-3]. In certain dynamic conditions the direct transfer can be dominant and pairing modes are more efficiently excited in a residual nucleus [4].

In the past, such spectroscopic studies were carried out mainly using (t,p) reactions [5]. During the course heavy ion beams were also available. Despite the apparently more complicated structure of heavy projectile, there are many reasons that lead to prefer the reactions between heavy ions rather than those induced by light ions. First and foremost the reaction mechanism is a much simpler for heavier projectiles. In fact, all quasi-elastic heavy-ion-induced processes can be treated in a semi-classical approximation. This simplicity often leads to a more clearly defined spectroscopy about the target and, in case of heavy ions, the projectile [6-7]. In fact there is the possibility of exciting the projectile as well as the target. Transfer reactions between heavy ions at energies above the Coulomb barrier have a large cross-section if certain kinematical conditions (known as Brink matching), on the *Q*-value of the reaction and on the angular momentum of the transferred nucleons in the initial and final nuclei, are satisfied [8]. In case of heavy-ion induced reactions, the angular distributions are bell shaped at incident energies close to the Coulomb barrier. At higher incident energies they display

forward rising and under favorable kinematic conditions they also show oscillations characteristic of the angular momentum transferred [6]. Finally since there are many heavy-ion beams, a great number of reaction channels can be used to produce the same residual nucleus [9].

If a pair of neutrons coupled to angular momentum zero is pre-formed in the projectile, the role of the pairing correlations is enhanced. This is what happens in (t,p) reactions; but nowadays triton beams are limited mainly due to restrictive radioprotection rules in many accelerator laboratories. Among the heavy-ion reactions there are many possibility such as (^{6}He, ^{4}He), (^{14}C, ^{12}C) and (^{18}O,^{16}O). The use of ^{6}He and ^{14}C beams is limited because they are radioactive beams and are characterized by low intensity. The ^{18}O beam is stable and so can be produced with high intensity. In this context the (^{18}O, ^{16}O) reactions are good spectroscopy probe to study the pairing interaction. We have chosen to perform such a reaction on ^{12}C target. The residual nucleus ^{14}C is well known and a vast literature is available as regards the configurations of its excited states [10-11]. Thus the study of the known ^{14}C states via the (^{18}O,^{16}O) reaction is a benchmark to learn about the reaction mechanism.

Another important factor is the incident energy. In fact at energies not for above the Coulomb barrier the angular distribution are sensitive to the angular momentum of the final populated states [9]. For these reasons the experiment was performed at about 3.5 times the Coulomb barrier. Furthermore according to the Brink's matching conditions the probability [8] to transfer $L = 0$ angular momentum is not negligible.

2 Experimental set-up and data reduction

The experiment was performed at the LNS-INFN in Catania, using a Tandem beam of ^{18}O at 84 MeV incident energy on a 50 μg/cm^2 self supporting ^{12}C target.

Fig. 1: MAGNEX at the INFN-LNS, Catania, Italy.

The outgoing ejectiles were momentum analysed by MAGNEX spectrometer [12] and detected by the focal plane detector FPD. In the data presented in this paper the spectrometer was located at 3 different angular settings, with the spectrometer optical axis centered at θ_{opt} = 8°, 12°, 18° in the laboratory frame. Due to the large angular acceptance of MAGNEX (-0.090 rad, +0.110 rad horizontally, ±0.125 rad vertically in the spectrometer reference frame), this setting covers an angular range of about 3° < θ_{lab} < 24°. The magnetic fields were set in order to focus the ^{16}O ejectiles. Particle identification is achieved through the simultaneous measurement of the position and angle, the energy loss and the residual energy as described in details in ref. [13]. The horizontal and vertical positions and angles of the oxygen ions, measured at the focal plane, are used as input of a 10th order ray-reconstruction of the scattering angle and kinetic energy, based on a differential algebraic method

implemented for MAGNEX [14]. This allows an effective compensation of the high order aberrations of the spectrometer [15-16]. The kinetic energy is then transformed, by the use of relativistic kinematic relations, in Q-value or equivalently in excitation energy $E^* = Q - Q_0$, where Q_0 represents the Q-value for the transfer to the ground states of the residual and ejectile nuclei.

3 Data analysis

The first evidence of the selectivity of the (^{18}O,^{16}O) reaction is the transfer yields. The isotopic yields for the different oxygen isotopes are shown in Fig.2. In order to measure the isotopic yields, the bound and resonance states of ^{14}C populated by (^{18}O,^{16}O) reaction were integrated.

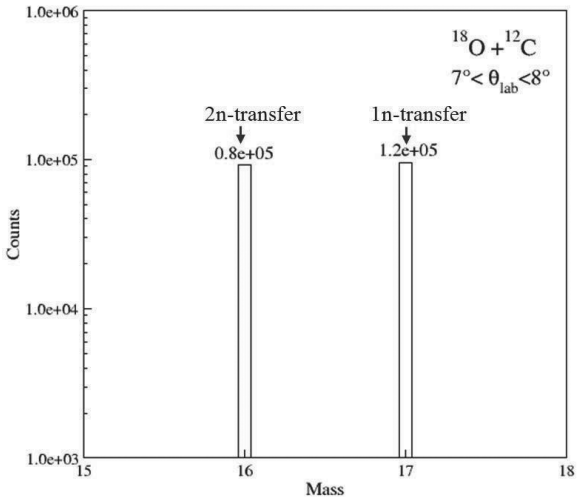

Fig. 2: Yields of ^{17}O, ^{16}O oxygen isotopes for the reactions ^{18}O + ^{12}C.

The striking results is that the two-neutron transfer process appears as probable as the one-neutron removal. This unexpected enhancement of ^{16}O ejectiles suggests that in the two-neutron removal process there is a relevant contribution from the direct transfer of the neutron pair, and not only a independent transfer (second order process). In fact, if the contribution from the sequential transfer of the two neutrons is dominant a transition amplitude given by the product of two independent terms is expected. Consequently the experimental yields for two-neutron transfer should be much lower than the one-neutron one.

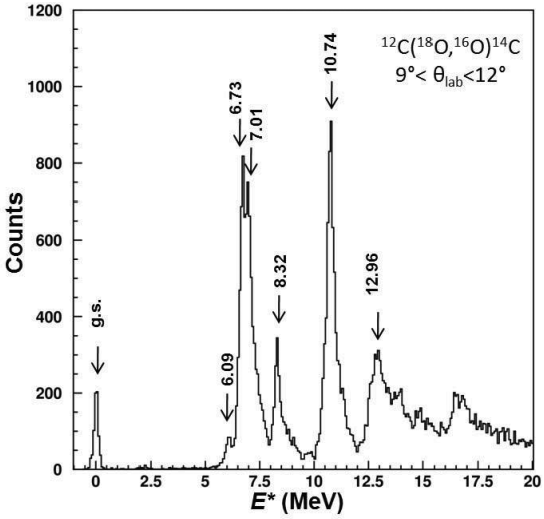

Fig. 3: Spectrum of ^{14}C the reconstructed excitation energy for $9° < \theta_{lab} < 12°$. The isolated peaks are labelled with the relative excitation energy.

A preliminary ^{14}C *Q*-value spectrum is shown in Fig. 3. Several bound and resonant states are observed and identified. All the labeled ^{14}C states have been observed by (t,p) [11] and other heavy-ion reactions [10]. In a tightly bound nucleus, as the ^{12}C, two-neutron transfer reactions can populate both single particle ($^{13}C_{gs}$ + n) and cluster states ($^{12}C_{gs}$ + 2n). The former definitely requires a mechanism of uncorrelated transfer of two neutrons, where the neutron pair in the initial ^{18}O ground state is broken. It is possible to observe, in the spectrum of Fig. 3, that the most populated states have a well known structure described by a two-neutron cluster coupled to the ^{12}C core. For example the states 7.01 and 10.74 MeV have a configuration $\left|\left[(^{12}C_{gs})^{0^+} \otimes (1d_{5/2}, 2s_{1/2})^{2^+}\right]^{2^+}\right\rangle$ and $\left|\left[(^{12}C_{gs})^{0^+} \otimes (1d_{5/2}, 2s_{1/2})^{2^+}\right]^{2^+}\right\rangle$ respectively [10]. This is an important indication of the dominance of the direct one-step nature of the transfer and the minor role of the two-step dynamics.

References

[1] N. Bohr and J.A. Wheeler, *Phys. Rev.* 56 (1939) 426.
[2] Bohr and B.Mottelson, *Nuclear Structure1-2*, Benjamin, New York, (1969-1970).
[3] W.Greiner and J.A.Maruhn, *Nuclear Models*, Springer-Verlag Berlin Heidelberg, (1996).
[4] W.von Oertzen, A.Vitturi, Rep.Prog.Phys.64(2001) 1247 and references therein.
[5] G.M. Crawley et al., Phys. Rev. Lett.39 (1977) 1451.
[6] S. Kahana and A.J. Baltz, *Adv. Nucl. Phys.* 9 (1977) 1.
[7] G.R. Satchler, *Direct Nuclear Reactions* Oxford University press, Oxford (1983).
[8] D.M. Brink, *Phys. Lett.* B40 (1972) 37.
[9] N. Anyas-Weiss et al., *Phys. Reports* C12 (1974) 201.
[10] W. von Oertzen, et al., *Eur. Phys. J.* A 21 (2004) 193-215 and references therein.
[11] S. Mordechai et al., *Nucl. Phys.* A301 (1978) 463.

[12] F. Cappuzzello et al., MAGNEX: an innovative large acceptance spectrometer for nuclear reaction studies in: Magnets: Types, Uses and Safety, Nova Publisher Inc., New York, 2011, pp 1-63.

[13] F. Cappuzzello, et al., Nucl. Instr. and Meth. A 621 (2010) 419 – 423.

[14] F. Cappuzzello, et al., Nucl. Instr. and Meth. A 638 (2011) 74 - 82.

[15] A. Cunsolo, et al., Nucl. Instr. and Meth. A 484 (2002) 56 - 83.

[16] A. Cunsolo, et al., Nucl. Instr. and Meth. A 481 (2002) 48 - 56.

Study of (n,xnγ) reactions on ^{235,238}U

A. Bacquias[1], *C. Borcea*[3], *Ph. Dessagne*[1], *M. Kerveno*[1], *J.C. Drohé*[2], *N. Nankov*[2], *A.L. Negret*[3], *M. Nyman*[2], *A. Plompen*[2], *C. Rouki*[2], *G. Rudolf*[1], *M. Stanoiu*[2], *J.C. Thiry*[1]
[1]CNRS, Université de Strasbourg, UMR7178, IPHC, 23 rue du Loess, 67037 Strasbourg, France
[2]EC - Joint Research Center, Institute for Reference Materials and Measurements, Retieseweg 111, B-2440 Geel, Belgium
[3]Horia Hulubei National Institute of Physics and Nuclear Engineering, Str. Reactorului 30, Bucharest–Magurele, Romania

Abstract
Prompt-gamma spectroscopy and time-of-flight techniques were used to measure (n,xnγ) cross-sections on several nuclei of interest for nuclear reactors. Experiments were performed at the GELINA facility which provides a pulsed white neutron beam of maximum energy about 20 MeV. Preliminary results concerning ^{235}U and ^{238}U will be presented.

1 Introduction

In the context of research and development of future nuclear reactors [1], satisfying to present constraints (environmental impact, security, resources management), studies on fast-neutrons induced reactions play a major role. Indeed, reactions with a threshold, like (n,xn), become important in reactors with a fast spectrum, since they contribute to the neutron multiplication, to the modification of the neutron spectrum and to the production of radioactive nuclei.

There are complementary approaches to measure (n,xn) reaction cross-sections: direct neutron detection, target activation, and prompt γ spectroscopy. Our collaboration chose to rely on that last method. The principle is to use experimental (n,xnγ) cross-sections, and account for unobserved transitions with theoretical predictions, to calculate the total (n,xn) cross-section. In order to reduce this model-dependency, it is primordial to observe a significant part of the total cross-section. In other words, a maximum of transitions has to be treated, especially those going directly to the ground state.

In this context, the aim of the present work is to measure, at high-level precision, the (n,xnγ) cross-sections on ^{235}U and ^{238}U. That latter belongs to the high-priority list of nuclear data [2], for which a significant improvement of accuracy is mentionned.

2 Experimental set-up

The Geel Electron LINear Accelerator (GELINA) located at the Joint Research Center - Institute for Reference Materials and Measurements (Geel, Belgium) provides an intense (compressed) pulsed electron beam. Typical figures for this beam are an energy of 100 MeV, a 1 ns pulse width and a peak-current of 120 A. The maximum repetition rate amounts to 800 Hz; it was used for the experiments mentioned in the present paper. As the electron beam hits the neutron-production target, consisting of Uranium, photons are emitted through the Bremsstrahlung process. Subsequent photonuclear reactions occur, leading to direct and delayed neutrons emission. The produced neutron beam covers a wide energy range, from a few eV to 20 MeV; the maximum of the flux sits between 1 and 2 MeV. The total average flux is about 3.4×10^{13} neutrons per second.

The experimental set-up GRAPhEME is located on Flight Path 16 (FP16), 30 meters away from the neutron-production target. It is represented on fig. 1. The incoming neutron beam passes through a Fission Chamber (FC), consisting of a UF_4 deposit (enriched beyond 99.5% of ^{235}U) embedded in an ionization chamber. The products of neutron-induced fission that escape the deposit leave a signal, whose time and amplitude are stored by the data acquisition system. Knowing the cross-section for ^{235}U(n,f)

from evaluations (ENDF/B-VII.0), the fission yields serve as a measure of the neutron flux as a function of the neutron energy.

The neutron energy was obtained using the Time of Flight (ToF) technique. The ToF measurement relied on the start signal T_0 given at the time electrons hit the neutron production target. This reference time is provided by the GELINA facility with a precision of 1 ns.

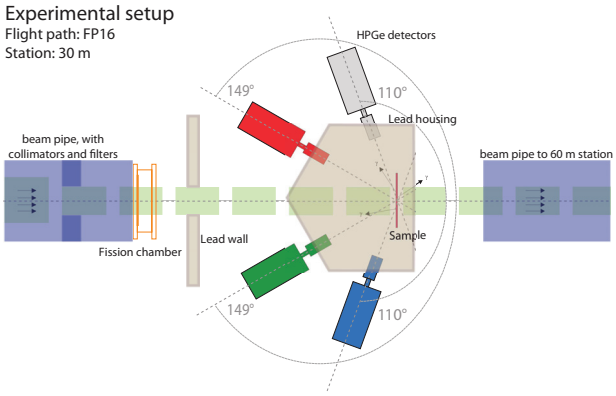

Fig. 1: The GRAPHEME set-up at the GELINA facility on the FP16 - 30m flight-path

In order to perform prompt γ spectroscopy, four planar High-Purity Germanium detectors (HPGe) have been set around a target, consisting of the sample of interest. Neutron-induced inelastic reactions leave the collided nuclei in an excited state. The following de-excitation operates (partly) by gamma-ray emission, detected by the surrounding HPGe.

These HPGe detectors as well as the fission chamber were connected to a fast digital acquisition system using TNT-2 cards working at 100 MHz, developed at IPHC Strasbourg [3]. Events could be recorded with a time precision of 10ns; the energy was coded over 32768 channels.

3 Data analysis

For each HPGe detector, the time distribution of events displays a similar structure as seen in fig. 2. The ambient radioactivity level coming from the set-up itself and surrounding materials adds up with the

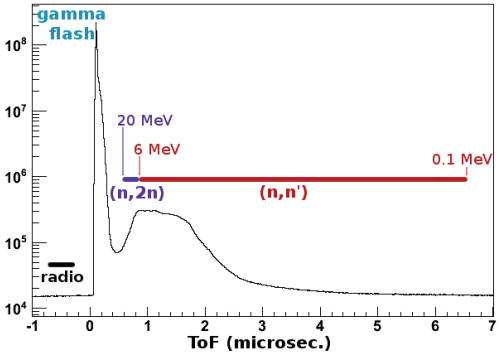

Fig. 2: Part of the ToF distribution, in one HPGe detector.

radioactivity of the sample of interest, forming a constant background, visible on the left on the figure. A

sharp peak occurs as a consequence of the brief emission of gamma rays at the neutron-production target; we refer to it as the "gamma flash". These events detected in the HPGe detectors are not correlated to neutron-induced reactions. After the gamma flash, gamma events can be linked with incoming neutrons. The first events, corresponding to smallest ToF, are (partially) induced by highest-energy neutrons. With larger ToF come events related to neutrons of less kinetic energy. A time window can be applied to select gamma events as a function of a corresponding neutron energy range. The neutron flux and the precision on the neutron ToF (over a relatively short flight path of 30 metres) put limits on the granularity in neutron energy that we can achieve.

A comparison between a time-gated energy spectrum before and after the gamma flash gives hints of neutron-induced reaction rays. As a function of the location of this gate in the time-distribution, i.e. as a function of the neutrons mean energy, peaks rise and disappear. This phenomenon is visible in two-dimensional histograms such as fig.3, where a part of the energy distribution is displayed as a function of a part of the ToF distribution. The gamma flash is seen as a strong vertical line. Horizontal lines starting from the left, so before neutrons arrive, correspond to radioactivity rays. On the right hand side of the gamma flash, i.e. when neutrons arrive, some rays appear, and slowly fade away.

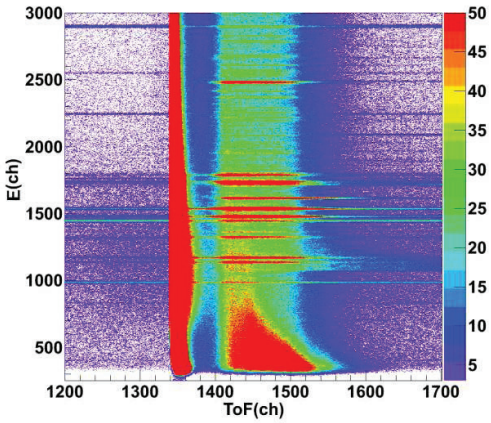

Fig. 3: Partial energy distribution vs partial ToF distribution (in channels), in one HPGe detector.

Once "spotted", a reaction ray is followed throughout the whole acquisition time gate. A collection of time intervals is prepared, for which we determine the corresponding neutron energy ranges. For each of these intervals, we determine the number of counts contained within the peak of interest. This procedure applies to each of our HPGe.

The formula expressing the reaction cross-section for one gamma transition as a function of our observables is as follows:

$$\sigma = \frac{N_\gamma}{\epsilon_\gamma}\frac{\epsilon_{\mathrm{FC}}}{N_{\mathrm{FP}}}\sigma_{235\mathrm{U}}(n,f)\frac{N_{235\mathrm{U}}}{N_{\mathrm{sample}}}\ , \tag{1}$$

with N_γ the number of detected gamma events, ϵ_γ the detector's efficiency for that γ energy, N_{FP} the number of detected fission products in the Fission Chamber (FC), ϵ_{FC} the FC efficiency, N_{sample} the number of atoms in the sample and $N_{235\mathrm{U}}$, the number of ^{235}U atoms in the FC deposit.

In the frame of high-precision studies, specific efforts were put on the quantification of the uncertainties. Besides the obvious need for large statistics with background reduction, careful simulations and calibrated-source measurements have been performed to determine detectors efficiencies. In addition, the Uranium deposit inside the FC and the target sample were precisely characterized (dimensions, mass, purity).

The integration of the differential cross-sections over all angles is performed using the Gauss quadrature. The method applied to γ-ray yields is explained in ref. [4]. In the present experiment, the measurement of the differential cross-section of a given transition at two appropriately chosen angles is sufficient to calculate the angle-integrated reaction cross-section:

$$\sigma = 4\pi \left[w_1 \frac{\mathrm{d}\sigma}{\mathrm{d}\Omega}(\theta_1) + w_2 \frac{\mathrm{d}\sigma}{\mathrm{d}\Omega}(\theta_2) \right] , \tag{2}$$

where angles $\theta_1 \approx (30.6^\circ \text{ or } 149.4^\circ)$ and $\theta_2 \approx (70.1^\circ \text{ or } 109.9^\circ)$ are roots of the Legendre polynomial $P_4(cos\theta)$, with associated coefficients $w_1 \approx 0.35$ and $w_2 \approx 0.65$.

4 Experimental results

We will present here the results concerning (n,n'γ) and (n,2nγ) reaction cross-sections for ^{235}U and ^{238}U. The characteristics of each sample used as a target are summed up in table 1.

Table 1: Specifications of the ^{235}U and ^{238}U targets

Isotope	Enrichment (%)	Total mass (g)	Diameter (cm)	Thickness (mm)
^{235}U	93.20(3)	37.43(1)	12.004(4)	0.211(6)
^{238}U	99.9(?)[a]	10.61911(7)	7.019(9)	0.18(4)[a]

[a] As given by the manufacturer; all other quantities were measured with high precision at IRMM.

4.1 The case of ^{235}U

The analysis and results of the (n,xnγ) reactions on ^{235}U will be discussed in more details in a forthcoming article [5]. Data were accumulated over more than 1400 hours of beam time. Angle-integrated cross-sections of one (n,n'γ) and three (n,2nγ) reactions have been obtained with a precision about 5-7 % below 9 MeV, degrading to about 20 % for higher energies (mainly due to low neutron flux).

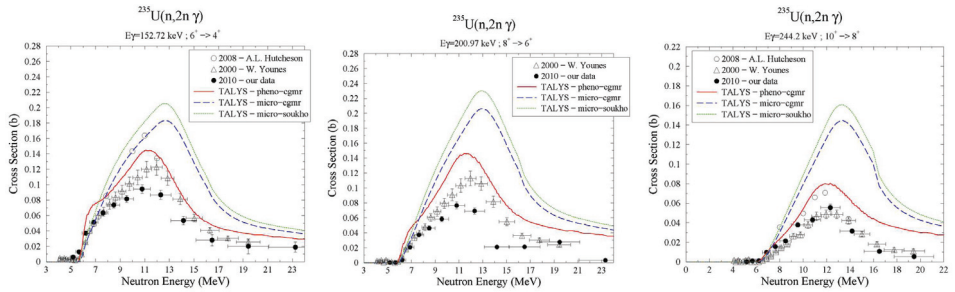

Fig. 4: Cross-sections of (n,2nγ) reactions on ^{235}U as a function of incident neutron energy.

The (n,2nγ) cross-sections for three γ transitions are plotted in fig. 4 as a function of incident neutron energy. Our data are compared to experimental results of Younes et al. [6] and Hutcheson et al. [7] when available. TALYS predictions are also displayed for three different calculations, using different input models. Data sets agree between themselves on the shape of these cross-sections. The shape is also well reproduced by the phenomenological approach with TALYS. The other two TALYS calculations yield substantial overestimation of the cross-sections, compared to data. Quantitative descrepancies between data sets remain.

4.2 The case of ^{238}U

Data were accumulated over more than 1200 hours of beam time. Angle-integrated cross-sections of (n,xnγ) for about 20 γ have been extracted, including three (n,2nγ) and four (n,3nγ) that are not shown here. The ^{238}U results are preliminary, especially in the sense that the determination of systematic uncertainties is still under process. The figure displayed below accounts only for statistical uncertainties.

We could extract several cross-sections for transitions in the main band, and many more from other rotational bands. A few transitions going to the ground state were analyzed, including the deexcitation of the first level at 45 keV (very preliminary results, with arbitrary error bars).

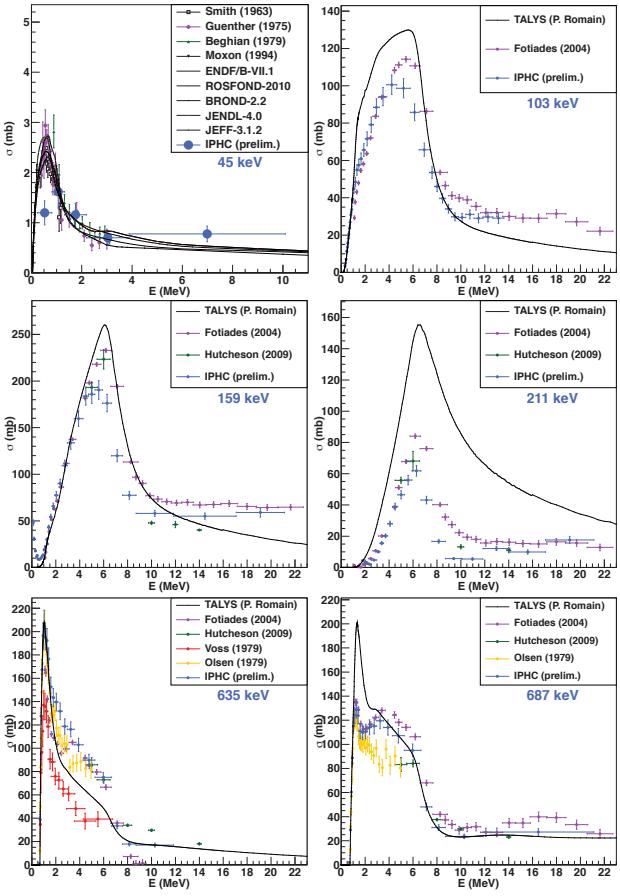

Fig. 5: Cross-sections of (n,n'γ) reactions on ^{238}U as a function of incident neutron energy.

Six transitions are presented in fig. 5: the four lowest transitions in the main band, 44.9 keV ($2^+ \rightarrow 0^+$), 103.5 keV ($4^+ \rightarrow 2^+$), 159.3 keV ($6^+ \rightarrow 4^+$), 211 keV ($8^+ \rightarrow 6^+$), and two transitions from second-band levels, 635 keV ($1^- \rightarrow 2^+$) and 687 keV ($3^- \rightarrow 2^+$). Our data are compared to experimental results from Voss [8], Olsen [9], Fotiades [10], Hutcheson [11] and their collaborators. Calculations performed by P. Romain [12] with TALYS are presented, except for the first level, where the disagreement goes out of scale. The cross-section for the first level (45 keV) is compared to direct neutrons measurements by Smith [13], Guenther [14], Beghian [15], Moxon [16] and their collaborators, and a list of evaluations: ENDF/B-VII.1, ROSFOND-2010, BROND-2.2, JENDL-4.0, and JEFF-3.1.2.

No strong tendency can be noticed from fig. 5. TALYS calculations are generally in good agreement with data regarding the shape of the cross-section, with the notable exception of the 687 keV (and a few other transitions, not shown here). Concerning the magnitude of these predictions, they are much too high for the 45 and the 211 keV. One of the limitations of these calculations is that despite the inclusion of thirty discrete levels, a few important levels decaying directly towards the ground state (e.g. 1279 keV) are not described. Data agree rather well between themselves. The compatibility between our data and direct neutron measurements of the first level production is encouraging.

5 Conclusion

For the two actinides ^{235}U and ^{238}U, the development of a dedicated set-up and analysis techniques allowed to perform experiments relying on prompt gamma spectroscopy and time of flight measurements. We could extract angle-integrated reaction cross-sections for (n,xnγ) processes with a typical precision ranging from 5 to 7 % below 9 MeV, and to about 20 % for higher energies. The authors bear in mind the importance of an exhaustive review of systematic uncertainties and of the determination of the covariance matrix.

The extremely sensible measurement of first levels' deexcitation is guiding further evolutions of the current GRAPhEME set-up. The minimization of the attenuation for low-energy gamma rays will be a first step, before considering the measurement of internally converted electrons.

Extensions of our experimental equipment will occur with two additional planar HPGe, that will be followed later by a 36-pixels planar HPGe. Measurements of (n,xnγ) reactions on very active targets like ^{233}U are foreseen in the near future.

Acknowledgements

The authors wish to thank the team of the GELINA facility for the preparation of the neutron beam and for their strong support day after day. This work was supported by the European Commission within the Sixth Framework Programme through I3-EFNUDAT (EURATOM contract no. 036434) and NUDAME (Contract FP6-516487), and within the Seventh Framework Programme through EUFRAT (EURATOM contract no. FP7-211499) and through ANDES (EURATOM contract no. FP7-249671).

References

[1] The Generation IV International Forum, http://www.gen-4.org/.
[2] OCDE-NEA, Nuclear Data High Priority List, http://www.oecd-nea.org/dbdata/hprl/.
[3] Electronics group for nucl. phys. at IPHC Strasbourg, http://www.iphc.cnrs.fr/-tnt-.html.
[4] C.R. Brune, Nucl. Instr. Meth. Phys. A 493 (2002) 106-110.
[5] J.-C. Thiry et al., *^{235}U(n,n'γ) and ^{235}U(n,2nγ) reaction cross sections*, to be submitted (2012).
[6] W. Younes et al., Tech. Rep. UCRL-ID-140313, U.S. Dept. of Energy, LLNL (2000).
[7] A.L. Hutcheson, Ph.D. thesis, Dept. of Physics in the Graduate School of Duke University (2008).
[8] F. Voss, Kernforschungszentrum Karlsruhe Reports, No.2379 (1976).
[9] D.K. Olsen, Conf.on Nucl.Cross Sections F.Techn.,Knoxville 1979, p.677.
[10] N. Fotiades et al., Phys. Rev. C 69, 024601 (2004).
[11] A.L. Hutcheson et al., Phys. Rev. C 80, 014603 (2009).
[12] Private communication.
[13] A.B. Smith et al., Nucl. Phys. 47 (1963), p.633.
[14] P. Guenther et al., Argonne National Laboratory Reports 16 (1975).
[15] L.E. Beghian et al., Nuclear Science and Engineering 69 (1979), p. 191.
[16] M.C. Moxon et al., Conf.on Nucl.Data for Sci.and Techn., Gatlinburg 1994, p.981.

Modelling secondary neutron cross section measurements performed at HIMAC

L. Heilbronn, M. Beach, L. W. Townsend, P. Tsai
Department of Nuclear Engineering, University of Tennessee, Knoxville, TN USA
R. M. Ronningen
National Superconducting Cyclotron Laboratory, Michigan State University, East Lansing, MI USA

Abstract
Comparisons are shown between transport model calculations and secondary-neutron cross sections from 400 MeV/nucleon Kr + Pb interactions measured at the HIMAC facility in Chiba, Japan. Because corrections are made to the experimental data to account for detector efficiencies, attenuation of neutrons between the target and detector, and to remove room-scattered neutrons and neutrons produced elsewhere besides the target, room-scattered neutrons, simplified "ideal" geometries have been used as input to transport codes for comparison with the data. However, corrections to the data may be imperfect, and as a result the input geometries to the codes and the methodology employed for comparison may need to be modified to produce a more direct, "realistic" comparison to the data. Here, PHITS transport calculations are made with both ideal and realistic geometries and are compared to each other and to data in order to determine which, if any, method is better.

1 Introduction

The process of validation and verification of transport model calculations with relevant experimental data can help lead to improvements in those models and, as a result, lead to reduced uncertainties in many applications where those codes are used. Currently, inclusive light-ion production from intermediate heavy-ion interactions is an area of interest with respect to current transport model calculations, especially for applications such as space radiation protection heavy-ion radiotherapy, due to the relative lack of experimental data. Secondary neutron cross sections measured over the past 15 years [1] provide one of the more complete heavy-ion induced light-ion data sets for comparison with transport calculations and have been compared previously with such codes as FLUKA [2] and PHITS [3]. If discrepancies exist between data and calculation in the comparison, those discrepancies may lead to modification of the physics engines that drive the event generators in transport codes. It is critical, then, to ensure that the calculations correctly model the experimental setup and data analysis, thereby ensuring that what is "measured" in the transport calculation is the same thing that is measured in the experiment.

In previous comparisons of transport calculations to secondary neutron cross sections measured at the Heavy Ion Medical Accelerator Center (HIMAC) in Chiba, Japan, modellers used what is referred to here as an "ideal" geometry to generate the output to compare with experimental data. In those comparisons, systematic differences between code and data indicate that some improvement to the codes may be necessary [4]. However, the question of whether or not an ideal geometry is the correct choice to compare with data must be answered. To define what is meant by an ideal geometry, the experimental methodology must first be described.

Figure 1 shows a schematic diagram of the experimental setup in the PH2 beam line at HIMAC. Neutrons are measured by the time-of-flight method, using the beam trigger plastic and neutron

detector as the starts and stops for the time of flight. Charged particles with enough energy to leave the target and enter the liquid scintillator neutron detector are detected by solid plastic scintillators placed in front of the neutron detector and eliminated from the data during the analysis. Long iron bars, called "shadow bars", are placed periodically between the target and the neutron detector in order to block neutrons coming directly from the target, allowing only room scattered neutrons (background neutrons) to enter the detectors. In a typical set up, seven detectors were placed at angles between 5 and 80 degrees. The number of beam particles incident upon the target was determined by the trigger plastic in front of the target.

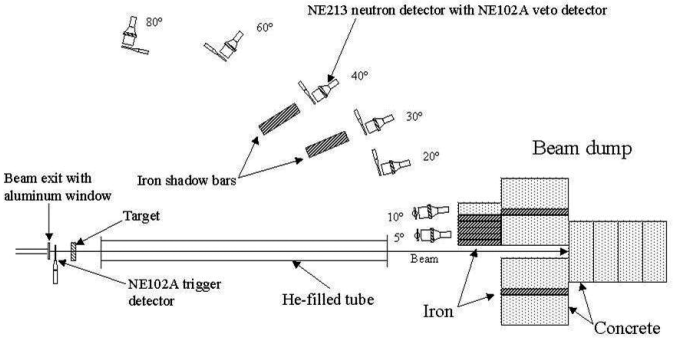

Figure 1. Schematic diagram of the experimental setup at HIMAC to measure neutron cross sections.

The neutron cross section at a particular angle is determined from data taken in four run configurations: (c1) beam + target, (c2) beam + target + shadow bar, (c3) beam + no target, and (c4) beam + no target + shadow bar. After normalizing for acquisition live time and the number of beam particles on target for each configuration, (c1) – (c2) gives the number of detected neutrons that came directly from the target and from materials in the beam near the target, such as the trigger plastic, beam exit window, and air in the vicinity of the target. Because of the placement and finite size of the shadow bars, there is no way to avoid blocking neutrons produced near the target by non-target materials, and as such the data are contaminated by non-target neutrons. To eliminate those neutrons, runs are made with no target in place, and (c3) – (c4) will give the number of detected neutrons that came directly from materials in the beam line that are close to the target. Thus, [(c1) – (c2)] – [(c3) – (c4)] will give the number of detected neutrons that only come directly from the target, after normalizing the runs for the number of beam particles on target. Once the data are corrected for detection efficiency and attenuation of neutron flux through the target and materials between the target and neutron detector, the time-of-flight method can be used to determine the secondary neutron production cross section.

2 Comparisons between experiment and model calculations

From a modelling standpoint, the experimental methodology and analysis is equivalent to an "ideal" geometry, where the experimental room has no other materials except for the target, neutron detector, and beam. There are no walls, floors, beam dumps, air, etc., and as such the modeller can take advantage of the axial symmetry to use ring detectors at each angle, as can be seen in Fig. A2 of Ref. [1], and reduce computational time and increase statistical accuracy. These types of ideal geometries have been employed before in model comparisons with the HIMAC neutron data.

There is an unavoidable effect in the experimental setup, however, that may invalidate the use of an ideal geometry in model calculations. For runs with the target, the beam exits the target at a reduced energy. For example, in the 400 MeV/nucleon Kr + Pb experiment, the beam exits that target at about 375 MeV/nucleon. When there is no target in place, the beam "exits" the same location at the incident energy of 400 MeV/nucleon. Thus, neutrons created downstream from the target location are created at different energies and arrive at the neutron detector at different times, depending if the configuration was either "target" or "no target". Although target thicknesses were minimized to keep that effect at a minimum, can it make enough of a difference in the data that the ideal geometry calculations cannot be compared directly with the data? This effect is most pronounced at forward angles, where previous comparisons of model and data show their greatest disagreements. Figure 2 shows PHITS calculations of secondary neutrons produced at 5º from 400 MeV/nucleon and 375 MeV/nucleon Kr in a non-target run (configuration 3). As can be seen, there is a significant shift in the peak location. If the contribution of neutrons from non-target materials is significant, then there could be a significant difference between the data and model predictions using an ideal geometry.

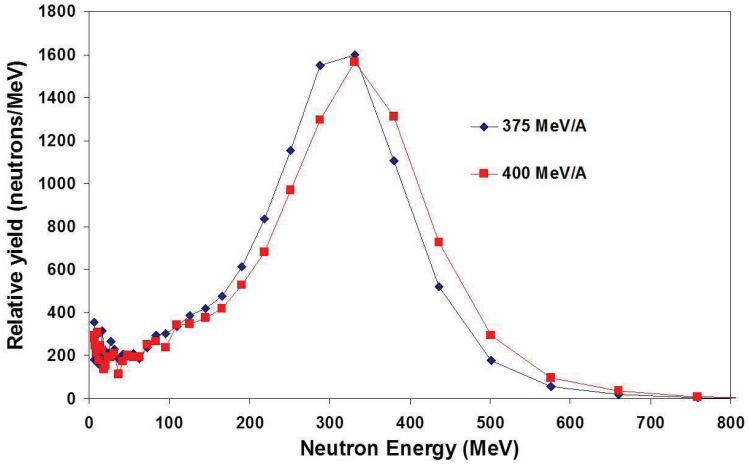

Figure 2. Comparison of neutron spectra at 5º from 375 MeV/nucleon and 400 MeV/nucleon Kr going through the beam exit window, trigger plastic, and air column (configuration c3).

To investigate the significance of the difference between the target and non-target runs, PHITS model calculations were run for all four run configurations, as was done in the experiment. Because the shadow bar runs make it no longer possible to use axial symmetry, all materials in the experiment (trigger plastic, target, air, veto detectors, shadow bars, etc.) were given their exact dimensions in the input geometry file. Also, tally regions were given the same exact dimensions as the neutron detectors used in the experiment. As a result, computational times were greatly increased during the realistic model runs, as opposed to the ideal model runs.

The following options were used in the PHITS calculations:

- Neutron cross section libraries were used up to 20 MeV
- JQMD and GEM were used as the event generators
- Heavy ion interactions were cut off at 1 MeV/nucleon
- The Tripathi model was used for the total reaction cross section
- Stopping powers were calculated with SPAR+NMTC

- Energy straggling was calculated using a Landau distribution
- Gamma emission was included.

The reported cross sections have been corrected for the attenuation of neutrons as they travel from the target to the detector [5]. To allow for a proper comparison with PHITS calculations, the corrections for neutron attenuation have been removed. Seven tally regions were set at 5º, 10º, 20º, 30º, 40º, 60º, and 80º in the calculations, at distances from the target that were equal to the flight paths used in the experiment. As was done in the experiment, the calculations were performed for four different geometries that depended on the placement of the shadow bars. Those geometries were: shadow bars placed at 5º and 10º, shadow bars placed at 20º and 30º, shadow bars placed at 40º and 60º, and a shadow bar placed at 80º. The shadow bars were placed in the same distances from target in the calculations as they were in the experiment. Four calculations were done for each of the target and non-target runs, so a total of eight PHITS calculations were performed in order to generate the data used to calculate the resultant double differential cross sections. At least one million histories were run for each of the eight calculations.

To generate the cross sections at a particular angle, the non-shadow bar runs were summed with the target in place (configuration c1) and with no target in place (configuration c3). The data for configurations c2 and c4 were generated from the shadow bar runs. The configurations were normalized to the same number of histories, and the cross sections were generated as they were in section 1, namely: [(c1) – (c2)] – [(c3) – (c4)].

Figure 3 shows a plot of the double differential cross section for 400 MeV/nucleon Kr + Pb at 80º. The experimental data (square symbols), ideal PHITS calculation (round symbols), and the four-configuration "realistic" PHITS calculation (diamond-shaped symbols) are shown. As expected, the statistical uncertainties with the realistic PHITS calculations are large due to the fact that the tally regions are much smaller than the tally regions for the ideal calculations. Both the ideal and realistic PHITS calculations match the shape of the experimental data well, but the ideal PHITS calculation overestimates the magnitude of the spectra. The realistic PHITS calculation predicts the magnitude of the spectrum very well.

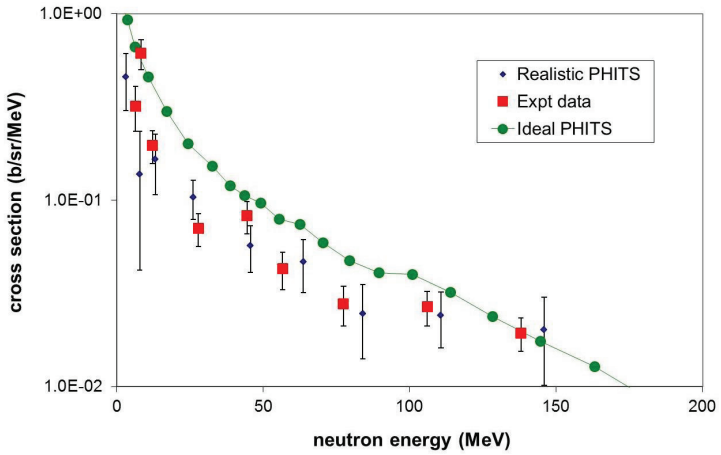

Figure 3. The double differential neutron cross section for 400 MeV/nucleon Kr + Pb at 80º. The experimental data are shown with the square symbols, the four-configuration "realistic" PHITS calculations are shown with the round symbols, and the "ideal" PHITS calculations are show with the diamond-shaped symbols.

The trends seen at 80º are also observed at angles down to 20º. For this particular system (400 MeV/nucleon Kr + Pb), it appears that the four-configuration realistic PHITS calculations show an improvement over the previous methodology employed with PHITS. However, when comparing calculations with the data at forward angles, it appears that the ideal PHITS calculations are in better agreement with the data than the realistic, four-configuration calculations. Figure 4 shows the comparisons of data to calculation at 5º. It is interesting to note that there is a marked shift in peak location between the two PHITS calculations, with the ideal PHITS calculation showing better agreement with the data.

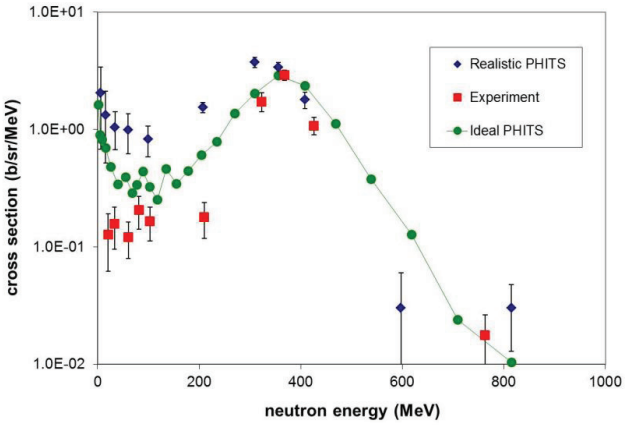

Figure 4. The double differential neutron cross section for 400 MeV/nucleon Kr + Pb at 5º. The symbols used for the data and calculations are the same as in Fig. 4.

3 Conclusions

To test the sensitivity of transport model calculations to the details of the methodology used for the experimental setup and data analysis that produced secondary neutron cross sections from 400 MeV/nucleon Kr + Pb, we ran PHITS calculations with two different geometries. One of the geometries assumed that all experimental corrections and analysis produced data that could be replicated with an ideal geometry of just a target and neutron detector, whereas the other geometry took many of the experimental details into account and replicated the analysis path used with the data. Using the realistic geometry resulted in better agreement between data and calculation at angles 20º and beyond, whereas the agreement at forward angles was better with the ideal calculations. Because the realistic geometry calculations require much smaller tally regions, the time needed to produce the double differential cross sections increases, as does the statistical uncertainty.

Acknowledgements

This work was support by a grant from the Nuclear Regulatory Commission (NRC-38-09-952) and from the NASA Langley Research Center (NNX12AL51A S01).

References

[1] T. Nakamura and L. Heilbronn, *Handbook on Secondary Particle Production and Transport by High Energy Heavy Ions*, (World Scientific Publishing, Singapore, 2006) pp. 1-224.

[2] A. Fasso`, A. Ferrari, J. Ranft, P.R. Sala Proc. IV Int. Conf. on Calorimetry in High Energy Physics, La Biodola (Italy) 21-26 September 1993, Ed. A. Menzione and A. Scribano, World Scientific, p. 493-502

[3] H. Iwase, K. Niita,N. Matsuda, Y. Iwamoto, H. Iwase, T. Sato, H. Nakashima, Y. Sakamoto and L. Sihver, JAEA Data/Code 2010-022 (2010). http://phits.jaea.co.jp

[4] I. Remec, R. M. Ronningen, L. Heilbronn, *Journal of ASTM International* **9**, no. 4, Paper ID JAI104227 (2012).

[5] L. Heilbronn, C. J. Zeitlin, Y. Iwata, T. Murakami, H. Iwase, T. Nakamura, T. Nunomiya, H. Sato, H. Yashima, R.M. Ronningen, and K. Ieki, *Nucl. Sci. and Eng.* **157**, p.142 (2007).

^{8}B production measurement at LNL

T. Marchi[1,2], V. L. Kravchuk[1], M. Cinausero[1], G. Collazuol[2,3], F. Gramegna[1]
for the EUROnu collaboration
[1] INFN, Laboratori Nazionali di Legnaro, Legnaro (PD), Italy
[2] Università di Padova, Dipartimento di Fisica, Padua, Italy
[3] INFN, Sezione di Padova, Padua, Italy

Abstract
The cross section for the reaction ^{6}Li(^{3}He,n)^{8}B at the bombarding energy of 5.77 MeV was measured. Eight liquid BC501 scintillators were used for the detection of the recoil neutrons, while the ^{3}He elastic scattering was used for the absolute cross section normalization. The capabilities of digital electronics have been exploited both for the neutron time of flight measurement and the neutron/gamma pulse shape discrimination.
Theoretical calculations were performed by means of the "Zero Range Knock-out Distorted Wave Born Approximation". Results show a good agreement between the calculations, our experimental data and earlier experimental data based on the time of flight technique.

1 Introduction

The phenomenon of neutrino oscillations is explained by the so-called Standard Neutrino Model (SνM), which uses a lepton mixing matrix with four parameters and two neutrino mass-differences ($\Delta m^2_{12} = m^2_2 - m^2_1$ and $\Delta m^2_{23} = m^2_3 - m^2_2$) to describe the observed data. Three of the mixing matrix parameters take the form of mixing angles (θ_{12}, θ_{23}, and θ_{13}), while the fourth is a phase parameter (δ_{CP}) which, if non-zero, introduces a CP asymmetry in the leptonic sector of the Standard Model, causing the oscillations of neutrinos to be different from those of anti-neutrinos.
The current challenge of the neutrino community is to measure all the mixing angles as precisely as possible, to determine the mass splittings and to seek for CP symmetry violation in neutrino oscillations, if it occurs. To this purpose the EUROnu collaboration, an European Commission co-funded collaborative project, has been studying the design of three types of facilities to provide neutrino beams: the Neutrino Factory, an intense, high-energy neutrino source based on the decay of a stored muon beam; the Beta Beam, in which electron neutrinos (and anti-neutrinos) are produced from the decay of stored radioactive-ion beams; and Super-Beams, high intensity conventional neutrino beams facility. The determination of which of these facilities should be built requires performances and costs comparisons to be made.
Beta Beams are competitive to produce well collimated pure electron neutrino or antineutrino beams to explore primarily neutrino oscillation physics including CP violation in the leptonic sector. The decay of radioactive isotopes with suitable decay time and reaction Q-values is exploited, suitable pairs of isotopes are needed to provide neutrinos and anti-neutrinos beams. The isotope pair ^{8}B and ^{8}Li, accelerated in the CERN (PS-SPS) complex, could provide respectively neutrinos and antineutrinos of energies matched to their CERN to Gran Sasso 732 km travel path. To understand if such pair can be really used for the Beta Beam project, the correspondent EUROnu work-package (WP4) contained a task to measure cross sections and angular distributions of the reaction products ^{8}B and ^{8}Li from the reactions:

- ^{3}He + ^{6}Li $\rightarrow$ ^{8}B + n (subject of this paper);
- ^{7}Li + d $\rightarrow$ ^{8}Li + p.

The ^{8}B nucleus is considered as a neutrino source producing relatively high-energy neutrinos according to its beta decay [1]: ^{8}B $\rightarrow$ ^{8}Be + e$^+$ + ν_e ($t_{1/2}$ = 770 ms).

Accurate knowledge of the reaction rates is necessary to design the tabletop accelerator and the other necessary equipment that will be used for the production of these isotopes, in particular to assess the performance of an internal target that also serves as a stripper and an absorber for ionization cooling of the circulating beam, as originally proposed by C. Rubbia *et al*. [2].
The total cross section of the ^{8}B production in the ^{6}Li(^{3}He,n)^{8}B reaction was measured previously using two different techniques, namely the positron counting and the neutron time of flight. The value obtained through the measurement of the positron decay, reorted in [3] and considered in the original proposal by C. Rubbia *et al*., is smaller at least by a factor 3 with restpect to the one evauated from the Time of Flight measurement reported in [4]. Moreover the experimental uncertainties of existing works are quite large reaching 15-20%. For this reason we proposed to measure with higher accuracy the absolute cross section and the angular distribution of the ^{8}B produced through the ^{6}Li(^{3}He,n)^{8}B reaction.For experimental reasons and for its higher reliability, the time of flight technique was chosen.

2 Experimental Setup

The experiment was performed at the CN 7 MV Van de Graaff accelerator facility of the Laboratori Nazionali di Legnaro (INFN). A pulsed $^{3}He^{+}$ beam of 6.1 MeV energy and 40 pnA intensity was provided by the electrostatic accelerator with a bunch width of less than 3 ns FWHM and a repetition rate of 3 MHz. A ^{6}LiF target with the thickness of 500 μg/cm^{2} evaporated on a ^{197}Au 500 μg/cm^{2} thick backing was used. The target was water cooled during the experiment to avoid Lithium evaporation and, for the same reason, placed with the Gold backing towards the incoming beam. The resulting beam energy at the middle of the ^{6}LiF layer was 5.77 MeV.
The emitted neutrons were measured using 8 large volume BC501 liquid scintillators of the RIPEN modular array [6] upgraded with digital electronics. The detectors were placed at the distance of 2 m from the target in the 15° - 140° angular range of the laboratory reference frame.

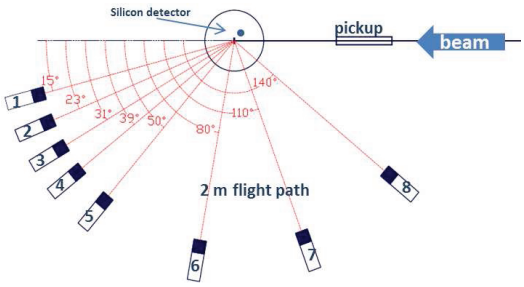

Fig. 1: Schematic view of the experimental setup.

In order to obtain a beam time reference, an inductive "pickup" was placed into the beam line. This tool emits a two-lobes signal every time a beam bunch gets through it and this signal can be properly shaped to be used as a stop for the time of flight measurements.
A ΔE (15 μm) - E (200 μm) Silicon Telescope was used for the detection of the ^{3}He particles elastically back-scattered from the Au backing. It was placed inside the scattering chamber at 150° in the laboratory reference frame and at the distance of 56 mm from the target. As already stated, this information served as a normalization to determine the ^{8}B production absolute cross section. A schematic view of the experimental setup is given in figure 1.
The energy calibration of the BC501 detectors was performed using ^{137}Cs, ^{60}Co and ^{88}Y gamma sources. This procedure is necessary to determine the neutron detection thresholds. Silicon detectors calibration

was performed using a triple Am-Pu-Cm alpha source.
Three different types of background measurements were performed:

- ^{3}He on ^{7}LiF with the thickness of 500 μg/cm^2 evaporated on the Au 500 μg/cm^2 thick backing (as the original ^{6}LiF target contained a small amount of ^{7}Li);
- ^{3}He on ^{12}C target 70 μg/cm^2 thick (to monitor the buildup of a carbon layer on the target during the experimental runs);
- a measurement without target in order to carefully subtract the environment background.

2.1 Digital Data Acquisition System

The setup was completely equipped with digital electronics. Signals from the liquid scintillators, the silicon detectors and the pickup were recorded using two CAEN V1720 digitizers (12 bit, 250 MS/s) in the 8 channels VME version. The two acquisition boards were synchronized propagating a master clock and a common software trigger but real triggers were handled on each module independently. Because of this the pickup and ΔE-E telescope signals were split and acquired in both boards. In this configuration each board is recording data from 4 neutron detectors, 2 silicon detectors and the pickup and the dead-time correction is no more required since each neutron detector channel is normalized to a number of ^{3}He particles measured at exactly the same count rate.
The Digital Front-End was interfaced to the data storage using a VME Bridge and an optical link connection (CAEN V1718 and A2818). The software used for the data acquisition is a customized version of CAEN WaveDump, properly updated in order to handle and synchronize the two (or more) digitizers. Sampled detector signals are written on disk in binary form using 2 μs acquisition windows and stored shapes are then offline analyzed to extract the required parameters.
Three different kinds of information are expected to be obtained processing the scintillators signals: the energy release of the impinging radiation, its time of flight and the pulse shape discrimination between neutrons and gammas. After proper baseline subtraction, the energy release is estimated by signal integration and time of flight is obtained as the difference between a digital constant fraction discriminator filter output value on the shape and the one obtained from the reference pickup signal.
The neutron/gamma discrimination is achieved using a digital implementation of the Zero-Crossing method, the result is a mono dimensional variable that can be directly plotted against time of flight or deposited energy to remove uncorrelated neutrons and gammas background and obtain clean time of flight spectra. This procedure will be illustrated in the next section.

3 Data Analysis

In figure 2 we show the two-dimensional plot of the Zero Crossing - deposited energy correlation for one of the BC501 detectors. The upper locus is connected to the detection of a neutron, while the lower one is due to a detected gamma; from this plot it is possible to estimate a neutron detection threshold of about 150 keVee, which corresponds to a minimum neutron energy close to 0.5 MeV. From two-body kinematics calculations the energy range of the neutron coming from the ^{6}Li(^{3}He,n)^{8}B reaction at 5.77 MeV is from 0.8 MeV at the most backward angle to about 3 MeV for the most forward detector that means mainly above and in few cases quite close to the detection threshold. These thresholds determine the efficiency of the BC501 detectors that can be calculated by a Monte Carlo code as reported in ref. [6].
As a cross check concerning the pulse shape analysis, figure 3 shows the Zero Crossing - time of flight correlation. Also here the neutron/gamma discrimination is evident and a gate on the neutron contribution can be done.

After the neutron signal selection previously discussed, one obtains the desired neutron time of flight spectrum, figure 4 shows one example for the most forward RIPEN detector. One can easily identify the two ^{8}B peaks (ground state and the first excited state at 0.78 MeV) and the peak from the reaction

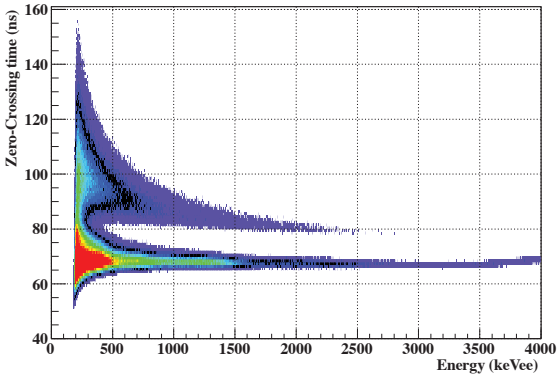

Fig. 2: Two-dimensional plot of the Zero-Crossing time vs the deposited energy for one BC501 detector where detected neutrons (upper blob) and gammas (lower blob) are clearly separated.

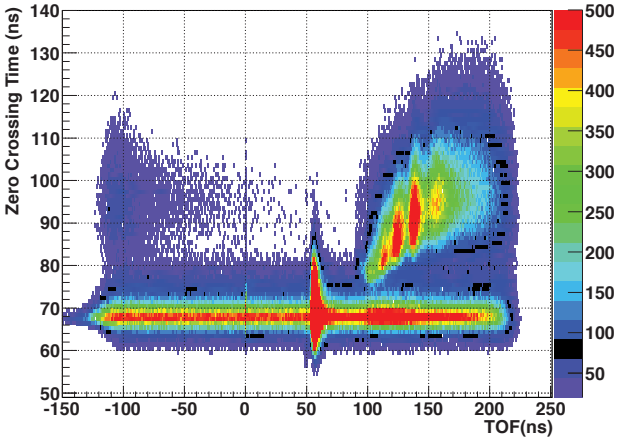

Fig. 3: Two-dimensional plot of the Zero-Crossing parameter vs Time of Flight for one of the BC501 detector. Detected neutrons (upper-right blob) and gammas (lower band) are identified. Prompt gammas can be separated from the uncorrelated background using time of flight information.

^{12}C(^{3}He,n)^{14}O due to the Carbon deposited on the target. The overall continuum is due to the three-body reaction ^{6}Li(^{3}He,np)^{7}Be and can be subtracted. This is done using the Sensitive Nonlinear Iterative Peak (SNIP) clipping algorithm implemented within the ROOT class TSpectrum [7]. The measured neutron energies extracted from the time of flight peaks are consistent with the values calculated from the reaction kinematics.

From the area under the peaks of interest one can infer the differential cross section at the considered angles after correction for the detection efficiency and normalization to the Rutherford scattering on the Gold backing. The experimental angular distribution obtained for the ^{8}B ground state population is shown in figure 5 (solid dots). The error bars take into account all the uncertainties of the measure (solid

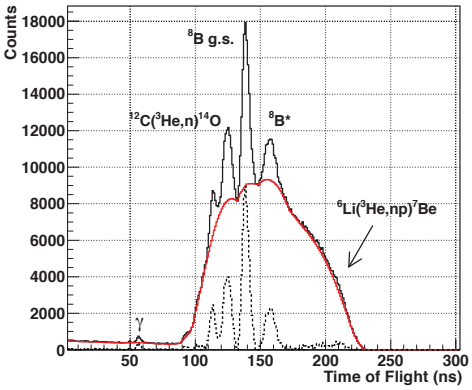

Fig. 4: Neutron time-of-flight spectrum at 15° in the laboratory reference frame from the reaction ^{6}Li(^{3}He,n)^{8}B at 5.77 MeV. The time calibration is 1 ns per channel. See text for details.

angle of the detectors, target thickness, detection efficiency) and are of the order of 10%.

4 Results and discussion

The ^{8}B ground state extracted cross sections were compared to theoretical calculations performed by S.A. Goncharov ([8]) in the "Zero Range Knock-out Distorted Wave Born Approximation" (ZR-KO-DWBA) framework [9] for two-nucleon transfer with microscopic Bayman-Kallio form factors [10] using the code DWUCK4 [11]. Results are given in figure 5 where the experimental and theoretical differential cross sections in the center of mass frame show a reasonably good agreement. The trend is not very well reproduced at center of mass angles higher than 120° (backward angles in the laboratory frame) where the neutrons energy is lower than 1 MeV. In this energy range the efficiency curve drops dramatically while approaching the detection threshold. This introduces a strong dependence of the evaluated cross section on the threshold estimation and requires more accurate information about the RIPEN detectors efficiency in this delicate energy range.
The integrated experimental cross section is 58±7 mb to be compared with the 75 mb calculated value.

5 Conclusions and outlook

The present result is in good agreement with the findings of earlier measurements using the neutron time of flight method [4], thus confirming the disagreement with the positron counting results [5].
To investigate this difference using the two methods we performed DWUCK4 calculations extending the projectile energy range up to 25 MeV. Even if the neutron angular distributions are more focused at the forward angles when increasing the projectile energy, the integrated cross section is not changing very much. Values are going from 75 mb of our case to 66 mb at 25 MeV with a maximum of about 85 mb at 10 MeV. The results of these calculation are thus in strong disagreement with the experimental results reported in ref. [5] and the difference is strongly increasing with the projectile energy reaching about a factor of 30 at the highest considered energy. This is strongly encouraging the experimental measurement of such differential cross sections in the 8 - 25 beam energy range.

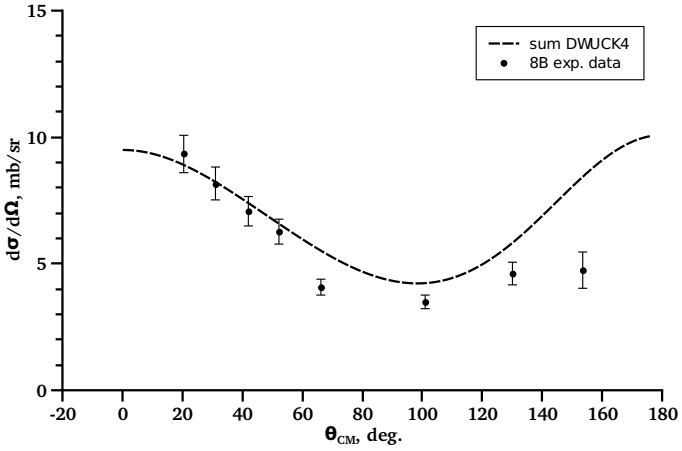

Fig. 5: Measured and calculated angular distributions. Experimental data are shown for the ^{8}B ground state.

6 Acknowledgments

This work was supported by the FP7 EUROnu Contract N. 212372. We would like to thank L. Maran, S. Marigo, A. Minarello, and L. Pranovi for the excellent technical support during the experiment. We are grateful to Prof. S.A. Goncharov for the theoretical ZR-KO-DWBA calculations and the fruitful discussions.

References

[1] W.T. Winter, S.J. Freedman. K.E. Rehm, I. Ahmad, J.P. Greene, A. Heinz, D. Henderson, R.V.F. Janssens, C.L. Jiang, E.F. Moore, G. Mukherjee, R.C. Pardo, T. Pennington, G. Savard, J.P. Schiffer, D. Seweryniak, G. Zinkann, and M. Paul, Phys. Rev. Lett. **91**, 252501 (2003).

[2] C. Rubbia, A. Ferrari, Y. Kadi, and V. Vlachoudis, Nucl. Inst. Meth. A **568**, 475 (2006).

[3] C.R. McClenahan and R.E. Segel, Phys. Rev. C **11**, 370 (1975) and ref. therein.

[4] P. Van der Merwe, W.R. McMurray, and I.J. Van Heerden, Nucl. Phys. A **103**, 474 (1967).

[5] R.E. Marrs, D. Bodansky, and E.G. Adelberger, Phys. Rev. C **8**, 427 (1973).

[6] N. Colonna, L. Celano, G. D'Erasmo, E.M. Fiore, L. Fiore, V. Paticchio, G. Tagliente, G. Antuofermo, G. Iacobelli, M. Sacchetti, P. Vasta, and A. Pantaleo, Nucl. Inst. Meth. A **381**, 472 (1996).

[7] ROOT data analysis framework. http://root.cern.ch

[8] S.A. Goncharov, Moscow State University, *private communication*.

[9] G.R. Satchler, *Direct Nuclear Reactions*, Clarendon Press, Oxford, 833 (1983).

[10] B.F. Bayman and A. Kallio, Phys. Rev. **156**, 1121 (1967).

[11] P.D. Kunz, University of Colorado, *The Code DWUCK4*, extendend version of J.R. Comfort, *unpublished*.

[12] C.-T. Liang, X.-H. Li, and C.-H. Cai, Journ. Phys. G **36**, 085104 (2009).

[13] J.H. Dave and C.R. Gould, Phys. Rev. C **28**, 2212 (1983).

Structure aspects of direct and sequential two-nucleon transfer reactions

B. Alex Brown[1] *,I. J. Thompson*[2]
[1]Department of Physics and Astronomy, and National Superconducting Cyclotron Laboratory, Michigan State University, East Lansing, Michigan 48824-1321, USA
[2]Lawrence Livermore National Laboratory, P.O. Box 808, L-414, Livermore, California 94551, USA

We investigate two-nucleon transfer reactions over a wide range of nuclei from ^{12}C to ^{208}Pb including (p,t), (t,p), (p,^{3}He) and (^{3}He,p) using the reaction code Fresco [1]. In all cases both direct and sequential transfer are included. The study is facilitated by a new wrapper code FR2IN which translates the microscopic matrix elements for two-nucleon overlaps obtained from shell-model codes such as Oxbash and NuShellX [2] into the appropriate format for direct and sequential transfers in Fresco. Overall agreement with data is reasonable given the uncertainties related to optical potentials. In most cases the sequential transfer is important. The use of these reactions for understanding aspects of nuclear structure such as T=1 paring and T=0 pairing in stable and exotic nuclei will be discussed.

Acknowledgments: We acknowledge support from NSF grant PHY-1068217. We thank the Institute for Nuclear Theory at the University of Washington for its hospitality and the Department of Energy for partial support during the completion of this work.

References

[1] I.J. Thompson, Comp. Phys. Rep. 7, 167 (1988); http://www.fresco.org.uk/
[2] www.nscl.msu.edu/∼ brown/resources/resources.html

Reaction dynamics and gamma spectroscopy of Ne isotopes by the heavy ion reaction ^{22}Ne+^{208}Pb

S. Bottoni[1,2], *G. Benzoni*[2], *S. Leoni*[1,2], *D. Montanari*[1,2], *A. Bracco*[1,2], *E. Vigezzi*[2], *F. Azaiez*[3], *L. Corradi*[4], *A. M. Stefanini*[4], *D. Bazzacco*[5], *E. Farnea*[5] *G. Montagnoli*[5,6] *F. Recchia*[5,6], *C. Ur*[5], *A. Gadea*[7], *S. Szilner*[8] *and G. Pollarolo*[9]

[1] Dipartimento di Fisica University of Milano, Milano, Italy
[2] INFN, Sezione di Milano, Milano, Italy
[3] IPN, Orsay, France
[4] INFN Laboratori Nazionali di Legnaro, Padova, Italy
[5] INFN, Sezione di Padova, Padova, Italy
[6] Dipartimento di Fisica, University of Padova, Padova, Italy
[7] CSIC-IFIC, Valencia, Spain
[8] Ruđer Bošković Institute, Zagreb, Croatia
[9] Dipartimento di Fisica Teorica, University of Torino and INFN, Sezione di Torino, Italy

Abstract

The heavy-ion reaction ^{22}Ne+^{208}Pb at 128 MeV beam energy has been studied using the PRISMA-CLARA experimental setup at Legnaro National Laboratories. Elastic, inelastic and one nucleon transfer differential cross sections have been measured and a comparison with semiclassical and distorted wave Born approximation (DWBA) calculations is presented. Similar results are discussed for the unstable ^{24}Ne nucleus, using existing data from the reaction ^{24}Ne+^{208}Pb at 182 MeV (measured at SPIRAL with the VAMOS-EXOGAM setup). In both cases the DWBA model gives a good reproduction of the experiment, pointing to a strong reduction of the β_2^C charge deformation parameter in ^{24}Ne.

1 Introduction

Low-energy transfer reactions with heavy ions have recently become a powerful tool for the production and investigation of exotic neutron-rich systems, making use of the combination of a large acceptance magnetic spectrometer with a high efficiency and high resolution multi-detector array for γ spectroscopy (based on Ge detectors) [1–3]. Recent works have clearly demonstrated the possibility to employ heavy-ion transfer reactions both for detailed particle-spectroscopy (with enhanced sensitivity to specific excited states by γ-gating techniques), and to perform full in-beam γ-spectroscopy [4–6].

In this work [7] we discuss the results of the analysis on light neutron-rich nuclei around ^{22}Ne populated by the reaction ^{22}Ne+^{208}Pb (at 128 MeV), performed at Legnaro National Laboratories with the PRISMA-CLARA setup. The analysis focuses on the measurement of differential cross sections for the elastic, inelastic and one particle transfer channels. The experimental data are interpreted by the semiclassical model GRAZING [8] and by the distorted wave Born approximation approach (DWBA), implemented in the code PTOLEMY [9]. In the case of the inelastic scattering to the 2^+ state of ^{22}Ne, the present results are also compared with existing data from the reaction ^{24}Ne+^{208}Pb (at 182 MeV), obtained in a similar experiment at GANIL using the VAMOS-EXOGAM setup and employing the radioactive ^{24}Ne beam from SPIRAL [10]. In both cases, a DWBA analysis is performed and β_2^C deformation parameters for the nuclear charge distributions are extracted.

2 The experiment

The experiment has been performed at Legnaro National Laboratories of INFN, using the PRISMA-CLARA experimental setup [11]. The ^{22}Ne beam, provided by the PIAVE-ALPI accelerator complex at 128 MeV of bombarding energy, impinged on a ^{208}Pb target 300 μg/cm^2 thick, sandwiched between two layers of ^{12}C (10 and 15 μg/cm^2 thick respectively) [7]. The magnetic spectrometer PRISMA, described in Refs. [12–15], was placed around the grazing angle for this reaction, which has been estimated to be $\theta_{lab} = 70°$. As described in detail in Ref. [4], the identification of the reaction products is achieved by the reconstruction of ion trajectories inside the spectrometer. The coupling of the PRISMA spectrometer with the γ-array CLARA, placed opposite to PRISMA, made possible particle-γ coincidence measurements for each ion detected.

3 The Analysis

The aim of the present work is the evaluation of absolute differential cross sections for elastic, inelastic and one-particle transfer channels, starting from the elastic case. Following the method described in Ref. [16] and successfully applied in previous works [4,10,16], total kinetic energy loss spectra (TKEL), defined as TKEL=-Q$_{value}$, have been constructed, as a function of the scattering angle, for ^{22}Ne ions. The elastic cross section has been determined by subtracting TKEL spectra of ^{22}Ne measured in PRISMA and the one measured in coincidence with γ transitions detected in the CLARA array (inelastic contribution), as shown in Fig.1. The angular distribution of the ratio of the elastic cross section with respect to the Rutherford cross section is presented in the inset of Fig.1. The data have been normalized to the theoretical ratio $\sigma_{el}/\sigma_{ruth}$ calculated by the semiclassical code GRAZING [8] and compared with the DWBA model implemented in the PTOLEMY code [9]. The first allows to extract a conversion factor between counts and mb/sr which has been used to study cross section on absolute scale, while the second provides the optical parameters of the potential of the colliding system.

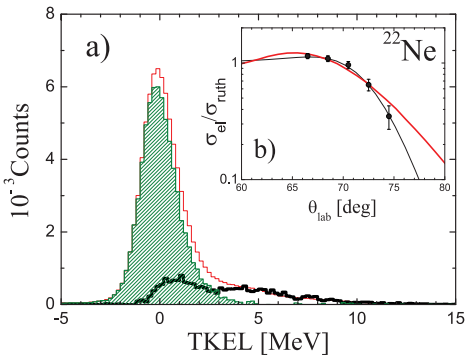

Fig. 1: (Color online) TKEL spectra for ^{22}Ne ions detected by PRISMA (thin red line) and in coincidence with γ transitions detected in CLARA (thick blue line). The shaded green area is the difference spectrum corresponding to elastic events. Inset: Elastic cross section over Rutherford cross section as a function of the scattering angle normalized in the Rutherford region to the theoretical calculation performed by the code GRAZING (thin black line). The calculation performed by the PTOLEMY code is shown by the thick red line.

Fig.2 (top) shows the inclusive (energy integrated) angular distribution for the elastic channel (^{22}Ne in panel a)), the one neutron pick-up channel (^{23}Ne in panel b)) and the one proton stripping channel (^{21}F in panel c)), which are the most intense reaction products. The experimental data are compared with theoretical calculation performed by the semiclassical GRAZING model. We see that the experimental angular distributions are rather well reproduced by the calculations, with a global agreement between data and theory. Similar quality of agreement was also obtained for the one-nucleon transfer channels in the work of Ref. [10], where the more exotic ^{25}Ne and ^{23}F channels were studied, following the heavy ion reaction ^{24}Ne+^{208}Pb. This indicates that the basic ingredients entering the prescription of the reaction dynamics by the GRAZING model are still valid in the case of heavy-ion reactions induced by rather light systems such as Ne isotopes, and moving away from the stability valley. In Fig. 2 (bottom) the γ spectra measured by the CLARA array in coincidence with ^{22}Ne, ^{23}Ne, ^{21}F are also presented.

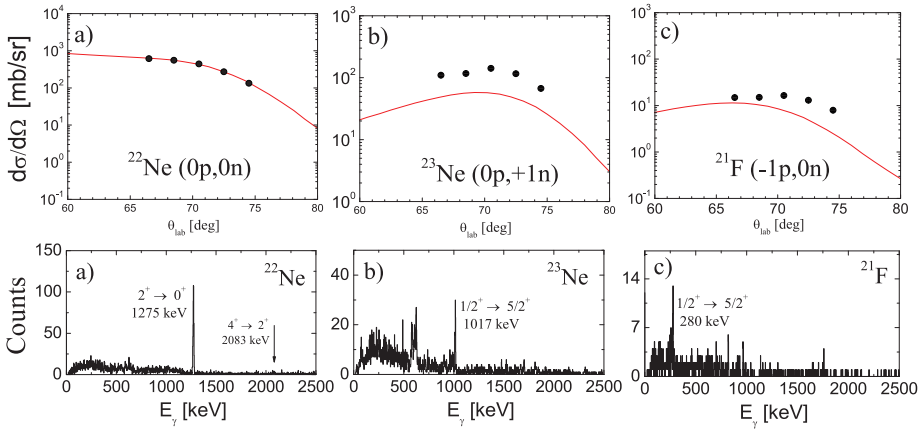

Fig. 2: (Color online) Top: inclusive angular distributions for the most intense reaction channels ^{22}Ne, ^{23}Ne and ^{21}F (panels a), b) and c)). Symbols correspond to experimental data, solid red lines to theoretical calculations by the semi-classical model GRAZING [8]. Bottom: gamma spectra of ^{22}Ne, ^{23}Ne and ^{21}F (panel a), b) and c), respectively). In each spectrum the γ transition from the first excited state to the ground state is clearly visible. In the case of ^{22}Ne, the arrow indicate the position of the $4^+ \rightarrow 2^+$ decay, at 2083 keV, not observed in this experiment.

In the case of ^{22}Ne, the $2^+ \rightarrow 0^+$ transition at 1275 keV has enough statistics to determine the differential cross section for the inelastic scattering to the 2^+ state. This has been done by integrating the area of the 1275 keV peak, for each θ_{lab} angle covered by the acceptance of PRISMA. As reported in Ref. [4], this procedure provides the direct population of the first excited state, after subtracting the feeding contribution from higher lying levels and taking into account the γ efficiency of the CLARA array. In this case, the feeding from the $4^+ \rightarrow 2^+$ decay is negligible, as indicated by the absence of the corresponding γ peak in Fig.2 a), while at most a 25% feeding contribution can be expected from higher-lying states around 5 MeV. This is suggested by the presence of a high-energy tail in the TKEL spectrum gated by the $2^+ \rightarrow 0^+$ γ-transition, as shown in the inset of Fig.3 a). In the same panel, the results (open symbols) are presented together with the data corrected for this feeding contribution (filled circles). In panel b) we present inelastic scattering data taken from Ref. [10], relative to the 2^+ state of the unstable ^{24}Ne, populated by the ^{24}Ne+^{208}Pb reaction at 182 MeV.

Calculations of the inelastic scattering to the 2^+ state have been performed for both experiments, using the Distorted Wave Born Approximation model, implemented in the code PTOLEMY [9]. For the Wood-Saxon optical model potentials we used the parameters obtained by the fit of the elastic distribution. Furthermore, we have put $\beta_2^C = \beta_2^N$, because the fit to the inelastic cross sections favored very similar values for the nuclear and Coulomb deformation parameters. We note that the fit of the inelastic distribution is not very sensitive to the value of β_2^N, while the variation of β_2^C influences the strength of the inelastic cross sections in a similar way for both nuclei. As a consequence, in the following we discuss our results in terms of charge deformation parameters β_2^C only. The results are shown in Fig.4 as filled diamonds. It is found that ^{22}Ne has a rather large quadrupole deformation ($\beta_2^C \approx 0.4$), with a value consistent with the one obtained by an earlier analysis of ^{22}Ne+^{208}Pb inelastic-scattering data, performed with a rotational coupled-channel model [17]. In that work the reaction ^{22}Ne+^{208}Pb was also studied, and a very similar value was obtained for ^{20}Ne (following the ^{20}Ne+^{208}Pb reaction), as shown by open diamonds in Fig.4 a). On the contrary, in the present analysis small values for the deformation parameters of ^{24}Ne are found ($\beta_2^C \approx 0.1$).

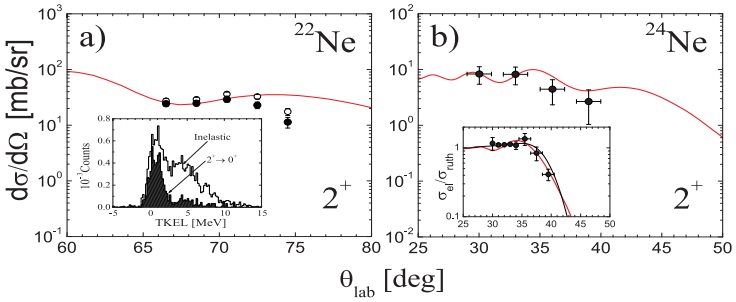

Fig. 3: (Color online) Panel a): Angular distribution of ^{22}Ne ions measured in coincidence with the $2^+ \rightarrow 0^+$ γ transition of 1275 keV. Filled (open) symbols refer to the analysis performed on the γ spectrum of ^{22}Ne taking (not taking) into account the feeding from high-lying states around 5 MeV. Inset of Panel a): inelastic TKEL spectrum of ^{22}Ne and the contribution coming from the $2^+ \rightarrow 0^+$ γ-decay (shaded blue area). Panel b): Angular distribution of ^{24}Ne, measured in coincidence with the $2^+ \rightarrow 0^+$ γ transition of 1982 keV. The inset of panel b) shows the elastic over the Rutherford cross section of ^{24}Ne, as a function of the scattering angle. Experimental data are indicated by symbols, while theoretical calculations performed by the code PTOLEMY (GRAZING) are given by thick (thin) red (black) lines. Data for ^{24}Ne are taken from Ref. [10].

It is interesting to compare our β_2^C values with the charge deformation parameters derived from experimental B(E2;$0^+ \rightarrow 2^+$) measurements (Coulomb excitation or lifetime analysis techniques). In Fig.4 a) we show by open circles the "adopted" β_2^C values [18], while filled circles refer to the most recent measurements, derived from intermediate energy Coulomb excitation experiments (at MSU and RIKEN) and from low-energy Coulomb excitation measurements (at ISOLDE) [19–22]. These recent values are systematically lower than the adopted ones, clearly indicating the difficulty in determining experimentally a firm value for the β_2^C parameter. Our results are also significantly smaller than the adopted value. They correspond to a 30% reduction in the case of ^{22}Ne (which could be accounted for by the uncertainty of the different experimental techniques), and to a much larger suppression (of the order of a factor of 5) for ^{24}Ne. In this case, the adopted value corresponds to the only existing $B(E2)$ measurement via lifetime technique, reported in Ref. [23]. Such a large discrepancy is rather puzzling and definitely calls for additional experimental investigation on the collectivity in ^{24}Ne, a nucleus of key importance for understanding the evolution of shell gaps in light systems, moving towards the neutron drip line.

In Fig.4 b) we show the deformation parameters of the ground state, β_2^{gs}, obtained in three recent theoretical calculations of the ground state of even Ne isotopes, such as the deformed Hartree-Fock plus BCS calculations with Skyrme interaction [24], the deformed mean-field approach including pair correlations treated by the BCS model [25] and the very recent relativistic Hartee-Fock-Bogoliubov model [26]. We note that these studies are found to reproduce quite accurately the experimental charge radii of Ne isotopes (determined by optical isotope shifts measurements [27]), across the sd neutron shell. As shown in the figure, the models predict that the deformation decreases close to the middle of the sd shell, as a consequence of the closure of the $d_{5/2}$ subshell [27,28]. Our data may suggest a similar trend, but a direct comparison is not possible, because the transition strengths are not calculated in these studies.

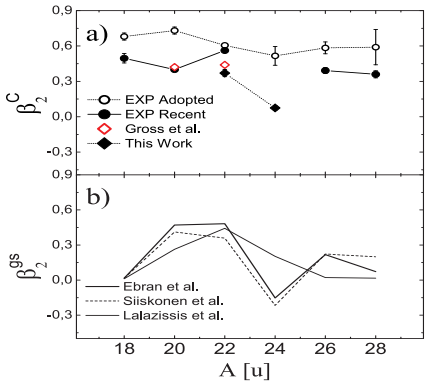

Fig. 4: (Color online) Panel a): Quadrupole deformation parameter β_2^C of the nuclear charge distribution, along the isotopic Ne chain, as derived from experiments. Filled diamonds refer to this work, open diamonds to a similar analysis performed by Gross et al. [17], open circles to the experimental adopted values [18], filled circles to the most recent results from Coulomb excitation experiments [19–22]. Panel b): Theoretical predictions for the ground state deformation parameter β_2^{gs}, as indicated by the legend [24–26]. (See text for details).

4 Conclusion

In this paper we have studied the dynamics of the heavy ion reaction ^{22}Ne+^{208}Pb at 128 MeV beam energy [7]. Elastic, inelastic and one nucleon transfer differential cross sections have been measured and compared with semiclassical and distorted wave Born approximation (DWBA) calculations, resulting in a global agreement between data and theory. A key point of the analysis was the study of the angular distribution of the 2^+ state of ^{22}Ne by the DWBA model, together with similar calculations performed for the 2^+ state of the unstable ^{24}Ne nucleus, based on existing data from the ^{24}Ne+^{208}Pb reaction at 182 MeV beam energy [10]. The analysis provides a very small β_2^C value for ^{24}Ne. This is consistent with the trend predicted for the evolution of ground state quadrupole deformation β_2^{gs} along the Ne isotopic chain, which suggests a subshell closure at N=14. Such a result calls, indeed, for additional experimental investigation on this nucleus, which is of key importance for the understanding of the shell structure along the Ne isotopic chain.

References

[1] L. Corradi, G. Pollarolo and S. Szilner, J. Phys. G **36**, 113101 (2009).
[2] J.J. Valiente-Dobon, et al., Phys. Rev. Lett. **102**, 242502 (2009).
[3] S. Bhattacharyya et al., Phys. Rev. Lett. **101**, 032501 (2008).
[4] D. Montanari et al., Phys. Rev. C **84**, 054613 (2011).
[5] D. Montanari et al., Phys. Lett. B **697**, 288 (2011).
[6] D. Montanari et al., Phys. Rev. C **85**, 044301(2012).
[7] S. Bottoni et al., Phys. Rev. C **85**, 064621(2012)
[8] A. Winther, Nucl. Phys. A **594**, 203 (1995).
[9] M. Rhoades-Brown et al., Phys. Rev. C **21**, 2417 (1980); Phys. Rev. C21, 2436 (1980).
[10] G. Benzoni et al., Eur. Phys. J. A **45**, 287 (2010).
[11] A. Gadea et al., Eur. Phys. J. A **20**, 193 (2004).
[12] A.M. Stefanini et al., Nucl. Phys. A **701**, 217c (2002).
[13] G. Montagnoli et al., Nucl. Instr. and Meth. A **547**, 455 (2005).
[14] S. Beghini et al., Nucl.I nstr. and Meth. A **551**, 364 (2005).
[15] D. Montanari et al., Eur. Phys. J. A **47**, 4 (2011).
[16] S. Szilner et al., Phys. Rev. C **76**, 024604 (2007).
[17] E.E. Gross et al., Phys. Rev. C **29**, 459 (1984).

[18] National Nuclear Data Center, Brookaven National Laboratory, http://www.nndc.bnl.gov/
[19] L. A. Riley et al., Phys. Rev. C **62**, 034306 (2000).
[20] H. Scheit et al., Eur. Phys. J. A**25**, 397 (2005).
[21] J. Gibelin et al., Phys. Rev. C **75**, 057306 (2007).
[22] H. Iwasaki et al., Phys. Lett. B **620**, 118 (2005).
[23] B. A. Watson, J. A. Becker and T. R. Fisher, Phys. Rev. C **9**, 1200 (1974).
[24] T. Siiskonen, P. O. Lipas and J. Rikovska, Phys. Rev. C **60**, 034312 (1999).
[25] G. A. Lalazissis, A. R. Farhan, and M. M. Sharma, Nucl. Phys. A **628**, 221 (1998).
[26] J.-P. Ebran, et al., Phys. Rev. C **83**, 064323 (2011).
[27] K. Marinova et al., Phys. Rev. C **84**, 034313 (2011).
[28] R.R. Rodriguez-Guzman, J.L. Egido, and L.M. Robledo, Eur. Phys. J. A **17**, 37 (2003).

Study of the ^{6}He,^{7}Be+^{9}Be reactions at low energy

K.C.C. Pires[1], R. Lichtenthäler[1], I. Mukha[2], A.M.Moro[3], M. Rodriguez-Gallardo[3], J. Gómez-Camacho[3,4], A. Lépine-Szily[1], V. Guimarães[1], M. Assunção[5], P.N. Faria[1] , E. Crema[1], A. Barioni[1], D.R.Mendes Junior[1], V. Morcelle[1], M.C. Morais[1], R. Pampa Condori[1], J. C. Zamora[1], J.M.B. Shorto[6], S. Mukherjee[7], M. Huyse[8], O. Ivanov[8] , D. Pauwels[8], J. Ponsaers[8], R. Raabe[8], D. Smirnov[8], I. Stefanescu[8], P. Van Duppen[8], C. Angulo[9], E. Casarejos[9], M. Loiselet[9], G. Ryckwaert[9], I. Martel[9],A.M. Sánchez Benítez[10] , L. Grigorenko[11], S. R. Lesher[12]

[1]Departmento de Física Nuclear, Instituto de Física, Universidade de São Paulo, Brazil
[2]Helmholzzentrum fuer Schwerionenforschung (GSI), D-64291 Darmstadt Germany
[3]Departmento de Física Atomica, Molecular y Nuclear, Universidad de Sevilla, Spain
[4]Centro Nacional de Aceleradores, E-41092 Sevilla, Spain
[5]Departamento de Ciências Exatas e da Terra, Universidade Federal de São Paulo, Brazil
[6]Instituto de Pesquisa Energeticas e Nucleares, Comissão Nacional de Energia Nuclear, São Paulo, Brazil
[7]Department of Physics, Faculty of Science, The M.S. University of Baroda, Vadodara, India
[8]Instituut voor Kern- en Stralingsfysica, Katholieke Universiteit Leuven, B-3001 Leuven, Belgium
[9]Institut de Physique Nucléaire and Centre de Recherches du Cyclotron, Université catholique de Louvain, B-1348 Louvain-la-Neuve, Belgium
[10]Departamento de Física Aplicada, Universidad de Huelva, E-21071, Spain
[11]Russian Research Center "The Kurchatov Institute", Kurchatov sq. 1, RU-123182 Moscow, Russia
[12]Department of Physics, University of Richmond, Richmond, Virginia 23173, USA

A study of the elastic scattering and nuclear reactions in light exotic systems ^{6}He+^{9}Be and ^{7}Be+^{9}Be is presented. The ^{6}He+^{9}Be collision was measured at the energies Elab = 12.1 MeV, 16.2 MeV and 21.3 MeV, using the RIBRAS system (Radioactive Ion Beams in Brazil) of the Institute of Physics of the University of São Paulo [1]. Angular distributions of the elastic, inelastic scattering and the alpha particles production in the ^{6}He+^{9}Be collision have been measured. The elastic scattering angular distributions were analyzed by Optical Model, Coupled Channels (CC) considering the ^{9}Be excitation and Continuum-Discretization Coupled-Channels (CDCC) calculations considering the breakup of the ^{6}He. The total reaction cross sections have been obtained from the elastic scattering analysis. The alpha-particle angular distributions were compared with the results of the CDCC calculations for the breakup of the ^{6}He projectile and, CC for the breakup of the ^{9}Be target and the angle-integrated cross section have been obtained. The data for the ^{7}Be+^{9}Be quasielastic scattering and the ^{9}Be(^{7}Be,^{8}Be)^{8}Be* transfer reaction has been measured at Elab = 23.7 MeV at CRC Radioactive Beam Facility at Louvainla-Neuve, Belgium [2]. The quasielastic angular distribution was analysed firstly using the optical model formalism, which provided the potential for the ^{7}Be+^{9}Be interaction and a normalization factor for the experimental data which was not obtained in the experiment. The contribution of the inelastic excitation of the ^{7}Be nucleus to quasielastic cross sections and the influence of the states of the continuum in the elastic scattering were investigated by Coupled Channels and CDCC calculations. The ^{9}Be(^{7}Be,^{8}Be)^{8}Be* transfer reaction was analysed in terms of the Distorted Wave Born Approximation (DWBA) and Coupled Channels Born Approximation (CCBA) methods. All the calculations have been performed using the computer code FRESCO [3]. Spectroscopic factors for the ^{9}Be$\rightarrow$ ^{8}Be+n states have been obtained and compared with shell-model predictions. The total reaction cross section ^{7}Be+^{9}Be has been obtained and compared with the ^{6}He+^{9}Be system and other systems of the literature.

References

[1] R. Lichtenthaler, A. Lepine-Szily, et al, European Physical Journal A 25: 259-260, Suppl. 1 (2005)
[2] M. Gaelens, M. Cogneau, et al, Nucl. Instr. and Meth. In Phys. Res. B (2003), 48
[3] I.J. Thompson, Comp. Phys. Rep. 7, (1988), 167

Analysis of Elastic Scattering of ^{6,8}He and ^{11}Li on Protons and ^{6}He on ^{12}C Using Microscopic Optical Potentials

A.N. Antonov[1], *D.N. Kadrev*[1], *M.K. Gaidarov*[1], *K. Spasova*[1,2], *V.K. Lukyanov*[3], *E.V. Zemlyanaya*[3], *K.V. Lukyanov*[3]

[1]Institute for Nuclear Research and Nuclear Energy, Bulgarian Academy of Sciences, Sofia 1784, Bulgaria

[2]University of Shumen "Bishop K. Preslavsky", Shumen 9712, Bulgaria

[3]Joint Institute for Nuclear Research, Dubna 141980, Russia

Abstract

The data of elastic scattering of ^{6,8}He and ^{11}Li on protons and ^{6}He on ^{12}C at beam energies less than 100 MeV/nucleon (MeV/N) are analyzed utilizing microscopic optical potentials obtained by a single (double)-folding procedure and also by using those inherent in the high-energy approximation. The calculated real and imaginary parts of the optical potentials are based on the neutron and proton density distributions of He and Li isotopes obtained within the large-scale shell-model (LSSM) method. The depths of the real and imaginary parts of the microscopic optical potentials are considered as fitting parameters using as a constrain the behavior of the volume integrals as functions of the incident energy. The ^{11}Li breakup effect on ^{11}Li+p elastic scattering at energy of 62 MeV/N is analyzed within a cluster model for ^{11}Li with ^{9}Li and $2n$ fragments. Predictions for the longitudinal momentum distribution of ^{9}Li fragments produced in the breakup of ^{11}Li on a proton target are given. The role of the spin-orbit and "surface" terms of the optical potential is also studied and estimations of the total cross sections within the both LSSM and breakup reaction model are made.

1 Introduction

The availability of radioactive ion beams facilities made it possible to carry out many experiments and to get more information regarding the structure of these nuclei and the respective reaction mechanisms (see, e.g., the review [1]). Experimental studies of exotic light nuclei, such as ^{6,8}He, ^{11}Li, ^{12}Be and others, with a localized nuclear core and dilute few-neutron halo or skin have also been an important test for various theoretical models used in the description of the data on cross sections of processes with such nuclei. Among the latter we should mention the microscopic analysis using the coordinate-space g-matrix folding method (e.g., Ref. [2]), as well as works where the real part of the optical potential (ReOP) is microscopically calculated (e.g., Ref. [3]) using the folding approach (e.g., Refs. [4, 5]). Usually the imaginary part of the OP's (ImOP) and the spin-orbit (SO) terms have been determined phenomenologically, which has led to the usage of a number of fitting parameters.

In this work we present results of our works [6–9] on calculations of ^{6}He+p [6], ^{8}He+p [7], ^{6}He+^{12}C [8], as well as on ^{11}Li+p [9] elastic differential cross sections in which we used microscopic both ReOP and ImOP. The latter was taken from the OP derived in [10,11] in the frameworks of the high-energy approximation (HEA) [12] that is known as the Glauber theory. Our main aim is to describe the existing experimental data using these microscopic OP's with a minimal number of fitting parameters. In particular we study: i) the limits of applicability of the HEA OP for different regions of angles and incident energies; ii) the sensitivities of the cross sections to the nuclear densities of ^{6,8}He and ^{11}Li; iii) the role of the SO interaction and the non-linearity in the calculations of the OP's; iv) the nuclear surface effects; v) the role of the renormalization of the depths of the ReOP and ImOP; vi) the possibility to involve additional physical criteria for a better description of limited number of experimental data.

2 Theoretical scheme

The optical potential used in our calculations has the form

$$U_{opt} = V^F(r) + iW(r). \tag{1}$$

The real part of the nucleon-nucleus OP is assumed to be a result of a single folding of the nuclear density and of the effective NN potential and involves the direct and exchange parts (e.g. Refs. [4,5]):

$$V^F(r) = V^D(r) + V^{EX}(r). \tag{2}$$

The direct part $V^D(r)$ is composed by the isoscalar (IS) and isovector contributions and expressions for them can be found in Ref. [6]. In our consideration the energy and density dependence of the effective NN interaction (of CDM3Y6-type) are taken in usual forms [5,6]. The isoscalar part of the exchange contribution to the ReOP has the form:

$$V_{IS}^{EX}(r) = g(E) \int \rho_2(\mathbf{r}_2, \mathbf{r}_2 - \mathbf{s}) F\left(\rho_2(\mathbf{r}_2 - \mathbf{s}/2)\right) \times v_{00}^{EX}(s) j_0(k(r)s) d\mathbf{r}_2, \tag{3}$$

where for the density matrix $\rho_2(\mathbf{r}_2, \mathbf{r}_2 - \mathbf{s})$ an approximation [13] is used. It is shown in Ref. [6] how the isovector part of the exchange ReOP can be obtained. The local momentum $k(r)$ of the incident nucleon in the field of the Coulomb $V_C(r)$ and nuclear potential (ReOP) is:

$$k^2(r) = \frac{2m}{\hbar^2} \left[E_{c.m.} - V_C(r) - V(r)\right] \left(\frac{1 + A_2}{A_2}\right). \tag{4}$$

One can see from Eq. (4) that nonlinearity effects appear as ingredient of the approach and they have to be taken into account.

In our work we use proton and neutron densities calculated microscopically within the LSSM method using the Woods-Saxon (WS) basis of single-particle wave functions with realistic exponential asymptotic behavior [14].

The complex HEA OP was derived in [10] on the basis of the eikonal phase inherent in the optical limit of the Glauber theory. In our procedure this OP or only its imaginary part together with the ReOP from the folding procedure is used to calculate the cross sections by means of the code DWUCK4 [15] for solving the Schrödinger equation. The HEA OP is obtained as a folding of the form factors of the nuclear density and the NN amplitude $f_{NN}(q)$ [10,11]:

$$U_{opt}^H = V^H + iW^H = -\frac{\hbar v}{(2\pi)^2}(\bar{\alpha}_{NN} + i)\bar{\sigma}_{NN} \times \int_0^\infty dq q^2 j_0(qr)\rho_2(q) f_{NN}(q). \tag{5}$$

In Eq. (12) $\bar{\sigma}_{NN}$ and $\bar{\alpha}_{NN}$ are, respectively, the NN total scattering cross section and the ratio of the real to imaginary part of the forward NN scattering amplitude, both averaged over the isospin of the nucleus (see, e.g., [16,17]).

The expression for the spin-orbit contribution to the OP used in our work is added to the right side of Eq. (1) and its form can be seen in e.g., Refs. [7,15,18].

In the case of the ^{11}Li+p elastic scattering we consider also the simplest ^{9}Li+2n model of ^{11}Li (see, e.g. [19]) in which two clusters are suggested, the ^{9}Li core (c) and the correlated pair of neutrons $h = 2n$ with the spin of the $2n$ cluster set to $s = 0$. In the framework of this model, the ^{11}Li+p OP can be estimated as folding of two OP's of interaction of the c- and h-clusters with protons and the density $\rho_0(s)$ corresponding to the wave function of the relative motion of two clusters:

$$U^{(b)}(r) = V^{(b)} + iW^{(b)} = \int d\mathbf{s}\rho_0(s) \left[U_c\left(\mathbf{r} + (2/11)\mathbf{s}\right) + U_h\left(\mathbf{r} - (9/11)\mathbf{s}\right)\right]. \tag{6}$$

The potentials U_c and U_h in Eq. (6) are calculated within the microscopic hybrid model of OP [10], in which a single-folding procedure is applied for the real part $V^{(b)}$, while the imaginary part $W^{(b)}$ is derived using the optical limit of the Glauber theory. For the n-p interaction we adopt the one introduced by Suzuki *et al*. [20] $v_{np} = v(r)(1 + i\gamma)$, where $v(r)$ is taken from the Minnesota potential [21].

The differential and total cross sections (for elastic scattering, as well as for diffractive breakup and absorption) all require calculations of the probability functions $d^3P(\mathbf{b}, \mathbf{k})/d\mathbf{k}$ that depend on the impact parameter $\mathbf{b}$. The general expression for the probability functions can be written as [22]

$$\frac{d^3P_\Omega(\mathbf{b}, \mathbf{k})}{d\mathbf{k}} = \frac{1}{(2\pi)^3} \left| \int d\mathbf{r} \phi_k^*(\mathbf{r}) \Omega(\mathbf{b}, \mathbf{r}_\perp) \phi_0(\mathbf{r}) \right|^2, \tag{7}$$

where $\Omega(\mathbf{b}, \mathbf{r}_\perp)$ is expressed by means of the two profile functions S_c and S_h of the core and the di-neutron clusters, respectively:

$$|S_i(b)|^2 = e^{-\frac{2}{\hbar v} \int_{-\infty}^{\infty} dz W_i(\sqrt{b^2+z^2})}, \quad i = c, h \tag{8}$$

where W is the imaginary part of the microscopic OP (6).

As shown in [22], the diffraction breakup elastic cross section (the longitudinal momentum distribution) has the form

$$\left(\frac{d\sigma}{dk_L}\right)_{diff} = \int_0^\infty b_h db_h \int_0^{2\pi} d\varphi_h \int_0^\infty dk_\perp \frac{d^2P(\mathbf{k}, \mathbf{b})}{dk_L dk_\perp}, \tag{9}$$

where $d^2P_\Omega(\mathbf{b}, \mathbf{k})/dk_L dk_\perp$ is obtained by integration of Eq. (7) over the transverse angle φ_k of the momenta.

3 Results and discussion

In the case of ^{6}He+p elastic cross sections ($E < 100$ MeV/N) the optical potential has the form

$$U_{opt}(r) = N_R V(r) + iN_I W(r), \tag{10}$$

where N_R and N_I are fitting parameters, the ReOP V is taken either from single-folding calculations (V^F) or from HEA (V^H), while ImOP has the form $W = W^H$ or $W = V^F$. In the case of ^{8}He+p process we introduce a surface component:

$$U'_{opt}(r) = U_{opt}(r) - i4aN_S \frac{dV^F(r)}{dr}. \tag{11}$$

For the ^{6}He+^{12}C cross sections the OP has the form

$$U_{opt}(r) = N_R V^{DF}(r) + iN_I W(r) + iN_I W^{SF}(r), \tag{12}$$

where the ReOP $V^{DF}(r)$ is a result of a double-folding procedure (using the charge density of ^{12}C obtained from electron-^{12}C scattering experiments) and $W^{SF}(r)$ has various forms related to the derivative $dW(r)/dr$ (e.g., $dW(r)/dr$, $rdW(r)/dr$, $r^2dW(r)/dr$, $dW(r-\delta)/dr$). It was shown in [6] that a good agreement in the case of ^{6}He+p is obtained when LSSM density is used (in comparison with the phenomenological densities) for $E = 41.6$ and 71 MeV/N with values of N_R and N_I close to unity. However, an agreement for the case of $E = 25.2$ MeV/N was obtained for rather smaller values of N_R (0.35) and N_I (0.03), thus showing the limitation of the approach for small energies ($E \leq 25$ MeV/N). In Fig. 1 we give the results for the ^{8}He+p elastic cross sections at energies $E = 15.7, 26, 32, 66$, and 73 MeV/N. It is known that because the procedure of fitting belongs to the class of the ill-posed problems (e.g., [23]), it is necessary to impose some physical constraints on the choice of the set of parameters N.

One of them is the total cross section of scattering and reaction. However, the corresponding values are missing at $E < 100$ MeV/N. Another physical criterion that was imposed on the choice of N's is the behavior of the volume integrals [4]

$$J_V = \frac{4\pi}{A}\int drr^2[N_R V^F(r)], \qquad J_W = \frac{4\pi}{A}\int drr^2[N_I W^H(r)] \tag{13}$$

as functions of the energy. It has been pointed out (see, e.g., [24]) that the values of J_V decrease with the increase of the energy at $0 < E < 100$ MeV/N, while J_W is almost constant in the same interval. In Fig. 1 one can see the result of the fitting procedure with the values of the parameters given in Table 1.

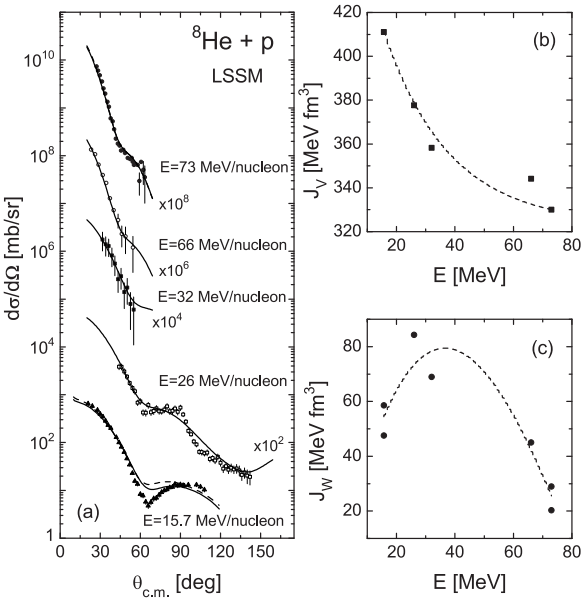

Fig. 1: The ^{8}He+p elastic scattering cross sections (a) at different energies using LSSM density of ^{8}He and parameters from Table 1. Experimental data are taken for 15.7 [25], 26 [26], 32 [27,28], 66 [27,28] and 73 MeV/N [27–29]. The obtained values of the volume integrals J_V (b) and J_W (c) (given by points) are shown as functions of the incident energy, while the dashed lines give the trend of this dependence.

It was shown in [6] that the inclusion of the surface term [see Eq. (11)] leads to a better agreement with the data for the lowest energy $E = 15.7$ MeV/N. Using the same physical constraint we obtained the best agreement of the calculations in the case of ^{6}He+^{12}C [by means of Eq. (11) and the surface term $(-iN_I^{SF} r^2 dW(r)/dr)$] that are presented in Fig. 2 for $E = 3$, 38.3, and 41.6 MeV/N. In Fig. 3 we show the results of our calculations of the ^{11}Li+p elastic cross sections for three energies $E = 62$, 68.4, and 75 MeV/N with and without accounting for the SO term.

Finally, in Fig. 4 we give as an example the calculated cross sections for the diffractive breakup elastic ^{11}Li+p reaction at $E = 62$ MeV/N. These results give predictions because there are not experimental data for such a process at ^{11}Li+p scattering at $E < 100$ MeV/N.

4 Conclusions

The results of the present work can be summarized:

1. The optical potentials and cross sections of ^{6}He+p ($E = 25.2$, 41.6 and 71 MeV/N), ^{8}He+p ($E =$

Table 1: The parameters N_R, N_I, N_R^{SO} and N_I^{SO}, the volume integrals J_V and J_W (in MeV.fm^3) as functions of the energy E (in MeV/N), and the total reaction cross sections σ_R (in mb) for the ^{8}He+p scattering in the case of LSSM density.

E	N_R	N_I	N_R^{SO}	N_I^{SO}	J_V	J_W	σ_R
15.7	0.630	0.064	0.139	0.070	411.1	58.6	722.0
15.7	0.630	0.052	0.166	0.057	411.1	47.6	701.2
26	0.644	0.128	0.035	0.026	377.7	84.35	381.2
32	0.648	0.120	0.062	0.022	358.3	69	302.7
66	0.852	0.131	0	0	344.2	45	95.2
73	0.869	0.090	0.004	0	330.0	29	60.9
73	0.869	0.063	0.010	0	330.0	20.25	43.9

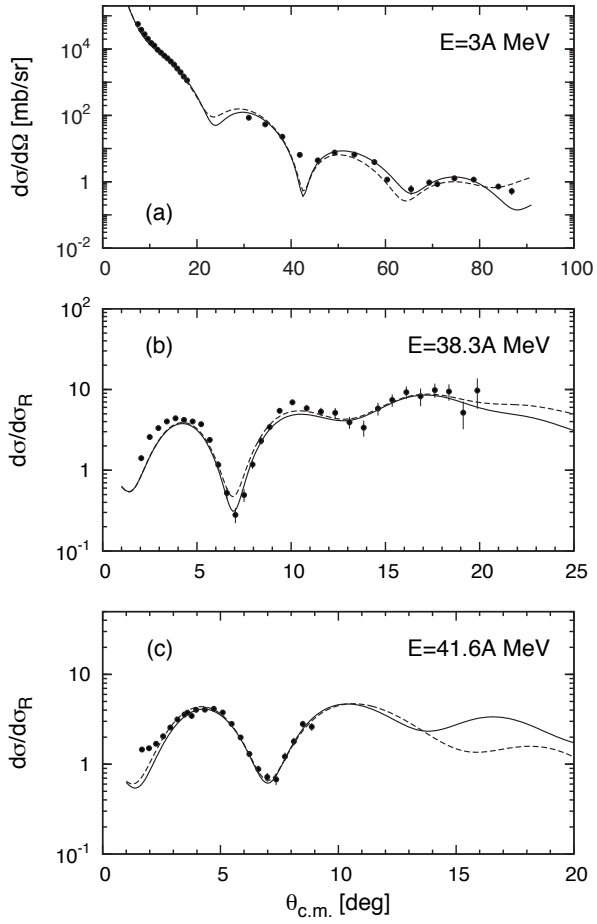

Fig. 2: Differential cross section of elastic ^{6}He+^{12}C scattering at $E = 3$ (a), 38.3 (b) and 41.6 MeV/N (c). Solid line: $W = W^H$, dashed line: $W = V^{DF}$. The experimental data are taken from Refs. [30–32].

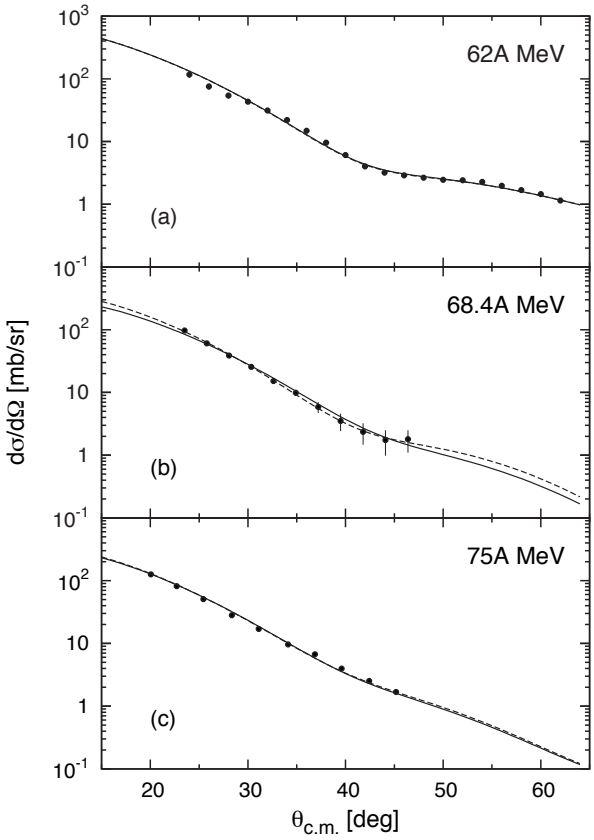

Fig. 3: The ^{11}Li+p elastic scattering cross section at $E = 62, 68.4$, and 75 MeV/N. Solid line: without SO term; dashed line: with SO term. The experimental data are taken from [33] for 62 MeV/N, [34] for 68.4 MeV/N, and [35] for 75 MeV/N.

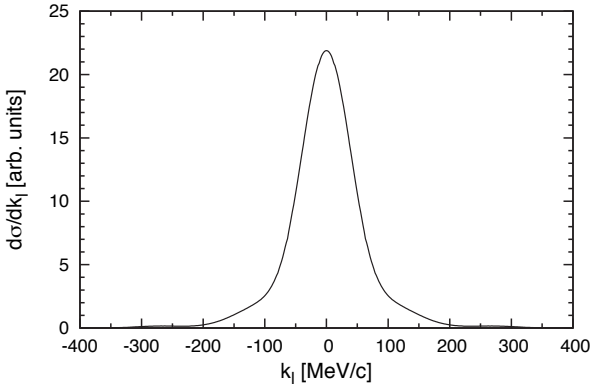

Fig. 4: Cross section of diffraction breakup in ^{11}Li+p scattering at $E = 62$ MeV/N.

15.7, 26, 32, 66 and 73 MeV/N), ^{11}Li+p (E = 62, 68.4 and 75 MeV/N), and ^{6}He+^{12}C (E = 3, 38.3 and 41.6 MeV/N) elastic scattering were calculated and comparison with the available experimental data was performed. The direct and exchange parts of ReOP (V^F) were calculated microscopically using the folding procedure and M3Y (CDM3Y6-type) effective interaction based on the Paris NN potential. The ImOP (W^H) was calculated within the high-energy approximation. Different model densities of protons and neutrons in ^{6}He, ^{8}He and ^{11}Li were used in the calculations: LSSM method, Jastrow correlation method (also Tanihata and COSMA). The SO contribution to the OP was included in the calculations. The cross sections were calculated by numerical integration of the Schrödinger equation by means of the DWUCK4 code using all interactions obtained (Coulomb plus nuclear optical potential).

2. The problem of the ambiguity of the values of the depths of OP's contributions: the parameters N_R, N_I, N_R^{SO}, and N_I^{SO} when the fitting procedure is applied to a limited number of experimental data is considered. A physical criteria imposed in our work on the choice of the values of the parameters N were the known behavior of the volume integrals J_V and J_W as functions of the incident energy in the interval $0 < E_{inc} < 100$ MeV/N, as well as the values of the total reaction cross section.

3. We considered also another folding approach that includes ^{11}Li breakup suggesting a ^{9}Li+2n cluster model, computing the potentials of the interactions of the two clusters with the proton. Predictions for the longitudinal momentum distributions of ^{9}Li fragments produced in the breaking of ^{11}Li at 62 MeV/N on a proton target are given and calculations of the diffraction and stripping reaction cross sections are performed. The necessity of experiments on these reactions of ^{11}Li+p at $E < 100$ MeV/N is emphasized.

Acknowledgements

The work is partly supported by the Project from the Agreement for co-operation between the INRNE-BAS (Sofia) and JINR (Dubna). Four of the authors (D.N.K., A.N.A., M.K.G. and K.S.) are grateful for the support of the Bulgarian Science Fund under Contract No. 02–285 and one of them (D.N.K.) under Contract No. DID–02/16–17.12.2009. The authors E.V.Z. and K.V.L. thank the Russian Foundation for Basic Research (Grant No. 09-01-00770) for the partial support.

References

[1] N. Keeley, N. Alamanos, K. W. Kemper, and K. Rusek, Prog. Part. Nucl. Phys. **63** (2009) 396.

[2] K. Amos, W. A. Richter, S. Karataglidis, and B. A. Brown, Phys. Rev. Lett. **96** (2006) 032503.

[3] M. Avrigeanu, G. S. Anagnostatos, A. N. Antonov, and J. Giapitzakis, Phys. Rev. C **62** (2000) 017001; M. Avrigeanu, G. S. Anagnostatos, A. N. Antonov, and V. Avrigeanu, Int. J. Mod. Phys. E **11** (2002) 249.

[4] G. R. Satchler and W. G. Love, Phys. Rep. **55** (1979) 183; G. R. Satchler, *Direct Nuclear Reactions* (Clarendon, Oxford, 1983).

[5] D. T. Khoa and G. R. Satchler, Nucl. Phys. A **668** (2000) 3; D. T. Khoa, G. R. Satchler, and W. von Oertzen, Phys. Rev. C **56** (1997) 954 (and references therein).

[6] K. V. Lukyanov, V. K. Lukyanov, E. V. Zemlyanaya, A. N. Antonov, and M. K. Gaidarov, Eur. Phys. J. A **33** (2007) 389.

[7] V. K. Lukyanov, E. V. Zemlyanaya, K. V. Lukyanov, D. N. Kadrev, A. N. Antonov, M. K. Gaidarov, and S. E. Massen, Phys. Rev. C **80** (2009) 024609.

[8] V. K. Lukyanov, D. N. Kadrev, E. V. Zemlyanaya, A. N. Antonov, K. V. Lukyanov, and M. K. Gaidarov, Phys. Rev. C **82** (2010) 024604.

[9] D. N. Kadrev, V. K. Lukyanov, A. N. Antonov, E. V. Zemlyanaya, K. V. Lukyanov, M. K. Gaidarov, and K. Spasova, in Nuclear Theory: Proc. 30th International Workshop on Nuclear Theory (Rila, Bulgaria, June 27-July 2, 2011) (2011) pp.126-137.

[10] K. V. Lukyanov, E. V. Zemlyanaya, and V. K. Lukyanov, Phys. At. Nucl. **69** (2006) 240.

[11] P. Shukla, Phys. Rev. C **67** (2003) 054607.

[12] R. J. Glauber, *Lectures in Theoretical Physics* (New York, Interscience, 1959), p.315; A. G. Sitenko, Ukr. Fiz. J. **4** (1959) 152; W. Czyz and L. C. Maximon, Ann. Phys. **52** (1969) 59; J. Formanek, Nucl. Phys. B **12** (1969) 441.

[13] J. W. Negele and D. Vautherin, Phys. Rev. C **5** (1972) 1472.

[14] S. Karataglidis, P. G. Hansen, B. A. Brown, K. Amos, and P. J. Dortmans, Phys. Rev. Lett. **79** (1997) 1447; S. Karataglidis, P. J. Dortmans, K. Amos, and C. Bennhold, Phys. Rev. C **61** (2000) 024319.

[15] P. D. Kunz and E. Rost, in *Computational Nuclear Physics*, edited by K. Langanke *et al*. (Springer-Verlag, New York, 1993), Vol.2, p.88.

[16] P. Shukla, arXiv: nucl-th/0112039; S. Charagi and G. Gupta, Phys. Rev. C **41** (1990) 1610; **46** (1992) 1982.

[17] C. Xiangzhow, F. Jun, S. Wenqing, M. Yugang, W. Jiansong, and Y. Wei, Phys. Rev. C **58** (1998) 572.

[18] F. D. Becchetti, Jr. and G. W. Greenless, Phys. Rev. **182** (1969) 1190; A. J. Koning and J. P. Delaroche, Nucl. Phys. A **713** (2003) 231.

[19] K. Ikeda, T. Myo, K. Kato, and H. Toki, Lect. Notes Phys. **818** (2010) 165–221.

[20] Y. Suzuki, K. Yabana, and Y. Ogawa, Phys. Rev. C **47** (1993) 1317.

[21] D. R. Thompson, M. LeMere, and Y. C. Tang, Nucl. Phys. A **286** (1977) 53; Y. C. Tang, M. LeMere, and D. R. Thompson, Phys. Rep. **47** (1978) 167.

[22] K. Hencken, G. Bertsch, and H. Esbensen, Phys. Rev. C **54** (1996) 3043.

[23] A. N. Tikhonov and V. Y. Arsenin, *Solutions of Ill-Posed Problems* (V. H. Winston and Sons/Wiley, New York, 1977).

[24] E. A. Romanovsky *et al*., Bull. Rus. Acad. Sci., Physics, **62** (1998) 150.

[25] F. Skaza *et.al*., Phys. Lett. B **619** (2005) 82.

[26] G. M.Ter-Akopian *et al*., in *Fundamental Issues in Elementary*, Proceedings of the Symposium in honor and memory of Michael Danos, Bad Honnef, Germany, 2000, ed. by W. Greiner (E P Systema, Debrecen, 2001), p.371.

[27] A. A. Korsheninnikov *et al*., Nucl. Phys. A **616** (1997) 189c.

[28] A. A. Korsheninnikov *et al*., Nucl. Phys. A **617** (1997) 45.

[29] A. A. Korsheninnikov *et al*., Phys. Lett. B **316** (1993) 38.

[30] M. Milin *et al*., Nucl. Phys. A **730** (2004) 285.

[31] V. Lapoux *et al*., Phys. Rev. C **66** (2002) 034608.

[32] J. S. Al-Khalili *et al*., Phys. Lett. B **378** (1996) 45.

[33] C.-B. Moon *et al*., Phys. Lett. B **297** (1992) 39.

[34] A. A. Korsheninnikov *et al*., Phys. Rev. Lett. **78** (1997) 2317.

[35] A. A. Korsheninnikov *et al*., Phys. Rev. C **53** (1996) R537.

Angular Distributions of the Analyzing Power in the Excitation of Low Lying States of ^{56}Co

J.J. van Zyl[1], *A.A. Cowley*[1,2], *R. Neveling*[2], *E.Z. Buthelezi*[2], *S.V. Förtsch*[2], *J.P. Mira*[1], *F.D. Smit*[2], *G.F. Steyn*[2], *J.A. Swartz*[1] *and I.T. Usman*[2,3]

[1]Department of Physics, Stellenbosch University, Private Bag X1, Matieland 7602, South Africa
[2]iThemba Laboratory for Accelerator Based Sciences, P. O. Box 722, Somerset West 7129, South Africa
[3]School of Physics, University of the Witwatersrand, Johannesburg 2050, South Africa

Abstract

We present new differential cross section and analyzing power measurements as a function of scattering angle for the reaction ^{58}Ni($\vec{p}$,^{3}He)^{56}Co at three incident energies, 80, 100 and 120 MeV. The experimental results are compared to macroscopic, zero-range DWBA calculations, assuming a direct single-step deuteron pickup mechanism. The dependency of the angular distributions on incident energy is investigated in order to evaluate the viability of such a simple one-step pickup process for the final stage in inclusive (p,^{3}He) reaction studies within a multistep formalism. It was found that the DWBA calculations give a good representation for the one-step direct pickup process and consistently follow the observed angular trends at all three incident energies.

1 Introduction

The current project involves the measurement of differential cross section and analyzing power angular distributions for a few discrete states in ^{56}Co at different incident energies. The investigation is largely motivated by studies done on the pre-equilibrium emission of light ^{3}He- and α-clusters from the interaction of medium energy polarized protons with target nuclei such as ^{58}Ni, ^{59}Co and ^{93}Nb [1–4].

These reactions were successfully described by the statistical multistep formalism of Feschbach, Kerman and Koonin (FKK), involving a final two-nucleon pickup or α-particle knockout process for the (p,^{3}He) and (p,α) reactions respectively, following a few intra-nuclear proton-nucleon collisions. In this context a one-step process, in the case of the (p,^{3}He) reaction for example, means a direct two-nucleon pickup. A two-step process means that the incident proton first collides with a nucleon in the target and then picks up a proton-neutron pair to exit as a ^{3}He-particle. Similarly for the three- and higher order steps. The final-step pickup processes have been described by means of the distorted-wave Born approximation (DWBA). The studies pointed out the sensitivity of the analyzing power to the contributions of the different steps. Large analyzing power values, seen at the lowest excitation energies, are dominated by direct single-step processes, while at larger excitation energies the analyzing powers decrease indicating the emerging prominence of higher order steps.

Most of the trends in the results are well understood from the theory, however some features are not that obvious. At larger incident energies the analyzing powers decrease, consistent with the multistep theory, but it is not certain why this decrease also appears at the very lowest excitation energies where one would rather expect the more direct single-step processes to be enhanced. In order to test the adequacy of the zero-range DWBA for the description of the final pickup process, the ^{58}Ni($\vec{p}$,^{3}He)^{56}Co reaction to a few low lying states of ^{56}Co has been investigated with a high resolution magnetic spectrometer at incident energies of 80, 100 and 120 MeV. The data are compared to a simple one-step, direct two-nucleon pickup description to see how well the DWBA theory is able to describe the direct reaction part.

2 Experimental

Measurements were performed at iThemba Laboratory for Accelerator Based Sciences (LABS) cyclotron facility near Faure, South Africa, using the K600 magnetic spectrometer, Fig. 1. Differential cross sec-

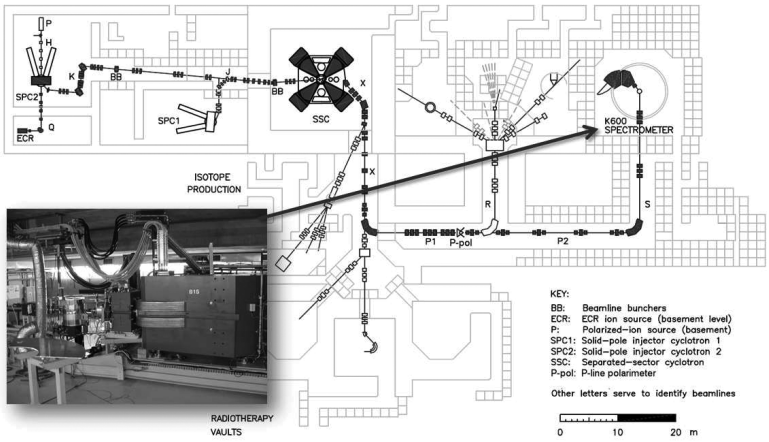

Fig. 1: Schematic overview of the cyclotron facility at iThemba LABS, Faure, South Africa.

tion and analyzing power angular distributions were measured for the $(p,^3\mathrm{He})$ reaction on ^{58}Ni at beam energies of 80, 100 and 120 MeV, and scattering angles between 25° and 60° in 5° steps for several discrete states. An inline polarimeter, consisting of two similar NaI(Tl) detectors at symmetrical angles on either side of the beam direction, was used to measure the polarization during the experiment. The polarization in the up(down) direction is determined form the known analyzing power for a fixed detector angle, e.g. $A_y = 0.74$ for the elastic scattering of protons from ^{12}C at $\theta = 40°$, using the expression

$$p^{\uparrow(\downarrow)} = \left(\frac{1}{A_y}\right)\frac{L^{\uparrow(\downarrow)} - R^{\downarrow(\uparrow)}}{L^{\uparrow(\downarrow)} + R^{\downarrow(\uparrow)}}\,, \tag{1}$$

where $L^{\uparrow(\downarrow)}$ and $R^{\downarrow(\uparrow)}$ are the number of elastically scattered events in the left and right detector when the beam polarization is up(down).

The average polarization achieved during the experiment was between 60% and 80% and the difference between up and down polarisation around 10% to 30%. Particle identification was done using standard time-of-flight (TOF) techniques and it was possible to clearly isolate the desired ^{3}He-particles as seen in Fig. 2. The energy calibration was done using the known Q-values for the ^{12}C$(p,^3$He), ^{16}O$(p,^3$He) and ^{27}Al$(p,^3$He) reactions to ground and excited states. The resulting excitation energy resolution, seen in Fig. 3, was about 100 keV, limited mostly by the thickness of the target. The most prominent states identified are those having large angular momentum transfers.

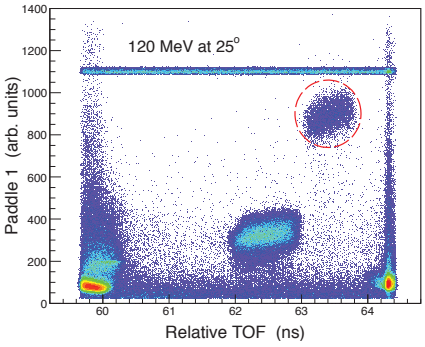

Fig. 2: Paddle 1 vs. time-of-flight (TOF) spectrum for the 120 MeV beam at 25° showing the ^{3}He locus (dashed circle)

The measured differential cross section (in mb sr^{-1}) for a specific lab angle is determined

from

$$\frac{d\sigma(\theta)}{d\Omega} = \left(\frac{10^{27}}{n}\right)\frac{N_c}{N_0\Delta\Omega}\,, \tag{2}$$

where n is the number of target nuclei per cm^2, N_c is the background corrected counts in an energy peak, N_0 is the total number of incident protons, and $\Delta\Omega$ is the acceptance solid angle of the spectrometer defined by the collimator. The absolute (unpolarized) differential cross section is then given by

$$\left(\frac{d\sigma(\theta)}{d\Omega}\right)_{unpol} = \frac{p^{\downarrow}\sigma^{\uparrow} + p^{\uparrow}\sigma^{\downarrow}}{p^{\downarrow} + p^{\uparrow}} \tag{3}$$

$$\approx \frac{\sigma^{\uparrow} + \sigma^{\downarrow}}{2}\,.$$

The last approximation is valid only if $p^{\uparrow} \approx p^{\downarrow}$. Similarly, the analyzing power is determined from

$$A_y = \frac{N^{\uparrow} - N^{\downarrow}}{p^{\downarrow}N^{\uparrow} + p^{\uparrow}N^{\downarrow}}\,, \tag{4}$$

where the number of event counts with the beam polarization in the up(down) direction is given by $N^{\uparrow(\downarrow)}$.

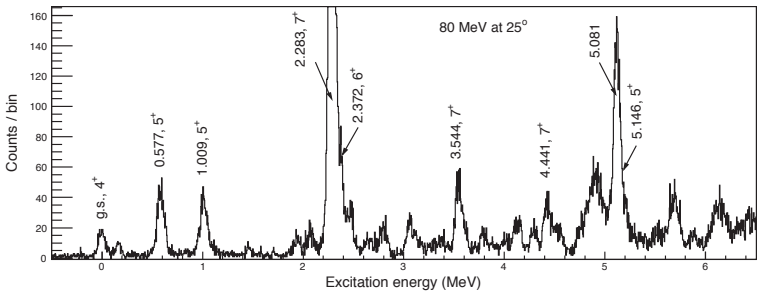

Fig. 3: Excitation energy spectrum of the ^{58}Ni(p,^{3}He)^{56}Co reaction at 80 MeV for θ_{lab} = 25°. A few prominent states are indicated with their known J^{π} assignments.

3 Theoretical

The differential cross sections and analyzing powers are calculated in terms of the DWBA with zero-range interaction using the code DWUCK IV [5]. The macroscopic cross section for deuteron pickup is given by

$$\left(\frac{d\sigma(\theta)}{d\Omega}\right)_{exp} = \frac{2S_{^3He}+1}{2S_p+1}\mathbf{C}\sum_{LSJ} b^2_{ST}D^2_{ST}\left\langle T_B N_B; TN|T_A N_A\right\rangle^2 \frac{2S+1}{2J+1}\left(\frac{d\sigma(\theta)}{d\Omega}\right)^{DW}\,, \tag{5}$$

where **C** is an overall normalization factor, the overlap function b^2_{ST} is 0.5, the interaction strengths D^2_{ST} between the transferred proton and neutron are 0.30 for $S = 0$ and 0.72 for $S = 1$, and the Clebsch-Gordan coefficients for the isospin transfers are 1 and 2 for the cases with $S = 0$ and $S = 1$ respectively. The last DW-factor is the output from DWUCK IV for a transfer with LSJ quantum numbers.

The analyzing power A_y is determined from the definition of polarization $p^{\uparrow(\downarrow)}$ for a beam polarization in the up(down) direction with respect to the scattering plane in terms of the cross section $\sigma^{\uparrow(\downarrow)}$, and is defined as

$$A_y = \frac{\sigma^{\uparrow} - \sigma^{\downarrow}}{\sigma^{\uparrow} p^{\downarrow} + \sigma^{\downarrow} p^{\uparrow}} \,. \tag{6}$$

The total A_y for a combination of different states with LSJ is written as

$$A_y = \frac{\sum_{LSJ} \left(\frac{d\sigma}{d\Omega}\right)^{LSJ} A_y^{LSJ}}{\sum_{LSJ} \left(\frac{d\sigma}{d\Omega}\right)^{LSJ}} \,. \tag{7}$$

4 Results and Conclusion

Figure 4 shows the differential cross section and analyzing power angular distribution for the $J = 7^+$ state at 2.283 MeV with known $L = 6$ transfer [6]. The DWBA calculations follow the angular trends well enough and especially the shape of the data for the different incident energies. Since the resolution did not allow the separation of closely spaced states, a small contribution of the $J = 6^+$, $L = 6$ state at 2.372 MeV was added to give the total fit. Of specific notice is the large negative analyzing powers which is sensitive to the J-value of the transferred pair.

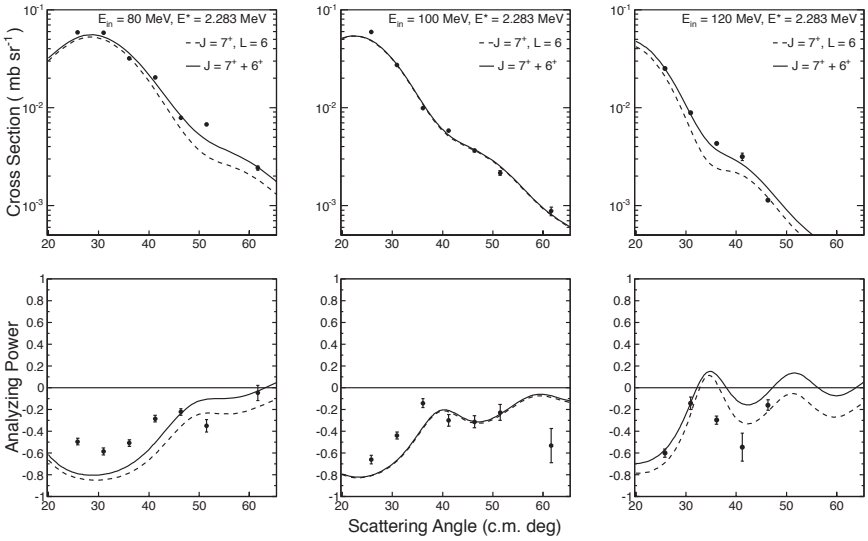

Fig. 4: Cross section (top) and Ay (bottom) for E^* = 2.283 MeV at 80 (left), 100 (middle) and 120 MeV (right)

Similarly, the results for the 0.577 MeV state with $J = 5^+$ and $L = 4 + 6$ are shown in Fig. 5. Two possible L-values can contribute, though the data seem to favour the $L = 4$ transfer. Again it is noticeable the definitive sign of the analyzing power angular distributions which, in this case, is largely positive.

In summary, we have provided new measured differential cross section and analyzing power angular distributions for a few discrete states of ^{56}Co at beam energies of 80, 100 and 120 MeV and at angles 25° to 60° by means of the reaction $(\vec{p},{}^3\mathrm{He})$ on ^{58}Ni. From the good correspondence between the calculations and the experimental data it would seem that the direct one-step deuteron pickup description

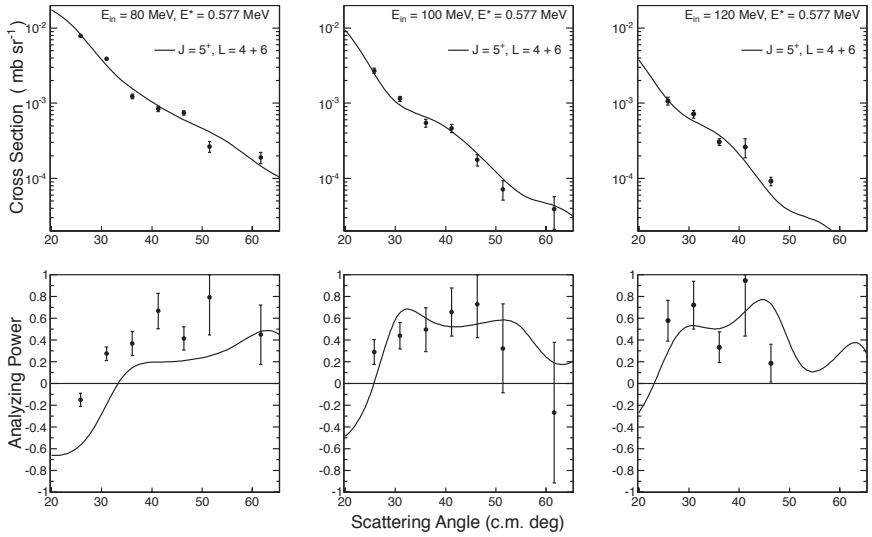

Fig. 5: Cross section (top) and Ay (bottom) for E^* = 0.577 MeV at 80 (left), 100 (middle) and 120 MeV (right)

in terms of the zero-range DWBA is indeed suitable to describe the pickup reaction for the range of incident energies investigated. The apparent quenching of the analyzing power at increasing incident energy is not obvious, though it can be expected that the combined effect from different discrete states with possible opposite phases can contribute in such a way to produce such a tendency. A future improvement to be investigated is a double folding potential for the ^{3}He-particles, and this will be done in collaboration with colleagues from the Institute for Nuclear Research and Nuclear Energy (INRNE) in Sofia, Bulgaria and the Joint Institute for Nuclear Research (JINR) in Dubna, Russia.

Acknowledgements

J.J. van Zyl thanks the Faculty of Science and the Division of Research Development, Stellenbosch University, South Africa as well as the National Research Foundation (NRF) of South Africa for their financial support.

References

[1] A.A. Cowley *et al*., *Phys. Rev. C* **75** (2007) 054617.

[2] A.A. Cowley, S.S. Dimitrova and J.J. van Zyl, In: *Proceedings of the 3rd International Conference on Frontiers in Nuclear Structure, Astrophysics, and Reactions - FINUSTAR 3*, Rhodes, Greece, 23-27 Aug. (2010) .

[3] A.A. Cowley *et al*., In: *Proceedings of the 23rd International Nuclear Physics Conference INPC2007*, Tokyo, Japan, 3-8 June 2007, edited by S. Nagamiya, T. Motobayashi, M. Oka, R.S. Hayano and T. Nagae, Vol. 1, Publisher: Elsevier, Amsterdam (2008) 473.

[4] K. Spasova, S.S. Dimitrova and P.E. Hodgson, *Phys. G.* **26** (2000) 1489.

[5] P.D. Kunz and E. Ross, *Computational Nuclear Physics*, edited by K. Langanke *et al*. Springer-Verslag, Berlin (1993) Vol. 2 Chap. 5.

[6] G. Bruge and R.F. Leonard, *Phys. Rev. C* **2** (1970) 2200.

Consistent analysis of all-inclusive deuteron-induced reactions at low energies

M. Avrigeanu and V. Avrigeanu
Horia Hulubei National Institute for Physics and Nuclear Engineering, P.O. Box MG-6, 077125 Bucharest-Magurele, Romania

Abstract
An extended analysis of the reaction mechanisms involved within deuteron interaction with nuclei, namely the breakup, stripping, pick-up, pre-equilibrium emission, as well as the evaporation from fully equilibrated compound nucleus, is presented. The overall agreement between the measured data and model calculations validates the description of nuclear mechanisms taken into account for the deuteron-nucleus interaction.

1 Introduction

The description of deuteron-nucleus interaction represents an important test for both the appropriateness of reaction mechanism models and evaluation of nuclear data requested especially by the ITER [1], IFMIF [2] and SPIRAL2-NFS [3] research programmes. The weak binding energy of the deuteron, B=2.224 MeV, is responsible for the high complexity of the interaction process that supplementary involves a variety of reactions initiated by the neutron and proton following the deuteron breakup (BU). The difficulties to interpret the deuteron-induced reaction data in terms of the usual reaction mechanism models have recently been re-investigated [4–10] looking for a consistent way to include the breakup contribution within the activation cross section calculations too.

On the other hand, the (d,p) and (d,n) stripping as well as the (d,t) pick-up direct reaction (DR) contributions have also been usually neglected or very poorly taken into account, in spite of being important at low incident energies (e.g., Refs. [4–10]). Finally, the reaction mechanisms such as the pre-equilibrium emission (PE) and evaporation from fully equilibrated compound nucleus (CN) become important when the incident energy is increased above the Coulomb barrier. Actually even the PE and CN analysis has to take into account the decrease of the deuteron total reaction cross section due to above-mentioned BU, stripping and pick-up processes. The present work concerns a deeper understanding, all together and consistently, of the deuteron breakup, stripping and pick-up reactions, and the better-known statistical emission.

2 Deuteron breakup effects on activation cross sections

The physical picture of the deuteron-breakup in the Coulomb and nuclear fields of the target nucleus considers two distinct chains, namely the elastic-breakup (EB) in which the target nucleus remains in its ground state and none of the deuteron constituents interacts with it, and the inelastic-breakup or breakup fusion (BF), where one of these deuteron constituents interacts with the target nucleus while the remaining one is detected.

An empirical parametrization of the total proton-emission breakup fraction $f_{BU}^{(p)} = \sigma_{BU}^{p}/\sigma_R$, of the deuteron total reaction cross section σ_R, and the elastic breakup fraction $f_{EB} = \sigma_{EB}/\sigma_R$ were obtained [4] through analysis of the experimental systematics [11,12] of the proton-emission spectra and angular distributions of deuteron-induced reactions on target nuclei from Al to Pb, at incident energies from 15 to 80 MeV. Their dependence on the deuteron incident energy E, and charge Z and atomic number A of the target nucleus is [4]:

$$f_{BU}^{(p)} = 0.087 - 0.0066Z + 0.00163ZA^{1/3} + 0.0017A^{1/3}E - 0.000002ZE^2, \quad (1)$$

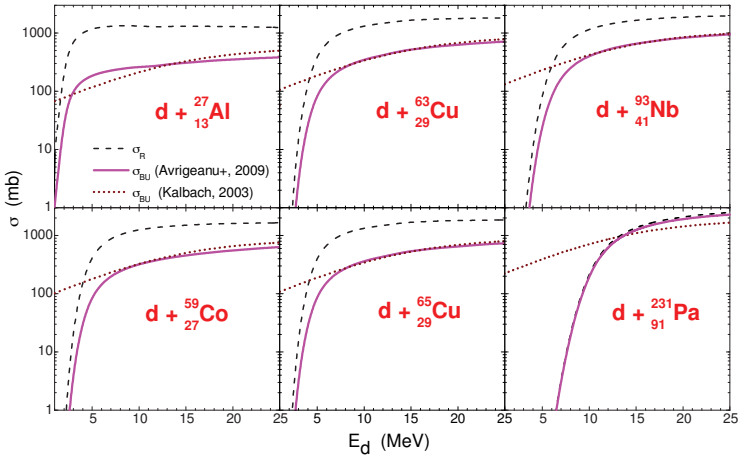

Fig. 1: The energy dependence of the deuteron total reaction cross section (dashed curves) and total breakup cross sections given by parametrizations of Avrigeanu *et al*. [4] (solid) and Kalbach [13] (dotted) for deuteron interactions with the ^{27}Al, ^{63,65}Cu, ^{59}Co, ^{93}Nb, and ^{231}Pa target nuclei.

$$f_{EB} = 0.031 - 0.0028Z + 0.00051ZA^{1/3} + 0.0005A^{1/3}E - 0.000001ZE^2. \quad (2)$$

Consequently, it results the inelastic breakup fraction

$$f^p_{BF} = f^p_{BU} - f_{EB} \quad , \quad (3)$$

and the corresponding nucleon inelastic–breakup cross sections, under the assumption that the inelastic–breakup cross section for neutron emission σ^n_{BF} is the same as that for the proton emission σ^p_{BF},

$$\sigma^{n/p}_{BF} = f^{(n/p)}_{BF}\sigma_R \quad . \quad (4)$$

A comparison with the total proton- and neutron-emission breakup cross-section parametrization of Kalbach [13],

$$\sigma^b_{BU} = K_{d,b}\frac{(A^{1/3}+0.8)^2}{1+exp\frac{(13-E)}{6}}, \;\; K_{d,p} = 21, \;\; K_{d,n} = 18 \;\; , \quad (5)$$

shows that the former parametrization [4], that considers equal breakup fractions for proton and neutron emission, supplementary provides all breakup components by means of the total, f^b_{BU}, elastic, f_{EB}, and inelastic f^b_{BF} fractions.

The comparison of the total breakup cross sections predicted by Avrigeanu *et al*. [4] and Kalbach [13] with the deuteron reaction cross sections for target nuclei from Al to Pa is shown in Fig. 1. Regardless of the differences between them, both parameterizations predict the increasing role of deuteron breakup with increasing the target nucleus mass/charge, pointing out the dominance of the breakup mechanism at the deuteron incident energies below and around the Coulomb barrier of, e.g., ^{231}Pa.

2.1 Phenomenological EB versus CDCC formalism

Concerning the energy dependence of the EB and BF components, the interest on deuteron activation cross sections for incident energies up to 60 MeV motivated an additional check [14] of the EB parameterization extension beyond the energies formerly considered for the derivation of its actual form. Actually, our parameterization [4] for the elastic-breakup was obtained through analysis of the empirical

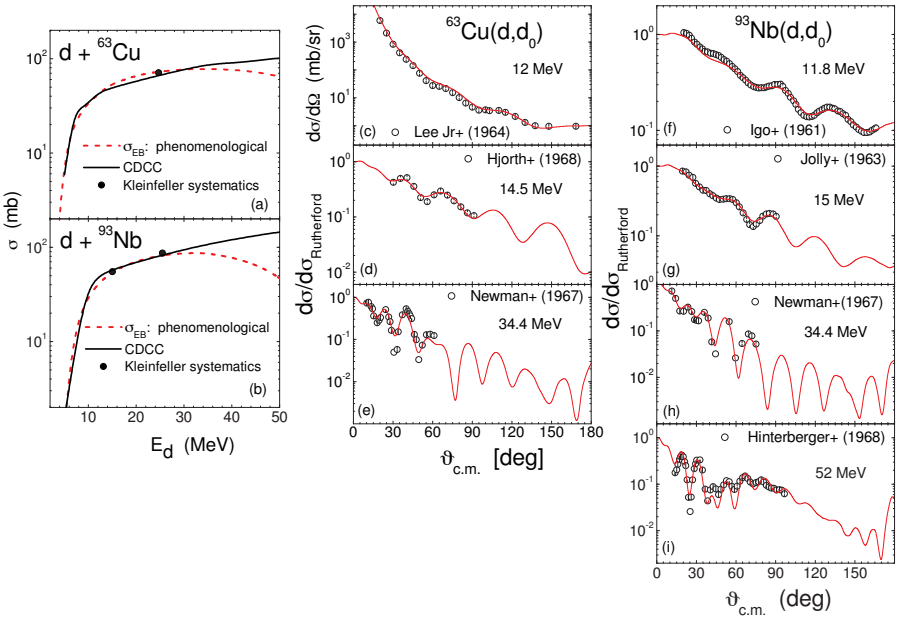

Fig. 2: (a,b) Energy dependence of empirical [4] (dashed curves) and CDCC [14] (solid) elastic breakup cross sections for deuterons on ^{63}Cu and ^{93}Nb target nuclei, and values of Kleinfeller systematics [11]. (c-i) Comparison of measured [20] and calculated (CDCC) angular distributions of deuteron elastic scattering on ^{63}Cu and ^{93}Nb.

systematics which covers an incident energy range from 15 to only 30 MeV. However, as it is shown in Fig. 2(a,b) for (a) the ^{63}Cu and (b) ^{93}Nb target nuclei, the elastic-breakup cross sections given by the empirical parameterization [4] decrease with the incident energy beyond the energy range within which it was established, while the total-breakup cross section has an opposite trend. Therefore, in the absence of available experimental deuteron elastic-breakup data at incident energies above 30 MeV, the correctness of an eventual extrapolation should be checked by comparison of the related predictions with results of a theoretical model as, e.g., the Continuum-Discretized Coupled-Channels (CDCC) method [15–18].

The elastic-breakup component is treated within the CDCC formalism as an inelastic excitation of the deuteron, coupling its unbound excited states in the solution of the scattering problem by means of the coupled channels approach. In order to deal with a finite set of coupled equations, the *binning* method [15, 16] has been used. The energy dependence of the EB cross sections provided by the excitation of the continuum spectrum (e.g the population of the virtual excited states) in the case of the deuteron interaction with ^{63}Cu and ^{93}Nb target nuclei, is compared with the prediction of empirical systematics [4] in Fig. 2(a,b). The calculations were performed with the coupled-channels code FRESCO [19]. The EB cross sections corresponding to the Kleinfeller *et el.* systematics (Table 3 of Ref. [11]) are also shown. The agreement of the CDCC elastic-breakup cross sections [14] and the latter systematics can be considered as a validation of the present advanced model approach. Moreover, the comparison shown in Fig. 2(a,b) points out that the CDCC calculations lead to EB cross sections that follow the total-breakup cross section behavior, and makes clear that the empirical parameterization extrapolation for the EB cross sections beyond the energies considered in this respect should be done with caution [14].

On the other hand, the check of the reliability of the CDCC parameters is given by the comparison between the experimental and CDCC deuteron elastic-scattering angular distributions. Therefore, the good agreement shown in Fig. 2(c-i) supports the consistent CDCC parametrization.

2.2 Inelastic-breakup enhancement of the deuteron activation cross sections

On the whole, the breakup process reduces the total reaction cross section that should be shared among different outgoing channels. On the other hand, the inelastic-breakup component, where one of deuteron constituents interacts with the target leading to a secondary composite nucleus, brings contributions to different reaction channels. Thus, the absorbed proton or neutron following the breakup emission of a neutron or proton, respectively, contributes to the enhancement of the corresponding (d, xn) or (d, xp) reaction cross sections. In order to calculate this breakup enhancement for, e.g., the (d, xn) reaction cross sections, firstly the inelastic-breakup cross sections were obtained by subtracting the EB cross sections from the phenomenological total breakup cross sections. Next, they have been multiplied by the ratios $\sigma_{(p,x)}/\sigma_R$ convoluted with the Gaussian line shape of the deuteron-breakup peak energies of the corresponding emitted constituent [21], for a given deuteron incident energy, where x stands for the γ, n, d, or α various outgoing channels [5–8].

A special point concerns the deuteron interactions with heavy nuclei, for which both breakup parameterizations [4, 13] point out the dominance of the breakup mechanism at the incident energies below and around the Coulomb barrier, as shown in Fig. 1 for deuteron interaction with ^{231}Pa target nucleus [10]. This is why recent measurements of the $^{231}\mathrm{Pa}(d,3n)^{230}\mathrm{U}$ and $^{231}\mathrm{Pa}(p,2n)^{230}\mathrm{U}$ reactions cross sections, between 11.2 and 19.9 MeV [22], and respectively 10.6 and 23.8 MeV [23], are particularly useful for the analysis of breakup effects on the former excitation function. The outgoing energy of the breakup–protons along the $^{231}\mathrm{Pa}(d,3n)^{230}\mathrm{U}$ data of Ref. [22] is covered by the $^{231}\mathrm{Pa}(p,2n)^{230}\mathrm{U}$ excitation function that can be used for the calculation of the BF enhancement of the $(d, 3n)$ reaction cross sections, as described above. Therefore, concerning the breakup mechanism dominance, it results that further calculations of deuteron activation cross sections have to take into account both the huge leakage of initial flux toward the breakup process, as well as the inelastic breakup enhancement brought by the BU nucleon interactions with the target nucleus.

These opposite effects of the breakup mechanism are shown in Fig. 3(d) for the $^{231}\mathrm{Pa}(d,3n)^{230}\mathrm{U}$ reaction. Thus, we have obtained firstly the PE and CN contributions to the $(d, 3n)$ reaction cross sections, under the assumption of no breakup process. Then the BU reduction of these results was addressed by using a reduction factor $(1 - \sigma_{BU}/\sigma_R)$ of the deuteron total reaction cross section.

Secondly, the significant BF enhancement comes from the absorbed proton, following the breakup neutron emission, through the $^{231}\mathrm{Pa}(p,2n)^{230}\mathrm{U}$ reaction. In order to calculate this breakup enhancement of the $^{231}\mathrm{Pa}(d,3n)^{230}\mathrm{U}$ reaction, the nucleon BF cross section σ^n_{BF} [10] was multiplied by the convolution of the ratio $\sigma_{(p,2n)}/\sigma_{(p,R)}$ with the Gaussian distribution of the breakup–proton energies corresponding to a given incident deuteron energy. The latest above-mentioned quantities are shown in Fig. 3(c) for three deuteron incident energies. The areas of the related convolution results correspond to the BF enhancement of the $(d, 3n)$ reaction cross sections at the given deuteron energies. The energy dependence of this BF enhancement of the $^{231}\mathrm{Pa}(d,3n)^{230}\mathrm{U}$ activation cross section is shown by dot-dashed curve in Fig. 3(d), while the corresponding total activation of ^{230}U is finally compared with the experimental data [22]. The realistic treatment of the BF enhancement by taking into account the quite large widths Γ of the breakup–proton energy distributions, shown in Fig. 3(a), has led to a rather accurate description of data. Further improvements of the breakup analysis may lead to a better account of the related energy dependence, while the present results prove the important role of breakup mechanism at the incident energies around the Coulomb barrier of a heavy target nucleus.

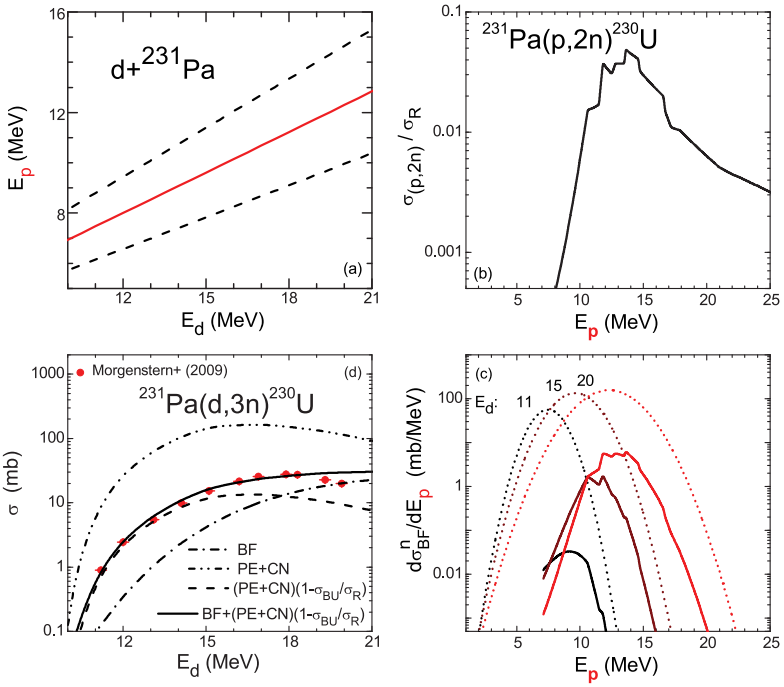

Fig. 3: (a) The centroid E_p of the Gaussian distribution of breakup-protons energies [21] versus the deuteron incident energy (solid curve) on ^{231}Pa, and the related $E_p \pm \Gamma/2$ values (dashed), (b) the cross section ratio $\sigma_{(p,2n)}/\sigma_{(p,R)}$ for the target nucleus ^{231}Pa, (c) the results (solid curves) of its convolution with the Gaussian distribution (dotted) of breakup-protons energies for deuterons on ^{231}Pa at incident energies of 10, 15 and 20 MeV noted above them, and (d) the corresponding BF enhancement (dash-dotted) of the ^{231}Pa$(d,3n)^{230}$U reaction, the PE+CN contributions to $(d,3n)$ reaction cross sections calculated without (dash-dot-dotted) and with (dashed) inclusion of the BU effect on σ_R, as well as the sum of all reaction mechanism contributions (solid).

3 One-nucleon transfer reactions

Apart from the breakup contributions to deuteron interactions, an increased attention has to be devoted to the direct reactions very poorly accounted so far in deuteron activation analysis. For low and medium mass target nuclei and deuteron energies below and around the Coulomb barrier, the interaction process proceeds largely through DR mechanism, while pre-equilibrium-emission and evaporation from fully equilibrated compound nucleus become also important with the increase of the incident energy.

The appropriate calculations of the DR contributions, like stripping and pick-up, that are important at the low energy side of the (d,p), (d,n) and (d,t) excitation functions [4–9], have been performed in the frame of the CRC formalism by using the code FRESCO [19]. The n-p interaction in deuteron [15] as well as d-n interaction in triton [24] are assumed to have a Gaussian shape, while the transferred nucleon bound states were generated in a Woods–Saxon real potential [7].

A particular note should concern the (d,t) pick-up mechanism contribution to the total (d,t) activation cross section, shown e.g. in Fig. 4(a). Usually neglected in the deuteron activation cross sections calculations, the (d,t) pick-up process is responsible for lowest-energy part of the excitation function, namely at the energies between its threshold and the (d,dn) and $(d,p2n)$ reaction thresholds, where the population of the same residual nucleus takes place [7–9].

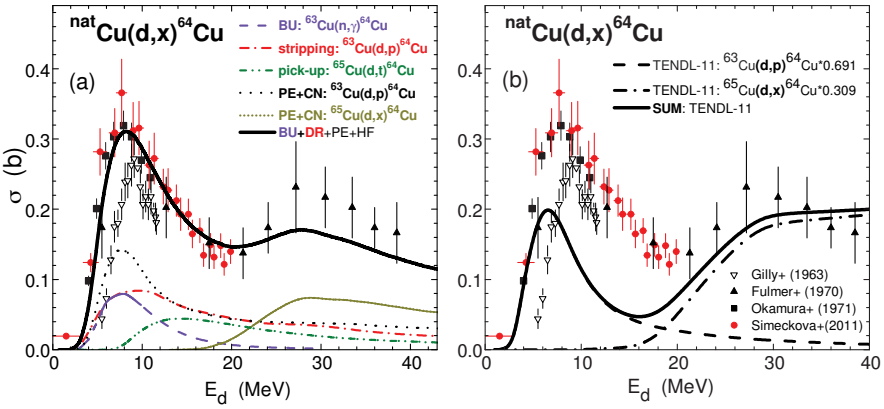

Fig. 4: Comparison of the ^{nat}Cu(d,x)^{64}Cu measured data ([7] and Refs. therein) with (a) the calculated related deuteron BF (dashed), DR stripping reaction ^{63}Cu(d,p)^{64}Cu (dash-dotted) and pick-up reaction ^{65}Cu(d,t)^{64}Cu (short dash-dot-dotted), PE+CN contributions, corrected for initial deuteron flux leakage through direct processes, to the ^{63}Cu(d,p)^{64}Cu reaction (dotted) and ^{65}Cu(d,x)^{64}Cu reaction (short-dotted), and their sum (solid curve), and (b) the corresponding TENDL-2011 predictions [27].

4 Statistical particle emission

The PE and CN reaction mechanisms become important at the incident energies above the Coulomb barrier. We have calculated the corresponding reaction cross sections by means of the codes STAPRE-H [25] and TALYS [26], taking into account also the breakup and DR results discussed above. Particularly, a consistent local parameter set was involved within the detailed analysis carried out using the code STAPRE-H [5,7].

As a sample case of complete analysis for deuteron interactions with nuclei, a comparison of the measured and calculated activation cross sections of ^{nat}Cu(d,x)^{64}Cu reaction [7] is shown in Fig. 4(a), the data being properly described by the local consistent parameter set within the PE+CN code STAPRE-H and taking into account also the breakup and DR contributions. These results substantiate the correctness of nuclear mechanism description that have been considered for the deuteron-nucleus interactions. Finally, Fig. 4(a) may be considered representative for the complexity of the deuteron interaction involving breakup, pick-up, PE and CN reaction mechanisms.

5 Conclusions

The overall agreement between the measured data and model calculations validates the description of nuclear mechanisms taken into account for the deuteron-nucleus interaction. On the other hand, the apparent discrepancies between the experimental data and corresponding TENDL-2011 [27] evaluation, shown in Fig. 4(b), stress out the effects of disregarding of the inelastic breakup enhancement, as well as of the stripping and pick-up processes.

However, while the associated theoretical frames are already settled for stripping, pick-up, PE and CN mechanisms, an increased attention should be paid to the breakup mechanism. Thus more work has to be done concerning its theoretical description including the inelastic component. The overall improvement of deuteron breakup description requires complementary experimental studies too.

Acknowledgments

This work was supported by a grant of the Romanian National Authority for Scientific Research, CNCS - UEFISCDI, project No. PN-II-ID-PCE-2011-3-0450.

References

[1] http://www.iter.org/proj.

[2] http://www.ifmif.org/b/.

[3] http://pro.ganil-spiral2.eu/spiral2/instrumentation/nfs.

[4] M. Avrigeanu *et al*., Fusion Eng. Design **84** (2009) 418.

[5] P. Bém *et al*., Phys. Rev. C **79** (2009) 044610.

[6] M. Avrigeanu and V. Avrigeanu, EPJ Web of Conf. **2** (2010) 01004; J. Phys: Conf. Ser. **205** (2010) 012014; E. Šimečková *et al*., EPJ Web of Conferences **8** (2010) 07002.

[7] E. Šimečková *et al*., Phys. Rev. C **84** (2011) 014605.

[8] M. Avrigeanu and V. Avrigeanu, J. Korean Phys. Soc. **59** (2011) 903; E. Šimečková *et al*., J. Korean Phys.Soc. **59** (2011) 1928.

[9] M. Avrigeanu and V. Avrigeanu, EPJ Web of Conf. **21** (2012) 07003.

[10] M. Avrigeanu, V. Avrigeanu, and A. J. Koning, Phys. Rev. C **85** (2012) 034603.

[11] J. Kleinfeller *et al*., Nucl. Phys. **A370** (1981) 205.

[12] J. Pampus *et al*., Nucl. Phys. **A311** (1978) 141; J. R. Wu *et al*., Phys. Rev. C **19** (1979) 370; N. Matsuoka *et al*., Nucl. Phys. **A345** (1980) 1; M. G. Mustafa *et al*., Phys. Rev. C **35** (1987) 2077.

[13] C. Kalbach Walker, TUNL Progress Report **XLII** (2002-2003) p. 82-83, Triangle University Nuclear Laboratory; www.tunl.duke.edu/publications/tunlprogress/2003/ .

[14] M. Avrigeanu and A. M. Moro, Phys. Rev. C **82** (2010) 037601.

[15] M. Kawai, M. Kamimura, and K. Takesako, Prog. Theor. Phys. Suppl. **184** (1969) 118.

[16] N. Austern *et al*., Phys. Rep. **154** (1987) 125.

[17] R. A. D. Piyadasa *et al*., Phys. Rev. C **60** (1999) 044611.

[18] A. M. Moro and F. M. Nunes, Nucl. Phys. **A767** (2006) 138; A. M. Moro *et al*., Phys. Rev. C **80** (2009) 054605; A. M. Moro *et al*., Phys. Rev. C **80** (2009) 064606.

[19] I. J. Thompson, Comput. Phys. Rep. **7** (1988) 167 (1988); v. FRES 2.3 (2007).

[20] L. L. Lee Jr. and J. P. Schiffer, Phys. Rev. **134** (1964) B765; EXFOR C1024 entry; S.A. Hjorth and E.K. Lin, Nucl. Phys. **A116** (1968) 1; EXFOR C1075 entry; E. Newman, L. C. Becker, and B. M. Freedom, Nucl. Phys. **A100** (1967) 225; EXFOR C1067 entry; R. K. Jolly *et al*., Phys. Rev. **130** (1963) 2391; EXFOR C1023 entry; F. Hinterberger *et al*., Nucl. Phys. **A111** (1968) 265; EXFOR D0225 entry; G. Igo *et al*., Phys. Rev. **124** (1961) 8332; EXFOR D0239 entry.

[21] C. Kalbach Walker, in: TUNL Progress Report, vol. XLVI (2007), p. 78; www.tunl.duke.edu/publications/tunlprogress/2007/tunlxlvi.pdf;

[22] A. Morgenstern *et al*., Phys. Rev. C **80**(2009) 054612.

[23] A. Morgenstern *et al*., Anal. Chem. **80** (2008) 8763; EXFOR D0562 entry.

[24] P. Guazzoni *et al*., Phys. Rev. C **83** (2011) 044614.

[25] M. Avrigeanu and V. Avrigeanu, IPNE Report NP-86-1995, Bucharest, 1995; News NEA Data Bank **17** (1995) 22.

[26] A. J. Koning, S. Hilaire, and M. C. Duijvestijn, in *Nuclear Data for Science & Technology, Nice, 2007* (EDP Sciences, Paris, 2008); v. TALYS-1.4, Dec. 2011, http://www.talys.eu/home/.

[27] A.J Koning and D. Rochman, *TENDL-2011: TALYS-Based Evaluated Nuclear Data Library*, Dec. 29, 2011, http://www.talys.eu/tendl-2011/.

Resonances near the 4α threshold through the ^{12}C (^{6}Li,d) reaction

T.Borello-Lewin[(a)], M.R.D.Rodrigues[(a)], H.Miyake[(a)], L.B.Horodynski-Matsushigue[(a)], J.L.M.Duarte[(a)], C.L.Rodrigues[(a)], M.A.Souza[(a)], A.Cunsolo[(b)], F.Cappuzzello[(b)], A. Foti[(b)], M. Cavallaro[(b)] and G.M.Ukita[(c)]

[(a)]Instituto de Física, Universidade de São Paulo Caixa Postal 66318, CEP 05314-970, São Paulo, SP, Brazil

[(b)]INFN - Laboratori Nazionali del Sud, via S.Sofia 62, 95125 Catania, Italy

[(c)]Faculdade de Psicologia, Universidade de Santo Amaro R. Prof. Eneas da Siqueira Neto, 340, CEP 04829-300, São Paulo, SP, Brazil

Abstract

Several narrow alpha resonant ^{16}O states were detected through the $^{12}C(^{6}Li,d)$ reaction, in the range of 12 to 17 MeV of excitation energy. The reaction was measured at a bombarding energy of 25.5 MeV employing the São Paulo Pelletron-Enge-Spectrograph facility and the nuclear emulsion technique. Experimental angular distributions associated with four quasi-bound states near the 4α threshold at 14.30, 14.40, 14.62 and 14.66 MeV of excitation are presented. The natural parity resonance transitions at 14.62 and 14.66 MeV are compared with DWBA predictions.

1 Introduction

Resonances around xα thresholds in light nuclei, as was primarily pointed out by Hoyle in ^{12}C, are recognized important in the production of elements in stars [1]. The main purpose of the research program in progress is the investigation of the alpha clustering phenomenon in (xα) and (xα + n) nuclei through the (^{6}Li, d) alpha transfer reaction [2-5]. In fact, there is scarce experimental information on the subject, in particular associated with odd-even nuclei and with resonant states predicted near the referred breakup thresholds. Alpha resonant states in the nucleus ^{16}O are the focus of the present work. The known 0^{+} state at 15.1 MeV of excitation , that has probably the gas-like configuration of the 4α condensate state with a very dilute density and a large component of α + ^{12}C(Hoyle) configuration [6], is of special concern. On the other hand, the existence of a rotational band with the α + ^{12}C (Hoyle) cluster state structure was recently demonstrated by Ohkubo and Hirabayashi [7]. In order to explore this region of renewed interest, measurements of the $^{12}C(^{6}Li,d)^{16}O$ reaction up to 17 MeV of excitation at an incident energy of 25.5 MeV, have been performed employing the São Paulo Pelletron-Enge Split-Pole facility and the nuclear emulsion detection technique.

2 Experimental Procedure

A 25.5 MeV ^{6}Li beam of the São Paulo Pelletron accelerator impinged a uniform and clean ^{12}C target. Two targets with 112 and 30 μg/cm^2, respectively, were used in the data acquisition. The deuterons emerging from (^{6}Li,d) reaction were momentum analyzed by the magnetic field of the Enge-Spectrograph and detected in emulsion plates (Fuji G6B 50 μm thick). Spectra associated with six scattering angles, from 5° to 29° in the laboratory frame, each one along 50 cm of the focal surface, were measured from 10 MeV up to 17 MeV excitation energy. After processing, the plates were scanned in strips of 200 μm and the spectra were obtained, displaying the number of tracks per strip versus the position along the focal plane. Several narrow resonances with a quasi-bound behavior embedded in the continuum were detected and the resolution of 30 keV and 15 keV, for the respective

targets, allowed for the separation of doublets not resolved before [8, 9]. Figure 1 displays, for further discussion, the region around the 4α threshold in the measured position deuteron spectrum associated with the scattering angle of 5°. The J^{π} and excitation energies in MeV of the detected states, taken from Tilley et al. [10], are indicated.

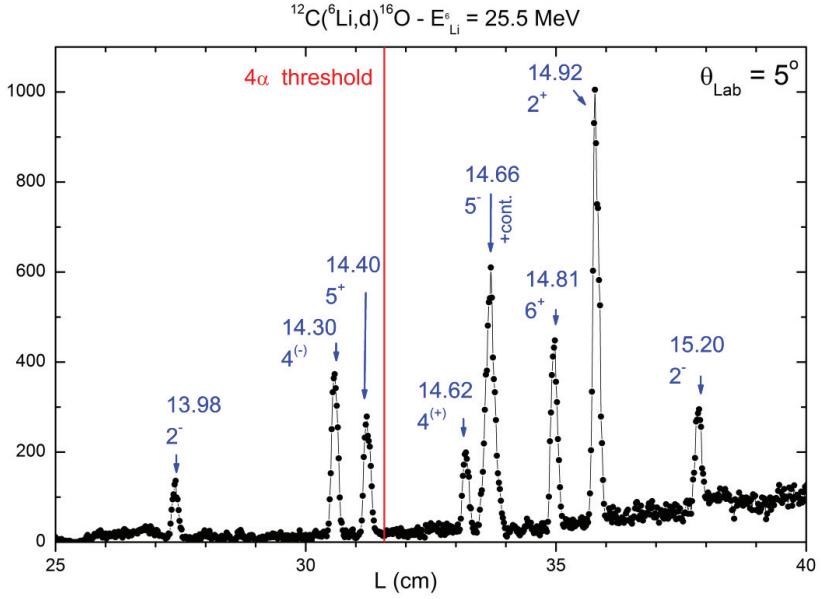

Figure 1: Position deuteron spectrum, corresponding to the indicated scattering angle, near the 4α threshold. The J^{π} and excitation energies in MeV of the detected states, taken from Tilley et al. [10], are indicated.

The relative normalization of the spectra and the absolute scale of the cross sections were, respectively, referred to the beam total charge collected in each run and to optical model predictions for elastic scattering measurements, in the same target and under similar conditions.

3 Results and Discussion

One step alpha transfer finite-range DWBA calculations, in this preliminary analysis, were performed to describe mainly the shape of those experimental angular distributions associated with resonances excited by a dominant direct process.

The optical model used for the entrance and exit channels, in the DWBA calculations, employed the global parameter sets of Cook [11] and of Daehnick et al. [12] respectively. The binding potential of Kubo and Hirata [13] was taken for the α + d description of ^{6}Li and, although resonant, the states under consideration were assumed to be bound by 100 keV in a Woods-Saxon binding potential (r_0 =1.25fm, a = 0.65 fm). Relative to the ^{12}C core, G [14] values 8 and 9 were considered, respectively, for positive and negative parity alpha states.

The experimental angular distributions, not previously reported, associated with four alpha narrow resonances, near the 4α threshold (14.44 MeV) at 14.30, 14.40, 14.62 and 14.66 MeV of excitation energy (see Fig. 1), are presented in Fig.2 [10]. The cross section uncertainties are relative

and the natural parity resonance transitions at 14.62 and 14.66 MeV are compared with DWBA predictions.

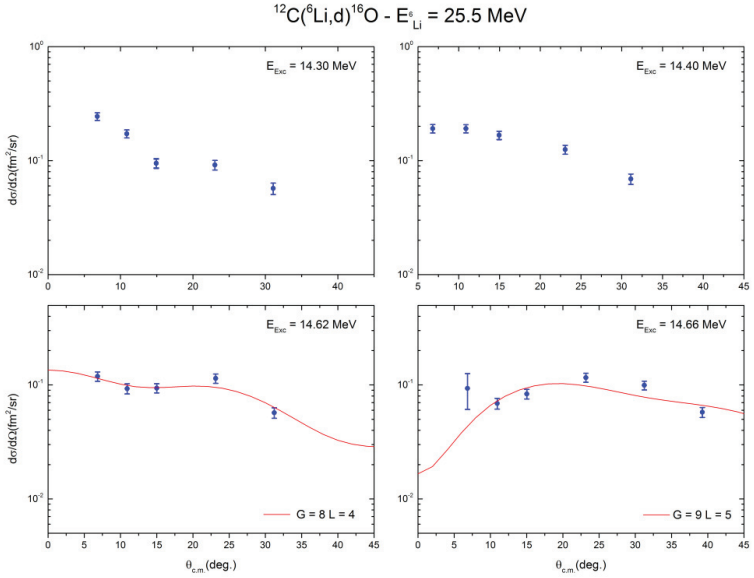

Figure 2: Experimental angular distributions. The DWBA predictions are shown for natural parity resonance transitions.

This preliminary DWBA analysis shows important direct contribution associated with the resonance at 14.62 and 14.66 MeV. It is to be noted that for the first one the positive parity is confirmed.

Note that the doublet resolved in the present work just above the 4α threshold, associated with $J^{\pi} = 4^{(+)}$ and 5^{-} at 14.62 and 14.66 MeV excitation energies, respectively [10], was also observed by Ames [15] in alpha elastic scattering on ^{12}C excitation function. The 5^{-} resonance was interpreted as a member of the $K^{\pi}=0^{-}$ alpha cluster band [10,15]. On the other hand, Wheldon et al. [9] detected through ^{12}C (^{6}Li,d) reaction at a higher incident energy only one state at 14.6 MeV associated with a strongly populated broad resonance which decays to the ^{12}C ground state. The unnatural parity resonances observed in the present work at 14.30 and 14.40 MeV were also reported and decay to the 2_1^{+} ^{12}C state [9] .

In the region of the 0^{+} state at 15.1 MeV of excitation that has probably the gas-like configuration of the 4α condensate state[6], was detected only one state, most like the state $J^{\pi} = 2^{-}$ at 15.20 MeV, as also indicated by Wheldon et al.[9].

4 Conclusions

The $^{12}C(^{6}Li,d)^{16}O$ reaction, measured at a bombarding energy of 25.5 MeV, populated several narrow resonances in ^{16}O from 12 to 17 MeV of excitation. Around the 4α threshold, the discrimination of at least three doublets, allowed by the excellent energy resolution of the data, also revealed a quasi-bound behavior of eight resonant states. The experimental angular distributions, not previously measured, associated with the resonances at 14.30, 14.40, 14.62,

and 14.66 MeV of excitation are presented and compared for the natural parity states with DWBA predictions. A parity doubt is resolved and new information in this region of interest is provided. The present work is in progress and further analysis is undergoing.

Acknowledgment

This work was partially supported by the Brazilian funding agencies FAPESP and CAPES.

References

[1] F. Hoyle, D. N. F. Dunbar, and W. A. Wenzel, *Phys*. *Rev*. **92**, 1095 (1953).

[2] M.R.D.Rodrigues et al., Investigation of the alpha-cluster states in ^{13}C via the (^{6}Li,d) reaction in *12th International Conference on Nuclear Reaction Mechanism, Varenna, Italy*, edited by F. Cerutti and A. Ferrari , CERN Proceedings, 2010-2, pp. 331- 335.

[3] T. Borello-Lewin et al., Proceedings of SOTANCP2, Brussels, Belgium 2010, edited by P. Descouvemount et al., *Int*. *J*. *Mod*. *Mod*. *Phys* **E** 20, 1018-1021 (2011).

[4] T. Borello-Lewin et al., "Alpha Resonant States in ^{13}C", In: XXXIII Brazilian Workshop on Nuclear Physics, 2011, Campos do Jordão, AIP Conference Proceedings, 2011. v. 1351. p. 125-130.

[5] T. Borello-Lewin et al., Alpha cluster states in light nuclear through the (^{6}Li,d) reaction *XXXIV Brazilian Workshop on Nuclear Physics, Foz do Iguaçu, Brazil, 2011,* edited by S. Duarte, Proceedings of Science ,XXXIV BWNP, 118 (2012).

[6] Y. Funaki, T. Yamada, A. Tohsaki, H. Horiuchi, G Ropke, and P. Schuck, *Phys*. *Rev*. *C* ***8*2,** 024312 (2010).

[7] S. Ohkubo and Y. Hirabayashi, *Phys*. *Lett*. **B** 684, 127 (2010).

[8] A. Cunsolo et al. , *Phys*. *Rev*. *C* **21**, 2345 (1980).

[9] C. Wheldon et al., *Phys*. *Rev*. *C* **83**, 064324 (2011).

[10] D. R. Tilley et al., *Nucl*. *Phys***. A 565** , 1-184 (1993).

[11] J. Cook, *Nucl*. *Phys*. **A388**, (1982) 153-172.

[12] W.W. Daehnick, J.D. Childs and Z. Vrcelj, *Phys*. *Rev*. *C* 21, (1980) 2253-2274.

[13] K.I. Kubo and M. Hirata, *Nucl*. *Phys***. A187**, (1972) 186-204.

[14] K. Wildermuth and Y. C. Tang, *A Unified Theory of the Nucleus* (Academic Press, N. Y.,1977).

[15] L. L. Ames et al., *Phys*. *Rev*. *C* **25**, 729 (1982).

Determination of ^{8}B(p,γ)^{9}C reaction rate from ^{9}C breakup

Tokuro Fukui[1*], *Kazuyuki Ogata*[1], *Kosho Minomo*[2], *and Masanobu Yahiroro*[2]
[1]Research Center for Nuclear Physics, Osaka University, Osaka 567-0047, Japan
[2]Department of Physics, Kyushu University, Fukuoka 812-8581, Japan

Abstract
The astrophysical factor of the ^{8}B(p,γ)^{9}C at zero energy, $S_{18}(0)$, is determined from three-body model analysis of ^{9}C breakup processes. The elastic breakup ^{208}Pb(^{9}C,p^8B)^{208}Pb at 65 MeV/nucleon and the one-proton removal reaction of ^{9}C at 285 MeV/nucleon on C and Al targets are calculated with the continuum-discretized coupled-channels method (CDCC) and the eikonal reaction theory (ERT), respectively. As a result of the present analysis, $S_{18}(0)$ extracted from the two reactions show good consistency, in contrast to in the previous studies.

1 Introduction

In low-metallicity supermassive stars, the proton capture reaction of ^{8}B, ^{8}B(p,γ)^{9}C ignites the explosive hydrogen burning [1]:

$$^8\mathrm{B}(p,\gamma)^9\mathrm{C}(\alpha,p)^{12}\mathrm{N}(p,\gamma)^{13}\mathrm{O}(\beta^+\nu)^{13}\mathrm{N}(p,\gamma)^{14}\mathrm{O}.$$

This process called hot pp chain is expected to be a possible alternative path to the synthesis of the CNO elements. Because of the difficulties in measuring the ^{8}B(p,γ)^{9}C cross section $\sigma_{p\gamma}$ at very low energies, several alternative reactions have been proposed [2–4] to indirectly determine the astrophysical factor $S_{18}(\varepsilon)$

$$S_{18}(\varepsilon) = \sigma_{p\gamma}\varepsilon \exp[2\pi\eta]. \tag{1}$$

Here, ε is the relative energy between p and ^{8}B in the center-of-mass (c.m.) frame and η is the Sommerfeld parameter. Because an astrophysical factor has quite weak energy dependence, several previous studies have paid special attention to the evaluation of $S_{18}(\varepsilon)$ at zero energy, $S_{18}(0)$ [1–5]. Experimental results seem to support the $S_{18}(0)$ obtained by a cluster model calculation [5]. There is, however, still a significant discrepancy of about 50% between the $S_{18}(0)$ obtained by Coulomb dissociation method [4] and the ANC method [2,3].

In this paper, we reinvestigate the Coulomb dissociation [4] (elastic breakup) and the proton removal process [3] of ^{9}C by means of coupled-channel calculation with a three-body ($p + {}^8\mathrm{B} + \mathrm{target}$) model. We adopt the continuum-discretized coupled-channels method (CDCC) [6–8] for the former and the eikonal reaction theory (ERT) [9,10] for the latter; we use the ANC method [11] for both reactions. The main purpose of the present study is to show the consistency between the two values of $S_{18}(0)$ extracted from these two types of breakup, and thereby determine $S_{18}(0)$ with high reliability.

2 Theoretical framework

In Fig. 1 we show schematic illustration of the three-body ($p + {}^8\mathrm{B} + \mathrm{target}$) system. The scattering between ^{9}C and a target nucleus A is described by the Schrödinger equation

$$\left[-\frac{\hbar^2}{2\mu}\nabla^2_{\boldsymbol{R}} + h + U(r_p, r_{\mathrm{B}}) - E\right]\Psi(\boldsymbol{r},\boldsymbol{R}) = 0, \tag{2}$$

*tokuro@rcnp.osaka-u.ac.jp

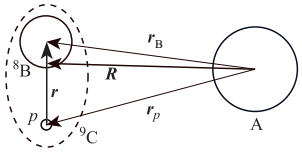

Fig. 1: Illustration of the three-body system.

where $\Psi(\boldsymbol{r}, \boldsymbol{R})$ is the tree-body wave function and $\boldsymbol{r}$ ($\boldsymbol{R}$) is the coordinate of ^{8}B (^{9}C) relative to p (A). The reduced mass between ^{9}C and A is denoted by μ and E is the total energy of the three-body system in the c.m. frame. The internal Hamiltonian of ^{9}C is shown by h. The interaction $U(r_p, r_{\rm B})$ is given by

$$U(r_p, r_{\rm B}) = V_p^{(\rm N)}(r_p) + V_p^{(\rm C)}(r_p) + V_{\rm B}^{(\rm N)}(r_{\rm B}) + V_{\rm B}^{(\rm C)}(r_{\rm B}), \tag{3}$$

where $V_{\rm X}^{(\rm N)}$ and $V_{\rm X}^{(\rm C)}$ are the nuclear and Coulomb interactions, respectively, between X and A; X represents a fragment particle of the projectile, i.e., p or ^{8}B. Similarly, $r_{\rm X}$ denotes the relative distance between X and A.

In the present analysis of the elastic breakup of ^{9}C, we solve Eq. (2) with eikonal-CDCC (E-CDCC) [12,13]. E-CDCC assumes eikonal approximation to the scattering wave between ^{9}C and A. As a result, the total wave function $\Psi(\boldsymbol{r}, \boldsymbol{R})$ is expressed by

$$\Psi(\boldsymbol{r}, \boldsymbol{R}) = \sum_c \Phi_c(\boldsymbol{r}) e^{-i(m-m_0)\phi_R} \psi_c(b, z) \phi^{\rm C}_{\boldsymbol{K}_c}(b, z), \tag{4}$$

where $\Phi_c(\boldsymbol{r})$ is the internal wave function of ^{9}C with c the channel indices $\{i,\ \ell,\ S,\ I,\ m\}$; $i > 0$ ($i = 0$) stands for the ith discretized-continuum (ground) state, and ℓ, S, and I are, respectively, the orbital angular momentum, the channel spin, and the total angular momentum of the p and ^{8}B system. m is the projection of I on the z-axis taken to be parallel to the incident beam; m_0 is the value of m in the incident channel. b is the impact parameter defined by $b = \sqrt{x^2 + y^2}$ with $\boldsymbol{R} = (x, y, z)$ in the Cartesian representation. The use of the Coulomb incident wave $\phi^{\rm C}_{\boldsymbol{K}_c}(b, z)$ instead of the plane wave $\exp(\boldsymbol{K}_c \cdot \boldsymbol{R})$ in the eikonal approximation is one of the most important features of E-CDCC; $\boldsymbol{K}_c$ is the asymptotic wave-number vector of ^{9}C in channel c from A. In the actual calculation, we use an approximate asymptotic form of $\phi^{\rm C}_{\boldsymbol{K}_c}(b, z)$. E-CDCC is shown to work very well for describing both the nuclear and Coulomb breakup processes with high accuracy and computational speed [12,13].

The one-proton removal reaction, its stripping component in fact (see below), is analyzed by means of the eikonal reaction theory (ERT) [9,10], which can calculate an inclusive cross section, such as a nucleon removal cross section, in the CDCC framework. ERT uses a formal solution (the scattering matrix S) to the coupled-channel equations of E-CDCC, and makes adiabatic approximation to only the nuclear part of S. Then one can obtain the most important result of ERT, i.e., the product form of S [9]

$$S = S_{\rm b} S_{\rm c}, \tag{5}$$

where $S_{\rm b}$ and $S_{\rm c}$ show the contributions from the constituents b and c of the projectile, respectively. At this stage, however, this result can be derived only when b or c is chargeless, which is not the case for the ^{9}C projectile consisting of p and ^{8}B. Therefore, in the present study, we neglect the Coulomb breakup process in the one-proton removal process and replace the Coulomb interaction $V_p^{(\rm C)}(\boldsymbol{r}_p)$ with

$$V_p^{(\rm C)}(r_p) \to V_p^{(\rm C)}(R). \tag{6}$$

Then we can calculate the one-proton removal cross section σ_{-p} with

$$\sigma_{-p} = \sigma_{\rm bu} + \sigma_{\rm str}, \tag{7}$$

as in Refs. [9, 10]. In Eq. (7), $\sigma_{\rm bu}$ and $\sigma_{\rm str}$ denote the elastic breakup cross section and the stripping cross section, respectively; ERT is used to evaluate $\sigma_{\rm str}$. The accuracy of the replacement of Eq. (6) can be examined by calculating σ_{-p} with and without the Coulomb breakup. It is confirmed that the Coulomb breakup contributes to σ_{-p} for C and Al targets by about 5%. Thus, we conclude that the Coulomb breakup by these two targets can be neglected with 5% errors. Below we include this amount in uncertainties of $S_{18}(0)$ extracted from σ_{-p}. The detail of our numerical setups are shown in the Ref. [14].

3 Results and discussion

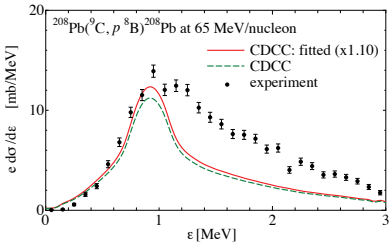

Fig. 2: Breakup spectrum of the ^{208}Pb(^{9}C,p^8B)^{208}Pb at 65 MeV/nucleon as a function of the relative energy ε between p and ^{8}B. The dashed line shows the result of calculation with a normalized p-^{8}B wave function, whereas the solid line is the result multiplied by 1.1 to fit the experimental data [4].

First, we analyze the elastic breakup ^{208}Pb(^{9}C,p^8B)^{208}Pb at 65 MeV/nucleon. In Fig. 2, we show the breakup cross section as a function of the relative energy ε between p and ^{8}B. We have included the experimental efficiency $e(\varepsilon)$ [15] and resolution Γ in the calculation. We adopt $\Gamma = 0.23$ MeV extracted from the experimental breakup spectrum of ^{12}C(^{9}C,p^8B)^{12}C at 65 MeV/nucleon [15]. In order to determine $S_{18}(0)$ we fit the theoretical result (dashed line) to the experimental data [4], and the solid line is obtained. The renormalization factor is 1.10, which results in $S_{18}(0) = 67.3$ eVb.

In Fig. 2, our calculation describes well the breakup spectrum below $\varepsilon \sim 1.0$ MeV, i.e., both the transition to the $1/2^-$ resonant state and breakup to low-energy nonresonant states of ^{9}C. It should be noted that we treat the resonant and nonresonant breakup continua on the same footing in the CDCC calculation. In the higher ε region than the resonance energy, however, the calculation significantly underestimates the experimental data. It is expected that this is due to incompleteness of our present framework. The back-coupling effects of three-body breakup states of ^{9}C to $p + p + ^7$Be on the $p + ^8$B state observed will become important as ε increases. In addition, more accurate description of the $p + ^8$B continua for higher partial waves with a proper p-^{8}B interaction $V_{p\rm B}^{(\rm N)}$ will be needed. At low ε, these possible problems will not exist, because only the tail of the overlap between ^{9}C and p-^{8}B contributes to the breakup process.

Table 1: Results of the one-proton removal reactions with ^{12}C and ^{27}Al targets. The experimental data of σ_{-p} are taken from Ref. [17].

Target	^{12}C		^{27}Al	
	calc.	expt.	calc.	expt.
σ_{-p} [mb]	44.9	48(8)	53.9	55(11)
$S_{18}(0)$ [eVb]	65.2		62.2	

Second, we analyze the one-proton removal reaction of ^{9}C at 285 MeV/nucleon on ^{12}C and ^{27}Al targets. We neglect the Coulomb breakup of ^{9}C in this case. We calculate $\sigma_{\rm bu}$ by CDCC and the stripping cross section $\sigma_{\rm str}$ by ERT, and obtain the one-proton removal cross section σ_{-p}, as the sum of the two. Then we renormalize the calculated σ_{-p} to fit the experimental value taken from Ref. [17], which determines $S_{18}(0)$. These values are summarized in Table 1. One sees that the two results of $S_{18}(0)$, corresponding to ^{12}C and ^{27}Al targets, agree well with each other. By taking an average of the two values, we obtain $S_{18}(0) = 63.7$ eVb.

We here remark that in our three-body coupled-channel analysis, the values of $S_{18}(0)$ extracted from two different breakup reactions, 67.3 eVb (elastic breakup) and 63.7 eVb (proton removal), show very good agreement. This indicates reliability of the present analysis and the result of $S_{18}(0)$. As a principal result of the present study, we obtain

$$S_{18}(0) = 66 \pm 10 \text{ eVb}. \tag{8}$$

In Fig. 3, the $S_{18}(0)$ extracted by the present work is compared with previous values. Previous results mentioned above can be categorized into two, i.e., one is around 80 eVb (Ref. [4,5]) and the other is around 45 eVb (Ref. [2,3]). Our result exists in between them, slightly favoring the former.

In Ref. [4], the E1 contribution to the elastic breakup of ^{9}C by ^{208}Pb at 65 MeV/nucleon was extracted by subtracting the contributions of the nuclear and E2 breakup processes ($\sim$ 10%) from the measured cross section, with a help of the ^{9}C breakup data by ^{12}C at the same energy. The rather good consistency between the present and previous results of $S_{18}(0)$ will indicate that the procedure for extracting the E1 contribution worked quite well. It was reported in Ref. [4], however, that about 80% of the peak in the ^{208}Pb(^{9}C,p^{8}B)^{208}Pb breakup spectrum around $\varepsilon = 0.9$ MeV was explained by nonresonant E1 breakup processes. On the other hand, in the present analysis, the peak is found to be mainly generated by the nuclear and E2 transition to the $1/2^{-}$ resonance state. Reason for this large discrepancy in the resonant part between the present and previous studies needs further investigation; this is our important future work. If we adopt a one-step calculation including nuclear and Coulomb breakup with all multipolarities, $S_{18}(0) = 54$ eVb is obtained, i.e., 20% difference appears. This behavior is the same as in the study of $S_{17}(0)$ for the ^{7}Be(p,γ)^{8}B reaction [12].

Our result is quite larger than the result of Ref. [3], in which the one-proton removal reactions (^{9}C,^{8}B) at 285 MeV/nucleon were analyzed by the extended Glauber model, with carefully evaluating the uncertainty regarding the nucleon-nucleon effective interactions (profile functions). By a detailed analysis, it is found that the difference between the $S_{18}(0)$ obtained in the present work and Ref. [3] is mainly due to the proton optical potential. In Fig. 4 of Ref. [3], the reaction cross section $\sigma_{\rm R}$ of the p-^{12}C (solid line) is compared with experimental data. As shown in the figure, the data have quite

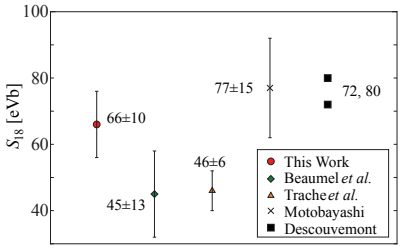

Fig. 3: $S_{18}(0)$ extracted by this work (circle) is compared with the results of the Coulomb dissociation method (cross) [4] and the analysis of σ_{-p} with the extended Glauber model (triangle) [3]. Theoretical results with a cluster model calculation (squares) [5] and the value extracted from the $d(^{8}\mathrm{B},^{9}\mathrm{C})n$ reaction (diamond) [2] are also shown.

large uncertainty; there seem to be two data groups between 250 MeV and 600 MeV. Our microscopic calculation based on the Melbourne g matrix gives $\sigma_{\rm R} = 198$ mb at 285 MeV, which is smaller than the value used in the previous study by about 10%. It should be noted that both the theoretical values of $\sigma_{\rm R}$ are consistent with the experimental data, within their uncertainty mentioned above. This 10% difference is indeed crucial for the evaluation of σ_{-p}, which eventually gives the difference in $S_{18}(0)$ by about 35%. Thus, more accurate and reliable data of $\sigma_{\rm R}$ is highly desirable to judge the microscopic theoretical calculations of $\sigma_{\rm R}$, although we have shown in this study a very good agreement between the two $S_{18}(0)$ extracted from different breakup reactions.

4 Summary

We have analyzed the elastic breakup of ^{9}C by ^{208}Pb at 65 MeV/nucleon and the one-proton removal reaction of ^{9}C at 285 MeV/nucleon on C and Al targets by a three-body coupled-channel framework, i.e., CDCC for the elastic breakup process and ERT for the stripping process. We determined the astrophysical factor at zero energy, $S_{18}(0)$, for the ^{8}B(p,γ)^{9}C reaction. Our principal result is $S_{18}(0) = 66\pm10$ eVb. We have confirmed that the results of $S_{18}(0)$ extracted from the two independent experimental data agree very well with each other, and thus resolved a significant discrepancy of $S_{18}(0)$ in the previous studies. Although the $S_{18}(0)$ is determined well in the present analysis, description of the breakup spectrum at higher p-^{8}B relative energies is not sufficient. Extension of the present reaction model to incorporate the $p + p + ^7$Be configuration will be very important for deeper understanding of the breakup of ^{9}C. Investigation on the $d(^8\mathrm{B}, ^9\mathrm{C})n$ transfer reaction, which gives a quite smaller $S_{18}(0)$ than in the present study, will also be important.

Acknowledgements

The authors wish to thank T. Motobayashi and Y. Togano for helpful discussions and providing experimental information on the elastic breakup reaction. The computation was carried out using the computer facilities at the Research Institute for Information Technology, Kyushu University. This research was supported in part by Grant-in-Aid of the Japan Society for the Promotion of Science (JSPS).

References

[1] M. Wiescher, J. Görres, S. Graff, L. Buchman, and F.-K. Thieleman, Astrophys. J. **343**, 352 (1989).
[2] D. Beaumel *et al*., Phys. Lett. **B514**, 226 (2001).
[3] L. Trache, F. Carstoiu, A. M. Mukhamedzhanov, and R. E. Tribble, Phys. Rev. C **66**, 035801 (2002).
[4] T. Motobayashi, Nucl. Phys. **A718**, 101c-108c (2003).
[5] P. Descouvemont, Nucl. Phys. **A646**, 261 (1999).
[6] M. Kamimura, M. Yahiro, Y. Iseri, Y. Sakuragi, H. Kameyama, and M. Kawai, Prog. Theor. Phys. Suppl. No. 89, 1 (1986).
[7] N. Austern, Y. Iseri, M. Kamimura, M. Kawai, G. Rawitscher, and M. Yahiro, Phys. Rep. **154**, 125 (1987).
[8] M. Yahiro, K. Ogata, T. Matsumoto, and K. Minomo, to be published in Prog. Theor. Exp. Phys. (2013) [arXiv:1203.5392 (2012)].
[9] M. Yahiro, K. Ogata, and K. Minomo, Prog. Theor. Phys. **126**, 167 (2011).
[10] S. Hashimoto, M. Yahiro, K. Ogata, K. Minomo, and S. Chiba, Phys. Rev. C **83**, 054617 (2011).
[11] A. M. Mukhamedzhanov and N. K. Timofeyuk, Yad. Fiz. **51**, 679 (1990) [Sov. J. Nucl. Phys. **51**, 431 (1990)].
[12] K. Ogata, S. Hashimoto, Y. Iseri, M. Kamimura, and M. Yahiro, Phys. Rev. C **73**, 024605 (2006).
[13] K. Ogata, M. Yahiro, Y. Iseri, T. Matsumoto, and M. Kamimura, Phys. Rev. C **68**, 064609 (2003).

[14] T. Fukui, K. Ogata, K. Minomo, and M. Yahiro, Phys. Rev. C 86, 022801(R) (2012).
[15] T. Motobayashi, Private Communication (2011).
[16] F. Ajzenberg-Selove, Nucl. Phys. **A413**, 1 (1984).
[17] B. Blank $et\ al.$, Nucl. Phys. **A624**, 242 (1997).

CDCC analysis for breakup of three-body projectiles

T. Matsumoto[1], *K. Minomo*[1], *K. Ogata*[2], *M. Yahiro*[1], *and K. Kato*[3]
[1]Department of Physics, Kyushu University, Fukuoka 812-8581, Japan
[2]Research Center for Nuclear Physics (RCNP), Osaka University, Osaka 567-0047, Japan
[3]Division of Physics, Graduate School of Science, Hokkaido University, Sapporo 060-0810, Japan

Abstract
We present a new method of smoothing discrete breakup cross sections calculated by the continuum-discretized coupled-channels method based on the complex-scaling method. One of advantages of this approach is applicable to many-body breakup reaction systems. In this work, we apply the new smoothing method to analyses of ^{12}C(^{6}He, nn^4He) and ^{208}Pb(^{6}He, nn^4He) reactions at 240 MeV/A.

1 INTRODUCTION

Exploring unstable nuclei far from the stable line is one of the most important subjects in nuclear physics. Two-neutron halo nuclei near the neutron drip line such as ^{6}He and ^{11}Li have exotic properties, i.e., soft dipole excitation and a di-neutron correlation. These properties can be investigated via breakup reactions, where the projectile breaks up into three fragments (core + n + n). One of the most reliable methods for treating the projectile breakup processes is the method of continuum-discretized coupled channels (CDCC) [1–3], which has been proposed as solving three-body scattering problems. Recently, we have developed CDCC as a method of treating four-body breakup processes in scattering of a three-body projectile [4–9].

Breakup cross sections include properties of continuum and resonance states of a projectile, and are obtained by the T-matrix elements in theoretically. The T-matrix elements estimated by CDCC, T_i, are discrete in the excitation energy ε of the projectile, although the exact ones $T(\varepsilon)$ are continuous. Thus one needs a way of smoothing T_i to analyze breakup reactions. For three-body breakup reactions, we have proposed the smoothing function method and confirmed the validity [6,7]. However, it is quite hard to adopt it to four-body breakup processes. Thus, it is highly expected that an accurate and practical method of smoothing T_i will be proposed.

In this work, we propose a new method to obtain the differential breakup cross section as a continuous function of ε accurately and practically, by using CDCC and the complex-scaling method (CSM) [10,11]. The new method is applied to the ^{12}C(^{6}He, nn^4He) reaction at 229.8 MeV/A. A merit of the present smoothing method is that one can see fast convergence of the calculated breakup cross section with respect to extending the model space. The method is also applied to ^{12}C(^{6}He, nn^4He) and ^{208}Pb(^{6}He, nn^4He) reactions at 240 MeV/A and compared with the experimental data. In principle, this method is applicable not only for four-body breakup reactions but also for many-body breakup reactions.

2 FORMULATION

We consider scattering of a projectile B from a target A. The scattering is described by the Schrödinger equation with outgoing boundary conditions,

$$[H - E_{\rm tot}]|\Psi^{(+)}\rangle = 0, \tag{1}$$

where the total energy $E_{\rm tot}$ is related to the corresponding incident energy of the center-of-mass system $E_{\rm in}^{\rm CM}$ as $E_{\rm tot} = E_{\rm in}^{\rm CM} + \varepsilon_0$ with the ground-state energy ε_0 of B. The total Hamiltonian H of this system is defined as

$$H \;=\; K_R + U(\boldsymbol{\xi}, \boldsymbol{R}) + H_{\rm B}, \tag{2}$$

where $\boldsymbol{R}$ is a coordinate between B and A, and $\boldsymbol{\xi}$ is a set of internal coordinates in B. The kinetic energy operator for $\boldsymbol{R}$ and internal Hamiltonian of B are represented by K_R and H_B, respectively, and U is a sum of nuclear and Coulomb potentials between constituents in B and A.

The most fundamental assumption in CDCC is that the scattering takes place in a modelspace,

$$\mathcal{P} = \sum_{\gamma} |\Phi_\gamma\rangle\langle\Phi_{n\gamma}|, \tag{3}$$

where Φ_γ is a γth eigenstate obtained by diagonalizing $H_{\rm B}$ with L^2-type basis functions. Therefore, the Schrödinger equation is solved in the modelspace:

$$\mathcal{P}[H - E_{\rm tot}]\mathcal{P}|\Psi^{(+)}_{\rm CDCC}\rangle = 0. \tag{4}$$

The T matrix amplitude for breakup processes, in which the final state of B has an excitation energy ε, is

$$T(\varepsilon) = \langle\psi^{(-)}_\varepsilon(\boldsymbol{\xi})\chi^{(-)}_\varepsilon(\boldsymbol{R})|\hat{U}|\Psi^{(+)}(\boldsymbol{\xi},\boldsymbol{R})\rangle_{\boldsymbol{\xi R}}, \tag{5}$$

$$\hat{U} = U(\boldsymbol{\xi},\boldsymbol{R}) - V^{\rm Coul}_{\rm B}(R), \tag{6}$$

where $V^{\rm Coul}_{\rm B}$ is the Coulomb interaction between B and A. The exact final channel wave function $\psi^{(-)}_\varepsilon(\boldsymbol{\xi})\chi^{(-)}_\varepsilon(\boldsymbol{R})$ with incoming boundary conditions satisfies

$$\left[K_R + V^{\rm Coul}_B(R) - (E_{\rm tot} - \varepsilon)\right]|\chi^{(-)}_\varepsilon(\boldsymbol{R})\rangle = 0, \tag{7}$$

$$[H_{\rm B} - \varepsilon]\,|\psi^{(-)}_\varepsilon(\boldsymbol{\xi})\rangle = 0. \tag{8}$$

Using Eq. (5), the differential cross section as a function of ε can be calculated as

$$\frac{d\sigma}{d\varepsilon} = \int d\varepsilon'\delta(\varepsilon - \varepsilon')|T(\varepsilon')|^2 = \frac{1}{\pi}{\rm Im}\mathcal{R}(\varepsilon) \tag{9}$$

with the response function

$$\mathcal{R}(\varepsilon) = \int d\boldsymbol{\xi}d\boldsymbol{\xi}'\mathcal{O}^\dagger(\varepsilon,\boldsymbol{\xi})\mathcal{G}^{(-)}(\varepsilon,\boldsymbol{\xi},\boldsymbol{\xi}')\mathcal{O}(\varepsilon,\boldsymbol{\xi}'), \tag{10}$$

where the Green's function $\mathcal{G}^{(-)}$ and operator $\mathcal{O}$ are defined by

$$\mathcal{G}^{(-)}(\varepsilon,\boldsymbol{\xi},\boldsymbol{\xi}') = \lim_{\eta\to+0}\langle\boldsymbol{\xi}|\frac{1}{\varepsilon - H_{\rm B} - i\eta}|\boldsymbol{\xi}'\rangle, \tag{11}$$

$$\mathcal{O}(\varepsilon,\boldsymbol{\xi}) = \langle\chi^{(-)}_\varepsilon(\boldsymbol{R})|\hat{U}|\Psi^{(+)}(\boldsymbol{\xi},\boldsymbol{R})\rangle_{\boldsymbol{R}}. \tag{12}$$

In order to evaluate $\mathcal{R}(\varepsilon)$, we use the complex scaling method (CSM), where the scaling transformation operator is represented by $C(\theta)$. The scaled Green's function is written as

$$\mathcal{G}^{(-)}_\theta(\varepsilon,\boldsymbol{\xi},\boldsymbol{\xi}') = \lim_{\eta\to+0}\langle\boldsymbol{\xi}|\frac{1}{\varepsilon - H^\theta_{\rm B} - i\eta}|\boldsymbol{\xi}'\rangle, \tag{13}$$

with the complex-scaled Hamiltonian

$$H^\theta_{\rm B} = C(\theta)H_{\rm B}C^{-1}(\theta). \tag{14}$$

The scaled Green's function $\mathcal{G}^\theta$ is a L^2-type operator when $-\pi < \theta < 0$, so that it can be expanded with L^2-type basis functions with high accuracy:

$$\mathcal{G}^\theta(\varepsilon,\boldsymbol{\xi},\boldsymbol{\xi}') \approx \sum_i \frac{|\phi^\theta_i\rangle\langle\tilde{\phi}^\theta_i|}{\varepsilon - \varepsilon^\theta_i}, \tag{15}$$

where ϕ_i^θ is a i-th eigenstate obtained by diagonalizing $H_{\rm B}^\theta = C(\theta) H_{\rm B} C^{-1}(\theta)$ in a modelspace spanned by L^2-type basis functions, $\langle \tilde{\phi}_i^\theta | H_{\rm B}^\theta | \phi_{i'}^\theta \rangle = \varepsilon_i^\theta \delta_{ii'}$. Note that the scaling angle should be taken as negative, because the Green's function $\mathcal{G}^{(-)}$ satisfies an incoming boundary condition.

Furthermore the modelspace approximation is applied to the Green's function and total wave function, that is, $\mathcal{G}^{(-)}$ and Ψ are replaced by $\mathcal{P}\mathcal{G}^{(-)}\mathcal{P}$ and $\Psi_{\rm CDCC}^{(+)}$, respectively. This leads to

$$\begin{aligned} \mathcal{R}(\varepsilon) \;\approx\; & \sum_i \sum_{\gamma',\gamma} \langle \Psi_{\rm CDCC}^{(+)} | \hat{U}^* | \chi_\gamma^{(-)} \Phi_{\gamma'} \rangle \\ & \frac{\langle \Phi_{\gamma'} | C^{-1}(\theta) | \phi_i^\theta \rangle \langle \tilde{\phi}_i^\theta | C(\theta) | \Phi_\gamma \rangle}{\varepsilon - \varepsilon_i^\theta} \\ & \times \langle \Phi_\gamma \chi_\gamma^{(-)} | \hat{U} | \Psi_{\rm CDCC}^{(+)} \rangle. \end{aligned} \tag{16}$$

Noting that $\langle \Phi_\gamma \chi_\gamma^{(-)} | \hat{U} | \Psi_{\rm CDCC}^{(+)} \rangle$ is a T-matrix element of CDCC, T_γ, to Φ_γ, we define scaled T-matrix elements by

$$\tilde{T}_i^\theta \equiv \sum_{\gamma'} \langle \tilde{\phi}_i^\theta | C(\theta) | \Phi_{\gamma'} \rangle T_{\gamma'}, \tag{17}$$

$$T_i^\theta \equiv \sum_\gamma T_\gamma^* \langle \Phi_n | C^{-1}(\theta) | \phi_i^\theta \rangle. \tag{18}$$

The final form of the differential cross section is then obtained by

$$\frac{d\sigma}{d\varepsilon} \;=\; \frac{1}{\pi} {\rm Im} \sum_i \frac{T_i^\theta \tilde{T}_i^\theta}{\varepsilon - \varepsilon_i^\theta}. \tag{19}$$

For the diagonalization of $H_{\rm B}$ and $H_{\rm B}^\theta$, we adopt the Gaussian expansion method (GEM) [12]. In GEM, the state of the ^{4}He + n + n system is described by a superposition of three channels, each channel with a different set of Jacobi coordinates, $(\boldsymbol{y}_c, \boldsymbol{r}_c)$. For each c (channel), the radial parts of the internal wave functions regarding $\boldsymbol{y}_c$ and $\boldsymbol{r}_c$ are expanded by a finite number of Gaussian basis functions

$$\begin{aligned} \varphi_{j\lambda}(\boldsymbol{y}_c) &= y_c^\lambda e^{-(y_c/\bar{y}_j)^2} Y_\lambda(\Omega_{y_c}), \\ \varphi_{i\ell}(\boldsymbol{r}_c) &= r_c^\ell e^{-(r_c/\bar{r}_i)^2} Y_\ell(\Omega_{r_c}), \end{aligned} \tag{20}$$

respectively. Here λ (ℓ) is the angular momentum regarding $\boldsymbol{y}_c$ ($\boldsymbol{r}_c$), and the range parameters are taken to lie in geometric progression:

$$\bar{y}_j \;=\; (\bar{y}_{\rm max}/\bar{y}_1)^{(j-1)/j_{\rm max}}, \tag{21}$$

$$\bar{r}_i \;=\; (\bar{r}_{\rm max}/\bar{r}_1)^{(i-1)/i_{\rm max}}. \tag{22}$$

The parameters depend on c, but we omitted the dependence in Eqs. (21) and (22) for simplicity; see Ref. [4] for the details of the diagonalization and the definition of Jacobi coordinates. As interactions V_{nn} and $V_{n\alpha}$ in H_B, we take the so-called GPT [13] and KKNN [14] potentials, respectively. These potentials with a Gaussian form reproduce well data of low-energy nucleon-nucleon and nucleon-^{4}He scattering, respectively. The particle exchange between valence neutrons and neutrons in ^{4}He is treated approximately with the orthogonality condition model [15].

3 RESULTS AND DISCUSSIONS

First, we prepare the three sets of parameters of basis functions shown in Table 1 to confirm the convergence of the breakup cross section. For the 0^+ and 1^- states, maximum internal angular momenta

Table 1: Gaussian range parameters.

Set	c	$j_{\max}$	$\bar{y}_1$ (fm)	$\bar{y}_{\max}$ (fm)	$i_{\max}$	$\bar{r}_1$ (fm)	$\bar{r}_{\max}$ (fm)
I	3	10	0.1	10.0	10	0.5	10.0
	1, 2	10	0.5	10.0	10	0.5	10.0
II	3	15	0.1	20.0	15	0.5	20.0
	1, 2	15	0.5	20.0	15	0.5	20.0
III	3	20	0.1	50.0	20	0.5	50.0
	1, 2	20	0.5	50.0	20	0.5	50.0

$\ell_{\max}$ and $\lambda_{\max}$ are both set to unity. For the 2^+ states, we take $\ell_{\max} = \lambda_{\max} = 1$ for $c = 1$ and 2, and $\ell_{\max} = \lambda_{\max} = 2$ for $c = 3$. Figure 1 shows the breakup cross sections $d\sigma/d\varepsilon$ to the 0^+, 1^-, and 2^+ continua for ^{12}C(^{6}He,nn^4He) reaction at 229.8 MeV. For all the cross sections, sets II and III yield the same result, whereas the result of set I is somewhat different from it. The convergence of CDCC solution with respect to expanding the model space is thus obtained with set II. Here, we take $\theta = -14^\circ$ as the scaling angle, since the converged spectra are obtained at this angle.

In Fig. 2, the breakup cross section $d\sigma/d\varepsilon$ calculated by the present method is compared with the experimental data for ^{6}He + ^{12}C and ^{6}He + ^{208}Pb reactions at 240 MeV/A [16]. These data have already been analyzed by four-body distorted-wave Born approximation (DWBA) [17] and the eikonal approximation [18]. In the present analysis, we estimate optical potentials for n-target and ^{4}He-target based on the double-folding model the Melbourne nucleon-nucleon g-matrix interaction [19] with the densities obtained by the spherical Hartree-Fock (HF) calculation with the Gogny D1S interaction. [20, 21]. For the result of the ^{12}C(^{6}He, nn^4He) reaction, one sees clear peak of the 2^+ resonance around 1 MeV as shown in Fig. 2(a). In this analysis, we found that Coulomb breakup effects are negligible and the present theoretical result is consistent with the experimental data except for the peak of the 2^+ resonance around $\varepsilon = 1$ MeV. On the other hand, Coulomb breakup to the 1^- continuum is dominant for the ^{208}Pb(^{6}He, nn^4He) reaction as shown in Fig. 2(b). For ^{208}Pb target, the present method underestimates the experimental data at $\varepsilon \geq 2$ MeV. A possible origin of this underestimation is that the inelastic breakup reactions are not included in the present calculation. As mentioned in Ref. [17], the inelastic breakup effect is not negligible, and the elastic breakup cross section calculated with four-body DWBA also underestimates the data.

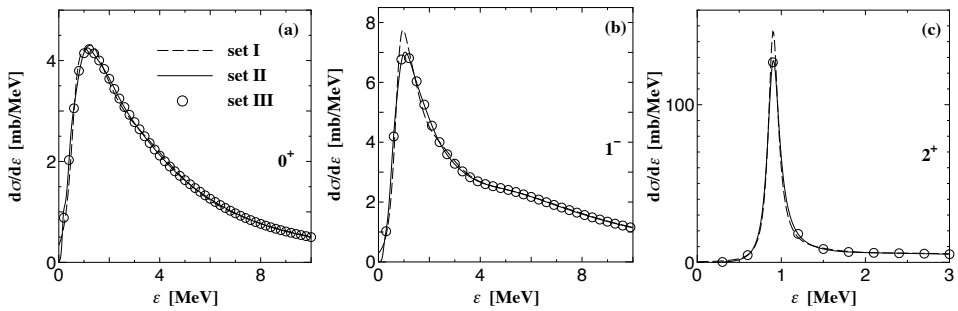

Fig. 1: Convergence of the breakup cross sections to the 0^+ (a), 1^- (b), and 2^+ (c) continua. In each panel, the dashed line, the solid line, and the open circles correspond to results of sets I, II, and III, respectively. The dotted line in (b) shows the result when Coulomb breakup processes are switched off.

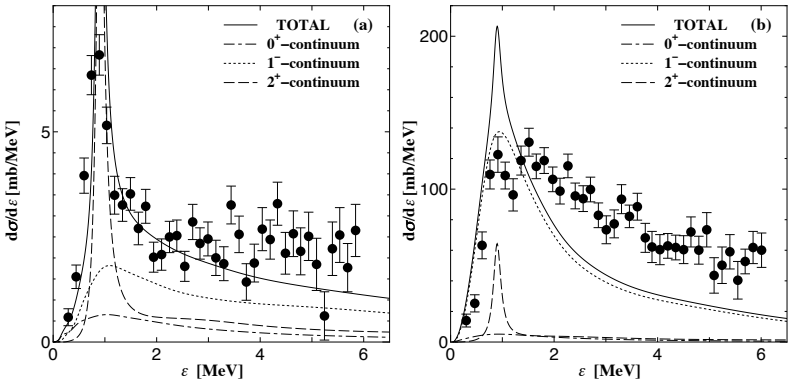

Fig. 2: Comparison of the breakup cross section calculated by CDCC (solid line) with experimental data for (a) the ^{6}He + ^{12}C scattering at 240 MeV/nucleon and (b) the ^{6}He + ^{208}Pb scattering at 240 MeV/nucleon. The dash-dotted, dotted, and dashed lines correspond to the contributions of the 0^+, 1^-, and 2^+ breakup, respectively, and the solid line is the sum of them. The experimental data are taken from Ref. [16].

4 SUMMARY

In summary, we have proposed a practical method of calculating the differential breakup cross section as a continuous function of the excitation energy of a projectile, by combining CDCC and CSM. One of advantages of this method is that we do not require to calculate the exact continuum wave functions of the projectile. In the present formalism, we have to do is just diagonalize the projectile Hamiltonian and the scaled Hamiltonian with L^2-type basis functions. Furthermore, the scaling operator $C(\theta)$ operates only on spatially damping functions and hence the differential breakup cross section converges quickly as the model space is extended. The method is successful in reproducing the data on ^{12}C(^{6}He, nn^{4}He) and ^{208}Pb(^{6}He, nn^{4}He) reactions at 240 MeV/A. In principle, the present formalism is applicable for many-body breakup reaction, if the diagonalization of the projectile Hamiltonian and the scaled Hamiltonian is feasible.

References

[1] M. Kamimura, M. Yahiro, Y. Iseri, Y. Sakuragi, H. Kameyama and M. Kawai, Prog. Theor. Phys. Suppl. **89**, 1 (1986).

[2] N. Austern, Y. Iseri, M. Kamimura, M. Kawai, G. Rawitscher and M. Yahiro, Phys. Rep. **154**, 125 (1987).

[3] M. Yahiro, K. Ogata, T. Matsumoto, and K. Minomo, Prog. Theor. Exp. Phys. **1**, 01A209 (2012); arXiv:1203.5392 (2012).

[4] T. Matsumoto, E. Hiyama, K. Ogata, Y. Iseri, M. Kamimura, S. Chiba, and M. Yahiro, Phys. Rev. C **70**, 061601(R) (2004).

[5] T. Matsumoto, T. Egami, K. Ogata, Y. Iseri, M. Kamimura, and M. Yahiro, Phys. Rev. C **73**, 051602 (2006).

[6] T. Matsumoto, T. Kamizato, K. Ogata, Y. Iseri, E. Hiyama, M. Kamimura, and M. Yahiro, Phys. Rev. C **68**, 064607 (2003).

[7] T. Egami, K. Ogata, T. Matsumoto, Y. Iseri, M. Kamimura, and M. Yahiro, Phys. Rev. C **70**, 047604 (2004).

[8] T. Matsumoto, E. Hiyama, M. Yahiro, K. Ogata, Y. Iseri and M. Kamimura, Nucl. Phys. **A 738c**, 471 (2004).

[9] M. Rodríguez-Gallardo, J. M. Arias, J. Gómez-Camacho, R. C. Johnson, A. M. Moro, I. J. Thompson, and J. A. Tostevin, Phys. Rev. C **77**, 064609 (2008).

[10] J. Aguilar and J.M. Combes, Commun. Math. Phys., 22, 1971, 269.
E. Balslev and J.M. Combes, Commun. Math. Phys., 22, 1971, 280.

[11] S. Aoyama, T. Myo, K. Kato, and K. Ikeda, Prog. Theor. Phys. 116, 1 (2006).

[12] E. Hiyama, Y. Kino and M. Kamimura, Prog. Part. Nucl. Phys. **51**, 223 (2003).

[13] D. Gogny *et al*., Phys. Lett. **B32**, 591 (1970).

[14] H. Kanada, *et al*., Prog. Theor. Phys. **61**, 1327 (1979).

[15] S. Saito, Prog. Theor. Phys. **41**, 705 (1969).

[16] T. Aumann *et al*., Phys. Rev. C **59**, 1252 (1999).

[17] S. N. Ershov, B. V. Danilin, and J. S. Vaagen, Phys. Rev. C **62**, 041001(R) (2000).

[18] D. Baye, P. Capel, P. Descoubemont, and Y. Suzuki, Phys. Rev. C **79**, 024607 (2009).

[19] K. Amos, P. J. Dortmans, H. V. von Geramb, S. Karataglidis, and J. Raynal, in *Advances in Nuclear Physics*, edited by J. W. Negele and E. Vogt(Plenum, New York, 2000) Vol. 25, p. 275.

[20] J. Decharge and D. Gogny, Phys. Rev. C **21** (1980), 1568.

[21] J. F. Berger, M. Girod, and D. Gogny, Comp. Phys. Comm. **63** (1991), 1365.

Breakup of ^{22}C studied by CDCC with Cluster-Orbital Shell-Model wave functions

K. Ogata[1]*, T. Myo*[2]*, T. Furumoto*[3]*, T. Matsumoto*[4] *and M. Yahiro*[4]
[1]Research Center for Nuclear Physics, Osaka University, Ibaraki 567-0047, Japan
[2] General Education, Faculty of Engineering, Osaka Institute of Technology, Osaka 535-8585, Japan
[3]RIKEN Nishina Center, Hirosawa 2-1, Wako 351-0198, Japan
[4]Department of Physics, Kyushu University, Fukuoka 812-8581, Japan

Abstract
The breakup cross section (BUX) of ^{22}C by ^{12}C at 250 MeV/nucleon is evaluated by the continuum-discretized coupled-channels method (CDCC) incorporating the cluster-orbital shell model (COSM) wave functions. Contributions of the low-lying 0^+_2 and 2^+_1 resonances predicted by COSM to the BUX are investigated. The 2^+_1 resonance gives a narrow peak in the BUX, as in usual resonant reactions, whereas the 0^+_2 resonant cross section has a peculiar shape due to the coupling to the nonresonant continuum. Mechanism of the appearance of this shape in the breakup of ^{22}C is discussed.

1 Introduction

Exploring the frontier of the nuclear chart is one of the most important subjects in nuclear physics. Properties of neutron drip-line nuclei, e.g., ^{11}Li, ^{19}B, and ^{22}C, are therefore crucial for that purpose. Very recently, evidence for an unbound ground state of ^{26}O was reported [1], which could extend the concept of drip-line nuclei to the unbound-state regions. In this situation, clarification of unbound states, i.e., resonance structures, of nuclei around the neutron drip-line will be a fascinating subject.

In this study we focus on ^{22}C, the drip-line nucleus of carbon isotopes. By measuring the reaction cross section [2] and the neutron removal cross section [3], ground state properties of ^{22}C have been intensively studied so far; the results strongly support the picture that ^{22}C is an s-wave two-neutron halo nucleus, in consistent with the theoretical prediction of Ref. [4] based on a $^{20}\mathrm{C}+n+n$ three-body model. On the other hand, possible resonance states of ^{22}C have never been observed and suggested.

In this paper, we investigate the resonance structure of ^{22}C with the cluster-orbital shell model (COSM) [5] through the breakup cross section (BUX) of ^{22}C by ^{12}C at 250 MeV/nucleon evaluated by the continuum-discretized coupled-channels method (CDCC) [6–8]. COSM is a powerful method to describe a system consisting of a core plus valence nucleons; it has successfully been applied to studies of the ground and resonance states of ^{6}He, ^{7}He, and ^{8}He [9–11]. One of the most important advantages of COSM is the description of radial wave functions of each nucleon by the superposition of Gaussian basis functions, covering a quite wide space. It is thus expected that COSM describes well both resonances and the nonresonant continuum of a system, in a model space required to evaluate breakup observables. CDCC is a sophisticated reaction model that has been applied to various breakup processes with high success. Our main purpose is to investigate how the resonance states of ^{22}C predicted by COSM are "observed" in the BUX.

Formalism of COSM-CDCC is described in Sec. 2 and numerical inputs are given in Sec. 2. In Sec. 3, results of the BUX of ^{22}C by ^{12}C at 250 MeV/nucleon are shown and discussion on the resonant and nonresonant contributions of the BUX is given. Finally, we give a summary in Sec. 5.

2 Formalism

In the present COSM calculation, a ^{20}C+$n+n$ three-body model is adopted for the ^{22}C wave function:

$$\Phi_{cIM_I}(\boldsymbol{\eta}_1,\boldsymbol{\eta}_2) = \sum_{l_1j_1l_2j_2}\sum_{i_1i_2} d^{i_1i_2}_{cl_1j_1l_2j_2I}\hat{\mathcal{A}}\left[\phi^{b_{i_1}}_{l_1j_1}(\boldsymbol{\eta}_1)\otimes\phi^{b_{i_2}}_{l_2j_2}(\boldsymbol{\eta}_2)\right]_{IM_I}, \tag{1}$$

where I and M_I are the total spin of ^{22}C and its third component, respectively, and $\boldsymbol{\eta}_i$ ($i=1$ or 2) is the relative coordinate of the ith neutron to the center of the ^{20}C core. $\hat{\mathcal{A}}$ represents the antisymmetrization operator for the two valence neutrons; antisymmetrization between a valence neutron and a neutron in ^{20}C is approximately taken into account with the orthogonal condition model [12]. ϕ in Eq. (1) is the Gaussian basis function

$$\phi^{b_i}_{ljm_j}(\boldsymbol{\eta}) = \varphi^{b_i}_l(\eta)\left[Y_l(\hat{\boldsymbol{\eta}})\otimes\xi_{1/2}\right]_{jm_j}, \tag{2}$$

where ξ is the spin $1/2$ wave function of neutron and

$$\varphi^{b_i}_l(\eta) = \sqrt{\frac{2}{\Gamma(l+3/2)}}\left(\frac{1}{b_i^2}\right)^{(l+3/2)/2}\eta^l\exp\left(-\frac{\eta^2}{2b_i^2}\right) \tag{3}$$

with Γ the Gamma function. The range parameters b_i ($i=1$–$i_{\max}$) are chosen to lie in a geometric progression:

$$b_i = b_1\gamma^{i-1}. \tag{4}$$

By diagonalizing an internal Hamiltonian h of ^{22}C with the basis functions, one obtains eigenstates, each of which is characterized by I, M_I, and the energy index c, with the expansion coefficients $d^{i_1i_2}_{cl_1j_1l_2j_2I}$. In the present case, there is only one bound state in $I=0$. All the other states are located above the ^{20}C+$n+n$ three-body threshold, which are called pseudostates (PS).

Since COSM describes the ^{22}C wave function covering a quite large model space, the PS can be regarded to a good approximation as discretized continuum states. Then the total wave function of the ^{20}C+$n+n+^{12}$C four-body reaction system with the total angular momentum J and its third component M can be expanded as

$$\Psi_{JM}(\boldsymbol{\eta}_1,\boldsymbol{\eta}_2,\boldsymbol{R}) = \sum_{cIL}\left[\Phi_{cI}(\boldsymbol{\eta}_1,\boldsymbol{\eta}_2)\otimes\chi_{cIL}(\boldsymbol{R})\right]_{JM}, \tag{5}$$

where $\chi_{cIL}(\boldsymbol{R})$ is the scattering wave of ^{22}C in the (c,I) state relative to ^{12}C; $L(\boldsymbol{R})$ is the corresponding relative angular momentum (coordinate).

By solving the four-body Schrödinger equation

$$[H-E]\,\Psi_{JM}(\boldsymbol{\eta}_1,\boldsymbol{\eta}_2,\boldsymbol{R}) = 0, \tag{6}$$

$$H = T_{\boldsymbol{R}} + U_{n_1}(\boldsymbol{R}_1) + U_{n_2}(\boldsymbol{R}_2) + U_{\rm c}(\boldsymbol{R}_{\rm c}) + h \tag{7}$$

with the standard boundary condition of $\chi_{cIL}(\boldsymbol{R})$, one may obtain the scattering matrix to the (c,I,L) channel. Here, E is the total energy of the four-body system in the center-of-mass (c.m.) frame, $T_{\boldsymbol{R}}$ is the kinetic energy operator associated with $\boldsymbol{R}$, U_{n_i} ($i=1$ or 2) is the neutron distorting potential, and $U_{\rm c}$ is the potential between the ^{20}C core and ^{12}C. This framework is *four-body CDCC* [13,14] incorporating the COSM wave functions, which we call *COSM-CDCC* below. We further adopt the prescription [15] based on the complex-scaling method (CSM) [16], the CSM smoothing method, to obtain a smooth breakup cross section $d^2\sigma/(d\epsilon d\Omega)$, i.e., the double differential breakup cross section (DDBUX). Here, ϵ is the breakup energy of the ^{20}C+$n+n$ system measured from the three-body threshold and Ω is the solid angle of the c.m. of ^{22}C after the breakup; the corresponding polar angle is denoted by θ below.

3 Numerical input

In the ^{20}C+$n+n$ three-body Hamiltonian h, we adopt the Minnesota nucleon-nucleon interaction [17] and a Woods-Saxon potential for the n-^{20}C system, consisting of the central and spin-orbit parts. As for the latter, we use Set B parameters of Ref. [4]; we have slightly changed V_1 and V_s to 20.00 MeV and 10.50 MeV, respectively, so that the 1s state is unbound. In the COSM calculation, we include the single-particle configuration of each n up to $l = 5$ ($l = 4$) for the 0^+ (2^+) state of ^{22}C, taking into account the spin of n. The radial wave function between n and ^{20}C in each single-particle orbit is described by 10 Gaussian basis functions; we use $b_1 = 0.3$ fm and $\gamma = 1.5$ fm in Eq. (4).

As a result of diagonalization of h, we obtain the 0^+ ground state at 289 keV below the ^{20}C+$n+n$ threshold, which is consistent with the experimental value 420 ± 940 keV [18], together with 604 (1,385) PS above the threshold in the 0^+ (2^+) state. In the CDCC calculation, we include the ground state and the 77 (164) PS for 0^+ (2^+) below $\epsilon = 10$ MeV, which are important for describing the breakup observables shown below.

As for the distorting potential of n-^{12}C and ^{20}C-^{12}C, we adopt microscopic single and double folding models, respectively, with the CEG07b nucleon-nucleon G-matrix interaction including the medium effects [19]. We use the nuclear densities of ^{12}C and ^{20}C given in Refs. [20] and [21], respectively, with a slight change in the parameters for the former. CDCC equations between ^{22}C and ^{12}C are solved up to $R = 30$ fm with the increment of 0.02 fm and the number of the partial waves is set to 600. In the CDCC calculation, we use the so-called no-recoil approximation to the ^{20}C core, as in the previous study of Ref. [22]; this approximation is considered to be valid when the mass of the core nucleus is much larger than the valence particle(s), which is satisfied well in the present case.

In the CSM smoothing method, we adopt the complex-scaling angle of 14°. The basis functions used in diagonalization of the scaled Hamiltonian h^θ are similar to those mentioned above, except that we need finer and wider bases. We show in Table 1 the number N of the Gaussian basis functions and its range parameters, b_1 and γ, for each single-particle orbit of neutron, used in the CSM smoothing method.

Table 1: Parameters of Gaussian basis functions used in the CSM-smoothing method.

neutron orbit	N	b_1 (fm)	γ (fm)
s	25	0.2	1.3
d	20	0.2	1.3
others	15	0.3	1.4

4 Results and discussion

Figure 1 shows the DDBUX $d^2\sigma/(d\epsilon d\Omega)$ of ^{22}C by ^{12}C at 250 MeV/nucleon calculated by COSM-CDCC. One sees some structures in the DDBUX, expected to reflect properties of the resonance and the nonresonant continuum of ^{22}C. In fact, COSM predicts some resonance states of ^{22}C and ^{21}C in the energy region shown in Fig. 1; the results are summarized in Table 2. The next question is thus how these resonances contribute to the DDBUX.

As a great advantage of the CSM-smoothing method, one can decompose the DDBUX into the components due to the three-body resonances (each of the 0^+_2, 2^+_1, and 2^+_2 states), the binary resonance of ^{21}C coupled with another neutron, and the nonresonant three-body continuum. Figure 2 shows the result of the decomposition of the breakup energy distribution $d\sigma/d\epsilon$, which is obtained by integrating the DDBUX over θ from 0° to 0.1°. The left and right panels correspond to the 0^+ and 2^+ states of ^{22}C, respectively. In each panel, the solid (dotted) line shows the total breakup cross section (contribution of the three-body nonresonant continuum). The contribution of the three-body resonance, 0^+_2 (2^+_1) in the

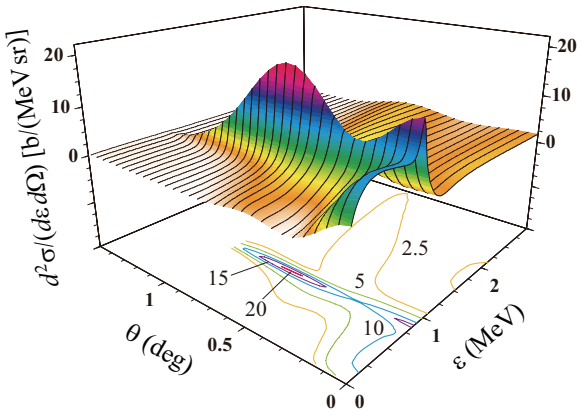

Fig. 1: Double differential breakup cross section (DDBUX) of ^{22}C by ^{12}C at 250 MeV/nucleon.

Table 2: Resonance energy $E_{\rm r}$ and width $\Gamma_{\rm r}$ of ^{22}C and ^{21}C.

nucleus	I^π	$E_{\rm r}$ (MeV)	$\Gamma_{\rm r}$ (MeV)	main configuration
^{22}C	0_2^+	1.02	0.52	$(0{\rm d}3/2)^2$
	2_1^+	0.86	0.10	$(1{\rm s}1/2)(0{\rm d}3/2)$
	2_2^+	1.80	0.26	$(0{\rm d}3/2)^2$
^{21}C	$3/2^+$	1.10	0.10	$(0{\rm d}3/2)$

left (right) panel, is denoted by the dashed line. In both I^π states, it is found that the contributions from the ^{21}C binary resonance are negligibly small. Similarly, the 2_2^+ resonance gives an inappreciable cross section. For the 2^+ state, one clearly sees that the peak in $d\sigma/d\epsilon$ is due to the 2_1^+ resonance, which has the standard Breit-Wigner form. On the other hand, as shown in the left panel of Fig. 2, the 0_2^+ resonance has a peculiar form due to the coupling with the nonresonant continuum. It is well known that resonant cross sections can have different shapes from the standard Breit-Wigner form because of the coupling to the nonresonant continuum. This is called the background-phase effect or the Fano effect [23]. There have been many examples of the Fano effect in various research fields, e.g., neutron scattering [24], Raman scattering [25], hypernucleus formation [26], optical absorption [27], and quantum transport in a mesoscopic system [28]. Nevertheless, the sizable Fano effect on the 0_2^+ resonant cross section in this study should be remarked.

One of the most important characteristics of ^{22}C is the dominance of the $(1{\rm s}1/2)^2$ configuration (more than 80%) in its ground state. This gives a large breakup cross section to the low-energy 0^+ nonresonant continuum with the same configuration, for which only the monopole transition is responsible. It should be noted that if neutron has a finite value of l, it hardly contributes to the low-energy nonresonant continuum of ^{22}C because of the centrifugal barrier. At the same time, the small but non-negligible $(0{\rm d}3/2)^2$ configuration of about 13% in the ground state of ^{22}C brings the low-lying 0_2^+ resonance. This is essentially due to the closely-located (1s1/2) and (0d3/2) single-particle orbits of ^{22}C. Thus, the resonant and nonresonant states with the same spin-parity (0^+) strongly affect each other. This is the main reason for the sizable Fano effect on the 0_2^+ resonant cross section. The coexistence of the 0^+ resonance and nonresonant continuum will rarely be realized when a core plus one neutron system is considered; an s-wave neutron cannot form a resonance, except through a compound process or a Feshbach reso-

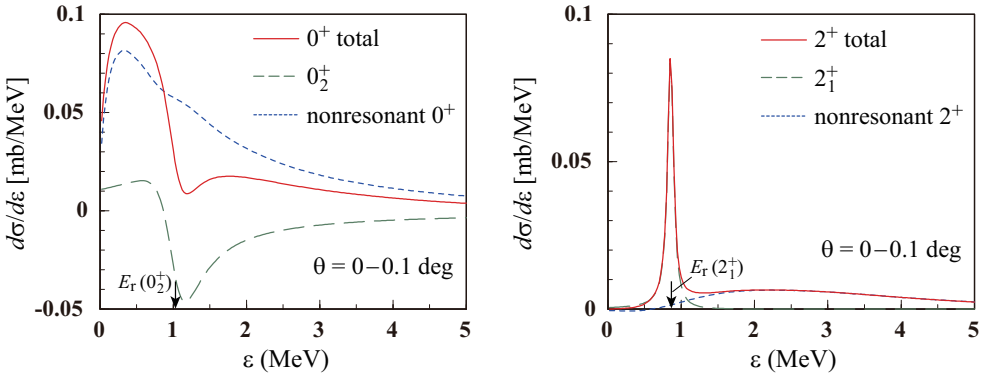

Fig. 2: Decomposition of the breakup energy distribution obtained by integrating the DDBUX over θ from 0° to 0.1°. The left (right) panel is the result of the 0^+ (2^+) state. The dashed lines represent the contributions of the 0^+_2 (left panel) and 2^+_1 (right panel) three-body resonances. The solid and dotted lines in each panel show the total breakup energy distribution and its nonresonant component, respectively. The arrow in the left (right) panel denotes the 0^+_2 (2^+_1) resonance energy E_r.

nance [29]. Therefore, the features of the resonant cross section shown in the present study are expected to be quite unique to an s-wave two-neutron halo nucleus, i.e., ^{22}C.

Experimental data of the DDBUX of ^{22}C are highly desirable to validate the interesting behavior of the 0^+ breakup cross section suggested here. For this purpose, one must eliminate the 2^+ cross section from the total DDBUX. This can be performed quite easily, because the 2^+ contribution will be described well by a standard Breit-Wigner form. To do this, however, we need experimental data with high energy resolution; they will hopefully be obtained at RIBF with utilizing the brand-new SAMURAI spectrometer.

5 Summary

We have proposed a new framework of four-body CDCC adopting COSM wave functions, *COSM-CDCC*, and applied it to the breakup process of ^{22}C by ^{12}C at 250 MeV/nucleon. We showed the 2^+_1 resonance gives a clear peak in the DDBUX, whereas the 0^+_2 resonant cross section has a remarkably different shape from the Breit-Wigner form. The latter is due to the coupling between the 0^+_2 resonance and the 0^+ nonresonant continuum, i.e., the Fano effect. The sizable Fano effect found in the present study is expected to be quite unique to an s-wave two-neutron halo nucleus, i.e., ^{22}C.

Experimental clarification of the sizable Fano effect on the 0^+_2 resonance will be very interesting. From the theoretical side, inclusion of the recoil of the core nucleus ^{20}C and its dynamical excitation during the breakup of ^{22}C will be important future work. Extension of COSM-CDCC to five- and six-body breakup reaction will be a very challenging subject of nuclear reaction studies.

Acknowledgements

K. O. thanks Y. Kikuchi, K. Mizuyama, and T. Fukui for valuable discussions. T. F. is supported by the Special Postdoctoral Researcher Program of RIKEN. This research was supported in part by Grant-in-Aid of the Japan Society for the Promotion of Science (JSPS).

References

[1] E. Lunderberg *et al*., Phys. Rev. Lett. **108**, 142503 (2012).

[2] K. Tanaka *et al*., Phys. Rev. Lett. **104**, 062701 (2009).

[3] N. Kobayashi *et al*., arXiv:1111.7196 (nucl-ex).

[4] W. Horiuchi and Y. Suzuki, Phys. Rev. C **74**, 034311 (2006).

[5] Y. Suzuki and K. Ikeda, Phys. Rev. C **37**, 410 (1988).

[6] M. Kamimura, M. Yahiro, Y. Iseri, Y. Sakuragi, H. Kameyama, and M. Kawai, Prog. Theor. Phys. Suppl. No. 89, 1 (1986).

[7] N. Austern, Y. Iseri, M. Kamimura, M. Kawai, G. Rawitscher, and M. Yahiro, Phys. Rep. **154**, 125 (1987).

[8] M. Yahiro, K. Ogata, T. Matsumoto, and K. Minomo, Prog. Theor. Exp. Phys. **1**, 01A209 (2012); arXiv:1203.5392 (2012).

[9] T. Myo, K. Kato, and K. Ikeda, Phys. Rev. C **76**, 054309 (2007).

[10] T. Myo, R. Ando, and K. Kato, Phys. Rev. C **80**, 014315 (2009).

[11] T. Myo, R. Ando, and K. Kato, Phys. Lett. **B691**, 150 (2010).

[12] S. Saito, Prog. Theor. Phys. **41** (1969), 705.

[13] T. Matsumoto, E. Hiyama, K. Ogata, Y. Iseri, M. Kamimura, S. Chiba, and M. Yahiro, Phys. Rev. C **70**, 061601(R) (2004).

[14] M. Rodríguez-Gallardo, J. M. Arias, J. Gómez-Camacho, A. M. Moro, I. J. Thompson and J. A. Tostevin, Phys. Rev. C **80**, 051601(R) (2009).

[15] T. Matsumoto, K. Kato, and M. Yahiro, Phys. Rev. C **82**, 051602(R) (2010).

[16] J. Aguilar and J. M. Combes, Commun. Math. Phys. **22**, 269 (1971); E. Balslev and J. M. Combes, Commun. Math. Phys. **22**, 280 (1971).

[17] D. R. Thompson, M. Lemere, and Y. C. Tang, Nucl. Phys. **A286**, 53 (1977).

[18] G. Audi, A. H. Wapstra, and C. Thibault, Nucl. Phys. **A729**, 337 (2003).

[19] T. Furumoto, Y. Sakuragi, and Y. Yamamoto, Phys. Rev. C **78**, 044610 (2008), *ibid*. **80**, 044614 (2009).

[20] J. W. Negele, Phys. Rev. C **1**, 1260 (1970).

[21] L. C. Chamon *et al*., Phys. Rev. C **66**, 014610 (2002).

[22] J. A. Tostevin and B. A. Brown, Phys. Rev. C **74**, 064604 (2006).

[23] U. Fano, Phys. Rev. **124**, 1866 (1961).

[24] R. K. Adair, C. K. Bockelman, and R. E. Peterson, Phys. Rev. **76**, 308 (1949).

[25] F. Cerdeira, T. A. Fjeldly, and M. Cardona, Phys. Rev. B **8**, 4734 (1973).

[26] O. Morimatsu and K. Yazaki, Nucl. Phys. **A483**, 493 (1988).

[27] J. Faist, F. Capasso, C. Sirtori, K. W. West, and L. N. Pfeiffer, Nature **390**, 589 (1997).

[28] K. Kobayashi, H. Aikawa, S. Katsumoto, and Y. Iye, Phys. Rev. Lett. **88**, 256806 (2002).

[29] H. Feshbach, Ann. Phys. **5**, 357 (1958), *ibid*. **19**, 287 (1962).

Comparison of breakup processes of ^{6}He and ^{6}Li with four-body CDCC

[1]*Shin Watanabe,* [1]*Takuma Matsumot,* [1]*Kosho Minomo,* [2]*Kazuyuki Ogata, and* [1]*Masanobu Yahiro*
[1]Kyushu University, Fukuoka, Japan,
[2]RCNP, Osaka University, Osaka, Japan

Abstract
We have investigated projectile breakup effects on ^{6}Li+^{209}Bi elastic scattering near the Coulomb barrier with the four-body version of the continuum-discretized coupled-channels method. In this analysis, the elastic scattering is well described by the $p + n + {}^4$He + ^{209}Bi four-body model. Four-body dynamics of the elastic scattering is precisely investigated, and we then propose a reasonable $d + {}^4$He + ^{209}Bi three-body model for describing the four-body scattering. This work is based on the article Phys. Rev. C **86**, 031601(R) (2012).

1 Introduction

The Continuum-Discretized Coupled Channels method (CDCC) is a fully quantum-mechanical method of describing not only three-body scattering but also four-body scattering [1–3]. We call CDCC for four-body (three-body) scattering four-body (three-body) CDCC. CDCC has succeeded in reproducing experimental data on both three- and four-body scattering [4–13].

^{6}He + ^{209}Bi scattering near the Coulomb barrier was analyzed with three-body CDCC [14]. Reference [14] based on a $^2n + {}^4$He + ^{209}Bi three-body model; that is to say a pair of extra neutrons in ^{6}He was treated as a single particle, dineutron (^2n). The three-body CDCC calculation, however, does not reproduce the angular distribution of the measured elastic cross section and overestimates the measured total reaction cross section by a factor of 2.5. This problem has been solved by four-body CDCC in which the total system is assumed to be a $n + n + {}^4$He + ^{209}Bi four-body system [10]. On the other hand, ^{6}Li + ^{209}Bi scattering has been analyzed only with three-body CDCC by assuming a $d + {}^4$He + ^{209}Bi three-body model [14] (see Fig. 1 (a)). However, the calculation could not reproduce the data without normalization factors for the potential between ^{6}Li and ^{209}Bi. These studies strongly suggest that ^{6}Li + ^{209}Bi scattering should also be treated with four-body CDCC as well as ^{6}He + ^{209}Bi scattering.

In this work, we analyze ^{6}Li + ^{209}Bi elastic scattering at 29.9 and 32.8 MeV with four-body CDCC by assuming the $p + n + {}^4$He + ^{209}Bi four-body model (see Fig. 1 (b)). This is the first application of four-body CDCC to ^{6}Li scattering. We deal with four-body dynamics of the elastic scattering explicitly, and propose a reasonable $d + {}^4$He + ^{209}Bi three-body model for describing the four-body scattering.

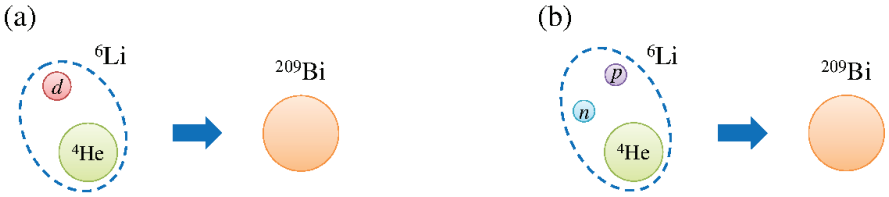

Fig. 1: (Color online) Schematic picture of three- and four-body systems. (a) represents $d + {}^4$He + ^{209}Bi three-body model, and (b) represents $p + n + {}^4$He + ^{209}Bi four-body model.

2 Theoretical framework

One of the most natural frameworks to describe ^{6}Li + ^{209}Bi scattering is the p + n + ^{4}He + ^{209}Bi four-body model. Dynamics of the scattering is governed by the Schrödinger equation

$$(H - E)\Psi = 0 \tag{1}$$

for the total wave function Ψ, where E is a total energy of the system. The total Hamiltonian H is defined by

$$H = K_R + U + h \tag{2}$$

with

$$U = U_n(R_n) + U_p(R_p) + U_\alpha(R_\alpha) + \frac{e^2 Z_{\rm Li} Z_{\rm Bi}}{R}, \tag{3}$$

where h denotes the internal Hamiltonian of ^{6}Li, $\boldsymbol{R}$ is the center-of-mass coordinate of ^{6}Li relative to ^{209}Bi, K_R stands for the kinetic energy operator associated with $\boldsymbol{R}$, and U_x describes the nuclear part of the optical potential between x and ^{209}Bi as a function of the relative coordinate R_x (see Fig. 2). As U_α, we adopt the optical potential of Barnett and Lilley [15]. Parameters of U_n are fitted to reproduce experimental data on n + ^{209}Bi elastic scattering at 5 MeV [16], where only the central interaction is taken for simplicity. The proton optical potential U_p is assumed to be the same as U_n. In the n + p + ^{4}He three-cluster model, we have numerically confirmed that the dipole strength is negligibly small. So, we can approximate the Coulomb part of p-^{209}Bi and α-^{209}Bi interactions into $e^2 Z_{\rm Li} Z_{\rm Bi}/R$, as shown in Eq. (3); $Z_{\rm A}$ is the atomic number of the nucleus A.

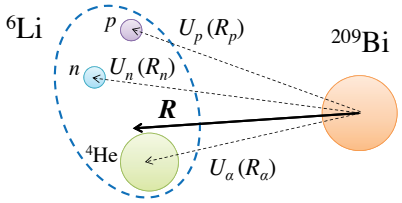

Fig. 2: (Color online) Illustration of coordinates of ^{6}Li + ^{209}Bi four-body system.

The internal Hamiltonian h of ^{6}Li is described by the p + n + ^{4}He orthogonality condition model [17]. The Hamiltonian of ^{6}Li agrees with that of ^{6}He in Ref. [10], when the Coulomb interaction between p and ^{4}He is neglected. Namely, the Bonn-A interaction [18] is taken in the p-n subsystem and the so-called KKNN interaction [19] is used in the p-α and n-α subsystems, where the KKNN interaction is determined from experimental data on low-energy nucleon-α scattering. In order to reproduce the measured binding energy of ^{6}Li, we introduce the effective three-body interaction. The calculated results for the ^{6}Li ground state are summarized in Table 1.

	I^π	ϵ_0 [MeV]	$R^{\rm m}_{\rm rms}$ [fm]
Calc.	1^+	-3.68	2.34
Exp.	1^+	-3.6989	2.44±0.07

Table 1: Calculated spin-parity (I^π), energy (ϵ_0) and matter radius ($R^{\rm m}_{\rm rms}$) of the ^{6}Li ground state. The experimental data are taken from Refs. [20,21].

Eigenstates of h consist of finite number of discrete states with negative energies and continuum states with positive energies. In four-body CDCC, the continuum states of projectile are discretized into a finite number of pseudostates by either the pseudostate method [4–12] or the momentum-bin method [13]. The Schrödinger equation (1) is solved in a model space $\mathcal{P}$ spanned by the discrete and discretized-continuum states:

$$\mathcal{P}(H-E)\mathcal{P}\Psi_{\rm CDCC}=0. \tag{4}$$

In the pseudostate method, the discrete and discretized continuum states are obtained by diagonalizing h in a space spanned by L^2-type basis functions. As the basis function, the Gaussian [5–7, 10] or the transformed Harmonic Oscillator function [4, 8, 9, 11, 12] is usually taken. In this paper, we use the Gaussian function. The model space $\mathcal{P}$ is then described by

$$\mathcal{P} \;=\; \sum_{nIm} |\Phi_{nIm}\rangle\langle\Phi_{nIm}|, \tag{5}$$

where Φ_{nIm} is the nth eigenstate of ^{6}Li with an energy ϵ_{nI}, a total spin I and its projection on the z-axis m.

The CDCC wave function $\Psi^{JM}_{\rm CDCC}$, with the total angular momentum J and its projection on the z-axis M, are expressed as

$$\Psi^{JM}=\sum_{\gamma}\chi^J_\gamma(P_{nI},R)/R\;\mathcal{Y}^{JM}_\gamma \tag{6}$$

with

$$\mathcal{Y}^{JM}_\gamma=\Big[\Phi_{nI}(\boldsymbol{\xi})\otimes i^L Y_L(\hat{\boldsymbol{R}})\Big]_{JM} \tag{7}$$

for the orbital angular momentum L with respect to $\boldsymbol{R}$. Here $\boldsymbol{\xi}$ is a set of internal coordinates of ^{6}Li and the expansion coefficient χ^J_γ, where $\gamma=(n,I,L)$, describes a motion of ^{6}Li in its (n,I) state with linear momentum P_{nI} relative to the target. Multiplying the four-body Schrödinger equation (4) by $\mathcal{Y}^{*JM}_{\gamma'}$ from the left and integrating it over all variables except R, one can obtain a set of coupled differential equations for χ^J_γ:

$$\left[\frac{d^2}{dR^2}-\frac{L(L+1)}{R^2}-\frac{2\mu}{\hbar^2}U_{\gamma\gamma}(R)+P^2_{nI}\right]\chi^J_\gamma(P_{nI},R)=\frac{2\mu}{\hbar^2}\sum_{\gamma'\neq\gamma}U_{\gamma'\gamma}(R)\chi^J_{\gamma'}(P_{n'I'},R) \tag{8}$$

with the coupling potentials

$$U_{\gamma'\gamma}(R)=\langle\mathcal{Y}^{JM}_{\gamma'}|U_n(R_n)+U_p(R_p)+U_\alpha(R_\alpha)|\mathcal{Y}^{JM}_\gamma\rangle+\frac{e^2Z_{\rm Li}Z_{\rm Bi}}{R}\delta_{\gamma'\gamma}, \tag{9}$$

where μ is the reduced mass between ^{6}Li and ^{209}Bi. The elastic and discrete breakup S-matrix elements are obtained by solving Eq. (8) under the standard asymptotic boundary condition [1,22].

In order to obtain Φ_{nIm}, we assume $I^\pi=1^+, 2^+$ and 3^+ states with isospin zero and diagonalize h with 10 Gaussian basis functions for each coordinate in which the range parameters are taken from 0.1 to 12 fm in a geometric series. As shown in Table 1, the calculated binding energy and the matter radius of the ^{6}Li ground state are in good agreement with the experimental data. The Φ_{nIm} with its eigenenergy $\epsilon_{nI}>20$ MeV are excluded from $\mathcal{P}$. The resulting numbers of discrete states are 64 (including the ground state of ^{6}Li), 56, and 57 for 1^+, 2^+, and 3^+ states, respectively. We have also confirmed numerically that other spin-parity states such as $I^\pi=0^+$ and negative parity states do not affect the present results. The model space thus obtained gives good convergence within 1% of the calculated elastic cross sections for the ^{6}Li + ^{209}Bi scattering at 29.9 and 32.8 MeV.

We also perform three-body CDCC calculations by assuming a d + ^{4}He + ^{209}Bi model, following Refs. [14, 23]. As an interaction between d and ^{4}He, we take the potential of Ref. [24], which was determined from experimental data on the ground-state energy (-1.47 MeV) and the 3^+-resonance state energy (0.71 MeV) of ^{6}Li and low-energy d-α scattering phase shifts. The continuum states between d and ^{4}He are discretized with the pseudostate method [5] and are truncated at 20 MeV in the excitation energy of ^{6}Li from the d-^{4}He threshold. The d-^{209}Bi optical potential ($U_d^{\rm OP}$) [25] is taken as U_d, i.e., the distorting potential between d and ^{209}Bi in a d + ^{4}He + ^{209}Bi three-body Hamiltonian, whereas U_α is common between three- and four-body CDCC calculations.

3 Results

Figure 3 shows the angular distribution of elastic cross section for ^{6}Li + ^{209}Bi scattering at 29,9 MeV and at 32.8 MeV. The dotted line shows the result of three-body CDCC calculation with $U_d^{\rm OP}$ as U_d. This result underestimates the measured cross section [26, 27]. The solid (dashed) line, meanwhile, stands for the result of four-body CDCC calculation with (without) projectile breakup effects. In CDCC calculations without ^{6}Li-breakup, the model space $\mathcal{P}$ is composed only of the ^{6}Li ground state. The solid line reproduces the experimental cross section, but the dashed line does not. The projectile breakup effects are thus significant and the present ^{6}Li scattering is well described by the p + n + ^{4}He + ^{209}Bi four-body model.

Now we consider d-breakup in the ^{6}Li scattering in order to understand four-body dynamics of the scattering. In the limit of no d-breakup, the interaction between d and ^{209}Bi can be obtained by folding U_n and U_p with the deuteron density. This potential is referred to as the single-folding potential $U_d^{\rm SF}$. Note that we use the same U_n and U_p as for four-body CDCC (see Eq. 3). In Fig. 3, the dot-dashed line show the result of the three-body CDCC calculation with $U_d^{\rm SF}$ as U_d. The result well simulates that of four-body CDCC calculation, i.e., the solid line. This result suggests d-breakup is suppressed in the ^{6}Li scattering. Thus we found that the reason why three-body CDCC with $U_d^{\rm OP}$ does not work may be because we manage to count d-breakup, which is almost absent in d in ^{6}Li scattering.

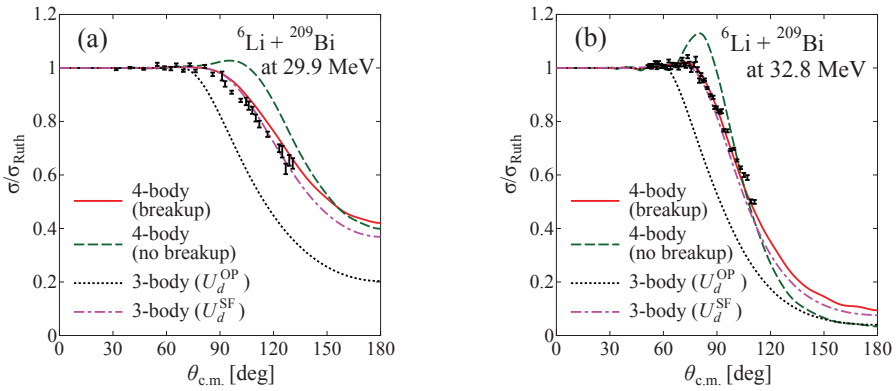

(i) ^{6}Li + ^{209}Bi scattering at 29.9 MeV (ii) ^{6}Li + ^{209}Bi scattering at 32.8 MeV

Fig. 3: (Color online) Angular distribution of the elastic cross section for ^{6}Li + ^{209}Bi scattering at 29,9 MeV (a) and at 32.8 MeV (b). The cross section is normalized by the Rutherford cross section. The dotted (dot-dashed) line stands for the result of three-body CDCC calculation in which $U_d^{\rm OP}$ ($U_d^{\rm SF}$) is taken as U_d. The solid (dashed) line represents the result of four-body CDCC calculations with (without) breakup effects. The experimental data are taken from Refs. [26,27].

Figure 4 shows the angular distribution of elastic cross section for d + ^{209}Bi scattering at 12.8 MeV.

The solid and dashed lines stand for the results of three-body CDCC calculations with and without d-breakup, respectively, in which the $p + n + {}^{209}$Bi model is assumed and both Coulomb and nuclear breakup effects are taken into account. In this calculation, the discretized continuum states of d, obtained by the pseudostate method, are truncated at 30 MeV in the excitation energy from the n-p threshold. As the relative angular momentum ℓ between n and p, we take up to $\ell = 4$. The resulting number of discretized states is 13 (14) for $\ell = 0$ and 1 ($\ell = 2, 3,$ and 4). The model space gives good convergence of the calculated elastic cross sections within 1%. The solid line reproduces the data fairly well, but the dashed line (one channel calculation with $U_d^{\rm SF}$) does not. Thus d-breakup is significant for the deuteron scattering. The deuteron optical potential $U_d^{\rm OP}$ (dotted line) yields fairly good agreement with the data, but the imaginary part of $U_d^{\rm OP}$ is much larger than that of $U_d^{\rm SF}$ mainly because of d-breakup effects. This is the reason why three-body CDCC calculations with $U_d^{\rm OP}$ as U_d cannot reproduce the measured elastic cross section for ^{6}Li + ^{209}Bi scattering. $U_d^{\rm OP}$ implicitly includes d-breakup effects, which is almost absent in d in ^{6}Li scattering.

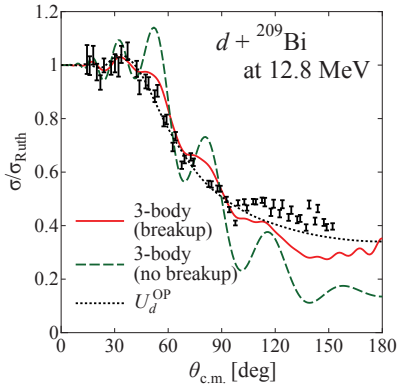

Fig. 4: (Color online) Angular distribution of the elastic cross section for $d + {}^{209}$Bi scattering at 12.8 MeV. The solid (dashed) line stands for the result of three-body CDCC calculation with (without) deuteron breakup, whereas the dotted line is the result of the deuteron optical potential $U_d^{\rm OP}$. The experimental data are taken from Ref. [25].

4 Summary

The ^{6}Li + ^{209}Bi scattering at 29.9 MeV and 32.8 MeV near the Coulomb barrier is well described by four-body CDCC based on the $p + n + {}^4$He + ^{209}Bi model. This is the first application of four-body CDCC to ^{6}Li scattering. In the ^{6}Li scattering, d-breakup is strongly suppressed, suggesting that the $d + {}^4$He + ^{209}Bi model becomes good, if the single-folding potential $U_d^{\rm SF}$ with no d-breakup is taken as an interaction between d and the target. For d+ ^{209}Bi scattering at 12.8 MeV, meanwhile, d-breakup is significant, so that the deuteron optical potential $U_d^{\rm OP}$ includes d-breakup effects. That is to say, the failure of three-body CDCC with $U_d^{\rm OP}$ may be because we manage to count d-breakup, which is almost absent in d in ^{6}Li scattering. However, we need to discuss carefully whether we can always neglect d-breakup in ^{6}Li. We will investigate the energy and target dependence of d-breakup effects in ^{6}Li scattering.

The authors would like to thank Y. Watanabe, K. Kato, and Y. Hirabayashi for helpful discussions. This work has been supported in part by the Grants-in-Aid for Scientific Research of Monbukagakusho of Japan and JSPS.

References

[1] M. Kamimura, M. Yahiro, Y. Iseri, Y. Sakuragi, H. Kameyama, and M. Kawai, Prog. Theor. Phys. Suppl. **89**, 1 (1986).

[2] N. Austern, Y. Iseri, M. Kamimura, M. Kawai, G. Rawitscher, and M. Yahiro, Phys. Rep. **154**, 125 (1987).

[3] M. Yahiro, K. Ogata, T. Matsumoto, and K. Minomo, M. Yahiro, K. Ogata, T. Matsumoto, and K. Minomo, Prog. Theor. Exp. Phys. 2012, 01A206 (2012).

[4] A. M. Moro, J. M. Arias, J. Gómez-Camacho, I. Martel, F. Pérez-Bernal, R. Crespo, and F. Nunes, Phys. Rev. C **65**, 011602(R) (2001).

[5] T. Matsumoto, T. Kamizato, K. Ogata, Y. Iseri, E. Hiyama, M. Kamimura, and M. Yahiro, Phys. Rev. C **68**, 064607 (2003).

[6] T. Matsumoto, E. Hiyama, K. Ogata, Y. Iseri, M. Kamimura, S. Chiba, and M. Yahiro, Phys. Rev. C **70**, 061601(R) (2004).

[7] T. Egami, K. Ogata, T. Matsumoto, Y. Iseri, M. Kamimura, and M. Yahiro, Phys. Rev. C **70**, 047604 (2004).

[8] M. Rodríguez-Gallardo, J. M. Arias, J. Gómez-Camacho, A. M. Moro, I. J. Thompson, and J. A. Tostevin, Phys. Rev. C **72**, 024007 (2005).

[9] A. M. Moro, F. Pérez-Bernal, J. M. Arias, and J. Gómez-Camacho, Phys. Rev. C **73**, 044612 (2006).

[10] T. Matsumoto, T. Egami, K. Ogata, Y. Iseri, M. Kamimura, and M. Yahiro, Phys. Rev. C **73**, 051602(R) (2006).

[11] M. Rodríguez-Gallardo, J. M. Arias, J. Gómez-Camacho, R. C. Johnson, A. M. Moro, I. J. Thompson, and J. A. Tostevin, Phys. Rev. C **77**, 064609 (2008).

[12] A. M. Moro, J. M. Arias, J. Gómez-Camacho, and F. Pérez-Bernal, Phys. Rev. C **80**, 054605 (2009).

[13] M. Rodríguez-Gallardo, J. M. Arias, J. Gómez-Camacho, A. M. Moro, I. J. Thompson, and J. A. Tostevin, Phys. Rev. C **80**, 051601(R) (2009).

[14] N. Keeley, J. M. Cook, K. W. Kemper, B. T. Roeder, W. D. Weintraub, F. Maréchal, and K. Rusek, Phys. Rev. C **68**, 054601 (2003).

[15] A. R. Barnett and J. S. Lilley, Phys. Rev. C **9**, 2010 (1974).

[16] J. Annand, R. Finlay, and P. Dietrich, Nuclear Physics A **443**, 249 (1985).

[17] S. Saito, Prog. Theor. Phys. **41**, 705 (1969).

[18] R. Machleidt, Adv. Nucl. Phys. **19**, 189 (1989).

[19] H. Kanada, T. Kaneko, S. Nagata, and M. Nomoto, Prog. Theor. Phys. **61**, 1327 (1979).

[20] D. R. Tilley *et al*., Nucl. Phys. A **708**, 3 (2002).

[21] A. V. Dobrovolsky *et al*., Nucl. Phys. A **766**, 1 (2006).

[22] R. A. D. Piyadasa, M. Yahiro, M. Kamimura, and M. Kawai, Prog. Theor. Phys. **81**, 910 (1989).

[23] K. Rusek, I. Martel, J. Gómez-Camacho, A. M. Moro, and R. Raabe, Phys. Rev. C **72**, 037603 (2005).

[24] Y. Sakuragi, M. Yahiro, and M. Kamimura, Prog. Theor. Phys. Suppl. **89**, 136 (1986).

[25] A. Budzanowski, L. Freindl, K. Grotowski, M. Rzeszutko, M. Słapa, J. Szmider, and P. Hodgson, Nuclear Physics **49**, 144 (1963).

[26] E. F. Aguilera *et al*., Phys. Rev. Lett. **84**, 5058 (2000).

[27] E. F. Aguilera *et al*., Phys. Rev. C **63**, 061603 (2001).

Possible anisotropy in the emission of fission fragments

A. Al-Adili[1,2] *and F.-J. Hambsch*[1] *and S. Pomp*[2] *and S. Oberstedt*[1]
1. European Commission, Joint Research Centre (IRMM), B-2440 Geel, Belgium
2. Division of Applied Nuclear Physics, Uppsala University, S-751 20 Uppsala, Sweden

Abstract
This study on ^{234}U(n,f) focused on the vibrational resonance at the incident neutron energy E_n=770 keV. Due to the strong angular anisotropy, fluctuations of the fission fragment (FF) properties were predicted. The bipolar angular anisotropy was verified in this work and a possible new correlation to anisotropic FF emission has been observed. The mass distribution was found to have the biggest difference in asymmetry, at the vibrational resonance and was less asymmetric in emission along the axis of the beam direction. A corresponding anisotropy in the total kinetic energy was also observed. The observed effect was consistent with the change in the mass distribution. At last, the experimental data were fitted based on the Multi-Modal Random Neck-Rupture (MMRNR) model. The yield of the standard-1 mode was found to increase at the resonance.

1 Introduction

The motivation for this study on ^{234}U(n,f) is the apparent need for nuclear data concerning this reaction. In addition to the importance of these data for nuclear applications, it can also be used to review parts of the modelling of fundamental fission dynamics due to the interesting properties of ^{234}U(n,f). Several works, e.g. Refs. [1–3], investigated the anisotropic fragment emission in ^{234}U(n,f) which is due to a prominent vibrational resonance in the sub-barrier region, at E_n=770 keV. However, to our knowledge, only one measurement exists on the energy distributions for ^{234}U(n,f) [4] and no measurement is available on the mass distribution.

2 Background

The angular anisotropy in fission has been well studied. However much less is known on possible correlations with other fission-fragment observables like the mass distribution. A few works suggested an angular-anisotropy dependence of the fragment masses [5–8], and others disproved these findings e.g. [9–12]. Classical models favour an anisotropy independent on the mass [13]. The reason can be found in the fission barrier, which is responsible for the angular distribution according to the theory of Bohr [14]. The fission barrier height, is assumed to be the same for all asymmetric fission events, therefore the FF angular distribution, is also assumed to be the same [8, 10]. In modern fission models, for instance the Multi-Modal Random Neck-Rupture model (MM-RNR), the angular anisotropy may be mass dependent. Basically, each fission mode which has its own mass distribution, could in fact have different angular distributions [15, 16]. In this study we searched for possible correlations between the mass distribution and the prominent angular anisotropy which is peaked at 835 keV incident neutron energy. Moreover, we performed a fission mode analysis to understand the possible influence on the fission observables.

3 Experiments

In total 14 different measurements were collected at the incident energies: 0.2, 0.35, 0.5, 0.64, 0.77, 0.835, 0.9, 1.0, 1.5, 2.0, 2.5, 3.0, 4.0 and 5.0 MeV. The experiment is performed using neutrons from

the 7 MV Van de Graaff accelerator (MONNET) at the Institute for Reference Materials and Measurements (IRMM) in Geel, Belgium. For FF detection, a Twin Frisch Grid Ionization Chamber (TFGIC) was utilized. It has two anodes, two Frisch grids and one common cathode (see Ref. [17] for more experimental details). The sample used for irradiation is a $^{234}UF_4$ target enriched to 99% ^{234}U and placed in the center of the cathode. P-10 counting gas was used in the chamber at a pressure of 1.05×10^5 Pa. By measuring the FF pulse height (proportional to the FF energy) and the emission angle, the pre-neutron emission masses could be calculated based on conservation of energy and momentum. A digital data acquisition system was used to store the raw signals from the charge sensitive pre-amplifiers. Several advantages were achieved by applying the digital techniques compared to conventional analogue techniques e.g. improving the angular resolution, verifying the correct grid-inefficiency correction and successfully correcting for α pile-up [17–19].

4 Analysis

The analysis of the data is based on the 2E method. As an absolute energy calibration, $^{235}U(n_{th},f)$ was measured with the same setup. Well known literature data on $\overline{\mathrm{TKE}}$ and $\langle A_H \rangle$ were used for this reaction in the calibration. The angular resolution is reduced at higher emission angles due to the energy losses in the sample, therefore only events with $\cos(\theta)\geqslant0.5$ were selected for the FF mass calculation. The analysis took into account the correction for the pulse-height defect, neutron-momentum transfer and the energy-losses in the sample. One crucial step in the analysis is the neutron multiplicity $\nu(A,TKE,E_n)$. Since it was not measured in this experiment, ν had to be parametrized based on data from neighbouring uranium isotopes, $^{233}U(n,f)$ and $^{235}U(n,f)$ [20]. The TKE dependence of $\nu(A,TKE)$ was parametrized as in Ref. [21] and the dependency on incident neutron energy was also corrected for using available data on $\bar{\nu}_{tot}(E_n)$ for $^{234}U(n,f)$ [22]. The angular anisotropy was calculated relative to the supposed isotropic thermal fission of ^{235}U. The angular distributions were fitted in the center-of-mass system, with Legendre polynomials. The fit range was set to $0.3<\cos(\theta)<0.9$ due to the degrading resolution outside this range.

5 Results

The angular anisotropy found in Refs. [1–3] were confirmed in our work. The maximum anisotropy at the vibrational resonance was peaking at E_n=835 keV and had a minimum at E_n=500 keV. The changes in $\overline{\mathrm{TKE}}$ were however different to the previous measurement. The $\overline{\mathrm{TKE}}$ as a function of neutron energy increases at the resonance, contrary to the findings of Ref. [4]. Several attempts were made to understand the possible reasons behind this difference. We now believe that the difference in solid angle coverage may be the reason since only a small angle coverage was allowed when using surface barrier detectors, as in Ref. [4]. We found that the high TKE events contributing to the increasing $\overline{\mathrm{TKE}}$ at the resonance, originate from events with higher emission angles. In fact, near 0° (relative to the incoming beam) the measurement at the resonance energy showed a slightly lower $\overline{\mathrm{TKE}}$ than outside of the resonance energy, as observed in Ref. [4]. In Ref. [4], two different geometries were used, at 0° and 90°, respectively. The $\overline{\mathrm{TKE}}$ was higher for the 90° run, however, probably due to the strong angular anisotropy the interpretation was different.

This apparent angle-dependent $\overline{\mathrm{TKE}}$ is not straight forward and needed better quantification. The change in $\overline{\mathrm{TKE}}$ as a function of $\cos(\theta)$ is probably not linear but a linear fit was anyhow applied as an approximation and for simplicity. The resulting change in slope was striking, showing a clear trend in correlation to the main vibrational resonance. The difference in $\overline{\mathrm{TKE}}$, between 0° and 90°, was at highest for the fission in the resonance. A similar fit was performed, now on the mass distribution as a function of $\cos(\theta)$. The trend observed in the $\overline{\mathrm{TKE}}$ must have a direct link to the mass distribution and a possible anisotropy there as well. Indeed, after plotting the slopes of the different fits, a clear trend showed a higher anisotropy in mass emission in correlation to the vibrational resonance at E_n=770 keV. The observed effect was a more symmetric mass distribution for higher emission angles. Since a

more symmetric yield distribution preferable leads to higher TKE, these findings are consistent with the changes in $\overline{\mathrm{TKE}}$ at the resonance.

To further study this effect, fission mode parametrizations based on Ref. [15] were used to fit the two-dimensional TKE vs. mass distributions. The 3 modes used, standard-1, standard-2 and super-long describe the asymmetric, very asymmetric and symmetric fission divisions, respectively. The mode-weight analysis showed that the standard-1 fission mode is actually increasing at the vibrational resonance and since it is giving higher TKE values, it is consistent with the higher $\overline{\mathrm{TKE}}$ found at the resonance. The combination of a possible anisotropic mass emission and the growing standard-1 yield at the vibrational resonance, could indicate an angle-dependent mode change. Since the mass distribution becomes more symmetric for higher emission angles, at the same time standard-1 increases and the $\overline{\mathrm{TKE}}$ becomes larger, the mode weight change could be angular-anisotropic. If true, the two standard modes may have slightly different angular distributions. As discussed earlier based on the Bohr theory, the angular distributions are closely related to the barrier height. So, could this be a (first) evidence on a different barrier height for the two standard fission modes?

Acknowledgements

The authors would like to thank the staff of the Van de Graaff accelerator at the IRMM Geel, Belgium, for providing a stable neutron beam. One of the authors (A. A.) is indebted to the European Commission for granting him a PhD fellowship.

References

[1] J. Simmons and R. L. Henkel, Phys. Rev. **120** (1960) p198.
[2] R. Lamphere Nucl. Phys. **38** (1962) p561.
[3] A. Behkami et. al., Phys. Rev. **171** (1968) p1267.
[4] A. Goverdovskii et. al., Sov. Jour. Nucl. Phys. **44** (1986) p287.
[5] B. L. Cohen et. al., Phys. Rev. **98** (1955) p685-687.
[6] S.S. Kapoor et. al., Phys. Rev. **B137** (1965) p511.
[7] H. Kudo and Y. Nagame and H. Nakahara, Phys. Rev. **C25** (1982) p909-917.
[8] B.M. Gokhberg et. al., Sov. Jour. Nucl. Phys. **47** (2), (1988) p320.
[9] R. Vandenbosch and J. P. Unik, and J. R. Huizenga, Proc. Of IAEA Symp. On Physics and Chemistry of Fission, Salzburg, Austria 1, (1965) 547.
[10] J. W. Meadows , Phys. Rev. **177** (1968) p1817-1825.
[11] V. G. Vorobeva et. al., Sov. J. Nucl. Phys. **26**, (1977) p508.
[12] Ch. Straede et. al., Nucl. Phys. **A462** (1987) p85-108.
[13] R. Vandenbosch and J.R.Huizenga, Nuclear Fission, ACADEMIC PRESS (1973) p209.
[14] A. Bohr, Proc. Intern. Conf. Peaceful Uses of Atom. Energy, Vol. **I**, (1956) p191.
[15] U. Brosa, S. Grossmann, and A. Müller, Phys. Rep. **197** (1990) p167.
[16] C. Wagemans, The Fission Process, CRC Press (1991) p494.
[17] A. Al-Adili et. al., Nucl. Instr. Methods **A624** (2010) p684.
[18] A. Al-Adili et. al., Nucl. Instr. Methods **A671** (2012) p103.
[19] A. Al-Adili et. al., Nucl. Instr. and Meth. **A673** (2012) p116.
[20] A. C. Wahl, At. Data and Nucl. data tables **39** (1988) p1-156.
[21] E. Birgersson et. al., Nucl. Phys. **A817** (20 09) p1.
[22] D.S. Mather, P. Fieldhouse and A. Moat Nucl. Phys. **66** (1965) p149.

Transient effects in proton-induced fission of ^{208}Pb

Y. Ayyad[1] *, J. Benlliure*[1] *, A. Kelić-Heil*[2] *, K.-H. Schmidt*[2] *, E. Casarejos*[1] *, A. Bacquias*[4] *, A.Boudard*[3] *, T. Enqvist*[5] *, M.V. Ricciardi*[2] *, M. Fernandez*[6] *, V. Henzl*[7] *, V. Henzlova*[8] *, B. Jurado*[9] *, T. Kurtukian*[9] *, S. Lukić*[10] *, P. Nadtochy*[11] *, D. Pérez-Loureiro*[1] *, R.Pleskac*[2] *, F. Rejmund*[12] *, M.V. Ricciardi*[2] *, C. Schmitt*[12] *, and Son Nguyen Ngoc*[13]
[1]University of Santiago de Compostela, Spain
[2]Gesellschaft für Schwerionenforschung, Darmstadt, Germany
[3]CEA, Saclay, France
[4]Universite Louis Pasteur, Strasbourg, France
[5]CUPP Project, P.O. Box 22, FI-86801, Phyasalmi, Finland
[6]CIEMAT, MAdrid, Spain
[7]MIT, 77 Massachusetts Ave, Cambridge, MA. 02139
[8]Los Alamos National Laboratory, Safeguards Science
and Technology Group (N-1), Los Alamos, NM, 87545
[9]Universite Bordeaux I, CNRS/IN2 P3, CENBG, BP 120, F-33175, Gradignan, France
[10]Karlsruhe Institute of Technology, D-76021 Karlsruhe, Germany
[11]Omsk State University, RU-644077 Omsk, Russia
[12]GANIL, BP 55027, F-14076 Caen Cedex 05, France
[13]Natural Centre of National Science and Technology, Ngiado-Tuliem, Hanoi, Vietnam

Peripheral heavy-ion collisions at relativistic energies represent an appropriate scenario to investigate the transient and nuclear dissipation effects on fissile systems. Using a new experimental approach [1,2], the de-excitation of the system and its degrees of freedom are studied. A dedicated experimental set-up using the inverse kinematics technique [3] make it possible to identify in atomic number both fission fragments simultaneously with high resolution and reconstruct the charge of the fissioning system. In this approach, the width of the fission-fragment nuclear charge distribution depends on the excitation energy of the system, and therefore, on its temperature at the saddle point (Tsad). These observables are compared with nuclear-reaction codes to extrapolate quantitative results concerning the strength of the dissipation coefficient and transient time of the system. In this work, we have investigated transient and dissipation effects in proton and deuteron induced fission on ^{208}Pb at 500 A MeV using these new experimental signatures. A comparison between different reaction codes was made to stress the main differences between them. For this purpose we used as a excitation stage ABRA (BURST) [4], INCL [5] and ISABEL [6]. For the de-excitation stage we used ABLA [4] and GEMINI++ [7]. The obtained results are consistent with other works showing the influence of the transient time and the nuclear dissipation in the fission process at high excitation energy [9].

References

[1] B. Jurado et al Phys. Rev. Lett. 93(2004) 072501.
[2] B. Jurado et al Nucl. Phys. A 700 (2002) 469.
[3] K.-H. Schmidt et al. Nucl. Phys. A 665 (2000) 221.
[4] J. J. Gaimard and K.-H. Schmidt Nucl. Phys. A 531 (1991) 709.
[5] A. Boudard, J. Cugnon, S. Leray and C. Volant Phys. Rev. C 66 (2002) 044615.
[6] Y. Yariv and Z. Fraenkel Phys. Rev. C 20 (1979) 2227.
[7] R. J. Charity, in Joint ICTP-IAEA Advanced Workshop on Model Codes for Spallation Reactions, p. 139, Trieste, Italy, 2008, IAEA, Report INDC(NDC)-0530.
[8] J. Benlliure et al. Nucl. Phys. A 700 (2002) 469.
[9] C. Schmidtt et al. Phys. Rev C 81 (2010) 064602

Fission Product Yields as a Diagnostics for Plutonium Burnup

M.B. Chadwick
Los Alamos National Laboratory, Los Alamos, NM 87545, USA

Abstract

I describe progress made in recent years in determining fission product yields for fast neutron reactions on plutonium. Discrepancies of the order of 5–10% have been partially resolved, allowing fission burnup to be determined to a few percent accuracy.

1 Introduction

This paper represents an extract from *"Fission Yields and Other Diagnostics for Nuclear Performance"*, LA-UR-12-00727 (2012): a talk on the occaion of receiving the E.O. Lawrence Award, and focuses on one aspect of that work - fission product yields.

Until recently Los Alamos and Livermore disagreed on the yields in kilotons assigned to a plutonium nuclear explosion. This wasn't always the case. Since the earliest days of nuclear science, Los Alamos developed methods to determine the yields from measurements of the fission products (FP) in the debris after the explosion, through use of calibrated laboratory experiments involving fission chambers inside critical assemblies. These critical assemblies allowed radiochemists to determine exactly how to translate the beta decay radioactivity of the fission products to the number of fissions that occurred, and hence to the yield. Originally Livermore followed Los Alamos' approach, and the labs were on a consistent "fission basis". Later, in the 1970s, Los Alamos repeated the calibration experiment using a critical assembly that better mimicked our applications (creating a fast spectrum, not a thermal neutron spectrum) as part of the Inter-Laboratory Reaction Rate (ILRR) collaboration, and found a different result compared to its original 1950s result: the key "Q_{99} value" [1] for ^{239}Pu was determined to be 1.015 instead of 0.966. The reason for the discrepancy was thought to be due to a self-shielding problem in the early experiment, and adopting the new experimental results led Los Alamos to lower its fission yield assessments. However, Livermore had – we concluded – remained on the original basis, so that for the last two decades the Laboratories have had an offset in their assessments. Livermore felt it prudent to be cautious before making a change to again be consistent with LANL. In part this was because, for the key fission product we use as an indicator (neodymium-147, ^{147}Nd) the fission product yield in use at Livermore happened to be in good agreement with an independent fast reactor measurement from Idaho National Laboratory by Maeck [2] (as I'll explain later, this puzzle was resolved by the identification of a neutron energy-dependence to the ^{147}Nd product yield).

Thus, we had a situation in the 1990s and 2000s where the equivalent sets of specialists at LANL and LLNL knew their results were different, but each group felt their results were correct! Additionally, Livermore had moved to use a different approach for much of their fission product work that involved measuring fission products using Germanium detectors for the decay gamma-rays, together with use of fission product yields. These methods differed from Los Alamos' more traditional beta decay radiochemical methods, and for a while at least some of the differences between the labs was due to different languages used between the specialists. LANL continued to use the somewhat archaic radchem language of "K factors and R and Q values" [3], that had its origins in the Manhattan project, while Livermore migrated to the more widely used "fission product yield". Only through numerous exchanges between the labs, and Don Barr's writings was it understood that the approaches are equivalent when care is taken in determining the physical constants.

The confusion continued. The Livermore radiochemists from the nuclear testing era had mostly retired and few records remained documenting the origins of their FPYs that were being used in their

yield assessment work. Livermore pointed to examples of their FPY evaluations based on measurements published in the open literature. But it was shown that, for the key fission products used in yield assessments such as ^{147}Nd, ^{95}Zr, ^{99}Mo, ^{144}Ce, *etc*, the values Livermore used almost certainly came from the same traditional methodology ("FPY= FPY-235-th. Q_{99}. R") used at LANL. This is no surprise since it reflects a desire for continuity in yield assessments made over the years. But it also showed *why* Livermore FPY values in use until recently were offset compared to LANL's: they used the old (deficient) 1950s LANL Q_{99}=0.966 value.

The challenge I faced was to assemble evidence that would elucidate what are the correct FPY values for fast neutrons on plutonium, and explain why LANL and LLNL values differed. The previous paragraphs summarize our conclusions on why the labs differed, but work was needed to determine which values were most correct. It was not enough to say that the esteemed radiochemists from Los Alamos – Barr, Knobeloch, and so on – undertook the LANL-ILRR 1970s experiments and obviously measured the key quantities correctly, or that the successive generations of excellent LANL researchers – Mac Innes, Inkret, Wilkerson, Selby, Keksis, Burns, Meade, Wallstrom *etc* – had carefully analyzed these data and found them to be trustworthy! Livermore could validly ask why we should trust this particular experiment, which had not (at that time) been documented in the open literature? And although we showed [4] that results from the 1970s LANL-ILRR experiment were in excellent agreement with many other accurate and independent measurements published in the literature (e.g. Maeck [2]; ILRR [5]), this was not the case for the key ^{147}Nd FPY. Here, Maeck's measurement agreed instead with Livermore's value (like LANL's historic 1950s value) and not the LANL-ILRR value that LANL is now recommending! Why was this?

There were two particular advances I made that helped solve this problem, described below: (a) an identification of a subtle energy dependency of the key ^{147}Nd FPY; and (b) use of a meta-analysis to expand our knowledge base of information on the magnitude of FPYs; the result of this analysis supported the validity of LANL's measured values.

2 Energy dependence of FPYs

I came to the conclusion that the apparent discrepancy between the LANL FPY data for ^{147}Nd and Maeck's fast-reactor ^{147}Nd value is due to the different neutron spectra in the two experiments: fast reactors have an average neutron energy of a few hundred keV, whereas the LANL data (appropriate for our applications) have an average energy closer to 1.5-2 MeV, and there are physical reasons why the ^{147}Nd FPY can have a positive energy dependence over this region. Thus, both the LANL and the Maeck values can be correct within their uncertainties; they just apply to different energy regimes.

It is well known that FPYs often have neutron energy dependencies. The mass distribution of FPYs is double-humped, owing to shell effects which favor a heavy peak near the closed-shell A=132 (plus the few extra nucleons captured back after the rupture of the neck between the two fragments, giving a peak at about A=135), and consequently a light peak near 102 (this comes from 240, the initial compound system mass before fission, – 135 for the heavy fragment – 3, the average number of prompt fission neutrons emitted). FPYs in the valley (near A=120) increase with incident energy as the symmetric fission breakup mode becomes energetically more possible, and the FPs in the wings also increase with energy, whilst the yields for the FPs at the peaks decrease slightly with energy. The FP indicators used by LANL and LLNL were chosen to be roughly energy-independent, lying nearer the peaks of the double-humped FPY distribution. And the lore at the labs had been that these FPs are energy *in*dependent. Whilst this is approximately true, at the few percent level energy dependencies can occur for all FPs, including ^{95}Zr, ^{144}Ce, and ^{147}Nd.

Fortunately LANL measured a rich database of 17 plutonium ^{147}Nd R-values within critical assemblies with varying neutron spectra, all the way from thermal up to fast energies (the hottest assembly with the highest energy neutrons being Jezebel, a sphere of plutonium). This allowed me to develop an

independent check of the ^{147}Nd FPY energy dependence since the FPY is proportional to the R-values, and indeed we do see a positive variation between the softest and hottest assemblies, supporting the hypothesis. The effect is subtle, though, since the energy-dependence magnitude (3–4 %-relative change over an MeV) is approximately the same as the variance of the data. Trends in the systematic behavior of FPY energy dependencies for the whole mass range of FPs, based on numerous independent experiments, build a phenomenological picture of the energy dependencies that makes physical sense, and A=147 is seen to be at the transition between negative and positive dependencies for plutonium (just on the positive side – see Fig.10 of Ref. [4]). My colleague John Lestone has recently developed a theoretical underpinning of these dependencies based on a model for fission [6], and his results support these conclusions.

Subsequent independent Livermore studies of the experimental ^{147}Nd FPY data (Thompson *et al*., Ref. [7]) have led to a similar energy-dependence result ($\sim 3.2\%$ per MeV). Dardenne of Livermore also developed another way of viewing the data based on taking FPY ratios to other FPs (so that certain systematical uncertainties cancel). This approach also confirms the ^{147}Nd FPY positive energy dependence over the 0.5-2 MeV range – when observing the ^{147}Nd FPY in ratio to ^{140}Ba (which we think is essentially energy-independent over this range) Thompson and Dardenne found an energy-dependence of about 4.5%-per-MeV [7], consistent with our result. A separate group of consultants commissioned by Livermore, led by Stan Prussin [8], studied the problem from a different and rather clever perspective (see also Maeck [9]), focusing only on the isotope dilution mass-spectrometry reactor data and again found a similar result (2.4–4.0%-per-MeV) for the A=147 energy-dependence.

FPY energy dependencies would be of little practical concern if significant uncertainties in our plutonium yield assessments could be tolerated, as was the case for much of the nuclear testing period. But now that our accuracy goals are much higher – of the order of a few % – such phenomena need to be considered.

3 Magnitude of fission product yields determined through a meta-analysis

Although the energy dependence hypothesis was able to explain part of the difference between LANL and LLNL's yield values, an important question remained to be settled: how sure can we be that LANL's overall FPY magnitudes are correct? Until the recent consensus between the labs there was a general offset in magnitude for all the important FPYs we use – ^{95}Zr, ^{99}Mo, ^{140}Ba, ^{144}Ce, as well as for ^{147}Nd. Energy dependence considerations weren't particularly relevant to resolving this discrepancy.

^{99}Mo is LANL's standard fission product – all other FPs are measured in ratio to ^{99}Mo (thus, ^{99}Mo is analogous to carbon in the field of atomic masses). The absolute scale of all of LANL's fast neutron+Pu FPY values, including ^{147}Nd, is therefore set by the ^{99}Mo Q_{99}=1.015 measurement in the seminal LANL-ILRR experiment. Livermore's values differed by an offset compared to this value, arising – we believed – from their use of the historic Q_{99}=0.966. I therefore sought to find independent information that would elucidate the correct value for Q_{99} to resolve this difference. But this was complicated by the fact that for ^{99}Mo there is a dearth of experimental information beyond LANL's measurements. One of the few other sets of reported ^{99}Mo fast neutron on plutonium FPY data came from Maeck, and agreed with LANL, but was interpolated from nearby nuclides. The other direct measurement, by Laurec [10], was discrepant with LANL's data – though all of Laurec's FPY data for fission-spectrum neutrons on plutonium tend to lie below other laboratory's measurements, a discrepancy we still do not understand.

I realized that the large suite of Los Alamos R-value measurements contained a hidden treasure of information on ^{99}Mo, it just needed to be teased out. The R-value measured data for various fission products j contains ratio information on the production of the fission product j to that of ^{99}Mo. (Actually it is a ratio of ratios, see Refs. [3,4]). These other fission product j FPYs are often known accurately from a variety of independent measurements published in the literature. Thus by using these other FPYs together with LANL's R-value ratio data, the ^{99}Mo FPY can be inferred. By following this prescription

I determined ^{99}Mo values, and found a consistent *meta-analysis* result Q_{99}=1.019±0.8% that supported LANL's direct measurement of Q_{99}=1.015±2% [4].

A meta-analysis is defined as procedure by which multiple data sets set can be combined to better determine a quantity, to overcome problems of small sample sizes. This well describes the above process, where information embodied in R-values was used to expand our knowledge of the ^{99}Mo fission product data. By expanding the available database from 1 to N values, the uncertainty on the FPY result was reduced by $1/\sqrt{N}$. The result I obtained for Q_{99} further supported LANL's yield assessments, and reduced the uncertainty.

Finally it is worth noting that in the two years that have passed since I published the meta-analysis results, a consistency check can be done based on new evaluated ^{99}Mo FPY data that have been published by LANL, LLNL, and by Prussin (see Table 1). This is done by computing Q_{99} from them by dividing the plutonium fission-spectrum FPY by the ENDF FPY for thermal reactions on uranium-235. When one does this, very good agreement is seen (LANL, 6.23/6.108=1.020; Prussin, 6.22/6.108=1.018; LLNL, 6.19/6.108=1.013; the average of these 3 is 1.017 which compares well with Q_{99}=1.019±0.8% from my meta-analysis).

Livermore has now conducted an independent evaluation effort on the magnitude of the FPY for fission spectrum neutrons on plutonium (Thompson *et al*. [7]). Unlike the older Livermore values, which were typically 5–9% lower than LANL's values, the magnitude of their new results agree with ours (within about 2% or better), see Table 1.

4 Conclusions

In this paper I haven't described the (less important for msny applications) 14 MeV range, where the laboratories still have some significant differences. At Los Alamos we have refined our understanding of our 14 MeV experiments and evaluations, and we recently documented our results in peer-reviewed open publications [12, 13]. But the resolution of our present differences at 14 MeV will require future experiments; see below.

There are some remaining puzzles to be solved, including unknown reasons for the systematically lower plutonium FPY measured by our excellent CEA colleagues [10]. We have initiated various experiments that aim to corroborate (or who knows, maybe invalidate?) our present understanding: new measurements being planned in Nevada using our critical assemblies will look at FPY energy dependencies between thermal and ∼1.5 MeV (thanks to Bob Little, Todd Bredeweg, and others in the Criticality Safety community); a detector being fabricated at LANSCE under an LDRD/DR project (Morgan White, Frederick Tovesson) will map out trends of FPY for all masses and energies; and measurements at TUNL through the NNSA Stewardship Science Academic Alliance program (with Jerry Wilhelmy, John Becker, Anton Tonchev, David Vieira, Mac Fowler, Mark Stoyer *et al*.) are looking at specific FPY ratios from fast to 14 MeV energies. What started as an effort to resolve a longstanding discrepancy between LANL and LLNL has evolved into the re-vitalization of fission physics research.

References

[1] Q_{99}, for ^{99}Mo, is the ratio of the fission product yield for fission spectrum neutrons on plutonium to that for thermal neutrons on ^{235}U. At Los Alamos it was not determined experimentally from ratios of FPY per se, but rather from ratios of count rates of the FP radioactive decay.

[2] W. J. Maeck, "Fast Reactor Fission Yields for ^{239}Pu and ^{241}Pu," Allied Chemical Corporation, Idaho Chemical Programs Rept., ICP-1050-II (1977).

[3] H. D. Selby, M. R. Mac Innes, D. W. Barr, A. L. Keksis, R. A Meade, C. J. Burns, M. B. Chadwick, and T. C. Wallstrom, "Fission Product Data Measured at Los Alamos for Fission Spectrum and Thermal Neutrons on ^{239}Pu, ^{235}U, and ^{238}U", Nuclear Data Sheets 111, 2891 (2010).

Table 1: Summary of FPYs from fission spectrum neutrons on ^{239}Pu in units of % per fission. The values are quoted for an average energy causing fission of 1.5 MeV (except for the ^{99}Mo data that are quoted at the relevant energy of the Bigten molybdenum experiment, ∼0.5 MeV).

	LANL-ILRR exp. Selby *et al*. [3]	LANL-eval ENDF/B-VII.1 Chadwick [4,13]	Prussin eval. Ref. [8]	LLNL-eval. (new) Thompson [7]	LLNL-eval. (old) Nethaway [11]
^{95}Zr	4.80±0.18	4.80±0.10	4.75 ±0.07	4.73 ±0.03	4.52
^{99}Mo	6.20±0.15	6.23±0.04	6.22 ±0.12	6.19 ±0.11	5.94
^{144}Ce	3.68±0.13	3.62±0.08	3.66 ±0.05,3.67 ±0.05	3.69 ±0.02	3.34
^{147}Nd	2.09±0.05	2.10±0.03	2.13 ±0.04, 2.11±0.04	2.05 ±0.06	1.97

[4] M.B. Chadwick, T. Kawano, D.W. Barr, M.R. Mac Innes, A.C. Kahler, T. Graves, H. Selby, C.J. Burns, W.C. Inkret, A.L. Keksis, J.P. Lestone, A.J. Sierk, P. Talou, "Fission Product Yields from Fission Spectrum n+^{239}Pu for ENDF/B-VII.1", Nuclear Data Sheets 111, No 12, 2923 (2010).

[5] W.D. McElroy, ed., "InterLaboratory Reaction Rate Program 11th Progress Report, Nov. 1975 - Oct. 1976", Hanford Engineering Department Laboratory Report HEDL-TME 77-34, UC-79 b,d (1977); Gilliam et al., "Reference and Standard Benchmark Field Consensus Fission Yields for U.S. reactor Dosimetry Programs", in ASTM/EURATOM Symposium on Reactor Dosimetry, NUREG/Cp-0004 (1977).

[6] J.P. Lestone, "Energy Dependence of Plutonium Fission-Product Yields", Nuclear Data Sheets 112, No. 12, 3120 (2011).

[7] I.J. Thompson, Y.M.X.M. Dardenne, J.M. Kenneally, A. Robertson, L.E. Ahle, C.A. Hagmann, R.A. Henderson, D. Vogt, C.Y. Wu and W. Younes, Nucl. Sci. Eng. 171, 85 (2012).

[8] H. C. Britt, J. M. Dairiki, R. W. Lougheed, D. P. McNabb, and S. Prussin, "Review of the Status of Cumulative Fission Yields from ^{239}Pu(n,f) of Interest to Nuclear Forensics," Lawrence Livermore Laboratory report, LLNL-TR-458777 (2010).

[9] W. J. Maeck, "The correlation of ^{239}Pu thermal and fast reactor fission yields with neutron energy," Allied Chemical Corporation — Idaho Chemical Programs Report, ENICO-1030 (1981).

[10] J. Laurec, A. Adam, T. de Bruyne, E. Bauge, T. Granier, J. Aupiais, O. Bersillon, G. le Petit, N. Authier, P. Casoli, "Fission Product Yields of ^{233}U, ^{235}U, ^{238}U, and ^{239}Pu in Fields of Thermal Neutron, Fission Neutrons, and 14.7 MeV Neutrons", Nuclear Data Sheets 111, No 12, 2965 (2010).

[11] D. Nethaway, "PROPHET fission yields", Livermore report LJW-45-85-189 (1985).

[12] M.R. Mac Innes, M.B. Chadwick, T. Kawano, "Fission Product Yields for 14 MeV Neutrons on ^{235}U, ^{238}U and ^{239}Pu"', Nuclear Data Sheets 112, 3135 (2011).

[13] M. B. Chadwick, M. Herman, P. Obložinský *et al*., "ENDF/B-VII.1 Nuclear Data for Science and Technology: Cross Sections, Covariances, Fission Product Yields and Decay Data". Nuclear Data Sheets, **112**, p. 2887 (2011).

Evolution of isotopic fission-fragment yields with bombarding energy

O. Delaune[1], *M. Caamaño*[1,2], *F. Farget*[1], *O.B. Tarasov*[3], *X. Derkx*[1], *K.-H. Schmidt*[1], *L. Audouin*[4], *A.M. Amthor*[1], *C.-O. Bacri*[4], *G. Barreau*[5], *B. Bastin*[1], *D. Bazin*[3], *J. Benlliure*[2], *B. Blank*[5], *L. Cacères*[1], *E. Casarejos*[6], *B. Fernández-Domínguez*[2], *L. Gaudefroy*[7], *C. Golabek*[1], *S. Grévy*[1], *B. Jurado*[5], *O. Kamalou*[1], *A. Lemasson*[1], *S.M. Lukyanov*[8], *W. Mittig*[3,9], *D.J. Morrissey*[3,10], *A. Navin*[1], *J. Pereira*[3], *L. Perrot*[4], *M. Rejmund*[1], *T. Roger*[1], *M.G. Saint-Laurent*[1], *H. Savajols*[1], *C. Schmitt*[1], *B.M. Sherrill*[3], *C. Stodel*[1], *J. Taieb*[7], *J.C. Thomas*[1] *and A.C.C. Villari*[11]

[1] GANIL, CEA/DSM-CNRS/IN2P3, BP 55027, F-14076 Caen cedex 5, France
[2] Univ. de Santiago de Compostela, E-15706 Santiago de Compostela, Spain
[3] NSCL, Michigan State University, East Lansing, MI 48824, USA
[4] Institut de Physique Nucléaire, CNRS/IN2P3, F-91406 Orsay, France
[5] CENBG, UMR 5797 CNRS/IN2P3, Université Bordeaux 1, F-33175 Gradignan, France
[6] University of Vigo, E-36310, Spain
[7] CEA, DAM, DIF, F-91297 Arpajon, France
[8] FLNR, JINR, 141980 Dubna, Moscow region, Russian Federation
[9] Dep. of Physics and Astronomy, Michigan State University, East Lansing, MI 48824, USA
[10] Dep. of Chemistry, Michigan State University, East Lansing, MI 48824, USA
[11] PANTECHNIK S.A., 13, rue de la Résistance, 14400, Bayeux, France

Abstract

Two fission experiments have been performed at GANIL using ^{238}U beams at different energies and light targets. Different fissioning systems were produced with centre of mass energies from 10 to 240 MeV and their decay by fission was investigated with GANIL spectrometers. Preliminary fission-fragment isotopic distributions have been obtained. The evolution with impinging energy of their properties, the neutron excess and the width of the neutron-number distributions, gives important insights into the dynamics of fusion-fission mechanism.

1 Introduction

The binding energy of the nucleus can be estimated in the framework of the liquid-drop model including shell effects and pairing. Produced in heavy ions collision, the compound nucleus has a certain excitation energy. Assessing the evolution of potential energy with the deformation of a fissioning nucleus, fission-fragment mass yields can be estimated [1]. Before reaching the saddle point, the compound nucleus may release a part of its excitation energy by evaporating particle. At saddle point, the remain excitation energy defines the potential energy landscape which influences the fission-fragment distributions. Therefore, the study of the properties of these distribution may reveal some informations about the formation and the deexcitation of the compound nucleus.

The use of inverse kinematics to measure the atomic number of all the fission fragments has been developed at GSI in the 1990s [2]. Previously, the charge of the heavy fragments was rather difficult to determine. Using a spectrometer allows to measure in the same time the mass of the fragments.

2 Experiments

Two different experiments have been performed at GANIL, using ^{238}U beams at different energies impinging ^{12}C or ^{9}Be targets. Depending on the impact parameter, different actinides are produced by transfer or fusion reactions, giving access to a broad excitation-energy regime. The fission-fragment distributions of these actinides were investigated using two spectrometers, VAMOS [3] and LISE [4], for the low-energy and high-energy experiments, respectively.

2.1 Specific features of the experiments

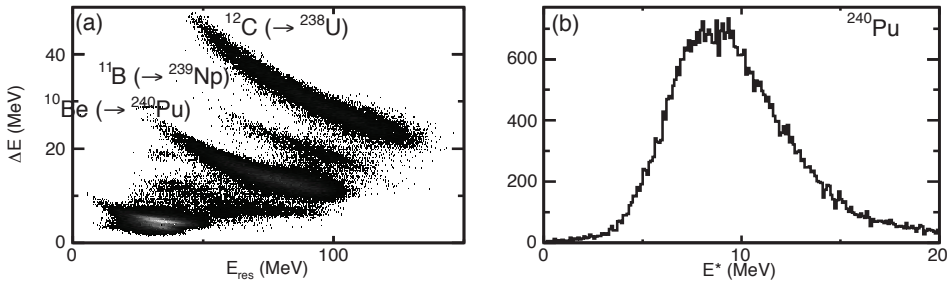

Fig. 1: (a) Energy loss (ΔE) of recoil nuclei as a function of their residual energy (E_{res}). (b) Excitation energy spectrum for ^{240}Pu.

In the first experiment, the beam impinged on a thin ^{12}C target with an energy of 6.1 A MeV. At this energy, transfer reactions represent about 10% of the total cross section [5]. The actinides produced by transfer reactions were tagged by the detection and the identification of the target recoils in a highly segmented annular silicon telescope, SPIDER [6], as shown in figure 1 (a). The excitation energy of the actinides produced by transfer reaction was determined from the angle and the energy of the target recoil assuming a two-body kinematics. The excitation energy distribution was measured with a mean value around 9 MeV (see figure 1 (b)). In this work, the two-proton transfer channel, i.e. the production of ^{240}Pu, is studied. A tiny beam-energy straggling into the thin target (0.1 mg/cm^2) led to the production of compound nuclei in fusion reaction with E*=45.4±0.3 MeV. In the case that fission occurred, one of the two fission fragments was identified with the VAMOS spectrometer.
In a second experiment at LISE, a ^{238}U beam of 24 A MeV has been used. Thick carbon and beryllium targets (15 mg/cm^2 for both targets) were used, which resulted in considerable beam-energy straggling. The centre of mass energy ranged from 164 to 208 MeV with the beryllium target, and from 210 to 274 MeV with the carbon target.

In summary, different fissioning systems with 4 different excitation energies are investigated: ^{240}Pu with E*≈9 MeV (VAMOS), ^{247}Cm with $E_{CM} \approx 185$ MeV (LISE) and ^{250}Cf with E*=45 MeV (VAMOS) and $E_{CM} \approx 240$ MeV (LISE).

2.2 Identification of fission fragments

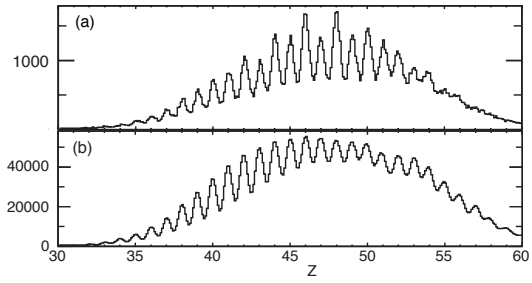

Fig. 2: Distribution of the fission-fragment atomic number Z for both experiments (the full data set for ^{250}Cf is presented). The resolutions are 1.6% for LISE experiment (a) and 1.7% for VAMOS experiment (b).

The fission-fragment identification was based in both experiments on the Bρ-ToF-ΔE-E technique [7], where Bρ is the magnetic rigidity of the fragment, ToF its time of flight through the spectrometer and E its total kinetic energy. The identification of the atomic number Z was obtained from energy-loss measurements. The atomic number distribution is shown in figure 2 for both experiments.

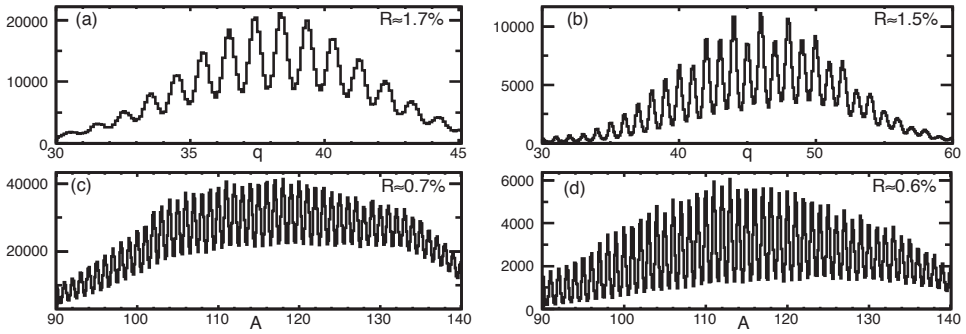

Fig. 3: Ionic charge state q and mass A distributions measured from the fission of ^{250}Cf in VAMOS (a) and (c) and in LISE (b) and (d), respectively. Resolutions R are indicated in figures.

From the measurement of positions at the focal plane, the path and the radius of curvature, ρ, were determined [7]. The measurement of ToF gave the ion velocity v. The radius of curvature is related to the velocity by the relation Bρ = Av/q, where B is the magnetic field applied to the dipoles of the spectrometers, A the mass of the ion, and q its ionic charge state. From Bρ and v measurements, the ratio A/q was determined. The mass, A_E, can also be derived using the velocity and the energy. The ionic charge state is then determined as $q=\frac{A_E}{A/q}$ (see figure 3 (a) and (b)). Finally, the mass A was obtained multplying A/q by the integer value of q (see figure 3 (c) and (d)). At VAMOS, a γ-ray detector located in the target region was used to validate the spectrometer identification [8] and at LISE the γ-ray detectors were installed at the focal plane and measured isomeric decay of fission fragments.

3 Fission yields

To determine isotopic fission yields Y(Z,A), the first step is the reconstruction of the momentum distribution for each ionic charge state, using different Bρ settings of the spectrometer. The different runs are normalised to the beam intensity using the elastic scattering of the target in SPIDER in the case of VAMOS experiment. A precision of 10% is obtained. In the case of the LISE experiment, the beam intensity was measured with a Faraday cup before and after each run.

3.1 Normalisation and spectrometer acceptance correction

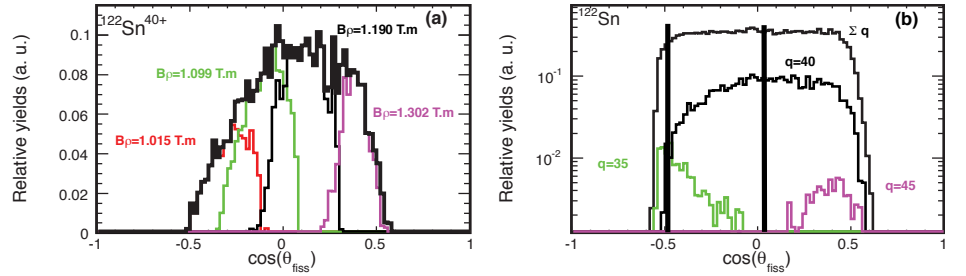

Fig. 4: (a) Angular distribution of the ion ^{128}Sn^{42+} (colour online). Angular distributions for different Bρ settings are plotted in colour. The total angular distribution was obtained taking the envelope of all the settings. (b) Angular distribution in the frame of the fissioning nucleus θ_{fiss} summing all ionic charge state contributions (colour online).

The acceptance of the spectrometer has been converted in the reference frame of the fissioning nucleus, where the kinematical properties and angular distributions are well known. Several Bρ values were needed to cover the angular distribution shown on figure 4 (a). The distributions were corrected by the azimuthal angle φ acceptance and normalised to the beam intensity. The acceptance on φ depends on the value of the polar angle θ and the magnetic rigidity Bρ [7]. Thus, the correction was applied on an event per event basis, for each value of θ and Bρ of the fragments. Considering the envelope spectrum — shown as a black line in figure 4 (a) — a first estimation of the yield Y_0(Z,A,q) for each ion was obtained. The isotopic yield estimation is given by $Y_1(Z,A) = \sum_q Y_0(Z,A,q)$. Finally, Y_1 was corrected following θ using the relation $Y(Z,A) = Y_1(Z,A)\frac{2}{\int_{\theta_{fiss,min}}^{\theta_{fiss,max}} \sin\theta d\theta}$. The angles θ_{min} and θ_{max} correspond to the range for which the angular distribution is not cut by the spectrometer acceptance. This range is determined by comparing the kinematics of each ion to the limits of the spectrometer acceptance as presented in figure 5.

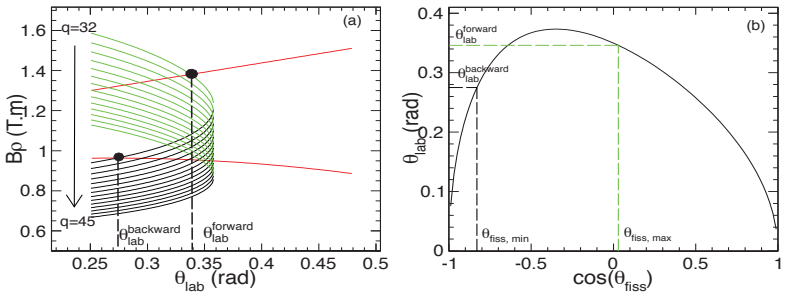

Fig. 5: (a) Kinematics of the different charge state of ^{122}Sn. Green curves correspond to the forward angles, blue ones to the backward angles and red ones to the limits of the acceptance that we measured (colour online). The intersections between the kinematics curve of $^{122}Sn^{32+}$ with the acceptance limits are represented by two black points. (b) Evolution of θ_{lab} as a function of $\cos(\theta_{fiss})$ (in black). The values $\theta_{fiss,min}$ (in blue) and $\theta_{fiss,max}$ (in green) associated respectively to the backward and the forward angles are shown.

The forward (in green) and the backward (in blue) kinematics of the different charge states of ^{122}Sn, from q=32 and q=45, are plotted. In the reference frame of the laboratory, the angle $\theta_{\text{lab}}^{\text{forward}}$ and $\theta_{\text{lab}}^{\text{backward}}$ are determined for each ion. They correspond to the intersection of the kinematics line with the spectrometer acceptance, shown in red in figure 5 (a). The transformation of these limits in the frame of the fissioning nucleus gives us the angular interval $(\theta_{fiss,min}, \theta_{fiss,max})$ in which the ion is measured without any cut (see figure 5 (b). For each isotope, the smallest interval among all the charge state correspond to the region of the angular distribution which is not cut by the acceptance. This range is plotted in blue in figure 4 (b) for the example of ^{122}Sn.

To correct the data of the LISE experiment from the spectrometer acceptance, a simulation based on the fission kinematics proposed by Wilkins was used [9]. We modelled also the charge state distribution to reproduce the measured one from the Schiwietz parametrisation [10]. Considering a square acceptance of 1° in angle and 0.8% in magnetic rigidity, we determine from the simulation the correction factor as the ratio between the number of ion produced and the number of ions transmitted. The methods that we used to get the yields and to correct the transmission are presented in detail in [11].

3.2 Preliminary results and discussion

Following the methods described above, isotopic yields were obtained for the four different fissioning systems investigated, and for the complete fragment production. In the following, the main characteristics of the isotopic distributions, namely the neutron excess defined as the ratio of the mean neutron

number value $\langle N \rangle$ over Z and the neutron-number width $\sigma(N)$ are studied.

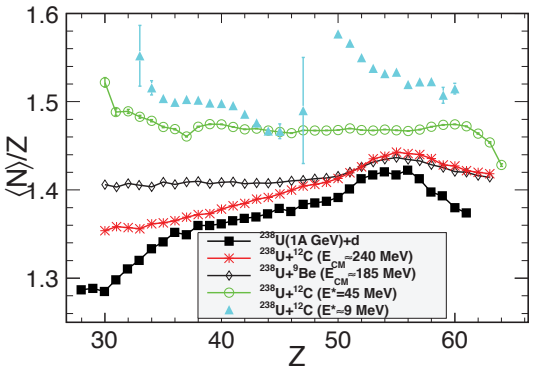

Fig. 6: Neutron richness $\langle N \rangle / Z$ as a function of the fission fragments atomic number Z for different systems (colour online).

Figure 6 shows the evolution of the mean neutron excess, $\langle N \rangle / Z$, with the fission-fragment atomic number Z for the different fissioning systems and different excitation energies. At low excitation energy (triangles), light fragments exhibit lower $\langle N \rangle / Z$ values than heavy ones. This can be understood as the result of the minimisation of the total potential energy of the emerging fragments: an excess of neutrons in the heavy fragments lowers the influence of the Coulomb energy contribution and symmetry energy in the total potential energy [9]. This trend is enhanced by shell effects around Z=50. For the fission of ^{250}Cf produced at 45 MeV (circles), $\langle N \rangle / Z$ gives a constant value of 1.47, which is consistent with the N/Z ratio of ^{242}Cf. This would mean that 8 neutrons in total would be evaporated by the compound nucleus and the fission fragments, independently of the mass of the fission fragment. At higher centre of mass energy (greater than 160 MeV) (diamonds and asterisks), the $\langle N \rangle / Z$ ratio decreases as the centre of mass energy increases, indicating more evaporated neutrons. A hump is formed around Z≈54. This can be understood as the effect of different entrance channels with different excitation energies. At high bombarding energy, pre-equilibrium particles emission may occur before the formation of the compound nucleus and consequently, the different compound nuclei are produced over a range of A and E*. Fission at a low excitation energy induces the hump around Z≈54 from shell effects which stabilise the mass and atomic-number distributions of heavy fission fragments [12]. This trend is confirmed by data from spallation-fission reactions performed at GSI [13], for ^{238}U at 1 A GeV impinging on a deuterium target (squares).

Figure 7 shows the width of the isotopic distribution $\sigma(N)$ as a function of the fission-fragment atomic number for the same fissioning systems. From statistical description of the fission process, $\sigma(N)$ is expected to increase with the temperature T and with the mass A [14], in agreement with the present data. The large energy straggling existing in the highest energy reactions certainly contributes to enlarge the distributions. Likewise for $\langle N \rangle / Z$, a large increase of the width is observed around Z≈54 at high bombarding energy, which most likely reflects the presence of different entrance channels with different excitation energies.

The fragments from the fission of ^{250}Cf produced at E*≈45 MeV show a different behaviour, with constant $\langle N \rangle / Z$ and a regular increase in $\sigma(N)$. In this reaction, shell effects are expected to be weak and entrance-channel effects to be limited. Thus, a liquid-drop behaviour is expected, i.e. $\langle N \rangle / Z$ at scission is expected to increase steadily with Z [15]. The observed constant value of $\langle N \rangle / Z$ with Z suggests that heavy fission fragments evaporate more neutrons than light ones and compensate exactly the neutron excess of fragments at scission. The absence of shell-gap influence, supported by the lack of

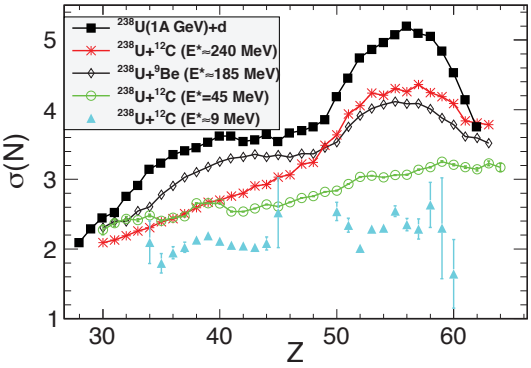

Fig. 7: The width of the neutron-number distribution $\sigma(N)$ as a function of the fission fragments atomic number Z for different systems (colour online).

hump in the evolution of $\sigma(N)$ with Z, puts forward that the compound nucleus has no time to evaporate neutrons before reaching the saddle deformation, i.e. first-chance fission is highly probable, as was already suggested in the study of similar fissioning systems at similar excitation energy [16].

4 Conclusion

The technique of the inverse kinematics combined with a spectrometer is a powerful tool to investigate fission-fragment distributions. The complete isotopic fission-fragment yields are measured for different fissioning systems at different excitation energies. The production of neutron-rich fission fragments reveals to be a complex process where the influence of the entrance channel effects is decisive. The neutron-excess degree of freedom shows to be very powerful in gaining information about time scales and dynamics of low-energy nuclear reactions. In particular, the present results indicate that at moderate excitation energy the compound nucleus reaches the saddle deformation before any significant cooling by neutron evaporation, and that the fission fragments release the remaining excitation energy.

References

[1] Goutte H. *et al*., *Phys. Rev. C* **71** (2005) 024316.
[2] Bernas M. *Nucl. Phys. A* **616** (1997) 352 - 362.
[3] Savajols H. *et al*., *Nucl. Instr. and Meth. B* **204** (2003) 146 - 153.
[4] Anne R. *et al*., *Nucl. Instr. and Meth. A* **257** (1987) 215 - 232.
[5] Biswas D. C. *et al*., *Phys. Rev. C* **56** (1997) 1926 - 1935.
[6] Derkx X. *et al*., EPJ Web of Conferences, 2010, 2, 07001 CNR09 - Second International Workshop on Compound Nuclear Reactions and Related Topics - Bordeaux, France
[7] Pullanhiotan S. *et al*., *Nucl. Instr. and Meth. A* **593** (2008) 343 - 352.
[8] Shrivastava A. *et al*., *Phys. Rev. C* **80** (2009) 051305.
[9] Wilkins B.D. *et al*., *Phys. Rev. C* **14** (1976) 1832.
[10] Schiwietz, G. and Grande, P. *Nucl. Instr. and Meth. B* **175 - 177** (2001) 125 - 131.
[11] Delaune O. (2012), *Thèse de l'Université de Caen Basse-Normandie*
[12] Böckstiegel, C. *et al*., *Nucl. Phys. A* **802** (2008) 12 - 25.
[13] Pereira J. *et al*., *Phys. Rev. C* **75** (2007) 014602.
[14] Yuri T.S. Oganessian and Yuri A. Lazarev, *Treatise on Heavy-Ion Science 4*, Plenum Press New York, 1985
[15] Berlanger M. *et al*. Z. Phys. A **291** (1979) 133 - 143
[16] Rubehn Th. *et al*., *Phys. Rev. C* **54** (1996) 3062 - 3067.

Fission Dynamics of Compound Nuclei

Yoritaka Iwata and Sophia Heinz
GSI Helmholtzzentrum für Schwerionenforschung, Darmstadt, Germany

Abstract
Collisions between ^{248}Cm and ^{48}Ca are systematically investigated by time-dependent density functional calculations with evaporation prescription. Depending on the incident energy and impact parameter, fusion, deep-inelastic and quasi-fission events are expected to appear. In this paper, possible fission dynamics of compound nuclei is presented.

1 Introduction

The synthesis of superheavy chemical elements [1,2] in the laboratory is one of the biggest challenges in nuclear physics. It is an attempt for clarifying the existence limits of all the chemical elements, as well as the completion attempt of the periodic table of chemical elements. We are concerned with heavy-ion collisions

$$^{248}\mathrm{Cm} \ + \ ^{48}\mathrm{Ca}$$

with different impact parameters in this paper. Let A and Z be the mass number and the proton number, respectively. The neutron number N is defined by $N = A - Z$, so that N/Z of ^{248}Cm and ^{48}Ca are 1.58 and 1.40, respectively. If fusion appears, ^{296}Lv (= $^{296}116$) with $N/Z = 1.55$ is produced.

Fast charge equilibration [3] is expected to appear in low-energy heavy-ion reactions with an incident energy of a few MeV per nucleon. It provides a very strict limitation for the synthesis of superheavy elements. Actually, the N/Z of final product is not above nor below the N/Z of the projectile and the target ($1.40 \leq$ N/Z ≤ 1.58 in this case) in the case of charge equilibration, so that the proton-richness of the final product follows. Although the actual value of N/Z depends on the two colliding ions, its value for the merged nucleus tends to be rather proton-rich for a given proton number of the merged system. This feature is qualitatively understood by the discrepancy between the β-stability line and the $N = Z$-line for heavier cases. Superheavy compound nuclei are very fragile and fission is a very frequent channel which leads to disintegration of the compound nuclei even at low excitation energies. In this paper, following the evaporation prescription shown in Ref. [4], a possible fission dynamics of compound nuclei is simulated based on the time-dependent density functional theory (TDDFT).

2 Methods

2.1 Treatment of the thermal property

Self-consistent time-dependent density functional calculations are employed in this paper. TDDFT reproduces the quantum transportation due to the collective dynamics. In this sense, what is calculated by the TDDFT can be regarded as products after several 10^{-21} s, which corresponds to a typical time-scale of low-energy heavy-ion reactions (1000 fm/c), as well as to the inclusive time interval of any collective oscillations such as giant dipole resonance, giant quadrupole resonance and so on. Meanwhile, thermal properties such as the thermal instability are not directly taken into account in TDDFT. Indeed, the Skyrme type interaction used in TDDFT (for example, see Ref. [5]) is determined only from several densities. It is important that the most effective cooling effect arises from the emission of particles, and therefore it is expected that the break-up or fission of fragments including rather high internal excitation energy is suppressed in the TDDFT final products. The additional thermal effects leading to the break-ups of fragments should be introduced.

Here is a fact that simplifies the treatment of thermal effects, that is, the difference of the time-scales. Different from the typical time scale of low-energy heavy-ion reactions, the typical time-scale

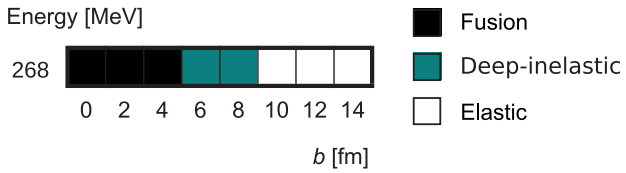

Fig. 1: (Colour online) Diagram of different reaction channels obtained in $^{48}\mathrm{Ca} + ^{248}\mathrm{Cm}$ collisions by TDDFT calculations. The preferred reaction channels for different beam energies and impact paramters are given. The beam energies are all located above the Coulomb barrier which is 209.0 MeV. The results show fusion, deep-inelastic and elastic events. The difference between fusion-fission and quasi-fission is defined in this paper by whether the fission products satisfy "1.40 $\leq$ N/Z $\leq$ 1.58" or not.

of the thermal effects is estimated by the typical time interval of collision-fission (fission appearing in heavy-ion collisions): several 10^{-19} s. It is reasonable to introduce an evaporation prescription simply to the TDDFT final products. In this context the TDDFT final fragments have the meaning of products just after the early stage of heavy-ion reactions (several 10^{-21} s).

2.2 Evaporation prescription

In complete fusion reactions the cross-section for the formation of a certain evaporation residue is usually given by three factors [6]:

$$\sigma_{ER}(E_{cm}) = \sum_J \sigma_{CP}(E_{cm}, J) \times P_{CN}(E_{cm}, J) \times P_{SV}(E_{cm}, J) \tag{1}$$

where σ_{CP}, P_{CN} and P_{SV} mean the capture cross-section, the probability for the compound nucleus formation, and the probability for survival of the compound nucleus against fission. All three factors are functions of the centre-of-mass energy E_{cm} and the total angular momentum J, where J can be related with the impact parameter. For light systems P_{CN} and P_{SV} are about unity and $\sigma_{ER} \approx \sum_J \sigma_{CP}$. But in superheavy systems the strong Coulomb repulsion and large angular momenta lead to small values of P_{CN} and P_{SV} and therefore to the small cross-sections of the evaporation residues observed in the experiments. This means, different from light systems, it is necessary to introduce additional thermal effects for the superheavy element synthesis. First, σ_{CP} is sufficiently considered in the TDDFT if we restrict ourselves to a sufficiently high energy exceeding the Coulomb barrier (cf. sub-barrier effects such as tunnelling are not taken into account in the TDDFT). Second, P_{CN} is fully considered in the TDDFT, which is a kind of mass equilibration also related to charge equilibration. Third, P_{SV} whose relative time-scale is by no means equal to the former two probabilities is not satisfactorily considered in the TDDFT. This probability is much more related to thermal effects. Consequently, further consideration is necessary only for P_{SV} as far as the energy above the Coulomb barrier is concerned.

Several factors are included in P_{SV} such as probabilities for fission of the compound nucleus, neutron-evaporation, proton-evaporation, deuteron-evaporation, alpha-particle-evaporation and so on. Probabilities of neutron and α-particle emissions are considered by

$$P_{SV} := (1 - P_{n,evap})(1 - P_{\alpha,evap}).$$

For the details of evaporation prescription, see our preceding research summarized in Ref. [4].

2.3 Fission dynamics

For given energy and impact parameter, long-lived compound nucleus with certain excitation energies (compared to the ground state) are obtained. Fission dynamics is obtained by additional TDDFT cal-

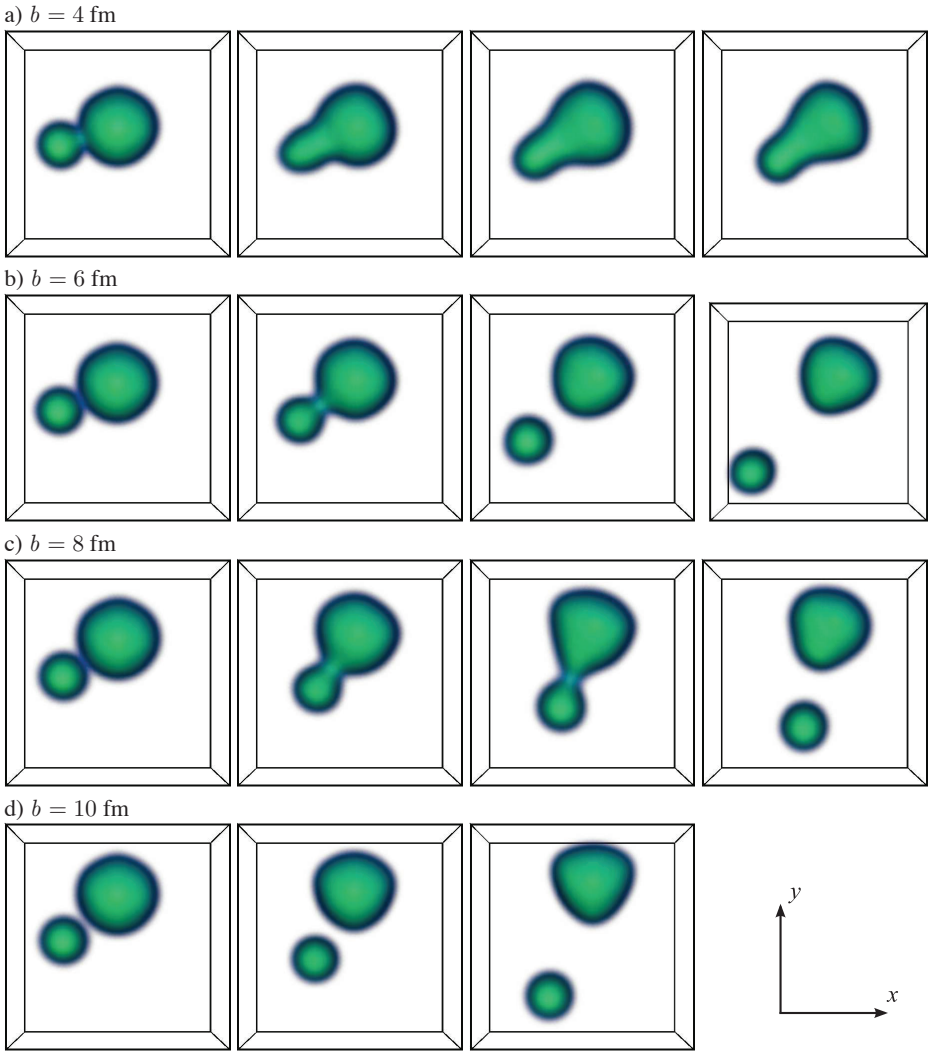

Fig. 2: (Colour online) Time evolution of $^{248}\mathrm{Cm} + ^{48}\mathrm{Ca}$ with a fixed incident energy 268 MeV in the centre-of-mass frame, where a box is fixed to $48\times48\times24$ fm^3. Snapshots at 2.3×10^{-22} s, 8.7×10^{-22} s, 15.1×10^{-22} s and 21.5×10^{-22} s are shown, where a snapshot at 21.5×10^{-22} s is not shown only for $b = 10$ fm. Fusion, deep-inelastic and elastic events appear depending on b. In particular, the life-time of composite nucleus for $b = 6$ and 8 fm is the order of $\times10^{-21}$ s.

culations, where no initial velocity is given. Let us take a residual nucleus of mass number A_R, proton number Z_R and excitation energy E_R. Consider the binary fission:

$$^{A_R}Z_R \rightarrow ^{A_1}Z_1 + ^{A_2}Z_2, \tag{2}$$

where $A_R = \sum_{i=1}^{2} A_i$ and $Z_R = \sum_{i=1}^{2} Z_i$. First, choose A_i and Z_i to determine the heavy-ion reaction being considered. A configuration of the two nuclei at a distance R_0 is prepared as an initial state of additional calculation. Second, choose R_0 such that the excitation energy agrees with that of the compound state found in the collision (Fig. 2), where the energy can be different depending on R_0. Note here that the TDDFT is a theory in which the total energy is strictly conserved, so that the total energy is conserved during the presented fission process. Third, the initial many-body wave function, which is given as a single Slater determinant, consists of single wave functions of two different initial nuclei, where a set of single wave functions are orthogonalized before starting TDDFT calculations (cf. the Gram-Schmidt orthogonalization method). In this way a configuration at the same excitation energy but closer to fission can be obtained; for given A_R, Z_R and E_R. The distance R_0 is uniquely determined for fixed $^{A_1}Z_1$ and $^{A_2}Z_2$.

3 TDDFT calculations for fission dynamics

Time-dependent density functional calculations with a Skyrme interaction (SLy6 [7]) are carried out in a spatial box of $48 \times 48 \times 24$ fm^3 with periodic boundary condition. The unit spatial spacing and the unit time spacing are fixed to 1.0 fm and $2/3 \times 10^{-24}$ s, respectively.

The initial positions of ^{248}Cm and ^{48}Ca are fixed to $(0, b, 0)$ and (-15,0,0), respectively. The initial ^{248}Cm is almost spherical the diameter for x, y, and z directions are 19 fm, 19 fm and 18 fm, respectively. ^{248}Cm (the right hand side on $x-y$-plane) does not have initial velocity on the frame, while the initial velocity parallel to the x-axis is given to ^{48}Ca (the left hand side on $x-y$-plane). The systematic results of TDDFT calculations for a given incident energy (268 MeV) are summarized in Fig. 1. These results, which include many fusion events, provide a quite optimistic view for producing superheavy elements. However, in comparison with experiments, the corresponding fusion cross-section of those low-energy heavy-ion reactions is too high to believe. Consequently, although these TDDFT results are still legitimate to show products just after the early stage of heavy-ion reactions, it is necessary to take into account P_{SV} in order to have comparable results to experiments.

In case of the incident energy 268 MeV, the pure TDDFT results show the following reactions (Fig. 2):

$$^{248}\mathrm{Cm} + ^{48}\mathrm{Ca} \rightarrow ^{296}\mathrm{Lv}$$
$$^{248}\mathrm{Cm} + ^{48}\mathrm{Ca} \rightarrow ^{247}\mathrm{Cf} + ^{49}\mathrm{Ar}$$
$$^{248}\mathrm{Cm} + ^{48}\mathrm{Ca} \rightarrow ^{246}\mathrm{Bk} + ^{50}\mathrm{K}$$
$$^{248}\mathrm{Cm} + ^{48}\mathrm{Ca} \rightarrow ^{248}\mathrm{Cm} + ^{48}\mathrm{Ca}$$

for $b = 4, 6, 8, 10$ fm, respectively. If we take into account the neutron and alpha emissions, they become

$$^{248}\mathrm{Cm} + ^{48}\mathrm{Ca} \rightarrow ^{280}\mathrm{Ds} + 3\alpha + 4n$$
$$^{248}\mathrm{Cm} + ^{48}\mathrm{Ca} \rightarrow ^{238}\mathrm{Pu} + ^{47}\mathrm{Ar} + 2\alpha + 3n$$
$$^{248}\mathrm{Cm} + ^{48}\mathrm{Ca} \rightarrow ^{237}\mathrm{Np} + ^{48}\mathrm{K} + 2\alpha + 3n$$
$$^{248}\mathrm{Cm} + ^{48}\mathrm{Ca} \rightarrow ^{248}\mathrm{Cm} + ^{48}\mathrm{Ca}$$

for $b = 4, 6, 8, 10$ fm, respectively.

Concerning the fission dynamics, here we take the case of $b = 4$ fm. For instance we consider the symmetric fission for ^{296}Lv, which corresponds to the pure TDDFT product. The distance R_0 =11.8 fm

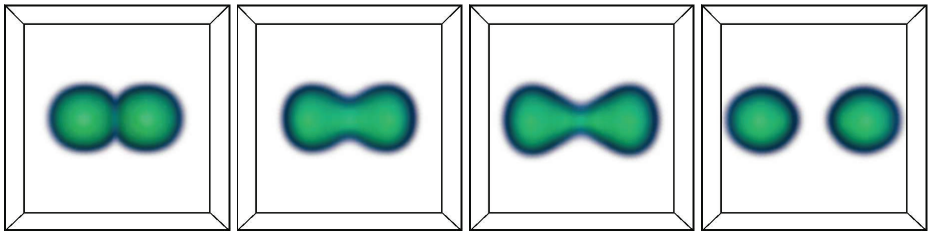

Fig. 3: (Colour online) Symmetric fission dynamics from the compound nucleus, which corresponds to the heavy-ion reaction shown in Eq. (3), is simulated. A calculation box is fixed to $48\times48\times24$ fm^3. Snapshots at 0.0×10^{-22} s, 8.3×10^{-22} s, 16.6×10^{-22} s and 24.9×10^{-22} s are shown. The distance R_0, which is deduced from the excitation energy, is equal to 11.8 fm. Note that the orthogonalization is applied to the initial state before starting TDDFT calculations, because the two initial nuclei are slightly overlapped.

is deduced from the excitation energy of the compound nucleus (^{296}Lv), where trial TDDFT calculations with several R_0 were performed to identify R_0. The fission dynamics

$$^{248}\mathrm{Cm} + {}^{48}\mathrm{Ca} \rightarrow {}^{296}\mathrm{Lv} \rightarrow {}^{148}\mathrm{Ce} + {}^{148}\mathrm{Ce} \tag{3}$$

is shown in Fig. 3. The magnitude of R_0 is related to the difficulty of fission, as well as the total time-scale of fission. In addition R_0 becomes larger for lower incident energies. Note that R_0 can be larger than the touching distance in which case the fission is suggested to be impossible. In this sense this method is applicable to the fission appearing in heavy-ion collisions. Although the duration of fission shown in Fig. 3 is quite short (similar to the typical duration time of low-energy heavy-ion reactions), the additional time is necessary to realize the initial state. The total duration time is expected to be significantly longer than 10^{-21} s, because the initial state shown in Fig. 3, which cannot be realized in the standard TDDFT at the least, cannot be easily realized.

4 Summary

A procedure of obtaining fission dynamics of excited compound nuclei has been presented, where the reproduction of microscopic fission dynamics was a long standing problem in nuclear theory (among a few preceding works on microscopic fission dynamics, see J. W. Negele [8]). The presented method allows us to have a self-consistent treatment of fission dynamics. The obtained dynamics treating the excited states under the strict total energy conservation is diabatic, which is essentially different from the adiabatic fission dynamics.

For the proposed method it is remarkable that the initial condition of fission dynamics is uniquely determined without having any intentional settings; i.e., it is automatically determined for a given set of A_R, Z_R, $^{A_1}Z_1$, $^{A_2}Z_2$ and E_R. As is seen in the comparison between Figs. 2 and 3, the presented fission dynamics is hidden if only pure TDDFT calculations are utilized. In this sense a new point of this method is to choose an ideal configuration (which is rarely realized in most cases if the excitation energy is not so high) as the initial state. As a matter of cause, a different choice of $^{A_1}Z_1$ and $^{A_2}Z_2$ brings about different fission dynamics even from an identical compound nucleus. It is also worth noting that this method with taking into account many different initial conditions can be utilized to distinguish whether fission arising from the collective dynamics can appear or not. Even though the proposed procedure might not be the ultimate solution for investigating fission dynamics, the obtained dynamics actually extracts important aspects of fission dynamics (for example, see the time evolution of the neck).

It was suggested by the calculation shown in Fig. 3 that symmetric fission of the compound nucleus (^{296}Lv) is possible in the collision: $^{248}\mathrm{Cm} + {}^{48}\mathrm{Ca}$ with an incident energy E =268 MeV. The

fission process itself takes only a few 10^{-21} s, but the preformation of the initial state might take significantly longer. The estimation of the total duration time for fission process is a future problem.

This work was supported by the Helmholtz alliance HA216/EMMI. The authors thank Prof. J. A. Maruhn for reading this manuscript carefully.

References

[1] S. Hofmann et al., Eur. Phys. J. **A32** 251 (2007).
[2] Yu. Ts. Oganessian et al., Phys. Rev. **C74** 44602 (2006).
[3] Y. Iwata, T. Otsuka, J. A. Maruhn and N. Itagaki, Phys. Rev. Lett. **104**, 252501 (2010).
[4] Y. Iwata and S. Heinz, J. Phys. Conf. Ser., to appear; arXiv:1208.6215.
[5] W. Greiner and J. A. Maruhn, Nuclear Models, Springer-Verlag Berlin Heidelberg, 1996.
[6] N. V. Antonenko et al., Phys. Lett. **B319** 425 (1993).
[7] E. Chabanat, P. Bonche, P. Haensel, J. Meyer and R. Schaeffer, Nucl. Phys. **A635** 231 (1998); **A643** 441(E) (1998).
[8] J. W. Negele, Rev. Mod. Phys. **54**, 913 (1982).

Excitation Energy Sorting Mechanisms in Fission

P.Talou[1]*, T.Kawano*[1]*, I. Stetcu*[1]*, and M.B. Chadwick*[2]
[1]Nuclear Physics Group, Theoretical Division, Los Alamos National Laboratory, Los Alamos, USA
[2]X-CP, Los Alamos National Laboratory, Los Alamos, USA

Abstract
We explore the excitation energy sorting mechanisms in binary fission that lead to the formation of two excited primary fission fragments, which quickly decay by emitting prompt neutrons and gamma rays. Using Monte Carlo Hauser Feshbach calculations to describe the characteristics of those evaporated particles, we infer significant constraints on the energy partitioning mechanisms at play near the point of scission. The example of the spontaneous fission of ^{252}Cf is used to illustrate this discussion.

1 Introduction

In a binary fission process of a heavy nucleus, two lighter fragments are produced in compound excited states. While the total excitation energy of the system may be known fairly accurately, the partitioning of this energy between the two fragments is a complicated and not fully understood problem. Since no direct observation of the scission process exists, looking at the decay of the primary fragments is certainly the next best thing to do to shed some light on the configurations of the fragments near the scission point. The excited primary fragments do indeed quickly evaporate neutrons and gamma rays until they reach a ground-state or a long-lived isomer. They may further β-decay, but we will ignore those in the current work.

The Hauser-Feshbach statistical theory of nuclear reactions [1] is perfectly suited to describe the de-excitation of the primary fragments, as nuclear fission constitutes perhaps the best example of the compound nucleus formation process. Recently, we have developed a Monte Carlo version [2] of the Hauser-Feshbach theory that tracks individual decay histories following probability laws for the neutron and gamma-ray emissions. An obvious advantage of the Monte Carlo technique over traditional deterministic Hauser-Feshbach codes is that it provides distributions and correlations of the emitted particles in a straightforward manner, and is a clear benefit for the purpose of the present work. It is worth noting, though, that even though the Hauser-Feshbach formalism seems to be well suited for modeling fission fragment decay, some of our recent work points to challenges and puzzles that need to be addressed, given differences between predicted and measured PFNS for n_{th}+^{235}U [3].

2 Energy Balance along the Fission Path

In low-energy fission, the total Q value of the reaction is the sum of the total kinetic energy TKE and the total excitation energy TXE that is later evaporated through the emission of prompt neutrons and gamma rays. If for a given fragmentation, Q and TKE are known, then TXE is also known. This energy is not necessarily fully available to the fragments right at the scission point, as part of it is often stored in deformation energies of the two fragments. The deformation energy is defined as the energy of the fragment in its scission shape minus the energy of the same fragment in its ground-state. These energies, along with excitation from collective modes normal to the fission axis, get quickly transformed and add to the intrinsic excitation energies that the fragments have accumulated in their descent from the saddle to scission points.

It is widely admitted that the deformation energies of the fragments at scission are responsible for the saw-tooth shape of the average prompt neutron multiplicity as a function of fragment mass. The deformation energy is strongly dependent on shell closures in the fragments. The total intrinsic

energy available at scission is shared differently. Recently, Schmidt and Jurado [4] proposed an energy sorting mechanism that maximizes the entropy of the full fissioning system, and follows our conventional understanding of two bodies in thermal contact: energy naturally flows from the hot body to the cold one. If the temperature of the light fragment is higher than the one of its heavy partner, then the excitation energy will go primarily into the heavy fragment. Note that this view implicitly assumes that the system is in equilibrium. In such a scenario, the average excitation energy in the light fragment is obtained as [4]

$$\langle U_l \rangle = \frac{\int dU U \rho_l(U) \rho_h(U_{int} - U)}{\int dU \rho_l(U) \rho_h(U_{int} - U)}, \tag{1}$$

where U_{int} corresponds to the total *intrinsic* excitation energy at scission, before the relaxation of the fragment deformation energies, and $\rho_{l,h}$ are the level densities in the light and heavy fragment respectively.

The purpose of this presentation is to discuss both collective and intrinsic mechanisms in view of prompt fission neutron and gamma-ray data that can be computed through Monte Carlo Hauser-Feshbach calculations.

3 Prompt Neutron and Gamma-Ray Data

Evaporated prompt neutrons take away a lot of excitation energy from the primary fragments but little angular momentum, while gamma rays will remove most of the angular momentum left after the neutron emission phase. The evidence for the emission of neutrons prior to the full acceleration of the fission fragments remains scarce and mostly inconclusive at this point, and has not been considered here.

In Monte Carlo Hauser-Feshbach (MCHF) calculations, the competition between neutrons and gamma rays is readily taken into account (see discussion in next section). However, because of the behavior of the respective transmission coefficients with excitation energy, most neutrons are emitted prior to gamma rays.

Experimental data on prompt neutrons and gamma rays are crucial as they put stringent constraints on the modeling of nuclear configurations near scission. While average quantities such as the average neutron multiplicity $\overline{\nu}$ or the average neutron energy spectrum $\langle \chi \rangle$ can be reproduced fairly well with simplified models (e.g. [5]), more detailed characteristics cannot be reproduced without a deeper understanding and more complex modeling of the evaporation stage. MCHF calculations can indeed predict distributions, e.g., P(ν), P(N_γ), mass- and kinetic energy-dependent quantities, e.g., $\overline{\nu}(A, KE)$, exclusive spectra for given multiplicities, correlations, etc.

Experimental data exist on some of these quantities, and more are needed to fully constrain fission model parameters. However, existing data on P(ν) and $\overline{\nu}(A)$ can already lead to specific conclusions, as discussed below.

4 Monte Carlo Implementation of the Hauser-Feshbach Theory

As mentioned earlier, the statistical Hauser-Feshbach theory of nuclear reactions is ideally suited to describing the evaporation stage of the primary fission fragments. For the excitation energies typically encountered in low-energy fission, only the statistical emissions of neutrons and gamma rays are probable, while the emission of charged particles is strongly hindered by the Coulomb barrier.

The probabilities of emitting prompt neutrons and gamma rays are calculated as

$$P(\epsilon_\gamma) d\epsilon_\gamma \propto T_\gamma(\epsilon_\gamma) \rho(Z, A, U - \epsilon_\gamma), \tag{2}$$

and

$$P(\epsilon_n) d\epsilon_n \propto T_n(\epsilon_n) \rho(Z, A-1, U - \epsilon_n - S_n). \tag{3}$$

The energy-dependent neutron transmission coefficients $T_n(\epsilon_n)$ are obtained from optical model calculations. In the present work, the global optical model potential of Koning and Delaroche [6] is used for all fragments. The gamma-ray transmission coefficients $T_\gamma(\epsilon_\gamma)$ are calculated from gamma-ray strength functions as

$$T_{XL}(\epsilon_\gamma) = 2\pi\epsilon_\gamma^{2L+1} f_{XL}(\epsilon_\gamma), \tag{4}$$

where XL defines the multipole type. In this work, only the three most important multipoles are considered: E1, E2 and M1.

The level density $\rho(U)$ appearing in Eqs. 2 and 3 is represented in the Gilbert-Cameron-Ignatyuk formalism [7, 8]. At the lowest excitation energies, a constant temperature regime dominates while a Fermi-gas representation is used at higher excitation energies. The washing-out of shell corrections with increasing excitation energy is taken into account through an energy-dependent level density parameter. The parity distribution is assumed to be equiprobable in the continuum, while the spin distribution is given by

$$f(J,U) \propto (2J+1)\exp\left\{-\frac{(J+1/2)^2}{2\sigma^2(U)}\right\}, \tag{5}$$

where $\sigma^2(U)$ is the energy-dependent spin cut-off parameter.

Our recent `CGMF` code [2, 11] solves the Hauser-Feshbach equations using the Monte Carlo technique to sample the probability distributions. Earlier works [9, 10] used the Weisskopf approximation, neglecting spin and parity conservations and treating the neutron-gamma competition in a crude way only. Other works [12, 13] use similar techniques, but none implements the Hauser-Feshbach theory as `CGMF` does.

5 Numerical Results

The fission fragments produced in the spontaneous fission of ^{252}Cf are indicated as black squares in Fig. 1 overlying a colored map of the ground-state deformations as calculated in the Finite-Range Droplet Model (FRDM) by Möller *et al.* [14]. The wide range of ground-state deformations observed for the fission fragments has an important impact on the overall form of the prompt fission neutron multiplicity as a function of the fragment mass $\overline{\nu}(A)$. The influence of the double spherical shell closure near $N = 82$ and $Z = 50$ is clearly visible in Fig. 1.

5.1 Level Density and Temperature

In thermodynamical terms, the temperature and level density are related through the entropy S by

$$\frac{1}{T} = \frac{\partial S}{\partial U} = \frac{\partial}{\partial U}\ln\rho(U). \tag{6}$$

Temperatures calculated as a function of excitation energy are shown in Fig. 2a in the case of specific fission fragment pairs produced in the spontaneous fission of ^{252}Cf. The result for the fragment pair (^{102}Zr,^{150}Ce) is qualitatively identical to what was reported by Schmidt and Jurado [4]: both fragments exhibit a constant-temperature regime at the lowest excitation energies, as expected from the Gilbert-Cameron representation used, and the light fragment temperature is significantly higher than the temperature of its heavy partner. However, this situation is reversed in the case of (^{120}Pd,^{132}Te) for which the expected important shell closure brings up the temperature of the heavy fragment higher than its light partner.

Following Schmidt [4], if the total intrinsic excitation energy is shared according to Eq. 1, one can calculate the average intrinsic excitation energies in both fragments. This was done for the same pairs of

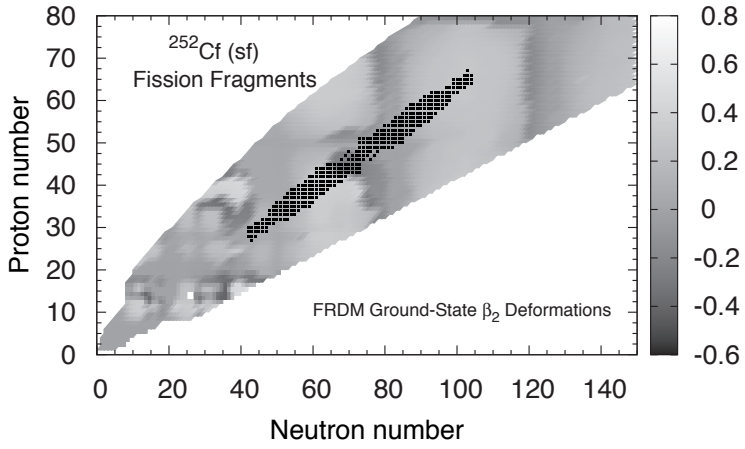

Fig. 1: Nuclear ground-state deformations calculated in the FRDM by Möller *et al.* [14]. The black squares indicate the fission fragments produced in the spontaneous fission of ^{252}Cf.

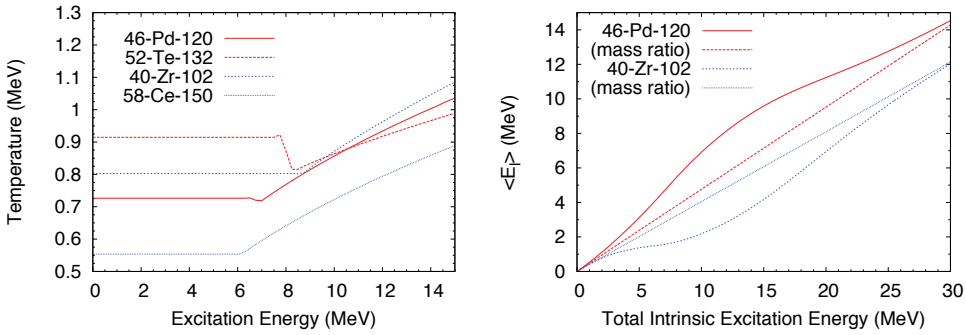

Fig. 2: (a) Nuclear temperatures, as calculated with Eq. 6, as a function of excitation energy for specific fission fragment pairs produced in the spontaneous fission of ^{252}Cf. (b) The average fission fragment excitation energies as a function of the total intrinsic excitation energy are calculated with Eq. 1 following K.-H. Schmidt [4]. "Mass ratio" indicate the results that would be obtained assuming a level density proportional to the mass of the fragment, and an equal temperature between the light and the heavy fragments. Results are similar to what was described in [4], except that the process can be inverted due to strong shell closures, i.e., the temperature in the heavy fragment can be higher than the one in its light partner, as seen for the pair (^{120}Pd,^{132}Te).

fission fragments, and the result is shown in Fig. 2b. Clearly, if correct, the energy sorting mechanism proposed in [4] does not necessarily happen in one direction only, i.e., from the light to the heavy, but can be strongly modulated by the presence of shell effects.

Of course, these results depend on the choice of the systematics used to describe the level density in the fission fragments, in particular near the scission point. Unfortunately, little is known about the nuclear structure of neutron-rich isotopes, and even less about their specific deformations near scission.

5.2 Monte Carlo Hauser-Feshbach Results

The average prompt fission neutron multiplicity as a function of the fragment mass $\overline{\nu}(A)$ was calculated for the spontaneous fission of ^{252}Cf, and is shown in Fig. 3 for two choices of the R_T parameter, which describes the ratio of temperatures in the light vs. heavy fragments T_l/T_h: (a) $R_T = 1.0$ and (b) $R_T(A)$ fitted to reproduce the $\overline{\nu}(A_l)/\overline{\nu}(A_h)$ experimental data.

One can see that the assumption $T_l = T_h$ works very well for very asymmetric fragment pairs, i.e., $A_l \leq 100$ and $A_h \geq 150$, but clearly fails for more symmetric masses. There, more excitation energy has to be transferred to the light fragment at the expense of the heavy fragment. At its most extreme near $A \simeq 130$, the difference between $\overline{\nu}$ calculated with $R_T = 1$ and the experimental data is close to one neutron, which would correspond to about 6 MeV of excitation energy. This difference can be explained by the role of deformation and collective energies of the nascent fission fragments near the scission point. Calculations are under-way to compute those deformation energies from FRDM shape predictions for fragments near scission and in their ground-state.

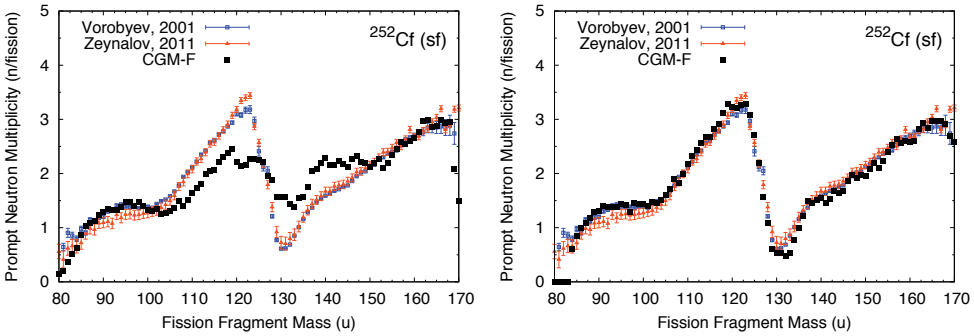

Fig. 3: Average prompt fission neutron multiplicity calculated as a function of the fragment mass $\overline{\nu}(A)$ with (a) $R_T = 1.0$ and (b) $R_T(A)$ chosen to fit the experimental ratio $\overline{\nu}(A_l)/\overline{\nu}(A_h)$.

6 Conclusion

The question of the excitation energy sorting mechanisms between nascent fission fragments was studied through the lens of post-scission data such as prompt fission neutron multiplicity distributions as a function of the fragment mass. Modern Monte Carlo Hauser-Feshbach calculations constitute a powerful tool to study the distributions and correlations of prompt neutrons and gamma rays emitted right after scission.

The role of collectivity versus intrinsic excitation energy sorting near scission was discussed. Deformation energies play a major role in shaping the saw-tooth form of $\overline{\nu}(A)$. The interesting developments brought by Schmidt and Jurado [4] are being studied in the context of actual MCHF calculations. It was shown that energy transfers can happen both ways between the heavy and light fragments, and that shell closures play an important role in the determination of the temperature of the fragments.

References

[1] W.Hauser and H.Feshbach, Phys. Rev. **87**, 366 (1952).
[2] T.Kawano, P.Talou, M.B.Chadwick, and T.Watanabe, J. Nucl. Sci. Tech. **47** (5), 462 (2010).
[3] T.Kawano, P.Talou, and M.B.Chadwick, *submitted to Phys. Rev. C*.
[4] K.-H.Schmidt and B.Jurado, Phys. Rev. Lett. **104**, 212501 (2010).
[5] D.G.Madland and J.R.Nix. Nucl. Sci. Eng. **81**, 213 (1982).

[6] A.J.Koning and J.P.Delaroche, Nucl. Phys. A **713**, 231 (2003).
[7] A.Gilbert, and A.G.W.Cameron, Can. J. Phys. **43**, 1446 (1965).
[8] A.V.Ignatyuk, G.N.Smirenkin, and A.S. Tishin, Yad. Fiz. **21**, 485 (1975).
[9] S.Lemaire, P.Talou, T.Kawano, M.B.Chadwick, and D.G.Madland, Phys. Rev. C**72**, 024601 (2005).
[10] P.Talou, B.Becker, T.Kawano, M.B.Chadwick, and Y.Danon, Phys. Rev. C**83**, 064612 (2011).
[11] B.Becker, P.Talou, T.Kawano, Y.Danon, and I.Stetcu, *submitted to Phys. Rev. C*.
[12] R.Vogt, J.Randrup, J.Pruet, and W.Younes, Phys. Rev. C**80**, 044611 (2009).
[13] O.Litaize and O.Serot, Phys. Rev. C**82**, 054616 (2010).
[14] P. Möller, J.R.Nix, W.D.Myers, and W.J.Swiatecki, At. Data Nucl. Data Tables **59**, 185 (1995).

Measurement of the fission fragment angular distribution for Th-232(n,f) at the CERN n_TOF facility

D. Tarrío[1)], L. Tassan-Got[2)], L. Audouin[2)], I. Duran[1)], L.S. Leong[2)], C. Paradela[1)], S. Altstadt[3)], J. Andrzejewski[4)], M. Barbagallo[5)], V. Bécares[6)], F. Bečvář[7)], F. Belloni[8)], E. Berthoumieux[8,9)], J. Billowes[10)], V. Boccone[9)], D. Bosnar[11)], M. Brugger[9)], M. Calviani[9)], F. Calviño[12)], D. Cano-Ott[6)], C. Carrapiço[13)], F. Cerutti[9)], E. Chiaveri[8,9)], M. Chin[9)], N. Colonna[5)], G. Cortés[12)], M.A. Cortés-Giraldo[14)], M. Diakaki[15)], C. Domingo-Pardo[16)], N. Dzysiuk[17)], C. Eleftheriadis[18)], A. Ferrari[9)], K. Fraval[8)], S. Ganesan[19)], A.R. Garcìa[6)], G. Giubrone[16)], M.B. Gómez-Hornillos[12)], I.F. Gonçalves[13)], E. González-Romero[6)], E. Griesmayer[20)], C. Guerrero[9)], F. Gunsing[8)], P. Gurusamy[19)], D.G. Jenkins[21)], E. Jericha[20)], Y. Kadi[9)], F. Käppeler[22)], D. Karadimos[15)], P. Koehler[23)], M. Kokkoris[15)], M. Krtička[7)], J. Kroll[7)], C. Langer[3)], C. Lederer[3,24)], H. Leeb[20)], R. Losito[9)], A. Manousos[18)], J. Marganiec[4)], T. Martìnez[6)], C. Massimi[25)], P.F. Mastinu[17)], M. Mastromarco[5)], M. Meaze[5)], E. Mendoza[6)], A. Mengoni[26)], P.M. Milazzo[27)], F. Mingrone[25)], M. Mirea[28)], W. Mondalaers[29)], A. Pavlik[24)], J. Perkowski[4)], A. Plompen[29)], J. Praena[14)], J.M. Quesada[14)], T. Rauscher[30)], R. Reifarth[3)], A. Riego[12)], F. Roman[9,28)], C. Rubbia[9,31)], R. Sarmento[13)], P. Schillebeeckx[29)], S. Schmidt[3)], G. Tagliente[5)], J.L. Tain[16)], A. Tsinganis[9)], S. Valenta[7)], G. Vannini[25)], V. Variale[5)], P. Vaz[13)], A. Ventura[26)], R. Versaci[9)], M.J. Vermeulen[21)], V. Vlachoudis[9)], R. Vlastou[15)], A. Wallner[24)], T. Ware[10)], M. Weigand[3)], C. Weiß[20)], T.J. Wright[10)], P. Žugec[11)]*

1) Universidade de Santiago de Compostela, Spain
2) Centre National de la Recherche Scientifique/IN2P3 - IPN, Orsay, France
3) Johann-Wolfgang-Goethe Universität, Frankfurt, Germany
4) Uniwersytet Łódzki, Lodz, Poland
5) Istituto Nazionale di Fisica Nucleare, Bari, Italy
6) Centro de Investigaciones Energeticas Medioambientales y Tecnológicas (CIEMAT), Madrid, Spain
7) Charles University, Prague, Czech Republic
8) Commissariat à l'Énergie Atomique (CEA) Saclay - Irfu, Gif-sur-Yvette, France
9) European Organization for Nuclear Research (CERN), Geneva, Switzerland
10) University of Manchester, Oxford Road, Manchester, UK
11) Department of Physics, Faculty of Science, University of Zagreb, Croatia
12) Universitat Politecnica de Catalunya, Barcelona, Spain
13) Instituto Tecnológico e Nuclear, Instituto Superior Técnico, Universidade Técnica de Lisboa, Lisboa, Portugal
14) Universidad de Sevilla, Spain
15) National Technical University of Athens (NTUA), Greece
16) Instituto de Fìsica Corpuscular, CSIC-Universidad de Valencia, Spain
17) Istituto Nazionale di Fisica Nucleare, Laboratori Nazionali di Legnaro, Italy
18) Aristotle University of Thessaloniki, Thessaloniki, Greece
19) Bhabha Atomic Research Centre (BARC), Mumbai, India
20) Atominstitut, Technische Universität Wien, Austria
21) University of York, Heslington, York, UK
22) Karlsruhe Institute of Technology, Campus Nord, Institut für Kernphysik, Karlsruhe, Germany
23) Oak Ridge National Laboratory (ORNL), Oak Ridge, TN 37831, USA
24) University of Vienna, Faculty of Physics, Austria
25) Dipartimento di Fisica, Università di Bologna, and Sezione INFN di Bologna, Italy
26) Agenzia nazionale per le nuove tecnologie, l'energia e lo sviluppo economico sostenibile (ENEA), Bologna, Italy
27) Istituto Nazionale di Fisica Nucleare, Trieste, Italy

[28] Horia Hulubei National Institute of Physics and Nuclear Engineering - IFIN HH, Bucharest - Magurele, Romania
[29] European Commission JRC, Institute for Reference Materials and Measurements, Retieseweg 111, B-2440 Geel, Belgium
[30] Department of Physics and Astronomy - University of Basel, Basel, Switzerland
[31] Laboratori Nazionali del Gran Sasso dell'INFN, Assergi (AQ),Italy
*Corresponding author: diego.tarrio@usc.es

Abstract

A fission reaction chamber was designed to measure the angular distribution of the fragments emitted in neutron-induced fission reactions at n_TOF. Up to ten Parallel Plate Avalanche Counters can be included and kept at controlled low-pressure gas. Counters are tilted 45º with respect to the neutron beam direction and up to nine targets can be interleaved in between. A first measurement of the ^{232}Th(n,f) was recently done and preliminary experimental results demonstrating the suitability of the setup are presented here.

1 Introduction

Accurate data on neutron-induced reactions at intermediate energies are crucial for different fields in physics. In particular, an accurate knowledge on the reactions involved in the so-called thorium cycle is of relevant interest for improving the existing nuclear energy-related technologies. With the aim of providing accurate values on the cross sections of neutron-induced reactions, an extensive experimental program is being carried out at the n_TOF facility at CERN [1, 2].

One of the experimental setups used at n_TOF for studying fission reactions is a reaction chamber containing Parallel Plate Avalanche Counters (PPACs). During the so-called Phase I (developed between 2002 and 2003), the fission cross section of several nuclei have been measured [3, 4] but, because of the limited angular acceptance exhibited by these detectors, the detection efficiency had to be corrected by the angular distribution of the emitted fragments, according to previous available data in the literature. In order to overcome this difficulty, and to get a simultaneous measurement of the fission cross section and of the angular distribution of the fragments emitted, a new geometrical configuration was developed and firstly used in the 2010 and 2011 campaigns to measure the ^{232}Th(n,f) reaction, demonstrating the suitability of the method described here.

2 Experimental setup

The experiment was performed at the CERN Neutron Time-of-Flight (n_TOF) facility [1, 2], where a very intense neutron flux is available covering a wide energy range, from thermal up to GeV neutrons. The long, 185-m flight path between the spallation target and the experimental area makes it possible to obtain high-resolution time-of-flight (TOF) measurements.

2.1 Parallel Plate Avalanche Counters and targets

The PPACs used in this experiment have a central anode flanked by two cathodes. A low-pressure gas fills the 3-mm gaps between the 1.5-μm aluminized Mylar foil electrodes. The cathodes of each PPAC are segmented in 2-mm wide strips separated 100 μm to provide the spatial position of the hitting. PPAC anode signals are very fast (9 ns width at half maximum), reducing the pileup probabilities and makes it possible to reach energies as high as 1 GeV.

The fission reaction chamber includes 10 PPACs with 9 targets in between, so that the fission events were identified as coincidence signals in the anodes of two consecutive PPACs. The samples used in this experiment have 8 cm diameter and were produced by electrodeposition on an aluminium foil of 0.75 μm thick (six ^{232}Th samples) and of 2.5 μm (for ^{235}U, ^{238}U and ^{237}Np samples). A schematic view of the samples and detectors can be seen in Fig. 1.

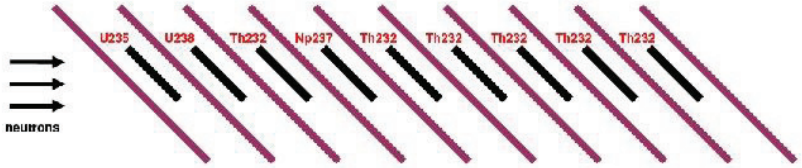

Fig. 1: Schematic view of the PPAC detectors and of the samples used in this experiment.

3 Simulation work

The angular acceptance and the total detection efficiency of this tilted experimental setup were investigated by means of Geant4 simulations, and compared with the situation where the detectors and targets are perpendicular to the beam direction. A simplified version of the real setup was implemented in Geant4, including only two PPAC detectors and one target in between. In order to study the geometrical detection efficiency, we are only interested in the slowing down of the fission fragments in the detection setup, so that we ignore the signal generation in the electrodes.

The event generator produced two complementary fission fragments that are emitted in opposite directions from a random point inside the target volume. The mass and charge of the fission fragments were randomly selected according to a probability distribution given by the fission yield provided by the ENDF/B-VII.1 evaluation [5]. The total kinetic energy released in the reaction was calculated using the Viola's systematic [6] and shared between both fission fragments in an inverse relation accordingly with their masses.

3.1 Detection efficiency

In the case where the PPACs and the target are perpendicular to the neutron beam direction, the distance travelled by the fission fragment inside the material layers is proportional to $\cos\theta$, so that the energy loss is minimal for fission fragments crossing the detectors in the direction of the beam (perpendicular to the detector surface) and it increases until the maximum polar angle θ is reached for the emitted fragments. Since both fission fragments must be detected, the most restrictive case occurs when the heavy fission fragment passes through the backing. Geant4 simulations indicate the maximum angle to be around 65º, as shown in Fig. 2(a), where the detected events are histogrammed as a function of $\cos\theta$ and φ. There is no dependence on the φ angle in this case.

However, in the tilted setup used in the present experiment, the angular range covers all the possible values for $\cos\theta$ between 0 and 1, although there is no axial symmetry in this case, being the efficiency dependent also on the φ angle. The detected events in this case are represented in Fig. 2(b).

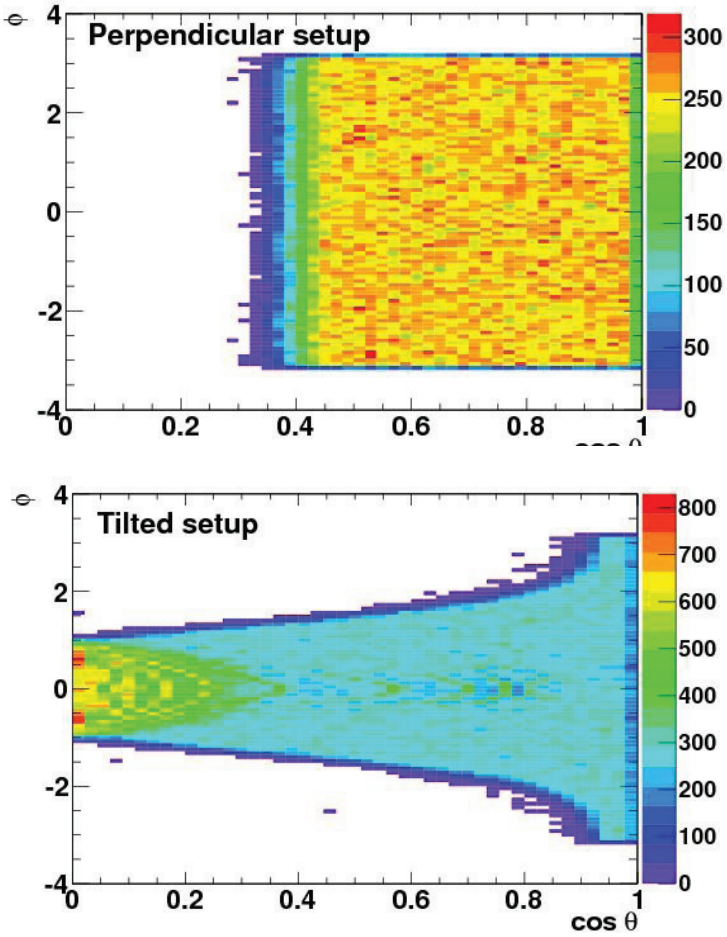

Fig. 2: Detected events as a function of $\cos\theta$ and φ for both geometrical setups: In the perpendicular configuration (Fig. 2(a)), the cosine of the polar angle θ is limited to angles below 65º and does not depend on the azimuthal angle φ around the beam axis. However, in the tilted setup (Fig. 2(b)), the angular acceptance covers all the possible values of θ but the acceptance in the azimuthal angle φ decreases as θ increases.

The detection efficiency, defined as the ratio between the number of detected and generated fission events, is shown in Fig. 3 as a function of $\cos\theta$ for both cases. In the perpendicular setup, the efficiency is very close to 1 for $\cos\theta \geq 0.48$ $(\theta \leq 61^{\circ})$ and drops quickly to zero for larger angles, while the tilted setup presents a non-zero efficiency for all values of θ, even though this is never constant. The fact that it is possible to detect fission fragments emitted at every θ angle converts this geometrical configuration into an excellent experimental setup for measuring fission fragment angular distributions. Despite the different behaviour of the angular acceptance in both cases, the overall detection efficiency is nearly the same (60% for both configurations).

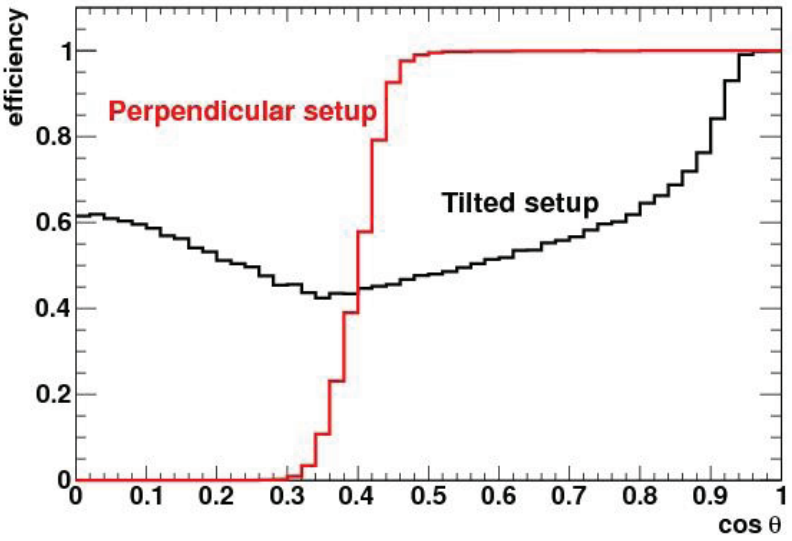

Fig.3: Comparison of the detection efficiency for perpendicular and tilted setups.

4 Data analysis

The detection principle of fission events is based on the detection in coincidence of both fission fragments in two adjacent PPACs in a coincidence window of 10 ns, as it was done in previous experiments [3, 4], rejecting most of the background produced by the α emission of the radioactive samples and by spallation reactions in the materials surrounding the samples. The stripped cathodes provide the spatial position and, therefore, the emission angle θ of the fragments can be calculated.

The fission fragment angular distribution (FFAD) is defined with respect to the cosine of the angle θ between the beam axis and the direction of the fission fragments, assumed to be emitted back to back. The detection efficiency (that is angle-dependent) was calculated by using the data from the ^{235}U (n,f) reaction at low energies measured in the same experiment, since it is well-known to be isotropic. After the efficiency correction, the angular distributions for ^{232}Th were fit to a serie of Legendre polynomials $P_L(\cos\theta)$, according to the expression:

$$W(\theta) = A_0\left[1 + \sum_{\substack{L=0 \\ L\,even}}^{L_{max}} A_L P_L(\cos\theta)\right] \tag{1}$$

where A_L are the fitting coefficients. Only even terms in $\cos\theta$ are used because of the backward-forward symmetry of the emitted fragments. The maximum order L_{max} used for each energy bin was chosen by a χ^2 test. A more detailed description of the analysis and of the results is given in Ref. [7].

5 Results

Two examples of the angular distributions obtained for the neutron-induced fission of ^{232}Th are given. Fig. 4(a) represents an emission peaked in the beam direction, while Fig. 4(b) shows a side-peaked emission with a maximum at 45º and a minimum at 0º. In both cases, fits including up 2nd, 4th, and 6th order polynomials are represented showing that, at least, the 4th order must be included in the fits.

A way to characterize the behaviour of the angular distribution with the neutron energy is the anisotropy parameter, defined as the ratio of the number of fragments emitted along the beam axis with respect to the perpendicular direction: A=W(0º)/W(90º). By inserting Eq. (1), the following analytical expression for the anisotropy parameter is obtained:

$$A = \frac{1 + A_2 + A_4 + A_6 + \ldots}{1 - \frac{1}{2}A_2 + \frac{3}{8}A_4 - \frac{5}{16}A_6 + \ldots} \tag{2}$$

The anisotropy parameter itself only provides information at 0º and at 90º, hiding the behaviour at intermediate angles. The main advantage of this setup is that fragments emitted at every θ angle can be measured, even along the neutron beam direction, thanks to the insensitivity of the PPACs to the neutrons, so that the full angular distribution can be measured.

The anisotropy parameter obtained for ^{232}Th(n,f) in the fission threshold region is represented in Fig. 5. The good agreement with previous data available in EXFOR [8] demonstrates the suitability of this setup to perform this kind of measurements. As it was shown in previous experiments at n_TOF, results up to 1 GeV can be obtained thanks to the excellent time properties of the PPACs. These results for the angular distribution in the whole energy range will be part of a forthcoming publication.

6 Summary and conclusions

A new fission chamber based on Parallel Plate Avalanche Counters tilted 45º with respect to the neutron beam direction was used to measure the angular distribution of the fragments emitted in neutron-induced fission. Preliminary results on the analysis of the first measurement of ^{232}Th(n,f) with this new reaction chamber at n_TOF were shown here, demonstrating the suitability of this setup to perform this kind of measurements. New experiments to measure other isotopes are already scheduled to be done at the n_TOF facility.

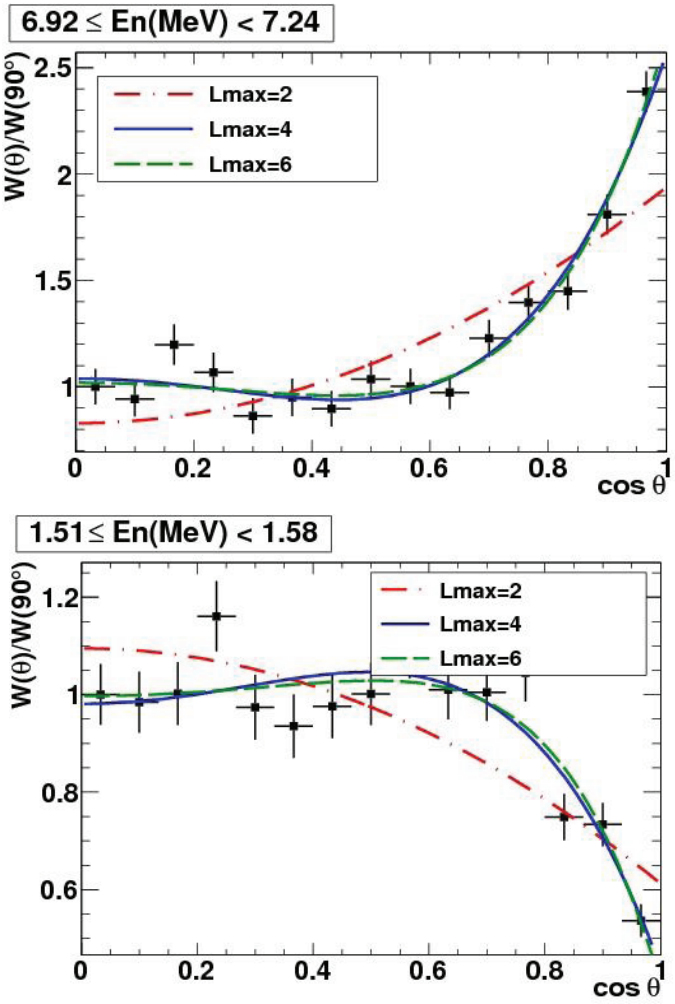

Fig.4: Examples of angular distributions of fragments emitted in neutron-induced fission of ^{232}Th. In Fig. 4(a) most of fission fragments are emitted in the beam direction, while in Fig. 4(b) the maximum of emission is at 45º and the minimum is along the beam direction. In both cases, fits to the 2nd, 4th, and 6th order are drawn.

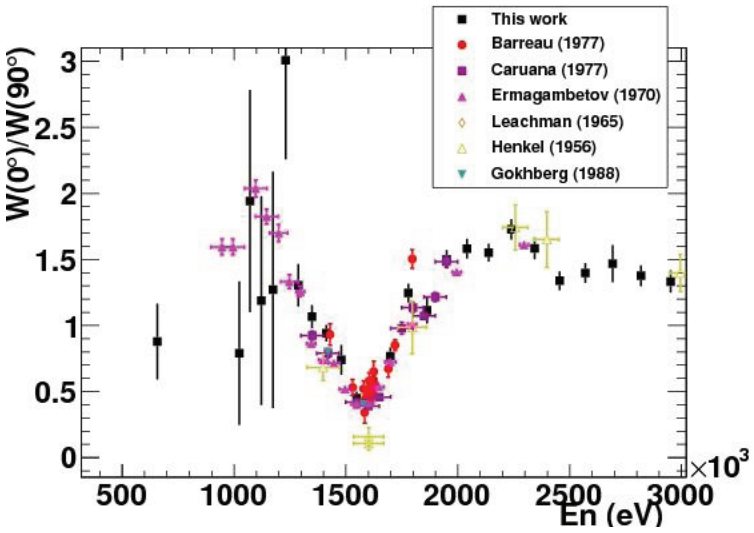

Fig.5: Dependence of the anisotropy parameter on the neutron energy for the ^{232}Th(n,f) reaction in the present experiment (black markers), compared with previous results from other authors.

References

[1] C. Rubbia, S. Andriamonje, D. Bouvet-Bensimon et al. *Proposal for a Neutron Time of Flight Facility*. CERN/LHC/98-02(EET) and CERN/LHC/98-02(EET)-Add. 1 (1998).

[2] The n_TOF Collaboration. European Collaboration for High-Resolution Measurements of Neutron Cross Sections between 1 eV and 250 MeV. CERN/SPSC 99-8 SPSC/P310 (1999).

[3] C. Paradela et al. *Phys*. *Rev*.*C* **82**, 034601 (2010).

[4] D. Tarrío et al. *Phys*. *Rev*. *C* **83**, 044620 (2011).

[5] M. B. Chadwick, M. Herman, P. Oblozinsky et al. *Nucl*. *Data Sheets* **112**, 2887 (2011).

[6] V. E. Viola, K. Kwiatkowski, and M. Walker. *Phys*. *Rev*. *C* **31**, 1550 (1985).

[7] D. Tarrío. *Neutron-induced fission fragment angular distribution at CERN n_TOF: The Th-232 case*. PhD thesis, Universidade de Santiago de Compostela, Spain (2012). Available at: http://igfae.usc.es/~genp/academic/tesis/DiegoTarrio_PhDthesis.pdf

[8] EXFOR (Experimental Nuclear Reaction Data). National Nuclear Data Center (NNDC) (Brookhaven), 2009. http://wwwnds.iaea.org/exfor/exfor.htm

Cluster-gas states in light nuclei

Hisashi Horiuchi
Research Center for Nuclear Physics, Osaka University,Ibaraki, Osaka 567-0047
International Institute for Advanced Studies, Kizugawa, Kyoto 619-0225

Abstract
We first discuss studies of alpha-condensate-like states in ^{12}C including the historical survey of the studies of the Hoyle state to which Morinaga assigned a linear-chain structure [1] of 3α clusters. A very important fact is that the wave function of the Hoyle state by the microscopic 3α cluster model (RGM/GCM) which could have reproduced many experimental data proved to be almost 100% equivalent [2] to a single THSR wave functions [3]. We next discuss studies of 4α-condensate-like states in ^{16}O which have been made by using the THSR wave function and also by OCM approach. The 4α OCM suggested that the 6th 0^+ state at 15.1 MeV excitation energy is a strong candidate of the 4α condensate-like state. We also give discussions on other systems which show the existence of cluster-gas-like states, including the possible existence of excited cluster states having the structures including ^{12}C cluster in Hoyle state.

1 Introduction

This talk is dedicated to Professor M. Kawai. In the graduate course I learned nuclear dynamics through the lectures by Professor Kawai on nuclear reaction. For me, "Nuclear Matter and Nuclear Reaction" by Kikuchi and Kawai has been an important textbook. I learned a theoretical foundation for my AMD study of proton inelastic scattering to continuum by the semiclassical distorted-wave model of proton inelastic scattering to continuum by Professor Kawai and his collaborators. Also for the subject of "cluster-gas states in light nuclei" which I discuss in this talk, I owe very much to Professor Kawai as is exlained in the following. Around 1970, I started my study of the 3α structure of the Hoyle state by the analysis of the reduced α-decay width of the Hoyle state. I noticed the fact that the observed reduced α-decay width of the Hoyle state is much larger than the Wigner limit value. I argued that this fact means the inadequacy of the assignment of 3α linear-chain structure [1] to the Hoyle state [4]. This argument is based on the recognition that the 3α linear-chain structure contains many partial waves than S-wave for the ^{8}Be(0^+) - α relative motion. Since the α-decay of the Hoyle state is only via the S-wave because of the very small Q-value of the decay, the 3α linear-chain structure necessarily gives much smller value than the Wigner limit for the reduced α-decay width of the Hoyle state. Thus the assignment of 3α linear-chain structure to the Hoyle state is in contradiction to the experimental observation. In the process of this investigation of the reduced α-decay width of the Hoyle state, the advices and encouragements by Professor Kawai were very much helpful and useful.

The large reduced α-decay width of the Hoyle state strongly suggests the dominance of the S-wave of the ^{8}Be(0^+) - α relative motion in the Hoyle state. The confirmation of the S-wave dominance was obtained by performing the full three-body calculation of 3α clusters in Ref. [5]. In Fig. 1 we shpw the calculated results of the α-reduced-width amplitudes of the ground state (0^+_1) and the Hoyle state (0^+_2). The large spectroscopic factor S^2 of the Hoyle state confirms the S-wave dominance.

A few yeas after the 3α OCM calculation of Ref. [5], the full microscopic 3α calculations with GCM [6] and RGM [7] methods were reported. They also confirmed the S-wave dominance of the ^{8}Be(0^+) - α relative motion in the Hoyle state. Table 1 shows good reproduction of many data of ^{12}C by Ref. [7]. As shown in this Table, 3α model calculations predicted a large radius of the Hoyle state, in other words a very dilute density of the Hoyle state which is about 1/3 of the ground-state density.

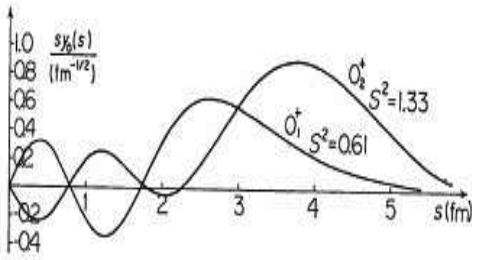

Fig. 1: α-reduced-width amplitudes of the ground state (0_1^+) and the Hoyle state (0_2^+) obtained by the 3α OCM calculation of Ref. [5].

Table 1: Reproduction of the ^{12}C data by 3α calculation of Ref. [7]

	Exp.	Theor.
Excitation energy (0_2^+) (MeV)	7.65	7.74
Width (0_2^+) (eV)	8.7 ± 2.7	7.7
$M(0_2^+ \to 0_1^+)$ (fm^2)	$5.4 \pm 0{,}2$	6.7
$B(E2: 0_2^+ \to 2_1^+)$ (e^2 fm^4)	13 ± 4	5.6
$B(E2: 2_1^+ \to 0_1^+)$ (e^2 fm^4)	7.8	9.3
$R_{\rm rms}(0_1^+)$ (fm)	2.43	2.4
$R_{\rm rms}(0_2^+)$ (fm)		3.37

The Hoyle state was considered to have three distinctive characters: the first is its weak binding energy measured from the 3α breakup threshold, the second is the S-wave dominance of the ^{8}Be(0^+) - α relative motion, and the third is its dilute density. Thus the Hoyle state was regarded as having a gas-like structure of 3α clusters. Actually in Ref. [6], the authors wrote that the Hoyle state could be called α-boson gas.

As we explain in the next section, about 25 years after these 3α cluster model investigations by the use of OCM, GCM, and RGM methods, a new proposal was given which regarded the 3α gas-like structure of the Hoyle state as being a 3α-condensate-like structure.

2 3α-condensate-like structure of the Hoyle state

Our study of α-condensate-like states in finite nuclei started on the excursion boat of the cluster conference at Rab, Croatia, in 1999. Peter Schuck asked me whether there is any possiblity of α-condensate-like structure in finite nuclei. He and Gerd Röpke gave talks on α condensation in nuclear matter at this conference. I explained the 3α cluster-model calculations [5–7] performed in 1970's which concluded that the Hoyle state is a 3α gas-like state with very dilute density.

In our paper [3] published in 2001 we proposed the so-called THSR wave function for expressing the α-condensate-like structure in finite nuclei and by using this THSR wave function we concluded that the Hoyle state can be regarded as having a 3α-condensate-like structure because the energy of the Hoyle state was reproduced quite easily in the vicinity of the 3α threshold. The THSR wave function for the 3α system is given as

$$\Phi_B(3\alpha) = \mathcal{A}\{\exp[-\frac{2}{B^2}(\boldsymbol{X}_1^2+\boldsymbol{X}_2^2+\boldsymbol{X}_3^2)]\ \phi(\alpha_1)\phi(\alpha_2)\phi(\alpha_3)\} \quad (1)$$

$$= \exp(-\frac{6}{B^2}\boldsymbol{\xi}_3^2)\mathcal{A}\{\exp(-\frac{4}{3B^2}\boldsymbol{\xi}_1^2-\frac{1}{B^2}\boldsymbol{\xi}_2^2)\ \phi(\alpha_1)\phi(\alpha_2)\phi(\alpha_3)\}, \quad (2)$$

$$\boldsymbol{\xi}_1 = \boldsymbol{X}_1-\frac{1}{2}(\boldsymbol{X}_2+\boldsymbol{X}_3),\ \boldsymbol{\xi}_2=\boldsymbol{X}_2-\boldsymbol{X}_3,\ \boldsymbol{\xi}_3=\frac{1}{3}(\boldsymbol{X}_1+\boldsymbol{X}_2+\boldsymbol{X}_3). \quad (3)$$

Here $\boldsymbol{X}_i$ and $\phi(\alpha_i)$ stand for the C.M. (center of mass) coordinate and the internal wave function of the i-th α cluster, respectively. As shown in Eq. (2), the THSR wave function can be regarded as expressing the cluster structure where a ^{8}Be(0^+_1)-like cluster $\mathcal{A}\{\exp(-(1/B^2)\boldsymbol{\xi}_2^2)\phi(\alpha_2)\phi(\alpha_3)\}$ and the α_1 cluster couple via S-wave with inter-cluster wave function $\exp(-(4/3B^2)\boldsymbol{\xi}_1^2)$. On the other hand, Eq. (1) shows that the THSR wave function represents the state where three α clusters occupy the same single $0S$-orbit $\exp(-(2/B^2)\boldsymbol{X}^2)$, namely a 3α condensate state which is the finite size counterpart of the macroscopic α-particle condensation in infinite nuclear matter at low density [8]. What the authors of Ref. [3] proposed was that the ^{8}Be(0^+_1) + α structure of the Hoyle state can be regarded as being a 3α condensate-like state and furthermore that one can expect in general the existence of $n\alpha$ condensate-like state in the vicinity of the $n\alpha$ breakup threshold in $4n$ self-conjugate nuclei.

Detailed comparison of the 3α THSR wave function with the 3α GCM and RGM wave functions was reported in Ref. [2]. A very astonishing fact reported in this paper is that each of the 3α GCM and RGM wave functions reported in Ref. [6] and in Ref. [7] has almost 100% overlap with a single THSR wave function:

$$|\langle \text{single THSR w.f.}|3\alpha \text{ RGM/GCM w.f. of Hoyle state}\rangle|^2 \approx 100\%. \tag{4}$$

In view of the complexity of the 3α GCM and RGM wave functions, the equivalence of each of these wave functions with a single THSR wave function which has the simplest form among 3α wave functions is very striking and forces us think that the Hoyle state structure has a strong relation with the α condensation physics in dilute infinite nuclear matter [8].

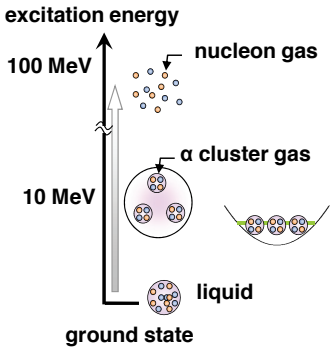

Fig. 2: Excitation energies of α-cluster gas state and nucleon gas state in the case of ^{12}C.

The α-condensate-like state is the lowest-energy state of the α-cluster gas state. In nuclear physics, gas state of nucleons has been an important subject of study for a long time. Such a state has a very high excitation energy and therefore has been a subject of nuclear matter and nuclear reaction rather than nuclear structure. On the other hand, the gas state of clusters is not so highly excited, and can be a discrete state accessible spectroscopically. This situation is shown in Fig. 2. Gas state of clusters is a new concept of nuclear structure and this concept was first proposed for the Hoyle state of ^{12}C in 1970's. However, the discussion at that time was confined only for the Hoyle state. Now after 2000, gas state of clusters is regarded as being universal and is studied in many nuclei both theoretically and experimentally.

The clustering structure in ^{12}C can now be studied without assuming the existence of α clusters by AMD [9] and FMD+UCOM [10] methods. Both methods adopt the 12-nucleon calculation by the use of nuclear force including non-central forces, Therefore the obtained wave functions are no more pure [4]-symmetry states in general, but the the wave function for the Hoyle state in these approaches proved to be a dominantly 3α-cluster state with large radius. Table 2 shows the good reproduction by the AMD calculation of the observed β^+ decay strengths to ^{12}C states from the ground 1^+ state of ^{12}N which are due to the components with broken spatial symmetry of ^{12}C wave function.

Table 2: The experimental data for β decays ^{12}N(β^+)^{12}C compared with the AMD results [9].

States in ^{12}C (MeV)	$J^{\pm}$	$(\log ft)_{\rm exp}$	$(\log ft)_{\rm AMD}$ $(J_f^{\pm})$
0	0^+	4.120 ± 0.003	3.8
4.44	2^+	5.149 ± 0.007	4.8 (2_1^+)
7.65	0^+	4.34 ± 0.06	4.0 (0_2^+)
10.3	(0^+)	4.36 ± 0.17	4.7 (0_3^+)
12.71	1^+	3.52 ± 0.14	3.8 (1_1^+)

3 4α-condensate-like states in ^{16}O

In ^{12}C there are only two states below the 3α threshold, but in ^{16}O there are many states below the 4α threshold. In the case of $T = 0$ and $J^\pi = 0^+$, there are five 0^+ states below the 4α threshold. The second and third 0^+ states are known [11] to have ^{12}C(0_1^+) + α (S-wave) and ^{12}C(2_1^+) + α (D-wave) structures, respectively. The 4α condensate-like state which we expect to be located near the 4α threshold is, of course, orthogonal to all these lower-lying 0^+ states. We can say that the formation of 4α condensate-like state is only possible by the assistance of this orthogonality to the lower-lying states. It is because the orthogonality to the ^{12}C + α states and the ground state works to prevent the 4α condensate-like state from collapsing into more compact configurations of 4α clusters. If we solve full four-body problem of α clusters, this orthogonality requirement to lower-lying states is automatically satisfied.

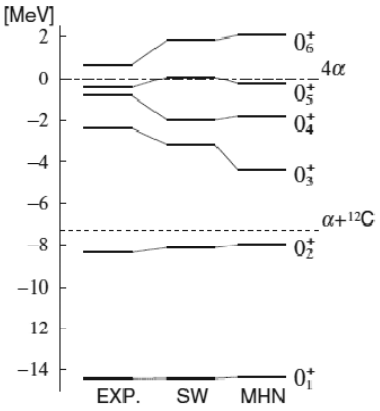

Fig. 3: Energy spectra by 4α OCM [12] with two kinds of effective nuclear force, SW and MHN.

Fig. 3 shows the calculated 0^+ levels by 4α OCM of Ref. [12]. We see that the calculated energies of the lowest six 0^+ states well correspond to the observed energies of lowest six 0^+ states up to the 0_6^+ state at 15.1 MeV. The calculated 0_1^+ has, as its dominant component, the wave function with the lowest total oscillator quanta $N_{total} = 12$. Thus it well corresponds to the ground state. From the analyses of the reduced-width amplitudes of various ^{12}C + α channels, the calculated 0_2^+ and 0_3^+ states proved to have, as their dominant components, the wave functions with ^{12}C(0_1^+) + α and ^{12}C(2_1^+) + α cluster structures, respectively. Therefore the calculated 0_2^+ and 0_3^+ states well reproduce the respective characters of the observed 0_2^+ and 0_3^+ states. As for the calculated 0_4^+ and 0_5^+ states, the analyses of the reduced width amplitudes in various ^{12}C + α channels show that the 0_4^+ and 0_5^+ states have dominantly ^{12}C(0_1^+) + α and ^{12}C(1^-) + α cluster structures, respectively. The assignment of the calculated 0_4^+, 0_5^+ and 0_6^+ states to the observed 0_4^+, 0_5^+ and 0_6^+ states is supported by the good reproduction of decay widths: the widths of the calculated 0_4^+, 0_5^+ and 0_6^+ states are ~ 600, ~ 200, and ~ 140 keV, respectively, while those of the observed 0_4^+, 0_5^+ and 0_6^+ states are 600, 185, and 166 keV, respectively.

Table 3: Partial α decay widths of the 0_6^+ state of the 4α OCM. Observed total width is 166 keV.

	^{12}C(0_1^+)+α (a = 8.0 fm)	^{12}C(2_1^+)+α (a = 7.4 fm)	^{12}C(0_2^+)+α (a = 8.0 fm)	Total
Γ_L (keV)	104	32	8×10^{-7}	136
$\theta_L^2(a)$	0.024	0.016	0.6	

A very important result of the 4α OCM of Ref. 12 is that the calculated 0_6^+ state has a character of 4α-condensate-like state. Figure 4 shows the reduced width amplitudes of various ^{12}C + α channels for the calculated 0_6^+ state defined by

$$y(r) = \langle \frac{\delta(r_{C-\alpha} - r)}{r^2}[Y_L(\hat{r}_{C-\alpha})\phi_L(^{12}C)]_0 \mid \Phi(^{16}O, 0_6^+) \rangle, \quad (5)$$

where $\phi_L(^{12}C)$ is the wave function of ^{12}C given by the 3α OCM calculation [13] with the same effective inter-α interaction. This figure shows clearly that the $y(r)$ has a large amplitude only in the ^{12}C(0_2^+) + α channel whereas the amplitudes in other channels are much suppressed. Since the $y(r)$ in the Hoyle state channel has a very long tail stretching out to about 20 fm and the Hoyle state has a 3α condensate-like structure, one can certainly say that the calculated 0_6^+ state has a character of 4α-condensate-like structure.

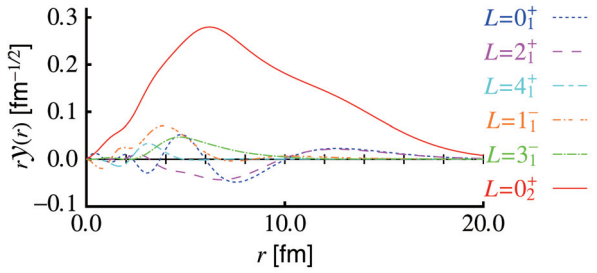

Fig. 4: The reduced width amplitudes defined by Eq. 5 for the 0_6^+ state with the MHN force.

The 4α threshold is about 7 MeV higher than the ^{12}C + α threshold. Thus one may think that the width of a 4α-condensate-like state expected to be around the 4α threshold must have a very large decay width. But as mentioned already, contrary to this conjecture, the width of the calculated 0_6^+ state which has a 4α-condensate-like character has a rather small width of 140 keV. The reason of this small width is simple and two-fold. One reason is the small overlap of the exotic structure of 4α-condensate-like state with the wave functions of ^{12}C + α channels except the Hoyle-state channel ^{12}C(0_2^+) + α. The small overlap is because the ^{12}C states other than the Hoyle state are compact. The other reason is the very small decay Q-value to the Hoyle-state channel, which makes the Coulomb-barrier penetration very small although the overlap of this channel with the 4α-condensate-like state is rather large. We can clearly see in Table 3 that these two reasons explain the small width of the calculated 0_6^+ state. These two-fold reasons are expected to be general and applicable to heavier $n\alpha$-condensate-like states. We can expect that generally the $n\alpha$-condensate-like states will have rather small width in spite of their high excitation energies. Smallness of decay widths can be expected on the basis of our above arguments. Smallness of the spreading width is expected from the very large difference of the structure of the $n\alpha$-condensate-like state from those of the background compound leves with mean-field structures.

In Fig. 5 taken from Ref. [14], we show that the fine structures of the isoscalar monopole strength function in the low energy region up to $E_x \approx 16$ MeV in ^{16}O are rather satisfactorily reproduced within

the 4α OCM. This figure shows that the observed fine structures can be attributed to the 0_3^+, 0_4^+, 0_5^+, and 0_6^+ states.

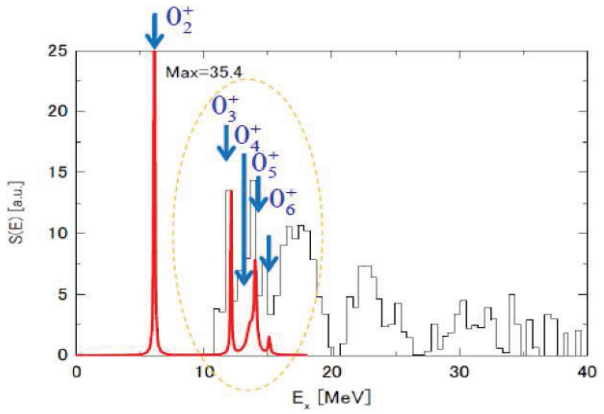

Fig. 5: Calculated isoscalar monopole strength function of ^{16}O (bold line) and experimental data (thin line). In calculating the strength function, theoretical values are used for monopole matrix elements and decay widths of the lowest six 0^+ states, while observed values are used for the excitation energies of the six 0^+ states.

4 Cluster-gas-like states in other nuclei

The third $3/2^-$ state of ^{11}B at Ex = 8.56 MeV and its mirror state in ^{11}C at Ex = 8.11 MeV are now considered to be candidates of the gas-like states which may correspond to the Hoyle state of ^{12}C. They became to attract attention rather recently by many unordinary characters of these states. The third $3/2^-$ state of ^{11}C is excited very weakly at zero degree by high-resolution reaction of ^{11}B(^{3}He, t)^{11}C* implying a very small B(GT) value of this state. This $3/2^-$ state was not reproduced by the recent no-core shell model calculation of Ref. [15] although the B(GT) values of the other populated states well agreed with the calculation of Ref. [15]. Furthermore recently it was found by ^{11}B(d, d') inelastic scattering that the third $3/2^-$ state has a markedly strong monopole transition strength [16]. The unusual properties of the third $3/2^-$ states of ^{11}B and ^{11}C were nicely reproduced by the AMD calculation of Ref. [16, 17]. In The $E0$ strength of the third $3/2^-$ state of ^{11}B, $B(E0$,IS) = 96 $\pm$ 16 fm^4, is of comparable magnitude with the $E0$ strength of the Hoyle state of ^{12}C, $B(E0$,IS) = 121 $\pm$ 9 fm^4. In Ref. [16], it wa noticed that the $E0$ strengths of cluster states in light nuclei including the Hoyle state of ^{12}C are generally comparable to the single-nucleon strength, and it was insisted that the large $E0$ strength of the third $3/2^-$ state of ^{11}B would imply that this $3/2^-$ state is a cluster state related to the Hoyle state. The density distribution of the third $3/2^-$ state by the AMD calculation shows that the third $3/2^-$ state of ^{11}B has a three-cluster structure of $2\alpha + t$ and that the calculated r.m.s. radius of the third $3/2^-$ state of ^{11}B is 3.0 fm and is remarkably larger than that of the ground $3/2^-$ state which is 2.5 fm.

In ^{13}C (^{13}N), the possible cluster-gas-like states of $3\alpha + n$ (p) have been studied by many authors as is reviewd in Ref. [18]. The possiblity of $n\alpha$-gas-like states around the core nuclues such as ^{16}O and ^{40}Ca has been also studied by many authors as is reviewd in Ref. [18]. Sakuragi and his collaborators [19] have discussed molecular resonances of the structures ^{12}C(0_2^+) + C and ^{12}C(2_2^+) + C, where C is ^{12}C(0_1^+), ^{12}C(2_1^+), or ^{12}C(0_2^+). The 4α OCM also suggests the existence of the states around $E_x \approx$ 17 MeV which have the structure of ^{12}C(0_2^+) + α [20].

5 Delocalized motion of clusters in nuclei

As was mentioned already, each of the 3α GCM and RGM wave functions of the Hoyle state has almost 100% overlap with a single THSR wave function. What is very interesting is the fact that each of the 3α GCM and RGM wave functions of the ^{12}C ground state has about 93 % overlap with a single THSR wave function. Recently it was found that the ^{16}O + α RGM/GCM wave function of the ^{20}Ne ground

state has the almost 100% overlap with a single THSR wave function [21].

$$|\langle \text{single THSR w.f.}|^{16}\text{O} + \alpha \text{ RGM/GCM w.f. of G.S.}\rangle|^2 \approx 100\%. \quad (6)$$

This is also true not only for the ground state but also for 2^+ and 4^+ members od the grpond band. These results for non-gas-like states imply that the motion of clusters in non-gas-like states in nuclei is rather delocalized, which is a large contrast to the traditional idea of the geometrical configuration of clusters.

6 Summary

1. 3α cluster model studies in 1970Afs reproduced almost all the observed data of the Hoyle state of ^{12}C and concluded that the Hoyle state has 3α-gas-like structure.

2. 3α cluster model wave function of the Hoyle state proved, after about 25 years, to have about 100 % overlap with a single THSR wave function which expresses α-condensate-like structure.

3. The 6th 0^+ state of ^{16}O has been assigned to have 4α-condensate-like structure by the full 4-body calculation of α-cluster model which reproduced well (i) the excited states which are known to have ^{12}C + α structures, and (ii) observed strength function of the monopole excitation.

4. Cluster-gas-like states are now discussed in many nuclei.

5. Studies of non-gas-like cluster states by using THSR wave functions suggest strongly the importance of delocalized motion of clusters in nuclei which is a large contrast to the traditional idea of the geometrical configuration of clusters.

This talk is dedicated to Professor Kawai. As I explained, I owe very much to Professor Kawai when I startted the study of the Hoyle state in my graduate-course days by analysing the decay width of the Hoyle state which eventually replaced the 3α-linear-chain structure by the S-wave-dominant structure for the Hoyle state. I close my talk by wishing Professor Kawai many more healthy and successful years.

References

[1] H. Morinaga, Phys. Rev. **101**, 254 (1956); Phys. Lett. **21**, 78 (1966).

[2] Y. Funaki, A. Tohsaki, H. Horiuchi, P. Schuck, and G. Röpke, Phys. Rev. C **67**, 051306(R) (2003).

[3] A. Tohsaki, H. Horiuchi, P. Schuck, and G. Röpke, Phys. Rev. Lett. **87**, 192501 (2001).

[4] Y. Suzuki, H. Horiuchi, and K. Ikeda, Prog. Theor. Phys. **47**, 1517 (1972).

[5] H. Horiuchi, Prog.Theor. Phys. **51**, 1266 (1974); **53**, 447 (1975).

[6] E. Uegaki, S. Okabe, Y. Abe, and H. Tanaka, Prog. Theor. Phys. **57**, 1262 (1977); E. Uegaki, Y. Abe, S. Okabe, and H. Tanaka, Prog. Theor. Phys. **59**, 1031 (1978); **62**, 1621 (1979).

[7] Y. Fukushima and M. Kamimura, Supple. of J. Phys. Soc. Japan **44**, 225 (1978); M. Kamimura and Y. Fukushima, Proc. INS Int. Symp. on Nuclear Direct Reaction Mechanism, Fukuoka, Japan, 1978, p.409; M. Kamimura, Nucl. Phys. A **351**, 456 (1981).

[8] G. Röpke, A. Schnell, P. Schuck, and P. Nozières, Phys. Rev. Lett. **80**, 3177 (1998).

[9] Y. Kanada-En'yo, M. Kimura, and H. Horiuchi, C. R. Physique **4**, 497 (2003); Y. Kanada-En'yo, Prog. Theor. Phys. **117**, 655 (2007).

[10] T. Neff and H. Feldmeier, Nucl. Phys. A **738**, 357 (2004); M. Chernykh, H. Feldmeier, T. Neff, P. von Neumann-Cosel, and A. Richter, Phys. Rev. Lett. **98**, 032501 (2007).

[11] Y. Suzuki, Prog. Theor. Phys. **55**, 175 (1976); **56**, 111 (1976).

[12] Y. Funaki, T. Yamada, H. Horiuchi, G. Röpke, P. Schuck, and A. Tohsaki, Phys. Rev. Lett. **101**, 082502 (2008).

[13] T. Yamada and P. Schuck, Eur. Phys. J. A. **26**, 185 (2005).

[14] T. Yamada, Y. Funaki, T. Myo, H. Horiuchi, K. Ikeda, G. Röpke, P. Schuck, and A. Tohsaki, Phys. Rev. C, to be published.

[15] P. Navrátil and E. Ormand, Phys. Rev. C **68**, 034305 (2003).
[16] T. Kawabata et al., Phys. Lett. B **646**, 6 (2007).
[17] Y. Kanada-En'yo, Phys. Rev. C **75**, 024302 (2007).
[18] H. Horiuchi, K. Ikeda, and K. Kato, Prog. Theor. Phys. Supple. **192** 1 (2012).
[19] M. Ito, Y. Sakuragi, and Y. Hirabayashi, Phys. Rev. C **63**, 064303 (2001); Phys. Rev. C **66**, 034307 (2002).
[20] Y. Funaki, et al., private communication.
[21] Bo Z., Z. Ren, C. Xu, Y. Funaki, T. Yamada, A. Tohsaki, H. Horiuchi, P. Schuck, and G. Röpke, Phys. Rev. C. to be published.

Symmetry Energy from Isobaric Analog States

P. Danielewicz
National Superconducting Cyclotron Laboratory Michigan State University East Lansing, Michigan 48824, USA

Extraction of the symmetry energy from systematic of excitation energies to isobaric analog states (IAS) of ground states is discussed. Understanding of the symmetry energy is essential when extrapolating from ïňAąnite nuclei to neutron matter. At diïňĂerent densities, the symmetry energy is explored within nuclear structure and heavy-ion reactions. The IAS systematic allows for an independent assessment of the magnitude and slope of the symmetry energy with density, for uniform matter. In the course of carrying through the assessment, new analytic criteria for stability of systems described by phenomenological Skyrme interactions are derived. Close to 40the literature turn out to produce unstable systems, even when employing only time-even terms within calculations.

Medium-light nuclei beyond the drip line: the proton-emitter ^{17}Na

P. R. Fraser[1,2]*, L. Canton*[1]*, K. Amos*[2,3]*, S. Karataglidis*[3]*, J. P. Svenne*[4] *and D. van der Kniff*[2]
[1] Istituto Nazionale di Fisica Nucleare, Sezione di Padova, I-35131, Italy
[2] School of Physics, The University of Melbourne, Victoria 3010, Australia
[3] Department of Physics, University of Johannesburg, P.O. Box 524 Auckland Park, 2006, South Africa
[4] Department of Physics and Astronomy, University of Manitoba and Winnipeg Institute for Theoretical Physics, Winnipeg, Manitoba, Canada R3T 2N2

Abstract
Measuring radioactive nuclei at or just beyond a drip line is very difficult. Conversely, many have mirror nuclei on or near the valley of stability, where properties are often well known. With a Multi-Channel Algebraic Scattering formalism (MCAS), we predict the spectrum of the proton emitter ^{17}Na by the use of its mirror ^{17}C. Firstly, model parameters are fixed for neutron-nucleus scattering where the compound system has a stable ground state, and then the protons and neutrons are interchanged to examine the unstable system. In the absence of a measured ground state with which to assess the MCAS prediction, we compare with values from mass equations and from systematic trends we have found in known nucleon separation energies of mirror systems.

1 Introduction

The masses of nuclei on and near the "valley of stability" are known, often to high precision, and can be found in the Ame2003 compilation [5] or TUNL project[13] tabulations (for light-mass systems). However, the study of radioactive nuclei is most challenging, especially of those at or just beyond a drip line. Presently, not even the ground state energy of many are known. Few, if any, excited levels have been identified, and the spin-parities of many of the states that are known have not been assigned with certainty. While the advent of radioactive ion beams allows the investigation of such exotic nuclei, theoretical approaches may provide some information in the interim.

We examine here the results of several of the various phenomenological methods available that offer some insight into the masses, using the unmeasured proton emitter ^{17}Na as an example.

2 MCAS study

The experimental observation of ^{17}Na presents a great challenge, with it being beyond the proton drip line. However, the first two eigenstates of ^{16}Ne, which has one proton less, have been measured. Additionally, the mirror to ^{17}Na, being ^{17}C, has also been measured to some extent, as has the nucleus with one less neutron, ^{16}C. Thus, with the MCAS formalism (Multi-Channel Algebraic Scattering) [2] we predict the spectrum of ^{17}Na as resonances of p+^{16}Ne by first setting the model parameters for the mirror system n+^{16}C→^{17}C, and then interchanging protons and neutrons and adding a Coulomb interaction.

MCAS solves the coupled-channel Lippmann-Schwinger equations:

$$T^{J^\pi}_{cc'}(p,q;E) = V^{J^\pi}_{cc'}(p,q) + \mu\left[\sum_{c''=1}^{\text{open}}\int_0^\infty V^{J^\pi}_{cc''}(p,x)\frac{x^2}{k^2_{c''}-x^2+i\epsilon}T^{J^\pi}_{c''c'}(x,q;E)\,dx - \sum_{c''=1}^{\text{closed}}\int_0^\infty V^{J^\pi}_{cc''}(p,x)\frac{x^2}{h^2_{c''}+x^2}T^{J^\pi}_{c''c'}(x,q;E)\,dx\right] \quad (1)$$

and is built upon: realistic nuclear interaction input potentials, $V_{cc'}^{J^\pi}$ (here from a Tamura collective model with rotor character [12]); the separation of these interactions into an 'optimal' set of functions (derived from sturmians) [15]; and constructing scattering matrices (and thus observables) for these interactions:

$$S_{cc'} = \delta_{cc'} \; - \; i^{l_{c'}-l_c+1}\pi\mu \sum_{n,n'=1}^{N} \sqrt{k_c}\hat{\chi}_{cn}(k_c) \left([\boldsymbol{\eta} - \mathbf{G}_0]^{-1} \right)_{nn'} \hat{\chi}_{c'n'}(k_{c'}) \sqrt{k_{c'}} \, , \tag{2}$$

where the Green's function is

$$[\mathbf{G}_0]_{nn'} = \mu \left[\sum_{c=1}^{\text{open}} \int_0^\infty \hat{\chi}_{cn}(x) \frac{x^2}{k_c^2 - x^2 + i\epsilon} \hat{\chi}_{cn'}(x) \, dx - \sum_{c=1}^{\text{closed}} \int_0^\infty \hat{\chi}_{cn}(x) \frac{x^2}{h^2 + x^2} \hat{\chi}_{cn'}(x) \, dx \right] \, , \tag{3}$$

with $\hat{\chi}_{cn}(x)$ determined from sturmian functions as specified in Ref. [2].

The advantages of this method include location of all resonance centroids and widths of the $A+1$ coupled system; determination of all subthreshold bound states using negative energies; and a mechanism to incorporate the Pauli principle, even with targets defined by collective models. The latter is done with orthogonalising pseudo potentials:

$$\mathcal{V}_{cc'}(r, r') = V_{cc'}(r)\delta(r - r') + \lambda A_c(r) A_{c'}(r') \delta_{c,c'} \, , \tag{4}$$

with $V_{cc'}(r)$ being the original potential, $\mathcal{V}_{cc'}(r, r')$ the resultant (non-local) potential which is expanded in a series of separable sturmian terms, and the added orthogonalising pseudo potentials consisting of $A_c(r)$ and $A_{c'}(r')$, the radial components of the single-particle wave functions of occupied states, and λ, a parameter that tunes Pauli-blocking to the level of shell occupancy.

The possibility of incorporating the Thomas-Ehrman shift is provided by the MCAS Hamiltonian formulation, which solves the single-particle equation in the coupled-channel formalism.

The parameters found for the n+^{16}C→^{17}C system, selected to give the best fit for the three measured subthreshold states, are shown in Table 1 (for further details, see Ref. [1]).

Table 1: The MCAS parameter values used to define the channel-coupling properties of the n+^{16}C system. Energy units are MeV, length units are fm.

V_0	V_{ll}	V_{ls}	V_{Is}
-36.7	-2.0	9.0	1.7
R	a	β_2	β_4
2.9	0.8	0.33	0.1
state in		OPP λ_{lj}	
^{16}C	$(1s_{\frac{1}{2}}, 1p_{\frac{3}{2}}, 1p_{\frac{1}{2}})$	$1d_{\frac{5}{2}}$	$2s_{\frac{1}{2}}$
0^+ (ground)	10^6	2.7	0.0
2^+ (1.766)	10^6	2.7	0.0
4^+ (4.142)	10^6	0.0	2.0

The spectrum that resulted is shown in Fig. 1, along with that of experiment (a combination of states listed in Table 4 of Ref. [7] and Fig. 5 of Ref. [11]), and the energies of the ^{16}C states used in the channel coupling. Only positive parity states are known in the low-excitation spectrum. The energies of the experimental spectrum are given relative to the n+^{16}C scattering threshold. Some states specified by Raimann *et al*. [11] are displayed by the dash-dot lines.

Clearly the three known subthreshold (n+^{16}C) states are matched well in energy and spin-parity by the MCAS results. The other known and uncertain spin-parity states also have matching MCAS partners in proximity of their excitation energies. Additionally, the uncertain states from Raimann *et al*. [11] seem

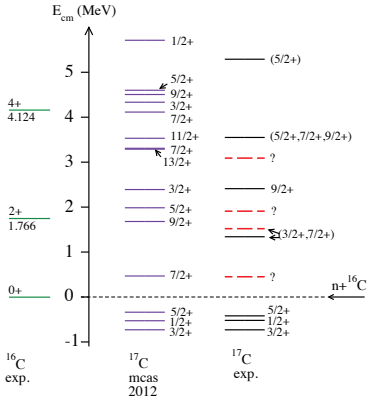

Fig. 1: MCAS results for the spectrum of ^{17}C compared with experimental data. The energy scale is set with the n+^{16}C threshold as zero.

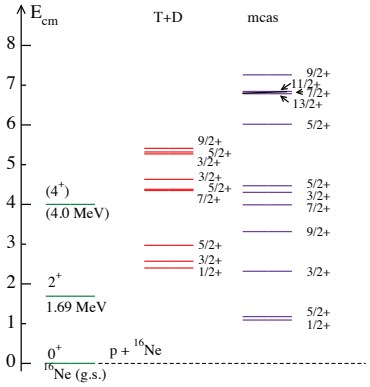

Fig. 2: Results from model evaluations of the spectrum of ^{17}Na. The energy scale is relative to the p+^{16}Ne threshold. See Sec. 3 for T+D levels.

to have possible matches, and the first low-lying state above threshold of that set we expect to be a $\frac{7}{2}^+$ resonance.

These results show two very narrow states of spin-parity $\frac{13}{2}^+$ and $\frac{11}{2}^+$ at 3.82 and 4.16 MeV excitation respectively. These two states are generated by the coupling of the neutron single-particle state with the "geometrical" collective states of ^{16}C, where there are no restrictions on momentum coupling. However, these states would not be found in a simplistic s-d shell model calculation because the maximum coupling in ^{17}C of $\left(d_{\frac{5}{2}}\right)^3$ is $\frac{9}{2}^+$, with the $\frac{11}{2}^+$ only possible as $\left(d_{\frac{5}{2}}\right)^2 d_{\frac{3}{2}}$ [1].

We exchange neutrons for protons to model ^{17}Na as p+^{16}Ne. The Coulomb potential added is derived from a Woods-Saxon charge distribution with the same geometry and deformation as the nuclear interaction. Where the 0^+ and 2^+ states of ^{16}Ne to which we couple the proton are experimentally known, the 4^+ is as yet unobserved, but is included, by symmetry arguments, at an estimated energy of 4 MeV above the scattering threshold. Results of this MCAS study are shown in the right-hand side of Fig. 2, and estimate a ^{17}Na ground state 1.03 MeV above the scattering threshold.

3 Comparison with other methods

Given the unmeasured status of the ^{17}Na ground state, a selection of methods of estimating it are sought in the literature for comparison (though others exist [8]).

A recent study [14] used a microscopic-cluster structure model for n+^{16}C$\rightarrow$ ^{17}C, and also then assumed charge symmetry to study p+^{16}Ne$\rightarrow$ ^{17}Na. The results of that study are shown in the centre column of Fig. 2. The ground state centroid energy (width) was predicted to be 2.4 (1.36) MeV.

Another approach, dating back to the 1950s [16] (and summarized in Ref. [6]), is the use of mass formulae for nuclei within an isobar multiplet. It is characterised by being model-independent. Kelson and Garvey [10] gave a parameter-free formula to relate masses of isobars, namely

$$M(A,T_z=-T)-M(A,T_z=T)=\sum_x\left[M(A+x,T_z=-1/2)-M(Z+x,T_z=1/2)\right], \quad (5)$$

where $-(2T-1)\leq x\leq(2T-1)$.

They found that their formula suggested a mass excess of 35.61 MeV for ^{17}Na. Using the same formula to estimate the mass excess of ^{16}Ne as 24.67 MeV, they predicted that the p+^{16}Ne threshold

would lie 3.65 MeV below, i.e. $Th(p^{16}\mathrm{Ne}) = 3.65$ MeV. However, using the masses of Ame2003 in Eq. (5), one obtains a ^{17}Na mass excess of 35.56 MeV. Considering the now-measured ^{16}Ne mass excess of 23.996 MeV and proton mass excess of 7.288 MeV [5], the Kelson and Garvey formula now gives $Th(p^{16}\mathrm{Ne}) = 4.28$ MeV. Obviously, these mass formulae are sensitive to the precision of known data.

Antony *et al*. [4] proposed another mass formula to specify isobaric mass multiplet energies for $A < 40$, for which they considered multiplets with $T \leq 2$. This formula is also parameter-free, being based on experimental data. The energy differences (ϵ) between ground states of isobar pairs are approximated. The energy of a generic (less-stable) ground-state nucleus is given with respect to that of a more stable one, taken as a 'base',

$$\epsilon = \epsilon(Z,A) = E(Z,A) - E(Z_s,A)\ ;\ E(Z,A) = M_{Z,A} - ZM_{\mathrm{H}} - (A-Z)M_{\mathrm{n}} - 0.6Z(Z-1)A^{\frac{1}{3}}. \quad (6)$$

In this formula, Z_s is the charge number of the base nucleus, M_{n} is the mass of the neutron, and M_{H} is the mass energy of the hydrogen atom. The units are MeV and the last term is an approximation for the Coulomb energy.

For ^{17}Na, we have two unknowns: the atomic mass and the gap energy. Given the close pairing of the ground-state energies for nuclei of the same T within an isobar multiplet, and noting that as T increases, so does the gap between these ground states, we estimate the gap between the $T = \frac{5}{2}$ ^{17}C and ^{17}Na ground states to be around 1 MeV [3]. Then, since the gap energy between ^{17}C and ^{17}O ground states is 26.54 MeV, we assume a gap energy for ^{17}Na above ^{17}O of 25.5±1.0 MeV. Thus the atomic mass of ^{17}Na is estimated as 17.03752 ± 0.00107, which is 3.66 ± 1.0 MeV above the proton-^{16}Ne threshold.

4 An approach based on nuclear data systematics

Given the lack of accord in the results of the above methods, we developed an experimental guide from energy systematics in Ref. [3].

Defining two mirror nuclei by $X = {}^{A}_{(\pi=Z)}X_{(\nu=N)}$ and $Y = {}^{A}_{(\pi=N)}Y_{(\nu=Z)}$, let the energies (in MeV) of the nucleon plus nucleus thresholds be

$$Th(nX) = E(n{+}X) - E_{\mathrm{g.s.}}\left[{}^{(A+1)}_{(\pi=Z)}X_{(\nu=N+1)}\right],\ \text{and}\ Th(pY) = E(p{+}Y) - E_{\mathrm{g.s.}}\left[{}^{(A+1)}_{(\pi=Z+1)}W_{(\nu=N)}\right]. \quad (7)$$

Data for $Th(nX)$ and $Th(pY)$ from the Ame2003 compilation [5] for all nuclei with known mass (A) and with core nucleus isospin (T) less than 3, are shown in Fig. 3. Core nuclei have been grouped according to isospin. For example, the values for the mirror pair, ${}^{13}_{6}\mathrm{C}_7 - {}^{13}_{7}\mathrm{N}_6$, are formed from the single, isospin $T = 0$, core nucleus, ${}^{12}_{6}\mathrm{C}_6$, while those for the mirror pair ${}^{13}_{5}\mathrm{B}_8 - {}^{13}_{8}\mathrm{O}_5$ have mirror core nuclei with $T = 1$, ${}^{12}_{5}\mathrm{B}_7$ and ${}^{12}_{7}\mathrm{N}_5$ respectively.

Defining $\Delta(Th)$ to be the difference $Th(nX) - Th(pY)$, the data in Fig. 3 can be recast as in Fig. 4, the left panel being the full set of $\Delta(Th)$ values (for $A \leq 100$), and the right being the light mass results ($A \leq 20$) shown at a larger scale. Therein the curves are theoretical results for $T = 0$ core nuclei ($N = Z = \frac{A}{2}$) with a proton. They were found from

$$\Delta(Th) = \frac{\alpha Z\hbar c}{R} = \frac{197.3269602}{137.035999679}\ Z\ \frac{1}{R}. \quad (8)$$

where R is as recently defined [9] with the proton radius, r_p, added, i.e.

$$R = c_1\ A^{\frac{1}{3}} + c_2\ A^{-\frac{2}{3}}\ + r_p. \quad (9)$$

Using $c_1 = 0.94$ and $c_2 = 2.81$ fm from Ref. [9], and taking the proton radius to be $r_p = 0.5$ fm, the dashed curve in Fig. 4 was found. Using a radius defined without any proton radius correction

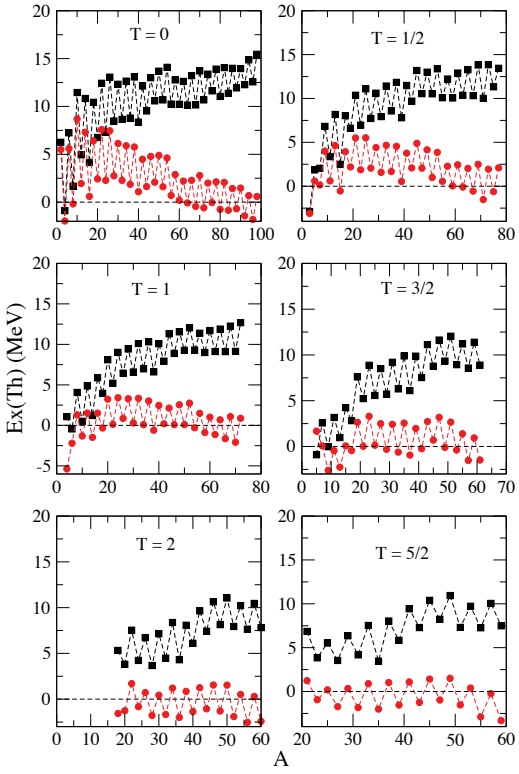

Fig. 3: Excitation energies of particle-emission thresholds, $Th(nX)$ (filled squares) and $Th(pY)$ (filled circles). The connecting lines are simply to guide the eye.

($r_p = 0$) and making a curve fit to the $T = 0$ data set to determine the coefficients $c_1 = 1.07585$ fm and $c_2 = 1.95514$ fm, the solid curve is obtained. Both show similar trends.

Examining the data for $A = 17$, one might expect the difference in the n+^{16}C and p+^{16}Ne threshold energies, relative to the ground states of ^{17}C and ^{17}Na respectively, to be within the range of ∼3.2 to ∼4.8 MeV. Then, as ^{17}Na lies beyond the proton drip-line and the n+^{16}C threshold lies 0.728 MeV above the ^{17}C ground state, the ground state of ^{17}Na is estimated to be between 2.5 and 4.1 MeV above the p+^{16}Ne threshold. Taking the line of fit into account, this can be summarised as 3.3±0.8 MeV.

The results of all methods outlined above are summarised in Table 2. Excluding the outdated result of the Kelson and Garvey formula from the 1966, there is clearly little accord between these values, and the MCAS result is significantly lower than the others, predicting a large Thomas-Ehrman shift.

Table 2: Predicted ground state energies of ^{17}Na relative to the p+^{16}Ne threshold (in MeV).

Systematics	KG_{old}	KG_{new}	Antony	cluster	MCAS
3.3(8)	3.65	4.28	3.66(1.0)	2.4	1.03

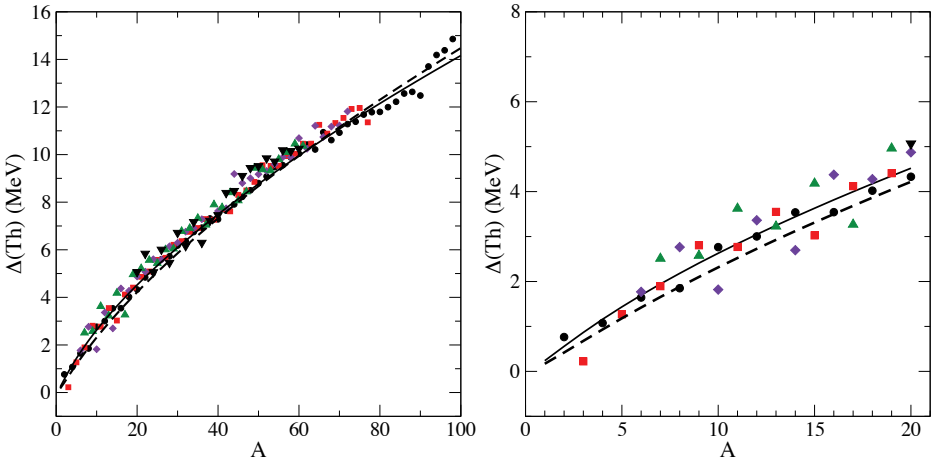

Fig. 4: $\Delta(Th)$ plotted against the mass number of the core nuclei for isospins $T \leq 2$. The nuclear isospins are shown by circles ($T = 0$), squares ($T = \frac{1}{2}$), diamonds ($T = 1$), up-triangles ($T = \frac{3}{2}$), and down-triangles ($T = 2$).

5 Conclusions

An MCAS calculation, a microscopic-cluster calculation, two mass equations, and a novel approach of systematics all predict different values for the ground-state energy of ^{17}Na relative to the p+^{16}Ne threshold. If the MCAS result is accurate, it could indicate a large Thomas-Ehrman shift. Thus, a direct measurement of the ^{17}Na ground state mass would be illuminating.

References

[1] K. Amos, L. Canton, P. R. Fraser, S. Karataglidis, J. P. Svenne, and D. van der Kniff. *Nucl. Phys.*, A879:132, 2012.

[2] K. Amos, L. Canton, G. Pisent, J. P. Svenne, and D. van der Knijff. *Nucl. Phys. A*, 728:65, 2003.

[3] K. Amos, D. van der Kniff, L. Canton, P. R. Fraser, S. Karataglidis, and J. P. Svenne. *Europhys. Lett.*, 99:12001, 2012.

[4] M. S. Antony, J. Britz, J. B. Bueb, and A. Pape. *At. Data and Nucl. Data Tables*, 33:447, 1985.

[5] G. Audi, A. H. Wapstra, and C. Thibault. *Nucl. Phys. A*, 729:337, 2003.

[6] W. Benenson and E. Kashy. *Rev. Mod. Phys.*, 51:527, 1979.

[7] H. G. Bohlen et al. *Eur. J. A*, 31:279, 2007.

[8] B. A. Brown and P. G. Hansen. *Phys. Lett. B*, 381:391, 1996.

[9] A. E. L. Dieperink and P. Van Isacker. *Eur. Phys. J. A*, 42:269, 2009.

[10] I. Kelson and G. T. Garvey. *Phys. Lett.*, 23:689, 1966.

[11] G. Raimann et al. *Phys. Rev. C*, 53:453, 1996.

[12] T. Tamura. *Rev. Mod. Phys.*, 37:679, 1965.

[13] D. R. Tilley et al. *Nucl. Phys.*, A636:155, 1998. and from *www.tunl.duke.edu/nucldata*.

[14] N. K. Timofeyuk and P. Descouvemont. *Phys. Rev. C*, 81:051301, 2010.

[15] S. Weinberg. In *Lectures on Particles and Field Theory*, volume Brandeis Summer Institute in Theoretical Physics vol 2., page 289. Prentice-Hall, 1965.

[16] E. P. Wigner. In *Proceedings of the Robert A. Welch Conferences on Chemical Research*, volume 1, page 67. Robert A. Welch Foundation, Houston, Texas, 1957.

Particle conserving approach to nuclear pairing

Alexander Volya[1] *and Vladimir Zelevinsky*[2]
[1]Department of Physics, Florida State University, Tallahassee, Florida 32306-4350, USA.
[2]National Superconducting Cyclotron Laboratory and Department of Physics and Astronomy, Michigan State University, East Lansing, Michigan 48824-1321, USA

Abstract
We discuss a method for treating the general pairing problem in a finite Fermi-system without violating the particle number conservation. The operator equations of motion are brought to the form of the recurrence relations with respect to the particle number. Examples of applications are shown. The results reproduce the exactly solvable models and consistently display an advantage compared to the conventional BCS solution. Extensions of the method are discussed.

1 Introduction

The conventional description of pairing in small systems usually employs the classical BCS [1] approach used in theory of superconductivity. This approximate solution is highly accurate for large systems and becomes exact in the asymptotic limit [2]. Following the works [3,4] the BCS approach and more general Hartree-Fock-Bogoliubov method have been widely used in nuclear physics. However, the particle number non-conservation and the instability of the BCS technique when the pairing is weak relative to the shell gaps are the major weaknesses of the approach when applied to physics of nuclei. In the density functional approaches, the problem of restoration of the particle number requires special serious efforts [5].

Below we present a variational particle conserving approximate solution in the form of a recurrence relation with respect to the number of particles N. Each step of the iterative solution is similar to the one in the BCS approach. For each value of N one is required to solve equations for the energy gap and chemical potential. The numerical procedure is simple and fast; the standard BCS theory results from additional approximations. The idea of the method goes back to [6–9]. The approach takes it roots in the exact operator equations of motion for a collective variable, here the gauge angle conjugate to the particle number [10]. In discrete space the corresponding equations are of recurrent type.

We start with the brief reminder of the BCS approach and in the derivation maintain the parallel to the BCS and Hartree-Fock-Bogoliubov (HFB) method. We show that once particle number dependence is ignored the method reduces to the BCS, in the well known degenerate model the solution coincides with the exact one. The weak pairing limit is examined in a two-level model where the particle-conserving solution is compared to the exact one and to the BCS solution; an improvement over the BCS is observed. Finally, the chain of tin isotopes is presented as a realistic example.

2 Pairing problem in BCS formulation

We use the language of second quantization with $a_1^\dagger$ and a_1 being creation and annihilation operators for single-particle orbitals labeled with subscript 1. The pairing Hamiltonian involves interaction of nucleon pairs on time-conjugated orbitals 1 and $\tilde{1}$. Here, we limit ourselves to systems with identical nucleons. The set of three pair operators is defined as $p_1^\dagger = a_1^\dagger a_{\tilde{1}}^\dagger$, $p_1 = a_{\tilde{1}} a_1$ and $n_1 = (a_1^\dagger a_1 + a_{\tilde{1}}^\dagger a_{\tilde{1}})/2$. These operators form the quasispin algebra $[p_1^\dagger, p_2] = 2\delta_{12}\, p_1^z$, $p_1^z = (n_1 - 1/2)$. We assume the following form of the pairing Hamiltonian:

$$H = 2\sum_{1>0} \epsilon_1 n_1 - \sum_{1,2>0} G_{12} p_1^\dagger p_2. \tag{1}$$

This Hamiltonian leaves the unpaired particles untouched, therefore single-occupied pair states are effectively blocked.

The BCS approach can be formulated with the help of the canonical transformation to new fermionic operators $b_1^\dagger$ and b_1, where $|u_1|^2 + |v_1|^2 = 1$,

$$b_1^\dagger = u_1^* a_1^\dagger - v_1^* a_{\tilde{1}} \quad b_1 = u_1 a_1 - v_1 a_{\tilde{1}}^\dagger. \tag{2}$$

With respect to time conjugation, $u_1 = u_{\tilde{1}}$ and $v_1 = -v_{\tilde{1}}$. Non-conservation of the number of particles requires an introduction of the chemical potential as a Lagrange multiplier, it is also advantageous to treat the diagonal terms G_{11} as a part of single-particle energy. Thus,

$$H' = H - \mu N = 2\sum_{1>0} \varepsilon_1 n_1 - \sum_{1\neq 2;1,2>0} G_{12} p_1^\dagger p_2,$$

where $\varepsilon_1 = \epsilon_1 - \mu - \frac{G_{11}}{2}$. Within the BCS approach the Hamiltonian H' is brought to a diagonal form $H' = 2\sum_{1>0} e_1 b_1^\dagger b_1$. This determines the parameters of the canonical transformation (2),

$$|u_1|^2 = \frac{1}{2}\left(1 + \frac{\epsilon_1}{e_1}\right), \quad |v_1|^2 = \frac{1}{2}\left(1 - \frac{\epsilon_1}{e_1}\right),$$

and the quasiparticle energies $e_1 = +\sqrt{\epsilon_1^2 + \Delta_1^2}$. The energy gaps Δ_1 satisfy the set of non-linear equations

$$\Delta_1 = \sum_{2>0} G_{12} u_2 v_2 = \sum_{2>0} G_{12} \frac{\Delta_2}{2e_2}$$

to be solved together with an equation for the chemical potential that assures a correct average number of particles $N = 2\sum_{1>0} |v_1|^2$.

3 Particle number conserving approach

Below we replace the ground state $|BCS\rangle$ of the BCS approach by a seniority zero ground state $|N\rangle$ of an even-particle system. The one-quasiparticle states $|1\rangle \equiv b_1^\dagger |BCS\rangle$ that carry the single-particle quantum number, 1, should now represent excitations in an odd-mass system $|N \pm 1; 1\rangle$. We introduce the one-nucleon amplitudes following the analogy to the BCS approach. For BCS, from Eq. (2) we find $\langle 1|a_1^\dagger|BCS\rangle = u_1^*$, $\langle \tilde{1}|a_1|BCS\rangle = v_1$; thus for the particle conserving approach we define

$$v_1(N) \equiv \langle N-1; \tilde{1}|a_1|N\rangle\,, \quad u_1^*(N) \equiv \langle N+1; 1|a_1^\dagger|N\rangle.$$

In the particle conserving approach we restrict the admixtures of states by seniority. For example, the particle number can be evaluated as $\langle N|a_1^\dagger a_1|N\rangle \simeq \langle N|a_1^\dagger|N-1, \tilde{1}\rangle\langle N-1, \tilde{1}|a_1|N\rangle = v_1^*(N)v_1(N)$, where the transition proceeds via a single intermediate state $|N-1,\ \tilde{1}\rangle$. The consistent application of these approximations leads to the BCS-like properties

$$|u_1(N)|^2 + |v_1(N)|^2 = 1,$$

$$N = \langle N|\sum_1 a_1^\dagger a_1|N\rangle \simeq \sum_1 |v_1(N)|^2 = \Omega - \sum_1 |u_1(N)|^2,$$

and allows for a similar definition of the number-dependent pairing gap

$$\Delta_1(N) \equiv \frac{1}{2}\langle N+2|\sum_2 G_{12} p_2^\dagger|N\rangle = \frac{1}{2}\sum_2 G_{12}\, v_2^*(N+2)\, u_2(N). \tag{3}$$

The transition between adjacent systems is determined by an equation of motion for the one-body operator

$$[a_1,\, H] = \epsilon_1 a_1 - \frac{1}{2}\sum_{12} G_{12} a_{\tilde{1}}^{\dagger} p_2 = \epsilon_1 a_1 - G_{11} a_1 - \frac{1}{2}\sum_{12} G_{12} p_2 a_{\tilde{1}}^{\dagger}.$$

The matrix element $\langle N-1;\, \tilde{1}|[a_1,\, H]|N\rangle$ of this equation gives

$$[E(N) - E_1(N-1) - \epsilon_1]\, v_1(N) + u_1(N-2)\Delta_1^*(N-2) = 0, \tag{4}$$

where the following approximation is used for decoupling:

$$\langle N-1;\, \tilde{1}|\frac{1}{2}\sum_{12} G_{12} a_{\tilde{1}}^{\dagger} p_2|N\rangle \simeq \langle N-1;\, \tilde{1}|a_{\tilde{1}}^{\dagger}|N-2\rangle\langle N-2|\frac{1}{2}\sum_{12} G_{12} p_2|N\rangle = -u_1(N-2)\Delta_1^*(N-2)$$

Analogously, from $\langle N+1; 1|[H,\, a_1^{\dagger}]|N\rangle$ it follows:

$$[E_1(N+1) - E(N) - \epsilon_1 + G_{11}]u_1(N) - v_1(N+2)\,\Delta_{\tilde{1}}(N) = 0. \tag{5}$$

The set of equations (4) and (5) can be brought to a BCS-like form using the definitions for the chemical potential $\mu(N)$, the quasiparticle energy $e_1(N)$, and the relative single-particle energy

$$E(N+2) = E(N) + 2\mu(N), \quad E_1(N+1) = E(N) + \mu(N) + e_1(N) - \frac{G_{11}}{2}, \tag{6}$$

$$\varepsilon_1(N) = \epsilon_1 - \mu(N) - \frac{G_{11}}{2}. \tag{7}$$

In terms of the new variables we obtain the final set of equations,

$$\begin{array}{c} -\Delta_1^*(N)\, u_1(N) + [e_1(N) + \varepsilon_1(N)]\, v_1(N+2) = 0 \\ [e_1(N) - \varepsilon_1(N)]\, u_1(N) - \Delta_1(N)\, v_1(N+2) = 0 \end{array}.$$

The non-trivial solution for this set of equations is possible when

$$e_1^2(N) = \varepsilon_1^2(N) + \Delta_1^2(N), \tag{8}$$

in which case the amplitudes for N and $(N+2)$-particle systems are related as

$$v_1(N+2) = \frac{\Delta_1(N)\, u_1(N)}{e_1(N) + \varepsilon_1(N)}. \tag{9}$$

The problem is now reduced to the N-dependent BCS theory. Assuming $n_1(N) = |v_1(N)|^2$ to be given, the set of gap equations follows from (3) and (9):

$$\Delta_1(N) = \frac{1}{2}\sum_{2} G_{12}\, \frac{\Delta_2(N)}{e_2(N) + \varepsilon_2(N)}\, [1 - n_2(N)]\,. \tag{10}$$

The occupation numbers for the system of $N+2$ particles are defined following (9):

$$n_1(N+2) = \frac{\Delta_1^2(N)\ [1 - n_1(N)]}{[e_1(N) + \varepsilon_1(N)]^2} = \frac{e_1(N) - \varepsilon_1(N)}{e_1(N) + \varepsilon_1(N)}\, [1 - n_1(N)]\,. \tag{11}$$

The unknown chemical potential $\mu(N)$ in the gap equation (10) is fixed to guarantee that

$$\sum_{1} n_1(N+2) = N + 2. \tag{12}$$

The solution for a given Hamiltonian can proceed in an iterative manner starting from the empty shell when $n_1(0) = 0$. Alternatively, one can reverse the procedure and start from a fully occupied shell, $n_1(\Omega) = 1$, in which case one could use

$$\Delta_1(N) = \frac{1}{2}\sum_2 G_{12}\,\frac{\Delta_2(N)}{e_2(N) - \varepsilon_2(N)}\,n_2(N+2). \tag{13}$$

Reduction to the standard BCS follows if one assumes that the density change due to an addition of a new pair into the system is small. Taking $n_1(N+2) \approx n_1(N)$ in Eq. (11) gives $n_1 = \frac{1}{2}\left(1 - \frac{\varepsilon_1}{e_1}\right)$ and the gap equation reduces to the one found in the BCS theory. If the difference of occupancies is non-zero but small, one can use simple Taylor expansion and recover the so-called moment of inertia for pair rotation in the gauge angle conjugate to the particle number [10].

By virtue of Eq. (10), the constant pairing strength $G_{12} \equiv G$ leads to a constant gap, $\Delta_1 \equiv \Delta$. For a degenerate model when all single-particle energies are equal, $\epsilon_1 \equiv \epsilon$, the solution is analytic and is similar to the BCS case with the subtle difference due to Eq (12): $\Delta^2(N) = \frac{G^2}{4}(\Omega - N)(N+2)$ and $\mu(N) = \epsilon - \frac{G}{4}(\Omega - 2N)$. This result reproduces the exact degenerate model solution, $E(N) = \epsilon N - \frac{G}{4}(N-\nu)(\Omega - N - \nu + 2)$, valid for both even N with $\nu = 0$ and for odd $N+1$ where $\nu = 1$.

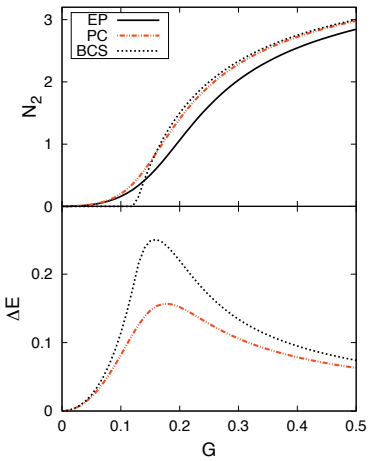

Fig. 1: Comparison of the BCS (BCS), particle-conserving (PC) and exact pairing (EP) solutions for the half-occupied two level model $N = \Omega_1 = \Omega_2 = \Omega/2 = 8$. The unit of energy is set by the level spacing between the two levels. Upper plot: the occupancy of the upper level N_2 as a function of the pairing strength G. Lower plot: the ground state energy difference of BCS and PC solutions relative to EP.

In Fig. 1 we examine the particle-number conserving method in the limit when pairing is weak relative to the shell gap. We introduce the shell gap using the two-level model. The most interesting situation occurs when the particle number is such that the Fermi surface is exactly between the two levels. The pairing excitations are suppressed by the energy required to promote particles across the shell gap. Below a critical value, G_c, of the pairing strength, the BCS theory does not support a non-zero pairing gap, so that only a trivial solution is possible with all particles occupying the lower level, $N_1 = N$, and the upper level is empty, $N_2 = 0$. The number of particle N_2 as a function of the pairing strength G is shown in the upper panel of Fig. 1. Here we solve the pairing problem using three methods: exact (EP), BCS (BCS), and with iterative particle conserving (PC). The BCS theory (blue dotted line) produces a non-zero gap and $N_2 \neq 0$ only if $G > G_c = 1/\Omega$. In the PC method (red dot-dot-dashed line) and in the exact solution (black solid line) virtual pair excitations contribute at an arbitrary small pairing strength, thus the pairing phase extends continuously into a region of weak pairing (no sharp phase transition). The ground state energy deviation between the approximate methods of BCS and PC and an exact solution is shown in the lower plot of Fig. 1.

In Fig. 2 we demonstrate a realistic application. Here we consider a chain of $^{100-132}$Sn isotopes in the valence space that includes five single-particle orbitals. Single-particle energies and pairing matrix elements are taken from the G-matrix calculations [11], the numerical values of the parameters are listed in Table 1 of Ref. [12]. We compare the solutions using the present particle conserving method (PC) with the BCS approach (BCS). In Fig. 3 the ground state energy difference relative to the exact eigenvalue from diagonalization is shown as a function of the mass number. While the PC approach is still an approximation it clearly represents an improvement over BCS.

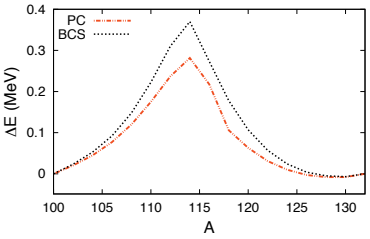

Fig. 2: The chain of $^{100-132}$Sn isotopes with the realistic (non-constant G) pairing Hamiltonian. The ground state energy difference of BCS and PC solutions relative to EP is shown as a function of the mass number.

4 PC-HFB

An interesting feature of the particle-number conserving approach is its density-dependent nature. A nucleon pair can be added to a system which is described by a certain density profile. Thus, the approach does not have to start from the spherical closed shell. The density of a new, enlarged system, is determined by Eq. (12), however other components of the interaction can be included at that time.

Below we outline the generalized procedure of the iterative particle-conserving HFB method. Here the equations of motion include the pairing and normal densities leading to a generalized iterative procedure. We extend our Hamiltonian by including all other interactions,

$$V = \frac{1}{4}\sum_{1234} V_{12;34} a_1^\dagger a_2^\dagger a_4 a_3.$$

The generalized Bogoliubov transformation defines the following matrices

$$v_{12}(N) = \langle N-1;\tilde{1}|a_2|N\rangle\,, \quad u_{12}(N) = \langle N+1;1|a_2^\dagger|N\rangle.$$

The operator equation of motion contains now

$$[a_1,\, V] = \sum_2 W_{12}\{\hat{R}\}a_2 = \sum_2 a_2\, W_{12}\{\mathbf{1}+\hat{R}\}, \tag{14}$$

where W_{12} is a linear functional of the generalized density matrix operator $\hat{R}_{21} = a_1^\dagger a_2$,

$$W_{12}\{\hat{R}\} = \frac{1}{2}\sum_{34} V_{13;24}\hat{R}_{43} = \frac{1}{2}\sum_{34} V_{13;24} a_3^\dagger a_4.$$

Note that $W_{12}^\dagger\{\hat{R}\} = W_{21}\{\hat{R}\}$. In the first term of (14), W acts on the identity matrix and the result is a c-number matrix renormalizing the one-body part of the Hamiltonian, $W_{12}\{\mathbf{1}\} \equiv \frac{1}{2}\sum_3 V_{13;23}$.

Similar to the previous section, we describe the paired state with the density matrix given as an expectation value $\langle N|\hat{R}_{21}|N\rangle = \sum_3 v_{31}^* v_{32} \equiv (v^T v^*)_{21} \equiv R_{21}(N)$. This c-number matrix we denote as $\mathbf{R}(N)$. Including pairing forces and evaluating the full commutator,

$$[a_1,\, H] = \epsilon_1 a_1 - \frac{1}{2}\sum_{12} G_{12} a_{\tilde{1}}^\dagger p_2 + \sum_2 a_2\, W_{12}\{\mathbf{1}+\hat{R}\},$$

in the matrix element $\langle N-1;\tilde{3}|[a_1,\, H]|N\rangle$, we obtain

$$[E(N) - E_3(N-1) - \epsilon_1]\, v_{31}(N) - \sum_2 W_{12}\left\{\mathbf{1}+\mathbf{R}(N)\right\} v_{32}(N) + u_{31}(N-2)\Delta_1^*(N-2) = 0.$$

As before, the Hermitian conjugate equation of motion can be used to construct the second equation resulting in the final set of matrix equations

$$\left[e_3(N) + \varepsilon_1(N) + \frac{G_{11}-G_{33}}{2}\right] v_{31}(N{+}2) + \sum_2 W_{12}\left\{\mathbf{1}+\mathbf{R}(N+2)\right\} v_{32}(N{+}2) - u_{31}(N)\Delta_1^*(N) = 0,$$

$$\left[e_3(N) - \varepsilon_1(N) + \frac{G_{11} - G_{33}}{2}\right] u_{31}(N) + \sum_2 W_{21}\left\{\mathbf{R}(N)\right\} u_{32}(N) - v_{31}(N+2)\,\Delta_1(N) = 0.$$

These equations still couple the matrix densities $v(N+2)$ and $u(N)$, because matrices u and v are subjects to constraints that retain the Bogoliubov transformation as canonical. In the absence of pairing, or in the limit of $V = 0$, these equations reduce to the HF equations and to the PC equations discussed above, respectively.

5 Conclusions

This short presentation is a continuation of our efforts in Refs. [12] and [13]; here we present a particle-number conserving method intended to deal with the problem of pairing in finite systems. The method is an extension of a conventional BCS approach, and represents a recursive solution of BCS-like equations for the energy gap and the chemical potential as functions of the total particle number. The results are in a better agreement with the exact solutions in all considered cases. The method appears to provide a better treatment of superconducting state when pairing is weak.

The appealing merits of the new technique are in its relative computational simplicity and broad applicability. There is no restrictions for the type of the single-particle spectrum or pairing matrix elements; extension to other pairing modes or/and introduction of time reversal non-invariant forces is also possible. As demonstrated, the method can be incorporated in the self-consistent scheme of the HFB approach taking into account on equal footing non-pairing components of the residual interaction. We expect the importance of exact particle number conservation to increase for the description of soft nuclei where the static mean field is unstable, in the cases where nuclear spectra reveal a stronger N-dependence, or near nuclear drip-lines. Next steps beyond the present approximation should include the intermediate states of higher seniority.

This work is supported by the DOE grant DE-FG02-92ER40750 and by the NSF grant PHY-1068217.

References

[1] J. Bardeen, L.N. Cooper, and J.R. Schrieffer, Phys. Rev. **108**, 1175 (1957).
[2] N.N. Bogoliubov, JETP **34**, 58 (1958); Physica **26**, 1 (1960).
[3] A. Bohr, B.R. Mottelson, and D. Pines, Phys. Rev. **110**, 936 (1958).
[4] S.T. Belyaev, Mat. Fys. Medd. Dan. Vid. Selsk. **31**, No. 11 (1959).
[5] T. Duguet, M. Bender, K. Bennaceur, D. Lacroix, and T. Lesinski, Phys. Rev. C **79**, 044320 (2009).
[6] E. Sahisti, Nuovo Cim. **37**, 199 (1965).
[7] M. Jean, Nuovo Cim. **40**, 1224 (1965).
[8] G. Do Dang and A. Klein, Phys. Rev. **147**, 689 (1966).
[9] S.C. Pang and A. Klein, Can. J. Phys. **50**, 655 (1972).
[10] S.T. Belyaev and V.G. Zelevinsky, Yad. Fiz. **16**, 1195 (1972).
[11] A. Holt, T. Engeland, M. Hjorth-Jensen, and E. Osnes, Nucl. Phys. A. **634**, 41 (1998).
[12] V. Zelevinsky and A. Volya, Phys. At. Nucl. **66**, 1829 (2003).
[13] A. Volya and V. Zelevinsky, in *Fifty years of nuclear BCS*, eds. R. Broglia and V. Zelevinsky, World Scientific, in press.

Compound nucleus decay: sequential evaporation vs. statistical multifragmentation

B.V. Carlson[1], *F.T. Dalmolin*[1], *M. Dutra*[1], *R. Donangelo*[2,3], *S.R. Souza*[2,4], *D.A. Toneli*[1]
[1]Departamento de Física, Instituto Tecnológico de Aeronáutica, 12228-900 São José dos Campos, Brazil
[2]Instituto de Física, Universidade Federal do Rio de Janeiro Cidade Universitária, CP 68528, 21941-972, Rio de Janeiro, Brazil
[3] Instituto de Física, Facultad de Ingeniería, Universidad de la República, Julio Herrera y Reissig 565, 11.300 Montevideo, Uruguay
[4]Instituto de Física, Universidade Federal do Rio Grande do Sul Av. Bento Gonçalves 9500, CP 15051, 91501-970, Porto Alegre, Brazil

Abstract
We examine the properties of hot nuclei within the context of the statistical multifragmentation model. We then relax the simultaneous emission hypothesis of the model to permit the calculation of partial widths and lifetimes. The model that results is essentially a compound nucleus evaporation one in which the time between successive evaporations is so short that they can be considered to be almost simultaneous. However, the compound nucleus in this case is not the usual low-energy one, but a greatly expanded one, roughly consistent in size with the multifragmentation breakup volume.

1 Introduction

The statistical multifragmentation model [1–5] assumes that a large fraction of excited compound nuclei desintegrate almost simultaneously into a number of small and intermediate mass fragments. The remaining fraction of compound nuclei, as well as the primary products of the multifragmentation, decay by emission of small or intermediate mass fragments or by fission. A drawback to the model is that it contains no lifetimes or partial widths that would permit comparison of the different decay modes. Here, we begin by examining the properties of hot nuclei in the context of the multifragmentation model. We then relax the simultaneous emission hypothesis of the model and extend it to include fluxes, which then permits the calculation of partial widths and lifetimes. The resulting model is essentially a compound nucleus evaporation one in which the time between successive evaporations is so short that they can be considered to be almost simultaneous. Such a model was considered long ago by Moretto and collaborators as an alternative to multifragmentation [6]. However, in our case the highly excited compound nucleus differs from the usual low-energy case in that it is greatly expanded, roughly consistent in size with the multifragmentation breakup volume.

2 The hot compound nucleus

A hot compound nucleus is a difficult object to study, both experimentally and theoretically as, at all but the lowest excitation energies, it decays extremely quickly. Experimentally, we must infer its characteristics through its decay. Theoretical studies of its structure are dubious due to the fact that it is not the stable long-lived object that theory must assume it to be to carry out such studies. With this proviso in mind, we have attempted to gain a better understanding of hot compound nuclei using two self-consistent temperature-dependent mean-field approaches [7].

In the first of these, which we denote as BS (bound states), we perform self-consistent relativistic Hartree calculations using a grand canonical ensemble of bound neutron states and proton states below the Coulomb barrier. As the temperature increases, the nucleus grows in size, as shown in Figure 1

for the case of ^{58}Ni. Unbound states can become bound as the size of the nuclear well increases with temperature and calculation of the nuclear mean field can be extended to arbitrarily high temperatures.

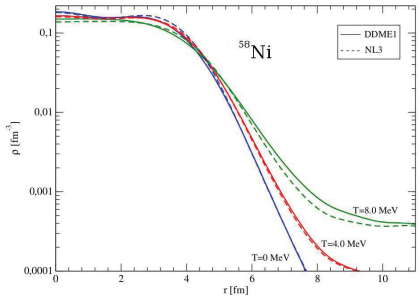

Fig. 1: Nuclear density of ^{58}Ni for two parameterizations of the relativistic mean field as a function of temperature including only bound nucleon states.

In the second approach we apply the method of Bonche, Levit and Vautherin [8, 9], which we denote by BLV, to self-consistent relativistic Hartree and nonrelativistic Thomas-Fermi calculations using the grand canonical ensembles of a nucleus+gas minus the background gas. This formalism includes bound states and single-particle resonances. We have performed self-consistent calculations in both the BS and BLV formalisms in the relativistic mean field approximation using the NL3 [10] and DDME1 [11] interactions. Again, as the temperature increases, the nucleus grows in size, as shown in Figure 2 for the case of ^{58}Ni. Here the background gas density increases with temperature until the nucleus melts into the gas and disappears.

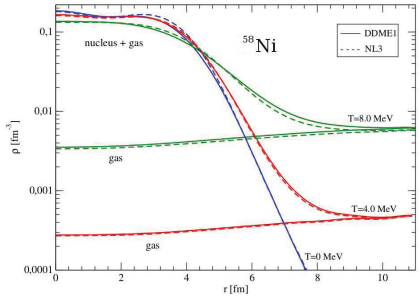

Fig. 2: Nuclear density of ^{58}Ni for two parameterizations of the relativistic mean field as a function of temperature in the formalism of Bonche, Levit and Vautherin [8, 9]

In the non-relativistic Thomas-Fermi approach, we have performed calculations of the BLV formalism using the Bsk14 [12] and NRAPR [13] Skyrme interactions. The BLV calculations were performed at integer values of T and stop at the last value at which they converged. In Figure 3, we show the rms radius of ^{58}Ni as a function of the temperature for all calculations. The rms radii of the relativistic and nonrelativistic calculations using the BLV formalism behave similarly, increasing slowly at low

temperatures and then diverging as they reach their limiting temperatures, which vary between 9 and 11 MeV in this case. The rms radii of the BS calculations grow more quickly at low temperature but do not diverge.

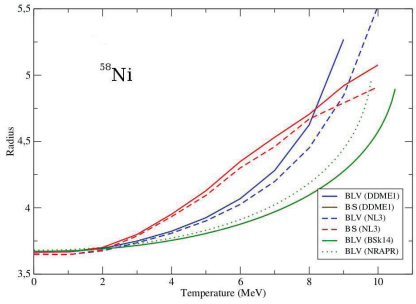

Fig. 3: Radius of the ^{58}Ni nucleus as a function of the temperature of the relativistic and nonrelativistic mean field calculations described in the text.

Turning now to the statistical multifragmentation model, we first note that it is usually assumed to apply at temperatures above about 4 MeV. The nuclear volume is taken to be from 2 to 3 (or more) times the cold nuclear volume. Here, these values of the volume correspond to rms radii of the order of 4.6 to 5.3 fm and to values of the temperature above 8 MeV. Such values of the radius are indeed reached close to the temperature at which the nucleus disappears in the BLV approach. However, the BLV and BS approaches suggest that the nuclear volume would be at most about 25% larger than the cold volume at 4 MeV.

3 Decay rates in the statistical multifragmentation model

In a recent paper [14], we have shown that the density of states of a configuration of n fragments in the statistical multifragmentation model can be written as the following generalized Fermi breakup phase-space integral,

$$\omega_n(\varepsilon_0) = \prod_{l=1}^{k} \frac{1}{N_l!} \left(\frac{V}{(2\pi\hbar)^3}\right)^{n-1} \int \prod_{j=1}^{n} d^3p_j \, \delta\left(\sum_{j=1}^{n} \vec{p}_j\right) \times \int \prod_{j=1}^{n} \left(\omega_{bj}(\varepsilon_j)\, d\varepsilon_j\right) \delta\left(\varepsilon_0 - B_0 - E_{c0} - \sum_{j=1}^{n} \left(\frac{p_j^2}{2m_j} + \varepsilon_j - B_j - E_{cj}\right)\right), \quad (1)$$

where the sums and products $j = 1, \ldots, n$ run over all fragments of the breakup mode, while the sum $l = 1, \ldots, k$ runs over the distinct noninteracting fragments and takes into account their multiplicities. Conservation of nucleon number and of charge require that

$$A_0 = \sum_{j=1}^{n} A_j = \sum_{l=1}^{k} N_l A_l \qquad \text{and} \qquad Z_0 = \sum_{j=1}^{n} Z_j = \sum_{l=1}^{k} N_l Z_l \,, \quad (2)$$

where Z_j and A_j are the charge and mass number, respectively, of fragment j. The excitation energy of the decaying nucleus is denoted by ε_0, while B_0 is its binding energy and E_{c0} is a term associated with

the Wigner-Seitz correction to the Coulomb energy of the system. V is the nuclear volume and is usually defined as

$$V = (1 + \chi) V_0 \,, \tag{3}$$

where V_0 is the ground state volume of the decaying nucleus and the expansion factor χ is usually taken to be $\chi = 1$. The excitation energy of fragment j is denoted by ε_j, with $\omega_{bj}(\varepsilon_j)$ its density of quasi-bound states and B_j its ground-state binding energy, while the E_{cj} represent the remaining Wigner-Seitz corrections to the Coulomb energy, taken to be

$$E_{cj} = \frac{C_{Coul}}{(1+\chi)^{1/3}} \frac{Z_j^2}{A_j^{1/3}} \,. \tag{4}$$

For a particle with no excited states, we have $\omega_{bj}(\varepsilon_j) = g_j \delta(\varepsilon_j)$, where g_j is the particle spin multiplicity.

We emphasize that the density $\omega_{bj}(\varepsilon_j)$ should contain only quasi-bound states, to avoid the double counting of configurations in which the fragment j is separated into smaller fragments. When the excitation energy ε_j of fragment j is extremely high, it is thus possible that the density corresponding to the fragment will be zero, due to the inexistence of quasi-bound states at the given energy. At sufficiently low excitation energy, when

$$\varepsilon_0 < B_0 + E_{c0} - \sum_{j=1}^{n} (B_j + E_{cj}) \,,$$

the density of states of a configuration will also be zero. The total density of states of the Z_0, A_0 system with excitation energy ε_0, $\omega(\varepsilon_0, Z_0, A_0)$, is obtained by summing the densities corresponding to all possible configurations of all numbers of fragments,

$$\omega(\varepsilon_0, Z_{tot}, A_{tot}) = \omega_{b1}(\varepsilon_0) + \sum_f \omega_{f2}(\varepsilon_0) + \sum_f \omega_{f3}(\varepsilon_0) + \ldots \,. \tag{5}$$

If the correct continuum interactions among the fragments in each configuration were included, this sum would describe the exact density of states. However, as the bound fragments in each configuration defined in Eq. 1 do not interact, it is only an approximation to this density.

The fragments of a multifragmentation reaction are usually considered to be produced simultaneously. Here we wish to reconsider the physical significance of such a claim. 1) It could simply be a reiteration of the assumption that the fragments in the initial multi-fragmentation volume are not interacting. If this is the case, the question of how they formed continues unanswered. We could then consider looking back to an earlier stage of the reaction to analyze the fragment formation in more detail. 2) It could be the assumption that all fragments leave the initial interaction volume simultaneously. For the case of two fragments, where only one separation is necessary, this seems quite reasonable. Simultaneous separation of a nucleus into three or more fragments would seem to be extremely improbably however, as it would require that two or more independent events (the separations) occur at exactly the same instant.

As neither of the two possibilities is very satisfying from a physical point of view, let us assume instead that fragment emission can be *almost* simultaneous. This would seem to be a reasonable assumption in the case of any two distinct but closely occurring events. In this case, we can arrange the n initial fragments into two larger fragments, $n_1 + n_2 = n$, that are the first to separate beyond the range of the nuclear interaction. We can write the corresponding n-fragment density of states of Eq. 1 in terms of the n_1- and n_2-fragment densities of states, as in Eq. 1, and their momenta, $\vec{p}_1$ and $\vec{p}_2$, as

$$\omega_{fn}(\varepsilon_0) \;=\; \frac{V}{(2\pi\hbar)^3} \int d^3p_1 \, d^3p_2 \, \delta(\vec{p}_1 + \vec{p}_2) \int \omega_{f_1 n_1}(\varepsilon_1) \, \omega_{f_2 n_2}(\varepsilon_2) \, d\varepsilon_1 d\varepsilon_2 \tag{6}$$

$$\times\delta\left(\varepsilon_0 - B_0 - E_{c0} - \sum_{j=1}^{2}\left(\frac{p_j^2}{2m_j} + \varepsilon_j - B_j - E_{cj}\right)\right) .$$

The SMM furnishes no estimate of the rate at which the fragmentation occurs. We can estimate a decay rate as the rate at which the two fragments separate beyond a given distance R, which we can approximate as the range of nuclear interaction between the fragments [15]. We first reduce the momentum integrals in the expression for the density of states, Eq. 6, to a single integral over the relative momentum and then rewrite this expression in terms of the relative momentum and separation of the two fragments,

$$\begin{aligned}\omega_{fn}(\varepsilon_0) &= \frac{1}{(2\pi\hbar)^3}\int d^3p\, d^3r \int \omega_{f_1 n_1}(\varepsilon_1)\,\omega_{f_2 n_2}(\varepsilon_2)\, d\varepsilon_1 d\varepsilon_2 \\ &\quad\times\delta\left(\varepsilon_0 - B_0 - E_{c0} - \frac{p^2}{2\mu} - \sum_{j=1}^{2}(\varepsilon_j - B_j - E_{cj})\right) .\end{aligned}$$

We then write the decay rate for the partition as

$$\begin{aligned}-\frac{d}{dt}\omega_{fn}(\varepsilon_0)_{\to f_1 n_1 f_2 n_2} &= \frac{1}{(2\pi\hbar)^3}\int d^3p\, d^3r\, \frac{\hat{r}\cdot\vec{p}}{\mu}\theta(\hat{r}\cdot\vec{p})\,\delta(r-R) \\ &\quad\times\int \omega_{f_1 n_1}(\varepsilon_1)\,\omega_{f_2 n_2}(\varepsilon_2)\, d\varepsilon_1 d\varepsilon_2 \\ &\quad\times\delta\left(\varepsilon_0 - B_0 - E_{c0} - \frac{p^2}{2\mu} - \sum_{j=1}^{2}(\varepsilon_j - B_j - E_{cj})\right) .\end{aligned} \tag{7}$$

We now wish to take into account all partitions whose first separation yields Z_1, A_1 and Z_2, A_2. Looking in turn at each of the configurations that furnish Z_1, A_1, we find that their sum is the total density $\omega_{tot}(\varepsilon_1, Z_1, A_1)$. This sum multiplies each of the partitions that furnish Z_2, A_2, which, in their turn, can be summed to yield $\omega_{tot}(\varepsilon_2, Z_2, A_2)$. The summed contributions of these partitions is then the contribution to the decay rate of the total density $\omega_{tot}(\varepsilon_0, Z_{tot}, A_{tot})$ into fragments Z_1, A_1 and Z_2, A_2,

$$\begin{aligned}-\frac{d}{dt}\omega_{tot}(\varepsilon_0, Z_{tot}, A_{tot})_{\to Z_1 A_1, Z_2 A_2} &= \frac{1}{(2\pi\hbar)^3}\int d^3p\, d^3r\, \frac{\hat{r}\cdot\vec{p}}{\mu}\theta(\hat{r}\cdot\vec{p})\,\delta(r-R) \\ &\quad\times\int \omega_{tot}(\varepsilon_1, Z_1, A_1)\,\omega_{tot}(\varepsilon_2, Z_2, A_2)\, d\varepsilon_1 d\varepsilon_2 \\ &\quad\times\delta\left(\varepsilon_0 - B_0 - E_{c0} - \frac{p^2}{2\mu} - \sum_{j=1}^{2}(\varepsilon_j - B_j - E_{cj})\right) .\end{aligned} \tag{8}$$

We can simplify the partial decay rate by integrating,

$$\frac{1}{(2\pi\hbar)^3}\int d^3p\, d^3r\, \frac{\hat{r}\cdot\vec{p}}{\mu}\theta(\hat{r}\cdot\vec{p})\,\delta(r-R) \to \frac{1}{2\pi\hbar}\int de_p\, \frac{2\mu e_p}{\pi\hbar^2}\,\pi R^2\,\theta(e_p) . \tag{9}$$

Defining the Q-value of the two-body reaction and an effective barrier in terms of the Coulomb energies,

$$Q = B_0 - B_1 - B_2 \qquad \text{and} \qquad V_c = E_{c0} - E_{c1} - E_{c2}, \tag{10}$$

as well as the asymptotic kinetic energy e, in terms of the kinetic energy immediately after separation e_p and the additional energy due to the posterior Coulomb acceleration V_c,

$$e = e_p + V_c = \frac{p^2}{2\mu} + V_c \,, \tag{11}$$

the decay rate becomes

$$\begin{aligned} -2\pi\hbar \frac{d}{dt} \omega_{tot} \left(\varepsilon_0, Z_{tot}, A_{tot}\right)_{\rightarrow Z_1 A_1, Z_2 A_2} &= \int_0^\infty de \, \frac{2\mu e}{\pi\hbar^2} \, \pi R^2 \left(1 - V_c/e\right) \theta \left(e - V_c\right) \\ &\times \int \omega_{tot} \left(\varepsilon_1, Z_1, A_1\right) \omega_{tot} \left(\varepsilon_2, Z_2, A_2\right) d\varepsilon_1 d\varepsilon_2 \\ &\times \delta \left(\varepsilon_0 - Q - e - \varepsilon_1 - \varepsilon_2\right) \,. \end{aligned} \tag{12}$$

This expression look remarkably like the Weisskopf approximation to the compound nucleus decay rate [16], if we make the common association with the absoprtion cross section,

$$\pi R^2 \left(1 - V_c/e\right) \theta \left(e - V_c\right) \rightarrow \sigma_{abs, Z_1 A_1 + Z_2 A_2} \left(e\right) \,. \tag{13}$$

We can thus estimate the partial decay widths for quasi-simultaneous fragment separations just as we would for normal sequential emission,

$$\begin{aligned} 2\pi \, \Gamma_{Z_{tot} A_{tot} \rightarrow Z_1 A_1, Z_2 A_2} \, \omega_{tot} \left(\varepsilon_0, Z_{tot}, A_{tot}\right) &= \int de \, \frac{2\mu e}{\pi\hbar^2} \, \sigma_{abs, Z_1 A_1 + Z_2 A_2} \left(e\right) \\ &\times \int \omega_{tot} \left(\varepsilon_1, Z_1, A_1\right) \omega_{tot} \left(\varepsilon_2, Z_2, A_2\right) d\varepsilon_1 d\varepsilon_2 \\ &\times \delta \left(\varepsilon_0 - Q - e - \varepsilon_1 - \varepsilon_2\right) \,, \end{aligned} \tag{14}$$

with the total decay width determined by summing over all possible two-body separations,

$$2\pi \, \Gamma_{Z_{tot} A_{tot}} \, \omega_{tot} \left(\varepsilon_0, Z_{tot}, A_{tot}\right) = \sum_{Z_2 \leq Z_1, A_2 \leq A_1} 2\pi \, \Gamma_{Z_{tot} A_{tot} \rightarrow Z_1 A_1, Z_2 A_2} \, \omega_{tot} \left(\varepsilon_0, Z_{tot}, A_{tot}\right) \,. \tag{15}$$

According to the statistical multifragmentation model and to our study of hot nuclei, the radius of the fragmenting nucleus is larger than that of a cold nucleus. We would expect the effective barrier to be proportionally lower. Secondary and further separations could be calculated in the same manner as we have calculated the first separation. In general, spectra, angular distributions and correlations must be calculated with more care at high temperatures, where the proximity of different fragments must be taken into account.

We illustrate this with the reaction ^{12}C + ^{48}Ca $\rightarrow$ ^{60}Fe $\rightarrow$ ^{11}B + ^{49}Sc at an initial excitation energy of 250 MeV. Using the Weisskopf approximation, we find the total decay width of either of the fragments to be $\Gamma \approx 8$ MeV, which furnishes a lifetime of $\tau \approx 24$ fm/c. From the relative velocity of the two fragments,

$$e_p = \frac{\mu}{2} v^2 \approx 2T \approx 9.4 MeV,$$

we find $\beta \approx$0.05 and a distance between the two fragments at the time of the second emission of $\Delta R \approx$ 1.2 fm. If the secondary emission were to be of a charged particle as well, the subsequent Coulomb repulsion among the three (or more) fragments could have important effects on their asymptotic properties.

W. Gawlikowicz considered the effects of proximity on fragment emission already some time ago [17]. Using the GEMINI Monte Carlo statistical emission code [18], he integrated the Coulomb trajectories of the fragments after their emission and compared these results to those of calculations assuming the asymptotic energies and angles upon emission. He found narrower spectra for intermediate mass fragments, due to repulsion from a more extended system, and larger correlations of low intermediate mass fragments at low relative velocity, due to their relative repulsion.

4 Conclusions

When the statistical multifragmentation model's assumption of simultaneous emission is replaced by one of quasi-simultaneity, we find that multifragmentation can be described by expressions very similar to those of sequential emission. Such a description of multifragmentation was proposed long ago by Moretto and collaborators [6].

We expect the effective cross sections and barriers for emission from very hot nuclei to be different from those of cold nuclei. More theoretical work and more precise experimental studies are needed to better determine these.

Due to the proximity of the fragments of quasi-simultaneous emissions, the usual Weiskopf-Ewing or Hauser-Feshbach formalisms cannot be used to calculate spectra and/or angular distributions and correlations, although they might suffice for calculating production cross sections. At present, Monte Carlo decay calculations seem to be the most efficient way to take into account correctly all of the characteristics of quasi-simultaneous decay.

However, it is still not clear to what extent the statistical multifragmentation model describes the physical process of multifragmentation. Lower effective intermediate mass fragment emission barriers seem to be needed for heavy-ion collisions than for spallation reactions [19]. This could be due to angular momentum effects not taken into account in the Weisskopf-type formalism used to describe intermediate mass fragment emission in GEMINI. However, it might also be the effect of collective expansion after compression suffered in the heavy-ion collision.

In closing, we note that the arguments we have given here can be be extended to include angular momentum conservation.

Acknowledgements

We acknowledge partial support from the CNPq, CAPES, FAPERJ, FAPESP, the PRONEX program, under contract No E-26/171.528/2006, and the International Atomic Energy Agency, under research contract No. 14568.

References

[1] J. P. Bondorf, R. Donangelo, I. N. Mishustin, C. J. Pethick, H. Schulz and, K. Sneppen, Nucl Phys. **A443** (1985) 321.

[2] J. Bondorf, R. Donangelo, I.N. Mishustin, H. Schulz, Nucl. Phys. **A444** (1985) 460.

[3] H. W. Barz, J. P. Bondorf, R. Donangelo, I. N. Mishustin, H. Schulz, Nucl. Phys. **A448** (1986) 753.

[4] A. S. Botvina, A. S. Iljinov, I. N. Mishustin, J. P. Bondorf, R. Donangelo, K. Sneppen, Nucl. Phys. **A475** (1987) 663.

[5] J. P. Bondorf, A. S. Botvina, A. S. Iljinov, I. N. Mishustin, K. Sneppen, Phys. Rep. **257** (1995) 133.

[6] L. G. Moretto, R. Ghetti, L. Phair, K. Tso, and G. J. Wozniak, Phys. Rep. **287** (1997) 249.

[7] F. T. Dalmolin, M. Dutra, B. V. Carlson, R. Donangelo, S. R. Souza, EPJ Web of Conferences **21** (2012) 10003.

[8] P. Bonche, S. Levit and D. Vautherin, Nuclear Physics **A427** (1984) 278.

[9] P. Bonche, S. Levit and D. Vautherin, Nucl. Phys. **A436** (1985) 265.
[10] G. A. Lalazissis, J. König and P. Ring, Phys. Rev. C **55** (1997) 540.
[11] T. Niksic, D. Vretenar, P. Finelli, and P. Ring, Phys. Rev. C **66** (2002) 024306.
[12] S. Goriely, M. Samyn, and J. Pearson, Phys. Rev. C **75** (2007) 064312.
[13] A. W. Steiner, M. Prakash, J. M. Lattimer, and P. J. Ellis, Phys. Rep. **411** (2005) 325.
[14] B. V. Carlson, R. Donangelo, S. R. Souza, W. G. Lynch, A. W. Steiner, M. B. Tsang, Nucl. Phys. **A876** (2012) 77.
[15] W. A. Friedman and W. G. Lynch, Phys. Rev. C **28** (1983) 16.
[16] V. F. Weisskopf and D. H. Ewing, Phys. Rev. **57** (1940) 472.
[17] W. Gawlikowicz, Acta. Phys. Pol. B **28** (1997) 1687.
[18] R. J. Charity, M. A. McMahan, G. J. Wozniak, R. J. McDonald, L. G. Moretto, D. G. Sarantites, L. G. Sobotka, G. Guarino, A. Panteleo, L. Fiore, A. Gobbi, and K. Hildenbrand, Nucl. Phys. **A483** (1988) 371.
[19] D. Mancusi, J. Cugnon, A. Boudard, J.-C. David, S. Leray, R. J. Charity, A. Kelíc-Heil, M. V. Ricciardi, Journal of the Korean Physical Society **59** (2011) 943.

Hauser Feshbach Calculations in Deformed Nuclei

S. M. Grimes
Ohio University
Athens, Ohio 45701

Abstract
Hauser Feshbach calculations for deformed nuclei are typically done with level densities appropriate for deformed nuclei but with Hauser Feshbach codes which enforce spherical symmetry by not including K as a parameter in the decay sums. A code has been written which does allow the full K dependence to be included. Calculations with the code have been compared with those from a conventional Hauser Feshbach code. The evaporation portion (continuum) is only slightly affected by this change but the cross sections to individual (resolved) levels are changed substantially. It is found that cross sections to neighboring levels with the same J but differing K are not the same. The predicted consequences of K mixing will also be discussed.

1 Introduction

Calculation of spectra and cross sections for reactions proceeding under the condition that the Bohr independence hypothesis is valid were first made by Weisskopf [1, 2]. Hauser and Feshbach [3] and Wolfenstein [4] then modified the formalism to allow for the possibility that the independence hypothesis applies separately to states of given J and π, i.e., the branching may be different for states of large J than those of small J.

In 1972, a revision to the Hauser-Feshbach formalism was proposed [5]. For nuclei with $A >\sim 40$, proton bombardment can produce compound states of two different isospin values (assuming $N > Z$), while alpha bombardment of a target chosen to produce the same compound nucleus only produces one value. Thus, one might expect different proton to alpha branching ratios for compound nuclei formed by alpha bombardment than by proton bombardment. A slight enhancement in the proton to alpha decay ratios for proton bombardment is predicted by the traditional Hauser Feshbach formalism ($\sim 15\%$) because of the different spin distribution in the two entrance channels, but the experimental measurements showed a 40% to 50% enhancement.

If one uses a Hauser Feshbach code which includes isospin [5], the factor increases to 60% to 65%. By invoking isospin mixing, one can infer that letting the upper isospin states mix into lower isospin states before decay $\sim 50\%$ of the time reproduces the experimental result [6]. It was later shown that isospin effects could be seen in alpha- and neutron-induced reactions as well [7].

There is a possibility that the situation is similar for deformed nuclei. Use of a conventional Hauser Feshbach code for calculations in deformed nuclei is forcing the decay of the compound nucleus to be independent of K, the angular momentum projection on the symmetry axis.

2 Development of a Hauser Feshbach Code Including K

It is obvious that the possible effects of K on branching ratios can only be investigated with a new formulation of the Hauser-Feshbach equation. In this case, the cross section will be

$$\sigma_{ab} = \frac{\pi\lambda^2}{(2I_1+1)(2I_2+1)} \sum_{J_1 K_1 \pi} \frac{\tau_a \tau_b}{\sum_c \tau_c}. \tag{1}$$

Here, λ is the reduced wavelength of the particle in the entrance channel, I_1 is the projectile spin and I_2 is the target spin. Each τ is the appropriate transmission coefficient multiplied by the square of the

appropriate Clebsh-Gordan coefficient to couple to J and K. The sum in the denominator is over all exit channels, outgoing energies and final J' and K' values coupled to the J and K of the compound nucleus. The formalism is entirely parallel to that introduced for isospin in Reference [5]. In that case, the Clebsh-Gordan coefficients are for coupling to a particular $T_z(=(N-Z)/2)$ and $T = T_z$ or $T = T_z + 1$. For the deformed case, the coupling is to J and particular values of $K \leq J$.

It turns out that an important difference between the isospin case and the deformed case is that the deformed case seems to have small effects on the continuum. On the other hand, there are substantial effects on the relative cross sections to resolved final states.

It was originally anticipated that introduction of K in the formalism would lead to differences in the population of final states with the same J and different K values. Some differences of this type are observed but they might be expected to be erased if K mixing is large. This would be analogous to that situation for isospin.

There is a more profound effect which is present even if K mixing is large. A level in a spherical basis is $2J+1$ degenerate, since each of the states with $-J \leq J_z \leq J$ has the same energy. This results in compound nuclear cross sections that are approximately proportional to $2J+1$ if J (the spin of the level) is comparable to or less than the spin cutoff parameter, σ. For a deformed nucleus, this degeneracy is changed. A level of spin J is now split into $J+1$ levels (even A) or $J+1/2$ levels (odd A). Each level has a degeneracy of 2 unless the spin projection K is zero, in which case the degeneracy is one [8].

The consequence of this change is that the cross sections calculated in a deformed basis have a tendency to vary less rapidly with J than those for a spherical Hauser Feshbach calculation. The use of a standard Hauser Feshbach code even with the deformed levels included in the level density forces a spherical symmetry on the calculations.

3 Calculations

A new Hauser Feshbach code [9] has been written which includes a sum over K as well as J and π and also includes the Clebsh-Gordan coefficients as described in Section 2. The code, because of the inclusion of the sums over K, is approximately eight to ten times slower in execution that a comparable spherical Hauser Feshbach code [10,11]. The code can make calculations in hybrid situations, e.e., one in which some residual nuclei are deformed and others are spherical. Finally, the code can be run with complete K conservation or with fractions of mixing before decay between 0 and 1.

Calculations were done for neutrons incident on ^{168}Er at energies of 1, 2, 4 and 6 MeV. For the three highest energies, the decay was predominately to the continuum. The shape and magnitude of the continuum were only slightly changed between calculations with HF2002 (spherical) and HF2012 (deformed). In each case the level densities used were those appropriate for deformed nuclei, i.e., rotational bands were included.

The results at all the bombarding energies were similar for the cross sections to resolved final states.

1. The removal of the $(2J+1)$ degeneracy made the cross sections increase for low J and decrease for high J when using the deformed Hauser Feshbach code. This conclusion was not changed when K mixing was introduced. This conclusion was valid in each exit channel (α, p, n).
2. The remaining degeneracy difference is between $K = 0$ and $K \neq 0$ states. This results in a enhancement of $K \neq 0$ compared to $K = 0$ levels of the same J. The degeneracy difference is a factor of two. The observed factor is slightly larger than a factor of two with no mixing. As the K mixing increases, the factor approached two. Thus, the K mixing does *not* remove the dependence of cross sections on K as well as J. For residual nuclei with even A, the dependence on K is weak if $K \neq 0$, but the states of given J with $K \neq 0$ are approximately twice as large as those with the same J and $K = 0$. Residual nuclei with odd A have no levels with $K = 0$; hence, all levels have

Table 1: Low-lying states in ^{168}Er

State	E_x	J	K	π
1	0.0	0	0	+
2	0.08	2	0	+
3	0.264	4	0	+
4	0.549	6	0	+
5	0.862	2	2	+
6	0.895	3	2	+
7	0.93	8	0	+
8	0.99	4	2	+
9	1.12	5	2	+
10	1.13	4	4	-
11	1.19	5	4	-
12	1.22	0	0	+
13	1.26	6	2	+
14	1.26	2	0	+
15	1.31	6	4	-

double degeneracy and the K dependence is very small. In both cases, the difference between no K mixing and complete K mixing is typically no more than 10%.

Table 1 lists the J, K, and π values for the lowest fifteen levels of ^{168}Er. In Table 2, the cross sections for neutron scattering at 2 MeV from ^{168}Er are presented for a Hauser Feshbach code based on spherical symmetry [10,11] (a conventional Hauser Feshbach code) and the cross sections calculated with a deformed Hauser Feshbach code [9]. In each case, the cross sections are presented as ratios to the calculated elastic cross section. This cross section is about 100% larger for the deformed calculations. All input parameters are identical for the two calculations. Nate the strong tendency in the cross sections calculated with the deformed code to enhance the relative cross sections for low J and reduce the cross sections for high J. There is also a tendency for states with the same J but different K to be larger for $K \neq 0$.

Table 3 presents the same results for 6 MeV neutrons. At this energy, the substantial inhibition of the population of states with $J \geq 6$ is largely removed. However, the tendency to reduce cross sections at high J is still observed. Note that for the spherical calculations eight of the cross sections are larger than the elastic; for the deformed calculation, only one cross section is larger than the elastic. Also, note that the spherical calculation predicts very similar cross sections for levels 3, 8 and 10. This is not surprising, since each level has $J = 4$. Since the K values differ, it is also not surprising that the deformed Hauser Feshbach predicts substantially different cross sections for the three states. The results quoted in Table 2 and Table 3 are for no mixing of K values. If one invokes complete K mixing, the trio of states 3, 8 and 10 move towards the asymptotic limit of twice as much cross sections for states 8 and 10 as for 3. Thus, state 8 has a virtually unchanged cross section, while the cross section for state 3 goes up about 12% and that for state 10 goes down 8%.

As has been previously noted, the continuum is virtually unchanged in moving to a deformed calculation. Both the cross section and average energy change by less than 5% for neutrons, protons and alpha particles. There are some higher order changes, however. The average J value of states populated in the continuum goes down about 15% in going to the deformed calculation and the average K value increases. These changes could potentially modify (n,2n) cross sections near threshold.

Table 2: Cross sections for scattering of 2 MeV neutrons from ^{168}Er (normalized to ground state cross section).

Level	Conventional HF Cross Section	Deformed HF Cross Section
1	1.0	1.0
2	1.84	0.39
3	0.28	0.04
4	10^{-9}	7×10^{-9}
5	1.66	0.78
6	0.86	0.31
7	8×10^{-10}	5×10^{-9}
8	0.25	0.08
9	0.08	0.02
10	0.25	0.10
11	4×10^{-6}	9×10^{-6}
12	0.89	0.90
13	2.5×10^{-9}	8×10^{-9}
14	1.56	0.33
15	1.4×10^{-6}	2.8×10^{-6}

Table 3: Cross sections for scattering of 6 MeV neutrons from ^{168}Er (normalized to ground state cross section).

Level	Conventional HF Cross Section	Deformed HF Cross Section
1	1.00	1.00
2	3.04	0.63
3	1.89	0.24
4	0.49	0.05
5	2.93	1.35
6	2.64	0.90
7	0.043	0.004
8	1.85	0.52
9	1.04	0.253
10	1.71	0.64
11	0.95	0.3
12	0.97	0.96
13	0.47	0.104
14	2.66	0.60
15	0.42	0.12

4 Summary

A new Hauser Feshbach code has been developed which includes K as a quantum number in calculating decay of the compound nucleus. Very small effects are found for the continuum. Cross sections for the population of resolved final levels are frequently changed by 40% or more. A systematic tendency is found such that cross sections for levels of large J are reduced and cross sections for low J states are enhanced. Cross sections for $K = 0$ states are reduced relative to those of states of the same J with $K > 0$.

References

[1] V. Weisskopf, *Phys. Rev.* **52**, 295 (1937).

[2] V. F. Weisskopf and D. H. Ewing, *Phys. Rev.* **57**, 472 (1940).

[3] W. Hauser and H. Feshbach, *Phys. Rev.* **87**, 366 (1952).

[4] L. Wolfenstein, *Phys. Rev.* **82**, 690 (1951).

[5] S. M. Grimes, J. D. Anderson, A. K. Kerman and C. Wong, *Phys. Rev. C* **5**, 85 (1972).

[6] C. R. Lux, N. T. Porile and S. M. Grimes, *Phys. Rev. C* **15**, 1308 (1977).

[7] S. M. Grimes, *Phys. Rev. C* **46**, 1064 (1992).

[8] S. M. Grimes, *Phys. Rev. C* **78**, 057601 (2008).

[9] S. M. Grimes, Ohio University Report **INPP 12-01**, "A Hauser Feshbach Code for Deformed Nuclei" (2012)

[10] S. M. Grimes, J. D. Anderson, J. W. McClure, B. A. Pohl and C. Wong, *Phys. Rev. C* **10**, 2373 (1974).

[11] S. M. Grimes, Ohio University Report **INPP 04-03** (2004).

Level density for large number of particle-hole states

*Adriana Pállfy and Hans A. Weidenmüller**
Max-Planck-Institut für Kernphysik, Saupfercheckweg 1, D-69117 Heidelberg, Germany
*Hans.Weidenmueller@mpi-hd.mpg.de

Nuclear spectroscopy using intense high-energy laser beams with ultrashort pulses has become a realistic possibility [1]. This fact calls for a theoretical exploration of the expected nuclear excitation processes. In the course of such investigations [2] the need arises to determine the nuclear level density at high excitation energy ($\approx$ several 100 MeV) and large particle-hole numbers (several units of ten). The results available in the literature [3] are essentially confined to small particle-hole numbers and/or to the vicinity of the Fermi surface and cannot be extended easily into the domain of interest. We use an independent-particle model with equidistant level spacing d and finite binding energies for particles and holes. In this model, the nucleon binding energy B = bd and the total energy $E_p = \epsilon_p$d of particles are given by integers b and ϵ_p. Then, the level density for p particles can be written as

$$\omega_b(p,\epsilon_p) = \sum_{1\le n_1<\ldots<n_p\le b} \delta_{n_1+n_2+\ldots+n_p,\epsilon_p} \tag{1}$$

and correspondingly for holes and for the combined particle-hole density. We deal with a combinatorial problem involving very large numbers. A combination of analytical and numerical methods is used to develop approximate level density formulas that are valid for excitation energies of several 100 MeV and for tens of particles and holes and that yield the characteristic dependence of these functions on the variables p, ϵ_p, h (number of holes), ϵ_h and the total energy ϵ.

References

[1] G. Morou and T. Tajima, Science 331 (20100) 41.

[2] H. A. Weidenmüller, Phys. Rev. Lett. 106 (2011) 122502.

[3] M. Boehning, Nucl. Phys. A 152 (1970) 529, F. C. Williams, Nucl. Phys. A 166 (1970) 231, K. Stankiewicz, A. Marcinowski and M. Herman, Nucl. Phys. A 435 (1985) 67, P. Oblozinsky, Nucl. Phys. A 453 (1986) 127.

Emerging simplicity: Evidence for the formation of collectivity from hadronic and EM probes

N. Pietralla[1,2], Th. Möller[1], T. Ahn[1,3,4], Ch. Bauer[1], L. Coquard[1], M. Danchev[5], K.A. Gladnishki[5], A. Krugmann[1], J. Leske[1], O. Möller[1], P. von Neumann-Cosel[1], V.Yu. Ponomarev[1], G. Rainovski[5], A. Scheikh Obeid[1], M. Scheck[1], Ch. Walz[1], and J. Wambach[1,2]

[1] Institut für Kernphysik, Technische Universität Darmstadt, 64289 Darmstadt, Germany
[2] GSI Helmholtzzentrum für Schwerionenforschung mbH, 64291 Darmstadt, Germany
[3] Wright Nuclear Structure Laboratory, Yale University, New Haven, CT, U.S.A.
[4] National Superconducting Cyclotron Lab, Michigan State University, East Lansing, MI 48824, USA
[5] Faculty of Physics, St. Kliment Ohridski University of Sofia, BG-1164 Sofia, Bulgaria

Abstract
The one-quadrupole phonon excitation of mixed symmetry, the $2^+_{1,\mathrm{ms}}$ state, is a fundamental building block of nuclear structure. This article gives a summary of our recent experimental research on this excitation mode in the $A = 90$ and $A = 130$ mass regions.

1 Introduction

The nuclear proton-neutron degree of freedom and its fundamental impact on nuclear structure represents one of the central aspects of nuclear structure physics. The evolution of nuclear shells as a function of proton and neutron numbers sets the conditions for the emergence of excited nuclear quantum states with wave functions that include many proton excitations and neutron excitations within the valence shell that collectively couple in phase. This in-phase coupling of proton and neutron valence-shell excitations simultaneously leads to the occurrence of orthogonal nuclear valence-shell excitations with partial out-of-phase coupling of proton and neutron components. These states represent a closely related aspect of the nuclear proton-neutron degree of freedom. Indeed, nuclear excitations may be classified according to the proton-neutron symmetry of their wave functions, either in terms of isospin in the framework of models that use nucleons as the fundamental degree of freedom or in terms of F-spin in approximate bosonic nuclear models for collective valence-shell excitations at low energies.

The formulation of the interacting boson model (IBM-2) in its F-spin limit [1–3] has emphasized the fundamental role of collective proton-neutron non-symmetric valence-shell excitations. Nuclear excitations with F-spin quantum number $F < F_{\max} = (N_\pi + N_\nu)/2$, where $N_{\pi(\nu)}$ is half the number of valence protons (neutrons), contain parts in their wave functions where proton bosons and neutron bosons are coupled antisymmetrically. These states have been called mixed-symmetry states (MSSs). Prominent examples of MSSs are the $J^\pi = 1^+$ scissors mode of deformed nuclei or the mixed-symmetry $2^+_{1,\mathrm{ms}}$ one-phonon vibration in heavy spherical nuclei. Information on the proton-neutron symmetry of the low-energy nuclear states, including the ground state, its collective excitations, and MSSs, is needed for a correct interpretation of the role of the nuclear proton-neutron degree of freedom in the formation of nuclear structure. After the discovery of the scissors mode [4] and the clarification of its quadrupole-collective character [5, 6] it became obvious that the isovector quadrupole excitation of the valence shell represents the building block of mixed-symmetric structures.

Vibrational nuclei exhibit a one-quadrupole phonon excitation as the lowest-lying state of mixed-pn symmetry, *i.e* the $2^+_{1,\mathrm{ms}}$ state. Its close relation to the 2^+_1 state is evident in the Q-phonon scheme [7], where the wave functions of the one-phonon excitations are well approximated by the expressions

$$|2^+_1\rangle \simeq Q_s\,|0^+_1\rangle = [Q_\pi + Q_\nu]\;|0^+_1\rangle \tag{1}$$

$$|2^+_{1,\mathrm{ms}}\rangle \simeq Q_m\,|0^+_1\rangle = N\left[\frac{Q_\pi}{N_\pi} - \frac{Q_\nu}{N_\nu}\right]\;|0^+_1\rangle\,. \tag{2}$$

Here, $Q_{\pi,\nu}$ ($N_{\pi,\nu}$) denote the proton and neutron quadrupole operators (boson numbers), $N = N_\pi + N_\nu$, and $|0^+_1\rangle$ is the (in general highly correlated) ground state of a collectively vibrating even-even nucleus. Despite its fundamental role in nuclear structure, the $2^+_{1,\mathrm{ms}}$ state has only recently been studied systematically, [8–12]. The dominant fragments of the one-phonon $2^+_{1,\mathrm{ms}}$ state are observed at about 2 MeV excitation energy. Due to their isovector character, MSSs decay rapidly by dipole transitions and are very short lived, typically a few tens of femtoseconds. Large $M1$ matrix elements of $\approx 1\ \mu_N$ are in fact the unique signatures for MSSs. Consequently, lifetime information is needed for making safe assignments of mixed symmetry to a nuclear energy level. A review article on the status of experimental information on mixed-symmetry states in vibrational nuclei has been published [13]. We report on our recent progress in this field. Due to the strong interest of the community in this topic we have been asked to do so on several occasions during this summer. Therefore, this contribution follows closely the presentations [14, 15] that we have recently tried to formulate as best as we can.

2 Experimental Method

Projectile-Coulomb excitation has been established as a powerful method for the identification and investigation of one-phonon MSSs [10]. After this approach has first been applied to the investigation of the $2^+_{1,\mathrm{ms}}$ state of ^{96}Ru [10], we have initiated a research programme on the $2^+_{1,\mathrm{ms}}$ state at Argonne National Laboratory with the nucleus ^{138}Ce as a case study [12]. Crucial influence of sub-shell closures on mixed-symmetry structures was observed [12], *i.e.*, MSSs sensitively test the effective proton-neutron interaction in microscopic valence shell models [16–18].

A sequence of experiments has been performed at ANL. The superconducting ATLAS accelerator provided beams of stable even-even isotopes of the Xenon, Barium and Cerium isotopic chains. Beam energies corresponded to ~ 85 % of the Coulomb barrier for a reaction on ^{12}C nuclei. The beam intensities amounted typically to $\sim$ 1pnA. The ions were impinging on a stationary carbon target of thickness 1 mg/cm^2. Light target ions were chosen in order to favor the one-step Coulomb excitation process over multi-step processes. The γ-rays emitted by Coulomb-excited states of the beam nuclei were detected in the Gammasphere array [19, 20]. An event was defined by a γ-ray of multiplicity 1 or higher. Doppler correction (recoiling velocity $\sim$ 6-8%) and background subtraction (difference between the "in-beam" spectrum and the "off-beam" spectrum scaled to eliminate the 1461 keV ^{40}K line) were applied. Figure 1 displays data from the projectile-Coulomb excitation reactions of a ^{136}Ce-ion beam on a carbon target.

The γ-ray spectra are dominated by the decays of low-spin states, such as 2^+ or 3^- states, that are predominantly populated by one-step Coulomb excitations. For each state observed we measured

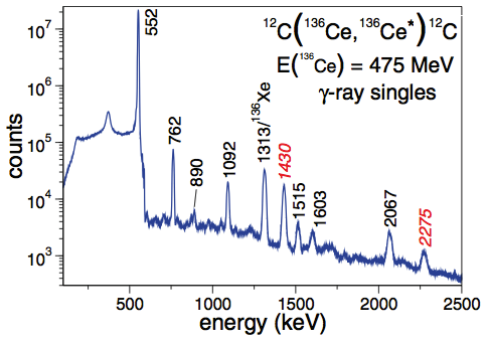

Fig. 1: Background-subtracted and Doppler-corrected singles γ-ray spectrum summed over all Ge detectors of the Gammasphere array at ANL after Coulomb excitation of ^{136}Ce on a carbon target [21].

the excitation cross section relative to that of the 2_1^+ state with an accuracy of 1 - 0.1 %. We deduced electromagnetic matrix elements corresponding to each transition of the excited states by calculating the Coulomb excitation cross sections with the multiple-Coulomb excitation code CLX and fitting them to our experimental data (normalized to the 2_1^+ state). The crucial multipole-mixing ratios of the $2^+_{(i>1)} \rightarrow 2_1^+$ transitions were obtained from γ-ray angular distributions if sufficient statistics had been obtained. A possible large $B(M1)$ value, signature of the MSS, can then be derived from the data. For a further description of this method, the reader is referred to Refs. [12, 13].

3 Evolution of $2^+_{1,\mathrm{ms}}$ states in the $A = 130$ region

The experiments [12, 21–23] allow for a nearly complete overview on the properties of the one-phonon MSS throughout the stable isotopes of the $A = 130$ region. A recent publication on the first identification of a MSS in the unstable nucleus ^{132}Te [24] expands the data on the $N = 80$ isotonic chain to the neutron-rich radioactive isotopes. Data currently under analysis on the nucleus ^{132}Ba [25] will complete our information on the one-phonon MSS in the stable even-even $N = 76$ isotones. An overview on the $B(M1; 2_i^+ \rightarrow 2_1^+)$ strength distributions in the $A = 130$ region is shown in Fig. 2.

In the stable $N = 80$ isotones the excitation energy of the $2^+_{1,\mathrm{ms}}$ state increases with proton number. This trend continues in the unstable nucleus ^{132}Te [24]. The evolution of one-quadrupole phonon MSSs along the $N = 80$ isotonic chain has been studied microscopically in the nuclear shell model either using large-scale diagonalization [17] or very recently using a new importance-sampling iterative algorithm for matrix diagonalization [18]. In the $N = 78$ isotonic chain, the energy of the MSS again increases with increasing proton number. In the neighboring $N = 76$ isotones, however, the opposite trend can be observed. It is also interesting to follow the evolution of the MSS excitation energies in the different isotopic chains. In the Ce and Ba isotopes, the excitation energy of the MSS increases with increasing neutron number, whereas in the Xe isotopes an increase in N_ν results in a decrease of $E(2^+_{1,ms})$. Apparently, the $2^+_{1,\mathrm{ms}}$ state evolves in different ways as a function of valence particle numbers. The evolution of $M1$ transitions between mixed-symmetry states and fully symmetric states in the γ-soft nuclei of the xenon isotopic chain have recently been described in a schematic microscopic approach [26] and in the nuclear shell model using the importance-sampling algorithm [27]. Whether or not the observed evolutions are related to a nuclear shape transition near ^{134}Ba is unclear up to now.

From data on $E(2_1^+)$ and $E(2^+_{1,ms})$, an estimate of the proton-neutron quadrupole-quadrupole interaction V_{pn}^{QQ} according to the two-state mixing scheme in [28] has been performed on the $N = 80$ isotones [22], the Xe isotopes [23], and, just recently, on the $N = 78$ isotones [21]. The results show,

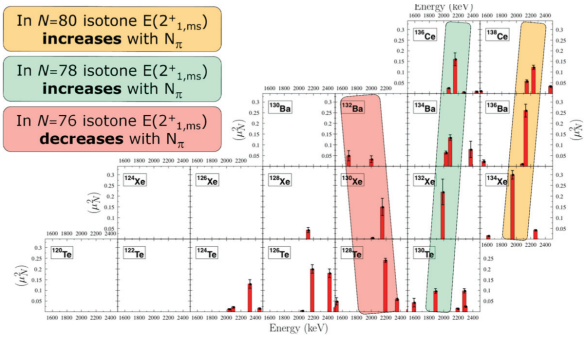

Fig. 2: Distributions of $B(M1; 2_i^+ \rightarrow 2_1^+)$ strengths for the stable even-even nuclei in the A=130 region.

that the value derived for the proton-neutron quadrupole-quadrupole interaction in the $N = 78$ isotonic chain is about 14% smaller than that for the $N = 80$ isotopic chain [22] and about 6% smaller than the value for the xenon isotopic chain [23].

4 Phase of proton- and neutron-components to MSSs: The case of ^{92}Zr

We studied the formation of quadrupole collectivity in the particularly simple case of a nucleus with a low-energy structure dominated by one pair of valence particles each for protons and neutrons. An example is ^{92}Zr with 2 neutrons beyond the $N = 50$ shell closure and 2 protons beyond the $Z = 38$ sub-shell closure. The lowest 2-quasiparticle (2qp) states will therefore have $\pi(1g_{9/2})^2$ and $\nu(2d_{5/2})^2$ configurations. Due to the residual proton-neutron interaction two different classes of collective excitations appear at low energy in which the amplitudes of the two most important 2qp configurations are coupled in a symmetric or antisymmetric way, respectively. In ^{92}Zr, these are experimentally identified as the 2^+_1 and 2^+_2 states [13, 30] with some degree of configurational isospin polarization [31, 32]. To shed light on the microscopic origin of the effective coupling strength in the valence shell we consider the quasiparticle-phonon model (QPM) [33]. The QPM wave functions are dominated by the lowest π and ν 2qp components, that show the expected in-phase and out-of-phase behavior for the $2^+_{1,\mathrm{fs}}$ fully symmetric and $2^+_{1,\mathrm{ms}}$ mixed-symmetry states. The electromagnetic properties and excitation energies are in good agreement with the data [34]. The magnetic moments of these states and the $M1$ transition between them originate almost entirely from the valence-shell configurations. However, up to 80% of the $B(E2)$ strengths are generated from many components beyond the valence shell although their total contribution to the wave function norm is small. This observation motivates a simple three-state mixing scenario between the proton-valence shell configuration, the neutron-valence shell configuration, and the Giant Quadrupole Resonance (GQR) for a deeper insight in the formation of the one-quadrupole phonon states with symmetric and mixed-symmetry character even on a semi-quantitative level [35]. For the nucleus ^{92}Zr which has a higher energy for the proton valence-shell component than the neutron valence-shell component at the $Z = 40$ sub-shell closure, the three-state mixing scheme requires that the neutron valence-shell component flips its phase with respect to the GQR component when going from the proton-neutron symmetric 2^+_1 state to the predominantly mixed-symmetric 2^+_2 state.

Two probes with different sensitivity to protons and neutrons are necessary to study this quantum interference experimentally. Electron scattering at low momentum transfer provides a measure of the charge transition radius. An (e, e') experiment was performed at the high-energy-resolution spectrometer [36] of the Darmstadt superconducting electron linear accelerator (S-DALINAC). A self-supporting zirconium metal target of 9.8 mg/cm^2 areal density and with enrichment to 94.6 % in the isotope ^{92}Zr was used. Data were taken covering a momentum transfer range between $q \sim 0.3 - 0.6$ fm^{-1} indicating

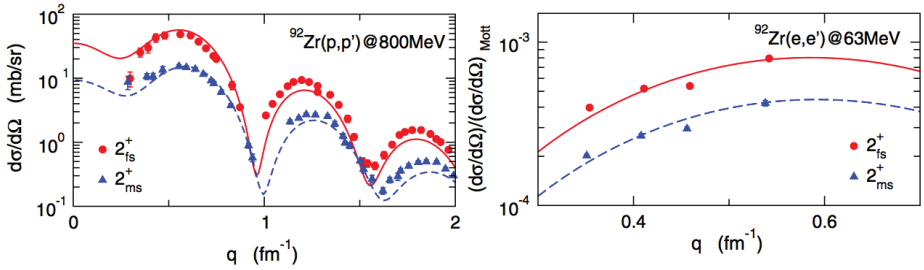

Fig. 3: Form factors for the $2^+_{1,\mathrm{fs}}$ (red, solid line) and $2^+_{1,\mathrm{ms}}$ (blue, dashed line) from $^{92}Zr(p, p')$ and $^{92}Zr(e, e')$ experiments (from [35]).

no difference between the charge transition radii of the 2_1^+ and 2_2^+ states within experimental uncertainties (Figure 3, bottom). Information about the neutron transition radii can be derived from the proton scattering data of Ref. [37]. At the incident energy of 800 MeV protons interact predominantly via the isoscalar central piece of the effective projectile-nucleus interaction [38]. Clearly, the refraction pattern of the (p, p') cross section for the $2^+_{1,\mathrm{ms}}$ state are shifted to higher q values as compared to those for the $2^+_{1,\mathrm{fs}}$ state (Figure 3, left) corresponding to a smaller transition radius.

We have studied [35] proton and neutron transition densities of the $2^+_{1,\mathrm{fs}}$ and $2^+_{1,\mathrm{ms}}$ states calculated in the full QPM approach. The full transition densities are decomposed into a collective part stemming from the GQR and the predominant $\nu(2d_{5/2})^2$ 2qp neutron contributions. The key point is the different radial behaviour of both parts and their relative signs. An out-of-phase coupling between the neutron valence shell contribution and the contribution from the GQR in the $2^+_{1,\mathrm{ms}}$ state leads to a destructive quantum interference that reduces the neutron transition density at large radii (due to the larger radius of the $\nu(2d_{5/2})^2$ orbital) and consequently shifts the maximum of the total neutron transition density to the interior with respect to that one for the 2_1^+ state. This effect reduces the neutron transition radius of the $2^+_{1,\mathrm{ms}}$ state with respect to the 2_1^+ state of ^{92}Zr. In contrast, the proton transition radius remains essentially unchanged since the $\pi(1g_{9/2})^2$ part couples in-phase to the GQR contribution in both states. The combination of both data sets unambiguously demonstrates for the first time that the phase of the neutron valence-shell configurations in ^{92}Zr changes its sign between the 2_1^+ and the $2^+_{1,\mathrm{ms}}$ state [35].

5 Summary

The isovector one-quadrupole phonon excitation of the valence shell has been systematically investigated in a large number of vibrational nuclei in the mass regions $A = 90$ and $A = 130$. It carries the signatures of the $2^+_{1,\mathrm{ms}}$ state with F-spin quantum number $F = F_{\max} - 1$. This state is generally observed from absolute $M1$ transition strengths when the experimental sensitivity is high enough. This state is typically concentrated in a single 2^+ state or distributed over two or three fragments. It is found at energies around 2 MeV and features an $M1$ transition matrix element to the 2_1^+ state between 0.5 and 1.5 μ_N. The details of its evolution as a function of particle number is not entirely understood. It may depend on the local shell structure around the Fermi level and on the evolution of quadrupole deformation.

Acknowledgements

We thank all those who have contributed to our research on various aspects of mixed-symmetry states. With respect to the data discussed here we want to acknowledge the scientists and staff members at Argonne National Laboratory, USA, at iThemba Labs, South-Africa, and at the S-DALINAC. Support from the DFG under grants Pi 393/2-2 and SFB 634, by the DAAD within the German-Bulgarian exchange program under grant Nos. PPP 50751591 and DNTS/01/2/2011, by the German Federal Ministry for Education and Research under grant Nos. 06DA9041I and 06DA7046, and by the Helmholtz International Center for FAIR funded in the LOEWE program by the state of Hesse is gratefully acknowledged.

References

[1] A. Arima, T. Ohtsuka, F. Iachello, and I. Talmi, *Phys. Lett.* **B 66** (1977) 205.

[2] F. Iachello and A. Arima, *The Interacting Boson Model* (Cambridge University Press, 1987).

[3] P. Van Isacker, K. Heyde, J. Jolie, and A. Sevrin, *Ann. Phys.* **171** (1986) 253.

[4] D. Bohle, A. Richter, W. Steffen, A. Dieperink, N. L. Iudice, F. Palumbo, and O. Scholten, *Phys. Lett.* **B 137** 1984) 27.

[5] W. Ziegler, C. Rangacharyulu, A. Richter, and C. Spieler, *Phys. Rev. Lett.* **65** (1990) 2515.

[6] N. Pietralla, P. von Brentano, R.-D. Herzberg, U. Kneissl, N. Lo Iudice, H. Maser, H. H. Pitz, and A. Zilges, *Phys. Rev. C* **58** (1998) 184.

[7] T. Otsuka, and K.-H. Kim, *Phys. Rev. C* **50** (1994) R1768.

[8] N. Pietralla, C. Fransen, D. Belic, P. von Brentano, C. Frießner, U. Kneissl, A. Linnemann, A. Nord, H. H. Pitz, T. Otsuka, I. Schneider, V. Werner, and I. Wiedenhöver, *Phys. Rev. Lett.* **83** (1999) 1303.

[9] N. Pietralla, et al., *Phys. Rev. Lett.* **84** (2000) 3775.

[10] N. Pietralla, C. J. Barton, R. Krücken, C. W. Beausang, M. A. Caprio, R. F. Casten, J. R. Cooper, A. A. Hecht, H. Newman, J. R. Novak, and N. V. Zamfir, *Phys. Rev. C* **64** (2001) 031301(R).

[11] N. Pietralla, et al., *Phys. Rev. C* **68** (2003) 031305(R).

[12] G. Rainovski, N. Pietralla, T. Ahn, C. J. Lister, R. V. F. Janssens, M. P. Carpenter, S. Zhu, and C. J. Barton, *Phys. Rev. Lett.* **96** (2006) 122501.

[13] N. Pietralla, P. von Brentano, and A. F. Lisetskiy, *Prog. Part. Nucl. Phys.* **60** (2008) 225.

[14] N. Pietralla, Th. Möller *et al.*, Proc. of *Beauty in Physics: Theory and Experiment*, Cocoyoc, Mexico, May 14-18, 2012, AIP, *in press*.

[15] N. Pietralla, Th. Möller *et al.*, Proc. of *Nuclear Structure and Related Topics*, Dubna, Russia, July 2-7, 2012, Eur. Phys. J. Web of Conferences, *in press*.

[16] N. Lo Iudice, C. Stoyanov, and D. Tarpanov, *Phys. Rev. C* **77** (2008) 044310.

[17] K. Sieja, G. Martinez Pinedo, L. Coquard, and N. Pietralla, *Phys. Rev. C* **80** (2009) 054311.

[18] D. Bianco, F. Andreozzi, N. Lo Iudice, A. Porrino, and F. Knapp, *Phys. Rev. C* **85** (2012) 034332.

[19] I. Y. Lee, *Nucl. Phys.* **A 520** (1990) 641c.

[20] P. Nolan, F. Beck, and D. Fossan, *Annu. Rev. Nucl. Part. Sci.* **45** (1994) 561.

[21] T. Ahn, G. Rainovski, N. Pietralla, L. Coquard, T. Möller, A. Costin, R. V. F. Janssens, C. J. Lister, M. P. Carpenter, and S. Zhu, *Phys. Rev. C* **86** (2012) 014303.

[22] T. Ahn, L. Coquard, N. Pietralla *et al.*, *Phys. Lett.* **B 679** (2009) 19.

[23] L. Coquard *et al.*, *Phys. Rev. C* **82** (2010) 024317.

[24] M. Danchev, G. Rainovski, N. Pietralla *et al.*, *Phys. Rev. C* **84** (2011) 061306.

[25] T. Möller *et al.*, in preparation.

[26] R.V. Jolos, N. Pietralla, N.Yu. Shirikova, and V.V. Voronov, *Phys. Rev. C* **84** (2011) 014315.

[27] D. Bianco, F. Andreozzi, N. Lo Iudice, A. Porrino, and F. Knapp, *Phys. Rev. C* **84** (2011) 024310.

[28] K. Heyde and J. Sau, *Phys. Rev. C* **33** (1986) 1050.

[29] B. Fazekas, T. Belgya, G. Molnar, and A. Veres, *Nucl. Phys.* **A 548** (1992) 249.

[30] V. Werner, D. Belic, P. von Brentano, C. Fransen, A. Gade, H. von Garrel, J. Jolie, U. Kneissl, C. Kohstall, A. Linnemann, A. Lisetskiy, N. Pietralla, H. Pitz, M. Scheck, K.-H. Speidel, F. Stedile, and S. Yates, *Phys. Lett.* **B 550** (2002) 140.

[31] J. D. Holt, N. Pietralla, J. W. Holt, T. T. S. Kuo, and G. Rainovski, *Phys. Rev. C* **76** (2007) 034325.

[32] A.P. Severyukhin, N.N. Arsenyev, and N. Pietralla, *Phys. Rev. C* **86** (2012) 024311.

[33] V. Soloviev, *Theory of Atomic Nuclei: Quasiparticles and Phonons*, (IoP Publ., 1992).

[34] N. Lo Iudice and C. Stoyanov, *Phys. Rev. C* **73** (2006) 037305.

[35] C. Walz, H. Fujita, A. Krugmann, P. von Neumann-Cosel, N. Pietralla, V. Y. Ponomarev, A. Scheikh-Obeid, and J. Wambach, *Phys. Rev. Lett.* **106** (2011) 062501.

[36] A. Lenhardt, U. Bonnes, O. Burda, P. von Neumann-Cosel, M. Platz, A. Richter, and S. Watzlawik, *Nucl. Instrum. Methods Phys. Res.* **A 562** (2006) 320.

[37] F. Baker, A. Scott, M. Grimm, W. Love, V. Penumetcha, C. Glashausser, G. Adams, G. Igo, G. Hoffmann, J. Moss, W. Swenson, and B. Wood, *Nucl. Phys.* **A 393** (1983) 283.

[38] M. A. Franey, and W. G. Love, *Phys. Rev. C* **31** (1985) 488.

The observation of a strong E0 component in the 2+2-2+1 transition in ^{184}Hg from the β-decay of laser-ionized thallium isotopes: a strong signature for shape coexistence.

E.Rapisarda
Instituut voor Kern- en Stralingsfysica, Katholieke Universiteit Leuven, B-3001 Leuven, Belgium

The mass region of neutron-deficient mercury and lead isotopes near the midshell (N=104) is well known for the phenomenon of shape coexistence. In neutron-deficient, even-even $^{180-188}$Hg isotopes an oblate ($\beta_2 \sim -0.15$) ground state band is found to coexist with an excited prolate ($\beta_2 \sim 0.25$) band at low spin and low-excitation energies. This band is built on top of a deformed excited 0^+ state, which is interpreted as resulting from proton excitations across the Z=82 closed shell. Such intruder states have been found to be a widely occurring structural feature of nuclei at and near closed shell.

The low-lying coexisting states in ^{180,182,184}Hg have been studied at ISOLDE, CERN through the β^+/EC decay of ^{180,182,184}Tl as part of a systematic α, β, and β-delayed fission study of neutron-deficient thallium isotopes. The β^+/EC decay is a very simple but still powerful tool which allows to effectively populate low-lying not-yrast states in the daughter nucleus, normally not easily accessible with other techniques, thus providing complementary information to the ones from in-beam γ-spectroscopy studies and from α−decay studies from the Pb parent nuclei.

Mass-separated Tl beams, produced at ISOLDE, CERN, in the bombardment of ^{238}U by 1.4 GeV protons and selectively laser ionized, were implanted on a carbon foil mounted on a rotating wheel. The implantation foil was surrounded by two Si detectors for α, β and electron detection while γ rays were detected with two high-resolution Ge detectors.

By means of unambiguously Si-γ and γγ coincidences, a detailed level scheme of the coexisting states has been built-up as well as a detailed description of their decay properties (γ intensities, E0 component of $2^+ \rightarrow 2^+$ transitions). The newly observed or better energy-determined 0_2^+, 2_2^+, 2_3^+ states in ^{180,182}Hg follow well the general trend of the prolate band. They confirm that the minimum of the parabolic behavior in excitation energy of the prolate band occurs in ^{182}Hg, as expected. The exceptionally large E0 component observed in the $2_1^+ \rightarrow 2_2^+$ transition in ^{184}Hg (23+/-5) confirm that the two states are strongly mixed and they have different deformation.

Isomerism is well-known in the heavier thallium isotopes and the population of low-spin states as well as high-spin states (up to 8^+ in ^{182,184}Hg) in the beta decay points to similar features in the lighter thallium isotopes.

The information gathered can be combined with the ones obtained with different techniques, such as in-beam γ and conversion-electron spectroscopy, Coulomb excitation on postaccelerated radioactive ions (recently performed at ISOLDE), lifetime measurements and laser spectroscopic studies to get a deeper knowledge of the shape-coexistence phenomenon.

Rotating hyperdeformed quasi-molecular states formed in capture of light nuclei and in collision of very heavy ions

G. Royer[1], *E. Zarrouk*[1], *J. Gaudillot*[1], *C. Beck*[2] *and W. von Oertzen*[3]
[1]Laboratoire Subatech, UMR : IN2P3/CNRS-Université-Ecole des Mines, Nantes, France
[2]IPHC, IN2P3-CNRS, UMR 7178, Université Louis Pasteur, Strasbourg, France
[3]Hahn-Meitner-Institut-GmbH, Berlin, Germany

Abstract
Within a rotational liquid drop model including the nuclear proximity energy the l-dependent potential barriers governing the capture reactions of light nuclei and of very heavy ions have been determined. Rotating quasi-molecular hyperdeformed states appear at high angular momenta. The energy range of these very deformed high spin states is given for light systems. The same approach explains the observation of ternary cluster decay from ^{56}Ni and ^{60}Zn through hyperdeformed shapes at angular momenta around 45 $\hbar$. The apparently observed superheavy nuclear systems in the U+Ni and U+Ge reactions at high excitation energy might correspond to these rotating isomeric states formed at very high angular momenta even though the shell effects vanish.

1 Introduction

The connection between nuclear clustering, quasi-molecular resonances and very high deformations in light nuclear systems remains an open domain in nuclear physics [1]. Indeed, resonances observed in the excitation functions of some reactions as well as the numerous detected superdeformed bands are indications of the existence of rotating highly deformed configurations in ^{36}Ar, ^{40}Ca, ^{44}Ti and ^{48}Cr [2–4]. Furthermore, binary and ternary decays of rotating hyper-deformed states formed in the ^{32}S+^{24}Mg and ^{36}Ar+^{24}Mg reactions at angular momenta of 45-50 $\hbar$ have been also observed recently [5,6].

Our purpose is to study the l-dependent entrance channel of reactions between light nuclei, the fission probability being very small for such light systems [7]; and also the possibility to form superheavy elements at high excitation energy. The potential energy is determined within a generalized liquid drop model previously used to investigate the fusion [8–10], fission [11,12], alpha emission [13] and cluster radioactivity [14] processes. The selected quasi-molecular one-body shape sequence (elliptic lemniscatoids) describes smoothly the formation of a deep neck between the incoming spherical nuclei while keeping almost spherical ends.

2 Generalized liquid drop model

The generalized liquid drop model (GLDM) energy is the sum of the volume, surface, Coulomb and proximity energies:

$$E = E_V + E_S + E_C + E_{\rm Prox} \, . \tag{1}$$

When the nuclei are separated:

$$E_V = -15.494 \left[(1 - 1.8 I_1^2) A_1 + (1 - 1.8 I_2^2) A_2 \right] \ \text{MeV}, \tag{2}$$

$$E_S = 17.9439 \left[(1 - 2.6 I_1^2) A_1^{2/3} + (1 - 2.6 I_2^2) A_2^{2/3} \right] \ \text{MeV}, \tag{3}$$

$$E_C = 0.6 e^2 Z_1^2 / R_1 + 0.6 e^2 Z_2^2 / R_2 + e^2 Z_1 Z_2 / r, \tag{4}$$

where I_i is the relative neutron excess.

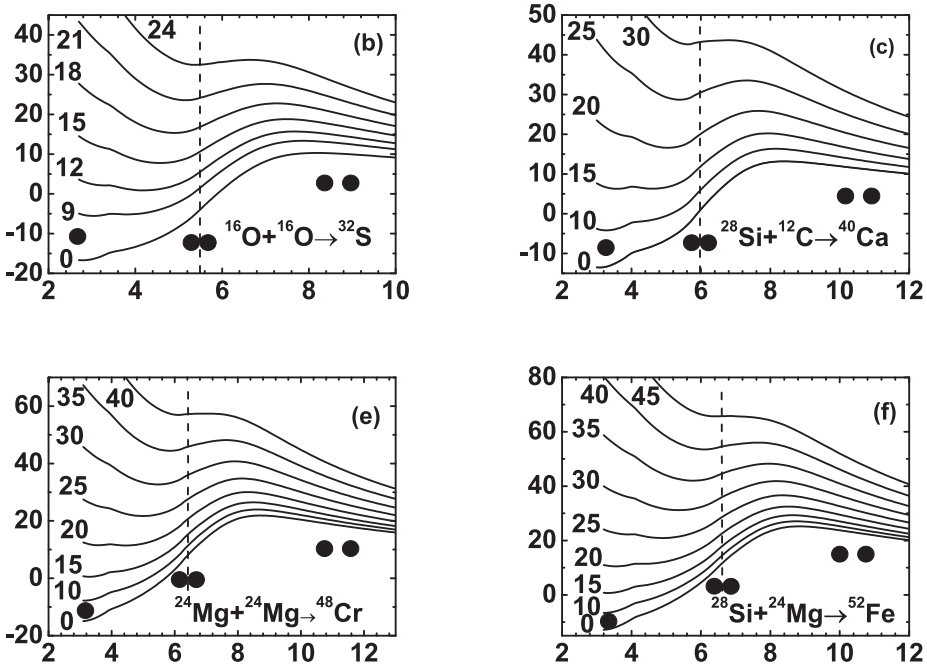

Fig. 1: Fusion barriers (in MeV) versus the angular momentum ($\hbar$ unit) and the distance r between the mass centres for the $^{16}O+^{16}O$, $^{28}Si+^{12}C$, $^{24}Mg+^{24}Mg$ and , $^{28}Si+^{24}Mg$ nuclear systems.

When there are nucleons in regard in a gap or a neck between incoming nuclei an additional term called proximity energy must be added to the surface energy to take into account the effects of the nuclear forces between the close surfaces.

3 Capture barriers

The *l*-dependent macroscopic capture barriers for four reactions between light nuclei are displayed in Fig. 1 as examples and the Q value and the barrier heights and positions are given in Table 1 for several reactions. The GLDM allows to reproduce satisfactorily the whole data set. With increasing angular momenta a macroscopic very deformed minimum appears and corresponds to a one-body configuration with a deep neck. Thus the formation of hyperdeformed quasi-molecular states is predicted in a large angular momentum range. Often the beam energy is not sufficient to reach the quasi-spherical compound nucleus assuming the angular momentum conservation. This prevents from a rapid compound nucleus formation and allows a relative stability of these highly deformed rotating states. In this mass range the quasi-fission exit channel is neglected.

The deformation of these minima increases with the angular momentum while the position of the barrier is closer to the contact point. Due to a more important mass inertia the maximal angular momenta that the nuclei are able to sustain increase with their masses. For these highly deformed shapes the calculations of the shell and pairing effects are very model dependent. They can move the position of these potential pockets but their basic origin is macroscopic and the existence of these hyperdeformed states must be a general phenomenon for light nuclei for which the fission channel is relatively narrow.

Table 1: Q values of the fusion reactions and experimental and theoretical barrier heights and positions.

Reaction	Q_{exp}(MeV)	B_{exp}(MeV)	$R_{exp}(fm)$	B_{GLDM}	R_{GLDM}
$^{13}C+^{13}C\rightarrow^{26}Mg^*$	22.47	6.0	7.83	5.85	8.1
$^{16}O+^{16}O\rightarrow^{32}S^*$	16.54	10.25	8.21	10.3	8.2
$^{28}Si+^{12}C\rightarrow^{40}Ca^*$	13.35	13.7	8.0	13.2	8.4
$^{28}Si+^{16}O\rightarrow^{44}Ti^*$	11.32	17.7	8.2	17.3	8.55
$^{24}Mg+^{24}Mg\rightarrow^{48}Cr^*$	14.95	21.5	8.4	21.9	8.7
$^{28}Si+^{24}Mg\rightarrow^{52}Fe*$	12.91	25.9	8.5	25.2	8.8
$^{28}Si+^{28}Si\rightarrow^{56}Ni^*$	10.92	28.7	9.06	29.0	8.95
$^{40}Ca+^{40}Ca\rightarrow^{80}Zr^*$	-14.44	55.6	9.1	55.6	9.6
$^{40}Ca+^{48}Ca\rightarrow^{88}Zr^*$	04.56	53.2	10.1	54.0	9.9
$^{48}Ca+^{48}Ca\rightarrow^{96}Zr^*$	-2.99	51.7	10.4	52.4	10.2

4 Fusion cross sections

The fusion cross sections have been determined using the usual partial-wave summation. Above the l-wave barrier the transmission coefficient is approximated by the Hill-Wheeler formula. Below the barrier the WKB method has been used. The Fig. 2 displays the fusion cross sections around the Coulomb barrier. The agreement is quite correct which indicates that the static approach is sufficient for these light systems when the fusion barriers are precisely determined. The quasi-fission events being neglected all the angular momenta leading to hyperdeformed rotating states contribute to the fusion cross sections which consequently are highly dependent on the angular momentum range. As for most one-dimensional static models using spherical shapes the theoretical fusion cross sections are slightly too low at very low energy below the barrier for some reactions. For heavier masses dynamical models are needed to reproduce the data since the barrier top is closer to the contact point and the dissipation due to the friction forces must be taken into account [8].

5 Characteristics of the rotating hyperdeformed states

In Tables II and III the angular momentum, moment of inertia and energy range of these highly deformed rotating quasi-molecular states are given for symmetric and asymmetric reactions as well as the l-dependent barrier heights and positions and the electric quadrupole moment and β parameter in the symmetric case. The state corresponding to a potential pocket is taken into account when there is a barrier height of at least two MeV both against decay in two fragments and in the path towards the quasi-spherical compound nucleus. The β parameter indicates clearly that the deformation is very large. Naturally these states probably will evacuate their excitation energy via γ cascades and will reach after the superdeformed minima mainly due to shell effects at smaller deformations.

The following analytical formula reproduces the energy of the quasi-molecular minima versus its angular momentum

$$E=-11.18A_1^{2/3}-16.025A_2^{2/3}+\frac{50.618A_1^{1/3}A_2^{1/3}}{A_1^{1/3}+A_2^{1/3}}+1.7624A+7.9856l^{0.5} \tag{5}$$
$$+\frac{1.05985(A_1+A_2)l^2}{A_1A_2(A_1^{1/3}+A_2^{1/3}-2)}-\frac{0.20305Z_1^2}{A_1^{1/3}}+\frac{0.06709Z_2^2}{A_2^{1/3}}+\frac{1.13156Z_1Z_2}{A_1^{1/3}+A_2^{1/3}-2}.$$

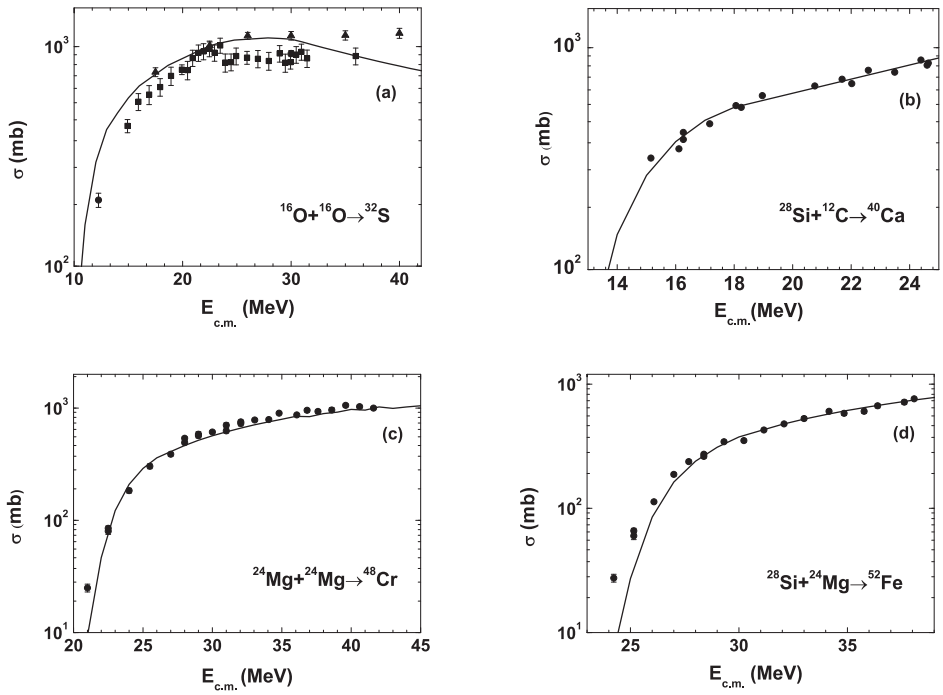

Fig. 2: Fusion cross sections around the Coulomb barrier for the $^{16}O+^{16}O$, $^{28}Si+^{12}C$, $^{24}Mg+^{24}Mg$ and $^{28}Si+^{24}Mg$ nuclear reactions.

6 Fission and ternary decay of hyper-deformed rotating ^{56}Ni and ^{60}Zn

In the experiments $^{32}S+^{24}Mg\rightarrow^{56}Ni$ (E*=84 MeV) and $^{36}Ar+^{24}Mg\rightarrow^{60}Zn$ (E*=88 MeV) narrow out-of-plane correlations corresponding to coplanar decay are observed when two fragments are emitted with missing charges from 4 up to 8. This ternary fission have been interpreted as the decay of hyper-deformed states with angular momenta around 45-50 $\hbar$ [5,6]. The Fig. 3 indicates that, within the GLDM, the very asymmetric ternary fission is favoured relatively to the symmetric ternary one. At high angular momenta around 45 $\hbar$ the potential energy minima is lower in the ternary fission path than in the binary fission path. The more negative Q-value for ternary fission is compensated for the smaller value of the rotational energy at the saddle point. Thus, the GLDM allows to explain simply that the ternary cluster fission of light nuclei becomes competitive with binary cluster fission at the highest angular momenta.

7 Formation of superheavy elements in the ^{238}U+Ni and ^{238}U+Ge reactions

Recently, the systems ^{238}U+Ni and ^{238}U+Ge have been studied at Ganil in reverse kinematics at high excitation energy of 6.62 MeV/u and 6.09 MeV/u possibly leading to composite systems of charge 120 and 124 respectively [15,16]. A coupled analysis of the involved nuclear reaction time distributions and of the measured K x rays provides evidence for nuclei with Z=120 and 124 living longer than 10^{-18} s and arising from highly excited compound nuclei.

Within the GLDM the capture barriers for these reactions have been calculated as a function of the angular momentum (see Fig. 4 where the shell effects are taken into account assuming that the next proton magic number is Z=114.) The excitation energy is very large and very high angular momenta are

Table 2: l, I, Q, β and E are respectively the angular momentum, the moment of inertia, the quadrupole moment Q, the β parameter and the center of mass energy (relatively to the energy of two infinitely separated nuclei) of the strongly deformed quasi-molecular minima for symmetric fusion reactions. B and R are the l-dependent fusion barrier heights and positions.

Reaction	$l(\hbar)$	I($\hbar^2$/MeV)	Q(e b)	β	E(MeV)	B(MeV)	R(fm)
$^{13}C+^{13}C$	12	4.31	1.0	0.78	1.7	13.2	7.2
$^{13}C+^{13}C$	18	5.34	1.4	0.94	20.8	23.5	6.5
$^{16}O+^{16}O$	12	4.45	0.6	0.39	2.13	15.7	7.7
$^{16}O+^{16}O$	23	7.81	2.3	0.96	29.4	31.6	6.8
$^{24}Mg+^{24}Mg$	22	11.1	2.4	0.68	15.4	31.8	8.25
$^{24}Mg+^{24}Mg$	37	15.1	4.3	0.94	49.3	51.6	7.5
$^{28}Si+^{28}Si$	27	14.2	3.1	0.67	24.3	40.9	8.5
$^{28}Si+^{28}Si$	44	19.5	5.5	0.93	60.0	62.2	7.75
$^{40}Ca+^{40}Ca$	38	25.9	5.5	0.65	52.7	69.3	9.2
$^{40}Ca+^{40}Ca$	62	35.9	10.15	0.93	91.3	93.5	8.6
$^{48}Ca+^{48}Ca$	48	34.2	5.7	0.61	47.8	68.4	9.8
$^{48}Ca+^{48}Ca$	80	49.3	11.6	0.93	96.6	98.8	9.1

Table 3: Angular momentum l, moment of inertia I and center of mass energy (relatively to the energy of two infinitely separated nuclei) of the strongly deformed quasi-molecular minima for asymmetric fusion reactions. B and R are the l-dependent fusion barrier heights and positions.

Reaction	l	I	E	B	R	l	I	E	B	R
$^{28}Si+^{12}C$	16	8.5	8.21	21.2	7.9	28	10.15	36.8	39.3	7.15
$^{28}Si+^{16}O$	17	9.86	9.34	24.5	8.15	32	12.7	42.1	44.4	7.3
$^{28}Si+^{24}Mg$	24	10.0	19.8	35.7	8.4	40	17.2	53.5	56.0	7.75
$^{28}Si+^{40}Ca$	31	19.95	35.6	52.1	8.9	53	27.1	74.1	76.8	8.2
$^{40}Ca+^{48}Ca$	52	30.0	57.1	76.1	9.4	78	41.2	104.8	107.0	8.25

populated while the shell effects are probably very small at these energies. For these very heavy systems the potential energy profile is very flat once the external barrier is passed allowing the possible formation and stability of rapidly rotating isomeric states without reaching a quasi-spherical nuclear shape and even though the shell effects vanish. This perhaps could help to explain the observation of these very heavy compound systems.

8 Conclusion

The l-dependent capture barriers in reactions between light nuclei have been determined within a generalized liquid drop model taking into account the proximity energy and the asymmetry. Deep strongly deformed quasi-molecular minima appear at very high angular momenta lodging possibly rotating isomeric states. Their energetic and geometrical characteristics are provided. The same approach explains the observation of ternary cluster decay from ^{56}Ni and ^{60}Zn through hyperdeformed shapes at angular momenta around 45 $\hbar$. The apparently observed superheavy nuclear systems in the U+Ni and U+Ge reactions at high excitation energy might correspond to these rotating isomeric states formed at very high angular momenta even though the shell effects vanish.

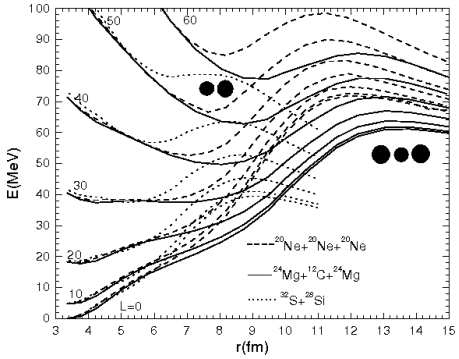

Fig. 3: Potential energies for selected binary and ternary channels for different angular momenta and ^{60}Zn.

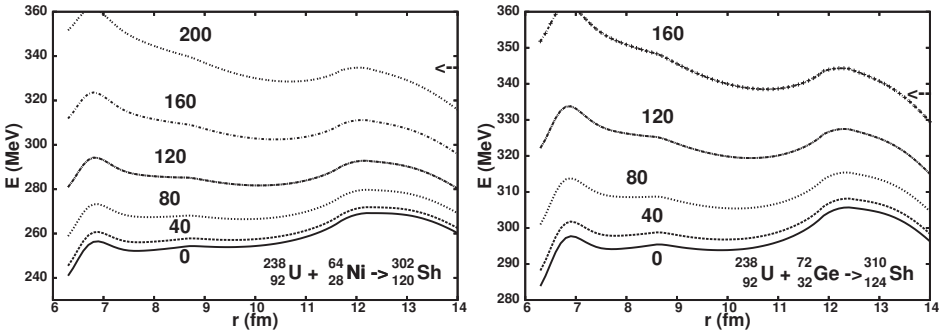

Fig. 4: L-dependent capture barriers for the U+Ni and U+Ge reactions. The arrows indicate the beam energy.

References

[1] C. Beck *et al*., *Acta Phys. Pol. B* **42** (2011) 747.

[2] S.J. Sanders *et al*., *Phys. Rep*. **311** (1999) 487.

[3] C. Beck *et al*., *Phys. Rev. C* **63** (2000) 014607.

[4] M. Rousseau *et al*., *Phys. Rev. C* **66** (2002) 034612.

[5] W. von Oertzen *et al*., *Eur. Phys. J. A* **36** (2008) 279.

[6] W. von Oertzen, V. Zherebchevsky, B. Gebauer, Ch. Schulz, S. Thummerer, D. Kamanin, G. Royer, Th. Wilpert, *Phys. Rev. C* **78** (2008) 044615.

[7] G. Royer, J. Gaudillot, *Phys. Rev. C* **84** (2011) 044602.

[8] G. Royer, B. Remaud, *Nucl. Phys. A* **444** (1985) 477.

[9] G. Royer, *J. Phys. G: Nucl. Phys*. **12** (1986) 623.

[10] G. Royer, C. Bonilla and R.A. Gherghescu, Phys. Rev. C **67** (2003) 034315.

[11] G. Royer, B. Remaud, *J. Phys. G: Nucl. Phys*. **10** (1984) 1057.

[12] G. Royer, K. Zbiri, *Nucl. Phys. A* **697** (2002) 630.

[13] G. Royer, *J. Phys. G : Nucl. Part. Phys*. **26** (2000) 1149.

[14] G. Royer, R. Moustabchir, *Nucl. Phys. A* **683** (2001) 182.

[15] M. Morjean et al, *Phys. Rev. Lett*. **101** (2008) 072701.

[16] M.O. Frégeau et al, *Phys. Rev. Lett*. **108** (2012) 122701.

Towards a Reconstruction of Thermal Properties of Light Nuclei from Fusion-Evaporation Reactions

G. Baiocco[1,2]*, L. Morelli*[1]*, F. Gulminelli*[2]*, U. Abbondanno*[3]*, M. Bruno*[1]*, M. D'Agostino*[1]*, S. Barlini*[4]*, M. Bini*[4]*, S. Carboni*[4]*, G. Casini*[4]*, M. Cinausero*[5]*, M. Degerlier*[6]*, F. Gramegna*[5]*, V. L. Kravchuk*[7]*, T. Marchi*[5,8]*, A. Olmi*[4]*, G. Pasquali*[4]*, S. Piantelli*[4]*, G. Poggi*[4]*, Ad. R. Raduta*[9]
(NUCL-EX collaboration)
[1] Dipartimento di Fisica dell'Università and INFN, Bologna,Italy
[2] CNRS, UMR6534, LPC ,F-14050 and ENSICAEN, UMR6534, LPC ,F-14050, Caen cédex, France
[3] INFN Trieste, Italy
[4] Dipartimento di Fisica dell'Università and INFN, Firenze, Italy
[5] INFN, Laboratori Nazionali di Legnaro, Italy
[6] University of Nevsehir, Science and Art Faculty, Physics Department, Nevsehir, Turkey
[7] Institute for Nuclear Research, RAS, Moskow, Russia
[8] Dipartimento di Fisica dell'Università di Padova, Italy
[9] NIPNE, Bucharest-Magurele, POB-MG 6, Romania

Abstract

An experimental campaign has been proposed at *Laboratori Nazionali di Legnaro* - INFN, in order to progress in our understanding of statistical properties of light nuclei at excitation energies above particle emission thresholds. Exclusive measurements from fusion-evaporation reactions are used. Light nuclei are interesting probes for high temperature nuclear thermodynamics and the role of structure effects in their decay is a subject of great interest. A first reaction: ^{12}C+^{12}C at 95 MeV beam energy has been measured using the GARFIELD+Ring Counter(RCo) apparatuses. A theoretical study of the system, performed with a dedicated Monte-Carlo Hauser-Feshbach code, will be shown, together with results of the data analysis. Constraints on the nuclear level density at high excitation energy for systems ranging from $\sim$C to Mg are given, and out-of-equilibrium effects, possibly favoured by α-structure, are put in evidence.

1 Introduction

Dissipative nuclear reactions are a tool to investigate nuclear properties at finite temperature, notably including the excitation energy dependence of the nucleon effective mass, symmetry energy and pairing correlations. A general concern is associated with such experimental studies: the final inclusive yields represent integrated contributions and, because of that, the information they bear on specific excitation energy (temperature) regions of the nuclei explored during the reaction may be model dependent. The experimental challenge is therefore to perform a highly exclusive detection of reaction products, in order to backtrace their origin, with the final aim of constraining nuclear properties at finite temperature [1]. An additional challenge comes into play in modelization: because of the strong interplay of nuclear structure and reactions, statistical (and dynamical) codes should be highly constrained by available nuclear data on ground state properties and information on low excitation energies, with the aim of gaining a better predictive power on finite temperature observables.

In this spirit, the NUCL-EX collaboration has recently proposed an experimental campaign, whose aim is to progress in the understanding of statistical properties of light nuclei at excitation energies above

particle emission thresholds, by measuring exclusive fusion-evaporation data.
The choice of investigating light systems is easily explained in the light of our preliminary remarks: the low expected multiplicity of fragments produced in light nuclei collisions (combined with a high detection coverage) increases the probability of achieving a quasi-complete recontruction of the event.
Furthermore, the high energy and angular resolution of the chosen GARFIELD+RCo [2] experimental setup allows the measurement of kinematic correlations among fragments, thus obtaining a global control on the decay mechanism.
The study of the fusion-evaporation channel is the only way to access the fundamental quantity governing the thermal behaviour of any nuclear property, *i.e.* the nuclear Level Density (LD), above the thresholds for particle decay, through the theory of compound nucleus decay (CN). For light nuclei reactions, the reproduction of the features of accurately selected events by means of statistical model calculations allows to strongly constrain the level density in a mass and excitation energy region where few data exist, altogether coming from rather inclusive measurements. Available data in the A$\sim 10 \div 20$ and $E^* \sim 2 \div 3$ A·MeV point indeed to the persistence of the compound nucleus description, provided that the level density parameter is correctly renormalized and deformation is included at high angular momentum [3]. These findings are also consistent with qualitative expectations from surface effects and excitation energy dependence of the effective mass [4], and with theoretical and experimental studies [5] pointing to a limiting nuclear temperature increasing with decreasing compound mass.
Nevertheless, it is especially for light nuclei that signatures of nuclear structure in the reactions are expected to be more evident even at high excitation energy. Thanks to the exclusive channel selection and to the accurate comparison with a highly constrained statistical code, we might therefore find evidence of possible deviations from a statistical behaviour in the decay of the hot fused source formed in the collision.

The first measurement of this campaign: ^{12}C+^{12}C at 95 MeV beam energy, has been measured using the GARFIELD + Ring Counter (RCo) [2] apparatuses at *Laboratori Nazionali di Legnaro* LNL - INFN, Italy. Preliminary results of this study are presented in the following.

2 The ^{12}C+ ^{12}C Experiment

The reaction: ^{12}C+ ^{12}C at 95 MeV has been measured using the GARFIELD + Ring Counter (RCo) [2] apparatuses at LNL - INFN, Italy. Some details on this setup are given in the following.
Exclusive data for the fusion-evaporation channel have been compared to the predictions of a dedicated Monte Carlo Hauser-Feshbach (HF) code for the decay of the compound nucleus [6], explicitly including all the experimentally measured particle unstable levels from the archive NUDAT2 (*http://www.nndc.bnl.gov/nudat2/*). A realistic parameterization for the nuclear level density from Ref. [7] has been implemented in the code, and other statistical model ingredients are optimized for the description of light nuclei.
In the measured reaction, the compound nucleus issued in case of complete fusion is ^{24}Mg, at $E^* = 2.6$ A·MeV and with even values of the initial angular momentum J_0, extracted from a triangular distribution with $J_{0\ max} = 12\ \hbar$ (PACE4).

2.1 Inclusive energy spectra

The fusion-evaporation channel can be selected at first thanks to static conditions on the total detected charge (in this case, $\geq 80\%$ of the charge available in the entrance channel) and on the coincidence between a residue at forward angles (RCo) ($5^\circ \leq \theta_{lab} \leq 17^\circ$) and light charged particles (LCP) detected in GARFIELD ($\theta_{lab} \geq 30^\circ$). Under these conditions, global observables as the charge distribution or LCP multiplicities, known to be less sensitive to the nuclear LD, are well reproduced by model calculations.
In what concerns the comparison of LCP energy distributions to model predictions, as it is evident from

the first two panels of Fig.1, a very good reproduction of the proton energy spectrum can be achieved, allowing us to constrain the level density model, while the same parameters choice cannot reproduce the energy spectrum of α particles. This deviation from a statistical behaviour could be attributed to out-of-equilibrium α emission, possibly favoured because of the α cluster-like nature of the ^{12}C projectile and target in the entrance channel [10]. This suggests that a contamination from other reaction mechanisms is present in the subset of events selected for the analysis.

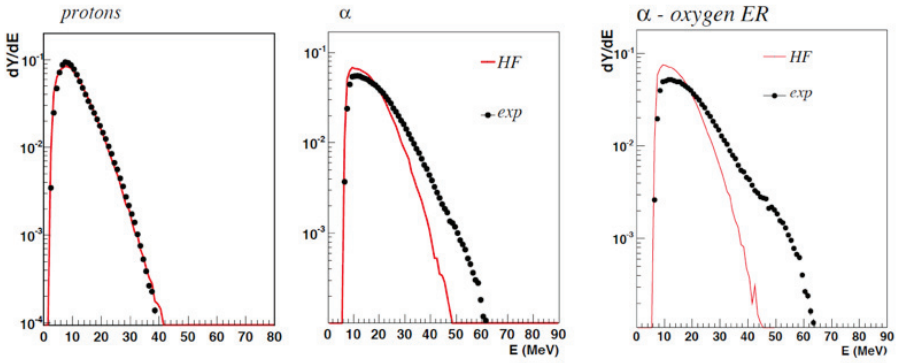

Fig. 1: From left to right, for the reaction ^{12}C (@95 MeV) + ^{12}C: in the angular range covered by GARFIELD, experimental data (dots) and filtered HF calculations (lines) for the laboratory energy spectra of protons and α particles in coincidence with any fragment at RCo angles, and for α in coincidence with a Z=8 fragment in the RCo, always under the condition of completeness of detection ($Z_{det} \geq 10$). In all spectra, normalization is to the total yield for p and α respectively.

2.2 The ^{12}C+^{12}C $\rightarrow$ ^{x}O+α + ... channel

In order to understand where the deviation from the maxwellian shape of the α energy spectrum stems from, we can investigate in more detail outgoing reaction channels in which α particles are detected. In particular, it is found that in the selected set of events, the largest cross section is related to the ^{12}C+^{12}C $\rightarrow$ ^{x}O+α + ... channel (Fig.1, third panel). The kinematic correlation between the oxygen fragment and the α particle(s) in this channel can be built, and it is shown in the top left panel of Fig.2. In the bottom left panel, the same correlation is shown for the Z=8 fragment and α particle(s) resulting from the decay of the ^{24}Mg CN, according to our HF calculations. As it is evident from the figure, there exists a locus of events in the experimental E(O) vs. E(α) matrix showing a strong correlation, which reminds of a not dissipative reaction kinematics. Such events are not easily attributed to the fusion-evaporation channel, but they have not been eliminated from the selected dataset, since they satisfy both requests on the completeness of detection and on the coincidence between a high Z fragment at forward angles and a particle at GARFIELD angles. It is also evident that even a discrimination of the reaction mechanism based on the velocity (or energy) of the "residue" [11] would not be enough to completely isolate such correlated events.

On the contrary, by building the correlation matrix of Fig.2, this discrimination can be easily performed,

and the energy spectrum of α particles from events falling in the non-correlated region (delimited by the graphical cut) is shown in the left part of Fig.2 (full dots), together with the corresponding code calculation for the same channel (line). As a reference, also the inclusive energy distribution of α particles detected in coincidence with an oxygen is plotted again (empty dots). The cut used to separate the correlated from the uncorrelated region corresponds to the locus: E(^{16}O) vs. E(α), which can be calculated on the basis of kinematic arguments for the 3-body decay channel ^{16}O+2α, with a Q-value of $\sim$ -15 MeV, corresponding to the opening of 4-body channels (see next section for more details). As it is evident from the figure, the agreement between experimental data and calculations is greatly improved by excluding 3-body decay channels, which are identified as the source of the largest discrepancy.

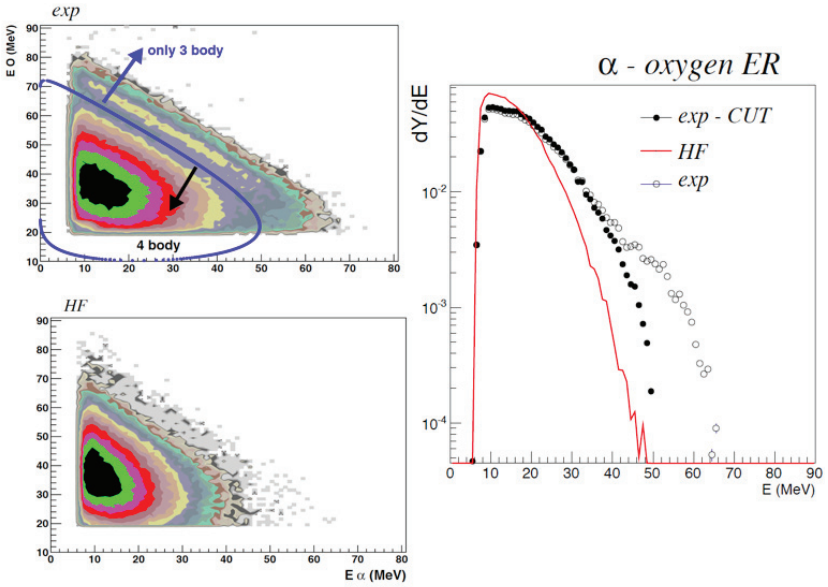

Fig. 2: Analysis of the ^{12}C+^{12}C $\rightarrow$ ^{x}O+α + .. reaction channel: on the left, top panel: experimental kinematic correlation between the oxygen (detected in the RCo) and the α particle(s) in GARFIELD; bottom panel: the same kinematic correlation as predicted by our HF calculations for the decay of the ^{24}Mg CN. On the right, full dots: energy distribution of α particles from dissipative events falling in the region identified by the kinematical cut in the experimental E(O) vs. E(α) matrix; red line: corresponding HF code calculation; empty dots: all α particles in coincidence with an oxygen. All distributions are normalized to the corresponding α particle yield.

2.3 The ^{12}C+^{12}C $\rightarrow$ ^{x}O+2α + ... channel

The ^{x}O+2α channel can be on turn investigated in more detail, even if a reduced statistics is available, due to the very stringent request on the complete charge reconstruction. For this latter case, the Q-value spectrum can be built, where:

$$Q = \sum_{i}^{mult} E_i - E_{beam} \tag{1}$$

and the sum of kinetic energies runs over all detected reaction products. The experimental distribution, plotted in the left panel of Fig.3, shows the same structure as the theoretical one on the right side, with two narrow peaks in the low Q-value region, and a broad distribution extending up to a high amount of energy shortage. By looking at model events, we can easily interpret such spectrum: the two narrow peaks correspond to decay chains in which the ^{16}O is produced either in its ground state (for the peak centered at Q $\sim$ 0.5 MeV), or in one of its first closely spaced excited states below the threshold for α particle emission (Q $\sim$ -6 MeV). The broad bump region corresponds to 4-body channels of the type ^{15}O+$2\alpha + n$, in which the missing energy is the kinetic energy of the emitted neutron. The Q-value at the opening of 4-body channels provides the best separation between the two regions, and it is used to calculate the kinematical cut in Fig.2. Despite the similarity in the structure of the two spectra, a clear discrepancy in the cross-sections for the population of the two regions is seen: in the experimental sample we have 30% of events falling in the narrow Q-value peaks region, while only $\sim$ 5% of model events fall in the same region according to the calculations. This discrepancy may be attributed to the contamination of direct reactions in the event selection, possibly favoured by the α-cluster like nature of projectile and target, which are expected to populated the same low Q-value region, without proceeding through a CN state. When enlarging the set of events to the $Z_{tot} \geq 10$ case (see previous section), this contamination cannot be totally excluded, since no real Q-value can be built for an incomplete charge detection. This might (at least partially) explain the persistence of a deviation from a statistical behaviour evident in the α energy spectrum of Fig.2.

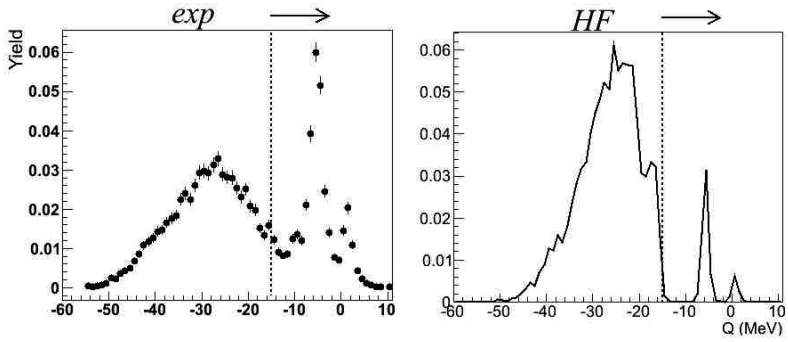

Fig. 3: For the ^{12}C+$^{12}C \rightarrow {}^{x}$O+$2\alpha$ + .. channel, experimental (left) and theoretical (right) Q-value distribution (eq.1). The experimental sample reduces here to 2.5% of the events considered in Fig.2. In both cases, the arrow identifies the region of 3 body exit channels ($^{16}O_{gs}/^{16}O^{*} + 2\alpha$), where a clear discrepancy in the measured and calculated population is observed. Normalization is to the number of events.

3 Conclusions and Perspectives

The results presented at this conference for the ^{12}C+^{12}C reaction have allowed us to put constraints to the level density of light nuclei in the A$\sim$ 10 $\div$ 20 and E* $\sim$ 2 $\div$ 3 A·MeV mass-excitation energy region, through the comparison with a dedicated Monte-Carlo Hauser-Feshbach code. An out-of-equilibrium component in α particle emission has been put in evidence, and tentatively attributed to the contamination of reaction mechanisms other than CN formation and decay, possibly favoured by the α structure of both projectile and target. The exclusive coincidence study for ^{12}C(^{12}C,^{x}O)(2)α discussed here in details will be extended by means of further analysis to other interesting decay channels in the same dataset. This will allow us to further refine the fusion-evaporation event selection, in order to understand if the contamination of non dissipative reaction mechanisms can be considered as the unique source of

deviation from a statistical behaviour.

Within the same experimental campaign, a new measurement is already scheduled at LNL, with the same GARFIELD + RCo setup, concerning the ^{14}N (@ 80 MeV)+^{10}B reaction, leading in case of complete fusion of the two N$\neq$ Z reaction partners to the same ^{24}Mg compound nucleus at similar excitation energies. In the perspectives of this campaign, deviations from a statistical behaviour are used as a tool to get information on nuclear clustering, both in the ground-state for projectile and target and eventually in the hot source formed in the collision. A disentanglement of these two aspects and an insight on the persistence of cluster correlations at high excitation energy should be possible thanks to the comparison between the two reactions.

References

[1] M. D'Agostino *et al.*, Nucl. Phys., A875 (2012) 139.

[2] F. Gramegna *et al.*, Nucl. Instr. and Meth., A389 (1997) 474;
A. Moroni et al., Nucl. Instr. and Meth., A556 (2006) 516,
M. Bruno *et al.*, in preparation;

[3] S. Adhikari *et al.*, Phys. Rev. C74 (2006) 024602.

[4] S. Shlomo and J.Natowitz, Phys. Rev. C44 (1991) 2878.

[5] J. B. Natowitz *et al.*, Phys. Rev. Lett. 89 (2002) 212701.

[6] G. Baiocco, Ph.D. thesis, Università di Bologna, Italy, and Université de Caen-Basse Normandie, France, 2012, *http://tel.archives-ouvertes.fr/lab/lpcc/*

[7] T. Von Egidy and D. Bucurescu, Phys. Rev., C72 (2005) 044311.

[8] J. Cabrera *et al.*, Phys. Rev. C 68 (2003) 034613.

[9] V. L. Kravchuk *et al.*, EPJ Web of Conferences 2 (2010) 10006.

[10] V. L. Kravchuk *et al.*, IJMPE 20, 4 (2011) 1050 and proposal to LNL-PAC (2012).

[11] M. E. Ortiz *et al.* , Phys. Rev. C82 (1436) 1982.

^{48}Ti(n,n′γ) gamma production cross section as a candidate for a reference cross section

S.P. Simakov[1], V.G. Pronyaev[2], R. Capote[1] and R.O. Nelson[3]
1) Nuclear Data Section, IAEA, Wagramer Strasse 5, A-1400 Vienna, Austria
2) Institute of Physics and Power Engineering, Bondarenko Sq. 1, Obninsk, Russian Federation
3) LANSCE-NS, Los Alamos National Laboratory, Los Alamos, NM 87545, USA

Abstract

The yield of 984 keV γ-rays from ^{48}Ti(n,n′) reaction has been evaluated from threshold up to 20 MeV. For this purpose all currently available measured discrete gamma production and neutron inelastic cross sections were thoroughly analysed and renormalised to the updated standards when possible. The TALYS and EMPIRE nuclear reaction codes were used to get an optimal description of these cross sections for natural Titanium and its main isotope ^{48}Ti. The final evaluation of the 984 keV γ-ray yield from ^{48}Ti(n,n′) reaction and covariance matrix was performed on the basis of collected experimental data and optimised model calculations employing the least squares code GMA.

1. Introduction

Despite many decades of research, and importance in a wide variety of applications, no recognized γ-ray reference cross sections exist for neutron-induced reactions. To address the need for useful and reliable inelastic neutron produced γ-ray reference cross sections, ^{48}Ti(n,n′γ_{984keV}) is being developed through new accurate measurements and comprehensive theoretical evaluation of all existing data and calculations.

Some issues with the often used ^{56}Fe(n,n′γ_{847keV}) cross section that make it problematic as a reference include: background contributions from Fe structural and other components in experimental setups, (n,p) activation of the Fe sample itself that adds a contribution to the same γ-ray following β-decay, and non-isotropic angular distribution effects. Ti, like Fe, has a large cross section that is fairly constant over a wide incident neutron energy range and has a large natural abundance for the main isotope of interest (^{48}Ti). Additionally, high-purity titanium is easily available, relatively cheap and not difficult to prepare as uniform density samples with appropriate thickness. The advantages of Ti over Fe are that Ti is generally not present in large quantities in experimental venues, and the (n,p) cross section and hence activation is reduced compared to Fe.

The status of cross section standards, evaluation techniques, and recent improvements and needs are described by A. Carlson et al. [1]. While no cross section standards exist for neutron inelastic γ-rays, Fe, Cr and Nb are mentioned in Ref. [1] as potential reference cross sections. Data acquired on ^{93}Nb(n,n′γ) with GEANIE at LANSCE have shown that Nb is not a suitable reference due to the existence of isomeric states that were not previously known. At an IAEA consultants meeting [2], plans for improvements to the data for ^{56}Fe(n,n′γ) and ^{52}Cr(n,n′γ) from LANSCE and IRMM Geel were presented, and potential γ-ray reference cross section materials Nb, Au, and ^{48}Ti were discussed. Following a reinvestigation of systematic uncertainties in the IRMM Geel data that resulted in corrections to the measured neutron flux, generally good agreement of the measured ^{56}Fe cross sections was observed. This was reported at an IAEA meeting in 2010 [3]. At this meeting, it was noted that there is good agreement between the recent measurements and the IRK evaluation [4] for Fe, Cr, and Ti, and that the evaluations can be updated easily using a Bayesian approach. In addition,

^{48}Ti(n,n′γ) and ^{48}Ti(n,2nγ) were identified as the best candidates for γ-ray reference cross sections. However, the paucity of ^{48}Ti(n,n′γ) data requires more experimental and theoretical work to establish it as a viable reference cross section in the incident neutron energy range from about 4 to 12 MeV.

This paper describes the modelling and evaluation work in progress towards the goal of establishing ^{48}Ti(n,n′γ) as a convenient and accurate gamma-ray reference cross section.

2. Experimental data

The available results of measurements of discrete γ-ray production and neutron discrete inelastic scattering cross sections relevant for ^{48}Ti(n,n′γ_{984}) cross section evaluation are summarised in Table 1. Since 1965 there are relatively few direct measurements of the 984 keV gamma yield versus incident neutron energy (the so-called excitation function): only one dataset [5,6] in the whole energy range of interest employing enriched ^{48}Ti sample and four sets [7-10] based mainly on natural samples from threshold up to 7.5 MeV.

Table 1. (n,n′γ_{984}) and (n,n_1) experiments carried out for Ti and suitable for present analysis.

Author and Ref.	Year Lab	Neutron Source Energy resolution	Sam-ple	Detector, Energy resolution, angle	EXFOR Entry
Registration of secondary discrete gammas from (n,n′γ) reaction					
D.L. Broder et al. [7]	1965 IPPE	1.1 - 3.2 MeV ΔE = 35 - 80 keV	^{nat}Ti	NaI 20° - 125°	40035011
E. Konobeevskij et al. [8]	1973 FIAN	1.0 – 1.23 MeV, ΔE = 17 keV	^{nat}Ti	GeLi, ΔE =4.0 keV	40213004
		1.0 – 1.49 MeV, ΔE = 38 keV	^{nat}Ti	GeLi, ΔE =4.0 keV	40213003
J.K. Dickens [9]	1974 ORNL	4.9, 5.4, 5.9 MeV ΔE = 0.15 - 0.20 MeV	^{nat}Ti ^{48}Ti	GeLi, 55° and 125°	10426
A.I. Lashuk et al. [10]	1994 IPPE	0.9 - 7.36, 15 - 16 MeV ΔE = 30 keV	^{nat}Ti	GeLi, ΔE =4.5 keV, ~ 90°	41186007 41186027
D. Dashdorj et al. [5,6]	2007 LASL	1.0 - 240 MeV, ΔE = 9 keV - 37 MeV	^{48}Ti	HPGe, 27°-142°	14162002
Registration of inelastically scattered neutrons from (n,n_1) reaction					
E. Barnard et al. [11]	1974 ANL	1.277 - 1.487 MeV "broad" ΔE ≈ 20 keV	^{nat}Ti	TOF 30° - 150°	10048006
	1974 Pelindaba	1.200 - 1.500 MeV "good" ΔE ≈ 5-10keV	^{nat}Ti	TOF 30° - 150°	10048089
I.A. Korzh et al. [12]	1977 Kiev	1.5 - 3.0 MeV	^{nat}Ti	TOF, Stilben 20° - 125°	40532016
W.E. Kinney et al. [13]	1977 ORNL	4.07 - 8.56 MeV ΔE = 60 - 70 keV	^{nat}Ti	TOF, NE213	10285019 10285031
A. Smith et al. [14]	1978 ANL	1.5 - 4.5 MeV ΔE = 25 - 50 keV	^{nat}Ti	TOF, Scintillator 30° - 134°	10048006
M.V. Pasechnik et al. [15]	1969 Kiev	2.9 MeV	^{nat}Ti	TOF, Scintillator 30° - 134°	40045006

D.L. Broder et al. [7] used moderate resolution NaI detector, rather thick sample and as a reference (0.53 ± 0.02) mb for Fe(n,n′$_{847}$) reaction cross section at 1.2 MeV neutron energy. E.S. Konobeevskij et al. [8] carried out measurements with thin and thick Ti samples (two sets of data with gamma energy losses of 17 and 38 keV, respectively) and using (0.17 ± 0.02) mb for the Fe(n,n′γ_{847}) reaction

cross section at 890 keV neutron energy as a reference. A.I. Lashuk et al. [10] also measured yield of 984 keV γ-rays from the natural titanium sample relative to the $Fe(n,n'\gamma_{847})$ reaction. J.K. Dickens [9] has measured yields for many γ-rays utilizing the samples of natural titanium and enriched ^{46}Ti and ^{48}Ti isotopes. He used the D(d,n) reaction to produce monoenergetic neutrons, the fluence was directly measured by a NE-213 scintillation detector. The results of experiments [7,8,10] were corrected to the updated monitor reaction cross sections taken from ENDF/B-VII.1 (IAEA) evaluation [1,16].

Below the incident energy 2.344 MeV, i.e. the excitation threshold of the second level 2.296 MeV, (n,n′) is identical to (n,n′γ) and thus the discrete inelastic could also be used in the analysis of the 984 keV gamma production. Such experiments have been carried out by E. Barnard et al. [11], I.A. Korzh et al. [12], W.E. Kinney et al. [13], A. Smith et al. [14] and M.V. Pasechnik et al. [15]. They have measured discrete and secondary energy smoothed inelastic scattering cross sections by TOF technique. The neutron scattering on hydrogen was used as a reference, except [14] where elastic scattering on carbon was selected for the absolute normalisation. If the authors reported the neutron inelastic cross section for the excitation of 984 keV level in ^{48}Ti as one for the natural titanium, we divided their results by factor 0.7372 (natural isotope abundance) to get cross section for $^{48}Ti(n,n_1)$.

At neutron energy around 14 MeV five experiments reported the 984 keV gamma yield from the natural Ti sample (in this case it is a sum of $^{48}Ti(n,n')$ and $^{49}Ti(n,2n)$ reactions). The comparative analysis [17] has shown that data measured by a NaI detector are 15-50% higher than those obtained by a Ge(Li) detector. Such a systematic difference is probably caused by interference from 889 keV photons that depopulate first 2^+ excited level of ^{46}Ti, the residual of $^{46,47}Ti(n,xn)$ reaction.

In the present analysis we additionally used neutron emission differential cross sections (secondary neutron spectra) measured by W.E. Kinney et al. [13] (at initial energies 5 - 8.5 MeV), D. Schmidt et al. [18] (8 - 15 MeV), H. Vonach [19], and M. Baba [20] (14 MeV).

3. TALYS default and optimised calculations

The TALYS code, version 1.4 [21], was employed to model neutron interaction with Ti isotopes to get an optimal prediction of photon production and neutron inelastic scattering cross sections from the threshold up to 20 MeV. The calculations were started with default input parameters: *optical model potential* - local and global ones by A.J. Koning and J.P. Delaroche [22] ; *nuclei structure* - 20 discrete levels for ^{48}Ti up to excitation energy 3.852 MeV taken from RIPL discrete level library; *level density* - matched constant temperature by Gilbert-Cameron and Fermi gas models (GCFG); *direct inelastic scattering* – DWBA calculation of excitation of the first 2^+ and 3^- vibrational states. These results are presented in Figs. 1 - 3 as red curves. The observed discrepancies prompted us to modify parameters and search for better agreement with experimental data.

Below the incident neutron energy of 2.5 MeV practically only the first level of ^{48}Ti is populated and thus results of calculations are not affected by discrete level scheme, decay branching or level density. However, we observed that both TALYS and EMPIRE codes overpredict the experimental cross section just above the reaction threshold, Fig. 1. To exclude the effect of incident energy resolution, the theoretical excitation function was convoluted with a Gaussian (given typical experimental resolution 60 keV). As seen this procedure smoothed out the curve near threshold; however, the systematic overprediction still remains. Additionally, the energy fluctuations observed in experiments below 2 MeV cannot be described as expected by statistical reaction models.

Replacement of the default DWBA model for collective state excitation by coupled channel calculations (where the imaginary surface potential depth was reduced by 15% and different optical model parameterisation was used for each excited state) had no effect on the cross section. To reach an agreement with experimental results in the first 200 keV interval, the imaginary surface potential depth should be unrealistically increased by factor 2. Further study of the impact of the optical model potential was undertaken with the EMPIRE code as described in the next Section.

Above 3 MeV the discrete level scheme and γ-branching ratios (BR) as well as level density of ^{48}Ti determine the computed results. Comparing the TALYS default discrete level scheme with ENSDF [23] (for A=48 chain it adopts evaluation [24]) and RIPL-3 [25] databases, we found inconsistency for several levels: *2.465 MeV (level #4)* - TALYS database specifies it as having spin J = 1^+ and 100% decay to g.s. (RIPL-3 assigns spin J = 5^+ and the same BR); ENSDF gives only excitation energy without specification of spin and γ-branching ratio (this weak level was observed only in [26] without spin and decay assignments); *3.062 MeV (level #6)* - TALYS default options are J = 2^+ and BR(1^{st}/g.s.) = 0.5/0.5, whereas RIPL-3 inscribes the same spin but 100% discharge to g.s.; since ENSDF adopts only energy and spin but no gamma transition we left TALYS default branching untouched; *3.711 MeV (level #16)* - TALYS default: J = 2^+ and BR(1^{st}/g.s.) = 0.5/0.5 (for comparison RIPL-3 has the same spin, but 100% decay to the first 2^+), ENSDF: no spin assignment, the same decay as RIPL-3.

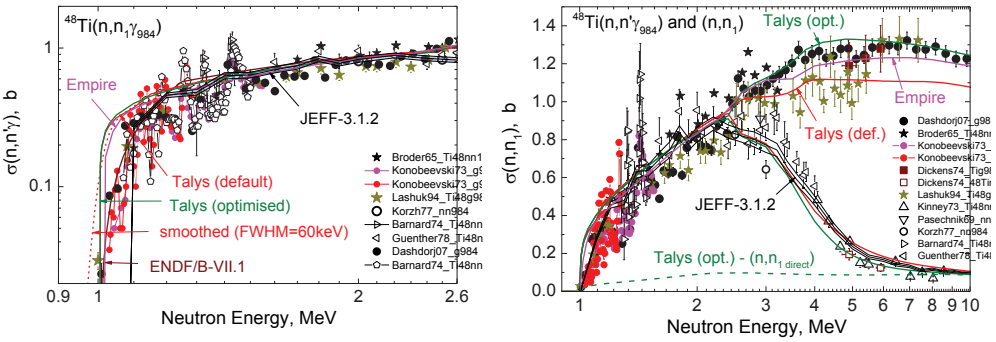

Fig. 1: ^{48}Ti(n,n′γ_{984}) and ^{48}Ti(n,n_1) cross sections near threshold (left) and up to 10 MeV (right): symbols – experimental data obtained by detection of gammas (closed) and neutrons (open).

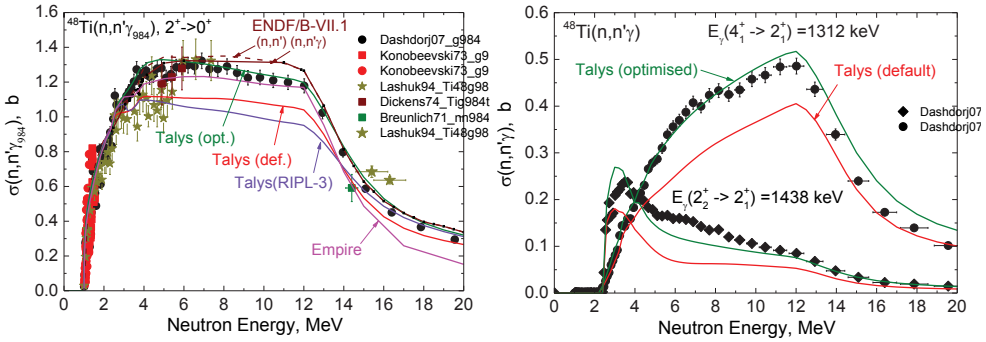

Fig. 2: ^{48}Ti(n,n′γ_{984}) (left) and ^{48}Ti(n, n′γ_{1312} γ_{1438}) (right) cross sections up to 20 MeV: symbols – experimental data; curves – TALYS & EMPIRE calculations and ENDF/B-VII.1 evaluation [16].

Since no γ-transition from the depopulation of 2.465 and 3.711 MeV levels was experimentally observed, we assumed that their excitation by neutron inelastic scattering is negligibly small and suppressed them in our calculations. This resulted in a much better agreement with measured ^{48}Ti(n,n′γ_{984}) excitation function up to incident energy 4 MeV, Figs. 1 - 2. The parameters of all other levels up to excitation energy 4.535 MeV (level #41) were also updated using information presently available in ENSDF database. When the spin, parity or BR were not known, we took them to be the same as for levels with the similar collective or single particle nature. As additional validation of

selected input parameters one may consider 1.312 and 1.438 MeV gamma transitions from the second and third levels with excitation energy U = 2.296 MeV (4^+) and 2.421 MeV (2^+) to the first excited state U = 0.984 MeV (2^+). As Fig. 2 (right) shows the selected input parameters for TALYS modelling improve the agreement between calculated and measured [5] data compared to the TALYS defaults.

As a result of the model parameters adjustment, the ratio (n,n′γ_{984})/(n,n′) (in other words, the factor that shows the probability of depopulating transition to pass through the first excited level in ^{48}Ti) increased from 0.85 to 0.90 at 5 MeV, Fig. 3. For comparison this ratio obtained in [4] from the known γ-branching ratios for the several first ^{48}Ti levels is also plotted there. The upper limit could also be estimated from the experimental data [5] as ratio of 984 keV γ-ray cross section to the sum of all measured transitions feeding the ground state (i.e., the sum of 984, 2421, 3328, 3699, 3371 and 3809 keV). It is seen that TALYS calculation, that optimally fits the measured (n,n′γ_{984}) cross section, predicts the (n,n′γ_{984})/(n,n′) ratio to be smaller than measured by up to 5%.

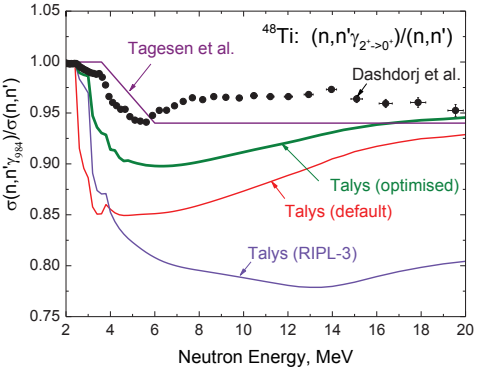

Fig. 3: Ratio (n,n′γ_{984})/(n,n′) vs. neutron energy: points - derived from experiment [5], curves - TALYS calculation with default parameters (red), with RIPL-3 discrete level scheme (violet) and after full optimisation (green) a swell as correction factor used in evaluation [4] (purple).

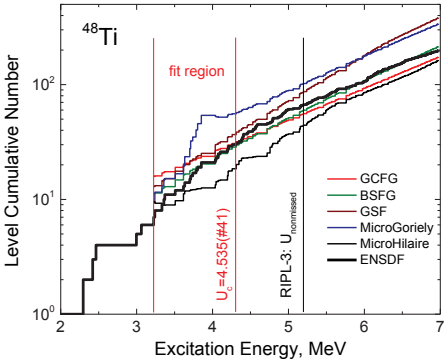

Fig. 4: ^{48}Ti cumulative number of levels: ENSDF (black), constant temperature and Fermi gas GCFG (red), back-shifted Fermi gas BSFG (green), generalised superfluid GSF (brown), microscopic level density tables of Goriely's (marine) and Hilaire's (blue).

Level density function becomes important above the incident neutron energy ~5 MeV. For the key isotope ^{48}Ti, the RIPL-3 database defines the cut-off energy (no level missed) $U_{cut\text{-}off}$ as 5.197 MeV (level #67). However the level spin and parity are only known up to 2.421 MeV (level #3). Fig. 4 displays the cumulative number of discrete levels of ^{48}Ti nucleus known from experiment (ENSDF) and calculated by different level density models in TALYS. It is worthwhile noting that TALYS adjusts the level density function in the preselected excitation energy interval (3.2 - 4.535 MeV) to the experimental spacing between s_0-resonances at neutron binding energy (D_0 as taken from RIPL [25]). As Fig. 4 shows, the back-shifted Fermi gas (BSFG) model matches better the observed cumulative number of discrete levels in ^{48}Ti in the interval 3-7 MeV compared to other models. Therefore BSFG was selected to model level density in further calculation.

For additional validation of the selected input parameters the secondary neutron spectra from ^{nat}Ti(n,xn) reaction were also calculated and compared with available experimental data at 8 MeV [13] and 14 MeV incident energies [19,20], Fig. 5. It is seen that extension of the cut-off limit for discrete levels U_{max} from the default 3.852 to 4.535 MeV improves the agreement with measured secondary neutron spectrum at 8 MeV and, in particular, confirms the preference of the back-shifted Fermi gas

level density model in comparison with default option. At 14 MeV the sensitivity to the model input parameters is relatively small in comparison with the spread of measured results [19, 20].

In the high energy part of secondary spectra the direct excitation of collective states makes a dominant contribution, Fig. 5. By default, TALYS performs DWBA calculations with an internal set of deformation parameters β_λ. We replace them by those available in ENSDF database for ^{48}Ti and performed coupled channels calculations for the strongest vibrational quadrupole one (and build upon them two) phonon states. The large spread and uncertainty of experimental data and interference from elastically scattered neutrons due to insufficient energy resolution do not allow to select a preferable set of deformation parameters.

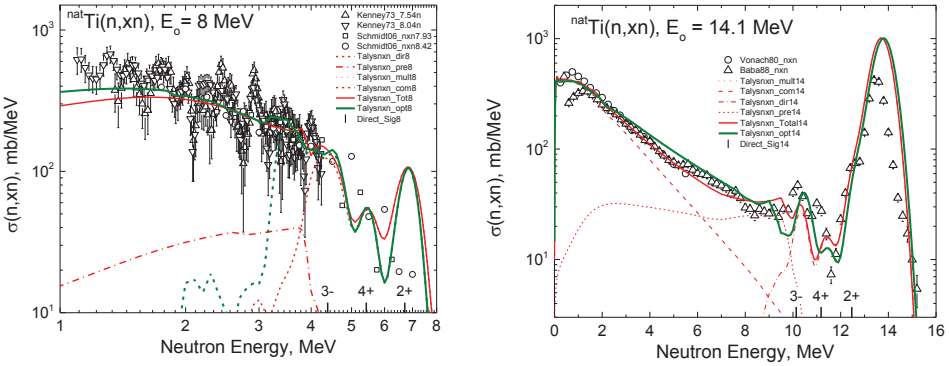

Fig. 5: Secondary neutron spectra from the ^{nat}Ti(n,xn) reaction at 8 and 14 MeV: symbols - experimental data, curves - TALYS calculations with default (red) and optimised (green) parameters.

4. EMPIRE calculations

The EMPIRE code [27], version 3.1.1, was also used to model neutron inelastic scattering on ^{48}Ti. The main goal was to study the impact of the soft rotator optical model on results. The reactions induced by neutrons on ^{48}Ti in the studied energy range occur through the direct, pre-equilibrium and compound nucleus mechanisms. EMPIRE utilizes the optical and direct reaction models, quantum-statistical pre-equilibrium model (MSD+MSC) and the full featured Hauser-Feshbach (HF) model. The direct interaction cross sections and transmission coefficients for the incident and outgoing neutron channels were obtained consistently from the soft-rotator coupled-channel optical model potential of Sukhovitskii et al. (RIPL set #2602 [25]) that couples the lowest 8 excited levels of the target nucleus [28]. The coupled-channel OPTMAN code [29] incorporated into the EMPIRE system was used in current optical model calculations. Default values of the pre-equilibrium model were used in calculations after adoption of optimised branching γ-transition ratios for discrete levels as discussed in the previous Section. The Enhanced Generalized Superfluid Model (EGSM) for nuclear level density [27] was used as default. Other parameters were retrieved from the RIPL-3 database [25].

The agreement of EMPIRE and TALYS calculations up to 3 MeV (discrete level region) perfectly shows that the impact of selected optical model at these energies is negligible. From 3 to 12 MeV EMPIRE calculations are slightly lower than TALYS results, this probably reflects the small differences in the level density models. Larger deviations from the experimental data are observed above 14 MeV. It is interesting that the predicted direct excitation of the coupled 984 keV level is about 50 mb, while TALYS DWBA calculation gives ~100 mb. Such differences could be explained by the different dynamical deformations used. Preequilibrium model may also have an impact at those high energies. Further studies are needed to clarify the discrepancy.

5. GMA evaluation

GMA evaluation of 983.5 keV γ-ray production cross section was done by taking into account the results of measurements carried out by direct registration of gammas and neutrons following the inelastic scattering. For later, the conversion to γ-ray production cross section was performed by application of the evaluated branching ratio of 984 keV gamma production to the total inelastic scattering. The branching ratio, Fig. 3, was calculated using experimental data [5] as ratio of 984 keV γ-ray production cross section to the sum of γ-transition feeding the ^{48}Ti ground state. Additionally the branching coefficients from ENSDF [23] were used for calculation of weak transitions to the ground state, which were not experimentally detected in [5]. Since the complete scheme of γ-transitions is reasonably known only up to excitation energy 5 MeV, the BR used to transform the inelastic scattering cross section to the 984 keV gamma production yield was taken from the evaluation based upon experimental data [5] up to 5 MeV and assumed equal to 0.95 between 5 and 20 MeV.

We used the least-squares method and GMA code [30] for non-model evaluation of the 984 keV γ-ray production cross section. In this approach the common energy grid (nodes) should be used for presentation of all data. To keep the resonance-like structure in the cross section below 3.2 MeV, we decided to use the energy grid of [5]. At higher energies up to 20 MeV, the cross section was considered to be smooth that allows the usage of the wider energy steps between nodes.

The following experimental data were used in the non-model GMA least squares fit: gamma-production data by D. Dashdorj et al. [5] as absolute cross section; the results from thin and thick samples measurements of 984 keV gammas by I.A. Konobeevskij et al. [8] treated as shape type data; and absolute inelastic cross section measurements by A.I. Korzh et al. [12] transformed to 984 keV gamma yield using BR evaluation described above and shown in Fig. 3. Beyond the neutron energy 3.2 MeV two model calculations were used in the GMA fits: the 984 keV gamma production cross section obtained from TENDL-2010 inelastic scattering cross section after correction for BR ratio shown in Fig. 3, and the result of the present optimized TALYS calculation.

The comparison of the evaluations of 984 keV gamma production cross section for two different model calculations used in the fit as a prior evaluations are shown in Fig. 6. Due to the excellent consistency between experimental data [6, 8 and 12] after interpolation to the same nodes below 3.2 MeV, no difference between GMA evaluation and experimental data [5] was observed there. The difference at level of 5 - 6% between two final evaluations in the energy range of the cross section maximum can be explained by the difference in the results of the model calculations used as a prior and having relatively small uncertainties (~ 3%) for the wide energy groups. Such modelling uncertainties are obviously underestimated, and further studies are required. Obviously a final evaluation will require better estimation of the model results and modelling covariances above 3 MeV.

Fig. 7 shows the results of GMA fit that used as a priori only experimental data or additionally the TALYS optimal excitation function. The observed fluctuations of the calculated uncertainty, when only experimental data are used, show that the experimental database used in fit is not complete. If TALYS results are used, then *a priori* model calculation pulls the final evaluation towards itself and slightly decreases uncertainties (due to the model uncertainty underestimation). Since the TENDL-2010 features stronger positive correlations, inclusion of modeling data in the GMA analysis results in increased energy-energy correlation in the final evaluation.

Results of independent evaluation of inelastic scattering cross section for ^{48}Ti were obtained by S. Tagesen, H. Vonach and A. Wallner (included in JEFF-3.1.2 library) using the Bayesian code GLUCS with combined non-model fit of experimental data for all reaction cross sections in the energy range from 1 to 20 MeV [4]. The strict relations between total and partial cross sections were accounted for in this fit. The evaluation was done in 2004 before experimental data [5] was published. For calculation of 984 keV γ-production from (n,n′) cross section the evaluated BR shown at Fig. 3 was used. The results of comparison of three evaluations are shown in Fig. 1. Rather large difference

at the maximum of the cross section is explained by large difference in the reaction (or non-elastic) cross section evaluation. Better optical models (e.g. based on soft-rotator structure model as Sukhovitskii et al. - RIPL set #2602 [25]) need to be used for a proper estimation of the non-elastic cross section, a magnitude which remains very uncertain to measure if the same method of evaluation will be used.

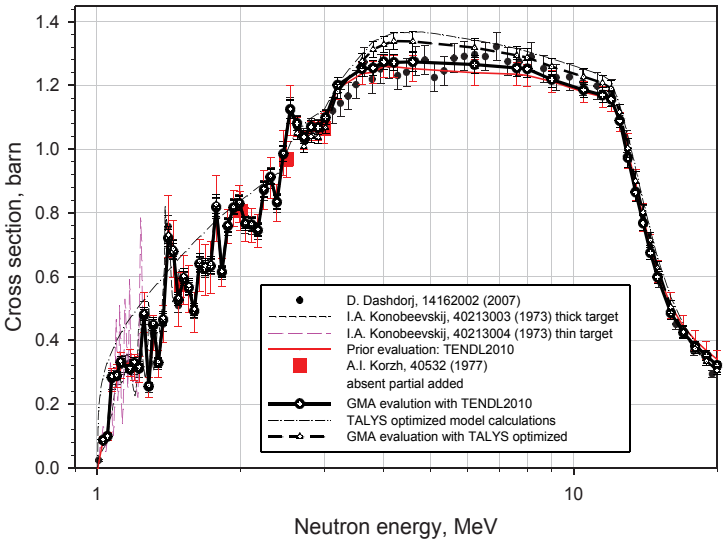

Fig. 6. Comparison of GMA fit with two different model calculations used as prior and independent GLUCS combined fit [4] including all total and partial cross sections. GLUCS fit did not include results of latest measurements by Dashdorj et al. [5].

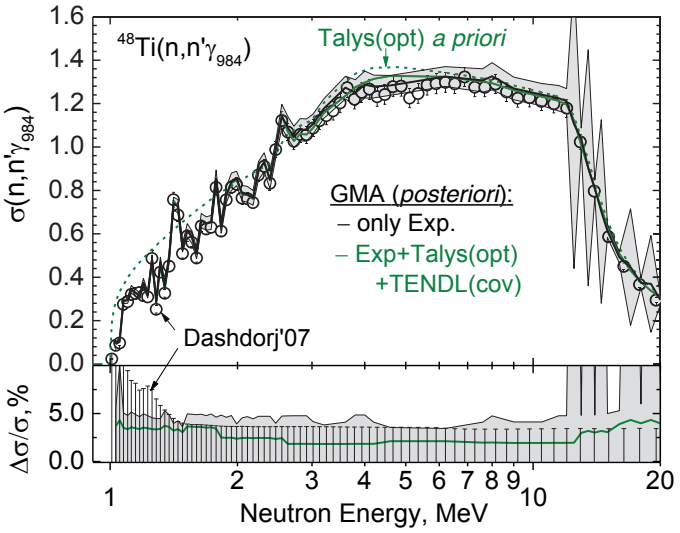

Fig. 7. Results of GMA fit with two *a priori*: only experimental data [5] (black) and together with optimised TALYS calculation (green).

Conclusions

Experimental data relevant for evaluation of $^{48}Ti(n,n'\gamma_{984})$ cross sections were collected and critically reviewed. Up to now there is only one experiment that delivers excitation function for this reaction in the whole energy range of our interest - from threshold up to 20 MeV. This experiment's data could be complemented by several other measurements near threshold and at 14 MeV. Regrettably many of them are rather old, used large samples, detectors with modest energy resolution and energy fluctuating monitor reactions. Regarding this and, in also because of the complex resonance structure of the $^{48}Ti(n,n'\gamma_{984})$ reaction cross section below 2 MeV, further precise and independent measurements would be highly valued.

Theoretical analysis has been performed with a goal to establish a theoretical model as predictive as possible. The preliminary calculations made with the TALYS code and default input parameters demonstrated non acceptable discrepancies with available experimental data. Similar discrepancies were observed for the default EMPIRE calculation. Optimization of discrete level scheme, level density and modes of calculation has been done on the base of all known information on nuclear structure and reaction mechanism. Nearly perfect prediction of the 984, 1312 and 1438 keV γ-rays from $^{48}Ti(n,n'\gamma)$ and neutrons from $^{48}Ti(n,n_1)$ and Ti(n,xn) reactions has been finally obtained. Exceptions, however, are the first 1 MeV interval above $^{48}Ti(n,n'\gamma_{984})$ reaction threshold, where model calculations failed to reproduce the average magnitude, and energies below 3 MeV where statistical reaction models are incapable to reproduce the resonance structure.

The final evaluation of $^{48}Ti(n,n'\gamma_{984})$ cross section has been performed by means of the GMA code. Below 3.2 MeV the evaluation relies on the experimental data and thus reproduces well the observed resonance structure and mean values. At higher energies the results of theoretical modelling could be additionally used as a prior. The outcome of GMA evaluation depends on modelling input within a few percent. The 984 keV γ-ray production cross section was estimated from threshold up to 20 MeV with uncertainty around 5%, a full covariance matrix was also obtained.

Acknowledgment

One of co-authors (S.S.) would like to thank A. Koning (NRG, Petten) for detailed explanation of models and approaches implemented in the TALYS code and practical advice during calculations.

References

[1] A.D. Carlson, V.G. Pronyaev, et al., International Evaluation of Neutron Cross Section Standards, Nuclear Data Sheets **110**, 3215–3324 (2009).
[2] V.G. Pronyaev, A. Mengoni, A.D. Carlson, Consultancy Meeting. Report INDC(NDS)-0540, IAEA, 2008.
[3] V. Pronyaev, A. Carlson et al., Consultancy Meeting. Report INDC(NDS)-0583, IAEA, 2011.
[4] S. Tagesen, H. Vonach et al., Evaluations of the fast neutron cross sections of $^{46,47,48,49,50}Ti$ including complete covariance information, Report JEFF/DOC–1002, NEA, Paris, 2004.
[5] D. Dashdorj, G.E.Mitchell et al., Gamma-Ray Production Cross Sections in Multiple Channels for Neutron-Induced Reaction on ^{48}Ti for En = 1 to 200 MeV, Nucl.Sc.& Eng. **157** (2007) 65.
[6] D. Dashdorj, T. Kawano, P. E. Garrett et al., Effect of preequilibrium spin distribution on ^{48}Ti + n cross sections, Phys. Rev. **C75**, 054612 (2007).
[7] D.L. Broder, A.G. Dovebenko et al. Inelastic neutrons scattering by C, Al, Ti, Fe, Bi nuclei, Preprint FEI-32, Obninsk, 1965, EXFOR 40035.
[8] E.S. Konobeevskij et al. Inelastic scattering of neutrons on Ti and Fe isotopes in energy range near threshold, Izv. Rossijskoi Akademii Nauk, Ser.Fiz. **37**, 1764 (1973), EXFOR 40213.

[9] J.K. Dickens, Neutron-Induced Gamma-ray Production in Titanium for Incident-Neutron Energies of 4.9, 5.4, and 5.9 MeV, Nucl.Sc.& Eng. **54** (1974) 191, EXFOR 10426.
[10] A.I. Lashuk et al., Gamma-quanta production cross-sections at inelastic scattering of the neutrons on the nuclei of reactor construction materials, Yad. Konst. **1** (1994) 26.
[11] E. Barnard, J. Devilliers et al., Neutron scattering from titanium; compound and direct effects, Nucl. Phys. **A229**,(1974) 189, (EXFOR 10048.
[12] I.A. Korzh, V.A. Mishchenko et al., Differential scattering cross sections of 1.5-3.0 MeV neutrons for Ti, Fe and Bi, Ukrainskij Fizicheskij Zhurnal **22** (1977) 87, EXFOR 40532.
[13] W.E. Kinney, F.G. Perey, Ti neutron elastic- and inelastic- scattering cross sections from 4.07 to 8.56 MeV, Oak Ridge National Lab. Reports, No. 4810 (1973), USA, EXFOR 10285.
[14] A. Smith, P. Guenther et al., Fast-neutron total and scattering cross sections of elemental titanium, Nucl. Phys. **A307** (1978) 224, EXFOR 10669.004.
[15] M.V. Pasechnik et al., Neutron scattering with initial energy of 2.9 MeV by Titanium and Chromium nuclei, Report Yad.-Fiz. Issledovaniya, No. 6 (1968) 106, EXFOR 40045.
[16] M.B. Chadwick et al., "ENDF/B-VII.1 Nuclear Data for Science and Technology: Cross Sections, Covariances, Fission Product Yields and Decay Data", *Nuclear Data Sheets* **12** (2011) 2987.
[17] S.P. Simakov, A. Pavlik, H. Vonach and S. Hlavac, Status of Experimental and Evaluated Discrete Gamma-Ray Production at E =14.5 MeV, Report INDC(CCP)-413, IAEA, 1998.
[18] D. Schmidt, W. Mannhart et al., Determination of Differential Elastic and Inelastic and Double-differential Neutron Scattering Cross Sections of Elemental Titanium at Energies between 7.93 MeV and 14.72 MeV, Report PTB-N-50, 2006, PTB Braunschweig, Germany, EXFOR 22961.
[19] H. Vonach, A. Chaluoka et al. Measurement of the angle-integrated secondary neutron spectra from interaction of 14 MeV neutrons with medium and heavy nuclei, Proc. of BNL Conf. 12-14 May 1980, Report ZFK-382, p. 159, 1979.
[20] M. Baba, M. Ishikawa, et al., Double differential neutron emission cross sections of Cu, Ti, Zr and C, Int. Conf. on Nucl. Data for Sci. and Technol., Mito 1988, p. 291, EXFOR 22077032.
[21] A.J. Koning et al., TALYS, http://www.TALYS.eu/home/
[22] A.J. Koning and J.P. Delaroche, Local and global nucleon optical models from 1 keV to 200 MeV, Nucl. Phys. **A713** (2003) 231.
[23] Evaluated Nuclear Structure Data File (ENSDF), http://www.nndc.bnl.gov/ensdf/
[24] T.W. Burrows, Nuclear Data Sheets **107** (2006) 1747.
[25] R. Capote, M. Herman et al, RIPL Reference Input Parameter Library for calculations of nuclear reactions and nuclear data evaluation, Nuclear Data Sheets **110** (2009) 3107; data available online at http://www-nds.iaea.org/RIPL-3/ .
[26] A. Higashi and K. Katori, Systematic behaviour of octupole strengths in ^{46,48,50}Ti, Phys. Rev. **C39** (1989) 1286.
[27] M. Herman, R. Capote, B.V. Carlson, et al., EMPIRE, Nuclear Reaction Code System for Data Evaluation, Nuclear Data Sheets **108** (2007) 2655; http://www-nds.iaea.org/EMPIRE .
[28] E. Soukhovitskii, S. Chiba and J. Lee , Proc. Int. Conf. on Nucl. Data for Sci. and Technology, Santa Fe, USA, Ed.by R.C.Haight et al., AIP **769** (2005) 1100.
[29] E. Soukhovitskij, G.B. Morogovskij, S. Chiba et al., Physics and Numerical Methods of OPTMAN: A Coupled-channels Method Based on Soft-rotator Model for a Description of Collective Nuclear Structure and Excitations, JAERI Data/Code 2004-002 (2004).
[30] W.P. Poenitz, Data interpretation, objective evaluation procedures and mathematical techniques for the evaluation of energy-dependent ratio shape and cross section data, Report BNL-NCS-51363, Brookhaven, 1981, v. 1, p. 249.

Neutron inelastic scattering, recent experiments and their interpretation

A.J.M. Plompen[1], *C. Rouki*[1], *S. Kopecky*[1], *A. Krása*[1], *N. Nankov*[1], *A. Bacquias*[2], *Ph. Dessagne*[2], *M. Kerveno*[2], *G. Rudolf*[2], *J.C. Thiry*[2], *C. Borcea*[3], *A. Negret*[3], *M. Stanoiu*[3], *A. Domula*[4], *K. Zuber*[4], *M. Angelone*[5], *M. Pillon*[5], *S. Hilaire*[6], *P. Romain*[6], *P. Archier*[7], *C. De Saint-Jean*[7], *G. Noguère*[7], *A.J. Koning*[8], *S. Goriely*[9], *A. Milocco*[10] *and A. Trkov*[10]
[1]EC-JRC-IRMM, Geel, Belgium
[2]CNRS-IPHC, Strasbourg, France
[3]IFIN-HH, Magurele-Bucharest, Romania
[4]Technische Universität Dresden, Dresden, Germany
[5]ENEA, Frascati, Italy
[6]CEA, DAM, DIF, Arpajon, France
[7]CEA, DEN, Cadarache, France
[8]NRG, Petten, The Netherlands
[9]ULB, Brussels, Belgium
[10]JSI, Ljubljana, Slovenia

Abstract
Measurements of inelastic scattering and (n,xn)-cross sections with the (n,xnγ)-technique are performed at the GELINA neutron time-of-flight facility with two arrays consisting of high purity germanium detectors, GAINS and GRAPHEME. These measurements provide important nuclear data for criticality, reactivity and power distribution estimates in current and advanced power reactors, for the development of active material interrogation techniques for security and safeguards, and for background studies supporting the search for neutrinoless double-beta decay in experiments like GERDA, and MAJORANA and for weakly interacting massive particles. Despite significant advances in modeling, such cross sections still pose a major challenge to nuclear theory at the level of the required accuracy. GAINS is an array consisting of 12 large volume detectors used to study inelastic scattering from C to Bi with high incident neutron energy resolution. GRAPHEME using four planar detectors, is tailored for the actinides. Recent and ongoing experimental work for ^{23}Na, ^{76}Ge, W and ^{232}Th is presented. The experimental work is supported and complemented by state-of-the-art nuclear modeling with the well-known TALYS code using both a phenomenological and a microscopic approach, and with resonance analysis for selected nuclides. Advances and open issues will be shown. For carbon interesting complementary results were obtained using single-crystal diamond detectors.

1 Introduction

Remarkably, there is still a strong current interest in neutron inelastic scattering and (n,xnγ)-reactions that derives from innovation in nuclear energy [1, 2], the development of active material interrogation techniques for security and safeguards, and from background studies supporting the search for neutrinoless double-beta decay in experiments like GERDA [3], and candidate dark matter particles [4]. Remarkable since the history of neutron inelastic scattering is a long one dating back from the period shortly after the discovery of the neutron. A brief recap.

Conclusive experimental evidence [5] for (n,2n) reactions (on ^{63}Cu and ^{65}Zn) was first established at the N.V. Philips Gloeilampenfabrieken, Eindhoven, Holland, by an activation method confirming the half-life, employing radiochemistry to eliminate the end products were neighboring elements and

deflecting the emitted particles to establish β^+-decay [6]. Inelastic scattering was established a year later. Following several indications of "excitation without capture" of materials by fast neutrons [5], as summarised by Livingston and Bethe in Part C of an extensive review of nuclear physics, experimental proof of neutron inelastic scattering was first established by Seaborg, Gibson and Grahame using a radium-beryllium neutron source, various configurations involving a large lead-block and a Geiger-Mueller counter [7]. The experiments demonstrated negligible loss of neutrons traversing the lead block with or without various other materials around the source, the ability of neutrons to excite the lead even after deep penetration, the minor role of slow neutrons in producing these gamma-rays and the reduced production of gamma-rays when other materials shield the source. Thus, it was established that 1) neutrons are not significantly captured as they produce gamma-rays and 2) their ability to excite lead is reduced when they lose energy. Implications for the nuclear reaction theory of Weisskopf and Ewing were sought by Dunlap and Little using D-D neutrons and a cloud chamber [8]. They were unsuccessful as the 2.5 MeV neutrons mostly scattered from discrete levels. The suggested discrete energies of the outgoing neutrons following inelastic scattering were exhibited using photographic emulsions and the Li(p,n) source reaction by Stelson and Preston for the first level of ^{56}Fe [9]. Quantitative studies detecting gamma-rays took off with the advent of NaI scintillator counters [10, 11] and for detection of neutrons through time-of-flight measurements at quasi mono-energetic pulsed neutron sources with fast hydrogenous scintillators as detectors. The latter technique was pioneered by Cranberg and Levin at Los Alamos for iron [12]. The highest resolution measurements of this type were developed much later by Haouat and co-workers and applied to ^{238}U [13]. The first neutron-gamma coincidence measurements were performed early fifties as well with the aim of curbing the ever important background in neutron experiments [14].

Measurements at incident-neutron time-of-flight facilities with a white neutron spectrum were established much later. At the Karlsruhe cyclotron a Ge(Li) detector was used for several elements [15], while at the Oak Ridge electron linear accelerator ORELA initially a NaI detector was employed [16] which was replaced with a germanium detector in later work [17]. A new impulse to this line of experimentation was due to the installation of the GEANIE high purity germanium array at the WNR spallation time-of-flight facility of Los Alamos [18]. This new facility gave easy access to gamma-rays from (n,xn) reactions tackling important targets such as ^{239}Pu [19] and ^{238}U [20]. The installation of GEANIE was inspired by the work of Vonach et al. who first demonstrated the potential of $(n, xn\gamma)$-measurements at WNR [21].

Early inelastic scattering studies drew inspiration from the Wolfenstein-Hauser-Feshbach model allowing a qualitative rather than a quantitative agreement with experimental results [22]. Detailed angular distribution measurements could be described by an extension of the WHF model allowing the derivation of transition multipolarities and the inference of level spins and sometimes parities [23]. Despite significant advances in modeling, predicting cross sections still poses a major challenge to nuclear theory at the level of the required accuracy. In particular, accurate criticality and reactivity estimates of advanced fast reactors and the power distribution in PWRs warrant low uncertainties $(2 - 8\%)$ for inelastic scattering cross sections of the most important isotopes (^{23}Na, ^{56}Fe and ^{238}U). Depending on the concepts considered the list may be extended to include Mg, Si, Cr, Ni, Zr, Mo and Th.

To meet these challenges accurate experiments must be complemented by state-of-the-art nuclear model calculations to take optimum benefit of the data and provide the required quantities. What may be achieved was recently demonstrated for the ^{241}Am(n,2n)^{240}Am reaction where consistent phenomenological model calculations from different origin were beautifully confirmed by experiment [24, 25]. In addition, we may now expect a performance from WHF calculations using level densities [26], strength functions [27] and optical model potentials [28] from (semi-)microscopic calculations at the level of the phenomenological approach [29]. The phenomenological approach itself has recently seen considerable development [30] through new dispersive (coupled-channels) optical-models [31–34], imposing Lane-consistency on optical models [35], investigating the minimum number of coupled-channels to attain

convergence [36], WHF calculations by Monte Carlo to understand coincidence data [37], and the determination of the spin distribution of residuals populated by the pre-equilibrium process [38]. For the light nuclei impressive results are obtained using an algebraic coupled-channel approach that takes account of the Pauli principle and describes bound and scattering states [39–42]. Model calculations are facilitated through a comprehensive numerical compilation of nuclear model parameters [43].

In the present collaboration neutron-inelastic scattering is studied experimentally at the IRMM GELINA neutron time-of-flight facility by observation of the emitted gamma-rays using two arrays based on high purity germanium detectors. GAINS, an array consisting of 12 large volume detectors, is used to study inelastic scattering from C to Bi with high incident neutron energy resolution [29, 44–48]. GRAPHEME, developed by IPHC and using four planar detectors, is tailored for the actinides and was also used for lead [49–51]. Recent and ongoing experimental work that concerns ^{23}Na, ^{76}Ge, W and ^{232}Th is presented. Interesting complementary results for carbon are shown as well.

2 ^{23}Na

Inelastic scattering data for sodium are important for the estimation of the void coefficient in advanced fast reactors, in particular when multiple recycling of high level radioactive waste is emphasized [1, 52]. For a sodium cooled fast reactor configured as a transuranic burner, the target uncertainty between 0.5 and 1.35 MeV is 4% on the energy average and 9% between 1.35 and 2.2 MeV. For other concepts such as the European Fast Reactor or the Advanced Breeder Test Reactor the requirement is less stringent (8-10%), but the currently achieved uncertainties are much worse (15-25%).

In a recent publication we describe measurements performed with the GAINS array at the neutron time-of-flight facility GELINA [44] that meet the target uncertainty for the inelastic scattering cross-sections averaged over the above-mentioned energy ranges. An uncertainty of less than 2.5% was claimed. The experiment was performed at the 200 m flight station where an energy dependent resolution is obtained (being about 1 keV at 1 MeV) that is largely determined by a fixed time-of-flight uncertainty of about 10 ns. Eight 8 cm diameter 8 cm long high purity germanium detectors were used which are placed 4 by 4 at angles of about 110^o and 150^o degrees for optimal integration over non-trivial gamma-ray angular distributions (Fig. 1). For the case of sodium the ratio of the 150^o yield over the 110^o yield was one within the uncertainties for the transitions (Fig. 1) for which cross sections were determined. Thus no significant deviation from isotropy was found.

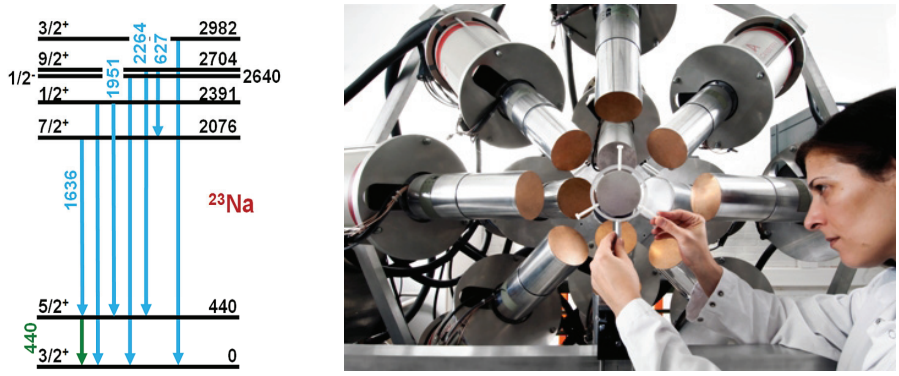

Fig. 1: Left: Partial level scheme of ^{23}Na showing the transitions measured in this work. Right: The current configuration of GAINS has twelve detectors at 110, 125 and 150 degrees.

The gamma-ray efficiency determinations are done by Monte Carlo simulations with detector models optimized by calibrations with well characterised sources [53]. The normalization to neutron flux is

obtained by a measurement with a ^{235}U fission ionization chamber that is placed less than 2 m upstream from the sample [54, 55]. The Na sample was a high purity metallic sample encased in an Al container. The sample diameter was about 80 mm diameter and 4.2 mm thick with an areal density of 0.389(1) g/cm^2. Further details may be found in reference [44].

In Rouki et al. also a complete overview of the results is given. These results show differences with the ENDF/B-VI.1 and JEFF-3.1 evaluations for energies above 1 MeV. Improvements are presently being sought. Since detailed nuclear modeling of n+^{23}Na reactions is out of scope of WHF calculations due to the resonance structure and since the algebraic model mentioned above is currently only applied to still lighter nuclei, the best that may be done is a description of the cross section using an R-matrix parametrization. Such a parametrization is being undertaken and will still require a number of modifications to come from the present status, which corresponds with JEFF-3.1(.1), to an agreement with the newly measured data (Fig. 2) at the higher energies.

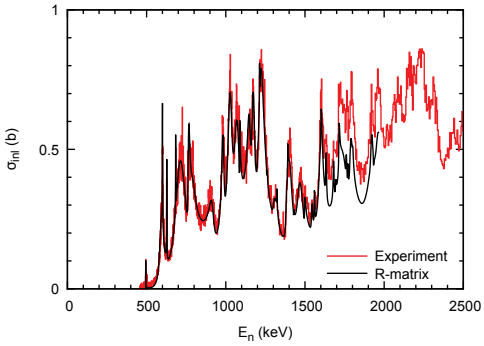

Fig. 2: Results obtained for sodium compared with a new R-matrix fit.

The (n,xnγ)-technique does not allow to extract angular distributions of the scattered neutrons. As a prestudy for new work and to facilitate new evaluations of earlier work the Märten et al. [56] data and their R-matrix analysis by Kopecky et al. [57] were re-analysed [58]. The R-matrix results are available for future evaluations. These concern the total cross section measured at ORNL and the inelastic cross section obtained by Märten et al. The elastic scattering data from that work are also of interest since they offer valuable experience with obtaining angle-dependent data. Figure 3 shows the result of a numerical integration of the differential cross section data for elastic scattering. Added to the inelastic scattering cross section these should yield the total cross section. It is shown that two methods of integration of the experimental data have negligible differences but the differences with the total cross section are substantial and energy dependent (Fig. 3).

Since the R-matrix fit provides a fairly good description of the total and the inelastic data, it is no surprise that the R-matrix estimates for elastic scattering and for the mean-cosine of the scattering angle differ substantially from the experimental data (Fig. 3). The original data of the experiment are no longer available and important aspects such as multiple scattering corrections cannot be undone and redone. It is therefore of utmost interest to reinvestigate these angular distributions by new measurements. Theoretical guidance for this still rather light nucleus with significant resonance structure in the range of interest would also be of high value.

3 ^{76}Ge

With a Q-value of 2039.0 keV the nucleus ^{76}Ge is one of a small set of nuclides that may exhibit (neutrinoless) double-beta decay. In the case of regular double-beta decay two neutrinos will be emitted and

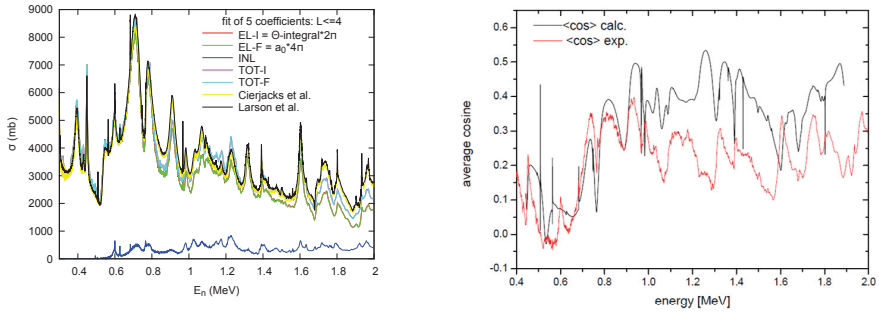

Fig. 3: Na data of reference [58]. Left: Elastic differential cross section data obtained were numerically integrated in the center of mass system (EL-I) or fitted with a 4^{th} order Legendre polynomial to obtain the integral (EL-F). Adding the experimental data for inelastic scattering (INL) results in two estimates for the total cross section (TOT-I and TOT-F). These are compared with data for the total cross section of Cierjacks et al., and Larson et al. Since the EL-I and EL-F, resp., the TOT-I and TOT-F curves are nearly identical, the "-I" are hidden behind the "-F" curves. Right: Mean cosine of the scattering angle in the center of mass system.

the sum of the energies of the two electrons will be a characteristic continuous distribution limited above by the Q-value. Neutrinoless double-beta decay goes beyond the standard model being possible only if the neutrino is its own antiparticle. The important characteristic is that the sum of the energies of the electrons is exactly the Q-value. The current lower limit on the process half life is $1.6 \cdot 10^{25}$ y [59]. The GERDA experiment [3] attempts to establish this mode of decay by employing a number of high purity germanium detectors 86% enriched in ^{76}Ge, following up on an early claim of observation of this decay mode [60, 61]. The detectors are suspended in an Ar cryostat for cooling and more importantly for shielding against background. The cryostat has 2 m radius and is further shielded by 3 m of water. The primary concern for the shielding are gamma-rays from the rock and concrete, next come the neutrons (same source) and finally the cosmic rays. The latter are vetoed using the water shield as Cerenkov counter. The experiment aims at a background at 2039 keV of less than 10^{-3} counts per year, per keV and per kg of germanium.

A possible background is through the excitation of a level at 3951.89 keV by neutron inelastic scattering. This level emits a 2040.7 keV gamma-ray with a probability of 3.6(9)% per decay. The energy of this gamma-ray is sufficiently close to the Q-value to be of concern and thus it was decided to study the cross section for the production of this level by neutron inelastic scattering with GAINS at GELINA. In the experiment the 2040.7 keV gamma-ray was not observed. Also the transitions with energy (emission probability) 3951.7 (46(4)%) and 3388.8 (31(2)%) keV were not observed. The inferred upper limit for the cross section of producing a 2040.7 keV gamma-ray by neutron inelastic scattering is 3 mb. Using the neutron-fluxes (3 10^{-7} n/cm^2/s [62, 63]) determined at LNGS where GERDA is located for unshielded detectors this implies an upper limit of 6-8 10^{-2} kg^{-1}y^{-1} emissions of 2040.7 keV gamma-rays. The GERDA shielding easily reduces this to rates that are insignificant compared to the present goal for the background. TALYS model calculations show that the cross section could actually be much smaller (<0.5μb) allowing an unshielded detector at LNGS. For the present generation of experiments this does not require further investigation, however future experiments may have considerably more stringent requirements.

Using the samples shown in figure 4 cross sections could be measured for four gamma-rays (of energy 562.9, 545.5, 431.0 and 1348.1 keV). Two of these are shown in comparison with TALYS model calculations in figure 5. The typical uncertainty of the measurement is about 10% and is primarily due to the irregular sample shape.

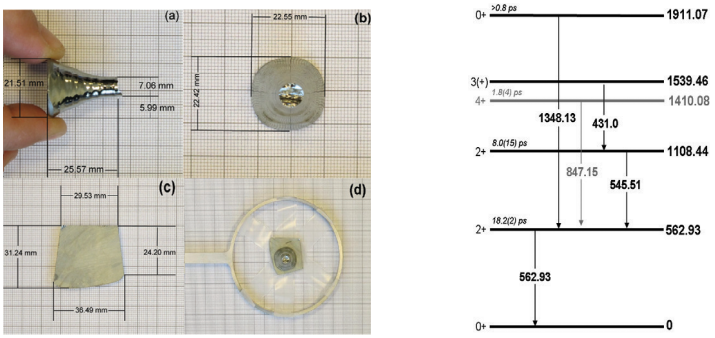

Fig. 4: Left: Samples used for the experiment on ^{76}Ge. Right: Portion of the level scheme of ^{76}Ge showing the gamma-rays observed in this work in black. The decay of the 4^+ level at 1410.08 keV was not observed.

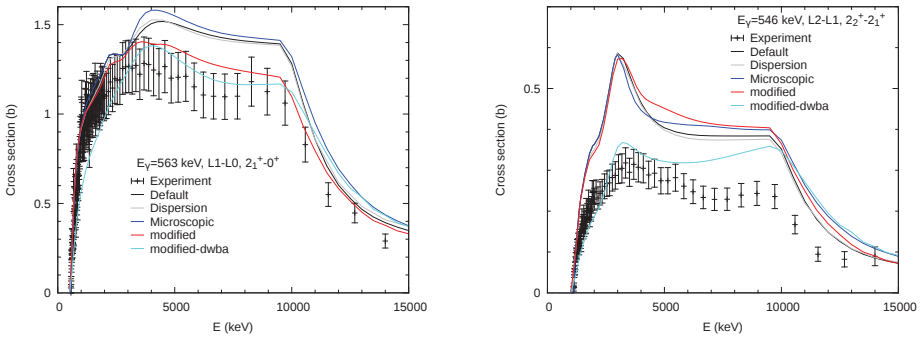

Fig. 5: Two gamma-ray production cross sections of ^{76}Ge.

The TALYS model calculations use various options available in the code. The so-called default calculation is a fully phenomenological calculation with parameters obtained earlier [64]. This is also the basis of the calculations labeled "Dispersion", "modified" and "modified-dwba". The "Dispersion" calculation uses the optical model potential of [64] adding the dispersive correction to the real potential. No significant differences are found. The modified calculation adjusts the optical model potential for better agreement with the data above 3 MeV incident neutron energy for the 563 keV gamma. The modified-DWBA calculation uses in addition a DWBA rather than a coupled-channels calculation to account for the vibrational character of the first excited states. This results in better agreement with the data for the 546 keV gamma in particular. The microscopic calculation uses the optical model of Bauge et al. [35], the level densities of Hilaire et al. [26] and the gamma-ray strength functions of Goriely et al. [27]. The result using ingredients from microscopic calculations is comparable in quality to that of the phenomenological calculation. It is however clear that model improvements are of interest in order to come to an overall satisfactory description of the experimental data.

4 W and ^{232}Th

Measurements with the GRAPHEME array of IPHC Strasbourg and installed at the GELINA time-of-flight facility in Geel at a 30 m flight path currently address the actinides. Recent work with this array for ^{235}U and ^{238}U is summarised in a separate contribution to this conference [49]. There too details are presented of this setup, which presently consists of four planar germanium detectors placed 2 by 2

at 110 and 150 degrees. A particular focus of work at this experimental setup is the Th/U fuel cycle. Data for (n,xnγ)-cross section were obtained for ^{232}Th and measurements for ^{233}U are being planned. In view of the difficulties of detecting low-energy gamma-rays which for actinides is compounded by natural radioactivity and gamma-rays due to the fission process, measurements were also made of natural and enriched tungsten samples. Since data for tungsten are simpler to obtain such data also allow to better study the experimental and analysis methods. Furthermore, the physics of tungsten nuclei is similar to that of the actinides in the sense that these are well-deformed rotational nuclides emitting low-energy intra-band gamma-rays and higher energy inter-band gamma-rays. Thus, comparisons with model calculations cover a wider mass range allowing a broader impact of the data. Some preliminary results are shown in figure 6 in comparison with model calculations with the TALYS code. The data analysis is still ongoing.

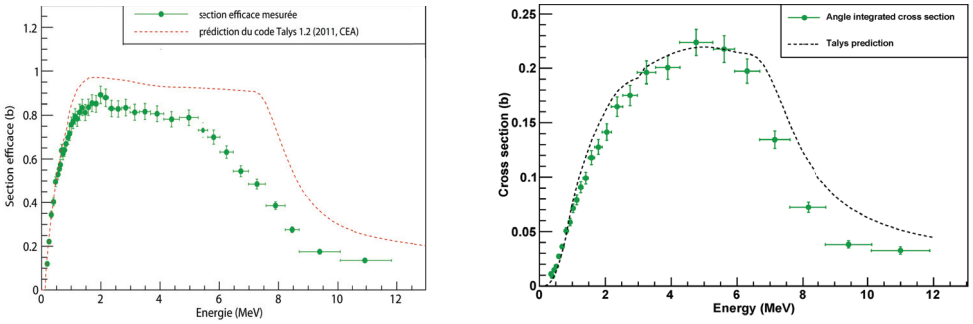

Fig. 6: Experimental inelastic scattering cross sections for the emission of the 122.64 keV gamma-ray of the $2_1^+ \rightarrow$ gs-transition in ^{186}W (Left) and the 112.75 keV gamma-ray of the $4_1^+ \rightarrow 2_1^+$-transition in ^{232}Th (Right).

5 ^{12}C

Inelastic neutron scattering on ^{12}C can be studied in a way quite different from the (n,xnγ)-technique and the neutron time-of-flight methods mentioned above. In recent work [65, 66] single crystal diamond detectors were exposed to quasi mono-energetic neutron fields at the IRMM van de Graaff laboratory. These detectors register the energy deposited by the charged particles left in the crystal following excitation of the carbon atoms by neutron inelastic scattering. The resulting pulse height spectrum in these very pure carbon detectors has better than 50 keV energy resolution and is determined by the Q-value of the reaction plus the incident neutron energy minus the sum of the emitted neutron and gamma energies. Gamma-emission is the dominant decay mode for the first level (2_1^+, $E_x = 4438.91$ keV) but is negligible for the higher lying levels. These decay into α+^{8}Be or 3αs. In view of the range of energies assumed by the outgoing neutron a range of energies in the pulse height spectrum is contributed by each of the excited levels in ^{12}C. In addition one observes in the detector full-energy peaks that are associated with the dissociation of the compound nucleus ^{13}C into charged particles only. In particular one observes the following binary exit channels: α+^{9}Be, p+^{12}B, or d+^{11}B. For these channels cross sections are readily obtained. A first attempt at modeling was undertaken by inspecting the data available in the ENDF/B-VII neutron library using MCNP. Using this Monte Carlo simulation code with a specially developed tally-ing subroutine it is possible to check the energy deposited by looking at the difference in energy of the incident neutron and the outgoing neutron(+gamma) [67]. The comparison of data and simulation is shown in figure 7. Here the data are taken for 16.6 MeV neutrons with a standard spread of 0.2 MeV.

At the highest deposited energy the ^{12}C(n,α)^{9}Be contribution is evident. From 4.5 to 9.5 MeV deposited energy the response is dominated by 3α breakup continuum. For deposited energies less than 4.5 MeV the response is dominated by elastic scattering for which this is the maximum deposited

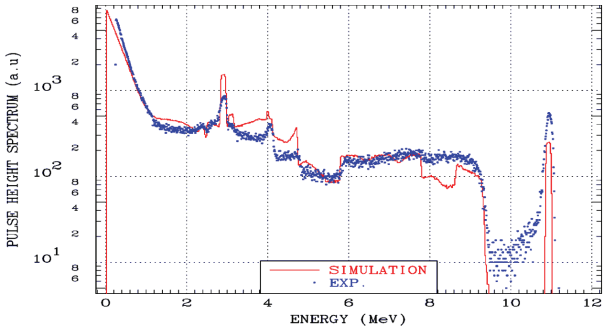

Fig. 7: Comparison of experimental data and Monte Carlo simulations based on ENDF/B-VII cross sections for n+^{12}C. The data correspond to the pulse height spectrum observed with a 4.7x4.7x0.5 mm^3 single crystal diamond detector obtained from Diamond Detectors Ltd.

energy [68]. The discrete peaks on top of the (in-)elastic scattering distribution correspond with the ^{12}C(n,p)^{12}B and ^{12}C(n,d)^{11}B reactions.

The figure clearly shows that some of the features in the spectrum are adequately described while others are not. In particular it appears that the description of inelastic scattering at large energy deposition and elastic scattering near the maximum recoil energy could be improved. Hence these data appear to offer an interesting test ground for the algebraic approach to coupled channel calculations for carbon described in references [41,42]. As is evident from our publication pulse height spectra and cross sections were obtained in the energy range from 7.3 to 20.5 MeV and the numerical data are available on request.

A good description of these data is of interest to applications aiming at neutron fluence and neutron spectrum measurements in various radiation fields in fission and fusion energy and in accelerator based neutron fields.

6 Summary

An overview is presented of recent measurements with the (n,xnγ)-technique with the GAINS and GRAPHEME setups. Cross sections were shown for ^{23}Na, ^{76}Ge, ^{186}W, ^{232}Th and in an accompanying contribution to this conference: ^{235,238}U. The data are compared with calculations in the interest of improving nuclear models and making the most of the data in the interest of applications. For applications in nuclear energy such data are in high demand and there remains considerable room for improved measurements and improved model calculations. Also shown are neutron inelastic scattering and reaction data obtained with a single-crystal diamond detector. These should be of interest to n+^{12}C model calculations that were recently performed. Describing these data better is of interest for the use of these detectors in complex neutron fields and involves the excitation spectrum of ^{12}C and ^{13}C and the angular distribution of emitted neutrons.

Acknowledgements

This work was supported by the European Commission within the Sixth Framework Programme through NUDAME (Contract FP6-516487), and within the Seventh Framework Programme through EUFRAT (EURATOM contract no. FP7-211499) and ANDES (EURATOM contract no. FP7-249671).

References

[1] M. Salvatores, coordinator, “Uncertainty and target accuracy assessment for innovative systems using recent covariance evaluations.” Organisation for Economic Co-operation and Development, Nu-

clear Energy Agency, International Evaluation Co-operation, Volume-26, NEA/WPEC-26, ISBN 978-92-64-99053-1, 2008.

[2] M. Salvatores, G. Palmiotti, G. Aliberti, R. McKnight, P. Obložinský, and W. Yang, "Needs and issues of covariance data application," *Nucl. Data Sheets*, vol. 109, p. 2725, 2008.

[3] A. Bettini, "GERDA. Germanium detector array. Search for neutrino-less $\beta\beta$ decay of ^{76}Ge," *Nucl. Phys. B*, vol. 168, p. 67, 2007.

[4] V. Kudryavtsev, L. Pandola, and V. Tomasello, "Neutron- and muon-induced background in underground physics experiments," *Eur. Phys. J. A*, vol. 36, p. 171, 2008.

[5] M. Livingston and H. Bethe, "Nuclear physics, C. Nuclear dynamics, experimental," *Revs. Mod. Phys.*, p. 245, 1937.

[6] F. Heyn, "Evidence for the expulsion of two neutrons from copper and zinc by one fast neutron," *Nature*, vol. 138, p. 723, 1936.

[7] G. Seaborg, G. Gibson, and D. Grahame, "Inelastic scattering of fast neutrons," *Phys. Rev.*, vol. 52, p. 408, 1937.

[8] H. Dunlap and R. Little, "The scattering of fast neutrons by lead," *Phys. Rev.*, vol. 60, p. 693, 1941.

[9] P. Stelson and W. Preston, "The inelastic scattering of fast neutrons from iron," *Phys. Rev.*, vol. 86, p. 132, 1952.

[10] V. Scherrer, R. Theus, and W. Faust, "Gamma-radiation from interaction of 14-MeV neutrons with iron," *Phys. Rev.*, vol. 89, p. 1268, 1953.

[11] R. B. Day, "Gamma rays from neutron inelastic scattering," *Phys. Rev.*, vol. 102, p. 767, 1956.

[12] L. Cranberg and J. S. Levin, "Inelastic scattering of neutrons from iron by time-of-flight," *Phys. Rev.*, vol. 100, p. 434, 1955.

[13] G. Haouat, J. Lachkar, C. Lagrange, J. Jary, J. Sigaud, and Y. Patin, "Neutron scattering cross sections for ^{232}Th, ^{233}U, ^{235}U, ^{238}U, ^{239}Pu, and ^{242}Pu between 0.6 and 3.4 MeV.," *Nucl. Sci. Eng.*, vol. 81, p. 491, 1982.

[14] R. Garrett, F. Hereford, and B. Sloope, "Inelastic neutron scattering in Al, Fe, Mg and Cu," *Phys. Rev.*, vol. 92, p. 1507, 1953.

[15] F. Voss, C. Cierjacks, and L. Kropp, "Measurement of high resolution gamma-ray production cross sections in inelastic neutron scattering on Al and Fe between 0.8 and 13 MeV," in *Conf. on Nuclear Cross Sections and Technology*, vol. 1, (Knoxville, USA), p. 218, 1971.

[16] J. K. Dickens, "^{28}Si$(n, n'\gamma)$ photon production cross sections for E_γ=1.78 MeV, 5.0$\leq E_n \leq$ 9.5 MeV," *Phys. Rev. C*, vol. 10, p. 958, 1974.

[17] Z. Bell, J. Dickens, D. Larson, and J. Todd, "Neutron-induced gamma-ray in ^{57}Fe for incident neutron energies between 0.16 and 21 mev," *Nucl. Sci. Eng.*, vol. 84, p. 12, 1983.

[18] L. Bernstein, J. Becker, W. Younes, D. Archer, K. Hauschild, G. Johns, R. Nelson, W.S.Wilburn, and D. Drake, "Probing reaction dynamics with the ^{196}Pt(n,xnγ) reactions for $x \leq 15$," *Phys. Rev. C*, vol. 57, p. R2799, 1998.

[19] L. Bernstein, J. Becker, P. Garrett, W. Younes, D. McNabb, D. Archer, C. McGrath, H. Chen, W. Ormand, M. Stoyer, R. Nelson, M. Chadwick, G. Johns, W.S.Wilburn, M. Devlin, D. Drake, and P. Young, "^{239}Pu(n,2n)^{238}Pu cross section deduced using a combination of experiment and theory," *Phys. Rev. C*, vol. 65, p. 021601(R), 2002.

[20] N. Fotiades, G. Johns, R. Nelson, M. Chadwick, M. Devlin, W. Wilburn, P. Young, D. Archer, J. Becker, , D. Archer, L. Bernstein, P. Garrett, C. McGrath, D. McNabb, and W. Younes, "Measurements and calculations of ^{238}U(n,xnγ) partial γ-ray cross sections," *Phys. Rev. C*, vol. 69, p. 024601, 2004.

[21] H. Vonach, A. Pavlik, M. B. Chadwick, R. C. Haight, R. O. Nelson, S. A. Wender, and P. G. Young, "^{207,208}Pb(n,xnγ) reactions for neutron energies from 3 to 200 MeV," *Phys. Rev. C*, vol. 50, p. 1952,

1994.

[22] D. A. Lind and R. B. Day, "Studies of gamma rays from neutron inelastic scattering," *Ann. Phys.*, vol. 12, p. 485, 1961.

[23] E. Sheldon and D. M. van Patter, "Compound inelastic nucleon and gamma-ray angular distributions for even- and odd-mass nuclei," *Revs. Mod. Phys.*, vol. 38, p. 143, 1966.

[24] C. Sage, Semkova, O. Bouland, P. Dessagne, A. Fernandez, F. Gunsing, C. Nästren, G. Noguère, H. Ottmar, A. J. M. Plompen, P. Romain, G. Rudolf, J. Somers, , and F. Wastin, "High resolution measurements of the ^{241}Am(n,2n) reaction cross section," *Phys. Rev. C*, vol. 81, p. 064604, 2010.

[25] A. Tonchev, C. Angell, M. Boswell, A. Crowell, B. Fallin, S. Hammond, C. Howell, A. Hutcheson, H. Karwowski, J. Kelley, R. Pedroni, W. Tornow, J. Becker, D. Dashdorj, J. Kenneally, R. Macri, M. Stoyer, C. Wu, E. Bond, M. Chadwick, J. Fitzpatrick, T. Kawano, R. Rundberg, A. Slemmons, D. Vieira, and J. Wilhelmy, "Measurement of the ^{241}Am(n,2n) reaction cross section from 7.6 to 14.5 MeV," *Phys. Rev. C*, vol. 77, p. 054610, 2008.

[26] S. Hilaire and S. Goriely, "Global microscopic nuclear level densities within the HFB plus combinatorial method for practical applications," *Nucl. Phys. A*, vol. 779, p. 63, 2006.

[27] S. Goriely, E. Khan, and M. Samyn, "Microscopic HFB + QRPA predictions of dipole strength for astrophysics applications," *Nucl. Phys. A*, vol. 739, p. 331, 2004.

[28] E. Bauge, J. Delaroche, and M. Girod, "Semimicroscopic nucleon-nucleus spherical optical model for nuclei with A$\geq$40 at energies up to 200 MeV," *Phys. Rev. C*, vol. 58, p. 1118, 1998.

[29] L. C. Mihailescu, C. Borcea, P. Baumann, P. Dessagne, E. Jericha, H. Karam, M. Kerveno, A. J. Koning, N. Leveque, A. Pavlik, A. J. M. Plompen, C. Quétel, G. Rudolf, and I. Trešl, "A measurement of (n, xnγ) cross sections for ^{208}Pb from threshold up to 20 MeV," *Nucl. Phys. A*, vol. 811, pp. 1–27, 2008.

[30] A. Plompen, T. Kawano, and R. Capote Noy, "Inelastic scattering and capture cross section data of major actinides in the fast neutron region." INDC(NDS)-0597, IAEA, Vienna, Austria, 2012.

[31] R. Capote, S. Chiba, E. Soukhovitskii, J. Quesada, and E. Bauge, "A global dispersive coupled-channel optical model potential for actinides," *J. of Nucl. Sci. and Technol.*, vol. 45, p. 333, 2008.

[32] B. Morillon and P. Romain, "Bound single-particle states and scattering of nucleons on spherical nuclei with a global optical model," *Phys. Rev. C*, vol. 76, p. 044601, 2007.

[33] P. Young, M. Chadwick, R. MacFarlane, P. Talou, T. Kawano, D. Madland, W. Wilson, and C. Wilkerson, "Evaluation of neutron reactions for ENDF/B-VII: $^{232-241}$U and ^{239}Pu," *Nucl. Data Sheets*, vol. 108, p. 2589, 2007.

[34] E. Soukhovitskii, R. Capote, J. Quesada, and S. Chiba, "Dispersive coupled-channel analysis of nucleon scattering from ^{232}Th up to 200 MeV," *Phys. Rev. C*, vol. 72, p. 024604, 2005.

[35] E. Bauge, J. Delaroche, and M. Girod, "Lane-consistent, semimicroscopic nucleon-nucleus optical model," *Phys. Rev. C*, vol. 63, p. 024607, 2001.

[36] F. S. Dietrich, I. Thompson, and T. Kawano, "Target-state dependence of cross sections for reactions on statically deformed nuclei," *Phys. Rev. C*, vol. 85, p. 044611, 2012.

[37] T. Kawano, P. Talou, M. Chadwick, and T. Watanabe, "Monte Carlo simulation of particle and γ-ray emissions in statistical Hauser-Feshbach model," *J. of Nucl. Sci. and Technol.*, vol. 47, p. 462, 2010.

[38] D. Dashdorj, T. Kawano, P. Garrett, J. Becker, U. Agvaanluvsan, L. Bernstein, M. Chadwick, M. Devlin, N. Fotiades, G. Mitchell, R. Nelson, , and W. Younes, "Effect of preequilibrium spin distribution on ^{48}Ti + n cross sections," *Phys. Rev. C*, vol. 75, p. 054612, 2007.

[39] K. Amos, L. Canton, G. Pisent, J. Svenne, and D. van der Knijff, "An algebraic solution of the multichannel problem applied to low energy nucleon-nucleus scattering," *Nucl. Phys. A*, vol. 728, p. 65, 2003.

[40] L. Canton, G. Pisent, J. P. Svenne, D. van der Knijff, K. Amos, and S. Karataglidis, "Role of the Pauli principle in collective-model coupled-channel calculations," *Phys. Rev. Letters*, vol. 94, p. 122503, 2005.

[41] G. Pisent, J. P. Svenne, L. Canton, K. Amos, S. Karataglidis, and D. van der Knijff, "Compound and quasicompound states in low-energy scattering of nucleons from ^{12}C," *Phys. Rev. C*, vol. 72, p. 014601, 2005.

[42] J. P. Svenne, K. Amos, S. Karataglidis, D. v. L. Canton, and G. Pisent, "Low-energy neutron-^{12}C analyzing powers: Results from a multichannel algebraic scattering theory," *Phys. Rev. C*, vol. 73, p. 027601, 2006.

[43] R. Capote, M. Herman, P. Obložinský, P. G. Young, S. Goriely, T. Belgya, A. V. Ignatyuk, A. J. Koning, S. Hilaire, V. A. Plujko, M. Avrigeanu, O. Bersillon, M. B. Chadwick, T. Fukahori, Z. G. Y. Han, S. Kailas, J. Kopecky, V. M. Maslov, G. Reffo, M. Sin, E. S. Soukhovitskii, and P. Talou, "RIPL reference input parameter library for calculation of nuclear reactions and nuclear data evaluations," *Nucl. Data Sheets*, vol. 110, p. 3107, 2009.

[44] C. Rouki, P. Archier, C. Borcea, C. De SaintJean, J. Drohé, S. Kopecky, A. Moens, N. Nankov, A. Negret, G. Noguére, A. Plompen, and M. Stanoiu, "High resolution measurement of neutron inelastic scattering cross-sections for ^{23}Na," *Nucl. Instrum. Methods Phys. Res. A*, vol. 672, p. 82, 2012.

[45] A. Negret, C. Borcea, and A. J. M. Plompen, "Cross sections for neutron inelastic scattering on ^{28}Si," *J. Korean Physical Society*, vol. 59, p. 1765, 2011.

[46] A. Negret, C. Borcea, J. Drohé, L. Mihailescu, A. J. M. Plompen, and R. Wynants, "A new setup for neutron inelastic cross section measurements." Proc. Int. Conf. on Nuclear Data for Science and Technology - ND2007, Apr. 22 - Apr. 27, 2007, Nice, France, EDP Sciences, ISBN 978-2-7598-0091-9, 2008.

[47] L. C. Mihailescu, C. Borcea, A. Koning, , A. Pavlik, and A. J. M. Plompen, "High resolution measurement of neutron inelastic scattering and (n,2n) cross-sections for ^{209}Bi," *Nucl. Phys. A*, vol. 799, pp. 1–29, 2008.

[48] L. Mihailescu, C. Borcea, A. Koning, and A. Plompen, "High resolution measurement of neutron inelastic scattering and (n,2n) cross-sections for ^{52}Cr," *Nucl. Phys. A*, vol. 786, p. 1, 2007.

[49] A. Bacquias, C. Borcea, P. Dessagne, M. Kerveno, J. Drohé, N. Nankov, A. Negret, M. Nyman, A. Plompen, C. Rouki, G. Rudolf, M. Stanoiu, and J. Thiry, "Study of (n,xnγ) reactions on ^{235,238}U." These proceedings, 2012.

[50] J. Thiry, C. Borcea, P. Dessagne, J. Drohé, E. Jericha, H. Karam, M. Kerveno, A. Koning, A. Negret, A. Pavlik, A. Plompen, P. Romain, C. Rouki, G. Rudolf, and M. Stanoiu, "Measurement of $(n, xn\gamma)$ reactions of interest for the new nuclear reactors," *J. Korean Physical Society*, vol. 59, p. 1880, 2011.

[51] A. Pavlik, P. Baumann, C. Borcea, E. Jericha, S. Jokic, M. Kerveno, S. Lukic, J. P. Meulders, L. C. Mihailescu, R. Nolte, A. J. M. Plompen, I. Raskynite, G. Rudolf, and the n_TOF collaboration, "Cross-section measurements for (n,xn) reactions by in-beam gamma-ray spectroscopy." Proc. Int. Conf. on Nuclear Data for Science and Technology - ND2004, Sep. 26 - Oct. 1, 2004, Santa Fe, USA, AIP conf. proceedings 769, 876, 2005.

[52] Working Party on International Evaluation Co-operation, "The High Priority Request List for nuclear data (HPRL)." NEA Nuclear Science Commitee, www.nea.fr/dbdata/hprl/, 2006.

[53] D. Deleanu, C. Borcea, P. Dessagne, M. Kerveno, A. Negret, A. J. M. Plompen, and J. C. Thiry, "The gamma efficiency of the GAINS spectrometer," *Nucl. Instrum. Methods Phys. Res. A*, vol. 624, p. 130, 2010.

[54] A. Plompen, C. Borcea, D. Deleanu, P. Dessagne, M. Kerveno, M. Mosconi, N. Nankov, A. Negret, R. Nolte, C. Rouki, G. Rudolf, M. Stanoiu, and J.-C. Thiry, "Method developing and testing for

inelastic scattering measurements at the GELINA facility," *J. Korean Physical Society*, vol. 59, p. 1581, 2011.

[55] M.Mosconi, R.Nolte, A.Plompen, C.Rouki, M.Kerveno, P.Dessagne, and J. Thiry, "Characterisation of fission ionisation chambers using monoenergetic neutrons." Proc. of the Final scientific EFNUDAT Workshop, p.99, 30 August - 2 September 2010, Ed. E. Chiaveri, ISBN 978-92-9083-365-9, CERN, Geneva, Switzerland, 2010.

[56] H. Märten, J. Wartena, and H. Weigmann, "Simultaneous high-resolution measurement of differential elastic and inelastic neutron cross section on selected light nuclei." Neutron Data report GE/R/ND/02/94, CEC-Joint Research Centre, IRMM, Geel, Belgium; unpublished, 1994.

[57] S. Kopecky, R. Shelley, H. Märten, and H. Weigmann, "High resolution inelastic scattering cross section of ^{23}Na and ^{27}Al," in *Proceedings of the International Conference on Nuclear Data for Science and Technology* (A. V. G. Reffo and C. Grandi, eds.), (Trieste, Italy), p. 523, Editrice Compositori, 40128 Bologna, Italy, May 19-24 1997.

[58] S. Kopecky and A. Plompen, "R-matrix analysis of total and inelastic scattering cross section of ^{23}Na." JRC Scientific and Technical Reports, LANA-25067-EN-N, ISBN 978-92-79-22214-6, European Union, 2011.

[59] C. Aalseth, F. Avignone III, R. Brodzinski, S. Cebrian, D. Gonzáles, E. García, W. Hensley, I. Irastorza, I. Kirpichnikov, A. Klimenko, H. Miley, A. Morales, J. Morales, A. Órtiz de Solórzano, S. O. V. Pogosov, J. Puimedón, J. Reeves, M. Sarsa, S. Scopel, A. Smolnikov, A. Starostin, A. Tamanyan, A. Vasenko, S. Vasiliev, and J. Villar, "Recent results of the IGEX ^{76}Ge double-beta decay experiment," *Physics of Atomic Nuclei*, vol. 63, p. 1225, 2000.

[60] H. Klapdor-Kleingrothaus and I. Krivosheina, "The evidence for the observation of $0\nu\beta\beta$ decay: the identification of $0\nu\beta\beta$ events from the full spectra," *Modern Physics Letters A*, vol. 21, p. 1547, 2006.

[61] H. Klapdor-Kleingrothaus, A. Dietz, L. Baudis, G. Heusser, I. Krivosheina, B. Majorovits, H. Paes, H. Strecker, V. Alexeev, A. Balysh, A. Bakalyarov, S. Belyaev, V. Lebedev, and S. Zhukov, "Latest results from the HEIDELBERG-MOSCOW double beta decay experiment," *Eur. Phys. J. A*, vol. 12, p. 147, 2001.

[62] H. Wulandari, J. Jochum, W. Rau, and F. von Feilitzsch, "Neutron flux at the Gran Sasso underground laboratory revisited," *AstroP*, vol. 22, p. 313, 2004.

[63] P. Belli, R. Bernabei, S. D'Angelo, M. De Pascale, L. Paoluzi, and R. Santonico, "Deep underground neutron flux measurement with large BF_3 counters," *Il Nuovo Cimento A*, vol. 101, p. 959, 1989.

[64] A. J. Koning and M. C. Duijvestijn, "New nuclear data evaluations for Ge isotopes," *Nucl. Instrum. Methods Phys. Res. B*, vol. 248, p. 197, 2006.

[65] M. Pillon, M. Angelone, A. Krása, A. J. M. Plompen, P. Schillebeeckx, and M. L. Sergi, "Experimental response functions of a single-crystal diamond detector for 5-20.5 MeV neutrons," *Nucl. Instrum. Methods Phys. Res. A*, vol. 640, p. 185, 2011.

[66] M. Pillon, M. Angelone, A. Krása, A. J. M. Plompen, P. Schillebeeckx, and M. L. Sergi, "Measurement of neutron reaction cross sections in carbon using a single crystal diamond detector." AIP Conference proceedings 1412, 121, doi:10.1063/1.3665305, 2011.

[67] A. Milocco, A. Trkov, and M. Pillon, "Simulation of charge collection in diamond detectors irradiated with deuteron-triton neutron sources." AIP Conf. Proc. 1412, 224, doi:10.1063/1.3665318, 2011.

[68] S. Gvozdev, V. Frunze, and V. Amosov, "Numerical simulation of the energy spectrum of recoil nuclei and alpha particles from interactions of fast neutrons with diamond," *Instr. Exp. Tech. (USSR, English translation)*, vol. 52, p. 637, 2009.

Nuclear data for neutron-induced reactions on U-235 measured at DANCE

M . Jandel
C-NR, Los Alamos National Laboratory

Many areas of applied nuclear physics such as nuclear forensics, stockpile stewardship, nuclear non-proliferation, and nuclear energy, require new or improved cross sections of neutron-induced reactions. High precision measurements of U-235 neutron capture cross section were performed at Los Alamos Neutron Scattering Center (LANSCE), Los Alamos National Laboratory (LANL). The measurements were performed using unique LANL facility: Detector for Advanced Neutron Capture Experiments (DANCE). Data on cross sections were obtained in incident neutron energy range from 4 eV to 1 MeV. Significant discrepancies were observed between the existing evaluations and the DANCE measurement.

In addition, the properties of the prompt-gamma ray emission in neutron-induced fission of U-235 were extracted in form of correlated data on gamma-ray multiplicity versus gammaray energy and total energy. The results from DANCE were used to constrain the theoretical models.

Improved capture γ-ray libraries for nuclear applications

A. M. Hurst[1], *B. W. Sleaford*[2], *R. B. Firestone*[1], *N. C. Summers*[2], *Zs. Revay*[3], *L. Szentmiklósi*[3], *S. Basunia*[1], *T. Belgya*[3], *J. E. Escher*[2], *M. Krticka*[4]
[1]Lawrence Berkeley National Laboratory, Berkeley, CA 94720, USA
[2]Lawrence Livermore National Laboratory, Livermore, CA 94550, USA
[3]Centre for Energy Research, Hungarian Academy of Sciences, Budapest, Hungary
[4]Charles University in Prague, Prague, Czech Republic

Abstract
The neutron-capture reaction is of fundamental use in identifying and analyzing the γ-ray spectrum from an unknown object as it gives unambiguous information on exactly what isotopes are absorbing the neutrons. There are many applications where this can be used passively (nonproliferation), or actively where an external neutron source is used to probe an unknown assembly (planetary studies). There are known capture-γ data gaps in the ENDF libraries used by transport codes for various nuclear applications. A new database, EGAF, containing thermal neutron-capture γ-ray data is used to improve the capture-γ information in the ENDF libraries. For many nuclei the unresolved quasi-continuum part of the γ cascade is not available experimentally. In this work, we have modeled this contribution using the Monte Carlo statistical-decay code DICEBOX, in addition to improving level-scheme evaluations. For capture of higher-energy neutrons there is little experimental data available, making evaluation of modeling codes problematic. We plan to continue the DICEBOX approach through the resolved resonance region where spin and parity information is partially known. In the unresolved resonance region, and up to 20-MeV incident neutron energy, we are applying Hauser-Feshbach models to predict the capture-γ spectrum.

1 Introduction

Improved prompt capture-γ spectra are needed for a variety of non-proliferation programs, e.g. Monte Carlo Neutron Transport Codes (MCNP) for National Security applications. Prompt γ rays are emitted following neutron capture and can, thus, be used to unambiguously identify compositions of unknown assemblies since the observed capture γ rays are themselves unique signatures of the elements/isotopes contained within the absorbing medium. Until recently, however, no reliable prompt neutron-capture γ-ray database existed for this type of analysis [1]. Since capture-γ data are an essential component for many basic and applied scientific purposes, a series of thermal-capture measurements were undertaken at the Budapest Reactor on all elemental targets corresponding to Z = 1-83, 90, and 92, with the exception of helium and promethium. This work led to the development of the Evaluated Gamma-ray Activation File (EGAF) and has been evaluated and published as part of an International Atomic Energy Agency (IAEA) coordinated research project [2].

For low-Z isotopes, neutron-decay schemes are likely near complete, however, for medium-heavy mass isotopes there may remain considerable gaps in the complete knowledge of the decay scheme. Furthermore, the contribution of feeding to the observed low-lying states from the quasi continuum is difficult to resolve experimentally for many nuclei. To account for this feeding and supplement the experimental data available in the EGAF database, the Monte Carlo statistical-decay code DICEBOX [3] has been utilized. New independent measurements of the total radiative thermal neutron-capture cross section (σ_0) can then be extracted as the sum of experimentally measured partial-capture γ-ray cross sections feeding the ground state directly, in addition to the DICEBOX-modeled contribution from the

continuum that feeds the ground state. Also, the comparison between DICEBOX simulations and the experimentally-determined cross sections in the EGAF database allows for optimization of the capture-state spin distribution as well as improved evaluations of the nuclear structure information that can ultimately be communicated back through the Evaluated Nuclear Structure Data File (ENSDF) [4] and the Reference Input Parameter Library (RIPL) [5], a nuclear reaction database containing reformatted structure information from ENSDF.

A future long-range goal of this work is to develop comprehensive neutron-data libraries with complete capture-γ information covering incident-neutron energies from the thermal region, through to the resolved and then unresolved resonance regions, all the way up to 20 MeV, the Hauser-Feshbach regime. This information is vital for neutron transport calculations and will be disseminated through the Evaluated Nuclear Data File (ENDF) [6]. Unfortunately, very little experimental data are available for prompt γ-ray emission resulting from higher-energy neutron capture. To address this problem, future neutron-time-of-flight measurements are being planned. The DICEBOX approach may then also be adopted in the resolved-resonance region where spin and parity information of the $l \geq 1$ resonances is partially known, while Hauser-Feshbach models [7] will be used to treat the remaining part of the high-energy neutron-capture γ-ray spectrum.

In these proceedings we are presenting results from a series thermal-capture measurements using enriched tungsten targets. This new information will be communicated through EGAF, ENSDF, and RIPL, and will form part of revised, more accurate capture-γ library that will be made available through the ENDF database for nuclear applications.

2 Experimental Setup

Partial neutron-capture γ-ray cross sections were measured with the mirror-guided thermal-neutron beam at the 10-MW Budapest Research Reactor [8,9]. A thermal flux of approximately 7.8×10^7 n·cm^{-2}·s-1 was incident upon samples of isotopically-enriched tungsten oxide compounds. An elemental sample of tungsten oxide was also irradiated with a thermal flux of 2×10^6 n·cm^{-2}·s-1. The samples were prepared in powder form and held in the beam line in Teflon bags. Due to the proximity of the evacuated target-sample holder, a distance some 35 m away from the reactor wall, a low-background environment permits for the detection of primary and secondary capture-γ rays. The Prompt Gamma Activation Analysis (PGAA) setup [10, 11] is located at this target station and, in its simplest operational mode, comprises a single Compton-suppressed n-type high-purity germanium (HPGe) detector with a closed-end coaxial-type geometry. The HPGe detector is positioned approximately 23.5 cm from the target-sample holder. The energy calibration and counting efficiency of the HPGe detector was accomplished using a variety of standard radioactive sources spanning an energy range of ~ 50 keV up to ~ 11 MeV. The γ-ray spectroscopy software package HYPERMET-PC [12] aided the generation of non-linear energy-calibration and efficiency fits to the data, in addition to the peak-fitting analysis of the capture γ-ray spectrum.

Partial γ-ray cross sections were extracted from the measured peak areas for all tungsten capture-γ lines using an internal-standardization procedure which normalizes the observed intensities to well-known comparator lines [13]. Hydrogen was used as the comparator in this case from a standard (n,γ) measurement with tungstic acid (H_2WO_4) [14]. Cross sections for all tungsten γ lines were then derived based on this standardization (n,γ) measurement. To ensure consistency over the observational range, a statistically-consistent set of normalization factors were required in five different regions encompassing the low-energy, turning-point, medium- and high-energy regions of the capture-(n,γ) spectrum. Furthermore, this requirement of consistency between low-, medium, and high-energy normalization factors for each sample, allowed for determination of independent sample thicknesses by considering, and correcting peak intensities for, γ-ray self absorption within the tungsten oxide powders themselves. The attenuation coefficients were calculated using data from XMUDAT [15] which is based on the prescription outlined in Ref. [16].

3 Statistical Model Calculations

The thermal neutron-capture γ cascade has been simulated by calculating theoretical feedings to the experimentally observed low-lying levels using the Monte Carlo code DICEBOX [3]. This program is based on the generalization of the extreme statistical model, proposed by Bohr [17], in the formation and decay of the compound nucleus. Thermal neutron capture is an s-wave process ($l = 0$) whereupon the compound product is formed with an excitation energy corresponding to its neutron separation energy. Using this information, and within this theoretical framework, the DICEBOX calculation is then constrained according to an experimental decay scheme up to a defined energy, referred to as the critical energy $E_{\rm crit}$. All experimental information characterizing the decay scheme including level energies, spins and parities, γ-ray transition energies and their corresponding branching ratios as well as internal-conversion coefficients, are regarded as complete and accurate up to $E_{\rm crit}$. The code then considers the region between $E_{\rm crit}$ and the neutron separation energy as the quasi continuum and uses a random discretization of an *a priori* known level density (LD) formula $\rho(E, J^{\pi})$ and photon strength function (PSF) $f^{(XL)}(E_{\gamma})$ to generate γ-ray transitions from within this region to the low-lying levels in the experimental decay scheme. A partial radiation width $\Gamma_{if}^{(XL)}$ describing the transition probability for a given γ-ray decay with an energy $E_{\gamma} = E_i - E_f$ is then assumed to be a random choice from a Porter-Thomas distribution [18], centred on a mean value given by

$$\langle \Gamma_{if}^{(XL)} \rangle = \frac{f^{(XL)}(E_{\gamma}) \cdot E_{\gamma}^{2L+1}}{\rho(E_i, J_i^{\pi_i})}. \tag{1}$$

In equation (1), $\rho(E_i, J_i^{\pi_i})$ represents the level density near the initial level i and XL denotes the multipolarity of the transition involved; selection rules are fully accounted for in the generation of the partial widths. The system of partial radiation widths fully describing the decay properties of the low-lying levels as well as the randomly-generated levels of the quasi continuum is known as a *nuclear realization*. Decay properties of the levels involved differ according to each independent nuclear realization i.e. level-scheme simulation, and thus, generate statistical fluctuations in the simulated level feedings. By using an appropriate number of realizations DICEBOX can be used to determine the nature of the Porter-Thomas fluctuations involved, and therefore, provide an estimate of the uncertainty attributed to the statistical nature of the decay processes. These proceedings describe calculations involving 50 separate nuclear realizations, with each realization comprising 100,000 capture-state γ-ray decay cascades.

Phenomenological models have been used to describe the influence of the PSF and LD on the simulated level feedings. Since the dominant decay mode from the capture state at the neutron separation energy is via an electric dipole transition ($E1$), Lorentzian-based models are used to describe the shape of the corresponding giant dipole electric resonance (GDER) observed in photonuclear reactions. Several different GDER-based PSFs are implemented in the DICEBOX code [3] and all were tested in this analysis. The Enhanced Generalized Lorentzian (EGLO) model [19, 20], which is dependent on both γ-ray energy as well as nuclear temperature, was found to reproduce the experimental absorption data for tungsten rather well and was employed as the principal $E1$ PSF in this work. The GDER parametrizations for the tungsten isotopes were taken from RIPL [5]. However, other models were also tested, and even the simpler Brink-Axel (Standard Lorentzian) [21, 22] model−dependent upon γ-ray energy alone−was found to produce statistically invariant results cf. the EGLO model. The next most important capture-state decay mode is through an $M1$ magnetic dipole transition, although this mode is significantly hindered by approximately an order of magnitude compared to the $E1$ contribution . For the $M1$ PSF, Lorentzian-based models were considered and tested, however, due to the paucity of experimental data available for the giant dipole magnetic resonance (GDMR), in a somewhat general sense and certainly in the case of tungsten, a single-particle (SP) PSF model was adopted. A final consideration was also given to the PSF for the much weaker $E2$ electric quadrupole primary transitions. In this case, a global parametrization [23, 24] has been used to describe the expected shape of the giant quadrupole electric resonance (GQER) for the adopted PSF model. The simulations in this work made use of both

the constant temperature formula (CTF) and back-shifted Fermi gas (BSFG) models for the adopted level density. The parametrizations for these models were taken from Ref. [25]. All possible combinations of PSF and LD were tested in these calculations.

4 Results

The four major tungsten isotopes i.e. ^{182}W (26.50 %), ^{183}W (14.31 %), ^{184}W (30.64 %), and ^{186}W (28.43 %), have been investigated through a series of isotopically-enriched tungsten (^{182,183,186}W) and elemental tungsten (^{184}W) thermal neutron-capture measurements. The extracted cross sections have then been compared to theoretical predictions using the DICEBOX code to simulate the thermal-capture γ-ray cascade. The quality of the results are assessed in terms of how well the modeled predictions for level populations compare with the experimental depopulation data for a given level. Thus, plotting these two quantities against each other gives an immediate impression of the validity of the statistical model in addition to the quality and completeness of the experimental data. This approach can then be used to postulate on the existence of missing γ rays, and indeed, search for them in the collected (n,γ) spectra. The statistical model can also be used to test various spin-parity (J^π) assignments for levels which have tentative assignments and even suggest new values in the case of strongly populated levels with no known J^π assignments. Other structural information may also be extracted such as confirmation of mixing ratios for γ-ray transitions with mixed multipolarities.

A complete summary of this analysis of the major tungsten isotopes, including new independent measurements of the total radiative thermal neutron-capture cross sections and γ-emission probabilities, will be made available in Ref. [26], while earlier developments in this work may be found in Refs. [27–29]. In these proceedings, we would like to highlight some of the methods that we have adopted in improving the capture-γ spectrum and structural information. Results from ^{186}W(n,γ) will be used as a case-in-point illustration. For the ^{187}W compound a cut-off energy corresponding to $E_{\rm crit} = 900$ keV was determined. Beneath this value of $E_{\rm crit}$, 40 low-lying levels (including the ground state) are known to exist. Figure 1 shows the corresponding population-depopulation plot for this nucleus up to $E_{\rm crit}$. In Fig. 1(a) it can be seen that population and depopulation data are all in good agreement with the exception of the low-lying level at $E_{\rm ex} = 364.2$ keV. This level is reported in ENSDF (and therefore, RIPL) to have only two γ rays depopulating it at around 162.7 and 286.9 keV [4, 5]. However, the plot clearly indicates that the DICEBOX-simulated population for the 364.2-keV level is significantly greater than experimental depopulation corresponding to the extracted partial γ-ray cross sections for the 162.7- and 286.9-keV transitions. Since the experimental data for all other levels compare well for this nucleus, the implication is that the statistical model provides an accurate simulation for the ^{187}W capture-γ decay scheme, and it is more likely that there could be something wrong or incomplete with regards to the experimental data for the 364.2-keV level. The $J^\pi = 9/2^-$ assignment for this level is firmly established [4, 5] and so an alternative scenario could be there is a missing γ-ray transition deexciting this level that would otherwise provide the extra amount of intensity needed to reach agreement with the DICEBOX calculation. Fig. 1(b) shows that inclusion of a $\sim$ 14-keV transition to the 350.43-keV level improves agreement between simulation and experiment dramatically; all data now fall along the slope indicating good agreement between population and depopulation for levels up to $E_{\rm crit}$. The cross section for the $\sim$ 14-keV transition has been estimated based on expected population predicted by DICEBOX. In fact, the recent work of Bonadarenko *et al*. [30] suggests that such a transition should exist due to inferred coincidence relationships, despite not actually observing the transition directly. The course of this work has, indeed, highlighted several other instances where low-energy transitions, that have not been observed in nuclear structure experiments, may well exist according to statistical model expectations [26]. It is important that such transitions should be considered in establishing an optimized and more-complete capture-γ library.

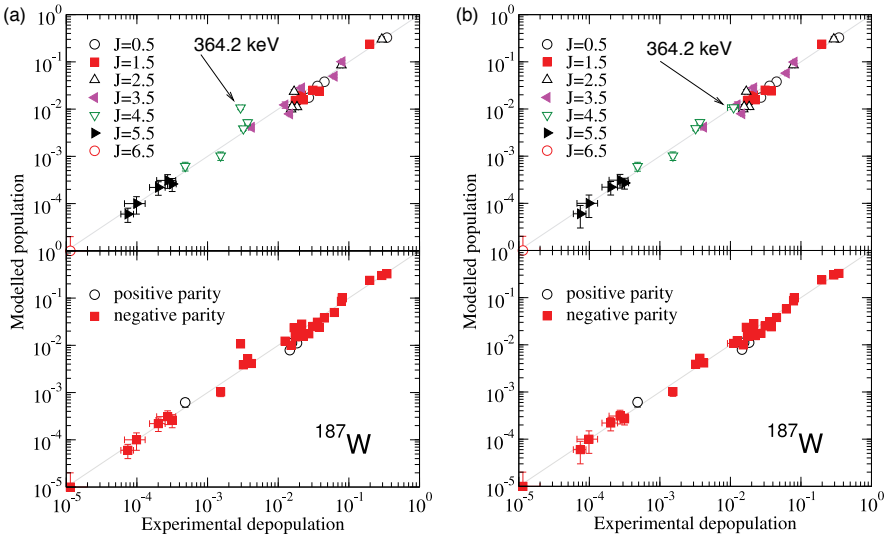

Fig. 1: Simulated populations (DICEBOX) plotted against experimental depopulations (capture-γ cross sections) for low-lying levels in ^{187}W up to $E_{\rm crit} = 900.0$ keV: (a) poor agreement between simulation and experiment for the 364.2-keV level; (b) good agreement between simulation and experiment for all levels.

5 Conclusion

Partial γ-ray cross sections have been measured for the major tungsten isotopes from a series of thermal neutron-capture experiments performed at the Budapest Research Reactor using isotopically-enriched and elemental tungsten samples. The quality and completeness of these data have been investigated by comparison to theoretical predictions of thermal capture onto tungsten isotopes using the Monte Carlo statistical-decay code DICEBOX. The combined experimental and theoretical effort has led to an increase in the cut-off energy $E_{\rm crit}$ compared to what is currently reported in RIPL [5] for all four tungsten compounds (^{183,184,185,187}W) investigated in this work. Furthermore, a more complete database of thermal-capture γ-rays and energy levels has been deduced for each of the compounds in this study, along with improved nuclear structure information such as confirmation of tentative J^π assignments in addition to newly-proposed assignments for certain levels. This information is currently in preparation for a forthcoming publication [26] and will be communicated back into the EGAF [2], ENSDF [4], and RIPL [5] libraries, and eventually disseminated as part of a complete capture-γ library to be made available through the ENDF [6] neutron-data library.

In the future we would like to extend our measurements with tungsten into the resolved-resonance and higher-energy neutron-capture regions, up to 20 MeV. These measurements will be accompanied by further statistical-model calculations using DICEBOX (resolved-resonance region) and Hauser-Feshbach (high-energy capture) techniques with the ultimate goal of generating a complete capture-γ library to be published through ENDF. This, in turn, will provide a more robust and reliable input-data-set for many applications using MCNP.

Acknowledgments

This work was performed under the auspices of the University of California, supported by the Director, Office of Science, Office of Basic Energy Sciences, of the U. S. Department of Energy at Lawrence Berkeley National Laboratory under Contract DE-AC02-05CH11231, and by the U. S. Department of Energy by Lawrence Livermore National Laboratory under Contract DE-AC52-07NA27344, the Hungar-

ian project OMFB 0018/2006 NAP VENEUS05, and by the research plan MSM 002 162 0859 supplied by the Ministry of Education of the Czech Republic. The operations staff at the Budapest research reactor are gratefully acknowledged.

References

[1] B. W. Sleaford *et al*., J. Kor. Phys. Soc. **59**, 1473 (2011).
[2] R. B. Firestone *et al*., IAEA STI/PUB/1263, 251 (2007).
[3] F. Becvár, Nucl. Instrum. Methods Phys. Res. A **417**, 434 (1998).
[4] Evaluated Nuclear Structure Data File, National Nuclear Data Center, Brookhaven National Laboratory.
http://www.nndc.bnl.gov/ensdf/.
[5] R. Capote *et al*., Nucl. Data Sheets, **110**, 3107 (2009).
http://www-nds.iaea.org/RIPL-3/.
[6] Evaluated Nuclear Data File, an electronic database of evaluated nuclear data maintained by the IAEA.
http://www-nds.iaea.org/exfor/endf.htm/.
[7] Walter Hauser and Herman Feshbach, Phys. Rev. **87**, 366 (1952).
[8] L. Rosta *et al*., Physica B, **234-236**, 1196 (1997).
[9] L. Rosta, Appl. Phys. A **74**, S52-S54 (2002).
[10] Zs. Révay *et al*., Nucl. Instrum. Methods Phys. Res. B **213**, 385 (2004).
[11] L. Szentmiklósi *et al*., J. Radioanal. Nucl. Chem. **286**, 501 (2010).
[12] Hypermet-PC Version 5.01 (v512), Institute of Isotopes (1995-97), Budapest, Hungary.
http://www.iki.kfki.hu/nuclear/hypc/.
[13] Zs. Révay and G. L. Molnár, Radiochim. Acta **91**, 361 (2003).
[14] L. Szentmiklósi, *private communication*.
[15] XMuDat: Photon attenuation data on PC, Version 1.0.1 of August 1998.
http://www-nds.iaea.org/publications/iaea-nds/iaea-nds-0195.htm/.
[16] J. H. Hubbel and S. M. Seltzer, Tables of X-Ray Mass Attenuation Coefficients and Mass Energy-Absorption Coefficients 1 keV to 20 MeV for Elements $Z = 1$ to 92 and 48 Additional Substances of Dosimetric Interest, NISTIR 5632 (1995).
http://physics.nist.gov/PhysRefData/XrayMassCoef/cover.html/.
[17] N. Bohr, Nature (London), **137**, 344 (1936).
[18] C. E. Porter and R. G. Thomas, Phys. Rev. **104**, 483 (1956).
[19] J. Kopecky and M. Uhl, Phys. Rev. C **41**, 1941 (1990).
[20] J. Kopecky, M. Uhl, and R. E. Chrien, Phys. Rev. C **47**, 312 (1993).
[21] D. M. Brink, Ph. D. Thesis, University of Oxford (1955).
[22] P. Axel, Phys. Rev. **126**, 671 (1962).
[23] J. Speth and A. van der Woude, Rep. Prog. Phys. **44**, 719 (1981).
[24] W. V. Prestwitch, M. A. Islam, and T. J. Kennett, Z. Phys. A **315**, 103 (1984).
[25] T. von Egidy and D. Bucurescu, Phys. Rev. C **72**, 044311 (2005).
[26] A. M. Hurst *et al*., to be submitted to Phys. Rev. C (2012).
[27] A. M. Hurst *et al*., J. Korean Phys. Soc. **59**, 1491s (2011).
[28] A. M. Hurst *et al*., AIP Conf. Proc. **1342**, 24 (2011).
[29] A. M. Hurst *et al*., Eur. Phys. J. Web of Conferences **21**, 10005 (2012).
[30] V. Bondarenko *et al*., Nucl. Phys. **A811**, 28 (2008).

Nuclear reaction modeling in nuclear data evaluation

M. Herman
NNDC, Brookhaven National Laboratory, Upton, NY 11793

mwherman@bnl.gov
http://www.nndc.bnl.gov

The US nuclear data community has recently released the ENDF/B-VII.1 library - the next generation of recommended nuclear data for nuclear science and technology applications. The library is the result of a coordinated five years effort of several US laboratories supported by collaboration with our colleagues in Japan, Europe, and at IAEA. The improvements focus on neutron cross sections, covariances, fission product yields and decay data and combine new developments in nuclear reaction modeling with measurements. Modern evaluations are essentially model based with experimental data used to constrain model parameters. This approach ensures physical consistency of the data but at the same time places stringent demands on the codes and employed models, which have to be flexible enough to reproduce experimental data with the desired accuracy. Over recent years there has been noticeable expansion of nuclear reaction modeling in the data evaluation. Simple eye-guided curves and least square fits were gradually giving room to the model calculations employing more and more powerful codes and more advanced reaction mechanisms. Various microscopic approaches start to compete with the phenomenological models. In this win-win combination nuclear data benefit from the better physics, which increases our confidence in the recommended data, while reaction physics gains the most thorough benchmark testing of concepts, models, and parametrizations. Since discovery of the neutron many advances in nuclear theory were driven by the needs of applications. Nowadays, nuclear data evaluation is the field in which the low energy nuclear reaction modeling finds its most extensive utilization.

In my talk I will briefly review status of reaction modeling used in the data evaluation, point out to recent advances and focus on those aspects that are still in need of further development. I will discuss areas in which until now we lack sufficient accuracy or predictive power and mention efforts that aim to close some of these gaps. Expanded availability of covariances, which quantify not only uncertainties but also correlations among data, offers exciting perspective of the global approach to nuclear data evaluation combining reaction modeling with differential and integral data. We are developing components of such a system being fully aware that its practical implementation presents enormous challenge related to reaction modeling, parametrization, selection of differential and integral experiments, reliable estimation of covariances and, last but not least, regarding scale of computation.

Processing of incident-neutron sub-library from ENDF/B-VII.1, JENDL-4.0 and JEFF-3.1.1

M.P.W. Chin, A. Ferrari, V. Vlachoudis
CERN (European Organization for Nuclear Research), CH-1211 Geneva, Switzerland

Abstract
FLUKA has so far achieved fully correlated/analog simulation for almost all projectile-target-energy combinations. This work reports some efforts in extending correlated transport to cover the <20 MeV neutron range, which is presently given, for the most part, multigroup treatment. The dynamics of correlated and multigroup transport will be demonstrated in the form of a sample history. Some issues arising from the processing of evaluated incident-neutron sub-libraries, using PREPRO and NJOY, will be presented. The representation of angular distribution of neutron elastic scatter will be discussed, with an attempt parameterize Legendre coefficients.

1 Correlated versus uncorrelated radiation transport

FLUKA [1,2] is capable of correlated simulation of all projectile-target combinations from eV to TeV – except for some cases where the neutron is below 20 MeV. In fact, even for low-energy (<20MeV) neutrons, correlated pointwise simulation is already available for selected channels. Wide-scale implementation of correlated pointwise transport is in progress; some aspects will be reported in Section 2.

In correlated/analog simulation, energy, momentum, A and Z are fully conserved at each collision – even before averaging over multiple samples; each secondary particle in the cascade fits a unique place in a *family tree*; the relation between every particle is uniquely defined.

Listing 2 is a sample history following a 20.1 MeV neutron in ^{10}B. FLUKA seamlessly switches to multigroup (non-correlated) transport when the neutron goes below 20.0 MeV (line 4). Before line 4, the neutron energy is exactly resolved (eg. 20.1 MeV at line 2). Once multigroup transport takes effect, however, the neutron energy becomes known between group-specific limits (eg. 19.6 and 20.0 MeV at line 4). The α produced at line 5 later collides, $\alpha +^{11} B \rightarrow^{14} C + p + \gamma$ (line 7), conserving A and Z. $^{10}B(n,\alpha)^{7}Li$ capture, the principle behind typical neutron detection, shielding and therapy, takes place in line 37; momentum and energy strictly conserved, FLUKA switches back to fully correlated transport. The accompanying 0.477 MeV γ, emitted explicitly as a sharp line, later interacts (line 39).

Estimation of integrated quantities (eg. dose and fluence) typically does not require correlation. Multigroup treatment is therefore a common technique in neutron transport; it offers greater details than the discrete ordinate technique. In fact, there are widely-used codes, where pointwise transport has been available, that are uncorrelated by design and philosophy. Correlated transport is optional, and challenging, in terms of code development.

There are applications which may be sensitive to the lack of correlation (eg. single event upsets and tissue equivalent proportional counters). Hence the importance of overcoming current exceptions where full correlation is absent in FLUKA. A point to note is that fully-correlated transport does not necessarily imply long run-times, as variance reduction techniques are always available.

2 Processing evaluated libraries: from ENDF to PENDF

A preliminary step towards implementing correlated low-energy neutron transport is to draw necessary data from evaluated libraries. Evaluated data in its raw form (ENDF [3]) are not readily usable feeds. Pointwise (PENDF) data may be obtained by processing ENDF using PREPRO [4] or NJOY [5].

	MeV	ns	cm
−>n	2.01000000000 e+01	0.000000000 e+00	0.000000000 e+00
∗elastic	2.01000000000 e+01	1.355819720 e−02	8.275412706 e−02
|−recoil	1.71238952200 e−01	1.355819720 e−02	8.275412706 e−02
∗multig	1.96e+01_2.00 e+01	2.396900352 e−01	1.453660049 e+00
−>2004	1.34750201500 e+01	2.396900352 e−01	1.453660049 e+00
|−step	2.17511493300 e+00	2.406580743 e−01	1.454112416 e+00
∗inelast	1.12999052200 e+01	2.406580743 e−01	1.454112416 e+00
−>6014	3.40657375900 e+00	2.406580743 e−01	1.454112416 e+00
|−step	3.40657375900 e+00	2.409063336 e−01	1.454126090 e+00
−>g	6.87132216600 e+00	2.406580743 e−01	1.454112416 e+00
∗Compton	6.87132216600 e+00	8.904385034 e−01	1.894811647 e+01
−>e−	6.29794025900 e+00	8.904385034 e−01	1.894811647 e+01
|−step	1.35455567600 e+00	9.025436869 e−01	1.929863451 e+01
|−step	9.07954558600 e−01	9.120798329 e−01	1.955831973 e+01
|−step	6.79128727100 e−01	9.198851972 e−01	1.966286332 e+01
|−step	6.33787894500 e−01	9.263898577 e−01	1.964319996 e+01
|−step	4.61618544000 e−01	9.316649092 e−01	1.954360203 e+01
|−step	3.72014477900 e−01	9.360452237 e−01	1.941729579 e+01
|−step	6.40817203300 e−01	9.397475699 e−01	1.931408822 e+01
|−step	1.91924358900 e−01	9.422203163 e−01	1.925041108 e+01
|−step	1.86279218600 e−01	9.441378768 e−01	1.920272774 e+01
∗Compton	5.73381906500 e−01	9.539757657 e−01	1.948346534 e+01
−>e−	1.61188100300 e−01	9.539757657 e−01	1.948346534 e+01
∗Compton	4.12193806200 e−01	1.034231071 e+00	2.145125437 e+01
−>e−	5.79735126300 e−02	1.034231071 e+00	2.145125437 e+01
∗Compton	3.54220293600 e−01	1.122923115 e+00	2.256353592 e+01
−>e−	1.10342679600 e−01	1.122923115 e+00	2.256353592 e+01
−>p	1.80576864000 e+00	2.406580743 e−01	1.454112416 e+00
|−step	1.80576864000 e+00	2.441490229 e−01	1.456045267 e+00
−>3007	8.76983895000 e+00	2.396900352 e−01	1.453660049 e+00
|−step	8.76983895000 e+00	2.405904497 e−01	1.454209451 e+00
|−recoil	3.64007707700 e+00	2.396900352 e−01	1.453660049 e+00
∗multig	1.92e+01_1.96 e+01	4.332574626 e−01	2.583124903 e+00
|−recoil	3.57532332400 e+00	4.332574626 e−01	2.583124903 e+00
∗multig	8.39e+00_8.61 e+00	2.335985032 e+00	9.579404378 e+00
|−recoil	1.93476781700 e+00	2.335985032 e+00	9.579404378 e+00
∗multig	8.19e+00_8.39 e+00	2.566380818 e+00	1.043058092 e+01
−>g	4.77610000000 e−01	2.566380818 e+00	1.043058092 e+01
∗Compton	4.77610000000 e−01	2.705250677 e+00	7.496920262 e+00
−>e−	2.03933671000 e−01	2.705250677 e+00	7.496920262 e+00
−>2004	7.93477174700 e+00	2.566380818 e+00	1.043058092 e+01
|−step	7.93477174700 e+00	2.570277887 e+00	1.043239819 e+01
−>3007	3.14540634600 e+00	2.566380818 e+00	1.043058092 e+01
|−step	3.14540634600 e+00	2.566780987 e+00	1.043058384 e+01
|−recoil	1.88226392500 e+00	2.566380818 e+00	1.043058092 e+01

Listing 1: Sample cascade from a slowing-down neutron in FLUKA. Time and distance are given with respect to source origin. The energy column shows 1) the kinetic energy at collision (arrows) or production (stars); 2) the kinetic energy range when multigroup (multig) treatment is in effect; 3) energy deposition for steps and recoils. Ions are represented in ZA notation. Indents denote the nth particle generation.

Fig. 1 shows the minimum cross section for different materials and reaction types. Data have been extracted from ENDF/B.VII.1 and JENDL-4.0. This is of particular interest given that PREPRO takes as input parameter a threshold in barns, below which cross sections would be copied verbatim. The default threshold is 1×10^{-10} barns, whereas the minimum cross sections do go well below this value (Fig. 1).

Fig. 2 shows the $(n, n'\alpha)$ cross section for ^{94}Nb after linearization and resonance reconstruction by NJOY and PREPRO. In this case it is easy to recognize which is correct. Plotted on a log-linear scale, with the ENDF file clearly specifying the interpolation scheme as log-linear, lines joining adjacent points should be straight. The disagreement at low energies is due to the above-mentioned threshold in PREPRO input. Lowering the threshold would solve the problem. The author of PREPRO, however, maintains that the threshold should be kept at 1×10^{-10} barns to avoid potential problems in the presence of resonance.

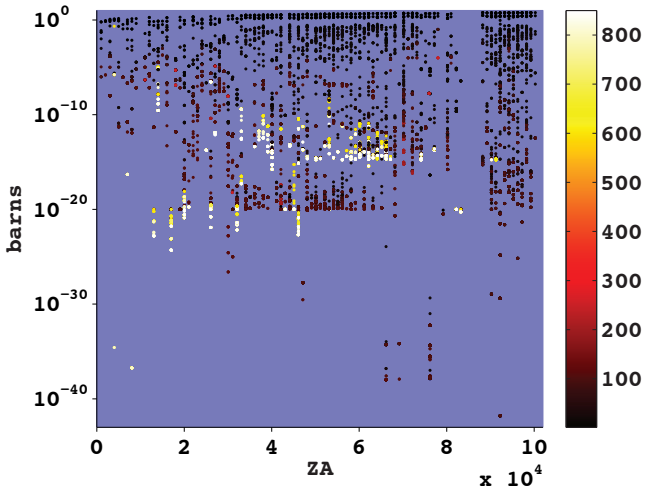

Fig. 1: The minimum cross section for various ZA available from the incident-neutron sub-library of ENDF/B-VII.1 and JENDL-4.0. Colour scales from low MT (dark) to high MT (bright).

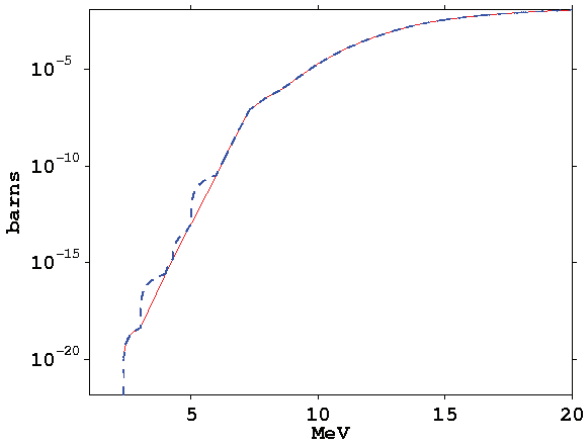

Fig. 2: Cross section after linearization and resonance reconstruction using PREPRO with default settings (dashed line) and NJOY (full line): Nb-94 MT=22.

Whereas either PREPRO or NJOY could have accomplished the task, we used both, as a tangential quality assurance exercise to spot vulnerabilities requiring attention. The amount of data calls for a balance between automation and human intervention, to address the risk of missing details (due to over-automation) and making mistakes (due to unnecessarily manual handling).

3 Angular distribution of neutron elastic scattering

Angular distribution (MF=4) of elastic scattering (MT=2) may be represented in several forms: 1) a flag indicating purely isotropic distributions, LTT=0, LI=1; 2) Legendre expansion coefficients, LTT=1;

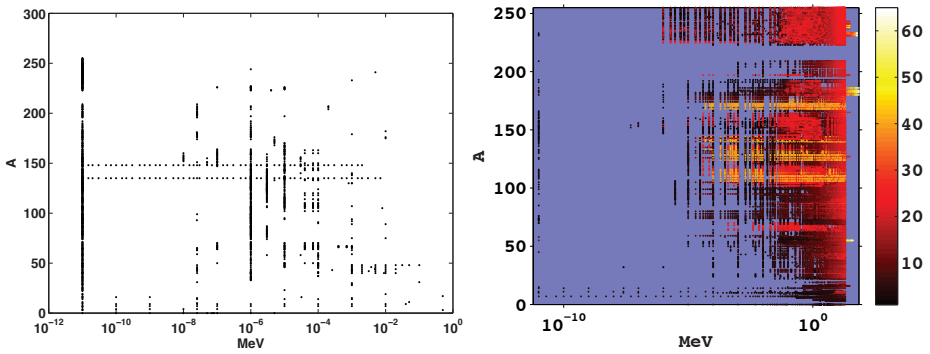

Fig. 3: A-E combinations where MF=4 MT=2 distribution are given as isotropic (left), or in Legendre representation (right) in ENDF/B-VII.1 and JENDL-4.0. Colour scales from low (dark) to high (bright) Legendre orders.

3) tabulated probabilities, LTT=2. Data storage demands understandably increases in this order. An additional factor is data availability. For instance, 74 materials were given as purely isotropic in JEFF-3.1.1 (2009), whereas no parallels could be found in the more recently released JENDL-4.0 and ENDF/B-VII.1. This does not necessarily negate the use of JEFF-3.1.1, since it contains materials and/or energy ranges still absent in the latter two libraries.

Fig. 3 summarizes the mass-energy (A-E) combinations where angular distribution is given as isotropic and that given in Legendre representation. Note that interpolation does not apply; the absence of a point indicates the absence of data rather than the continuity of data.

The first Legendre coefficient is of special interest because it allows the calculation of average energy loss. Its bi-variate A-E variation (Fig. 4) suggests trends of parameterization potential. Univariate plots (Fig. 5) suggest a straight-forward sigmoid dependence in the form of

$$Y = a + \frac{b}{1 + e^{-\frac{X+c}{d}}} \tag{1}$$

with the energy scale in logarithmic form. The A-dependence, however, merits a closer scrutiny (Fig. 6). The A-dependence at different energies exhibits common peaks and valleys at A around 53, 85, 143 and 209. It is therefore foreseeable that the Legendre coefficients may be further condensed as parameterized functions of A and E.

References

[1] A. Ferrari, P. Sala, A. Fassò, and J. Ranft, "FLUKA: a Multi-Particle Transport Code," Tech. Rep. CERN-2005-10, INFN/TC_05/11, SLAC-R-773, CERN, INFN, SLAC, 2005.

[2] G. Battistoni, S. Muraro, P. Sala, F. Cerutti, A. Ferrari, S. Rősler, A. Fassò, and J. Ranft, "Proceedings of the Hadronic Shower Simulation Workshop 2006, Fermilab 6–8 September 2006," vol. 896, pp. 31–49, AIP Conference Proceedings, 2007.

[3] M. Herman and A. Trikov, "ENDF-6 Formats Manual," Tech. Rep. Doc ENDF-102, BNL-XXXXX-2009, Brookhaven National Laboratory, 2009.

[4] D. E. Cullen, "PREPRO 2010," Tech. Rep. IAEA-NDS-39, IAEA, 2010.

[5] R. E. MacFarlane and A. C. Kahler, "Methods for Processing ENDF/B-VII with NJOY," *Nuclear Data Sheets*, vol. 111, pp. 2739–2889, DEC 2010.

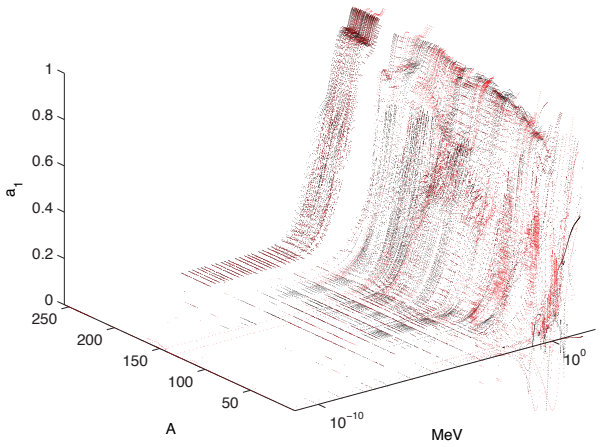

Fig. 4: The first Legendre coefficient given for MF=4 MT=2 by ENDF/B-VII.1 (red) and JENDL-4.0 (blue) as a function of A and E.

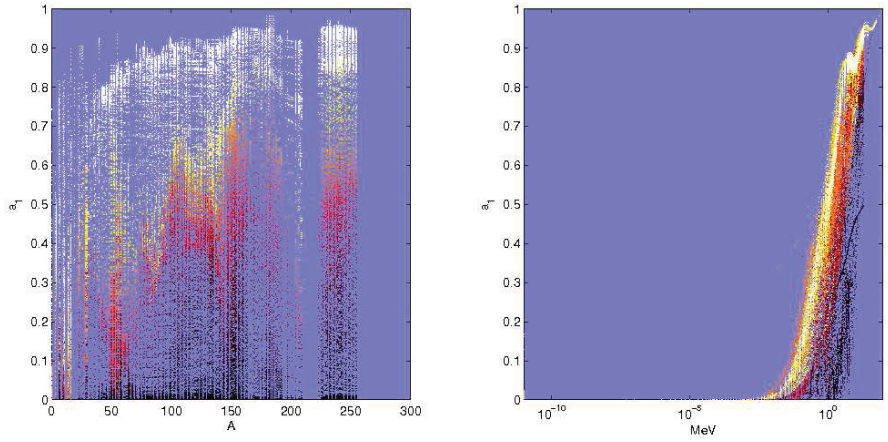

Fig. 5: The first Legendre coefficient given for MF=4 MT=2 by ENDF/B-VII.1 and JENDL-4.0. Left: variation with A, colour scales from low energy (dark) to high energy (bright). Right: variation with E, colour scales from low A (dark) to high A (bright).

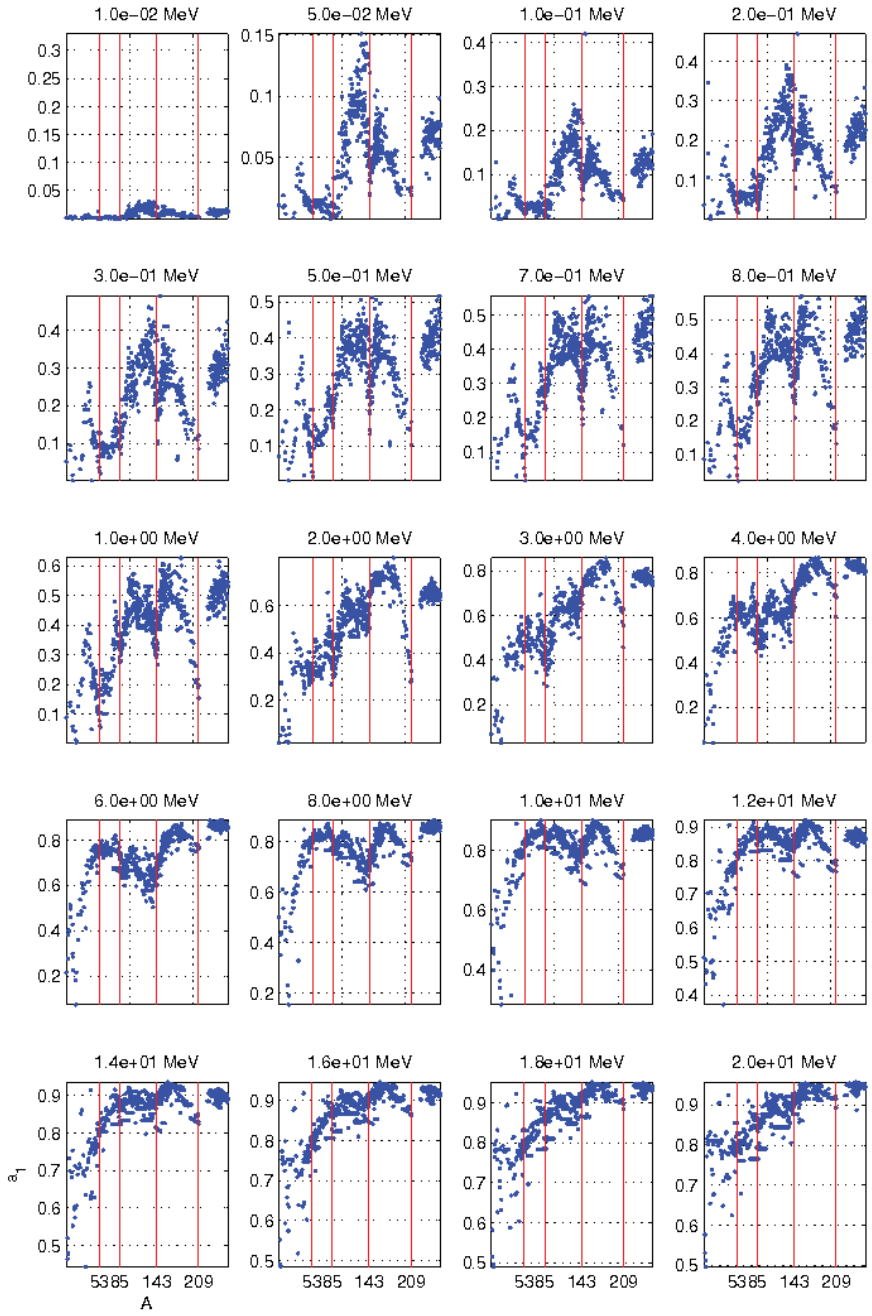

Fig. 6: Variation of the first Legendre coefficient with A, plotted at selected energies between 10 keV and 20 MeV. All subplots have been overlayed with lines A=53, 85, 143 and 209.

Outlook and perspectives for the n_TOF Experiment at CERN

E. Chiaveri
Spokesperson of n_TOF Collaboration

Abstract
The outstanding features of the existing CERN n_TOF neutron beam are the very high instantaneous neutron flux, excellent TOF resolution, low intrinsic backgrounds and coverage of a wide range of neutron energies, from thermal to a few GeV. These characteristics provide a unique possibility to perform neutron-induced cross-section and angular distribution measurements for applications in nuclear astrophysics, nuclear reactor technology and basic nuclear physics. A wide variety of measurements have already been performed since the facility became operational in 2001 and made available to the nuclear data and nuclear physics community. The most relevant measurements of the period 2009/2011 will be presented in this contribution. The overall efficiency of the experimental program and the range of possible measurements achievable with the construction of a second experimental area (EAR-2), vertically located 20 m on top of the n_TOF spallation target, might offer a substantial improvement in measurement sensitivities. Few selected aspects of the study for the realisation of the installation upgrade will be also presented.

1 Introduction

High precision neutron cross-section data are of major importance for a wide variety of research fields in basic and applied nuclear physics [1]. In particular, neutron data on neutron-nucleus reactions are essential in Nuclear Astrophysics for understanding the production rate of heavy elements in the Universe, which occurs mainly through slow and rapid neutron capture processes during the various phases of stellar evolution [2,3]. In the field of nuclear technology new studies aimed at developing future generation nuclear system which would address major safety, proliferation and waste concerns are requiring more accurate data in neutron-induced fission and capture cross-section on radioactive isotopes. Based on these motivations the neutron time-of-flight facility n_TOF has been constructed at CERN, Geneva in 2001 and operated since then.

2 n_TOF Facility

The idea of a new neutron time-of-flight facility at CERN was proposed by C. Rubbia in 1998 [4], as a follow up of the TARC experiment, also conducted at CERN in the previous years.

The concept of the n_TOF neutron beam [5] makes use of both the specifically high flux of neutrons attainable using the spallation process of 20 GeV/c protons on a massive lead target, able to contain practically the whole spallation shower, thanks to the remarkable beam density of the CERN Proton Synchrotron (PS) [6]. After the initial proposal, in a short amount of time the facility was accepted for construction by CERN. The CERN n_TOF facility has been set in operation and commissioned in 2001 with performances matching the expectations. The PS machine of CERN can generate high intensities up to 8.5×10^{12} ppp (protons per pulse) - high enough to produce the vast number of 2×10^{15} neutrons per pulse - in the form of short (6 ns 1σ width) pulses with a repetition

time varying from 1.2 s to 16.7 s and a prompt "flash" considerably smaller compared to electron machines based on the bremsstrahlung process. The high neutron flux, the low repetition rates and the excellent energy resolution of 5.5x10-4 (at 1keV) have opened new possibilities for high precision cross section measurements in the energy range from thermal to GeV, for stable and, in particular, for radioactive targets (see Fig.1).

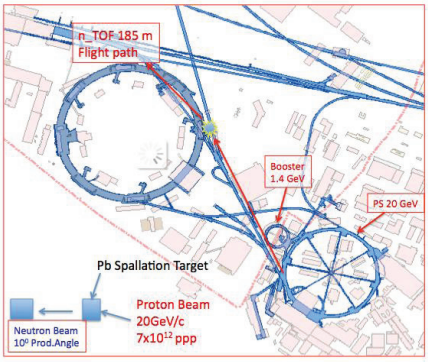

Main features of the n_TOF:

- Proton **intensity** $8x10^{12}$ *p/pulse*
- Proton beam **momentum** *20 GeV/c*
- Proton **pulse width** *6 ns (rms)*
- high **instantaneous n flux** 10^{5} *n/cm*^{2} */pulse*
- wide energy **spectrum** $25\ meV<E_n<1GeV$
- low **repetition** rate *< 0.8 Hz*
- good energy **resolution** $\Delta E/E = 10^{-4}$

Fig.1: The figure show the configuration of the installation as well as the main parameters of the installation.

3 Upgrade of the Facility: Class A and Borated Water

After the new target commissioning phase, which started in November 2008 and continued during mid-2009, two other significant upgrades have been implemented in the last 3 years.

The first is the implementation of a different moderator material other than light water. In particular, the program has envisaged the use of water enriched in ^{10}B, which has greatly enhanced the measuring capabilities of neutron-induced capture cross-section, by reducing significantly the presence of the in-beam photon component, and in particular the 2.2 MeV γ-rays, produced by neutron capture in hydrogen. Since this photon contribution is delayed, i.e. emitted after about 1 microsecond from the proton interaction (due to the fact that it is produced by thermalized neutrons), it would results in a background component in the 1-100 keV neutron energy range, which is problematic for capture reaction measurements performed with C_6D_6 detectors. The conceived system has reduced the 2.2 MeV photon components by a factor of about 10, leaving the neutron fluence unchanged above 1 eV.

Another upgrade performed during the 2010 run has been the transformation of the n_TOF experimental area into a Work Sector Type A, which has allowed the possibility to perform measurements of capture and fission cross-section of "unsealed" samples of highly radioactive isotopes, such as actinides like ^{241}Am, ^{243}Am and $^{240-2}Pu$, taking full advantage of the facility's high instantaneous neutron flux. This has required a complete revision of the experimental area and of the related technical services. The milestone of n_TOF facility is summed-up on Fig. 2

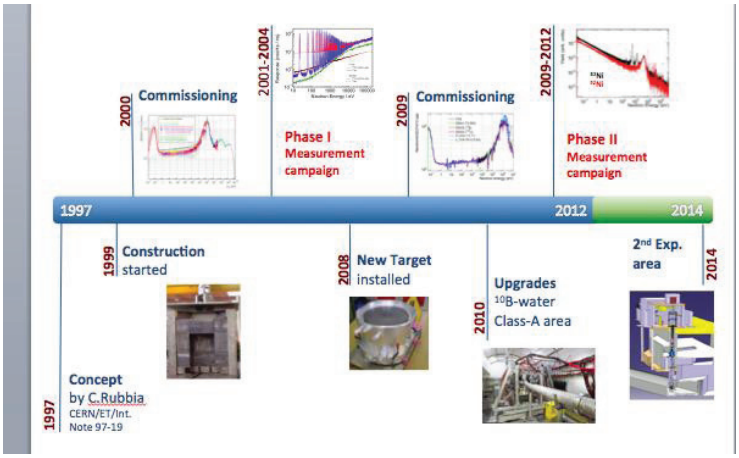

Fig.2: The figure shows the timeline of the n_TOF installation, from its conception to the foreseen major upgrades in 2014 ending with the construction of a new experimental area.

4 Experimental Campaign 2009/2011

During the years of operation 2009-2011 the n_TOF Collaboration has attained a rich experimental program measuring in total 19 isotopes, as highlighted in Figure3.

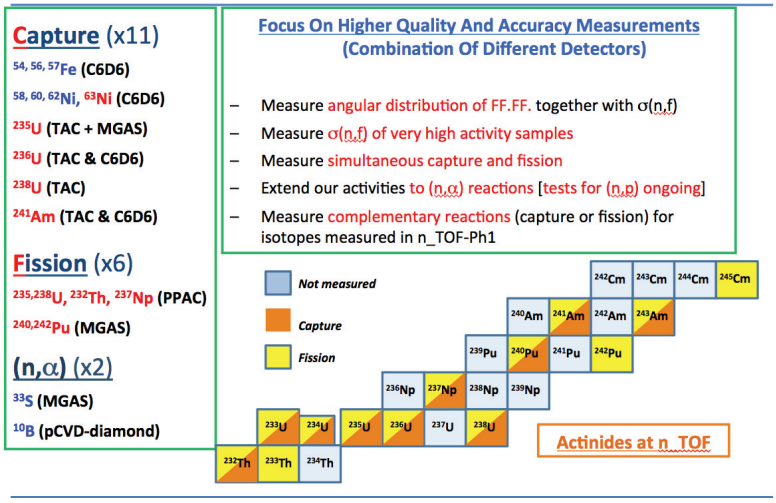

Fig.3: The figure shows the list of isotopes measured between 2009 and 2011 at n_TOF, together with the physics objectives associated with them.

5 Measurements Performance

Out of all the neutron induced cross sections that play a role in nuclear technology applications, those for which improvement is considered of utmost importance are included in the High Priority Request List [7] of the International Atomic Energy Agency IAEA. This list is continuously updated by the Nuclear Energy Agency (NEA).

Half of the capture cross section measurements included in this list (^{nat}Hf, ^{233,235,238}U, ^{239,241,242}Pu, ^{241}Am) are on fissile isotopes; some of these are very difficult to measure due to the fact that γ-rays generated in fission reactions may constitute a very large background when measuring γ-rays emitted in neutron capture reactions.

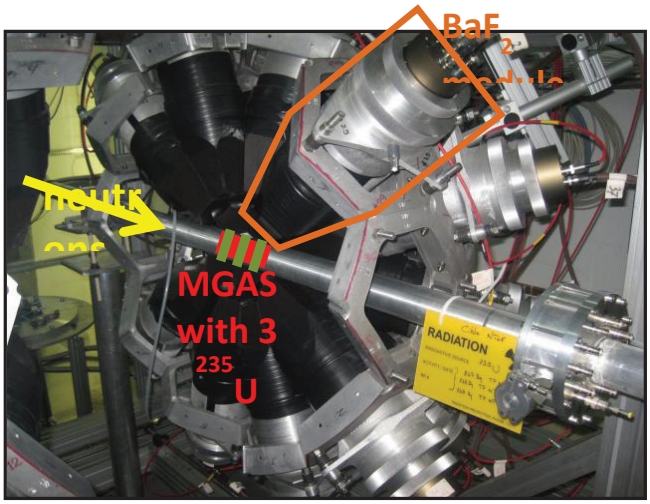

Fig.4: The photo shows one hemisphere of the 4π Total Absorption Calorimeter (TAC) and the long gas chamber inserted along its axis.

The measurement of capture cross sections of fissile isotopes is of utmost importance in the field of nuclear technology but it poses a challenge from the experimental point of view: the γ-ray background emitted in fission reactions complicates the measurement of weaker γ-signals associated with (n,γ) reactions. We have built and tested a new set-up at the CERN n_TOF facility that allowed us to measure simultaneously neutron-induced fission and capture reactions by combining a 4π Total Absorption Calorimeter (TAC) with several MicroMegas (MGAS) detectors loaded with a total of 3 mg of ^{235}U.(Fig. 4)

A detailed analysis of the measured data including the optimization of the coincidence algorithm and the determination of the several detection efficiencies involved in the process has confirmed the successful and unambiguous identification of capture and fission events. The analysis of the extracted capture and fission cross sections shows that the results are in good agreement with the ENDF/B-VII.0 evaluation in the energy region under study (6-22 eV).

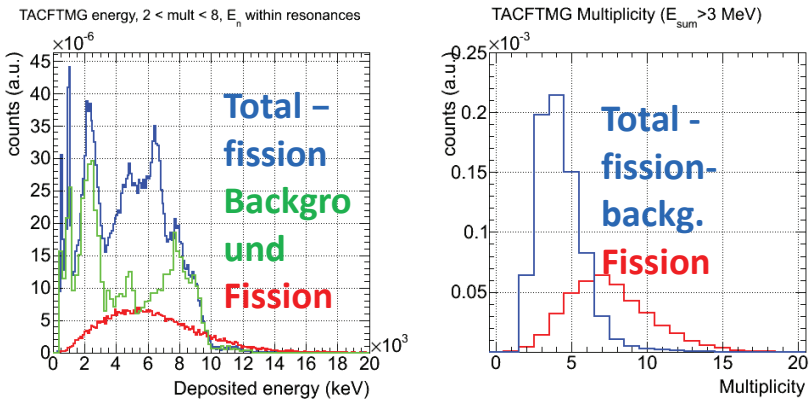

Fig.5: The figures show the distribution of deposited energy corresponding to fission captures and background.

In view of the present results, (Fig.5) a new experimental campaign is envisaged at n_TOF for measuring capture cross sections of fissile isotopes such as ^{233,235}U, ^{239,241}Pu and ^{245}Cm, always considering the very limited availability of suitable samples. The first measurement using 30 mg of ^{235}U is scheduled for 2012 [8].

Another important measurement during the present campaign was the 63Ni(n,γ) cross section.

Is the first time that such a measurement has been done at the neutron time-of- flight facility n_TOF from thermal neutron energies up to 200 keV. In total 16 resonances could be identified and capture kernels have been determined for 14 of these resonances. Maxwellian averaged cross sections were calculated for thermal energies from kT = 5 keV to 90 keV with uncertainties around 20%. Stellar model calculations for a 25 M⊙ star show that the new data have a significant effect on the s-process production of ^{63}Cu, ^{64}Ni, and ^{64}Zn in massive stars.

Up to now the stellar cross section of ^{63}Ni(n,γ)^{64}Ni relied on calculations or extrapolations of experimental values at thermal neutron energies (0.025 eV).Theoretical predictions for the Maxwellian Averaged Cross Section (MACS) at kT = 30 keV are ranging from 24 to 54 mb. The currently recommended value quoted by the compilation KADoNiS is 31 ± 6 mb. Because such calculations are vulnerable to large systematic uncertainties, measurements have been attempted at Los Alamos National Laboratory and at CERN.

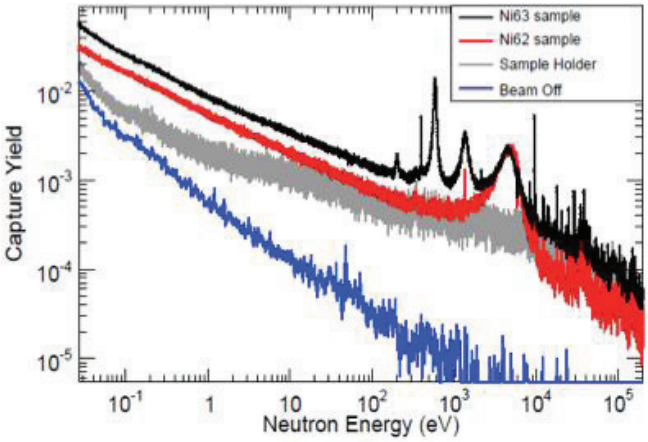

Fig.6: Capture yield of the 63Ni sample (black) compared to the empty sample holder and to the spectrum obtained with a pure 62Ni sample.

The energy-dependent ^{63}Ni(n,γ) cross section has been measured at the n TOF facility providing the first experimental results for MACSs at stellar neutron energies (Fig.6). The MACSs ranging from kT = 5 to 90 keV exhibit total uncertainties of ≈ 20 − 22% and are about a factor of 2 higher than the theoretical prediction of the KADoNiS compilation. Our results improve one of the main nuclear uncertainties affecting theoretical predictions for the abundances of ^{63}Cu, ^{64}Ni and ^{64}Zn in s-process rich ejects of core collapse supernovae. Furthermore, these results are a fundamental step to constrain the contribution from explosive nucleosynthesis to these species [9]

6 Experimental Area 2 project

The overall efficiency of the experimental program and the range of possible measurements could be significantly improved with the construction of a 2nd Experimental Area (EAR2), vertically located 20 m on top of the n_TOF spallation target (see Fig.7) [10]

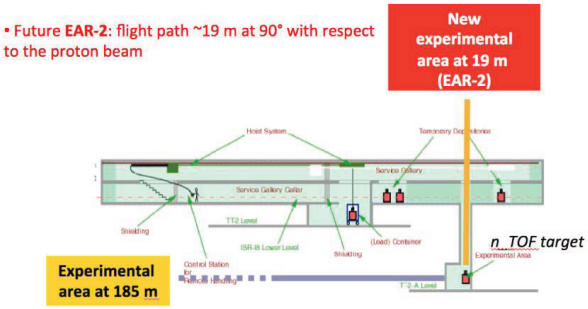

Fig.7: Schematic view of the EAR1 and of the proposed EAR2

Being closer to the spallation target (flight path of 20 m) the configuration provides a higher instantaneous neutron flux with respect to the present neutron fluence in EAR1 (flight path of 185m from the spallation target); this is a clear advantage for the measurement of reactions on samples with very small masses or reactions with very small cross sections. The reduced energy resolution important for resolved resonances due to the smaller distance does not affect the measurements at high neutron energies (see Fig. 8).

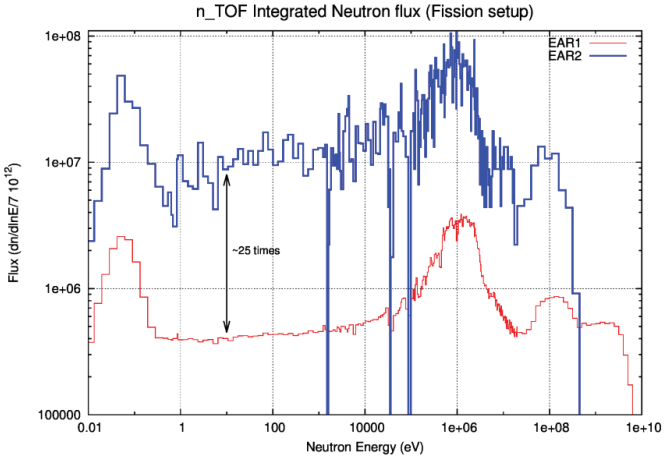

Fig.8: Comparison between the neutron fluence of the proposed EAR2 and the existing EAR1. The significant absorption dips in the EAR2 fluence are due to the large amount of structural Al between the spallation target and the vertical vacuum tube leading to EAR2.

The realization of the 2nd Experimental Area, with its short flight path, will contribute to a substantial improvement in experimental sensitivities and will open a new window to stellar nucleosynthesis, technological issues (such as transmutation or design of safety of future nuclear energy systems) and basic nuclear physics by allowing to measure neutron-induced reactions which are not accessible so far at any other installation. The main advantages will be:

Neutron-induced reaction measurements can be performed on very small mass samples. This feature is crucial to reduce the activity of unstable samples and in cases where the available sample material is limited.(ex. ^{238}Pu, ^{241}Pu ^{243}Cm, ^{244}Cm, ^{245}Cm, ^{242}mAm, ^{231}Pa, ^{233}Pa)

Measurement can be performed on isotopes with very small cross sections for which the optimization of the signal/background ratio is an essential prerequisite (ex. ^{86}Kr, ^{138}Ba, ^{140}Ce, ^{208}Pb)

Measurement can be performed on much shorter time scales. Repeated runs with modified conditions are essential to check corrections and to reduce systematic uncertainties.

Measurements of neutron-induced cross sections at high energies (E_n>10-100 MeV), which are not possible in the existing EAR1, will benefit from largely reduced the γ-flash. This will be particularly important for measurements of (n, charged particle) reactions at high energies because Si and Ge detectors are most strongly affected by the γ-flash.

7 Conclusion

There is need of accurate new data on neutron cross-section both for astrophysics and advanced nuclear technology. CERN n_TOF has proven to be a unique facility in the world for its performance. Since 2001, n_TOF has provided an important contribution to the field, with an intense activity on capture and fission measurements. The transformation of the Experimental Area into Work Sector of Type A has allowed performing measurement of capture and fission cross section of "unsealed" samples of highly radioactive isotopes. With the construction of the Experimental Area 2, the n_TOF installation is going to open new perspectives in the measurements of fission and capture cross-section with lower samples masses.

References

[1] E.Chiaveri et al. Past,Present and future of the n_TOF facility, Journal of the Korean Physical Society, Vol. 59, No. 2, August 2011, pp. 1620_1623
[2] F.Kaeppeler, Progr.Particles Nucl. Phys. 43(1999) 439
[3] G.Wallestein et al. Rev.Mod.Phys. 69(1997) 995
[4] C.Rubbia et al., A high Resolution Spallation Driven Facility at the CERN-PS to measure Neutron Cross Sections in the Interval from 1eV to 250MeV, CERN/LHC/98-02(EET)+Add1
[5] S. Abramovich et al.(the n_TOF Collaboration) European Collaboration for High Resolution Measurements of Neutron Cross Sections between 1eV and 250MeV,CERN/SPSC 99-8,1999
[6] R.Billinge, The CERN PS Complex: A multipurpose Particle Source, Proc.Of XIIth Int. Conf. on High Energy Acc., 1983
[7] NEA Nuclear Data High Priority Rquest List, http://www.nea.fr/dbdata/hprl/index.html
[8] Eur. Phys. J.A. (2012) 48:29
[9] to be submitted to Phys. Rev. Letter
[10] E.Chiaveri and the n_TOF Collaboration, Proposal for n_TOF Experimental Area 2, CERN-INTC-2012-029, INTC-O-015 (2012)

Recent results with the magnetic spectrometer PRISMA

E. Fioretto[1], *L. Corradi*[1], *S. Szilner*[2], *D. Montanari*[3], *C. Michelagnoli*[3], *T. Mijatović*[2], *G. Montagnoli*[3], *F. Scarlassara*[3], *A.M. Stefanini*[1], *C.A. Ur*[3], *G. Pollarolo*[4], *N. Soić*[2] *and the PRISMA and CLARA collaborations*
[1]INFN - Laboratori Nazionali di Legnaro, Viale dell'Università 2, Legnaro (PD), I-35020, Italy
[2]Ruđer Bošković Institute, Bijenička 54, Zagreb, HR-10001, Croatia
[3]Dipartimento di Fisica dell'Università di Padova and INFN, Via Marzolo 8, Padova, I-35131, Italy
[4]Dipartimento di Fisica Teorica dell'Università di Torino and INFN, Via P. Giuria 1, Torino, I-10125, Italy

Abstract
Large acceptance magnetic spectrometers have come into operation in the last decade, such as PRISMA installed at Laboratori Nazionali di Legnaro, and have given a further boost to the renewed interest for multinucleon transfer reactions. The large solid angles of these devices and the high resolving powers of their detection systems allowed to investigate the transfer process around and well below the Coulomb barrier and to perform nuclear structure studies in several mass regions of the nuclide chart when coupled with large γ-ray arrays such as CLARA or the AGATA Demonstrator. Recent results of reaction dynamics and nuclear structure obtained with PRISMA and PRISMA-CLARA as well as a new ancillary detector for the spectrometer will be presented in this paper.

1 Introduction

The renewed interest in the last decade for multinucleon transfer reactions, mainly due to the realization that this process could be used to populate nuclei moderately rich in neutrons, benefited from the construction of the new generation tracking spectrometers, based on the trajectory reconstruction, and the use of the state-of-art large area particle detectors.

PRISMA [1, 2, 3] is the large acceptance magnetic spectrometer designed to be used with heavy-ion beams accelerated at energies up to E = 10*A* MeV by means of the Tandem/PIAVE-ALPI accelerator complex of Laboratori Nazionali di Legnaro. It can operate as a standalone device or coupled to large γ-ray arrays such as the CLARA [4] set-up until March 2008 or the AGATA Demonstrator [5] until the end of December 2011. Its coupling with the CLARA array allowed to make in-beam γ-spectroscopy of moderately neutron-rich nuclei populated by multinucleon transfer reactions through the identification of individual excited states and their population pattern. The experimental campaign of the PRISMA-CLARA set-up started in 2004 and has been completed at the end of March 2008 making use of about 50% of the total beam-time available at the Tandem/PIAVE-ALPI accelerator complex of LNL. Experiments performed with PRISMA and PRISMA-CLARA were mainly addressed to obtain information on the nucleon-nucleon correlation and the connection between multinucleon transfer process and other competing reaction channels, on the shell evolution and the onset of new regions of deformation (collectivity, critical point symmetries) in medium-mass moderately neutron-rich nuclei.

Selected results obtained with the PRISMA and PRISMA-CLARA set-ups in sub-barrier transfer measurements and in odd argon isotopes populated by using the multinucleon transfer process are presented in this contribution. Moreover, the status of an ancillary detector which is being developed for PRISMA in order to perform kinematical coincidence measurements is also reported.

2 Sub-barrier transfer measurements

Multinucleon transfer in heavy ion reactions is a mechanism ranging from the quasi-elastic regime (i.e. few nucleon transfer and low total kinetic energy loss (TKEL)) to the deep-inelastic collisions (i.e. many nucleon transfer and large TKEL) which takes into account the largest fraction of the total reaction cross section at energies close to the Coulomb barrier [6]. In the sub-barrier region nuclei enter into contact through the tail of their density distributions and nucleon transfer processes take place between levels close to the Fermi surfaces of the donor and acceptor. At such large distances between the centres of the interacting nuclei the reaction mechanism conditions are much simplified compared to those near the strong absorption radius. Nuclei are only slightly influenced by the nuclear potential and follow almost pure Coulomb trajectories. Excitation energies are restricted to few MeV and uncertainties in calculations associated with optical potentials can be minimized. These peculiar conditions should in principle allow to extract more quantitative information on the mechanism of multiple transfer processes, for example on the relative contribution of single particle and more complex degrees of freedom which include nucleon-nucleon correlations. However, available data for heavy ion transfer reactions in the sub-barrier region are extremely scarce or almost not existing due to the significant experimental difficulties of this kind of measurements (such as the strongly backward peaked angular distributions, the low kinetic energy for the backscattered projectile like fragments and the low cross sections). A suitable way to overcome these limitations is to make use of inverse kinematics detecting the lighter targetlike fragments with magnetic spectrometers at very forward angles [7, 8]. The coming into operation of large solid angle spectrometers has renewed the interest for the study of the transfer process in the sub-barrier region where a high efficiency is required.

In this framework we measured with the spectrometer PRISMA the excitation functions for the neutron transfer channels populated in the inverse kinematics ^{96}Zr+^{40}Ca reaction [9] from the Coulomb barrier (330 MeV) to ~ 25% below (275 MeV). Projectile and target are closed or near-closed shell nuclei for both neutrons and protons, thus representing a good reference for a quantitative comparison with theoretical calculations. This experimental and theoretical environment provides very suitable conditions for a proper study of the mechanism of multiple transfer processes. The ^{96}Zr beam was accelerated by the Tandem-ALPI accelerator complex of LNL onto a 50 μg/cm^2 $^{40}CaF_2$ target supported on a 15 μg/cm^2 C backing. Mass spectra of the targetlike fragments, measured with magnetic spectrometer PRISMA placed at 20°, have evidenced the population of more than four neutron pick-up channels at energies close to the Coulomb barrier while at sub-barrier energies only one or at most two neutron transfers survive. Making use of semiclassical conditions, one can extract the transfer probability P_{tr} as a function of the distance of closest approach D, with P_{tr} defined as the ratio of transfer cross sections to the Rutherford one. This representation is significant only if semiclassical conditions are fulfilled and one deals with (almost) pure Coulomb trajectories. The case studied here well fulfils these requirements, with the further advantage that the Q-value distributions at the measured sub-barrier energies are quite narrow and corresponding to few MeV of excitation energy. At large ion-ion separation the radial behaviour of the form factor is governed by the exponential form of the bound-state wave function and the transfer probability is approximated by:

$$P_{tr}(\theta) \cong e^{-2\alpha D(\theta)} \tag{1}$$

where the parameter α is related to the binding energy E_b of the transferred nucleon, $\alpha = (2mE_b)^{1/2}/\hbar$, and $D(\theta)$ is the distance of closest approach. The excitation functions of transfer processes as a function of the distance of closest approach D are thus represented (in a semi-logarithmic plot) by straight lines with a slope $-\alpha$. Such behaviour is independent of the way in which transfer proceeds, as a successive process or as a simultaneous transfer. Contradictory results have been obtained in previous experiments around the Coulomb barrier, where slopes smaller than predicted were found [8], and at lower energies where no anomaly in the slope behaviour has been clearly identified [10]. Figure 1 displays the transfer probabilities extracted from the yields of the +1n (full circles), +2n

(empty circles) and +3*n* (full triangles) transfer channels as a function of the distance of closest approach *D*, together with the solid lines which are the results of the fitting procedure. Data for the +4*n* channel (empty triangles) are available only at the highest energies, therefore a reliable fit could not be performed. The extracted experimental slopes agree well with those expected by the binding energies. Given the correct behaviour of P_{tr} and keeping in mind the simplified assumptions mentioned before, we can make a phenomenological analysis which compares the probabilities for transfer channels with those expected from an independent particle transfer mechanism. It turns out that $P_{2n} = 3(P_{1n})^2$ and $P_{3n} = 3(P_{1n})^3$.

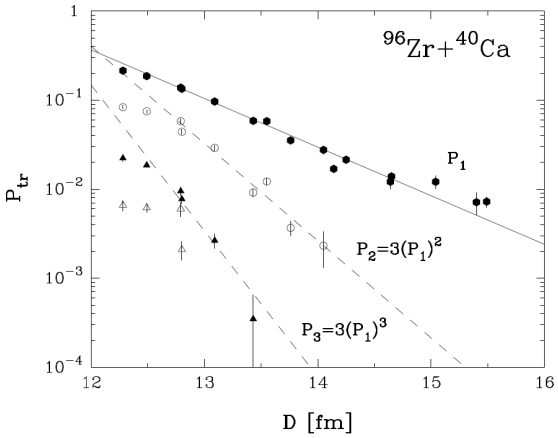

Fig. 1: Extracted transfer probabilities P_{tr} as function of the distance of closest approach *D* for neutron transfer channels

The two-neutron transfer channel has been analyzed with a semiclassical model that calculated, in the successive approximation, transitions to 0^+ states. Figure 2 shows the results of these calculations where the full line represents the inclusive transfer probability for one neutron transfer, the dotted line the ground state to ground state transition for the two-neutron transfer and the dashed line the transition to the first 0^+ excited state at 5.76 MeV in ^{42}Ca. It appears that the transfer probability for the transition to the excited 0^+ state in ^{42}Ca is much larger than the ground state one. But, by considering only 0^+ transitions the experimental cross section is underestimated by a factor of ~3. This

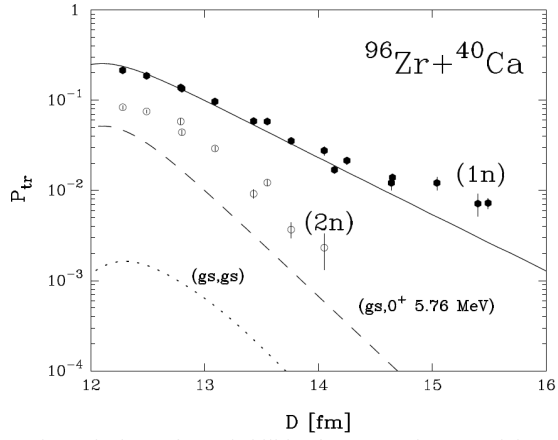

Fig. 2: Theoretical transfer probabilities for one- and two-particle transfer (lines) in comparison with the experimental data (points)

enhancement is ascribed to transitions to states with large angular momentum and to transitions of non-natural character, indicating that more complex two-particle correlations have to be considered in the transfer process.

In experimental conditions similar to those already successfully exploited in the ^{96}Zr+^{40}Ca case, as a further step we investigated the ^{116}Sn+^{60}Ni system whose ground to ground state Q-values are close to zero for neutron transfers, matching their optimum Q-value (~ 0 MeV). In particular, we measured the excitation functions in steps of 5 MeV from the Coulomb barrier (500 MeV) down to about 25% below (420 MeV) for the transfer channels populated in the inverse kinematics reaction. For this system one expects to have a main population close to the ground to ground state transitions and, in particular for the +2n channel, it is interesting to see how calculations including only transfer to the 0^+_{gs} states compare with the experimental data. The ^{116}Sn beam was delivered by the PIAVE injector and the ALPI superconducting booster with an average current of ~2 pnA onto a 100 μg/cm^2 ^{60}Ni target with a 15 μg/cm^2 C-backing. Ni-like recoils have been detected by PRISMA at θ_{lab}=20°, corresponding to $\theta_{c.m.}\simeq$140° and transfer yields have been measured down to ~ 16 fm of distance of closest approach. Figure 3 shows the Total Kinetic Energy Loss (TKEL) spectra for the elastic and one (+1n) and two (+2n) neutron pick-up channels at the representative bombarding energy of E_{lab} = 475 MeV, close to the Coulomb barrier. The elastic (+inelastic) peak has a width of ~ 3 MeV close to the expected energy resolution. The position of the Q-value for the elastic scattering (Q_{gs}=0) is marked with vertical dashed lines for the different channels in the figure. For neutron transfers (Q^{+1n}_{gs} = −1.7 MeV and Q^{+2n}_{gs} = +1.3 MeV) one observes a significant population close to these (ground to ground state) Q-values. At the same time one sees a tail toward larger TKEL, more marked for the +2n channel, typical of the energy regime close to the barrier. These energy loss components tend to disappear far below the barrier.

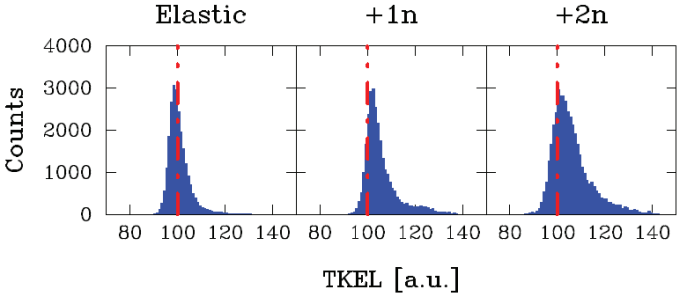

Fig. 3: TKEL loss spectra for the elastic and +1n, +2n transfer channels at the bombarding energy E_{beam} = 475 MeV. See text for details.

At present stage the data are being analyzed in the whole measured energy range, with the main aim to extract the transfer cross sections for the one and two neutron pick-up channels and for channels involving proton stripping. Proton stripping channels are in general more difficult to get experimentally far below the barrier since they drop off more rapidly than neutron channels, therefore a careful evaluation of the angular distribution (and transmission of the spectrometer) is mandatory. The −1p channel, together with the +1n channel, is one of basic building blocks defining the more complex multiple particle transfer and the comparison of its behaviour as a function of the bombarding energy with the microscopic calculations will tell about the shape of the form factors [11]. Part of the excitation functions for transfer channels have been measured with sufficient statistics to allow making cuts in the angular acceptance of PRISMA. In this way differential cross sections may be extracted for different angles at each energy, thus increasing significantly the number of points which define the transfer probability as a function of the distance of closest approach. Thus, a careful evaluation of the PRISMA response function is being studied via a Montecarlo simulation to assess

the influence of the transport of the ions through the spectrometer on the measured yields. A successful application of these studies has been employed in the ^{48}Ca+^{64}Ni system [12, 13] where experimental angular distributions for elastic as well as for transfer channels, have been corrected for the response of the spectrometer. Such corrections involved a case where measurements have been performed at energies much higher than the Coulomb barrier and where deep-inelastic components contribute significantly to the yields. In the case of sub-barrier energies the Q-values are quite narrow and one expects that the effect of the transmission is relevant mostly at the edges of the spectrometer. The reconstructed experimental angular distribution for the elastic scattering at E_{lab} = 440 MeV, obtained applying the response function of the spectrometer to the experimental data, follows quite well the Rutherford scattering in almost the whole angular range, with the except of the extreme edges. Similar calculations are now being performed for the neutron transfer channels and for all other measured energies.

3 Particle-phonon states populated in multinucleon transfer reactions

The coupling of single particle degrees of freedom to nuclear vibration quanta is very important for the understanding of the transfer strength distribution. These effects, still largely unexplored, are essential for the description of many basic states in the vicinity of closed shells. To this end we studied the population of states with a particle-phonon character in neutron transfer channels produced in the ^{40}Ar+^{208}Pb reaction [14]. The ^{40}Ar beam was extracted from an ECR ion source and accelerated by means of the superconducting Linac ALPI at E_{lab} = 255 MeV onto a 300 μg/cm^2 ^{208}Pb target. The yields of the projectile like fragments have been measured with PRISMA at three different angles θ_{lab} = 46°, 54° ($\approx\theta_{grazing}$) and 59° in order to cover most of the transfer flux in the reaction. The coincident γ-rays were detected with the CLARA array, located in the hemisphere opposite to PRISMA. The normalization for the different measured angles was ensured by a silicon SSBD monitor detector positioned at a forward angle.

The γ spectra measured in coincidence with ^{40,41,42,43}Ar corresponding to inelastic scattering, +1n, +2n and +3n channels are plotted in Fig. 4. They contain transitions from particle states as well as from states involving combinations of single-particle with a collective boson. New transitions have

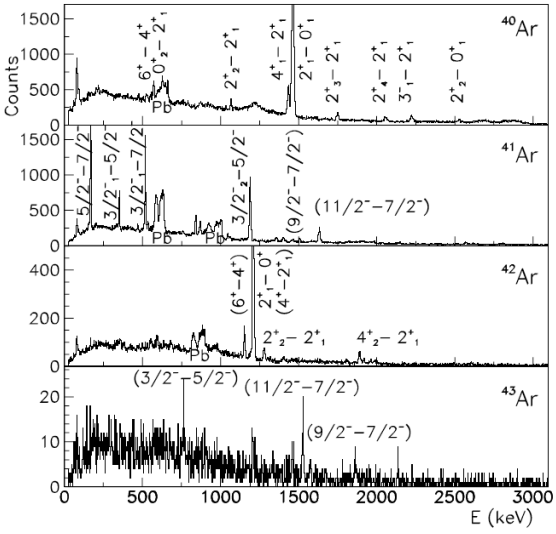

Fig. 4: Doppler corrected γ-ray spectra for ^{40,41,42,43}Ar

been identified in ^{41}Ar and ^{43}Ar ($9/2^- \rightarrow 7/2^-$ and $11/2^- \rightarrow 7/2^-$), and in ^{42}Ar ($6^+ \rightarrow 4^+$). A very strong population of the 2^+ states has been observed in ^{40}Ar and ^{42}Ar that act as cores in odd isotopes when a neutron is added. The energies, spins and parities of identified states agrees well with the results of *sd-pf* large-scale shell model (SM) calculations [15]. In ^{41}Ar and ^{43}Ar we observed, in addition to the known γ transitions of the low-lying states, strong lines at 1629.7(3) keV and at 1527.4(5) keV which we attribute to the population of the yet unknown $11/2^-$ states. These states can be understood as a coupling of collective boson to single-particle states (i.e. $|2^+, (f_{7/2})_1>$ giving an $11/2^-$ stretched configuration). It is expected that the properties of these particle-phonon states are to a large extent determined by the properties of the corresponding phonon states.

Figure 5 shows the comparison of the measured and SM calculated energies for the 2^+ and $11/2^-$ states of argon isotopes in the N = 20 – 28 region evidencing an excellent agreement for all argon isotopes shell. Solid circles are SM calculated energies, open squares are the adopted levels, whereas open triangles and the cross symbol correspond to the energies of $11/2^-$ in ^{41}Ar and ^{43}Ar from our experiment and in ^{45}Ar from Ref. [16]. The behavior of their energies displays that the evolution of the collectivity, in the even isotopes (2^+ energies) and in the odd isotopes ($11/2^-$ energies), is very similar. This further corroborates the particle-phonon character of these $11/2^-$ states. We expect that heavy ion induced transfer reactions populate states of similar character in more neutron rich isotopes. Argon isotopes with N≥28 have been populated in ^{238}U+^{48}Ca reaction [17], and the populated states in the ^{47}Ar behave similarly to odd-argon isotopes discussed here.

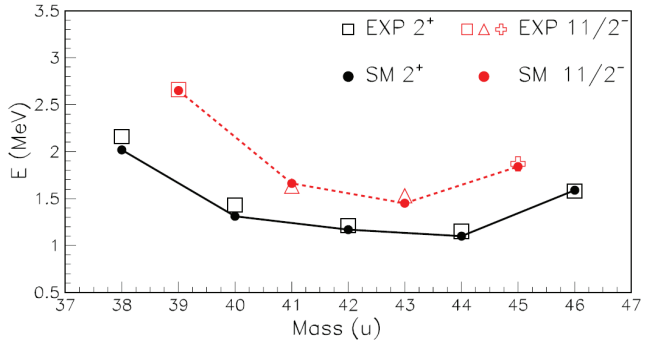

Fig. 5: Energies of the 2^+ and $11/2^-$ states of argon isotopes with N = 20–28

Experimental transfer yields have been interpreted within a reaction model [18] that explicitly treats the internal degrees of freedom of the two ions in terms of elementary modes, surface vibration and single particles. The significant population of particle-vibration states, reached via neutron transfer, demonstrates the importance of excitation of the states whose structure can be explained with the same degrees of freedom which are needed in the reaction model, i.e. coupling of the valence neutron to the vibration quanta.

4 An ancillary detector for the PRISMA spectrometer

A relevant aspect to be further investigated in transfer reactions that involves heavy ions is the influence of secondary processes, evaporation and fission that is important for the heavy partner. The determination of the survival probability against fission of heavy targetlike fragments (TLF) would help to understand how effectively multinucleon transfer reactions may be used to populate heavy nuclei [19]. We remark that data on the transfer induced fission are very scarce.

In order to check the relevance of the fission process in the population of the heavy fragments, we are planning to perform kinematical coincidence measurements where light fragments identified at

the focal plane of PRISMA will be used to tag heavy partners entering into position sensitive device located at the correlation angle in the scattering chamber. To this end the magnetic spectrometer PRISMA is being equipped with a position sensitive detector composed of a single-sided silicon strip detector (SSSD) with a thickness of 300 μm and an active area of 5x5 cm^2. The detector (shown in Fig. 6) is segmented in 16 resistive strips providing X and Y position information, timing and energy

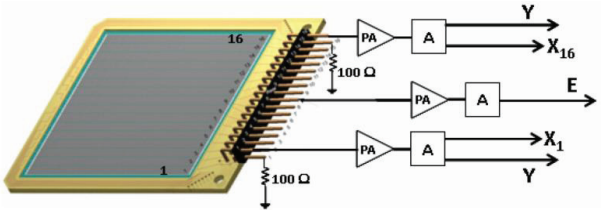

Fig. 6: Si strip detector for kinematical coincidence measurements

signals. In order to minimize the number of electronic channels, one end of each strip is grounded through a 100 Ω resistor and the position along the strip is obtained from the amplitude of the signal collected on the other end. Energy and position resolutions of about 80 keV and 1 mm along the strip, respectively, were obtained in laboratory tests performed with 5.486 MeV α particles.

A preliminary in-beam test has been performed by using the $^{40}Ca+^{90}Zr$ reaction at E_{lab} = 120 MeV. Figure 7 shows the X-Y scatter-plot (Zr ions) obtained with the entrance detector of PRISMA tagged by elastically scattered Ca ions entering into the SSSD. It was placed at 10 cm of

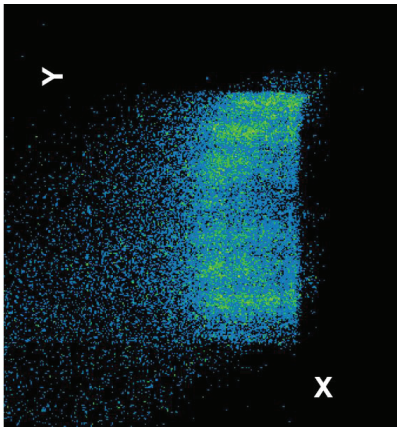

Fig. 7: X-Y plot measured with the start detector of PRISMA

distance from the target and covered with an aluminum mask composed of 8 by 10 holes, 1 mm diameter spaced 1.5 mm. Correlated Zr events in PRISMA cover only about half detector.

5 Summary

An enhancement by a factor 3 has been evidenced in the transfer probability extracted from the excitation function of the +2*n* transfer channel populated in the inverse kinematics reaction $^{96}Zr+^{40}Ca$. Data analysis of the excitation functions for the main transfer channels populated in the $^{116}Sn+^{60}Ni$ reaction is in progress to deduce the cross sections and transfer probabilities for neutron pick-up channels as well as for channels involving proton stripping. The comparison between data and theory

for both systems, namely superfluid and near closed shells nuclei, will significantly improve our understanding of nucleon-nucleon correlations in the transfer process. Excitation functions have been measured with sufficient statistics to extract angular distributions. Corrections of the experimental data based on the PRISMA response function are being performed for the neutron transfer channels.

In odd Ar isotopes populated via neutron transfer in the ^{40}Ar+^{208}Pb reaction, we observed a significant population of proposed $11/2^-$ states which well match a stretched configuration of the valence neutron coupled to the vibration quanta. The properties of such states are closely connected with the properties of the vibration quanta, allowing to follow the development of collectivity in odd argon isotopes.

A new ancillary detector for the PRISMA spectrometer has been developed and a preliminary in-beam test has been carried out. It will allow to perform kinematic coincidence measurements in order to study the effect of secondary processes such as the fission in the population of the TLF yields.

Acknowledgements

The authors are grateful to the LNL Tandem/PIAVE-ALPI staff for providing us with good quality beams and to the target laboratory for the excellent target preparation. The research leading to these results has received funding from the European Union Sixth Framework Programme FP6 under the EURONS Contract (No. RII3-CT-2004-506065) and the European Union Seventh Framework Programme FP7/2007- 2013 under Grant Agreement No. 262010 - ENSAR. This work was also partly supported by the Croatian Ministry of Science, Education and Sports (Grant No. 0098-1191005-2890).

References

[1] A.M. Stefanini *et al*., *Nucl*. *Phys*. **A701** (2002) 217c.
[2] G. Montagnoli *et al*., *Nucl*. *Instrum*. *Methods Phys*. *Res*. **A547** (2005) 455.
[3] S. Beghini *et al*., *Nucl*. *Instrum*. *Methods Phys*. *Res*. **A551** (2005) 364.
[4] A. Gadea *et al*., *Eur*. *Phys*. *J*. **A20** (2004) 193.
[5] A. Gadea *et al*., *Nucl*. *Instrum*. *Methods Phys*. *Res*. **A654** (2011) 88.
[6] L. Corradi, G. Pollarolo and S. Szilner, *J*. *of Phys*. **G**: Nucl. Part. Phys. 36 (2009) 113101.
[7] C.L. Jiang *et al*., *Phys*. *Lett*. **B337** (1994) 59.
[8] C.L. Jiang *et al*., *Phys*. *Rev*. **C57** (1998) 2393.
[9] L. Corradi *et al*., *Phys*. *Rev*. **C84** (2011) 034603.
[10] K.E. Rehm *et al*., *Phys*. *Rev*. **C47** (1993) 2731; R.B. Roberts *et al*., *Phys*. *Rev*. **C47** (1993) R1831.
[11] J.M. Quesada, G. Pollarolo, R.A. Broglia, A. Winther, *Nucl*. *Phys*. **A442** (1985) 381.
[12] D. Montanari *et al*., *Eur*. *Phys*. *J*. **A47** (2011) 4.
[13] D. Montanari *et al*., *Phys*. *Rev*. **C84** (2011) 054613.
[14] S. Szilner *et al*., *Phys*. *Rev*. **C84** (2011) 014325.
[15] F. Nowacki and A. Poves, *Phys*. *Rev*. **C79** (2009) 014310.
[16] D. Mengoni *et al*., *Phys*. *Rev*. **C82** (2010) 024308.
[17] S. Bhattacharyya *et al*., *Phys*. *Rev*. *Lett*. 101 (2008) 032501.
[18] A. Winther, *Nucl*. *Phys*. **A572** (1994) 191; A. Winther, *Nucl*. *Phys*. **A594** (1995) 203.
[19] L. Corradi *et al*., *Phys*. *Rev*. **C66** (2002) 024606.

The PANDA experiment : physics goals and experimental setup

*Gianluigi Boca on the behalf of the PANDA collaboration**
GSI Helmoltzzentrum für Schwerionenforschung, Darmstadt, Germany

Abstract
PANDA (antiProton ANnihilation at DArmstadt) is an experiment that will run at the GSI laboratory, Darmstadt, Germany, in 2018. A high intensity antiproton beam with momentum up to 15 GeV/c will collide on a fixed proton target (pellet target or jet target). A wide range of physics topics will be investigated : charmonium states and open charm states above the $D\overline{D}$ threshold; exotic states like glueballs, oddballs, hybrids, multiquarks, molecules; the spectroscopy of the excited states of strange and charm baryons; non-perturbative QCD dynamics in the $p\overline{p}$ production cross section of charm and strange baryons and their spin correlations; the behaviour of hadrons in nuclear matter; hypernuclear physics; electromagnetic proton form factors in the time-like region; the CP violation in the charm sector, rare and forbidden decays of charm baryons and mesons.

PANDA is an experiment that will run at the GSI laboratory in Darmstadt (Frankfurt, Germany) around 2010. It will continue and extend the successful physic program started at Cern with LEAR and Fermilab with E760/E835. Presently the PANDA collaboration is composed by a group of 420 physicists from 53 institutions of 16 countries. The experiment will use a very high intensity antiproton beam with momentum ranging from 1.5 GeV/c to 15 GeV/c, on a fixed proton target (pellet target or jet target). The range of energy in the center of mass covered goes from $\sqrt{s} = 2.25$ up to $\sqrt{s} = 5.47$ enabling the study a wide physics topic range, some of them described in the following sections. The $\overline{p}$ beam will be accumulated in the HESR storage ring in two modes : a high intensity mode, with a beam current of $\sim 2 \times 10^7$ $\overline{p}$/sec and stochastic cooling leading to a luminosity of $2 \times 10^{32}\,\mathrm{cm}^{-2}\mathrm{s}^{-1}$ and $\delta p/p = 10^{-4}$, and a high resolution mode with electron cooling, a luminosity of $2 \times 10^{31}\,\mathrm{cm}^{-2}\mathrm{s}^{-1}$ and $\delta p/p = 10^{-5}$.

1 Some of the Panda Physics goals

For lack of space it is impossible here to describe all physics measurements feasible in PANDA. Only a few are briefly described in the following. For a more detailed description see the PANDA Physics Book [1].

1.1 Charmonium physics

The $p\overline{p}$ system can form (non-exotic) states with any J^{PC} not just 1^{--} as in the e^+e^- experiments. Consequently all the charmonium states predicted by the potential models, can be studied in PANDA. The mass and width resolution of the states formed is driven essentially by the resolution of the $\overline{p}$ momentum and less by the detector performances, as demonstrated by the experience of the experiment E835 at Fermilab.
with $2 \times 10^{32}\,\mathrm{cm}^{-2}\mathrm{s}^{-1}$ luminosity PANDA will accumulate $8pb^{-1}$ integrated luminosity per day (assuming overall 50% efficiency) and $10^4 \div 10^7$ $c\overline{c}$ states/day. In 6 months data taking $1.5fb^{-1}$ will be accumulated, approximately 10 times better than the Fermilab experiments E760/E835 with a better detector, with better angular coverage, with magnetic field and the ability of detecting hadronic decay modes.

*On leave from Dipartimento di Fisica, Pavia University

The charmonium states can be divided in 'conventional' $c\overline{c}$ states predicted by the quark model and 'unconventional' states whose interpretation is still far from obvious. Some of the 'conventional' state that needs to be experimentally further investigated are : 1) the charmonium ground state η_c; it has been measured by eight experiments in the past, still there is poor agreement on the mass and the width. PANDA will measure this state with high statistics; 2) the η_c' discovered by Belle [2] in the $\eta_c' \to K\overline{K}\pi$ channel in 2002 and subsequently confirmed by BaBar and Cleo in 2004. The width is presently measured only with a 40% error, clearly new high statistics measurements are needed; 3) the charmonium $n^{2s+1}l_J = 1^1P_1$ state (h_c) mass and width are very important for the determination of the spin dependent components of the $q\overline{q}$ confinement potential. The BES3 (2010) [3] and CLEO (2008) [4] measurements confirm the mass value obtained earlier by E835 (in 2005) [5]. For the width there is still only an upper limit ($\Gamma < 1$ MeV); again larger statistic experiments are needed.
Concerning the physics of the charmonium 'unconventional' states, PANDA will be able to study many of them in great detail; for instance the X(3872). This state was discovered by Belle in 2003 [6] in the decay $X(3872) \to J/\psi\,\pi^+\pi^-$ and confirmed later by CDF, D0 and BaBar. Several hypothesis have been suggested to explain this narrow state : excited charmonium (1^3D_2 or 1^3D_3), a D^0D^{*0} molecule, $c\overline{c}g$ hybrid.
The X(3872) state is not the only puzzle in the mass spectrum. PANDA can study many of the reported states that need confirmation [7] : the X(3940), Y(4008), Z_1^+(4051), Y(4140), X(4160), Z_2^+(4250), Y(4274), X(4350), Z_2^+(4430), X(4630), Y(4660). In particular the Z states, if confirmed, would be the first unambiguos sign of non-$q\overline{q}$ states.

1.2 Open charm physics

PANDA will run at full luminosity above the open charm threshold at the $\psi(3770)$ resonance. A $D\overline{D}$ pair will be produced almost at rest. In a running time of 10^7 seconds in a year and with 50% reconstruction efficiency for the D decays, $\sim 10^9$ $D\overline{D}$ golden mode pairs/year will be detected. PANDA will be the next generation charm factory continuing the very successful charm physics program of experiments like Cleo, FOCUS, BaBar, BELLE. The PANDA large sample will made possible studies on the direct CP violation and T-violation of the D meson, on the mixing in the $D^0\overline{D}^0$ system, on rare and forbidden decays, on semileptonic decays, on Dalitz plots of hadronic decays, on the determination of D absolute branching ratios, of new allowed, singly, and doubly Cabibbo forbidden D decays.

1.3 Gluonic excitations (hybrids, glueballs) and other exotics

QCD allows for a state spectrum richer than the one predicted by the quark model. Gluons can be principal components of new hadrons : glueballs and hybrids. The additional gluons make possible exotic J^{PC} forbidden to SU3 quark model hadrons. That is a powerful experimental signature for their discovery. Their properties are determined by the long distance features of QCD and for this reason they are very interesting. For many of these states the latest LQCD calculations improved the precision of the predictions on the mass and the width. LQCD predicts about 15 glueball states with mass accessible to PANDA (for instance the first 2^{+-} state is predicted at $4.3\,\mathrm{GeV}/c^2$). Some of them have exotic quantum numbers (oddballs) and a width of $\sim 100\,\mathrm{MeV}/c^2$. Glueballs decay color blindly in $u\overline{u}$, $d\overline{d}$, $s\overline{s}$ and $c\overline{c}$ and can mix with normal hadronic resonances in the same mass range. Oddballs, due to their exotic J^{PC} are predicted to be narrower and easier to discover in partial wave analysis. The glueball decays most favourable to PANDA are those into $\phi\phi$ or $\phi\eta$ if their mass is $< 3.6\,\mathrm{GeV}/c^2$ or into $J/\psi\,\eta$ or $J/\psi\,\phi$ if it is above. PANDA can form glueballs in the $p\overline{p} \to \phi\phi$ channel, with statistics two orders of magnitude better than JETSET, or $p\overline{p} \to \omega\omega$,$\rho\rho$, $K\overline{K}^*$. The $\eta(1475) \to K\overline{K}\pi$ state published by the OBELIX collaboration [8] can be studied in detail.
As far as the hybrids are concerned, non-charmonium candidates are the $\pi_1(1400)$ decaying into $\eta\pi$,$\rho\pi$, the $\pi_1(1600)$ decaying into $\eta'\pi$, $\rho\pi$, $b_1\pi$, $f_1\pi$, $\omega\pi\pi$ the $\pi_1(2000)$ decaying in $f_1\pi$, $\omega\pi\pi$ and the $h_2(1950)$ decaying in $\omega\pi\pi$. PANDA will have the best chance to detected the $c\overline{c}g$ states with exotic quantum num-

bers since they are predicted to be relatively narrow and to have mass in the region above $3.5\,\mathrm{GeV}/c^2$ where the spectrum is not so populated by other large resonances.
As far as the tetraquarks and pentaquarks is concerned, PANDA will have access to these states up to $\sim 5.5\,\mathrm{GeV}/c^2$; the reaction $p\overline{p} \to \Theta^+\Theta^-$, if it exists, could be studied near threshold.

1.4 Electromagnetic form factors of the proton in the time-like region

The electromagnetic form factors in the time-like region can be studied in the $p\overline{p} \to e^+e^-$ reaction. To first order QCD

$$\frac{d\sigma}{d\cos\theta^\star} = \frac{\pi\alpha^2}{8EP}[|G_M|^2(1+cos^2\theta^\star) + \frac{4m_p^2}{s}|G_E|^2(1-cos^2\theta^\star)]$$

where E and P are the energy and momentum of the $\overline{p}$ in the $p\overline{p}$ reaction center of mass. Presently data exist up to a maximum of $Q^2 \equiv s \sim 15\,\mathrm{GeV}^2$ but higher Q^2 data are crucial to check the theory predictions and to check the equality between the space-like and time-like form factors for corresponding Q^2. Only the experiments E760 and E835 measured the form factors up to $15\,\mathrm{GeV}^2$ but, due to low statistics, they had to assume $|G_E| = |G_M|$. In PANDA it will be possible to measure them without assumptions, up to $Q^2 = 29\,\mathrm{GeV}^2$, with much wider angular acceptance and higher statistics.

2 The PANDA detector

In order to achieve its wide physics program, the detector must have full angular acceptance and good angular resolution both for charged particles and for γ. The particle identification (π, K, e and μ) should be excellent up to a momentum of $\sim 8\,\mathrm{GeV}/c$. High momentum resolution for a relatively wide momentum range is required. The detector has to work at a very high rate (2×10^7 Hz) in order to achieve the desired luminosity. A top view of the detector is shown in fig. 1. There are two magnets.

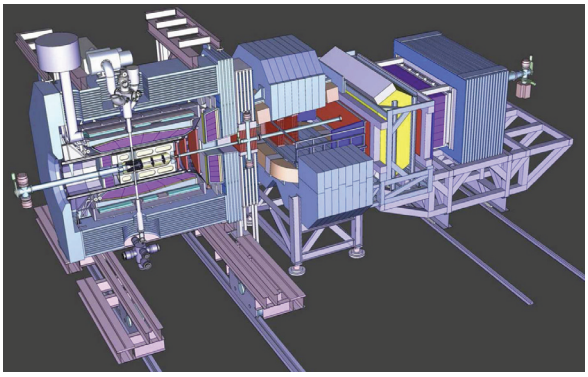

Fig. 1: Top view of the PANDA apparatus

A solenoid with 2 T field for the central region, a dipole with an integrated field of 2 Tesla·meter in the forward region. The $\overline{p}$ beam has a moment ranging from 1.5 up to $15\,\mathrm{GeV}/c$ and collides on a fixed target, a pellet target (the option of a gas jet target is also being considered). A microvertex detector made of pixel sensors and microstrip sensors with a barrel geometry surrounds the interaction region. The central detector is completed by a inner tracking detector (straw tubes), a DIRC for particle identification and an electromagnetic calorimeter. An inner time of flight detector (SciTil) made of by scintillator tiles is placed around the DIRC. Outside and around the solenoid a system of scintillator counters and drift chambers for muon detection will be placed. In the forward direction, for polar angles less than 22^0, the

dipole and 8 stations of multiwire drift chambers will help determining the track momentum. Particle identification will be ensured by a forward DIRC and a RICH and by time of flight counters scintillator walls. An electromagnetic calorimeter and hadron calorimeter will detect neutral particles like γ and neutrons. In the following sections the most relevant parts of the detector are described.

2.1 The pellet target

Presently the preferred solution is a pellet target like the one used in the CELSIUS/WASA facility. The desired density of the frozen droplets of hydrogen in order to achieve the PANDA luminosity requirements is 3.8×10^{15} atoms/cm^2 and presently the CELSIUS/WASA facility is very close to this goal : 2.8×10^{15} atoms/cm^2. The pellets are blown into the vacuum beam pipe through a tube which should be as small as possible. In the present design its inner diameter is 2 cm.

2.2 The microvertex detector

The microvertex detector [9] is placed around the beam pipe and it has a barrel geometry with 5 layers. The first 3 layers are pixels $100 \times 100\,\mu\mathrm{m}^2$. In order to reduce the material the 2 outer layers are double sided strips. There are also 5 forward wheels. The first 3 are pixels and the last two are double sided strips. In total $\sim$ 12 million pixels redout channels in the barrel and forward region and ~ 200000 strip readout channels. The pixel technology is the same used for LHC. The pixel total thickness (including the frontend) is $\sim 500\mu m$. The digitization is performed locally with the time over threshold method, in an ASIC using the $0.13\mu m$ technology. The resolution forseen with this detector is $100\mu m$.

2.3 The central tracker

The Central Tracker [10] consists of a Straw Tube system , used as tracker and for $\frac{dE}{dx}$ measurement. The straw tube system will be made of layers (from 20 up to 31 layers) of drift tubes 150 cm long, placed in hexagonal symmetry. They fill the cylindrical zone of inner radius 15 cm and outer radius 42 cm. The first 16 and last layers are aligned parallel to the beam axis, while the 16 central layers are arranged at skew angles of 3^0 enabling the measurement of the z position of the hit with better than 1 cm precision. Adiacent layers are staggered with respect to each other to help resolving the left-right ambiguity. The straw diameter is 10 mm; the gold-plated tungsten-rhenium wire diameter is $27\mu m$ and the wall thickness of the aluminized Mylar is $24\mu m$. The total number of straws is ~ 5300. The gas mixture is Ar-CO_2 with gain $\sim 10^5$. The x and y resolution on the single hit is $\leq 100\mu m$, while the z resolution is better than 0.4 cm; the typical momentum resolution of the straw system together with the microvertex system is 1.5% at 1 GeV/c total momentum.

2.4 The forward GEM detector

Particles emitted at angles below 22° not covered fully by the Straw Tube system will be tracked by three stations of GEM detectors placed 1.1 m, 1.4 m and 1.9 m downstream of the target. With the envisaged luminosity, the expected particle flux in the first chamber in the vicinity of the 5 cm diameter beam pipe is about $3{\cdot}10^4$ cm^{-2}s^{-1}. Besides this very high flux, this detector also has to work in the 2 T magnetic field. Gaseous micropattern detectors based on GEM foils as amplification stages are suitable to function under these conditions. In the current layout there are three double planes with two projections per plane. The readout plane is subdivided in an outer ring with longer and an inner ring with shorter strips. The strips are arranged in two orthogonal projections per readout plane. Owing to the charge sharing between strip layers a strong correlation between the orthogonal strips can be found giving an almost 2D information rather than just two projections. The readout is performed by the same front-end chips as are used for the silicon microstrips. The first chamber has a diameter of 90 cm, the last one of 150 cm. The readout boards carrying the ASICs are placed at the outer rim of the detectors.

2.5 Charged particle identification systems

The charged particle identification is essential in PANDA in all the physics channels. It is achieved with a DIRC, with a RICH, by means of $\frac{dE}{dx}$, with the Time of Flight system and with the muon counters.
The central barrel DIRC is placed in the solenoid, just around the straw tube tracker, at approximately 42 cm radius. It is made by quartz (fused silica) bars, where the Čerenkov light is produced, arranged in cylindrical fashion with axis coinciding with the one of the solenoid. It measures the Čerenkov cone of particle crossing the quartz bars and from that it is possible to derive the β of the particle. The quartz bars with $n = 1.47$ will enable kaon identification starting at $460\,\mathrm{MeV}/c$. The readout of the light will be achieved either with an array of 7000 photomultipliers located outside the magnetic field of the solenoid, coupled with purified water to the quartz bars, or by MicroChannelPlate PhotoMultipliers placed just outside the bars. Another option considered is the use of silicon PhotoMultipliers.
A DIRC for the forward particles at polar angles between 10^0 and 22^0 will be placed inside the solenoid, at the downstream end. The present design idea is to use a disk of fused silica as radiator, read out in ~ 3200 pixels. The design will ensure π/K separation from $1\,\mathrm{GeV}/c$ up to $10\,\mathrm{GeV}/c$ at $\theta = 0$ and up to $5\,\mathrm{GeV}/c$ at $\theta = 25^0$.
In the forward direction (polar angles $< 10^0$) the particle identification will be ensured by a RICH located downstream the dipole. The radiator is made of 3^{rd} generation aerogel, hydrophobic, with $> 80\%$ transmittance. For the Čerenkov cone light readout a new type of multipixel hybrid GaAsP photocathode with 60 % quantum efficiency in the $300 - 700$ nm range is being considered. It is an avalanche diode, with 64 pixels $2 \times 2\,\mathrm{mm}^2$ with $< 100\mathrm{ps}$ resolution in 1.5 T field.
The $\frac{dE}{dx}$ technique is used in PANDA to separate $\pi/K/p$ typically below $800\,\mathrm{MeV}/c$. In the central region the straw tube system (which works in proportional mode) will measure the energy released by the charged particles. The electromagnetic and hadronic calorimeters will be able to identify γ's and neutrons.
Another technique exploited in PANDA is the Time of Flight measurement for charged particles. In the central region the SciTil placed around the DIRC will serve this scope. The present design uses $2.85 \times 2.85\,\mathrm{cm}2$ tiles of fast scintillator with thickness 0.5 cm mechanically mounted together with the DIRC. About 5000 tiles are forseen, each read by two APDs. A time resolution of 100 fs is expected with this detector.
A ToF scintillator wall will be placed in the forward region, behind the dipole and the forward electromagnetic calorimeter, at a distance of $\sim$ 7 m downstream the target. The wall will be 5.6 m wide and 1.4 m tall and it will consist of 60 vertical scintillator strips from 5 to 10 cm wide. Inside the dipole 5 vertical strips, each 10 cm wide and 1 m long will be placed and read out with fibers by phototubes placed outside the dipole magnetic field. Simulations show that with the help of the tracking system a time resolution of 50 ps can be achieved by this ToF system.
The muon identification will be achieved with a set of Iarocci proportional tubes and with scintillator counters. They will be placed outside and around the solenoid and the dipole magnets, in the inner gap of the solenoid yoke and between the hadron calorimeter planes. In that way the iron of the yoke or several planes of hadron calorimeter will act as filter for all the other particles. The angular coverage will be from 0^0 up to 60^0 in polar angle.

2.6 The electromagnetic calorimeter

The detection of γ's, with the largest possible angular coverage is crucial in PANDA. This motivates the use of four calorimeters, one inside the solenoid, in the central barrel region, covering the polar angle from 22^0 to 140^0; one in the backward end cap region of the solenoid, covering the angles from 140^0 to almost 180^0; one in the downstream (forward) end cap region, covering the angles from 10^0 to 22^0 and one in the forward region behind the ToF wall and covering the the angles $0^0 - 10^0$. The calorimeters must be fast, radiation hard and have excellent resolution for γ energies from $22\,\mathrm{MeV}$ to $4\,\mathrm{GeV}$. The presently favoured option is the use of $\mathrm{PbWO_4}$ crystals $2\,\mathrm{cm} \times 2\,\mathrm{cm} \times 22\mathrm{X}_0$ read out by

Date	Description
2014	preassembly of the experiment
2016	installation at FAIR
2017	commissioning
2018	data taking

Table 1: Schedule with milestones of the PANDA experiment

APDs (necessary for the strong magnetic field). The barrel calorimeter has a cylindrical symmetry, 2.5 long, 0.54 m thick in the radial direction, and it is made of 11360 $\mathrm{PbWO_4}$ crystals. The upstream end cap has 816 crystals, segmented in 16 slices; the forward end cap has 1 m radius with 6864 crystals. The expected resolution of all the first three calorimeters is $< \frac{2\%}{\sqrt{E}} + 1\%$. The forward calorimeter is composed of Shashlyk modules of lead and scintillator sandwich read out by fibers. The expected resolution is $\frac{\sigma(E)}{E} = (1.96 \pm 0.1)\% \bigoplus \frac{(2.74 \pm 0.05)\%}{\sqrt{E}}$ with the energy in GeV.

2.7 The hadronic calorimeter

The hadronic calorimeter will detect K_L and neutrons in the forward region. It is located 8 m downstream the target. We plan to reuse the MIRAC calorimeter from experiment WA80 at CERN. The PANDA arrangement consists of 20+20 modules in two rows. Each module contains 100 layers composed of steel and scintillator. The total dimensions are 1.8 m height, 4.4 m wide, and 1.12 m long, in the beam direction, for a total of 4.8 absorption lengths. According to GEANT4 simulations it is expected to have a resolution $\frac{\sigma(E)}{E} = \frac{0.40}{\sqrt{E}}$.

3 Time schedule of the project

The time schedule of the PANDA project depends on the time schedule of FAIR, the project of the entire accelerator complex at GSI. The milestones of the PANDA project are summarized in Tab. 1. The data taking wil be in 2018.

References

[1] M. F. M. Lutz *et al*. [PANDA Collaboration], "Physics Performance Report for PANDA: Strong Interaction Studies with Antiprotons," arXiv:0903.3905 [hep-ex].

[2] S. Choi et al., Phys. Rev. Lett. **89**, 102001 (2002).

[3] M. Ablikim et al. (BES III Collab.), Phys. Rev. Lett. **104**, 132002 (2010).

[4] S. Dobbs et al. (CLEO Collab.), Phys. Rev. Lett. **101**, 182003 (2008).

[5] M. Andreotti et al. (FNAL E835 Collab.), Phys. Rev. **D72**, 032001 (2005).

[6] S. Choi et al., Phys. Rev. Lett. **91**, 262001 (2003).

[7] J. Beringer et al. (Particle Data Group), Phys. Rev. **D86**, 010001 (2012).

[8] F.Nichitiu et al.(OBELIX Collab.), Phys. Lett. **B545**, 261 (2002).

[9] W.Erni *et al*. [PANDA Collaboration], "Technical Design Report for the: PANDA Micro Vertex Detector," arXiv:1207.6581 [physics.ins-det].

[10] W.Erni *et al*. [PANDA Collaboration], "Technical Design Report for the: PANDA Straw Tube Tracker," arXiv:1205.5441 [physics.ins-det].

The FIRST experiment at GSI: Detector performances with a 400 MeV/u ^{12}C beam

Z. Abou-Haidar[p,x], C. Agodi[f], M.A.G. Alvarez[p], T. Aumann[a], F. Balestra[h,k], G. Battistoni[b], A. Bocci[p], T.T. Böhlen[v,w], A. Boudard[u], A. Brunetti[c,i], M. Carpinelli[c,m], G.A.P. Cirrone[f], M.A. Cortés-Giraldo[q], G. Cuttone[f], M. De Napoli[d], M. Durante[a], J.P. Fernández-García[q], C. Finck[r], M.I. Gallardo[q], B. Golosio[c,m], E. Iarocci[e,j], F. Iazzi[h,k], G. Ickert[a], R. Introzzi[h], D. Juliani[r], J. Krimmer[t], N. Kurz[a], M. Labalme[s], A. Lavagno[h,k], Y. Leifels[a], A. Le Févre[a], S. Leray[u], F. Marchetto[h], V. Monaco[h,l], M.C. Morone[i,n], D. Nicolosi[aa,f], P. Oliva[c,m], A. Paoloni[e], V. Patera[e,j], L. Piersanti[e,j], R. Pleskac[a], J.M. Quesada[q], N. Randazzo[d], F. Romano[f,o], D. Rossi[a], V. Rosso[y,z], M. Rousseau[r], R. Sacchi[h,l], P. Sala[b], A. Sarti[e,j], C. Scheidenberger[a], C. Schuy[a], A. Sciubba[e,j], C. Sfienti[f,w], H. Simon[a], V. Sipala[d,m], E. Spiriti[g], L. Stuttge[r], S. Tropea[f] H. Younis[h,k],

[a]GSI Helmholtzzentrum für Schwerionenforschung, Darmstadt, Germany
[b]Istituto Nazionale di Fisica Nucleare - Sezione di Milano, Italy
[c]Istituto Nazionale di Fisica Nucleare - Sezione di Cagliari, Italy
[d]Istituto Nazionale di Fisica Nucleare - Sezione di Catania, Italy
[e]Istituto Nazionale di Fisica Nucleare - Laboratori Nazionali di Frascati, Italy
[f]Istituto Nazionale di Fisica Nucleare - Laboratori Nazionali del Sud, Italy
[g]Istituto Nazionale di Fisica Nucleare - Sezione di Roma 3, Italy
[h]Istituto Nazionale di Fisica Nucleare - Sezione di Torino, Italy
[i]Istituto Nazionale di Fisica Nucleare - Sezione di Roma Tor Vergata, Italy
[j]Dipartimento di Scienze di Base e Applicate per l'Ingegneria, "La Sapienza" Università di Roma, Italy
[k]Dipartimento di Fisica, Politecnico di Torino, Italy
[l]Dipartimento di Fisica, Università di Torino, Italy
[m]Università di Sassari, Italy
[n]Dipartimento di Biopatologia e Diagnostica per Immagini, Università di Roma Tor Vergata, Italy
[o]Centro Studi e Ricerche e Museo Storico della Fisica "Enrico Fermi", Roma, Italy
[p]CNA, Sevilla, Spain
[q]Departamento de Física Atómica, Molecular y Nuclear, University of Sevilla, 41080-Sevilla, Spain
[r]Institut Pluridisciplinaire Hubert Curien, Strasbourg, France
[s]LPC-Caen, ENSICAEN, Université de Caen, CNRS/IN2P3, Caen, France
[t]IPN-Lyon, Université de Lyon, Université Lyon 1, CNRS/IN2P3, Villeurbanne, France
[u]CEA-Saclay, IRFU/SPhN, Gif sur Yvette Cedex, France
[v]European Organization for Nuclear Research CERN, Geneva, Switzerland
[w]Medical Radiation Physics, Karolinska Institutet and Stockholm University, Stockholm, Sweden
[x]Universität Mainz Johann-Joachim-Becher, Mainz, Germany
[y]Dipartimento di Fisica, Università di Pisa, Italy
[z]Istituto Nazionale di Fisica Nucleare - Sezione di Pisa, Italy
[aa]Dipartimento di Fisica, Università di Catania, Italy

Abstract

FIRST (Fragmentation of Ions Relevant for Space and Therapy) is an experiment aimed at the measurement of double-differential cross sections, with respect to kinetic energy and scattering polar angle, of nuclear fragmentation processes in the energy range between 100 and 1000 MeV/u. The experiment was performed with the SIS accelerator at GSI (Darmstadt, Germany). During August 2011 a first set of data was collected using a 400 MeV/u ^{12}C ion beam on carbon and gold targets. We present a description of the experimental apparatus and some preliminary results from the data acquisition and from the data analysis.

1 Introduction

Hadron therapy has well known advantages with respect to conventional radiation therapy using photons. The ion beam energies can be chosen in such a way that the Bragg peak, the sharp peak of the released dose at the end of the ion range, falls inside the tumour, while sparing surrounding normal tissues. Compared to proton therapy, hadron therapy using ^{12}C beams has further advantages, among

these are a sharper lateral dose fall-off and a higher potential to treat radioresistant tumours due to its increased linear energy transfer (LET) at the end of the particle range. However, since the secondary fragments produced by the nuclear interactions of the beam with the tissue significantly contribute to the absorbed dose [1], fragmentation effects cannot be neglected. Currently, treatment planning systems for hadron therapy are generally based on deterministic codes for dose calculations which are relatively fast [2, 3]. These deterministic dose engines are often benchmarked against Monte Carlo simulations in order to test and improve their accuracy [4, 5]. The predictions of various theoretical models for the fragmentation process differ up to an order of magnitude for double-differential quantities (in energy and angle). Several measurements were made in the past of fragment yields and total cross sections (for a review see [6]), but double-differential cross section (DDCS) measurements are scarce. Accurate knowledge of fragmentation cross sections would also be important in the field of radiation protection in space missions. Recently, NASA completed a large database of nuclear fragmentation measurements [7] and observed that there are ion types and kinetic energy ranges where such measurements are missing. In particular, DDCS measurements for light ions in the energy range of interest for hadron therapy applications are lacking. The FIRST experiment is aimed at filling some of this lacking knowledge by measuring DDCS for light ions in the kinetic energy range between 100 and 1000 MeV/u.

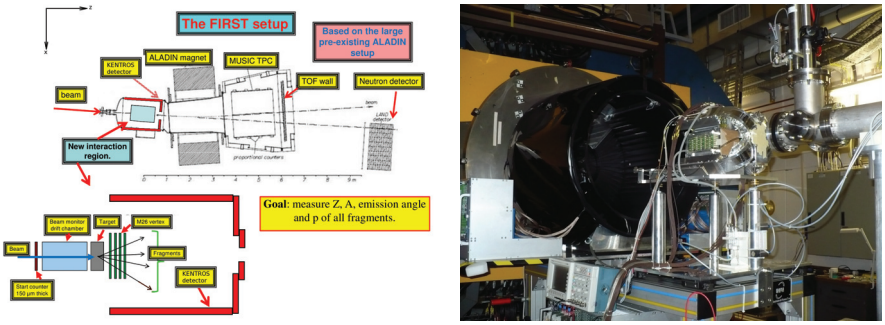

(a) (b)

Fig. 1: (a) Layout of the FIRST experiment with expanded interaction region. (b) The FIRST Interaction Region detectors during the installation.

2 Experimental setup

A detailed description of the experimental apparatus is reported in ref. [8]. Here only a short description will be given. A schematic layout of the FIRST experimental setup is shown in Fig. 1(a). The interaction region, shown in the enlarged portion of Fig. 1(a) and in the picture of Fig. 1(b), is composed of small area detectors that surround the target, before the ALADiN horizontal bending magnet. All these detectors have been specifically designed and built for this experiment. Following the beam path:

- the Start Counter [9] measures the starting time for the time-of-flight measurement. The active part of this detector is an EJ-228 fast scintillator foil (52 mm diameter, 250 μm thick). The scintillation signal is driven by four optical fibre bundles to four fast photomultipliers (Hamamatsu H10721-201);
- the Beam Monitor [9] measures the incoming ion direction and the impact point on the target. It consists of a drift chamber filled by an Ar-CO_2 80%-20% gas mixture and is composed of 36 sensing wires, arranged in six planes perpendicular to the beam, with the wires oriented alternatively in the horizontal and in the vertical direction;
- the Vertex Detector measures the tracks of charged particles originating from the target. It is based on the MIMOSA-26 silicon pixel sensor [10], which features an active area of $21.2 \times 10.6\,\mathrm{mm}^2$ segmented in 1152×576 pixels, with a 18.4 μm pitch. The layout of the detector (see Fig. 5(b)) is composed of four planes of about $2 \times 2\,\mathrm{cm}^2$ area, each plane being made of two partially overlapping MIMOSA-26 detectors spaced by 3 mm and with the long side oriented vertically. It

can measure tracks with an angular resolution of about 0.3 degrees up to polar angles of about 40 degrees;
- the KENTROS (Kinetic ENergy and Time Resolution Optimized on Scintillator) detector measures the time of flight and energy release of fragments with polar angles between about 5 degrees and 90 degrees. These measurements are used to identify the particle charges and to evaluate their kinetic energy. The KENTROS detector is divided in three subdetectors: a small endcap, which detects fragments with polar angles between 5 and 15 degrees, a big endcap for polar angles between 15 and 37 degrees, and a barrel for polar angles between 37 and 90 degrees. Each subdetector is composed of EJ-200 fast plastic scintillator modules. The scintillation signal is driven by plexiglass light guides to AvanSiD Silicon PhotoMultipliers (SiPM) with an active area of $4 \times 4\,\mathrm{mm}^2$. The SiPM signal is read by custom readout boards, with individual supply voltage control, signal amplification, reshaping and splitting to QDCs and to TDCs.

Behind the ALADiN bending magnet, large area detectors inherited from previous experiments were used. Following the beam path:

- the TP-MUSIC IV (Time Projection MUltiple Sampling Ionization Chamber) detector is a time projection chamber that measures the tracks of charged particles which exit the ALADiN magnet. The active volume is filled with a P10 (Ar-CH_4 90%-10%) gas mixture. It is divided in two symmetric parts by a central vertical cathode plane. The track projections on the non-bending (yz) plane[1] are determined by proportional counters located on the opposite sides of the detector, while the track projections on the horizontal bending (xz) plane are evaluated by measuring the ionization electron drift time from the track to the proportional counters. The readout is based on 14-bit FADC boards which digitize the signals coming directly from the preamplifiers. The MUSIC IV detector is able to measure with high efficiency and high resolution the charge and momentum of ions from He up to Au [11];
- the TOFWALL [12] measures the arrival time, energy release and impinging position of the fragments produced with polar angles smaller than about 6.5 degrees. It is composed of two layers, each made of 12 modules. Each module is composed of 8 BC-408 plastic scintillator slats, 110 cm long, 2.5 cm wide and 1 cm thick, oriented in the vertical direction. Each slat is read on both ends by two R3478 Hamamatsu photomultipliers. The signal is split and read out by Fastbus QDCs and by TDCs for charge and time measurements, respectively;
- the Large Area Neutron Detector (LAND) [13] is a large scintillation detector, having an active volume of about $2 \times 2 \times 1\,\mathrm{m}^3$, specifically designed for neutron detection. It is composed of 200 paddles having a volume of $200 \times 10 \times 10\,\mathrm{cm}^3$. Each paddle is made of 10 sheets of scintillator separated by sheets of iron. The scintillation light is collected on both ends of the paddles by stripe light guides, which drive it to the photomultipliers. The difference in the arrival times of the two signals is used to localize the position where the neutron interacts with the scintillator material, while the mean time is used to evaluate the neutron arrival time.

3 The first data taking at the GSI laboratory

The FIRST experiment was instrumented at the GSI laboratories in Darmstadt, and a first set of data was collected in 2011 between July and August. A total number of about 37 million events were collected and grouped in about 250 runs. Most of these measurements (about 32 million events) were made using a 400 MeV/u ^{12}C beam impinging on a 8 mm thick carbon target, while the remaining 5 million events were collected using a 5 mm thick gold target. Additional runs with special detector and target conditions were also taken for calibration and alignment purposes. The data acquisition was developed using the framework of the GSI Multi Branch System (MBS) [14]. This system can handle all the readout electronics standards (FASTBUS, CAMAC and VME) used in the experiment. Each readout crate was equipped with a trigger module connected through a single trigger bus to distribute the trigger and dead-time signals and to ensure event synchronization. The trigger signals from different detectors were fed into a programmable coincidence module where a logical combination of the signals could be used to produce the global trigger decision. Basically, this decision was based on an unbiased trigger provided

[1] The right-handed coordinate system used in this paper has the z axis pointing in the beam direction, the x axis pointing horizontally and the y axis pointing upwards. Polar and azimuthal angles are defined with respect to the z direction.

by the Start Counter. Other pre-scaled triggers with logical combinations of the Start Counter with other detectors were used for efficiency and calibration studies.

4 Detector performance

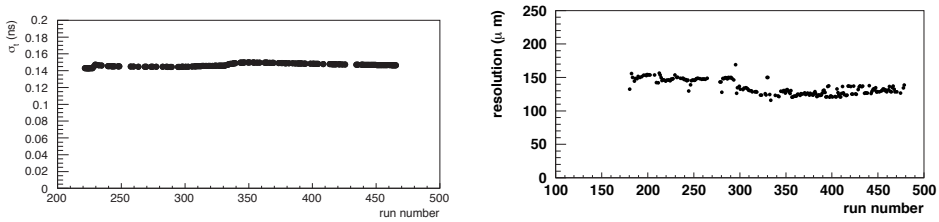

(a) (b)

Fig. 2: (a) Standard deviation of the time difference between pairs of Start Counter PMTs as a function of the run number. (b) Track spatial resolution of the Beam Monitor as a function of the run number.

The Start Counter efficiency was measured by using the unbiased sample of events triggered with the forward scintillator. It was found to be well above 99% in each of the runs even when requiring the coincidence of all the 4 PMTs, thus providing an indication of the high quality of the light collection system. The time resolution was determined by means of a gaussian fit of the distribution of the time difference between pairs of PMTs. The resulting sigma was in all runs better than 150 ps, as shown in Fig. 2(a). The time resolution, estimated as the standard deviation of the time difference between pairs of PMT divided by $\sqrt{2}$, is around 100 ps.

The performance of the Beam Monitor was also stable, as shown in Fig. 2(b). The space time relations used in the BM track reconstruction have been calibrated on a dedicated test beam [9] on a carbon beam of 80 MeV/u, with the same gas mixture at different high voltages. While the use of those calibrations is somewhat suboptimal, since they were obtained for carbon ions at a different energy, the results obtained are not far from the expected values: O(100 μm) [9]. Figure 2(b) shows that a track spatial resolution of 130-160 μm was achieved for all the C-C runs which is in agreement with the expected performances for the BM detector. This resolution corresponds to the standard deviation of the gaussian fit to the distribution of the difference between the hit and reconstructed track coordinates. The Beam Monitor measurement of the beam spot size, a Gaussian distributed circular spot of 1.3 mm σ was found to be in very good agreement with measurements performed by the Vertex Detector downstream of the target. The good performance of the Vertex Detector is evidenced in Fig. 3(a) where the number of clusters belonging to a track is shown for a single run. Although a minimum of 3 clusters are needed to build a track, the large majority of tracks incorporates one cluster in each of the four planes, indicating

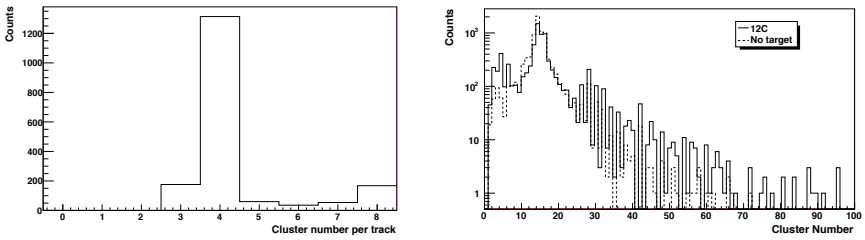

(a) (b)

Fig. 3: (a) Number of clusters per track in the Vertex Detector for ^{12}C on carbon run. (b) Number of pixels per cluster in the Vertex Detector for a run with the carbon target (solid line) and for a run without the target (dashed line).

a good tracking performance of this detector. In addition, a class of tracks crossing the planes in the overlap region between the two sensors is shown which incorporates up to eight clusters. For the same run, the total number of clusters belonging to a track in each of the eight sensors where about equal for sensors on the left side as well as for sensors on the right side. From this evaluation the efficiencies of the sensors appear to be uniform, the difference in the absolute number of tracked clusters, between sensors on the left or on the right with respect to the beam, being due to the beam not impinging perfectly centred on the Vertex Detector. Fig. 3(b) represents the distribution of the number of pixels belonging to a cluster, both for a run with the carbon target and for a run without the target. As expected the distributions are similar for carbon, gold and no target, since most of the events are non-fragmented events (i.e. mostly carbon ions). In Fig. 4(a), a section of the KENTROS TDC counts distribution, obtained requiring the

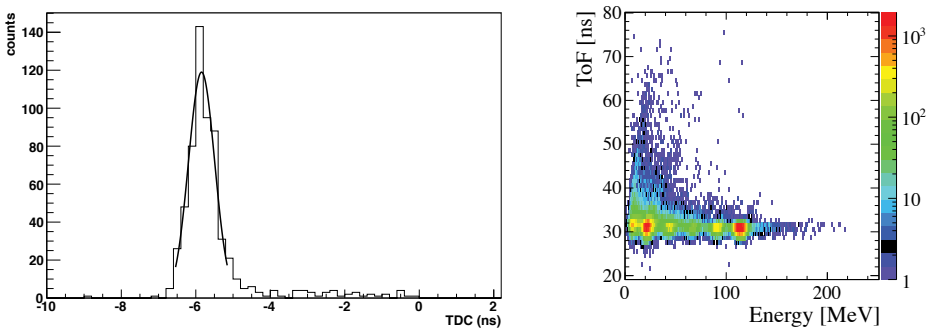

(a) (b)

Fig. 4: (a) TDC distribution on a Small Endcap module of the KENTROS detector, without time-walk correction, for QDC counts between 2200 and 2400. A gaussian fit to the peak of the histogram within $\pm 2\sigma$ shows a standard deviation of $\sigma \simeq 0.35$ ns. (b) ToF vs energy release ΔE_{TOF} in the TOFWALL. The six regions in the plot correspond to the ion fragments with $Z = 1, \ldots, 6$ from left to right.

related QDC counts to be consistent with the α particles energy release, was projected on the TDC axis. A gaussian fit to the peak of the histogram within $\pm 2\sigma$ shows a standard deviation of $\sigma \simeq 0.35$ ns. This value is influenced by the time-walk effect and by fluctuations of the scintillation signal transit time, which depends on the particle impact point on the detector module and will be corrected using the global track reconstruction information. Therefore, the standard deviation obtained by the fit should be regarded as an upper limit for the time resolution in our experimental conditions. The time of flight and the energy release, combined with the information on the tracks reconstructed by the Vertex Detector, will be used to evaluate the fragment kinetic energy. For the TOFWALL detector, the length of each slat (110 cm) requires to combine the values of the TDCs at both ends as average and the values of the ADCs as product, in order to cancel the dependence of the one-side measurement on the impact point. We shall denote the difference between the average time value of the TDCs and the time measured by the Start Counter as ToF; this quantity is related to the time of flight by a time offset to be determined individually for each slat. Similarly the square root of the ADCs product, converted to particle energy lost in the slat, is denoted as ΔE_{TOF}. Some special runs with no target and with the magnetic field of the ALADiN continuously varied were dedicated to the calibration of the TDCs and ADCs. The ToF calibration for the ^{12}C ion beam at 400 MeV/u, over all slats of the TOFWALL was tuned with a time offset chosen in each slat such that the ToF distribution for non-fragmented carbon ions at 400 MeV/u was centred at $\sim$32 ns. An upper limit for the real time resolution σ of 0.5 ns, was obtained, to be compared with a minimum time of $\sim$28 ns spent by the fastest fragments to reach the TOFWALL. The scatter plot of ToF versus ΔE_{TOF} measured by a single slat in all runs with carbon as target and a beam energy of 400 MeV/u is shown in Fig. 4(b). The six separated regions which appear in the plot correspond to ion fragments $Z = 1, \ldots, 6$ from left to right. They suggest a good charge identification capability of this detector. The time of flight information will be used together with the global track reconstruction to evaluate the kinetic energy of the fragments. The tracking performance of the detectors of the Interaction Region:

Beam Monitor, Vertex Detector and KENTROS, are easily monitored by means of a 3D event display, as shown in Figs. 5(a) and 5(b).

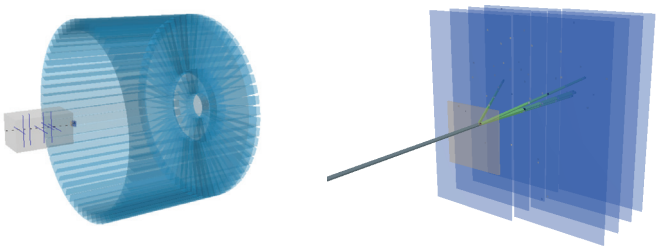

(a) (b)

Fig. 5: (a) Interaction Region event display. (b) Vertex Detector event display.

5 Conclusion

The FIRST experiment was designed for the measurement of nuclear fragmentation cross sections, double differential with respect to kinetic energy and scattering polar angle, for light ions in the range between 100 and 1000 MeV/u. The experiment was instrumented at the GSI laboratory and a first data acquisition took place during summer 2011. About 37 million events were acquired using a 400 MeV/u ^{12}C beam impinging on carbon (32 M) and gold (5 M) targets. The data analysis is still in progress. However from the preliminary analysis the measured values of the detector resolutions and the quality of the data match perfectly the expected performance.

Acknowledgement

We would like to acknowledge M. Arba, L. La Delfa and M. Tuveri (INFN Sez. Cagliari), M. Anelli, S. Cerioni, G. Corradi, D. Riondino and R. Rosellini (INFN, LNF), M. Capponi and A. Iaciofano (INFN, Sez. Roma3) for the technical design and mechanical work on the Interaction Region, and Filippo Bosi (INFN Sez. Pisa) for his help and suggestions. We also acknowledge Dr. Håkan T. Johansson for the invaluable help in setting up the trigger. This work has been supported by the European Community FP7 - Capacities, contract ENSAR n° 262010 and People PITN-GA-2008-215840-PARTNER. This work was also supported by Junta de Andaluca and the Spanish Ministerio de Ciencia e Innovación Contracts P07-FQM-02894, FIS2008-04189 and FPA2008-04972-C03. Finally some of the authors would like to thank CNRS-In2p3 for the support.

References

[1] E. Haettner *et al.*, Radiat. Prot. Dosim. **122**(1-4) (2006) 485.

[2] M. Krämer and M. Durante, Eur. Phys. J. D **60**(1) (2010) 195.

[3] L. Sihver and D. Mancusi, Radiat. Meas. **44**(1) (2009) 38.

[4] K. Parodi *et al.*, Proc. 12th Int. Conf. on Nucl. Reac. Mechan. (Varenna, Italy, 15th-19th June 2009), available at http://cdsweb.cern.ch/record/1238366/files/p509.pdf.

[5] T. T. Böhlen *et al.*, Phys. Med. Biol. **55**(19) (2010) 5833.

[6] D. Schardt *et al.*, Rev. Mod. Phys. **82**(1) (2010) 383.

[7] J.W. Norbury and J. Miller, 47th NCRP Annual Meeting, Bethesda, MD (2011) 24.

[8] R. Pleskac *et al.*, Nucl. Instrum. Meth. *A678* (2012) 130.

[9] Z. Abou-Haidar *et al.*, J. Instrum. **7** (2012) P02006.

[10] http://www.iphc.cnrs.fr/-CMOS-ILC-.html

[11] C. Sfienti *et al.*, "Isotopic dependence of the nuclear caloric curve", Phys. Rev. Lett. **102**(15) (2009) 152701.

[12] A. Schüttauf *et al.*, Nucl. Phys. A **607**(4) (1996) 457.

[13] K. Boretzky *et al.*, Phys. Rev. C **68**(2) (2003) 243171.

[14] H.G. Essel and N. Kurz, IEEE TNS **47**(2) (2000) 337.

Results from the experimental campaign of the AGATA Demonstrator at LNL

E. Farnea on behalf of the AGATA Collaboration
INFN Sezione di Padova, 35131 Padova, Italy

Abstract
The AGATA Demonstrator Array has recently concluded a two-years campaign of measurements at the Laboratori Nazionali di Legnaro, Italy. In this contribution, the principles of operation of the device and the status of the AGATA project will be reviewed. The performance of the array will be discussed and highlights from a few selected measurements will be presented.

1 Introduction

In the past 20 years, valuable Nuclear Structure information has been obtained with γ spectroscopy techniques, by using arrays of Compton-suppressed hyperpure germanium (HPGe) detectors. These devices rely on the combination of several crystals to obtain full peak efficiencies of the order of a few percent (up to 10% for arrays such as EUROBALL and GAMMASPHERE [1]). The peak-to-total (P/T) ratio of the resulting spectra is maximised by collimating the detectors, which limits the scattering of photons in between crystals, and, most importantly, by using veto detectors (Compton-suppression shields) to detect photons which made only a partial energy deposition within the germanium crystals. A major problem with these devices is the Doppler broadening of photons emitted from nuclei in motion with typical recoil velocity of a few percent of the speed of light. In order to limit this effect, the crystals should cover as small a solid angle as possible.

The above described devices are not well suited to the experimental conditions at the planned and under construction radioactive ion beam facilities such as SPES, SPIRAL-2, FAIR. Full peak efficiencies of the order of 30-40% will be needed to cope with the low beam intensities. In case of fragmentation facilities with high-energy beams, where the nuclei emitting the radiation will move with relativistic velocities, Doppler broadening will dominate the effective energy resolution of the detectors. "Conventional" arrays should be composed of thousands of crystals in order to keep these effects to acceptable values, which would hardly be manageable and, most likely, economically unfeasible.

In the early 2000s an innovative approach to this problem was proposed, namely to use the germanium crystals in position-sensitive mode. This requires using crystals with electrically segmented outer electrodes and digital electronics. The energy and position of each interaction within the crystals is extracted by comparison of the observed signal shapes with a reference set of signals representing the response of the system to a single-interaction event in a grid of known locations inside the crystal. This process is known as *signal decomposition* or *pulse shape analysis*, PSA. Once the full set of interaction points seen in all detectors in a specific event is determined, the energy and direction of each photon can be determined (*tracked*) by means of computer algorithms, which, as a side effect, can also perform efficient Compton suppression, or, in other words, identify and discard partial energy depositions. The full-peak efficiency of a 4π tracking array of HPGe detectors, as estimated by realistic Monte Carlo simulations, can as high as 50%, with a P/T ratio of 60%. Since each interaction point is determined with a precision of a few millimeters, hence much smaller than the typical crystal size, the Doppler correction can be performed with a much better quality than in case of "conventional" Compton-suppressed arrays.

Presently, the construction of a tracking array inspired by the above mentioned principles is pursued by two projects, both using 36-fold segmented crystals closely packed into multi-crystal cryostat (*clusters*) and digital electronics sampling all signals at 100 Ms/s with a resolution of 14 bits. The US-based array GRETA [2] will be built out of 120 crystals, arranged into 30 quadruple clusters, while the

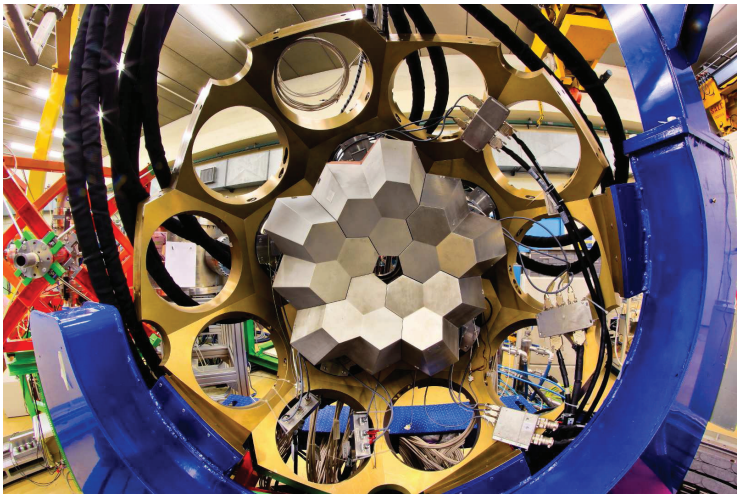

Fig. 1: Photo of the AGATA Demonstrator Array installed at the target point of the PRISMA magnetic spectrometer at the Laboratori Nazionali di Legnaro.

European array AGATA [3] will be composed of 180 crystals, arranged into 60 triple clusters. The two projects are very ambitious, technically challenging and, clearly, economically compelling. Therefore, they will be completed in stages, starting with the realization of a sub-set of the full array to "demonstrate" the soundness and feasibility of the chosen technical solutions. A key point in both projects is the capability of reducing the huge data flow (200 MB/s/segment, i.e. 8 GB/s/crystal) to values which can be handled by the available computer technology. For the full arrays, it will be impossible to store the original digitized data, implying that pulse shape analysis and γ-ray tracking should be performed in real time, and only the final results of the tracking process should be stored.

2 The AGATA Demonstrator at LNL

The AGATA Demonstrator consists of five AGATA triple clusters, arranged in the compact configuration shown in the Figure 1. Given that this configuration lacks spherical symmetry and that, contrary to conventional arrays, the detectors are not bound to a single source-detector distance, the performance of the AGATA Demonstrator depends on its position relative to the source. According to the Monte Carlo simulations reported in [4], the full peak efficiency of the array for 1 MeV photons ranges between 3% and 7% with a P/T ratio close to 60%. These values, later confirmed by the experimental data, are comparable to existing arrays of Compton-suppressed detectors. Therefore, in the initial phase, the emphasis to prove that AGATA will be a much superior device is put on the quality of the Doppler correction. This means that the AGATA Demonstrator is best exploited in combination with devices to track the incoming beam or the recoiling nuclei. The AGATA Demonstrator has been first installed at the Laboratori Nazionali di Legnaro (LNL), Italy, at the target point of the large-acceptance magnetic spectrometer PRISMA [5]. The initial goal of the campaign of measurements was to prove that indeed PSA and γ-ray tracking could be successfully performed in real time, on the most demanding conditions achievable in a low-energy stable-beam facility, i.e. with reactions with velocities of the γ-emitting products up to β 10% and with relatively high-intensity beams. Once this was achieved, the Demonstrator was used for physics experiments, mostly in coupled operation with PRISMA and with the array of MCP detectors DANTE [6] to study moderately neutron-rich nuclei populated by multi-nucleon transfer or deep inelas-

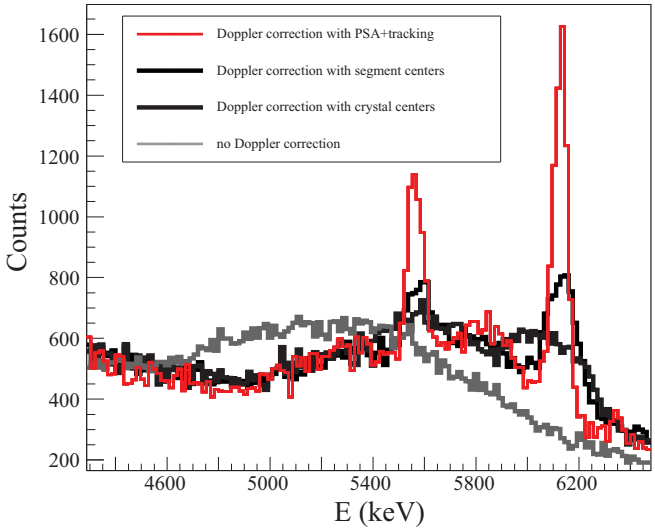

Fig. 2: Quality of the Doppler correction obtained with the AGATA Demonstrator coupled to the segmented silicon detectors of the TRACE project. Spectra obtained in coincidence with a ^{16}O nucleus detected within TRACE are shown, performing Doppler correction under different conditions. See text for details.

tic collisions with the stable beams delivered by the Tandem-PIAVE-ALPI accelerator complex. AGATA was also successfully coupled with other complementary detectors in order to exploit experimental possibilities such as direct, Coulomb excitation or fusion-evaporation reactions. The technical details on the installation of the Demonstrator at LNL are discussed in [7].

3 Performance of the AGATA Demonstrator at LNL

The commissioning campaign of the AGATA Demonstrator at LNL was carried out during 2009, through a series of source and in-beam tests. The overall performance of the device was quite satisfactory and has been the subject of technical reports, see for instance [8] or [9]. In the present contribution, we will just discuss the overall quality of the Doppler correction. The spectra shown in Figure 3 were obtained with the ^{17}O(340 MeV)+^{208}Pb reaction, where the projectile-like ^{16}O nuclei were detected in the 4 mm x 4 mm pads of the silicon detectors of TRACE [7]. In this particular example, Doppler correction was performed using the velocity corresponding to the scattering of a ^{16}O nucleus into the centre of the firing pad. Considering the AGATA crystals as a whole, no peaks are visible, but they clearly start standing out when the segmentation information is used and most importantly when the full information from PSA and tracking is available. The FWHM for the 6130 keV line in ^{16}O is 58 keV, which, although far from the intrinsic energy resolution of the germanium detectors, is fully consistent with the kinematics of the reaction, as verified with Monte Carlo simulations. The quality of the Doppler correction reflects the underlying performance of the pulse shape analysis. As shown in [10], the position resolution obtained with PSA techniques is slightly better than 4 mm FWHM for energies above 1 MeV.

4 The Physics Campaign at LNL

The AGATA Demonstrator has been exploited in a two-year experimental campaign at the Laboratori Nazionali di Legnaro, Italy. A total of 20 PAC-approved measurements were performed, plus 3 in-

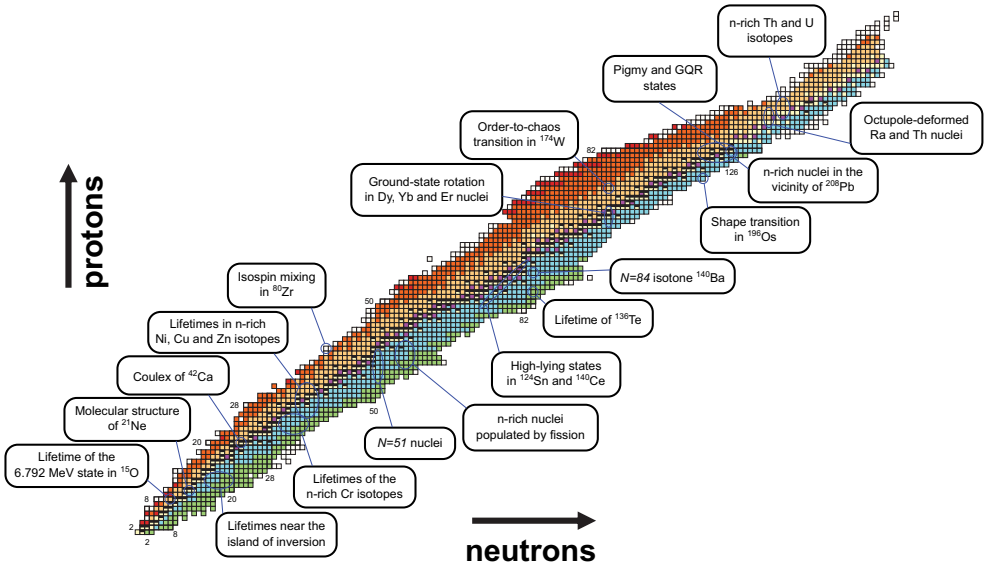

Fig. 3: Visual summary of the first experimental campaign of the AGATA Demonstrator, performed at the Laboratori Nazionali di Legnaro, Italy.

beam tests, for a grand total of 148 days of beam time. A visual summary of the campaign is shown in Figure 4. The campaign has focused mainly on the study of moderately neutron-rich nuclei populated via multi-nucleon transfer or deep-inelastic reactions in order to best exploit the possibilities offered by the coupling with PRISMA. However, the proton-rich side of the nuclides chart has been explored as well by coupling AGATA with complementary devices such as the silicon detectors of TRACE or the scintillators of HELENA [11] and HECTOR+ [12]. Given the novelty and relative complexity of the PSA and γ-ray tracking methods, the experiments are still in the analysis phase. Therefore, in this contribution we will just discuss a few preliminary results.

4.1 Lifetime measurement in Zn isotopes

A large fraction of the AGATA-PRISMA experiments at Legnaro aimed at measuring transition probabilities of neutron-rich nuclei populated in multi-nucleon transfer reactions, applying the Recoil Distance Doppler Shift method [13] with the differential plunger device developed at IKP Köln [7]. As a matter of fact, the technique was previously tested at LNL during the CLARA-PRISMA campaign [14]. As an example, we report here on an experiment aimed at studying the onset of collectivity in the zinc isotopes, which was performed with the ^{76}Ge(577 MeV)+^{238}U reaction. The systematics of B(E2; $2^+ \rightarrow 0^+$) for the even neutron-rich zinc isotopes, measured with Coulomb excitation experiments at the REX-ISOLDE facility [15], suggest that collectivity rapidly develops at $N = 40$ when moving away from ^{68}Ni, which shows instead a doubly-magic nature as suggested by the high excitation energy for its first excited state, together with a low B(E2; $2^+ \rightarrow 0^+$) value. Since the statistics in these experiments was not sufficient to extract the angular distribution of the ejectiles, an independent evaluation of the B(E2) via lifetime measurement is needed to derive the deformation of the involved isotopes. A paper on this measurement is forthcoming [16], here we will just mention that the B(E2) for ^{72}Zn, obtained via differential decay curve method [17] analysis, are in agreement with known values from the literature, while the corresponding values for ^{74}Zn are lower than the previously accepted values, thus shifting back

the maximum of B(E2; $2^+ \rightarrow 0^+$) for the Zn chain from $N = 44$ to $N = 42$.

4.2 Lifetime measurement in ^{15}O

As a second (and final) example, we report on a lifetime measurement to gather nuclear structure information of astrophysical interest related to the core metallicity of the Sun [18]. Assuming that all the relevant reaction cross sections are known, the carbon and nitrogen content in the center of the Sun can be deduced from the CNO neutrino fluxes. The overall energy production rate is determined by the slowest reaction of the cycle, namely by the ^{14}N(p,γ)^{15}O reaction. In particular, the width of the sub-threshold resonance corresponding to the 6.79 MeV excited state in ^{15}O plays a crucial role in the evaluation of the total astrophysical S-factor at zero energy, as discussed in [19]. To improve the accuracy of such value, a new direct measurement of the lifetime of this level was performed by means of the Doppler Shift Attenuation Method (DSAM) [13]. The technique was pushed to the fs range in which the lifetime of the level of interest is expected to lie by populating the excited level in ^{15}O in inverse kinematics, producing the ^{14}N beam at 32 MeV energy with the Tandem accelerator and using a deuterated gold target. The Demonstrator, used in standalone mode, consisted of 4 triple clusters. The details and the results of the analysis will be the subject of a forthcoming publication [20], here we will just mention that it was possible to construct energy versus angle matrices and to perform DSAM with an almost continuous angular distribution by exploiting the position-sensitive capabilities of the AGATA crystals. The level lifetime will be extracted through a comparison with detailed Monte Carlo simulations of the experimental setup and of the reaction process, which is mostly direct nucleon transfer with an admixture of fusion-evaporation. The method was validated with a known level in ^{15}N, populated during the same run. The preliminary results on ^{15}O point to a very short lifetime of the order of 1 fs, in agreement with the literature [21].

The author would like to thank all of the AGATA collaboration for the support during the experimental campaign at Legnaro. In particular, the author would like to thank Corinne Louchart and Caterina Michelagnoli for sharing their preliminary results.

References

[1] J. Eberth and J. Simpson, Prog. Part. Nucl. Phys. **60**, 283 (2008).
[2] M.A. Deleplanque et al., Nucl. Instr. and Meth. **A430**, 292 (1999).
[3] S. Akkoyun et al., Nucl. Instr. and Meth. **A668**, 26 (2012).
[4] E. Farnea et al., Nucl. Instr. and Meth. **A621**, 331 (2010).
[5] A.M. Stefanini et al., Nucl. Phys. **A701**, 217c (2002); S. Szilner et al., Phys. Rev. **C76**, 024604 (2007).
[6] A. Gottardo et al., Nucl. Phys. **A805**, 606 (2008).
[7] A. Gadea et al., Nucl. Instr. and Meth. **A654**, 88 (2011).
[8] F. Recchia et al., INFN-LNL-234, 60 (2011).
[9] B. Bruyneel et al., INFN-LNL-234, 64 (2011).
[10] P.-A. Söderström et al., Nucl. Instr. and Meth. **A638**, 96 (2011).
[11] M. Mattiuzzi et al., Nucl. Phys. **A612**, 262 (1997).
[12] R. Nicolini et al., Nucl. Instr. and Meth. **A582**, 554 (2007); F.G.A. Quarati et al., Nucl. Instr. and Meth. **A629**, 157 (2011).
[13] T.K. Alexander, J.S. Forster, in: M. Baranger, E. Vogt (Eds.), Advances in Nuclear physics, Vol.10, Plenum Publishing Corporation (1978)

[14] J.J. Valiente-Dobón et al., Phys. Rev. Lett. **102**, 242502 (2009).
[15] J. Van de Walle et al., Phys. Rev. Lett. **99**, 142501 (2007).
[16] C. Louchart et al., in preparation (2012)
[17] A. Dewald et al., Z. Phys. **A334**, 163 (1989).
[18] A.M. Serenelli et al., Astrop. Journ. Lett. **705**, L123 (2009).
[19] C. Broggini et al., Annu. Rev. Nucl. Sci., **60**, 53 (2010) and references therein.
[20] C. Michelagnoli et al., in preparation (2012)
[21] C. Michelagnoli et al., proceedings of the 11^{th} International Symposium on Origin of Matter and Evolution of Galaxies, Wako, Saitama, Japan, 2011 (in press).

Neutronics Analysis Around The Spalaltion Target For The MYRRHA ADS Design

Anna Ferrari
Helmholtz-Zentrum Dresden-Rossendorf, PF 510119, 01314 Dresden, Germany
a.ferrari@hzdr.de

The present study has been done in the framework of the Central Design Team European project (CDT), which has the goal to design the FAst Spectrum Transmutation Experimental Facility (FASTEF), able to demonstrate efficient transmutation of high level waste and associated ADS technology. On the FASTEF design will be based the MYRRHA facility at SCK·CEN in Mol (Belgium), which should start the construction phase in 2015. The heart of the system is a 100 MW lead-bismuth eutectic (LBE) cooled reactor, working both in critical and sub-critical modes. The neutrons needed to sustain fission in the sub-critical mode are produced via spallation processes by a 600 MeV, 4 mA proton beam, which is provided by a linear accelerator and hits a LBE spallation target located inside the reactor core.

Starting from the initial need to assess the shielding of the reactor building and to characterize the irradiation of the materials in the last part of the proton beam-line, an extensive simulation study has been done to define the radiation fields around the spallation target, with special attention to the neutron component. Using a description that includes the last part of the proton beamline and the LBE spallation target, neutron yields and spectra have been computed with both Monte Carlo codes FLUKA (version 2011.2) and MCNPX (version 2.6.0), where in the second case different fragmentation/evaporation models have been used and compared. As second step the neutron fluence behavior has been estimated in the whole structure around the reactor core, including fission neutrons. In this case a full MCNPX model has been used, including the vertical part of the proton beamline, the spallation target, the reactor core and the structure around, from the coolant until the external vessel, the reactor cover and the shielding walls. With the aim to compare the results, an additional simulation has been performed with the FLUKA code, using neutron source terms evaluated in the previous MCNPX calculations on suitable surfaces close to the reactor core.

All the results of the neutronics analysis are presented and discussed, together with the main implications on the design solutions.

Spectroscopy of neutron-rich nuclei at REX-ISOLDE with MINIBALL

Th. Kröll for the MINIBALL and REX-ISOLDE collaborations
Institut für Kernphysik, Technische Universität Darmstadt, Darmstadt, Germany

Abstract
In this contribution, recent results obtained in nuclear structure studies with post-accelerated radioactive ion beams from the REX-ISOLDE facility at CERN are presented. The method employed is γ-ray spectroscopy with the MINIBALL array following "safe" Coulomb excitation and nucleon-transfer reactions.

1 Introduction

ISOLDE at CERN is the world-leading ISOL ("Isotope Separation OnLine") facility with more than 45 years of experience in producing low-energy radioactive ion beams (RIBs) [1]. So far, more than 1000 different isotopes have been delivered to experiments. The 1.4 GeV proton beam from the PS Booster impinges on a thick production target, in most cases discussed in this contribution consisting of UC_x/graphite ($\approx$ 50 g/cm^2 ^{238}U). Alternatively, the protons irradiate a Ta or W rod next to the production target and the generated neutrons induce the fission of the uranium. Compared to the direct proton impact, the chemical or isotopical composition of the fragments is changed. The produced nuclei diffuse within the heated target and reach the ion source. Here, a selection of the chemical element is intended. Sometimes it is possible to ionise only a certain isotope or even a single long-lived state of the nucleus. The highest selectivity is offered by the RILIS ("Resonant Ionisation Laser Ion Source"). The singly charged ions are extracted and sent through one of the two mass separators available at ISOLDE (GPS and HRS). In principle, the selection of the chemical element and the mass allows for isotopically pure beams. However, most of the beams contain a cocktail of different isobars because non-selective thermal ionisation is unavoidable. After passing the separator, a 30-60 keV low-energy beam can be sent to the experiments.

The idea of the REX-ISOLDE facility has been to post-accelerate these beams enabling nuclear reaction studies [2]. Firstly, the ions are cooled and bunched in a penning trap (REXTRAP). Then, they are sent to a second trap where the ions are charge bred, i.e. their charge state is increased by collisions with an intense electron beam (REX-EBIS). At a mass to charge ratio of about $A/q = 4$, the ions are injected into a linac (REX-LINAC) where the energy is boosted to currently up to 3 MeV/u. REX-ISOLDE operates now successfully for 10 years and post-accelerated ISOL beams of more than 80 isotopes of elements ranging from Li to Ra have been delivered to experiments.

The most important instrument for the study of exotic nuclei at REX-ISOLDE is the highly efficient MINIBALL spectrometer consisting of 8 triple clusters of six-fold segmented HPGe detectors [3]. MINIBALL was the first large γ-ray spectrometer equipped with fully digital electronics. The γ-rays are usually measured in coincidence with beam- and target-like nuclei detected by arrays of segmented Si detectors.

2 Coulomb excitation

Many experiments at REX-ISOLDE with MINIBALL employ γ-ray spectroscopy following "safe" Coulomb excitation as a tool to study collective properties of exotic nuclei. Here, the beam energy is chosen such that projectile and target interact only via the well-known electromagnetic interaction. The radioactive isotope of interest impinges as beam on a target and either of them (or both) can be excited. From the double-differential cross sections, extracted from the measured γ-ray–particle yields, the electromagnetic matrix elements are determined. As the cross section depends on both transitional

but also diagonal matrix elements, reduced transition probabilities $B(E\lambda)$ as well as electric quadrupole moments Q_2 can be measured. In the analysis, the experimental data are compared with results of calculations solving a system of coupled differential equations to obtain the cross sections for a set of matrix elements. The use of a target nucleus with known properties allows for a analysis of the projectile excitation relative to the target excitation avoiding the necessity to determine absolute efficiencies and beam intensities. Other observables, like lifetimes or g factors, have been measured too by adapting methods used with stable beams to the requirements for experiments at REX-ISOLDE.

However, as isobaric contaminants in the beam excite the target as well the beam composition has to be determined. Different methods have been developed for this task comprising switching on/off the RILIS, stopping the beam inside MINIBALL and analysing the characteristic decay γ-rays, or using a $\Delta E - E$ telescope or a Bragg detector mounted in the beam dump downstream of MINIBALL.

One corner stone of the physics programme aims for the study of the evolution of collectivity near shell closures in exotic nuclei. Some key isotopes investigated at REX-ISOLDE are ^{30,32}Mg [4], ^{68}Ni [5], neutron-rich Cu isotopes [6–8], ^{80}Zn [9, 10], ^{96}Kr [11] and the region around ^{132}Sn.

The isotope ^{132}Sn is the heaviest doubly-magic nucleus below ^{208}Pb which is experimentally accessible. As the astrophysical r process is expected to pass via this region, the understanding of the nuclear structure is also important for modelling the nucleosynthesis. At REX-ISOLDE, the Cd and Xe isotopical chains have been investigated. For the even isotopes $^{138-144}$Xe, the preliminary $B(E2; 0^+_{\rm gs} \rightarrow 2^+)$ values obtained at REX-ISOLDE are well within the range of predictions by both a simple Grodzins-type systematics and theory calculations [12, 13]. The same regular behaviour is observed for the Ba isotopes. Recently, it was possible by the combination of the cross section for Coulomb excitation and the lifetime from a DSAM measurement, both experiments were performed at REX-ISOLDE with MINIBALL, to determine the quadrupole moment of the first 2^+ state in ^{140}Ba [14].

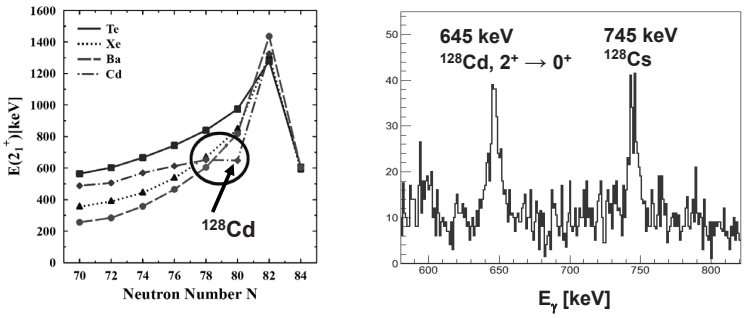

Fig. 1: Systematics of excitation energies $E(2^+)$ around ^{132}Sn (left) and preliminary Doppler corrected γ-ray spectrum following "safe" Coulomb excitation of ^{128}Cd (right) [16]. An additional γ-ray at 745 keV has been assigned as new transition to ^{128}Cs, an isobaric contaminant in the beam.

Below Sn, the Cd isotopes are of particular interest. The even isotopes $^{122-128}$Cd and the odd ^{123}Cd have been investigated at REX-ISOLDE [12, 13, 15, 16]. A special case is the isotope ^{128}Cd, a short-lived nucleus ($T_{1/2} = 280$ ms) which is already 12 neutrons off stability. Although being nearer to the shell closure at $N = 82$, the excitation energy of the first 2^+ state is lower than in the lighter neighbour ^{126}Cd (Fig. 1, left). This strikingly irregular behaviour cannot be explained by shell model calculations. Only beyond-mean-field calculations are able to reproduce the energy and predict a considerable deformation for this nucleus having only two protons and two neutrons less than the doubly-magic ^{132}Sn [17]. At REX-ISOLDE, the quadrupole collectivity of ^{128}Cd has been studied recently [16]. Fig. 1

(right) shows the preliminary γ-ray spectrum obtained after Doppler correction with respect to the scattered Cd ions. The obtained $B(E2)$ value will challenge the predictions from theory.

Recently, also very heavy nuclei became available as beams at REX-ISOLDE. E.g the phenomenon of shape coexistence has been investigated in light Hg and Po isotopes. Other important results obtained from Coulomb excitation concern the investigation of octupole collectivity in Rn and Ra isotopes with $^{224}\mathrm{Ra}$ being the first isotope for which a $B(E3)$ value has been measured at REX-ISOLDE [18].

3 Transfer reactions

In the last some years, one- and two-neutron transfer reactions became an important tool to study single-particle properties at REX-ISOLDE. A dedicated set-up of segmented Si detectors with a large solid angle coverage, T-REX, has been constructed allowing to measure energy and position of light charged particles as well as to identify the species [19]. So far, (d,p) and (t,p) reactions in inverse kinematics have been studied with T-REX and MINIBALL.

The transfer data are analysed using the DWBA approach which is based on the use of empirical optical potentials. The observed cross section is described by the calculated cross section multiplied by a "spectroscopic factor" which is given by the overlap of the neutron(s) coupled to the inital state and the wave function of the final state. However, the concept of "spectroscopic factors" is highly debated. In practice, a problem is that the parameters of the optical potentials are not known for radioactive nuclei. They have to be extrapolated from parameter sets determined for stable beams or fitted to the elastic scattering measured in the actual experiment. We can conclude that the extracted cross sections in the experiments presented below depend only slightly on the actual choice. In Fig. 2, the experimental differential cross section for elastic scattering of $^{30}\mathrm{Mg}$ at an energy of 1.8 MeV/u on protons and tritons is shown in comparison with results from DWBA calculations using different optical potentials [20].

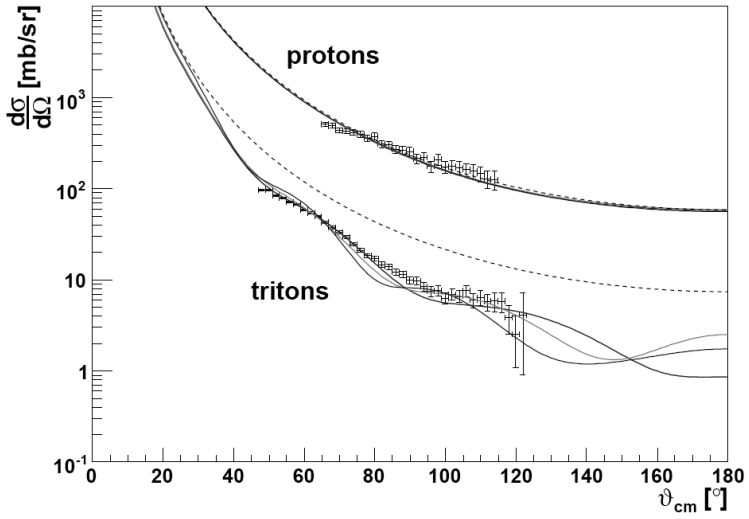

Fig. 2: Elastic scattering of $^{30}\mathrm{Mg}$ on protons and tritons at 1.8 MeV/u. Pure Coulomb potential (dashed lines) and extrapolated or fitted optical potentials (solid lines) [20].

One physics case studied in experiments performed at REX-ISOLDE was the investigation of

the nuclear structure at the border of the "island of inversion", a region of the nuclear chart where the traditional shell closure at $N = 20$ disappears. Excited states in the isotopes ^{31,32}Mg have been populated by (d,p) and (t,p) reactions in inverse kinematics [20–22].

Most prominent result was the discovery of the long-sought second 0^+ state in ^{32}Mg. From most experimental data and theory calculations it has been concluded that in ^{30}Mg exists a coexistence between two 0^+ states with different shapes, the nearly spherical ground state and a deformed excited 0^+ state. Hence, ^{30}Mg is outside of the "island of inversion", see e.g. [4, 23]. For ^{32}Mg, the situation is not so clear yet. The large $B(E2; 0^+_{\rm gs} \rightarrow 2^+)$ value indicates a deformed ground state with a fp intruder configuration, hence the nearly spherical sd configuration forming the ground state of ^{30}Mg is expected as an excited 0^+_2 state in ^{32}Mg. However, such a state has never been observed experimentally before. At REX-ISOLDE, the population of an excited 0^+ state was unambiguously identified by the angular distribution of the protons following a (t,p) reaction on a ^{30}Mg beam which was characteristic for an orbital angular momentum transfer $\Delta L = 0$. As the two-neutron transfer will populate only $0p - 0h$ or $2p - 2h$ configurations in ^{32}Mg, the wave functions of the populated states will have the respective configurations and, consequently, large cross sections for the ground state ($2p - 2h$) and the 0^+_2 state ($0p - 0h$) are expected. Such an experiment became feasible because of the use of a tritium loaded Ti foil as target, the first radioactive target at REX-ISOLDE. The cross section for the population of the newly found 0^+ state is consistent with the assumption of a sd-configuration with a $p_{3/2}$ admixture, similar as the ground state of ^{30}Mg. However, the low excitation energy remains a challenge for nuclear theory.

Further experiments performed during the last years are still under analysis. The nuclei investigated were ^{12}Be, ^{46}Ar, ^{67,68}Ni, and ^{79}Zn. Aim is to investigate the evolution of shell closures at $N = 8, 28, 40$, and 50.

Currently, transfer reactions are limited by the available beam energy to medium-mass nuclei up to $A = 80$, because for heavier beams the angular distributions of the light products become more and more flat and featureless. This prevents to extract the transferred orbital angular momentum from the data. However, cross sections at low energy are of importance for astrophysical scenarios.

4 Summary and Outlook

The concept of the REX-ISOLDE facility at CERN, the post-acceleration of low-energy ion beams from ISOLDE, has been proven to be highly successful. With a broad range of isotopes at energies of up to 3 MeV/u available, many aspects and questions concerning the structure of exotic nuclei far-off the valley of stability have been addressed. Most important method is the γ-ray spectroscopy following "safe" Coulomb excitation and nucleon-transfer reactions. The experimental set-up consisting of the efficient high-resolution HPGe spectrometer MINIBALL in combination with arrays of segmented Si detectors is a powerful and versatile instrumentation to perform such studies.

In the near future REX-ISOLDE will be upgraded step-wise to HIE-ISOLDE [24]. By the end of 2014, beam energies of up to 5.5 MeV/u will be available. In a second step, the energy will be increased further up to 10 MeV/u. This is achieved by replacing the resonators of the REX linac with superconducting cavities. Additionally, higher beam intensities and an improved beam quality are envisaged.

The higher beam energy will allow to extend the physics programme considerably. In Coulomb excitation experiments with heavy targets, the probability for multi-step processes as well as for one-step excitation of high-lying states will be strongly enhanced. In particular, transfer reactions will profit as at HIE-ISOLDE such reactions can be studied also with heavy beams, some of them are unique to ISOLDE as low-energy beams. Such experiments aim at the investigation of single-particle properties in heavy nuclei. The investigation of the evolution of single-particle orbitals near shell closures will challenge modern shell model calculations. One aspect e.g. is the spin-orbit coupling in exotic nuclei which may be altered by a more diffuse surface of neutron-rich nuclei. Two-neutron transfer reactions

are an excellent tool to populate shape-coexisting 0^+ states as well as to study pairing correlations far-off stability.

The success of REX-ISOLDE and the perspectives at HIE-ISOLDE have initiated also ideas for additional new instrumentation to be operated at HIE-ISOLDE like a helical orbit spectrometer, HELIOS, to study nucleon-transfer reactions. A major step will be the installation of the storage ring TSR [25]. It will allow for the study of reactions of stored exotic nuclei with an internal gas target.

These developments will extend the physics programme conducted at ISOLDE to new horizons and the study of exotic nuclei at CERN has a bright future.

Acknowledgements

This contribution represents the work of many groups, in particular PhD students and young postdocs, from all over Europe. The success of the REX-ISOLDE is owed to the large commitment of the ISOLDE and REX teams resulting in a continuous improvement of the facility.

The author acknowledges support by the German BMBF under grants 06MT238, 06DA9036I, 06DA7040, HIC for FAIR, EU through EURONS (No. 506065) and ENSAR (No. 262010) as well as the MINIBALL/REX-ISOLDE collaborations.

References

[1] `http://isolde.web.cern.ch/ISOLDE/`.
[2] D. Habs *et al.*, *Nucl. Instr. and Meth.* **B 139** (1998) 139; `http://isolde.web.cern.ch/ISOLDE/REX-ISOLDE/index.html`.
[3] J. Van de Walle *et al.*, *Eur. Phys. J. A* (in preparation).
[4] O. Niedermaier *et al.*, *Phys. Rev. Lett.* **94** (2005) 172501.
[5] N. Bree *et al.*, *Phys. Rev.* **C 78** (2008) 047301.
[6] I. Stefanescu *et al.*, *Phys. Rev. Lett.* **98** (2007).
[7] I. Stefanescu *et al.*, *Phys. Rev. Lett.* **100** (2006) 112502.
[8] E. Rapisarda *et al.*, *Phys. Rev.* **C 84** (2011) 064323.
[9] J. Van de Walle *et al.*, *Phys. Rev. Lett.* **99** (2007) 142501.
[10] J. Van de Walle *et al.*, *Phys. Rev.* **C 79** (2009) 014309.
[11] M. Albers *et al.*, *Phys. Rev. Lett.* **108** (2012) 062701.
[12] Th. Kröll *et al.*, INPC2007 proceedings, *Nucl. Phys.* **A 805** (2008) 394.
[13] T. Behrens, PhD thesis (TU München, 2010).
[14] C. Bauer *et al.*, *Phys. Rev.* **C** (in press).
[15] S. Ilieva et al., in preparation.
[16] S. Bönig *et al.*, ISOLDE Workshop 2011.
[17] T. R. Rodríguez *et al.*, *Phys. Lett.* **B 668** (2008) 410.
[18] L. Gaffney, PhD Thesis (University of Liverpool, 2012); to be published.
[19] V. Bildstein *et al.*, *Eur. Phys. J.* **A 48** (2012) 85.
[20] K. Wimmer, PhD Thesis (TU München, 2010).
[21] K. Wimmer *et al.*, *Phys. Rev. Lett.* **105** (2010) 252501.
[22] V. Bildstein, PhD Thesis (TU München, 2010); to be published.
[23] W. Schwerdtfeger *et al.*, *Phys. Rev. Lett.* **103** (2009) 012501.
[24] `http://hie-isolde.web.cern.ch/hie-isolde/`.
[25] M. Grieser *et al.*, *Eur. Phys. J. Special Topics* **207**, (2012) 1.

Status of J-PARC after the Earthquake on 2011 March 11

K.H. Tanaka
Particle and Nuclear Physics Division, J-PARC Center, and
Institute of Particle and Nuclear Studies (IPNS),
High Energy Accelerator Research Organization (KEK),
Oho 1-1, Tsukuba-shi, Ibaraki-ken, 305-0801 JAPAN.

Abstract
Recovery of J-PARC from the big earthquake happened on 2011 March 11 is reported. Recovery itself was favourable for us and its essential part was completed by the beginning of December 2011. We then stared the accelerator operation from December 9. Experiments with slow extraction started in February 2012 and the neutrino experiment with fast extraction followed it. Recent activities of J-PARC on particle and nuclear physics are described, too.

1 Accelerators and facilities of J-PARC

Japan Proton Accelerator Research Complex (J-PARC) [1, 2] is the brand new and state of the art accelerator complex in Japan. The construction of the J-PARC started in 2001 and completed its Phase-1 construction in the early 2009. The construction site of J-PARC is near the beautiful seashore facing Pacific Ocean in the Tokai campus of Japan Atomic Energy Agency (JAEA) since J-PARC is a joint project of High Energy Accelerator Research Organization (KEK) and JAEA.

J-PARC consists of three stages of accelerators, the proton linear accelerator (LINAC) of 181 MeV, the rapid-cycle 3 GeV proton synchrotron (RCS), and the main 50 GeV Proton Synchrotron (50 GeV-PS). The photograph of the J-PARC completed in Tokai is shown in Fig. 1.

The design value of the beam intensity of J-PARC's main accelerator, 50 GeV-PS, is 15 μA, which means the beam power of 750 kW. By using this high-power primary proton beam, the intense production of kaons, pions, and many other rare secondary and tertiary particles such as antiprotons and neutrinos will be made in order to promote unprecedented progress in both nuclear and particle physics. In this meaning the J-PARC 50 GeV-PS is the first real KAON Factory [3] accelerator in the world.

The J-PARC 50 GeV-PS has two extractions. One is for the slow extraction for the fixed-target experiments at the Hadron Experimental Hall, and the other is the single-turn fast extraction for the neutrino beam production. The latter beam is solely used for T2K experiment [4], i.e. Japanese accelerator based long baseline neutrino oscillation experiment. Many other experiments are running or under preparation in the Hadron Experimental Hall.

A cascade acceleration scheme was employed for J-PARC. The 3 GeV RCS is used as an injector to the 50 GeV-PS. However only a few percent of the extracted 3 GeV proton beam from RCS is injected to 50 GeV-PS. Then the rest of the extracted beam can be used solely for driving spallation neutron source and pulsed muon source at Material and Life Science Research Facility (MLSF). The design value of RCS beam power for MLSF is 1 MW.

Now construction of J-PARC was completed and the beam has already been accelerated by 50 GeV-PS up to 30 GeV, which is project's first goal at the Phase-1 construction. The first slow beam from the 50 GeV-PS was extracted to the Hadron Hall in January 2009 and the first fast beam was delivered to T2K experiment in April 2009. Beam power for T2K increased gradually and has reached

approximately 145 kW for steady operation in March 2011. Beam power of slow beam was limited up to 5 kW by the beam loss at the extraction devices from 50 GeV-PS. However, very high extraction efficiency of 99.6%, which is almost the theoretical limit of slow extraction, has been achieved after the stimulated beam study. Higher beam power operation was then promising and the first high intensity run has been scheduled in April 2011. Beam power of RCS reached 200 kW for steady operation and 300 kW for short term trial in early 2011. Intensity of spallation neutrons and pulsed muons of MLFS increased gradually and continued to break its own world records day by day.

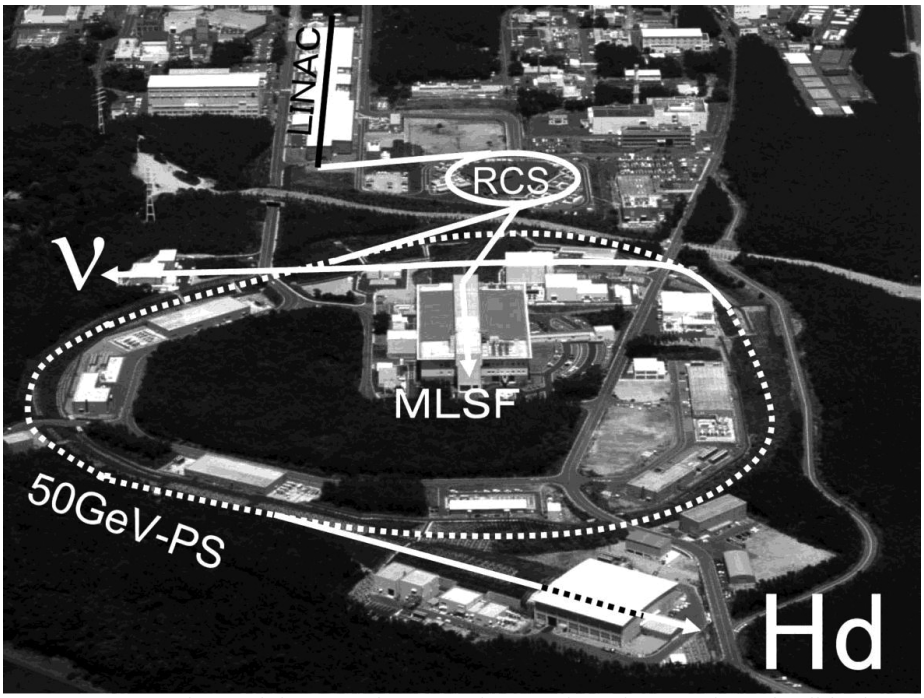

Fig. 1: J-PARC site at Tokai campus of JAEA. "Hd" means the Hadron Experimental Hall for the fixed target experiments with slow extraction. "**ν**" indicates the neutrino experimental facility with fast extraction. "MLSF" indicates the Material and Life Science Research Facility where the spallation neutron and pulsed muon sources are operated by using intense 3 GeV proton beam provided from Rapid Cycle Synchrotron (RCS).

2 Influence of the earthquake

At 2:46pm on March 11 in 2011, Tohoku Region Pacific Coast Earthquake hit J-PARC. Approximately 40 minutes later, tsunami of a height of about 4m and the maximum run-up of about 6m attacked the shore of the J-PARC site. After the careful inspection of the mark of the tsunami left at the seashore, it was understood later that it had been exactly a near miss to the worst situation that the tsunami flows in the J-PARC site. Thanks to geographical features around the J-PARC, the worst case had been fortunately avoided. Finally it was found that no one was injured by the earthquake and tsunami at the J-PARC site. In addition, no radiation problem happened in J-PARC.

Fig. 2: Road around LINAC was completely destroyed by the earthquake. Approximately 1.5m drop of road surface was observed at wide area. Electric wires and water pipes set in the underground were all seriously damaged.

Fig. 3: At the neutrino experimental facility, ground surface around beam dump (i.e. area covered by grey tent in the photograph) seriously subsided. Beam dump itself was sustained by many underground pins and less damaged. Land around the target station subsided also.

After the earthquake, we had to concentrate to recover our own life for almost a week and we could perform the first inspection throughout the J-PARC facilities on March 17. At that time electricity was not recovered at all and no detailed inspection was possible. Then we found, fortunately, there was almost no obvious structural damage in the accelerators and experimental facilities due to many underpins underneath the buildings. However, all roads around the buildings and the utilities such as water pump stations and electric transformer yards had severe damages. In Figs 2-3, one can see the serious influence of the earthquake to J-PARC. It should be noted that we found small water leaks at the wall of the accelerator tunnel at the first inspection after the earthquake and, however, the leakage grew up day by day. Finally, especially in LINAC tunnel, water depth from the floor increased approximately 10cm a day. It was one of the most serious challenges to us. We had to collect water pumps to rescue LINAC and had to find engine generators to operate the pumps since no electricity was available at LINAC area for a long time. The same kind of water leaks were found at 50 GeV-PS tunnel also. After those inspections and urgent rescue actions we could start regular recovery works of our J-PARC facilities. Japanese Government supported us strongly, too.

After detailed inspections of our facilities, it was found that all the magnets and related beam devices such as beam monitors slipped off in the range of mm to cm from their appropriate positions. These were relatively small troubles but number of devices which should be restored was so big. Then we understood that we need very long time for re-alignment of all the devices slipped off.

In the late May, electricity and cooling water were not recovered at whole J-PARC area then, we decide the recovery schedule of J-PARC. We should complete the rebuilding of our experimental facilities by the end of year 2011 and our accelerator complex should start the beam acceleration at the same time. Experimental programs should be re-started in the spring run period (January-March) in 2012. We aimed to perform at least 2-cycle (two months) beam operation for experiments then. For the operation of next Japanese Fiscal Year, 2012, we should request the budget to operate J-PARC for full 9 cycles (200 days) for users. These Goals seemed too high. However should be achieved if we would stay at the top of the accelerator science. Fortunately the recovery schedule was accomplished early for a few days.

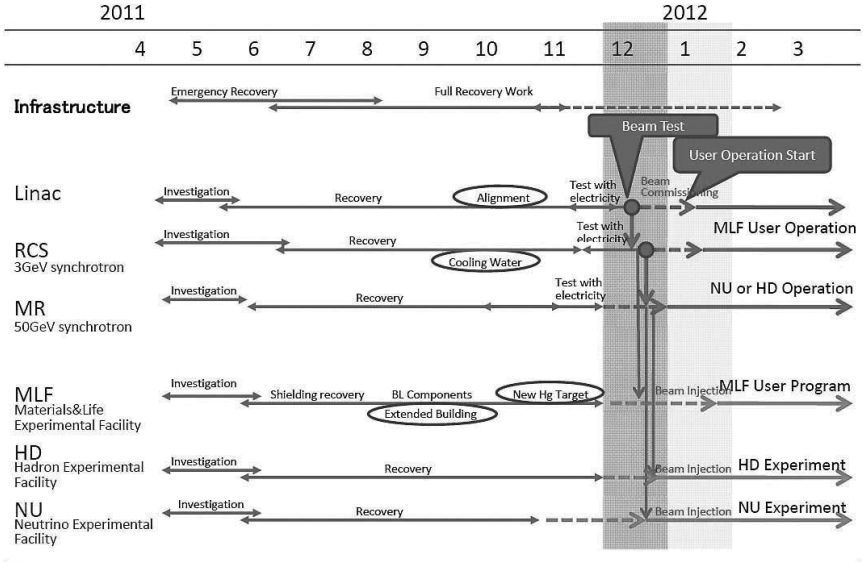

Fig. 4: Recovery schedule of J-PARC decided in the late May 2011. We aimed at recovering by the end of year 2011, and expecting to have 2-cycle (approximately two months) running by March 2012. Fortunately the recovery schedule was accomplished early for a few days.

3 Scientific activities after the earthquake

Even during the hard work days for J-PARC recovery, our scientific motivation to bring new physics results was still continuing. Though we could not perform experiments with beams, experimental data accumulated before the earthquake were analyzed intensively. The first good indication of new physics had come from T2K collaboration. Based on the analysis of all data collected before the earthquake, it was found that 88 neutrino events were detected by the Super-Kamiokande, i.e. the far detector of T2K experiment. Among them, six candidate events were cleanly identifiable as electron neutrino interactions. In the current T2K experiment, possible background for electron neutrino event was simulated to be approximately 1.5. Then the probability of the existence of electron neutrino appearance was estimated to be 99.3%, suggesting the appearance of electron neutrinos for the first time. Details of this T2K result can be seen in the published paper [5]. Now the number of electron event increased to be 10 as seen in Fig. 5 and we can say that the probability of the existence of electron neutrino appearance is 99.92% (3.2σ). The other interesting result came from E19 experiment at Hadron Experimental Hall. Experiment to produce pentaquark Θ^+ by strong interaction was performed via $p(\pi^-,K^-)$ reaction [6]. Unfortunately no significant peak indicating Θ^+ production was seen. However possible structure of Θ^+ was strongly limited by this E19 result.

Scientific activity at both Hadron Hall and Neutrino Facility was so high even after the earthquake. Especially in the Hadron Hall, several experimental teams are constructing new detector systems and are waiting for the beam time scheduled in the autumn 2012. For example, E14 (KOTO) collaboration, search for rare K decay in $K_L \rightarrow \pi^0\nu\nu$, completed the construction of CsI calorimeter wall, which was once used at KTeV experiment at FNAL, before the earthquake, and the wall itself was found healthy even after the earthquake. Then KOTO experiment will be ready in the late 2012 as scheduled. DO NOT MISS new physics outputs from 2012-2013 beam season of J-PARC.

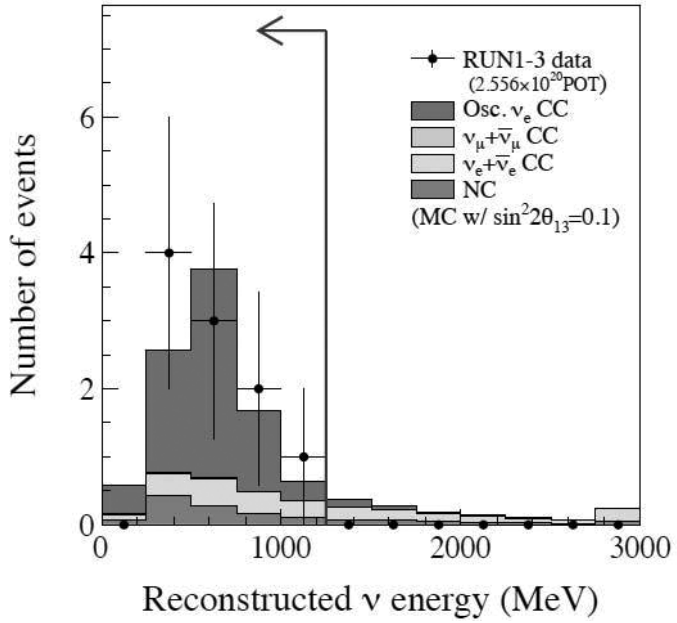

Fig. 5: Energy spectrum of electron neutrinos observed at Super-Kamiokande. Ten candidate events have been observed with possible background of 2.73. It indicates the probability of the existence of electron neutrino appearance is estimated to be 99.92% (3.2σ).

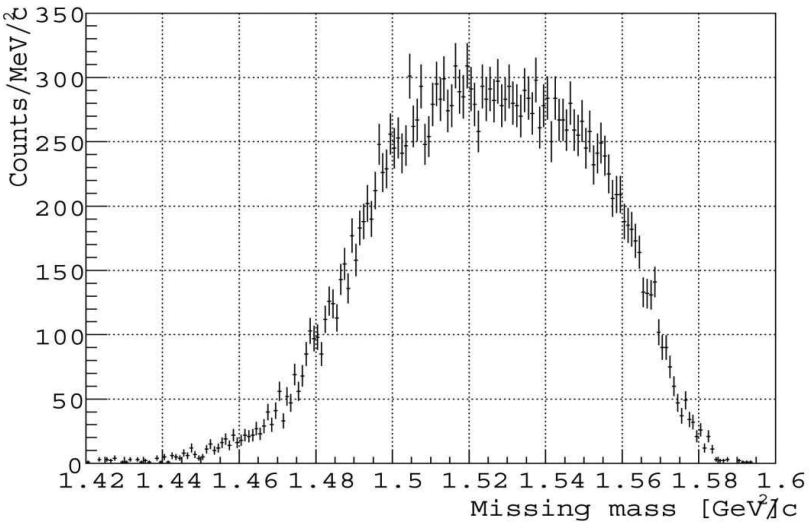

Fig. 6: Missing mass spectrum observed in (π^-, K^-) reaction on hydrogen target. No significant peak is seen in the spectrum, which indicates upper limit of Θ^+ production with this process is approximately 0.4μb (90%C.L.)

Acknowledgement

The author would like to express his thanks to professors and doctors A. Suzuki, S. Nagamiya, K. Nishikawa and Y. Ikeda of KEK, JAEA and J-PARC directorates for their warm encouragement throughout the present recovery works. The author would like to thank those who extended their warm-hearted support during the most serious days of J-PARC after the earthquake.

References

[1] J. Chiba et al., JHF98, *KEK Proceedings 98-5* (1998).

[2] Joint Project team of JAERI and KEK, The joint project for high-intensity proton accelerators, *KEK Report* 99-4 and *JAERI-Tech* 99-056, July 1999.

[3] TRIUMF, Kaon Factory Proposal, 1985.

[4] Y. Itow et al., The JHF-Kamioka Neutrino Project, *KEK-Report* 2001-4, 2001, and *arXiv:hep-ex*/0106019v1.

[5] G K. Abe et al., Indication of Electron Neutrino Appearance from an Accelerator-produced Off-axis Muon Neutrino Beam, *Phys*. *Rev*. *Lett*. 107 (2011) 041801.

[6] K. Shirotori et al., Search for the Θ^+ pentaquark via the $\pi^- p \to K^- X$ reaction at 1.92 GeV/c, *Phys*. *Rev*. *Lett*. 109, 132002 (2012) and *arXiv:nucl-ex*/1203.3604.

The Fazia initiative: more powerful detectors for a more detailed investigation on the origin and the decay of charged fragments

G.Casini[1], *S.Barlini*[1], *G.Pasquali*[1], *S.Carboni*[1], *N.Le Neindre*[2], *M.Bini*[1], *B.Borderie*[3], *R.Bougault*[2], *P.Edelbruck*[3], *M.Merciai*[1], *A.Olmi*[1], *G.Poggi*[1], *M.F.Rivet*[3], *A.A.Stefanini*[1], *E.Scarlini*[1], *G.Baiocco*[2,4], *R.Berjillos*[5], *E.Bonnet*[6], *M.Bruno*[4], *A.Chbihi*[6], *J.A.Dueñas*[5], *F.Gramegna*[7], *A.Kordyasz*[8], *T.Kozik*[9], *V.L.Kravchuk*[7], *O.Lopez*[2], *T.Marchi*[7], *L.Morelli*[4], *M.Parlog*[2], *S.Piantelli*[1], *E.Rosato*[10], *E.Vient*[2], *M.Vigilante*[10] *for the FAZIA collaboration*
[1]INFN and University of Florence, Italy
[2]LPC Caen, ENSICAEN University of Caen, CNRS/IN2P3, Caen, France
[3]IPN Orsay, CNRS/IN2P3 and University of Paris-Sud XI, Orsay, France
[4]INFN and University of Bologna, Italy
[5]Huelva University, Spain
[6]GANIL, Caen, France
[7]INFN-LNL and University of Padua, Italy
[8]Warsaw University, Poland
[9]Jagellonian University, Kracow, Poland
[10]INFN and University of Naples, Italy

Abstract

The main results of the R&D program of the FAZIA collaboration are described. The objective was to improve particle identification capabilities from solid-state telescopes made of Silicon detectors and CsI(Tl) scintillators in view of a new large acceptance apparatus to be used for heavy-ion physics. Important progresses have been made on silicon detectors thanks to a careful control of the material, of its doping uniformity and of the crystal orientation. Moreover, the use of appropriate fast digital electronics allowed to extract maximum information via Pulse Shape Analysis and to propose new configurations of CsI(Tl) readout. Some of the recent results of the telescopes are discussed here, together with some perspective and preliminary data on the physics program at intermediate bombarding energies

1 Introduction

In recent years, heavy-ion physics put the focus on the isospin degree of freedom which can be particularly stressed when using radioactive beams to perform experiments. With their employment, important steps can be done both in nuclear structure and in reaction mechanisms because one can explore ground state properties and excited states of nuclei which are far from the beta stability. Fundamental aspects of nuclear science like the evolution of shell closures and of the level lifetimes, the modification of basic reaction processes like fusion or fission, the finding of exotic decay modes and correlation phenomena related to unusual shapes, all these subjects can be investigated in the scarcely explored region towards the nuclear drip lines.
Let's focus on reaction processes: it is particularly interesting to study how the reaction cross section varies, at the different energy and mass scales, with changing isospin. There are, for example, specific effects related to loosely bound neutrons which have been investigated in light n-rich halo-nuclei [1] but which have been so far poorly known for heavier systems in relation with neutron skin or surface [2]. A big subject is the symmetry energy term, which favours the same number of protons and neutrons in nuclei. This term is not well known for systems at densities far from the saturation value and at high excitation energies; indeed, several behaviors have been theoretically proposed [3,4]. In heavy-ion reactions,

as a function of the energy and of the impact parameter, the interacting system heats up and experiences density variations (compression and expansion); thus, isospin dynamics can suitably investigated and the effects are obviously enhanced in nuclei far from the β-stability.

Coming to the decay modes, it is well known that "hot" and rapidly spinning systems are formed in ion collisions. Therefore, also the description of the decay of these systems, possibly with unusual isospin values, can be an other interesting field, where the interplay between structure and dynamics for exotic species is strong. In this context, we just cite results on (alpha-)cluster phenomena observed in weakly excited N=Z systems [6] or in fusion-like reactions between very light systems [7]. Moreover, we mention the ongoing developments of theory, in the different sectors of collective [8], stochastic [9] or TDHF [5] models to better describe the trend of the reaction cross section from low to intermediate energies (5 to 50 MeV/u).

As the isospin is a crucial variable, it is important that the reaction products be identified both in charge and in mass. This can be reached using powerful spectrometers which offer so far the best mass and charge resolution up to the heaviest ions. A limitation of these devices is their acceptance, which is typically poor and doesn't allow for a (almost) complete event reconstruction, as recommended in collisions with production of many fragments (in particular at the Fermi energy regime).

All above considered, the european FAZIA collaboration [10] was born some years ago in order to improve the operation of silicon and scintillation detectors and to push at the limits their particle identification capabilities also by means of fast-sampling digital electronics. The technological research has led to excellent results and to the definition of a powerful three layer telescope Si-Si-CsI(Tl), a typical choice of modern set-up (see e.g. Reff. [11,12]). Some recent results [13–18]) are discussed here together with some preliminary data which show the FAZIA capabilities for isospin studies at intermediate energies, as planned for our first future experimental campaign. Indeed, a modular array of about 200 telescopes is under construction and should be commissioned in 2014.

2 The FAZIA activities and the Telescope concept

FAZIA is an european collaboration of France, Italy, Poland, Romania and Spain. As said, the driving idea of the initiative, also pushed by the development of Radioactive Ion Beams (RIB) facilities at GANIL and at Legnaro, was to improve the performance of detectors to identify ions, also through the Pulse Shape Analysis (PSA), this latter hugely benefiting of the versatile digital treatment of signals. PSA is important, because one of the main efforts is to keep identification energy thresholds low, in order to recognize also slow ions which stop in thin silicon junctions.

FAZIA adopted a three-layer Silicon-Silicon-CsI(Tl) telescope as the basis module for a future large acceptance array. Many aspects of the telescope operation have been investigated along the years and special solutions have been proposed to improve the results. In 2011 a Memomrandum of Understanding was signed by the five countries in order to rule the construction of a demonstrator. This ongoing phase will last till 2015 and foresees the construction of an array of 192 telescopes with optimum performances. The detectors have an active area 20x20 mm^2, thicknesses 300 and 500 μm for the silicon stages and 100 mm for the slightly tapered CsI(Tl). The silicon resistivity is around 3-4 kOhm*cm while the Tl doping of the CsI is from 1500 to 2000 ppm. In the demonstrator, the modules will be mounted in 16 blocks, each one consisting of four 2x2 matrices with 4 telescopes. They will be mounted at 100 cm from the target, each block covering 0.64 msr solid angle.

2.1 PSA and fast sampling electronics

In certain detectors the signals formed by the passage of ions have a time-development which depends also on the ion nature itself. In silicon junctions, this dependence is due to a combined effect of electric field profile, ion penetration, different mobility of charge carriers (electrons and holes) and, last but not least, to the time delay before that the opposite charged carriers feel the electric field and drift towards electrodes (plasma erosion time) [19]. For different ions of the same energy, the penetration depth

inside the bulk changes depending on the specific energy losses. Charge carriers are therefore differently distributed and sample variable electric field values, so that the study of the signal shapes allows for their identification.
In inorganic crystals, fluorescence presents several decay constants whose relative weight depends on the particle. In typical CsI(Tl) crystals, widely employed as stop detectors in heavy-ion experiments, the two components have decay constants of around 1 to 4-6 μs [17], respectively. In general, the fast contribution increases with the Z of the adsorbed ion; therefore, different ions with fixed energy can be separated by means of an analysis based on these fast-slow components.

FAZIA activity started from these detection bases trying to improve their application by means of sampling electronics. Digital signal processing, indeed, is very versatile and the availability of commercial fast sampling ADC permits its use also in case of the rapid signals (wide bandwidths) produced in nuclear detectors. The processing can be done, shape by shape, in real time by using front-end computation units (DSP or FPGA) to extract the relevant parameters or, as chosen by FAZIA, via off-line analysis applied to the whole waveforms, stored on disk. Off-line analysis is more powerful since it allows to singularly study each waveform, to upgrade identification algorithms whenever available, to implement special analysis types (e.g. related to radiation damage or to border effects). During its R&D phases, FAZIA strongly benefited of this "off-line" approach in particular for silicon detectors [13,20].
Since digital PSA relies on the sampling of intrinsic waveforms produced by the ions, the preamplification stage is an issue, in particular for silicons where PSA applications are mor crucial. Special low-noise preamplifiers [21] have been developed within the collaboration, with both current and charge ouputs. For silicon detectors, two gains have been adopted for the charge outputs in order to better exploit the dynamics: 250 MeV@Si-eq and 3/4 GeV@Si-eq. For CsI(Tl) the only charge output is exploited with a sensitivity of $\approx$ 300 MeV@Si-eq.
The sampling stages are 14bit-ADC with clock at 250 MS/s and 100 MS/s for silicons and CsI, respectively. Indeed, the bandwidth of scintillators is less extended than in silicon, where transient times down to 20 ns should be measured. Preamplifiers and ADC circuits, together to other stages (e.g., the programmable logic arrays, the slow controls, the pulser generation, the bias voltage supply and tuning), are all hosted in "custom" boards, each hosting 6 channels (2 complete telescopes). Also noise contributions should be kept low enough in order not to spoil the information brought by the waveforms. In other words, the effective number of bits (ENOB) of the channels must be as highest as possible, possibly not too far from the NOB of the chosen ADC in order to save its resolution typical FAZIA values are ENOB$\approx$11-12, overall.

2.2 Silicon detectors

The two silicon stages (Si1 and Si2) of the FAZIA telescope are the core of the module and thus they have been the objective of careful investigation. The silicon chips have a twofold purpose: i) ion identification and ii) energy measurement. Particles which punch-through the first Si1 and stop in Si2 are recognized, in charge and mass via the usual $\Delta E - E$ method, while the kinetic energy is given by the sum of the two contributions $\Delta E + E$. This method cannot be used with ions stopping in Si1 and thus it presents a energy threshold that can be severe: for instance, for a 300 μm thickness, the threshold is 6 MeV/u for protons and alphas and it increases to about 22 MeV/u for Z=30. For ions adsorbed in Si1, an estimate of the particle mass can be obtained from the energy and the time-of-flight (tof) variables. It is thus important to preserve good timing properties for silicons and this fact would suggest to mount silicons in "front" configuration, where particles hit the high electric field (junction) side and produce faster signals. However, PSA applications demand to reconsider this aspect. As a matter of fact, FAZIA chose the rear mounting configuration, in which particles enter the ohmic side of the junction (for both silicon layers) where the electric field is at the minimum. This choice, as discussed in the literature [22,23], is preferable to improve PSA because this way signal shape differences are enhanced with respect to the front mounting. This is shown, as an example, in Figure 1, where experimental charge signals for

Ti ions of two initial energies are shown for rear (red) and direct (blu) configuration. The two energies correspond to ions stopping at the end of the thickness (910 MeV) or with a range of about 2/3 of it (i.e. 190 μm). Clearly, signal shapes appear to differ more in the rear mounting and this reflects in a greater sensitivity of any signal-related parameter for PSA. Attempts to microscopically describe the (charge or current) signals produced by heavy-ions in silicon detectors are on progress within FAZIA and recently they gave promising results [19]. Besides the optimisation of the electronics, FAZIA devoted

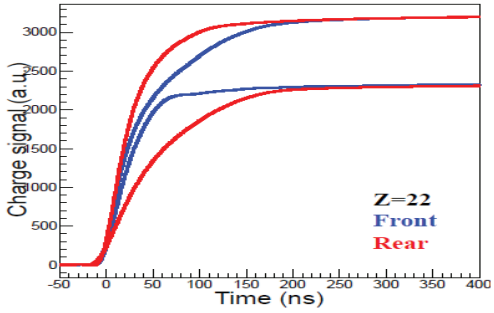

Fig. 1: Charge signals for Titanium ions of two energies as measured for a 300 μm silicon detector in front (blu) or rear (red) configurations. From Ref [18].

many efforts in studying and reducing the effects which intrinsecally degrade the PSA. They are related both to the silicon structure (like crystalline nature and doping homogeneity) and to the detector use (like radiation damage). For the latter we refer to Ref. [24]. Here we briefly discuss the structural aspects which affect PSA in silicon detectors. Good PSA performances need that signal shape variations are only due to different ion/range combinations with negligible fluctuations introduced by spurious sources. Channeling effects of heavy-ions in silicon detectors have been observed since many years, showing up as a spoiling of the energy resolution with humped energy distributions even for monochromatic ions [25]. When ion beams with narrow emittance impinge on silicon junctions with directions close to crystallographic axes and/or planes, the ion-electron interactions along the tracks are strongly position dependent; the effective charge of the slowing ions fluctuates as function of the track details and this produces the humps in the spectra. The powerful sampling techniques allow to better evidence the signal shape fluctuations due to channeling, as FAZIA demonstrated with specific experiments [13]. It was shown that these spurious shape variations can be strongly reduced with almost random irradiation, corresponding to incident angles far from crystallographic directions. In this case the crystalline structure is almost hidden to impinging ions and a smooth behavior is obtained with reduced fluctuations.

The doping homogeneity is an other crucial aspect for PSA with silicon detectors. In fact, dis-homogeneities of dopants create local changes of the electric field inside the device which, again, produce spurious signal smearing. This is known since the pioneering works on PSA which suggested the use of neutron trasmutation doped (nTD) detectors, having better doping uniformity with respect to FZ-implanted ones. FAZIA clearly evidenced the effect of doping inhomogeneities on PSA [15]; therefore, only nTD wafers were adopted, with resistivity which should be constant, for each detector, within 6-7%. To check this figure in the final ready-to-mount pads, FAZIA implemented a tool to probe the homogeneity of the silicon detectors without need of beam tests. The method, based on very fast UV-laser flashes [14], leads to a resistivity map for each pad over its active area; only the pads with the flattest resistivities are retained. Best homogeneities are less than 1% but typical values are 4 to 6%. Recently, a method has been proposed to compensate for the residual doping inhomogeneity, by further thermal neutron irradiation of the wafer with purposely shaped Cadmium masks [26]. The method, still at its concept phase, needs the previous knowledge of the resistivity map in order to shape the mask for each

wafer.

2.3 CsI(Tl) scintillators

The selected CsI(Tl) are slightly tapered piramidal crystals; their front square face (20.3x20.3mm^2) contains the silicon dimensions. Tipically, the luminescence is read by a photodiode (PD) glued with soft

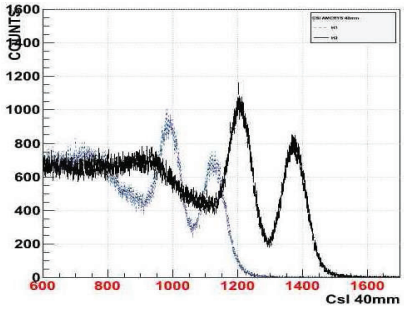

Fig. 2: ^{60}Co gamma ray spectrum for a 40 mm long CsI crystal wrapped with a diffusive paper (blu) or with the 3M-Vikuiti (black) reflector

optical epoxy to the crystal. The square PD are specifically produced for FAZIA; they are 300 μm thick single pads with ρ=6000 ohm*cm, whose main feature is the very narrow lateral dead zone (active area 19.6x19.6 mm^2, 81% of the total area); commercial devices couldn't be used except loosing a relevant fraction of light sensitive area. The crystal length (10 cm) allows to stop even the most energetic light particles in reactions at intermediate energies. Particular care has been devoted in selecting the surface type and the wrapping materials. The front and rear faces are polished while the lateral ones are slightly roughed after polishing. The wrapping material was chosen after laboratory tests with gamma and alpha sources on several crystals. The use of a new high-reflecting polymer [27] gave an enhancement of light output of about 18-20% with respect to previously used white diffusive papers (see Figure 2). Tests under vacuum were done to verify the good operation also in typical experimental conditions and to exclude major de-gassing effects of this polymer.

3 In beam performances

We now discuss a few examples of the under-beam performances of the FAZIA telescopes, prepared as described above. The results refer to experiments done at Laboratori Nazionali del Sud (Catania, Italy). Pulsed beams of ^{84}Kr and ^{129}Xe at 35 MeV/u were sent on thin (0.2-2.0 mg/cm^2) foils made of various enriched isotopes of tin and nickel. The telescopes were positioned at distances 100 to 250 cm from the targets.

3.1 ion identification via ΔE-E

Ions with enough energy punch-through the first stage of a telescope and can be identified via $\Delta E - E$ technique. We can use the Si1 or the Si1+Si2 as the first lens of the telescope, for particles stopping in Si2 or CsI(Tl), respectively. A rich set of the FAZIA results is reported in Ref [16,18]; here, we stress that unprecedented mass separation is reached by our telescopes. For example, isotopes are resolved up to Z≈24-25 for both Si1 vs. Si2 and (Si1+Si2) vs. CsI as shown in Figure 3.1 a). This opens the door to more complete isospin studies at Fermi energies because one can afford isospin reconstruction of the very fast quasi-projectiles (at least for medium-heavy mass) produced in semi-peripheral collisions and

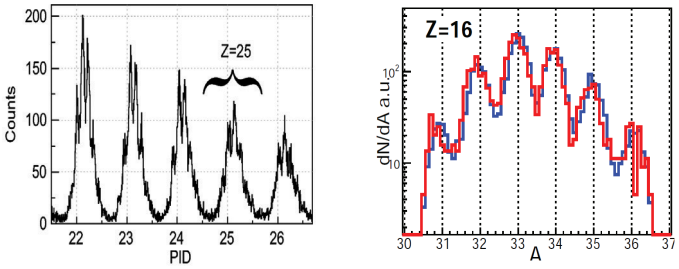

(a) (b)

Fig. 3: a): Isotopic distribution in the iron region for ions stopped in CsI(Tl). The identification is obtained with the $\Delta E - E$ technique applyied to one FAZIA telescope (from [16]). b): Comparison of the isotopic distributions for Sulphur as measured via the $\Delta E - E$ method for a given pair of Si1-Si2, mounted in reverse (red) or direct (blu) configuration (from [18]).

not only of the lighter fragments as done so far.
An important conclusion has been drawn by FAZIA on a debated subject, namely the quality of the $\Delta E - E$ technique with silicon detectors in front or reverse geometry. In a specific beam-test, we compared the the method with front and reverse mounting by flipping the Si1 and Si2 stages in two phases of the same experiment. This way, the comparison is strictly conclusive. No difference was found as demonstrated in Figure 3.1 b), which shown the sulphur isotopic yield obtained in the two silicon configurations [18].

3.2 Ion identification via digital PSA

The strong interest in the identification of less energetic ions which stop in the first layer is due to the fact that they represent a large fraction of the population of the ejectiles at moderate bombarding energies, as those of the next exotic beam facilities. Also, fragments emitted by the rather slow big sources formed in central collisions or by quasi-target nuclei at larg impact parameters typically demand low thresholds. The good quality of the FAZIA silicon material allowed to reach promising results. About charge identification, the limit has been amply extended: in our reverse mounted silicon pads the elements have been separated up to the maximum values of the test reactions (Z=54). Concerning isotopic separation the situation is more critical because it depends quite sensitively on the various parameters (doping homogeneity, channeling suppression, radiation damaging, overall operation stability). So far, we verified that, PSA permits a safe separation up to carbon ions with energies greater than MeV/u [15].

3.3 The single chip configuration

The use of fast sampling electronics pushed the FAZIA collaboration to better investigate the Single Chip Telescope (SCT) configuration, proposed years ago [28]. The idea is to use the second silicon Si2 as the photodiode for the following CsI(Tl) crystal. The SCT solution can be useful to spare electronic channels (and money) in large apparatus. In a SCT, the Si2 acts both as an ionization detector and as a photosensor: thus, the signal waveforms for ions stopping in the CsI(Tl) are given by different contributions, extending on different timescales, from many nanoseconds to microseconds. From the sampled recorded shapes one can first recognize the signals of ions stopped in Si2 (no scintillation component) and those for ions stopped in the CsI(Tl). Then, for these latter, one can perform an appropriate analysis (e.g. based on various shaping times) and disentangle the fast silicon contribution from the slow one(s) of the scintillator. The behaviour of a SCT has been accurately compared with that of a reference standard Telescope and the results are described in Ref. [17]. We show in Figure 4 the $\Delta E - E$ identification

plot of the reconstructed SCT signals. The quality is very good and in particular the hydrogen isotopes (in the zoomed inset) are well distinguishable. As a matter of fact, the SCT is almost equivalent to the standard read-out for Z=1,2 ions while for Z$\geq$ 2 it is worse for energies below 20 MeV/u, although the isotopic separation is preserved. Therefore, the SCT concept appears to be appealing and also other groups adopted this solution [**?**].

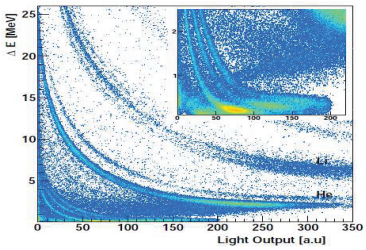

Fig. 4: $\Delta E - E$ identification plot obtained from a Single Chip Telescope. Lithium isotopes are separated. In the inset, hydrogen isotopes are shown (from Ref. [17]).

4 Towards the demonstrator phase

During the last test under beam at the INFN-LNS (Catania), we measured reactions induced by a ^{84}Kr beam with 35 MeV/u on targets of enriched tin isotopes. The idea was to prove that the perfomance of the FAZIA telescopes permits to measure isospin variables with unprecedented quality at the Fermi regime. First, we wanted to investigate the role of the isospin diffusion and drift [3,4] occuring in the transient systems formed in semi-peripheral binary reactions which finally lead to excited quasi-projectile (QP) and quasi-target (QT) fragments. Secondly, we aimed at studying odd-even staggering effects which are ruled both by reaction mechanisms and nuclear structure. In the experiment, only QP were detected and identified in charge up to the maximum Z=36 (Kr); isotopes were separated up to about Chromium as described above (Figure 3.1 a)). The use of ^{124}Sn and ^{112}Sn targets permits to verify the effect on QP characteristics due to changes of the isospin content of the target; indeed, the N/Z of Kr (1.33) is in between those of the n-rich ^{124}Sn (N/Z=1.48) and of the n-deficient ^{112}Sn (N/Z=1.24). Event types

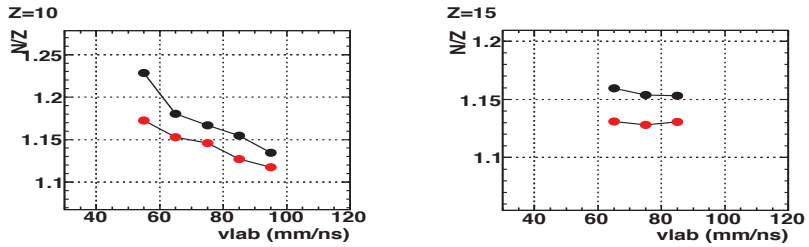

(a) (b)

Fig. 5: Preliminary results of average isospin N/Z of fragments Ne (a) and P (b) as function of their lab velocity. Red dots for ^{112}Sn, black dots for ^{124}Sn

were selected on the basis of the $Z - v$ correlation where v is the laboratory velocity of the detected ions. This correlation has been widely used in the past to characterize different event types [29]. The

analysis of these data is on progress and it will be reported in the future [30]. Here we just anticipate some preliminary results which allow to appreciate the goodness of the data and give some hints of the physics cases. This is done in Figure 5 where the average N/Z ratio is presented versus v for neon and phosphor isotopes. Red (black) points refer to the ^{112}Sn (^{124}Sn). The following observations can be done. The detected (cold) fragments show a memory of the different isospin target content, although they are mainly associated with QP. Then, lighter fragments with v compatible with the intermediate QP-QT region (midvelocity region) appear to be more neutron rich than those having v close to the QP. This trend is quite in agreement with results, among others, of a very recent study [31]. Finally, we observe that the region above Z=9-10 was unaccessible for this kind of variable by modern multidectors, so far. The example of Z=15 isotopes (Figure 5, right) is, in this sense, new and give an idea on how isospin related quantities can be extended by the next experiments with the FAZIA demonstrator.

References

[1] A.Di Pietro *et al*., *Phys. Rev. Letters* **105** (2010) 022701.
[2] M.Veselsky *et al*., *Nucl. Phys* **A 765** (2006) 252.
[3] V. Baran *et al*., *Nucl. Phys*. **A 730** (2004) 329.
[4] M. DiToro *et al*., *Journ. Phys*. **G 37** (2010) 083101.
[5] C. Simenel *et al*., *Phys. Rev.* **C 76** (2007) 024609.
[6] W. Van Oertzen *et al*., *Phys. Rev.* **C 78** (2008) 044615.
[7] G. Baiocco, contribution to this Conference
[8] Sh. A.Kalandarov *et al*., *Phys. Rev.* **C83** (2011) 054611.
[9] L. Shvedov *et al*., *Phys. Rev.* **C 81** (2010) 054605.
[10] FAZIA website `http://fazia2.in2p3.fr/spip`.
[11] M. Alderighi *et al*., *IEEE Trans. Nucl. Sci*. **N53–1** (2006) 279.
[12] S. Wuenschel *et al*., *Nucl. Instr. and Meth*. **A604** (2009) 578.
[13] L. Bardelli *et al*., *Nucl. Instr. and Meth*. **A605** (2009) 353.
[14] L. Bardelli *et al*., *Nucl. Instr. and Meth*. **A602** (2009) 501.
[15] L. Bardelli *et al*., *Nucl. Instr. and Meth*. **A654** (2011) 272.
[16] S. Carboni *et al*., *Nucl. Instr. and Meth*. **A664** (2012) 251.
[17] G. Pasquali *et al*., accepted for publication.
[18] R. Bougault *et al*., submitted for publication.
[19] Z. Sosin *Nucl. Instr. and Meth*. **A693** (2012) 170.
[20] S. Barlini *et al*., *Nucl. Instr. and Meth*. **A600** (2009) 244.
[21] H.Hamrita *et al*., *Nucl. Instr. and Meth*. **A531** (2004) 607.
[22] M. Mutterer *et al*., *IEEE Transactions on Nucl. Sci*. **47** (2000) 756.
[23] G. Pausch *et al*., *Nucl. Instr. and Meth*. **A 443** (2000) 304.
[24] S. Barlini *et al*., accepted for publication and contribution to this Conference.
[25] G. Poggi *et al*., *Nucl. Instr. and Meth*. **B 119** (1996) 375.
[26] A. Kordyasz *et al*., to appear in *Nucl. Instr. and Meth*. **A** (2012).
[27] Vikuiti 3M Enhanced Specular Reflector.
[28] G. Pasquali *et al*., *Nucl. Instr. and Meth*. **A301** (1991) 101.
[29] E. Galichet *et al*., *Phys. Rev.* **C 79** (2009) 064614.
[30] S. Piantelli *et al*., in preparation.
[31] E. De Filippo *et al*., subm. *Phys Rev* **C 86** (2012) .

Effects of irradiation of energetic heavy ions on digital pulse shape analysis with silicon detectors

S.Barlini[1] *,S.Carboni*[1] *,N.Le Neindre*[2] *,M.Bini*[1] *,B.Borderie*[3] *,R.Bougault*[2] *,G.Casini*[1] *,P.Edelbruck*[3] *, A.Olmi*[1] *,G.Pasquali*[1] *,G.Poggi*[1] *,M.F.Rivet*[3] *,A.A.Stefanini*[1] *,E.Scarlini*[1] *,A.Catelani*[1] *,G.Baiocco*[2,4] *,R.Berjillos*[5] *, E.Bonnet*[6] *,M.Bruno*[4] *,A.Chbihi*[6] *,J.A.Dueñas*[5] *,F.Gramegna*[7] *,A.Kordyasz*[8] *,T.Kozik*[9] *,V.L.Kravchuk*[7] *,O.Lopez*[2] *, T.Marchi*[7] *,L.Morelli*[4] *,M.Parlog*[2] *, S.Piantelli*[1] *, E.Rosato*[10] *,E.Vient*[2] *,M.Vigilante*[10]
for the FAZIA collaboration
[1]INFN and University of Florence, Italy
[2]LPC Caen, ENSICAEN University of Caen, CNRS/IN2P3, Caen, France
[3]IPN Orsay, CNRS/IN2P3 and University of Paris-Sud XI, Orsay, France
[4]INFN and University of Bologna, Italy
[5]Huelva University, Spain
[6]GANIL, Caen, France
[7]INFN-LNL and University of Padua, Italy
[8]Warsaw University, Poland
[9]Jagiellonian University, Kracow, Poland
[10]INFN and University of Naples, Italy

Abstract
Detected energy, charge rise-time and pulse shape identification capabilities of nTD silicon detectors under prolonged irradiation by energetic heavy ions have been studied. Sizeable effects on the amplitude and the risetime of the charge signal have been found for detectors irradiated with large fluences of stopped heavy ions, while much weaker effects were observed for punching-through ions. The robustness of ion identification based on digital pulse shape techniques has been evaluated.

1 Introduction

The energy thresholds for charge and mass identification of the different reaction fragments is a crucial point for a modern nuclear physics apparatus. The FAZIA collaboration [1] is developing a new Si-Si-CsI(Tl) telescope with fully digitized signals in order to perform Pulse Shape Analysis (PSA) and Time of Flight (ToF) measurements for fragment identification. Many experiments have been performed to study and improve the behaviour of silicon detectors with respect to PSA, and nTD (neutron Transmutation Doped) silicon crystals in reverse mount configuration (i.e. with particles entering the detector through the low field side) with a bulk resistivity of about 3 kΩcm have been chosen as final solution. Moreover, a "random" crystal orientation in order to avoid channeling directions [2] and doping inhomogeneities at a low level ($\leq 3\%$) [3,4] have been recognized to be crucial points for good PSA performances. Following these recipes and adopting especially designed low-noise digital fast sampling electronics, excellent results on PSA were obtained by the FAZIA group, but the robustness of detector operation must be evaluated and proved in view of future long experimental campaigns. Many studies have addressed this subject, mainly silicon pixel and microstrip detectors for tracking applications in high energy physics (see [5] and [6] as examples). In such experiments, the detectors are irradiated with low-Z particles at relativistic energies and/or subjected to strong neutron fluxes, a situation completely different from our case. where heavy-ion collisions at beam energies from the Coulomb barrier to over 30 MeV/nucleon will be investigated.
The major source of damage in silicon detectors is the loss of ion kinetic energy via nuclear interactions with lattice atoms. The incident particles interact with silicon atoms which are displaced from the

crystal lattice, creating lattice defects. Low-energy recoils create only "fixed point" defects, while energetic recoils could create a dense agglomeration of defects at the end of the primary ion track ("defect clusters"). Both of them introduce energy levels within the forbidden energy gap, acting as recombination/generation centers of electron-hole pairs. So they are responsible for an increase of reverse current and they can also affect the charge collection efficiency ([5], [7]).
Our purpose is to observe the changes in detected signal shapes and their consequences on the related physical observables of interest (energy and charge rise-time) as a function of the increasing fluence.

2 Experimental setup

Data were collected at the "Laboratori Nazionali del Sud" in Catania using 35 MeV/nucleon ^{129}Xe beam bombarding targets of ^{nat}Ni (1050 μg/cm^2) and ^{120}Sn (2500 μg/cm^2). Seven different telescopes were mounted in the "Ciclope" scattering chamber, at distances ranging from 250 cm to 300 cm from the target. A more complete description of the whole apparatus can be found in [8]. The effects of irradiation with heavy ions were studied using two different detectors: a 310 μm nTD silicon detector (RD-detector) and a "standard" three stage FAZIA telescope (TeleA) made of two Silicon detectors Si1 and Si2 (thickness 310 μm and 504 μm, respectively) followed by a 4 cm thick CsI scintillator. The silicon detectors were mounted in the "reverse" configuration (low field side facing the target); their main specifications are shown in Table 1. The position of RD-detector was changed during the experiment in a way that is explained below with the help of Fig. 1.

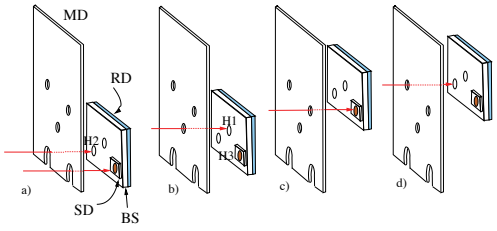

Fig. 1: Scheme of the irradiation cycle for the RD detector. The drawing is not to scale and it is meant to visually explain the irradiation cycle. Abbreviations and figure parts are defined and discussed in the text.

Table 1: Some experimental details of the used silicon detectors.

Heading	RD-Si	TeleA Si1	TeleA Si2
Area	20X20 mm	20X20 mm	20X20 mm
Manufacturer	FBK	FBK	CANBERRA
Thickness	310 μm	310 μm	504 μm
Depletion Voltage	120 V	130	228 V
Bias Voltage	140 V	140 V	250 V
Bulk type	n-type	n-type	n-type
Resistivity	2970 Ω·cm	2540 Ω·cm	4160 Ω·cm
Resistivity unif. (FWHM)	2.3%	4 %	0.4%
Distance from target	301 cm	258 cm	258 cm
Θ position in lab.	0.3°/ 1.4°	2.35°	2.35°

The measurement cycle consisted essentially of two phases: the first where the "transmission" and "stopping" regions (H2, H3) were slid well under the grazing angle ["irradiation" phase, see Fig. 1 a)]

while the "no damage" hole H1 was protected. In the second "measurement" phase, the three holes were sequentially exposed to the reaction products and the signal shapes were acquired. This second phase was performed in different steps [cfr Fig. 1 b), c), d)] in order to acquire, each time, only the pulses associated to the desired region. The angles of the "irradiation" phase were decreased during the experiment in order to quickly produce sizeable changes in the RD. In order to keep the acquisition dead time to an acceptable level during "irradiation"(count rates reached up to 700 Hz for each hole), the signals were not acquired, but they were simply counted by fast scalers, estimating the ion fluence. A typical irradiation-measurement cycle lasted slightly more than one hour, with a short pause (3 minutes long) between the two phases.
The n-side of the reverse mounted silicon detectors was directly connected to a charge and current "PACI" pre-amplifier [9] whose outputs were fed, through 6 m long differential cables, to custom digitizer boards placed outside the reaction chamber. Two kinds of boards have been used: the RD-detector was connected to a 125 MS/s-12 bits ADC card [10] while the TeleA signals were sampled by a 100 MS/s-14 bits ADC board. For each detector the bias voltage was provided by a remotely controlled power supply module, also featuring reverse current monitoring. In this way, the supply voltage was continuously automatically corrected (in 1V steps) as a function of the reverse current change in order to maintain the actual bias voltage across the silicon junction constant.

3 The RD-silicon analysis

Fixing the mass, charge and energy of the impinging particle, the signal shape strongly depends on the electric field profile in the depleted region of the detector. As already said, during the present measurement the bias was kept constant on the detectors. So the variation of the pulse shapes of elastically scattered Xe ions in our collimated zones as a function of fluence can be attributed to changes in detector properties due to damaging. A detailed analysis of the amplitude and rise-time of charge the signal as a function of the fluence is presented in Fig.2. To optimize the signal to noise ratio, the collected charge is measured taking the maximum value of the output of a semi-Gaussian shaper-filter applied to the digitized charge signals (called Qmax in the following). The filter has a time constant of 1.5 μs and unitary gain. The charge signal rise-time (Qrisetime in the following) is calculated as the difference between two digital constant fraction discriminators [8,11], with thresholds set at 20% and 70% of the total signal amplitude.

For the "stopping" zone, at the final fluence of 6×10^8 ions/cm^2 we observe a relative drop of Qmax of 16% with respect to the beginning of the experiment. A "pulse height defect" associated to irradiation is also reported in Ref. [12], for fission fragments from ^{235}U detected using an Au-Si-Al surface barrier transmission detector. More recently, in Ref. [13], a position-sensitive Silicon detector has been irradiated by elastically scattered ^{28}Si of 80 MeV stopped in the device. After 1.5×10^9 ions/cm^2 of implanted ^{28}Si a decrease of the detected energy around 3.5% was observed, accompanied by a worsening of the energy resolution. It is not obvious how one can scale our data to compare with Ref. [13]. From TRIM calculations one can estimate that the linear density of vacancies in silicon at the end of the ion range is about 5 times greater for ^{129}Xe than for ^{28}Si. Our fluence, however, is a factor of 2.5 smaller than in Ref. [13]. In any case, in ref. [12,13], the increase of reverse current was not compensated, and this could lead, depending on the bias resistor, to a reduction of the field and a worse charge collection efficiency compared with our setup. Concerning the shape of the signals, ref. [13] states that no variation of the charge rise time was observed, contrary to our case where for stopped Xe ions the Qrisetime drops of a factor 2. A saturation of Qrisetime towards about 100 ns in the "stopping" zone is suggested by the data of Fig. 2. Unfortunately, it is not possible to confirm this asymptotic behaviour because the measurement had to be stopped, having used up the whole allotted time.
As expected, in the "transmission" zone the effects are lower. The decrease of Qmax at the end of the measurement is less than 2 %, while the Qrisetime remains constant within 5%. This is due to the fact that in this case the defects are distributed along the ion track and they are not concentrated in the last few

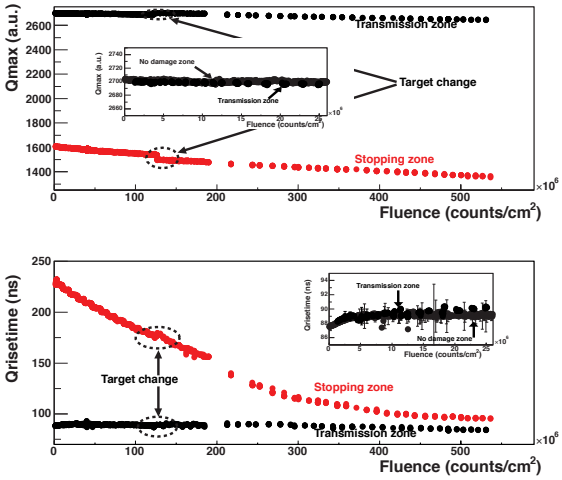

Fig. 2: Qmax (top panels) and Qrisetime (bottom panel) of scattered ^{129}Xe ions impinging on the "transmission" and "stopping" regions. For each panel, in the inset the results for the "no damage" area are compared to the low fluence points of the "transmission" region.

microns of the range as for stopped ions. This is a crucial information for planning future experiments with silicon detectors placed at relatively small angles with respect to the beam. Finally, the response of the "no damage" zone is expected to be very similar to the transmission zone because also in this case Xe ions are punching through. Moreover, this zone was shielded during irradiation at small angles so that the fluence spans a reduced range. The fluence on the no damage zone can be calculated directly from the number of ions whose shapes are collected, taking into account the dead time of the acquisition system.

Both effects of reduction of Qmax and decrease of Qrisetime with increasing fluence are a consequence of the creation of recombination or trapping centers for electrons and holes. However, the explanation of the decrease of Qrisetime is not straightforward, as it involves the interplay between charge recombination or trapping and plasma erosion time. In any case, the observed behaviour of the data shows that the plasma delay is significantly reduced by the increasing number of irradiation-generated defects. To our knowledge, this is the first time that such phenomenon is measured so precisely.

4 The TeleA analysis

TeleA is a three stage Si-Si-Csi(Tl) telescope mounted at 2.35^{o} with respect to the beam at a distance of 258 cm from the target (the subtended angle is slightly less than 0.5^{o}). The study of the PSA performance of this telescope (i.e. the ion separation capability) as a function of the ^{129}Xe fluence is particularly interesting. The results shown in the following concern the first part of the experiment, i.e. the ^{129}Xe+^{nat}Ni at 35 MeV/nucleon reaction. For such reaction, the grazing angle is 2.3^{o}. We estimated an average value of the ^{129}Xe fluence from the number of detected elastic events (corrected for the dead-time of the acquisition system which was of the order to 20-30 %) divided by the detector area inside the grazing angle of the reaction. We have tested the second silicon detector, where the Xe ions are stopped and the radiation damage more evident.

A correlation commonly used in the FAZIA project for PSA identification of imping fragments is the "energy vs. Qrisetime " (see [8] for more details). This plot features separate ridges for different atomic

numbers (Z-ridges), at least above a Z-dependent energy threshold. At energies under the threshold the ridges join in a common "back-bending" ridge. At the end of the experiment the widths of the back-bending region and of the Z-ridges were larger, leading to a poorer identification. In order to perform a quantitative comparison of PSA capability as a function of Xe ions fluence, we applied the linearization procedure adopted in [3] and [8]: starting from the bidimensional plots of energy vs. Qrisetime, we draw identification-lines overlapped to the various Z-ridges, assigning a Particle IDentification (PID) value to each line. Interpolating between adjacent identification lines, a unique PID value is attributed to each detected particle. In a Qmax vs. PID correlation, each ridge is ideally parallel to the Qmax axis. Projecting on the PID axis, the PID "spectrum" is obtained, where each peak is associated to a different ion-element. When adjacent peaks have similar statistics, the so called "Figure of Merit" (or FOM) [14] is a useful parameter to quantify the separation between different elements. The FOM is defined as

$$FOM = \frac{|\mu_1 - \mu_2|}{(\sigma_1 + \sigma_2) * 2.35} \tag{1}$$

where μ_1 and μ_2 are the centroids, σ_1 and σ_2 the standard deviations of two Gaussians fitted to adjacent peaks.

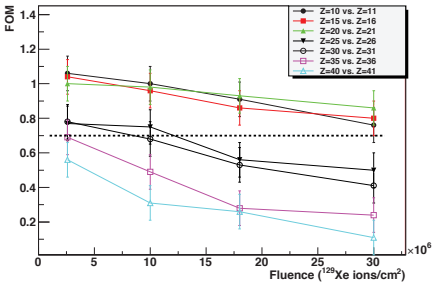

Fig. 3: FOM for adjacent elements versus Xenon ions fluence

In Fig. 3, the FOM values calculated for different element pairs are shown as a function of ^{129}Xe fluence. The original energy vs. Qrisetime correlations from which PID spectra are derived have been obtained analyzing a suitable number of signals immediately after reaching the associated fluence value. FOM=0.7 (dotted horizontal line in Fig. 3) is used as a reference threshold above which we conventionally assume a good peak separation. The obtained FOM values clearly decrease as a function of the fluence. The contribution to this effect due to the increase of the reverse current during the experiment is negligible. To better distinguish the effects of a non-uniform impinging particles rate on the detector with respect to the damaging, we can look at the Qmax and Qrisetime distribution of the elastically scattered Xe ions in the two different studied detectors.

Figure 4 shows the Qmax [panels a) and c)] and Qrisetime [panels b) and d)] distributions normalized to the initial mean value for the Si2 of TeleA (left panels) and for the RD-detector (right panels). Around one thousand of elastically scattered ^{129}Xe ions stopped in the silicon are considered for each distribution. Data refer to the beginning (continuous line) and after 30×10^6 ions/cm^2 (dashed line). For the RD-detector data are also displayed after a fluence of 4.8×10^8 ions/cm^2 (dotted line). In the RD-detector data, the event selection is performed using a threshold on the collected charge (due to the RD polar angle, practically the overwhelming majority of detected particles are elastically scattered ^{129}Xe ions). For Si2 of TeleA, elastically scattered ^{129}Xe ions are selected with a graphical cut in the ΔE-E plot. One can note the asymmetric form of the distribution of the charge risetime variation for the Si2 of TeleA

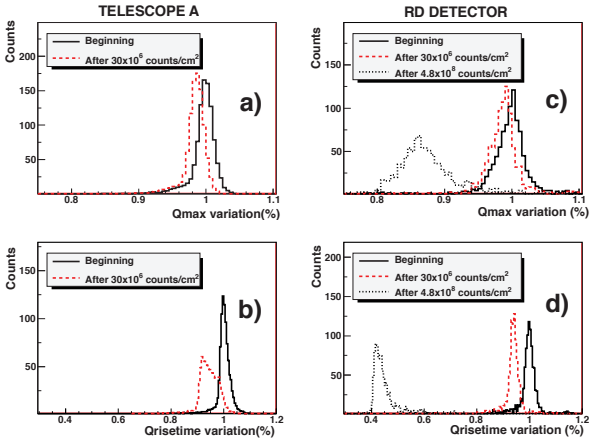

Fig. 4: Qmax [panels a),c)] and charge rise-time [panels b),d)] distributions for the Si2 of TeleA (left part) and "RD-detector" (right part) at the beginning (continuous line), after 30×10^6 ions/cm^2 (dashed line) and 4.8×10^8 ions/cm^2 (dotted line). The distributions are normalized to the mean values at the beginning of the test.

after 30×10^6 ions/cm^2 [Fig. 4, panel b), dashed line]. Such asymmetric behaviour is not present in the collimated RD-detector at the same fluence [Fig. 4, panel d), dashed line]. This difference can be related to a non uniform rate of elastically scattered Xe ions (and consequently a non uniform damaging of the detector) in the TeleA due to the fact that this detector was mounted in a region of rapidly varying cross section and was not collimated. This can be the major reason for the progressive decrease of PSA performance shown in Fig. 3. Nevertheless, the presence of the broadening also in the collimated RD-detector after 4.8×10^8 ions/cm^2 [Fig. 4, panel d), dotted line] suggests that even when the impinging rate is rather uniform, the detector loses resolution. In other words, the effect of increasing fluence can not be considered as a "rigid" shift in the observed quantities Qmax and Qrisetime. The signals of the detector experience increasingly larger fluctuations, resulting in a worsening of the performances.

References

[1] for more information, see http://fazia2.in2p3.fr/spip
[2] L.Bardelli et al., Nucl. Instr. and Meth. A605(2009), 353
[3] L.Bardelli et al., Nucl. Instr. and Meth. A654(2011), 272
[4] L.Bardelli et al., Nucl. Instr. and Meth. A602(2009), 501
[5] G.Lindsrom, Nucl.Instr. and Meth. A512(2003), 30
[6] CSM Technical Proposal, CERN/LHCC794-38, 1994;
[7] M.Jaksić et al., Nucl. Instr. and Meth. B231(2005), 502
[8] S.Carboni et al., Nucl. Instr. and Meth. A664 (2012), 251
[9] H.Hamrita et al., Nucl.Instr. and Meth. A531(2004), 607
[10] G.Pasquali et al., Nucl.Instr. and Meth. A570(2007), 126
[11] L.Bardelli et al., Nucl.Instr. and Meth. A521(2004), 480
[12] F.Shiraishi, Nucl.Instr. and Meth. 69(1969), 316
[13] Norihisa Kato, Nucl.Instr. and Meth. B51 (1990), 425
[14] R.A.Winyard et al., Nucl.Instr. and Meth. 95(1971), 141

Measurement of high energy gamma rays with large volume $LaBr_3$:Ce scintillators

L.Pellegri [1,2], *S.Brambilla*[2], *S.Riboldi*[1,2], *F.Camera*[1,2], *A. Giaz*[1,2], *A.Krasznahorkay*[3], *L.Stuhl*[3], *M.Csatlòs*[3], *J.Gulyàs*[3], *G.Benzoni*[2], *N.Blasi*[2], *S.Bottoni*[1,2], *A.Bracco*[1,2], *C.Boiano*[2], *F.C.L.Crespi*[1,2], *S.Leoni*[1,2], *B. Million*[2], *R.Nicolini*[2], *V.Vandone*[1,2], *O.Wieland*[2]

[1] Università degli Studi e INFN sezione di Milano, Via Celoria 16, 20133, Milano, Italy.

[2] INFN sezione di Milano, Via Celoria 16, 20133, Milano, Italy.

[3] Institute of nuclear research of the Hungarian Academy of Science (ATOMKI), P.O. Box 51, H-4001 Debrecen Hungary

Abstract

In the last few years, the Lanthanium Bromide scintillators are attracting the scientific community in nuclear spectroscopy because of their "almost ideal" scintillator properties. An array composed of 10 large volume $LaBr_3$:Ce (3.5" $\times$ 8") detectors, named HECTOR$^+$, was developed by the gamma-ray spectroscopy group of University of Milan. A R&D activity was performed on such large detectors and their general performances, especially for high energy gamma rays, have been studied. In fact no information about such large volume crystals is present in literature as they are available since very few years only.

1 Introduction

Recent studies have shown that a $LaBr_3$:Ce detector gives an optimal energy resolution for scintillators (<3% at 662keV), an excellent time resolution (<1ns), a good efficiency and a negligible variation of the light output with temperature. Furthermore, the study of the signal line-shape allows to discriminate between alpha particle and gamma-rays, using Pulse Shape Analysis techniques [1]. The availability of $LaBr_3$:Ce crystals in volumes larger than 1000cc could make these scintillators a possible alternative to HPGe detectors for gamma-ray measurements. An array based on $LaBr_3$:Ce scintillators (eventually coupled with HPGe detectors) will constitute an extremely performing, efficient, cost-effective and easy to handle array for gamma spectroscopy experiments. Indeed the good energy resolution and high efficiency allow the measurement of low and high-energy gamma-rays in nuclear physics experiments in a wide energy range (0-40 MeV), as for example the measurements of the gamma decay of the Giant Dipole Resonance and of the Pygmy Dipole Resonance [6] [7]. The sub-nanosecond time resolution enables an extremely efficient rejection of background radiation not originating from target position. Moreover thanks to the fast time constant (16 ns), these detectors could be used with count rates of hundreds of KHz. Recently these detectors have been used in the AGATA campaign at Legnaro Laboratories while, at the moment, they are located at the PRESPEC setup at GSI coupled again with AGATA.

For these reasons the gamma-ray spectroscopy group of the University of Milan has been working on the development of an array composed of 10 large volume $LaBr_3$:Ce (3.5" $\times$ 8"), named HECTOR$^+$. The $LaBr_3$:Ce have been coupled to a standard SBA PhotoMultiplier Tube (PMT) Hamamatsu R10233-100SEL and a specifically designed active Voltage Divider (VD) developed by the electronic group of INFN Milano [4]. Unfortunately the performances of $LaBr_3$:Ce (3.5" $\times$ 8") crystals cannot be easily scaled from those of smaller ones [2], because of possible self absorption or possible incomplete reflections of the scintillation light, count rate effects, large PMTs, crystal in-homogeneities and a much higher sensitivity to high energy gamma rays. For these reasons we measured mono-energetic gamma-rays from 1 MeV up to 22.6 MeV at Debrecen ATOMKI Laboratories (Hungary) to investigate the PMT linearity, the detectors energy resolution and their response functions to different count rates.

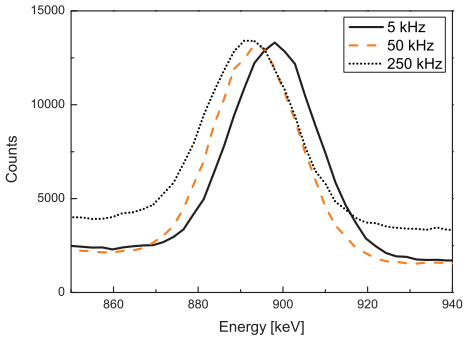

Fig. 1: The 898 keV peak from a ^{88}Y source measured in a $LaBr_3$:Ce (3.5" × 8") detector for different count rates.

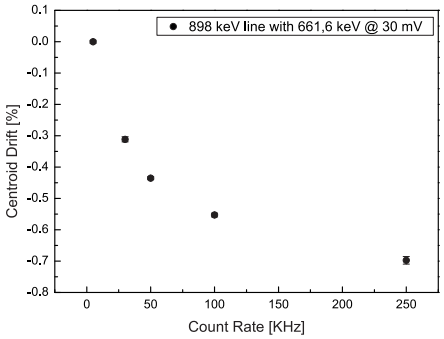

Fig. 2: The centroid drift measured in a $LaBr_3$:Ce (3.5" × 8") detector is displayed as a function of the count rate.

2 Studies of the detector properties

The aim of this work is the characterization of the HECTOR$^+$ array in term of count rate, pulse distortion and energy resolution.

2.1 Detector response as a function of Count Rate

In principle it is possible to use large volume $LaBr_3$:Ce detectors at very high count rates thanks to their fast pulses (150 ns). However, in such conditions, the average current inside the PMT increases and affects the values of the voltage at the last dinodes. If the count rates is not stable these gain drifts could deteriorate the detector energy resolution. In order to study this behaviour the response of the $LaBr_3$:Ce to different count rates was investigated using as a reference line the gamma-rays emitted by the ^{88}Y source. Different count rates were achieved by placing a 400 MBq ^{137}Cs source at different position relative to the detector. The plots in Fig. 1 shows the centroids drift as a function of count rate (from a few kHz to 250 kHz), obtained using the in house developed active VD [4]. Signals have been digitized at a frequency of 2 GHz and then integrated to produce the energy spectra. As can been seen from the Fig. 2 the centroid drift is smaller than 0.7% at 250 kHz with this VD. In case of stable count rates no significant deterioration of the energy resolution was measured.

2.2 Pulse Distortion

As a consequence of the high light yield of the new Lanthanum Bromide scintillators (63000 ph/MeV), the coupled PMTs generally show saturation effects for high energy gamma rays and such non linearity affects time and energy resolution. Therefore, it is extremely important to account and correct for these effects. An indication of this non ideal behaviour of the PMT+VD is the presence of a distortion in the pulse line-shape [5]. The Fig. 3 shows the pulse line-shape measured in a $LaBr_3$:Ce (3.5" × 8") detector coupled to the active VD for monochromatic gamma-rays from 1 MeV up to 17 MeV. As can be observed a very small distortion of the pulse is present. It has to be pointed out that in case one uses a passive VD this distortion becomes relevant. Fig. 4 summarizes the rise time, fall time and FWHM of the pulses displayed in Fig. 3.

2.3 Energy Resolution

The energy resolution was measured using different mono-energetic gamma-rays from 1 MeV up to 22.6 MeV. The monochromatic gamma-rays were obtained using (p, γ) reactions [3]. The $LaBr_3$:Ce (3.5" × 8") crystals were coupled to a PMT+activeVD and a in house spectroscopy amplifier (BaFPro) for

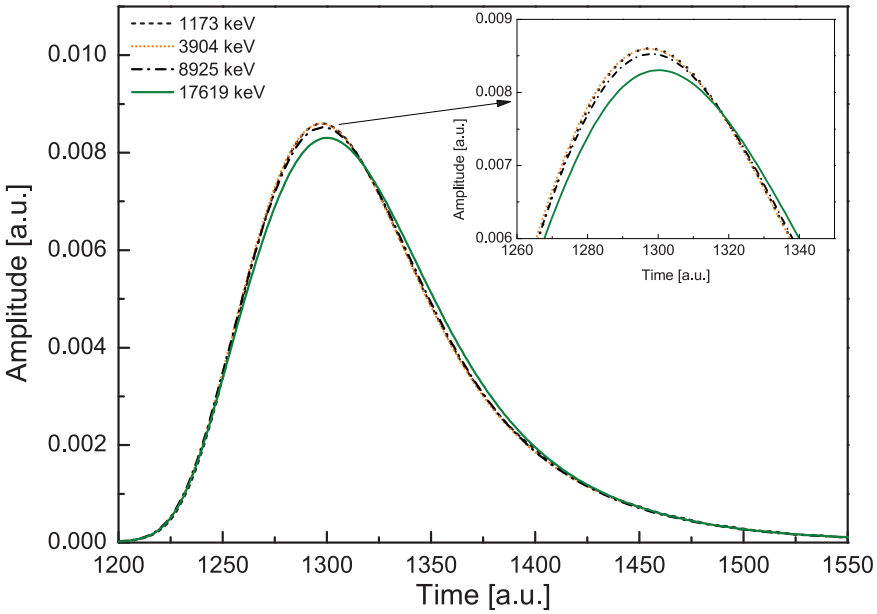

Fig. 3: The pulse line-shape measured in a $LaBr_3$:Ce (3.5" × 8") detector with the active VD for different gamma-ray energies.

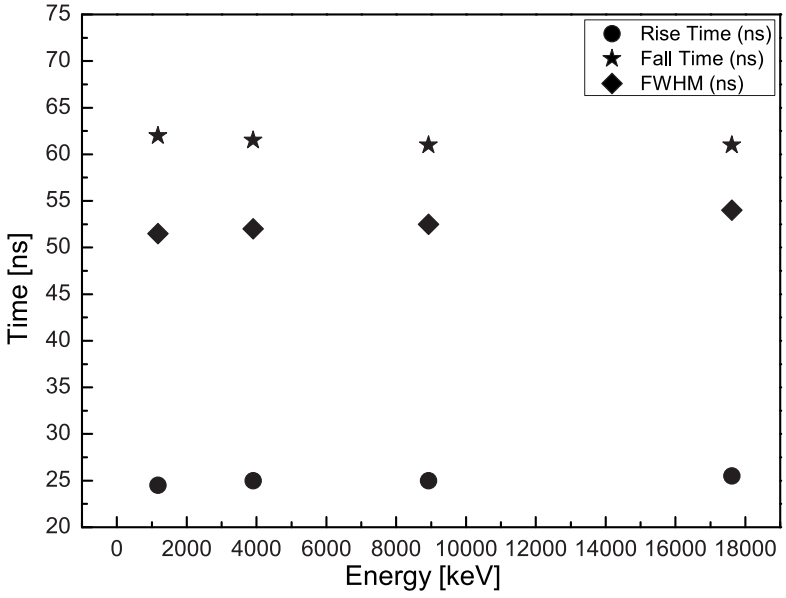

Fig. 4: The pulse line-shape parameters extracted from Fig. 3 .

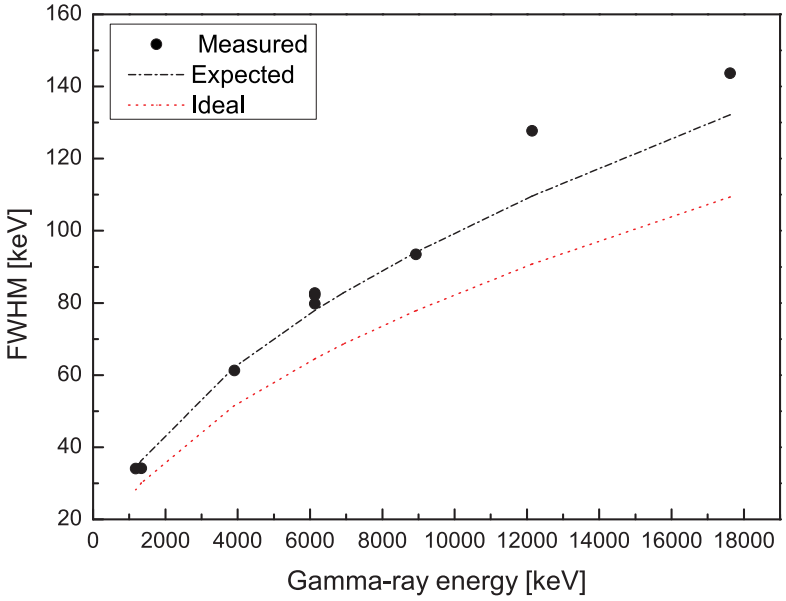

Fig. 5: The measured energy resolution for a $LaBr_3$:Ce (3.5" $\times$ 8") detector with the active VD. The filled points are the results obtained at ATOMKI Debrecen Laboratory using an analog electronics (BaFPro modul). The dashed black line indicates the expected $1/\sqrt{E}$ trend. The dashed red line indicates the values obtained at University of Milan from digitalized pulses

the shaping of signals was used. The detector HV was chosen in order to have an anode signal of 30 mV for an event which deposit 661.6 keV inside the crystal. The results are showed in Fig. 5. The energy resolution reflects the expected trend up to 10 MeV. Due to the crystal in-homogeneities or, alternatively, to small gain drift of the PMT gain down to temperature or voltage a deterioration of the energy resolution from the $1/\sqrt{E}$ trend was observed for the two highest gamma-ray energies. The dotted red line shows the energy resolution measured (up to 9 MeV) and expected (for E$\gamma > 9$ MeV) in our R&D laboratory using digitized pulses. Fig. 6 shows a comparison between energy spectra measured with a $LaBr_3$:Ce (3.5" $\times$ 8") detector and a HPGe detector. The used source is a AmBe-Ni source. In such a source, a core of ^{9}Be and alpha-unstable ^{241}Am is surrounded by a thick layer of paraffin; some metal discs of natural Nickel are also placed inside the paraffin layer. The radiative capture of thermal neutrons in natural Nickel produces several gamma rays of which those at 8.997 MeV is the strongest one. The AmBe-Ni source is very useful because the ^{58}Ni(n, γ) neutron capture reaction produces gamma-rays up to 9 MeV of energy, and this is one of the few ways to have such high energy gammas without using an accelerator. The 9 MeV gamma-ray is resolved in both spectra.

3 Conclusions

We studied the performances of large volume $LaBr_3$:Ce (3.5" $\times$ 8") detector in terms of the PMT+VD response, the detectors energy resolution and their response functions to different count rates. The characteristics of these detectors were investigated in a wide energy range, from 1 MeV up to 22.6 MeV. These tests were performed in preparation to the experimental campaign at GSI Laboratories (Germany) where the HECTOR^{+} array will be used in the PRESPEC-AGATA setup.

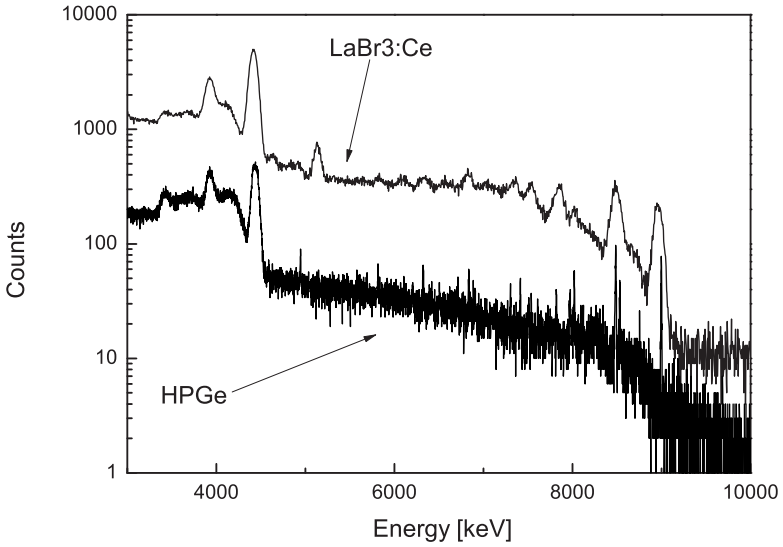

Fig. 6: The energy spectra measured using a $LaBr_3$:Ce (3.5" × 8") detector with the active VD in black and a HPGe in red. An AmBe-Ni source was used.

References

[1] F.C.L. Crespi et al., Nucl. Instr. and Meth. A602 (2007) 520
[2] R. Nicolini et al., Nucl. Instr. and Meth. A582 (2007) 554
[3] M. Ciemala et al., Nucl. Instr. and Meth. A608, (2009) 76
[4] S. Riboldi et al., IEEE NSS (2011) 776-778
[5] S. Riboldi et al., IEEE NSS (2010) 1809
[6] O. Wieland et al., PRL (2009), vol. 102, no. 9, p. 092502.
[7] A.Corsi et al., PRC (2012) 381 012045.

Scintillators with high-energy-resolution and low-intrinsic-activity

F. Quarati[ab], J. van de Biezen[c], P. Dorenbos[a], G. von der Goenna[d], C. Hansson[c], Alan Owens[c], L. Parthier[e], P. Schotanus[f], F.Seifert[e], M. Selle[e], T. Toepfer[d] and A. Weisleder[d]*

[a]Delft University of Technology, TNW, Mekelweg 15, 2629JB Delft , The Netherlands
[b]Praesepe BV, Lorentzplein 7, 2012 HG Haarlem, The Netherlands
[c]European Space Agency, ESTEC, Keplerlaan 1, 2201AZ Noordwijk, The Netherlands
[d]Hellma Materials GmbH, Moritz-von-Rohr Strasse 1, 07745 Jena, Germany
[e]Schott AG, Advanced Materials, Moritz-von-Rohr Strasse 11, 07745 Jena, Germany
[f]Scionix BV, Regulierenring 5, 3981LA Bunnik, The Netherlands

Lanthanum halides scintillators, namely $LaBr_3$ and $LaCl_3$, have superior scintillation properties and provide the best energy resolution for gamma-ray detection. However, the presence of natural isotope ^{138}La generates an intrinsic activity, well above 1 Bq/cm^3, which represents a major shortcoming for their application in low count rate experiments. Among other applications, for space applications it is desired the development of low intrinsic activity scintillators which also maintain the spectroscopic performances of $LaBr_3$, in terms of energy resolution and detection efficiency. At now two scintillators have been developed by our collaboration with capabilities to fulfill this requirement: $CeBr_3$ and SrI_2.

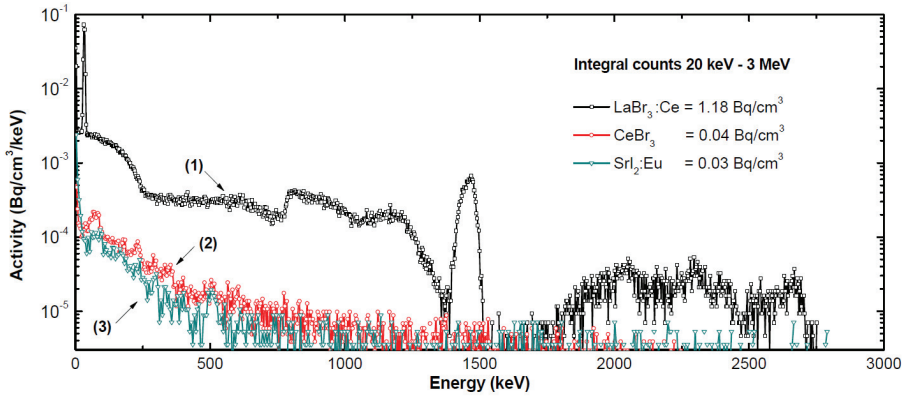

Fig.1: Comparison of intrinsic activity pulse high spectra collected with $LaBr_3$:Ce (1), $CeBr_3$ (2) and SrI_2:Eu (3).

In this communication we briefly summarize the origin of $LaBr_3$ intrinsic activity and quantify the limitation it might pose. Then, we show the results we have already obtained with $CeBr_3$ and SrI_2. Nowadays $CeBr_3$ is available in size of 2″×2″ and larger and does not present any detectable intrinsic activity, neither at level of contaminants. Energy resolution achieved so far is less than 4% at 662 keV and its fundamental limit currently under investigation. At the energy of 1.4 MeV, used for the detection of ^{40}K, which is of interest for gamma-ray remote sensing of planetary surfaces, a $CeBr_3$ spectrometer is about 8 times more sensitive than $LaBr_3$.

* *corresponding author; e-mail: f.g.a.quarati@tudelft.nl*

Application of the HICAM Camera for Imaging of Prompt Gamma Rays in Measurements of Proton Beam Range

R. Peloso[1], P. Busca[1], A.Celani[2], C. Fiorini[1], I.Perali[1], M. Basilavecchia[2], T. Frizzi[2], J. Smeets[3], F. Roellinghoff[4], D.Prieels[4], F. Stichelbaut[4] , A. Benilov [4]

[1] Politecnico di Milano, Dipartimento di Elettronica e Informazione, Milano, Italy and INFN, Sezione di Milano, Milano, Italy.
[2] XGLab, Milano, Italy.
[3] Université Libre de Bruxelles, Service de Métrologie Nucléaire, Brussels, Belgium and funded by the Belgian FNRS (aspirant).
[4] Ion Beam Applications S.A., Louvain-la-Neuve, Belgium.

Abstract

The HICAM gamma camera is an imaging device recently developed in the framework of a European project, based on Silicon Drift Detectors (SDDs) as photodetectors. Although originally designed for low-energy gamma-ray imaging in nuclear medicine (140 keV of ^{99m}Tc), in this work we attempt to use the camera, suitably modified, to image high energy prompt gamma rays (2 to 7 MeV) emitted by a target irradiated by protons. The final objective of our experiment is to assess the feasibility of proton beam range measurements by prompt gamma imaging with a slit camera, and the HICAM camera was chosen for a first prototype. Although a SDD-based camera would not be fast enough for real treatment conditions, the prototype here employed benefited from the camera modularity, compactness, high resolution and low noise. The camera here employed is composed of 25 SDDs of 1 cm^2 active area each, arranged in a 5x5 format, already used in clinical and research environments with a high intrinsic spatial resolution (~1 mm). The SDD matrix has been coupled to a LYSO crystal (1cm thickness), to improve efficiency with high-energy gammas, and has been characterized preliminarily with a ^{60}Co source. Good imaging performances have been obtained in this test. Moreover, results of a first test of the camera to detect prompt gammas emitted with a proton beam impinging on a plastic target are presented in this work.

1 Introduction

Particle therapy is nowadays considered an advantageous option in cancer treatment and growing research efforts are dedicated to its development. Strength of this kind of therapy, in particular proton therapy, is related to the possibility to release the maximum of the dose in the target site destroying tumoral cells and limiting otherwise the dose to healthy tissues.

For this purpose, the measurement of the proton beam range in the target is very important but although the energy of therapeutic proton beams is usually controlled with a high level of accuracy, corresponding to a sub-mm range accuracy in water, the real range of such proton beams in patients may contain uncertainties of up to 10-15 mm (due to uncertainties on tissue composition, internal organ motions, anatomical and physiological changes, patient positioning, etc.).

The proposed method to improve the quality control of the treatment is based on the detection of prompt gamma rays emitted by excited nuclei during proton irradiation [1].

In fact, during a proton irradiation, the secondary emissions generate by nuclear interactions within the target include prompt gammas with energies up to 10 MeV and previous studies have shown that the location of these prompt gammas is correlated to the position of the Bragg peak [2-3]. The development of a prompt gamma camera could be a solution which allows checking in real-time the range of a single pencil beam with a 'mm' accuracy in patients [4].

Prompt gammas emitted along the proton tracks are selected with a tungsten slit collimator and detected with a 10mm LYSO scintillator to obtain a reversed 1D image of the proton beam path in the target, as visible in Fig.1.

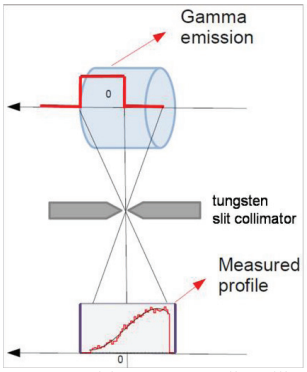

Fig. 1: Scheme of a prompt gamma camera with a tungsten slit collimator and a LYSO scintillator to detect selected prompt gamma emitted.

The challenge of this method is to detect high energy photons in an important neutron background. A dedicated concept was designed with Monte Carlo simulations and an example of the response is reported in Fig.2 for an energy window of 3 to 7 MeV. The profile of the photons correlated to the Bragg peak is indicated in green color and in pink the contribution of neutrons which only generate an offset that does not perturb the overall correlation with the Bragg peak.

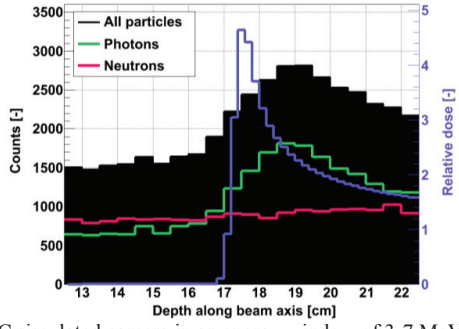

Fig. 2: .Response of a MC simulated camera in an energy window of 3-7 MeV when sending 10^9 protons of 160 MeV on the water target. Photon and neutron count rates are about 1000 counts per 5 mm bin.

To preliminarily verify the effectiveness of this concept we use the HICAM gamma camera, recently developed in the framework of the HICAM (HIgh resolution CAMera) project supported by the European Community, under coordination of Politecnico di Milano [5].

2 The HICAM Gamma Camera

HICAM is an Anger camera, designed for medical applications with low energy gamma sources (typ. 140keV of ^{99m}Tc), based on Silicon Drift Detector (SDD) photodetectors which are characterized by high quantum efficiency (>80%) and low electronic noise. The basic detection unit is a monolithic array of 5 SDD of 1 cm^2 active area each. During the project two prototypes in a format 5 x 5 and 10 x 10 were realized assembling several SDDs units, Fig. 3 shows a photograph of the 25 SDDs matrix. The photodetectors were coupled with a CsI crystal (10mm thickness). A custom designed ASIC reads and filters the signals from each SDD.

Fig. 3: Photograph of the detection module of the small HICAM prototype. The whole active area is 5 cm x6 cm.

The HICAM camera is characterized by a very high intrinsic resolution (~1 mm) [6] and has recently shown good performances both in clinical and pre-clinical applications [7].

For this work we used the small prototype with a 5 cm x 6 cm active area. Originally developed only for low-energy gamma-ray imaging, in this work it has been suitably modified to image higher energy prompt gamma rays (2 to 7 MeV) emitted by the target irradiated by protons. The photodetectors are now coupled with a LYSO crystal of 1 cm thickness, a good compromise between improved detection efficiency and still satisfactory ratio between thickness/FOV. The light collection was purposely limited covering the top side and the lateral ones with black absorbing tapes to match the readout ASIC dynamic range, originally designed for 200 keV. The natural emission of Lutetium gives a significant background to the energy spectrum and suitable processing of signals has been introduced to minimize its contribution in the images.

3 Laboratory characterization of the camera

A first measurement session was made in Politecnico laboratory, to assess the imaging capability of the system with a ^{60}Co source (1.17 MeV, 1.33 MeV).

As schematically represented in Fig. 4, the ^{60}Co point source was placed on the edge of a lead block (3 cm thickness) and moved from one boundary of the active area of the camera to the opposite one with steps of 0.5 cm in order to cover all the detection area in longitudinal direction. Fig.5. shows the

reconstructed image, by means of centroid algorithm, of the irradiation of the source when placed in the middle of the camera.

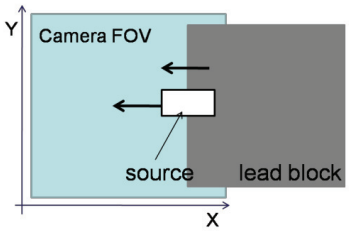

Fig. 4: A ^{60}Co point source is placed on the edge of a lead block (thickness of 3 cm) and moved from one boundary of the active area to the opposite one with steps of 0.5 cm.

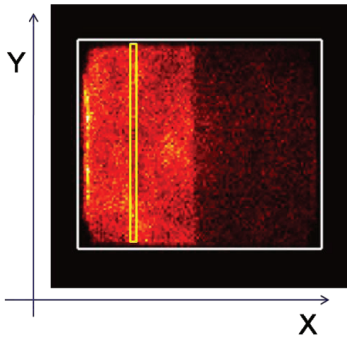

Fig. 5: Reconstructed irradiation of the ^{60}Co point source next to the middle of the camera. The centroid algorithm produces a reduction of the useful active area, pointed out by the white box.

From the figure, it is possible to notice that the irradiated region and the dark one (covered by the lead block) are separated quite sharply. The counts of the image are then integrated along the vertical axis, with 1 mm bin (yellow box in figure), to compute the 1D profile. All the acquired profiles of the moving source along the whole area, are overlapped and shown in Fig. 6, each one visualized only in a proper region of interest.

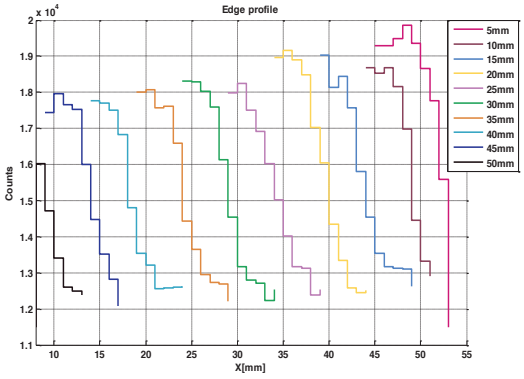

Fig. 6: Edge profiles of the source moving across the field of view with steps of 0.5 cm.

4 Proton range measurements

The first experiment with prompt gammas was carried out in the new WPE proton therapy center in Essen, Germany. The experimental set up, schematically shown in Fig. 7, consists in a proton beam impinging on a PMMA target of 20 cm length and 7.5 cm radius. A tungsten, knife-edge slit collimator, with an aperture of 6 mm, is set at a distance of 15 cm to detect the prompt gammas emitted in perpendicular direction with respect to the beam one. HICAM camera is placed at the same distance of 15 cm from the collimator. Both the camera and the read out electronics are shielded with a lead box, 5 mm of thickness. A photograph of the set-up is shown in Fig. .

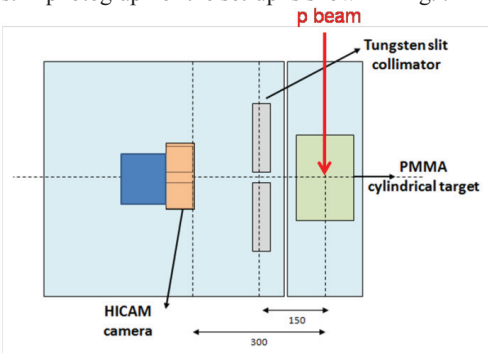

Fig. 7: Scheme of the set up for prompt gammas measurements. The slit collimator is set at a distance of 15 cm to detect the prompt gammas emitted in perpendicular direction with respect to the beam one. The same distance is kept between HICAM and the collimator.

In the energy spectrum of prompt gammas, as shown in the measurement of Fig., the significant component of the natural emission of Lutetium is visible but the selected energy window from 3 to 7 MeV, set for all the following acquisitions, cuts off its contribution.

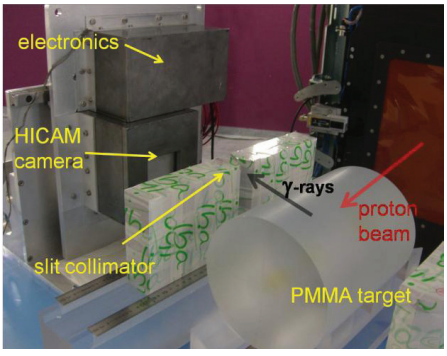

Fig. 8: Photograph of the set up used in the radiotherapy facility. The slit collimator, aperture 6mm, and the Hicam camera are in perpendicular direction with respect the proton beam one.

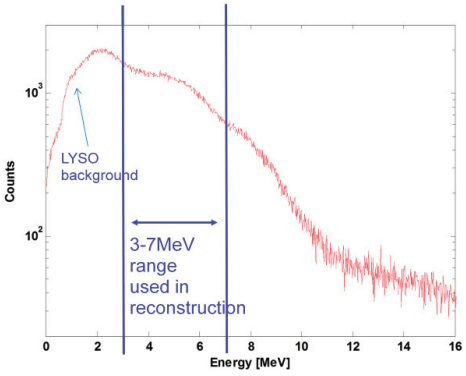

Fig. 9: Energy spectrum of prompt gammas. The energy window of 3-7 MeV is selected for the reconstruction.

We first present an acquisition (5 min long) in which the proton beam was set at an energy of 160 MeV.

In the default configuration of the setup, the dose peak is aligned with the collimator slit and the center of the camera FOV (see Fig. 7). The HICAM camera has also a mobile support that allows to place the camera in two other positions at distances of 4 cm toward right and left. The same acquisition was thus repeated with the camera in these two positions and the reconstructed profiles are overlapped in the same graph. This allows to better image the whole profile despite the limited FOV of HICAM.

The profiles obtained from the three acquisitions are shown in Fig. 10a. Another set of three measurements was carried out substituting the slit collimator with a tungsten block, 4 cm of thickness, in order to acquire signal due to neutrons and scattered gamma–rays and the result is reported in Fig. 10b. This profile is rather flat and represents a constant contribution that could be subtracted from the previous acquisition. The resulting profile is presented in Fig. 10c and is in good agreement with simulations.

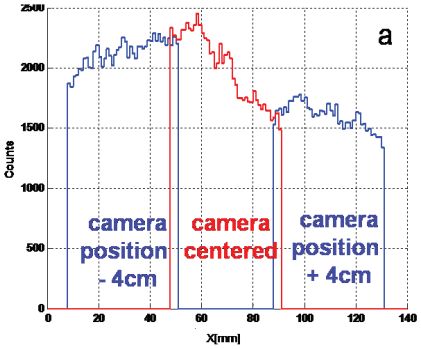

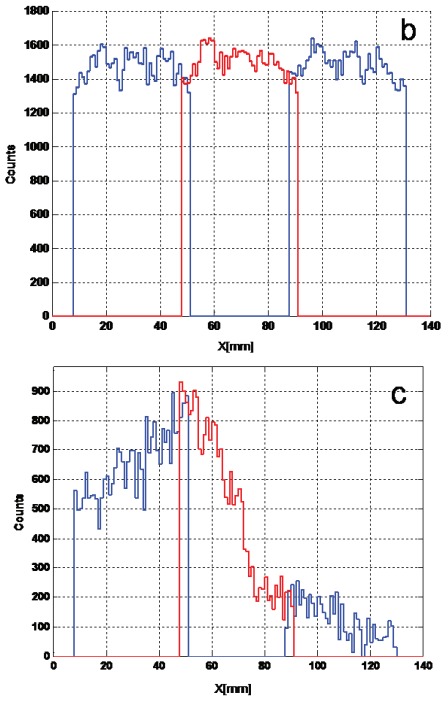

Fig. 10: (a) Profiles of three overlapped acquisitions, each of 5 min, with HICAM moving with respect to the collimator aperture; (b) contribution from neutrons and scattered photons acquired interposing a tungsten block; (c) profile obtained subtracting the last profile from the first one, that can be attributed to prompt gamma photons.

With the camera fixed in the central position another set of acquisitions was carried out changing the position of the PMMA target, with beam energy of 100 MeV. From the central position, the target was moved with steps of different length, from 1 mm to 10 mm, toward both the right and the left directions, in order to evaluate the capability of the system to track also small shifts. Acquisitions time was of 5 min each.

The fits of the measured profiles are reported in Fig. 11. All the fitted profiles are well defined and separated and even the difference between 1 mm shifts of the target could be clearly identified by eye.

To preliminarily evaluate the accuracy of the measured shift, a reference value x_0 was derived from the intersection between the curve acquired in the central position and the vertical axis in the middle of the camera FOV (30 mm). For each profile the distance with respect to this point is evaluated along the horizontal axis (Fig. 12). The accuracy of this measurement is preliminarily evaluated as the difference between the measured value and the expected one, as shown in Fig. 12, and it turns out to be in the 'mm' range.

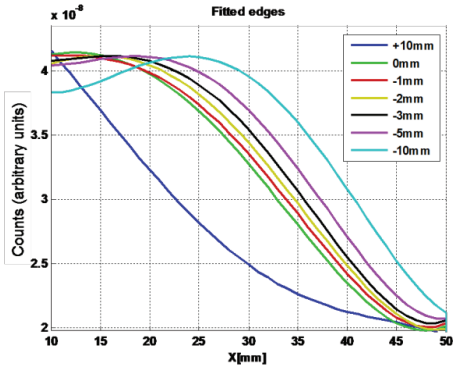

Fig. 11: Fitted profiles of the acquisitions with the moving target. Each acquisition is 5min long and corresponds to $7 \cdot 10^{10}$ absorbed protons.

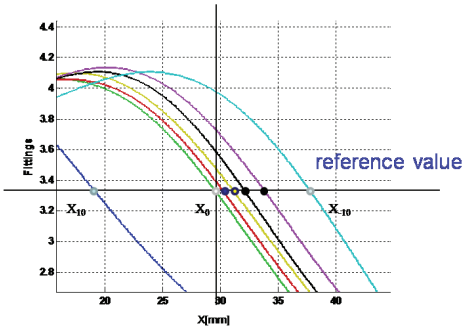

Fig. 12: The reference value x_0 was defined from the intersection between the profile of the base position and the vertical axis in the middle of the camera FOV (30mm). For each profile the distance with respect to this point is evaluated along a horizontal axis.

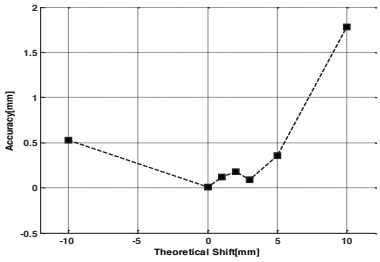

Fig. 13: Plot of the difference between exact range shift and measured shift.

Measurements were then extended to 230 MeV to cover the full clinical range of beam energies.The profiles obtained from the three acquisitions, after the subtraction of the contribute due to neutrons and scattered gamma–rays, are shown in Fig. 10.

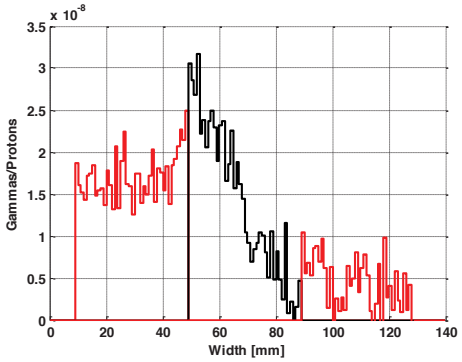

Fig. 14: Profiles of three overlapped acquisitions at 230 MeV, each of 450 sec, with HICAM moving with respect to the collimator aperture. The contribution from neutrons and scattered photons was subtracted.

Also in this case, the target was moved from the central position with steps of lengths from 1 mm to 10 mm, toward both the right and the left directions. Acquisitions time was of 450 sec each. The fits of the measured profiles are reported in Fig. 15.

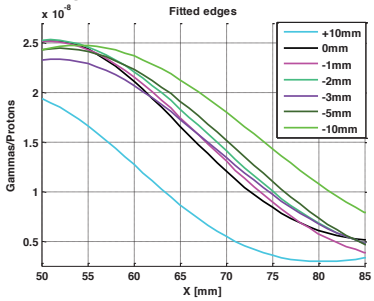

Fig. 15: Fitted profiles of the acquisitions with the moving target. Each acquisition is 450 sec long and corresponds to $4 \cdot 10^{10}$ absorbed protons.

5 Conclusions

Measurements of prompt gammas correlated to proton range were successfully made using the HICAM gamma camera. Although not optimized for 1 to 10 MeV energy range (low efficiency, low scintillator light collection) a satisfactory accuracy in the 'mm' range was first measured.

Although suitable for the measurements performed in this work, the SDD-based camera shows intrinsic limitations in terms of speed, which make it unsuited to patients treatments. The camera, however, thanks to its high intrinsic spatial resolution, compactness and versatility has allowed demonstrating the concept of slit camera for prompt gamma detection in proton therapy.

Acknowledgement

The authors thank D. Clivio, P.Compagnoni, S. Masci and S. Incorvaia for their support.

References

[1] F. Stichelbaut, Y. Jongen," Verification of the proton beam position in the patient by the detection of prompt gamma-rays emission", 39th PTOCG meeting, San Francisco (2003).

[2] C.-H. Min, C.H. Kim, M.-Y. Youn, J.-W. Kim, "Prompt gamma measurements for locating the dose falloff region in the proton therapy", Applied Physics Letters 89: 183517 (2006).

[3] D. Kim, H. Yim, J.-W. Kim, "Pinhole camera measurements of prompt gamma-rays for detection of beam range variation in proton therapy", Journal of the Korean Physical Society 55(4): 1673-1676 (2009).

[4] D.Prieels, J.Smeets, F.Stichelbaut, A.Benilov, J.C.Dehaes, A.Dubus, F.Roellinghoff, "Towards a practical solution for real-time measurement of the proton beam range in patients", 50th PTCOG meeting, Philadelphia (2011).

[5] www.hi-cam.org.

[6] R.Peloso, P.Busca, C.Fiorini, A.Abba, A.Geraci, A.Manenti, A. Longoni, G.Padovini, C.Bianchi, G.L.Poli, K.Erlandsson, B.F.Hutton, P.Lechner, H.Soltau, L.Strüder, A.Pedretti, P.Van Mullekom, "The HICAM Gamma Camera" Nuclear Science Symposium Conference Record (NSS/MIC), 2010 IEEE , ISBN # 978-1-4244-9104-9, 4 Pages.

[7] P.Busca, R.Peloso, C.Fiorini, A.Gola, A.Abba, K.Erlandsson, B.F.Hutton, C.Bianchi, G.L.Poli, U.Guerra, G.Virotta, L.Ottobrini, C.Martelli, G.Lucignani, A.Pedretti, P.Van Mullekom, S.Incorvaia, F.Perotti, "Applications of the HICAM Gamma Camera", Nuclear Science Symposium Conference Record (NSS/MIC), 2010 IEEE , ISBN # 978-1-4244-9104-9, 4 Pages.

Electromagnetic Dissociation Cross Sections for Double Nucleon Removal using Weisskopf-Ewing Theory

Anne Marie Adamczyk
University of Tennessee, Department of Nuclear Engineering
315 Pasqua Engineering Building, Knoxville, TN, 37996, USA
aadamczy@utk.edu

Abstract
The continued development of accurate particle interaction cross section models are necessary for calculating reliable space radiation exposure assessments when using space radiation transport codes. The nuclear fragmentation model NUCFRG3, which has been incorporated into various space radiation transport codes, calculates Electromagnetic Dissociation (EMD) cross sections using Weisskopf-Ewing (WE) theory. However, only single nucleon removal EMD cross sections are calculated. For total space radiation exposure estimates, single nucleon emission is most important, but multiple particle emission is also significant. In this work, EMD cross sections for double nucleon removal are calculated using the WE theory, which is the formalism currently utilized by NUCFRG3. Comparisons are made to a previously developed double nucleon removal parameterization for cosmic ray nuclei and experimental data.

1 Introduction

The deleterious effects from space radiation exposure to astronauts and electronics are an important concern for space operational development. Reliable radiation exposure estimates from Galactic Cosmic Rays (GCRs), require an accurate description of the nuclear interactions between particles of the ambient radiation environment and the shielding material. It has been shown by Norbury and Maung [1] that reactions proceeding via the electromagnetic force are of major importance to nuclear reactions of interest to space radiation assessments. The deterministic space radiation transport code HZETRN2010 (High charge (Z) and Energy TRaNsport) was developed at NASA Langley Research Center as a computational tool for space radiation studies and shield design [2]. The code utilizes the nuclear fragmentation model NUCFRG3 [3] to calculate ElectroMagnetic Dissociation (EMD) cross sections. Currently, multiple nucleon emission is not included in NUCFRG3. The present work provides an extension of the EMD framework of NUCFRG3 to provide the ability to calculate double nucleon removal cross sections.

2 EMD cross section

The NUCFRG3 EMD cross section for one nucleon removal assumes both electric dipole (E1) and electric quadrupole (E2) excitations. Other electromagnetic multipoles were excluded, since their effect is much less important. Adopting a similar formalism, which includes both E1 and E2 excitations, the total photonuclear dissociation cross section for double nucleon removal is expressed as

$$\begin{aligned} \sigma^{\mathrm{EMD}}(ab) &= \sigma_{\mathrm{E1}}^{\mathrm{EMD}}(ab) \; + \; \sigma_{\mathrm{E2}}^{\mathrm{EMD}}(ab) \\ &= \int_{E_0(ab)} \left[N_{\mathrm{E1}}(E_\gamma) \; \sigma_{\mathrm{E1}}(E_\gamma, ab) + N_{\mathrm{E2}}(E_\gamma) \; \sigma_{\mathrm{E2}}(E_\gamma, ab) \right] dE_\gamma \; , \end{aligned} \tag{1}$$

where $\sigma_{\mathrm{E1}}^{\mathrm{EMD}}(ab)$ and $\sigma_{\mathrm{E2}}^{\mathrm{EMD}}(ab)$ are the E1 and E2 photonuclear dissociation cross section components, respectively. The lower limit of integration in Eq. (2) is evaluated at the photonuclear threshold energy,

$E_0(ab)$, for the production of particles ab. The NUCFRG3 formalism for the Weizsacker-Williams E1 and E2 virtual photon spectras, $N_{\mathrm{E1}}(E_\gamma)$ and $N_{\mathrm{E2}}(E_\gamma)$, where E_γ represents the photon energy, is documented in Ref. [3] and is utilized in this work. Also contained in Eq. (1) are $\sigma_{\mathrm{E1}}(E_\gamma, ab)$ and $\sigma_{\mathrm{E2}}(E_\gamma, ab)$, the E1 and E2 total photonuclear reaction cross sections for the production of particles ab, respectively.

2.1 Photonuclear cross section

The total photonuclear reaction cross section for the production of particles ab is expressed as

$$\begin{aligned} \sigma_\gamma(E_\gamma, ab) &= \sigma_{\mathrm{E1}}(E_\gamma, ab) \; + \; \sigma_{\mathrm{E2}}(E_\gamma, ab) \\ &= G_{ab}(E_\gamma) \; \sigma_{\mathrm{abs}}(E_\gamma) \\ &= G_{ab}(E_\gamma) \; [\sigma_{\mathrm{abs-E1}}(E_\gamma) \; + \; \sigma_{\mathrm{abs-E2}}(E_\gamma)] \; , \end{aligned} \tag{2}$$

where the photoabsorption cross section, σ_{abs}, is given by the sum of the E1 and E2 photoabsorption cross section components, namely $\sigma_{\mathrm{abs-E1}}$ and $\sigma_{\mathrm{abs-E2}}$, respectively. The formalism for the photoabsorption cross section utilized in this work has been discussed in Ref. [3] and will not be reproduced herein. Eq. (2) also contains $G_{ab}(E_\gamma)$, the branching ratio or probability of producing particles ab, which will be discussed in the subsequent section.

2.1.1 Branching Ratio using WE theory

The single particle removal EMD calculations of NUCFRG3 currently employ WE theory to calculate the branching ratio for the input photonuclear cross sections. Therefore, utilizing the WE formalism to calculate double nucleon removal cross sections was seen as a natural extension of the NUCFRG3 EMD framework. A statistical description of the compound nucleus model, based on WE theory, was employed, which follows work by Büttner et al., Ref. [4]. According to the scheme of successive evaporation of particles, it is assumed that the reaction $X(x, ab)B$ can be separated as

$$\begin{aligned} x \; + \; X \; \longrightarrow \; Z \; \longrightarrow \; a + \quad & A \\ \hookrightarrow \quad & b \; + \; B \; . \end{aligned} \tag{3}$$

Here, particle x (note that for a photonuclear reaction, x corresponds to a photon) strikes a projectile nucleus X to produce a residual nucleus A and an arbitrary outgoing particle a. Note that the reaction proceeds through an intermediate compound state, labeled Z. If the excitation energy of the residual nucleus A is higher than the binding energy of an arbitrary particle b, then nucleus A may subsequently decay into the residual nucleus B and the arbitrary outgoing particle b. Note that x, a, and b may be particles, such as a photon, neutron, or proton, but also may be nuclei, such as a deuteron, triton, helion, or alpha particle.

A schematic representation of the energy level diagram for two particle emission after compound nucleus formation is presented in Fig. 1. It can be seen from the energy level diagram, that the excitation energies of the residual nuclei A and B are given as

$$E^*_A = E_x + Q_{x,a} - E_a \tag{4}$$

$$E^*_B = E_x + Q_{x,ab} - E_a - E_b \; , \tag{5}$$

respectively, where $*$ signifies an excited state. Eq. (4) and/or Eq. (5) contain E_x, E_a, and/or E_b, the kinetic energy of particle x, a, and b, respectively, as well as $Q_{x,a}$ or $Q_{x,ab}$, the Q-values for the reactions (x, a) and (x, ab), respectively. Note that for a photonuclear reaction, Eq. (3) will be expressed as

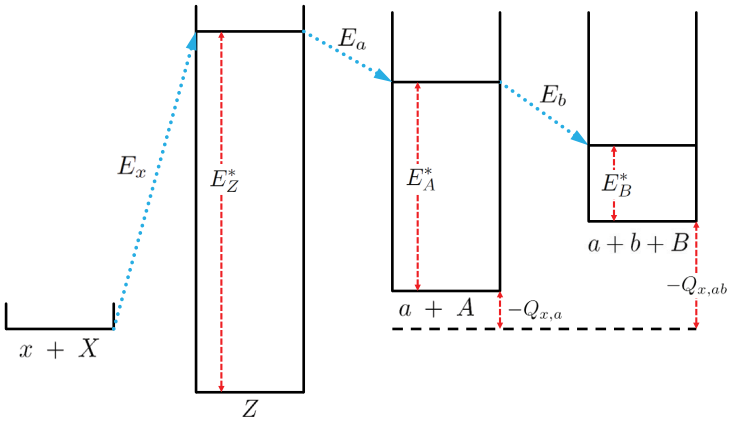

Fig. 1: Schematic representation of the energy level diagram for two particle emission after compound nucleus formation. Diagram adapted from Fig. 1 of Ref. [5].

$$\begin{aligned} \gamma + X \longrightarrow X^* \longrightarrow a + \quad & A \\ \hookrightarrow \quad & b + B\,. \end{aligned} \tag{6}$$

Therefore, the excitation energy of the compound nucleus Z is given as

$$E_Z^* = E_X^* = E_x = E_\gamma\,. \tag{7}$$

2.1.1.1 Branching ratio formalism

The branching ratio $G_{ab}(E_\gamma)$, given in Eq. (2), is calculated using a scheme of successive evaporation of particles, based on WE theory, and is generalized here as

$$G_{ab}(E_x) = \frac{\int_0^{E_x+Q_{x,ab}} dE_a\; S(E_x,E_a)\; G_b^A(E_x,E_a)}{\sum\limits_{a'} \int_0^{E_x+Q_{x,a'}} dE_{a'}\; S(E_x,E_{a'})}\,, \tag{8}$$

where the probability that the nucleus A will decay by emission of particle b is expressed as

$$G_b^A(E_x,E_a) = \frac{\int_0^{E_x+Q_{x,ab}-E_a} dE_b\; S(E_x,E_a,E_b)}{\sum\limits_{b'} \int_0^{E_x+Q_{x,ab'}-E_a} dE_{b'}\; S(E_x,E_a,E_{b'})}\,. \tag{9}$$

Note that the sum in the denominator of Eq. (8) and Eq. (9) should include all possible decay channels; However, herein it is assumed that a and b can be a neutron, proton, deuteron, triton, helion, or alpha particle. Other decay modes may be considered in future work. Eq. (8) and Eq. (9) contain $S(E_x,E_a)$ and $S(E_x,E_a,E_b)$, respectively, which are expressed as

$$S(E_x, E_a) = g_a\, k_a^2(E_a)\, \sigma_a(E_a)\, \rho^A(E_A^*) \quad (10)$$
$$S(E_x, E_a, E_b) = g_b\, k_b^2(E_b)\, \sigma_b(E_b)\, \rho^B(E_B^*)\,. \quad (11)$$

If $i = a$ or b, the variables g_i, k_i, and σ_i represent the statistical weighting factor, wave number, and inverse cross section for either particle a or b. The formalism of the inverse cross section, which herein describes the cross section for the absorption of the emitted particle a or b by the nucleus Z or A, respectively, has been discussed in Ref. [6] and will not be repeated here. Note that

$$g_i\, k_i^2(E_i) \;=\; (2s_i + 1)\, (2m_i\, E_i\, \hbar^{-2})\,, \quad (12)$$

with s_i, m_i, and E_i representing the spin, mass, and kinetic energy for the particle i, respectively (where $i = a$ or b). Eq. (10) and Eq. (11) also contain $\rho^A(E_A^*)$ and $\rho^B(E_B^*)$, which signify the level density of the residual nucleus A or B, at excitation energy E_A^* or E_B^*. More information regarding the form of the nuclear density is given in Ref. [3].

2.1.2 Energy independent branching ratio

A branching ratio can be modeled as energy dependent, as in Eq. (2), or as energy independent. Utilizing an energy independent branching ratio formalism for double nucleon removal EMD cross section calculations increases computational speed; When substituting a photonuclear cross section, which utilizes an energy independent branching ratio, into the formula for the total photonuclear dissociation cross section, namely Eq. (1), the branching ratio can be brought outside of the integral, allowing for faster computations.

Energy independent branching ratios for double nucleon removal were suggested by Norbury and Mueller in 1994, Ref. [7]. The two neutron and two proton branching ratios are approximated as

$$G_{nn} = (1 - G_n)^2 \quad (13)$$
$$G_{pp} = G_p^2\,, \quad (14)$$

where G_n and G_p are the single neutron and proton branching ratio, respectively. The emission of other channels was thought to compete insignificantly with proton and neutron emission, therefore, G_n was defined as $G_n = 1 - G_p$, where

$$G_p = \begin{cases} 0.5 & \text{for } Z_A < 6 \\ 0.6 & \text{for } 6 \le Z_A \le 8 \\ 0.7 & \text{for } 8 < Z_A < 14 \\ \text{Min}\,[Z_A/A_A,\ 1.95\exp(-0.075\ Z_A)] & \text{for } Z_A \ge 14 \end{cases} \quad (15)$$

with Z_A and A_A as the atomic number and mass number of the projectile nucleus A, respectively. Due to the dependence on only the atomic number and mass number, the double nucleon removal branching ratios can be applied to a compound nucleus reaction, as in Eq. (3), or to a direct reaction.

3 Results

EMD cross sections for two neutron and two proton removal, calculated with either a WE, Eq. (8), or an energy independent, Eq. (13) or Eq. (14), branching ratio are compared to experimental data in

Table 1. Reactions include both projectile and target excitation. In Table 1, only the reactions which undergo target excitation, namely ^{59}Co and ^{197}Au, proceed through a compound nucleus state. Note that the reactions involving ^{18}O and ^{28}Si (projectile) excitations have one or more channels which proceed directly. The energy dependent branching ratio, based on WE theory utilized herein, was formulated for compound nucleus reactions. Overall, when comparing the EMD cross sections, calculated with either a WE or energy independent branching ratio, to the experimental target excitation data, it can be seen in Table 1 that the WE results provide a better fit.

The branching ratio models utilized herein, namely WE and energy independent, can be qualified by comparing the model results to experimental data and displaying the results in tabular or graphical form. However, this type of validation does not quantify uncertainty and error. By using the cumulative uncertainty distribution method of Ref. [12], the accuracy can be quantified. This validation metric provides a global perspective on accuracy, and quantifies how well a model will perform for the application of interest compared to all validation data.

To assess the global accuracy of the EMD branching ratio methods, the models were compared to the available EMD experimental data in the assembled database using the cumulative uncertainty distribution method. Fig. 2 displays the cumulative uncertainty distribution as a function of the fraction of the data in the EMD experimental database, which consists of the sparse 24 cross sections given in Table 1. In the region of approximately 0.92 to 1.0 fraction of data, it can be seen that the EMD model which incorporates the WE branching ratio has a lower cumulative uncertainty than that which uses the parameterized energy dependent branching ratio. However, for most values of the fraction of data, the uncertainty due to experiment is larger than the difference between the EMD model results. Here, the experimental uncertainty swamps the model analysis. Consequently, the branching ratio methods cannot be differentiated until additional experimental results become available.

Table 1: EMD Cross Sections for double nucleon removal. $\sigma_{\rm expt}^{\rm EMD}$ are experimental EMD cross sections from Refs. [8–11]. $\sigma_{\rm NUCFRG2}^{\rm param}$ are theoretical EMD cross sections calculated with parameterized energy independent branching ratios from Ref. [7]. $\sigma_{\rm WE}^{\rm EMD}$ are theoretical EMD cross sections calculated using WE theory.

Projectile	Target	$T_{\rm lab}$ (GeV/n)	Decay Channel	$\sigma_{\rm expt}^{\rm EMD}$ (mb)	$\sigma_{\rm param}^{\rm EMD}$ (mb)	$\sigma_{\rm WE}^{\rm EMD}$ (mb)
^{197}Au	^{197}Au	1.0	^{195}Au	643 ± 105	100.1	398.1
^{139}La	^{197}Au	1.26	^{195}Au	335 ± 49	73.8	293.7
^{56}Fe	^{197}Au	1.7	^{195}Au	73 ± 13	25.1	99.8
^{40}Ar	^{197}Au	1.8	^{195}Au	76 ± 18	13.4	53.4
^{20}Ne	^{197}Au	2.1	^{195}Au	49 ± 15	5.2	20.7
^{12}C	^{197}Au	2.1	^{195}Au	9 ± 17	2.0	8.0
^{139}La	^{59}Co	1.26	^{57}Co	32 ± 16	15.0	58.3
^{56}Fe	^{59}Co	1.7	^{57}Co	13 ± 6	5.6	21.7
^{20}Ne	^{59}Co	2.1	^{57}Co	3 ± 5	1.2	4.8
^{12}C	^{59}Co	2.1	^{57}Co	6 ± 4	0.49	1.9
^{28}Si	Pb	13.7	^{26}Mg	73.11 ± 0.80	23.7	44.3
^{28}Si	Sn	13.7	^{26}Mg	31.7 ± 0.41	9.6	18.1
^{28}Si	Cu	13.7	^{26}Mg	12.55 ± 0.16	3.5	6.7
^{28}Si	Al	13.7	^{26}Mg	4.35 ± 0.10	0.79	1.5
^{28}Si	Pb	13.7	^{26}Si	1.9 ± 0.11	10.3	17.9
^{28}Si	Sn	13.7	^{26}Si	0.74 ± 0.07	4.3	7.5
^{28}Si	Cu	13.7	^{26}Si	0.27 ± 0.04	1.6	2.9
^{28}Si	Al	13.7	^{26}Si	0.12 ± 0.02	0.37	0.66
^{18}O	U	1.7	^{16}O	74.3 ± 1.7	36.0	141.2
^{18}O	Pb	1.7	^{16}O	65.2 ± 2.3	30.1	118.0
^{18}O	W	1.7	^{16}O	50 ± 4.3	25.6	100.5
^{18}O	Sn	1.7	^{16}O	27.5 ± 4.0	13.6	53.2
^{18}O	Cu	1.7	^{16}O	9 ± 3.5	5.5	21.6
^{18}O	Ti	1.7	^{16}O	6.3 ± 2.5	3.4	13.5

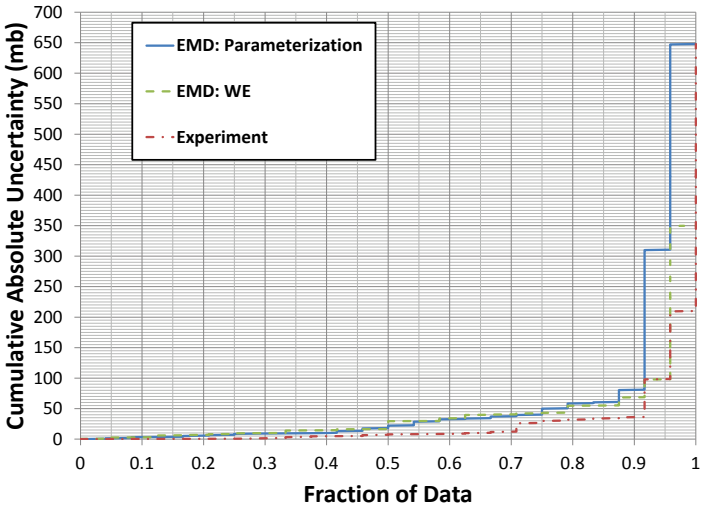

Fig. 2: Cumulative uncertainty distributions for the EMD cross section, calculated using either a parameterized energy independent branching ratio or WE theory, compared to the experimental EMD cross sections given in Table 1. The distribution for the cumulative uncertainty due to experiment is also shown.

4 Conclusions

In this work, the framework for calculating EMD double nucleon removal cross sections, using WE theory, was developed. Results were compared to EMD cross sections calculated with an energy independent branching ratio parameterization. For reactions which proceeded through a compound nucleus state, it was found that the EMD cross sections calculated with a WE branching ratio provided a better fit to experiment. However, when examining all of the available EMD cross section data, it was found that within the limited datasets and accuracy of experiments, it could not be determined whether the EMD cross sections calculated with a parameterized energy independent or WE branching ratio are more accurate in a global sense. Overall, the WE model provides a physics-based description for EMD reactions. The WE branching ratio can be used to calculate not only double nucleon emission, but also any allowed two particle emission combination. The WE formalism presented herein can also be extended to three particle emission.

References

[1] J. Norbury and K. Maung, *Acta Astronaut.* **60** (2007) 770.
[2] T. Slaba, S. Blattnig, and F. Badavi, *J. Comput. Phys.* **229** (2010) 9397.
[3] A. Adamczyk *et al.*, *Nucl. Instrum. Meth.* **A 687** (2012) 21.
[4] H. Büttner, A. Lindner and H. Meldner, *Nucl. Phys.* **63** (1965) 615.
[5] H. Liskien, *Nucl. Phys.* **A118** (1968) 379.
[6] A. Adamczyk, Ph.D. thesis, Worcester Polytechnic Institute, 2009.
[7] J. Norbury and C. Mueller, *Astrophys. J. Suppl. S.* **90** (1994) 115.
[8] D. Olsen et al., *Phys. Rev.* **C 24** (1981) 1529.
[9] J. Barrette et al., *Phys. Rev.* **C 41** (1995) 865.
[10] J. Hill et al., *Phys. Rev.* **C 39** (1989) 524.
[11] T. Aumann et al., *Phys. Rev.* **C** (1993) 1728.
[12] R. Norman and S. Blattnig, A Comprehensive Validation Methodology for Sparse Experimental Data, NASA TP 2010−216200 (2010).

Extensions of the INCL model to light ion induced reactions for medical and space applications

A. Boudard[1], *B. Braunn*[1], *J. Cugnon*[2], *J.C. David*[1], *P. Kaitaniemi*[1], *S. Leray*[1], *D. Mancusi*[1]
[1]CEA Saclay, Irfu/SPhN, 91191 Gif-sur-Yvette, FRANCE
[2]Université de Liège, AGO Department, Bât. B 5, B-4000 Liège, BELGIUM

Abstract
This contribution describes recent extensions of the Intra Nuclear Cascade code INCL to light ion projectiles and to low beam energies. Examples of carbon beam fragmentations at GANIL and at GSI energies on thick water or PMMA targets are compared with experimental data. The production of astatine isotopes from proton beams around 1 GeV on a thick Pb-Bi target (ISOLDE experiment) demonstrates the need of a good description of the helium production in the first interaction at the beam energy and of helium induced reactions at low energy in secondary interactions.

1 Introduction

Accelerator Driven Systems have renewed the interest for good models of spallation reactions describing especially the production of neutrons and of residual nuclei from proton beams on heavy nuclei in the GeV regime. This type of reactions is efficiently descried in terms of an Intra Nuclear Cascade - sequence of free and incoherent NN interactions in a realistic target nuclear density - followed by a de-excitation of the excited remnant nucleus mainly by evaporation of particles and possibly by fission.

The intra nuclear cascade code INCL originally built at Liège University [1] and more recently developed in collaboration with the CEA/Irfu/SPhN [2] is based on realistic physical ingredients and a very reduced number of parameters. This makes it a predictive semi-classical model of nuclear reactions. Coupled with modern de-excitation codes as ABLA [3], it fully specifies final states with all correlations and statistical fluctuations and is consequently also well adapted as a realistic event generator. It has been recognized as one of the best cascade in the frame of an inter-comparison of many codes organized by IAEA [4] and dealing with nuclear reactions induced by nucleons of 60 MeV to 2.5 GeV mainly on thin Iron and Lead targets.

We have recently tested and improved the model in other sectors. Composite projectiles up to alpha particles were already implemented with promising results at the GeV per nucleon [2]. We have extended the capabilities up to projectiles of mass sixteen and we have paid attention to the low energy domain, interesting in itself and really needed for most of applied calculations of thick target configurations. Potential applications are in the medical domain (tumor treatment by carbon beams) and in the evaluation of irradiation by cosmic rays (including heavy ions) on men and electronics in space vehicles.

There are presently a Fortran version of the code INCL4.6 coupled with the de-excitation ABLA07 in a still private version of MCNPX [5] and a fully redesigned C++ version INCL++5.1 implemented in GEANT4 [6] and using the GEANT4 de-excitation handler.

2 Treatment of light projectiles (4<A<17)

Light composite projectiles are treated in the following way. The ion comes from infinity at a random impact parameter (see Fig. 1a). It is described as a set of (A,Z) nucleons in the ion rest frame whose positions and momenta are randomly chosen in a realistic spacial and momentum density. A constraint is applied to have the sum of the vectors equal to zero in both spaces. For each configuration the depth of a binding potential is determined so that the sum of the nucleon energies is equal to the tabulated mass of the projectile nucleus.

A Lorentz boost with the nominal projectile velocity is applied to the off-shell nucleon four-vectors to define them in the laboratory system (target at rest). Nucleons are no more on mass shell but the sum of energies and vector momenta are equal to the nominal energy and momentum of the projectile.

The ion follows globally a classical Coulomb trajectory until one of its nucleon impinges on a sphere of calculation around the target nucleus, large enough for simulating all reaction events in practice. Considering the individual nucleon velocities, some of them will never interact with this sphere and will be combined together in the "projectile spectator".

All other nucleons are entering the calculation sphere. They will move globally (with the beam velocity) until one of them interact, being close enough to a target nucleon. The NN interaction is computed with the proper nucleon momenta, and if not Pauli-blocked, outgoing nucleons propagate independently until further collisions. Nucleons having crossed the sphere of calculation without any NN interaction are combined also in the "projectile spectator" at the end of the cascade.

This projectile spectator nucleus is kinematically defined by its nucleon content and its excitation energy obtained by an empirical particle-hole model based on the energy configuration of the current projectile and the removed nucleons (interacting with the target). This nucleus can then be de-excited by any model; typically a Fermi Breakup for the light projectiles considered up to now.

It is quite clear that this "projectile spectator" has not received any explicit contribution from the zone of interaction which is entirely contained in the target remnant. This has two consequences. The calculation is not at all symmetric (if we compute C on C for example) and we believe that the residue of the target is more realistic than the "projectile spectator" at this stage of the model.

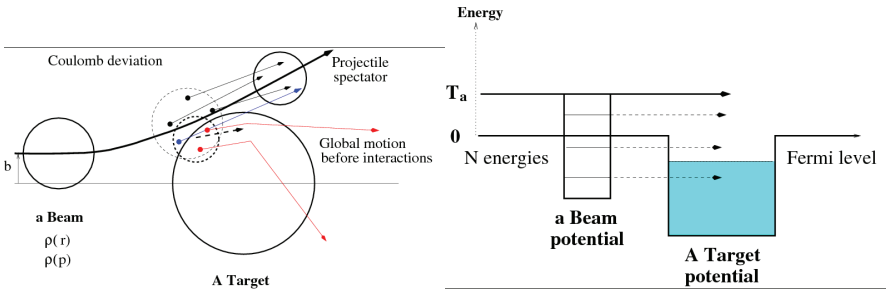

(a) Coulomb deviation (b) Compound nucleus at low energy

Fig. 1: Composite projectile treatment in INCL

3 Very light projectiles (d, t and He) and low energy

At very low energy, the nuclear reaction proceeds by a total absorption of the projectile and the formation of a compound nucleus which will then decay. To account for this, we have introduced a smooth empirical description of the transition between the full absorption and the usual intra nuclear cascade regime (actually only for projectiles with A<=4) in the following way.

The projectile content in terms of nucleons and the Coulomb deviation is realized as described above, but the kinetic energy of individual nucleons can be negative and some times can even be lower than the Fermi level in the target nucleus (see Fig. 1b), a situation hardly acceptable in the cascade picture. Up to alphas, nucleons missing the sphere are put on shell and the necessary energy for this is equally taken from all nucleons entering in the sphere and named participants.

If at least one participant has an energy lower than the target Fermi level and one participant will cross the "hard" part of the target density, a target-participants compound nucleus is produced and treated

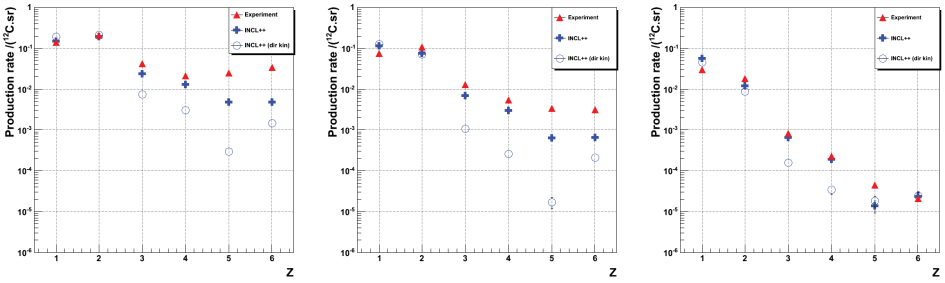

(a) *Fragments emitted at* 7° (b) *Fragments emitted at* 10° (c) *Fragments emitted at* 16°

Fig. 2: Production of fragments identified in charge (Z) and produced by a ^{12}C beam of 95 MeV per nucleon on a PMMA target. For three angles, the measured production rate [8] (red triangles) is compared with calculations using INCL++ in GEANT4 with the "direct" mode (open blue circles) or the recommended "reverse" mode (blue crosses).

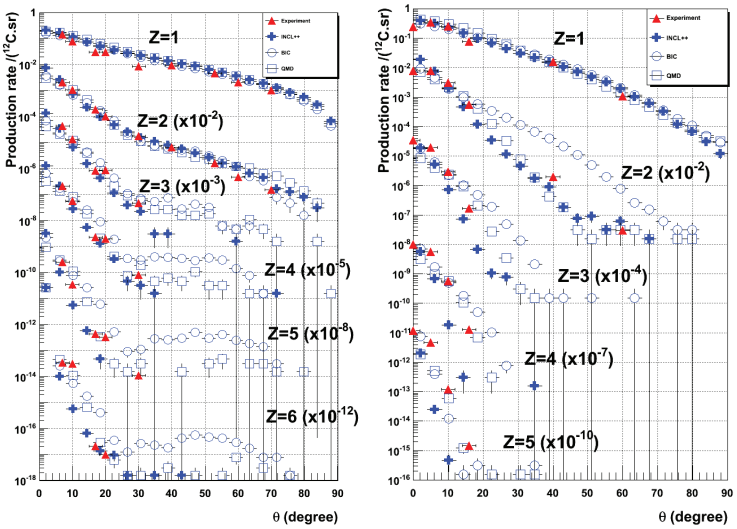

(a) *target thickness* : 5*mm* (b) *target thickness* : 25*mm*

Fig. 3: Angular distributions of fragments identified in charge (Z) and produced by a ^{12}C beam of 95 MeV per nucleon on a PMMA target. Data measured at GANIL [8] (red triangles) are compared to calculations with INCL++ (blue crosses), BIC (blue circles) and QMD (blue squares) in GEANT4.

by the de-excitation as the usual remnant nucleus of the cascade. There is no more "cascade" calculation in that case.

We have also taken into account the tabulated [7] masses of nuclei and particles so that the Q-values in all outgoing channels are now correct and the global conservation of energy-momentum is at

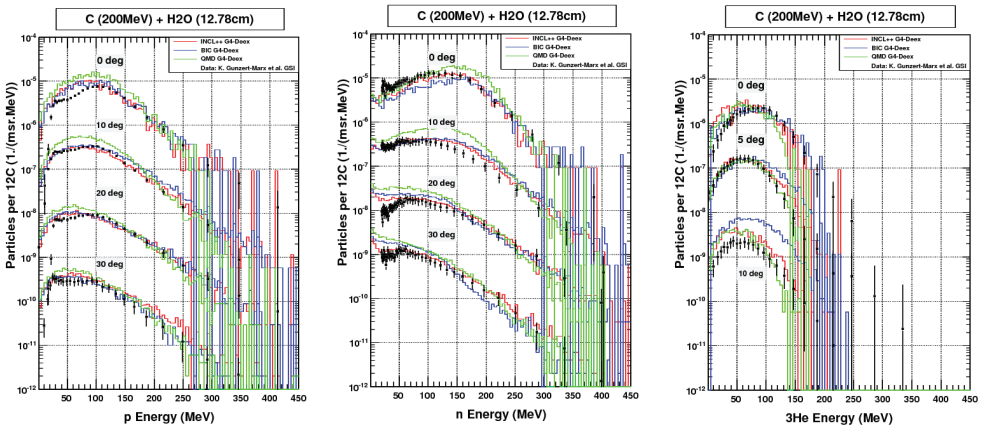

(a) *proton production* (b) *neutron production* (c) ^3He *production*

Fig. 4: Proton, Neutron and ^3He double differential production rates from a ^{12}C beam of 200 MeV per nucleon stopped in a thick water target. Data measured at GSI [9] (black points) are compared with INCL++ (red line), BIC (blue line) and QMD (green line) models in GEANT4. Convenient powers of 10 are used to display the various angles on the same picture.

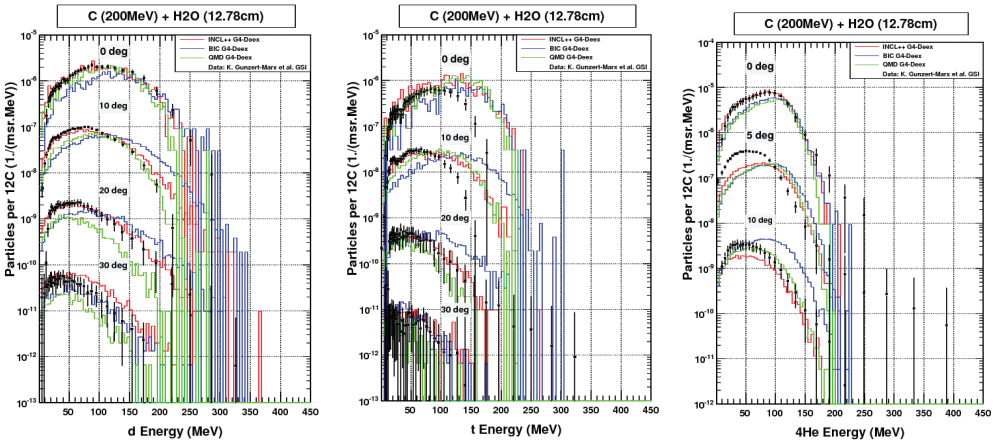

(a) *deuteron production* (b) *tritium production* (c) ^4He *production*

Fig. 5: Same as Fig. 4 for deuteron, tritium and ^4He production except that all calculations are divided by 3 for d and t and by 10 for ^4He.

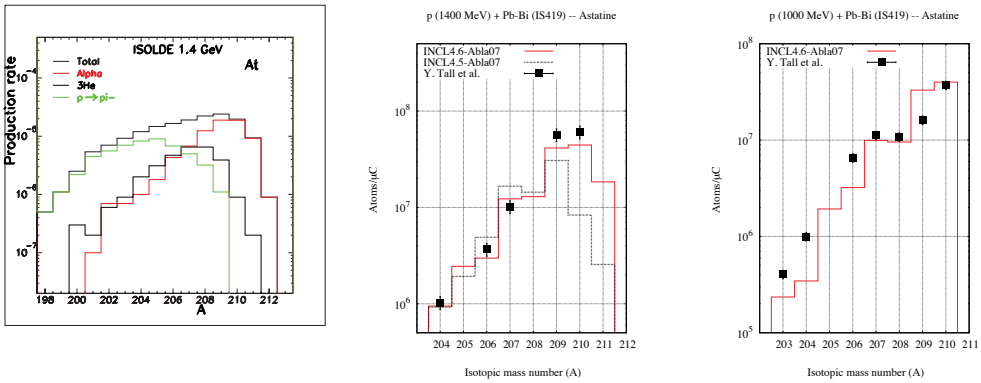

(a) *Contributions* (b) *At production at* 1.4 *GeV* (c) *At production at* 1.0 *GeV*

Fig. 6: Production of astatine isotopes by a proton beam of 1.4 GeV and 1.0 GeV on a 20 cm thick Pb-Bi target as measured at ISOLDE [10] and compared to INCL4.6-ABLA07 predictions with MCNPX.

the tenth keV level at the end of the cascade.

4 Ganil experiment

A collaboration has measured [8] at GANIL the fragmentation of a ^{12}C beam of 95A MeV stopped in a PMMA ($C_5H_8O_2$) target. In Fig. 2 the production of fragments emitted at 7° , 10° and 16° is compared with INCL calculations in GEANT4 either in the "direct" mode or the "reverse" mode. In "direct" mode the ^{12}C is really the beam particle interacting with the target nucleus (C or O here) and due to the asymmetric beam/target treatment as discussed above, fragments of the projectile are poorly described. So for each interaction the actual calculation ("reverse" mode) in GEANT4 is done with a Carbon target and a C or O projectile with all produced particles boosted in the correct system after each interaction for further transport. More precisely, the choice is dependent of the observable. The "direct" mode is an "accurate target" mode and the "reverse" an "accurate projectile" mode.

In Fig. 3 the angular distribution of fragments for a 5mm and a 25mm thick PMMA target measured by the same collaboration are compared with INCL, BIC (Binary Cascade) and QMD (Quantum Molecular Dynamics) calculations in GEANT4 [6]. The INCL calculation is better than the BIC one and quite comparable to the QMD one but much faster.

5 GSI experiment

At GSI, double differential production rates of n, p, d, t, ^3He and ^4He produced by a ^{12}C beam of 200A MeV stopped in a 12.8 cm thick water target have been measured [9]. In Fig. 4 and Fig. 5, data are compared with the same 3 dynamical models available in GEANT4 (INCL, BIC and QMD). All calculations are divided by 3 for deuterons and tritons and by 10 for ^4He but are absolute for neutrons, protons and ^3He. We don't understand the origine of these factors but these detailed observables are rather precisely described in shape, and on the overall better by INCL than by the other models.

6 ISOLDE experiment (At production)

The production of astatine isotopes released from a 20 cm thick Pb-Bi target and produced by proton beams of 1.4 GeV and 1.0 GeV has been measured [10] at ISOLDE. To increase by 2 units the charge of the bismuth target, a one step process by a $Bi(p,\pi^-)At + xn$ reaction or a two step process $Pb - Bi(p, He)X$ followed by a $Bi(He, xn)At$ reaction are possible.

The total production (black curve in Fig. 6a) is decomposed into these various contributions showing that the one step process is dominant for the light isotopes whereas the two step is dominant for the heavy ones. Taking into account the history of irradiation (decay of nuclei during irradiation) leads to the final rather satisfactory calculations of Fig. 6b and Fig. 6c.

Fig. 6b illustrates the effect of a better treatment of He projectiles at low energy between the version INCL4.5 in blue and the present one INCL4.6 in red.

7 Conclusion

We have explained how the cascade code INCL has been improved in the sector of composite beams up to oxygen nuclei and for low beam energies. This led to a Fortran version (INCL4.6 soon publicly available in MCNP6, projectiles up to ^4He) and a fully redesigned C++ version (INCL++5 already available in Geant4, projectiles up to ^{16}O).

We have shown promising first results on the fragmentation of ^{12}C beams on thick targets at 95A MeV and 200A MeV. INCL calculations are here better than the BIC model and comparable to but faster than the QMD model. Energy distributions of light particles (up to ^4He) are very good. The correct prediction of astatine production measured at ISOLDE illustrates the importance of a good He production and of the low energy treatment in the code.

The new open sector has certainly to be more systematically tested especially to disentangle the contribution of the de-excitation. The main drawback is at the moment the asymmetric treatment between the projectile and the target nuclei. This force a choice of the kinematics (beam nuclei as target or as beam in the INCL calculation) favoring the fragmentation of the beam and will be the subject of future developments.

References

[1] J. Cugnon, *Nucl. Phys. A462 (1987) 751*

[2] A. Boudard, J. Cugnon, S. Leray and C. Volant, *Phys. Rev. C66 (2002) 044615*

[3] A. Kelić, M.V. Ricciardi and K.-H. Schmidt, *arXiv_ nucl-th 0906.4193v1*; Proc. of Joint ICTP-IAEA Adv. W. on Model Codes for Spal. Reac., Trieste, 2008, report INDC(NDS)-530, Vienna, August 2008, Editors: D. Filges et al.

[4] *http://www-nds.iaea.org/spallations/* and Report IAEA INDC(NDS)-530, Vienna, August 2008, Editors: D. Filges et al.

[5] D. B. Pelowitz. MCNPX User's Manual - Version 2.6.0. LA-CP-07-1473, 2008

[6] GEANT4-S. Agostinelli et al. *Nucl. Inst. and Phys. A506 (2003) 250* and Geant4.cern.ch (Physics Reference Manual).

[7] J.K. Tuli, *Nuclear Wallet Cards 2010*, Broohkaven Nat. Lab. USA

[8] B. Braunn et al. *Nucl. Inst. and Meth. B269 (2011) 2676*

[9] K. Gunzert-Marx et al. *New Journal of Phys. 10 (2008) 075003* and D. Schardt private communication.

[10] Y. Tall et al. *Proceeding of Internat. Conf. on Nucl. Data for Science and Tech., April 2007 Nice, France, Editors: O. Bersillon et al., EDP Science (2008) p1069*

A Monolithic Silicon Detector for pre-treatments verification in Intensity Modulated Radiotherapy

M. Bruzzi[1], *C. Talamonti*[2], *M. Scaringella*[1] *and M. Bucciolini*[2]
[1] INFN Firenze and Dip. Energetica , Univ. Florence, Via S. Marta 3, Firenze, Italy
[2] INFN Firenze and Dip. Fisiopatologia Clinica, Univ. Florence, Largo Brambilla 3, Firenze, Italy

We report on the development of a large area bidimensional detector, adequate for 2D pre-treatment dose verifications, developed for clinical dosimetry in Intensity Modulated Radiation Therapy (IMRT). The detector is a monolithic segmented sensor obtained by n-type implantation on a 50 μm thick p-type epitaxial silicon layer, with improved radiation hardness against the accumulated dose. The detector is composed by up to nine modules each composed of a matrix of 21×21 pixels with a size of 2×2 mm2.

A dosimetric characterization of the detector has been performed and results are compared with those obtained with ion chambers as well as with a matrix of Si diodes (MapCHECK™, Sun Nuclear). Results show that our modular detector represents a valuable tool for quality assurance in IMRT dose delivery in high precision radiotherapy techniques.

Charged and Neutral Particles Production from 80 MeV/u ^{12}C ion beam on a PMMA target

C. Agodi[f], G. Battistoni[g], F. Bellini[a,b], G.A.P. Cirrone[f], F. Collamati[a,b], G. Cuttone[f], E. De Lucia[c], M. De Napoli[f], A. Di Domenico[a,b], R. Faccini[a,b], F. Ferroni[a,b], S. Fiore[a], P. Gauzzi[a,b], E. Iarocci[c,d], M. Marafini[a,e], I. Mattei[c,h], S. Muraro[g], A. Paoloni[c], V. Patera[c,d], L. Piersanti[c,d], F. Romano[e,f], A. Sarti[c,d], A. Sciubba[c,d], E. Vitale[g], C. Voena[a,b]

[a] Dipartimento di Fisica, Sapienza Università di Roma, Roma, Italy; [b] INFN Sezione di Roma, Roma, Italy; [c] Laboratori Nazionali di Frascati dell'INFN, Frascati, Italy; [d] Dipartimento di Scienze di Base e Applicate per Ingegneria, Sapienza Università di Roma, Roma, Italy; [e] Museo Storico della Fisica e Centro Studi e Ricerche "E. Fermi", Roma, Italy; [f] Laboratori Nazionali del Sud dell'INFN, Catania, Italy; [g] INFN Sezione di Milano, Milano, Italy; [h] Dipartimento di Fisica, Università Roma Tre, Roma, Italy

Abstract

We have measured the properties of the secondary particles produced in the interaction of carbon ion beams with homogeneous targets, in order to reconstruct the profile of the dose delivered in an hadrontherapy treatment. Our measurements have been done with a 80 MeV/u fully stripped carbon ion beam at the INFN Laboratori Nazionali del Sud (LNS), Catania, with a Poly-methyl methacrylate target (PMMA).Both the neutral and the charged component of the secondaries have been measured, the neutral component including prompt photons and β^+-annihilation photons (γ-PET).

1 Introduction

Protons and carbon ion beams are presently used to treat many different solid cancers [1,2] and several new centers based on hadron accelerators are operational or under construction [3,4]. The main advantage of this technique, in comparison to the standard radiotherapy with X-ray beams, is the better localization of the irradiation dose in the tumor affected region sparing healthy tissues and possible surrounding organs at risk. This feature can be achieved because the heavy charged particles loose most of the energy at end of their range, the Bragg peak, in comparison to the exponentially decreasing energy release of the X-ray beam. New dose monitoring techniques need to be developed and introduced into clinical use, to meet the improved capability of hadrontherapy to match the dose release with the cancer position. The R&D effort should be then focused to develop novel imaging methods to monitor, preferably in real time, the 3-dimensional distribution of the radiation dose effectively delivered during hadrontherapy. This holds true especially for treatments using carbon ion beams since the dose profile is very sensitive to anatomical changes and minor patients' positioning uncertainties. Conventional methods for the assessment of patients' positioning used in all X-ray based radiation therapy, where a non-negligible fraction of the treatment beam is transmitted through the patient, cannot be used to pursue this task due to the different physics underlying.

We report on the measured properties of the secondary particles produced in the interaction of a 80 MeV/u fully stripped carbon ion beam at the INFN Laboratori Nazionali del Sud (LNS), Catania, with a Poly-methyl methacrylate target (PMMA). Both the neutral and the charged component of the secondaries have been measured, the neutral component including prompt photons and β^+-annihilation photons (γ-PET).

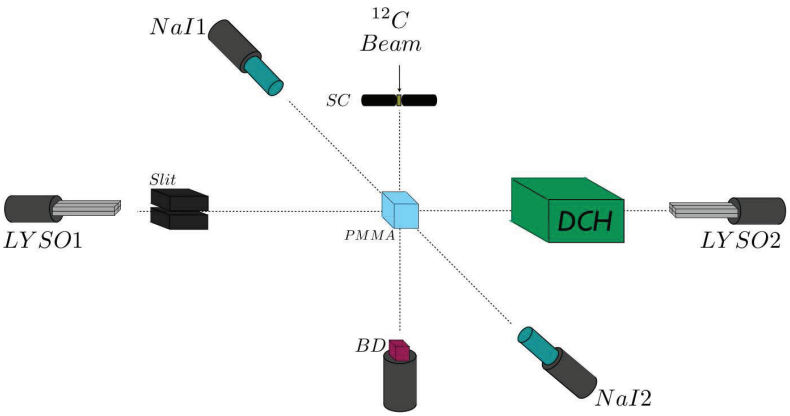

Fig. 1: Schematic view of the experimental setup; for prompt photon the acquisition is triggered by the Start Counter in coincidence with the LYSO, while for the γ-PET the NaI crystals are required.

2 Experimental setup

The experimental setup at LNS is shown in Fig. 1: a $4 \times 4 \times 4$ cm^3 PMMA target is placed on a fully stripped ^{12}C ion beam. The beam rate, ranging from hundred kHz to $\sim$ 2 MHz, was monitored with a 1.1 mm thin scintillator on the beam line read-out with two photomultiplier tubes (PMT) (Hamamatsu 10583) put in coincidence (Start Counter) and placed at 17 cm from the PMMA.
A pair of cylindrical Thallium-doped sodium iodide crystals NaI(Tl) (r = 2.5 cm and h = 5 cm) was placed at 45° (225°) with respect to the beam line, at 20 cm from the PMMA. The scintillation light of the two crystals was detected by two Scionix V 14-EI PMTs triggered in coincidence within a time window of 80 ns.
An array of 4 LYSO crystals, each measuring 1.5x1.5x12 cm^3, was placed at 90° with respect to the beam line, at 74 cm from the PMMA center. The scintillation light of the crystals was detected with a PMT (EMI 9814B).
A 21 cm long drift chamber (DCH) was placed at 51 cm from the PMMA center, along the flight line connecting the PMMA to the LYSO crystals. We have chosen the configuration at 90° with respect to the beam line to maximize the sensitivity to the Bragg peak position along the beam.

3 Prompt photons measurement

Photons are detected by the LYSO calorimeter, and selected from charged particles by requiring no signal in the DCH. Prompt photons are discriminated by measuring the time difference between the beam impact on the Start Counter and the photon detection consistent with a particle emitted instantaneously and traveling at the speed of light.

We measured the energy spectrum, Fig. 2(left), and rate of prompt photons with a time resolution of 300 ps for photons with energies above 3 MeV, allowing for a much stronger neutron background rejection with respect to previous measurements [5]. The fit of the peak gives a fraction of $f_{^{12}\mathrm{C}}$ = (13.9$\pm$0.6)% for prompt photons over carbon ions at 4.44 MeV. Fig. 2(right) shows the data distribution compared to the MonteCarlo simulation from GATE [7] with G4QMDReaction for ions' inelastic process and ^{12}C-PMMA interactions, folded with detector response. The spectra, normalized to the number of incident carbons, show the level of agreement between data and MonteCarlo simulation: both the normalization and the fraction of E=4.44 MeV photons require further investigation.

The rate of photons per carbon ions triggered (N_{C}) $\mathrm{F}_{\mathrm{prompt}}$ =(3.04$\pm$0.01$_{\mathrm{stat}}\pm$0.20$_{\mathrm{sys}}$)$\times 10^{-6}$ has

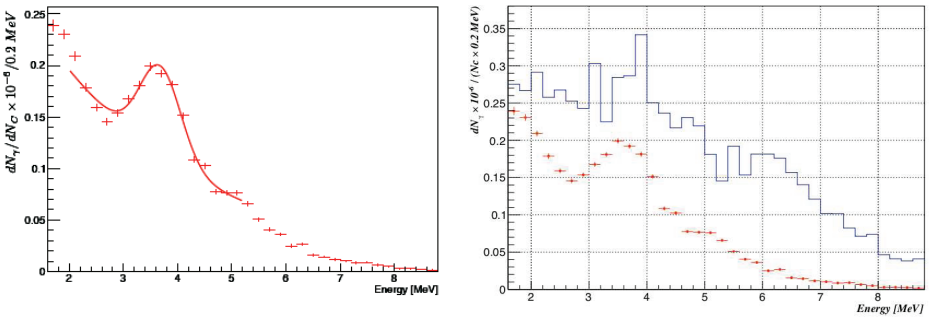

Fig. 2: (Left) Measured prompt photons spectrum obtained with the LYSO detector. The fit of the peak gives a fraction of $f_{^{12}\mathrm{C}}$ = (13.9±0.6)% for prompt photons over carbon ions at 4.44 MeV. (Right) Data-MC comparison of the prompt photons energy spectrum, normalized to the number of incident carbon ions.

been measured together with the differential production rate $dN_\gamma/(dN_\mathrm{C}d\Omega)(E > 2MeV, \theta = 90°)$ = (2.92±0.19)×10^{-2} sr^{-1} [6].

4 γ-PET measurement

NaI crystals have been used to detect the $\gamma-$PET signals, the collinear 511 keV photons produced by positrons annihilation from β^+ emitters. The rate of β^+ decays and the isotopic composition of the emitters has been measured as a function of time both during irradiation and in the intervals in between. The time dependence of the emission during the irradiation results from two main contributions: (i) the creation of new emitters induced by the passage of the carbon ions in the PMMA, and (ii) the decay of the previously created ones. When the irradiation time is comparable to the decay time of the emitters, the relation between the β^+ decays and dose rate is non-trivial. With the acquired data we have demonstrated the possibility to estimate the number of impinging carbon ions from the number of observed $\gamma-$PET. We measured the ratio between the number of activated ^{11}C and ^{13}N to be A_C/A_N = 16.6±2.7 and a number of (10.3±0.7)×10^{-3} generated ^{11}C ions, per impinging carbon ion, undergoing β^+ decay [8].

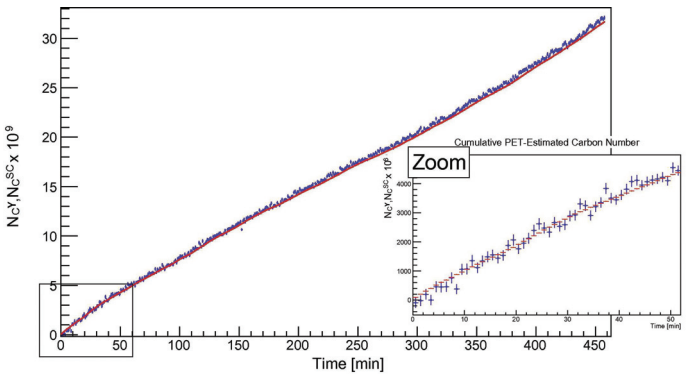

Fig. 3: Cumulative distribution of the number of carbon ion measured with the Start Counter, N_C (magenta dashed data), compared to the number of ions estimated by the measurements of γ-PET, N_C^γ (blue dot points). The plot on the right is a zoom of the first 50 min of acquisition.

With these data we also validated a model to describe the activated nuclei β^+ decay during the irradiation. Figure 3 shows the cumulative distribution of the number of ions estimated by the measurements of γ-PET, N_C^{γ}, blue dot points, compared to the cumulative number of carbon ions measured with the Start Counter N_C , magenta dashed data. A good agreement is visible, also at times comparable with the lifetimes of the decaying isotopes.

Finally we measured the mean position of the β^+ emission to be $D_{\beta+}$ = (5.3±1.1) mm from the beam entrance face of the PMMA, to be compared to the FLUKA simulated Bragg peak position D_{Bragg} = (11.0±0.5) mm. The D_{Bragg} value is confirmed from the direct observation of the PMMA deterioration after data taking, visible as a light yellow band and shown in Fig.12 of Ref [8]. All this information can be used as a benchmark for the β^+ emitters MonteCarlo simulation of hadrontherapy.

5 Charged particles

Charged secondary particles, produced at 90° with respect to the beam axis, have been tracked with the DCH, while their energy and time of flight has been measured by means of the LYSO scintillator. Secondary protons have been identified exploiting the energy and time of flight information (ToF), Figure 4 and their emission region has been reconstructed backtracking from the drift chamber to the target. In order to evaluate the setup acceptance and efficiency, and to optimize the particle identification analysis a detailed simulation has been developed using the FLUKA software release 2011.2 [10,11]. The interaction of a sample of 10^9 carbon ions with 80 MeV/u, equivalent to 10^3 s of data taking at the typical 1 MHz rate of beam, has been simulated.

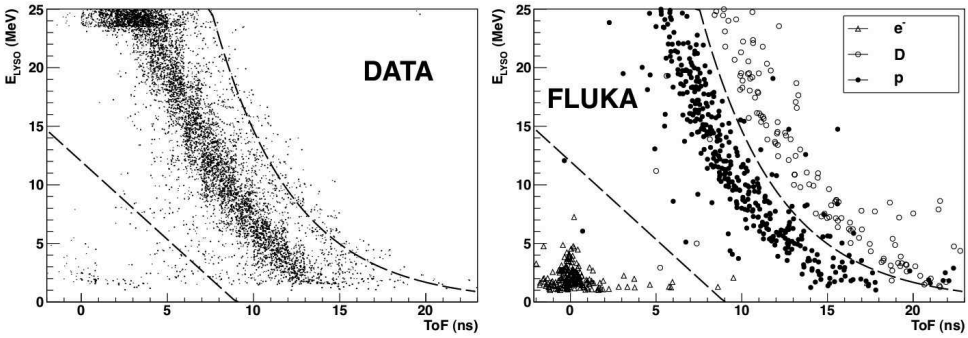

Fig. 4: Distribution of the detected energy in the LYSO crystals as a function of the Time of Flight: Data (Left) and FLUKA Simulation (Right).

The existence of a correlation between the reconstructed production region of secondary protons ($\bar{x}_{\mathrm{PMMA}}$) and the Bragg peak position (x_{Bragg}) has been observed, performing a position scan of the PMMA target (Figure 5). The expected position of the Bragg peak has been obtained with the FLUKA simulation and its value confirmed from visual inspection of the PMMA deterioration after data taking, as mentioned above. A proton kinetic energy at emission time $\mathrm{E}_{\mathrm{kin}}^{\mathrm{Prod}} > 83$ MeV has been required to account for the crossing of some centimeters of patient's tissue when using these secondary particles for monitoring purposes. The FLUKA simulation has been used to relate the detected proton kinetic energy to $\mathrm{E}_{\mathrm{kin}}^{\mathrm{Prod}}$.

The achievable accuracy on the Bragg peak determination exploting this procedure has been estimated to be in the submillimeter range, using the described setup and selecting secondary protons with kinetic energy at emission $\mathrm{E}_{\mathrm{kin}}^{\mathrm{Prod}} > 83$ MeV. The obtained accuracy on the position of the released dose should be regarded as an indication of the achievable accuracy for possible applications of this technique

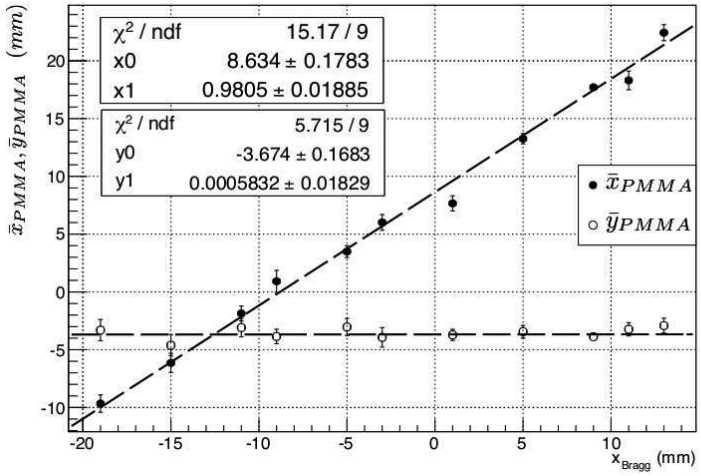

Fig. 5: Reconstructed peak position of the secondary proton emission distribution $\bar{x}_{\mathrm{PMMA}}$,$\bar{y}_{\mathrm{PMMA}}$ as a function of the expected Bragg Peak position x_{Bragg}, with $\mathrm{E}_{\mathrm{kin}}^{\mathrm{Prod}} > 83$ MeV.

to monitor the Bragg peak position in hadrontherapy treatment.

We measured the differential production rate for protons with $\mathrm{E}_{\mathrm{kin}}^{\mathrm{Prod}} > 83$ MeV and emitted at 90° with respect to the beam line: $dN_{\mathrm{P}}/(dN_{\mathrm{C}}d\Omega)(E_{\mathrm{kin}}^{\mathrm{Prod}} > 83\,\mathrm{MeV}, \theta = 90°) = (2.69 \pm 0.08_{\mathrm{stat}} \pm 0.12_{\mathrm{sys}}) \times 10^{-4} sr^{-1}$ [9].

6 Conclusions

The measurement of the fluxes of the secondary particles produced by the hadron beam is of fundamental importance in the design of any dose monitoring device and is eagerly needed to tune Monte Carlo simulations.

Charged and Neutral Particles Production from the 80 MeV/u fully stripped carbon ion beam on a PMMA target at the INFN Laboratori Nazionali del Sud (LNS), Catania, provided us with several results.

With prompt photons we measured: energy spectrum, rate and differential production rate per triggered carbon ion and at 90° with respect to the beam line.

With γ-PET we validated a model to describe the activated nuclei β^+-decay during the irradiation, we estimated the number of carbon ions from the number of observed γ-PET, we measured the ratio between the number of activated ^{11}C and ^{13}N and the average position of β^+ emitters in the PMMA.

With secondary protons we observed the existence of a correlation between the reconstructed production region of these secondaries and the Bragg peak position. The achievable accuracy on the Bragg peak determination exploiting the proton signal has been estimated to be in the submillimeter range. The differential production rate per triggered carbon ion and at 90° with respect to the beam line has been also measured.

References

[1] O. Jäkel et al., *The future of heavy ion radiotherapy*, *Med. Phys.* **35** (2008) 5653

[2] M. Durante and J.S. Loeffler, *Charged particles in radiation oncology*, *Nat. Rev. Clin. Oncol.* **7** (2010) 37

[3] U. Amaldi and G. Kraft, *Radiotherapy with beams of carbon ions*, *Reports on Progress in Physics* **68** (2005) 1861.

[4] D. Schardt et al., *Heavy-ion tumor therapy: pysical and radiobiological benefits Rev. Mod. Phys.* **82** (2010) 383

[5] E. Testa *et. al.*, *Dose Profile monitoring with carbon ions by means of prompt-gamma measurements*, *Nucl. Instr. and Meth. Phys. Reserch B* **267** (2009) 993–996.

[6] C. Agodi *et al.*, *Precise measurement of prompt photon emission for carbon ion therapy*, *JINST* **7** (2012) P03001

[7] S. Jan *et. al.*, *Gate: a simulation toolkit for pet and spect*, *Phys. Med. Biol.* **49** (2004) 4543.

[8] C. Agodi *et al.*, *Study of the time and space distribution of β^+ emitters from 80 MeV/u carbon ion beam irradiation on PMMA*, *Nucl. Instrum. Methods* **B**. **283** (2012) 1

[9] C. Agodi *et al.*,*Charged particle's flux measurement from PMMA irradiated by 80 MeV/u carbon ion beam*, *Phys. Med. Biol.* **57** (2012) 5667

[10] A. Fasso *et al.*, *The physics models of FLUKA: status and recent development*, *arXiv: hep-th/0306267* (2003)

[11] A. Ferrari *et al.*, *FLUKA: A Multi Particle Transport Code*,*CERN-2005-10, INFN/TC_05/11, SLAC-R-773* (2005)

95MeV/u ^{12}C nuclear fragmentation measurements on thin targets for hadrontherapy

J. Colin[1], *D. Cussol*[1], *J. Dudouet*[1], *J.M. Fontbonne*[1], *M. Labalme*[1], *P. Henriquet*[2], *J. Krimmer*[2]
C. Finck[3], *D. Juliani*[3], *M. Rousseau*[3], *B. Braunn*[4], *M.G. Saint-Laurent*[5]
[1] LPC Caen
[2] IPN Lyon
[3] IPHC Strasbourg
[4] CEA/IRFU/SPhN Saclay
[5] GANIL

To keep the benefits of the use of carbon ions in radiation therapy, a very high accuracy on the dose location is required. A part of the uncertainties on the dose deposition rely on the fragmentation of the ion along its path in the patient (fragmentation tails behind the tumor, RBE fluctuation in depth). Up to now, the simulation codes are not able to reproduce the fragmentation process with the required accuracy for clinical treatments. The constraints on nuclear models and fragmentation cross sections in the energy range used in hadrontherapy (30 to 400MeV/u) are not yet sufficient.

A first experiment, on thick water equivalent targets has been performed on May 2008 at GANIL. The goals were the measurements of energy and angular distributions of the fragments coming from the nuclear reaction between 95MeV/u ^{12}C and thick PMMA targets. Comparisons between experimental data and Geant4 simulations (BIC, QMD, INCL) show discrepancies up to one order of magnitude for production rates. The shapes of the angular and energy distributions are also not well reproduced.

To improve the models and reach the precision required for a reference simulation code for hadrontherapy, a second experiment has been performed on thin targets on May 2011 at GANIL. The experimental set-up included five three stages ΔE-E telescopes composed of two Si detectors (thickness: 150µm and 1mm) and one CsI scintillator (thickness: 10cm). These telescopes were mounted on rotating stages to cover angles from 0 to 45°. We have measured the double differential cross section ($\frac{\partial^2\sigma}{\partial E\,\partial\Omega}$) of fragments resulting of the nuclear reaction from 95MeV/u ^{12}C ions with thin targets (C; CH_2; Ti; Al; Al_2O_3). The data of this experiment are still under analysis but the energy calibration of the detectors and the identification of the fragments have been achieved. As shown in the figures for the ^{4}He particles, the first results of fragments production (from proton to carbon) on the carbon targets are already available. The double differential cross sections for the other targets will be soon available. The experimental setup and the results for the different targets will be presented.

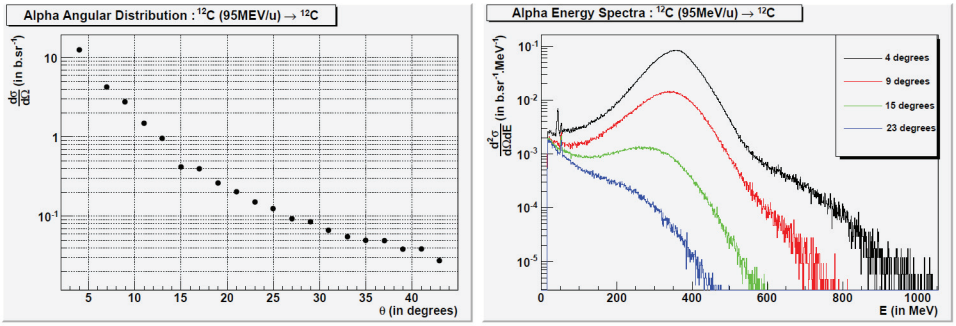

(a) ^4He angular distribution (b) ^4He energy spectra at five different angles.

Fig.1: Preliminary results for the reaction ^{12}C(95MeV/u) → ^{12}C.

Comparisons with Geant4 simulations will be achieved in order to evaluate the accuracy of the nuclear reaction models (BIC, QMD...) included in the Geant4 toolkit for hadrontherapy purposes.

FLUKA Monte Carlo calculations for hadrontherapy application

G. Battistoni[1], V. Boccone[2], T. Boehlen[3,4], F. Broggi[1], M. Brugger[3], G. Brunetti[5], M. Campanella[1], F. Cappucci[6,7], F. Cerutti[3], M. Chin[3], P. Colleoni[8], A. Empl[9], A. Fassò, A. Ferrari[3], A. Ferrari[10], E. Gadioli, P. Garcia Ortega[3], M.V. Garzelli[11], L. Lari[12], M. Lantz[13], A. Lechner[3], K. T. Lee[14], G. Lukasik, A. Mairani[6], A. Margiotta[5], A. Mereghetti[3], M. C. Morone[15], S. Murano[1], R. Nicolini[1], K. Parodi[16], V. Patera[17], M. Pelliccioni[18], L. Pinsky[9], J. Ranft[19], I. Rinaldi[20], S. Roesler[3], S. Rollet[21], P.R. Sala[1], M. Santana[22], L. Sarchiapone[23], M. Sioli[5], G. Smirnov[3], C. Theis[3], S. Trovati[24], R. Versaci[3], H. Vincke[3], H. Vincke[3], V. Vlachoudis[3], J.Vollaire[3]

[1]INFN Milano, Italy
[2]University of Geneva, Switzerland
[3]CERN, Geneva, Switzerland
[4]Stockholm University and Medical Radiation Physics, Karolinska Institutet, Sweden
[5]INFN and University Bologna, Italy
[6]CNAO Pavia, Italy
[7]University of Milano, Italy
[8]Ospedali Riuniti di Bergamo, Italy
[9]University of Houston, USA
[10]FZR Rossendorf, Germany
[11]Nova Gorica University, Slovenia
[12]University of Valencia, Spain
[13]Uppsala University, Sweden
[14]NASA, Houston, USA
[15]University of Roma II, Italy
[16]LMU, Munich, Germany
[17]INFN Frascati and University of Roma La Sapienza, Italy
[18]INFN Frascati and CNAO, Pavia, Italy
[19]University of Siegen, Germany
[20]HIT, Heidelberg, Germany
[21]AIT, Austria
[22]SLAC, USA
[23]INFN Legnaro, Italy
[24]EBG MedAustron, Austria

Abstract
Monte Carlo (MC) codes are increasingly spreading in the hadrontherapy community due to their detailed description of radiation transport and interaction with matter. The suitability of a MC code for application to hadrontherapy demands accurate and reliable physical models for the description of the transport and the interaction of all components of the expected radiation field (ions, hadrons, electrons, positrons and photons). This contribution will address the specific case of the general-purpose particle and interaction code FLUKA. In this work, an application of FLUKA will be presented, i.e. establishing CT (computed tomography)-based calculations of physical and RBE (relative biological effectiveness)-weighted dose distributions in scanned carbon ion beam therapy.

1 Introduction

A major advantage for the application of carbon ion beams in tumour therapy is their so called "inverse" depth-dose profile with a pronounced maximum at the end of range (Bragg peak), in conjunction with their increased relative biological effectiveness (RBE) in the tumour volume in comparison to the lower effectiveness in the surrounding health tissue [1]. Besides these advantages due to electromagnetic interaction, carbon ion beams experience nuclear reactions which cause a significant alteration of the radiation field. This shows mainly through a loss of primary beam particles and a build-up of secondary lower-charge fragments [2]. In particular, the lower-charge fragments, having longer ranges than the primary beam, give rise to the characteristic dose tail beyond the Bragg peak. Moreover, the light fragments scatter more than the heavier primaries thus broadening the irradiation field in the patient. Furthermore, the biological effectiveness of the fragments is different from that of the primary carbon ions [3] and it has to be included in the biological effect calculations. At the GSI Helmholtzzentrum für Schwerionenforschung Darmstadt, Germany, the analytical treatment planning system (TPS) TRiP98 (TReatment planning for Particles, 1998) [4,5] has been clinically used in connection with the GSI pilot project for carbon ion beam therapy [6]. TRiP98 is coded for being applied to the GSI 3D active beam delivery, which combines intensity-controlled lateral deflection based on the raster scan system [7] with discrete selection of accelerator beam parameters (energy, focus, intensity). The physical beam model of TRiP98 relies on an external database which takes into account the energy loss, the energy loss straggling and the projectile fragmentation [8,4]. For RBE-weighted dose calculations, TRiP98 is based on the Local Effect Model (LEM) [3,9,10] which is used to reproduce the dependency of the RBE on the type of the irradiated tissue, on the biological endpoint and on the ion beam characteristics. For biological inverse planning, an optimization process is implemented in TRiP98 in order to provide a uniform RBE-weighted dose distribution in the target volume according to the planning prescription. The result of the optimization is an output file containing the beam phase space information for each treatment field: pencil beam energy, lateral width and position (x,y) at the isocenter as well as fluence distribution.

In this work, we describe a novel methodology for establishing CT (Computed Tomography)-based calculations of physical dose and RBE-weighted dose distributions in carbon ion beam therapy using the FUKA MC code [11,12]. We performed CT-based forward re-calculations of absorbed and RBE-weighted dose for a clivus chordoma patient treated at GSI. The patient case has been planned with TRiP98. MC CT-based calculations required the proper handling of the patient CT images and of the TRiP98 WEPL (water-equivalent path length) – HU (Hounsfield unit) calibration curve (as described in section 2.1) as well as the coupling of FLUKA to the LEM model for the evaluation of RBE-weighted dose distributions [2] (as outlined in section 2.2). Among the simulated beam ports of the total treatment fraction, section 3 shows a representative comparison of the MC dose/RBE-weighted dose results (dose to tissue) with the corresponding TRiP98 quantities (dose to water).

2 Material and Methods

2.1 Handling of patient CT with related information

In view of re-calculating patient plans, we have used the approach proposed in Schneider *et al* [13] and already applied in Paganetti *et al* [14] and Parodi *et al* [15] in proton therapy to convert the CT data, expressed in HUs, into mass density and chemical composition. The patient CT data are processed before the starting of the simulation and converted into an appropriate file format to be input into FLUKA. According to the logic of FLUKA, all voxels with the same HU value are identified as a spatial region. In order to reduce the number of materials to be used in FLUKA the segmentation of the CT in several HU intervals proposed by Schneider *et al* [13] and extended by Parodi *et al* [14] have been applied. The materials defined in FLUKA are characterized via the mentioned segmentation and the 'nominal' density, i.e. the density at the HU corresponding to the center of the HU intervals. Nuclear and electromagnetic processes depend, in first approximation, on the mass density and on the stopping power ratio, varying with the HU values within each material

characterized only by the 'nominal' density in the MC. To account for this, CT number dependent scaling factors for electromagnetic and nuclear interactions are introduced to adjust the stopping power values and mass density, respectively [15].

TPSs are essentially based on the assumption of water targets and the main idea to account for longitudinal density variations is to apply the concept of WEPL when an ion traverses a CT voxel. High density voxels correspond to water-equivalent path lengths larger than that for water, low density voxels to shorter water-equivalent path lengths. In this way the trajectory of an ion is transformed from the CT system into a water-equivalent system in the beam-eye-view. TRiP98 adopts an experimentally established WEPL curve based on the measurements of residual ranges behind tissue-equivalent phantom materials as well as bovine and human bony tissue in comparison to ranges in water [16,17]. This calibration curve has to be matched by the MC calculations for assuring a correct estimation of the experimental carbon ion range as a function of HUs.

Starting from the electron density and mean ionization energy for the nominal materials corresponding to the segmentation implemented in FLUKA, the carbon ion stopping power relative to water (ρ_s) has been calculated using the approximation proposed in Schneider *et al* [18] for proton therapy application, neglecting the shell and density corrections of the Bethe-Bloch formula (which are only minor for the energy range and materials of therapeutic relevance [19,20]):

$$\rho_S = \rho_e \frac{\log\left[\frac{2m_e c^2 \beta^2}{I_m(1-\beta^2)}\right] - \beta^2}{\log\left[\frac{2m_e c^2 \beta^2}{I_{water}(1-\beta^2)}\right] - \beta^2} \quad , \tag{1}$$

where ρ_e is the relative electron density, βc is the carbon ion velocity, m_e is the electron mass and I_m is the mean ionization energy of the target atoms. The carbon ion stopping power relative to water ρ_s represents a good approximation of the WEPL. Hence, in order to match the same experimental WEPL calibration as used in TRiP98 for determining the Bragg peak position in dependence of the HU value, the electromagnetic scaling factors (f_{EM}) for FLUKA have been calculated as:

$$f_{EM} = \frac{WEPL}{\rho_S} \quad . \tag{2}$$

For validating the introduced approach and the related f_{EM} calculations, we simulated the irradiation of phantoms, corresponding to different CT numbers, with several mono-energetic carbon ion pencil beams. The obtained Bragg peak positions were compared with the TRiP98 results. In figure 1 a satisfactorily comparison between TRiP98 (solid line) and FLUKA (dashed line) results using the calculated scaling factors is shown for 270 MeV/u carbon ion pristine Bragg peaks simulated in phantoms corresponding to different HU values. Both TRiP98 and FLUKA results are normalized using the same number of primary carbon ions. It should be noticed that adjusting the FLUKA stopping power calculations for reproducing the same semi-empirical HU-WEPL calibration curve used by the TPS does not mean to benchmark the MC dose calculation engine against the TRiP98 predictions, but only to ensure their consistency in terms of calculated Bragg-peak positions.

2.2 Calculation of absorbed dose and RBE-weighted dose

In our simulations, we calculate dose correcting the 'nominal' material density to the 'real' value by means of the same factors used to rescale nuclear processes [15] and for RBE-weighted dose simulations [2]. RBE-weighted dose distributions are calculated using the same RBE tables as in TRiP98 by applying, prior to the start of the simulation, the *low dose approximation approach*

described in [10].

The RBE database consists of α_D and β_D, i.e. the coefficients of the linear and quadratic terms of cell survival after ion irradiation, for the components of the mixed radiation field as a function of the particle energy, particle type and cell line. In the simulation, whenever energy is deposited by a certain radiation type, the following two quantities, in addition to the dose D, are stored: $\alpha_D \cdot D$ and $\sqrt{\beta_D} \cdot D$. Then applying the methods described in [2] one can derive RBE-weighted dose results. Dose and RBE-weighted dose results of TRiP98 are saved with the same spatial resolution of the CT image of the treated patient; the FLUKA grid for scoring dose/RBE-weighted dose has been thus chosen according to the planning CT.

3 Results

Figures 2 and 3 show representative comparisons between FLUKA and TRiP98 calculations of 2D distributions (Fig. 2) and profiles (Fig. 3) of absorbed and RBE-weighted dose for a clivus chordoma patient treated at GSI. The FLUKA particle transport was performed on a CT scan of 106 slices with 256 x 256 transaxial pixels each. The pixel dimension is about 1.21 mm and the distance between two consecutive slices is 3 mm. The cranial carbon ion treatment field enters the patient from the right side of the Fig. 2 (sagittal views). The depth-profiles are sampled along the lines shown in the upper-left panels of Fig. 2.

4 Discussion

An important aspect in view of re-calculations of clinical treatment plans is the implementation of CT-dependent stopping power correction factors in order to force the MC to follow the same CT-range calibration curve as the TPS. Our implementation has been validated by calculating Bragg peaks in phantoms of different CT numbers with carbon ion beams at 270 MeV/u. The differences between the Bragg peak positions calculated by FLUKA on the basis of the introduced stopping power correction factors and by TRiP98, as shown in Fig. 1, are less than 1 mm (the histogram bin width is 0.5 mm). The discrepancies in the absolute value are due to the different weighting of the energy deposition calculating *dose to water* in the TRiP98 and *dose to tissue* in FLUKA and to the different description of electromagnetic/nuclear processes in FLUKA and in TRiP98. In fact, as described in the section 2.2, TRiP98 considers the CT phantoms as equivalent to water by stretching the ion path using the WEPL table (*dose to water*), while in our calculations we divide the energy deposition (already normalized per unit volume) by the real density of tissue corresponding to the CT number (*dose to tissue*). The differences in the fragmentation tails are mainly influenced by the different composition of the mixed radiation field due to differences in nucleus-nucleus reactions modeling [2] and in target definition: water in TRiP98 and various materials in FLUKA.

In Figs. 2 and 3 we presented dose/RBE dose calculations for a treatment field delivered to a clivus chordoma patient at GSI. In general, the shapes of the MC calculated distributions agree with the TRiP98 ones. Exceptions occur in the cases more sensitive to the limitations of the analytical dose calculations similarly to the findings in proton therapy simulations [14,15]. These especially include regions of large density variation. In fact TPSs are typically less accurate than the MC computational engines in the transport of the radiation in the presence of large tissue heterogeneities. This is due to the intrinsic limitations of the water-equivalent stretching in depth, i.e. they account for the specific tissue composition only by corresponding adjustment of the penetration depth. In contrast, MC codes accurately model electromagnetic and nuclear processes keeping into account the specific tissue elemental composition obtained from a stoichiometric calibration of the CT scan. A clear example is given by Fig. 3 which shows a dose/RBE-weighted dose profile sampled along the line depicted in upper-left panel of Fig. 2. In the plateau region the FLUKA and the analytical results agree

satisfactorily while in the high dose region they differ where the CT values are considerably different from 0, i.e., when the mass density is substantially different from that of water, such as in bony structures. Finally differences have been found in the tail of dose distributions. The low dose tail is due to energy deposition by the fragments, mainly H and He, produced in nuclear fragmentation. As already pointed out in Mairani *et al* [2] the different handling of nuclear reactions in the analytical code and in the MC code can explain the differences in the tails. Using the interface to LEM outlined in section 2.3 it has been possible to calculate RBE-weighted dose distributions as shown in the bottom-left panels of Fig. 2 and in the right panels of Fig. 3. In the high dose/RBE-weighted dose region of the profiles depicted in Fig. 3, the dose/RBE-weighted dose by primary carbon ions only contributes as 81 % and 89% to the total absorbed/RBE-weighted dose respectively. The enhancement in the biological dose is due to the higher values of RBE of carbon ions compared to fragments at these depths.

5 Conclusion

Among the manifold applications of the FLUKA MC code for hadrontherapy, in this work we have presented a first contribution towards the goal of making a MC validation tool of analytical carbon ion beam treatment planning. In particular, it has been described a methodology for establishing CT-based calculations of absorbed/RBE-weighted dose. Reasonably good agreement has been observed with the calculations of the TRiP98 TPS for a clinical case treated at GSI. Differences between MC and TPS were mainly observed in those situations more sensitive to the well known limitations of pencil beam calculations, such as the handling of nuclear interactions as well as the beam transport in large tissue heterogeneities.

Acknowledgments

We would like to thank Michael Krämer for the usage of TRiP98.

References

[1] Krämer M, Weyrather W and Scholz M “The Increased Biological Effectiveness of Heavy Charged Particles: From Radiobiology to Treatment Planning” Technology in Cancer Research & Treatment Vol. **2** 427-436 (2003)

[2] Mairani A, Brons S, Cerutti F, Fassò A, Ferrari A, Krämer M, Parodi K, Scholz M and Sommerer F “The FUKA Monte Carlo code coupled with the Local Effect Model for biological calculations in carbon ion therapy” Phys. Med. Bio. **55** 4273-4289l (2010)

[3] Elsässer T, Weyrather W K, Friedrich T, Durante M, Iancu G, Krämer M, Kragl G, Brons S, Winter M, Weber K J and Scholz M “Quantification of the relative biological effectiveness for ion beam radiotherapy: direct experimental comparison of proton and carbon ion beams and a novel approach for treatment planning” Int. J. Radiation Oncology Biol. Phys. **78** 1177-1183 (2010)

[4] Krämer M, Jäkel O, Haberer Th, Kraft G, Schardt D and Weber U “Treatment planning for heavy-ion radiotherapy: physical beam model and dose optimization” Phys. Med. Biol. **45** 3299-3317 (2000)

[5] Krämer M and Scholz M “Treatment planning for heavy-ion radiotherapy: calculation and optimization of biologically effective dose” Phys. Med. Biol. **45** 3319-3330 (2000)

[6] Jäkel O, Krämer M, Karger C P and Debus J ”Treatment planning for heavy ion radiotherapy: clinical implementation and application” Phys. Med. Biol. **46** 1101-1116 (2001)

[7] Haberer Th, Becher W, Schardt D and Kraft G “Magnetic scanning system for heavy ion therapy” Nucl. Instr. Meth. **A 330** 296-305 (1993)

[8] Haberer Th Entwicklung eines magnetischen Strahlführungssystems zur tumorkonformen Strahlentherapie mit schweren geladenen Teilchen GSI Report 94-01 (1994)
[9] Scholz M, Kellerer A M, Kraft-Weyrather W and Kraft G "Computation of cell survival in heavy ion beams for therapy - the model and its approximation" Radiat. Environ. Biophys. **36** 59-66 (1997)
[10] Krämer M and Scholz M 2006 "Rapid calculation of biological effects in ion radiotherapy" Phys. Med. Biol. **51** 1959-1970 (2006)
[11] Ferrari A, Sala P R, Fassò A and Ranft J "FLUKA: a multi-particle transport code" CERN-2005-10, INFN/TC_05/11, SLAC-R-773 (2005)
[12] Battistoni G, Muraro S, Sala P R, Cerutti F, Ferrari A, Roesler S Fassò A and Ranft J "The FLUKA code: description and benchmarking" AIP Conference Proceeding **896** 31-49 (2007)
[13] Schneider W, Bortfeld T and Schlegel W "Correlation between CT numbers and tissue parameters needed for Monte Carlo simulations of clinical dose distributions" Phys. Med. Biol. **49** 459-478 (2000)
[14] Paganetti H, Jiang H, Parodi K, Slopsema R and Engelsman M "Clinical implementation of full Monte Carlo dose calculation in proton beam therapy" Phys. Med. Bio. **53** 4825-4853 (2008)
[15] Parodi K, Ferrari A, Sommerer F and Paganetti H "Clinical CT-based calculations of dose and positron emitter distributions in proton therapy using the FLUKA Monte Carlo code" Phys. Med. Biol. **52** 3369-3387 (2007)
[16] Jäkel O, Jacob C, Schardt D, Karger C P and Hartmann G H "Relation between carbon ion ranges and x-ray CT number" Med. Phys. **28** 701-703 (2001)
[17] Rietzel E, Schardt D and Haberer Th "Range accuracy in carbon ion treatment planning based on CT-calibration with real tissue samples" Radiation Oncology **2**:14 (2007)
[18] Schneider U, Pedroni E and Lomax A "The calibration of CT Hounsfield units for radiotherapy treatment planning" Phys. Med. Biol. **41** 111-124 (1996)
[19] Ziegler J F "The stopping of energetic light ions in elemental matter" J. Appl. Phys. **85** 1249-1272 (1999)
[20] Sternheimer R M, Seltzer S M and Berger M J "Density effect for the ionization loss of charged particles in various substances" Phys. Rev. B **26** 6067-76 (1982)

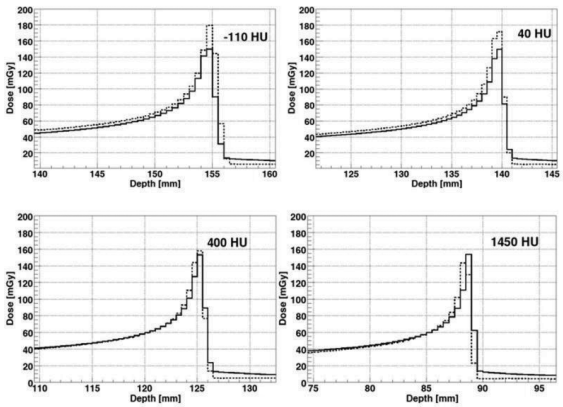

Figure 1 Comparison between TRiP98 (solid line) and FLUKA (dashed line) results for 270 MeV/u carbon ion pristine Bragg peaks calculated in phantoms corresponding to the indicated HU value. Both TRiP98 and FLUKA results are normalized using the same number of primary carbon ions

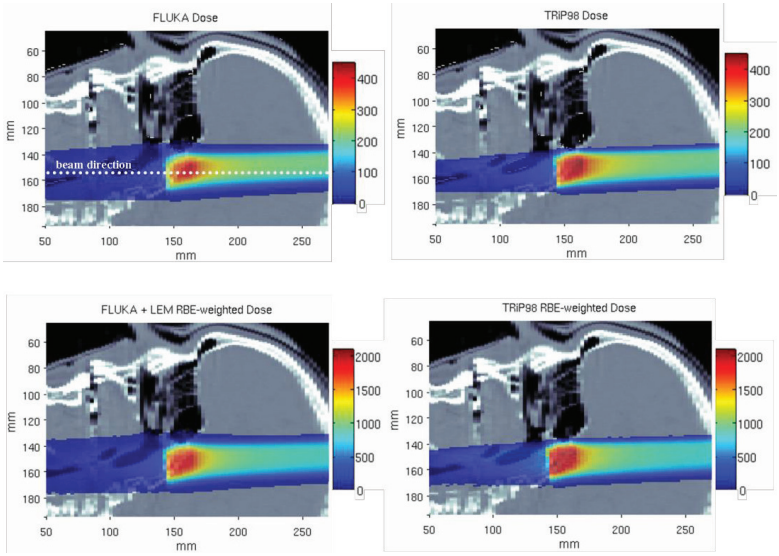

Figure 2 2D MC calculated dose (top-left panel) and RBE-weighted dose (bottom-left panel) distributions (color wash) in comparison to the planned treatment (top-right panel: dose; bottom-right panel: RBE-weighted dose) and overlaid to the gray-scale planning CT for a clivus chordoma patient treated at GSI with carbon ion beams. The carbon ion beam enters the patient from the right side of the figure. The color-bars display dose/RBE-weighted dose values in mGy/mGyE. The dotted line in the top-left panel depicts the position where the profiles shown in figure 3 are sampled.

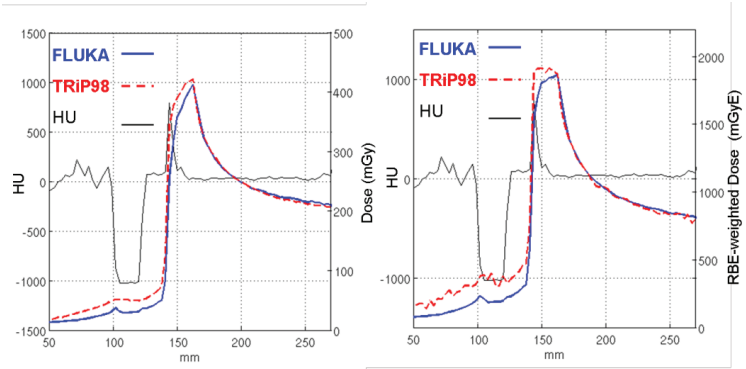

Figure 3 Comparison between MC (thick solid line) and TRiP98 (thick dashed line) calculated absorbed depth-dose (left panel) and RBE-weighted dose (right panel). The depth-dose profiles are sampled along the line depicted in upper-left panel of figure 2. The thin solid line represents the HU profile.

New Developments in FLUKA

F. Cerutti[1], *A. Ferrari*[1], *A. Mairani*[2], P.R. Sala[0]
[1] European Laboratory for Particle Physics (CERN), CH-1211 Geneva 23, Switzerland
[0] INFN, Via Celoria 16, 20133, Milan, Italy
[2] CNAO foundation, Pavia, Italy

Abstract
FLUKA is a general purpose tool for calculations of particle transport and interactions with matter. It handles all hadrons, ions, and electromagnetic particles. The FLUKA applications range from LHC or cosmic energies down to hadron-therapy and microdosimetry. It is the standard tool at CERN for beam-machine interactions and radioprotection. All FLUKA models and algorithms are object of a long and constant development that benefits to a wide range of applications. The present paper will focus on selected new developments in the nuclear interaction models, namely: hadronic interactions in the few GeV energy range and their effect on neutrino induced reactions; interactions of α particles below 150 MeV/A; improvements in the latest stages of nuclear reactions.

1 Introduction

FLUKA [1,2] is a general purpose tool for calculations of particle transport and interactions with matter, covering an extended range of applications spanning from proton and electron accelerator shielding to target design, calorimetry, activation, dosimetry, detector design, Accelerator Driven Systems, cosmic rays, neutrino physics, radiotherapy. Sixty different particles plus heavy ions can be transported by the code. The energy range covered for hadron-hadron and hadron-nucleus interaction is from threshold up to 10000 TeV, while electromagnetic and μ interactions can be dealt with from 1 keV up to 10000 TeV. Nucleus-nucleus interactions are also supported up to 10000 TeV/n. Neutron transport and interactions below 20 MeV down to thermal energies are treated in the framework of a multi-group approach, with cross section data sets developed for FLUKA starting from standard evaluated databases (mostly ENDF/B-VI, JENDL and JEFF).

Transport in arbitrarily complex geometries, including magnetic field, can be accomplished using the FLUKA combinatorial geometry. A suitable voxel geometry module allows to model properly CT scans or other detailed 3D representations of human beings, typically for dosimetry or therapy planning purposes.

The code has the ability to run either in fully analogue mode, or in biased mode exploiting a rich variety of variance reduction techniques.

FLUKA is jointly developed by the European Laboratory for Particle Physics (CERN), and the Italian National Institute for Nuclear Physics (INFN).

2 The FLUKA hadronic models

The approach to hadronic interaction modeling behavior adopted in FLUKA has been described in several papers [3–6].

Hadron-nucleon inelastic collisions are described in terms of resonance production and decay up to a few GeV. At higher energies, a model [5] based on the Dual Parton Model [7] (DPM) takes over. The Dual Parton Model is a particular quark/parton string model, and provides reliable results up to several tens of TeV. In DPM, hadron-hadron interactions result in the creation of two or more QCD color strings, from which hadrons have to be generated.

the FLUKA nuclear interaction model called PEANUT [3–6] can be schematically described as a sequence of the following steps:

- Glauber-Gribov cascade and high energy collisions
- (Generalized)-IntraNuclear cascade
- Preequilibrium emission
- Evaporation/Fragmentation/Fission and final deexcitation.

Some of the steps could be missing depending on the projectile energy and identity. PEANUT has proved to be a precise and reliable tool for intermediate energy hadron-nucleus reactions. Its "nuclear environment" is also used in the modelization of (real and virtual) photonuclear reactions, neutrino interactions, nucleon decays, muon captures.

Interactions originated by ions are handled by three different generators depending on the projectile energy. The Boltzmann Master Equation (BME [21]) model has been implemented into FLUKA to deal with the lowest energies, below about 150 MeV/A. At higher energies, the interfaces with a modified version of rQMD-2.4 [8–11] and with DPMJET-III [12] take over. Ion electromagnetic dissociation is also simulated, through the emission of virtual photons and the coupling with the PEANUT environment [13].

All nuclear interaction models, including those genetrated by ions, share parts of the common PEANUT framework. In particular, all nuclear fragments, irrespective of the originating reaction, are deexcited through the same evaporation/fragmentation and gamma production chain. This approach allows to share all the new developments and improvements among all the target, projectile and energy combinations, all will be shown in the following. It allows also to factorize the benchmark of the different models, thus gaining knowledge and enhancing reliability. At the same time, this integrated approach needs a consistent behavior and information sharing of all the building blocks.

3 Improvements to the DPM at its lower limit

Strong experimental effort is ongoing on particle production from beams in the few to tens of GeV range [14–17]. Hadroproduction in this energy range is of utmost importance, for instance, for a precise determination of neutrino spectra in neutrino oscillation experiments. From the theoretical point of view, this is a very challenging region, since the energy is too high for resonance formation models, and too low for for quark gluon based models. This was true also for FLUKA, that describes the interactions in the DPM framework as chain production and chain hadronization. Indeed, the "standard" hadronization is outside its validity region when low mass chains are involved, mainly because of strong mass effects. The same is true also for the simulation of reaction induced by neutrinos. Their description in FLUKA include the QuasiElastic, resonant and deep inelastic scattering (DIS) channels. Hadron production after DIS is modeled with the same chain hadronisation as for hadronic interactions. A description of the FLUKA neutrino generator (called NUNDIS) can be found in [18,19]. A correct simulation of neutrino interactions in the GeV energy range is of utmost importance for the next generation neutrino experiments at accelerators.

To better cope with hadron production and neutrino interactions in the few-GeV range, a new treatment of low mass chain has been implemented in FLUKA. These chains gradually migrate from standard hadronization to a "phase space explosion", analogue to the Fermi Break up of light nuclei. The chain is thus hadronised in a single step, emitting baryons, mesons and resonances with multiplicity and momenta sampled according to phase space density. Two constraints are enforced through random rejection. First of all, the most energetic particle is preferentially the carrying one of the projectile quarks. Second, in order to comply with the experimentally observed transverse momentum distributions, configurations where the product of all transverse momenta largely exceeds $N \cdot 0.3$ GeV (N being the number of secondaries) are disfavored. Results of this new approach agree well with thin target experimental data, as shown for instance in figure 1.

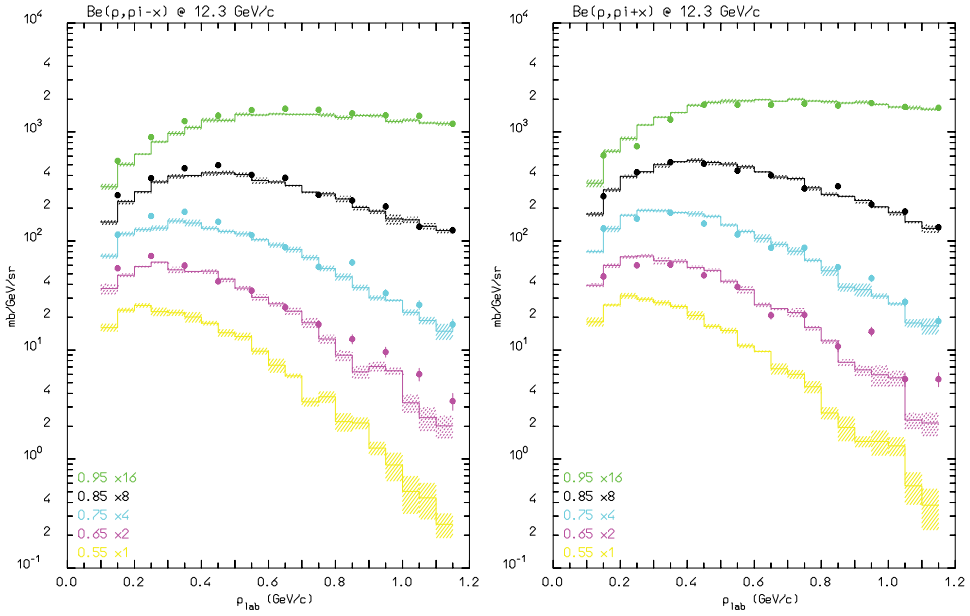

Fig. 1: Pion production from proton interactions on Be at 12.3 GeV Emitted pion spectra at different angles in the range 300 - 600 mrad Dots: data (BNL910 expt. [17]), histograms : Fluka

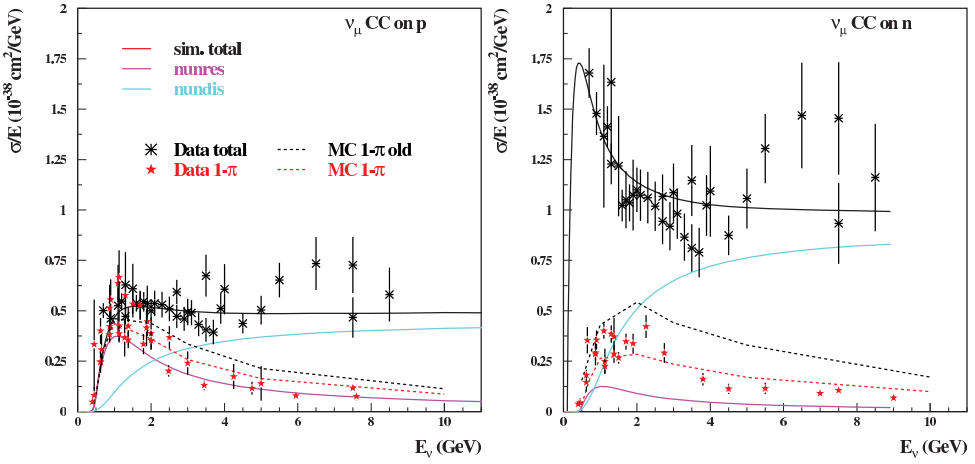

Fig. 2: Cross sections for reactions induced by muon neutrinos on protons(left) and protons (right). Data (symbols, from the compilation in [20]) are presented for the total cross section (black) and for the so called "single π" cross section (red). The total simulated cross section (black line) is composed by the QE, resonant (magenta line) and DIS (cyan line) channels. The red dotted line shows the calculated "single π" cross section in the present FLUKA version, while the dotted blue line correspons to the old FLUKA results

For what concerns neutrino interactions, this new chain treatment has a spectacular impact on the prediction of the so-called "single pion production" reactions, such as, for example, $\nu_\mu + p \rightarrow \mu^- + p + \pi^+$. These are the natural outcome of the resonant channel: the above example could come

from $\nu_\mu + p \to \mu^- + \Delta^{++} \to \mu^- + p + \pi^+$. However, the DIS channel can also result in a single pion production. Both processes must be considered when comparing to experimental data. FLUKA results after the latest improvement are in nice agreement with data, while they previously overestimated the single pion channels (see Fig. 2).

4 Alpha-induced reactions at low energy

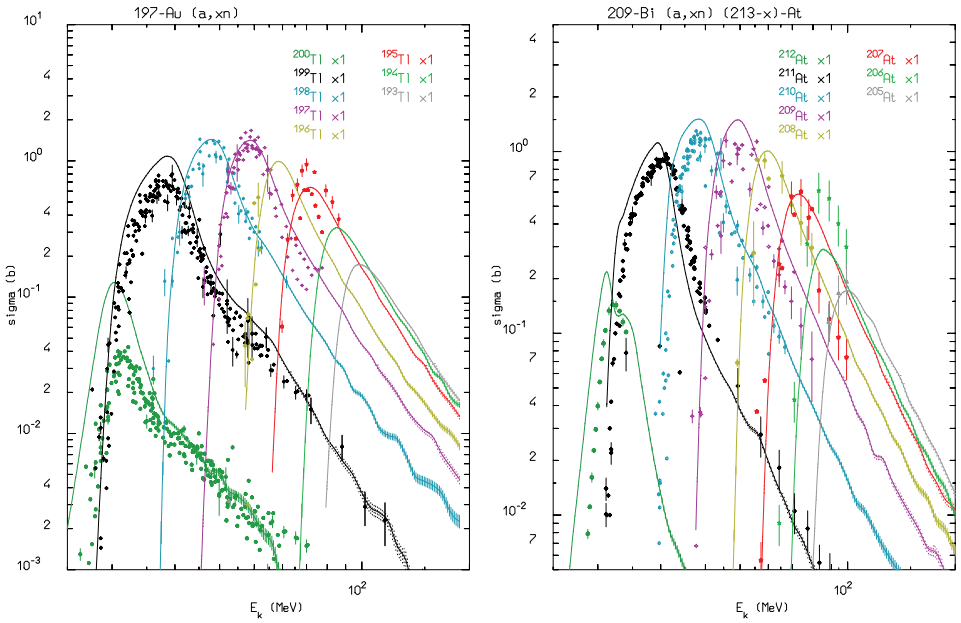

Fig. 3: Excitation functions for the production of radioisotopes from α interactions on Au (left) and Pb (right) (Data (points) from [22] lines: Fluka

Reactions induced by alpha particles are of relevance in different fields. For instance αs are abundant in the fragmentation tail of hadrontherapy beams, they can cause radiation damage to electronics, and they can produce dangerous radioisotopes, like the chemically reactive Astatine isotopes from reactions on Bismuth , and Polonium from reactions on Lead. Some of these isotopes have exemption limits 3-4 order of magnitudes smaller than most other radioisotopes commonly produced at accelerators. One of the latest development in FLUKA is the implementation of α induced reactions at low energy (E $<$ 150 MeV/A) through the BME model. At higher energies these reactions were already handled by the rQMD-2.4 and DPMJET-3 interfaces. The BME event generator [23] in FLUKA simulates thermalization of a composite nucleus, created in the complete or incomplete fusion of two ions, by sampling from the results of the numerical integration of the BMEs. These equations describe the time evolution of the momentum distributions of the nucleons of the composite nucleus via two body elastic scatterings and particle emissions into the continuum (both single nucleons and clusters such as a light particle) [21]. The final de-excitation of the remaining equilibrated nucleus is handled by the FLUKA evaporation/fission/fragmentation module. While complete fusion covers the lowest impact parameter interval, for more peripheral collisions a three body picture of the reaction is implemented, envisaging the production of rather cold projectile-like and target-like nuclei and a middle source preferentially excited. The mass of the last is calculated by the integration of the projectile and target Fermi densities over their overlapping region. At even higher impact parameters, single nucleon mode break-up/transfer

is modeled. Due to the specificity of the extremely light ion projectile, alpha-induced reactions are not included in the BME database. Nevertheless, pre-equilibrium emissions play a key role in accounting for the high energy tails of the excitation functions displayed in figure 3, which cannot be reproduced by the only evaporation of the complete fusion system. The adopted strategy, yielding the results presented here, has been to interface the BME event generator with the PEANUT pre-equilibrium module, based on the exciton model, in order to treat the first de-excitation stage of all nuclei for which BME information is not (yet) available.

5 Gamma De-excitation in Fluka

At the end of the nuclear eveporation stage, the PEANUT model dissipates the residual excitation energy through emission of cascades of γ rays. Photon energies are sampled according to statistical assumptions at high excitation, and to a rotational approximation at low excitations. A partial database of experimentally known excited levels was also implemented and used to constrain the gamma cascading. Details and comparison with data are available in [24]. Since the FLUKA2011.2 release, the database of known levels and transitions has been extended according to RIPL-3 [28] data provided by IAEA, and the evaporation stage has been constrained to proceed through known levels when they are available. In the latter case, a first attempt to account for the angular distribution of emitted photons has also been implemented, following the formalism in [25] with the approximation of the absence of mixed multipolarity. The orientation of the nuclear spin is calculated starting from the initial stage of the reaction through the INCC stage, with the further assumption of $l = 0$ emission during the early steps of the evaporation. Whenever the level compilation is nonexistent or incomplete, the statistical/rotational approximation is still used. Checks of its validity were already performed comparing with experimental data in [24]. Further comparisons have been carried out enabling/disabling the use of the RIPL-3 database for reaction involving isotopes with well known level schemes. Apart from the obvious presence/absence of characteristic photon peaks, the obtained deexcitation spectra are amazingly similar. The average γ multiplicity and average energy differ by a few percent only, which ensures that the FLUKA results are reliable also outside the extent of the database

Further improvements are ongoing, also in view of applications in the field of in-vivo hadron therapy monitoring with prompt photons.

6 Spin-parity in Fermi-Break-up

For low mass excited fragments (A<16), the evaporation stage in PEANUT is substituted by Fermi break-up [26,27],where the excited nucleus is supposed to disassemble just in one step into two or more fragments. All particle stable states with A$\leq$16 are included as possible fragments, plus the particle unstable levels with sizable γ decay branching ratios. The probability for each possible fragment configuration is calculated on the basis of the total available kinetic energy with the appropriate fragment spin multiplicity factors. Once the final state configuration has been selected, the kinematic quantities of each fragment are chosen according to n-body phase space distribution and Coulomb effects (see [27] for a more detailed description). In cases where spin and parity of the excited nucleus are known, conservation laws, constraints on available configurations and centrifugal barrier (if L=0 is forbidden), are now enforced in the fragment production. For the time being, this possibility is limited to specific entrance channel, since the FLUKA generators are not yet tracing the spin and parity evolution. However, apart from future developments, there are already applications that profit from this break-up constraints, for instance the background from induced activity in underground experiments. In these relatively radiation-free environment a major source of induced activity are photonuclear interactions from muons and associated showers. A typical possibility is the production of ^{11}C through the $^{12}C(\gamma, n)\ ^{11}C$ reaction. For photon energies in the Giant Dipole Resonance region, the initial exited ^{12}C state in this reaction has $J^{\pi} = 1^{-}$. The energetically favored disintegration channel would be the one in three α particles. However, being all the intrinsic spins equal to zero, this decay cannot proceed with angular momentum $l = 0$. (The same

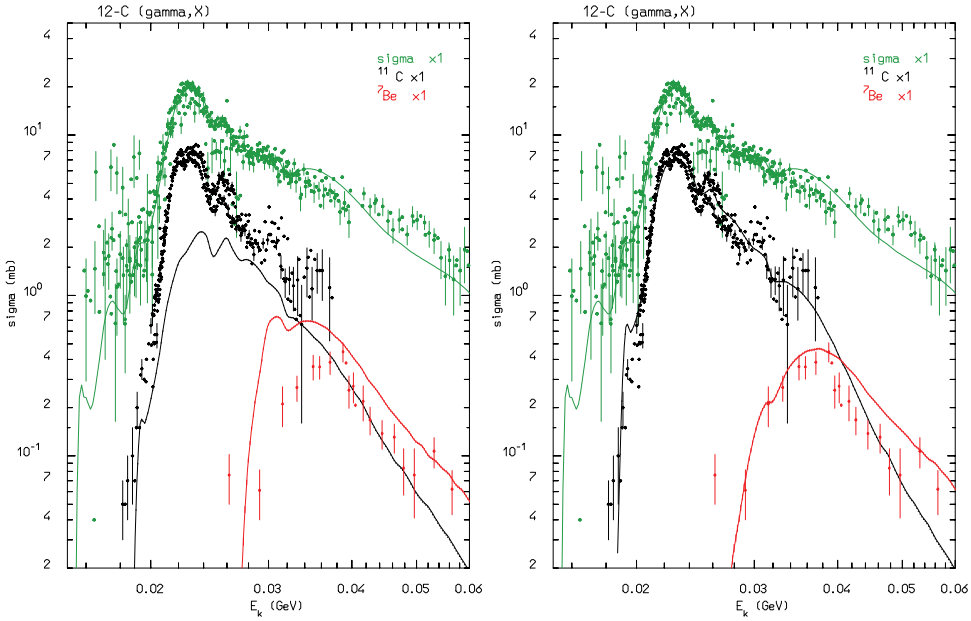

Fig. 4: Excitation functions for photon reactions on carbon. Dots are experimental data [22], lines are FLUKA results. In green the total cross section, in blue the production of ^{11}C, in red the production of ^{7}Be. Left: old FLUKA results, right, results with the latest Fermi break-up developments.

applies to the less probable α+^{8}Be channel). The inclusion of a centrifugal barrier in the energy balance for the *alpha* channels with $l > 1$ strongly suppresses their branching ratio, increasing the competitor n,^{11}C channel by a large factor (≈ 3), and brings the simulated cross sections in fair agreement with data, as shown in figure 4.

References

[1] A. Fassò, A. Ferrari, J. Ranft, and P.R. Sala, CERN 2005-10 (2005), INFN/TC_05/11, SLAC-R-773.

[2] G. Battistoni *et al.*,AIP Conf. Proc. **896** (2007) 31.

[3] A. Fassò, A. Ferrari, J. Ranft, and P.R. Sala, Proceedings of the MonteCarlo 2000 Conference, Lisbon, October 23–26 2000, A. Kling, F. Barão, M. Nakagawa, L. Távora, P. Vaz eds., Springer-Verlag Berlin, 955 (2001).

[4] A. Fassò, A. Ferrari, J. Ranft, and P. R. Sala, Proceedings of the "Specialists' Meeting on Shielding Aspects of Accelerators, Targets & Irradiation Facilities", Arlington, April 28-29 1994, published by OECD/NEA, p. 287-304 (1995).

[5] A. Ferrari, and P.R. Sala, Proceedings of Workshop on Nuclear Reaction Data and Nuclear Reactors Physics, Design and Safety, A. Gandini, G. Reffo eds., Trieste, Italy, April 1996, **2**, 424 (1998).

[6] G. Battistoni et al., Proceedings of 11th International Conference on Nuclear Reaction Mechanisms, Varenna, Italy, 12-16 Jun 2006

[7] A. Capella, U. Sukhatme, C.-I. Tan and J. Tran Thanh Van, Phys. Rep. **236**, 225 (1994).

[8] H. Sorge, H. Stöcker, and W. Greiner, Nucl. Phys. **A498**, 567c (1989).

[9] H. Sorge, H. Stöcker, and W. Greiner, Ann. Phys. (N.Y.) **192**, 266 (1989).

[10] V. Andersen et al., Advances in Space Research, **34(6)**, 1302 (2004).

[11] H. Aiginger et al. [the FLUKA collaboration] Advances in Space Research, **35** (2005), 214-222

[12] S. Roesler, R. Engel and J. Ranft, Proceedings of the MonteCarlo 2000 Conference, Lisbon, October 23–26 2000, A. Kling, F. Barão, M. Nakagawa, L. Távora, P. Vaz eds., Springer-Verlag Berlin, 1033 (2001).

[13] F. Ballarini et al. AIP Conf. Proc. **769**, (2005) 1197

[14] The HARP Collaboration, Nucl. Phys. **B732**, 1 (2006).

[15] A. Bolshakova et al.,Eur. Phys. J. **C72** (2012) 1882

[16] R. Raja et al.,AIP Conf.Proc. 896 (2007) 225-234

[17] I. Chemakin et al., Phys.Rev. **C65** (2002) 024904

[18] G. Battistoni, A. Ferrari, M. Lantz, P. R. Sala and G. I. Smirnov, Proceedings of 12th International Conference on Nuclear Reaction Mechanisms, Varenna, Italy, 15-19 Jun 2009, pp.387-394.

[19] G. Battistoni, A. Ferrari, M. Lantz, P. R. Sala and G. I. Smirnov, "Generator of neutrino-nucleon interactions for the FLUKA based simulation code," AIP Conf. Proc. **1189** (2009) 343.

[20] J Beringer et al. (Particle Data Group), Phys. Rev. D86, 010001 (2012).

[21] M. Cavinato et al.,Nucl. Phys. A643, (1998) 15.

[22] www-nds.iaea.org/exfor/

[23] F. Cerutti et al., Proceedings of 11th International Conference on Nuclear Reaction Mechanisms, Varenna, Italy, 12-16 Jun 2006

[24] A. Ferrari, J. Ranft, S. Roesler, P.R.Sala, Z.Phys. C **71** (1996), 75.

[25] H.A. Tolhoek and J.A.M. Cox, Physica **XIX** (1953), 101.

[26] E. Fermi, Prog. Theor. Phys., **5**, 1570 (1950).

[27] A. Ferrari, J. Ranft, S. Roesler, P.R.Sala, Z.Phys. C **70** (1996), 413.

[28] R. Capote et al., Nuclear Data Sheets **110** (2009), 3107

Imaging techniques in ion beam therapy: status and perspective

Ilaria Rinaldi
University Hospital Heidelberg, Im Neuenheimer Feld 400, 69120 Heidelberg, Germany

Abstract
An overview of the current and proposed imaging modalities in ion beam therapy is presented. In particular, the review starts describing the work already done in the field of Positron Emission Tomography, underlying its potentiality and limiting factors. Afterwards, the techniques under investigation using the detection of fragments produced during nuclear interactions are presented. The attention is concentrated on the Interaction Vertex Imaging based on the detection of charged particles (e.g., protons in case of carbon ion beams) emerging from a patient and on techniques based on the detection of prompt gammas originated from de-excitation of nuclear fragments. Finally, the approach of the heavy ion radiography and tomography is introduced.

1 Introduction

The main physical advantages of ion beam therapy are due to the increased energy deposition towards the finite range of ions in tissue, the Bragg peak, which allows a precise dose delivery. However, the ion beam selectivity can also cause adverse therapeutic results in the case of tumour miss and/or accidental exposure of organs at risk from incorrect delivery of the intended dose. This may occur due to uncertainties related to the accuracy of the ion-range calibration of the patient Computed Tomography (CT) at the treatment planning stage (Hounsfield Unit - Water Equivalent Path Length (HU-WEPL) calibration curve), in addition to reproducibility issues at the treatment site due the accuracy of the patient set-up and immobilization, to the issue of organ motion for specific anatomical sites like the lung, the liver, the rectum, and the prostate as well as to anatomical modifications (e.g., tumour shrinkage) and displacements (e.g., due to rectum or bladder filling) during the fractionated treatment course. Thus, the improvements in the achievable selectivity of the dose delivery using ion beams have been accompanied over the last years by an increasing role of imaging techniques to support not only precise diagnosis and identification of the target volume at the planning stage, but also in-vivo confirmation of the actual treatment delivery.

Nowadays, Positron Emission Tomography (PET) is the most extensively clinically investigated method for this purpose, which exploits the surrogate signal from the irradiation-induced positron emitters, such as ^{11}C, ^{15}O and ^{13}N, produced inside the patient by nuclear fragmentation reactions between the projectiles and the target nuclei of the traversed tissue. Imaging can be performed during or after irradiation. Treatment verification can be obtained from a comparison of the actual measurement with an expected pattern calculated on the basis of the planned treatment and actual time course of beam delivery and imaging.

In addition to the PET-based monitoring, several alternative or complementary techniques are currently being explored for in-vivo quality assurance of ion beam therapy. These novel concepts either try to exploit the emerging prompt secondary radiation (e.g., photons as well as light fragments produced during nuclear interactions), or make use of primary ions at higher energy than used in a treatment for obtaining low dose transmitted planar (radiographic) or volumetric (tomographic) images of the patient.

Prompt emerging secondaries from the therapeutic ion beams can be used for in-vivo verification simultaneously to the treatment delivery. In particular, prompt gamma based imaging techniques have recently gained remarkable interest and several groups are working on simulation studies as well as on the development of optimized detector set-ups (e.g., Compton camera, collimated prompt gamma camera).

Transmitted high energy primary particles could be employed to evaluate the correct patient positioning and verify the ion range before or in between the treatment, especially to reveal morphological

modification and motion. In the extension to tomographic imaging, the distribution of relative stopping power in the patient could be reconstructed and be directly used by the treatment planning system, without resorting to or complementing the use of the X-ray planning CT.

This contribution will present an overview of the status and perspectives of imaging techniques in ion beam therapy.

2 Positron Emission Tomography

Presently, PET is the only clinically investigated method for in-vivo and in-situ monitoring in charged particle therapy (Enghardt et al. 1992). The physical principle of PET-based verification of ion beam therapy is that during therapeutic irradiation, positron emitters, such as ^{11}C, ^{15}O and ^{10}C, are produced inside the patient by nuclear fragmentation reactions between the projectiles and the target nuclei of the traversed tissue. PET scanners can detect the photon pairs resulting from the annihilation of the positrons in a patient either during (on-line) or after (shortly after: in-room, with greater delay: off-line) treatment. These measured activities are successively compared with Monte Carlo (MC) simulations based on the prescribed beam plan providing a non-invasive validation method of the whole treatment planning and delivery chain (Parodi et al. 2008).

Promising results were achieved so far for ion-based PET imaging for in-vivo verification of ion treatment and beam range. The first clinical activities showed the usefulness but also the limitations of in-vivo PET range verification. The pioneering investigations were performed at the GSI Helmholtz Centre for Heavy Ion Research during the pilot project using a dedicated in-beam double-head detector integrated into the experimental treatment room for carbon ion therapy (Enghardt, Crespo, Fiedler, Hinz, Parodi, Pawelke & Pönisch 2004, Parodi 2004). Afterwards, at Massachusetts General Hospital (MGH) in Boston, a commercial PET/CT scanner was also used for post-treatment imaging in proton therapy (Parodi et al. 2007, Parodi et al. 2008).

The differences of these two technical implementations of PET are summarized in the following. At GSI, the acquisition was performed in between the spill extraction pauses with a data acquisition system synchronized with the beam delivery and for approximately 40 s after each irradiation with a limited angle detector (Enghardt, Crespo, Fiedler, Hinz, Parodi, Pawelke & Pönisch 2004). It is evident that in-beam solutions are technically very demanding but, on the other hand, offer the possibility of monitoring individual fields in the treatment position without losing the significant activity contribution from the short-lived ^{15}O emitter. At MGH, the patient is moved, shortly after the irradiation, to a commercial PET/CT scanner in close proximity to the treatment site (Parodi et al. 2008, Unholtz et al. 2011, Parodi et al. 2011). The off-line solution is used nowadays also at the Heidelberg Ion Therapy centre (HIT) (Haberer et al. 2004). It has been also investigated at the HIMAC facility, although it is not yet used in clinical routine for carbon ion dose verification (Schardt et al. 2010). An advantage of the off-line PET is the use of commercially available full-ring PET scanners that typically offer better imaging performance with respect to in-beam limited angle detectors. The main drawbacks are patient re-positioning issues as well as the loss of signal from short-lived positron emitters and the larger influence of metabolic processes in the time elapsed between irradiation and imaging. Moreover, post-treatment imaging only detects the integral beam delivery, with a loss of range information in the case of multiple treatment fields (Parodi et al. 2008).

The characteristics of PET imaging depends on the primary beam used in the treatment. In figure 1, the differences between PET monitoring performed for an irradiation with proton and carbon ion beams are depicted. For irradiation with carbon ions (left panel of figure 1), a peak in the β^+-activity is formed in close proximity to the Bragg peak since the main contributions to the PET signal are given by the positron emitters ^{10}C and ^{11}C projectile fragments. In fact, carbon isotope projectile fragments keep approximately the same velocity as the primary carbon ions and therefore have almost the same range due to the A/Z^2 dependence. Consequently, the maximum of positron radioactivity is formed at the end of

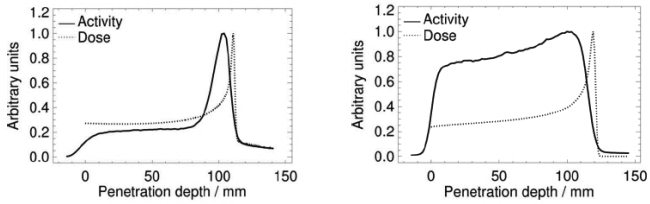

Fig. 1: Measured auto-activation of thick PMMA targets by means of 260 MeV/u carbon ions (left) and 140 MeV protons (right). The solid lines show the depth profiles of the measured β^+-activity. For comparison the depth-dose profile of the primary beam is shown as dotted line. Figure from (Parodi 2004).

the β^+-activity profile not far away from the Bragg peak position in the primary depth-dose distribution. On the contrary, the correlation between the proton depth-dose curve and the β^+-activity profile (right panel of figure 1) is poorer due to the lack of projectile fragmentation which implies that no maximum of positron radioactivity is formed at the end of the primary proton range (Parodi et al. 2002). Nevertheless, this lack of peak structure in the activity profile for proton beams is balanced to some extent by the three times higher total induced activity for the same range and dose delivery (Parodi et al. 2002), which is due to the about 20 times higher number of protons compared to carbon ions necessary to deliver the same physical dose (Kraft 2000). The ratio could further increase in favour of protons when comparing the same biological effective dose.

Applications of proton off-line PET for range monitoring were feasible for head and neck cases in well co-registered low perfused bony structures, however challenges for millimetre accurate range verification were encountered especially in extra-cranial anatomical locations due to limiting factors such as physiological washout, co-registration, and motion (Knopf et al. 2011).

In any case, the main drawback of PET imaging applied to particle therapy is the low β^+-activity[1] induced by fragmentation: about 200 Bq Gy^{-1} cm^{-3} for ^{12}C and about 600 Bq Gy^{-1} cm^{-3} for protons (Enghardt, Parodi, Crespo, Fiedler, Pawelke & Pönisch 2004). Moreover, the positron activity is correlated but not directly proportional to the spatial pattern of the delivered dose (Schardt et al. 2010).

In clinical routine, the therapy control is achieved by visually comparing the measured β^+-activity distribution with a MC prediction based on the treatment plan and the specific time course of the irradiation (cf. figure 2). In case of observed discrepancies between the measured and expected PET images, the radio-oncologist is provided with a quantitative estimation of the deviation between the planned and actually applied physical dose (Parodi 2004). Before the next irradiation fraction, the radiotherapist can, e.g., expose the patient to a new X-ray CT for further investigation of possible anatomical changes and, in case of significant deviation between the planned and applied dose, a new treatment plan can be elaborated.

To summarize, the PET monitoring technique, especially in the on-line implementation, allows to monitor the maximum ion range, to verify the field position, and to detect deviations in the patient positioning or local changes of the patient anatomy in the course of the fractionated treatment (Schardt et al. 2010). On the other hand, unfortunately, 3D tomographic in-beam PET solutions are, nowadays, not commercially available, but research is ongoing in several groups to realize new generation dedicated detector solutions.

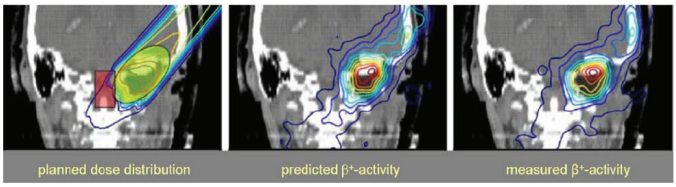

Fig. 2: Example of in-beam PET monitoring showing the irradiation of a skull base tumour at GSI. Left: Planned dose distribution superimposed on the CT image. The target volume and the brain stem as an OAR are highlighted. Middle: Predicted β^+-activity distribution calculated from the treatment plan and time course of the irradiation. Right: Measured β^+-activity distribution. By comparison with the prediction it was verified that the carbon ions were correctly stopped before the brain stem (Crespo et al. 2006).

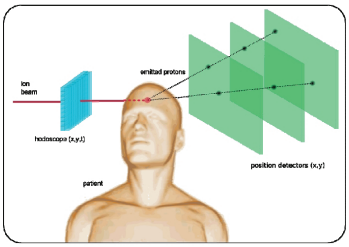

Fig. 3: Artistic scheme of the IVI system. The hodoscope tags the ions in time and space coordinates. In single-track vertexing, the vertex is reconstructed as the intersection of the emerging particle trajectory and the beam direction provided by the hodoscope. In multi-track vertexing, the vertex is reconstructed by the intersection of two or more emerging particle trajectories arising from the same fragmentation point. Figure adapted from (Dauvergne et al. 2009).

3 Interaction Vertex Imaging

An alternative technique for ion therapy monitoring and range verification is the Interaction Vertex Imaging (IVI, c.f figure 3), especially attractive in the case of pencil beam scanned delivery. The IVI is based on the detection of secondary charged particles emerging from the patient, that were generated in nuclear interactions between the incoming ions and target nuclei. This technique is currently under investigation, e.g., by a collaboration between the groups of Lyon (Institut de Physique Nucléaire de Lyon and CNDRI-INSA, working on the Regional Research Program for Hadron Therapy (ETOILE)) and the TERA (Therapy with Hadronic Radiations) foundation (Henriquet 2010) and also in the framework of the Advanced Quality Assurance project (AQUA, `http://project-aqua.web.cern.ch/project-aqua`) for the National Centre for Oncological Treatment (CNAO). There are two main advantages which make IVI a potentially attractive technique: The detection of charged particles is easier and the counting statistic potentially achievable is larger (i.e., 2-3 orders of magnitude (Henriquet 2010)) compared to systems that detect, e.g., photons (Braunn et al. 2010, Gunzert-Marx et al. 2008, Testa et al. 2010). This possible new technique is based on the reconstruction of the trajectories of the emerging particles which are then extrapolated back to their production point (Dauvergne et al. 2009). Indeed, the position of the fragmentation points are expected to be correlated with the ion range, and the amount of emerging charged particles could be, in principle, correlated to the dose. Figure 4 illustrates the possible correlations of proton interaction vertex profiles and the Bragg peak position obtained with a GEANT4 (Agostinelli et

[1]The irradiation-induced activity is 2-3 orders of magnitude lower than in conventional tracer imaging in nuclear medicine PET.

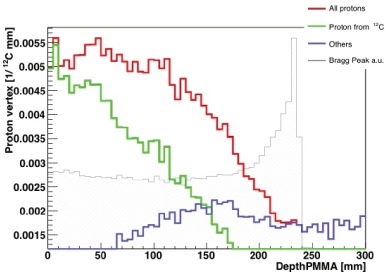

Fig. 4: Vertex distribution of emerging primary, secondary and total protons created by 400 MeV/u carbon ions impinging onto a PMMA target simulated with the GEANT4 MC code. The respective Bragg curve is also illustrated in arbitrary units. While not directly representing the dose distribution, a measurement of the interaction vertex distribution is somewhat correlated with the Bragg peak position. Figure adapted from the AQUA project website (`http://project-aqua.web.cern.ch/project-aqua`).

al. 2003, Allison et al. 2006) MC simulation of 400 MeV/u carbon ion beams hitting a PMMA target.

The vertex reconstruction can be done with two different techniques based on the particle multiplicity arising from each fragmentation vertex. In the simplest form, also named single-track vertexing, the vertex is reconstructed as the intersection of the emerging particle trajectory and the beam direction provided by the hodoscope. While in the more complex so-called multi-track vertexing, the vertex is reconstructed by the intersection of two or more emerging particle trajectories arising from the same fragmentation point (cf. figure 3 and (Henriquet 2010)).

4 Prompt gamma radiation

Prompt gammas are mainly produced in de-excitation processes during nuclear interactions. The detection of prompt gamma profiles can be, in principle, correlated to the Bragg peak position providing one dimensional information on the ion range in a patient, especially suitable for pencil beam scanning.

In the case of protons, the measurement of the emitted prompt photons, detected at an angle of 90◦ with respect to the incident direction of a 100 MeV proton beam, has verified the correlation with the Bragg peak position with an accuracy of 1-2 mm (cf. figure 5 (Min et al. 2006)).

More recently, the discussion about the potential use of prompt gamma emission as a method to verify the accuracy and efficacy of doses delivered with proton radiotherapy was raised by (Polf et al. 2009*a*, Polf et al. 2009*b*).

The first proof of principle for carbon ion beams was performed by the Lyon groups at the GANIL facility (Caen, France) in 2007 with 73 MeV/u $^{13}C^{6+}$ ions impinging on a PMMA target. The correlation between 90◦ angled prompt photon profiles and the Bragg peak position, obtained for a carbon ion beam in which both, target nuclei and primary ions, undergo nuclear fragmentation (Testa et al. 2008), is shown in figure 6, when properly discriminating the photon signal.

Other experimental investigations with carbon beams were performed in the following years at GANIL and GSI (Testa et al. 2009, Testa et al. 2010). The main feature of these experiments is the introduction of time of flight (TOF) discrimination between prompt photons and background radiation, especially neutrons, avoiding the use of bulky neutron shielding like in the case of the work presented by (Min et al. 2006). This feature is of particular importance since it allows the use, in case of scanned ion beam delivery, of a stacked multi-detector set-up that, in principle, can be employed clinically for real-time in-situ ion range monitoring.

The major drawback of this technique, on the other hand, is the low achievable counting statistic of

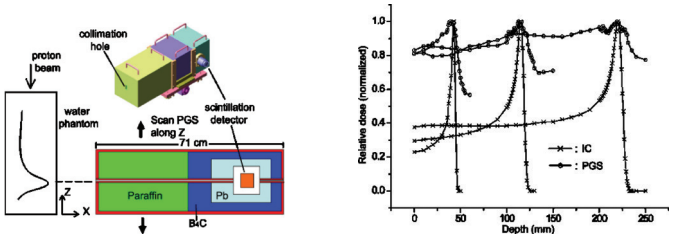

(a) Experimental set-up

(b) Correlation between the Bragg peak locations and prompt gamma scans along the beam penetration in water

Fig. 5: (a) Experimental set-up used by (Min et al. 2006) for right-angled measurement of prompt gamma induced by proton beams slowing down in water. A collimator system consisting of lead, paraffin and B_4C powder is used to suppress the considerable background from scattered photons and neutrons, respectively. The gamma detector is a CsI(Tl) scintillator. (b) The resulting prompt gamma scans (PGS) along the beam penetration in water are compared in the 5(b) to depth dose measurements taken with an ionization chamber (IC) to illustrate the correlation with the Bragg peak location.

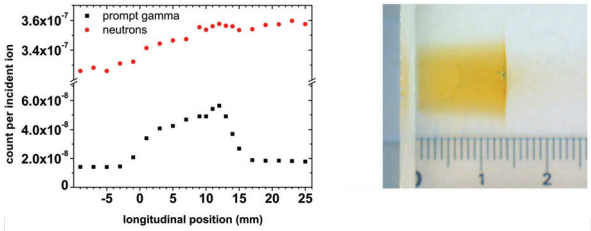

Fig. 6: Details of the experiment performed at the GANIL facility in 2007 by the Lyon groups with 73 MeV/u $^{13}C^{6+}$ ions impinging onto a PMMA target. Left: 90◦ angled prompt gamma detection rates as a function of the longitudinal position of target applying a TOF selection. The neutron (round symbols) background is also shown. Right: scaled photograph of the irradiated PMMA sample. Figure adapted from (Testa et al. 2008).

measured gammas, also related to the detector efficiency. The Lyon groups have measured the net gamma count rate along the primary ion path per incident carbon ion, unit solid angle, and unit path length for a primary beam of 95 MeV/u ^{12}C impinging onto a PMMA target and using a single scintillator (e.g., BaF_2) for gamma detection. The value was found to be $\approx 1 \cdot 10^{-7}$ gammas ion^{-1} msr^{-1} mm^{-1} (Testa et al. 2010). A patient treatment plan in which, e.g., $7 \cdot 10^8$ carbon ions are required to deliver an absorbed dose of 1 GyE to a tumour volume of 120 cm^3, divided in 39 slices of 3 mm width (Krämer et al. 2000) corresponds on average to $1.8 \cdot 10^7$ delivered carbon ions per slice. Therefore, according to the above mentioned value of $1 \cdot 10^{-7}$ photons ion^{-1} msr^{-1} mm^{-1}, about 7 gamma counts per slice within the ion path would be obtained for the considered set-up.

Detector developments will allow to improve the counting statistic of measured gammas and thus determine the prompt gammas applicability to 3D total delivery or isoenergy slice/pencil beam based imaging. To obtain 3D information, not only prompt gamma profiles have to be detected but also precise information on the transverse position of the beam is required (e.g., from a hodoscope). Prompt gamma based imaging techniques for ion beam therapy have recently gained remarkable interest and several groups are working on developing an optimized experimental set-up (e.g., Compton camera, collimated prompt gamma camera).

5 Ion-based radiography and tomography

The use of energetic ion beams to obtain low dose transmitted planar (radiographic) or volumetric (tomographic) images of the patient prior to or in between the treatment could be one alternative method to improve the accuracy of the calculated ion ranges in tissue and to avoid range uncertainties correlated to the usage of X-ray-based calibration curves. Primary ions lose their energy in matter mostly in inelastic Coulomb collisions with atomic electrons. This transferred energy is characterized by the stopping power, which depends on the properties of the traversed material (i.e., electron density, atomic number and atomic weight). Due to the weak energy dependence of the stopping power ratio in a traversed material relative to water, the radiographic images obtained at higher energies than used for therapeutic purposes could serve for verification of the HU-WEPL calibration curve used in the treatment planning. In addition, ion radiographic images could be made at the treatment site and employed to monitor the patient positioning and to check the primary ion range in the target volume, which is important especially in case of morphological modifications and motions.

In the extension to tomographic imaging, the distribution of relative WEPL in the patient could be reconstructed directly based on the knowledge of the Bethe-Bloch formula and by irradiating the patient from several different angles with an energetic ion beam and measuring the corresponding residual energy or range behind the traversed volume. A so obtained 3D WEPL map could then be directly used by the treatment planning system, without resorting to the use of the X-ray planning CT and HU-WEPL calibration curve.

The history of heavy charged particle radiography began already in 1968 with the pioneering work of Koehler. In (Koehler 1968) it is shown that images obtained on a radiographic film irradiating objects with a thickness slightly smaller than the range of the incident 160 MeV proton beam had a much greater contrast than images produced with X-rays under the same conditions. In the following years, publications about proton radiography (Koehler & Steward 1974) and tomography (pCT (Cormack & Koehler 1976)) addressed proton imaging as a diagnostic tool (Hanson et al. 1981, Hanson et al. 1982).

In those decades, however, most of the technological effort was put forward to improve X-ray CT, so that the interest in developing medical pCT stagnated until the advent of the first medical proton gantries at LLUMC. With the worldwide installation of proton gantries and the increased number of patients treated with proton therapy, the need of an accurate prediction of the proton range and verification of the patient position increased. Therefore, the development of accurate imaging techniques led to the construction of a first radiographic system at PSI (Schneider & Pedroni 1995, Schneider et al. 1996, Schneider et al. 2004), shown in figure 7(a). In the same year, within the LLUMC project, a design study concluded that a pCT scanner, depicted in figure 7(b), should utilize instrumentation developed for high-energy physics such as silicon track detectors and crystal calorimeters equipped with fast read-out electronics, allowing one-by-one registration of protons traversing the body during a full revolution of the proton gantry (Schulte et al. 2004).

One technical challenge of pCT is due to the fact that the range/energy measurements are strongly dependent on the precise knowledge of the most probable trajectories of the protons through the patient, since protons are affected by multiple Coulomb scattering. To develop algorithms to accurately reconstruct their path through matter, it is a very complex task (Li et al. 2006). To improve the spatial resolution of proton radiography or tomography to meet clinical standards, each incident proton has to be labelled and the range (PSI approach) or the energy (LLUMC approach) for the corresponding proton exiting the target has to be revealed (cf. figure 7).

PCT also requires fast data taking methods in order to scan the patient in a tolerable time (Pemler et al. 1999). The dose received by the patient during a proton radiographic exposure was found to be smaller than during the acquisition of a comparable X-ray CT image by approximately a factor of 50-100 (Schneider et al. 2004).

Although the proven advantages of proton-based imaging techniques such as superior density

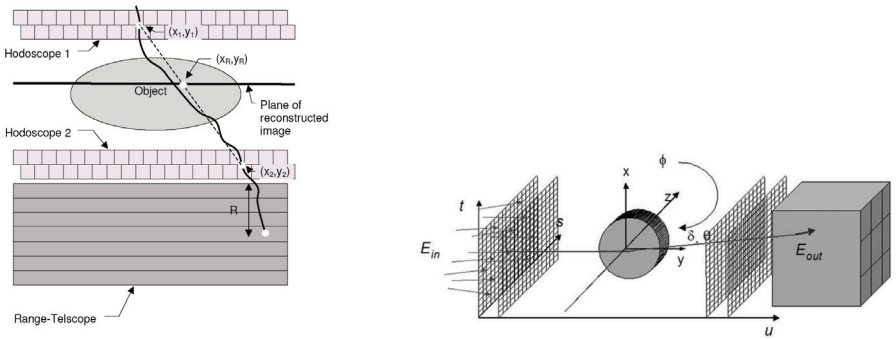

(a) PSI experimental set-up (b) LLUMC experimental set-up

Fig. 7: (a) Schematic view of the PSI radiographic experimental apparatus. The hodoscopes for the measurement of the proton coordinates in front (Hodoscope 1) and behind the object (Hodoscope 2) are shown as well as the range telescope for the range measurement (R). A proton trajectory is delineated. The white dots mark the measured coordinates (x_1,y_1,x_2,y_2) in the hodoscopes and the reconstructed coordinate (x_R,y_R) on a straight line for the plane of image reconstruction (Schneider et al. 2004). (b) Schematic representation of the LLUMC approach. Primaries with known entry energy (E_{in}) are recorded one-by-one in the detector reference system (s; t; u) as they traverse the image object from many different projection angles θ. The recorded data can include entry and exit positions and entry and exit angles as well as initial and exit energy prior to and after the imaged object as well as in the detector (E_{out}) (Reinhard W. et al. 2005).

resolution at lower dose exposure have been experimentally demonstrated (Schneider et al. 2005, Reinhard W. et al. 2005), this technique is not yet used in the clinical routine.

In 2006 in Japan at HIMAC, the first attempt was made to implement a CT, using broad carbon ion beams and measuring the residual energy behind the targets (Shinoda et al. 2006, Ohno et al. 2004). Since both, primary and fragmented secondary ions, add to the residual energy, revealed e.g., by a calorimeter, the discrimination of their contributions to the signal is difficult. On the other hand, the Bragg peak position is determined only by primary ions, suggesting the use of a range telescope as alternative detector in carbon ion-based transmission imaging applications. Contrarily to protons, the trajectories of high energy carbon ions can be assumed to be straight in first approximation, thus simplifying a lot the path reconstruction problem.

Difficulties related to carbon ion-based CT concern the financial and technical effort needed to accelerate therapeutic ion beams to sufficiently high initial energy (e.g. $\approx$ 400 MeV/u) and to deliver heavy ions with a suitable isocentric system, e.g., with a gantry for carbon ions. At HIT, carbon ion beams of initial energy up to $\approx$ 430 MeV/u, a 3D fast and precise active raster scanning beam delivery system as well as the worldwide first heavy ion gantry are available and offer the ideal scenario to develop ion-based radiography and tomography (Rinaldi et al. 2011, Voss et al. 2010, Rinaldi et al. 2012).

6 Conclusions

The novel imaging techniques listed in this work present interesting potentialities for future clinical applications to in-vivo range verification on different time scales of the treatment(i.e., prior to, during, and in-between treatment), thus encouraging further investigations and developments. It is expected that they will provide valuable information complementary to techniques being currently clinically evaluated (i.e., PET), with the final goal to integrate several imaging modalities to reduce range uncertainties and thus provide full clinical exploitation of the physical advantages of ion beams for high precision radiation therapy.

In such a scenario, ion-based tomography could be employed to supplement and/or replace the use of X-ray CT and HU-WEPL calibration curve in the treatment planning and ion-based radiography to evaluate the correct patient positioning and to verify the ion range prior to and in-between treatment. Prompt gamma imaging and IVI could serve for real-time in-vivo range monitoring of single pencil beams or isoenergy slices during a treatment. PET could be adopted for tomographic confirmation of the irradiated volume and for dose reconstruction.

References

Agostinelli et al. S 2003 *Nuclear Instruments and Methods in Physics Research Section A: Accelerators, Spectrometers, Detectors and Associated Equipment* **506**(3), 250–303.
URL: *http://www.sciencedirect.com/science/article/pii/S0168900203013688*

Allison et al. J 2006 *Nuclear Science, IEEE Transactions on* **53**(1), 270 –278.

Braunn B, Labalme M, Ban G, Cussol D, Fontbonne J, Lecolley F, Pautard C, Haas F, Lebhertz D, Rousseau M, Stuttge L, Chevallier M, Dauvergne D, Le Foulher F, Ray C, Testa E, Testa M & Salsac M 2010 *in* A. F F. Cerutti, ed., 'Proceedings of the 12th International Conference on Nuclear Reaction Mechanisms 12th International Conference on Nuclear Reaction Mechanisms' Vol. Vol. 2 Cern Varenna Italy pp. 531–537.
URL: *http://hal.in2p3.fr/in2p3-00449227/en/*

Cormack A M & Koehler A M 1976 *Physics in Medicine and Biology* **21**(4), 560.
URL: *http://stacks.iop.org/0031-9155/21/i=4/a=007*

Crespo P, Shakirin G & Enghardt W 2006 *Physics in Medicine and Biology* **51**(9), 2143.
URL: *http://stacks.iop.org/0031-9155/51/i=9/a=002*

Dauvergne D, Battaglia M, Montarou G & Testa E 2009.
URL: *http://hal.in2p3.fr/in2p3-00363382/en/*

Enghardt W, Crespo P, Fiedler F, Hinz R, Parodi K, Pawelke J & Pönisch F 2004 *Nuclear Instruments and Methods in Physics Research, Section A: Accelerators, Spectrometers, Detectors and Associated Equipment* **525**(1-2), 284–288.

Enghardt W, Fromm W D, Geissel H, Heller H, Kraft G, Magel A, Manfrass P, Munzenberg G, Nickel F, Pawelke J, Schardt D, Scheidenberger C & Sobiella M 1992 *Physics in Medicine and Biology* **37**(11), 2127.
URL: *http://stacks.iop.org/0031-9155/37/i=11/a=009*

Enghardt W, Parodi K, Crespo P, Fiedler F, Pawelke J & Pönisch F 2004 *Radiotherapy and Oncology* **73**(Supplement 2), S96 – S98. Carbon-Ion Theraphy.
URL: *http://www.sciencedirect.com/science/article/B6TBY-4H0RR0H-V/2/a9591cbd746c27d7fec18b9a57ada89b*

Gunzert-Marx K, Iwase H, Schardt D & Simon R S 2008 *New Journal of Physics* **10**(7), 075003.
URL: *http://stacks.iop.org/1367-2630/10/i=7/a=075003*

Haberer T, Debus J, Eickhoff H, Jäkel O, Schulz-Ertner D & Weber U 2004 *Radiother Oncol* **73**, S186–S190.
URL: *http://linkinghub.elsevier.com/retrieve/pii/S016781400480046X?showall=true*

Hanson K, Bradbury J, Cannon T, Hutson R, Laubacher D, Macek R, Paciotti M, & Taylor C 1981 *Phys. Med. Biol.* **26**, 965–983.

Hanson K, Bradbury J, Koeppe R, Macek R, Machen D, Morgado R, Paciotti M, Sandford S & Steward V 1982 *Phys. Med. Biol.* **27**, 25–36.

Henriquet P 2010 Etude de l'emission de particules chragées secondaires dans l'optique d'une dosimetrie en ligne en hadrontherapie PhD thesis Institut de physique nucléaire de Lyon Université Claude Bernard Lyon 1.

Knopf A C, Parodi K, Paganetti H, Bortfeld T, Daartz J, Engelsman M, Liebsch N & Shih H 2011 *International Journal of Radiation Oncology*Biology*Physics* **79**(1), 297–304.
URL: *http://www.sciencedirect.com/science/article/pii/S0360301610002518*

Koehler A M 1968 *Science* **160**, 303–304.

Koehler A & Steward V 1974 *Nature* **245**, 38–40.

Kraft G 2000 *Progress in Particle and Nuclear Physics* **45**(Supplement 2), S473 – S544.
URL: *http://www.sciencedirect.com/science/article/B6TJC-424M60R-5/2/24ba8d6d0b0f6bb65924c97fd646b6fd*

Krämer M, Jäkel O, Haberer T, Kraft G, Schardt D & Weber U 2000 *Physics in Medicine and Biology* **45**(11), 3299.
URL: *http://stacks.iop.org/0031-9155/45/i=11/a=313*

Li X A, Stepaniak C & Gore E 2006 *Medical Physics* **33**(1), 145–154.
URL: *http://link.aip.org/link/?MPH/33/145/1*

Min C H, Kim C H, Youn M Y & Kim J W 2006 *Applied Physics Letters* **89**(18), 183517.
URL: *http://link.aip.org/link/?APL/89/183517/1*

Ohno Y, Kohno T, Matsufuji N & Kanai T 2004 *Nuclear Instruments and Methods in Physics Research Section A: Accelerators, Spectrometers, Detectors and Associated Equipment* **525**(1-2), 279 – 283. Proceedings of the International Conference

on Imaging Techniques in Subatomic Physics, Astrophysics, Medicine, Biology and Industry.
URL: *http://www.sciencedirect.com/science/article/B6TJM-4C47R64-8/2/c5855503f2f52b5be264fdbc934bbbf0*

Parodi K 2004 On the feasibility of dose quantification with in-beam PET data in radiotherapy with ^{12}C and proton beams PhD thesis Technische Universität Dresden, Germany.

Parodi K, Bauer J, Mairani A, Sommerer F, Unholtz D, Haberer T & Debus J 2011 *Conference Record of IEEE 2011 Nuclear Science Symposium and Medical Imaging Conference* .

Parodi K, Bortfeld T, Enghardt W, Fiedler F, Knopf A, Paganetti H, Pawelke J, Shakirin G & Shih H 2008 *Nuclear Instruments and Methods in Physics Research Section A: Accelerators, Spectrometers, Detectors and Associated Equipment* **591**(1), 282 – 286. Radiation Imaging Detectors 2007 - Proceedings of the 9th International Workshop on Radiation Imaging Detectors.
URL: *http://www.sciencedirect.com/science/article/B6TJM-4S3S2BK-W/2/7451f192076cee119aee41143c477230*

Parodi K, Enghardt W & Haberer T 2002 *Physics in Medicine and Biology* **47**(1), 21.
URL: *http://stacks.iop.org/0031-9155/47/i=1/a=302*

Parodi K, Ferrari A, Sommerer F & Paganetti H 2007 *Phys Med Biol* **52**(12), 3369–87.
URL: *http://ukpmc.ac.uk/abstract/MED/17664549*

Pemler P, Besserer J, de Boer J, Dellert M, Gahn C, Moosburger M, Schneider U, Pedroni E & Stäuble H 1999 *Nuclear Instruments and Methods in Physics Research Section A: Accelerators, Spectrometers, Detectors and Associated Equipment* **432**(2-3), 483 – 495.
URL: *http://www.sciencedirect.com/science/article/B6TJM-3X3K963-14/2/90849e49134df2c303ea1d298c2f252d*

Polf J C, Peterson S, Ciangaru G, Gillin M & Beddar S 2009*a Physics in Medicine and Biology* **54**(22), N519.
URL: *http://stacks.iop.org/0031-9155/54/i=22/a=N02*

Polf J C, Peterson S, Ciangaru G, Gillin M & Beddar S 2009*b Physics in Medicine and Biology* **54**(3), 731.
URL: *http://stacks.iop.org/0031-9155/54/i=3/a=017*

Reinhard W. S, Vladimir B, Márgio, C. Loss K, Tianfang L, Andrew J. W, Ivan E, David C. W & Todd S 2005 **32**(4), 1035–1046.
URL: *http://dx.doi.org/doi/10.1118/1.1884906*

Rinaldi I, Brons S, Gordon J, Jäkel O, Panse R, Voss B & Parodi K 2012 *Phys Med Biol* **submitted**.

Rinaldi I, Brons S, Jäkel O, Mairani A, Panse R, Voss B & Parodi K 2011 *Conference Record of IEEE 2011 Nuclear Science Symposium and Medical Imaging Conference* .

Schardt D, Elsässer T & Schulz-Ertner D 2010 *Rev. Mod. Phys.* **82**(1), 383–425.

Schneider U, Besserer J, Pemler P, Dellert M, Moosburger M, Pedroni E & Kaser-Hotz B 2004 *Medical Physics* **31**(5), 1046–1051.

Schneider U & Pedroni E 1995 *Medical Physics* **22**(4), 353–363.
URL: *http://link.aip.org/link/?MPH/22/353/1*

Schneider U, Pedroni E & Lomax A 1996 *Physics in Medicine and Biology* **41**(1), 111.
URL: *http://stacks.iop.org/0031-9155/41/i=1/a=009*

Schneider U, Pemler P, Besserer J, Pedroni E, Lomax A & Kaser-Hotz B 2005 *Medical Physics* **32**(1), 195–199.
URL: *http://link.aip.org/link/?MPH/32/195/1*

Schulte R, Bashkirov V, Li T, Liang Z, Mueller K, Heimann J, Johnson L, Keeney B, Sadrozinski H W, Seiden A, Williams D, Zhang L, Li Z, Peggs S, Satogata T & Woody C 2004 *IEEE Trans. Nucl. Sci.* **51**, 866–872.

Shinoda H, Kanai T & Kohno T 2006 *Physics in Medicine and Biology* **51**(16), 4073.
URL: *http://stacks.iop.org/0031-9155/51/i=16/a=013*

Testa E, Bajard M, Chevallier M, Dauvergne D, Foulher F L, Freud N, Letang J M, Poizat J C, Ray C & Testa M 2008 *Applied Physics Letters* **93**(9), 093506.
URL: *http://link.aip.org/link/?APL/93/093506/1*

Testa E, Bajard M, Chevallier M, Dauvergne D, Foulher F L, Freud N, Létang J, Poizat J, Ray C & Testa M 2009 *Nuclear Instruments and Methods in Physics Research Section B: Beam Interactions with Materials and Atoms* **267**(6), 993 – 996. Proceedings of the Seventh International Symposium on Swift Heavy Ions in Matter.
URL: *http://www.sciencedirect.com/science/article/B6TJN-4VKDMP2-J/2/71c6688f42e84e61d9cb8732497bf8ab*

Testa M, Bajard M, Chevallier M, Dauvergne D, Freud N, Henriquet P, Karkar S, Le Foulher F, Létang J, Plescak R, Ray C, Richard M H, Schardt D & Testa E 2010 *Radiation and Environmental Biophysics* **49**, 337–343. 10.1007/s00411-010-0276-2.
URL: *http://dx.doi.org/10.1007/s00411-010-0276-2*

Unholtz D, Sommerer F, Bauer J, van Straaten D, Haberer T, Debus J & Parodi K 2011 *Conference Record of IEEE 2011 Nuclear Science Symposium and Medical Imaging Conference* .

Voss B, Rinaldi I, Brons S, Jäkel O, Panse R & Parodi K 2010 *GSI Scientific Report 2010* **Volume 2011-1**, 484.

In Memoriam to: Prof. Kazuo Furukawa "Champion for the Th-MSR" who passed away 14 Dec. 2012.

An Alternative Source for Venezuelan Nuclear Energy Production: The Thorium Molten Salt Reactor

L. Sajo-Bohus, H. Barros, M. Sajo-Castelli, M. Asuaje, S. Croquer, J. Clarembaux, E. D. Greaves
Universidad Simón Bolívar, Apdo 89000 Caracas 1080A, Venezuela

Abstract

The Thorium Molten Salt Reactor (MSR), as the FUJI reactor project by Furukawa and collaborators, is considered as one of the generation IV six innovative concepts for alternative nuclear power plants. The thorium cycle for its several advantages should be the future energy source for developing countries. Recently Venezuela signed an agreement with the Russian Federation to install in the near future a PWR-type Nuclear Power Plant, since is the more used and standard technology. However, in the near future the Country should orient his nuclear program toward the thorium cycle MSR due to simplicity, safety and non proliferation properties. This technology is suitable for Venezuela having proved thorium resources and experience with molten salt at industrial scale. We report theoretical calculations for a sub-critical assembly dealing with energy transfer and the effect on the neutron balance of delayed neutrons.

Keywords: Molten Salt Reactor, Thorium cycle, nuclear energy.
PACS: 28.41.-i,28.41.Bm, 28.50.-k

1 Introduction

The energy consumption is a direct evidence of any country productivity; the GDP *per capita* is often assumed as an indicator of a country's living standard. Since the tendency is to improve it, necessarily the energy demand will increase and may double in the next 30 years. The development and introduction of new technologies to tap wind and solar renewable energy is currently on the agenda. However, they are low in energy density, irregular in output and so far it seems to be uneconomical and impractical for large industrial power plants. There is evidence that the nuclear option is still a strong candidate to be employed and increasingly technological interest arises in this field in spite of the opposition of some from the general public.. Today 436 Nuclear Power Plant (NPP) are in operation and already 63 new installations are in construction in spite of all the policy makers declarations that in few leading countries the nuclear program halted. To mention an example Rosatom (Russian Federation) is planning this year to connect to the electric grid a 1.2GW Novovoronezh-2-1 type VVER-NPP and further 16 units are planned to enter operation by 2020; among them, some of a more advanced GenerationIV^{+} (GEN-IV^{+}) reactors are considered.

So far all commercial NNP are based on the uranium cycle, however it is not the only option. Already several initiatives have started toward new concepts e.g. employing the thorium fuel cycle. Initiatives toward development of nuclear plants employing this cycle rose during the past years in several countries motivated for its inherent technical advantages[1]. For instance its superior performance over PWR or BWR (most often commercially employed NPP) was demonstrated during the Thorium Molten Salt Reactor Experiment (MSRE) constructed and successfully operated at Oak

Ridge National Laboratory (ORNL), USA during the decade 1960´s [2]. The 8-MW(t)-MSR had a ^{7}LiF-BeF_2 salt nd graphite moderator; this is a material that is compatible with the corrosive fluoride salt having a stable performance during neutron irradiation[3]. The mentioned research reactor prototype was a good demonstration assembly toward safety operation, neutron balance due to a removal system of xenon and krypton from the fluid fuel, and the employment of different fissile materials such as ^{235}U, ^{233}U, and plutonium. This unit operated successfully for 13,000 equivalent full-power hours between 1965 and 1968. Later on the ORNL-MSR design was further development e.g. the FUJI reactor project by Furukawa and collaborators (1980s – 2000s)[4]. A concept scheme of a MSR-NPP is given in figure 1.

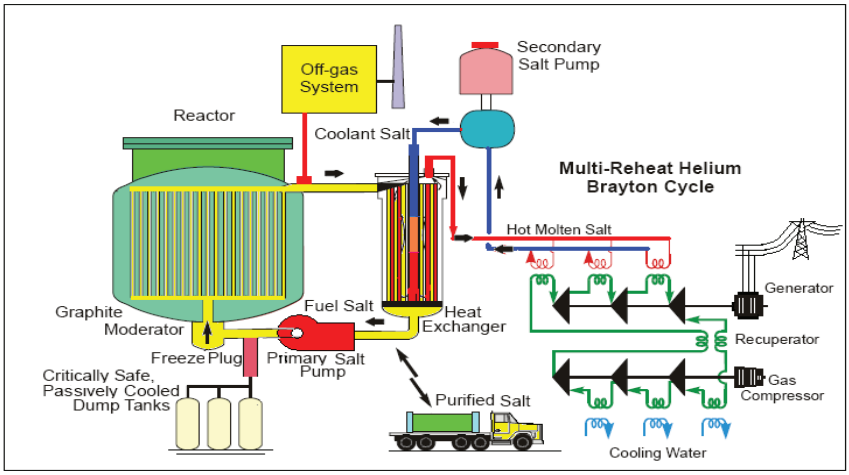

Fig.1: Concept scheme of a MSR-NPP adapted from Forsberg 5. Main features are described in the text.

The main features of the MSR, scheme of Figure 1, consist in having a graphite reactor core crossed by the molten salt fluid followed by an off-gas system at the core out-let and a heat exchanger; after the primary salt pump, an actively cooled freeze plug being a safety valve connecting the primary circuit to dump tanks. The secondary circuit is a conventional one, in which hot molten salt and multy-reheat helium Brayton cycle is considered for its inherent thermodynamical advantages. In fact, since it employs helium (or nitrogen) gas, this cycle efficiently convert high-temperature heat to mechanical energy; in opposition to the steam cycle where the maximum value set on temperature is ~550^{o}C that in turns imposes a limiting mechanical conversion capability. The development of the technology related to high-temperature Brayton cycles, allows higher conversion efficiency and therefore provide higher electrical energy output compared to any other thermodynamical cycle found in commercial NPP.

Other conceptual NPP schemes are under review and several ¨generation IV¨ concepts already have been proposed. For instance, Mazzini et al.[6], started recently the EU-PUMA project based on Th-Pu fuel cycles working in pebble-bed High Temperature Reactor (HTR) concept. The outcome has pointed out that the thorium breeder, due to its liquid fuel characteristics, offer a better and less risky reprocessing operation mainly due to the fact that actinides could be returned to the reactor core. In this way fission fragments are modified and radio-toxicity reduced accordingly. Therefore these highly radioactive waste products should not be removed from the reactor by costly processes and transported

to reprocessing centers; consequently, further advantages exist from the resulting reduction of risk and accidents.

A few others design concepts are worth mentioning briefly: one is the TMSR-NM (non-moderated thorium molten salt reactor) being so far the GEN-IV reactor with the highest energy density. This could be considered as an extreme industrial NPP concept being a combination of the thorium-based fuel cycle with accelerator driven systems (ADS-MSR known as the Rubbia proposal[7]). The other method is the hybrid fusion driven system concept proposed by H. Bethe (1970)[8] related to two step power generation i.e. nuclear fusion to produce the neutron field and fission that will take advantage of it[9]. The last one to which we refer is the modified Liquid Metal Fast Reactor, known as the traveling-wave reactor proposed in the 1950s; that could breed its own fuel inside the reactor core, consume wastes from LWRs and run on depleted Uranium as a fuel[10]. In table 1, we give an overview of some MSR elements to show the broad on going research interest in MSR and fuel compound.

Reactor type	**Neutron Spectrum**	**Application**	**Solute**	**Solvent**
MSR-Breeder	Thermal	Fuel	7Li-BeF2	ThF4-UF4
	Fast	Fuel	7Li	ThF4-PuF4
	TNM	Secondary coolant	NaF-NaBF4	
MSR-Burner	Fast	Fuel	LiF-NaF	LiF-(NaF)-AnF4-AnF3
MSR-Burner	Fast	Fuel	LiF-(NaF)-BeF2	LiF-(NaF)-BeF2-AnF4-AnF3
MSR-Burner	Fast	Fuel	LiF-NaF-ThF4	
MS-Advanced High-Temp. Reactor	Thermal	Primary coolant	7LiF-BeF2	

Tab.1: Fuel and coolant salts composition for different thorium cycle reactor assembly

The renewed interest in the systems mentioned is related not only to new development in material science, surface treatment technologies, viability and advantages in energy economy but also to other aspects that justify the MSR technology as follows:

i.- Th-MSR has been proposed as one of the six innovative concepts by the prestigious ¨GEN-IV International Forum¨, it was selected on the basis of sustainability, economics, proliferation resistance and physical protection; ii.- the proven possibility to increase nuclear fuel resources by breeding ^{233}U from thorium, *de facto* extending nuclear energy lifespan resources by two or more orders of magnitude; iii.- fuel utilization improvement; iv.- enrichment requirements are reduced significantly; v.- the build-up of Pu is not a primary objective; vi.- existing Pu stockpiles and long lived radio-toxic isotopes or other radioactive waste could be incinerated lowering considerably the environmental burden. These, among other observations, support the MSR technology to be considered one of the best ways to continue and spread nuclear energy generation, not only for a future Venezuelan nuclear program, but take the advantages of Th-MSR for emerging and developing countries in general.

In recent years the Venezuelan Government signed an agreement with the Russian Federation (RF) to develop nuclear activities related to the installation of a research reactor and electric

generation[11]. It was announced officially and given diffusion by the media that Rosatom (RF) should install a NPP, probably of 1200MWe type Novovoronezh (VVER-1200). However, due to different causes including the Fukushima accident and its impact in the public opinion, it is highly probably that the program will be delayed at least few years.

Also, in the 1970s the Venezuelan Government received proposals from U.K. to install relatively small NPP to cope with the requirement of large amount of high-temperature heat by industrial plant of Petroleos de Venezuela SA, for example at Paraguana refinery complex producing 956,000 bbl/d (i.e. 152,000 m^3/d), or the Orinoco Basin oil extraction fields including areas for tertiary oil recovery.

On the other hand, the advantages of thorium fuel being more abundant in the Earth crust compared to natural U suggests that it is plentiful also because worldwide supply includes also by-product of rare earth element production. Natural Th is almost 100% ^{232}Th, so that costly fuel enrichment is avoided. However, fissile material must be added to the fuel to start a Th-MSR, e.g. weapons grade ^{235}U or ^{239}Pu from stockpiles and in this case a bonus of weapons dismantling could be provided at low cost.

Additionally the Th-Molten Salt Reactor will help to ensure the maintenance of nuclear weapons free Latin American-continent and so avoiding foreign powers interference with national nuclear programs. It will help also that most countries achieve energy independence and for several of them to make use of their own indigenous sources of thorium e.g. Venezuela occupying the sixth place for its Th resource at Cerro Impacto (World Nuclear org) and Brazil with proven large deposits, just to mention a few.

2 Preliminary studies on reactor dynamics

2.1 The sub-critical training assembly

Preliminary studies have been performed with aim to master computer codes related to the dynamical behavior of small assembly for a MSR structure. Yamamoto et al.,[13] studied small MSR by steady-state analysis estimating the effects of fuel flow.

Based on their results, zero power structure for student training at the USB, was started as a project to assembly a small sub-critical system. This is designed to hold solid fuel having a salt composition with Th+Unat. The fuel, being natural element, is available on the market; our laboratory already received financial support for thorium rich mineral processing; it is planned to produce Th-salt fuel to feed the projected sub-critical assembly. It is devised to employ a radioisotope neutron source (either a 252 Cf, a purpose made Ra-Be, Am-Be source already being used for on-going applied projects). The possibility exists of employing a modified ion implanter, operating it with a deuteron beam on a titanium target to induce low energy D-D reaction and provide neutrons to experiment with a subcritical assembly. The produced neutrons are relatively of low energy (E_n = 2.5 MeV) that by diffusion in a graphite assembly provides a facility for a broad reactor simulation and neutron related experiments. The sub-critical assembly main material is the moderator being a pirolytic graphite pile assembled with blocks of 20x20x60 cm^3 (in the past employed as reflector to lower neutron leakage in research reactors). This material was donated by the Atomic Energy Research Institute AEKI of Budapest, Hungary, in the frame of collaboration with USB and the International Atomic Energy Agency (Vienna, Austria) from which originated the project VEN/8/014. Details of the sub critical assembly including the two strata biological shielding, can be seen in the schematic lay-out of figure 2.

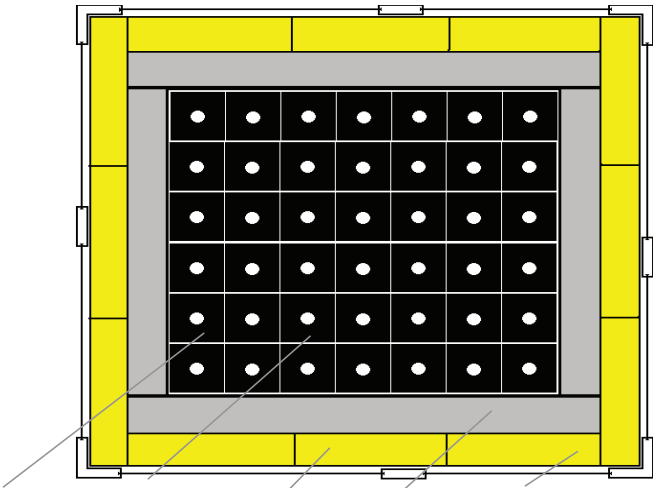

Fig.2: Schematic lay out of zero power graphite assembly (a) has a radioisotope source (252Cf) that is positionable at different places indicated by the accessing holes (b). These are also suitable for fuel loading and neutron or gamma measuring devices. This assembly has an external biological paraffin shield (c) that covers the neutron absorber slabs Li-Polyethylene (d). For safety purpose against possible displacement due to an earthquake shake, a tightly holding non-ferrous structure (e) is included and it holds on place also the biological external shield. Spacing between loading holes is 20cm. Figure not to scale.

Neutron diffusion equation with two or more energy groups is often employed to determine reactor response time. The reactivity depends on the neutrons released from prompt fission and those from decay processes of precursors. The latter are delayed neutrons and without them the reactor could not reach criticality. Meaning that are important and have to be taken into account in the estimation of the neutron balance. Since fissions occur in a flowing media[15], precursors may release delayed neutrons outside the moderating assembly and being lost without inducing new fissions. This means that the reactor neutron-kinetics depends on the precursors drift and therefore on the fuel-flow velocity and the reactor volume (sub-critical assembly in our case. The number of neutron groups depends on the precursor life time and it is known that almost 240 precursors take part in the balance equation given below as follows:

$$\partial C(z,t)/\partial t + \partial(vC(z,t))/\partial z = Q(z,t) - \lambda C(z,t), \partial t \qquad (1)$$

where C is the precursors concentration, v is the fuel cycle speed, Q is the source function, and λ is the decay constant for the given group. It is common to consider six groups to determine neutron balance with fuel speed. Delayed neutron groups kinetic equation can be solved numerically with MATLAB as suggested by F. Reisch[14]. Following that procedure we determined the time behavior at zero power operation under the condition that fuel and moderator temperature have negligible increment. We obtained some indicative results that allow us to establish from the observable graphics (calculations are performed for zero power operation):

- the reactivity is changing as shown in figure 3

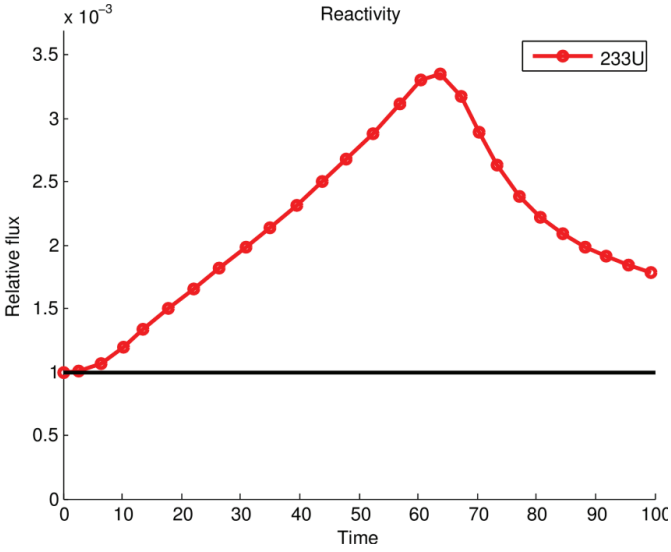

Fig.3: Relative neutron flux variation with time for 233U-fuel

- the characteristics temperature change of the fuel and moderator for zero power operation, is given in Figure 4

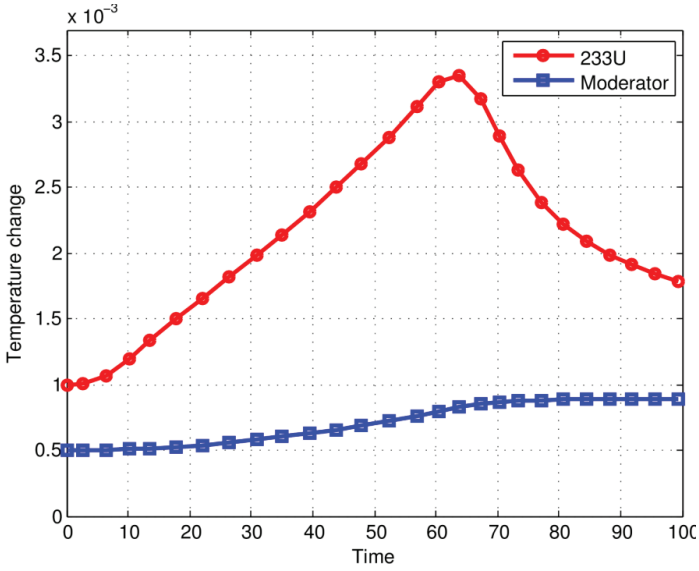

Fig.4: Temperature variation for 233U-fuel and moderator calculated employing MATLAB program.

From these curves we learn fuel's thermal and neutron balance time constant for graphite moderator.

2.2 Thermal and Hydro dynamical effect on reactivity

As an excise we considered the case of a small size nuclear reactor where heath production is not neglected. Its transference to the moderator before reaching the steady state and its time variation with fluid speed is given by the following expression:

$$\partial (\rho h)/ \partial t + \partial/\partial z (\rho v h) = Q \qquad (2)$$

where: ρ , h, v parameters indicate fuel density, enthalpy, and velocity respectively. The heath Q represent the sum of the following terms $Q_{fission} + Q_{delay} + Q_{graphite}$ i.e. $Q_{fission}$, due to fissile material in the fuel, the decay heat Q_{delay}, and the heat exchange between graphite and salt $Q_{graphite}$. The latter represents the heat release and its diffusion in the graphite pile including that it will be exchanged between graphite and fuel. The method of effective heat transfer coefficients determines the temperature gradient in the moderator. The ANSYS-CFX, computer code was employed for a larger assembly than that suggested for laboratory training. Results are given in figure 5. For the simulation of the reactor core, a duct of OD= 0,15m and 4,3m long was assumed and a fuel flow rate of 1m/s. Temperature of the salt was modeled by setting an energy balance considering heat production from delayed neutron in the salt, heat transfer through duct walls and the thermal capacity of the salt.

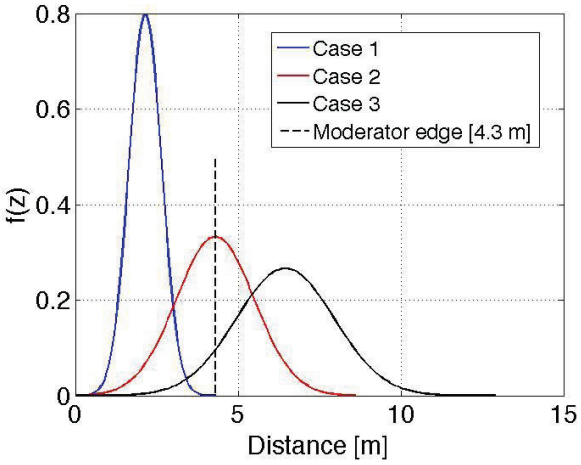

Fig.5: Delayed neutron number with varying flow speed. Segmented line indicates the moderator edge.

As the fuel speeds up the number of delayed neutrons are emitted increasingly out side of the reactor core. Independently of the speed values (limited by the precursor decay constant) always some delayed neutron will be emitted to induce further fission before leaving the core. However it is critical to maintain the delayed neutrons in a window of values to obtain fission rate at given values. For instance delayed neutron precursors changing the transit time from 8.13 s to 60 s induces a variation for neutron multiplication factor by about 0.03%Δk/k. That means that the neutron balance can be modified by changing the fuel flow velocity (see ref.: ORNL-LR-Dwg.75653 pag. 15).

Figure 6 shows heat transfer interactions at duct walls (into and from the graphite moderator). Figures 7 and 8 show temperature distribution over a plane at duct center and temperature evolution over duct axis respectively. As delayed neutron production varies with speed, so is the heat production term affecting the salt's energy balance and the temperature distribution inside the duct.

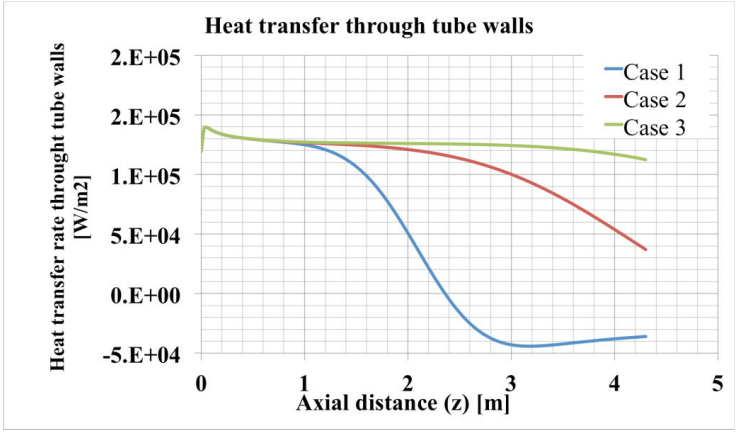

Fig.6: Heat transfer rate distribution along fuel housing tube axis.

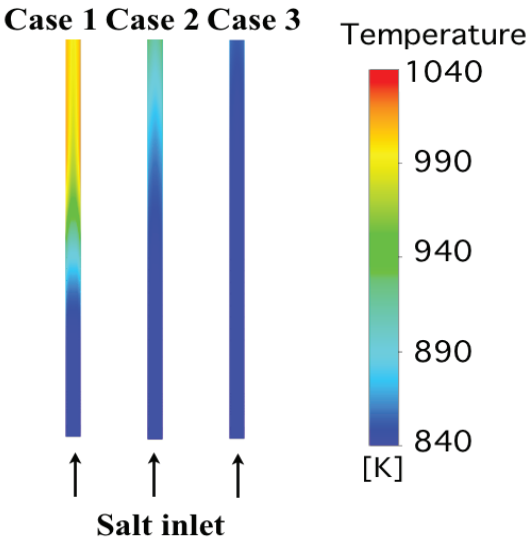

Fig.7: Temperature variation over a plane located at tube middle longitudinal section.

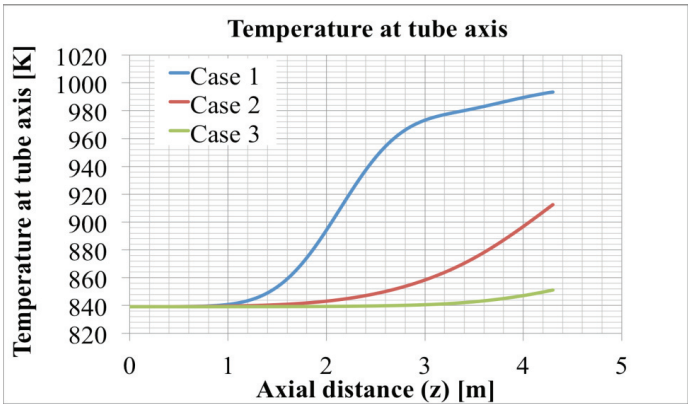

Fig.8: Temperature variation along tube axis.

3 Conclusions

The future of energy production should rely on nuclear fission since other sources do not provide comparably high density energy within the present known technology. Based on reactor experiences of the early 1970s, a 1000 MW(e) MSR using the thorium cycle is at reach. In spite of low development for several decades, the Th-MSRs are now being positively reexamined suggesting that energy independence following this technology is not only possible but affordable with low risk due to the inherently advantages of thorium as fuel. Several countries have initiated Research and Development with molten salt assembly and a project is already at its final design stage as it is the miniFUJI-MSR. This could be built in a relatively short time scale to produce: electricity, space heating and desalinate water. We suggest that the nuclear programs of developing or even emerging countries should include the possibility to follow the MSR technology for electric energy generation. The first step is training young professionals and promoting further technological solution still required by MSR. Preliminary studies recently initiated at the USB, are encouraging and we are setting up a sub-critical assembly first a small one to be enlarged up to 120x120x180 cm^3. To gain experience we have studied the heat transfer form fuel to moderator. The overall experience this induce us to continue promoting MSR with the aim to convince policy makers that the road to follow on short terms, is to accept the nuclear technology to satisfy future energy requirements.

Venezuela has an interesting potential in this way since we have important Thorium deposits and also experience with molten salt at industrial scale, specifically in the production of aluminum, and this experience can be transferred.

Acknowledgments

One of the authors (LS-B) acknowledge financial support from the Uni1versita di Padova, Instituto Nazionale di Fisica Nucleare dei Laboratori Nazionali di Legnaro, USB Research Dean and the Organizers of the Varenna – 2012 meeting.

References

[1] C. Renault, M. Hron, R. Konings and D.E. Holcomb., "The Molten Salt Reactor (MSR) – R&D Status and Perspectives in Europe",FISA 2009, Prague, June 22-24, 2009

[2] M.W. Rothental, P. N. Haubenreich and R. B. Briggs (1972). The Developmental Status of Molten-Salt Breeder Reactors, OR.NL-4812

[3] ORNL-5132, (1976). Molten-salt Reactor Program, Semiannual Progress report for Period ending February 29, 1976, 7-12;

[4] K. Furukawa, et al., (17 coauthors) A road map for the realization of Global scale Thorium Breeding Fuel Cycle by single Molten-Fluoride Flow. Energy Conversion & Manag. **49**, (2008) 1832-1845.

[5] C. W. Forsberg, C. Renault, C. LeBrun, and V. Ignatev, "Liquid Salt Applications and Molten Salt Reactors,"CD-ROM¨ , Paper 7596, Proc. 2007, International Congress on Advances in Nuclear Power Plants.

[6] G. Mazzini, E. Bomboni, N. Cerullo, E. Fridman, G. Lomonaco and E. Shwageraus. The Use of Th in HTR: State of the Art and Implementation in Th/Pu Fuel Cycles. Science and Technology of Nuclear Installations.(2009), ID 749736, 13 p., doi:10.1155/2009/749736

[7] *www.energychallenge.com/**rubbia**2.pdf*

[8] H. Bethe, (1979). "The fusion hybrid". Physics Today: 44-51. ISSN 0031-9228. Retrieved 16 May 2012).

[9] E. Gerstner, (2009). "Nuclear energy: The hybrid returns". Nature 460 (7251): 25–8. DOI:10.1038/460025a. PMID 19571861.

[10] Saveli M. Feinberg, "Discussion Comment", Rec. of Proc. Session B-10, ICPUAE, United Nations, Geneva, Switzerland 1958

[11] Venezuelan Government **Gaceta Oficial 39.558 del 23 de noviembre de 2010.** *Ley Aprobatoria del Acuerdo entre el Gobierno de la República Bolivariana de Venezuela y el Gobierno de la Federación de Rusia Sobre la Cooperación para el Desarrollo del Programa Nucleoeléctrico en la República Bolivariana de Venezuela, la Construcción y Operación de un Reactor de Investigación para la Producción de Radioisótopos de Usos Pacíficos en Medicina e Industria y de una Central Nucleoeléctrica en el Territorio de la República Bolivariana de Venezuela*.

[12] http://www.world-nuclear.org/info/inf45.html

[13] T. Yamamoto, K. Mitach, T. Suzuki. Steady State Analysis of Small Molten Salt Reactor. (Effect of Fuel Salt Flow on Reactor Characteristics) JSME Int´l J. B 48, 3, 2005

[14] F. Reisch, Reactor Kinetics Equations applied to the start-up phase of a Ringhals. 2006. http://www.euronuclear.org/e-news/e-news-14/pwr.htm

PHITS - Applications to Radiation Biology and Radiotherapy

L. Sihver[1], T. Sato[2], K. Niita[3], N. Matsuda[2], Y. Iwamoto[2], S. Hashimoto[2], H. Iwase[4], H. Nakashima[2], and S. Chiba[2,5]*
[1]Chalmers University of Technology, Sweden
[2]Japan Atomic Energy Agency, JAEA, Japan
[3]Research Organization for Information Science and Technology, RIST, Japan
[4]High Energy Accelerator Research Organization, KEK, Japan
[5]Tokyo Institute of Technology, Japan
[*] E-mail: sihver@chalmers.se, Phone: +46-31-772 2921

Abstract

PHITS is a 3-dimensional general-purpose Monte Carlo code, which can transport of all varieties of hadrons and heavy ions with energies up to around 100 GeV/nucleon. To be able to estimate the biological damage from neutrons with PHITS, a feature has been included to treat low energy neutron collisions as "events" which means that the energy and momentum is conserved in each event and makes it possible to extract the kinetic energy distributions of all the residual nuclei without using any local approximation. To estimate the direct biological effects of radiation, mathematical functions, for calculating the microdosmetric probability densities in macroscopic material, have been incorporated in PHITS. This makes it possible to instantaneously calculate the probability densities of lineal and specific energies around the trajectories of high energetic charged particle tracks. A method for estimating the biological dose has also been established by using the improved PHITS coupled to a microdosimetric kinetic model.

1 Introduction

The health risks associated with exposure to various components of radiation are of great concern in many different situations, e.g. when planning manned long-term interplanetary missions, such as future missions to Mars, during and after radiotherapy, and after nuclear accidents. Since it is not possible to measure the radiation environment inside of human organs, simulations based on radiation transport/interaction codes are used. When dealing with radiation risks, it is important to be able to predict deterministic as well as stochastic radiation effects. Deterministic effects are observed only at doses above a threshold and their severity increases with dose, while stochastic effects do not seem to have a threshold and their severity is not directly dependent on the dose. The estimation of biological effects is very complicated and has large uncertainties. Although knowledge of the dose is not sufficient for estimating the biological effects of radiation, it is still a basic important component when estimating the risks associated with exposure to ionizing radiation. Using quality factors based on LET spectra, absorbed doses are then converted into dose equivalents, which in turn are converted into risk using appropriate risk coefficients. However, when estimating the direct biological effects of radiation lineal and specific energies are better indexes in comparisons to LET, since LET does not take the energy dispersion due to the created delta electrons into consideration. This paper describes the 3-

dimensional general purpose particle and heavy-ion MC transport code PHITS (Particle and Heavy-Ion Transport code System), and some of it features related to radiation biology and radiotherapy.

2 PHITS (Particle and Heavy Ion Transport code System)

PHITS (Particle and Heavy-Ion Transport code System) [1] is a 3-dimensional general purpose particle and heavy-ion MC transport code, developed and maintained by RIST, JAEA and KEK in Japan together with Chalmers in Sweden, which can transport neutrons from thermal energies up to 200 GeV, and the same method as in the MCNP4C code [2] is employed for neutrons with energies between 1 meV and 20 MeV based on the Evaluated Nuclear Data such as the ENDF-B/VI [3], JENDL-3.3 [4,5]; and for p and n up to 3 GeV for the JENDL-HE [6,7] file. Above 20 MeV, the Bertini model with free p-p and n-n cross sections parameterized according to Niita et al. [8] is used up to 3 GeV, while the simulation model JAM (Jet AA Microscopic Transport Model) developed by Nara et al. [6] is used above 3 GeV for nucleons, above 2.5 GeV for pions, and for all energies for all other baryons. JAM is a hadronic cascade model, which explicitly treats all established hadronic states including resonances with explicit spin and isospin as well as their anti-particles. For protons and other hadrons, JAM is used above 1 MeV, but for charged particles below 1 MeV only the ionization process is considered until the particles are stopped. PHITS also uses Evaluated Nuclear Data for photon and electron transport below 1 GeV in the same manner as in the MCNP4C code based on the ITS code, version 3.0 [9]. The energy range of electrons and photons is restricted to the energy region 1 keV - 1 GeV at the present, but the extension of the maximum energy of these particles is in progress. PHITS can also transport nuclei in any solid, gas or liquid material. Below 10 MeV/n, only the ionization process for the nucleus transport is taken into account, but above 10 MeV/n the nucleus-nucleus collisions up to 100 GeV/n is described by the simulation model JQMD (JAERI Quantum Molecular Dynamics) developed by Niita et al. [10]. In the QMD model, the nucleus is described as a self-binding system of nucleons, which are interacting with each other through the effective interactions in the framework of molecular dynamics. One can estimate the yields of emitted light particles, fragments and excited residual nuclei resulting from the heavy ion collision. The QMD simulation, as well as the JAM simulation, describes the dynamical stage of the reactions. At the end of the dynamical stage, excited nuclei are created and must be forced to decay in a statistical way to get the final observed state. In PHITS the GEM model [11] (Generalized Evaporation Model) is default employed for light particle evaporation and fission process of the excited residual nucleus.

When simulating the transport of charged particles and heavy ions, the knowledge of the magnetic field is sometimes necessary to estimate beam loss, heat deposition in the magnet, and beam spread. This is also of importance when simulating the beam transport in accelerators, e.g. for proton and heavy ion therapy. PHITS can provide arbitrary magnetic fields in any region of the setup geometry. PHITS can simulate not only the trajectory of the charged particles in the field, but also the collisions and the ionization process at the same time. For the ionization process of the charged particles and nuclei, the SPAR code [12] is default used for the average stopping power dE/dx, the first order of Molière model for the angle straggling, and the Gaussian, Landau and Vavilov theories for the energy straggling around the average energy loss according to the charge density and velocity. In addition to the SPAR code, the ATIMA package, developed at GSI [13, 14], has been implemented as an alternative code for the ionization process.

The total reaction cross section, or the lifetime of the particle for decay, is an essential quantity in the determination of the mean free path of the transported particle. According to the mean free path, PHITS chooses the next collision point using the MC method. To generate the secondary particles of the collision, we need the information of the final states of the collision. It is therefore very important that reliable data of total non-elastic and elastic cross sections is used for the particle and heavy ion transport. In PHITS, the Evaluated Nuclear Data is used for neutron-induced reactions below 20 MeV. For neutron-induced reactions above 20 MeV a parameterization is used. As for the elastic cross

sections, the Evaluated Nuclear Data is also used for neutron-induced reactions below 20 MeV, and a parameterization is used above 20 MeV [8]. Parameterizations are also used for proton induced reactions for all energies, and for the double differential cross sections of elastic nucleon-nucleus reactions [8]. We have adopted the NASA systematics developed by Tripathi et al., [15-17] for the total nucleus-nucleus reaction cross section, as an alternative to the Shen formula [18], and a careful benchmarking of the mayor total reaction cross section models used in particle and heavy ion transport codes has been made [19-21]. PHITS has also been extensively used and benchmarked for many different applications, including different space applications e.g. [22-32].

2.1 Simulations of biological effects

When estimating the local biological effects of high energetic photons and charged particles, the contribution from the neutrons created both outside and inside the human must be considered. It is therefore important to be able to calculate the kinetic energy distributions of the created secondary charged particles from photonuclear and neutron induced reactions. For low energetic neutrons, nuclear data is normally used. However, based on the one-body Bolzman equation, energy and momentum is not conserved in an event during the transport calculations. They are only conserved as an average over many randomly calculated events since the Bolzman equation only include mean values of the one-body observables in the phase space and cannot give two-body and higher correlations. A feature has therefore been included in PHITS to treat low energy neutron collisions as "events" which means that the energy and momentum is conserved in each interaction and makes it possible to extract the kinetic energy distributions of the residual nuclei, two particle correlations, etc. In PHITS, the transport algorithm has been changed for the low-energy neutrons from that on solving Bolzmann equation to an algorithm based on an event generator. By using this event generator mode, energy and LET distributions for all charged particles, created by all charged particles and neutrons, can be calculated.

When estimating the direct biological effects of radiation, microdosimetric quantities, such as the lineal and specific energies, are better indexes for expressing the RBE of the primary and secondary particles in comparisons to the conventionally often used LET, since LET does not take the energy dispersion due to the created delta electrons into consideration. Though, the use of microdosimetric quantities in macroscopic transport codes is limited because of the difficulty in calculating the provability distributions on macroscopic matter. Therefore mathematical functions, for calculating the microdosmetric probability densities in macroscopic material, have been incorporated in PHITS. This makes it possible to instantaneously calculate the probability densities of lineal and specific energies around the trajectories of high energetic primary and secondary charged particle tracks. A method for estimating the biological dose, the product of physical dose and RBE of cell survival, for charged particles has also been established by using the improved PHITS coupled to a microdosimetric kinetic (MK) model [33, 34]. Fig 1. shows an example of calculated RBE_{10} for HSG cells in a slab phantom irradiated by several different heavy ion beams, together with experimental values from [35]. Since the energy distributions of the secondary charged particles from neutron induced reactions can be estimated by using the "event generator" in PHITS, an estimation of the RBE of the neutrons can also be made. The accuracy of this will be evaluated in the near future.

In addition to the direct effects, indirect effects due to radicals or reactive oxygen species (ROS), which are formed along the particle tracks, can further damage the DNA, and induce oxidative stress to the cells and therefore compromise the cellular functions. We have therefore developed a method to use experimentally deduced G-values to estimate the G-values as a function particle and energy in PHITS [36]. This model enables calculation of the radical distribution in an extended volume, e.g. inside an organ, taking into account nuclear interactions calculated with PHITS.

3 Summary and conclusions

When estimating the local biological damage of high energetic photons and charged particles, the contribution from the neutrons created both outside and inside the human must be included. This is also the case when estimating single and multiple event upsets of semi-conductor devices exposed to neutron radiation. In PHITS, an approach has therefore been developed to calculate the deposited energy distributions for the thermal neutron transport and the averaged quality factor for neutrons. This feature treat low energy neutron collisions as "events" which means that the energy and momentum is conserved in each event and makes it possible to extract the kinetic energy distributions of all the residual nuclei, two particle correlations, as well as calculate the dose equivalent based on Q(L) relationship, DNA damage, cell survival, etc. without using the local Kerma factor. In treatment planning of charged particle therapy, it is necessary to estimate not only the physical dose, but also the biological dose defined as the product of the physical dose and the RBE of cell killing, inside the patients. In PHITS, the former quantity can be calculated by macroscopic particle transport simulation, while the latter can be estimated by calculating the α and β parameters using PHITS coupled with a microdosimetric kinetic (MK) model. By doing so, the biological dose can be calculated both in the tumor cells and in the healthy tissue inside the patients. This makes PHITS a great tool for treatment planning of charged-particle therapy.

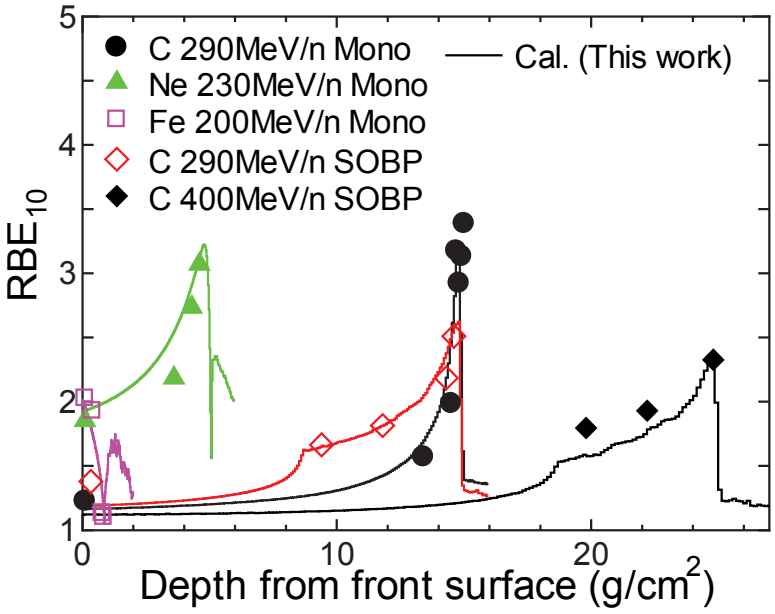

Fig 1. Shows an example of calculated RBE_{10} for HSG cells in a slab phantom irradiated by several different heavy ion beams together with experimental values are from [35].

References

[1] K. Niita, et al., PHITS: Particle and Heavy Ion Transport code System, Version 2.23, JAEA-Data/Code 2010-022 (2010).

[2] J. F. Briesmeister, et al., MCNP General Monte Carlo N-Particle Transport Code, Los Alamos National Laboratory report; LA-12625-M (1997).

[3] V. McLane, et al., ENDF/B-VI Summary Documentation, BNL-NCS-17541 (1996).

[4] K. Shibata, et al., Japanese Evaluated Nuclear Data Library Version 3 Revision-3: JENDLE-3.3, J. Nucl. Sci. Technol. 39, 1125 (2002).

[5] Watanabe, Y. et al. Nuclear data evaluations for JENDL high-energy file. Proceedings of International Conference on Nuclear Data for Science and Technology, Santa Fe, USA, Sep.26-Oct.1, 2004; AIP CP769, p326-331, 2005.

[6] Nara, Y. et al. Relativistic nuclear collisions at 10A GeV energies from p+Be to Au+Au with the hadronic cascade model. Phys. Rev. C61:024901, 1999.

[7] T. Fukahori, et al., JENDL High Energy File. J. Nucl. Sci. Technol., Suppl. 2, 25-30 (2002).

[8] K. Niita, H. Takada, S. Meigo, Y. Ikeda, High-energy particle transport code NMTC/JAM, Nucl. Instrum. Methods, B184, 406 (2001).

[9] J. A. Halbleib, et al., ITS Version 3.0: The Integrated TIGER Series of Coupled Electron/Photon Monte Carlo Transport Codes, SAND91-1634 (1992).

[10] K. Niita, et al., Analysis of the (N,xN') reactions by quantum molecular dynamics plus statistical decay model, Phys. Rev. C52, 2620 (1995).

[11] S. Furihata, Statistical analysis of light fragment production from medium energy proton-induced reactions, Nucl. Instr. and Meth. B171, 251 (2000).

[12] T. W. Armstrong, and K. C. Chandler, A Fortran program for computing stopping powers and ranges for muons, charged pions, protons, and heavy ions, ORNL-4869, Oak Ridge National Laboratory, (1973).

[13] H. Geissel, C. Scheidenberger, Slowing down of relativistic heavy ions and new applications, Nucl. Instr. Meth. B136-138, 114-124 (1998).

[14] C. Scheidenberger, H. Geissel, Penetration of relativistic heavy ions through matter, Nucl. Instr. Meth. B136-138, 114-124 (1998).

[15] R. K. Tripathi, F. A. Cucinotta, J. W. Wilson, Accurate universal parameterization of absorption cross sections, Nucl. Instr. and Meth. B117, 347 (1996).

[16] R. K. Tripathi, J. W. Wilson F. A. Cucinotta, Accurate universal parameterization of absorption cross sections II – neutron absorption cross sections, Nucl. Instr. and Meth. B129, 11 (1997).

[17] R. K. Tripathi, F. A. Cucinotta, J. W. Wilson, Accurate universal parameterization of absorption cross sections III – light systems, Nucl. Instr. and Meth. B155, 349 (1999).

[18] W. Shen, et al., Total reaction cross section for heavy-ion collisions and its relation to the neutron excess degree of freedom, Nucl. Phys. A 491 (1) 130-146 (1989).

[19] L. Sihver, et al., A Comparison of Total Reaction Cross Section Models Used in Particle and Heavy Ion Transport Codes, IEEEAC paper 1476, ISBN/ISSN: 978-142443888-4 (2010).

[20] L. Sihver, et al., A comparison of total reaction cross section models used in particle and heavy ion transport codes, Adv. Space Res. 49, 812-819 (2011), doi:10.1016/j.asr.2011.11.029.

[21] L. Sihver, et al., A comparison of total reaction cross section models used in FLUKA and PHITS, IEEEAC papper. (in press).

[22] T. Sato, et al., Applicability of particle and heavy ion transport code PHITS to the shielding design of spacecrafts, Rad. Meas. 41, 1142-1146 (2006).

[23] L. Sihver, et al., Benchmarking of calculated projectile fragmentation cross sections using the 3-D, MC codes PHITS, FLUKA, HETC-HEDS, and MCNPX", Acta Astronautica 63, 865-877 (2008).

[24] T. Sato, L. Sihver, K. Gustafsson, D. Mancusi and K. Niita, Shielding Design of Spacecrafts Using PHITS, American Nuclear Society Transactions, 99, 592 (2008).

[25] L. Sihver, T. Sato, K. Gustafsson, V.A. Shurshakov, and G. Reitz, Simulations of the MTR-R and MTR Experiments at ISS, and Shielding Properties Using PHITS, IEEEAC paper 1015 (2009).

[26] L. Sihver, et al., An update about recent developments of the PHITS code, Adv. Space Res. 45, 892-899 (2010).

[27] L. Sihver, T. Sato, M. Puchalska, and G. Reitz, Simulations of the MATROSHKA experiment at the International Space Station using PHITS, Radiat. Environ. Biophys. 49:351-357 (2010).

[28] K. Gustafsson, L. Sihver, D. Mancusi, T. Sato, PHITS simulations of the Matroshka experiment", Adv. Space Res.46, 1266–1272 (2010).

[29] L. Sihver, et al., Monte Carlo simulations of MATROSHKA experiment outside ISS, IEEEAC paper 1585, ISSN: 978-142447350-2 (2011).

[30] T. Sato, et al., "Evaluation of Dose Rate Reduction in a Spacecraft Compartment due to Additional Water Shield", ISSN 0010_9525, Cosmic Research, Vol. 49, No. 4, pp. 319–324. © Pleiades Publishing Ltd. (2011).

[31] L. Sihver et al., Simulations of absorbed dose on the phantom surface of MATROSHKA-R experiment at the ISS, Adv. Space Res. 49, 230-236 (2011).

[32] M. Puchalska, L. Sihver, T. Sato, T. Berger, and G. Reitz, Simulations of MATROSHKA experiments at ISS using PHITS, Adv. Space Res. (accepted).

[33] T. Sato, et al., Biological Dose Estimation for Charged-Particle Therapy Using an Improved PHITS Code Coupled with a Microdosimetric Kinetic Model", Rad. Res. 171, 107-117 (2009).

[34] T. Sato et al., Analysis of Cell-Survival Fractions for Heavy-Ion Irradiations Based on Microdosimetric kinetic Model Implemented in the Particle and Heavy Ion Transport code System, Rad. Prot. Dos., 1-6, 2010.

[35] Y. Kase et al., Microdosimetric measurements and estimation of human cell survival for heavy-ion beams. Radiat. Res. 166, 629-638 (2006).

[36] T. Maeyama et al., Production of a Fluorescence Probe in Ion-beam Radiolysis of Aqueous Coumarin-3-carboxylic Acid Solution 2: Effects of nuclear fragmentation and its simulation with PHITS, Rad. Phys. Chem. 80, 1352-1357 (2011).

Nuclear Astrophysics at n_TOF, CERN

G Tagliente[1], U Abbondanno[2], G Aerts[3], H Alvarez[4], F Alvarez-Velarde[5], S Andriamonje[3], J Andrzejewski[6], L Audouin[8], G Badurek[9], P Baumann[10], F Bečvář[11], F Belloni[2], E Berthoumieux[3], S Bisterzo[12], F Calviño[13], M Calviani[14], D Cano-Ott[5], R Capote[15,16], C Carrapiço[17], P Cennini[18], V Chepel[19], E Chiaveri[18], N Colonna[1], G Cortes[13], A Couture[20], J Cox[20], M Dahlfors[18], S David[10], I Dillman[8], C Domingo-Pardo[21], W Dridi[3], I Duran[4], C Eleftheriadis[22], M Embid-Segura[5], A Ferrari[18], R Ferreira-Marques[19], K Fujii[2], W Furman[24], R Gallino[12], I Goncalves[19], E Gonzalez-Romero[5], F Gramegna[14], C Guerrero[5], F Gunsing[3], B Haas[25], R Haight[26], M Heil[8], A Herrera-Martinez[18], M Igashira[27], E Jericha[9], F Käppeler[8], Y Kadi[18], D Karadimos[7], D Karamanis[7], M Kerveno[10], P Koehler[28], E Kossionides[29], M Krtička[11], H Leeb[9], A Lindote[19], I Lopes[19], M Lozano[16], S Lukic[10], J Marganiec[6], S Marrone[1], T Martinez[5], C Massimi[30], P Mastinu[14], A Mengoni[15], P M Milazzo[2], M Mosconi[8], F Neves[19], H Oberhummer[9], J Pancin[3], C Papachristodoulou[7], C Papadopoulos[31], C Paradela[4], N Patronis[7], A Pavlik[32], P Pavlopoulos[33], L Perrot[3], M T Pigni[9], R Plag[8], A Plompen[34], A Plukis[3], A Poch[13], J Praena[14], C Pretel[13], J Quesada[16], T Rauscher[35], R Reifarth[26], C Rubbia[36], G Rudolf[10], P Rullhusen[34], J Salgado[17], C Santos[17], L Sarchiapone[18], I Savvidis[22], C Stephan[23], J L Tain[21], L Tassan-Got[23], L Tavora[17], R Terlizzi[1], G Vannini[30], P Vaz[17], A Ventura[37], D Villamarin[5], M C Vincente[5], V Vlachoudis[18], R Vlastou[31], F Voss[8], S Walter[8], H Wendler[18], M Wiescher[20] and K Wisshak[8]

[1] INFN, Bari, Italy; [2]INFN, Trieste, Italy; [3]CEA/Irfu, Gif-sur-Yvette, France; [4]Univ. Santiago de Compostela, Spain; [5]CIEMAT, Madrid, Spain; [6]Univ. Lodz, Poland; [7]Univ. Ioannina, Greece; [8]FZK, Institut fűr Kernphysik, Germany; [9]Technische Universität Wien, Austria; [10]CNRS/IN2P3 - IReS, Strasbourg, France; [11]Univ. Prague, Czech Republic; [12]Dip. Fisica Generale, Univ. Torino, Italy; [13]Univ. Politecnica Catalunya, Barcelona, Spain; [14]INFN, Laboratori Nazionali di Legnaro, Italy; [15]IAEA, Vienna, Austria; [16]Univ. Sevilla, Spain; [17]ITN, Lisbon, Portugal; [18]CERN, Geneva, Switzerland; [19]LIP - Coimbra & Dep. Fisica Univ. Coimbra, Portugal; [20]Univ. Notre Dame, USA; [21]Inst. Fisica Corpuscular, CSIC-Univ. Valencia, Spain; [22]Aristotle Univ. Thessaloniki, Greece; [23]CNR S/IN2P3 - IPN, Orsay, France; [24]JINR, Frank Lab. Neutron Physics, Dubna, Russia; [25]CNRS/IN2P3 - IPN, Orsay, France; [26]LANL, USA; [27]Tokyo Inst. Technology, Japan; [28]ORNL, Physics Division, USA; [29]NCSR, Athens, Greece; [30]Dip. Fisica, Univ. Bologna, & INFN, Bologna, Italy; [31]National Technical Univ. Athens, Greece; [32]Inst. fűr Fakultät fűr Physik, Univ. Wien, Austria; [33]Pôle Univ. L. de Vinci, Paris, France; [34]CEC-JRC-IRMM, Geel, Belgium; [35]Dep. Physics and Astronomy, Univ. Basel, Switzerland; [36]Univ. Pavia,Italy; [37]ENEA, Bologna, Italy. The n_TOF Collaboration

Abstract

The neutron time of flight (n_TOF) facility at CERN is a spallation neutron source with white neutron energy spectrum (from thermal to several GeV), covering the full energy range of interest for nuclear astrophysics, in particular for measurements of the neutron capture cross section required in s-process nucleosynthesis. This contribution presents an overview on the astrophysical program carried on at the n_TOF facility, the main results and their implications.

1 Stellar nucleosyntesis

The origin of the elements is an important topic to understand the evolution of the universe. Hydrogen and helium, and small amounts of lithium, were formed in the period between about 100 seconds and 20 minutes after the big bang [1]. This period of primordial nucleosynthesis was followed by galactic condensation and the formations of the stars. All elements heavier than lithium have been formed in

stars, and the elements heavier than iron have been formed via neutron capture processes in the stars. The isotopic abundances in the solar system reflect the average composition of the galaxy as it was 5.5 x 10^9 years ago. Spectral information of stellar environments and isotopic analyses of presolar dust grains provide important observation to validate stellar evolution models.

1.1 The s-process

Stellar nucleosynthesis has first been extensively reviewed in the reference work [2] and more recently in [3][4]. The isotopes up to ^{56}Fe can be synthesized by fusion reactions during the different stages of the evolution of a star. It is nowadays well established that neutron capture processes in red giant stars and supernovae are responsible for the formation of nearly all isotopes with higher masses [1][5]. This was first recognized by the discovery of technetium in red giant [6].

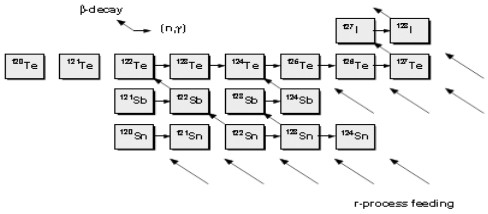

Fig.1 s-process path in the Sn region with s-only and r-only isotopes

The neutron capture mechanisms are known as s- and r-processes, where "s" stands for slow and "r" for rapid referring to the time scale of the β-decay. The s- and r- processes are important for the stable and neutron rich isotopes. A thorough knowledge of the s-process, for which much more experimental data is available, constrains the possibilities of the r-process. A competing mechanism is the p-process, referring to photodisintegration reaction like (γ,n), (γ,p) and (γ,α), they influence the abundances from the proton rich side.

isotopes from ^{56}Fe to ^{209}Bi are formed. Heavier nuclei than Bi are unstable and cannot be formed by neutron capture anymore. The s-process path follows closely the valley of stability in the chart of the nuclei and ends at ^{209}Bi. The neutron source of the s-process are manly the ^{22}Ne(α,n)^{25}Mg and ^{13}C(α,n)^{16}O reactions

In the r-process the neutron capture process is much faster and occurs on much shorter time scales. The time between consecutive neutron captures is of the order of seconds. To achieve the according extremely high neutron fluxes, the astrophysical site for the r-process is believed to be of explosive nature, like in a supernova or in merging neutron stars.

Neutron capture cross section are a key ingredient in the development of stellar models using the calculation of nuclear abundances in stellar environments. At the branching points uncertainties in the cross sections can propagate into large differences in the production of higher mass nuclei within a given model.

In a very schematic quantitative description of the s-process, starting from the seed nucleus ^{56}Fe and assuming constant temperature and neutron density, for a s-only nucleus the product of the average capture cross section $\langle\sigma_\gamma\rangle_{kT,A}$ and the abundance of the isotope $N_{s,A}$ constant

$$\langle\sigma_\gamma\rangle_{kT,A}\, N_{s,A} = \text{constant} \qquad (1)$$

Indeed this is roughly the case, except for the nuclei with magic numbers (N = 28,50,82,126) around A = 88, 140, and 208, which have very low cross sections. These nuclei are bottlenecks in the s-process paths, and show up as abundance peaks. The s-only nuclei are shielded from r-process by stable isobars of nuclei with lower Z and which contributions from proton rich side of the valley of stability are commonly neglected. In the same way r-only nuclei have no contribution from the s-process.

In fig 1 a simplified part of the s-process is shown in the Z = 50 vicinity starting from ^{120}Sn. Some stable nuclides, like ^{124}Sn and ^{130}Te are not reached by the s-process put but are shielded from r-process by the nuclei ^{122}Sb, ^{123}Sb and ^{124}Sb. These are s-only isotopes. The about 30 s- and about 40 r-only isotopes provide a means to distinguish between the two processes.

2 The n_TOF facility

The n_TOF facility, based on an idea by Rubbia at al. [7], locate at CERN Geneva Switzerland became fully operational in May 2002, when the scientific program has started. A detailed description can be found in ref [8]. Neutrons are produced by spallation reaction induced by a pulsed, 6 ns wide, 20 GeV/c proton beam with up to $7x10^{12}$ proton per pulse, impinging on a 80x80x60 cm^3 lead target. A 5.8 cm water slab surrounds the lead target acting as a coolant and as moderator of the initial fast neutron spectrum. An isolethargic neutron flux distribution is produced over a wide range of energy (1 eV – 250 MeV).

Neutrons emerging from the target propagate in the vacuum pipe inside the time-of-flight tunnel 200 m long. Two collimators are present along the flight path, one of the diameter of 13,5 cm placed at 135 m from the lead target and one at 180 m with a diameter of 2 cm for the capture measurements. This collimation results in a Gaussian-shaped beam profile [9]. A 1.5 T sweeping magnet placed at 40 m upstream of the experimental area is used to deflect outside the beam charged particles travelling along the vacuum pipe. For an efficient background suppression, several concrete and iron walls are placed along the time-of-flight tunnel.

The measuring station is located inside the tunnel, centered at 187.5 m from the spallation target.

The neutron beam is monitored up to 1 MeV by a low-mass system, based on thin mylar foil with ^{6}Li deposit places in the beam, surrounded by an array of silicon detectors place outside the beam. The detection by the silicon detectors of the triton and α s produced in the ^{6}Li(n,α) reaction gives a direct measure of the neutron flux. The small amount of material in the beam ensures a negligible level of scattered neutrons. The scattering chamber is made in carbon fibre to minimize the neutron-induced γ background.

Measurements of neutron capture cross-sections in the first stage of the project were performed with specifically made C_6D_6 detectors, and in the second stage of the measurements a 4π calorimeter made of 40 BaF_2 crystal has been used.

The data acquisition system is based on flash ADCs with sampling rate up to 1 GHz for recording the detector signals during nearly 20 ms off-line analysis. This generate a high data rate but ensures an almost zero dead-time.

In the first phase of the n_TOF project, neutron capture measurements were carried with an array of C_6D_6 liquid scintillator cells. These detectors have the advantage of being the less sensitive to scattered neutron. Specifically designed C_6D_6 where used at n_TOF, in order to reduce the neutron sensitivity all the material that could produce a neutron capture in the detector were removed or substituted, all the aluminum part were substituted with carbon fibre [10] and also the support material was minimized, allowing to perform measurement of isotopes with a large scattering to capture ratio.

Due to the small solid angle coverage and the low intrinsic efficiency the C_6D_6 detectors, which result in an overall efficiency of ~10%, only one γ-ray per event is detected from the de-excitation cascade following neutron capture. For an accurate cross-section determination, the efficiency of the set-up has to be made independent on the details of the de-excitation cascade, in particular of the γ-ray multiplicity.

To this end the pulse height weighting function (PHWF) has been used. It consists in suitably modifying by software the detectors response so that the efficiency ε_γ is proportional to the photon energy E_γ. Under these conditions the efficiency for detecting a cascade becomes proportional to the known cascade energy Ec and independent of the actual cascade path.

In the second phase of n_TOF project the neutron capture measurements have been performed with Total Absorption Calorimeter (TAC). The design of the n_TOF TAC is based o 42-fold segmentation consisting of 15 cm thick BaF_2 crystal in the form of truncated pyramids. Each of the 12 pentagonal and 30 hexagonal crystals extends the same solid angle with respect to the sample centre.

On average the crystals exhibit an average energy resolution of 14% at 662 keV and an excellent time resolution of about 500 ps.

Due to the low cross-section of most the samples of Astrophysics interest measured at n_TOF, the C_6D_6 were preferred for these measurements since the background due to the in-beam γ for those detectors is lower.

3 Experimental campaign

The Astrophysics experimental campaign was focus on neutron magic nuclei, which act as bottle neck for the flow of s-process, nuclei with A < 120, branching points isotopes and isotopes of special interest as the Os important for nuclear cosmochronology.

In the following the description and results of the measurements.

3.1 ^{151}Sm(n,γ) cross section measurements

The ^{151}Sm is a branching point in the s-process path, in particular, this branching is sensitive to the temperature at which the s-process is taking place. The accurate determination of the neutron capture cross-section of this isotope can thus provide crucial information on the thermodynamics condition of the AGB stars.

The measurement had been performed with the C_6D_6 liquid scintillator. The result obtained at n_TOF is $\langle\sigma(n,\gamma)\rangle$ = 3100±160 mb, a value much larger than previous estimated, all based on model calculation, which ranged from 1500 and 2800 mb [11].

The firm estimate of the capture rate for the first time base on experimental value allowed reaching two important conclusions with respect to the s-process nucleosynthesis in this mass region: i) the classical model, based on the phenomenological study of the s-process fails to produce consistent result of the branching at ^{151}Sm and ^{147}Pm, ii) the p-process contribution to the production of ^{152}Gd can amount up 30% of the solar-system observed abundance [11]

3.2 ^{90,01,92,93,94,96}Zr(n,γ) measurements

Zr is a typical s-process element belonging to the first s-process peak of solar abundance distribution. Predictions of the production of the various Zr isotopes are critical for s-process modelling. Several of

them are close to the magic number of neutron N =50, with ^{90}Zr having exactly N=50. Hence, production of ^{90,91,92,93,94}Zr is sensitive to the overall neutron flux, which is mostly defined by the ^{13}C neutron source. The abundance of the remaining stable isotope, ^{96}Zr, is determined by the activation of the branching point at the unstable ^{95}Zr. Hence, its production is sensitive to the neutron density, which is mostly defined by the ^{22}Ne neutron source. Furthermore, most of the abundance of the element Nb is due to the radiogenic decay of the long living ^{93}Zr (1.6 My).

The capture cross sections of the ^{91,92,93,94,96}Zr in term of resonance parameter were measured in a wide neutron energy range. The results [12,13,14,15,16] show sizeable differences with respect to previous experimental data and allow extracting the related nuclear quantities with improved accuracy.

3.3 ^{204,206,207}Pb and ^{209}Bi(n,γ) measurements

The Pb isotopes and the ^{209}Bi have a special role in the nucleosynthesis, these isotopes represent the termination point of s-process nucleosynthesis, this point is reached since the α-recycling of Po and heavier Bi isotopes is always faster than further neutron captures. It is important to know the cross section information for the Pb and Bi isotopes with very high accuracy in order to determine more exactly the amounts and ratios of these isotopes being produced.

Capture widths and radioactive kernels were determinate in a large range of energy for all isotopes. From these results the MACS have been derived and in many cases large discrepancy were found with values of the previous experiment, in figure 2 is reported the comparison between the ^{204}Pb MACS calculated with n_TOF and the values reported by Bao [17],

For all isotopes the systematic uncertainties could be improved by a factor two, this allowed to have a firm calculation of the abundances of the s-process component and to constrain the estimation of the r-process component, the results are reported in [18][19][20][21].

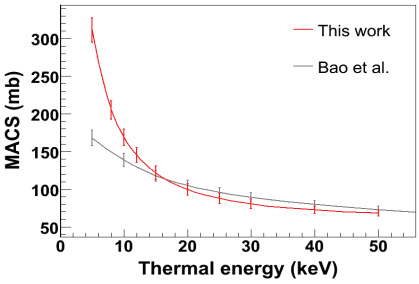

Fig. 2 Comparison between the ^{204}Pb MACS calculated with n_TOF data and Bao et al.

3.4 ^{186,187,188}Os measurements

The time duration of the nucleosynthesis of the heavy elements produced by neutron capture processes can be used to set limits on the age of the universe [22]. Among several cosmic clock based on the abundances of long-lived radioactive isotopes, the ^{187}Os/^{187}Re is one of the most interesting.

The clock is based on the extremely long half-life of ^{187}Re($\tau_{1/2}$ = 43.3Gyr), decaying to ^{187}Os, and on the fact that ^{186}Os and ^{187}Os are shielded against direct r-process production. Thanks to the well

established s-process abundances of the ^{186}Os and ^{187}Os, the age of the Universe can be inferred, in the the Re/Os clock, by the enhancement in the abundance of ^{187}Os due to ^{187}Re $\rightarrow$ ^{187}Os decay.

The neutron capture cross sections of ^{186,187,188}Os have been measured at the CERN n_TOF facility with improved accuracy and over a wide energy range of neutron energies from 1 eV to 1 MeV. In Fig. 3 a comparison between the n_TOF result and the previous data is shown. Based on the n_TOF data, Maxwellian averaged cross sections have been obtained with uncertainties between 3 and 4%. These results have been complemented by a detailed resonance analysis. Average level spacing, radiative widths, and neutron strength functions have been deduced by statistical analysis to establish a consistent set of input data for detailed cross section calculations with the Hauser-Feshbach statistical model. Based on these calculations stellar enhancement factors were obtained to correct the Maxwellian averaged cross sections determined from experimental (n,γ) data for the effect of thermally excited states in the hot, dense photon bath at the *s*-process site. The corresponding stellar (n,γ) cross sections have been used to separate the radiogenic part of the ^{187}Os abundance from its *s*-process component and to define the mother/daughter ratio ^{187}Re/^{187}Os. With a schematic model that assumes an exponentially decreasing production rate for ^{187}Re, an age of the Universe of 15.3+-0.8+-2 Gyr was obtained from the Re/Os cosmo-cronometer, with an accuracy, mostly related to the remaining nuclear physics uncertainties, of less than 1 Gyr. More details can be found in [23,24,25]

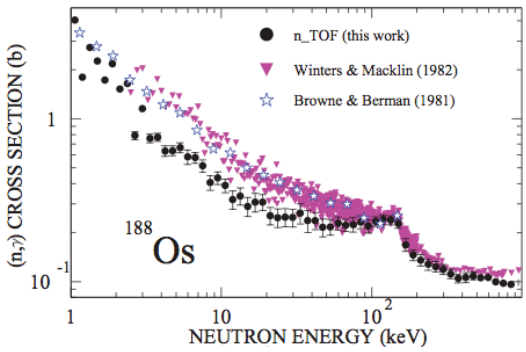

Fig. 3 Comparison between the present results and the previous data [24]

4 Conclusion

Neutron capture cross sections of astrophysical interest have been measured at the CERN n_TOF facility. The major motivation of these measurements was to reduce the uncertainties on nuclear data to a few percent, as required to improve the stellar s-process model.

In 2010 the facility was upgraded, the spallation target and moderator were substitued, the upgrade improved the n_TOF apparatus resulting in a significantly reduction of the uncertainty in the measured cross-sections, with a valuable impact on studies of s-process nucleosynthesis. New measurements on neutron-magic nuclei and, especially, on branching-point radioactive isotopes, have been done at n_TOF, called n_TOF phase II, while a much higher neutron flux in a second experimental area at 20 m from the spallation target should be available in 2014. The new experimental area will open the way to measurements of relatively short-lived isotopes, produced at ISOLDE, involved in r-process nucleosynthesis.

References

[1] R. A. Alpher, H. A. Bethe, G. Gamow, Phys. Rev. 73 (1948) 803.

[2] E. M. Burbidge, G. R. Burbidge, W. A. Fowler, F. Hoyle, Synthesis of the elements in stars, Rev. Mod. Phys. 29, (1957) 547.

[3] G. Wallerstein, et al., Synthesis of the elements in stars: forty years of progress, Rev. Mod. Phys. 62(1999)395.

[4] M. Arnould, K. Takahash, Nuclear astrophysics, Rep. Prog. Phys. 62(1999)395.

[5] A. G. W. Cameron, Pub. Astr. Soc. Pacific 69 (1957) 201.

[6] P.W. Merrill, Science 115(1952)484.

[7] C. Rubbia et al., Tech. Rep. CERN/LHC/98-02 CERN(1998)

[8] U. Abbondanno et al., Tech. Rep. CERN/SL/2002-053 ECT(2003)

[9] S. J. Pancin et al., Nucl. Instr. Meth. A 524 (2004)102.

[10] R. Plag et al., Nucl. Instr. Meth. A 496 (2003)425.

[11] *U. Abbondanno et al.,* Phys. Rev. Letters 93 (2004)161103.

[12] G. Tagliente et al., Phys. Rev. C 77 (2008) 035802.

[13] G. Tagliente et al., Phys. Rev. C 78 (2008) 045804.

[14] G. Tagliente et al., Phys. Rev. C 81 (2010) 055801.

[15] G. Tagliente et al., Phys. Rev. C 84(2011) 015801

[16] G. Tagliente et al., Phys. Rev. C 84(2011) 055802

[17] Z.Y. Bao et al., At. Data Nucl. Data Tables 76 (2000).

[18] C. Domingo-Pardo et al., Phys Rev. C75 (2007) 15806.

[19] C. Domingo-Pardo et al., Phys Rev. C74 (2006) 55802.

[20] C. Domingo-Pardo et al., Phys Rev. C74 (2006) 25807.

[21] C. Domingo-Pardo et al., Phys Rev. C76 (2007) 45805.

[22] D. D. Clayton et al., *Cosmoradiogenic chronologies of nucleosynthesis* // Ap. J. – 1964 – Vol. 139. – P. 637.

[23] M. Mosconi et al., Neutron physics of the Re/Os clock. I. Measurement of the (n,γ) cross sections of ^{186,187,188}Os at the CERN n TOF facility// Phys. Rev. C 82 (2010) 015802.

[24] M. Mosconi et al., Neutron physics of the Re/Os clock. II. The (n,n') cross section of 187Os at 30 keV neutron energy // Phys. Rev. C 82 (2010) 015803.

[25] K. Fujii et al., Neutron physics of the Re/Os clock. III. Resonance analyses and stellar (n,γ) cross sections of ^{186,187,188}Os // Phys. Rev. C 82 (2010) 015804.

Construction of deformed neutron stars steming from DBHF

E. Běták[1,2]*, M. Urbanec*[2] *and Z. Stuchlík*[2]
[1] Institute of Physics, Slovak Academy of Sciences, 84511 Bratislava, Slovakia
[2] Faculty of Philosophy and Sciences, Silesian University, 74601 Opava, Czech Rep.

Abstract
Using the parameterized approximation to the DBHF equations of state of relativistic nuclear matter, we obtained the macroscopic description of neutron stars based on different equations of state and also with allowing for hyperonic degrees of freedom. We put our main attention to posibilities of nonspherical shapes of the stars, like the moment of inertia, deformation etc., and what is the influence of the equations of state in this aspect.

1 Introduction

Neutron stars are one of bridges between micro- and macro-cosmos, specifically, they relate macroscopic quantities of the stars, like radius, mass, pressure, deformation, etc. with the equation of state (EoS) of asymmetric nuclear matter with allowance for hyperons. A wide variety of EoSs and their applications to astrophysical problems has been reported in the literature (see, e.g., [1–5]).

Our calculations use the Dirac-Brueckner-Hartree-Fock (DBHF) mean field approach [1,6] in its parameterized form [7] which effectively approximates full nuclear matter calculations [8–10].

Frequently reported and/or calculated quantities of neutron stars are their mass M and radius R, but sometimes also quantities like the radiation radius R_∞, ratio of baryon to gravitational mass and others [2,5,11–33] are considered.

Mass of a neutron star can be deduced from different kinds of observations (see, e.g., [2,19], and also the relevant discussion in [27]). Unfortunately, extracting mass from the observations is usually strongly dependent on the assumptions used. Thus, till recently, the maximal one, related to the source, was usually quoted to be $M = (2.1 \pm 0.2)M_\odot$ (see the review [2]), but it has been consequently lowered to $M = (1.26 \pm 0.14)M_\odot$ [23]. Recent measurement of PSR J1614-2230 using Shapiro delay effect yielded $M = (1.97 \pm 0.04)M_\odot$ [25], and it can be probably considered as the heaviest neutron star reliably found. Other tests use the ratio of mass to baryon number [18], the mass-radius relation [5,11, 12,17,22,26,28] and the moments of inertia [2,13,15,24].

As the precise measurements of neutron star radii R are not reported, these are usually estimated from observations of thermal emission, which give the so-called radiation (or Eddington) radius R_∞ that is related to R (e.g. [2])

$$R_\infty = R/\sqrt{1 - 2GM/Rc^2}; \tag{1}$$

obviously, $R < R_\infty$. Whereas the papers (depending on the analysis model) published just few years ago preferred radii close to 14 km and extending up to 15 km or even 20.9 km; the recent studies favored the radii to tend to lower values, typically $R \approx (9 - 12)$ km, even though their apparent radius R_∞ may still be above 20 km [5].

2 Equations of state of neutron star matter

We follow the DBHF mean field approach (see e.g. [1,6,20]), which allows to consider various compositions of the neutron star matter, and also some inclusion of non-nucleonic degrees of freedom.

The model Lagrangian includes the nucleon ψ, isoscalar scalar meson σ, isoscalar vector meson $\boldsymbol{\omega}$, isovector vector meson $\boldsymbol{\rho}$, and isovector scalar meson δ fields, vector cross-interaction, and also Λ^0

and Σ^- hyperonic degrees of freedom. Lagrangian density is [7]

$$\begin{aligned}
\mathcal{L}(\psi_{\mathrm{p},n},\sigma,\boldsymbol{\omega},\boldsymbol{\rho},\delta) &= \bar{\psi}[\gamma_\mu(i\partial^\mu - g_\omega\boldsymbol{\omega}^\mu) - (m_\mathrm{N} - g_\sigma\sigma)]\psi \\
&+ \frac{1}{2}(\partial_\mu\sigma\partial^\mu\sigma - {m_\sigma}^2\sigma^2) - \frac{1}{4}\boldsymbol{\omega}_{\mu\nu}\boldsymbol{\omega}^{\mu\nu} + \frac{1}{2}{m_\omega}^2\boldsymbol{\omega}_\mu\boldsymbol{\omega}^\mu \\
&- \frac{1}{3}b_\sigma m_\mathrm{N}(g_\sigma\sigma)^3 - \frac{1}{4}c_\sigma(g_\sigma\sigma)^4 + \frac{1}{4}c_\omega({g_\omega}^2\boldsymbol{\omega}_\mu\boldsymbol{\omega}^\mu)^2 \\
&+ \frac{1}{2}(\partial_\mu\delta\partial^\mu\delta - {m_\delta}^2\delta^2) + \frac{1}{2}{m_\rho}^2\boldsymbol{\rho}_\mu\boldsymbol{\rho}^\mu - \frac{1}{4}\boldsymbol{\rho}_{\mu\nu}\boldsymbol{\rho}^{\mu\nu} \\
&+ \frac{1}{2}\Lambda_V({g_\rho}^2\boldsymbol{\rho}_\mu\boldsymbol{\rho}^\mu)({g_\omega}^2\boldsymbol{\omega}_\mu\boldsymbol{\omega}^\mu) - g_\rho\boldsymbol{\rho}_\mu\bar{\psi}\gamma^\mu\tau\psi + g_\delta\delta\bar{\psi}\tau\psi \\
&+ \Sigma_Y\bar{\psi}_Y[\gamma_\mu(i\partial^\mu - g_{\omega Y}\boldsymbol{\omega}^\mu - g_{\rho Y}\boldsymbol{\rho}_\mu\bar{\psi}\gamma^\mu\tau - g_{\phi Y}\phi^\mu) \\
&- (M - g_{\sigma Y}\sigma - g_{\delta Y}\delta\bar{\psi}\tau\psi - g_{\sigma^* Y}\sigma^*)]\psi_Y \\
&+ \frac{1}{2}(\partial_\mu\sigma^*\partial^\mu\sigma^* - {m_{\sigma^*}}^2\sigma^{*2}) + \frac{1}{2}{m_\phi}^2\phi_\mu\phi^\mu \\
&- \frac{1}{4}\phi_{\mu\nu}\phi^{\mu\nu} + \Sigma_{\mathrm{e},\mu}\bar{\psi}_{\mathrm{e},\mu}(i\gamma_\mu\partial^\mu - m_{\mathrm{e},\mu})\psi_{\mathrm{e},\mu}. \qquad (2)
\end{aligned}$$

The full mean-field DBHF calculations of nuclear matter [8–10] were parameterized [7]. We choose two (in some cases three) parameterizations, which were shown to yield the best fits to the well-known properties of nuclear matter, namely: the best RMF fit to results of Huber *et al*. [9], denoted Hu in figures, Lee *et al*. [10] (marked Le), and finally the results of [8] (labelled as Ma), respectively, in all cases to the parameter set denoted in their papers as the A set. For details as well as for the values of coupling constants for the individual sets of parameterization, we refer to the original paper [7].

3 Energy and pressure radial dependence

The matter in neutron stars is in β-equilibrium, which determines the particle fractions at each density.

The nuclear EoS is the dominant input for the calculations in the high-density region, namely $\rho \geq 10^{14}$ g/cm^3. For lower densities, the EoS Feynman-Metropolis-Teller [35], for 7.9 g/cm^3 $\leq \rho \leq$ 10^4 g/cm^3 where matter consists of e^- and $^{56}_{26}$Fe; Baym-Pethick-Sutherland [36] for 10^4 g/cm^3 $\leq$ $\rho \leq 4.3 \times 10^{11}$ g/cm^3 with Coulomb lattice energy corrections; and Baym-Bethe-Pethick EoS [37] 4.3 g/cm^3 $\times 10^{11} \leq \rho \leq 10^{14}$ g/cm^3 are used.

In the spherically symmetric case, the hydrostatic equilibrium is given by the Tolman-Oppenheimer-Volkoff equation relating the pressure $P(r)$ and the energy density $\rho(r)$ [38],

$$\frac{\mathrm{d}P}{\mathrm{d}r} = -(\rho + P)\frac{m(r) + 4\pi r^3 P}{r(r - 2m(r))}, \qquad (3)$$

with obvious condition of zero pressure at the star surface, $P(R) = 0$.

Calculations yielding mass-radius relation obtained in this way for two parameterizations (both with inclusion of the hyperon degrees of freedom) are in Fig. 1. The typical radii (of static spehrically symmetric neutron stars) are not much influenced by the hyperon presence (compare, e.g., [27]) and they are close to 12.5 km; the neutron star masses with hyperons are a bit higher than in the case of nucleonic neutron stars.

4 Rotating neutron stars

To study rotation and deformation of neutron stars, we use the slow-rotation Hartle-Thorne approximation method [40] and the basis of our earlier calculation of spherical (static) neutron stars both without [27] and with [30] hyperonic degrees of freedom, where we thoroughfully tested their properties against the most strict constraints given by astrophysical data.

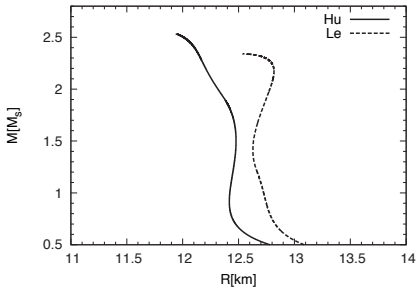

Fig. 1: Relation between mass and radius of a neutron star with hyperon degrees of freedom.

In the following, we refer to the essential ideas on their rotation and deformation, as they were formulated by one of us recently [39]. The basic equation that describes the centrifugal force in a star depending on the local spin frequency $\bar{\omega}$ measured in a local inertial reference frame satisfies in its lowest order the differential equation (see, e.g., [21])

$$\frac{1}{r^4}\frac{\mathrm{d}}{\mathrm{d}r}\left(r^4 \mathrm{e}^{-\Phi-\lambda}\frac{\mathrm{d}\bar{\omega}}{\mathrm{d}r}\right) + \frac{4}{r}\left(\frac{\mathrm{d}}{\mathrm{d}r}\mathrm{e}^{-\Phi-\lambda}\right)\bar{\omega} = 0, \tag{4}$$

where Φ and λ are metric functions of a non-rotating star.

The total moment of inertia $I = J/\Omega$, where J is the total stellar angular momentum, is given by [21]

$$I = \frac{8}{3}\pi \int_0^R r^4(\rho + P/c^2)\frac{\bar{\omega}}{\Omega}\exp(-\Phi-\lambda)\mathrm{d}r. \tag{5}$$

In the Newtonian limit, $\bar{\omega} = \Omega$, $\lambda = \Phi = 0$, $P \ll \rho c^2$, what gives $I_{\mathrm{Newton}} = \frac{8}{3}\pi \int_0^R r^4 \rho \mathrm{d}r$.

In this presentation we focus also on the ratio of equatorial R_{eq} and polar R_{pol} radii. These are given by the shape of isobaric surface

$$\mathcal{R}(r,\theta) = r(P) + \xi_0(r) + \xi_2(r)P_2(\cos\theta), \tag{6}$$

where $r(P)$ is the shape of isobaric surface of the nonrotating star, functions ξ_0 and ξ_2 are perturbation functions (for details see [40]) and $P_2(\cos\theta)$ is Legendre polynomial. Radial and polar coordinates of the star are given as $R_{\mathrm{eq}} = \mathcal{R}(R, \pi/2)$, $R_{\mathrm{pol}} = \mathcal{R}(R, 0)$.

The resulting inertia moment vs. compactness for six parameterizations of the equation of state (see [27, 34]) as well as the ratio of the equatorial to the polar radii vs. compactness, as calculated for the rotation frequency of 716 Hz (the most rapidly rotating star), are presented in Fig. 2. We see that all calculated curves lie very close one to each other (especially in the case of the inertia moment), what suggests that these quantities are generally very weakly dependent on the exact form of the equation of state, even if hyperons are included.

To show the influence of the speed of rotation, we have calculated the polar and equatorial radii dependent on the rotational frequency for two DBHF parameterizations; they are presented in Fig. 3.

5 Conclusions

We calculated the properties of neutron stars stemming from the parametrized DBHF approach. In addition to usual quantities, like mass, radius, etc., we calculated also the neutron star deformation and moment of inertia vs. compactness. The nonzero deformation, which was obtained also for small compactness, suggests that the deformation is a common feature for these stellar objects. Therefore,

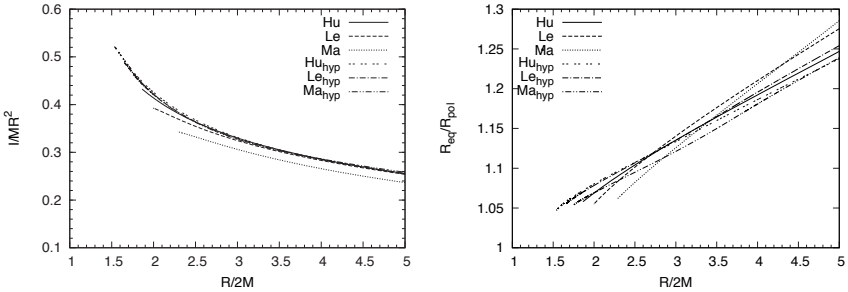

Fig. 2: Inertia moment *(left)* and the ratio of the equatorial to the polar radii *(right)* vs. compactness for six parameterizations of the equation of state, three with and three without hyperons (from [34]).

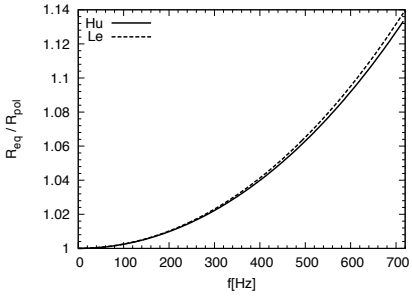

Fig. 3: Ratio of equatorial to polar radius of a rotating neutron star vs. its rotational frequency. The calculations for parameters fitting the Huber and Lee full DWBA calculations are very close one to the other and are difficult to be distinguished in this scale.

there emerges a new bridge between nuclear physics and general relativity, namely the possibility to study the gravitational waves also from this point of view.

5.1 Acknowledgements

The authors are grateful to J. Kotulič Bunta and Š. Gmuca for the availability of their computer codes. The work has been supported by the VEGA, APVV and GAČR grants Nos. 2/0029/10, 0177-11 and P209/12/P740, respectively. The authors further acknowledge the internal student grant of the Silesian University in Opava (SGS/1/2012) and the project CZ.1.07/2.3.00/20.0071 Synergy in the frame of Education for Competitiveness Czech Operational Programme supporting the international collaboration of the Institute of Physics.

References

[1] F. Weber, *Pulsars as Astrophysical Laboratories for Nuclear and Particle Physics* (IoP Publishing, Bristol, 1999).

[2] J.M. Lattimer and M. Prakash, *Astrophys. J.* **550** (2001) 426; *Phys. Rep.* **442** (2007) 109.

[3] F. Weber, R. Negreiros and P. Rosenfeld, *Neutron star properties and the equation of state of superdense matter* (2007) arXiv:0705.2708.

[4] C. Burgio, *J. Phys. G* **35** (2008) 014048.

[5] H. Steiner, J. Lattimer and E. Brown, *Astrophys. J.* **722** (2010) 33.

[6] J.D. Walecka, *Theoretical Nuclear and Subnuclear Physics*, 2nd ed. (Imper. College & World Sci., London & Singapore, 2004).
[7] J. Kotulič Bunta and Š. Gmuca, *Phys. Rev. C* **68** (2003) 054318; *ibid*. **70** (2004) 054309.
[8] G.Q. Li, R. Machleidt and R. Brockmann, *Phys. Rev. C* **45** (1992) 2782.
[9] H. Huber, F. Weber and M.K. Weigel, *Phys. Rev. C* **51** (1995) 1790.
[10] C-H. Lee, T.T.S. Kuo, G.Q. Li and G.E. Brown, *Phys. Rev. C* **57** (1998) 3488.
[11] F. Walter and L. Matthews, *Nature* **389** (1997) 358.
[12] J.A. Pons *et al*., *Astrophys. J*. **564** (2002) 981.
[13] M. Bejger and P. Haensel, *Astron. and Astrophys*. **396** (2002) 917.
[14] P. Haensel, J-L. Zdunik and F. Douchin, *Astron. and Astrophys*. **385** (2002) 301.
[15] M. Bejger, T. Bulik and P. Haensel, *Monthly Not. Royal Astron. Soc*. **364** (2002) 635.
[16] J. Rikovska Stone, P.A.M. Guichon, H.H. Matevosyan and A.W. Thomas, *Phys. Rev. C* **68** (2003) 034324.
[17] J. Trümper, V. Burwitz, F. Haberl and V.E. Zavlin, *Nucl. Phys. B Proc. Suppl*. **132** (2004) 560.
[18] P. Podsiadlowski *et al*., *Monthly Not. Royal Astron. Soc*. **361** (2005) 1243.
[19] T. Klähn *et al*, *Phys. Rev. C* **74** (2006) 035802.
[20] P.G. Krastev and F. Sammarruca, *Phys. Rev. C* **74** (2006) 025808.
[21] P. Haensel, A.Y. Potekhin and D. Yakovlev, *Neutron Stars 1* (Springer, Heidelberg, 2007).
[22] V. van Kerkwijk and D. Kaplan, *Astrophys. J. Suppl*. **308** (2007) 191.
[23] D. Nice, I. Stairs and L. Kasian, *AIP Conf. Proc*. **983** (2008) 453.
[24] Z. Stuchlík, G. Török, S. Hledík and M. Urbanec, *Class. Quant. Gravity* **26** (2009) 035003.
[25] P.B. Demorest *et al*., *Nature* **467** (2010) 1081.
[26] T. Güver, P. Wroblewski, L. Camarota and F. Özel, *Astrophys. J*. **719** (2010) 1807.
[27] M. Urbanec, E. Běták and Z. Stuchlík, *Acta Astron*. **60** (2010) 149.
[28] S. Gandolfi, J. Carlson and S. Reddy, *The maximum mass and radius of neutron stars and the nuclear symmetry energy* (2011) arXiv:1101.1921.
[29] R. Neuhäuser *et al*., *Proc. Sci*. **NIC XI** (2011) 037.
[30] M. Urbanec, E. Běták and Z. Stuchlík, *AIP Conf. Proc*. **1377** (2011) 275.
[31] M. Malheiro, R.P. Negreiros, F. Weber, V. Usov, *J. Phys. Conf. Ser.* **312** (2011) 042018.
[32] S. Weissenborn, D. Chatterjee and J. Schaffen-Bielich, *Nucl. Phys. A* **881** (1012) 62.
[33] R. Neuhauser, V.V. Hambaryan, M.M. Hohle and T. Eisenbeiss, *J. Phys. Conf. Ser.* **337** (2012), 012703.
[34] M. Urbanec, E. Běták and Z. Stuchlík, *J. Phys. Conf. Ser.* **337** (2012) 012021.
[35] R. Feynman, N. Metropolis and E. Teller, *Phys. Rev.* **75** (1949) 1561.
[36] G. Baym, C. Pethick and P. Sutherland, *Astrophys. J*. **170** (1971) 299.
[37] G. Baym, H. Bethe and C. Pethick, *Nucl. Phys. A* **175** (1971) 225.
[38] R.C. Tolman, *Phys. Rev.* **55** (1939) 364; J.R. Oppenheimer and G.M. Volkoff, *ibid*. 374.
[39] M. Urbanec, *PhD Thesis* (Silesian University, Opava, 2010); M. Urbanec, J.C. Miller and Z. Stuchlík, *to be published*.
[40] J. B. Hartle and K. Thorne, *Astrophys. J*., **153**, (1968) 807; S. Chandrasekhar, J. C. Miller, *Monthly Not. Royal Astron. Soc*., **167**, (1974) 63; J. C. Miller, *Monthly Not. Royal Astron. Soc*., **179**, (1977) 483.

Review of nuclear structure calculations in the sd shell for the rp process

W. A. Richter[1],[2] *and B. Alex Brown*[3]
[1] iThemba Labs, P.O.Box 722, Somerset West 7129, South Africa [2] Department of Physics, University of the Western Cape, Private Bag X17, Bellville 7535, South Africa, [3] Department of Physics and Astronomy, and National Superconducting Cyclotron Laboratory, Michigan State University, East Lansing, Michigan 48824-1321, USA

Abstract
We have embarked on a systematic study of important astrophysical rp-process rates for sd shell nuclei. Calculations and results for the ^{25}Al(p,γ)^{26}Si, ^{35}Ar(p,γ)^{36}K and ^{29}P(p,γ)^{30}S reactions are discussed, as well as general principles for doing such calculations.

1 Introduction

In explosive stellar environments, such as classical novae and x-ray bursters, thermonuclear radiative capture reactions on unstable nuclei determine the path of nucleosynthesis towards the proton drip line. These processes are often dominated by resonant capture to excited states above the particle-emission threshold and therefore depend critically on the nuclear properties of the levels involved. However, since the required spectroscopic information on proton-rich nuclei is difficult to obtain, one often has to rely on input from theory, or the use of measured properties of the mirror nuclei. For the present work the gamma and proton decay widths have been calculated with several Hamiltonians to find their values and to estimate their theoretical uncertainties. The determination of the level energies to be used for the resonance Q values is discussed in the next section.

2 Procedure for determining energy levels in the final nucleus.

Because of the exponential dependence of the reaction rate on the resonance energy of the final nucleus of the (p,γ) reaction [1], it is imperative to use as accurate energies as possible. Generally there are three different sources for the energies of the final T=1 nucleus that are input into the reaction rate calculations. In order of preference they are: 1) well-established experimental energies 2) in the case of a T=1 nucleus, predicted levels based on the Isobaric Mass Multiplet Equation (IMME) which uses the measured binding energies of the T=1 partners and a theoretical value of the c-coefficient of the IMME [2] 3) level energies calculated with reliable sd-shell two-body interactions, such as USDA and USDB [3].

The method used for 2) is explained in Ref. [15].

According to the IMME

$$B = a + bT_z + cT_z^2, \tag{1}$$

where B is the binding energy of a state. For the three T=1 isobaric states one can then, with $T_z = (N-Z)/2$, substitute $T_z = 1, 0, -1$ alternately, and by rearranging

$$B_p = 2B_o - B_n + 2c \tag{2}$$

for the proton-rich member, where c can be expressed as

$$c = (B_n + B_p - 2B_o)/2. \tag{3}$$

As a specific example, for ^{26}Si one has

$$B_{th}(^{26}\mathrm{Si}) = 2B(^{26}\mathrm{Al}) - B(^{26}\mathrm{Mg}) + 2c_{th}. \tag{4}$$

For the calculation of the b- and c-coefficients of the IMME we use the USDB Hamiltonian [3] for the charge-independent part and add the Coulomb, charge-dependent and charge-asymmetric nuclear Hamiltonian obtained by Ormand and Brown for the sd shell [2]. This composite interaction is called usdb-cdpn in NuShellX [4]. The cd refers to charge-dependent and pn because the calculations are done in the pn formalism. For the nuclei considered in [2], A=18-22 and A=34-39, the 42 b-coefficients were reproduced with an rms deviation of 27 keV and the 26 c-coefficients were reproduced with an rms deviation of 9 keV. There is considerable state-dependence in the c-coefficients (ranging in values from 130 keV to 350 keV) that is nicely reproduced by the calculations (see Fig. 9 in [2]).

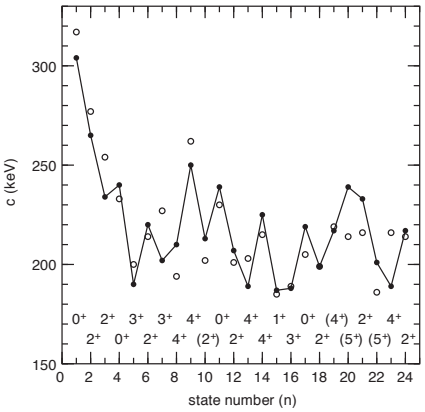

Fig. 1: c-coefficients from the isobaric mass multiplet equation (IMME: $E = a + bT_z + cT_z^2$) versus state number (in order of increasing energy) in ^{26}Si based on experimental energies (closed circles) and energies calculated from USDB (crosses).

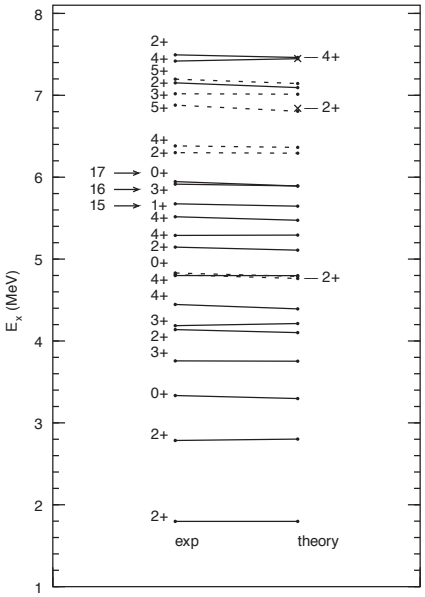

Fig. 2: Adopted experimental excitation energies in ^{26}Si [5] versus predicted energies E_{th} based on experimental binding energies of ^{26}Mg and ^{26}Al and the theoretical c-coefficient (USDB) (Eq. (4)). Dashed lines indicate the uncertain J^π assignments from [5]. The crosses correspond to predicted energies without experimental counterparts.

3 ^{26}Si as the final nucleus

Because many levels in ^{26}Si have uncertainties in terms of energy, spin and parity, a procedure often adopted is to make assignments in ^{26}Si based on known levels in the mirror nucleus ^{26}Mg. We have also made use of experimental information on the levels of excited states in ^{26}Si from Ref. [5]. Using the new sd-shell interactions USDA and USDB [3], as well as the older USD interaction [6], assignments between theory and experiment of corresponding levels in ^{26}Mg levels have been confirmed, and new ones suggested [7]. It has also been shown previously that the new interactions reproduce most observables in the sd shell reliably, and in some cases better than USD [8].

In Fig. (1) values of c from experiment and theory are compared for states in ^{26}Si ordered ac-

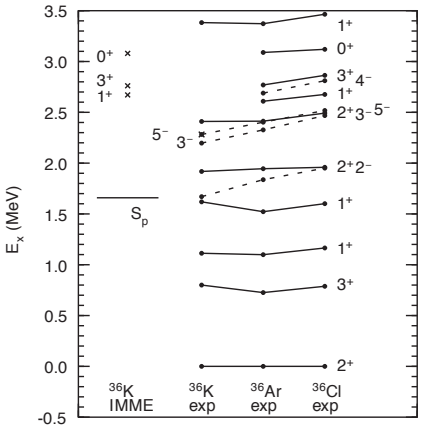

Fig. 3: Experimental energies of the isobaric T=1 triplets for A=36. The energies of ^{36}Ar are relative to the lowest 2^+ T=1 state at 6.611 MeV. Negative parity states are connected by dashed lines. The solid lines connect positive parity states considered to be analogs on the basis of our IMME predictions. The proton separation energy in ^{36}K is shown by the horizontal line on the left-hand side.

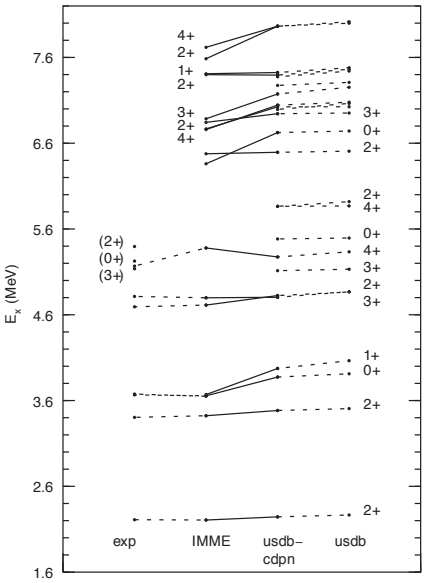

Fig. 4: Experimental excitation energies, predicted IMME-based energies, and usdb-cdpn and usdb energies in ^{30}S.

cording to increasing experimental energy. The experimental values are obtained for states where all three members of the multiplet are known. In general a good correspondence can be seen, the largest deviations being less than 30 keV. There is considerable state dependence with c values ranging from 300 keV (for the 0^+ ground state) down to 180 keV. This IMME method was used in [9] for the T=1 states of the odd-odd nuclei with mass 28, 32 and 36. The agreement with experiment [Fig. (1)] for our even-even case appears to be better than obtained in [9] for the odd-odd cases.

Fig. (2) shows the excitation energies for ^{26}Si obtained from Eq. (2) on the right compared to experiment on the left. The calculated values can then be used as a guide to the correct spin/parity assignments for measured levels in ^{26}Si. Where no levels in ^{26}Si are known, levels can be predicted. Two such levels are indicated by crosses in Fig. (2). The three levels that are just above the proton-decay separation energy of 5.51 MeV and of potential importance for the capture reaction at low temperatures are indicated by the arrows in Fig. (2).

Based on the foregoing discussion, the ^{26}Si energies used for the rate calculations are firstly the established experimental values, then values based on the IMME where data is lacking, and finally values calculated from USDA and USDB when there is insufficient information on the T=1 analog states. The gamma and proton decay widths have been calculated with USDA and USDB.

4 ^{36}K as the final nucleus

Fig. (3) shows the experimental excitation energies of the T=1 analog states for A=36. A number of levels of ^{36}K measured recently by Wrede et al [10] above the proton separation are included, and all other excitation energies are from Ref. [11]. The cross on the 2.282 MeV 5^- state in ^{36}K indicates what this level was associated with the 2^+_3 state by Wrede et al. Our reasons for associating the 2^+_3 level with

the higher state at 2.446 MeV state are discussed in Ref. [12]. The levels labeled ^{36}K IMME are based on Eq. (2) with the experimental binding energies of ^{36}Cl and ^{36}Ar and the theoretical c-coefficient (Eq. (3)). The crosses correspond to predicted energies without experimental counterparts.

In the present case there are two negative parity states, 3^- and 5^- as shown in Fig.(3), close to some of the important resonances, and their contributions should be taken into account. In view of the correspondence between mirror states for A = 36 it would be reasonable to substitute experimental values of the spectroscopic factors and lifetimes from the mirror nucleus ^{36}Cl in cases where a calculation is not feasible. In this way the contributions from these negative parity levels can be taken into account approximately.

5 ^{30}S as the final nucleus

In Fig. (4) experimental energies, energies based on the IMME, and theoretical energies for usdb-cdpn and USDB are shown for ^{30}S. In general the experimental energies and those based on the IMME agree quite well. The experimental energies below 5 MeV are from Ref. [13]. Some new measured energies above 5 MeV from Ref. [14] have also been included (from their Table II). For three of these the energies in the nucleus ^{30}P are uncertain so that IMME values cannot be determined. Where energies could not be predicted from the IMME, values based on usdb-cdpn were used. It is also seen from Fig. (4) that the usdb-cdpn and USDB values do not differ much. Unlabeled theoretical levels (due to space considerations) are, with usdb-cdpn energies given in brackets, 5^+(6.99 MeV), 2^+(7.27 MeV) and 0^+(7.37 MeV).

6 Calculation of the reaction rates

The resonant reaction rate for capture on a nucleus in an initial state i, $N_A < \sigma v >_{\mathrm{res}\,i}$ for isolated narrow resonances is calculated as a sum over all relevant compound nucleus states f above the proton threshold [1]

$$N_A < \sigma v >_{\mathrm{res}\,i} = 1.540 \times 10^{11} (\mu T_9)^{-3/2} \times \sum_f \omega\gamma_{if} \ \mathrm{e}^{-\mathrm{E_{res}}/(kT)} \ \mathrm{cm}^3\,\mathrm{s}^{-1}\mathrm{mole}^{-1}. \quad (5)$$

Here T_9 is the temperature in GigaK, $\mathrm{E}_{res} = \mathrm{E}_f - \mathrm{E}_i$ is the resonance energy in the center of mass system, the resonance strengths in MeV for proton capture are

$$\omega\gamma_{if} = \frac{(2J_f+1)}{(2J_p+1)(2J_i+1)} \frac{\Gamma_{\mathrm{p}\,if}\Gamma_{\gamma f}}{\Gamma_{\mathrm{total}\,f}}. \quad (6)$$

$\Gamma_{\mathrm{total}\,f} = \Gamma_{\mathrm{p}\,if} + \Gamma_{\gamma f}$ is a total width of the resonance level and J_i, J_p and J_f are target, the proton projectile ($J_p = 1/2$), and states in the final nucleus, respectively. Approximations made in calculating the proton width are discussed in Refs. [15], [12].

The total rp reaction rates have been calculated for each of the interactions USD, USDA and USDB for ^{26}Si. The Q values required for ^{26}Si were based on measured energies, and where they were not known values calculated from Eq. (4) were used. Above 8 MeV we used the energies obtained with USDB that includes the addition of about 170 states with $J^\pi \leq 5^+$ up to 14 MeV in excitation energy. Fig. (5) shows the results for the resonance-capture rate obtained using the levels adopted for ^{26}Si (given in Table I, Ref. [15]).

In Fig. (6) the reaction rates leading to ^{36}K are shown. It should be noted that the contribution of the negative parity state 3^- is significant and cannot be neglected, even if it has to based on measured spectroscopic factors and gamma widths of the mirror nucleus ^{36}Cl.

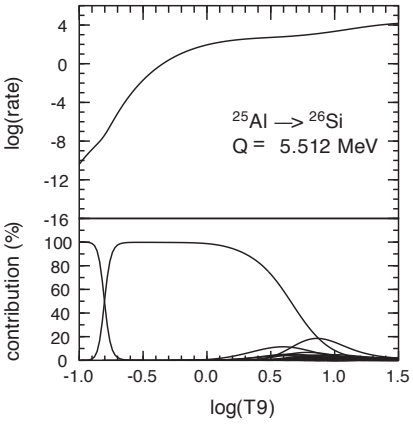

Fig. 5: The total rp reaction rate versus temperature T9 (GigaK) (top panel) and the contribution of each of the final states (lower panel) with USDB. In the lower panel the dominant contribution below log(T9) = −0.8 is from the 1^+ state at 5.675 MeV, and above from the 3^+ state at 5.915 MeV. Γ_γ calculated for ^{26}Si levels.

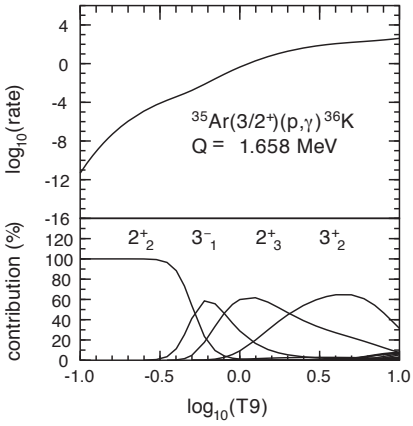

Fig. 6: The total rp reaction rate versus temperature T9 (GigaK) (top panel) and the contribution of each of the final states (lower panel) with usdb-cdpn. Γ_γ was calculated for ^{36}K levels.

In Fig. (7) the results for ^{30}S are shown, indicating that the dominant contributions are from the $3^+(1)$, $2^+(3)$ and $2^+(4)$ states.

7 Uncertainties in the resonant capture reaction rates

A detailed analysis of error sources in the rate calculations has been given in Ref. [15]. A general indication of the variation caused by the use of different interactions can be obtained by comparing the corresponding reaction rates. As an example this is shown in Fig. (8) for the reaction ^{35}Ar(p,γ)^{36}K. Comparisons with the 2010 Evaluation of Monte Carlo-based Thermonuclear Reaction Rates [16] have been made for ^{26}Si and ^{36}K in Refs. [15] and [12] respectively.

8 Conclusions

We have summarized the results of rp reaction rate calculations for three T=1 sd-shell final nuclei. When experimental energies are not available to determine the Q values of the proton capture process, we resorted to the IMME method which is empirically based, except for a contribution from a theoretical c-coefficient. We have demonstrated that a good correspondence between theoretical and experimental values of the c-coefficient for sd-shell nuclei generally exists. The method leads to a reliable prediction of energy levels in the final nucleus provided the energies of the T=1 analog partners are known. The required spectroscopic factors and gamma decay lifetimes for rate calculations were obtained from shell-model calculations using the new sd-shell interactions USDA and USDB (or usda-cdpn and usdb-cdpn) for the charge-independent parts of the interactions. Where some negative parity states occur in the region close to the threshold energy, their contributions to the reaction rate were estimated by using spectroscopic factors and lifetimes of their mirror counterparts. In this way the contributions of such states could be taken into account approximately.

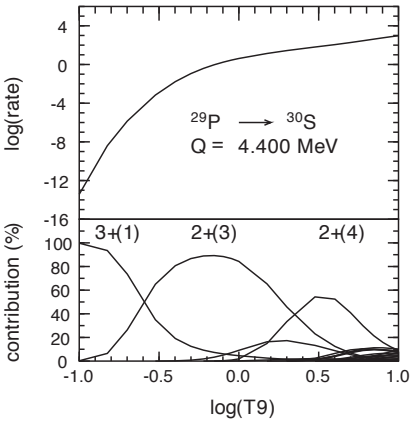

Fig. 7: The total rp reaction rate versus temperature T9 (GigaK) (top panel) and the contribution of each of the final states (lower panel) with usdb-cdpn.

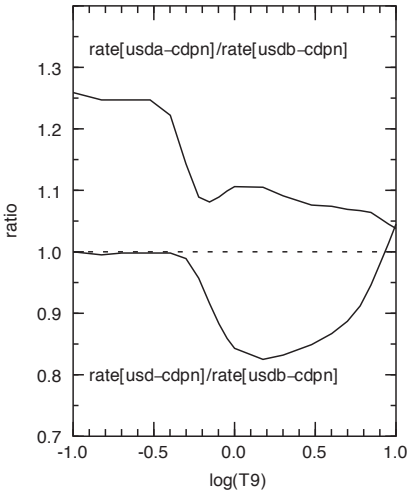

Fig. 8: The total rp reaction rate ratios of usda-cdpn and usd-cdpn versus usdb-cdpn compared.

Acknowledgments This work is partly supported by NSF Grant PHY-1068217 and the National Research Foundation of South Africa under Grant No. 76898.

References

[1] W. A. Fowler and F. Hoyle, Ap. J. Suppl. **9**, 201 (1964).

[2] W. E. Ormand and B. A. Brown, Nucl. Phys. A **491**, 1 (1989).

[3] B. A. Brown and W. A. Richter, Phys. Rev. C **74**, 034315 (2006).

[4] www.nscl.msu.edu/∼brown/resources/resources.html

[5] A. Matic et al., Phys. Rev. C **82**, 025807 (2010).

[6] B. H. Wildenthal, Prog. Part. Nucl. Phys. **11**, 5 (1984).

[7] W. A. Richter and B. A. Brown, Phys. Rev. C **80**, 034301 (2009).

[8] W. A. Richter, S. Mkhize and B. A. Brown, Phys. Rev. C **78**, 064302-1 (2008).

[9] C. Iliadis, P. M. Endt, N. Prantzos and W. J. Thompson, The Astrophysical Jour. **524**, 434 (1999).

[10] C. Wrede, J. A. Clark, C.M. Deibel, T. Faestermann, R. Hartenberger, A. Parikh, H.-F. Wirth, S. Bishop, A. A. Chen, K. Eppinger, B. M. Freeman, R. Krucken, O. Lepyoshkina, G. Rugel and K. Setoodehnia, Phys. Rev. C **82**, 035805 (2010)

[11] P. M. Endt, Nucl. Phys. A **633**, 1 (1998)

[12] W. A Richter and B. A. Brown, Phys. Rev. C **85**, 045806 (2012).

[13] http://www.nndc.bnl.gov/ (2012).

[14] K. Setoodehnia, A. A. Chen, J. Chen, J.A.Clark, C.M. Deibel, S. D. Geraedts, D. Kahl, P. D. Parker, D.Seiler, and C. Wrede, Phys. Rev. C **82**, 022801 (2010)

[15] W. A Richter, B. A. Brown, A. Signoracci and M. Wiescher, Phys. Rev. C **83**, 065803 (2011)

[16] C. Iliadis, R. Longland, A. E. Champagne, A. Coc and R. Fitzgerald, Nucl. Phys. A **841**, 31 (2010).

Meson photoproduction from the nucleon at CLAS

D.P. Watts for the CLAS collaboration at Jefferson Lab
SUPA, University of Edinburgh, UK

Abstract

The excitation spectrum of the nucleon provides a stringent constraint on the dynamics and interactions of its internal constituents and therefore probes the mechanism of confinement in the light quark sector. Our detailed knowlege of this excitation spectrum is poor, with many predicted states not yet observed in experiment and many "established" states having poorly known properties. To address these shortcomings a worldwide effort is currently underway exploiting the latest generation of electron and photon beams in detailed studies of meson photoproduction from nucleon targets. A major contribution to this effort will come from the experimental programme at Jefferson Lab exploiting the frozen spin target (FROST) with the CLAS spectrometer. The status of this project will be presented along with preliminary results and analyses.

1 Introduction

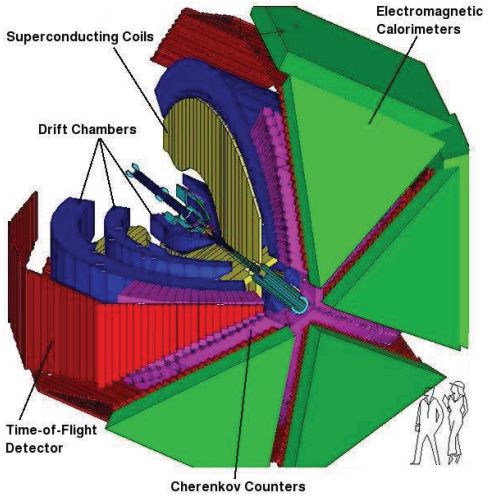

Fig. 1: Schematic diagram of the CLAS detector.

Obtaining an accurate determination of the excitation spectrum of the nucleon would provide stringent constraints on our understanding of the dynamics and degrees of freedom of its constituents. Significant advances in theory aiming to understand this spectrum have taken place in recent years. One recent highlight is the emergence and expected progression of Lattice QCD predictions, which provide a more direct link between the properties of the excitation spectrum and the underlying non perturbative QCD processes in the light quark sector [2]. Better establishing the excitation spectrum would also guide refinements to QCD-based phenomenological models such as constituent quark models. The recent lattice results tend to support the finding of many constituent quark models that there should be many more excited states of the nucleon than have currently been observed, particularly in the mass region above 1.8 GeV/c^2.

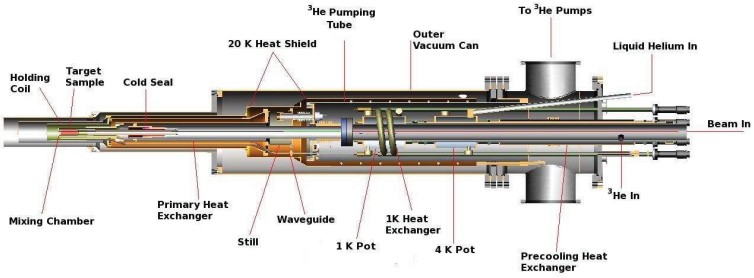

Fig. 2: Schematic diagram of FROST.

It remains a major challenge to current hadron physics to establish whether this "missing resonance" problem is due to deficiencies in the coverage, quality, or completeness of the world data set to date or whether these states are absent in nature, with significant consequences to our understanding of nucleon dynamics. As well as hunting for unseen resonances, it is important to better establish the properties of "known" resonances, reaching a situation where they are consistently evident in different analyses and have consistent electromagnetic couplings, masses and widths.

Meson photoproduction is an excellent tool to study the nucleon resonance spectrum. The photon offers a clean well understood probe, with the advantage over previous studies with spinless pion beams that the response of the nucleon to polarisation degrees of freedom can be utilised. The new generation of measurements of meson photoproduction carried out or planned at many of the world's electromagnetic beam facilities will provide a step change in the quality of available experimental data. The use of photon beams and targets with high degrees of polarisation, coupled with large acceptance particle detectors is essential for disentangling the spectrum of excited states, which can only be revealed from the data by a detailed partial wave analysis (PWA). The inadequacies of the current world data set are highlighted by the differences in the composition of the resonance spectrum by different partial wave analyses of the same data (for a review see [3]). Significant advances in PWA analyses themselves are also currently underway, including the SAID [5], MAID [6], Bonn-Gatchina [7] and EBAC [1]. One recent highlight from these developments comes from the coupled channel models developed by the EBAC group at Jefferson Lab, which recently led to the suggestion that the low mass of the Roper resonance may arise from strong coupled channel effects [1]. A common problem for all the PWA's in meson photoproduction is that they are currently under-constrained and require more comprehensive experimental data to permit more consistent interpretations of the contributing resonances and reaction mechanisms.

The CLAS measurements presented in this contribution will form a crucial part of this world effort to improve the world data base available for PWA studies. The FROST experiment will provide complete or nearly complete measurements for a whole range of meson photoproduction reactions such as $\gamma p \rightarrow N\pi, p\eta, p\omega, K^+Y$ and $p\pi^+\pi^-$. A "complete" measurement corresponds to the determination of sufficient experimental quantities to eliminate experimental ambiguities in extracting the scattering amplitude for the reaction and thereby putting as tight constraints on the various PWA's as possible. Achieving a complete measurement requires the precise determination of at least eight well chosen experimental observables (for a recent discussion see [4]). One combination is the cross section, three

single-spin and four double-spin observables. For hyperon production channels the ability to determine the polarisation of the recoiling hyperon from the angular distribution of its weak decay allows this complete determination to be achieved entirely from observables measured in the CLAS programme. For non-strange production channels a close to complete set can be obtained at CLAS.

The experimental facilities will be discussed in section 2. A selection of preliminary results for beam-target observales will be presented in sections 3-6.

2 Experimental Setup

The Continuous Electron Beam Accelerator Facility (CEBAF) provides high-intensity electron beams of up to 6 GeV with approximately 100% duty cycle simultaneously to three experimental halls: A, B and C. The upgrade to 12 GeV will be completed in 2014, with associated upgrades to the equipment in the three current experimental halls and a fourth hall, D, currently under construction. The CEBAF accelerator consists of two anti-parallel superconducting RF-linacs connected by recirculation arcs to create a racetrack with a combined length of 1.4 km. The accelerator produces a continuous-wave electron beam which can circulate around the linacs up to 5 times, gaining 1.2 GeV of energy with each pass.

Hall B houses the CEBAF Large Acceptance Spectrometer (CLAS), which can be used with both electron and photon beams. A schematic diagram of CLAS is shown in Fig.1. CLAS is a multi-layered magnetic spectrometer, divided into six independent sectors by six superconducting coils arranged symmetrically around the beamline producing a toroidal magnetic field. There is a magnetic field free region in the centre of the detector, allowing for the use of polarised targets such as FROST. For photon beam experiments the innermost detector is a scintillator start counter surrounding the target providing timing and triggering information on charged reaction products. Outside the start counter, the first three layers of detectors consist of drift chambers to determine the curved trajectories and hence momenta of charged particles. Surrounding the drift chambers, gas Cherenkov Counters identify electron events and allows for the differentiation of electrons from pions. This is then surrounded by a layer of plastic scintillation bars for time-of-flight measurements. The outermost detector system is made up of electromagnetic calorimeters for the detection of photons, electrons and high-energy neutrons.

Near the entrance to Hall B the electrons from CEBAF impinge on a thin radiator in which they undergo bremsstrahlung. The recoiling electrons from this process are momentum analysed in a magnetic spectrometer containing a highly segmented focal plane comprised of thin plastic scintillation detector elements. The device can tag photons in the energy range 0.35 to 5.8 GeV. Circularly polarised photons can be produced by utilising a longitudinally polarised electron beam. The direction of the electron polarisation (and therefore photon circular polarisation) was flipped at a rate of 30 Hz. Linear photon polarisation can be achieved by using a thin diamond radiator. For such cases the lattice structure coherently enhances the momentum transfer direction in the scattering process to directions related to the reciprocal lattice vectors of the crystal, producing linear polarisation for the bremsstrahl photons.

The frozen spin target (FROST) is placed at the centre of the CLAS detector and provides a highly polarised proton target for use in a wide range of experiments. A schematic of the FROST apparatus is shown in Fig. 2. The target material consists of frozen, 1-2 mm beads of butanol (C_4H_9OH) mixed by weight with 5% H_2O and 0.5% TEMPO (2,2,6,6-tetramethylpipendine- 1-oxyl), and is placed inside the target cup which is 50 mm long and 15 mm in diameter. The target material was chosen to have a high maximum polarisation, a high ratio of polarisable nucleons to the total number of nucleons (the quality factor), a high resistance to ionising radiation, and a small number of unwanted polarisable nuclei. In butanol the non-hydrogen components, carbon and oxygen, are spinless particles, so pure butanol has no background polarisation to correct for. To subtract the yield from the unpolarised nuclei the frost target was run simultaneously with a separate carbon and polythene detector downstream of FROST. Events from these targets could be identified from the vertex tracking information of CLAS and their contribution to the butanol yield could be assessed for any variable of interest in the analysis. In operation

the FROST target achieved polarisation levels immediately following the polarising process of 85% to 90% and the polarisation degraded at a rate of 0.9% (spin paralell to beam) to 1.5% (anti-parallel to beam axis) per day.

In the following sections some of the preliminary analysis results from the first round of FROST data using a longitudinally polarised proton target will be presented.

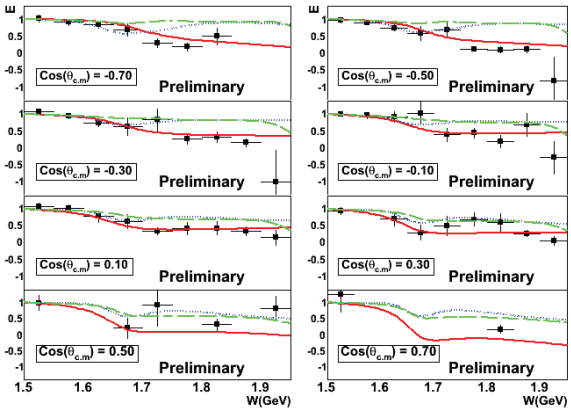

Fig. 3: Preliminary results for E in $\vec{\gamma}\vec{p} \to p\eta$ for energies $W = 1.525 - 1.925$ GeV . Curves: η-MAID (dotted line), Bonn-Gatchina PWA (dashed line), and SAID (solid line).

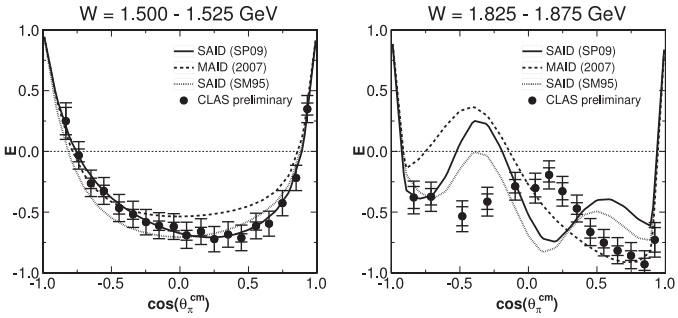

Fig. 4: Preliminary results of the double-polarisation observable E (helicity difference) for $\vec{\gamma}\vec{p} \to n\pi^+$ [11]. The inner error bars indicate stat. uncertainties; the outer error bars include a 10 % sys. uncertainty, which is expected to be reduced in the final analysis. The curves show solutions of the SAID SP09 [5], MAID [6] and SAID SM95 PWA.

3 The beam-target helicty asymmetry, E, in η photoproduction

The measurement of a wide range of final states in meson photoproduction is highly desirable, not only to constrain coupled channel analyses but also as certain channels are expected to filter contributions of nucleon resonances to the scattering amplitude. One example of this is η photoproduction which due to the I=0 isospin of the η can be produced in a single step mechanism only via intermediate nucleon resonances having isospin, I=$\frac{1}{2}$. This restriction simplifies the data interpretation and theoretical efforts to predict the excited states contributing to these reactions.

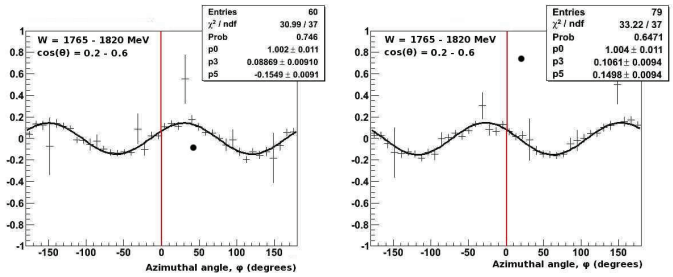

Fig. 5: (Upper) phi asymmetry for the positively polarised target setting. (Lower) phi asymmetry for negative target setting. The vertical red line at 0^0 is present to help demonstrate the phase shift in the asymmetry due to the G contribution to the cross section [8]

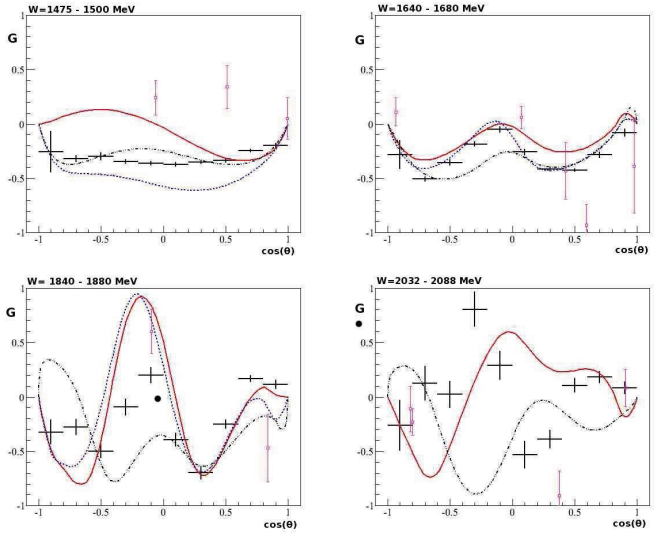

Fig. 6: Preliminary FROST values of the double-polarisation observable G (black points) plot as a function of *cos(θ)* for a small fraction of the available mass (W) bins [8]. Overlaid on the plots are the current SAID [5] (solid-red line) and MAID2007 [6] (dashed-blue line) solutions. The open pink squares show the previous experimental data for G.

The polarised cross section for the reaction $\vec{\gamma}\vec{p} \to p\eta$ of circularly-polarised photons on longitudinally-polarised protons is given by:

$$\frac{d\sigma}{d\Omega} = \frac{d\sigma}{d\Omega}_0 \left(1 - P_z\, \delta_\odot\, E\right), \tag{1}$$

where $d\sigma/d\Omega_0$ is the unpolarised cross section. P_z and $\delta_\odot$ are the degrees of target and beam polarisation, respectively. E denotes the helicity asymmetry.

The asymmetry is extracted from the difference in reaction yields between the photon and target nucleons spins aligned or antialigned. Preliminary results [9] of the helicity asymmetry, E, for $\vec{\gamma}\vec{p} \to p\eta$ are shown in Fig. 3. Since the η threshold is dominated by the N(1535)S_{11} resonance, the observable exhibits values close to unity for W $\leq$ 1.6 GeV/c^2 . The preliminary results indicate that the observ-

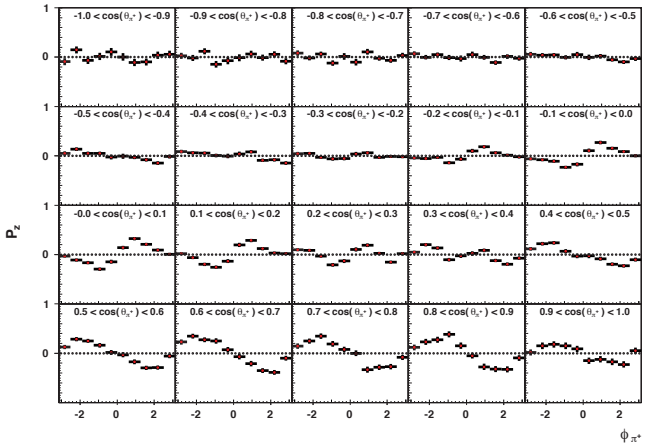

Fig. 7: Preliminary target asymmetry, P_z, from FROST for the reaction $\vec{\gamma}\vec{p} \rightarrow p\pi^+\pi^-$ for $E_\gamma \in [0.7,\ 0.8]$ GeV [10]. Error bars are statistical only.

able remains positive below about W = 2 GeV, providing new information to constrain the partial wave analyses for this channel.

4 The beam-target helicity asymmetry E in π^+ photoproduction

Comprehensive measurement of the pion production reaction is important as, of all the production channels accesible, the pion photoproduction is expected to give sensitivity to the largest set of resonances. The current database for pion photoproduction is mainly populated by unpolarised cross section data and single-spin observables and is therefore significantly under-constrained.

Figure 4 shows preliminary results [11] of the double polarisation E for $\vec{\gamma}\vec{p} \rightarrow \pi^+ n$ (Eqn. 1). While the predictions shown in Fig. 4 agree nicely with the new data at low energies, discrepancies emerge at higher energies for W $\geq$1.7 GeV/c^2. Single-pion photoproduction in this region appears less well understood than previously expected. The implications for the resonance spectrum and properties will be explored when the finalised results are included in the various PWAs.

5 The beam-target linear asymmetry G in π^+ photoproduction

The use of a linearly polarised photon beam with a longitudinally polarised proton target gives access to the observable G, for which only sparse data exists in the current world data base. The differential cross section for the case of a linearly polarised photon beam and longitudinally polarised proton target can be written as:

$$\frac{d\sigma}{d\Omega} = \left(\frac{d\sigma}{d\Omega}\right)_0 (1 - P_L \Sigma \cos(2\phi) + P_L \delta_\odot G \sin(2\phi)), \tag{2}$$

where $d\sigma/d\Omega_0$ is the unpolarised cross section. P_L and $\delta_\odot$ are the degrees of linear beam and target polarisation, respectively. G denotes the beam-target linear asymmetry observable and Σ is the single beam polarisation observable.

There were two possible settings for the photon beam polarisation in the first FROST experiment: PARA ($||$) in which the electric field vector was parallel to the floor and PERP ($\perp$) in which the electric

field vector was perpendicular to the floor. In addition, the target was polarised either parallel or anti-parallel to the beam direction, defined as positive and negative target polarisation, respectively. The combination of these resulted in a total of four possible combinations of polarised beam-polarised target settings during the run. An asymmetry in the reaction yield as a function of pion azimuthal angle with respect to the photon polarisation plane can be obtained:

$$\frac{N(\phi)_{\perp} - N(\phi)_{||}}{N(\phi)_{\perp} + N(\phi)_{||}} = P_L \Sigma \cos(2\phi) - P_L \delta_{\odot} G \sin(2\phi). \tag{3}$$

The value of G could be extracted by fitting these phi asymmetry spectra. Typical plots for positive and negative target polarisation settings are shown in Fig. 5. The effect of G in equation (3) gives the expectation of a change in sign of the ϕ offset when the target is polarised in the positive or negative direction. This is clearly seen when comparing the 2 plots in the Fig. 5 .

Preliminary values for G for a sample of the available W bins are shown in Fig. 6. It should be noted that the systematics in the degree of linear polarisation of the beam are still being evaluated so the results are at an early stage. Despite the preliminary nature it is clear that the new data show a great improvement in accuracy and kinematic coverage compared to previous measurements. Even in the low lying part of the excitation spectrum near to the Roper resonance it is seen that current PWAs give different expectations for G. These significant differences highlight how the current world data does not constrain this reaction even in the low lying part of the spectrum. The new data will therefore give valuable new constraints on PWAs over the mass range from 1400 up to 2300 MeV.

6 Polarisation observables for $\pi^+\pi^-$ production on the proton

One of the key experiments in the search for yet unobserved states is the investigation of double-pion photoproduction. Quark models predict large couplings of those states to $\Delta\pi$, for instance. The five-dimensional cross section for the photoproduction of two pseudoscalar mesons using longitudinal target polarisation and circularly-polarised (or unpolarised) beam can be written in the form [12]:

$$I = I_0 \{ (1 + \Lambda_z \cdot P_z) + \delta_{\odot} (I^{\odot} + \Lambda_z \cdot P_z^{\odot}) \},$$

where I_0 denotes the unpolarised cross section and $\delta_{\odot}$ and Λ_z denote the degree of beam and target polarisation, respectively. The additional polarisation observables, P_z and $I^{\odot}$, for the two-meson final state arise since the reaction is no longer restricted to a single plane.

Figure 7 shows an example for the observable P_z in $\gamma \vec{p} \rightarrow \pi^+\pi^-$ [10]. The variables θ and ϕ denote the polar and azimuthal angle of the π^+ in the rest frame of the two mesons. The observable acquires surprisingly large values for positive cos θ_{π^+} with the statistical errors in some cases smaller than the symbol size. The expected odd behaviour of the distribution is clearly visible.

7 Conclusion

Nucleon spectroscopy is undergoing an exciting period with major advances in theory being complemented by a step change in the quality of experimental data. Experimental programmes of meson photoproduction measurements at the world's electromagnetic beam facilities will provide the long sought extensive data sets to constrain the various partial wave analyses and more reliably extract the excitation spectrum of the nucleon and its properties. The FROST programme at Jefferson Lab will provide a large proportion of this new high quality experimental data. In the coming decade the combined efforts of experimentalists and theorists in this area is expected to allow deeper insights into our understanding of QCD confinement in the light quark sector.

8 Acknowlegements

The work is supported by DOE and NSF grants. The author thanks the Science and Technology Funding Council (UK) for support.

References

[1] H.Kamano and S. X. Nakamura and T. -S. H. Lee T. Sato, Phys. Rev. **C81**, 065207 (2010).

[2] Bulava, J. and Edwards, R. G. and Engelson, E. and Joó, B. and Lin, H-W. and Morningstar, C. and Richards, D. G. and Wallace, S. J Phys. Rev. **D82**, 014507 (2010); arXiv:1104.5152 [hep-ph]

[3] E. Klempt, J-M Richard, Rev. Mod. Phys. 82, 1095 (2010)

[4] B. Dey, M.E. McCracken, D.G. Ireland, C.A. Meyer, Phys Rev **C83** 055208 (2011)

[5] M. Dugger *et al*. [CLAS Collaboration], Phys. Rev. **C79**, 065206 (2009) and references therein; http://gwdac.phys.gwu.edu/

[6] D. Drechsel, O. Hanstein, S. S. Kamalov, L. Tiator, Nucl. Phys. **A645**, 145-174 (1999); http://wwwkph.kph.uni-mainz.de/MAID/

[7] E. Klempt, A.V. Anisovich, V.A. Nikonov, A.V. Sarantsev, U. Thoma., Eur.Phys.J.A24:111-128,2005; http://pwa.hiskp.uni-bonn.de/

[8] J. McAndrew, Ph.D thesis University of Edinburgh, UK, 2011 *submitted*

[9] B. Morrison, NSTAR 2011, Jefferson Lab.

[10] S. Park, NSTAR 2011, Jefferson Lab;

[11] S. Strauch, arXiv:1108.3050 [nucl-ex].

[12] W. Roberts, T. Oed, Phys. Rev. **C71**, 055201 (2005).

Strangeness Production on Nuclei

H. Lenske, T. Gaitanos, A. Obermann
Institut für Theoretische Physik, U. Giessen,
Heinrich-Buff-Ring 16, D-35392 Giessen

Abstract
Strangeness production on nuclei leading to the formation of hypernuclei is investigated by various probes ranging from high-energy photons to hadronic probes as pions, protons and heavy ions and antinucleon annihilation on nuclei with associated hadron production. Photo- and hadro-induced strangeness production is considered for coherent reactions, transforming a target nucleon into a bound hyperon. $K\Lambda$ production is described in a fully quantum mechanical approach accounting for initial and final sate interactions and state-of-the art nuclear wave functions. The production vertex is described by a resonance model where the incoming projectile first excites a target nucleon into resonance, subsequently decaying into the $K\Lambda$ channel. Recent results for in-medium hyperon interactions are discussed. The production of $S = -2$ hypernuclei is investigated by exploratory transport-theoretical studies of antiproton-nucleus collisions.

1 Introduction

Investigations of hypernuclei and their production in various types of reactions are a natural extension of traditional nuclear physics. Such studies are allowing to gain new insight into the dynamics of a system under strong interactions, the interactions of baryons of different flavor and the evolution of many-body dynamics of a mixed flavor system. Our purpose is to study the production and the spectroscopy of hypernuclei with strangeness $S = -1$ and $S = -2$. Even after decades of research on single-strangeness, i.e. single Λ, hypernuclei, our knowledge is sparse, mainly because of the limited set of data on YN interactions and the lack of high resolution spectroscopic data on hypernuclei. Hence, on the theoretical side the task is challenging because at present we have to derive the properties of YN interactions from a rather limited knowledge base. However, in the not too far future the situation will improve because of the ongoing or planned experiments on hypernuclear physics at various facilities around the world, ranging from JLAB (and RHIC) in the US, over the activities at MAMI, GSI and the upcoming FAIR facility in Germany to J-PARC in Japan. A comprehensive recent review on the status of hypernuclear physics is found on [1].

In section 2, we present the details of our theoretical approach to strangeness production by coherent photon- and hadron-nucleus scattering. The model has been used to investigate especially kaon production on nuclei by incoming photons [2,3], protons [4], and pions [5], respectively, presented for the (π^+, K^+) reaction data for ^{12}C, ^{40}Ca, ^{51}V, and ^{89}Y targets, measured some time ago at KEK by Hotchi et al. [6]. As a typical case, in sect. 4, we present numerical results for pion- and proton-induced kaon production on nuclei, analyzing KEK data in sect. 4.1. Proton-induced hypernuclear production, discussed in sect. 4.2 may be of potential interest for future activities at J-PARC. In section 5 our recent results [7] on the production of $S = -2$ double-Λ hypernuclei by antiprotons at PANDA are briefly presented. Last but not least, in section 6 we report on first results on YN interactions, obtained by a coupled channels Lippmann-Schwinger approach. Results are summarized in section 7.

2 Covariant Model for Hadro-Production of Kaons

Most of the theoretical models used so far to describe the (π^+, K^+) reaction employ a non-relativistic distorted wave impulse approximation (DWIA) framework [8] (see also ref. [9] for a comprehensive re-

view of these models). In these calculations, the Λ bound states are generated by solving the Schrödinger equation with Woods–Saxon or harmonic oscillator potentials. However, for processes involving momentum transfers of typically 300 MeV/c or more, a non-relativistic treatment of the corresponding wave functions may not be adequate as in this region the lower component of the Dirac spinor is no longer negligible in comparison to its upper component. The approach is discussed in detail in ref. [5].

In that paper, we have studied the $\mathrm{A}(\pi^+, K^+)_\Lambda\mathrm{A}$ reaction in a fully covariant model by retaining the field theoretical structure of the interaction vertices and by treating the baryons as Dirac particles. In this model, the kaon production proceeds via the collision of the projectile pion with one of the target nucleons. This excites intermediate baryon resonance states (N^*) which decay into a kaon and a Λ hyperon. The hyperon is captured in the respective nuclear orbit while the kaon re-scatters onto its mass shell. A similar picture has been used to describe the $A(p, K^+)_\Lambda B$ and $A(\gamma, K^+)_\Lambda B$ reactions in refs. [2–4]. In our model, the intermediate resonance states included are $N^*(1650)[\frac{1}{2}^-]$, $N^*(1710)[\frac{1}{2}^+]$, and $N^*(1720)[\frac{3}{2}^+]$ which have dominant branching ratios for the decay to the $K^+\Lambda$ channel [2–5]. Terms corresponding to the interference among various resonance excitations are included in the total reaction amplitude.

The structure of our model for the (π^+, K^+) reaction is described by the elementary strangeness production amplitude through excitation of a nucleon resonance N^* decaying into the $K^+\Lambda$ channel. Obviously, those resonances with a large $K^+\Lambda$ branching ratio are of special interest. In the energy region considered here, these are the $N^*(1650)[\frac{1}{2}^-]$, $N^*(1710)[\frac{1}{2}^+]$, and $N^*(1720)[\frac{3}{2}^+]$ baryon resonances. Terms corresponding to the interference between various amplitudes are retained. As found in our previous investigations the s-channel resonance mechanism dominates by far strangeness production in elementary reactions on the nucleon [10,11] and on nuclei [5], respectively.

2.1 Interaction Lagrangians

For the interaction terms of the spin-$1/2$ resonances, we have vertices of *pseudoscalar* (PS) or *pseudovector* (PV) form. The pseudovector coupling is consistent with the chiral symmetry requirement of the fundamental theory of strong interactions (quantum chromodynamics (QCD)). In contrast to that, the pseudoscalar one does not have this property, but it is easier to calculate. The couplings are in both cases fixed in such a way that they are equal on-shell; for off-shell cases, their difference is suppressed due to the denominator of the resonance propagator. It is, therefore, arguable which Lagrangian to use. The best approach would be to introduce a mixing parameter, which was investigated in [4].

In order to avoid the introduction of additional parameters due to a PS-PV mixing [4] we use the convention of either choosing the PS or the PV couplings for these vertices.

The pseudoscalar interaction Lagrangians for the spin-$1/2$ resonances are given by

$$\mathcal{L}^{\mathrm{PS}}_{\pi N N^*_{1/2}} = -g_{\pi N N^*}\bar{\psi}_{N^*}\Gamma(\boldsymbol{\tau}\cdot\boldsymbol{\phi}_\pi)\psi_N + \mathrm{h.\,c.}\,, \tag{1a}$$

$$\mathcal{L}^{\mathrm{PS}}_{N^*_{1/2} K \Lambda} = -g_{N^*\Lambda K}\bar{\psi}_{N^*}\Gamma\phi_K\psi_\Lambda + \mathrm{h.\,c.}\,, \tag{1b}$$

where the Γ takes care of parity conservation. We use

$$\Gamma = \begin{cases} \mathbb{1} & \text{for odd parity} \\ \mathrm{i}\gamma^5 & \text{for even parity}\,, \end{cases}$$

and h. c. in Eqs. (1) denotes the *hermitean conjugate*.

The pseudovector Lagrangians involve the derivative of the pion wave function rather than the wave function itself. This introduces an additional mass dimension, which is taken care of by a "rescaling" of the coupling constant. It also ensures the matching of the on-shell behaviour the two types of Lagrangians. The pseudovector Lagrangians are given by

$$\mathcal{L}^{\mathrm{PV}}_{\pi N N^*_{1/2}} = -\frac{g_{\pi N N^*}}{m_{N^*} \pm m_N}\bar{\psi}_{N^*}\gamma^\mu\Gamma\partial_\mu(\boldsymbol{\tau}\cdot\boldsymbol{\phi}_\pi)\psi_N + \mathrm{h.\,c.}\,, \tag{2a}$$

$$\mathcal{L}^{\mathrm{PV}}_{N^*_{1/2}K\Lambda} = -\frac{g_{N^*K\Lambda}}{m_{N^*} \pm m_\Lambda}\bar{\psi}_{N^*}\gamma^\mu\Gamma\partial_\mu\phi_K\psi_\Lambda + \mathrm{h.\,c.}\,, \tag{2b}$$

where Γ is given by

$$\Gamma = \begin{cases} \mathrm{i} & \text{for odd parity} \\ \gamma^5 & \text{for even parity}\,, \end{cases}$$

and the upper and lower signs are used for even and odd parity resonances, respectively.

The spin-$3/2$ resonance Lagrangians are given by

$$\mathcal{L}_{\pi NN^*_{3/2}} = \frac{g_{\pi NN^*}}{m_\pi}\bar{\psi}^\mu_{N^*}\partial_\mu(\boldsymbol{\tau}\cdot\boldsymbol{\phi}_\pi)\psi_N + \mathrm{h.\,c.}\,, \tag{3a}$$

$$\mathcal{L}_{N^*_{3/2}K\Lambda} = \frac{g_{N^*K\Lambda}}{m_K}\bar{\psi}^\mu_{N^*}\partial_\mu\phi_K\psi_\Lambda + \mathrm{h.\,c.}\,. \tag{3b}$$

The values and signs of the various coupling constants are taken from [5]. These parameters describe well the associated $K^+\Lambda$ production in proton-proton collisions within a similar resonance picture. All the pion-resonance-kaon vertices that are of interest in this paper are involved in this reaction.

2.2 Resonance Propagators

The initial πN and the final $K\Lambda$ interaction vertices are connected by a propagator describing the evolution of the intermediate N^* resonance. For the spin-$1/2$ and spin-$3/2$ resonances the propagators are given by

$$\mathcal{D}_{1/2} = \mathrm{i}\frac{\gamma_\mu p^\mu + m}{p^2 - (m - \mathrm{i}\Gamma_{N^*}/2)^2} \tag{4}$$

and

$$\mathcal{D}^{\mu\nu}_{3/2} = -\mathrm{i}\frac{\gamma_\lambda p^\lambda + m}{p^2 - (m - \mathrm{i}\Gamma_{N^*}/2)^2}P^{\mu\nu}\,, \tag{5}$$

respectively. In eq. 5 we have defined

$$P^{\mu\nu} = \eta^{\mu\nu} - \frac{1}{3}\gamma^\mu\gamma^\nu - \frac{2}{3m^2}p^\mu p^\nu + \frac{1}{3m}\left(p^\mu\gamma^\nu - p^\nu\gamma^\mu\right)\,. \tag{6}$$

Γ_{N^*} in Eq. (4) and Eq. (5) is the total width of the resonance. It is introduced in the denominator to account for the finite life time of the resonances for decays into various channels. This is a function of the centre of mass momentum of the decay channel, and it is taken to be the sum of the widths for pion and rho decay (the other decay channels are considered only implicitly by adding their branching ratios to that of the pion channel) [5]. At this time, we neglect corrections to the resonance propagators from in-medium self-energies as no major change is expected in our results due to these effects. As pointed out in [5], the in-medium effects on the widths of the s- and p-wave resonances, which make the dominant contribution to the cross sections investigated here, are not substantial. The reason is that for the present purpose resonances occur only as intermediate states which implies an integration over their respective spectral distributions.

3 Nuclear Model

The spinors for the final bound hypernuclear state (corresponding to momentum p_Λ) and for the intermediate nucleonic state (corresponding to momenta p_N) are required to perform numerical calculations of various amplitudes. We assume these states to be of pure-single particle or single-hole configurations with the core remaining inert. In experimental measurements, however, core excited states have also been detected (see, eg. [1]). A covariant description of the core polarization can, in principle, be achieved by nuclear many-body theory. However, those procedures are tedious and they are out of the scope of our

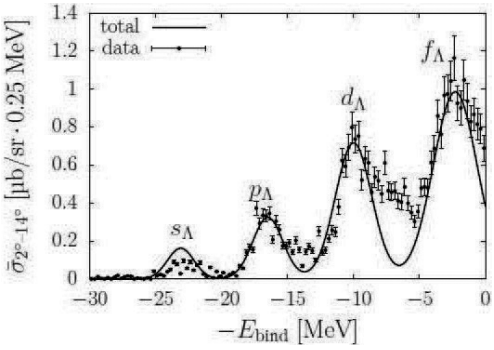

Fig. 1: The total averaged cross section for the ${}^{89}_{\Lambda}$Y hypernucleus [5]. The date are taken from [6].

present study. Therefore, here we concentrate on those transitions which involve pure single-particle and single-hole states.

The spinors in momentum space are obtained by a Fourier transformation of the corresponding coordinate space spinors which are solutions of the Dirac equation with self-energies consisting of an attractive scalar part ($V_{\rm s}$) and a repulsive vector part ($V_{\rm v}$), both including isoscalar and isovector contributions [12,13]. For numerical convenience, the self-consistent Dirac-Hartree-Fock self-energies obtained by our DDRH approach [12,13] are parametrized in terms of static potentials with Wood–Saxon form factors [5].

4 Associated Strangeness Production in Hadron-Nucleus Reactions

4.1 Pion-induced Strangeness Production

After having established the effective Lagrangians and the coupling constants, one can write down the matrix elements, by following the well known Feynman rules. As an example, let us consider in some detail the case of a π^+, K^* reaction [5]. The isospin part is treated separately which gives rise to a constant factor for each graph. Thus, the matrix element for our process is given by

$$\mathcal{M} = \int \frac{\mathrm{d}^4k_N}{(2\pi)^4}\int \frac{\mathrm{d}^4k_\Lambda}{(2\pi)^4}\int \frac{\mathrm{d}^4p}{(2\pi)^4}\,\phi_K^*(p-k_\Lambda)\bar{\psi}_\Lambda(k_\Lambda)\Gamma_\alpha \times \mathrm{i}\frac{\gamma_\mu p^\mu + m_{N^*}}{p^2-(m_{N^*}-\mathrm{i}\Gamma_{N^*}/2)^2}\Gamma_\beta\phi_\pi(p-k_N)\psi_N(k_N)\ . \quad (7)$$

In Eq. (7), the factors Γ_α and Γ_β are given according to the interaction Lagrangians, Eqs. (1)–(3) where the indices distinguish different kinds of vertex operators. The meson wave functions are denoted by ϕ, and the in-medium Dirac spinors ψ are the solutions of the single-particle Dirac equations.

The incident pion and outgoing kaon fields are given by

$$\phi_\pi^{(+)}(p'_\pi) = \delta(p'_{\pi 0}-E_\pi)\sum_{\ell_\pi m_\pi}(-1)^{\ell_\pi}Y^*_{\ell_\pi m_\pi}(\hat{p}_\pi)Y_{\ell_\pi m_\pi}(\hat{p}'_\pi) \times f_{\ell_\pi}(k'_\pi,k_\pi)\ , \quad (8)$$

$$\phi_K^{(-)*}(p'_K) = \delta(p'_{K0}-E_K)\sum_{\ell_K m_K}(-1)^{\ell_K}Y_{\ell_K m_K}(\hat{p}_K)Y^*_{\ell_K m_K}(\hat{p}'_K) \times f_{\ell_K}(k'_K,k_K)\ , \quad (9)$$

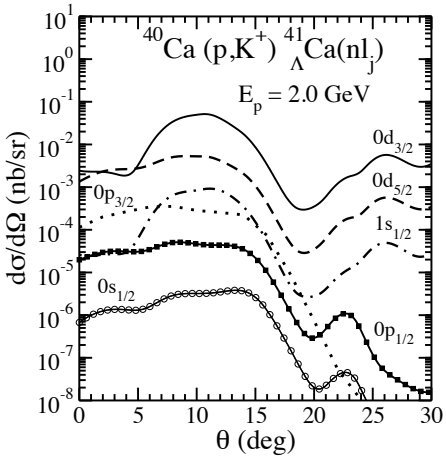

Fig. 2: Angular distributions for proton-induced hypernuclear production on a ^{40}Ca target nucleus at T_{lab} =2 GeV. Results for various final Λ single particle orbitals are shown [4].

where E_π and E_K represents the energies of the incident pion and outgoing kaon, respectively; p_K and p_π denote the meson on-shell momenta. The functions f_ℓ are given by

$$f_\ell(k',k) = \frac{1}{2\pi^2}\int_0^\infty j_\ell(k'r) f_\ell^C(r) r^2 \mathrm{d}r \ , \tag{10}$$

where the wave function f_ℓ^C is the coordinate space solution of the Klein–Gordon equation with a meson-nucleus optical potential and on-shell momentum k. Corresponding expressions for photo-production and proton-induced strangeness production on nuclei are found in refs. [2–4].

Besides the genuine production vertex, the size of reaction cross section is also determined by initial and final state interactions of the incoming pion and the outgoing kaon, respectively. In both cases we use a relativistic eikonal approach [5,14]. A typical result of our π^+, K^+ model calculations is shown in Fig.1 where we compare theoretical results for the production of the $^{89}_{\Lambda}$Y hypernucleus to data measured at KEK by Hotchi et al. [6].

4.2 Proton-induced Strangeness Production

Obviously, the production process can be induced by a variety of probes. Another important hadronic reaction scenario is proton-induced strangeness production, measured e.g. at COSY for elementary targets and at J-PARC for nuclear targets. Different types of reactions are possible, like $p + A(N,Z) \rightarrow {}_\Lambda B(N-1,Z)+n+K^+, p+A(N,Z) \rightarrow {}_\Lambda B(N,Z-1)+p'+K^+$, and $p+A(N,Z) \rightarrow {}_\Lambda B(N,Z)+K^+$ where N and Z are the target neutron and proton numbers, respectively. Here, we study the last reaction [to be referred to as $A(p,K^+)_\Lambda B$] which is exclusive in the sense that the final channel is a two body system. In this reaction the momentum transfer to the nucleus is much larger than in (π^+, K^+) reaction, about 1.0 GeV/c as compared to about 0.330 GeV/c in forward direction.

The elementary kaon production process proceeds as discussed before mainly through intermediate nucleon resonances via a collision of the projectile nucleon with one of its target counterparts, thereby exciting intermediate baryonic resonances decaying subsequently into a kaon and a Λ hyperon. The $N^*(1650)$, $N^*(1710)$, and $N^*(1720)$ states are especially important. The nucleon and the hyperon involved in the production process are captured into nuclear orbitals while the kaon is scattered onto its

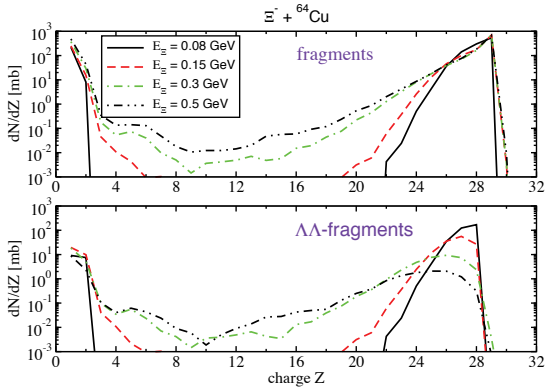

Fig. 3: GiBUU+SMM calculations for the charge distributions of nuclear fragments (upper panel) and double-Λ clusters (lower panel) for antiproton+^{64}Cu reactions at various kinetic energies of the Ξ-beam in the laboratory frame, as indicated [7].

mass shell. Three active bound state baryon wave functions are taking part in the reaction allowing the large momentum transfer to be shared among the participants.

Angular distributions for associated strangeness production in a (p, K^+) reaction at E$_p$ =2 GeV on a ^{40}Ca target are shown in Fig.2. Although initial and final state interactions are at present not included the magnitude of the cross sections in the nano- to picobarn range can be expected to be realistic, ranging at the lower end of the experimental feasibility. The shapes of the angular distributions are depending sensitively on the quantum numbers of the orbits into which the Λ is captured.

5 Production of $S = -2$ Hypernuclei in Antiproton-Nucleus Collisions

Experimental information on single-Λ hypernuclei is conventionally provided by spectroscopy using pion or kaon beams, by high energy protons, and by electro-production. In these cases the structure of rather cold hypernuclei at ground state density is explored. In reactions induced by intermediate energy heavy-ion beams, however, a quite different scenario is encountered: hyperons are produced at densities above saturation, in turn being captured by nuclear fragments. In such reactions one might explore the high density behavior of the hyperon-nucleon interaction. The production of single-Λ hypernuclei in reactions between heavy nuclei was first theoretically proposed by Kerman and Weiss as early as 1973 [15]. Complementary studies then followed by several groups [16–18]. Observations on hypernuclei and antihypernuclei in relativistic heavy-ion collisions have been reported recently by the STAR Collaboration [19] (see also for an experimental overview Ref. [20]). Furthermore, the HypHI and FOPI Collaborations [21,22] at GSI have performed heavy-ion experiments.

The formation of double-Λ hypernuclei is in the focus of strangeness-nuclear physics since the experimental discovery of the ${}^{10}_{\Lambda\Lambda}Be$ and the ${}^{6}_{\Lambda\Lambda}He$ hypernuclei. For this purpose the copious production of rather slow Ξ-hyperons is necessary. One of the key projects in the new FAIR facility is the experimental investigation of $S = -2$ hypernuclei by the PANDA Collaboration [20]. Here one intends to form hypernuclei by two-step reactions induced first by a $\bar{p}$-beam at momenta around 3 GeV/c, i.e. close to the $\Xi\overline{\Xi}$ production threshold ($P_{lab}^{thr} = 2.62$ GeV/c), and then by low energy Ξ-beams, produced in the reaction of the first target with $\bar{p}$-beams. In contrast to reactions induced by protons/heavy-ions, here the main production mechanism for hypernuclei arises from in-medium $\overline{p}N$-annihilation with high cross section at PANDA energies.

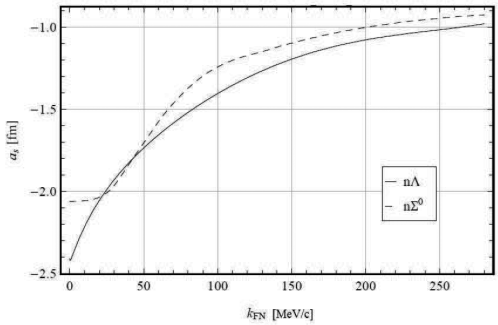

Fig. 4: In-medium $N\Lambda$ and $N\Sigma^0$ scattering lengths as a function of the nucleon Fermi momentum.

An appropriate theoretical approach, being able to describe the complexity of the reaction process, is a combination of covariant transport theory (GiBUU) [23] and a statistical fragmentation model (SMM) as used in [7]. Results of such a calculation are displayed in Fig. 3, where results for the fragment yields concerning the reaction with the secondary target are shown. According these theoretical calculations a copious production of double-Λ hyperclusters is possible at PANDA.

6 Hyperon-Nucleon Interactions in Nuclear Matter

A central question of hypernuclear physics is to understand the dynamics of hyperons in nuclear matter. Hyperon-nucleon (YN) and hyperon-hyperon (YY) interactions are the key quantities to be derived from the formation and spectroscopy of hypernuclei. The derivation of YN and YY interactions is a challenge to theory. At present, the data base is extremely poor, by far not broad enough in order to determine the free space interactions unambiguously, as e.g. seen in [24,25]. We have started a new survey, attempting a comprehensive description of free space and in nuclear matter [26]. Using the Bonn NN-potential as a starting point, guaranteeing an accurate description of NN-scattering observables, the model is being extended into the $S = -1$ YN region and further extensions into the $S = -2$ YY sector are envisioned. Our final goal is to have at hand a reliable BB interaction model in the lowest $SU(3)$ octet sector for asymmetric nuclear matter. A new feature of YN interactions is the mixing among the various $S = -1$ YN configurations of the same total charge Q and isospin I, e.g. for $Q = 0, I = \frac{1}{2}$ channel mixing occurs for the $\Lambda n, \Sigma^0 n$ states. Hence, in general we solve a coupled channels problem in free space and in nuclear matter for the YN interactions:

$$T_{ij}(q,q') = V_{ij}(q,q') + \sum_k \int \frac{d^4p}{(2\pi)^4} V(q,p) g_k^*(p) Q_{Fk}(p) T_{kj}(p,q') \tag{11}$$

describing the propagation of the intermediate $(BB')_k$ pair by he in-medium propagator g_k^*. In nuclear matter, we account for the Pauli-exclusion principle in the intermediate states by the projector Q_{Fk} ($Q_{Fk} \to 1$ in free space), blocking states inside the Fermi spheres of the different baryon species in hypermatter. The Lippmann-Schwinger equation, eq.11, is solved in the particle basis, taking care of the different thresholds in the $N - \Lambda - \Sigma$ system. As a typical result, the variation of the s-wave scattering length as a function of the nucleon density in symmetric nuclear matter is shown in Fig.4.

7 Summary

Strangeness production on nuclei was considered by various reaction scenarios. Coherent pion- and proton-induced reactions leading to the $K^+\Lambda$ final channel were investigated. Starting from a Lagrangian

formulation explicit expressions for the production vertices and reaction matrix elements were derived. Nuclear wave functions are obtained in the microscopic DDRH approach, expressing Dirac-Brueckner-Hartree-Fock interactions by density dependent meson-baryon coupling constants. KEK data for hypernuclear production by (π^+, K^+) reactions were well described. The production of $S = -2$ double-Λ hypernuclei in antiproton-nucleus collisions in the PANDA energy regime was explored in a transport theoretical approach. A first quantitative prediction on $\Xi\overline{\Xi}$ production and the formation of secondary Ξ beams was obtained. Hyperon-nucleon interactions in free space and asymmetric nuclear matter were studied in a coupled channels Brueckner G-matrix approach.

Acknowledgements:
Supported in part by HGF, GSI, BMBF, and DFG, contract Le439/7, Le439/8, and Le439/9.

References

[1] O. Hashimoto and H. Tamura, Prog. Part. Nucl. Phys. **57** (2006) 564.
[2] R. Shyam, H. Lenske, and U. Mosel, Phys. Rev. C**69** 065205 (2004).
[3] R. Shyam, H. Lenske, and U. Mosel, Nucl. Phys. A**764** 313 (2006).
[4] R. Shyam and O. Scholten, Phys. Rev. C**78** 065201 (2008).
[5] S. Bender, R. Shyam, H. Lenske, Nucl. Phys. A**839** 51 (2010).
[6] H. Hotchi et al., Phys. Rev. C**64** 044302 (2001).
[7] T. Gaitanos , A.B. Larionov, H. Lenske, U. Mosel, Nucl. Phys. A**881** 240 (2012).
[8] R. E. Chrien and C. B. Dover, Ann. Rev. Nucl. Part. Sci. **39** (1989) 113.
[9] H. Bando, T. Motoba, and J. Žofka, Int. J. Mod. Phys. A**5** (1990) 4021.
[10] V. Shklyar, H. Lenske, and U. Mosel, U., Phys. Rev. C**72** (2005) 015210.
[11] V. Shklyar, H. Lenske, U. Mosel, Phys. Lett. B**650** 172 (2007).
[12] C. M. Keil, F. Hofmann, and H. Lenske, Phys. Rev. C**61** 064309 (2000).
[13] C. Keil and H. Lenske, Phys. Rev. C**66** 054307 (2002).
[14] C. J. Joachain, *Quantum collision theory*, North-Holland Publishing Company, Amsterdam, 1975.
[15] A.K. Kerman, M.S. Weiss, Phys. Rev. C**8** 408 (1973).
[16] Z. Rudy, et al., Z. Phys. A**351** 217 (1995).
[17] J. Aichelin, K. Werner, Phys. Lett. B**274** (1992) 260 (1992).
[18] M. Wakai, Nucl. Phys. A**547** 89c (1992).
[19] STAR Collaboration, Science**328** 58 (2010).
[20] J. Pochodzalla, Acta Phys. Polon. B**42** 833 (2011).
[21] C. Rappold, T.R. Saito, S. Bianchin, O. Borodina, et al., Nucl. Instrum. Meth. A**622** 231 (2010).
[22] T.R. Saito, S. Bianchin, O. Borodina, J. Hoffmann, et al., Int. J. Mod. Phys. E**19** 2656 (2010).
[23] O. Buss, T. Gaitanos, K. Gallmeister, H. van Hees, M. Kaskulov, O. Lalakulich, A. B. Larionov, T. Leitner, J. Weil, U. Mosel, Transport-theoretical Description of Nuclear Reactions Phys. Rept. **512** 1 (2012).
[24] T. A. Rijken, V. G. J. Stoks, Y. Yamamoto, Phys. Rev. C**59** 21 (1999).
[25] E. Epelbaum, H.-W. Hammer, Ulf-G. Meiσner, Rev. Mod. Phys.**81** 1773 (2009).
[26] A. Obermann, Thesis, JLU Giessen, Oct. 2011.

Plasma Nuclear Science

D.P.McNabb
Lawrence Livermore National Laboratory, Livermore, USA

NIF and Omega provide new capabilities for studying the interplay between nuclear and plasma processes. The temperature and density conditions of the dynamic plasma environment created by ICF facilities probe new, as yet unachievable degrees of freedom in nuclear reaction mechanisms and nuclear-atomic interactions, enabling new research directions in nuclear physics and fostering the growth of a new interdisciplinary field: Plasma Nuclear Science.* These new research directions include the explorations of the effects of a hot, dense plasma environment on stellar and Big Bang nucleosynthesis, the role of the coupling between nuclear and plasma degrees of freedom on nuclear excitations and reaction rates, and the use of nuclear techniques to obtain a better understanding of thermonuclear hydrodynamics and transport phenomena. We recently used the Omega Laser Facility to make precise measurements of a fundamental nuclear process -- the elastic scattering of neutrons off heavy forms of hydrogen, deuterium (D) and tritium (T). This is the first time that a fundamental nuclear physics experiment has been achieved using a high-energy-density laser facility. An overview of this and some of the other plasma nuclear science experiments that have been performed will be provided.

*Basic Research Directions for User Science at the National Ignition Facility, Report on the National Nuclear Security Administration – Office of Science Workshop on Basic Research Directions on User Science at the National Ignition Facility, chaired by John Sarrao, Kimberly Budil, and Michael Wiescher (2010).

One and Two-pion production in pp reactions with the High Acceptance Di-Electron Spectrometer at GSI

B. Ramstein[14], *G. Agakishiev*[6], *C. Behnke*[7], *D. Belver*[16], *A. Belyaev*[6], *J.C. Berger-Chen*[8], *A. Blanco*[1], *C. Blume*[7], *M. Böhmer*[9], *P. Cabanelas*[16], *S. Chernenko*[6], *C. Dritsa*[10], *A. Dybczak*[2], *E. Epple*[8], *L. Fabbietti*[8], *O. Fateev*[6], *P. Fonte*[1,a], *J. Friese*[9], *I. Fröhlich*[7], *T. Galatyuk*[4,b], *J. A. Garzón*[16], *K. Gill*[7], *M. Golubeva*[11], *D. González-Díaz*[4], *F. Guber*[11], *M. Gumberidze*[14], *S. Harabasz*[4], *T. Hennino*[14], *R. Holzmann*[3], *P. Huck*[9], *C. Höhne*[10], *A. Ierusalimov*[6], *A. Ivashkin*[11], *M. Jurkovic*[9], *B. Kämpfer*[5,c], *T. Karavicheva*[11], *I. Koenig*[3], *W. Koenig*[3], *B. W. Kolb*[3], *G. Korcyl*[2], *G. Kornakov*[16], *R. Kotte*[5], *A. Krása*[15], *E. Krebs*[7], *F. Krizek*[15], *A. Kozuch*[2], *H. Kuc*[2,14], *A. Kugler*[15], *A. Kurepin*[11], *A. Kurilkin*[6], *P. Kurilkin*[6], *V. Ladygin*[6], *R. Lalik*[8], *S. Lang*[3], *K. Lapidus*[8], *A. Lebedev*[12], *L. Lopes*[1], *M. Lorenz*[7], *T. Liu*[14], *L. Maier*[9], *A. Mangiarotti*[1], *J. Markert*[7], *V. Metag*[10], *J. Michel*[7], *C. Müntz*[7], *R. Münzer*[8], *L. Naumann*[5], *M. Palka*[2], *Y. Parpottas*[13,d], *T. Perez-Cavalcanti*[10], *V. Pechenov*[3], *O. Pechenova*[7], *J. Pietraszko*[7], *W. Przygoda*[2], *B. Ramstein*[14], *L. Rehnisch*[7], *A. Reshetin*[11], *A. Rustamov*[7], *A. Sadovsky*[11], *P. Salabura*[2], *T. Scheib*[7], *H. Schuldes*[7], *J. Siebenson*[8], *Yu.G. Sobolev*[15], *S. Spataro*[e], *B. Spruck*[10], *H. Ströbele*[7], *J. Stroth*[7,3], *P Strzempek*[2], *C. Sturm*[3], *O. Svoboda*[15], *A. Tarantola*[7], *K. Teilab*[7], *P. Tlusty*[15], *M. Traxler*[3], *H. Tsertos*[13], *T. Vasiliev*[6], *V. Wagner*[15], *M. Weber*[9], *C. Wendisch*[5,c], *M. Wisniowski*[2], *J. Wüstenfeld*[5], *S. Yurevich*[3], *Y. Zanevsky*[6].

(HADES collaboration)

[1]LIP-Laboratório de Instrumentação e Física Experimental de Partículas , 3004-516 Coimbra, Portugal

[2]Smoluchowski Institute of Physics, Jagiellonian University of Cracow, 30-059 Kraków, Poland

[3]GSI Helmholtzzentrum für Schwerionenforschung GmbH, 64291 Darmstadt, Germany

[4]Technische Universität Darmstadt, 64289 Darmstadt, Germany

[5]Institut für Strahlenphysik, Helmholtz-Zentrum Dresden-Rossendorf, 01314 Dresden, Germany

[6]Joint Institute of Nuclear Research, 141980 Dubna, Russia

[7]Institut für Kernphysik, Goethe-Universität, 60438 Frankfurt, Germany

[8]Excellence Cluster 'Origin and Structure of the Universe' , 85748 Garching, Germany

[9]Physik Department E12, Technische Universität München, 85748 Garching, Germany

[10]II.Physikalisches Institut, Justus Liebig Universität Giessen, 35392 Giessen, Germany

[11]Institute for Nuclear Research, Russian Academy of Science, 117312 Moscow, Russia

[12]Institute of Theoretical and Experimental Physics, 117218 Moscow, Russia

[13]Department of Physics, University of Cyprus, 1678 Nicosia, Cyprus

[14]Institut de Physique Nucléaire (UMR 8608), CNRS/IN2P3 - Université Paris Sud, F-91406 Orsay Cedex, France

[15]Nuclear Physics Institute, Academy of Sciences of Czech Republic, 25068 Rez, Czech Republic

[16]LabCAF. Dpto. Física de Partículas, Univ. de Santiago de Compostela, 15706 Santiago de Compostela, Spain

[a] also at ISEC Coimbra, Coimbra, Portugal

[b] also at ExtreMe Matter Institute EMMI, 64291 Darmstadt, Germany

[c] also at Technische Universität Dresden, 01062 Dresden, Germany

[d] also at Frederick University, 1036 Nicosia, Cyprus

[e] also at Dipartimento di Fisica Generale and INFN, Università di Torino, 10125 Torino, Italy

Abstract

We present exclusive meaurements of the pp→pnπ^+ and pp→ppπ^0 reactions at 1.25 GeV, 2.2 GeV and 3.5 GeV and of the pp→pp$\pi^+\pi^-$ reaction at 1.25 GeV with the High Acceptance Di-Electron Spectrometer at GSI. Total and differential cross-sections for the one-pion production channels are analyzed with the resonance model to extract the differential baryonic resonance contributions. A comparison of the two-pion production channels to effective

lagrangian model predictions is on-going. The two-pion invariant mass and opening angle distributions show sensitivity to the double $\Delta(1232)$ and N(1440) $\rightarrow \Delta\pi$ decays.

1 Introduction

The High Acceptance DiEelectron Spectrometer (HADES) [1] installed at GSI in Darmstadt was built to investigate dielectron production in heavy-ion collisions in the 1-3.5 AGeV range [2] in order to study the properties of vector mesons in the hot and dense nuclear medium. Proton-nucleus reactions are also investigated to probe cold nuclear matter [3]. Moreover, the experimental programme also comprises elementary reactions (pp, quasi-free np and a project of measurements with a pion beam) to study more selectively the different dilepton sources. In particular, baryonic resonances are important sources of dileptons through two mechanisms: their Dalitz decays (e.g. Δ/N$^\star \rightarrow Ne^+e^-$) and the mesonic decay with subsequent dilepton decay ($\pi^0 \rightarrow \gamma e^+e^-$, $\eta \rightarrow \gamma e^+e^-$, $\omega/\rho \rightarrow e^+e^-$). The possibility to measure simultaneously one and two-π production with the HADES detector is therefore a great advantage, since it constrains the hadronic cocktail used to describe the dilepton production. More generally, such data provide quantitative information on hadronic interactions, as well as resonance excitations and resonance properties.

Although one-pion production was studied quite extensively in the past, only very few experiments measured precise differential spectra (see [4] and references therein). When the incident energy increases from 1 to 3.5 GeV, the effect of resonances heavier than the $\Delta(1232)$ is expected and little is known about their production mechanisms. The production of $\pi^+\pi^-$ pairs is very complementary, since most baryonic resonances have a large, but poorly determined branching ratio into this channel. The reaction pp$\rightarrow$pp$\pi^+\pi^-$ has also been studied in the past between 0.7 and 2 GeV using bubble chambers [5]. Recently, exclusive high-statistics measurements have become available for incident proton kinetic energies of 650 MeV (*i.e.* near threshold) up to 1.36 GeV from the PROMICE/WASA [6, 7], CELSIUS/WASA [8], COSY-TOF [9] and ANKE [10] experiments. At energies around 1.3 GeV, the branching ratios of the N(1440) resonance into the $\Delta(1232)\pi$ and N$(\pi\pi)_{Swave}$ are an important issue related to the intrinsic structure of the N(1440) resonance. Of high interest is also the relative contribution of double $\Delta(1232)$ and N(1440) excitations, since it depends on their respective production mechanisms and is sensitive e.g. to the exchange of ρ mesons. We report here on exclusive meaurements in the channels pp$\rightarrow$pnπ^+, pp$\rightarrow$ppπ^0 at 1.25 GeV, 2.2 GeV and 3.5 GeV and pp$\rightarrow$pp$\pi^+\pi^-$ at 1.25 GeV.

2 One-pion production channels

The pp$\rightarrow$pn$\pi^+$and pp$\rightarrow$ppπ^0 channels were selected using events with the reconstruction of one proton and one π^+ or two protons. Particle identification was provided by the correlation between time-of-flight measurements and momentum reconstruction. Events from pp elastic scattering were rejected using their angular correlation and events from the two-pion production processes using the missing mass. The absolute normalization of the data was provided with a precision of 6% at 1.25 GeV and 10% at 2.2 GeV and 3.5 GeV by the elastic scattering events for which the cross-section is known. In addition, the data were corrected for reconstruction efficiencies which were determined using simulations, with a precision ranging from 8% at 1.25 GeV to 17% at the highest energies.

Under the assumption that intermediate baryon resonances play a dominant role in π, η and ρ production, a model was developed by Teis et al. [11], based on an incoherent sum of various resonance contributions. The matrix element of the $\Delta(1232)$ production was calculated within the OPE model [12], which had been adjusted to available differential distributions of pion production in the pp$\rightarrow$pnπ^+ channel at incident kinetic energies in the range 0.9-1.5 GeV. The other matrix elements were kept constant and were determined by fitting the total meson production cross sections. As this model, with some variants, is the basis for different transport models (*e.g.* [13]) it is instructive to compare its predictions to the

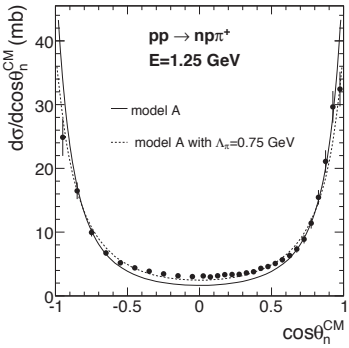

Fig. 1: (Color on-line) Angular distribution of neutron in center-of-mass system after acceptance correction for the pp→pnπ^+ reaction at 1.25 GeV. Data (black points) are compared to simulations based on model A (see text) with Λ_π=0.63 GeV (solid curve) and the modified version with Λ_π=0.75 GeV (dashed curve). Both simulation curves are normalized to reproduce the integrated experimental yield.

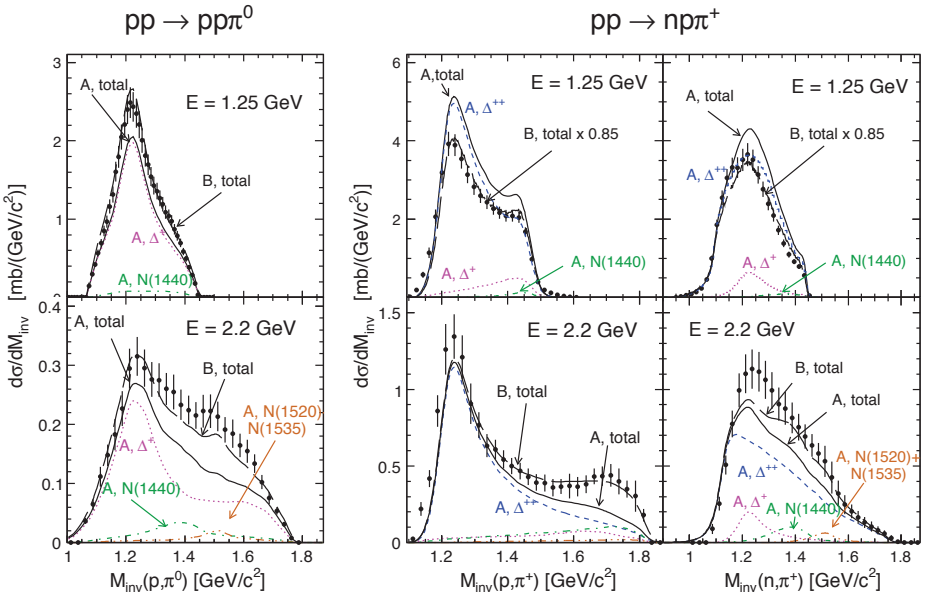

Fig. 2: (Color on-line) πN invariant mass distributions (full dots) measured in pp→ppπ^0 and pp→pnπ^+ reactions at 1.25 GeV (top row) and 2.2 GeV (bottom row). The data are compared inside the detector acceptance on an absolute scale to the predictions of the model A (see text) with contributions of Δ^+(1232) (pink dotted curve), Δ^{++}(1232) (dashed blue curve), N(1440) (green short dash-dotted curve) and N(1520)+N(1535) (long dash-dotted light brown curve). The long dashed curve shows the result of the model B (see text) with a scaling factor of 0.85 applied in the case of pp→pnπ^+ at 1.25 GeV.

measured differential distributions. Fig. 1 shows the neutron angular distribution in the center of mass system measured in the pp→pnπ^+ channel, after acceptance corrections. The error bars on the picture

include statistical and point-to-point systematic errors. Since the dominant process is pp→nΔ^{++}, this distribution reflects the forward/backward peaked Δ resonance production, as expected from the peripheral character of the process. The data are compared with the resonance model A, which is a variant of the Teis model, where we introduced pp and pn Final State Interaction, an anisotropic angular distribution for the N(1440) production, as well as an anisotropic $\Delta(1232)$ decay angular distribution (see [4] for details). The model underestimates the data around 90° by 40%. This discrepancy can be reduced to 15% by changing the cut-off parameter Λ_π of the πNΔ vertex.

The distributions of the (p,π^0), (p,π^+) and (n,π^+) invariant masses for T_p = 1.25 and 2.2 GeV are shown in Fig. 2. They are compared both to model A, as above, and to model B which contains modifications allowing for a better reproduction of both angular distributions, yields and invariant masses simultaneously. These modifications are described in more details in [4]. At 1.25 GeV, the Λ_π cut-off parameter was changed from 0.63 GeV to 0.75 GeV and the $\Delta(1232)$ production angular distribution was further adjusted to describe the neutron angular distribution in the pp→pnπ^+ channel. In this way, the proton angular distribution in the pp→ppπ^0 channel was also better reproduced. At 2.2 GeV, the production cross sections for N(1440), N(1520) and N(1535) resonances were increased and a non-resonant contribution was introduced. Absolute cross sections could be determined after acceptance corrections (Table 1) and were found to be in agreement with existing systematics.

An analysis of the data obtained in the pp→pnπ^+ and pp→ppπ^0 channels at 3.5 GeV is also being finalized. The cross-sections for the production of the various resonances were estimated using simultaneous fits of the invariant masses and angular distributions obtained in both isospin channels. For the production of the $\Delta(1232)$, the t dependence given by the OPE model [12] was used, while for the other resonances, a dependence of the form $d\sigma/dt = A/t^\alpha$ was chosen, and the parameters A and α were fitted to the data. These cocktails of baryonic resonances are then used to calculate the dielectron yields in the pp→ppe^+e^- reaction.

reaction	pp→pnπ^+		pp→ppπ^0	
energy	1.25 GeV	2.2 GeV	1.25 GeV	2.2 GeV
cross section (mb)	17.1 ± 2.0	14.45 ± 3.2	3.74 ± 0.48	4.15 ± 0.85
acceptance corrections	± 1.0	±1.1	± 0.2	±0.2
normalization	± 1.1	± 1.6	± 0.25	± 0.46
efficiency	± 1.3	±2.5	±0.33	± 0.65
event selection	± 0.3	± 0.7	± 0.12	± 0.2
statistics	± 0.01	± 0.01	± 0.003	± 0.004

Table 1: Cross sections for exclusive one-pion production channels measured by HADES are given with the total error, calculated as the quadratic sum of the statistical and systematic errors listed in the following rows.

3 Two-pion production

Figure 3 exhibits experimental distributions of the invariant mass and opening angle of $\pi^+\pi^-$ in the center-of-mass system in comparison to pure phase space (PHSP) calculations, which have been normalized to reproduce the area of the experimental distribution. Only statistical errors are presented. The systematic errors are about 10% due to the correction on the efficiency and normalisation on pp elastic scattering. It is seen, that both experimental distributions deviate from PHSP calculations. An enhancement can be observed at low $\pi^+\pi^-$ invariant masses which is not present in the simulation with the PHSP only. Correlatively, the PHSP distribution underestimates the yield at small opening angles. A similar effect can be seen with the preliminary data obtained by the HADES collaboration in the pn→pn$\pi^+\pi^-$ channels [14].

Such effects were also studied by the WASA and COSY-TOF collaborations in the pp→pp$\pi^+\pi^-$ channel from threshold up to 0.8 GeV [6,7,9] as well as in pp→pp$\pi^0\pi^0$ from 0.775 GeV up to 1.3 GeV [15,16]. Two lagrangian models were used to analyse these data, [17,18], from respectively Chinese and Spanish groups. A common feature of these models is the dominance of the N(1440) excitation close to threshold and the increase of the double Δ excitation when the incident energy increases. However, the models differ by the importance of the ρ-exchange contribution to the double $\Delta(1232)$ excitation and by the relative branching ratios of the N(1440) resonance into the $\Delta(1232)\pi$ and $N(\pi\pi)_{Swave}$. Modifications of the Spanish model have been proposed in [16], which allow for a good description of the differential spectra measured in the pp→pp$\pi^0\pi^0$ reaction by CELSIUS/WASA from 1 to 1.3 GeV. A comparison of the data obtained in the pn→pn$\pi^+\pi^-$ and pp→pp$\pi^+\pi^-$ to the Chinese and Spanish models [17,18] and to the modified version of the Spanish model [16] is on-going. The invariant mass ($M_{\pi^+\pi^-}$) and the opening angle in center-of-mass ($\cos\delta_{\pi^+\pi^-}$) of the pion pair are the most sensitive distributions to the different model contributions. A double-hump structure in the $\pi^+\pi^-$ invariant mass distribution, as observed in the experimental data (Fig. 3) also appears in the models as being due either the $\Delta\Delta$ excitation via ρ exchange or to the decay channel of the Roper resonance N(1440) into $\pi\Delta$. No structure in the $\pi\pi$ invariant mass is expected for pure N(1440) →$N(\pi\pi)_{Swave}$ decay. In the pn→d$\pi^0\pi^0$ reaction, a prominent peak at invariant masses is observed (the ABC effect) and interpreted as being due to the presence of an isoscalar resonance in the pn system [19] around 2.4 GeV/c^2. To check this interpretation, a consistent description of the different $\pi\pi$ production channels in pp and pn reactions needs to be achieved. Thus, in addition to the pp→pp$\pi^+\pi^-$ and pn→pn$\pi^+\pi^-$ channels, an analysis of the pn → d $\pi^+\pi^-$ channel measured by HADES is also on-going.

The OPER model [20] based on the exchange of reggeized pions had been successfully used to describe bubble chamber data on np → np$\pi^+\pi^-$ reaction at momenta above 3 GeV/c [21]. This model can be applied for the description of the NN→NN$\pi\pi$ reaction at momenta below 3 GeV/c by taking into account the mechanism of one baryon exchange (OBE) and is therefore also used for the analysis of two pion production channels measured by HADES.

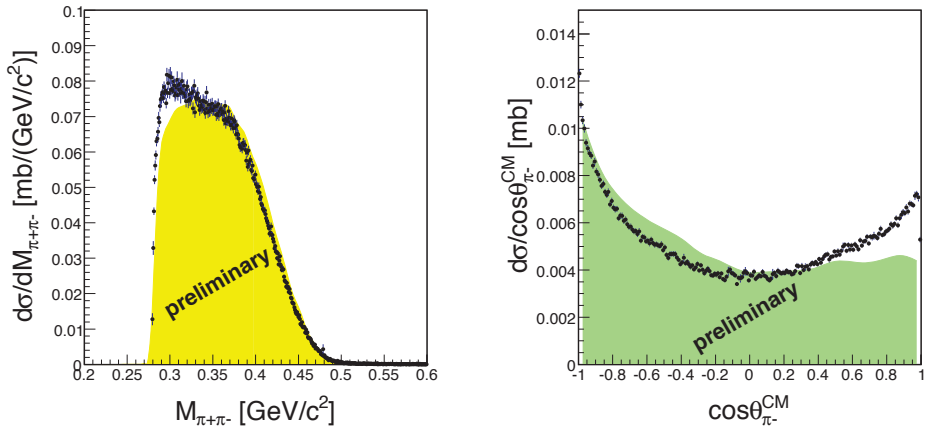

Fig. 3: Distributions of the $\pi^+\pi^-$ invariant mass $M_{\pi^+\pi^-}$ (left) and the $\pi^+\pi^-$ opening angle in the center of mass $\delta_{\pi^+\pi^-}$ (right) for the pp → $pp\pi^+\pi^-$ reaction at an incident beam energy of 1.25 GeV measured in HADES acceptance are shown to corresponding distributions from a phase space calculation. Only statistical errors are shown.

4 Conclusion

The measurement of one and two-pion production in elementary reactions with the HADES experimental set-up allows to test and improve the resonance model, which is the basis of transport models. More generally, the high statistics differential distributions provided by such measurements bring detailed information on baryonic resonance excitation and decay. The $\pi^+\pi^-$ invariant mass and opening angle distributions show sensitivity to the baryonic resonance excitation and decay. The analysis of the $\pi^+\pi^-$ production channels with effective lagrangian models will complement the extensive investigations made by the WASA collaboration in the $\pi^0\pi^0$ channel and will provide tests for a consistent description of double pion production in different isospin states.

5 Acknowledgments

The collaboration gratefully acknowledges the support by CNRS/IN2P3 and IPN Orsay (France), by SIP JUC Cracow (Poland) (NN202 286038, NN202198639), by HZDR, Dresden (Germany) (BMBF 06DR9059D), by TU München, Garching (Germany) (MLL München, DFG EClust 153, VH-NG-330, BMBF 06MT9156 TP5, GSI TMKrue 1012), by Goethe-University, Frankfurt (Germany) (HA216/EMMI, HIC for FAIR (LOEWE), BMBF 06FY9100I, GSI F&E), by INFN (Italy), by NPI AS CR, Rez (Czech Republic) (MSMT LC07050, GAASCR IAA100480803), by USC - Santiago de Compostela (Spain) (CPAN:CSD2007-00042).

References

[1] G. Agakichiev *et al*. (HADES collaboration), Eur. Phys. J. **A41**, 243 (2009).

[2] G. Agakichiev *et al*. (HADES collaboration), Phys. Rev. Lett. **98**, 052302 (2007); Phys. Lett. **B663**, 43 (2008); G. Agakishiev *et al*. (HADES collaboration), Phys. Rev. **C84**, 014902 (2011).

[3] G. Agakichiev *et al*. (HADES collaboration), Phys. Lett. **B715**, 304 (2012)

[4] G. Agakishiev *et al*. (HADES collaboration), Eur. Phys. J. **A48**, 74 (2012).

[5] A. M. Eisner *et al*., Phys. Rev. **138**, B670 (1965); D. C. Brunt *et al*., Phys. Rev. **187**, 1856 (1969). F. Shimizu *et al*., Nucl. Phys. **A389**, 445 (1982). L.G. Dakhno *et al*., Sov. J. Nucl. Phys. **37**, 540 (1983).

[6] W. Brodowski *et al*., Phys. Rev. Lett. **88**, 192301 (2002).

[7] J. Patzold *et al*., Phys. Rev. **C67**, 052202 (2003).

[8] T. Skorodko *et al*., Phys. Lett. **B679** (2009) 30.

[9] S. Abd El-Bary *et al*., Eur. Phys. J. **A37**, 267 (2008).

[10] S. Dymov *et al*., Phys. ReV. Lett. **102**, 192301 (2009).

[11] S. Teis *et al*., Z. Phys. **A356**, 421 (1997).

[12] V. Dmitriev, O. Sushkov, and C. Gaarde, Nucl. Phys. **A459**, 503 (1986).

[13] H. W. Barz et al., The Open Nuclear & Particle Phys. J. **3**, 1 (2010); J. Weil, H. van Hees, and U. Mosel, Eur. Phys. J. **A48**, 111 (2012).

[14] A. Kurilkin *et al*. (HADES collaboration), proceedings of HSQCD conference, Saint-Petersburg, July2012, to be published.

[15] T. Skorodko *et al*., Eur. Phys. J. **A35**, 317 (2008).

[16] T. Skorodko *et al*., Phys. Lett. **B695**, 115 (2011).

[17] L. Alvarez-Ruso, E. Oset, and E. Hernandez, Nucl. Phys. **A633**, 519 (1998).

[18] X. Cao, B.-S. Zou, and H.-S. Xu, Phys. Rev. **C81**, 065201 (2010).

[19] M. Bashkanov *et al*., Phys. Rev. Lett. **102**, 052301 (2009).

[20] A. Jerusalimov, (2012) arXiv:1203.3330.

[21] C. Besliu *et al*., Sov. J. Nucl. Phys. **43**, 565 (1986).

Production of double Λ- Hypernuclei at the PANDA Experiment

A. Sanchez Lorente on behalf of the PANDA collaboration[*]
Helmholtz Institut Mainz, Mainz Country

Abstract
Hypernuclear research will be one of the main topics addressed by the PANDA experiment at the planned Facility for Antiproton and Ion Research FAIR at Darmstadt (Germany). Thanks to the use of stored $\overline{p}$ beams, copious production of double Λ hypernuclei is expected at the PANDA experiment, which will enable high precision γ spectroscopy of such nuclei for the first time, and consequently a unique chance to explore the hyperon-hyperon interaction. One of the main challenge of this experiment is to evaluate to what extent excited particle stable states of these systems can be produced. In the present talk we explore this problem following the micro-canonical break-up of an initially excited double hypernucleus which is created by the absorption and conversion of a stopped Ξ^- hyperon. It will also be shown that independently on the spectrum of possible excited states in the produced double hypernuclei the formation of excited states dominates in our model. In addition, it will be seen that the ability to assign the various observable γ-transitions in a unique way to a specific double hypernuclei by exploring various light targets as proposed by the PANDA Collaboration requires a devoted hypernuclear detector setup, whose main aspects will be briefly introduced. The former setup consists of a primary nuclear target for the production of $\Xi^- + \overline{\Xi}$ pairs, a secondary active target for the hypernuclei formation and the identification of associated decay products and a germanium array detector to perform γ spectroscopy.

1 Introduction

The simultaneous production and implementation of two Λ particles into a nucleus is intricate. There is a possibility to produce multi-strange hypernuclei in heavy ion collisions via coalescence [1, 2]. The first observation of antihypernuclei by the STAR collaboration impressively illustrates the potential of this method [3]. However, high resolution spectroscopy of excited states is not feasible. To produce double hypernuclei in a more 'controlled' way the conversion of a captured Ξ^- and a proton into two Λ particles can be used. This process releases ignoring binding energy effects only 28 MeV. For light nuclei there exists therefore a significant probability of the order After an atomic cascade, the Ξ^- hyperon is eventually captured by a secondary target nucleus and converted via the $\Xi^- p \rightarrow \Lambda\Lambda$ reaction into two Λ hyperons. In a similar two-step process relatively low momentum Ξ^- can also be produced using antiproton beams in $\overline{p}p \rightarrow \Xi^-\overline{\Xi}^+$ or $\overline{p}n \rightarrow \Xi^-\overline{\Xi}$ reactions if this reactions happens in a complex nucleus where the produced Ξ^- can re-scatter [4, 6]. The advantage as compared to the kaon induced reaction is that antiprotons are stable and can be retained in a storage ring. This allows a rather high luminosity even with very thin primary targets. Because of the two-step mechanism, spectroscopic studies, based on two-body kinematics like in single hypernucleus production, cannot be performed. Spectroscopic information on double hypernuclei can therefore only be obtained via their decay products. The kinetic energies of weak decay products are sensitive to the binding energies of the two Λ hyperons. While the

[*]This research is part of the EU integrated infrastructure initiative Hadron- Physics Project under contract number RII3-CT-2004-506078. We acknowledge financial support from the Bundesministerium für Bildung und Forschung (bmb+f) under contract number 06MZ225I. We also thank the European Community-Research Infrastructure Integrating Activity Study of Strongly Interacting Matter (HadronPhysics2, Grant Agreement n. 227431; SPHERE network) under the Seventh Framework Programme of EU for their support

double pionic decay of light double hypernuclei can be used as an effective experimental filter to reduce the background [6] the unique identification of hypernuclei ground states only via their pionic decay is usually hampered by the limited resolution. Instead, γ-rays emitted via the sequential decay of excited double hypernuclei may provide precise information on the level structure.

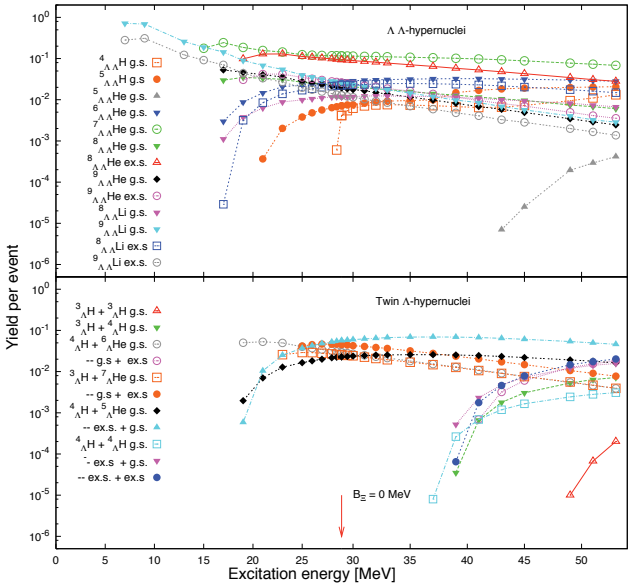

Fig. 1: Relative production probability of double hypernuclei top part) and single hypernuclei (lower part) for an excited $^{10}_{\Lambda\Lambda}Li$ nucleus as a function of its excitation energy.

2 Statistical decay of excited doubly Strange Nuclei

In order to limit the number of possible transitions and thus to increase the possible signal to background ratio, the experiment will focus on light secondary target nuclei. To describe this break-up process of the excited primary $\Lambda\Lambda$ nucleus and in order to estimate the population of individual excited states in double hypernuclei after the conversion of the Ξ^-, we have developed a statistical decay model which is reminiscent of the Fermi break-up model.We assume that the nucleus decays simultaneously into cold or slightly excited fragments. In the case of conventional nuclear fragments, we adopt their experimental masses in ground states, and take into account their particle-stable excited states. For single hypernuclei, we use the experimental masses and all known excited states. For double hypernuclei we apply theoretically predicted masses and excited states.

In the model we consider all possible break-up channels, which satisfy the mass number, hyperon number, charge, energy and momentum conservation, and take into account the competition between these channels. Since the excitation energy of the initially produced double hypernuclei is not exactly known,we performed the calculations as a function of the binding energy of the captured Ξ^-.

As an example Fig.1 shows excitation function of the relative production probability of double hypernulei top part) and single hypernuclei (lower part) for a primary $^{10}_{\Lambda\Lambda}Li$. Since the conversion of the Ξ^- is expected to take place close to B_Ξ=0 MeV the production of excited double hypernuclei is predicted to dominate in the PANDA experiment [5].

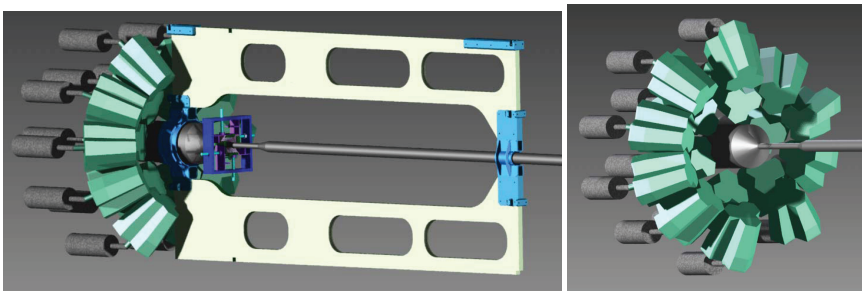

Fig. 2: Schematic view of the hypernuclear setup in PANDA. The figure on the top shows a side view of the hypernuclear experimental setup. The picture on the bottom, shows a detailed view of the interaction point surrounded by the secondary active target and the HPGe cluster array. In both pictures, the beam is coming from the left.

3 Integration inside the PANDA spectrometer

A big challenge to be solved in order to place the hypernuclear detector setup, is the limited space available at the entrance of the PANDA spectrometer. As a consequence, some modifications of the innerpart of the former spectrometer is needed. In particular, due to the fact that doubleΛ-Hypernuclei formation proceeds in a two-steps process, a dedicated target system consisting of a primary and secondary interaction point with an associated beam line is required (See Fig. 2). Since this target system has to be placed outside the interaction region of the PANDA spectrometer, detectors such as the MVD and Backward EndCap Calorimeter will be removed to avoid unnecessary radiation damage. In addition, the central frame dedicated to hold the beam line and the central tracker detectors will also be accordingly adapted to the hypernuclear setup.

3.1 Primary target

The main role of the primary target will be the production of low momentum Ξ hyperons. For this issue, light targets will be preferred in order to avoid a high hadronic background into the backward direction. Additionally, it is required that the luminosity of the $\overline{p}$-beam remains as constant as possible. As a consequence, beam losses, mainly due to coulomb scattering, must be kept low. The best candidate will be a 12C micro-wire target. On the other hand, high interaction rates will be avoided by choosing an appropiate fraction of the beam halo onto the target, what can be achieved by an monitoring mechanism where the beam as well as the target can be steered till the desired interaction rate is reached(See Fig.3).

3.2 Secondary active target

The purpose of the active volume of the secondary target is the tracking of charged particles generated during the first and the secondary interaction. As a consequence, its geometry is based on a compact structure where silicon microstrip detectors layers are in direct contact with absorber material [6]. In analogy to the germanium detectors array, this device has to be able to operate in extreme conditions such as a large hadronic environment, since it is close to the interaction point. Furthermore, the material budget on the detector volume must be kept low. The feasibility of such a device has recently been studied in Mainz, by evaluating the influence of putting layers of absorber material directly on a silicon sensor [11]. Results have not shown any significant change on the preamplifier signal caused by the vicinity of an boron layer [11]. The sensor utilized is a double sided microstrip detector with dimensions of $2\times2\,\mathrm{cm}^2$, a strip pitch of 50 μm, punch-through biasing and AC coupled contact pads. The sensor [13] is mounted on a L-shaped PCBoard displayed in Fig.4 and is bonded to a APV25-S1 front-end chip which features 128 channels. In order to avoid a huge load of hadronic flux on the readout electronics,

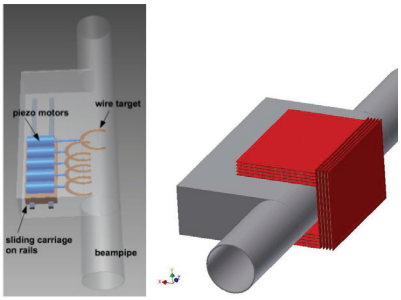

Fig. 3: Overview of the monitoring target system. The picture on the right shows the mechanism which held the target at a constant interaction rate by an automatic feedback system which continuously adjusts the wire positions via stepping motors. The target mechanism is mounted inside the vertex vessel, surrounded by the moveable parts of the secondary active target.

the use of Ultra-thin Al-Polyimide microcables([12]) is foreseen. The reason for that, is the routing of analog signals from silicon sensors to the readout system outside the interaction region and as a result to decrease the amount of material budget on the detecting volume. A prototype of such cables has already

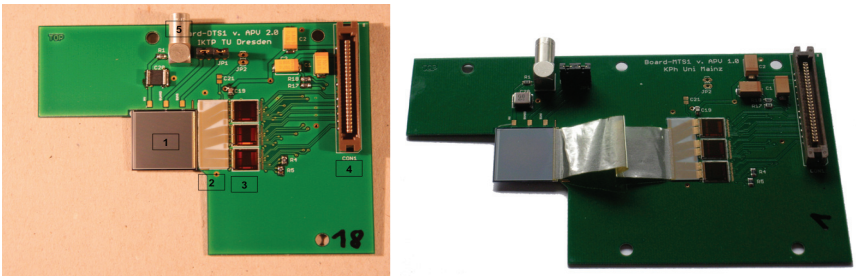

Fig. 4: Overview of the old and new PCB prototypes. The two pictures on the top show a photograph of a sensor module equipped to perform a double sided readout of the sensor(1) consisting of a PCB. Main components of each board are:(2) pitch adapter;(3) APV25 front-ends; (4) high density connector. The detector bias voltage (5) is supplied via one board. The picture on the right pannel shows a modified board to enable the connexion to a flexible ultra-thin cable(See Fig. 5).

been manufactured in SE SRTIIE, Kharkov, Ukraine. The cables were made on the basis of adhesiveless aluminium-polyimide foiled dielectrics(See Fig. 5). In addition, the PCB used for testing the analog signals, has to be modified accordingly (See Fig.4). This cable will be connected to the chip via bonding wires and to the readout electronics via a fine pitch connector. Further activities dedicated to investigate the effect of the cable length on the signal transmission are in progress. In addition, the performance of a holding structure for the whole device, is being studied. The mechanics of such a device has to be optimized considering thermal and mechanical properties of the holding structure.

4 The HPGe cluster Array

In order to increase the detection efficiency needed for a high resolution γ-Spectroscopy, the HPGe detectors array has to be placed as close as possible to the interaction point and cover a wide solid angle. Due to the limited space of the PANDA spectrometer, the arrangement of the germanium detector array

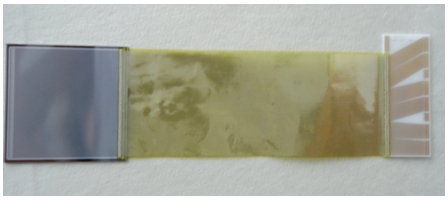

Fig. 5: First prototype of a flexible ultra-thin cable for the readout of the secondary active target. This cable has been made on the basis of adhesiveless aluminium-polyimide foiled dielectrics and it will be connected to the chip via bonding wires and to the readout electronics via a fine pitch connector.

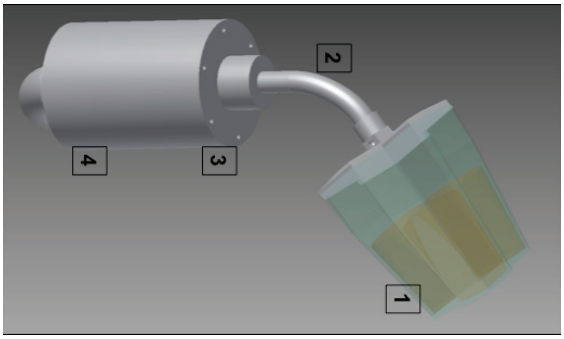

Fig. 6: HPGe triple cluster array assembled to a X-Cooler device. The encapsulated n-type coaxial HPGe crystals (EUROBALL) are arranged in a triangular form. The free space behind the crystals is foreseen for electronics. The connection of the crystal vessel to the cold head of the cooler is flexible to enable the placement of each cluster at backward axial angles. (1) encapsulated crystals, (2) flexible neck, (3) X- Cooler cold head, (4) X-Cooler Cable

will only be possible at backward axial angles. That means for instance, that the operation of these detectors will have to withstand a large flux of hadronic background and a high magnetic field [7], which can influence the good energy resolution (~ 3 keV at the 1,332 MeV line of Co^{60}) of these detectors. A possible solution for the space limitation has been to replace the standard cooling system, based on liquid nitrogen dewars, by a mechanical cooling device [8]. Fig. 6 shows a prototype for a triple germanium cluster array cooled by a electromechanical device. After installation of each of the encapsulated germanium crystals in the cryostat or vacuum vessel, the system has to reach optimum vacuum conditions to be properly operated.

The cooling efficiency of these devices has been successfully tested for three encapsulated germanium crystals without observing any additional worsening of the energy resolution [9]. Further investigations are currently taking place in Mainz at a dedicated test station. The scope of these studies is to evaluate to what extend the energy resolution of a Germanium detector, cooled electromechanically, can be influenced. For this reason, an ORTEC GEM-75205P device and analog readout electronics has been used. The energy resolution of such device has been measured with a ^{60}Co source considering two different cooling devices, namely a standard liquid nitrogen dewar and a X-Cooler device. For the case of a standard cooling system, the energy resolution was found to be 1.86 KeV for 1.332 keV line [1]. The one achieved by the X-cooler device has been 1.97 keV, which seems to be consistent. Figure 7 shows the energy spectra corresponding to the 1.332 keV line of ^{60}Co, obtained by considering the two cooling systems named above. The dashed spectrum corresponds to the case where the germanium crystal has been cooled electromechanically and although the energy resolution for this case is slightly worse, one

[1] The energy resolution provided by Ortec is about 2.05 keV

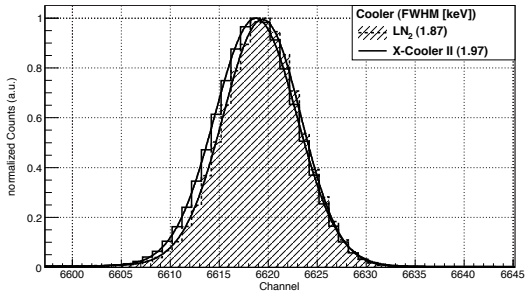

Fig. 7: Energy spectra corresponding to the 1,332 keV line of ^{60}Co for two different cooling devices. The dashed spectrum corresponds to the case where the germanium crystal has been cooled electromechanically showing a slightly worsening of the energy resolution.

can see that the use of the X-Cooler as a cooling option seems to be nevertheless acceptable. Further information about temperature effects and their impact on the spectroscopy properties as well as the performance of the detector and the X-Cooler assembly is in progress. In addition, activities concerning the use of digital electronics to evaluate pile-up effects, and radiation damages in a high flux hadronic environment are also under preparation [10].

References

[1] A.K.Kerman and M.S. Weiss, Phys. Rev. C 8, **408** (1973).

[2] A.S. Botvina and J. Pochodzalla, Phys. Rev. **C 76**, 024909 (2007)

[3] The STAR Collaboration, Science 328, 58-62 (2010).

[4] `http://www-panda.gsi.de/db/papersDB/PC19-050217\_panda\_tpr.pdf`

[5] A. Sanchez Lorente, A. Botvina, J. Pochodzalla, Phys. Lett. **B 697** (2011) 222-228.

[6] Physics Performance Report for PANDA: Strong Interaction Studies with Antiprotons, `arXiv:0903.3905v1`.

[7] A. Sanchez Lorente *et al.*, Nucl. Inst. Meth A **573**, 410 (2007).

[8] ORTEC. X-Cooler$^{\mathbf{TM}}$ II- Mechanical Cooler for HPGe detectors user manual.

[9] M. Wolf, J. Kojouharova, I. Kojouharov et al. Proceedings COMSOL Users Conference, Gronble, 2007.

[10] M. Steinen, Master Thesis, under preparation.

[11] S. Bleser, PhD.Thesis, under preparation.

[12] J. M. Heuser *et al*. HadronPhysics2, `\http://hadronphysics2.eu`, work package 26, ULISI

[13] Th. Würschig, L. Ackermann, F. Krüger, R. Schnell, H.-G. Zaunick, Panda-MVD - note 005, `http://panda-wiki.gsi.de/pub/Mvd/MvdPublic/PandaMVDnote-005.pdf`, April (2010)

Cosmic ray induced micro black hole showers

M.V. Garzelli, M. O'Loughlin and S. Nafooshe
University of Nova Gorica, Laboratory for Astroparticle Physics, SI-5000 Nova Gorica, Slovenia

Abstract
Extended air showers originate from interactions between ultra-high-energy cosmic rays and nuclei in the Earth's atmosphere. At present there are some discrepancies between experimental observed properties of these air showers and theoretical predictions obtained by using standard hadronic interaction models for cosmic ray primaries with laboratory energies above 10^5-10^6 TeV. In this contribution, we will present a preliminary discussion of the possibility (in the framework of TeV gravity models) that shower development may begin with the production of a microscopic black hole (MBH) at the moment of the primary collision, which then evaporates and decays, by emitting gravitons and Standard Model quanta. From our preliminary investigations it appears that lepton distributions are more likely to reveal the presence of a MBH than photon distributions.

When making a comparison between coupling constants related to different types of interaction, one finds $G_{grav}/G_{Fermi} \sim 10^{-34}$ so that $G_{grav} << G_{Fermi}$. In terms of the corresponding enegy scales this means that the Planck scale $\Lambda_{Planck} \sim 10^{16}$ TeV, at which gravity becomes strongly coupled and its effects cannot be neglected any more, is far larger than the electroweak (EW) symmetry breaking scale $\Lambda_{EW} \sim 0.25$ TeV. The absence of a clear explanation for a difference of so many orders of magnitude, is a manifestation of the so-called hierarchy problem. A possible solution, dating back to 1998 [1–3], proposes the existence of n extra-dimensions where gravitational interactions can extend (the "bulk"), thus diluting their effect in our 4-dimensional world (the "brane") where the strong and electroweak interactions would be confined. Thus, beside the Λ_{Planck} scale related to the strength of gravitational interactions in our 4-dimensional world, i.e. $\Lambda_4 = \Lambda_{Planck}$, a fundamental gravity scale in D-dimensions ($D = 4 + n$) is introduced which may be as low as $\Lambda_D \sim \Lambda_{EW}$ and possibly also lead to the unification of the fundamental forces. If this would be the case then the effects of gravity would begin to manifest themselves already at this (low) unification energy scale and thus would be within reach of terrestrial accelerator experiments. In particular, one of the most intriguing phenomenological consequences of this scenario would be the possible formation of microscopic black-holes (MBH)'s in collisions between two hadrons with a Center-of-Mass (CM) energy as low as $E_{CM} \sim 5 - 20$ TeV.

This contribution deals with hadronic collisions in a wide interval of energies, ranging from LHC energies ($E_{CM} \sim 10$ TeV) up to the highest cosmic ray energies ($E_{lab} \sim 10^6 - 10^8$ TeV, equivalent to $E_{CM} \sim 40 - 140$ TeV). In this energy range gravitational effects are usually neglected. These energies are higher than those tipically covered by nuclear physics studies[1], however it is possible to establish some parallelism between concepts familiar to nuclear physicists, which determine the evolution of an excited nuclear system formed in the collision between two nuclei at energies of the order of hundreds MeV/nucleon, and concepts that characterize the evolution of a MBH formed by the collision of two hadrons or nuclei at much higher energies as predicted by the Hoop Conjecture [4]: *if in the collision of two hadronic objects a large amount of energy/mass is concentrated in a spatial region that can be surrounded by a hoop with a radius $R < R_{Schwarzschild}$ corresponding to a Schwarzschild black hole of that energy, then a MBH is formed*.

Although the hoop conjecture provides some basic necessary conditions for the formation of a MBH in collisions, the actual formation process and the initial phase of its evolution is a very complex

[1] as those discussed in many contributions to this Conference

non-linear phenomenon, subject to many uncertainties, evolving from an asymmetric configuration out of thermal equilibrium, to a highly symmetric static configuration with a well-defined Hawking temperature. Numerical Monte Carlo simulations may be the best way to model this type of process. The same happens when describing the formation of an excited nuclear system from the collision of two nuclei. In both cases the key parameters determining the evolution of the system are E_{CM} and the total angular momentum J, related to the impact parameter b between the initial colliding objects.

At the end of the dynamical phase, it is commonly believed that the MBH undergoes a Hawking evaporation phase during which its temperature evolves following the law $T \propto k/M_{MBH}$, and this can be described by statistical/thermodynamical models together with corrections to the trajectory of the emitted particles as a consequence of the curved geometry through which they subsequently propagate via the so-called grey-body factors. Analogously, the evaporation of nucleons by excited nuclei at the end of the pre-equilibrium phase is commonly described by statistical methods.

In particular the dynamical + statistical MBH evolution is commonly divided in four sequential phases (for a more detailed discussion see e.g. Ref [5] and references therein):

- *Balding phase*: the MBH just formed, initially characterized by a deformed shape,"loses its hairs" (i.e. the higher angular momentum powers), by emitting charge, energy and angular momentum in the form of gravitational radiation and gauge fields, becoming more symmetric (elliptical) in the process.
- *Spin-down phase*: the now stationary rotating MBH continues to gradually lose its energy/mass $(60 - 80\%)$ and angular momentum, until it reaches a non-rotating static (spherical) configuration.
- *Schwarzschild/Evaporation phase*: the MBH loses its mass by emitting all possible particle degrees of freedom (Standard Model particles: quarks, leptons, photons, W, Z, gluons + gravitons, and, if they exist, other heavy particles beyond the SM). At this stage, the emission is assumed to be democratic: each degree of freedom is equally weighted, i.e. has the same probability of being emitted (thus colored particles are favoured with respect to the uncolored ones, high spin particles are favoured with respect to scalar ones, etc....). Furthermore, the emission is assumed to follow an adiabatic evolution: a homogeneous MBH temperature can be identified and slowly increases during the major part of the process of isotropic radiation.
- *Planck phase*: in the final stages of evaporation when $M_{MBH} \sim M_D$, the semi-classical and adiabatic approximation of General Relativity (which justifies a thermodynamical evolution of the evaporation process) breaks down and Quantum Gravity (QG) effects becomes much more important in defining the ultimate MBH fate. The possibilities range from a final remnant, an explosive break-up, or a complete evaporation, with each hypothesis still under discussion. In particular, the role of discontinuous emissions with backreaction in this context must still be investigated.

Each of the phases described above is subject to uncertainties. In particular, a better understanding of the balding phase requires dynamical simulations that should also take into account the possible formation of exotic shapes ("saturn"-like configurations) or multiple MBH's immediately following the collision. The democracy of the emissions that characterize the Schwarzschild phase is not present in the earlier phases where the MBH still retains a memory of the way in which it was created (it has hairs). In order to preserve unitarity it has recently been pointed out that democracy should be reached gradually, and that two scales should be introduced, instead of just one, to fully characterize the MBH evolution: in addition to the already mentioned gravitational scale/radius (at which gravitation becomes strong), a second (lower energy/higher distance) scale (e.g. the compactification radius in extra dimension models at which gravity deviations from the Einsteinian regime begin to manifest themselves), characterizes the transition from the non-democratic to the democratic emission regime [6]. Furthermore, the emission of particles during MBH evolution is modified by gravitational effects, related to the curved geometry near the MBH horizon. These modifications are codified in grey-body factors and many results concerning their precise determination have recently appeared in the literature, thanks to increasingly more

sophisticated computations. However, some of the factors are still unknown or very uncertain, like those for graviton emission in extra-dimensions from a rotating MBH. Finally, still unknown QG effects are expected to determine the evolution of the final MBH remnant in the Planck phase. While many works agree on the hypothesis of a complete evaporation, it is still possible that there may remain a finite MBH remnant.

Following progress in theoretical understanding, several numeric event generators have been developed in the last ten years for the simulation of MBH generation and decay, in particular `Groke` [8] in the framework of cosmic ray studies, and `Charybdis` [9], `Catfish` [10], `BlackMax` [11,12] and `QBH` [13] in the framework of LHC physics.

The heavy particles (top quarks, Higgs and EW bosons, etc.) emitted by MBH evaporation decay quickly, i.e. before entering the detectors, and the partons and charged leptons emitted both by MBH evaporation and by these decays are further subject to parton and photon shower emissions, degrading their energy down to a scale where perturbative QCD can not be applied anymore, and hadronization takes place, followed by hadron decays. Non-perturbative effects in this context are described by means of phenomenological models. This same chain of processes also occurs in p-p collisions in the framework of the SM and the corresponding physics and model parameters have been constrained over the years by results obtained at accelerators. In particular, shower Monte Carlo (SMC) programs like `PYTHIA`, `HERWIG` and `SHERPA` are commonly used to describe these processes [14]. The largest uncertainties in this framework concern the complications that may arise when considering beams with a nuclear structure (as for instance in p-A and A-A collisions) and the propagation of the MBH decay products in a medium instead of the vacuum [2].

Searches for MBH's have been conducted by the CMS and ATLAS experimental collaborations at LHC in the framework of the more general "searches for exotica". The analyses conducted so far [15–18] have not lead to any evidence for MBH formation in p-p collisions at E_{CM} = 7 TeV. However, these analyses have been criticized, since QG effects, expected to be important at LHC energies, have been neglected or treated too naively in the event generators used. Very recently, some theoretical work has also appeared in the literature pointing out, on the basis of other arguments like the generalized uncertainty principle or the extrapolation of the results of numerical simulation of colliding self-gravitating fluid objects, that the present LHC energy is in any case too low for the formation of MBH's [7,19]. However, the situation is globally still controversial, and the exclusion at the present LHC energy certainly does not limit the possible formation of MBH's at higher energies.

In this contribution we investigate the behaviour of event generators, usually adopted (and adapted) at LHC energies, at higher energies such as those reachable in the interactions of ultra-high-energy cosmic rays with the Earth's atmosphere, leading to extended air showers (EAS). In particular, we work with the last version of `BlackMax` (2.02.0), both in the standalone mode, and interfaced to the `PYTHIA` SMC code [20]. We perform simulations of the formation of non-rotating MBH's in p-p collisions in the 14 TeV $< E_{CM} <$ 100 TeV energy range, two different values for the fundamental gravity mass scale, i.e. $M_D = 4$ and 15 TeV, a MBH mass constrained in the range 2 $M_D < M_{MBH} < E_{CM}$, and $n = 2$ spatial extra dimensions without fermion splitting. In the simulation of MBH evolution, the mass, linear and angular momentum loss fractions were assumed to be equal to 0.3, whereas angular momentum, charge and color suppression factors were assumed to be equal to 0.2, and baryon and lepton numbers, as well as their difference, conserved. With these settings we investigated the kinematical properties of particles emitted during the MBH evolution as computed by `BlackMax` and also after the Parton Shower + Hadronization + Hadron decay chain, as computed by the interface of `BlackMax` with `PYTHIA`. Examples of selected results are presented in Figs.1, 2, 3 and 4.

In Fig.1.a and 1.b the longitudinal and transverse momentum distributions (expressed in terms of number of particles/bin/event) are shown for different SM particle species for the case of MBH produc-

[2] Actually, in case of p-p collisions medium effects reduces to the so-called "underlying event" effect, that is already one of the sources of the largest uncertainties in SMC simulations.

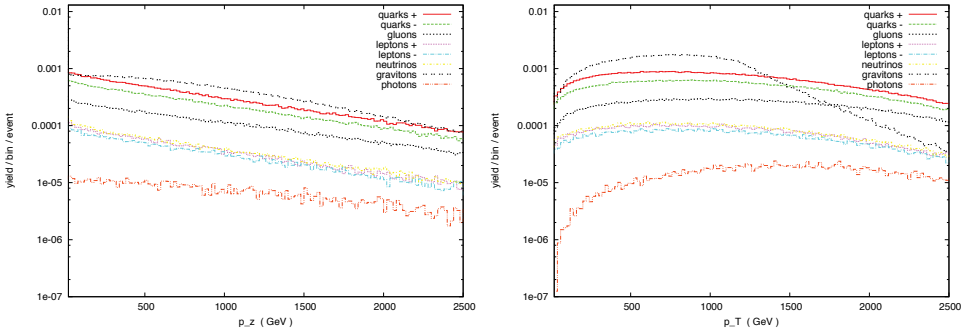

Fig. 1: Parallel ($left$) and transverse ($right$) momentum distributions for different SM degrees of freedom (quarks and antiquarks with positive charge, quarks and antiquarks with negative charge, gluons, positively charged leptons, negatively charged leptons, neutrinos, photons) and gravitons as computed by `BlackMax` for a MBH formed at a CM p-p collision energy E_{CM} = 50 TeV for M_D = 4 TeV. See text for more detail.

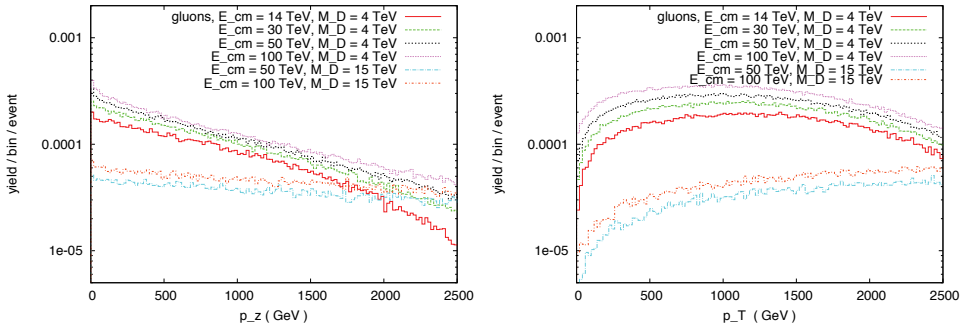

Fig. 2: Gluon parallel and transverse momentum distributions as computed by `BlackMax` for a MBH formed at four different CM p-p collision energies (E_{CM} = 14, 28, 50, 100 TeV) for M_D = 4 TeV and at two different CM energies (E_{CM} = 50, 100 TeV) for M_D = 15 TeV. See text for more detail.

tion at $E_{CM} = 50$ TeV. After evaporation of the MBH the (anti-)quarks give rise to the largest contributions followed by gluons, (anti-)leptons and photons. Contributions from particles with opposite charges are shown separately: for any given flavour the contribution of positively charged particles is larger than that coming from negatively charged particles, probably due to the fact that during the final burst in the MBH evolution (`BlackMax` implements the hypothesis of complete evaporation), positive charged particles are predominantly emitted, because the majority of MBH's are positively charged (see also Ref. [12] for similar conclusions in a lower energy p-p study). The p_z distributions are almost monotonically decreasing with similar slopes for all SM particles, whereas the p_T distributions show some broad peaks, located at different p_T values according to the particle species. (Anti-)leptons are emitted in pairs, i.e. as $\ell\nu_\ell$, $\ell^+\ell^-$ or $\nu_\ell\bar{\nu}_\ell$, due to imposed lepton number conservation. Graviton distributions are also shown, and display a high p_T profile with a slope that decreases more rapidly than do those for SM particles, leading to a suppression of gravitons with respect to SM degrees of freedom at high p_T.

In Fig.2.a and Fig.2.b, the p_z and p_T distributions of a specific particle species, i.e. the gluon in this example, are shown as a function of the p-p collision E_{CM} (leading to the formation of a MBH), for different values of M_D. It is evident that, for a fixed value of M_D, the shape of the distributions at

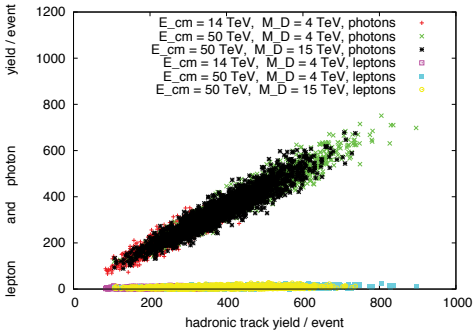

Fig. 3: Photon (upper part) and all lepton (lower part) yields as a function of the yield of all hadronic tracks after `BlackMax + PYTHIA`. Each point correspond to a different simulated event. Regions with different colors correspond to different E_{CM} and M_D parameters adopted in the MBH simulation, as labelled in the figure. See text for more detail.

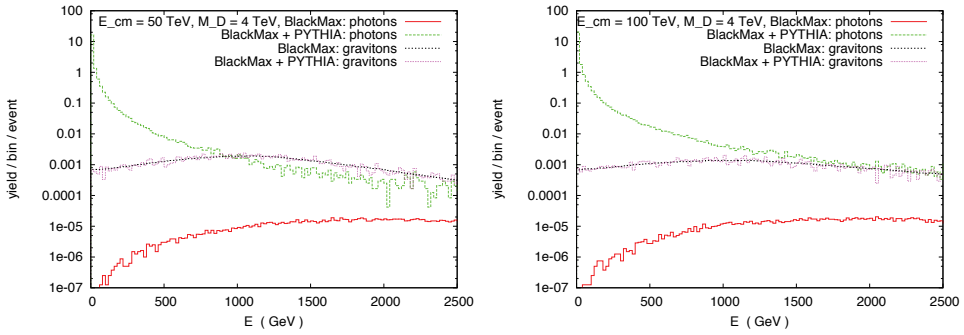

Fig. 4: Energy distributions of photons and gravitons emitted by a MBH at a CM p-p collision energy E_{CM} = 50 TeV (*left*) and E_{CM} = 100 TeV (*right*), for M_D = 4 TeV. Results after both `BlackMax` and `BlackMax + PYTHIA` are presented in each panel for comparison. See text for more detail.

different E_{CM}'s is preserved with the total number of gluons increasing with E_{CM}. This is as expected because the cross-section for MBH formation increases with E_{CM}. On the other hand, changing the value of M_D leads to distributions with different shapes in addition to a changing value of the total cross-section. In particular, the position of the p_T maximum for gluon emission increases with M_D, ranging from $p_T \sim 1.1$ TeV for $M_D = 4$ TeV to $p_T \sim 4.3$ TeV for $M_D = 15$ TeV.

The SM yields from MBH evaporation are in general modified after parton and photon shower + hadronization + hadron decay, as simulated by SMC codes, such as `PYTHIA`, which leads to hundreds of hadrons and photons. In particular, the number of emitted photons in each event turns out to be correlated to the number of emitted hadronic tracks, with a constant slope at increasing E_{CM}, as shown in Fig.3. This slope is also independent of M_D, at a fixed E_{CM}. On the other hand, the total yield of emitted leptons turns out to be small (a few tens of particles) and does not show evident correlations with the number of hadronic tracks. This points towards the conclusion that the large number of photons is probably due light hadron (in particular π^0) decays, whereas electromagnetic shower effects are suppressed.

It is also interesting to compare the shapes of particle spectra at different stages of the evolution of the entire system. In particular this can be carried out for distributions of particles that are not subject

to hadronization, such as leptons, photons and gravitons. In Fig.4.a and 4.b the energy distributions of photons and gravitons at the parton level after MBH evaporation and at the hadron level after PYTHIA are shown, for two different E_{CM} energies. It is evident that the contributions of the parton shower, the hadronization and hadron decay lead to a complete distorsion of the original photon spectrum, disproportionately populating the region of low energies with photons emitted in these last processes. The photon distributions at the evaporation level are very similar for both $E_{CM} = 50$ and 100 TeV, whereas, at the hadron level, the photon distribution at $E_{CM} = 100$ TeV is clearly much more populated than the corresponding one for $E_{CM} = 50$ TeV due to the stronger SMC effects. On the other hand, the graviton distributions are completely unaffected by shower effects, and in the case of $E_{CM} = 100$ TeV display a flatter profile in comparison to that at $E_{CM} = 50$ TeV.

In conclusion, we have provided some examples of theoretical simulations demonstrating how parton shower + hadronization + hadron decay effects may dramatically modify particle distributions after MBH evaporation, especially in the case of some SM quanta, such as photons. This is certainly a challenge that must be confronted when trying to distinguish the effects of different MBH models, potentially observable through MBH formation, evaporation and decay in high-energy and ultra-high-energy collisions, such as those explored at LHC and in cosmic ray experiments. From our preliminary investigations it appears that lepton distributions are less affected than photon ones and should thus be preferred for these MBH studies.

References

[1] N. Arkani-Hamed, S. Dimopoulos and G.R. Dvali, *Phys. Lett. B* **429** (1998) 263, [arXiv:hep-ph/9803315].

[2] I. Antoniadis, N. Arkani-Hamed, S. Dimopoulos and G.R. Dvali, *Phys. Lett. B* **436** (1998) 257, [arXiv:hep-ph/9804398].

[3] L. Randall and R. Sundrum, *Phys. Rev. Lett.* **83** (1999) 3370, [arXiv:hep-ph/9905221].

[4] K. Thorne, Nonspherical gravitational collapse: A short review. In J. Klauder, editor, Magic Without Magic: John Archibald Wheeler, page 231. Freeman, San Francisco, 1972.

[5] S.C. Park, *Progress in Particle and Nuclear Physics* **67** (2012) 617, [arXiv:1203.4683].

[6] G. Dvali and O. Pujolas, *Phys. Rev. D* **79** (2009) 064032, [arXiv:0812.3442].

[7] A.F. Ali, *JHEP* **09** (2012) 067, [arXiv:1208.6584].

[8] E-J. Ahn and M. Cavaglia, *Phys. Rev. D* **73** (2006) 042002, [arXiv:hep-ph/0511159].

[9] C.M. Harris, P. Richardson and B.R. Webber, *JHEP* **08** (2003) 033, [arXiv:hep-ph/0307305].

[10] M. Cavaglià, R. Godand, L. Cremaldi, D. Summers, *Comput. Phys. Commun.* **177** (2007) 506, [arXiv:hep-ph/0609001].

[11] J.A. Frost, J.R. Gaunt, M.O.P. Sampaio, M. Casals, S.R. Dolan, M.A. Parker and B.R. Webber, *JHEP* **10** (2009) 014, [arXiv:hep-ph/0904.0979].

[12] D.C. Dai, G. Starkman, D. Stojkovic, C. Issever, E. Rizvi and J. Tseng, *Phys .Rev. D* **77** (2008) 076007, [arXiv:hep-ph/0711.3012].

[13] D.M. Gingrich, *Comput. Phys. Comm.* **181** (2010) 1917, [arXiv:hep-ph/0911.5370].

[14] A. Buckley, J. Butterworth, S. Gieseke *et al.*, *Phys. Rept.* **504** (2011) 145, [arXiv:1101.2599].

[15] CMS Collaboration, CMS-EXO-10-017, *Phys. Lett. B* **697** (2011) 434, [arXiv:1012.3375].

[16] CMS Collaboration, CMS-EXO-11-071, *JHEP* **04** (2012) 061, [arXiv:1202.6396].

[17] ATLAS Collaboration, *Phys.Lett. B* **716** (2012) 122, [arXiv:1204.4646].

[18] CMS Collaboration, CMS-EXO-11-059, *JHEP* **1209** (2012) 094, [arXiv:1206.5663].

[19] L. Rezzolla and K. Takami, [arXiv:1209.6138].

[20] T. Sjostrand, S. Mrenna, P. Skands, *JHEP* **0605** (2006) 026, [arXiv:hep-ph/0603175].

IL NUCLEARE

1. Ettore Gadioli
   Energia nucleare e effetti biologici delle radiazioni
   ISBN 88-548-4004-1, formato 17x24 cm, 344 pagine, 25 euro

2. Giorgio Bendiscioli, Alberto Panzarasa
   La datazione con il radiocarbonio
   ISBN 978-88-548-5134-4, formato 17x24 cm, 144 pagine, 10 euro

3. Francesco Cerutti, Mark Chadwick, Alfredo Ferrari, and Toshihiko Kawano, with Simone Bottoni and Luna Pellegri
   Proceedings of the 13th International Conference on Nuclear Reaction Mechanisms
   ISBN 978-88-548-5882-4, formato 17x24 cm, 564 pagine, 40 euro

Compilato il 19 marzo 2013, ore 06:21
con il sistema tipografico LaTeX 2_ϵ

Finito di stampare nel mese di marzo del 2013
dalla «ERMES. Servizi Editoriali Integrati S.r.l.»
00040 Ariccia (RM) – via Quarto Negroni, 15
per conto della «Aracne editrice S.r.l.» di Roma